THE PHYSICAL REVIEW

VOLUME 95 Second Series NUMBER 6

SEPTEMBER 15, 1954

Published for the

AMERICAN PHYSICAL SOCIETY

by the

AMERICAN INSTITUTE OF PHYSICS

LANCASTER, PA. AND NEW YORK, N. Y.

THE
PHYSICAL REVIEW

A journal of experimental and theoretical physics established by E. L. Nichols in 1893

SECOND SERIES, VOL. 95, NO. 6 SEPTEMBER 15, 1954

Film Flow and Bulk Formation of Helium II in Capillaries*

R. V. DYBA,† C. T. LANE, AND C. H. BLAKEWOOD
Sloane Physics Laboratory, Yale University, New Haven, Connecticut
(Received June 7, 1954)

The formation and maintenance of bulk liquid in capillaries caused by the mobile film flowing from a liquid helium II bath below the capillaries has been observed. Experiments with parallel plates, cylindrical capillaries, and annular capillaries indicate that bulk will form initially only when the width of the capillary space is below some critical value, depending on the geometry. However, bulk liquid once present in a capillary will be maintained by the film even if the width is greater than the critical value for initial formation. Measurements of film flow rates and equilibrium capillary rise in these capillaries give values in agreement with measurements of these quantities, under other experimental conditions, made by various other observers. The effects observed are discussed in terms of the known properties of liquid helium II.

INTRODUCTION

THE principal flow properties of the mobile helium film have been established by extensive investigation over the past fifteen years. The mass rate of flow of the film between two baths of bulk helium II has been found to be directly proportional to the smallest perimeter crossed by the film above the upper level of the bulk liquid; it has also been found to be independent of either the gravitational potential gradient or the temperature gradient driving it, except under certain very special conditions. Such flow at a constant rate, independent of the driving force, indicates the absence of frictional forces in the fluid for velocities of flow up to a certain critical velocity corresponding to the velocity at the perimeter controlling the mass rate of flow. Atkins[1] has shown that this film behavior can be regarded as a limiting case of the flow of helium II in narrow channels, in which there is a critical velocity for frictionless flow which increases as the channel width is decreased, and where flow subject to frictional retardation tends to become vanishingly small as the channel width is decreased. In the case of the film, the thickness of the film ($\sim 10^{-6}$ cm) corresponds to the channel width.

It has been observed that when the perimeter crossed by the film at some point below the upper bulk level is made smaller than the controlling perimeter, the film retains its equilibrium thickness (which is a function of the height above the level, and possibly of the nature of the substrate), and the excess flow is converted into droplets of bulk liquid. According to Jackson and his co-workers[2,3] these droplets are several tenths of a millimeter in diameter and move with a velocity of about one cm/sec, considerably below the critical velocity of the film, which is of the order of 20 cm/sec. The appearance of such droplets is consistent with a reduced critical velocity and with the appearance of some frictional flow associated with a substantial increase of channel width.

EXPERIMENTS WITH CAPILLARIES

We have recently performed some experiments with capillaries held vertically above an evaporating bath of helium II and connected to it by a surface over which the mobile film can flow. We have found that, under appropriate conditions, the film can form bulk liquid in such capillaries and a report based on preliminary experiments with a pair of parallel plates was published earlier.[4] We have now varied the experimental conditions and we have also verified that the flow rate of the film, and the capillary rise of liquid helium, in

* Assisted by the U. S. Office of Naval Research.
† This paper is based in part on a dissertation presented by R. V. Dyba for the degree of Doctor of Philosophy at Yale University.
[1] K. R. Atkins, Proc, Roy. Soc. (London) **A203**, 241 (1950).
[2] L. C. Jackson and D. G. Henshaw, Phil. Mag. **41**, 1081 (1950); **44**, 14 (1953).
[3] A. C. Ham and L. C. Jackson, Phil. Mag. **44**, 214 (1953).
[4] C. T. Lane and R. V. Dyba, Phys. Rev. **92**, 829 (1953).

capillaries of the dimensions used here, are in agreement with values obtained from measurements made under other conditions.

The various capillaries were suspended vertically just above the level of the liquid helium bath. They were attached with special holders to the bottom of a stainless steel tube that passed through an O-ring seal in the Dewar cap; the vertical position of the capillaries was adjusted by moving this tube up and down. The holders were designed to present to the film a constricted periphery so there would not be a large film flow up the stainless steel tube. A low-power fluorescent light with heat-absorbing glass filters provided illumination for viewing of the bath level and the meniscus in the capillary through a cathetometer telescope. Measurements of the height of the two levels were usually taken as a function of time as the bath level dropped by evaporation.

I. Parallel Plates

In our preliminary report,[4] we described the results of experiments with parallel plates having a 36-micron spacing, and with one plate extending below the other.[5] A similar pair of plates with 47 micron spacing was also used. The behavior of each was found to be essentially the same. That is, a meniscus appeared in the capillary space when the lower plate was immersed in the liquid even though the bath level was below the bottom of the capillary gap. The meniscus rose rapidly to an equilibrium height above the bath, equal to the ordinary surface tension rise, as confirmed when the plates were immersed further such that the bath level was above the bottom of the gap. Then, as the bath level dropped by evaporation, the meniscus remained at this same height above the bath level, until the meniscus reached the bottom of the capillary space.

However, with a pair of similar plates with a gap of about 90 microns the meniscus did not form until the bath level was brought into contact with the bottom of the capillary space. Only then was there a rapid rise to the equilibrium height. But again, when the bath level dropped by evaporation, the meniscus maintained this equilibrium height above the bath level.

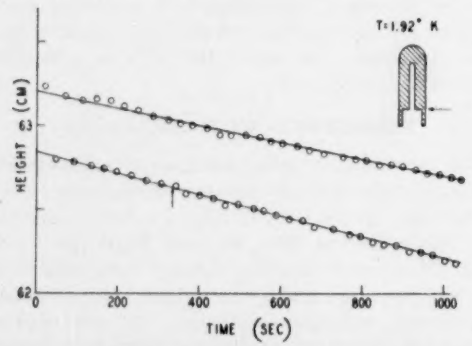

FIG. 1. The height of the meniscus and bath (lower curve) as a function of time for a circular capillary 226 microns in diameter. The arrow indicates the point at which the evaporating bath just reaches the bottom of the capillary. Temperature 1.92°K.

[5] The statement in reference 4 about the effect in spaces of 75 microns width is incorrect to the extent indicated by the details of the experiment described here.

II. Cylindrical Capillaries

A cylindrical capillary was constructed by joining a Pyrex tube with a 226-micron bore to another Pyrex tube with a 1.15-mm bore without distortion at the joint. The end of the narrow bore was sealed off.

When the open end of the wide bore was dipped into helium II, the meniscus appeared in the narrow bore although the liquid level was below the bottom of the latter. The meniscus rose in a few seconds to a height corresponding to the equilibrium capillary rise, as determined by immersing the narrow bore in the bath. After such an immersion, the heights of the meniscus in the capillary and of the bath level were measured as a function of time while the bath level dropped by evaporation. A typical plot of the data is shown in Fig. 1. The meniscus remained at the same height above the bath level even after the latter had dropped

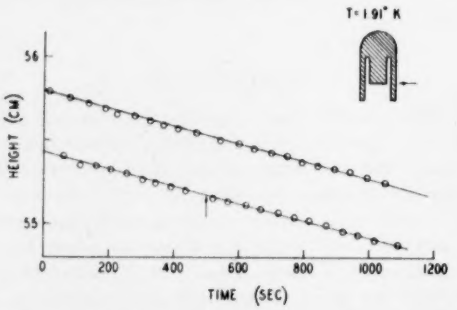

FIG. 2. The height of the meniscus and bath (lower curve) as a function of time for an annular capillary 100 microns wide. The arrow indicates the point at which the evaporating bath just reaches the bottom of the annular space. Temperature 1.91°K.

below the capillary region, and the same relative position of the meniscus and bath level was maintained until the meniscus reached the bottom of the capillary. The measurements were repeated at several different temperatures, and the equilibrium height was consistent with that calculated from the known surface tension.

A similar capillary using a 1-mm bore for the capillary space and a 2-mm bore for the lower tube was also tested. However, the small capillary rise of liquid helium in a 1-mm tube (order of 0.5 mm) made it impossible to determine whether the effects observed with the 226-micron bore were present or not.

III. Annular Capillaries

The desirability of performing the experiments with a geometry equivalent to that of the parallel plates,

yet with the top of the capillary space sealed so that the paths available to the film could be controlled, led to experiments with annular capillaries. Several such capillaries were made from Pyrex rods centrally aligned in Pyrex true-bore tubing of slightly larger diameter; the annular gaps were of the order of 100 microns and less in width, while the over-all diameter of the tubes was about 6 mm. The upper end of these capillaries was sealed off and because the gap width was so small compared to the radius, these annular capillaries corresponded essentially to parallel plates sealed off at the top. A sketch of one of these devices is shown in Fig. 2.

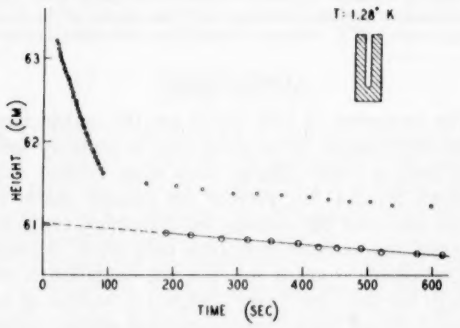

FIG. 3. An "emptying" process for a 185-micron circular capillary beaker. The bath level (lower curve, large circles) was, at all times, in contact with the outside of the beaker. Temperature 1.28°K.

In the first such capillary, with a gap width of about 100 microns, the outer tube was longer than the inner rod; therefore, the inner surface of the tube provided the path for film flow from the liquid helium bath to the annular gap. When the outer tube was immersed in the bath, no meniscus appeared in the annular gap until the bottom of the gap was in actual contact with bulk liquid. However, after the annular space was immersed, a meniscus appeared due to ordinary surface tension rise. Then alternate readings of meniscus and bath level were taken as the latter dropped by evaporation. A typical result is shown in Fig. 2. The meniscus remained at the equilibrium surface tension height above the bath even when the latter dropped below the bottom of the capillary bore, until the meniscus reached the bottom of the bore.

In the second annular capillary, the inner rod was longer than the outer tube; therefore the surface of the rod, instead of the inner surface of the tube, now provided the path for film flow from the bath to the annular space which was again about 100 microns wide. However, the behavior of the meniscus was essentially the same as in the first annular capillary.

In the third annular capillary, rod and tube were of the same length, but 1 cm of the lower end of the rod was reduced in diameter so the lower annular space was 1 mm wide, the capillary gap being about 75

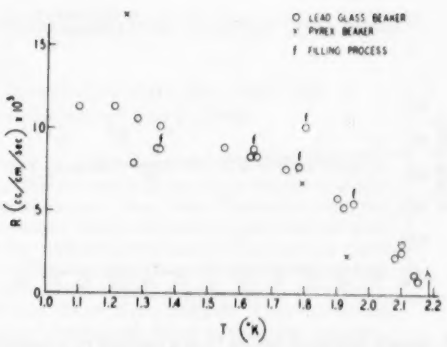

FIG. 4. The film transfer rate (R) as a function of temperature deduced from the capillary beaker experiments.

microns. In this case, therefore, the film could flow over both the surface of the rod and the inner surface of the tube from the bath to the annular capillary space. However, again the behavior of the meniscus was the same as in the other two arrangements.

From these experiments on annular capillaries it was concluded that the particular path available for the film had no effect on whether or not bulk formed in the annular capillary space.

The fourth annular capillary was similar to the first, except that the gap width was reduced to approximately 50 microns. When the outer tube was immersed in the bath, a meniscus appeared in the capillary space even though the bath level was below the bottom of this space. When the bath dropped by evaporation after the capillary was immersed, the meniscus remained at the surface tension equilibrium height above the bath level as in all the other cases.

From the experiments with the annular capillaries and the parallel plates, there therefore appears to be a critical spacing for the formation of bulk liquid from the film. For these geometries, it appears to be between 50 and 100 microns.

IV. Capillary Beaker Experiments

Since measurements of film flow rates have been made in the past using beakers with larger internal diameters than those of the capillaries in the preceding experiments, it was thought advisable to verify that the flow of the film was not significantly different in such capillaries. Consequently, flow rates were determined in a lead glass beaker with a 184-micron bore and a Pyrex beaker with a 185-micron bore, by the usual technique of measuring the rate of rise or fall of the liquid level in the beaker as the latter fills or empties by film flow. It was observed that, in general, a beaker raised partly clear of the bath after filling emptied only until the level in the beaker was at a height corresponding to the equilibrium surface tension rise above the bath level;[6] a similar effect was

[6] The same effect occurred for a "filling" process.

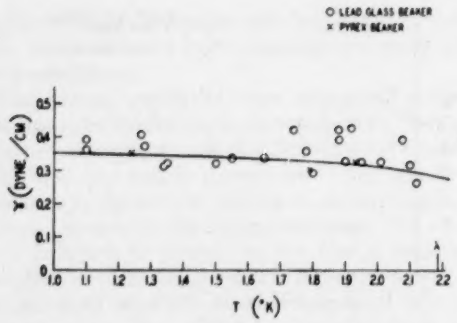

FIG. 5. Surface tension of helium II as a function of temperature. The solid curve represents smoothed values given by reference 9.

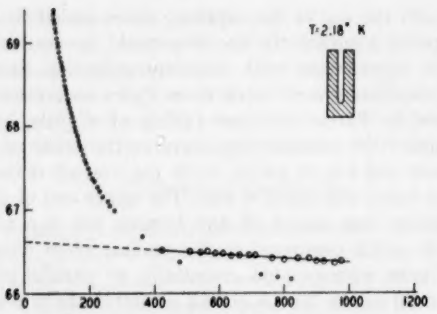

FIG. 6. An emptying process, very close to the λ point, for a 185-micron circular capillary beaker. The bath level (large circles) was, at all times, in contact with the outside of the beaker. Temperature 2.18°K. Ordinate: height in cm. Abscissa: time in sec.

observed by Atkins[7] in his determination of film thickness from the oscillations of the liquid level about its equilibrium position. A typical emptying curve is shown in Fig. 3. The deduced flow rates (in cm³/sec cm periphery) are shown as a function of temperature in Fig. 4; they are in fair agreement with the published results of Mendelssohn[8] and others for beakers with larger internal diameters. Surface tension as a function of temperature and calculated from the equilibrium heights is shown in Fig. 5 and compared with the smoothed data of Allen and Misener;[9] the agreement is satisfactory within the estimated error of about 10 percent.

Above about 2.15°K the meniscus (indicating the level in the beaker) did not remain at the expected equilibrium height above the bath but instead continued to drop below it; a typical run of this type is shown in Fig. 6. The rate of evaporation would not be expected to change much with small changes in temperature just below the λ point at which temperature the flow rate rapidly approaches zero. Hence, above 2.15°K the film flow cannot compensate for the loss of liquid from the beaker by evaporation. At the somewhat lower temperature where the equilibrium height is maintained (e.g., at 1.28°K, Fig. 3) the film flow must therefore have reversed direction, when this equilibrium height was reached, to compensate for evaporation. In the case of capillary rise, in general, the meniscus and the bath level must be at the same gravitational potential once the equilibrium rise is attained. This is true also for the special case presented by these capillary beakers; here the mobile film connects two liquid surfaces at the same potential. Normal evaporation of the meniscus will tend to lower the potential here as compared to that of the bath. Hence, the film reversal strongly suggests that the mobile film, in beaker experiments in general, is driven by a gravitational potential difference only.

[7] K. R. Atkins, Proc. Roy. Soc. (London) **A203**, 119 (1950).
[8] K. Mendelssohn and G. K. White, Proc. Phys. Soc. (London) **A63**, 1328 (1950).
[9] J. F. Allen and A. D. Misener, Proc. Cambridge Phil. Soc. **34**, 299 (1938).

CONCLUSIONS

The formation of bulk liquid via the mobile film,in these experiments, takes place only in capillary spaces that have a width smaller than some critical value, between 50 and 100 microns for parallel plates and annuli and over 200 microns for cylindrical capillaries. However, as we have seen, once bulk liquid is present in any capillary space the film will maintain it even though the bath level drops below the bottom of such a space. If one takes into account the surface tension, this latter effect is simply an example of the fact that the film connecting two quantities of bulk liquid flows until each is at the same gravitational potential, whence the film flow ceases. The only problem that remains, therefore, is to account for the initial formation of bulk liquid in the capillaries in those cases where this occurs.

Our capillary beaker experiments indicate that the film flow rate and the equilibrium height of the bulk liquid in such capillaries are, in general, consistent with the corresponding properties of liquid helium II under other conditions. One might expect the formation of bulk liquid in the capillary to be associated with some excess film flow, as in the other known cases of bulk formation from the film. (See reference 2.) In the cylindrical capillary, the formation of an initial droplet of bulk liquid covering the bottom of the gap could possibly be accounted for by the initial excess flow caused by the contraction of the periphery at the bottom of the capillary bore (see the reverse case in reference 2). This explanation, however, cannot hold in the cases of either the parallel plates or the annular capillaries since here no abrupt change in periphery takes place at the bottom of the capillary gap. Hence, the way in which bulk liquid is formed from the film in these capillaries remains unclear.

We wish to thank H. N. V. Temperley for first suggesting to us the possibility of a critical spacing with regard to the formation of bulk liquid from the film. We are also indebted to R. G. Wheeler for valuable assistance with the experiments.

Electrostatic Energy Calculations for Sodium Tungsten Bronze (Na_xWO_3)*

J. F. SMITH
Institute for Atomic Research and Department of Chemistry, Iowa State College, Ames, Iowa
(Received March 5, 1954; revised manuscript received June 11, 1954)

Recent measurements of the activation energy for diffusion of sodium in the metallic sodium tungsten bronze, $Na_{0.78}WO_3$, gave a value of 51.8 kcal/mole. To determine whether ionic bonding could be responsible for this high activation energy, electrostatic energy calculations have been made. Calculated activation energies for sodium diffusion using a model with random sodium distribution do not agree well with the measured value, but this discrepancy may be because of the consideration of ions as point charges which must be a poor approximation at small interionic distances. Further calculations of the total electrostatic energy as a function of sodium concentration have been made on the basis of random sodium distribution, point charges of Na^+, W^{+6}, and O^{-2}, and a uniform neutralizing charge of free electrons. These calculations indicate that cubic sodium tungsten bronze should be unstable or metastable below $x=0.35$. This calculated value of sodium concentration is in good agreement with the known phase transition occurring at a sodium concentration between $x=0.30$ and $x=0.38$.

INTRODUCTION

NONSTOICHIOMETRIC sodium metatungstate, Na_xWO_3, is known as sodium tungsten bronze. The range of sodium concentration x is limited to the region $0<x<1$. Presumably the metallic luster[1,2] at higher sodium concentration ($x>0.5$) is responsible for the appendage of the term "bronze" to this material.

The measured activation energy[3] for the diffusion of sodium in the sodium tungsten bronze, $Na_{0.78}WO_3$, is 51.8 kcal/mole. This measured value for the activation energy was considerably higher than expected. As a possible explanation Rundle[4] suggested that, since higher interaction energies were more typical of ionic compounds, the interaction forces in sodium tungsten bronze might be primarily electrostatic. To check this possibility the calculation of the electrostatic activation energy for the diffusion of sodium in sodium tungsten bronze was undertaken. Additional calculations of the total electrostatic energy as a function of sodium concentration in both the cubic structure and in an assumed tetragonal structure were made. These latter calculations were made in order to determine whether electrostatic forces would predict a phase transition[5] such as is known to occur in sodium tungsten bronze at lower sodium concentration ($x\approx0.3$).

BASIC ASSUMPTIONS AND METHODS OF CALCULATION

Gardner and Danielson[6] have shown by a determination of electrical conductivity and Hall coefficient that each sodium atom present in sodium tungsten bronze contributes one electron to the conduction band. This conclusion is substantiated by magnetic susceptibility measurements made by Kupka and Sienko[7] and by Stubbin and Mellor.[8] The measured values of the susceptibility show that sodium tungsten bronze is weakly paramagnetic, which is consistent with the dissociation of sodium atoms to sodium ions and free electrons. The susceptibility measurements further imply that ionic tungsten should be present as W^{+4} or W^{+6} and not as W^{+5}. A charge of +6 and not +4 was assigned to the tungsten ion in these calculations because the ionic character of tungsten in the solvent matrix WO_3 should be hexavalent, and because the sodium electrons in the conduction band should not affect the tungsten valence. In the calculations the assumed charge distribution was electrically neutral and consisted of a point charge distribution of W^{+6} ions, a point charge distribution of Na^+ ions, a point charge distribution of O^{-2} ions, plus a uniform neutralizing charge distribution of the electrons from the conduction band. It was further assumed that the sodium distribution was random in the sense that the probability of occupancy of any given sodium site in a bronze was proportional to the sodium concentration x.

The method of calculation employed in evaluating the electrostatic interactions in sodium tungsten bronze was based upon the method of Ewald.[9] The possible use of a uniform neutralizing charge is implicit in the Ewald calculation. Consider the charge density $\rho(\mathbf{r})$ as a function of position in a periodic lattice to be expressed as a Fourier series,

$$\rho(\mathbf{r})=\sum_k \rho_k e^{i(\mathbf{q}_k\cdot\mathbf{r})}, \quad (1)$$

where

$$\mathbf{q}_k=2\pi(k_1\mathbf{b}_1+k_2\mathbf{b}_2+k_3\mathbf{b}_3),$$

with k_i representing the Miller indices, $\mathbf{b}_i$, the reciprocal lattice vectors, and $\mathbf{r}$, the position vector. To evaluate

* Contribution No. 327 from the Institute for Atomic Research and Department of Chemistry, Iowa State College, Ames, Iowa. Work was performed in the Ames Laboratory of the U. S. Atomic Energy Commission.

[1] G. Hägg, Nature **135**, 874 (1935).
[2] M. E. Straumanis, J. Am. Chem. Soc. **71**, 679 (1949).
[3] J. F. Smith and G. C. Danielson, J. Chem. Phys. **22**, 266 (1954).
[4] R. E. Rundle, Iowa State College (private communication).
[5] G. Hägg, Z. physik. Chem. **B29**, 192 (1935).
[6] W. Gardner and G. C. Danielson, Phys. Rev. **93**, 46 (1954).
[7] F. Kupka and M. J. Sienko, J. Chem. Phys. **18**, 1296 (1950).
[8] P. M. Stubbin and D. P. Mellor, J. Proc. Roy. Soc. (N. S. Wales) **82**, 225 (1948).
[9] P. P. Ewald, Ann. Physik **64**, 253 (1921).

ρ_k, multiply by the complex conjugate and integrate,

$$\int \rho(\mathbf{r}) e^{-i(\mathbf{q}_{k'}\cdot\mathbf{r})} d\tau_0 = \int \sum_k \rho_k e^{i(\mathbf{q}_k\cdot\mathbf{r}-\mathbf{q}_{k'}\cdot\mathbf{r})} d\tau_0, \quad (2)$$

where $\int d\tau_0 = \Omega_0$, the volume of the unit cell. Then,

$$\begin{aligned} \int \rho(\mathbf{r}) e^{-i(\mathbf{q}_{k'}\cdot\mathbf{r})} d\tau_0 &= \rho_k \Omega_0 \quad \text{for} \quad k = k', \\ &= 0 \quad \text{for} \quad k \neq k'. \end{aligned} \quad (3)$$

This results from the cyclic nature of the charge distribution in a periodic lattice and the fact that the integration is over one complete cycle. Rearranging Eq. (3) gives

$$\rho_k = (1/\Omega_0) \int \rho(\mathbf{r}) e^{-i(\mathbf{q}_k\cdot\mathbf{r})} d\tau_0, \quad (4)$$

with the restriction that

$$\rho_0 = (1/\Omega_0) \int \rho(\mathbf{r}) d\tau_0 = 0, \quad (5)$$

because the charge density over a unit cell must be zero to maintain electrical neutrality.

If one considers a lattice of point charges with the electrical neutrality maintained by a uniform density distribution of opposite charge, one can write

$$\rho(\mathbf{r}) = \sum_i z_i \epsilon \delta(\mathbf{r} - \mathbf{r}_i) + \bar{\rho}, \quad (6)$$

where $z_i\epsilon$ represents the charge on a lattice point as the valence times unit charge, $\delta(\mathbf{r}-\mathbf{r}_i)$ represents the ordinary delta function, and $\bar{\rho}$ is a constant representing the uniform neutralizing charge. Then

$$\rho_k = (1/\Omega_0)\left[\sum_i z_i \epsilon \int \delta(\mathbf{r}-\mathbf{r}_i) e^{-i(\mathbf{q}_k\cdot\mathbf{r})} d\tau_0 + \bar{\rho} \int e^{-i(\mathbf{q}_k\cdot\mathbf{r})} d\tau_0\right]. \quad (7)$$

The second term is zero,

$$\bar{\rho} \int e^{-i(\mathbf{q}_k\cdot\mathbf{r})} d\tau_0 = 0, \quad (8)$$

unless $k=0$, because of the cyclic nature of the integration. Thus for $k \neq 0$ Eq. (7) becomes

$$\begin{aligned} \rho_k &= (1/\Omega_0) \sum_i z_i \epsilon \int \delta(\mathbf{r}-\mathbf{r}_i) e^{-i(\mathbf{q}_k\cdot\mathbf{r})} d\tau_0 \\ &= (1/\Omega_0) \sum_i z_i \epsilon e^{-i(\mathbf{q}_k\cdot\mathbf{r}_i)}. \end{aligned} \quad (9)$$

If $\bar{\rho}$ is chosen equal to $-\sum z_i\epsilon/\Omega_0$, then ρ_0 as calculated from Eq. (7) will vanish in accord with Eq. (5). Thus, the uniform neutralizing charge $\bar{\rho}$ contributes nothing to the coefficients ρ_k in the Fourier expression of the charge distribution.

This Fourier expression of the charge distribution $\rho(\mathbf{r})$ may be substituted in the Poisson equation, and the regular procedure of the Ewald method[10] may be employed to calculate an electrostatic potential at any point. The resulting equations for calculating the potential for a cubic structure are

$$\phi = \phi_1 + \phi_2, \quad (10)$$

where for a general point

$$\phi_1 = (1/\pi a) \sum_k{}' \frac{S_k \exp(-\pi^2/\eta^2)(k_1^2+k_2^2+k_3^2)}{k_1^2+k_2^2+k_3^2}, \quad (11a)$$

and

$$\phi_2 = (1/a) \sum_j{}' \left\{ \frac{z_j\epsilon[1-\psi(\eta r_{0j}/a)]}{r_{0j}} - \frac{z_j\epsilon\pi}{\eta^2} \right\}. \quad (11b)$$

In these equations η is an arbitrary parameter; two or more values of this parameter may be chosen to check numerical computation. A prime on the summation is used to indicate that the term for the zero index is to be omitted. The letter a represents the lattice parameter, $\psi(\eta r/a)$ is the normal probability integral, and

$$S_k = \sum_{i=1}^{\gamma} z_i \epsilon e^{-i(\mathbf{q}_k\cdot\mathbf{r}_i)},$$

where the limits 1 to γ indicate summation over one unit cell and where S_k is a function of the field point. Because the potential contribution of an ion becomes infinite as $r \to 0$, calculation of the potentials for points occupied by ions must exclude the contribution of the occupying ion. The potential for points occupied by ions may be calculated from the following equations:

$$\phi_1 = \frac{1}{\pi a} \sum_k{}' \frac{S_k \exp(-\pi^2/\eta^2)(k_1^2+k_2^2+k_3^2)}{(k_1^2+k_2^2+k_3^2)} - \frac{2z_0\epsilon\eta}{a(\pi)^{\frac{1}{2}}}, \quad (12a)$$

$$\phi_2 = (1/a) \sum_j{}' \frac{z_j\epsilon[1-\psi(\eta r_{ij}/a)]}{r_{ij}}. \quad (12b)$$

Since electrostatic potentials are additive, it is possible to calculate the potential at a specified point in any structure composed of interpenetrating simple cubic lattices of point charges by summing the contributions to the potential at that point due to each of the interpenetrating lattices. Because of this it was possible to calculate all potentials of interest in sodium tungsten bronze from the four potentials tabulated in Table I. In this table the origin was assumed to be occupied by an ion, and the potential at the origin was calculated

[10] M. Born and M. Göppert-Mayer, *Handbuch der Physik* (Julius Springer, Berlin, 1933), Vol. 24, Part 2, p. 710; see also R. Courant and D. Hilbert, *Methoden der Mathematischen Physik* (Julius Springer, Berlin, 1937), Vol. 2, p. 158 for a discussion of the theta-function transformation.

from Eqs. (12a) and (12b). The other three potentials were calculated using Eqs. (11a) and (11b). The electrostatic energy is obtained directly from the potentials by using the equation,

$$E=(\tfrac{1}{2})\textstyle\sum_i z_i\epsilon\phi_i. \qquad (13)$$

The factor of $\frac{1}{2}$ arises because double summation causes the interaction of each pair of ions to be considered twice.

It is also possible to calculate electrostatic energies of ionic arrays having a uniform neutralizing charge distribution by utilizing Emersleben's tabulation[11] of the Born ground potentials.[12] When using Emersleben's tabulation for calculating electrostatic energies of arrays in which the sum of the point charges over a unit cell is not equal to zero, it is necessary to include an additional term in the energy calculation for the potential at the origin. In Emersleben's article the value of this potential at the origin is listed in the body of the article rather than in the table with the rest of the ground potentials. The inclusion of a term for the potential at the origin must be noted when applying Emersleben's computational checks. Calculated electrostatic energies for cubic sodium tungsten bronze were checked by this method. The tabulated ground potentials are not, however, readily adaptable to the computation of potential barriers for diffusion calculations.

TABLE I. Calculated potentials in a simple cubic lattice of point charges.

Coordinates in a unit cell	Calculated potential[a]
000	$-2.8373z_i\epsilon/a$
$\frac{1}{2}00$	$-0.0959z_i\epsilon/a$
$\frac{1}{2}\frac{1}{2}0$	$-0.5830z_i\epsilon/a$
$\frac{1}{2}\frac{1}{2}\frac{1}{2}$	$-0.8017z_i\epsilon/a$

[a] z_i = ionic valence, ϵ = unit electrostatic charge, and a = lattice parameter

ACTIVATION ENERGY FOR THE DIFFUSION OF SODIUM

Calculations were made of the electrostatic activation energy as a function of sodium concentration for the diffusion of sodium in cubic sodium tungsten bronze. The structure of the cubic bronze is perovskite[13,5] and is illustrated in Fig. 1. The potential barrier was computed as the difference between the potential at the saddle point,

$$\phi_s=x\phi_{\frac{1}{2}00}{}^{Na}+2\phi_{\frac{1}{2}00}{}^{O}+\phi_{\frac{1}{2}\frac{1}{2}\frac{1}{2}}{}^{O}+\phi_{\frac{1}{2}\frac{1}{2}0}{}^{W}, \qquad (14)$$

and the potential at the equilibrium position,

$$\phi_{eq}=x\phi_{000}{}^{Na}+3\phi_{\frac{1}{2}\frac{1}{2}0}{}^{O}+\phi_{\frac{1}{2}\frac{1}{2}\frac{1}{2}}{}^{W}. \qquad (15)$$

The saddle point is the position midway between two

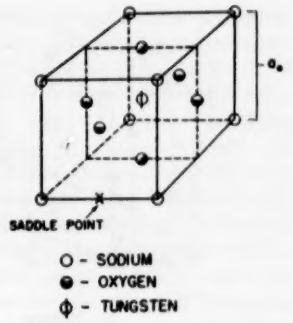

FIG. 1. Structure of the cubic phase of sodium tungsten bronze.

equilibrium positions of the sodium ion. A sodium ion attaining this jump position has equal probability of moving to either of the two adjacent equilibrium positions. The factor x which multiplies the potentials due to the sodium ion lattice is the sodium concentration in the formula, Na_xWO_3, and represents the random probability of any given sodium site being occupied by a sodium ion.

The potentials in Eqs. (14) and (15) are calculated with all ions in their equilibrium positions. In the process of diffusing the sodium ion moves from an equilibrium site to a saddle point. Therefore in calculating the activation energy for diffusion a second term must be added to compensate for the movement of the sodium ion which leaves vacant the original equilibrium site of the migrating ion. The resulting electrostatic activation energy is

$$\begin{aligned}\Delta H_a&=z_{Na}\epsilon(\phi_s-\phi_{eq})-x(z_{Na}\epsilon)^2/\tfrac{1}{2}a\\&=(0.7414x-0.1988)\epsilon^2/a.\end{aligned} \qquad (16)$$

This relation is shown graphically in Fig. 2. The units are left in terms of ϵ^2/a because of the variation of the lattice parameter with sodium concentration. On the basis of this equation the activation energy for sodium diffusion in $Na_{0.8}WO_3$ is approximately 40 kcal/mole, or 10 kcal/mole less than the measured value.

It should be recognized that this value for the activation energy is based upon an extremely simple model.[14] The above calculation allows only a $1-x$

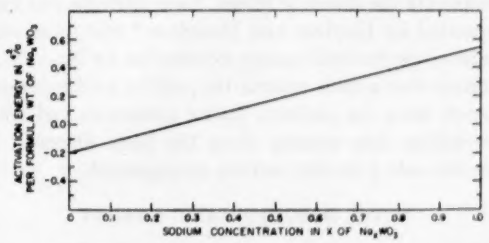

FIG. 2. Electrostatic activation energy as a function of sodium concentration.

[11] O. Emersleben, Physik. Z. **24**, 97 (1923).
[12] M. Born, Z. Physik **7**, 124 (1921).
[13] W. F. deJong, Z. Krist. **81**, 314 (1932).

[14] The author wishes to thank the referee for his comments on this topic.

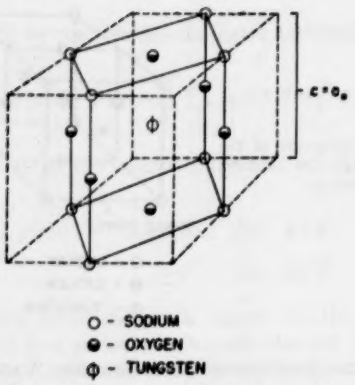

FIG. 3. Assumed structure for the tetragonal phase of sodium tungsten bronze.

probability for vacancy of the site into which the sodium ion is migrating. For diffusion to occur this probability should be unity. No satisfactory method for incorporating this requirement into the calculations has been found. An attempt to create such a vacancy by redistributing the charge from the vacated site uniformly among nearest neighbor sites resulted in a reduction in activation energy. An attempt to create a vacancy by abstracting the charge to infinity resulted in a negative activation energy for all sodium concentrations.

It would thus appear that the model used is inadequate to account for the high value of the activation energy which was measured. This is not too surprising when it is remembered that when a sodium ion moves from an equilibrium site to a saddle point the sodium-oxygen distance is reduced by approximately 30 percent. With this drastic change in interatomic distance the point charge approximation is probably very poor. It is suggested, therefore, that an adequate explanation of the high value of the activation energy might be the repulsive interaction between the bound electrons at the short interatomic distances which occur during sodium migration. In addition there is some experimental evidence for a possible ordered arrangement of the sodium ions near $Na_{0.75}WO_3$ which would further complicate the diffusion model. Such ordering was first suggested by Gardner and Danielson,[6] and some preliminary electrostatic energy calculations for $Na_{0.75}WO_3$ indicate that a cubic superlattice, with a lattice parameter of twice the ordinary lattice parameter and with the sodium ions missing along the body diagonal, is favored over a random sodium arrangement.

TOTAL ELECTROSTATIC ENERGY

A more interesting aspect of the activation energy calculations is shown in Fig. 2, where the activation energy becomes negative at low sodium concentrations. A negative activation energy would imply spontaneous diffusion and hence a region of instability for the cubic phase of sodium tungsten bronze.

In an attempt to determine the stability limit of the cubic phase of sodium tungsten bronze, calculation of the total electrostatic energy as a function of sodium concentration was undertaken. Sodium tungsten bronze is known to have a tetragonal phase[5] at lower sodium concentrations. The calculated electrostatic energy of the cubic phase was compared with the calculated electrostatic energy of an assumed tetragonal structure to determine whether the known transition could be predicted on the basis of an electrostatic model. It was necessary to assume a structure for the tetragonal phase since the actual structure[15] is incompletely known. The actual structure is somewhat complex, and only the x and y parameters of the tungsten positions are known with any accuracy. The assumed unit cell of the tetragonal phase was based upon the indicated tendency of the sodium ions to migrate to the saddle points at low sodium concentrations; the assumed unit cell is shown in Fig. 3. A comparison of the assumed tetragonal structure with the known cubic structure will show only one difference. The single primitive cubic lattice of sodium ions in the cubic phase is transformed to two interpenetrating primitive cubic lattices in the tetragonal phase; the tetragonal sodium lattices are translated

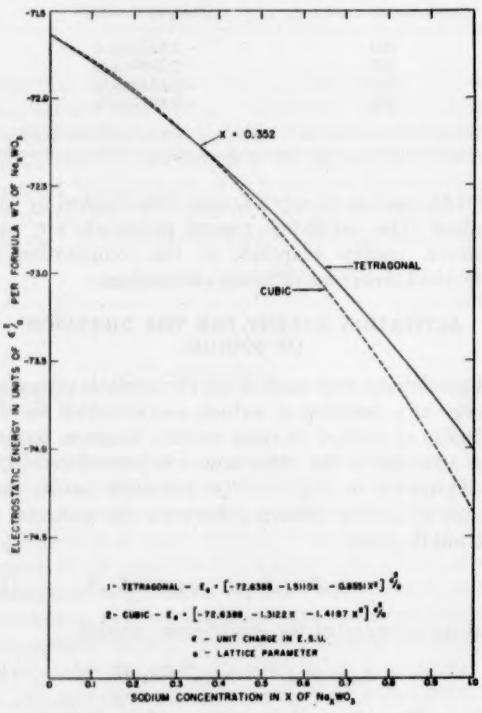

FIG. 4. Electrostatic energy as a function of sodium concentration for cubic and tetragonal sodium tungsten bronze (based on assumption of random sodium distribution).

[15] A. Magneli, Arkiv Kemi, Mineral. Geol. 1, 269 (1949).

by $\frac{1}{2}00$ and $0\frac{1}{2}0$ from the lattice position in the cubid structure. The random sodium distribution is retained by placing $x/2$ sodium ions in each of the sodium lattices of the tetragonal phase. The tungsten and oxygen positions are identical in the two phases. The c parameter of the tetragonal phase is equal to the lattice parameter of the cubic phase which is consistent with reported data[2,5,15] for the actual tetragonal phase; the a parameter of the assumed tetragonal phase is $\sqrt{2}/2$ times the cubic parameter, and the c/a ratio is $\sqrt{2}$. In addition the average tungsten-tungsten distance[15] of the actual tetragonal structure is very nearly equal to the tungsten-tungsten distance of the cubic phase and of the assumed tetragonal phase.

The calculations were carried out in the manner described, and the resulting electrostatic energy as a function of sodium concentration for the cubic phase is

$$_cE(Na_xWO_3) = (-71.6388-1.3122x-1.4187x^2)\epsilon^2/a. \quad (17)$$

The corresponding relationship for the tetragonal phase is

$$_tE(Na_xWO_3) = (-71.6388-1.5110x-0.8551x^2)\epsilon^2/a. \quad (18)$$

Figure 4 shows graphically both equations. The electrostatic energies of the two phases are equal at $x=0$ and $x=0.352$. The correspondence at $x=0$ is expected since both phases degenerate to the same structure at this point. The crossing of the energy curves at $x=0.352$ indicates that electrostatically the cubic phase should be unstable or metastable below this concentration.

CONCLUSION

The calculated stability limit of $x=0.352$ is in excellent agreement with reported data. Hägg[5] has reported the preparation of cubic sodium tungsten bronze with sodium concentration as low as $x=0.3$, while Magneli[15] has reported preparation of tetragonal bronze with sodium concentration as high as $x=0.38$.

It is to be emphasized that since the tetragonal structure used in the calculation is only an assumed structure; the strongest statement that can be made is that there is a structure below $x=0.352$ which has a lower Coulombic energy than the cubic perovskite structure. If the repulsive interaction between the closed electron shells at small sodium-oxygen distances is as important as indicated by the diffusion energy calculations, then the cubic structure would be favored and a lower stability limit for the cubic phase relative to the assumed tetragonal phase would be expected. However, it may well be that the assumed tetragonal phase is a poor approximation to the real structure. A tetragonal potassium tungsten bronze[16] is known, and additional structures[17] for sodium tungsten bronze below sodium concentration of $x=0.2$ have been reported. None of these structures approximate closely the assumed tetragonal structure used in these calculations. Even though the assumed tetragonal structure may differ markedly from the real structure, the calculations do indicate an energy dissatisfaction in the cubic structure and a tendency toward a phase change. In view of the simplicity of the model used, the agreement between the calculated transition point and the observed transition range is rather striking.

ACKNOWLEDGMENT

The author is deeply indebted to Dr. J. M. Keller for his helpful discussions throughout the progress of this investigation, especially with regard to the methods of calculation. The author also wishes to express his appreciation to Dr. R. E. Rundle for suggesting the problem, to Miss Suzanne Shaw for her assistance in the computational work, and to Dr. G. C. Danielson for his interest and encouragement in this research.

[16] A. Magneli, Arkiv Kemi, Mineral. Geol. **1**, 213 (1949).

[17] See A. Magneli and B. Blomberg, Acta Chem. Scand. **5**, 372 (1951) and A. Magneli, Acta Chem. Scand. **5**, 670 (1951) for a second tetragonal phase. See also O. Glemser and H. Sauer, Z. anorg. u. allgem. Chem. **252**, 147 (1943) for the tungsten oxide structures.

Time-Dependent Correlations between Spins and Neutron Scattering in Ferromagnetic Crystals*

LÉON VAN HOVE
Institute for Advanced Study, Princeton, New Jersey
(Received May 25, 1954)

The pair correlation between spins considered at different times in a ferromagnetic crystal is used to derive a general formula for the angular and energy distribution of magnetically scattered neutrons. The qualitative properties of the correlation are established for various temperature ranges and a number of characteristic features of the scattering and of its temperature variation are thus accounted for. From the study of the long-range part of the correlation an explicit expression is derived for the "critical magnetic scattering" produced in the neighborhood of the Curie point by the large spontaneous fluctuations of the magnetization.

I. INTRODUCTION

As was shown in an earlier paper,[1] the Born approximation scattering cross section can be simply expressed in terms of the four-dimensional Fourier transform of a pair distribution function depending on a space vector and a time variable. The formula thus obtained provides a new and physically very intuitive method of analyzing the properties of slow neutron scattering by systems of particles, in the most interesting energy region where energy transfers are of the order of the incident neutron energy or larger. The formula is the natural extension to neutron scattering of the classical Zernike-Prins formula[2] for scattering of x-rays. In full analogy with the latter, it is expected to be of most practical interest in the case of scattering systems of complicated dynamical and statistical structure, like liquids or dense gases, for which a theoretical calculation of the scattering is not possible.

This general method of describing slow-neutron scattering in terms of a time-dependent pair distribution function finds a very fruitful application in the case of magnetic inelastic scattering by ferromagnetic crystals. The total magnetic cross section of iron has been measured by Palevsky and Hughes for neutrons of wavelengths ranging from 5 to 13 A, from very low temperatures to well above the Curie point.[3] Similar measurements were made by Squires for iron and nickel.[4] As was briefly shown in an earlier paper,[5] striking features in the temperature variation of the total cross section are readily understood in terms of the general properties of the time-dependent pair distribution (or correlation) for spin orientations. The present paper is devoted to the detailed derivation and discussion of these properties as well as to a more complete account of the predictions which can be made on their basis for the magnetic inelastic scattering of slow neutrons. Despite the well-known impossibility to deal in any exact way with the dynamical properties of a ferromagnetic spin system, it turns out that all the most important qualitative properties of the correlation, and thus of the scattering, can be derived by means of general statistical arguments completed with macroscopic considerations. The success of this approach must be ascribed to the simple and direct physical meaning of the correlation as a function of space and time variables. It therefore illustrates in a striking way the practical usefulness of the concepts introduced and studied in II in more abstract terms.

The general formula expressing the magnetic scattering cross section in terms of the pair correlation between spins is derived and discussed in the next section. Section III deals with the correlation calculated by spin wave theory for temperatures very low compared to the Curie temperature. The qualitative properties of the correlation and of the magnetic inelastic scattering are discussed in Sec. IV for general temperatures, neither too small nor too close to the Curie point. The long range part of the correlation present at temperatures close to the Curie point and resulting from the occurrence of large spontaneous fluctuations in the magnetization is studied in the following section, where it is also used to derive the characteristic features of the "critical magnetic scattering" produced by those fluctuations. The experimental evidence confirming the existence of the critical magnetic scattering is mentioned. The final section is devoted to a few concluding remarks.

II. SCATTERING FORMULA

For the description of ferromagnetic crystals we adopt the atomic (Heisenberg) model of ferromagnetism which attributes to each atom a spin of fixed length s_0. Apart from assuming not too large overlap integrals, this model can be a fair approximation only when the magneton number ν_0 per atom is close to an integer. This is the case for iron ($\nu_0=2.2$), for which s_0 must be given the value 1. For nickel ($\nu_0=0.6$) the model does not hold.

Although there is no difficulty in writing down

* Part of this work was done at Brookhaven National Laboratory where it was supported by the U. S. Atomic Energy Commission.

[1] Léon Van Hove, Phys. Rev. **95**, 249 (1954). This paper will be referred to as II, and its equations denoted by Eq. (II ···).

[2] F. Zernike and J. A. Prins, Z. Physik **41**, 184 (1927).

[3] H. Palevsky and D. J. Hughes, Phys. Rev. **92**, 202 (1953).

[4] G. L. Squires (to be published).

[5] Léon Van Hove, Phys. Rev. **93**, 268 (1954), henceforth referred to as I.

formulas taking polarization effects into account,[6,7] we limit ourselves to scattering of unpolarized neutrons by a ferromagnetic crystal and leave the polarization of the scattered beam out of consideration. The differential cross section $d^2\sigma/d\Omega d\epsilon$ per unit solid angle and unit interval of outgoing neutron energy ϵ is then the sum of a term entirely due to the nuclear interaction of the neutron with the nuclei of the crystal, and a term $d^2\sigma_{\text{magn}}/d\Omega d\epsilon$ resulting from the magnetic interaction of the neutron with the magnetic electrons of the crystal.[8] Following Halpern and Johnson,[9] the magnetic cross section is

$$\frac{d^2\sigma_{\text{magn}}}{d\Omega d\epsilon}=\left(\frac{2ge^2}{m_0c^2}\right)^2\frac{1}{h}\frac{k}{k_0}|F(\kappa)|^2 \times\sum_{\alpha,\beta}\left(\delta_{\alpha\beta}-\frac{\kappa_\alpha\kappa_\beta}{\kappa^2}\right)S_{\alpha\beta}(\boldsymbol{\kappa},\omega), \quad (1)$$

$$S_{\alpha\beta}(\boldsymbol{\kappa},\omega)=\sum_{n_0}p_{n_0}\sum_n\left[\sum_R S_R{}^\alpha\exp(-i\boldsymbol{\kappa}\cdot\mathbf{r}_R)\right]_n^{n_0} \times\left[\sum_{R'}S_{R'}{}^\beta\exp(i\boldsymbol{\kappa}\cdot\mathbf{r}_{R'})\right]_{n_0}^n \cdot\delta\left(\omega+\frac{E_{n_0}-E_n}{h}\right), \quad (2)$$

where e and m_0 are the electron charge and mass, $g=1.91$ is the neutron magnetic moment in nuclear magnetons, c is the velocity of light, $\mathbf{k}_0$ and $\mathbf{k}=\mathbf{k}_0-\boldsymbol{\kappa}$ are the initial and final wave vectors of the neutron, whereas $\omega=\hbar(k_0{}^2-k^2)/2m$, m being the neutron mass. The indices $\alpha, \beta=x, y, z$ refer to rectangular coordinates in space. The function $F(\kappa)$ is the form factor of the magnetic electrons normalized to $F(0)=1$. The atoms in the crystal have their equilibrium positions $\mathbf{R}$ at the sites of a lattice which we assume to be of Bravais type (one particle per cell). We denote their actual position vectors by $\mathbf{r}_R=\mathbf{R}+\mathbf{u}_R$ and the resultant spin vector of their electron cloud by $\mathbf{S}_R$.[10] The initial and final quantum states of the crystal (including the spin system) are labeled by n_0, n; their energies are E_{n0}, E_n; the bracket $[\cdots]_n{}^{n_0}$ denotes a matrix element and p_{n0} is the Boltzmann factor,

$$p_{n0}=Z^{-1}\exp(-E_{n0}/k_BT), \quad \sum_{n_0}p_{n0}=1,$$

containing the temperature T and Boltzmann's constant k_B.

[6] F. Bloch, Phys. Rev. **50**, 259 (1936).
[7] J. Schwinger, Phys. Rev. **51**, 544 (1937).
[8] The weak neutron-electron interaction of nonmagnetic nature is neglected.
[9] O. Halpern and M. H. Johnson, Phys. Rev. **55**, 898 (1939).
[10] R stands for $\mathbf{R}$ when in suffix. We make the assumption that the orbital motion of the electrons does not contribute to the magnetic moment of the atom.

By the method of II, Eq. (2) is transformed into

$$S_{\alpha\beta}(\boldsymbol{\kappa},\omega)=(2\pi)^{-1}N\int\exp[i(\boldsymbol{\kappa}\cdot\mathbf{r}-\omega t)]\cdot\Gamma_{\alpha\beta}(\mathbf{r},t)d\mathbf{r}dt, \quad (3)$$

where N is the number of atoms in the crystal. The pair distribution $\Gamma_{\alpha\beta}$ is defined by

$$\Gamma_{\alpha\beta}(\mathbf{r},t)=N^{-1}\sum_{R'}\sum_R\left\langle\int d\mathbf{r}'\cdot S_{R'}{}^\alpha(0)\cdot\delta(\mathbf{r}+\mathbf{r}_{R'}(0)-\mathbf{r}') \times S_R{}^\beta(t)\cdot\delta(\mathbf{r}'-\mathbf{r}_R(t))\right\rangle_T, \quad (4)$$

where, for each operator A, one writes

$$A(t)=\exp(itH/\hbar)\cdot A\cdot\exp(-itH/\hbar) \quad (5)$$

in terms of the Hamiltonian H of the crystal (including spins), and also

$$\langle A\rangle_T=\sum_{n_0}p_{n0}[A]_{n_0}^{n_0}.$$

All atoms being identical, the sum over $\mathbf{R}'$ in Eq. (4) may be restricted to $\mathbf{R}'=0$ and the factor N^{-1} dropped.

It is a good approximation to assume that there is no coupling between atomic positions $\mathbf{r}_R$ and atomic spins $\mathbf{S}_R$. The correlation (4) then becomes

$$\Gamma_{\alpha\beta}(\mathbf{r},t)=\sum_R\gamma_R{}^{\alpha\beta}(t)G_R(\mathbf{r},t). \quad (6)$$

$\gamma_R{}^{\alpha\beta}(t)$ is the time-dependent correlation between pairs of spins,

$$\gamma_R{}^{\alpha\beta}(t)=\langle S_0{}^\alpha(0)S_R{}^\beta(t)\rangle_T. \quad (7)$$

It is complex-valued and satisfies the hermiticity condition,

$$\gamma_R{}^{\alpha\beta}(t)=\{\gamma_{-R}{}^{\beta\alpha}(-t)\}^*.$$

The function G_R, already introduced and calculated in II, describes the pair distribution in space and time of two atoms with equilibrium positions separated by $\mathbf{R}$:

$$G_R(\mathbf{r},t)=\left\langle\int d\mathbf{r}'\delta(\mathbf{r}+\mathbf{r}_0(0)-\mathbf{r}')\delta(\mathbf{r}'-\mathbf{r}_R(t))\right\rangle_T. \quad (8)$$

The theoretical discussion of the magnetic scattering reduces thus to the study of the time-dependent correlation (7) between pairs of spins. It could be carried out in full detail if an actual calculation of this correlation were possible. Except for temperatures small compared to the Curie temperature, where spin wave theory is applicable,[11] such a calculation presents great difficulties, comparable to the difficulties involved in the theoretical determination of pair distribution functions in liquids (see II). As in the case of liquids one has to proceed by deriving, rigorously when possible and qualitatively

[11] The discussion of magnetic scattering of neutrons by spin wave theory has been given by R. G. Moorhouse, Proc. Phys. Soc. (London) **A64**, 1097 (1951).

otherwise, as many general properties of the correlation $\gamma_R{}^{\alpha\beta}(t)$ as can be found. On the basis of these one could further select approximate methods to obtain more quantitative results. Our present aim is to deal with the first problem and to derive from its solution the main qualitative properties of the magnetic scattering of slow neutrons.

By far the main part of the interaction between atomic spins is of the exchange type, so that the main term in the Hamiltonian H_0 of the spin system is of form

$$H_0=-\sum_{\mathbf{R}\neq\mathbf{R}'} J_{R-R'}\mathbf{S}_R\cdot\mathbf{S}_{R'}, \tag{9}$$

where $-2J_R$ is the negative exchange energy of two atoms separated by a lattice vector $\mathbf{R}$, negligible for all but the shortest lattice vectors. Additional terms in the Hamiltonian, like the dipole-dipole interaction between spins, are very much smaller. If they are neglected, the cross-section formula (1) greatly simplifies for scattering by a polycrystal: averaging over crystal orientations gives

$$\frac{d^2\sigma_{\text{magn}}}{d\Omega d\epsilon}=\left(\frac{2ge^2}{m_0c^2}\right)^2\frac{2}{3h}\frac{k}{k_0}\cdot|F(\kappa)|^2\cdot\mathcal{S}(\boldsymbol{\kappa},\omega), \tag{10}$$

where $\mathcal{S}$, the trace of the 3×3 matrix $\mathcal{S}_{\alpha\beta}$, is the 4-dimensional Fourier transform of Γ, trace of $\Gamma_{\alpha\beta}$:

$$\mathcal{S}(\boldsymbol{\kappa},\omega)=(2\pi)^{-1}N\int\exp[i(\boldsymbol{\kappa}\cdot\mathbf{r}-\omega t)]\cdot\Gamma(\mathbf{r},t)d\mathbf{r}dt. \tag{11}$$

Equations (6) and (7) reduce to

$$\Gamma(\mathbf{r},t)=\sum_R\gamma_R(t)G_R(\mathbf{r},t), \tag{12}$$

$$\gamma_R(t)=\langle\mathbf{S}_0(0)\cdot\mathbf{S}_R(t)\rangle_T. \tag{13}$$

As was discussed in II, the separation between elastic and inelastic scattering can be obtained by separating the pair distribution $\Gamma_{\alpha\beta}(\mathbf{r},t)$ into its asymptotic value for $t=\pm\infty$ and a term converging to zero when $|t|\to\infty$. It will be seen in Sec. IV that (for large N)

$$\gamma_R{}^{\alpha\beta}(t)=N^{-2}\langle S^\alpha\rangle_T\langle S^\beta\rangle_T+\gamma'_R{}^{\alpha\beta}(t),$$

$$\lim_{|t|\to\infty}\gamma'_R{}^{\alpha\beta}(t)=0, \tag{14}$$

with $\mathbf{S}=\sum_R\mathbf{S}_R$ the total spin of the system.[12] Similarly

$$G_R(\mathbf{r},t)=G_R^{(\infty)}(\mathbf{r})+G_R'(\mathbf{r},t),\quad\lim_{|t|\to\infty}G_R'(\mathbf{r},t)=0, \tag{15}$$

$G_R^{(\infty)}$ has been calculated in II. Insertion of (14) into (6) gives

$$\Gamma_{\alpha\beta}(\mathbf{r},t)=N^{-2}\langle S^\alpha\rangle_T\langle S^\beta\rangle_T G(\mathbf{r},t)$$

$$+\sum_R\gamma'_R{}^{\alpha\beta}(t)G_R(\mathbf{r},t), \tag{16}$$

where

$$G(\mathbf{r},t)=\sum_R G_R(\mathbf{r},t) \tag{17}$$

is the pair distribution function of the crystal which determines the coherent nuclear scattering (see II).

The part $d^2\sigma_1/d\Omega d\epsilon$ of the magnetic scattering originating from the first term in the right-hand side of Eq. (16) will thus be very similar to the coherent nuclear scattering.[13] The main difference results from the magnetic form factor $F(\kappa)$ occurring in Eq. (1), which will strongly depress all scattering processes with κ^{-1} of the order of atomic dimensions or smaller, and from the factor $N^{-2}\langle S^\alpha\rangle_T\langle S^\beta\rangle_T$ in (16) obviously related to the magnetization of the system. This scattering is elastic as far as the spin system is concerned. As far as the crystal vibrations are concerned it subdivides into an elastic and an inelastic subpart, obtained respectively by replacing G by $\sum_R G_R^{(\infty)}$ and $\sum_R G_R'$. The former subpart, i.e., the truly elastic magnetic scattering, is readily calculated to be

$$\left(\frac{d\sigma_{\text{magn}}}{d\Omega}\right)_{el}=\frac{1}{N}\left(\frac{2ge^2}{m_0c^2}\right)^2|F(\kappa)|^2\langle(\mathbf{S}\cdot\mathbf{S})-\kappa^{-2}(\mathbf{S}\cdot\boldsymbol{\kappa})^2\rangle_T$$

$$\times\sum_R\int\exp(i\boldsymbol{\kappa}\cdot\mathbf{r})G_R^{(\infty)}(\mathbf{r})d\mathbf{r}.$$

Inserting the explicit expression of $G_R^{(\infty)}$ found in II, one gets

$$\left(\frac{d\sigma_{\text{magn}}}{d\Omega}\right)_{el}=\frac{8\pi^3}{Nv_0}\left(\frac{2ge^2}{m_0c^2}\right)^2|F(\kappa)|^2$$

$$\cdot\langle(\mathbf{S}\cdot\mathbf{S})-\kappa^{-2}(\mathbf{S}\cdot\boldsymbol{\kappa})^2\rangle_T$$

$$\times\exp\{-\langle(\boldsymbol{\kappa}\cdot\mathbf{u})^2\rangle_T\}\sum_\tau\delta(\boldsymbol{\kappa}-\boldsymbol{\tau}), \tag{18}$$

where v_0 is the volume of the crystal cell, $\mathbf{u}$ is the displacement vector of any atom, and the $\boldsymbol{\tau}$'s are the reciprocal lattice vectors.[14] The exponential is the familiar Debye-Waller factor.

Whereas the total spin, i.e., the total magnetization, is the only magnetic property affecting the part $d^2\sigma_1/d\Omega d\epsilon$ of the cross section, the rest of the magnetic scattering, the cross section of which will be denoted by $d^2\sigma_2/d\Omega d\epsilon$, involves the last term in Eq. (16) and depends through $\gamma'_R{}^{\alpha\beta}(t)$ on the full space and time variation of the correlation (7). Only this part, which is inelastic in the spin system and will hereafter be called magnetic inelastic scattering, requires therefore a further analysis. We are at present interested in its main qualitative properties and for this purpose we can neglect the atomic displacements, thus replacing $G_R(\mathbf{r},t)$ by $\delta(\mathbf{r}-\mathbf{R})$. One

[12] In the ferromagnetic case, where $\langle\mathbf{S}\rangle_T\neq0$, our considerations apply to scattering by one ferromagnetic domain. Except for very small angle effects (angles of the order of a few minutes), the scattering of various domains adds up incoherently.

[13] For a discussion of nuclear scattering by crystals and for a list of earlier papers devoted to it, see G. Placzek and L. Van Hove, Phys. Rev. 93, 1207 (1954).

[14] We define them as the vectors $\boldsymbol{\tau}$ for which $(2\pi)^{-1}(\boldsymbol{\tau}\cdot\mathbf{R})$ is an integer for each lattice vector $\mathbf{R}$. In suffix τ stands for $\boldsymbol{\tau}$.

gets

$$\frac{d^2\sigma_2}{d\Omega d\epsilon}=\left(\frac{2ge^2}{m_0c^2}\right)^2\frac{N}{2\pi\hbar}\cdot\frac{k}{k_0}\cdot|F(\kappa)|^2\cdot\sum_{\alpha,\beta}\left(\delta_{\alpha\beta}-\frac{\kappa_\alpha\kappa_\beta}{\kappa^2}\right)$$
$$\times\sum_R\int dt\exp[i(\boldsymbol{\kappa}\cdot\mathbf{R}-\omega t)]\gamma'_R{}^{\alpha\beta}(t), \quad (19)$$

and, for a polycrystal,

$$\frac{d^2\sigma_2}{d\Omega d\epsilon}=\left(\frac{2ge^2}{m_0c^2}\right)^2\frac{N}{3\pi\hbar}\cdot\frac{k}{k_0}\cdot|F(\kappa)|^2$$
$$\times\sum_R\int dt\exp[i(\boldsymbol{\kappa}\cdot\mathbf{R}-\omega t)]\gamma_R'(t), \quad (20)$$

with

$$\gamma_R'(t)=\gamma_R(t)-N^{-2}|\langle\mathbf{S}\rangle_T|^2. \quad (21)$$

At first sight it would seem that the atomic displacements could be approximately taken into account by simple insertion of the Debye-Waller factor $\exp\{-\langle(\boldsymbol{\kappa}\cdot\mathbf{u})^2\rangle_T\}$ into Eqs. (19) and (20). This would amount to the replacement of $G_R(\mathbf{r},t)$ by its asymptotic value $G_R{}^{(\infty)}(\mathbf{r})$ in the last term of Eq. (16). The improvement obtained in this way is however in general illusory, since the differences,

$$G_R'=G_R-G_R{}^{(\infty)}, \quad G_R{}^{(\infty)}-\delta(\mathbf{r}-\mathbf{R}),$$

are of the same order of magnitude. It is only with the exact expression of $G_R(\mathbf{r},t)$, Eq. (II 53), that the effect of atomic vibrations can be calculated properly. Such a calculation is completely unwarranted at present in view of our poor knowledge of the magnetic correlation function $\gamma_R{}^{\alpha\beta}(t)$, with the exception of the low-temperature region where spin wave theory applies[11] and of the critical magnetic scattering occurring near the Curie point (Sec. V).

We now begin the discussion of the spin correlation function and of the effect of its properties on magnetic scattering. Only for temperatures small compared to the Curie temperature T_c is a complete calculation possible. It is briefly outlined in the next section. A general, qualitative discussion is then given for higher temperatures, comparable to T_c but not too close to it. The special long-range effects occurring near the Curie point are studied separately.

III. SPIN WAVE THEORY OF CORRELATION FUNCTION

For temperatures T small compared to T_c, in a ferromagnetic domain magnetized in the z direction, the spin operators $\mathbf{S}_R$ can be approximately represented by[15]

$$\left.\begin{aligned}S_R{}^x&=(s_0/2N)^{\frac{1}{2}}\textstyle\sum_q\exp(i\mathbf{q}\cdot\mathbf{R})(a_q{}^*+a_{-q})\\ S_R{}^y&=(s_0/2N)^{\frac{1}{2}}i\textstyle\sum_q\exp(i\mathbf{q}\cdot\mathbf{R})\cdot(a_q{}^*-a_{-q})\\ S_R{}^z&=s_0-N^{-1}[\textstyle\sum_q\exp(i\mathbf{q}\cdot\mathbf{R})a_q{}^*]\\ &\quad\times[\textstyle\sum_q\exp(-i\mathbf{q}\cdot\mathbf{R})a_q]\end{aligned}\right\}. \quad (22)$$

We assume the domain to have $N^{\frac{1}{3}}$ cells along each of the three lattice axes. The vector $\mathbf{q}$[16] runs then over the values

$$\mathbf{q}=N^{-\frac{1}{3}}(n_1\boldsymbol{\tau}_1+n_2\boldsymbol{\tau}_2+n_3\boldsymbol{\tau}_3),$$

where $\boldsymbol{\tau}_1$, $\boldsymbol{\tau}_2$, $\boldsymbol{\tau}_3$ are basic vectors of the reciprocal lattice, and n_1, n_2, n_3 take all integral values in the interval $-\frac{1}{2}N^{\frac{1}{3}}<n_i\leqslant\frac{1}{2}N^{\frac{1}{3}}$. The only nonvanishing commutators of the operators a_q, $a_q{}^*$ are

$$a_qa_q{}^*-a_q{}^*a_q=1.$$

Equations (22) are valid apart from terms of third and higher order in the a_q and $a_q{}^*$. In the same approximation the Hamiltonian (9) of the spin system reduces to

$$H_0=-Ns_0{}^2(\textstyle\sum_R J_R)+h\sum_q\omega_qa_q{}^*a_q, \quad (23)$$

with

$$\hbar\omega_q=2s_0\textstyle\sum_R J_R[1-\cos(\mathbf{q}\cdot\mathbf{R})]. \quad (24)$$

The operators $a_q{}^*$ and a_q respectively create and annihilate an excitation of wave vector $\mathbf{q}$ and frequency ω_q. Following Bloch[17] such excitations are called spin waves. In the present approximation there is no interaction between spin waves.

On the basis of Eqs. (22) and (23) the calculation of the time-dependent correlation (7) is straightforward. It leads to the following result, valid in the limit of large N:

$$\gamma_R{}^{xx}(t)=\gamma_R{}^{yy}(t)=\frac{v_0s_0}{16\pi^3}\int d\mathbf{q}\cdot\{1-\exp(-\hbar\beta\omega_q)\}^{-1}$$
$$\times\{\exp[-i(\mathbf{R}\cdot\mathbf{q}-t\omega_q)]$$
$$+\exp(-\hbar\beta\omega_q)\cdot\exp[i(\mathbf{R}\cdot\mathbf{q}-t\omega_q)]\},$$

$$\gamma_R{}^{xy}(t)=-\gamma_R{}^{yx}(t)=\frac{v_0s_0i}{16\pi^3}\int d\mathbf{q}\cdot\{1-\exp(-\hbar\beta\omega_q)\}^{-1}$$
$$\times\{\exp[-i(\mathbf{R}\cdot\mathbf{q}-t\omega_q)]$$
$$-\exp(-\hbar\beta\omega_q)\cdot\exp[i(\mathbf{R}\cdot\mathbf{q}-t\omega_q)]\},$$

$$\gamma_R{}^{zz}(t)=N^{-2}\langle S_z\rangle^2{}_T=N^{-2}|\langle\mathbf{S}\rangle_T|^2$$
$$=s_0{}^2-\frac{v_0s_0}{4\pi^3}\int d\mathbf{q}\frac{\exp(-\hbar\beta\omega_q)}{1-\exp(-\hbar\beta\omega_q)},$$

$$\gamma_R{}^{xz}(t)=\gamma_R{}^{yz}(t)=0.$$

β is the reciprocal of k_BT and the integration extends over one cell of the reciprocal lattice. The vector $\mathbf{S}$ is the total spin $\sum_R\mathbf{S}_R$.

[15] T. Holstein and H. Primakoff, Phys. Rev. **58**, 1098 (1940).

[16] q stands for $\mathbf{q}$ when in suffix.

[17] F. Bloch, Z. Physik **61**, 206 (1930).

TABLE I. Magnetic inelastic cross section from spin wave theory.

T in °K	0	100	200	300	400	500	600
σ_2/λ_0 in mb per A	0	0.4	1.7	3.5	5.5	8	10

From these formulas a closed expression of the magnetic scattering cross section $d^2\sigma_2/d\Omega d\epsilon$ at low temperature is obtained by insertion into (19). The result is of course equivalent with what follows from a direct spin wave treatment of the scattering problem, as given by Moorhouse.[11] We refer to this author for a detailed discussion. It will be enough to mention here, for comparison with the transmission measurements of Palevsky and Hughes[3] and of Squires,[4] the numerical values of the total cross section,

$$\sigma_2=\int (d^2\sigma_2/d\Omega d\epsilon)d\Omega d\epsilon,$$

in the long wavelength region ($\lambda_0=2\pi/k_0\gg 2A$) where it is proportional to the incident wavelength λ_0. They have been calculated for iron, with the value $s_0=1$ for the atomic spin and the value $J=205$°K for the exchange interaction between nearest neighbors.[18] Table I gives the values of σ_2/λ_0 in millibarns per angstrom for various temperatures T. A comparison with the observations of Palevsky and Hughes is shown in the figure of I.[5] It gives a crude idea of the domain of validity of spin wave theory for the magnetic cross section σ_2. It is certainly limited to the low-temperature region ($T\lesssim 300°$) where σ_2 is quite small compared to the nuclear scattering cross section, and where the magnetic scattering could thus better be separated by its peculiar angular and energy distribution, as discussed by Moorhouse.[11]

As far as our present aims are concerned, the main interest of spin wave theory is to provide us with an explicit expression for the correlation $\gamma_R{}^{\alpha\beta}(t)$ for at least one temperature region, however restricted it may be. One can, for example, discuss the convergence of the correlation toward its asymptotic value $N^{-2}\langle S^\alpha\rangle_T\langle S^\beta\rangle_T$ when R or $|t|\to\infty$. It is determined by the convergence to zero of $\gamma_R{}^{xx}(t)$ and $\gamma_R{}^{xy}(t)$ as expressed in the formulas above. At any nonvanishing temperature and for $R\to\infty$, the convergence is in R^{-1}, as a consequence of the singularity of $\{1-\exp(-\hbar\beta\omega_q)\}^{-1}$ at $\mathbf{q}=0$,

$$\{1-\exp(-\hbar\beta\omega_q)\}^{-1}\simeq(\hbar\beta\omega_q)^{-1}\propto q^{-2}.$$

For $|t|\to\infty$ the convergence is in $|t|^{-1}$; this last result is best obtained by the method of stationary phases already used in the section of II devoted to crystals. The slow convergence, especially in R, is characteristic of the low-temperature region. As the temperature goes up, the number of spin waves excited increases rapidly and their interactions start playing a predominant role. The main effect of these interactions on the correlation is to make it converge much more rapidly toward its asymptotic value. The energy distribution of magnetically scattered neutrons, highly singular at low temperature, becomes correspondingly smoother.

Another interesting point concerns the time-dependent correlation at absolute zero. It has the following expression:

$$\gamma_R{}^{zz}(t)=\gamma_R{}^{yy}(t)=-i\gamma_R{}^{xy}(t)=i\gamma_R{}^{yx}(t)$$
$$=\frac{v_0 s_0}{16\pi^3}\int \exp[-i(\mathbf{R}\cdot\mathbf{q}-t\omega_q)]d\mathbf{q}, \quad (25)$$
$$\gamma_R{}^{xz}(t)=s_0{}^2, \quad \gamma_R{}^{xz}(t)=\gamma_R{}^{yz}(t)=0.$$

Although the convergence of the first four components toward zero is again in $|t|^{-\frac{3}{2}}$ for large times, the convergence in R for finite t is quite different from what it is at positive temperatures: from the expression (24) of the spin wave frequency one can show it to be exponential with a range of order of a few interatomic distances for all times not very large compared to $\hbar/J$, where J is the exchange interaction for nearest neighbors. In this case, however, despite the rapid convergence of the correlation for $R\to\infty$, the angular and energy distribution of scattered neutrons is still highly singular. This is possible only in view of the very special functional form of the right-hand side in Eq. (25).

IV. THE CORRELATION FUNCTION AT GENERAL TEMPERATURES

At temperatures too high for the application of spin wave theory, no explicit calculation is possible for either the inelastic scattering cross section $d^2\sigma_2/d\Omega d\epsilon$ or the time-dependent correlation $\gamma_R{}^{\alpha\beta}(t)$. It is in such a situation that the description of the scattering in terms of the correlation is actually useful, since the properties of the correlation, with their more direct significance in space and time, are easier to discuss on an approximate basis than those of the scattering. We limit ourselves in the present paper to the most qualitative features of the correlation and to their consequences for the temperature dependence of the magnetic inelastic scattering.

The first point to discuss is the limiting value of

$$\gamma_R{}^{\alpha\beta}(t)=\langle S_0{}^\alpha(0)S_R{}^\beta(t)\rangle_T \quad (26)$$

for R or $|t|\to\infty$. Under the assumption that the spin system is large (N large), as is usually the case in statistical mechanics, the two factors in the right-hand side of Eq. (26) will be statistically independent as soon as they refer to locations sufficiently distant in space or instants sufficiently distant in time. We thus have, for large R or $|t|$,

$$\gamma_R{}^{\alpha\beta}(t)\simeq\langle S_0{}^\alpha(0)\rangle_T\langle S_R{}^\beta(t)\rangle_T,$$

[18] This value is determined from the low-temperature variation of the magnetization. See C. Kittel, Revs. Modern Phys. **21**, 541 (1949), especially Eq. (2.1.17).

and, since $\langle S_R^\beta(t)\rangle_T$ is independent of $\mathbf{R}$ and t,

$$\gamma_R^{\alpha\beta}(t)\simeq N^{-2}\langle S^\alpha\rangle_T\langle S^\beta\rangle_T = s_T^\alpha s_T^\beta, \tag{27}$$

where $\mathbf{S}=\sum_R \mathbf{S}_R$ is the total spin and $\mathbf{s}_T=N^{-1}\langle\mathbf{S}\rangle_T$ is the average spin vector per atom. Above the Curie point $\mathbf{s}_T=0$. Below the Curie point, the foregoing argument and equations apply to a single ferromagnetic domain, in which the magnetization has a definite orientation, so that $\mathbf{s}_T\neq 0$.

Equation (27) requires a further comment. It is possible to derive an apparently different asymptotic formula for the correlation, namely,

$$\gamma_R^{\alpha\beta}(t)\simeq N^{-2}\langle S^\alpha(0)S^\beta(t)\rangle_T. \tag{28}$$

For t finite and $R\to\infty$, it follows from the fact that if $\gamma_R^{\alpha\beta}(t)$ has a limit, the latter can be written for large N in the form $N^{-1}\sum_R \gamma_R^{\alpha\beta}(t)$, leading readily to (28). For R fixed and $|t|\to\infty$, Eq. (28) is also found to hold if one makes the assumption that the Hamiltonian is invariant for simultaneous rotations of all spins, as in Eq. (9). Actually, of course, Eqs. (27) and (28) are equivalent in the limit of large systems, $N\to\infty$. The total spin, although of order N, has then a mean square fluctuation of the same order, so that the average of the product in Eq. (28) can be replaced by the product of the averages, the error in the equation being of order N^{-1} and thus negligible.

The consequences of the asymptotic formula (27) for scattering have been discussed in Sec. II. The asymptotic value of the correlation was shown to determine the part $d^2\sigma_1/d\Omega d\epsilon$ of the scattering which is elastic in the spin system.

We consider next the *range* r_0 and *relaxation time* t_0 of the correlation (26), i.e., the distance and time interval such that Eq. (27) holds for $R\gg r_0$, t arbitrary and for $|t|\gg t_0$, R arbitrary. They have meaning only when the convergence of the correlation toward the asymptotic value (27) is rapid, a condition which is expected to be always verified except at very low temperature (see foregoing section) and near the Curie point, where long-range and slowly varying spontaneous fluctuations of the magnetization affect the correlation (see Sec. V).[19]

Unless one solves first the difficult theoretical problem of finding reliable approximate methods for the calculation of the time-dependent correlation, it is not possible, outside the exceptional temperature regions mentioned above, to determine the actual dependence of $\gamma_R^{\alpha\beta}(t)$ or $\mathbf{R}$ and t, nor even to give an accurate theoretical definition of the range r_0 and the relaxation time t_0. All that can be done is to predict their orders of magnitude. Whereas r_0 must be of order of a few interatomic distances, t_0 is presumably of order of a somewhat larger multiple of the period $\hbar/J$ associated with the interaction J between spins. These estimates, which are known to be correct for liquids (J being replaced by the intermolecular interaction) and can be sharpened on the basis of the experimental data (see below), must hold for temperatures both below and above the Curie point. One would also expect that r_0 and t_0 do not vary too rapidly with the temperature T as long as it does not approach absolute zero or the Curie temperature T_c. It is clear however that, quantitatively, there must be a definite variation with T and a definite difference between the regions $T<T_c$ and $T>T_c$.

Beyond asymptotic value, range and relaxation time, another very important aspect of the time-dependent correlation about which one would like to have at least some qualitative information is its decomposition into real and imaginary parts. In the low-temperature region where spin wave theory applies, the situation is quite simple. As seen immediately from the expressions given in Sec. III, only the real part of the correlation varies with temperature, the imaginary part retaining always the value it has at absolute zero. Although so simple a behavior cannot rigorously prevail at higher temperatures, it is probably always true that the imaginary part $\mathrm{Im}\gamma_R^{\alpha\beta}(t)$, which is due to the noncommutativity of $S_0^\alpha(0)$ and $S_R^\beta(t)$, has a much weaker temperature dependence than the real part. Definite support for this prediction is obtained by considering the asymptotic value of $\mathrm{Im}\gamma_R^{\alpha\beta}(t)$ for R or $|t|\to\infty$ and the range over which it converges toward this value for $R\to\infty$. As follows from Eq. (27), the asymptotic value is zero for all temperatures. From what was said in Sec. III on the correlation at absolute zero and from the discussion of r_0 in the present section, one concludes that the range of $\mathrm{Im}\gamma_R^{\alpha\beta}(t)$ for $R\to\infty$ is of microscopic magnitude at low as well as at general temperatures. This remains true even in the neighborhood of the Curie point since the long-range part which is then present in the correlation originates from macroscopic fluctuations and is therefore real (see Sec. V). Both the asymptotic value of $\mathrm{Im}\gamma_R^{\alpha\beta}(t)$ and the order of magnitude of its convergence range are thus independent of temperature.

Returning now to magnetic scattering of neutrons, we want to extract from the admittedly very crude and incomplete considerations just developed some equally

[19] Even away from these exceptional temperatures, the convergence of the correlation for $|t|\to\infty$ is not strictly short ranged. The actual situation is very likely to be the following. For sufficiently small $|t|$, the $\mathbf{R}$ dependence of $\gamma_R^{\alpha\beta}(t)$ extends only over R values of microscopic dimension of which r_0 gives a measure and which do not exceed a few interatomic distances. This microscopic $\mathbf{R}$ dependence of the correlation is completely damped after a certain time interval, namely for $|t|\gg t_0$, thus giving a slightly more precise definition of the relaxation time t_0. For $|t|\gg t_0$, $\gamma_R^{\alpha\beta}(t)$ reduces to a small macroscopic function, practically constant over microscopic distances, decreasing with time as $|t|^{-1}$ and having a macroscopic range in space which increases as $|t|^{\frac{1}{2}}$. This macroscopic part of the correlation, which is entirely due to macroscopic fluctuations, plays no appreciable role in neutron scattering. Although it was not mentioned in II, a similar long-range part should exist for the pair distribution function $G(\mathbf{r},t)$ in liquids and dense gases. Although again unimportant for neutrons in the presently available wavelength range, it affects light scattering, the properties of which were deduced directly from macroscopic fluctuation theory by L. Landau and G. Placzek, Physik Z. Sowjetunion, **5**, 172 (1934). A detailed exposition and discussion of the above remarks will be left to another publication.

crude consequences concerning the temperature dependence of the magnetic inelastic scattering (total cross section σ_2 in the notation of Sec. II). We restrict ourselves to polycrystals. We have thus to consider only the scalar correlation $\gamma_R(t)$ defined in Eq. (13), and the difference $\gamma_R'(t)$ defined in Eq. (21). As far as these functions are concerned, the results of our discussion can be summarized as follows:

(i) For R or $|t|\to\infty$, $\gamma_R(t)$ converges to s_T^2 and $\gamma_R'(t)$ converges to zero.

(ii) $\gamma_0(0)=s_0(s_0+1)$ and $\gamma_0'(0)=s_0+s_0^2-s_T^2$.

(iii) The convergence in (i) takes place over distances and time intervals which do not change rapidly with temperature, the low-temperature region and the neighborhood of the Curie point T_c being excepted.

(iv) The common imaginary part of $\gamma_R(t)$ and $\gamma_R'(t)$ depends much less on temperature than the real parts of these functions.

These qualitative facts indicate that, if the temperature is increased from the upper limit of validity of spin wave theory (around 200°K or 300°K at most for iron) up to a temperature close to the Curie point T_c (some 100°K below $T_c=1043$°K for iron), the main variation in the function $\gamma_R'(t)$ affects its real part, and, without radical change in its range of convergence toward zero, its value $\gamma_0'(0)$ at $R=t=0$ increases from a number very close to s_0 to a number close to $s_0+s_0^2$. Such a rapid variation of magnitude is on the contrary absent in the temperature range starting somewhat above T_c (around T_c+100°K for iron). As a consequence, in view of Eq. (20), one expects a marked increase of the magnetic inelastic scattering (cross section σ_2) when the temperature varies from low values up to the neighborhood of the Curie point, whereas the temperature variation should be less pronounced beyond the neighborhood of the Curie point. The rapid increase of the cross section σ_2 with temperature below T_c must be particularly striking when the incident neutrons are very slow, so that practically no magnetic scattering takes place at low temperature. One expects then an increase roughly proportional to

$$\gamma_0'(0)-[\gamma_0'(0)]_{T=0}=s_0^2-s_T^2, \tag{29}$$

i.e., proportional to $1-(I_T/I_0)^2$, where I_T is the intensity of magnetization of the magnetic domains at temperature T and I_0 the same quantity at absolute zero. Qualitatively, as shown in I, this expectation is in agreement with the temperature variations of σ_2 for iron, measured by Palevsky and Hughes[3] for neutrons of wavelength ranging from 5 to 13 A, and by Squires[4] for neutrons of 7 A.

No quantitative agreement can of course be hoped for since the actual shape of $\gamma_R(t)$ must unavoidably change to a certain extent with temperature. A measurement of the angular and energy distribution of scattered neutrons would indeed reveal a much more complicated temperature dependence than the simple proportionality factor (29). All we can say at present about this distribution concerns a rough order of magnitude for average momentum and energy transfers in magnetic scattering. From the Fourier transformations in Eqs. (19) and (20) the transfers have to be of order $\hbar/r_0$ and $\hbar/t_0$, respectively, for all incident neutron wavelengths λ_0 for which the collective properties of the spin system appreciably affect the scattering ($\lambda_0\gtrsim 1$ A).

As already mentioned, in order to go beyond the quite crude considerations of this section, in particular to obtain more theoretical information on the angular and energy distribution of scattered neutrons, one has to develop proper approximate methods for the quantitative determination of the correlation. Although this problem falls outside the scope of the present paper, we would like to stress its importance and its interest from the standpoint of general statistical mechanics. Regarding the absolute magnitude of the total cross section, although its accurate calculation would also require a complete determination of the correlation, it is possible to check the consistency of the observed values with the expected orders of magnitude of correlation range r_0 and relaxation time t_0 by choosing some reasonable analytical form for the $\mathbf{R}$ and t dependence of $\gamma_R(t)$. This has been done by C. E. Porter for the case of iron, using the experimental data of Palevsky and Hughes[3] and of Squires.[4] Consistency is obtained for $r_0\simeq 2.3v_0^{\frac{1}{3}}$ (v_0 volume per particle) and $t_0\simeq 23\hbar/J$, and the requirement that reasonable values be obtained for both r_0 and t_0 turns out to determine the two quantities within surprisingly narrow limits, especially t_0 (within some 50 percent). The fact that the microscopic relaxation time t_0 can be determined with fair accuracy from a total scattering cross section measurement is noteworthy and illustrates strikingly the close relationship between inelastic scattering and time-dependence of the correlation between spin orientations.

To the main qualitative feature encountered for the temperature dependence of the magnetic inelastic scattering, namely, a rapid increase with temperature below the Curie point, roughly governed by the decrease of the magnetization, and a less pronounced temperature variation above T_c, one has, of course, to superimpose the very sudden and sharp increase in scattering when the Curie point is approached from below and from above. This additional scattering, the study of which is the object of the next section, is responsible for the sharp peaks observed at the Curie point by Palevsky and Hughes as well as by Squires in the σ_2 *versus* temperature curve for iron.

V. THE NEIGHBORHOOD OF THE CURIE POINT

From the fact that the susceptibility of a ferromagnet increases without limit as the Curie point is approached, there results an unbounded increase in magnitude for the spontaneous fluctuations of the magnetization. These fluctuations in turn scatter neutrons with in-

creasing intensity. Since the fluctuations extend over distances large compared to interatomic distances and decay over times long compared to the microscopic relaxation time t_0 considered above, they produce magnetic scattering with an angular and energy distribution radically different from what is expected at general temperatures. At the same time, from the theoretical standpoint, the applicability of macroscopic methods makes a more complete discussion possible, at least for temperatures above T_c.

Basically the phenomenon under study is very similar to the abnormally abundant scattering occurring in a liquid or a dense gas near critical conditions. In this case, as the critical point is approached, the spontaneous density fluctuations at constant pressure increase indefinitely in magnitude and produce an increasing amount of scattering both for electromagnetic waves (x-rays or light; for light the phenomenon is known as critical opalescence) and for neutrons. In the case of electromagnetic waves it is a very good approximation to neglect the energy transferred by scattering in comparison to the incident energy. The scattering depends then only on the average instantaneous shape of the density distribution as seen from a particle. This shape, expressed by the familiar pair distribution $g(\mathbf{r})$, has been calculated near critical conditions, for T above the critical temperature and r macroscopic, by Ornstein and Zernike, who thus were able to derive the properties of critical scattering in the electromagnetic case.[20] The extension of this theory to neutrons, for which the ratio of energy transfers to incident energy is much larger, requires a knowledge of the time variation of the average density distribution as seen from a point where a particle passed at some initial time. The proper description is given by the time-dependent pair distribution $G(\mathbf{r},t)$ introduced in II, and its calculation near critical conditions, for macroscopic distances and arbitrary times, is carried out in Sec. IV of that paper on the basis of the phenomenological equation for heat conduction.

An entirely analogous procedure can be followed to deal with the present problem of what we might call *critical magnetic scattering*, at temperatures above the Curie point and close to it. One has to calculate the correlation $\gamma_R^{\alpha\beta}(t)$ for R large compared to interatomic distances by determining first, from statistical considerations analogous to those of Ornstein and Zernike, the instantaneous correlation $\gamma_R^{\alpha\beta}(0)$, and by then deriving the time dependence from the phenomenological theory of macroscopic irreversible processes. These two steps will now be carried out under the simplifying assumption that the properties of the spin system are invariant with respect to simultaneous relations of all spins. The correlation $\gamma_R^{\alpha\beta}(t)$ is then of the form $\frac{1}{3}\delta_{\alpha\beta}\gamma_R(t)$, at least in the absence of external magnetic field, and the calculation can be restricted to the scalar correlation $\gamma_R(t)$.

Following the Ornstein-Zernike method in the improved form given to it by Klein and Tisza,[21] we imagine the crystal to be divided into a cubic array of identical cells, of macroscopic size but small compared to the total dimensions of the crystal. We denote by $\mathbf{M}_j$ the magnetic moment of the jth cell. Since the temperature T is assumed larger than T_c, $\mathbf{M}_j$ fluctuates around a vanishing mean value. In view of the macroscopic size of the cells the joined probability distribution of the vectors $\mathbf{M}_j$ is Gaussian:

$$\text{prob}=A\exp\{-\tfrac{1}{2}a_0\sum\mathbf{M}_j\cdot\mathbf{M}_j+a_1\sum\mathbf{M}_j\cdot\mathbf{M}_{j'}\},$$

where the first sum extends over all cells and the second over all pairs of adjacent cells. a_0 and a_1 are positive constants depending on the temperature. A is a normalization constant. Consider now the correlation $\langle\mathbf{M}_j\cdot\mathbf{M}_l\rangle_T$ between the magnetic moments of two cells. It depends only on the relative position of the cells j and l and verifies the equation,

$$a_0\langle\mathbf{M}_j\cdot\mathbf{M}_l\rangle_T-a_1\sum_{j'}\langle\mathbf{M}_{j'}\cdot\mathbf{M}_l\rangle_T=3\delta_{jl}, \tag{30}$$

with the sum extending over the cells adjacent to j. This equation results from the Gaussian character of the probability distribution. It gives immediately for the fluctuation of the total magnetic moment $\mathbf{M}=\sum_j\mathbf{M}_j$,

$$\langle\mathbf{M}\cdot\mathbf{M}\rangle_T=3n(a_0-za_1)^{-1},$$

where n and z are the number of cells in the crystal and the number of cells adjacent to a given cell. The same fluctuation is obtained independently from thermodynamical fluctuation theory,

$$\langle\mathbf{M}\cdot\mathbf{M}\rangle_T=3Vk_BT\chi,$$

V being the volume of the crystal and χ the magnetic susceptibility. From the two last equations,

$$(a_0-za_1)^{-1}=vk_BT\chi, \tag{31}$$

with v the cell volume.

As the Curie point is approached χ increases indefinitely; a_0-za_1 is thus seen to approach zero, so that the correlation occurring in Eq. (30) must have a longer and longer range for the equation to be satisfied. When this range is long compared to the cell dimension $v^{\frac{1}{3}}$, the correlation between cells separated by a distance $R\gg v^{\frac{1}{3}}$ can be identified with the instantaneous correlation $\gamma_R(0)$ according to the equation

$$\langle\mathbf{M}_j\cdot\mathbf{M}_l\rangle_T\simeq(2\beta v/v_0)^2\gamma_R(0),$$

where $\beta=he/2m_0c$ is the Bohr magneton. In this case the long-range part of $\gamma_R(0)$ can thus be obtained from the solution of Eq. (30), itself easily derived by Fourier

[20] L. S. Ornstein and F. Zernike, Proc. Am. Acad. Arts. Sci. **17**, 793 (1914).

[21] M. J. Klein and L. Tisza, Phys. Rev. **76**, 1861 (1949).

analysis.[22] Taking the asymptotic expression of the solution for small values of $v^{\frac{1}{3}}/R$ and of a_0-za_1 (T near T_c), and using further Eq. (31), one finds

$$\gamma_R(0)\simeq(4\pi r_1^2R)^{-1}v_0s_0(s_0+1)\cdot\exp(-\kappa_1R) \quad (32)$$

in terms of two lengths r_1 and κ_1^{-1}, related by the formula

$$(\kappa_1r_1)^2=\chi_1/\chi, \quad (33)$$

where χ_1 is the value which the susceptibility would have at temperature T if there were no exchange interaction between the spins (paramagnetic susceptibility),

$$\chi_1=4\beta^2s_0(s_0+1)/(3k_BTv_0).$$

In contrast with the product κ_1r_1 the length r_1 is unavoidably obtained in terms of the cell size and of the constant a_1,

$$r_1^2=\tfrac{1}{6}k_BT\chi_1za_1v^{\frac{2}{3}}, \quad (34)$$

although its occurrence in Eqs. (32) and (33) clearly establishes its independence of the cell system. Equation (34) shows that r_1 does not vary rapidly with temperature even in the neighborhood of the Curie point. Its order of magnitude is easily obtained from the following remark. For T rising to values substantially larger than T_c, the ratio χ/χ_1 decreases rapidly to values of order one, and, from Eq. (33), the range κ_1^{-1} decreases toward values of order r_1. We know, on the other hand, that the range has to decrease to microscopic size, so that r_1 must certainly be of microscopic dimension, probably of the same order as the correlation range r_0 for temperatures outside the neighborhood of the Curie point (Sec. IV). Whereas r_1 is thus seen to be a microscopic length changing little with temperature, κ_1^{-1} behaves, of course, quite differently. Indeed, for T decreasing toward T_c, the right-hand side of (33) approaches zero and the range κ_1^{-1} of $\gamma_R(0)$ grows beyond any limit until the Curie point is reached and the correlation becomes

$$\gamma_R(0)\simeq(4\pi r_1^2R)^{-1}v_0s_0(s_0+1).$$

Our derivation of Eq. (32) holds only when R and the range κ_1^{-1} are large compared to the cell size. Since the cell size can be chosen at will with the only restriction that it be macroscopic, the essential limits of validity of Eq. (32) are

$$R\gg v_0^{\frac{1}{3}}, \quad \kappa_1v_0^{\frac{1}{3}}=(v_0^{\frac{1}{3}}/r_1)(\chi_1/\chi)^{\frac{1}{2}}\ll 1,$$

or, more quantitatively,

$$R\gtrsim 10v_0^{\frac{1}{3}}, \quad \kappa_1v_0^{\frac{1}{3}}\lesssim 0.1. \quad (35)$$

The last condition defines the upper limit T_1 of the temperature interval $T_c\leqslant T\lesssim T_1$ to which the considerations of the present section apply. Its actual determination is, however, difficult, even with full knowledge of the susceptibility χ, because of the uncertainty concerning the actual magnitude of r_1. The best procedure at present would probably be to consider r_1 as a parameter and to determine its value from neutron scattering data.

Before turning to the time variation of the correlation we want still to draw attention to the complete similarity between Eqs. (32), (33) and the analogous Eqs. (II 36), (II 37) derived in II for the long-range pair distribution function in gases near critical conditions. In particular, the part played there by the isothermal compressibility χ_T is taken here by the magnetic susceptibility χ and the isothermal compressibility in absence of forces $(\rho k_BT)^{-1}$ (ideal gas) is here replaced by the paramagnetic susceptibility χ_1.

The time dependence of the correlation $\gamma_R(t)$ must now be derived for macroscopic R. For the reasons explained in II in the case of gases near critical conditions, the time dependence is given by the average decay in time of fluctuations of the magnetization, itself described by the phenomenological equations for irreversible processes in the spin system. A formal derivation of the latter from the conservation equations and the equation for entropy production can be obtained by the methods of the thermodynamics of irreversible processes in a way entirely similar to the derivation of the Navier-Stokes equations.[23] The situation is here particularly simple above the Curie point if, with a good approximation, the system is invariant for simultaneous rotations of all spins. For reasons of invariance the phenomenological equations contain then no coupling between the magnetization and any other macroscopic variable. The equation for the density of magnetization $\mathfrak{M}(\mathbf{r},t)$ is of the diffusion type

$$\partial\mathfrak{M}/\partial t=(\lambda/\chi)\Delta\mathfrak{M}, \quad (36)$$

where Δ is the Laplacian in $\mathbf{r}$ and λ a phenomenological constant related by

$$\tau(S)=\frac{\lambda}{T\chi^2}\sum_{\alpha,\beta}\left(\frac{\partial\mathfrak{M}_\alpha}{\partial x_\beta}\right)^2 \quad (37)$$

to the amount $\tau(S)$ of entropy produced per unit volume and unit time by the dissipative processes occurring when the system returns to equilibrium from a state characterized by an inhomogeneous distribution of magnetization of small magnitude. The constant λ in Eqs. (36) and (37) is so chosen that the entropy production $\tau(S)$ does no longer contain the susceptibility χ when (37) is expressed in terms of the intensive variable conjugate to $\mathfrak{M}$ in the sense of thermodynamics. This variable (the magnetic field which would produce the

[22] For this solution see Klein and Tisza (reference 21), also F. Zernike, Physica 7, 565 (1940) where a similar equation is studied in connection with the order-disorder problem.

[23] For the phenomenological theory of irreversible processes, see I. Prigogine, *Etude Thermodynamique des Phènomènes Irrèversibles* (Editions Desoer, Liège, 1947), and S. R. de Groot, *Thermodynamics of Irreversible Processes* (North-Holland Publishing Company, Amsterdam and Interscience Publishers, New York, 1951).

magnetization) retains spontaneous fluctuations of normal size even when T approaches T_c, so that λ remains finite in the neighborhood of the Curie point.[24] It would clearly be desirable to get some insight into the actual mechanism of the dissipative processes here involved and to obtain in this way for Eq. (36) and for the finiteness of λ a more reliable justification than the highly formal derivation sketched above. One would then get also a theoretical estimate of the order of magnitude of λ. No attempt will be made to answer these questions here.

Accepting the validity of Eq. (36) we conclude immediately that the decay in time of a plane wave fluctuation of the magnetization is given by the factor $\exp(-\Lambda_1 k^2 t)$ for $t>0$, with $\mathbf{k}$ the wave vector and $\Lambda_1=\lambda/\chi$.[25] Proceeding as in II, one obtains

$$\gamma_R(t)\simeq(4\pi r_1^2)^{-1}v_0 s_0(s_0+1)(4\pi\Lambda_1|t|)^{-\frac{3}{2}} \times\int\exp\left\{-\frac{|\mathbf{R}-\mathbf{R}'|^2}{4\Lambda_1|t|}-\kappa_1 R'\right\}\cdot\frac{d\mathbf{R}'}{R'}, \quad (38)$$

or

$$\gamma_R(t)\simeq(4\pi r_1^2 R)^{-1}v_0 s_0(s_0+1)\Psi[\kappa_1(4\Lambda_1|t|)^{\frac{1}{2}},R(4\Lambda_1|t|)^{-\frac{1}{2}}],$$

in terms of the function Ψ defined in II, Eq. (II 43). These equations hold in the R and T ranges defined by Eqs. (35), for all macroscopic times.

The cross section for critical magnetic scattering can now be obtained by replacing $\gamma_R{}'^{\alpha\beta}(t)$ in Eq. (19) by $\frac{1}{3}\delta_{\alpha\beta}\gamma_R(t)$ as given by Eq. (38). The calculation is straightforward and gives for a single crystal

$$\left(\frac{d^2\sigma}{d\Omega d\epsilon}\right)_{\text{crit}}=\left(\frac{2ge^2}{m_0c^2}\right)^2\frac{2N}{3\pi\hbar}s_0(s_0+1)\frac{k}{k_0}|F(\kappa)|^2 \times\sum_{\tau}\frac{1}{r_1^2\{|\kappa-\tau|^2+\kappa_1^2\}}\cdot\frac{\Lambda|\kappa-\tau|^2}{\Lambda_1^2|\kappa-\tau|^4+\omega^2}. \quad (39)$$

This formula, which is applicable only in the temperature interval $T_c\lesssim T\lesssim T_1$ here defined by the condition $\kappa_1 v_0^{\frac{1}{3}}\lesssim 0.1$, must be understood as describing a special type of scattering which appears in addition to the general scattering described in the last section when the Curie point is approached. Since both Λ_1 and κ_1 tend to zero when $T\to T_c$, this scattering is characterized by small energy transfers and by momentum transfers $\hbar\kappa$ with κ close to some reciprocal lattice vector τ

$$|\kappa-\tau|\ll v_0^{-\frac{1}{3}}, \quad \hbar\omega\ll J, \quad (40)$$

where J gives the order of magnitude of energy transfers in noncritical scattering. The conditions (40) give at the same time the limits of applicability of Eq. (39). It is seen in particular that in the sum over reciprocal lattice vectors only one term can be significant for each scattering, namely, the term belonging to the vector τ for which the first condition (40) holds.

Equation (19), and thus Eq. (39), neglect the atomic vibrations. In the case of the critical scattering, in view of the slow variation of the long-range correlation (38) with $\mathbf{R}$ and t, it is consistent to take the atomic vibrations partly into account by replacing $\delta(\mathbf{r}-\mathbf{R})$ by $G_R^{(\infty)}(\mathbf{r})$ in the derivation of Eq. (19). The improvement thus obtained in Eq. (39) is the multiplication of the cross section by the Debye-Waller factor $\exp\{-\langle(\kappa\cdot\mathbf{u})^2\rangle_T\}$. It does not affect the very special distribution of momentum and energy transfers described by the conditions (40). In view of the first of these, the cross section can be written[26]

$$\left(\frac{d^2\sigma}{d\Omega d\epsilon}\right)_{\text{crit}}=\left(\frac{2ge^2}{m_0c^2}\right)^2\frac{2N}{3\pi\hbar}s_0(s_0+1)\frac{k}{k_0}|F(\kappa)|^2 \times\sum_{\tau}\frac{\exp\{-\langle(\tau\cdot\mathbf{u})^2\rangle_T\}}{r_1^2\{|\kappa-\tau|^2+\kappa_1^2\}}\cdot\frac{\Lambda_1|\kappa-\tau|^2}{\Lambda_1^2|\kappa-\tau|^4+\omega^2}. \quad (41)$$

The experimental conditions under which critical magnetic scattering is observable are immediately determined by its distribution (40) of momentum and energy transfers. To the term with $\tau=0$ in the cross section corresponds scattering with $\kappa\ll v_0^{-\frac{1}{3}}$, i.e., small angle scattering whenever the incident wavelength is not too large compared to the interatomic spacing $v_0^{\frac{1}{3}}$. In our approximations this scattering is independent of crystal orientation. It occurs in single crystals or polycrystals alike. Critical scattering corresponding to a term with $\tau\neq 0$ can only be observed if the form factor $F(\kappa)$ is not too small at $\kappa=\tau$ and if it is possible to satisfy simultaneously both conditions (40). The latter requirement can only be fulfilled for incident wavelengths close to or shorter than the Bragg cut-off wavelength, and, for a single crystal, near Bragg position. In the case of a polycrystal the critical scattering for $\tau\neq 0$ is greatly weakened by the averaging process over orientations and its observation is further hampered by its proximity to the intense Debye-Scherrer rings.

Whereas we had noticed, as far as correlations are concerned, an almost perfect analogy between the considerations of the present section and the discussion of gases near the critical point presented in II, we have met with an important difference regarding the scattering, namely the occurrence in the cross section (41) of the terms with $\tau\neq 0$, evidently absent in the gas case. These terms reflect, of course, the fact that, despite the

[24] The situation is here analogous to the case of a gas or liquid near the critical point, where the coefficient of heat conduction remains finite.

[25] Λ_1 corresponds to one-fourth of the constant Λ_0 defined in II, Eq. (II 40).

[26] To take the effect of atomic vibrations completely into account one would still have to add to Eq. (41) a small amount of critical scattering coming formally from the difference between $G_R(\mathbf{r},t)$ and $G_R^{(\infty)}(\mathbf{r})$. This scattering, in contrast with the scattering described by (41), is inelastic in the lattice vibrations and, apart from being much smaller, it has an entirely different distribution of momentum and energy transfers. It is of more restricted experimental interest.

intense disorderly fluctuations of the magnetization, the spin system retains the regular arrangement of positions in space imposed by the lattice structure of the underlying crystal. Their occurrence is of considerable practical interest by permitting the observation of critical scattering in absence of any elastic peak for a single crystal rotated slightly from Bragg position.

Our theoretical discussion has dealt with a ferromagnetic spin system at temperatures higher than the Curie point. The situation for $T<T_c$ is complicated by the presence of permanent magnetization and would therefore require a special discussion. It is, however, to be expected that the properties of the critical magnetic scattering derived above hold true without essential modifications for $T<T_c$, T being again in the vicinity of T_c, since the magnetization has there also abnormally large fluctuations.

Both in transmission (total cross section) and in differential measurements there is clear evidence that the critical magnetic scattering has been experimentally observed. The peak at the Curie point obtained by Palevsky and Hughes[3] as well as by Squires[4] in the transmission *versus* temperature curve for iron is undoubtedly to be ascribed to critical scattering. It comes from the contribution of the term $\tau=0$ of (41) to the total cross section. As the Curie point is approached, this contribution, unlike that of the other terms, would increase indefinitely in the ideal case of a perfect geometry. The greater height and sharpness of the peak obtained by Squires is a consequence of a better temperature control than in the experiment of Palevsky and Hughes.

The occurrence of abundant small angle scattering of 0.9-A neutrons in polycrystalline iron for temperatures in the vicinity of T_c has been observed by Wilkinson and Shull,[27] with a pronounced maximum in the amount of scattering at the Curie point itself. McReynolds and Riste,[28] investigating the magnetic structure of a single crystal of Fe_3O_4 with 1.3-A neutrons, have established the existence, around the Bragg directions, of diffuse magnetic peaks of rapidly increasing intensity as the Curie point is approached from either side. The results of both experiments are in good agreement with the theoretical predictions presented above. They tend to indicate that, at least for Fe and Fe_3O_4, critical scattering takes place over a rather wide neighborhood of the Curie point, extending roughly to some 100° below and above T_c.

[27] M. K. Wilkinson and C. G. Shull, Phys. Rev. **95**, 1439 (1954), and private communication.
[28] A. W. McReynolds and T. Riste (to be published).

VI. CONCLUDING REMARKS

Our discussion of the time-dependent correlation between spins and of magnetic neutron scattering in ferromagnetic crystals has dealt only with the points of greatest importance for the qualitative understanding of the phenomena. Several questions have been raised without any attempt being made at their solution. Some of them, although difficult, are of considerable interest from the standpoint of general statistical mechanics, and further experimentation is likely to make their study desirable also from a more practical standpoint.

The present paper is entirely based on the atomic (Heisenberg) model of ferromagnetism, ascribing a spin of fixed length to each atom. The general method, however, consisting in the use of time-dependent correlations between pairs of spins and founded on Eqs. (1), (3), and (4), is, of course, applicable to magnetic scattering by the spins of an arbitrary system of electrons. The spin vectors in Eq. (4) have only to be taken as belonging to the individual electrons.[29] One could thus attempt to carry out our whole discussion for the collective (electron band) theory of ferromagnetism. No deep alteration of our main qualitative conclusions is probably to be expected. Some support for this view is given by the case of nickel which, having an average of 0.6 electron spin per atom, clearly requires a collective treatment. The results of transmission experiments of Squires[4] with 7-A neutrons seem to be in rough agreement with the main qualitative predictions one would obtain from our methods: the transmission *versus* temperature curve has a peak at the Curie point, and the magnitude of the magnetic cross section, although very uncertain as a consequence of its small size, is compatible with what would be obtained from the observed magnitude in iron by correcting for the smaller average atomic spin.

Another problem deserving attention concerns the case of antiferromagnetic crystals. The dynamics of such systems is certainly less well understood than is the case for ferromagnets, and instructive information would undoubtedly be revealed by inelastic neutron scattering experiments. The extension of our theoretical discussion to antiferromagnets raises also a number of questions which might be worth investigating.

We would finally like to express our appreciation to D. J. Hughes, H. Palevsky, G. L. Squires, C. G. Shull, and A. W. McReynolds for making their experimental results available before publication and for many stimulating discussions, to G. Placzek for various useful comments, and to C. E. Porter for communicating the results of unpublished calculations.

[29] The vectorial indices R, R' must be replaced by numerical indices labeling the electrons.

Magnetoresistance Effect in Cubic Semiconductors with Spheroidal Energy Surfaces

MOTOICHI SHIBUYA
Electrotechnical Laboratory, Tokyo, Japan

(Received February 26, 1954; revised manuscript received March 30, 1954)

The collision frequency of electrons having a spheroidal energy surface with acoustical modes of vibration is calculated without neglecting phonon energy. Using an asymptotic form in which the collision frequency is proportional to the square root of their energy, the electronic current in a semiconductor in combined magnetic and weak electric fields can be calculated in a closed form by the formal theory of conductivity. The magnetoresistance effect in oriented single crystals of n- and p-type germanium observed by Pearson and Suhl may be discussed consistently at least semiquantitatively with this calculation in both weak and strong magnetic fields.

1. INTRODUCTION

A FRUITFUL study of the magnetoresistance effect in oriented single crystals of germanium was performed by Pearson and Suhl.[1] They compared their results with theories developed by Seitz[2] for weak magnetic fields and by Harding[3] for strong fields, and they found certain discrepancies between the theories and experiment. They pointed out that the theory based upon anisotropies in the relaxation time alone did not agree with their observations and that the idea of nonspherical energy surfaces in the Brillouin zone should be included in a better theory.

It seems, however, that the theory based upon anisotropy in the relaxation time would agree with their observations in p-type samples at least qualitatively, if one took into account the proper sign of the integral I in the electronic theory proposed by Seitz.[4]

There still remain some discrepancies between theory and experiment even when the proper sign of this integral is taken into account. First, Seitz's weak field theory leads to the result that β is negative and both γ and δ are positive, whereas in Pearson and Suhl's experiment δ is negative in the n-type samples; and second, large saturation values of magnetoresistance are observed which cannot be explained with Harding's strong-field calculations.

Johnson and Whitesell[5] have recently studied the effects of both impurity scattering and intrinsic conduction upon the magnetoresistance, and found that the former increases the gap between theory and experiment and the latter decreases the gap. But there are no experimental investigations satisfying the latter condition.

In order to overcome the main discrepancies mentioned above, we here assume cubically equivalent families of spheroidal energy surfaces, the simplest nonspherical form, in the Brillouin zone. First, in the appendix, the collision frequency of electrons having a spheroidal energy surface with acoustical modes of vibration will be calculated along the same lines as in Seitz's theory.[6] The collision frequency of rather high-energy electrons may be proved to be proportional to the square root of their energy; this is the generalization of constant mean free path in the case of a spherical surface. Using this asymptotic form of the collision frequency, in the next section, the current density may be expressed in a closed form as a function of both magnetic and weak electric fields with the same procedure as that used by Blochinzev and Nordheim[7] in discussing the electrical properties of divalent metals. Only three typical but special cases are considered: cubically symmetric families of spheroidal surfaces may be found along six (100) axes (Case a), along twelve (110) axes (Case b), and along eight (111) axes (Case c). In the final section, we show that the observed effects in p- and n-type germanium samples may be semiquantitatively discussed for (Case a) and (Case c), respectively. The validity of the approximations and simplifications in this calculation will be discussed there briefly.

2. THE MAGNETORESISTANCE EFFECT

As shown in the appendix, the asymptotic form of the collision frequency is dependent upon the wave number only through energy. Using this, we can derive the magnetoresistance of a cubic semiconductor in a closed form with the same procedure as that used by Blochinzev and Nordheim[7] who discussed the magnetoresistance in divalent metals.

In the formal theory of conductivity, when the collision frequency depends upon the wave number $\mathbf{K}$ simply through energy and the energy surface is ellipsoidal, the solution of the Boltzmann equation in a weak electric field $\mathbf{E}$ can be obtained in the following finite form without any assumption about the magnitude of the magnetic field $\mathbf{H}$:

$$f=f_0-\phi(df_0/dW), \tag{1}$$

where

$$\phi=(2\pi/h)(\mathbf{G}\cdot\nabla_k W), \tag{2}$$

[1] G. L. Pearson and H. Suhl, Phys. Rev. **83**, 768 (1951).
[2] F. Seitz, Phys. Rev. **79**, 372 (1950).
[3] J. W. Harding, Proc. Roy. Soc. (London) **140**, 205 (1933).
[4] The integral I in Seitz's paper (reference 2) should be negative; Eq. (22c) should read $I=-ne(9\pi\mu^3)/16c^3$.
[5] V. A. Johnson and W. J. Whitesell, Phys. Rev. **89**, 941 (1953).
[6] F. Seitz, Phys. Rev. **73**, 549 (1948).
[7] D. Blochinzev and L. Nordheim, Z. Physik **84**, 168 (1933).

in which

$$\mathbf{G}=\frac{-e\{\nu^2\mathbf{E}-\nu(e/c)[(\mathfrak{M}^{-1}\mathbf{E})\times\mathbf{H}]+(e/c)^2(\mathbf{E}\cdot\mathbf{H})\mathfrak{M}H/\|\mathfrak{M}\|\}}{\nu^2+(e/c)^2(\mathfrak{M}\mathbf{H}\cdot\mathbf{H})/\|\mathfrak{M}\|}, \tag{3}$$

where $\mathfrak{M}$ is the effective mass tensor and $\|\mathfrak{M}\|$ its determinant. Using this distribution function, we can readily calculate the current density $\mathbf{I}$:

$$\mathbf{I}=-(e/2\pi^3\hbar)\int\int\int f\nabla_k W d\mathbf{K}. \tag{4}$$

When the energy surface is given by Eq. (A.1) and the corresponding collision frequency is given by Eq. (A.14), the three components of $\mathbf{I}$ may be expressed in the following closed form, f_0 being Maxwellian:

$$\begin{aligned}
I_1&=NeA\tau[E_1+\pi^{\frac{1}{2}}B(E_2H_3-E_3H_2)P(X)\\
&\qquad+\{B^2(\mathbf{E}\cdot\mathbf{H})H_1-XE_1\}Q(X)],\\
I_2&=NeA[E_2+\pi^{\frac{1}{2}}B(E_3H_1-\tau E_1H_3)P(X)\\
&\qquad+\{B^2\tau(\mathbf{E}\cdot\mathbf{H})H_2-XE_2\}Q(X)],\\
I_3&=NeA[E_3+\pi^{\frac{1}{2}}B(\tau E_1H_2-E_2H_1)P(X)\\
&\qquad+\{B^2\tau(\mathbf{E}\cdot\mathbf{H})H_3-XE_3\}Q(X)],
\end{aligned} \tag{5}$$

where N is the carrier density, τ and M_1 are given by Eq. (A.5), and three quantities A, B, and X and two functions P and Q are introduced which are defined by the following equations:

$$A=\mu_0 M_1^{-5/2}\tau^{-2}, \tag{6}$$

$$B=\pm 3\pi^{\frac{1}{2}}A/4c, \tag{7}$$

$$X=B^2\{H_1^2+\tau(H_2^2+H_3^2)\}, \tag{8}$$

$$P(X)=\{\tfrac{1}{2}-X+\pi^{\frac{1}{2}}X^{\frac{1}{2}}e^X[1-\mathrm{Erf}(X^{\frac{1}{2}})]\}, \tag{9}$$

and

$$Q(X)=1+Xe^X\,\mathrm{Ei}(-X), \tag{10}$$

in which c is the velocity of light and μ_0 is the conductivity mobility in the case of a spherical energy surface, that is, with scalar mass m_0, already obtained by Seitz. Ei is the exponential integral and Erf is the error function integral. In Eq. (7), the plus sign should be taken for hole carriers, and the minus sign for electrons.

To satisfy the cubic symmetry in the Brillouin zone, we must introduce several families of spheroidal surfaces in the case of cubic crystals. Only three special cases are considered in this calculation.

(Case a): We assume that the band edges may occur at six cubically equivalent points $(\pm j, 0, 0)$, $(0, \pm j, 0)$, $(0, 0, \pm j)$, and that at each point we may find a spheroidal energy surface of the same kind, whose rotational axis coincides with each (100) axis, as shown in Fig. 1.

(Case b): In this case, we assume that twelve spheroidal surfaces of the same kind may occur along twelve (110) axes just as in (Case a).

(Case c): In this case, we assume that eight spheroids may occur along eight (111) axes just as in (Case a).

In order to utilize the results obtained above, we assume further that these several families of surfaces are far apart from one another and that the transition of electrons from one family to a different one is forbidden. Thus the total current may be obtained by simply adding the independent currents arising from each family.

In the preceding calculation, for instance in Eq. (5), the coordinate axes defined with suffixes 1, 2, and 3 are so chosen that they form a normal right-hand system in ascending order of suffixes and the 1 axis coincides with the rotational axis of the spheroid. In the following calculation another normal right-hand system with suffixes x, y, and z is introduced, which is formed with the cubic axes (100), (010), and (001) in cubic crystals. The final results will be discussed with this system because of the many advantages which t offers.

(Case a). 6 Spheroids along the (100) Axes

In this case, the component of the total current density parallel to one of the cubic axes may easily be obtained with the following procedure.

The carrier density of each family is $N/6$, and the current density from the $(\bar{1}00)$ family is equivalent to that from the (100) family; and the same relation also holds for the other two pairs. Therefore, permuting the suffixes 1, 2, and 3 in Eq. (5), with x, y, and z, with y, z, and x, and with z, x, and y, successively, summing up the components of current density, and dividing by three, we can obtain the total current density. We will write down only the expression for the x component because the two other components may easily be obtained by changing the suffixes x, y, and z cyclically in this expression:

$$\begin{aligned}
I_x&=(NeA/3)[(\tau+2)E_x\\
&\qquad+\pi^{\frac{1}{2}}B\{E_yH_z[\tau P(X_x)+\tau P(X_y)+P(X_z)]\\
&\qquad-E_zH_y[\tau P(X_x)+P(X_y)+\tau P(X_z)]\}\\
&\qquad+\tau B^2(\mathbf{E}\cdot\mathbf{H})H_x[Q(X_x)+Q(X_y)+Q(X_z)]\\
&\qquad-E_x[\tau X_xQ(X_x)+X_yQ(X_y)+X_zQ(X_z)]],
\end{aligned} \tag{11}$$

where

$$X_x=B^2[H_x^2+\tau(H_y^2+H_z^2)], \tag{12}$$

and X_y and X_z are obtained by cyclically changing the suffixes x, y, and z in X_x. The two functions P and Q were already defined in Eqs. (9) and (10), respectively.

(Case b). 12 Spheroids along (110) Axes

In this case, the twelve families may be divided into three groups:

x group: (011), $(0\bar{1}\bar{1})$, $(01\bar{1})$, $(0\bar{1}1)$,
y group: (101), $(\bar{1}0\bar{1})$, $(10\bar{1})$, $(\bar{1}01)$,
z group: (110), $(\bar{1}\bar{1}0)$, $(1\bar{1}0)$, $(\bar{1}10)$.

Now the $(0\bar{1}\bar{1})$ family is equivalent to the (011) family as far as the contribution to the total current density is concerned, and the same relation holds also for the other five pairs. Thus the contribution from the x group is obtained when the current density from both the (011) and $(01\bar{1})$ families is given. The cubic components of the current density from the (011) family will be obtained in the following manner. We choose three principal axes of this spheroid for convenience of calculation as follows:

1 axis; (011), 2 axis; $(0\bar{1}1)$, and 3 axis; (100).

The three components of **I** along these principal axes, given by Eq. (5) with carrier density $N/12$, can be transformed to the cubic components by

$$I_x=I_3,\quad I_y=2^{-\frac{1}{2}}(I_1-I_2),\quad \text{and}\quad I_z=2^{-\frac{1}{2}}(I_1+I_2). \tag{13}$$

Also, the components of the vectors **E** and **H** in Eq. (5) may be given as the following linear combinations of cubic components:

$$\begin{aligned}&E_1=2^{-\frac{1}{2}}(E_y+E_z),\quad E_2=2^{-\frac{1}{2}}(-E_y+E_z),\quad E_3=E_x,\\ &H_1=2^{-\frac{1}{2}}(H_y+H_z),\quad H_2=2^{-\frac{1}{2}}(-H_y+H_z),\ \text{and}\ H_3=H_x.\end{aligned} \tag{14}$$

As the current density from the $(01\bar{1})$ family can also be obtained with a similar orthogonal transformation, the current density from the x group can readily be calculated. Those from the y and z groups can easily be obtained by cyclically changing the suffixes as usual. Thus the x component of the total current density in this case becomes:

$$\begin{aligned}I_x=&(NeA/3)[(r+2)E_x+(B\pi^{\frac{1}{2}}/4)\\ &\times\{(r+1)(E_yH_z-E_zH_y)[P(X_+)+P(X_-)\\ &+P(Y_+)+P(Y_-)+P(Z_+)+P(Z_-)]\\ &+(r-1)[E_yH_z(P(Z_+)+P(Z_-))\\ &-E_zH_y(P(Y_+)+P(Y_-))+(E_yH_y-E_zH_z)\\ &\times(P(X_+)-P(X_-))+E_yH_z(P(Y_+)-P(Y_-))\\ &-E_zH_x(P(Z_+)-P(Z_-))]\}\\ &+(rB^2/2)(\mathbf{E}\cdot\mathbf{H})H_x[Q(X_+)+Q(X_-)\\ &+Q(Y_+)+Q(Y_-)+Q(Z_+)+Q(Z_-)]\\ &-(r+1)(E_x/4)[X_+Q(X_+)+X_-Q(X_-)\\ &+Y_+Q(Y_+)+Y_-Q(Y_-)+Z_+Q(Z_+)+Z_-Q(Z_-)]\\ &+[(r-1)/4]\{E_x[X_+Q(X_+)+X_-Q(X_-)]\\ &+E_y[Z_+Q(Z_+)-Z_-Q(Z_-)]\\ &+E_z[Y_+Q(Y_+)-Y_-Q(Y_-)]\}],\end{aligned} \tag{15}$$

where

$$X_\pm=(B^2/2)[(r+1)H^2+(r-1)(H_x^2\pm 2H_yH_z)], \tag{16}$$

and $Y_\pm$ and $Z_\pm$ are given by cyclically changing the suffixes. Also I_y and I_z are obtained with the same procedure.

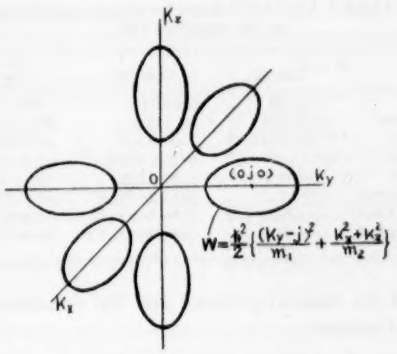

FIG. 1. Schematic diagram of the energy-momentum surfaces in (Case a).

(Case c). 8 Spheroids along (111) Axes

With nearly the same procedure as used in the above two cases, we can obtain I_x in this case as follows,

$$\begin{aligned}I_x=&(NeA/3)[(r+2)E_x+(B\pi^{\frac{1}{2}}/4)\\ &\times\{(2r+1)(E_yH_z-E_zH_y)(P_a+P_b+P_c+P_d)\\ &-(r-1)[(E_yH_y-E_zH_z)(P_a+P_b-P_c-P_d)\\ &+H_x((E_y-E_z)(P_a-P_b)+(E_y+E_z)(P_c-P_d))]\}\\ &+(3rB^2/4)(\mathbf{E}\cdot\mathbf{H})H_x(Q_a+Q_b+Q_c+Q_d)\\ &-(r+2)(E_x/4)(X_aQ_a+X_bQ_b+X_cQ_c+X_dQ_d)\\ &-[(r-1)/4][(E_y+E_z)(X_aQ_a-X_bQ_b)\\ &-(E_y-E_z)(X_cQ_c-X_dQ_d)]],\end{aligned} \tag{17}$$

where P_i and Q_i $(i=a, b, c, \text{or } d)$ are the abbreviations of $P(X_i)$ and $Q(X_i)$, respectively, and

$$\begin{aligned}X_a=&(B^2/3)[(2r+1)H^2\\ &+2(1-r)(H_yH_z+H_zH_x+H_xH_y)],\\ X_b=&(B^2/3)[(2r+1)H^2\\ &+2(1-r)(H_yH_z-H_zH_x-H_xH_y)],\\ X_c=&(B^2/3)[(2r+1)H^2\\ &+2(1-r)(-H_yH_z+H_zH_x-H_xH_y)],\\ X_d=&(B^2/3)[(2r+1)H^2\\ &+2(1-r)(-H_yH_z-H_zH_x+H_xH_y)].\end{aligned} \tag{18}$$

Now the current density **I** in a weak electric field **E** may be written in the following matrix form with the conductivity tensor $\mathfrak{L}$,

$$\begin{pmatrix}I_x\\ I_y\\ I_z\end{pmatrix}=\begin{pmatrix}L_{xx}, & L_{xy}, & L_{xz}\\ L_{yx}, & L_{yy}, & L_{yz}\\ L_{zx}, & L_{zy}, & L_{zz}\end{pmatrix}\cdot\begin{pmatrix}E_x\\ E_y\\ E_z\end{pmatrix}. \tag{19}$$

For the three special cases mentioned above, we have already obtained the complicated expressions for this conductivity tensor in a magnetic field. The resistivity tensor $\mathfrak{W}$ can be readily calculated, as it is the inverse tensor of $\mathfrak{L}$. The magnetoresistivity ρ_H will be calculated by the following equation with nine components

TABLE I. Calculated magnetoresistance constants at low magnetic field.

	Case (a)	Case (b)	Case (c)
σ/NeA	$(r+2)/3$	$(r+2)/3$	$(r+2)/3$
$2\alpha/NeAB_x^2$	$(2r+1)/3$	$(2r+1)/3$	$(2r+1)/3$
$\beta/NeAB^2$	$-(r^2+r+1)/3$	$-(r+1)^2/4$	$-(r+2)(2r+1)/9$
$\gamma/NeAB^2$	r	$(r^2+4r+1)/6$	$(r+2)(2r+1)/9$
$\delta/NeAB^2$	$(r-1)^2/3$	$-2(r-1)^2/12$	$-2(r-1)^2/9$
$-\epsilon'/NeAB^2x^2$	$(2r^2+1)/3$	$(3r^2+2r+1)/6$	$(2r+1)^2/9$
$-\lambda'/NeAB^2x^2$	$r(r+2)/3$	$(7r^2+2r+3)/12$	$(2r^2+1)/3$
$-\eta'/NeAB^2x^2$	$r(r+2)/3$	$(7r^2+2r+3)/12$	$(2r^2+1)/3$

W_{ij} of the resistivity tensor and the direction of the current vector:

$$\rho_H I^2 = W_{xx}I_x^2+W_{yy}I_y^2+W_{zz}I_z^2+(W_{xy}+W_{yx})I_xI_y +(W_{yz}+W_{zy})I_yI_z+(W_{zx}+W_{xz})I_zI_x, \quad (20)$$

and the generalized Hall constant R_H in a magnetic field is calculated by

$$R_H=-(\mathbf{E}\cdot[\mathbf{I}\times\mathbf{H}])/(IH)^2. \quad (21)$$

Now we return to our three special cases. Before discussing the magnetoresistivity and generalized Hall constant, some properties of the conductivity tensor are investigated.

The magnetoresistance constants at low magnetic field strength, introduced by Seitz in his equation

$$\mathbf{I}=\sigma\mathbf{E}+\alpha[\mathbf{E}\times\mathbf{H}]+\beta H^2\mathbf{E}+\gamma(\mathbf{E}\cdot\mathbf{H})\mathbf{H}+\delta\mathfrak{T}E+\cdots, \quad (22)$$

can readily be obtained with an ascending power series expansion in $\mathbf{H}$ of each component of $\mathfrak{L}$. These are listed in Table I. The normal conductivity and Hall constant are certainly scalar quantities, but they depend differently upon r; thus the relation between the conductivity mobility μ_σ and the Hall mobility μ_H becomes

$$\frac{\mu_H}{\mu_\sigma}=\frac{3\pi}{8}\frac{3(2r+1)}{(r+2)^2}. \quad (23)$$

This relation between the Hall and conductivity mobilities has already been discussed qualitatively with the idea of the re-entrant energy surface by Shockley,[8] but here we consider it quantitatively with spheroids.

There are also some linear relations among the constants which we think are due to the spheroidal approximation. For instance,

$$\beta+\gamma+\delta=0 \quad \text{for Case (a)}, \quad (24)$$

$$\beta+\gamma-\delta=0 \quad \text{for Case (b)}, \quad (25)$$

$$\beta+\gamma=0 \quad \text{for Case (c)}, \quad (26)$$

and

$$\lambda'=\eta' \quad \text{for all of the three cases.} \quad (27)$$

When we put r equal to 1, these small field constants are reduced to those obtained by Seitz in his electronic theory without anisotropy of the relaxation time.

[8] W. Shockley, *Electrons and Holes in Semiconductors* (D. Van Nostrand Company, Inc., New York, 1950).

The magnetoresistivity and Hall constant in a strong magnetic field may be discussed with Eqs. (20) and (21), respectively, but it is in general very tedious. However, it becomes somewhat less laborious when $\mathbf{H}$ is parallel to one of the special crystal axes, for instance, (100), (110), or (111).

When $\mathbf{H}$ is parallel to the (100) axis, the conductivity tensor $\mathfrak{L}$ has the following form, for all three cases:

$$\mathfrak{L}\equiv\begin{bmatrix}L_1, & 0, & 0\\ 0, & L_2, & L_3\\ 0, & -L_3, & L_2\end{bmatrix}. \quad (28)$$

Similarly the resistivity tensor has the same form, and thus the longitudinal magnetoresistivity ρ_{11}, the transverse magnetoresistivity $\rho_\perp$, and the Hall constant R_H become:

$$\rho_{11}=W_1=1/L_1, \quad \rho_\perp=W_2=L_2/(L_2^2+L_3^2), \quad HR_H=W_3=L_3/(L_2^2+L_3^2). \quad (29)$$

It is very interesting to note that in this case both $\rho_\perp$ and R_H are independent of the vector $\mathbf{I}$.

When $\mathbf{H}$ is parallel to the (111) axis, the resistivity tensor has the following form:

$$\mathfrak{W}\equiv\begin{bmatrix}W_1, & W_2, & W_3\\ W_3, & W_1, & W_2\\ W_2, & W_3, & W_1\end{bmatrix}. \quad (30)$$

Thus ρ_{11}, $\rho_\perp$, and R_H become:

$$\rho_{11}=W_1+W_2+W_3=(L_1+L_2+L_3)^{-1},$$
$$\rho_\perp=W_1-(W_2+W_3)/2=(2L_1-L_2-L_3)/[(L_1-L_2)^2+(L_2-L_3)^2+(L_3-L_1)^2], \quad (31)$$
$$HR_H3^{-\frac{1}{2}}=(W_2-W_3)/2=(L_2-L_3)/2[(L_1-L_2)^2+(L_2-L_3)^2+(L_3-L_1)^2].$$

When $\mathbf{H}$ is parallel to the (110) axis, $\mathfrak{L}$ has the following form:

$$\mathfrak{L}\equiv\begin{bmatrix}L_1, & L_3, & -L_4\\ L_3, & L_1, & L_4\\ L_4, & -L_4, & L_2\end{bmatrix}, \quad (32)$$

and

$$\rho_{11}=(W_1+W_3)=(L_1+L_3)^{-1},$$
$$\rho_\perp=(W_1-W_3)-Z^2(W_1-W_2-W_3) =\{L_2+Z^2(L_1-L_2-L_3)\}/\{2L_4^2+L_2(L_1-L_3)\}, \quad (33)$$
$$2^{-\frac{1}{2}}HR=W_4-XZ(W_1-W_2-W_3) =\{L_4+XZ(L_1-L_2-L_3)\}/\{2L_4^2+L_2(L_1-L_3)\},$$

where X and Z are the direction cosines of $\mathbf{I}$ to the (100) and (001) axes, respectively. That is, in this case, the transverse magnetoresistance and the Hall constant depend upon the direction of $\mathbf{I}$.

If we make an asymptotic expansion in $\mathbf{H}$ of the components of the conductivity tensor, the saturation

TABLE II. Calculated saturation magnetoresistance.

H direction	Case (a)	Case (b)	Case (c)
		Saturation values of $\Delta\rho_\infty/\rho_0$ when $\mathbf{I}\parallel\mathbf{H}$	
(100)	0	$(r-1)^2/(5r+1)$	$2(r-1)^2/9r$
(110)	$(r-1)^2/(5r+1)$	$3(r-1)^2/(3r^2+20r+1)$	$(r-1)^2/3(2r+1)$
(111)	$2(r-1)^2/9r$	$(r-1)^2/3(2r+1)$	$2(r-1)^2/3r(2r+7)$
		Saturation values of $9\pi\rho_\infty/32\rho_0$ when $\mathbf{I}\perp\mathbf{H}$[a]	
(100)	$(r+2)(2r+1)/9r$	$(r+2)(3r^2+8r+1)/18r(r+1)$	$(r+2)^2/3(2r+1)$
(111)	$(r+2)^2/3(2r+1)$	$(r^2+4r+1)/6r$	$(r+2)(5r+4)/3(8r+1)$
(110)	$\dfrac{(r+2)[(r+5)+Z^2(r-1)^2/r]}{9(r+1)}$	$\dfrac{(r+2)[(11r+1)(r+1)-Z^2(r-1)^2]}{18r(3r+1)}$	$\dfrac{(r+2)(2r+1)-Z^2(r-1)^2}{9r}$

[a] Z is the direction cosine of $\mathbf{I}$ along the (001) axis.

values of the magnetoresistivity, ρ_∞, and of the Hall constant, R_∞, are easily obtained. To our great surprise, for all of the three cases the saturation Hall constant has the same form

$$R_\infty=(Nec)^{-1}. \tag{34}$$

Thus the same relation as that between drift and Hall mobilities seems to be kept between normal and saturation Hall constants, with the spheroidal approximation, as follows:

$$(R_0/R_\infty)=(\mu_H/\mu_0). \tag{35}$$

Some saturation values of $\Delta\rho_\infty/\rho_0=(\rho_\infty-\rho_0)/\rho_0$ and ρ_∞/ρ_0 are listed in Table II. If one takes $r=1$, these results reduce to those already obtained by Harding, that is, the longitudinal effects disappear and the transverse effects becomes as follows:

$$\Delta\rho_\infty/\rho_0=(32/9\pi)-1=0.132, \tag{36}$$

$$R_0/R_\infty=8/(3\pi)=0.849. \tag{37}$$

Several functions of r listed in Table II are plotted in Fig. 2. One may easily see that in the spheroidal approximation, spherical surfaces give the smallest magnetoresistance effect.

Indeed, all the magnetoresistance effects observed by Pearson and Suhl are at least qualitatively explained with our calculation in this section. In the following section we shall make a semiquantitative discussion and find some quantitative discrepancy between theory and experiment due to the many simplifications and approximations made in this calculation.

3. COMPARISON WITH EXPERIMENT AND DISCUSSION

First, we recalculate the phenomenological magnetoresistance constants β, γ, and δ for small magnetic field, using the experimentally determined values of $\Delta\rho_H/\rho_0H^2$ listed in Table I in the paper by Pearson and Suhl. They determined these constants from the values in the lower three rows of that table, and hence their values are too inaccurate to be used in this discussion; for instance, a magnetoconductive effect would be observed in some cases in p type at 77°K, if they were true. Therefore we use all five rows in that table and determine the average values for the constants. The values thus determined are listed in Table III. One may find there fairly large allowable ranges of average values, which arise from their experiment. This shows that either there were some experimental difficulties or the samples used were not actually cubic.

In Table III, we show also three values of $\beta+\gamma+\delta$, $\beta+\gamma-\delta$, and $\beta+\gamma$ which are used to decide, as a first approximation, with which of those cases considered in the preceding section we may continue to discuss the experimental data semiquantitatively. From this table we can see that Case (a) fits best for p-type samples, and Case (c) fits best for n-type.

(i) p Type

As is seen from Table III, the values of β, γ, and δ satisfy Eq. (24) within the limits of experimental accuracy. Thus we put $\beta+\gamma+\delta$ equal to zero and we use hereafter the following values for β, γ, and δ, respectively: -4.66×10^{-9}, 4.15×10^{-9}, and 0.51×10^{-9}, in the case of p-type germanium at 300°K; and -300×10^{-9}, 273×10^{-9}, and 27×10^{-9} at 77°K, for the following semiquantitative discussion with (Case a).

From the ratio of γ and δ we can determine r, but

TABLE III. Low-field magnetoresistance constants calculated from the experimental data.

	p type		n type	
$10^9\times$	300°K	77°K	300°K	77°K
β	$-4.73\begin{cases}+0.10\\-0.44\end{cases}$	$-300\begin{cases}+14\\-6\end{cases}$	$-0.209\begin{cases}+0.017\\-0.009\end{cases}$	$-66.8\begin{cases}+2.1\\-7.6\end{cases}$
γ	4.08 ± 0.44	274 ± 20	0.187 ± 0.025	57.9 ± 9.7
δ	0.44 ± 0.44	$27\begin{cases}+19\\-22\end{cases}$	$-0.140\begin{cases}+0.029\\-0.022\end{cases}$	$-45.5\begin{cases}+10.1\\-9.4\end{cases}$
$\beta+\gamma+\delta$	$-0.21\begin{cases}+0.98\\-1.32\end{cases}$	$1\begin{cases}+53\\-48\end{cases}$	$-0.162\begin{cases}+0.071\\-0.056\end{cases}$	$-54.4\begin{cases}+21.9\\-26.7\end{cases}$
$\beta+\gamma-\delta$	$-1.09\begin{cases}+0.98\\-1.32\end{cases}$	$-53\begin{cases}+56\\-45\end{cases}$	$0.118\begin{cases}+0.064\\-0.063\end{cases}$	$36.6\begin{cases}+21.3\\-27.4\end{cases}$
$\beta+\gamma$	$-0.65\begin{cases}+0.54\\-0.88\end{cases}$	$-26\begin{cases}+34\\-26\end{cases}$	$-0.022\begin{cases}+0.042\\-0.034\end{cases}$	$-8.9\begin{cases}+11.8\\-17.3\end{cases}$

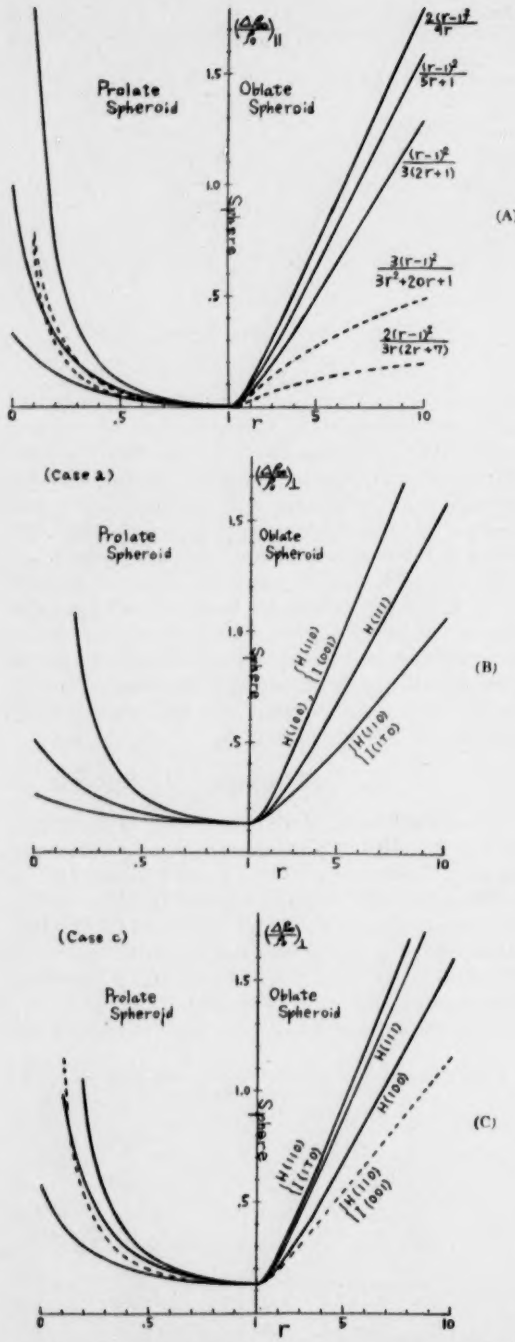

FIG. 2. (A) Saturation values of $\Delta\rho_\infty/\rho_0$ *versus* r, when $\mathbf{H}\|\mathbf{I}$. (B) Saturation values of $\Delta\rho_\infty/\rho_0$ *versus* r, when $\mathbf{H}\perp\mathbf{I}$, in (Case a). (C) Saturation values of $\Delta\rho_\infty/\rho_0$ *versus* r, when $\mathbf{H}\perp\mathbf{I}$, in (Case c).

the equation which determine r is quadratic ,so we obtain both oblate and prolate solutions. Once r is determined, we can readily obtain the ratio of Hall mobility and drift mobility and also some saturation values of the magnetoresistivity with the formulas in the preceding section. Using the experimental values of the normal conductivity, B will be fixed. With this B value, we can obtain the normal Hall constant R_0, which should be equal to the experimental value, for we already used it in recalculating the magnetoresistance constants. However, unfortunately the discrepancy is large for the case of p-type samples at 300°K. These calculated values are listed in Table IV with the experimental values for comparison. Both the oblate solution and the prolate one explain the observed results to nearly the same extent.

(ii) *n* Type

The data obtained with n-type samples are also treated semiquantitatively with Case (c) in a similar way. The results are listed in Table V. Comparing the calculated values with the experimental ones, we are likely to conclude that the prolate solution fits better for n-type samples.

The experimentally expected saturation values of magnetoresistance in both p- and n-type samples are at least twice as large as the calculated values in this calculation with r, which is determined from the data measured in weak magnetic field. The ratio of the Hall mobility to the drift mobility is given by Eq. (23) in this calculation, but it is about 1.8 for p-type samples at 300°K in the recent experiments at Bell Telephone Laboratories.[9] Closer quantitative agreement between this calculation and those experiments should not be expected at this stage, in consequence of the many simplifications and approximations employed in our calculation.

We may reproduce almost all the curves obtained in Pearson and Suhl's experiment with the appropriate

TABLE IV. Comparison between the calculated values of some magnetoresistance constants in Case (a) and the observed values in p-type Ge.

		300°K			77°K		
Values used in this calculation		σ 2.6 β -4.66×10^{-9} γ 4.15×10^{-9} δ 0.51×10^{-9}			4.6 -300×10^{-9} 273×10^{-9} 27×10^{-9}		
		Calculated	Observed		Calculated	Observed	
r		0.55	1.82		0.58	1.72	
$B\times10^5$		4.97	3.33		30.3	21.1	
$R_0\times10^5$		1.4	1.4	0.84	5.1	5.1	4.4
$8\mu_H/3\pi\mu_\sigma$		0.97	0.95	1.5	0.97	0.96	1.0
Directions of **H**	**I**		$\Delta\rho_\infty/\rho_0$			$\Delta\rho_\infty/\rho_0$	
(100)	(100)	0	0	~0.1	0	0	~0.1
(110)	(110)	0.054	0.067	~0.1	0.045	0.054	~0.2
(111)	(111)	0.082	0.082		0.068	0.068	
(100)	$I\perp H$	0.23	0.23	~0.5	0.21	0.21	~0.5
(111)	$I\perp H$	0.17	0.19		0.16	0.18	
(110)	(001)	0.23	0.23		0.21	0.21	
(1̄10)	(110)	0.15	0.16	~0.5	0.15	0.16	~0.5

[9] M. B. Prince, Phys. Rev. **92**, 681 (1953); and F. J. Morin, Phys. Rev. **93**, 62 (1954).

values of r and the equations derived in the foregoing section. This is true, for example, of $\Delta\rho_H/\rho_0$ *versus* H, $\Delta\rho_H/\rho_0 H^2$ *versus* H, and $\Delta\rho_H/\rho_0$ *versus* the direction of **H**, but is not true for the finite longitudinal effect along the (100) axis observed in a p-type sample, which cannot be treated with the Case (a). The magnetoresistance effect depends upon temperature only through the generalized mobility A in our calculation. The qualitative agreement between theory and experiment is quite satisfactory. A small part of the quantitative discrepancies between theory and experiment will be corrected in future experiments, but a larger part of them should be corrected in a future, more elaborate, theory. For this reason, we shall restate the simplifications and approximations used in this calculation.

In spite of the complicated energy surfaces in actual crystals, we assume, as one of the simplest nonspherical energy surfaces, spheroids, and we consider only three special cases. It seems rather remarkable that with such a simplification, we have been able to discuss the effects both in n- and p-type germanium semiquantitatively. So we think that the triply degenerate surfaces of complicated form at the top of the valence band may be approximated with three (100) spheroids in the first approximation in connection with the magnetoresistance effect. We also suppose that the bottom of the conduction band may be found nearly along the (111) axis in a future theory of the energy bands of germanium. Herman and Callaway[10] calculated the energy bands in germanium along the (100) axis in the Brillouin zone, and found a shallow minimum along this axis for the conduction bands. Calculations along other axes such as the (110) or the (111) axis are expected, for the magnetoresistance effect in n type cannot be explained with Case (a) but with Case (c) in the present calculation.

We have also assumed that transitions of electrons or holes from a certain family of spheroids to another one are forbidden. This assumption may be quite satisfactory in n type but not in p type. For the normal temperature dependence of electron mobility can be explained with this assumption, but not the anomalous temperature dependence of hole mobility. Of course, this anomaly is due originally to the complicated structure of the top of the valence band; but when we employ the three spheroid approximation mentioned above, it may perhaps be interpreted in terms of the transitions forbidden in this calculation.

The asymptotic form of the collision frequency has been used. This amounts to neglecting the correct behavior of slow electrons, on one hand, but simplifies the calculation a great deal, on the other. The slow electron contribution to the magnetoresistance seems to be very important, however, in many respects. Impurity scattering, which is not considered in this study, is large for slow electrons. Further, even in the case of simple spherical energy surface, using the asymptotic collision frequency (in other words, with the assumption of a constant mean free path), the usual weak magnetic field approximation of expanding the distribution function in ascending powers in H diverges, for this expansion is just the expansion in descending powers of collision frequency which is proportional to the wave number of the electrons. This apparent divergence difficulty can readily be removed by considering the actual collision frequency which is finite for cold electrons whose velocity is smaller than the acoustical velocity. Although we have not encountered such a divergence in this calculation because of the closed form, in spite of using the asymptotic collision frequency which is divergent at $\mathbf{K}=0$, we fear that we may have a little under- or overestimated the magnetoresistance in this calculation by neglecting the actual contribution of slow electrons. One may see the difference between the asymptotic and actual collision frequencies in the figures in the Appendix. The actual collision frequency does not depend simply on **K** only through the energy, so even with the model used in Case (a), the (100) parallel effect seems to be expected, if we can perform the calculation with the actual collision frequency.

As already discussed by Wilson,[11] the fundamental equation used in this study is inadequate for strong magnetic field, but at any rate, qualitative discussions can be made as mentioned above.

Just as was done by Johnson and Whitesell in the case of intrinsic conduction, we can formally combine the results obtained in three cases with appropriate weights, in order to approximate the complicated energy band structure in actual crystals, but it seems meaningless to do this without improving the approximations mentioned above.

TABLE V. Comparison between the calculated values of some magnetoresistance constants in Case (c) and the observed values in n-type Ge.

Values used in this calculation		300°K: σ 0.387, β -198×10^{-12}, γ 198×10^{-12}, δ -140×10^{-12}			77°K: 0.59, -64.7×10^{-9}, 64.7×10^{-9}, -45.5×10^{-9}		
		Calculated		Observed	Calculated		Observed
r		0.078	12.8		0.079	12.6	
$-B\times10^8$		7.7	1.60		53.3	11.2	
$-R_0\times10^4$		4.4	2.9	4.4	4.5	3.0	4.8
$8\mu_H/3\pi\mu_e$		0.80	0.36	0.87	0.80	0.34	0.86
Directions of **H**	**I**		$\Delta\rho_\infty/\rho_0$			$\Delta\rho_\infty/\rho_0$	
(100)	(100)	2.4	2.4	~4.0	2.4	2.4	~3.0
(110)	(110)	0.25	1.7	~0.5	0.24	1.7	0.5
(111)	(111)	1.01	0.22		1.00	0.22	
(100)	$I\perp H$	0.41	2.1	~1.0	0.41	2.1	~1.0
(111)	$I\perp H$	1.12	2.7		1.11	2.7	
(110)	(001)	1.50	1.50		1.48	1.48	
(1̄10)	(110)	2.9	2.9	~6.0	2.8	2.8	~6.0

[10] F. Herman and J. Callaway, Phys. Rev. **89**, 518 (1953).

[11] A. H. Wilson, *The Theory of Metals* (Cambridge University Press, Cambridge, 1936).

We can say in conclusion that the major part of the two main discrepancies between experiment and the previous theories concerning the magnetoresistance effect in cubic semiconductors, mentioned in the first section, is removed. Moreover, the relation between drift and Hall mobiiities is discussed, using the simplest nonspherical energy surfaces without introducing any anisotropic relaxation time.

The writer is much indebted to G. M. Hatoyama under whom this research was planned and to W. Sasaki for valuable qualitative discussions. Also he expresses his thanks to Professor F. Seitz, Professor J. Bardeen, and Professor T. Muto who gave him some important comments about the results in Case (a).

APPENDIX (COLLISION FREQUENCY)

The collision frequency of electrons with scalar effective mass in nonpolar crystals has been extensively studied by Seitz. He has pointed out that the acoustical modes of lattice vibration mainly control the collision frequency in actual diamond-type crystals. Therefore, taking only acoustical modes into account, we try here to extend his theory a little further for electrons having spheroidal energy-momentum surface:

$$W=(h^2/8\pi^2)[K_1^2/m_1+(K_2^2+K_3^2)/m_2]. \quad \text{(A.1)}$$

If we permit the high-temperature approximation, and assume that the unknown matrix component C would be constant independent of the wave number $\mathbf{K}$, but do not neglect the phonon energy, the collision frequency ν can be obtained as follows:

$$\nu=-(C^2k_0T/9\pi c^2n_0Mh)\Big[\iint_{\substack{A+B\leq 0,\\ 0\leq\theta\leq\pi,\\ 0\leq\varphi\leq 2\pi,}} d\varphi d\theta(\sin\theta)(A+B)D^{-2} + \iint_{\substack{A-B\leq 0,\\ 0\leq\theta\leq\pi,\\ 0\leq\varphi\leq 2\pi,}} d\varphi d\theta(\sin\theta)(A-B)D^{-2}\Big], \quad \text{(A.2)}$$

where

$$A=(h^2/2\pi^2)\{(K_1\cos\theta)/m_1+(K_2\cos\varphi+K_3\sin\varphi)(\sin\theta)/m_2\}, \quad \text{(A.3)}$$

$$B=hc/2\pi, \quad D=(h^2/8\pi^2)\{(\cos^2\theta)/m_1+(\sin^2\theta)/m_2\},$$

and all other constants have the same meaning as in Seitz's theory. When the phonon term B is neglected and the scalar mass m_0 is used instead of m_1 and m_2, Eq. (A.2) can readily be integrated and gives

$$\nu_0=32\pi^2C^2k_0Tm_0K/9c^2h^2n_0M, \quad \text{(A.4)}$$

which was already obtained by Seitz. But now, if one takes into account the effects of the phonon term and the tensor mass in this calculation, the two integrals in Eq. (A.2) have rather complicated ranges of integration and cannot be integrated analytically. In a region near the center of the spheroid, on a $(0,K_2,K_3)$ plane and on a K_1 axis and also in the special case of a spherical energy surface, however, the integration can be done analytically. The collision frequency will be given as a function of the collision frequency ν_0 given by Eq. (A.4), two effective mass ratios M_1 and r which are defined by

$$M_1=m_1/m_0, \quad r=m_2/m_1, \quad \text{(A.5)}$$

and four velocity ratios,

$$V_0=2\pi m_0c/hK, \quad V_1=V_0M_1, \quad V_2=V_1r \quad \text{and} \quad V_3=V_1r^{\frac{1}{2}}. \quad \text{(A.6)}$$

Case (1): A Spherical Surface

In this case, D becomes independent of the anguiar variables, so the collision frequency ν_1 of all the electrons in the Brillouin zone can be obtained rigorously, in spite of taking the phonon term B into account:

$$\nu_1=\nu_0\times\begin{cases}2V_0 & \text{for } V_0\geq 1,\\ 1+V_0^2 & \text{for } V_0\leq 1.\end{cases} \quad \text{(A.7)}$$

We see in this equation that the collision frequency of rather high-energy electrons can be approximated with the constant mean free path assumption but that of cold electrons is constant independent of the wave number $\mathbf{K}$.

Case (2): $(K_1/m_1)^2+(K_2^2+K_3^2)/m_2^2\leq(2\pi c/h)^2$

In this case, for cold electrons, their velocity is so slow that $A+B$ is always positive; in other words, a phonon-emitting transition is impossible, and $A-B$ is always negative. Thus the range of integration of the

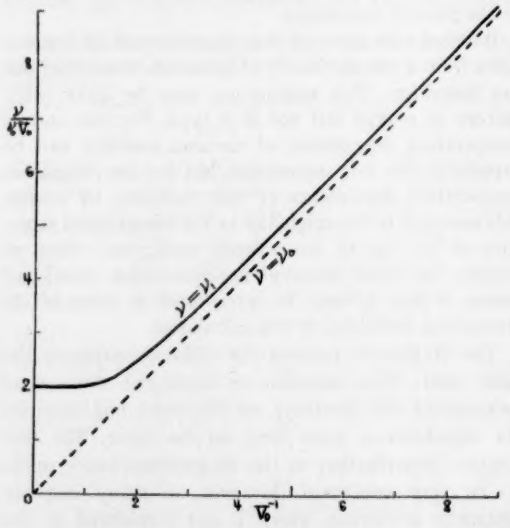

FIG. 3. The collision frequency and its asymptote in the case of spherical energy surface.

second integral corresponding to the phonon-absorbing process becomes very simple. Accordingly the collision frequency ν_2 is readily obtained:

$$\nu_2=\nu_0 M_1 V_2[1+S(r)], \tag{A.8}$$

where

$$S(r)=\begin{cases} r(r-1)^{-\frac{1}{2}}\arctan[(r-1)^{\frac{1}{2}}] & \text{for } r\geq 1, \\ r(1-r)^{-\frac{1}{2}}\operatorname{arctanh}[(1-r)^{\frac{1}{2}}] & \text{for } r\leq 1. \end{cases} \tag{A.9}$$

Thus the collision frequency of cold electrons having a spheroidal energy surface is also finite and constant independent of the wave number **K**.

Case (3): On the K_1 Axis Where $V_1\leq 1$

In this case, although both the phonon-emitting and phonon-absorbing processes are possible, the ranges of integration become independent of an angle variable φ,

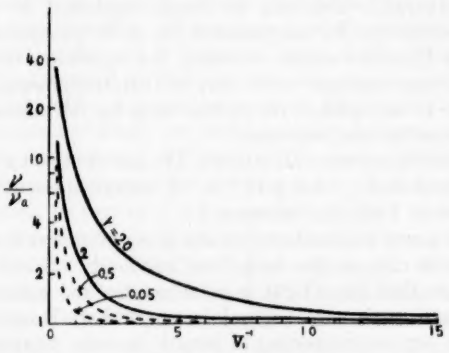

FIG. 4. The ratio of collision frequency and its asymptotic form along the K_1 axis.

and the collision frequency ν_3 can be easily obtained:

$$\nu_3=\nu_0 M_1 r[1+V_1 T(r,V_1)], \tag{A.10}$$

where

$$T(r,V_1)=\begin{cases} r(r-1)^{-\frac{1}{2}}\arctan[V_1(r-1)^{\frac{1}{2}}] & \text{for } r\geq 1, \\ r(1-r)^{-\frac{1}{2}}\operatorname{arctanh}[V_1(1-r)^{\frac{1}{2}}] & \text{for } r\leq 1. \end{cases} \tag{A.11}$$

Case (4): On a $(0,K_2,K_3)$ Plane Where $V_2\leq 1$

In this case, after a certain transformation of integral variables, the ranges of integration become dependent upon only one angle variable just as in Case (3), and the following expression can be easily obtained:

$$\nu_4=\nu_0 M_1 r^{\frac{1}{2}}\{[1+(1-r)V_3^2]^{\frac{1}{2}}+V_3 U(r,V_3)\}, \tag{A.12}$$

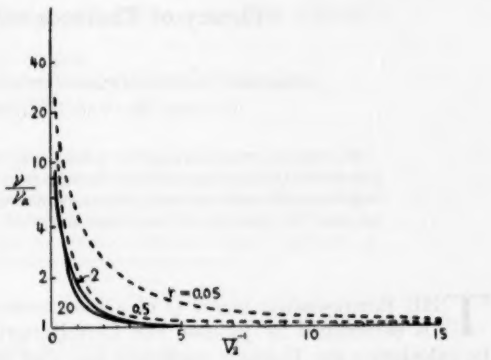

FIG. 5. The ratio of collision frequency and its asymptotic form along the K_2 axis.

where

$$U(r,V_3)=\begin{cases} r(r-1)^{-\frac{1}{2}}\arctan\{V_3(r-1)^{\frac{1}{2}} \\ \quad\times[1+(1-r)V_3^2]^{-\frac{1}{2}}\} & \text{for } r\geq 1, \\ r(1-r)^{-\frac{1}{2}}\operatorname{arctanh}\{V_3(1-r)^{\frac{1}{2}} \\ \quad\times[1+(1-r)V_3^2]^{-\frac{1}{2}}\} & \text{for } r\leq 1. \end{cases} \tag{A.13}$$

From these results rigorously obtained above, we can deduce the asymptotic expression ν_a for the high-energy electrons:

$$\nu_a=\nu_0(m_1m_2^2)^{\frac{1}{2}}(m_0K)^{-1} \times\{K_1^2/m_1+(K_2^2+K_3^2)/m_2\}^{\frac{1}{2}}. \tag{A.14}$$

That is, the collision frequency of rather high-energy electrons is approximately proportional, not to their velocity, but to the square root of their energy.

Indeed it is a very inadequate approximation, for slow or cold electrons, to substitute the actual collision frequency with this asymptotic form, but one may be permitted as a first approximation to use it for all the electrons in the Brillouin zone in the formal theory of electronic conduction, because the calculation then becomes quite simple. Further, the assumption of constant mean free path is used in all the previous theory, and that assumption is also inadequate for slow electrons.

We shall show in the following figures the difference between the actual collision frequency ν and its asymptotic form ν_a. In Fig. 3, ν_1 is plotted as a full line and ν_0, which is the asymptotic form of ν_1, as a dotted line. In Fig. 4, curves of ν/ν_a *versus* **K**, with $r=0.05$, 0.5, 2, and 20, are shown along the K_1 axis, the rotational axis of the spheroid, and in Fig. 5, such curves are shown along any, axis perpendicular to the K_1 axis. We can see in these figures that the larger the eccentricity of the spheroid, the less valid is the asymptotic approximation for medium-energy electrons.

Theory of Thermoelectric Power in Semiconductors

J. TAUC
Institute of Technical Physics, Czechoslovak Academy of Sciences, Prague, Czechoslovakia
(Received March 18, 1954; revised manuscript received June 14, 1954)

An error occurring in a paper by Johnson and Lark-Horowitz is corrected by calculating the thermoelectric power directly from the electrical current density expression. A general equation for the thermoelectric power is given which holds for semiconductors with one or two kinds of current carriers in thermal equilibrium governed by classical or Fermi-Dirac statistics.

THE thermoelectric power Q of a semiconductor is determined by Johnson and Lark-Horowitz,[1] by calculating the Thomson coefficient and then integrating the Thomson relation. However, it is possible to obtain an expression for Q directly from Eq. (I-6),[2] the equation for the electric current density. It can be shown that this procedure yields in general an expression for Q which differs slightly from that given by Johnson and Lark-Horowitz and which seems to be more correct. For the sake of simplicity we shall discuss here explicitly the case of a semiconductor in the intrinsic range when the assumptions (A), (B), (C) in part III of reference 1 are valid. Putting $j_x=0$ into Eq. (I-6), we obtain after a simple rearrangement

$$E_x=-\frac{1}{e}\left\{\frac{cn_1}{cn_1+n_2}\left[T\frac{d}{dx}\left(\frac{\zeta}{T}\right)+\frac{1}{T}\frac{L_2(1)}{L_1(1)}\frac{dT}{dx}\right]-\frac{n_2}{cn_1+n_2}\left[-T\frac{d}{dx}\left(\frac{E_G+\zeta}{T}\right)+\frac{1}{T}\frac{L_2(2)}{L_1(2)}\frac{dT}{dx}\right]\right\}. \quad (1)$$

The thermoelectric power Q can be determined from the relation,

$$Q=\frac{d}{dT}\oint E_x dx. \quad (2)$$

The integration on the right side of Eq. (2) is easily carried out in the intrinsic range when $n_1=n_2$. Integrating by parts, one obtains

$$\oint T\frac{d}{dx}\left(\frac{\zeta}{T}\right)dx=-\oint\frac{\zeta}{T}dT,$$

$$\oint T\frac{d}{dx}\left(\frac{E_G+\zeta}{T}\right)dx=-\oint\frac{E_G+\zeta}{T}dT,$$

as the integration in Eq. (2) must be performed over the whole circuit whose two ends are in the same state. Assuming the validity of Eq. (I-28), we thus obtain for Q the following expression:

$$Q=-\frac{k}{e}\left[\frac{c-1}{c+1}\left(\frac{E_G}{2kT}+2\right)+\tfrac{3}{4}\ln\frac{m_1}{m_2}\right], \quad (3)$$

differing from Eq. (I-19) by a constant, $-\frac{3}{4}(k/e)\times\ln(m_1/m_2)$. This can be simply explained in the following way. By integration of Eq. (I-18) Johnson and Lark-Horowitz obtain in reality the expression (I-19) plus some constant which they put arbitrarily equal to zero. In our opinion, the correct value for this constant is found by our procedure.

Putting $m_2/m_1=1.6$ into Eq. (3), one obtains for a a value of about -3.41×10^{-4} ev/°K instead of the values given in Table I of reference 1.

It is easy to calculate Q by the given procedure in the general case, as has been done previously.[3] It can be shown that Eq. (I-24) is valid exactly and not only approximately as stated by Johnson and Lark-Horowitz. It is perhaps interesting to remark that the expression for Q can be put into a general form with a simple physical interpretation (see reference 3):

$$Q=\frac{cn_1}{cn_1+n_2}Q_1+\frac{n_2}{cn_1+n_2}Q_2. \quad (4)$$

$$Q_1=-\frac{k}{e}\frac{\zeta-L_2(1)/L_1(1)}{kT},$$

$$Q_2=-\frac{k}{e}\frac{\zeta+E_G+L_2(2)/L_1(2)}{kT}.$$

Equation (4) holds for thermal equilibrium governed by classical or Fermi-Dirac statistics. It reduces to Eqs. (3), (I-24), (I-26a), or (I-26b) under special assumptions. For $n_2=0$ and a highly degenerate electron gas it gives the well-known expression for the thermoelectric power of metals.

[1] V. A. Johnson and K. Lark-Horowitz, Phys. Rev. 92, 226 (1953).
[2] Equation numbers like (I-6) refer to the equations in reference 1. The symbols used in the present note are the same as in reference 1.
[3] J. Tauc, Czechoslov. J. Phys. 3, 282 (1953).

Temperature and Field Dependence of the de Haas-van Alphen Effect*†

F. J. DONAHOE‡ AND F. C. NIX
Randal Morgan Laboratory of Physics, University of Pennsylvania, Philadelphia, Pennsylvania
(Received May 24, 1954)

The functional dependence of the observed de Haas-van Alphen effect in zinc has been compared with the predictions of the free electron theory. The dependence of the period on the magnetic field, and of the amplitude on the temperature appear to be correctly given. However, the predicted dependence of the amplitude on the magnetic field is in disagreement with the experimental results. An empirical formula for the amplitude dependence is given which differs from the free electron formula in that it contains an additional factor of $1/H$. This formula is in good agreement with the experimental results.

INTRODUCTION

THE de Haas-van Alphen effect is an oscillatory component of the diamagnetic susceptibility of certain conductors. It has been observed in some elements such as bismuth,[1] zinc,[2] and beryllium[3] at liquid hydrogen temperatures and in magnetic fields less than ten thousand oersteds. Other elements, such as lead,[4] only show the effect at temperatures of the order of one degree Kelvin and in magnetic fields of the order of eighty thousand oersteds. In all cases, except possibly lead, the effect is highly anisotropic. This is true even in aluminum[5] where the lattice has cubic symmetry.

No satisfactory calculation of the diamagnetism of conduction electrons has yet been made. The thermodynamic properties of a free electron gas in a uniform magnetic field may, however, be calculated to any desired accuracy.[6,7] An oscillatory component of susceptibility is found which possesses many features of the observed de Haas-van Alphen effect. In order to obtain any sort of quantitative agreement, it is necessary to assume values for the electron mass and for the electrochemical potential which are smaller by several orders of magnitude than those expected for a free electron gas having the particle density of a conduction band. The use of these quantities as adjustable parameters is usually justified by an appeal to the results of the Bloch theory.[8,9]

The dominant functional dependence of this oscillatory term on the absolute temperature T and magnetic field H is given by

$$\chi(T,H)=AT(1/H)^{\frac{1}{2}}\operatorname{csch}(aT/H) \times\exp(-b/H)\sin\pi[(1/dH)-\tfrac{1}{4}], \quad (1)$$

where A, a, b, and d are constants which are determined in terms of fundamental atomic constants by the theory.

In the first three mentioned elements, bismuth, zinc, and beryllium, the experimental parameters which characterize the effect are of such a magnitude that almost the whole range of the phenomena from the strong field case in which the power of $1/H$ is dominant, to the weak field case in which the exponential form of the hyperbolic cosecant dominates, may be observed at liquid helium temperatures using an electromagnet capable of producing ten thousand oersteds maximum. The effect in bismuth and beryllium is complicated by geometrical factors which will be explained in the following.

We present here the results of a detailed comparison of the observed de Haas-van Alphen effect, in a zinc single crystal containing 0.03 atomic percent aluminum, with the functional form predicted by the free electron theory. We find that quantitative agreement cannot be obtained without using two free parameters in addition to those permitted by the Bloch theory. These two parameters are the phase of the oscillations and the exponent of the factor $1/H$. An empirical formula will be given which is in satisfactory agreement with experiment.

FREE ELECTRON THEORY

The Landau formula[10] for the oscillatory part of the grand canonical potential $\Omega(T,V,\zeta,H)$ of a free electron gas is

$$\Omega_{\text{osc.}}=\frac{kTV}{4\pi^2}\left(\frac{eH}{\hbar c}\right)^{\frac{1}{2}}\sum_{r=1}^{\infty}\frac{(-1)^r\cos\pi(r\zeta/\beta H-\frac{1}{4})}{r^{\frac{1}{2}}\sinh(r\pi^2kT/\beta H)}. \quad (2)$$

Here ζ is the electrochemical potential, β is $eh/2mc$, and the other symbols have their usual significance. This formula is valid for arbitrary values of the magnetic field. The error is temperature dependent and is of the order of $\exp(-\zeta/kT)$.

* Based on a dissertation submitted by F. J. Donahoe in partial fulfillment of the requirements for the degree of Ph.D. at the University of Pennsylvania.

† Work supported by the U. S. Atomic Energy Commission.

‡ Present address: The Franklin Institute Laboratories for Research and Development, Philadelphia, Pennsylvania.

[1] W. J. de Haas and P. M. van Alphen, Proc. Koninkl. Akad. Wetenschap Amsterdam **33**, 680, 1106 (1930).

[2] J. A. Marcus, Phys. Rev. **71**, 559 (1947).

[3] Verkin, Lazarev, and Rudenko, Doklady Akad. Nauk. S.S.S.R. **73**, 59 (1950).

[4] D. Shoenberg, Nature **170**, 569 (1952).

[5] D. Shoenberg, Nature **167**, 647 (1951).

[6] E. H. Sondheimer and A. H. Wilson, Proc. Roy. Soc. (London) **A210**, 173 (1951).

[7] R. B. Dingle, Proc. Roy. Soc. (London) **A211**, 500, 517 (1952); **212**, 38, 47 (1952).

[8] H. Jones, Proc. Roy. Soc. (London) **A147**, 396 (1934).

[9] M. Blackman, Proc. Roy. Soc. (London) **A166**, 1 (1938).

[10] D. Shoenberg, Proc. Roy. Soc. (London) **A170**, 341 (1939).

Dingle has shown that if an electron spends a mean time τ in a given quantized state before making a transition to another state under the influence of some perturbation such as impurity scattering, the rth harmonic in the above expression is reduced by the factor $\exp(-r\pi\hbar/\tau\beta H)$.

Blackman[9] has shown that if one assumes a generalized form for the energy relation $2mE=\mathbf{p}\cdot\boldsymbol{\alpha}\cdot\mathbf{p}$, where $\boldsymbol{\alpha}$ is a tensor of rank two whose components in space coordinates are $\alpha_{ij}=(m/\hbar^2)(\partial^2E/\partial k_i\partial k_j)$, the resulting relations between energy, momenta, coordinates, and field may be reduced to spherical form by the substitutions $p_i'=\alpha_i^{\frac{1}{2}}p_i$; $q_j'=\alpha_j^{-\frac{1}{2}}q_j$, and $H_k'=(\alpha_i\alpha_j)^{\frac{1}{2}}H_k$. The coordinate system has been chosen to diagonalize $\boldsymbol{\alpha}$. To complete the substitution, one must replace V by $V'=(\alpha_1\alpha_2\alpha_3)^{-\frac{1}{2}}V$ and H by $H'=(\alpha_1\alpha_2H_3^2+\alpha_2\alpha_3H_1^2+\alpha_3\alpha_1H_2^2)^{\frac{1}{2}}$ in Eq. (2) above.

The magnetic moment is then given by

$$\mathbf{M}=-\operatorname{grad}_H\Omega(T,V',\zeta,H')=\mathfrak{M}\chi(T,V',\zeta,H')\begin{Bmatrix}\alpha_2\alpha_3H_1\\ \alpha_3\alpha_1H_2\\ \alpha_1\alpha_2H_3\end{Bmatrix}, \tag{3}$$

where $\mathfrak{M}$ is the total mass and χ the susceptibility per unit mass.

The effect of electron spin is to include the factor $2\cos(r\pi H/H')$ in the rth harmonic in Eq. (2).

The complete expression for χ thus includes harmonic terms which have been omitted from Eq. (1). Once the fundamental has been obtained, it is possible to estimate the magnitude of the error made in neglecting them.

METHOD OF MEASUREMENT

In general, a body with magnetic moment $\mathbf{M}$ in a magnetic field $\mathbf{H}$ experiences a translational force $-(\mathbf{M}\cdot\boldsymbol{\nabla})\mathbf{H}$ and a torque $\mathbf{M}\times\mathbf{H}$. Either the force or the torque may be used as a measure of the susceptibility of nonferromagnetic bodies. For a measurement of the field independent susceptibility, the body force (Faraday) method is to be preferred, since it is capable of yielding absolute values of the susceptibility. The torsion method is capable of measuring only the susceptibility difference in various directions in anisotropic media. For the measurement of field dependent susceptibility, the torsion method has the distinct advantage that homogeneous magnetic fields may be used. If the susceptibility be strongly dependent on the field, the body force method will reveal only a value of the susceptibility averaged over the different fields along the specimen.

The z component of the torque on a body having a magnetic moment described by Eq. (3) above is

$$C_z=(\mathbf{M}\times\mathbf{H})_z=-\mathfrak{M}H^2\{a_{21}a_{22}\alpha_1\alpha_3+a_{11}a_{12}\alpha_2\alpha_3+a_{31}a_{32}\alpha_1\alpha_2\}\chi(T,V',\zeta,H'), \tag{4}$$

where the a_{ij}'s are components of the matrix which transforms the coordinate system from the space coordinates in which the torque is measured in the z direction and the magnetic field is applied along the x axis to the body coordinate system in which the tensor $\boldsymbol{\alpha}$ is diagonal. H' is now

$$H\{a_{11}^2\alpha_2\alpha_3+a_{21}^2\alpha_3\alpha_1+a_{31}^2\alpha_1\alpha_2\}^{\frac{1}{2}}.$$

If ϕ be the angle between the magnetic field and the line of nodes of the body system, θ the angle between the z axis and the 3 axis of the body system, and ψ the angle of rotation of the 1 axis of the body system from the line of nodes about the 3 axis, these components are

$$\begin{aligned}
a_{11}&=\cos\phi\cos\psi-\cos\theta\sin\phi\sin\psi,\\
a_{12}&=\sin\phi\cos\psi+\cos\theta\cos\phi\sin\psi,\\
a_{21}&=-\cos\phi\sin\psi-\cos\theta\sin\phi\cos\psi,\\
a_{22}&=-\sin\phi\sin\psi+\cos\theta\cos\phi\cos\psi,\\
a_{31}&=\sin\theta\sin\phi,\\
a_{32}&=-\sin\theta\cos\phi.
\end{aligned} \tag{5}$$

An hexagonal crystal has sixfold rotational symmetry in the basal plane. Unless one assumes isotropy in the basal plane ($\alpha_1=\alpha_2$), at least three such tensor distributions arranged so that they go into each other under a rotation through $2\pi/3$ must be chosen. Since this is the simplest nontrivial case, we shall assume it for further computation.

The three distributions will each contribute to the torque. One contribution will be that given above and the other two may be obtained from it by replacing functions of ψ by functions of $\psi\pm2\pi/3$. In these experiments, we attempted to put the 1 and 3 axes of the crystal in the plane of the magnetic field. Therefore, let $\theta=\frac{1}{2}\pi+\eta$ and $\psi=\xi$ where $\eta,\xi\ll1$.

$$\begin{aligned}
H_0'&=H\{\alpha_1\alpha_2\sin^2\phi+\alpha_2\alpha_3\cos^2\phi\}^{\frac{1}{2}},\\
H_\pm'&=H\{\alpha_1\alpha_2\sin^2\phi+\tfrac{1}{4}(\alpha_2\alpha_3+3\alpha_3\alpha_1)\cos^2\phi\\
&\quad\mp\tfrac{1}{2}\sqrt{3}(\alpha_2\alpha_3-\alpha_3\alpha_1)(\xi\cos^2\phi-\eta\sin\phi\cos\phi)\}^{\frac{1}{2}},
\end{aligned} \tag{6}$$

$$\begin{aligned}
C_z/\mathfrak{M}H^2=&\{[\alpha_1\alpha_2-\alpha_2\alpha_3]\chi(H_0')+[\alpha_1\alpha_2-\tfrac{1}{4}(\alpha_2\alpha_3+3\alpha_3\alpha_1)]\\
&\cdot[\chi(H_+')+\chi(H_-')]\}\sin\phi\cos\phi\\
&+\tfrac{1}{2}\sqrt{3}[\alpha_3\alpha_1-\alpha_2\alpha_3][\chi(H_+')-\chi(H_-')]\\
&\cdot[\xi\sin\phi\cos\phi-\tfrac{1}{2}\eta(\cos^2\phi-\sin^2\phi)].
\end{aligned}$$

We can see that small errors in orientation are negligible except where ϕ is close to zero or to $\frac{1}{2}\pi$. For $\phi=\frac{1}{2}\pi$ the torque vanishes regardless of the value of ψ. It is this feature which leads Shoenberg[11] to suggest that the vanishing of the de Haas-van Alphen effect be used to determine the position of the 3 axis rather than the vanishing of the couple at room temperature, since any anisotropy in the suspension may shift the angle at which the couple vanishes.

As we shall subsequently show, our experimental value of the product $\alpha_1\alpha_2$ is so much greater than either $\alpha_2\alpha_3$ or $\alpha_3\alpha_1$ that the effect in zinc has a very simple

[11] D. Shoenberg, Trans. Roy. Soc. (London) **A245**, 1 (1952).

dependence on the angle ϕ. It is this feature which makes the analysis of the temperature and field dependence in zinc considerably less difficult than is the case for bismuth or beryllium.

THE TORSION BALANCE[12]

The torsion balance used in these experiments differs from those previously used in that the torsion head is replaced by a wall type galvanometer modified by drilling an extra hole through its base. The quartz rod holding the specimen is cemented to the galvanometer coil. Light reflected from the galvanometer mirror falls on a split photocell. The output of the photcell is amplified and the voltage applied to the galvanometer coil in such a way as to oppose its motion. The current in this feedback loop is thus proportional to the torque acting on the speciment. This scheme has several advantages. One is the very high effective spring constant of the balance so the actual deflections of the specimen are negligible, of order of a few minutes of arc for the largest torques. With this small motion, the effect of eddy currents in the specimen is not noticeable and equilibrium is achieved almost immediately. Another advantage is the possibility of using an ayrton shunt to vary the sensitivity of the balance. The circuit may be used for automatic recording as in the block diagram given in Fig. 1.

PREPARATION OF SPECIMEN

The single-crystal specimen, in the form of a sphere approximately $\frac{5}{16}$ inches in diameter, was grown by the method of Tammann in a graphite mold. The furnace was cooled from about 30°C above the melting point to 20°C below at a rate of about $\frac{1}{2}$°C per hour. A helium atmosphere was used to protect the melt from oxidation. The crystal was etched with ten percent hydrochloric acid in ethyl alcohol. The strongest etch plane is parallel to the basal plane (001) and three secondary etch planes are parallel to crystal planes of type (010).

To achieve the desired orientation with respect to the specimen holder, the specimen was placed in the holder on the stage of a metallurgical microscope. The vertical illuminator of the microscope was used to provide light having a known direction. The specimen was rotated until one of the secondary etch planes reflected strongly. The specimen was raised slightly without altering its orientation and the holder carefully wet with Duco cement. The specimen was then replaced in the holder and the brilliance of the reflection checked while minor adjustments in orientation could still be made. After the cement had dried, the reflection was again observed. If nothing had changed, the assembly of holder and specimen was cemented to the quartz rod connected to the torsion balance. The error in orientation could hardly be greater than a few degrees of arc.

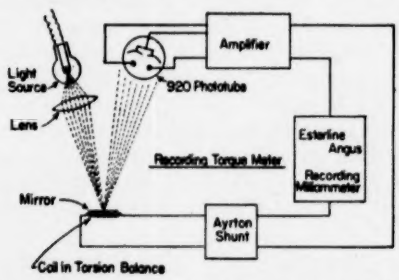

FIG. 1. Block diagram of circuit for recording torsion balance.

[12] The final form of this balance was the result of contributions by W. F. Love and G. T. Croft as well as the authors.

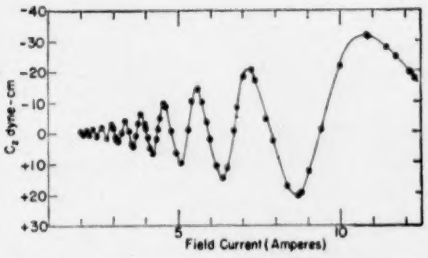

FIG. 2. Typical torque *vs* magnet field current curve for a zinc crystal at liquid helium temperatures. The angle ϕ between the hexagonal axis of the crystal and the magnetic field is 40°.

Measurements at room temperature were made primarily to determine the relative orientation of the crystal axes with respect to the reference scale on the magnet base. The torque at constant field was measured at fifteen-degree intervals through three hundred and sixty degrees of arc. The orientation of the crystal axes with respect to the reference angle ω was determined by the method of least squares.

As a precaution against the presence of ferromagnetic impurity, either in the specimen or on the suspension, the torque was also measured as a function of field at constant angle. The computed values of the susceptibility difference were plotted as a function of reciprocal field (Honda plot). If a significant amount of ferromagnetic impurity be present, the susceptibility difference will depart from constancy, and if the impurity can be assumed saturated, the slope of the Honda plot gives the magnetic moment and the intercept at infinite field gives the true susceptibility difference. Those specimens which showed ferromagnetic contamination were discarded.

MEASUREMENTS AT LIQUID HELIUM TEMPERATURES

A typical result of measurements at liquid helium temperature is shown in Fig. 2. The zinc-aluminum crystal weighted 1.6377 grams. There are more points at the low field end of the graph than could conveniently be shown. The especial virtue of the torsion balance used is that it permits one to measure these small torques with the same relative ease and accuracy

TABLE I. Reciprocal field at crossover points, in 10^4(oersted)$^{-1}$.

Integer n	Pure zinc ω	349°	82.8°	15°	45°	Zinc-aluminum 105°	240°	30°	75°	255°
	ϕ	45°	41.2°	70°13′	40°13′	75°	60°	30°	15°	75°
4				1.170		1.193	1.057			1.188
5		1.157	1.032	1.490		1.513	1.357			1.505
6		1.408	1.250	1.803	1.197	1.829	1.627			1.834
7		1.648	1.463	2.120	1.418	2.154	1.905	1.088		2.149
8		1.884	1.676	2.446	1.619	2.493	2.193	1.263		2.478
9		2.142	1.892	2.765	1.832	2.815	2.482	1.427		2.809
10		2.392	2.111	3.087	2.042	3.142	2.778	1.584		3.132
11		2.646	2.329	3.416	2.266	3.457	3.066	1.747		3.454
12		2.900	2.558	3.737	2.476	3.809	3.358	1.912		3.789
13		3.157	2.788	4.062	2.698	4.133	3.644	2.078	1.098	
14		3.412		4.391	2.913	4.478	3.961	2.249	1.193	
15		3.666		4.717	3.108			2.412	1.290	
16		3.924		5.053	3.336			2.583	1.378	
17		4.176			3.573			2.750	1.467	
18		4.448			3.760				1.522	
19		4.697			4.008				1.643	
20					4.229				1.728	
21					4.447				1.817	
22					4.667				1.892	
23					4.896				1.997	
24					5.104				2.087	
25					5.328					

as the large torques at high fields. The magnetic field at the highest point shown (field current 12.19 amperes) is 9570 oersteds.

PERIOD AND PHASE OF THE OSCILLATIONS

After the results of observation have been transformed, that is, the magnetic field current converted to field strength, and the torques weighted by the factor H^{-2}, the next and most straightforward step is to determine the period and phase of the oscillations. A large-scale plot is made with abscissa proportional to H^{-1} and ordinate proportional to C_zH^{-2}. The contribution of the field independent susceptiblity difference is taken as the mean of the oscillations. The values of the reciprocal field at which the graph crosses this mean value are tabulated. The crossover points should satisfy the relation

$$(1/H)_{\text{crossover}} = d(n+\delta), \qquad (7)$$

where n is an integer and δ is the phase in multiples of π radians. [See Eq. (1).]

The n corresponding to the first observed crossover may be assigned arbitrarily, but has been taken even or odd to conform to the sign convention of the free electron theory.

Table I gives the values of these crossover points measured at various angles ϕ between the 1 axis of the crystal and the magnetic field. Results for two specimens are tabulated, one pure zinc and the other zinc-aluminum. The results for zinc-aluminum are also shown graphically in Fig. 3.

The results of the calculations of the period and phase are given in Table II. The precision indices are the standard, or root mean square deviations which were computed according to formula given for example in Worthington and Geffner.[13]

We have included in this table the results of measurements of the period and phase at liquid hydrogen temperatures. Within the experimental error, these are the same as at 4.2°K.

The phase of the oscillations is markedly different from that predicted by the free electron theory. There is considerable scatter in the values obtained at various angles. The average value is about 0.4π radian as compared with -0.25π radian predicted by the free electron theory. This value is in agreement with the results of Mackinnon[14] with pure zinc, but not with those of Sydoriac and Robinson[15] who reported a phase of zero.

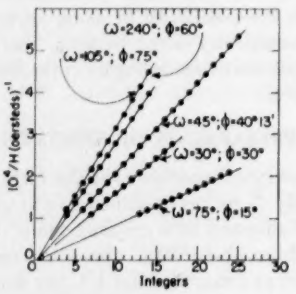

FIG. 3. Crossover points of oscillations *vs* integers for various orientations of magnetic field with respect to the crystal axes.

The square of the quantity d which we have given for various angles in Table II has been shown to be a linear function of $\sin^2\phi$. We assume that the values of d^2 are known more accurately than those of $\sin^2\phi$. Moreover, errors in ϕ and not in $\sin^2\phi$ are assumed equiprobable. For this reason, we assign a weighting factor w proportional to $(\sin\phi\cos\phi)^{-2}$. Because the standard deviation of d also differs from angle to angle, we make the weight w proportional to $(d\sigma_d)^{-2}$ as well. The weights so assigned are listed in the column headed w in Table III. They have been normalized such that $\sum w=9$, the number of observations. Figure 4 shows the graph of $\sin^2\phi$ against d^2.

From the intercept at $d^2=0$ in principle, one could

TABLE II. Period and phase of oscillations.

T°K	ω	ϕ	$d\times10^4$ (oersted)$^{-1}$	δ (radian/π)
		Pure zinc		
4.2°	349°	45°	2.534±0.007	0.512±0.037
4.2°	82.8°	41.2°	2.186±0.003	0.308±0.019
		Zinc-aluminum		
4.2°	15°	70°13′	3.233±0.007	0.422±0.020
4.2°	45°	40°13′	2.177±0.006	0.589±0.040
4.2°	105°	75°	3.282±0.011	0.408±0.028
4.2°	240°	60°	2.888±0.012	0.366±0.042
4.2°	30°	30°	1.655±0.005	0.414±0.033
4.2°	15°	15°	0.888±0.005	0.538±0.104
4.2°	255°	75°	3.251±0.006	0.366±0.014
14.1°	345°	40°	2.186±0.009	0.424±0.041
18.0°	345°	40°	2.189±0.015	0.477±0.059
20.4°	345°	40°	2.201±0.027	0.494±0.109

[13] A. G. Worthington and J. Geffner, *Treatment of Experimental Data* (John Wiley and Sons, Inc., New York, 1943), p. 249.
[14] L. Mackinnon, Proc. Phys. Soc. (London) **B62**, 170 (1949).
[15] G. Sydoriac and J. E. Robinson, Phys. Rev. **75**, 118 (1949).

determine the ratio $\alpha_3/\alpha_1-\alpha_3$. The parameters are such that our value for this ratio is $-10^{-3}\pm10^{-2}$. The negative sign is hardly significant in view of the uncertainty, but it is at least consistent with the known positive Hall coefficient of zinc. From the intercept at $\sin^2\phi=1$, the effective temperature $(\alpha_1\alpha_2)^{\frac{1}{2}}T_0$ may be computed. The value obtained is 1.98 ± 0.01°K which agrees within the stated error with the value published by Mackinnon of 1.96 ± 0.02°K for pure zinc. In this expression T_0 is the degeneracy temperature ζ/k of the electrons responsible for the effect.

The calculated errors in angle from the fitted curve are also listed in Table III. There are no errors in excess of the expected accuracy in orientation of the crystals.

TEMPERATURE DEPENDENCE OF THE AMPLITUDE

In this section, and in the following, whenever we refer to the magnitude of an extremum it is understood that the correction for the contribution of the field independent susceptibility has been made. At constant field and angle, the amplitude of an extremum $|C_z|_{\text{ext}}$ should obey the equation [see Eqs. (1) and (6)]:

$$|C_z|_{\text{ext}}=A'T\,\text{csch}(a'T).$$

Dividing through by T and taking logarithms of both sides gives

$$\log(|C_z|_{\text{ext}}/T)=\log A'-\log\sinh(a'T), \qquad (8)$$

which for large enough values of the argument of the hyperbolic function becomes the equation of a straight line. Such a plot for the extremum at H equal 5800 oersteds, ϕ equal 40° of arc, for temperatures between 1.5 and 4.2°K is given in Fig. 5. The pronounced positive curvature of the graph shows that the asymptotic formula for the logarithm of the hyperbolic function cannot be used. The graph is a plot of $-\log\sinh(0.3T)$ with the constant chosen so that the curve passes through the point at T equal 3°K.

The temperature range available through the use of liquid helium is not great enough to obtain much more than order of magnitude accuracy for the parameters involved. Consequently, the measurements were repeated at liquid hydrogen temperatures. Values were obtained at 20.4° at 18.0°, and at 14.1°K. All the points are shown in Fig. 6.

TABLE III. Quantities used to compute $(\alpha_1\alpha_2)^{\frac{1}{2}}T_0$.

ω	ϕ	$\beta^2\times10^{10}$ (oersted)$^{-2}$	$\sin^2\phi$	w	$\Delta\phi$
		Pure zinc			
349°	45°	6.419	0.5000	0.009	−3°27′
82.8°	41.2°	4.778	0.4339	0.557	+0°59′
		Zinc-aluminum			
255°	75°	10.57	0.9330	0.982	+1°12′
105°	75°	10.77	0.9330	0.327	−0°47′
15°	70°13′	10.45	0.8854	0.533	−2°32′
240°	60°	8.341	0.7500	0.098	+1°27′
45°	40°13′	4.739	0.4169	0.448	+0°12′
30°	30°	2.739	0.2500	1.069	+0°44′
15°	15°	0.7886	0.0670	4.977	−0°13′

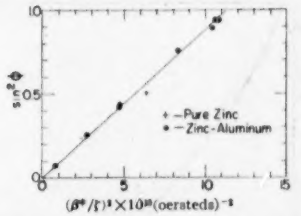

FIG. 4. $\sin^2\phi$ plotted against the square of the period of the oscillations. A linear relation is predicted by the theory.

The asymptotic form of the logarithm of the hyperbolic sine may be used in the liquid hydrogen temperature range. In an effort to get a good value for the parameters of the curve the logarithm of the hyperbolic sine was rewritten as

$$\log\sinh a'T=-\log2+\log[1-\exp(-2a'T)]+\log\exp(a'T).$$

The quantity $\log[1-\exp(-2a'T)]$ was calculated for each point using the value of the constant a' equal to 0.26 estimated from the slope in the asymptotic region. This quantity was then used to linearize the curve and the slope taken. This procedure yielded a new value of the constant a' equal to 0.264. An iteration of this procedure resulted in a new value of the constant, but negligibly different from the old. The curve drawn in Fig. 5 is computed from the fitted parameters.

FIELD DEPENDENCE OF THE AMPLITUDE

By reasoning similar to that used for the temperature dependence, we expect that at constant temperature

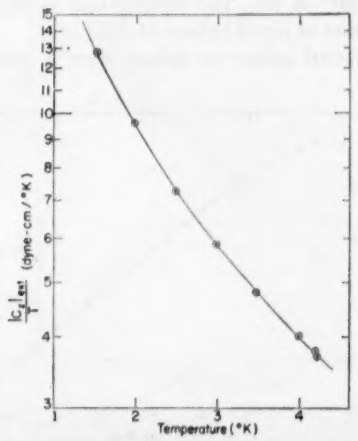

FIG. 5. The logarithm of the amplitude at constant field minus the logarithm of the temperature plotted against temperature from 1.5 to 4.2°K. Positive curvature is expected of the logarithm of a hyperbolic sine for small values of the argument.

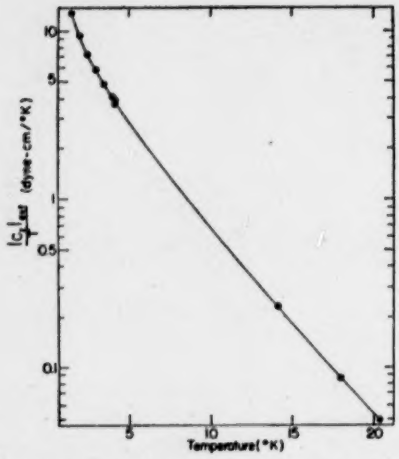

FIG. 6. Log(amplitude) minus log(temperature) *vs* temperature from 1.5 to 20.4°K. At hydrogen temperatures, the argument of the hyperbolic sine is large so that it may be approximated by the exponential function.

and angle the equation,

$$\log\left\{\frac{|C_z|_{\text{ext}}}{\mathfrak{M}\cos\phi}\left(\frac{\sin\phi}{H}\right)^{\frac{1}{2}}\right\}=\log A''-\log\sinh(a''/H\sin\phi)$$
$$-\log\exp(b''/H\sin\phi), \quad (9)$$

will be satisfied by the values $|C_z|_{\text{ext}}$ marking the envelope of the oscillations, and that the graph will approach a straight line at large values of the reciprocal field.

Forewarned by the results of the temperature measurement, we shall expect that considerable curvature will be shown at small values of the reciprocal field if the temperature be in the liquid helium range.

The actual results are shown in Fig. 7. The angle ϕ is again 40° of arc. The temperature is the normal boiling point of liquid helium (4.2°K).

The plotted points do indeed show a pronounced curvature, and exactly in the expected region, but the curvature has the wrong sign.

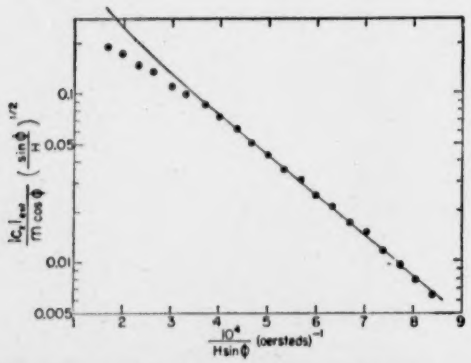

FIG. 7. Log(amplitude) minus $\frac{1}{2}\log H$ *vs* H^{-1}. The solid curve is the theoretical relation. The experimental points show negative curvature at high fields where theory predicts positive curvature.

This negative curvature may be found in the results of Shoenberg[10] for the amplitude dependence of the de Haas-van Alphen effect in bismuth and in those of Sydoriac and Robinson[15] and of Mackinnon[14] with zinc. They tended to place more confidence in the high field points than in the low field points and, in consequence, drew straight lines through the points taken at high fields (small values of the reciprocal field) and observed that the amplitude falls off more rapidly at low fields than the theory predicts.

EMPIRICAL RELATION FOR FIELD DEPENDENCE

If one wishes to preserve the theoretical form of the temperature dependence, and we see no reason to abandon it, the left-hand side of Eq. (9) must be altered. We have found that the addition of $\log(H\sin\phi)$ is sufficient to give to the graph of the experimental points the correct sign and magnitude of the curvature. Figure 8 shows a log plot of the quantity $(|C_z|_{\text{ext}}H^{\frac{1}{2}}\sin^{\frac{1}{2}}\phi)/(\mathfrak{M}\cos\phi)$ as a function of $(H\sin\phi)^{-1}$.

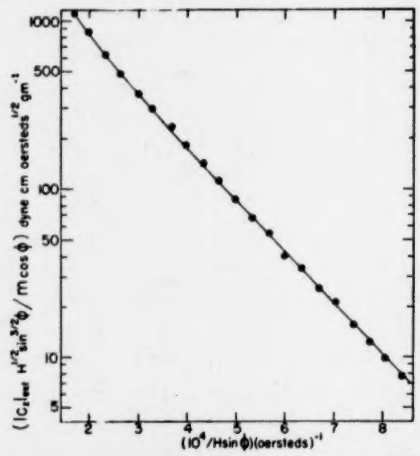

FIG. 8. Log(amplitude) plus $\frac{1}{2}\log H$ *vs* H^{-1}. The empirical equation is a good fit to the experimental points.

To illustrate the agreement more fully, we show in Fig. 9 a plot of the same set of points as are shown in Fig. 8 except that the ordinates have been corrected by the factor $[1-\exp(-2a''/H\sin\phi)]$, where the constant a'' has been computed from the parameters determined from the temperature dependence. The graph has become a straight line.

Since the phase of the oscillations is close to $\pi/2$ the series is almost a cosine series. Thus, the second and all even harmonics tend to alternately increase and decrease the magnitude of successive extrema. The fact that this is not observed in the high field points of Figs. 8 and 9 may be due to this effect being partially compensated by a small H^2 term in the monotonic susceptibility.

COMPARISON OF COMPUTED CURVES WITH ORIGINAL DATA

We have combined the results of the measurement of the phase and period for this particular angle from Table II and have computed the solid curve shown in Fig. 10, taking the amplitude from the logarithmic plot of Fig. 8. The envelope taken from Fig. 7 is lightly dashed. Against this background, we display the points computed from those shown in Fig. 1 as torque *versus* magnet field current.

If we had elected to obtain the 3/2 power parameters from the high-field measurements, the lightly dashed envelop would diverge at the low-field end, becoming too large by a factor of two.

The assumed 5/2 power dependence fits very nicely, both at high fields where the power is dominant and at low fields where the exponential dominates. The points

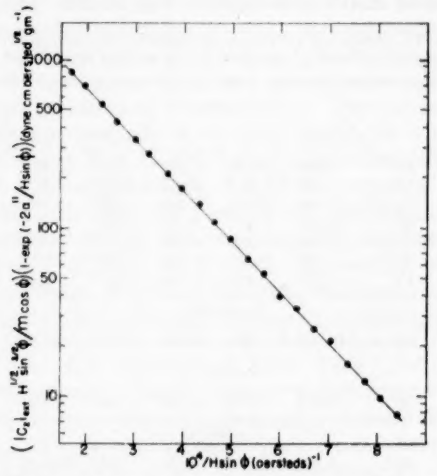

FIG. 9. Log(amplitude) plus ½ log$H$ plus a correction factor calculated from the temperature dependence plotted against H^{-1}.

at highest field are beginning to deviate from sinusoidal behavior. This can be attributed to the influence of the higher harmonics in the series. The second harmonic is estimated to be about 15 percent of the fundamental for these points.

FIELD DEPENDENCE AT OTHER ORIENTATIONS

Figures 11 and 12 show the field dependence of the amplitude at other angles in the same manner as in Figs. 7 and 8. The curvature has the wrong sign at every angle if the 3/2 power dependence of the susceptibility be assumed. The separation of the curves is a measure of the scatter in the amplitude. The slopes of the curves differ slightly. Some of these discrepancies are no doubt due to errors in determining ϕ. Functions of this angle appear in both ordinate and abscissa.

We have rectified the curves based on the assumption of a 5/2 power dependence of the susceptibility on the

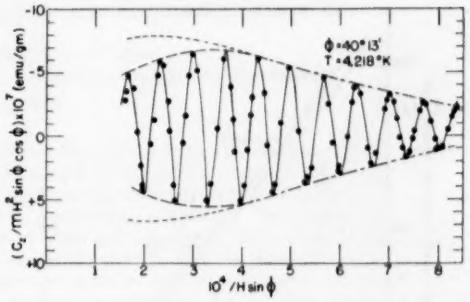

FIG. 10. Field-dependent susceptibility of zinc as a function of H^{-1}. The solid curve is computed from the empirical parameters. The lightly dashed curve indicates where the envelope should be if the amplitude dependence of the free electron theory were correct. These points were calculated from the experimental points shown in Fig. 2.

reciprocal field using the constant a'' computed from the temperature dependence. The values of the slopes and intercepts for the various orientations are listed in Table IV.

The best we can say for the intercept is that within the possible error of 30 percent it is independent of the angle ϕ. This constant A has a value of approximately 330 dyne-cm (oersteds)$^{\frac{1}{2}}$ per gram per degree Kelvin. In the absence of a reliable theory to relate this quantity to fundamental constants, we can proceed no further.

We identify the constant b'' with the scattering factor $\pi\hbar/\tau\beta^*$.[16] From the table, it can be seen that this factor is roughly constant as ϕ ranges from 75° to 40° of arc. It reaches a maximum at ϕ equal to 30° of arc and is slightly smaller at ϕ equal to 15° of arc. Croft, Love,

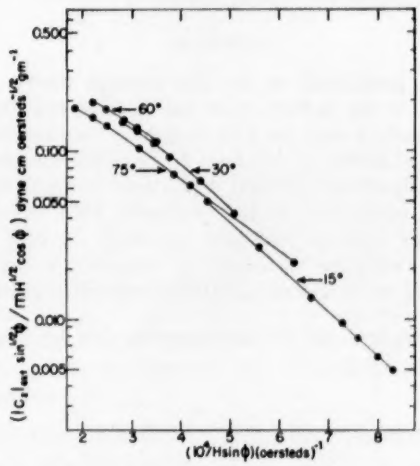

FIG. 11. Log(amplitude) minus ½ log$H$ *vs* H^{-1} shown for other orientations of the crystal with respect to the field. The negative curvature at high fields is contrary to the predictions of the free electron theory.

[16] β^* is an effective Bohr magneton defined such that $\beta^*H=\beta H'$.

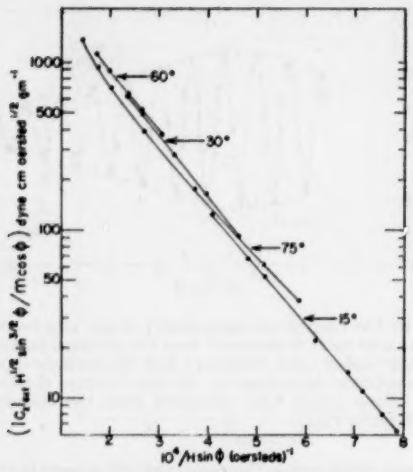

FIG. 12. Log(amplitude) plus $\frac{1}{2}\log H$ *vs* H^{-1} for various orientations of the crystal with respect to the magnetic field.

and Nix[17] observed similar variation with angle in tin-antimony alloys. The custom is to report this parameter as an effective temperature X which is $b''T/a''$. This effective temperature is also given in Table IV.

ELECTRONIC PARAMETERS

From the measurements of the angle variation of the period of the oscillations, the parameter $(\alpha_1\alpha_2)^{\frac{1}{2}}T_0 = 1.98°\text{K}$ was obtained. On the assumption that the parameter a' appearing in the temperature dependence relation can be identified with the constants given by the free electron theory, we compute the value of $(\alpha_1\alpha_2)^{\frac{1}{2}}$ to be 148. This leads directly to a value of 292°K for the degeneracy temperature T_0.

SUMMARY

The predictions of the free electron theory with regard to the periodicity of the de Haas-van Alphen effect and its variation with angle have been verified.

Our chief interest has been in the functional form of the temperature and field dependence of the envelope of the oscillations. It had previously been reported[14] that the variation with field was nearly correctly predicted, while the variation with temperature was not. We find, to the contrary, that the temperature variation could be fitted quite well to the predicted functional relation. Even with very generous allowance for experimental error, we have been unable to account for the observed field dependence on the basis of the predictions of the free electron theory. We propose an empirical modification of the formula for the oscillatory susceptibility which we have shown to be consistent with our experimental results.

$$\chi(T,H) = AT(1/H)^{5/2}\,\text{csch}(aT/H) \times\exp(-b/H)\,\sin\pi[(1/dH)+\delta]. \quad (10)$$

It should be mentioned that a term having this functional dependence has been calculated for the contribution of the surface states of a finite volume of free electron gas.[18,19] However, it appears improbable that this surface term could be used to justify the empirical formula above since, for the field strengths employed in this investigation, it is smaller than the volume term by many orders of magnitude except if the electrons be confined to volumes whose linear dimensions are of the order of a few lattice spacings.

TABLE IV. Slopes and intercepts of rectified 5/2 power plots. The constants a'' and b'' are given in units of 10^{-4}(oersted)$^{-1}$.

ω	ϕ	logA''	a''	b''	X (°K)	log$A$	No. of points
			$T=4.2$°K				
105°	75°	3.069	0.420	0.294	2.97°	2.444	8
255°	75°	3.101	0.417	0.333	3.34°	2.477	8
15°	70°13′	3.094	0.420	0.249	2.52°	2.468	12
240°	60°	3.145	0.417	0.270	2.70°	2.521	5
45°	40°13′	3.145	0.420	0.282	2.85°	2.520	21
30°	30°	3.250	0.417	0.378	3.79°	2.626	6
15°	15°	3.133	0.420	0.354	3.58°	2.508	8
			$T=14.1$°K				
345°	40°	3.665	1.404	0.304	3.05°	2.516	9
			$T=18.0$°K				
345°	40°	3.814	1.792	0.297	2.98°	2.559	7
			$T=20.4$°K				
345°	40°	3.708	2.033	0.137	1.29°	2.406	5

ACKNOWLEDGMENTS

We are indebted to Dr. W. F. Love for valuable discussions and are grateful for his and Mr. F. Witt's assistance in the preparation and handling of the liquefied gases used in these experiments.

[17] Croft, Love, and Nix, following paper, Phys. Rev. **95**, 1403 (1954).

[18] M. C. Steele, Phys. Rev. **88**, 451 (1952).

[19] R. B. Dingle, Proc. Roy. Soc. (London) **A219**, 463 (1953).

De Haas-van Alphen Effect in Tin and Tin-Antimony Alloys*†

G. T. CROFT,‡ W. F. LOVE, AND F. C. NIX
Randal Morgan Laboratory of Physics, University of Pennsylvania, Philadelphia, Pennsylvania
(Received May 24, 1954)

The de Haas-van Alphen effect has been studied in a series of dilute alloys of tin with antimony at field strengths below 10 000 gauss. Over the range of compositions studied (0–0.23 atomic percent Sb) there was no observable change in the parameters characterizing the de Haas-van Alphen effect other than the collision broadening parameter X, which increased uniformly with concentration of antimony. The temperature dependence of the amplitude of the susceptibility oscillations agrees with the theoretical predictions, but there is evidence that the field dependence does not. An angular dependence of X was observed and interpreted in terms of the lattice geometry. The room temperature magnetic anisotropy was also measured and found to increase by approximately 25 percent for an antimony concentration of 0.23 atomic percent.

I. INTRODUCTION

SINCE the original discovery by de Haas and van Alphen[1] of the oscillating behavior of the magnetic moment of a bismuth crystal as a function of the magnetic field strength, this effect has been discovered and studied in a number of different metals. The object of this investigation was to determine the various effects on this phenomenon due to alloying. The system tin-antimony was chosen as the most suitable for a study of this kind since its tin-rich alloys are substitutional solid solutions possessing a sufficient range of solid solubility to determine these effects, and because its composition and thermal equilibrium state can be easily controlled. In addition, it allows the variation of the concentration of valence electrons, an important parameter in the theory of the de Haas-van Alphen effect. The effect was first observed in tin by Shoenberg[2] and has also been reported by Croft, Love, and Nix,[3] Berlincourt,[4] and Verkin, Lazarev, and Rudenko.[5]

The theory as developed by Landau,[6] Peierls,[7] Blackman,[8] Dingle,[9] and Robinson[10] gives for the difference of susceptibilities of the conduction electrons (considered free, but with tensor effective mass) along two crystallographic directions the following formula:

$$\chi_3-\chi_1=\Delta\chi=\frac{e^2(m_1-m_3)}{12\pi^2c^2\hbar m_1}\left(\frac{2\zeta}{m_3}\right)^{\frac{1}{2}}\left\{1-3\pi\zeta^{\frac{1}{2}}kT(\beta H)^{-\frac{1}{2}}\times\sum_{n=1}^{\infty}\frac{(-1)^n\sin(n\pi\zeta/\beta H-\frac{1}{4}\pi)}{n^{\frac{1}{2}}\exp(-n\pi^2kX/\beta H)\sinh(\pi^2kT/\beta H)}\right\},\quad(1)$$

which can be approximated by

$$\Delta\chi=\frac{e^2(m_1-m_3)}{12\pi^2c^2\hbar m_1}\left(\frac{2\zeta}{m_3}\right)^{\frac{1}{2}}\left\{1-6\pi\zeta^{\frac{1}{2}}kT(\beta H)^{-\frac{1}{2}}\times\exp\left(-\frac{\pi^2k(T+X)}{\beta H}\right)\sin\left(\frac{\pi\zeta}{\beta H}-\frac{\pi}{4}\right)\right\}\quad(2)$$

if $\pi^2kT/\beta H\gg1$. The symbols are defined as follows:

χ_1, χ_3 = magnetic susceptibilities along the 1 and 3 axes, respectively;
ζ = effective Fermi level of the electrons responsible for the effect;
m_1, m_3 = effective mass parameters of the relevant electrons along the 1 and 3 axes, respectively;
$X=\hbar/\pi k\tau$ = collision broadening parameter, where
τ = mean free time between collisions for the relevant electrons;
ϕ = angle between the 3 axis of the crystal and the magnetic field H, and

$$(2\beta)^2=\frac{e^2\hbar^2}{c^2}\left(\frac{\cos^2\phi}{m_1^2}+\frac{\sin^2\phi}{m_1m_3}\right).\quad(3)$$

The other symbols have their usual meaning.

In deriving this formula, it is assumed that the electrons responsible for the effect occupy electronic states in **k** space on the surface of an ellipsoid of revolution and that the electrons are in an infinitely large volume.

By adjusting the parameters m_1, m_3, ζ, and X, the experimental data can be fitted to the theoretical expression. In order to obtain a fit for tin, values of the following order of magnitude must be assigned to these parameters:

$$\zeta=0.20\text{ ev},\quad X=0.1^\circ\text{K},\quad m_1\cong0.1m_0,\quad m_3\cong1.0m_0,$$

where m_0 is equal to the free electron mass. Using these values, the total number of electrons responsible for the effect is approximately 10^{-3} electron per atom. On the basis of these results, it seems reasonable to attribute the effect to those electrons which occupy states

* Based on the Ph.D. dissertation of G. T. Croft at the University of Pennsylvania.
† Supported by the U. S. Atomic Energy Commission.
‡ Now at the Edison Research Laboratory, of Thomas A. Edison, Inc., West Orange, New Jersey.
[1] W. J. de Haas and P. M. van Alphen, Leiden Comm. No. **212a** (1930).
[2] D. Shoenberg, Nature **164**, 225 (1939).
[3] Croft, Love, and Nix, Phys. Rev. **86**, 650 (1952).
[4] T. G. Berlincourt, Phys. Rev. **88**, 242 (1952).
[5] Verkin, Lazarev, and Rudenko, J. Exptl. Theoret. Phys. (U.S.S.R.) **20**, 995 (1950).
[6] L. D. Landau, see Appendix to D. Shoenberg, Proc. Roy. Soc. (London) **A170**, 341 (1939).
[7] R. Peierls, Z. Physik **80**, 763 (1933).
[8] M. Blackman, Proc. Roy. Soc. (London) **A166**, 1 (1938).
[9] R. B. Dingle, Proc. Roy. Soc. (London) **A211**, 517 (1952).
[10] J. E. Robinson, thesis, Yale University, 1950 (unpublished).

in **k** space just under or overlapping a Brillouin zone boundary.

The expected effects of adding antimony to tin should be to increase the electron concentration and the amount of impurity scattering. If the effect is due to holes, an increase in electron concentration should decrease ζ, and if the effect is attributable to electrons, ζ should increase. Depending on the direction in which ζ tends, it should be possible to determine whether electrons or holes are responsible for the effect. Increasing the number of antimony atoms in the lattice should cause a decrease in the mean free time τ, or an increase in the collision broadening parameter X.

II. THE SAMPLES

The alloys used in these experiments were prepared from spectographically pure components. An analysis of the tin (supplied by A. D. MacKay, Inc.) and antimony (Johnson Mathey No. 660, laboratory No. 4470) gave the following impurities:

For Sn:	Pb—0.0012 percent,	S —0.00003 percent,	Bi—0.00012 percent,
	Fe—0.00027 percent,	Sb—0.001 percent,	As—0.0002 percent,
	Cu—0.0002 percent,	Sn—99.997 percent,	
For Sb:	Ni—0.0087 percent,	Fe—0.0013 percent,	Co—Trace,
	Other impurities—0.064 percent,	Sb—99.9 percent.	

The compositions of the alloys used in these experiments and other relevant data are given in Table I.

The alloys were made by melting Sb and Sn in proper proportions *in vacuo* in a sealed Pyrex tube. To insure a homogeneous alloy, the melt was vigorously shaken before it was allowed to solidify.

Spherical $\frac{5}{16}$-in. diameter single crystals were then grown in very high purity graphite molds. These crystals were then annealed in evacuated Pyrex tubes. For annealing times and temperature, as well as the general condition of the samples, refer to Table I. Great care was taken in handling the crystals to avoid straining them in any way.

Each sample was checked for ferromagnetic impurities by the method of the Honda plot.[11] Only samples with no detectable trace of ferromagnetic impurity were used in these experiments.

After etching in concentrated HCl, the crystals were oriented by observing the reflections from the etch planes using standard optical techniques. They were then carefully mounted on the suspension of the torsion apparatus with a binary axis directed along the axis of the suspension.

TABLE I. Composition, heat treatment, and condition of samples studied.

Nominal conc. at. % Sb	Spec. analysis at. % Sb	Wt. of sample grams	Annealing[a] time (days)	Condition of sample
0.0	0.002	1.936	1	Single crystal
0.02	0.026	1.802	3	Single crystal
0.05	0.043	1.906	30	Small surface crystallite 1% of total surface
0.10	0.12	1.840	2	Small surface crystallite 1% of total surface
0.20	0.23	1.964	25	Single crystal

[a] Annealing temperature of all samples is 145°C.

[11] L. F. Bates, *Modern Magnetism* (Cambridge University Press, Cambridge, 1951), third edition, p. 133.

III. THE INSTRUMENTATION

If a spherical single crystal of tin is suspended in a homogeneous magnetic field H such that a binary axis is along the suspension, the torque acting on the sample about the axis of suspension is

$$C=(\chi_3-\chi_1)H^2\sin\phi\cos\phi, \tag{4}$$

where χ_3 and χ_1 refer to the susceptibility along the tetragonal and binary axes, respectively, and ϕ is the angle between the tetragonal axis and the magnetic field vector.

In these experiments, the torque C was measured at different temperatures as a function of H, and at various angles. From these data, $\Delta\chi$ was easily calculated using the formula given above.

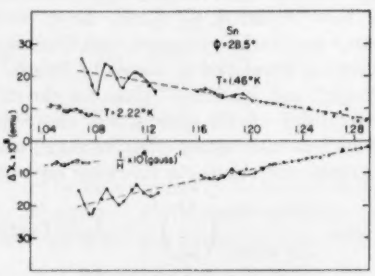

FIG. 1. Typical results for the de Haas-van Alphen effect in tin.

In the case of tin, this low-temperature measurement of the torque by measuring the angular deflection of a torsion suspension presents difficulties not encountered at room temperature. At low temperatures, the conductivity of tin is considerably higher than at room temperature. As a result of this high conductivity, eddy currents induced by the motion of the sample in the field create such strong damping that excessively long times to reach equilibrium deflections are required for a sensitive suspension, and the problem of taking detailed data becomes extremely tedious and time-con-

suming. Another difficulty arises from small changes in orientation of the crystal relative to the magnetic field vector brought about by rotation of the crystal under the influence of the torque due to the de Haas-van Alphen effect alone. Since the period and amplitude of the susceptibility are very sensitive to changes in orientation, rotation of this sort is objectionable and may lead to erroneous results.

Both of the above effects may be eliminated by using a sufficiently stiff suspension in the torsion apparatus. This has been accomplished by an especially designed recording electronic torque meter,[12] which works as follows: The sample was suspended from the suspension coil of a standard wall type galvanometer. By sending a current through this coil, the torque due to the magnetic field could be counterbalanced. This current provided a measure of the torque. A beam of light was reflected from the mirror of the suspension to a split-photocell, high-gain dc amplifier whose output was fed back degeneratively to the suspension coil. The feedback current was made of the order of milliamperes by properly shunting the suspension coil and recorded on a recording milliammeter. This arrangement is tantamount to a very stiff suspension. The maximum angular displacement of the sample was estimated to be 10^{-8} radian in these measurements. The current through the magnet was provided by motor driven powerstats which supplied voltage to a three-phase full wave rectifier circuit, and was recorded by a recording potentiometer. Effectively, the two quantities, torque and magnetic field, were then recorded simultaneously as the field was slowly decreased, the rate of change of field strength being kept so small that no torques due to eddy currents were produced. This was checked by suddenly stopping the reduction of the field and observing no change in the torque measured.

TABLE II. Comparison of data on Sn.

	ζ in ev	$2\beta\times10^{20}$ $(\text{erg})^{-1}$	ϕ	m_1	m_2
Berlincourt	0.204	16.1	29°	$0.10m_0$	...
Croft *et al.*	0.193	16.2	28.5°	$0.10m_0$	$2.0m_0$
Shoenberg	0.19	...		$0.10m_0$	$2.0m_0$

The electromagnet used had 4-in. diameter pole faces with a 2-in. gap, and was capable of producing magnetic fields up to 9500 gauss. It was calibrated using nuclear resonance techniques. No detectable inhomogeneity in the field was present in the region occupied by the sample.

IV. THE EXPERIMENTAL RESULTS

1. Pure Tin

Qualitatively, the results for pure Sn are similar to those obtained by Shoenberg[13] and Berlincourt.[4] Even though the range of field strengths is below that of previous workers, the phenomenon of "beats" is still observed. An example of the results for pure Sn is shown in Fig. 1.

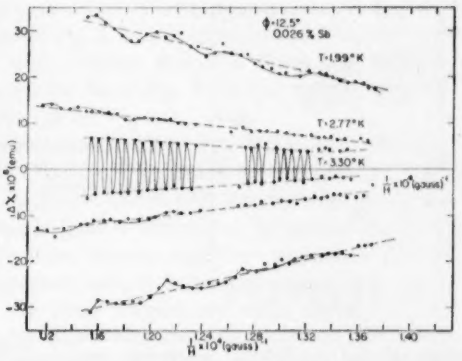

FIG. 2. The de Haas-van Alphen effect in Sn+0.026 atomic percent Sb at $\phi=12.5°$.

Quantitative comparison of the pure Sn data with the results of Shoenberg and Berlincourt (where comparison was possible) is shown in Table II. As far as parameters associated with the period and temperature dependence of the oscillations are concerned, the agreement is good. Comparison of absolute values of $\chi_3-\chi_1$ was not made

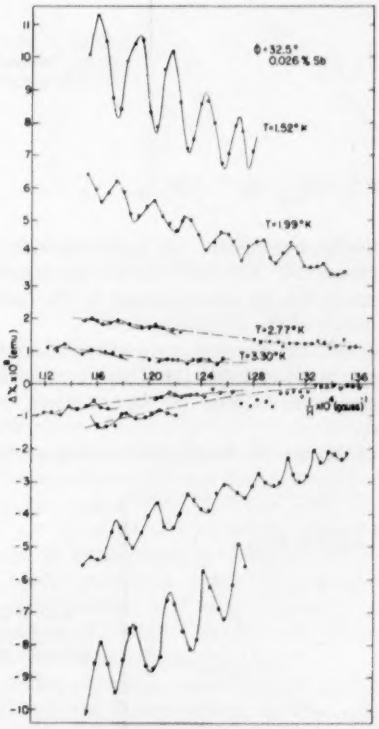

FIG. 3. The de Haas-van Alphen effect in Sn+0.026 atomic percent Sb at $\phi=32.5°$.

[12] Rev. Sci. Instr. (to be published).
[13] D. Shoenberg, Proc. Roy. Soc. (London) **A245**, 1 (1952).

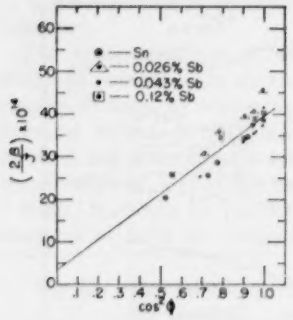

FIG. 4. Plot of $(2\beta/\zeta)^2$ *vs* $\cos^2\phi$ for the tin-antimony alloys.

because of the conditions governing reproducibility from sample to sample have not yet been clearly determined.

2. The Alloys

Examples of the de Haas-van Alphen effect in the 0.026 atomic percent Sb alloy are shown in Figs. 2 and 3. Qualitatively, the features of the effect are similar to those for pure Sn. The phenomenon of beats becomes less noticeable as the Sb concentration is increased and

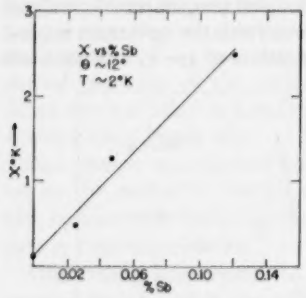

FIG. 5. Plot of X *vs* atomic percent Sb at $T \simeq 2°K$ and $\phi \simeq 12°$.

is practically nonexistent at concentrations of 0.12 atomic percent Sb. The most obvious qualitative effect of increasing the Sb concentration is the decrease in the amplitude of the oscillations.

The significant electronic parameters which occur in Eq. (1) are listed in Table III. These were obtained by fitting the data to Eq. (1) by methods describde elsewhere.[13]

Part of the motivation for the present work was to determine the effect of increasing the electron concentration on the parameter ζ in an effort to decide whether hole or electron motion is responsible for the de Haas-van Alphen effect in Sn. Inspection of Table III shows that within the limits of experimental error (± 10 percent) there is no change in ζ. It appears that the question of holes *versus* electrons as the relevant carriers for the de Haas-van Alphen effect in Sn cannot be decided easily by this method. However, there is evidence that this method is applicable to Bi.[14]

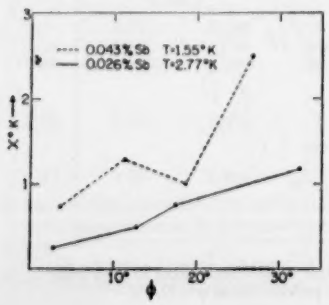

FIG. 6. Plot of X *vs* ϕ for two tin-antimony alloys.

The effect of alloying on the period of the oscillations, is shown in Fig. 4, showing a plot of $(2\beta/\zeta)^2$ *vs* $\cos^2\phi$. There is no detectable change in $2\beta/\zeta$ as the antimony content is increased. In view of the constancy of ζ, this shows that β is also not affected within the limits of experimental error by increasing the Sb concentration in Sn. Thus, the effective mass parameters are not affected by alloying.

TABLE III. Tabulation of parameters characterizing the de Haas-van Alphen effect in tin-antimony alloys.

ϕ (deg)	$(2\beta/\zeta)\times10^7$ (gauss^{-1})	Sn X (°K)	ζ (ev)	$2\beta\times10^{20}$ (ergs/gauss)
1.5	6.21		0.189	18.8
13.5	6.11	0.11	0.198	19.4
16.5	5.89		0.193	18.2
28.5	5.37		0.189	16.2
31.5	5.06	0.10	0.196	15.9
43.5	4.54			
			Average = 0.193 ev	
		Sn + 0.026% Sb		
2.5	6.77	0.26	0.186	19.6
12.5	6.38	0.61	0.192	19.7
17.5	6.27	0.78	0.186	18.7
27.5	6.00	0.69	0.177	17.0
32.5	5.55	1.20	0.186	16.5
			Average = 0.185 ev	
		Sn + 0.043% Sb		
3.5	6.46	0.73		
11.5	5.99	1.29		
18.5	5.80	1.00		
33.5	5.03	2.45		
2.2	6.13		0.190	18.6
12.8	5.97		0.203	19.4
17.2	5.85		0.201	18.8
			Average = 0.198 ev	
		Sn + 0.12% Sb		
3	6.34	2.3	0.183	18.5
12	6.24	2.4	0.199	19.9
18	5.86	2.5	0.210	19.7
27	5.89	1.9	0.193	18.1
42	5.10			
			Average = 0.196 ev	

Another reason prompting the present work was to determine X, the collision broadening parameter, as a function of the Sb content in Sn under conditions of carefully controlled composition and thermal equilibrium state. In Fig. 5, X as determined at $T \simeq 2°K$

[14] D. Shoenberg and M. Z. Uddin, Proc. Roy. Soc. (London) **A156**, 687 (1936)., Proc. D. Shoenberg Roy. Soc. (London) **A170**, 341 (1939).

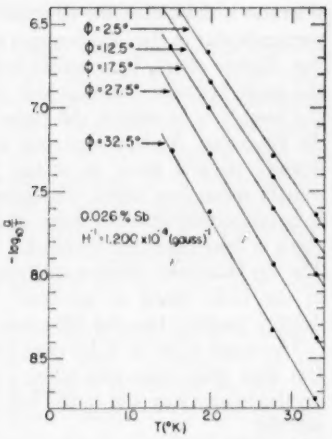

FIG. 7. Plot of $-\log_{10}(a/T)$ *vs* T for Sn+0.026 atomic percent Sb at various angles, ϕ.

and $\phi \simeq 12°$, is plotted as a function of the atomic percentage of Sb added to the Sn. X is an approximately linear function of the Sb concentration and the value for pure Sn is about 0.1°K. This value of X for pure Sn is about ten times smaller than previously quoted values.[13]

In Fig. 6, X *vs* ϕ is plotted for the 0.026 and 0.043 atomic percent Sb samples. Even though the error in X may be about ± 20 percent, there seems to be a definite dependence of X on ϕ.

In order to compare the theoretical predictions regarding the temperature and field dependence of the amplitude a of the oscillatory part of the susceptibility, $\log_{10}(a/T)$ *vs* T has been plotted in Fig. 7 and $\log_{10}(aH^{\frac{1}{2}})$ *vs* H^{-1} in Fig. 8. These data are taken from measurements on the 0.026 atomic percent Sb sample.

If the theoretical predictions are correct, these plots should be straight lines with negative slopes. The temperature dependence of a appears to be accurately predicted, but the field dependence of a shows marked deviations from the predictions. The best average over the beats, which is indicated, for example, by the dashed lines in Fig. 1, is used to determine a. Further evidence of this deviation from the theoretical predictions is shown for Sn in Fig. 9. Similar results have been observed in Zn.[15]

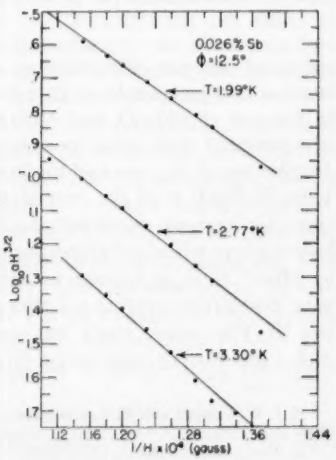

FIG. 8. Plot of $\log_{10}(aH^{\frac{1}{2}})$ *vs* $1/H$ for Sn+0.026 atomic percent Sb at $\phi = 12.5°$ and different T.

Since X is obtained from the slope of the $\log_{10}(aH^{\frac{1}{2}})$ *vs* H^{-1} curves, it should be pointed out that the values of X quoted above were obtained by fitting the best straight lines to the curves. In cases where the deviation from linearity was very marked, X was not interpretable and, therefore, not determined.

The room temperature value of $|\chi_3 - \chi_1|$ for the Sn-Sb alloys was also measured and the results are shown in Fig. 10. $|\chi_3 - \chi_1|$ increases linearly by about 25 percent over its value for pure Sn as the percentage of Sb increases by 0.2 atomic percent.

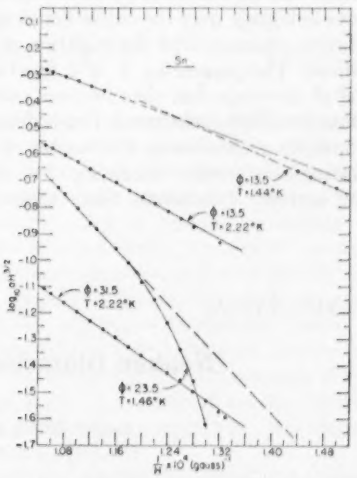

FIG. 9. Plots of $\log_{10}(aH^{\frac{1}{2}})$ *vs* $1/H$ for pure tin showing strong deviations from linearity.

V. DISCUSSION OF RESULTS

In view of the insensitivity of ζ to increasing electron concentration, the decision between hole conduction or electron conduction as the mechanism responsible for the de Haas-van Alphen effect in Sn cannot be made.

If, for purposes of argument, it is assumed that all the electrons added to Sn as a result of alloying become de Haas-van Alphen effect electrons, there should be a change in ζ given by $\Delta\zeta/\zeta = \frac{2}{3}\Delta N/N$. This amounts to 17 percent at 0.026 atomic percent Sb and 80 percent at 0.12 atomic percent Sb. Since the experimental error in the determination of ζ is ± 10 percent, it follows that less than 0.15×10^{-3} electron per atom become de Haas-van Alphen effect electrons.

The added electrons could become uniformly distributed over the Fermi surface, in which case $(\Delta\zeta/\zeta)$

[15] F. J. Donahoe, and F. C. Nix, preceding paper, Phys. Rev. **95**, 1395 (1954).

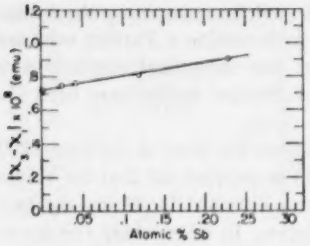

FIG. 10. Variation of $|\chi_3-\chi_1|$ with atomic percentage of antimony at room temperature.

$\times 100$ would be about 0.2 percent in the 0.12 atomic percent Sb sample, for example, and would not be detectable in the data.

The large change in $\chi_3-\chi_1$ at room temperature with a very small increase of Sb in the Sn indicates that the added electrons go into a more or less localized region in $\mathbf{k}$ space, removed from the regions responsible for the de Haas-van Alphen effect, rather than distribute themselves uniformly over the entire Fermi surface.

A tentative explanation of the variation of X with ϕ is as follows: The parameter X is a function of the reciprocal of the mean free time between collisions for the de Haas-van Alphen electrons. This is demonstrated by Fig. 5, which shows that as the number of Sb atoms in Sn increases, thereby increasing the number of scattering centers, X increases. Since theoretical considerations show that the electron motion in the plane perpendicular to the field is responsible for the de Haas-van Alphen effect, it therefore seems plausible that as the angle between the field and the tetragonal axis of the sample is increased, the plane of the orbits of the de Haas-van Alphen electrons rotates into a more densely packed plane of atoms, which gives rise to shorter mean free times, therefore larger values of X. It is interesting that the value of X at $\phi \cong 30°$ is about three or four times the value of X between 0° and 20°. The de Haas-van Alphen electrons would be rotating in the (101) plane at $\phi = 28.5°$. This plane is more densely packed than the 100 plane in Sn.

The small value of X for pure tin is attributed to the fact that great care was taken to avoid straining the crystal in any way and to the heat treatment given the sample.

At first sight, one might think that the nonlinearity of the $\log_{10}(aH^{\frac{1}{2}})$ *vs* H^{-1} plots is due to failure to include sufficient terms of the series given in Eq. (3). A calculation of the contribution of the second term, at a reasonable field strength and temperature, to the amplitude shows that it is too small to account for the observed deviations.

It appears that a higher power of H than 3/2 would give a better fit to the experimental results.

PHYSICAL REVIEW VOLUME 95, NUMBER 6 SEPTEMBER 15, 1954

Neutron Diffraction Studies of a Nickel Zinc Ferrite*

V. C. WILSON AND J. S. KASPER
General Electric Research Laboratory, Schenectady, New York

(Received June 8, 1954)

Neutron diffraction studies have been made of a ferrite powder of composition $Zn_{0.5}Ni_{0.5}Fe_2O_4$. The crystal structure is of the spinel type with 4 Zn^{++} and 4 Fe^{+++} ions in the tetrahedral positions and 4 Ni^{++} and 12 Fe^{+++} ions in the octahedral positions. The magnetic structure at 25°C appears to have an antiparallel arrangement of the Fe^{+++} spins on the two sites and a random orientation of the Ni^{++} spins.

INTRODUCTION

RECENT neutron diffraction studies of ferrites[1–4] have clearly demonstrated the special advantages of neutron diffraction for determining both the chemical and magnetic structures of these substances. Thus, while with x-rays it is difficult to ascertain the distribution of the respective cations and even more difficult to obtain a precise value of the oxygen parameter, the use of neutrons readily provides both kinds of information. Even more important is the opportunity by means of neutron diffraction to obtain directly the location and magnitude of atomic magnetic moments. In the case of $ZnFe_2O_4$ and $NiFe_2O_4$[2] the findings are in agreement with prior postulates as to both the distribution of the ions and the magnetic structures.[5,6] Thus, $ZnFe_2O_4$ is of the normal spinel type with no magnetic moment alignment, and $NiFe_2O_4$ is of the inverted type with the ferrimagnetic structure proposed by Néel.[6] It is of interest to ascertain whether the same postulates apply to a ferrite containing both Zn and Ni. The present study was made for this purpose with a specimen of composition $Ni_{0.5}Zn_{0.5}Fe_2O_4$.

* The observations were made at the Brookhaven National Laboratory.

[1] Shull, Wollan, and Koehler, Phys. Rev. **84**, 912 (1951).
[2] J. M. Hastings and L. M. Corliss, Revs. Modern Phys. **25**, 114 (1953).
[3] Corliss, Hastings, and Brockman, Phys. Rev. **90**, 1013 (1953).
[4] G. E. Bacon and F. F. Roberts, Acta Cryst. **6**, 57 (1953).
[5] E. J. W. Verwey and E. L. Heilmann, J. Chem. Phys. **15**, 174 (1947).
[6] L. Néel, Ann. Physik **3**, 137 (1948).

EXPERIMENTAL PROCEDURE

The ferrite was prepared according to the reaction $0.5NiO+0.5ZnO+Fe_2O_3 \rightarrow Ni_{0.5}Zn_{0.5}Fe_2O_4$. The components were pure powders intimately mixed in a colloid mill using distilled water. The water was then evaporated in an oven at 120°C and the resulting cake was pulverized and screened through a 30 mesh screen. This material was fired in air in mullite boats for 4 hours at 1350°C and furnace cooled. The x-ray diffraction pattern of the product corresponded to a spinel structure, which accounted for all the lines that were observed.

A bar of the ferrite was made from the same powder mixture and fired at the same temperature as the powder sample. The magnetic saturation for this bar was 4260 gauss which corresponds to 3.0 Bohr magnetons per formula $Ni_{0.5}Zn_{0.5}Fe_2O_4$. Guillaud[7] reports an extrapolated value of 5.4 Bohr magnetons per molecule at absolute zero; therefore, a value of 3 Bohr magnetons seems reasonable at room temperature.

For the neutron diffraction experiments, the powdered product was sieved through 100 mesh screen and loosely packed into a flat cell of dimensions $\frac{1}{2}$ in.$\times 2\frac{1}{4}$ in.$\times 4$ in.

TABLE I. Observed parameters.[a]

	Nickel	Ferrite at 338°C	Ferrite at 25°C
a_0	3.524 A	8.43 A	8.38 A
h	1.29 cm	1.37 cm	1.37 cm
ρ'	5.736 g/cm³	2.54 g/cm³	2.59 g/cm³
$e^{-\mu h}$	0.227	0.624	0.597

[a] P_{111}(nickel) = 1513 (arbitrary scale), $F_{111}^2 = 17.11$.

The two large surfaces of the cell were of thin boron-free glass. The $\frac{1}{2}$-in. thick specimen was set in the transmission arrangement and was irradiated with a 2-in. square beam of neutrons of 1.05 A wavelength. The "monochromatic" beam was obtained by reflection of the neutron source from a (200) face of a large lead crystal. Collimation was accomplished by means of Soller slits, and the diffracted rays were detected by a BF_3 proportional counter. A detailed description of the apparatus is to be published elsewhere.[8]

The diffracted intensity was recorded at intervals of 10′ of arc. The number of diffracted neutrons was recorded for a fixed number of incident neutrons on the sample as determined by a beam monitor counter. Integrated intensities were determined by measuring with a planimeter the areas under the peaks and were placed on an "absolute" basis by reference to the area of a (111) peak of Ni. For the calculations the following expression, appropriate for the integrated power of a diffraction peak obtained in transmission through a

[7] C. Guillaud, J. phys. et radium **12**, 244 (1951).
[8] Wilson, Roberts, Geisler, Kasper, and Roth, Rev. Sci. Instr. (to be published).

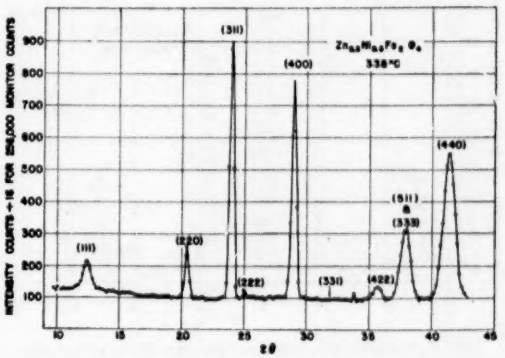

FIG. 1. Neutron diffraction pattern of a 50–50 nickel-zinc ferrite at 338°C.

cell, was used:

$$P_{hkl}=\left(P_0\lambda^3\frac{l}{4\pi r}\right)\left(N^2h\frac{\rho'}{\rho}\right)\left(\frac{e^{-\mu h\sec\theta}}{\sin^2 2\theta}\right)TgJ_{hkl}F_{hkl}^2, \quad (1)$$

where P_0 = number of neutrons striking the sample in unit time, λ = neutron wavelength, l = counter slit height, r = distance from counter slit to sample, N = number of unit cells per cm³, h = thickness of sample, ρ' = apparent density of powder, ρ = density of solid crystal, μ = effective linear absorption coefficient, T = temperature correction = $\exp[-2B(\sin\theta/\lambda)^2]$, g = geometrical correction factor for thick samples, J_{hkl} = multiplicity, and F_{hkl} = the structure factor.

The quantity $e^{-\mu h}$ was determined directly by measuring the transmission through the sample at $\theta=0$. The geometrical factor, g, is a special one for the conditions of our experimental arrangement. Its derivation is given in the appendix.

In normalizing to a nickel reflection the terms in the first bracket drop out. Table I gives the observed quantities necessary for application of Eq. (1).

CRYSTAL STRUCTURE

For $Ni_{0.5}Zn_{0.5}Fe_2O_4$, the structure determination consists of ascertaining the distribution of the three metal ions among the positions 8*a* (tetrahedral) and 16*d* (octahedral) of space group $Fd3m-O_h^7$, and of a

TABLE II. Intensities at 338°C for $Zn_{0.5}Ni_{0.5}Fe_2O_4$.

hkl	Observed	Calculated
111	155	149
220	113	139
311	643	653
222	14	10
400	603	601
331	0	3
422	75	72
511, 333	408	449
440	1001	1085

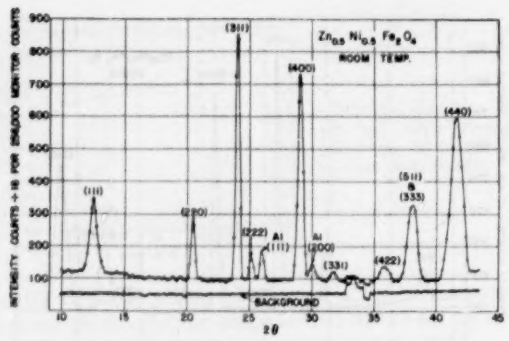

FIG. 2. Neutron diffraction pattern of a 50–50 nickel-zinc ferrite at room temperature.

determination of the oxygen parameter, u. The diffraction data at 338°C shown in Fig. 1 were used primarily for this purpose. Since the Curie temperature of this material is 260°C, it was assumed that at 338°C no magnetic contribution was present in any of the observed peaks.

The best fit of the calculated to the observed intensities was obtained for a model in which the tetrahedral positions were filled with 4 Zn^{++} ions and 4 Fe^{+++} ions distributed at random and that the octahedral positions were occupied by 12 Fe^{+++} ions and 4 Ni^{++} ions also distributed at random. In this case the best value for u was 0.383 ± 0.002 (see Table II). For these calculations a Debye-Waller temperature correction was used with the constant $B=1.4\times10^{-8}$ which corresponds to a characteristic temperature of 385°K. The following values of the nuclear scattering amplitudes were used:

$$b_{Ni}=1.03\times10^{-12}\text{ cm}; \quad b_{Zn}=0.59\times10^{-12}\text{ cm};$$
$$b_{Fe}=0.96\times10^{-12}\text{ cm}; \quad b_{oxygen}=0.58\times10^{-12}\text{ cm}.$$

Among other models that were considered were those wherein (a) the separate ions are ordered in tetrahedral or octahedral sites, or both; and (b) there is a partial inversion (some Ni^{++} in tetrahedral, some Zn^{++} in octahedral sites). None of these models was as satisfactory as the one above, regardless of the parameter value u.

MAGNETIC STRUCTURE

The diffraction pattern obtained at room temperature (25°C) is shown in Fig. 2. At this temperature for the most part there is superposition of magnetic and nuclear intensities. Only the (331) reflection appears to be purely magnetic. The nuclear intensities can be expected to differ from those at 338°C because of a different temperature factor and perhaps a slightly different u parameter. It was assumed that u remained at 0.383. The nuclear intensities at room temperature were obtained by correcting the observed intensities of the lines at 338°C to the value they would have without the Debye-Waller temperature effect, then by applying to these data a new temperature factor appropriate to room temperature. These results are shown in column 3 of Table III. The observed intensities are in column 4 and the difference between columns 4 and 3 gives the magnetic intensity, column 5.

Several arrangements and orientations of the magnetic ions were considered and F^2 values determined for each arrangement. To calculate F values it was assumed that an Fe^{+++} ion has 5 Bohr magnetons and a scattering amplitude of 1.35×10^{-12} cm; Ni^{++}, 2 Bohr magnetons, and 0.54×10^{-12} cm. In this case, $F^2=F_{nucl}^2+f^2q^2F_{mag}^2$, where f is the form factor given by Corliss and Hastings,[2] and q is the factor relating the orientation of the magnetic moment of the scattering particle to the orientation of the scattering plane. For a powder sample with cubic symmetry and with no magnetic field applied $q^2=\frac{2}{3}$ for all diffracted lines. The five arrangements that most nearly fitted the observed data are shown as cases I to V of Table III. In these five cases it was assumed that any magnetic alignment in a tetrahedral site was 180° to any alignment in the

TABLE III. Magnetic intensities for $Zn_{0.5}Ni_{0.5}Fe_2O_4$.

hkl	Obs. nucl. 338°C	Nucl. 25°C	Obs. 25°C	Diff. =mag. obs.	Calculated magnetic I	II	III	IV	V
111	155	157	332	175	136	263	164	305	294
220	113	118	156	38	9	38	13	38	33
311	643	668	671	3	12	4	11	8	10
222	14	15	66	51	39	51	44	66	68
400	603	657	690	33	30	55	36	65	64
331	0	0	34	34	27	53	33	61	59
422	75	85	82	−3	3	12	5	12	10
511, 333	408	472	468	−4	3	4	2	1	2
440	1001	1200	1193	−7	3	2	4	4	5

octahedral sites. Except in case V, considerations were given only to arrangements that would yield a net magnetic moment of 3 Bohr magnetons per molecule. As at 338°C, it was assumed that for each unit cell 4 Fe^{+++} ions were in the tetrahedral sites, 8a, and 12 Fe^{+++} and 4 Ni^{++} ions were in the octahedral sites, 16d. Case I is for one-half the magnetic spins lined up in both sites. Case II is for the iron in the 8a sites perfectly oriented and the Ni and Fe in the 16d sites both 0.647 oriented. Case III is for the Fe in 8a and 16d 0.6 oriented, Ni not oriented. Case IV is for Fe in 8a perfectly oriented, Fe in 16d 0.733 oriented, Ni not oriented. As before, the calculated intensities are in reference to the Ni-powder standard.

Niessen[9] has published a theoretical treatment to calculate the spontaneous magnetization of the nickel zinc ferrites. Using his equations one would expect that at room temperature a 50–50 Ni-Zn ferrite would have 3.26 Bohr magnetons per molecule, and the average moments of the ions would be: Fe^{+++} in 8a, 4.65 Bohr magnetons; Fe^{+++} in 16d, 3.24 Bohr magnetons; and

[9] K. F. Niessen, Physica **18**, 449–468 (1952).

Ni^{++} in 16*d*, 1.44 Bohr magnetons. Case V is the calculation of the neutron diffraction intensities to be expected for this distribution.

It appears that model III (Fe 0.6 lined up and Ni not lined up) gives the best fit with observed intensities, though some of the other models, notably I, cannot be ruled out. Except for (220), the agreement is quite satisfactory for III. The value of 38 (column 5), obtained by the difference procedure for (220), may well be quite too high, resulting from a too low value for the nuclear contribution at 338°C, as can be seen with reference to Table III. Attaching most weight to (111), (222), and (331), which are least sensitive to the nuclear contributions, model III would be definitely favored.

Additional support for model III is given by a comparison of the calculated and observed total intensities at 25°C (Table IV).

CONCLUSIONS

The arrangement of the metal ions is as one would predict from Verwey's observations on the family of ferrites. The antiparallel arrangement of the iron spins on the 8*a* and 16*d* sites was predicted by the Néel theory; however, the apparent lack of lineup of the nickel magnetic moments is a little surprising. The theories are not sufficiently well developed to rule out this possibility.

TABLE IV. Total intensities (nuclear+magnetic) at 25°C.

		Calculated				
hkl	Observed	I	II	III	IV	V
111	332	285	412	313	454	444
220	156	150	179	154	179	173
311	671	695	687	694	691	693
222	66	50	61	54	76	78
400	690	669	693	675	703	702
331	34	30	56	36	64	62
422	82	82	91	84	91	89
511, 333	468	511	512	511	510	510
440	1193	1273	1271	1273	1273	1274

APPENDIX I

Geometric Correction Factor, *g*

The monochromatic incident neutron beam striking the sample has a cross section of 2 in. by 2 in. The BF_3 proportional counter detector has a solar slit system before it so that the effective cross section of the detector is also 2 in. by 2 in. From Fig. 3 one can see that the neutrons scattered in the direction 2θ from the two small shaded areas will pass outside the detector. Equation (1) of this paper is based upon the assumption that all the neutrons diffracted by the sample are detected. Therefore, a correction factor must be used which is the ratio of the area *ABCDEF* to the area *GCHF*. The sample is rotated to an angle θ when the detector arm is rotated to an angle 2θ from the axis of the beam. If *W* is the width of the beam and the detector and *h* is the thickness of the sample, then

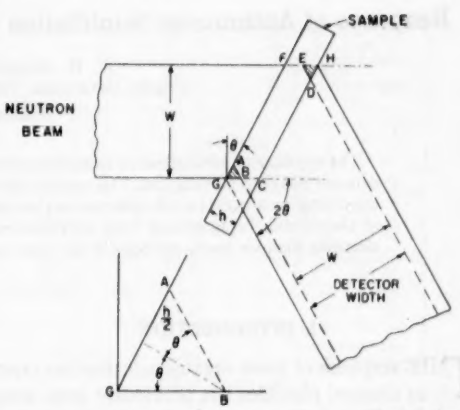

FIG. 3. Diagram for calculating geometric correction factor.

$$g=\frac{\text{area } ABCDEF}{\text{area } GCHF}=\frac{\text{area } GCHF-2\text{ area } GAB}{\text{area } GCHF},$$

$$g=\frac{hW/\cos\theta-2(t/2\times t/2\tan\theta)}{hW/\cos\theta},$$

$$g=1-\frac{h\sin\theta}{2W}.$$

In the case $h=\frac{1}{2}$ in. and $W=2$ in., we therefore obtain $g=1-\frac{1}{8}\sin\theta$.

Response of Anthracene Scintillation Crystals to Monoenergetic Soft X-Rays*

W. H. Robinson† and W. Jentschke
Physics Department, University of Illinois, Urbana, Illinois
(Received June 15, 1954)

The response of anthracene to monoenergetic x-rays in the range from 9 kev to 24 kev in a scintillation detector has been investigated. The results show that the response to short-range electrons produced within the crystal by x-rays is about the same as the response to electrons with equal energy incident on the surface of the crystal. In agreement with previous results, the specific fluorescence (dL/dx) is smaller for slow electrons than for heavy particles of the same specific energy loss (dE/dx).

I. INTRODUCTION

THE response of some organic scintillation crystals to charged particles has previously been investigated by Birks,[1] Franzen *et al.*,[2] Hopkins,[3] Cross,[4] Taylor *et al.*,[5] and King and Birks.[6] The results obtained by Taylor *et al.*[5] indicated that both anthracene and stilbene have slightly different fluorescence efficiencies for protons and alpha particles of the same specific energy loss. However, for electrons of energies below 30 kev they found a fluorescence efficiency considerably lower than that of protons and α particles of the same specific energy loss. In their experiment, radioactive sources of internal conversion electrons provided single electrons with energies from 30 kev to 600 kev. In the range from 0.5 kev to 5 kev a pulsed beam of electrons was used. No measurements were performed in the range from 5 kev to 30 kev.

The use of external electron sources and the resulting surface effects and back-diffusion of electrons in the experiments of Taylor *et al.*[5] might explain part of the difference between the fluorescence efficiency for electrons and heavy charged particles. The purpose of the present experiment, therefore, was the investigation of the response of anthracene to electrons produced inside the crystal where these effects are not present. Electrons with energies between 9 kev and 24 kev were used. Measurements with energies below 9 kev were not made since the signal pulses were not distinguishable from photomultiplier tube noise. The results show that the response of short-range electrons produced within the crystal by x-radiation is within the limits of error the same as the response to electrons with equal energy incident on the surface of the crystal. In agreement with previous results, the specific fluorescence (dL/dx) for slow electrons is smaller than that for heavy particles of the same specific energy loss (dE/dx).

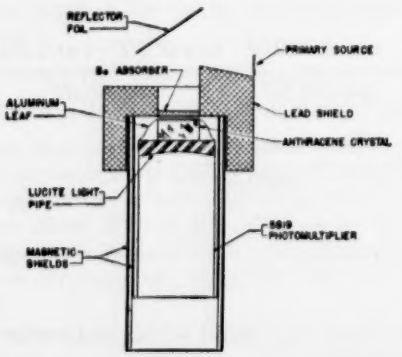

FIG. 1. Experimental arrangement for the measurement of the response of anthracene to fluorescent x-rays.

II. EXPERIMENTAL PROCEDURE

Monoenergetic photoelectrons were produced inside the anthracene crystal (2 cm×2 cm×1 cm) by incident x-radiation. X-rays in the range from 9 kev to 24 kev were obtained in two ways: (1) directly from a radioactive source decaying by K capture, and (2) from fluorescent x-radiation excited in suitable metal foil "reflectors" by radiation from a primary x-ray source following a method described by Insch.[7] For the first method we used the K x-rays of gallium and indium which are emitted after the K capture of Ge^{71} and Sn^{113}, respectively. The arrangement for the second method (using reflectors) is shown in Fig. 1. The reflector foils were about 0.01 cm thick and their area was about 40 cm². Sn^{113} was used as the primary x-ray source for the production of the fluorescence radiation in Zr, Rh, and Ag. Table I gives the energies for the

TABLE I. Energies of the K_α and K_β x-rays in Ga, Zr, Rh, Ag, and In.

Element	Energy in kev K_α	K_β
Ga	9.1	10.2
Zr	15.5	17.6
Rh	19.8	22.6
Ag	21.7	24.8
In	23.7	27.1

* Assisted by the joint program of the U. S. Office of Naval Research and the U. S. Atomic Energy Commission.
† Now at Carnegie Institute of Technology, Pittsburgh, Pennsylvania.
[1] J. B. Birks, Proc. Phys. Soc. (London) **A64**, 874 (1951).
[2] Franzen, Peele, and Sherr, Phys. Rev. **79**, 742 (1950).
[3] J. I. Hopkins, Rev. Sci. Instr. **22**, 29 (1951).
[4] W. G. Cross, Chalk River Laboratory (private communication).
[5] Taylor, Jentschke, Remley, Eby, and Kruger, Phys. Rev. **84**, 1034 (1951).
[6] J. W. King and J. B. Birks, Phys. Rev. **86**, 568 (1952).
[7] G. M. Insch, Phil. Mag. **41**, 857 (1950).

K_α and K_β radiation in these elements. The approximate intensity ratios of K_α/K_β are 5:1. (Since the binding energy of the K shell in Ag is 25.5 kev, only the K_β x-rays of indium are able to produce the fluorescence radiation of Ag.) Conversion electrons from Cs^{137} and Hg^{203} which give linear response were used for calibration purposes.

The pulses from the photomultiplier tube were amplified by a linear, nonoverloading amplifier with a rise-time of 0.25 microseconds and a time constant of 2.5 microseconds. A single-channel pulse-height analyzer was used for the pulse-height selection.

III. RESULTS

Two typical pulse-height distributions are shown in Figs. 2 and 3. The distribution in Fig. 2 was obtained using Ge^{71} and represents the lowest energy measured. Figure 3 is a pulse-height distribution obtained by

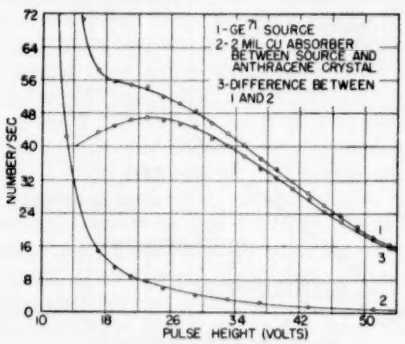
1-GE71 SOURCE
2-2 MIL CU ABSORBER BETWEEN SOURCE AND ANTHRACENE CRYSTAL
3-DIFFERENCE BETWEEN 1 AND 2
NUMBER/SEC
PULSE HEIGHT (VOLTS)

FIG. 2. Pulse-height distribution resulting from the fluorescence radiation of anthracene when excited by x-rays of a Ge^{71} source. The photomultiplier tube noise is responsible for the large number of small pulses. The statistical errors are not indicated since they are smaller than the circles.

using fluorescence x-rays from a Zr foil. About 15 percent of the x-ray counts are due to the K_β radiation. Since the K_α and K_β peaks cannot be resolved, a small correction for the evaluation of the true pulse-height maximum which belongs to the K_α x-rays was necessary. This introduces an uncertainty of the fluorescence energy relation of about ± 2 percent.

Plots of pulse height *vs* energy are shown in Figs. 4 and 5. The arbitrary pulse-height scale is normalized to 624 for the 624-kev Cs^{137} K conversion electrons. The accuracies of the pulse-height determinations are ± 1 percent at 600 kev, ± 2 percent at 200 kev, and ± 5 percent in the region from 10 kev to 30 kev. In the range from 20 kev to 30 kev the Compton effect and the photoelectric effect are of the same order of magnitude, but the Compton events will not be counted unless they are followed by a photoelectric event. The slight broadening of the pulse-height distributions on the low-energy side by Compton events is taken into account in the assignment of errors in this energy range.

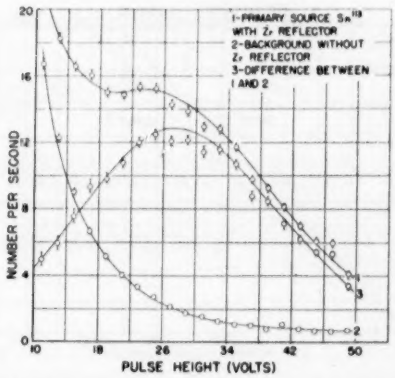
1-PRIMARY SOURCE Sn113 WITH Zr REFLECTOR
2-BACKGROUND WITHOUT Zr REFLECTOR
3-DIFFERENCE BETWEEN 1 AND 2
NUMBER PER SECOND
PULSE HEIGHT (VOLTS)

FIG. 3. Pulse-height distribution resulting from the fluorescence radiation of anthracene when excited by x-rays of Zr.

As a check on the calibration of the electronics, the response of sodium iodide to electrons of energies from 20 kev to 660 kev was measured; the response was found to be linear over this region in agreement with previous results.[6,8]

The present experimental response curve (Figs. 4 and 5), is linear above 130 kev with an extrapolation intersecting the abscissa at 23 kev in good agreement with previous experiments.[3,5] It also agrees with the previous curve at lower energies within the accuracy claimed in that experiment, but lies somewhat higher. This agreement suggests that the response to short range electrons incident on the surface of the crystal is not very different from the response to electrons produced within the crystal by x-radiation. The discrepancy between the heavy particle and electron-fluorescence efficiency therefore remains and cannot entirely be attributed to the escape of excitons or photons from the crystal surface, as suggested by Birks.[9]

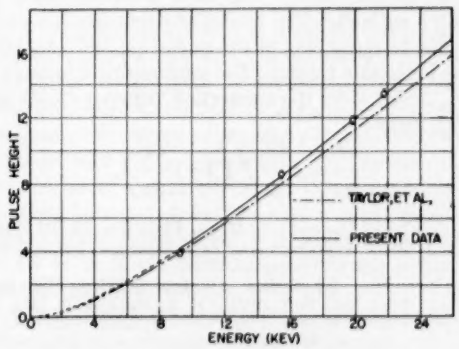

FIG. 4. Pulse heights from the fluorescence radiation of anthracene as a function of electron energy. The arbitrary pulse-height scale is normalized to 624 for 624-kev electrons.

[8] West, Meyerhof, and Hofstadter, Phys. Rev. **81**, 141 (1951).
[9] J. B. Birks, Phys. Rev. **86**, 569 (1952).

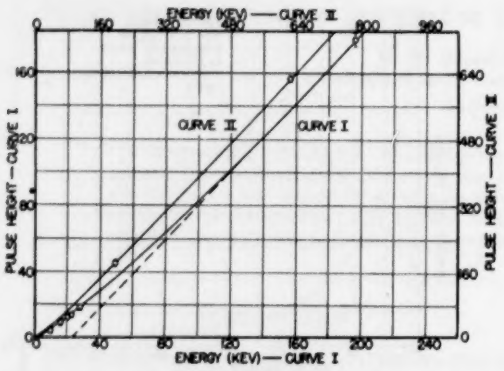

FIG. 5. Pulse heights from the fluorescence radiation of anthracene as a function of electron energy. The arbitrary pulse-height scale is normalized to 624 for 624-kev electrons.

IV. DISCUSSION OF RESULTS

It is known that the fluorescence efficiency of an organic crystal depends on the density of the ionization along the path of the particle in the crystal. Figure 6 is a plot of the specific fluorescence dL/dx as a function of specific energy loss dE/dx for alpha particles, protons, and electrons. The curves for alpha particles and protons were recalculated from the pulse height *vs* energy curves obtained by Taylor *et al.*[5] and Franzen *et al.*,[2] using dE/dx values which were computed from Hirschfelder and Magee's[10] work on the stopping power of protons in hydrogen and carbon. The curve for electrons was calculated from the curve of pulse height *vs* energy obtained in the present experiment. The values of dE/dx for electrons were calculated from Bethe's[11] theoretical formula. These curves show that the specific fluorescence for large dE/dx values depends on the specific energy loss and on the nature of the incident particle.[5]

Theories of the dependence of the specific fluorescence on the specific energy loss have been proposed by different authors.[12] The nonlinear dependence is probably due to quenching of the excitation and ionization in the ionization column. The semiempirical formula of Birks, which gives the connection between dL/dx and dE/dx, reads

$$\frac{dL}{dx}=A\frac{dE}{dx}\Big/\left(1+B\frac{dE}{dx}\right),$$

where A and B should have the same constant value independent of the nature of the particle. Therefore, particles which have the same specific energy loss should give the same specific fluorescence.

The experimental points for protons and, except for very low energy, for α particles can be accurately fitted by Birks' formula. However, choosing the same value of A for both curves, the B value for protons is slightly larger than that for alpha particles. Recent, very accurate measurements of Cross agree essentially with these results. His data yield for protons a B value of 6.4 and for alpha particles 5.0, if one assumes that $A=1$ in both cases.

In contrast to the proton and alpha curves, Birks' formula does not fit the electron curve. If the constant A is taken the same as for the heavy particles, B can be chosen to fit the response below 150 kev only at the expense of an 8 percent deviation from linearity at 150 kev and a 5 percent deviation at 600 kev. This is outside the experimental error quoted for this region by Hopkins,[3] Taylor *et al.*,[5] and the present authors, all of whom found linearity at least within ±2 percent above 150 kev.

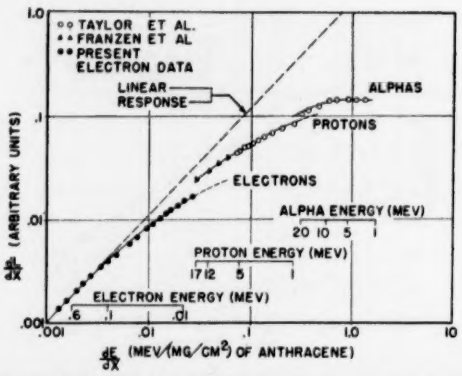

FIG. 6. Variation of the specific fluorescence, dL/dx (expressed in arbitrary units per mg/cm²), of anthracene with the specific energy loss, dE/dx, of the incident alpha particles, protons, and electrons of different energies. The straight line indicates linear response of the crystal.

The different energy spectra of the secondary electrons from alpha particles, protons, and electrons with the same specific energy loss may provide a possible explanation for their different response.[5]

ACKNOWLEDGMENTS

We thank W. G. Cross for valuable discussions and for communication of his data prior to publication.

[10] J. O. Hirschfelder and J. L. Magee, Phys. Rev. **73**, 207 (1948).
[11] H. A. Bethe, *Handbuch der Physik* (Springer, Berlin, 1933), Vol. 24, Part 1, p. 521, formula (56.10).
[12] J. B. Birks, *Scintillation Counters* (McGraw-Hill Book Company, Inc., New York, 1953); F. A. Black, Phil. Mag. **44**, 263 (1953); G. T. Wright, Phys. Rev. **91**, 1282 (1953); C. N. Chou, Phys. Rev. **87**, 904 (1952).

Theory of Electron Multiplication in Silicon and Germanium

P. A. WOLFF
Bell Telephone Laboratories, Murray Hill, New Jersey
(Received June 11, 1954)

Using methods similar to those employed to treat the gas discharge, a theory is developed to explain the multiplication of electrons (and holes) in Si and Ge junctions. The calculations take into account the effects of electron-phonon and pair-producing collisions on the distribution function. In Si, the only element for which complete measurements have been made, the calculated ionization rate *versus* field curve is in agreement with experiment if one assumes a mean free path of 200A for interactions between electrons and optical phonons.

I.

A RECENT series of experiments by McKay and McAfee[1] have demonstrated that in $p-n$ junctions of Si or Ge it is possible to obtain charge multiplication similar to that observed below breakdown in a gas. In the high-field region of the junction the electrons and holes attain sufficient energy to create additional charge by electron-hole pair production. The multiplication obtained in this way is small for low reverse bias but grows rapidly with increasing voltage and eventually approaches a large value at the critical breakdown potential. This process, as McKay[2] emphasizes, is quite analogous to that taking place in a gas discharge, a fact which permits him to apply a considerable part of the gas discharge theory to the solid state case. In particular, by using the formulas of Townsend's[3] β mechanism, he derives values of the ionization rates per unit path length, α_i, from the data. The resultant curve of α_i *versus* field is one of the most significant features of his work since α_i, though it is used to describe the nature of the discharge, is a quantity which is determined by the properties of the material in which the multiplication takes place. It is the parameter which relates the microscopic solid state properties of the junction to the macroscopic characteristics of the breakdown taking place in it. A theoretical calculation of the α_i *versus* field ($\mathcal{E}$) curve would, therefore, be of special interest since from it one would not only obtain an understanding of breakdown in junctions, but could also infer something about the properties of the materials of which they are made. Such a program is the aim of the present work.

The actual calculation of α_i is straightforward and parallels rather closely similar ones which have been made for ionization rates in gases.[4] Basically, the method consists in solving Boltzmann's equation for the motion of electrons (or holes) in a high field, taking into account the effect of electron-phonon and pair-producing collisions on the distribution functions. Having once obtained the distribution function, it is then a simple matter to calculate α_i, as well as other properties of interest such as the drift velocity. The final expressions contain parameters typical of the solid under consideration, not all of which are known at present. Fortunately, however, it turns out that the only one of these that plays a critical role in determining α_i is the mean free path for electron-phonon scattering. Its value is obtained by matching the theoretical α_i *vs* $\mathcal{E}$ curve to experiment at a single point, the theory then being evaluated by how well the rest of the curve fits the data. As will be seen, reasonably good agreement is obtained in this way, the discrepancies possibly being explainable in terms of fluctuations in donor (or acceptor) density within the junctions.

II.

As outlined in the previous section, the main difficulty in calculating α_i is the solution of the Boltzmann equation for the electron (or hole) velocity distribution functions. However, before one can attack this problem it is necessary to decide what the forces and interactions are that can affect the state of motion of electrons or holes within the solid. In the present case these particles are moving in an electric field and will, of course, be accelerated by it. In addition, they interact with the lattice vibrations of the crystal, emitting and absorbing phonons in such a way that the net effect is a resistive or frictional one opposing the accelerating field. Finally, when the electrostatic field is large enough, they will reach sufficient energy to produce electron-hole pairs in collisions with valence electrons. The question of the exact value of the threshold for this process will be discussed later, but it is clear that it must be at least as great as the forbidden gap in the material in question, i.e., 1.0 ev for Si and 0.7 ev in Ge. Thus pair production and multiplication will only occur when an electron has an appreciable chance of having energy of 1 ev or more. At energies such as these the coupling between electrons and the lattice is quite different from that for slow (thermal) electrons. Experiments of Ryder and Shockley[5] indicate that the fast electrons lose energy principally to the optical modes of the lattice. Few details as

[1] K. G. McKay and K. B. McAfee, Phys. Rev. **91**, 1079 (1953).
[2] K. G. McKay, Phys. Rev. **94**, 877 (1954).
[3] L. B. Loeb, *Fundamental Processes of Electrical Discharge in Gases* (John Wiley and Sons, Inc., New York, 1939).
[4] See, for example, W. P. Allis and Sanborn C. Brown, Phys. Rev. **87**, 419 (1952).
[5] E. J. Ryder and W. Shockley, Phys. Rev. **81**, 139 (1951).

yet are known about this interaction, but the theoretical work of Shockley,[6] as well as that of Seitz,[7] suggests that it is most reasonable to choose a constant mean free path for collisions between electrons and optical phonons. This assumption will be made in the succeeding work of this paper. Actually, the form of the α_i *vs* $\mathcal{E}$ curve appears not to depend critically upon it so that a small velocity dependence of the mean free path should not invalidate the results.

Another question of importance is that of the mean free path for hole-electron pair production. Fortunately, as will become clear later, the exact value of this quantity is not necessary in calculating α_i, it only being required that it be small compared to the mean free path for electron-phonon interaction. For the latter process the value needed to fit the experiments turns out to be about 200A. On the other hand, an estimate of the mean free path for pair production gives 15A for an electron energy 0.5 ev above threshold. This figure is obtained by treating the ionizing collision as a Coulomb scattering, the total cross section being found by integrating Rutherford's formula over values of the scattering angle such that energy greater than the gap width is transferred in the interaction. This value is also a reasonable one from the experimental point of view. Johnson and McKay[8] have shown that secondary electron emission from Ge is similar to that from metals, and for a metal a mean free path for internal secondaries of 15A is about right. Thus the criterion that the electron-phonon mean free path be long compared to that for pair production is satisfied, provided the electron energy is at least a few tenths of an electron volt above threshold. Right at threshold, of course, the pair cross section is zero, but it rises rapidly (quadratically if one counts available phase space) with increasing energy and, as the above figures show, soon surpasses that for electron-phonon scattering.

III.

The next step in the calculation of α_i is the solution of the Boltzmann equation. Since the cross section for pair production is large, this process will have a big effect on the distribution function. This fact will necessitate different treatments in the regions above and below the pair production threshold. In the low-energy region the velocity distribution is simple and can be expressed in terms of tabulated functions. For higher velocities the situation is more complicated, and it is only possible to obtain an explicit solution of the Boltzmann equation for energies far enough above the pair threshold that the mean free path is small compared to that for phonon scattering. The intermediate region is quite difficult and would require the use of numerical techniques. Considering the many uncertainties inherent in this problem such effort hardly seems

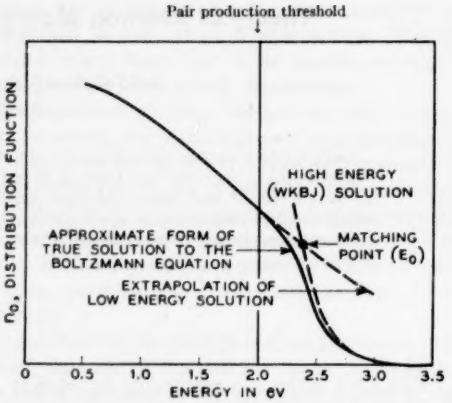

FIG. 1. Approximate form of electron energy distribution.

warranted. Instead, the high- and low-velocity solutions will be extrapolated into the rather narrow intermediate range and there matched. Figure 1 illustrates in a qualitative way the sort of procedure that will be used. This method, in effect, replaces the problem described above by a slightly different one in which the pair-production cross section has a threshold about 0.2 ev higher than formerly but also has a finite value there. The shape of the α_i *vs* $\mathcal{E}$ curve is mainly determined by the ability of the electrons to overcome the phonon drag and reach the threshold. This process will be the same in both these cases so they should give substantially the same results for α_i. Of course, if really accurate values of α_i ever become necessary it is always possible to carry out the numerical integration of the differential equations.

From Wannier's[9] paper on high-field mobilities it is evident that the solution of the Boltzmann equation is generally difficult. The expansion of the distribution function, which depends on the magnitude and direction of the electron velocity, into spherical harmonics leads to an infinite set of coupled differential equations which is very hard to handle. However, in certain limiting cases the problem simplifies considerably. For instance, if the charges lose only a small fraction of their energy at each collision the velocity distribution is nearly spherically symmetric and only the first two Legendre polynomials are needed in its expansion. The Boltzmann equation then reduces to a pair of fairly manageable, coupled differential equations. The solid-state breakdown being discussed here satisfies this criterion since, as was mentioned earlier, to obtain appreciable multiplication the average electron (or hole) energy must be approximately 1.0 ev, whereas the energy of the optical phonons is of the order of 0.1 ev.

Within the approximation mentioned above, the velocity distribution function can be written in the form

$$n(c,\theta)=n_0(c)+n_1(c)\cos\theta, \qquad (1)$$

[6] W. Shockley, Bell System Tech. J. **30**, 990 (1951).
[7] F. Seitz, Phys. Rev. **73**, 550 (1948).
[8] J. B. Johnson and K. G. McKay, Phys. Rev. **93**, 668 (1954).
[9] G. H. Wannier, Bell System Tech. J. **32**, 170 (1953).

where c is the magnitude of the electron or hole velocity and θ is the angle it makes with the electric field. When the electron energy is below the pair-production threshold, n_0 and n_1 are solutions of the equations

$$\frac{a}{3}\left(\frac{dn_1}{dc}+\frac{2n_1}{c}\right)=\frac{-n_0}{\tau}+4\pi\int F_0(c,c')\frac{n_0(c')}{\tau(c')}dc' \quad (2)$$

and

$$a\frac{dn_0}{dc}=-\frac{n_1}{\tau}+4\pi\int F_1(c,c')\frac{n_1(c')}{\tau(c')}dc'. \quad (3)$$

Here $a=e\mathcal{E}/m$ is the acceleration, τ the collision time, and

$$F_n(c,c')=\int P_n(\cos\theta)F(c,c',\cos\theta)d\Omega, \quad (4)$$

where $F(c,c',\cos\theta)$ is the probability that in an electron-phonon interaction an electron of velocity c' is scattered through the angle θ with final velocity c. The pair of equations, (2) and (3), are just those given in Wannier's paper for the motion of electrons in a gas.

At room temperatures in Si or Ge very few optical phonons are excited, so an electron will almost always lose energy in an interaction with the lattice vibrations. $F(c,c',\cos\theta)$ then takes the form

$$F(c,c',\cos\theta)=\delta(c-(c'^2-2\hbar\omega/m)^{\frac{1}{2}})g(c,\theta)/c^2, \quad (5)$$

where $\int g(c,\theta)d\Omega=1$, δ is the Dirac delta function, and ω is the frequency of the optical mode which, in the following, will be assumed constant. $F_0(c,c')$ is now given by

$$F_0(c,c')=\delta(c-(c'^2-2\hbar\omega/m)^{\frac{1}{2}})/c^2, \quad (6)$$

and Eq. (2) becomes

$$\frac{a}{3}\left(\frac{dn_1}{dc}+\frac{2n_1}{c}\right)=-\frac{n_0}{\tau}+\int\delta\left(c-\left(c'^2-\frac{2\hbar\omega}{m}\right)^{\frac{1}{2}}\right)\times\frac{n_0(c')}{\tau(c')}\frac{c'^2dc'}{c^2}. \quad (7)$$

After performing the c' integration, advantage may be taken of the fact that $2\hbar\omega/mc^2$ is generally small compared to unity by making a power series expansion in this parameter. The result, to lowest order, is

$$\frac{a}{3}\left(\frac{dn_1}{dc}+\frac{2n_1}{c}\right)=\frac{\hbar\omega}{mc^2}\left[c\frac{d}{dc}\left(\frac{n_0}{\tau}\right)+\frac{n_0}{\tau}\right]. \quad (8)$$

By multiplying through by c^2, this equation can be written in the form

$$\frac{a}{3}\frac{d}{dc}(c^2n_1)=\frac{\hbar\omega}{m}\frac{d}{dc}\left(\frac{cn_0}{\tau}\right). \quad (9)$$

To the same order of approximation, i.e., neglecting $2\hbar\omega/mc^2$ compared to 1, Eq. (3) becomes

$$ad n_0/dc=\langle\cos\theta-1\rangle n_1/\tau, \quad (10)$$

where

$$\langle\cos\theta-1\rangle=\int g(c\theta)(\cos\theta-1)d\Omega. \quad (11)$$

Equation (9) integrates immediately to give the relation

$$\tfrac{1}{3}ac^2n_1=(\hbar\omega cn_0/m\tau)+\text{constant}. \quad (12)$$

Substituting into Eq. (10) gives the differential equation

$$\frac{dn_0}{dc}+\left[\frac{3\langle1-\cos\theta\rangle\hbar\omega}{mca^2\tau^2}\right]n_0=\frac{\text{const}\langle\cos\theta-1\rangle}{a\tau c^2}. \quad (13)$$

This equation has the integrating factor

$$\exp\left[\int\frac{3\langle1-\cos\theta\rangle\hbar\omega}{ma^2\tau^2}\frac{dc}{c}\right], \quad (14)$$

with which it is possible to construct the general solution, but the result is so complicated as to be almost worthless for practical purposes. At this point, therefore, the approximation of constant mean free path will be made ($\tau=\lambda/c$). In addition, the velocity dependence of the factor $\langle1-\cos\theta\rangle$, which should not be great, will be neglected. With these simplifications the solution of Eq. (13) is

$$n_0=Ae^{-E/W}+\tfrac{1}{2}Be^{-E/W}\mathrm{Ei}(E/\omega), \quad (15)$$

where

$$W=\frac{(e\mathcal{E}\lambda)^2}{3\langle1-\cos\theta\rangle\hbar\omega}, \quad (16)$$

and A and B are constants of integration. The Ei function used here is that defined and tabulated in the WPA tables.[10]

A qualitative understanding of why W is the important parameter can be obtained by considering the average rate of energy gain by electrons in a spherically symmetric velocity distribution. After being accelerated for a time τ, an electron with initial velocity $c\cos\theta$ along the field will have a speed $c\cos\theta+e\mathcal{E}\tau/m$ in this direction. The average energy gain in time τ, obtained by squaring this expression and averaging over θ, is then $(e\mathcal{E}\lambda)^2/2mc^2$. On the other hand, an electron loses energy $\hbar\omega$ in this time. At equilibrium the rates of energy gain and loss must be equal, which gives the condition

$$(e\mathcal{E}\lambda)^2/4E\sim\hbar\omega, \quad \text{or} \quad E/W\sim1, \quad (17)$$

which is exactly the result one would obtain from a consideration of the distribution function, n_0. From this argument one sees that the form of the velocity distribution and the average energy of the electrons are determined by a competition between the process of

[10] *Tables of Sine, Cosine, and Exponential Integrals* (Work Projects Administration for City of New York, New York, 1940), Vol. 1.

energy gain from the field and that of energy loss to the phonons.

IV.

In the high-velocity region, the equations which determine the distribution function are

$$\frac{a}{3}\frac{d}{dc}(n_1c^2)=\frac{\hbar\omega}{m\lambda}\frac{d}{dc}(c^2n_0)-\frac{c^2n_0}{T}, \tag{18}$$

and

$$an_0'=-\langle 1-\cos\theta\rangle\frac{cn_1}{\lambda}-\frac{n_1}{T}, \tag{19}$$

where T is the mean free time for pair production. With the exception of the terms involving T, they are identical with Eqs. (9) and (10). These terms describe a continual loss of high-energy electrons. For each electron so lost it is assumed that another enters the distribution at zero velocity, thus keeping the total number of particles constant. Of course, this is somewhat of an oversimplification, since, in producing a pair, an electron will not drop exactly to zero energy, although, almost invariably, it will have quite a small energy after such an ionization. The gas discharge calculations[4] have shown that such an approximation hardly changes the values of ionization rate that one calculates. Its only effect is to cause an unimportant singularity in the distribution function at $c=0$.

As was pointed out earlier, the solution of Eqs. (18) and (19) for all values of c is very difficult because of the presence of the velocity dependent term $1/T$. This is particularly true near the threshold for pair production, where the percentage change in $1/T$ with velocity is large. For higher values of c, however, the situation is simpler, since the $1/T$ term changes fairly slowly and also becomes big enough to control the behavior of n_0 and n_1. In this range both n_0' and n_1' are very large, so that in terms such as $(d/dc)(c^2n_1)$ it is permissible to neglect the derivative with respect to c^2 since $cn_1'/n_1\sim c/aT\gg 1$ if one uses values of the mean free path for pair production estimated in Sec. II and field strengths below 10^6 volts/cm. With this approximation Eq. (18) becomes

$$\frac{a}{3}n_1'=\frac{\hbar\omega}{m\lambda}n_0'-\frac{n_0}{T}. \tag{20}$$

The other equation is

$$an_0'=\langle\cos\theta-1\rangle\frac{cn_1}{\lambda}-\frac{n_1}{T}\cong-\frac{n_1}{T}. \tag{21}$$

Differentiating gives the relation

$$n_1'\cong-aTn_0''-aT'n_0', \tag{22}$$

which, to the same approximation as used above, can be written

$$n_1'\cong-aTn_0''. \tag{23}$$

Combining this result with Eq. (20) then gives

$$-\frac{a^2}{3}Tn_0''=\left(\frac{\hbar\omega}{m\lambda}\right)n_0'-\frac{n_0}{T}. \tag{24}$$

This equation has a solution of the form $n_0=e^S$ where, because of the slow percentagewise change in $1/T$ for energies more than a few tenths of an electron volt above threshold, $S''<(S')^2$. Using the quadratic threshold law discussed at the end of Sec. II, one estimates that this approximation is valid for energies greater than 0.3 ev above threshold. In this range S is then determined by the equation

$$-\frac{a^2T}{3}(S')^2-\frac{\hbar\omega}{m\lambda}(S')+\frac{1}{T}=0. \tag{25}$$

From this formula S' is found to be

$$S'=-\Delta/T, \tag{26}$$

where

$$\Delta=\frac{1}{2}\left\{\frac{3\hbar\omega}{ma^2\lambda}+\left[\frac{9}{a^4}\left(\frac{\hbar\omega}{m\lambda}\right)^2+\frac{12}{a^2}\right]^{\frac{1}{2}}\right\}. \tag{27}$$

The quantity n_0 is then given by the relation

$$n_0=D\exp\left(-\Delta\int_{c_0}^{c}\frac{dc}{T}\right), \tag{28}$$

where c_0 is the velocity at the matching point and D an integration constant. It will be recognized that the method of solution used here is entirely analogous to the WKBJ method, T/Δ representing a large and relatively slowly varying "wavelength."

Having found forms for the velocity distribution, the final step in the calculation of α_i is the matching of these solutions at $c=c_0$. The constants A, B, and D must be determined such that n_0 and n_1 are continuous through the matching point and such that the total number of particles is unity. Calling the two independent solutions in the low-velocity region $\psi_1(c)$ and $\psi_2(c)$, respectively, one obtains the following set of algebraic equations to determine A, B, and D:

$$\begin{aligned}&A\psi_1(c_0)+B\psi_2(c_0)-D=0,\\&A\psi_1'(c_0)+B\psi_2'(c_0)+Ac_0D/\lambda=0,\\&A\int_0^{c_0}c^2\psi_1(c)dc+B\int_0^{c_0}c^2\psi_2(c)dc=1.\end{aligned} \tag{29}$$

The contribution of the high-velocity region to the normalization has been neglected in the last equation since n_0 falls very rapidly in this range (see Fig. 1).

The ionization rate per unit time, I, is given by

$$I=\int_{c_0}^{\infty}\frac{c^2n_0dc}{T}, \tag{30}$$

which, from Eq. (18), equals

$$I=\frac{\hbar\omega}{m\lambda}c_0^2n_0(c_0)-\frac{a}{3}c_0^2n_1(c_0). \tag{31}$$

Using formulas (10) and (15), this expression becomes

$$I=\frac{a^2\tau c_0}{3\langle 1-\cos\theta\rangle}B=\frac{a^2\lambda}{3\langle 1-\cos\theta\rangle}B. \tag{32}$$

α_i, the ionization rate per unit distance travelled along the field, is obtained by dividing I by the drift velocity, $\bar{c}$. This quantity is given by

$$\bar{c}=\frac{1}{3}\int n_1c^3dc=-\frac{1}{3}\int\frac{\lambda a n_0'c^2dc}{\langle 1-\cos\theta\rangle}, \tag{33}$$

where, for simplicity, the small number of electrons having velocity above c_0 is neglected in evaluating $\bar{c}$. Integrating by parts then yields

$$\bar{c}=\frac{2}{3}\int\frac{\lambda a n_0cdc}{\langle 1-\cos\theta\rangle}, \tag{34}$$

or

$$\bar{c}=\frac{2}{3}\int_0^{c_0}\frac{\lambda ac}{\langle 1-\cos\theta\rangle}[A\psi_1(c)+B\psi_2(c)]dc. \tag{35}$$

A and B are given by the following expressions obtained from Eq. (29):

$$A=\frac{1}{(\text{det.})}\left(\frac{\psi_2(c_0)\Delta c_0\langle 1-\cos\theta\rangle}{\lambda}+\psi_2'(c_0)\right), \tag{36}$$

$$B=\frac{-1}{(\text{det.})}\left(\frac{\psi_1(c_0)\Delta c_0\langle 1-\cos\theta\rangle}{\lambda}+\psi_1'(c_0)\right).$$

The factor (det.) is the determinant of the coefficients in Eqs. (29). Both of these formulas can be simplified by noting that

$$\Delta c_0\langle 1-\cos\theta\rangle/\lambda=\left(\frac{\Omega E_0}{Wc_0}\right),$$

where Ω is the dimensionless parameter

$$\Omega=[1+(1+4\langle 1-\cos\theta\rangle W/\hbar\omega)^{\frac{1}{2}}], \tag{37}$$

and W is defined in Eq. (16). The following expressions for A and B are obtained:

$$A=\frac{1}{c_0}\left[\frac{E_0}{W}(\Omega-2)\psi_2(c_0)+1\right]\frac{1}{(\text{det.})}, \tag{38}$$

$$B=-\frac{(\Omega-2)E_0\psi_1(c_0)}{Wc_0(\text{det.})}. \tag{39}$$

The formula for α_i now takes a form which is amenable to numerical calculation, namely,

$$\alpha_i=\tfrac{1}{2}aB\Big/\left[A\int_0^{c_0}c\psi_1(c)dc+B\int_0^{c}c\psi_2(c)dc\right]. \tag{40}$$

Notice that to evaluate α_i it is not necessary to calculate the denominator of A or B since this term enters in the same way in I and $\bar{c}$ and thus cancels in the expression for α_i. With Eq. (40) the calculation for α_i is complete and it is only necessary to compute to obtain its values. These will be presented and discussed in the next section.

V.

Before using Eq. (40) to evaluate α_i it is necessary to choose a value for E_0, the energy at which the high and low velocity solution of the Boltzmann equation are matched. The discussion of Sec. II indicates that E_0 should be taken a few tenths of an electron volt greater than the threshold for pair production. Unfortunately, however, this threshold is a quantity whose value is difficult to ascertain with any accuracy. It is true that if one assumes spherical, nondegenerate energy bands with equal masses for electrons and holes that the conservation laws for energy and crystal momentum require that the threshold should fall at one and a half times the gap width, but the band structures in Ge and Si are certainly more complicated than this and, in addition, such a calculation takes no account of umklapp or phonon processes. The latter certainly permit some pair production at somewhat lower energies but they probably have little importance in determining the energy of principal importance here, namely the energy at which the mean free path for pair production becomes smaller than that for the electron-phonon interaction. On the other hand, the form of the energy bands has a marked influence on this value as can be seen by repeating the energy-momentum argument mentioned above with different band shapes or different effective mass ratios. In silicon (the element on which most of McKay and McAfee's work has been done) the shape of the energy bands is in doubt. Calculations of Herman and Callaway[11] suggest that the valence band has a triply degenerate maximum at $k=0$ and that the conduction band edge occurs away from $k=0$, but the details of this structure are still obscure. This lack of knowledge makes any estimate of the pair-production threshold quite risky, but calculations using the Herman-type bands with the minimum in the conduction band halfway to the edge of the Brillouin zone suggest that, unless the effective masses have rather special values, the threshold obtained from the conservation laws will be somewhat greater than one and a half times the gap width, perhaps somewhat over 2.0 ev in Si. Clearly, this figure is not a very reliable one but, without more information about the bands in

[11] Frank Herman and Joseph Callaway, Phys. Rev. **89**, 518 (1953).

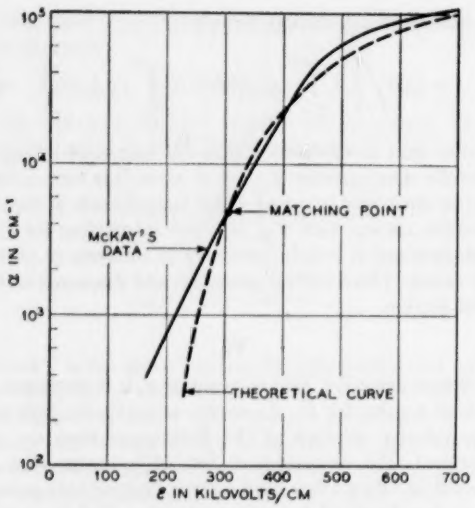

FIG. 2. Ionization rate *versus* electric field for silicon.

Si, it is hard to do better. The value of over 2.0 ev seems high but there is a certain amount of experimental evidence to support it. McKay and McAfee[1] have done experiments in which they bombarded Si with α particles and observed the amount of energy required to produce a hole-electron pair. The result was 3.6 ev per pair, a surprisingly large figure compared to the gap width of 1.0 ev, suggesting that the pair-production threshold is, indeed, abnormally high in silicon. As was mentioned earlier, the value of E_0 is a few tenths of an electron volt greater than the pair threshold and consequently will be taken to be 2.3 ev. The shape of the α_i *vs* $\mathcal{E}$ curve is not too dependent on this value of E_0, but a change in it would affect the value of λ deduced from the experiments.

Using the value for E_0 of 2.3 ev, the best fit of Eq. (40) to experiment is obtained with a mean free path, λ, of about 200A. This value is uncertain mainly because of lack of knowledge of E_0. An estimate of what sort of error to expect can be made by fitting to experiment with various values for E_0. Outside limits for this quantity are $1.5 \text{ ev} < E_0 < 3.5$ ev from which one obtains the mean-free-path range, $160\text{A} < \lambda < 260\text{A}$.

The α_i *versus* $\mathcal{E}$ curve is shown in Fig. 2. Agreement between theory and experiment is good in the high-field region but considerably poorer for lower values of $\mathcal{E}$.* Experimental error is large in this region but, in addition, there may be another factor which makes the observed α_i values larger than those calculated. In the experiments of McKay and McAfee it was assumed that the electric field could be calculated from the average donor and acceptor densities. However, small local fluctuations in these quantities cause considerable deviations of the field from the mean, and, since α_i varies so rapidly with $\mathcal{E}$, it is possible that the observed α_i values are typical of an electric field that is larger than the average. Unfortunately, any quantitative estimate of this effect is exceedingly difficult since variations in donor density, besides being caused by statistical fluctuations, may also be produced during the growing of the junctions.

Although there is no simple expression for α_i as a function of $\mathcal{E}$, the numerical calculations show that the general form of the curve is determined by the factor $e^{-E/W}$ which appears in Eq. (15). Physically this means that α_i is limited by the inability of electrons to go rapidly from low to high energy against the drag of the phonon field. In the neighborhood of $\mathcal{E}=6\times10^5$ volts/cm, however, the field becomes large enough that there is an appreciable chance for an electron to be accelerated from zero velocity to the pair-production threshold before it makes a collision with a phonon. At this point the phonon field ceases to play an important role and α_i is approximately given by the inverse of the distance an electron has to travel in the electric field to go from zero energy to 2.3 ev. In this high-field region the variation of α_i with $\mathcal{E}$ is linear as compared with the exponential dependence at lower $\mathcal{E}$. This fact explains why the α_i curve rises rapidly for low $\mathcal{E}$ and then appears to saturate for field strengths in the neighborhood of 6×10^5 volts/cm.

VI.

In the preceding sections of this paper, gas discharge theory has been used to describe the breakdown process in Si and Ge junctions. These calculations explain the course of the α_i *vs* $\mathcal{E}$ curve and thus support the interpretation McKay has placed on his data as well as giving one confidence in the application of gas theory to the solid-state discharge. A by-product of this investigation is the value of the mean free path for electron-phonon scattering in Si at 2.3 ev. The figure of 200A quoted in the text is uncertain mainly because of lack of knowledge of E_0 and could be in error by about 30 percent. Finally, it is suggested that certain deviations of theory from experiment are explainable in terms of fluctuations in donor or acceptor density within the junctions.

In conclusion the author would like to express his thanks to Dr. K. G. McKay and Dr. D. J. Rose with whom he has had numerous fruitful conversations on the topics set forth here. He would also like to express his thanks to them and to Conyers Herring for reading and commenting on the manuscript.

* *Note added in proof.*—In a private conversation Dr. McKay has informed the author that his latest experiments give somewhat smaller values of α_i at low fields than those plotted in Fig. 2. This change will considerably improve the agreement between theory and experiment.

Temperature-Dependent de Haas-van Alphen Parameters in Zinc

TED G. BERLINCOURT AND M. C. STEELE
United States Naval Research Laboratory, Washington, D. C.

(Received June 10, 1954)

The magnetic susceptibility of a single crystal of zinc has been investigated from 4.2°K to 300°K in fields up to 25 kilogauss. Traces of the de Haas-van Alphen effect persisted at temperatures as high as 200°K. The period of the characteristic susceptibility oscillations increased with increasing temperature, rising from 6.4×10^{-5} gauss^{-1} at 4.2°K to 12.5×10^{-5} gauss^{-1} at 61.2°K. If present interpretations of the de Haas-van Alphen parameters are valid, temperature dependent effective masses, or chemical potential, or both are implied for the pertinent electrons. A rough calculation indicates that temperature dependences of the right order of magnitude might arise from alteration of the overlap of Brillouin zone boundaries by the Fermi surface as a result of anisotropic thermal expansion of the lattice.

In addition to the main oscillations, terms exhibiting periods of approximately 2×10^{-7} gauss^{-1} were observed at 4.2°K but were not investigated in detail.

INTRODUCTION

THE low temperature periodic dependence of magnetic susceptibility upon magnetic field characteristic of the de Haas-van Alphen effect is of interest not only because it yields values for the effective masses and chemical potential of the pertinent electrons, but perhaps more so because of its correlation with the low temperature magneto-oscillatory behavior of magnetoresistance,[1-3] Hall effect,[4,5] thermoelectric effect,[6] and thermal conductivity.[7] The magnetic susceptibility oscillations were first observed by de Haas and van Alphen[8] in bismuth in 1930 and have since been observed in a total of fifteen metal single crystals. They were observed in zinc by Marcus[9-11] in 1947, and since then the effect in zinc has been studied in the liquid helium and liquid hydrogen temperature ranges by Sydoriak and Robinson,[12] Mackinnon,[13] Verkin, Lazarev, and Rudenko,[14] Verkin,[15] and Donahoe.[16]

Marcus had noted that a field dependence persisted in χ_3, the component of magnetic susceptibility per unit mass parallel to the hexagonal axis of zinc, at temperatures as high as 60°K, and in 1951 McClure and Marcus[17] reported that χ_3 was field dependent up to 85°K. Furthermore, they observed that, "The behavior of χ_3 at liquid nitrogen temperatures somewhat resembles the de Haas-van Alphen effect with the amplitude of oscillation sharply decreased and the maxima and minima displaced in field strength." The present investigation was undertaken in order to clarify the relation between these field dependences of susceptibility in the low and intermediate temperature ranges. As will be evident from the experimental results of this investigation, both are indeed manifestations of the same phenomenon, for oscillations which are strictly periodic in reciprocal magnetic field, as is characteristic of de Haas-van Alphen oscillations, were observed up to 61.2°K. However, in contrast to the de Haas-van Alphen effect at lower temperatures, the period of oscillation becomes temperature dependent at the higher temperatures, increasing with increasing temperature. Although such a dependence of period upon temperature has not been reported for any of the other fourteen metal single crystals known to exhibit the de Haas-van Alphen effect, it is unlikely that the property is exclusive to zinc alone. In any event, such behavior implies either temperature dependent effective masses, or chemical potential, or both for the pertinent electrons as will be evident from the theory.

According to the usual interpretations of Landau's[18] theory for the de Haas-van Alphen effect, the constant energy surface in momentum space for the pertinent electrons can often be accurately represented by an ellipsoid. Such an ellipsoidal surface may occur where the Fermi surface overlaps a Brillouin zone boundary producing a "pocket" of low effective mass electrons or holes. In the case of zinc, a suitable representation (see reference 12) for our purposes is

$$E_0=(p_1^2+p_2^2)/2m_1+p_3^2/2m_3, \qquad (1)$$

where the subscripts 1, 2, and 3 correspond respectively to digonal axes of type I, digonal axes of type II, and the hexagonal axis. m_1 and m_3 are the effective masses perpendicular and parallel respectively to the hexagonal

[1] P. B. Alers and R. T. Webber, Phys. Rev. **91**, 1060 (1953).
[2] Ted G. Berlincourt, Phys. Rev. **91**, 1277 (1953).
[3] T. G. Berlincourt and J. K. Logan, Phys. Rev. **93**, 348 (1954).
[4] Laird C. Brodie, Phys. Rev. **93**, 935 (1954).
[5] Reynolds, Leinhardt, and Hemstreet, Phys. Rev. **93**, 247 (1954).
[6] M. C. Steele and J. Babiskin, Phys. Rev. **94**, 1394 (1954).
[7] J. Babiskin and M. C. Steele, Phys. Rev. **95**, 602 (1954).
[8] W. J. de Haas and P. M. van Alphen, Leiden Comm. No. 212A (1930).
[9] Jules A. Marcus, Phys. Rev. **71**, 559 (1947).
[10] Jules A. Marcus, Phys. Rev. **76**, 413 (1949).
[11] Jules A. Marcus, Phys. Rev. **76**, 621 (1949).
[12] S. G. Sydoriak and J. E. Robinson, Phys. Rev. **75**, 118 (1949).
[13] L. Mackinnon, Proc. Phys. Soc. (London) **B62**, 170 (1949).
[14] Verkin, Lazarev, and Rudenko, Doklady Akad. Nauk. S.S.S.R. **73**, 59 (1950).
[15] B. I. Verkin, Doklady, Akad. Nauk. S.S.S.R. **81**, 529 (1951).
[16] F. Donahoe, Annual Report, Contract AT-30-1-597, University of Pennsylvania, 1952 (unpublished).
[17] J. W. McClure and J. A. Marcus, Phys. Rev. **84**, 787 (1951).
[18] L. Landau, see Appendix to D. Shoenberg, Proc. Roy. Soc. (London) **A170**, 341 (1939).

axis (i.e., isotropy in the basal plane is assumed), and E_0 is the chemical potential measured from the bottom of the relevant zone in the case of electrons (or the top in the case of holes). For this case, Landau's final expression for the anisotropy $\Delta\chi=\chi_3-\chi_1$, is

$$\Delta\chi=\frac{(m_1-m_3)A}{\rho}\left\{\frac{\pi^2}{6}\left(\frac{k}{E_0}\right)^{\frac{1}{2}}-\frac{1}{T^{\frac{1}{2}}}\left(\frac{2\pi^2 kT}{\beta H}\right)^{\frac{1}{2}}\times\sum_{p=1}^{\infty}\frac{(-1)^{p+1}\sin(2\pi pE_0/\beta H+\delta)}{2p^{\frac{1}{2}}\sinh(2\pi^2 pkT/\beta H)}\right\},\quad(2)$$

provided that $E_0\gg kT$ and $E_0\gg\beta H$, which, as will be evident later, is not fulfilled at the highest temperatures or highest fields in this investigation. ρ is the density, $\delta=-\pi/4$, and A is a constant given by

$$A\equiv\frac{e^2E_0}{\pi^4c^2\hbar(2k)^{\frac{1}{2}}m_1(m_3)^{\frac{1}{2}}}.\quad(3)$$

β is a double effective Bohr magneton given by

$$\beta=\frac{e\hbar}{cm_1(m_3)^{\frac{1}{2}}}(m_1\sin^2\phi+m_3\cos^2\phi)^{\frac{1}{2}},\quad(4)$$

where ϕ is the angle between the hexagonal axis and the magnetic field. The remaining quantities have their usual meanings. Note that $\Delta\chi$ consists of a field-independent term upon which is superposed a summation of oscillating terms. We will be concerned chiefly with the first term of the summation, for under the conditions of our experiments the harmonics were not in general important. This first term exhibits a period of oscillation β/E_0 in reciprocal field, which, according to the theory, is temperature independent. Hence, the observed dependence of β/E_0 on temperature is not accounted for by the theory but might be included by making β or E_0 or both suitable functions of temperature.

THE EXPERIMENTAL WORK

I. The Torsion Balance and Crystal

The general techniques used for measuring $\Delta\chi$, the difference of susceptibility per unit mass along two perpendicular directions in a metal single crystal, by observation of the vertical couple acting on the crystal placed in a homogeneous horizontal magnetic field, have been described adequately elsewhere.[19] However, it should be mentioned that in the present work the maximum observed couples never exceeded 13 dyne-cm which corresponded to angular deflections of the crystal of less than 0.3°.

The zinc single crystal used in this investigation was kindly donated by Dr. John K. Logan of this Laboratory. It was grown from New Jersey zinc (99.99 percent purity) and weighed 0.709 gram. All of the measurements were made with the hexagonal or 3 axis and a digonal axis of type I in a horizontal plane such that $\Delta\chi=\chi_3-\chi_1$.

II. Temperature Attainment and Measurement

Several methods were used to reach and maintain the desired temperatures. In all cases, the crystal was suspended on the lower end of a quartz rod inside a long glass tube containing helium thermal exchange gas. A copper-constantan thermocouple (which was shown to be magnetic field independent) was attached to the outside of this glass tube directly opposite the crystal permitting temperature measurement to an estimated accuracy of ±1°K above 28°K. (In the liquid helium range, the temperature was determined from the vapor pressure of the helium bath.) Surrounding the glass tube, but not in direct contact with the thermocouple, was a copper tube (approximately 0.5 mm wall and 13 cm long) to the upper end of which was attached a carbon resistor heater. The copper tube, which helped minimize temperature gradients, was surrounded by necked down portions of two concentric Dewar flasks. Temperatures above 90°K were reached by passing liquid nitrogen cooled helium gas into the inner flask at appropriate flow rates. Temperatures between 59°K and 90°K were attained by pumping on liquid nitrogen and liquid oxygen baths in the inner flask. In checking temperatures using the vapor pressure of the oxygen bath, it was necessary to correct for the dependence of vapor pressure upon field.[20]

In order to cover the range from 4.2°K to 59°K, liquid nitrogen was placed in the outer flask, about 100 cm³ of activated charcoal were added to the large diameter upper portion of the inner flask just making contact with the upper end of the copper tube, and liquid helium was bled into the inner flask until the lowest desired temperature was reached. The activated charcoal constituted a good heat sink because of its large thermal capacity and also permitted cooling via the desorption of helium gas when pumped under reduced pressure. In the absence of pumping, warm up took place at the rate of about 3°K per hour above 20°K. The temperature could be held constant to better than ½°K during the course of a field sweep (about 20 minutes) by adding heat to the carbon resistor heater for a short time, thus warming the copper tube but not appreciably warming the charcoal because of its poor thermal conductivity. With a little practice, a situation could be realized in which the normal heat leak to the copper tube (after the flow of current to the heater was stopped) was just compensated by the cooling from the charcoal. This method would probably have been applicable throughout the entire temperature range from a bit above 4.2°K to room temperature, but

[19] D. Shoenberg, Trans. Roy. Soc. (London) **245**, 1 (1952).

[20] A. Van Itterbeck and A. de Bock, Ann. Physik **20**, 231 (1945).

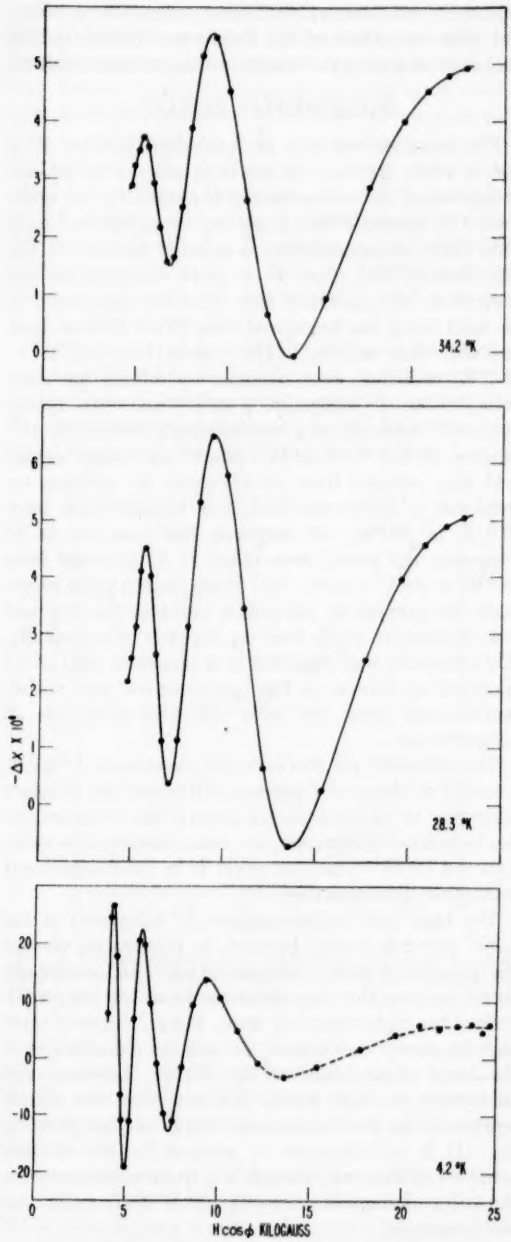

FIG. 1. $-\Delta\chi$ in emu g^{-1} as a function of the component of magnetic field parallel to the hexagonal axis of a zinc single crystal for various temperatures.

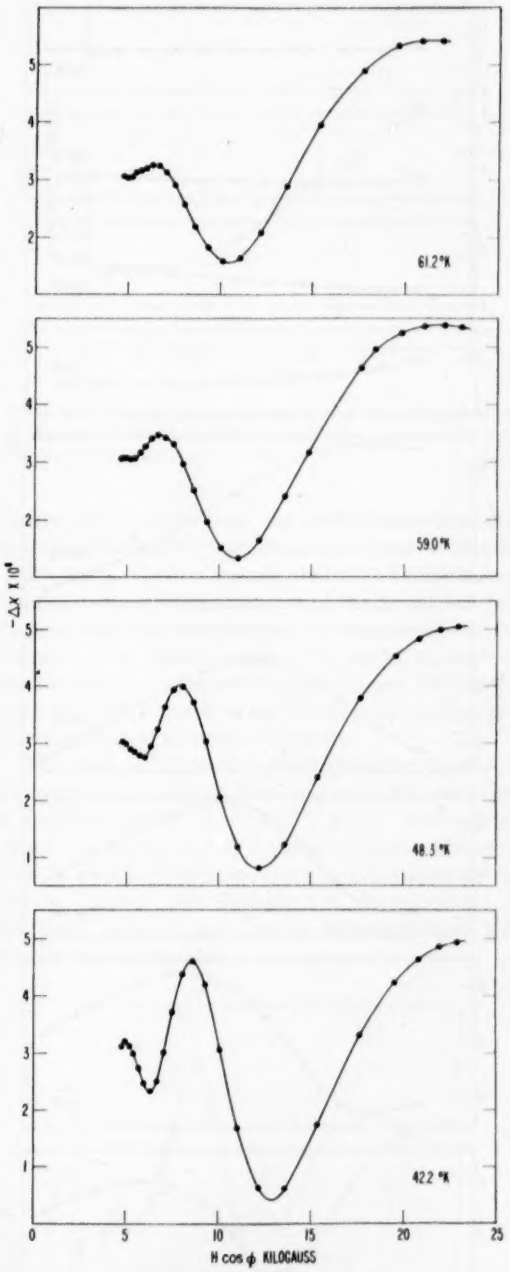

FIG. 2. $-\Delta\chi$ in emu g^{-1} as a function of the component of magnetic field parallel to the hexagonal axis of a zinc single crystal for various temperatures. Note the displacement to lower fields of the last maximum as the temperature is increased.

it was not tried until after the data above 59°K had already been obtained.

III. The Magnet

An Arthur D. Little electromagnet capable of rotation about a vertical axis supplied horizontal magnetic fields up to 25 kilogauss in strength. Pole pieces 5.75 inches in diameter and a gap of 1.75 inches assured field homogeneity to a few gauss over the volume of the crystal. The magnet was calibrated with a nuclear

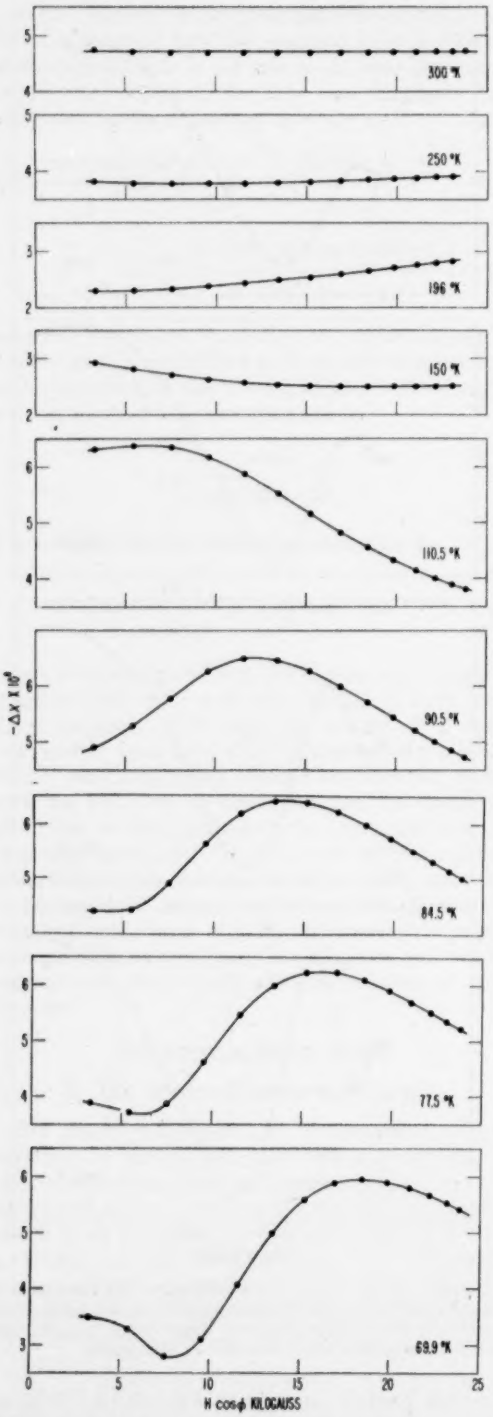

FIG. 3. $-\Delta\chi$ in emu g^{-1} as a function of the component of magnetic field parallel to the hexagonal axis of a zinc single crystal for various temperatures.

fluxmeter to an accuracy of better than 0.02 percent, and time variations of the field were limited to less than 5 gauss during the course of a single measurement.

EXPERIMENTAL RESULTS

The experimental data are presented in Figs. 1, 2, and 3, where $\Delta\chi=\chi_3-\chi_1$ has been plotted for several temperatures as a function of $H\cos\phi=H_3$, the component of magnetic field along the hexagonal or 3 axis. This mode of presentation is suitable because of the experimental fact that at a given temperature $\Delta\chi$ depends to high accuracy only upon the component of the field along the hexagonal axis. (This verifies, incidentally, that $m_3\gg m_1$.) The curves from 4.2°K to 61.2°K, inclusive, were obtained by setting the magnetic field at 25 kilogauss, ϕ at 0°, and then taking data at 5° intervals as ϕ was increased from 0° to 45°. Finally, with ϕ fixed at 45°, points were taken as the field was reduced from 25 kilogauss by uniform increments in reciprocal field. For temperatures from 69.9°K to 300°K, the magnetic field was set at 25 kilogauss, and points were taken at 5° intervals from $\phi=90°$ to $\phi=0°$ to $\phi=-90°$. Each plotted point represents the average of the points obtained for $+\phi$ and $-\phi$. In order to verify that $\Delta\chi$ depends only upon H_3, this procedure was repeated in a magnetic field of 15 kilogauss at several of the temperatures, and within experimental error the data coincided with the 25 kilogauss data.

The estimated relative error for the curves of Figs. 1, 2, and 3 is about ±1 percent. Although the absolute error may be as much as ±2 percent due to uncertainties in balance calibration, the room temperature value $\Delta\chi=-4.7\times10^{-8}$ emu per gram is in good agreement with other determinations.[12,13]

The high field portion (above 12 kilogauss) of the 4.2°K curve is dashed because, in this region, shorter (by a factor of about 300) period oscillations were observed making the data uncertain to within the amplitude of the high-frequency term. The existence of these high-frequency oscillations, as well as anisotropies in the basal plane observed by Verkin, Lazarev, and Rudenko[14] at high fields, indicate that the simple representation for the constant energy surface given by Eq. (1) is not adequate to account for the detailed behavior of zinc even though it is quite satisfactory for the long period oscillations with which this investigation was concerned.

ANALYSIS AND EVALUATION OF PARAMETERS

I. Period, Phase, and Mean of the Oscillations

In order to obtain values for the period β/E_0 of the oscillations of χ_3 in reciprocal field, the mean of the oscillations was first ascertained for each temperature. Then, values of reciprocal field at which the observed curve crossed the mean were plotted against even integers. In general, good straight lines were obtained,

from the slopes of which β/E_0 could be calculated. When values of reciprocal field at which maxima and minima occurred were plotted against odd integers, they fell on the same lines, but since fewer uncertainties arise in the determination of crossover points they were more heavily weighted. β/E_0 is plotted as a function of temperature in Fig. 4 where the probable error is indicated by the size of the points. The 4.2°K value is in good agreement with other determinations.[12,13,16] That the upward trend of β/E_0 continues to considerably higher temperatures than 60°K is suggested by the continued displacement of the highest-field maximum in $-\Delta\chi$ toward lower fields.

The phase δ of the oscillations is also of interest and may be obtained from the intercept on the integer axis of the plots of crossover points *versus* integers used in the determination of β/E_0. (It should be pointed out that the sign of the oscillating term follows that of

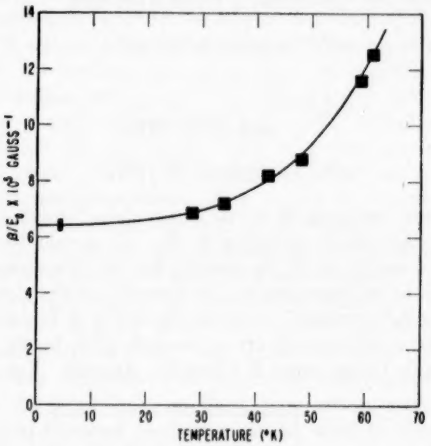

FIG. 4. The dependence upon temperature of the period β/E_0 of the de Haas-van Alphen (magnetic susceptibility) oscillations in zinc parallel to the hexagonal axis.

$+\sin(2\pi E_0/\beta H+\delta)$ since $m_3>m_1$.) δ has been plotted as a function of temperature in Fig. 5, and we note that, like the period, it increases with increasing temperature. Furthermore, it differs considerably from the theoretical value $-\pi/4$.

The dependence of the mean of the oscillations (i.e., $\lim_{H\to 0}\Delta\chi$) upon temperature is illustrated in Fig. 6. While there is some evidence for a kink between 20°K and 60°K, this might arise from uncertainties in determining the actual mean. The maximum in $-\Delta\chi$ at roughly 110°K is perhaps noteworthy because, below this temperature, Marcus[9,11] observed that χ_1 (the field-independent susceptibility perpendicular to the hexagonal axis) was temperature-independent while above it χ_1 increased strictly linearly at least to 380°K. Very recently, Elcock[21] has considered the theoretical

[21] E. W. Elcock, Proc. Roy. Soc. (London) **A222**, 239 (1954).

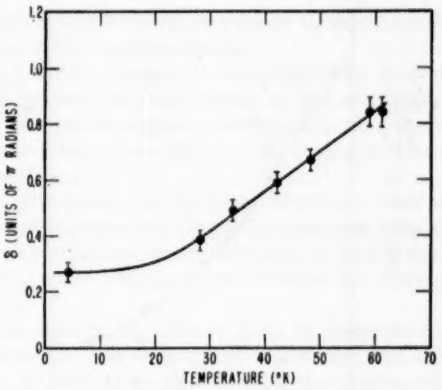

FIG. 5. The dependence upon temperature of the phase δ of the de Haas-van Alphen (magnetic susceptibility) oscillations in zinc. The theoretical value is $\delta=-\pi/4$.

temperature variation of the field-independent diamagnetic susceptibility of orbital electrons in metals. In his model, electron transfer across the Brillouin zone boundary arises from departure of the Fermi function from a true step function as the temperature is increased above absolute zero. This might account at least in part for the observed effects in zinc, but incomplete knowledge of the energy surface prohibits rigorous interpretation in terms of this theory.

The short-period oscillations observed at the lowest temperature and highest fields and at $\phi=8.5°$ exhibited a dominant period of 2.1×10^{-7} gauss^{-1} and a beat period of roughly 15×10^{-7} gauss^{-1}. These oscillations may be associated in some way with those observed by Verkin, Lazarev, and Rudenko[14] in the anisotropy of the basal plane of zinc, but an investigation of this feature was not pursued.

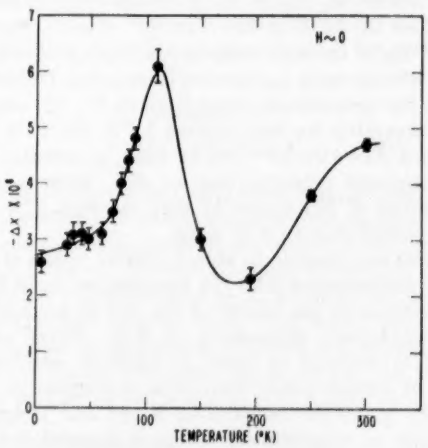

FIG. 6. The dependence upon temperature of the mean of the susceptibility oscillations in zinc. $-\Delta\chi$ is in emu g^{-1}.

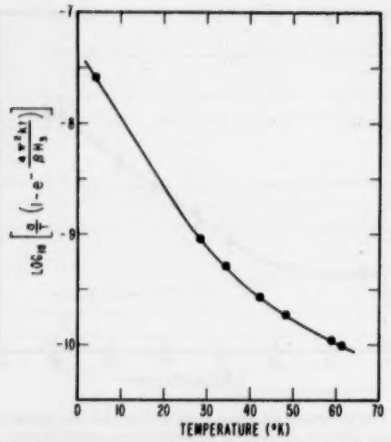

FIG. 7. The temperature dependence of the amplitude a of the susceptibility oscillations in zinc is illustrated. A value for β at 4.2°K can be derived from the slope of the linear portion.

II. Chemical Potential and Effective Mass

Provided Eq. (2) is valid, a plot of $\log_e\{aT^{-1}\times[1-\exp(-4\pi^2kT/\beta H_3)]\}$ (where a is the amplitude of the oscillations) against T for fixed H_3 should yield a straight line of slope $-2\pi^2k/\beta H_3$ (where β is referred to $\phi=0$). Thus a first approximation to β may be obtained from the slope of a plot of $\log_e(a/T)$ against T. This value of β may then be used in a plot of $\log_e\{aT^{-1}[1-\exp(-4\pi^2kT/\beta H_3)]\}$ against T, the slope of which yields a second approximation to β. This process may be repeated until a value for β of the desired accuracy is obtained.

Despite the fact that β/E_0 is temperature-dependent and hence Eq. (2) is not strictly valid, a value for β was calculated on the above basis using values of a at 4.207°K and 28.3°K for $H_3=7350$ gauss. A value of $\beta=2.65\times10^{-18}$ erg gauss^{-1} was obtained such that $m_1=7.0\times10^{-3}m_0$ (where m_0 is the free electron mass), and since at 4.2°K $\beta/E_0=6.4\times10^{-5}$ gauss^{-1}, $E_0=4.1\times10^{-14}$ erg at the same temperature. Such a calculation is not without some justification inasmuch as Donahoe[16] found the temperature dependence in Eq. (2) obeyed quite accurately for zinc between 1.5°K and 20°K and obtained $E_0=4.0\times10^{-14}$ erg in what is probably the most accurate determination for zinc, whereas a recalculation of Mackinnon's[12] data between 2°K and 20°K yielded $E_0=4.1\times10^{-14}$ erg.

It was not possible to obtain reliable values of β at higher temperatures from the temperature dependence of a because of the failure of Eq. (2) to account for the temperature dependence of β/E_0. Nevertheless, Fig. 7 is included in order to facilitate analysis in terms of possible future theoretical developments. The linearity of this plot between 4.2°K and 28.3°K despite the lack of experimental points is favored by the agreement between the above independent determinations of E_0. It should be mentioned that, even if the uncertainties in β were as great as a factor of two at the higher temperatures, the plot is a valid one since at 28.3°K $1\gg\exp(-4\pi^2kT/\beta H_3)$ for $H_3=7350$ gauss.

III. The Field-Dependence of Amplitude

In principle, one could calculate β at any given temperature from the field-dependence of amplitude. Such a calculation would then yield the temperature-dependences of β and hence m_1 and E_0. Unfortunately, attempts to fit the observed field-dependence to the theoretical dependence,

$$aH_3^{3/2}\propto\frac{1}{\sinh(2\pi^2kT/\beta H_3)}, \tag{5}$$

from Eq. (2) revealed a wide divergence between experiment and theory. Consequently, in an attempt to ascertain an empirical relation for the field dependence of amplitude, the following forms were tried

$$aH_3^{3/2}\propto\exp(-2\pi^2kT/\beta H_3) \tag{6}$$

$$aH_3^{5/2}\propto\frac{1}{\sinh(2\pi^2kT/\beta H_3)} \tag{7}$$

$$aH_3^{5/2}\propto\exp(-2\pi^2kT/\beta H_3). \tag{8}$$

The best empirical fit by far to the data [ignoring the harmonics which according to Eq. (2) should be important only at 4.2°K] is given by Eq. (8). The accuracy of this fit is illustrated by the linearity of the plots of $\log_{10}(aH_3^{5/2})$ *versus* H_3^{-1} appearing in Fig. 8. Donahoe[16] favored a field-dependence of the form given by Eq. (7) for fields below about 6 kilogauss. Actually, Eqs. (7)

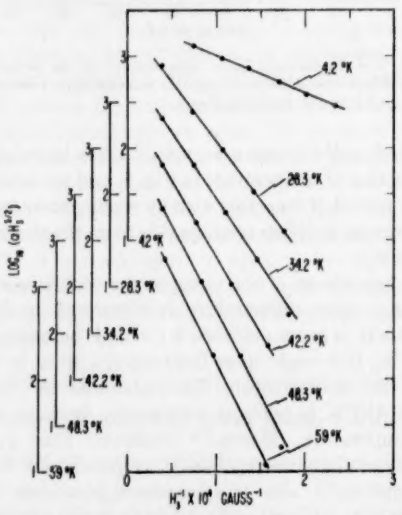

FIG. 8. The magnetic field dependence of the amplitude a of the susceptibility oscillations in zinc is illustrated. The linearity is indicative of the accuracy of the empirical relation given in Eq. (8).

and (8) are equivalent for all of our data except that for 4.2°K. Taking the harmonics in Eq. (2) into account for the 4.2°K data could conceivably favor Eq. (7), but uncertainties in the phase δ prohibit any conclusive analysis.

In any event, an attempt was made to ascertain in a qualitative way the temperature-dependence of β from the field-dependence of amplitude. Inspection of Eq. (8) reveals the fact that values for β can be deduced from the slopes of such plots as appear in Fig. 8. Equivalent plots for the field-dependences given by Eqs. (5), (6), and (7) yield linear portions at low fields, from the slope of which other values for β can be deduced. Before continuing, it is necessary to point out that according to an addition to the theory by Dingle,[22] collision broadening of the electronic energy levels should reduce the amplitude of the oscillations by a factor $\exp(-2\pi^2 kx/\beta H_3)$ where x is an effective temperature related to the collision time. Consequently, in calculating values for β by the scheme described above, the 4.2°K values of β were adjusted to the value obtained from the temperature dependence of amplitude by appropriate adjustment of x. Then, using this value of x, β was calculated at the higher temperatures. Although the assumption that x is temperature-independent is probably unwarranted, a rather violent temperature-dependence of x would be required to alter the calculated values of β appreciably at temperatures above 28.3°K. In all cases, the calculated values for β were within 30 percent of each other at a given temperature, and, in all cases, β increased by a factor of 1.5 to 2 in going from 4.2°K to 59°K. On this basis, it would appear that β does indeed increase (and m_1 therefore decrease) with increasing temperature and that E_0 is at least no more temperature-dependent than β. However, such speculation must be regarded with caution in view of the inadequacies of the theory which was derived in the approximations $E_0 \gg kT$ and $E_0 \gg \beta H$. Actually, at 60°K and 15 kilogauss, $E_0 \cong \beta H_3 \cong 5kT$, so differences between theory and experiment are not unexpected.

CONCLUDING REMARKS

This investigation has yielded the following information:

1. Traces of the de Haas-van Alphen effect persist in zinc at temperatures up to 200°K.

2. The period β/E_0 of the oscillations of χ_3 in zinc increases with increasing temperature from liquid helium temperatures to well above 60°K. This accounts in part for the persistence of the effect at high temperatures since in general the larger β/E_0 the stronger the de Haas-van Alphen effect.

3. The phase δ increases with increasing temperature.

4. It appears that β increases (and therefore m_1 decreases) with increasing temperature, although the evidence is not conclusive because of discrepancies between theory and experiment.

5. Over the ranges of temperature and field of this investigation, the dependence of the amplitude a of the de Haas-van Alphen oscillations in zinc upon field is better represented by Eq. (8) than the theoretical dependence, Eq. (5).

6. In addition to the long-period term with which this investigation was primarily concerned, very short-period oscillations observable only at high fields and low temperatures exist in the de Haas-van Alpen effect in zinc.

The observed dependence of the de Haas-van Alphen parameters upon temperature might very well arise in part at least from alteration of the overlap of the pertinent Brillouin zone by the Fermi surface brought about by thermal expansion of the crystal. Despite the possibility that the de Haas-van Alphen parameters could be somewhat artificial (as pointed out by Adams[23]), some idea of the orders of magnitude involved was obtained as follows. Using the thermal expansion coefficients for a single crystal of zinc as measured by Grüneisen and Goens,[24] the proportionate change $\Delta n/n$ in the number n of electrons per cm^3 for an increase of temperature from 40°K to 60°K was found. Since the Fermi energy ζ is proportional to $n^{2/3}$, the proportionate change $\Delta\zeta/\zeta$ in the Fermi energy was found to be

$$\Delta\zeta/\zeta \cong -6\times 10^{-4}.$$

The ratio of the overlap energy $E_0 = 4.1\times 10^{-14}$ erg $= 0.026$ electron volt at 4.2°K to the Fermi energy $\zeta = 11$ electron volts from soft x-ray measurements on zinc[25] is

$$E_0/\zeta \cong 2\times 10^{-3}.$$

Therefore $E_0 \sim 3|\Delta\zeta|$. Furthermore, in the same temperature interval, 40°K to 60°K, the proportionate changes in the Brillouin zone dimensions l_3 and l_1 parallel and perpendicular respectively to the hexagonal axis are

$$\Delta l_3/l_3 \cong -10^{-3},$$
$$\Delta l_1/l_1 \cong 4\times 10^{-5}.$$

Hence, if the overlap takes place in the perpendicular or 1-direction (which is most likely since $m_3 \gg m_1$) where the zone boundary is almost unchanged as the temperature is increased, the overlap energy E_0 could be altered by an amount of the order of $\Delta\zeta$, which as we have seen is comparable with E_0 itself. This would also change the number of overlapping electrons and possibly their effective masses. Of course this is not the only mechanism capable of giving rise to the transfer of electrons

[22] R. B. Dingle and D. Shoenberg, Nature **166**, 652 (1950).

[23] E. N. Adams II, Phys. Rev. **89**, 633 (1953).

[24] E. Grüneisen and E. Goens, Z. Physik **29**, 141 (1924).

[25] See A. H. Wilson, *The Theory of Metals* (Cambridge University Press, Cambridge, 1954), second edition, p. 94.

across the zone boundary, and it is quite likely that the mechanism discussed by Elcock[21] is also operative as well as others. Nevertheless, on the above model one might predict observable temperature-dependent de Haas-van Alphen parameters in other crystals having very anisotropic thermal expansion coefficients, low Debye characteristic temperatures, and small overlap energies, but the scarcity of data on low-temperature thermal expansion coefficients precludes any concrete conclusions along this line.

We are indebted to the members of the Cryogenics Branch for many stimulating discussions.

PHYSICAL REVIEW VOLUME 95, NUMBER 6 SEPTEMBER 15, 1954

Specific Heats of Metals Below One Degree Absolute*

JOHN RAYNE†
Department of Physics, University of Chicago, Chicago, Illinois
(Received June 9, 1954)

The heat capacities of a number of metals have been measured in the region below 1°K, using the technique of adiabatic demagnetization. Copper, silver, platinum, palladium, tungsten, molybdenum, and sodium have been investigated. Apart from sodium, all exhibit a linear dependence of electronic specific heat on temperature. The values of γ are in agreement with those obtained in the liquid helium region, except in the case of tungsten, which gives $\gamma=3.5\pm0.2\times10^{-4}$ cal/mole deg^2 in contrast to the previous value $\gamma=1.8\pm0.7\times10^{-4}$ cal/mole deg^2 reported in the literature. Sodium exhibits an anomalous peak in its specific heat curve. A low-temperature, martensitic-type transformation is advanced as a likely cause of this behavior.

In the course of the experiments, an independent measurement of the heat capacity of copper potassium sulfate has been made. The relation $C=A/T^3$ appears to be obeyed, the value of the specific heat constant A being $5.8\pm0.2\times10^{-4}R$ deg^2/mole.

INTRODUCTION

ACCORDING to the simple one-electron approximation,[1] the electronic specific heat of a normal metal is given by an expression

$$C=\frac{\pi^2}{3}k^2T\left(\frac{dN}{dE}\right)_{E=E_0}=\gamma T, \qquad (1)$$

where $(dN/dE)_{E=E_0}$ is the density of states at the top of the Fermi distribution. Experimental data in the liquid helium region seem to be in agreement with this prediction. The resulting values of γ are explained in terms of the variation of the density of states at the Fermi surface. Thus, in the case of the noble metals, where the d shell is completely full, the density of states corresponds roughly to that of a free electron gas with one electron per atom. Again, in the transition metals like platinum, with incomplete d shells and narrow d bands, the density of states is much higher, corresponding to the large values observed experimentally.

Equation (1) is based on the explicit assumption that the energy levels of a solid can be described correctly by a self-consistent field approximation. In particular, it is assumed that the total wave function can be represented by a simple product of one-electron wave functions, which are solutions of a Schrödinger equation for a periodic, self-consistent potential. Such a wave function cannot be correct since it does not give any recognition to the fact that the electrons in a metal, which interact strongly, tend to keep as far apart as possible. Thus the resulting energies must be too high. Admittedly, it is still possible that their differences may still give correctly the energy level spacings, but this would have to be established. It is thus a matter of conjecture as to whether Eq. (1) really does describe the behavior of an actual metal.

Now it is known that in the case of atomic systems, the Hartree-Fock approximation, which uses antisymmetrized wave functions, is more satisfactory than the Hartree approximation. Thus it gives lower energies and, furthermore, it produces a correct qualitative description of the spectroscopic terms actually observed in atoms. It might therefore be expected (although this expectation proves to be incorrect) that a similar situation exists in metals.

Here, the application of the Hartree-Fock approximation leads to an additional energy known as the exchange energy. For free electrons this exchange term is given by an equation

$$E_{ex}=-\frac{e^2k_0}{\pi}\left(1+\frac{k_0^2-k^2}{2kk_0}\ln\frac{k+k_0}{|k-k_0|}\right), \qquad (2)$$

where k_0 is the value of the wave number corresponding to the surface of the Fermi distribution. It will be seen

* Submitted in partial fulfillment of the requirements for the degree of Ph.D. at the University of Chicago. The work was done at the low-temperature laboratory of the Institute for the Study of Metals, University of Chicago.

† Now at Division of Physics, Commonwealth Scientific and Industrial Research Organization, Sydney, Australia.

[1] F. Seitz, *The Modern Theory of Solids* (McGraw-Hill Book Company, Inc., New York, 1940), pp. 15–159.

that the resulting curve of E *versus* k has an infinite slope at $k=k_0$. As a consequence, the assumptions made in deriving Eq. (1) break down, and a more careful analysis must be made to obtain the electronic specific heat.

A number of workers[2-5] have investigated the effect of the exchange energy on the electronic heat capacity. In the case of sodium, it is found that the heat capacity is now given by an equation

$$C=\frac{C_s}{8.9-1.7\log_{10}T}, \tag{3}$$

where C_s is the usual free-electron value. Thus the linear relationship with temperature is no longer obeyed, and the magnitude of the heat capacity is much lower than that predicted by the simple theory.

These results appear to be in contradiction with experiment and so it seems that the Hartree-Fock approximation does not correctly describe the behavior of a metal. As Wigner[6] points out, this conclusion is supported by considerations regarding the magnetic properties of an electron gas of low density. Here the Hartree-Fock theory predicts that the system should be ferromagnetic, whereas it is known from an exact solution that such is not the case.

Wohlfarth[4] has shown that the peculiar specific heat behavior given by Eq. (3) disappears if the exchange term is evaluated using a screened Coulomb potential. A similar potential was employed by Landsberg[7] to explain the soft x-ray emission spectrum of sodium. In both cases, the procedure was purely an *ad hoc* one. Recently, however, Macke,[8] and Bohm and Pines[9] have made considerable progress in justifying the use of a screened Coulomb field from a fundamental point of view. Although their work cannot be regarded as complete, the results seem promising.

In view of such progress, it appears likely that a theory really capable of being compared with experiment will be produced in the near future. Since sodium is the closest approximation to an ideal metal, experimental data on its electronic heat capacity would provide the best means of comparison with such a theory. It is thus of some importance to measure the temperature dependence of its electronic specific heat over as wide a temperature range as possible.

The present series of experiments extends specific heat measurements down to 0.2°K for a representative group of metals including sodium. Over the region of interest, the lattice heat capacity is negligible, so that it has been unnecessary to make any assumption regarding its temperature dependence.

[2] J. Bardeen, Phys. Rev. **50**, 1098 (1935).
[3] H. Koppe, Z. Naturforsch. **2a**, 185 (1947).
[4] E. P. Wohlfarth, Phil. Mag. **41**, 534 (1950).
[5] A. B. Lidiard, Phil. Mag. **42**, 1325 (1951).
[6] E. Wigner, Trans. Faraday Soc. **34**, 678 (1938).
[7] P. T. Landsberg, Proc. Phys. Soc. (London) **62**, 806 (1949).
[8] W. Macke, Z. Naturforsch. **A5**, 192 (1950).
[9] D. Bohm and D. Pines, Phys. Rev. **92**, 609 (1953).

Except in the case of sodium, the results indicate that the linear variation of electronic heat capacity with temperature holds down to the lowest temperatures obtainable in these experiments. The corresponding γ values are in substantial agreement with those obtained in the liquid helium region.

Previous work[10] on sodium revealed an anomaly in its specific heat at 7°K. As a consequence, no data concerning its electronic heat capacity had been obtained. It was hoped that measurements below 1°K would provide such data. Unfortunately, however, experiments here also fail owing to the presence of an anomaly at 0.87°K. It is thought that the anomaly arises from a martensitic-type transformation similar to that reported in lithium.[11] Some evidence for such a transformation is given by x-ray studies on cold-worked sodium.[12]

APPARATUS

Essentially the method consisted in measuring the combined heat capacity of the metal specimen and a paramagnetic salt. The heat capacity of the salt being known, that of the metal could be obtained by subtraction. The low temperatures were obtained by adiabatic demagnetization of the salt pill, starting from a temperature of 1.30°K and an initial field of about 6000 gauss. The latter was produced by a Weiss-type electromagnet having a 4-inch pole gap and mounted on rails so as to permit easy removal after demagnetization. Thermal contact between the salt pill and the helium bath was obtained using exchange gas at a pressure of approximately 10^{-4} mm of mercury. A mercury diffusion pump was used to produce an insulating vacuum when required.

The only item requiring detailed description is the vacuum can. Details of this are shown in Fig. 1. The outer case is in two sections, the upper half A being made of brass. Glass construction is used in the lower half B to eliminate disturbances arising from eddy currents in the circuit for measuring the susceptibility of the paramagnetic salt. Junction between the two parts is effected by a copper-glass seal C. The glass section of the can is necked down over its lower portion so as to accommodate the coil system used in measuring the susceptibility of the salt.

The exterior of the vacuum can is completed by the cap D which slides snugly into the top of the can, a seal between the two being obtained by a Rose's metal joint. Passing through the cap is the super-nickel pumping tube E, which communicates with the interior of the vacuum can by means of the aperture F. Radiation is prevented from entering the can by means of the trap G, by positioning the pumping hole on the side

[10] G. L. Pickard and F. E. Simon, Proc. Phys. Soc. (London) **61**, 1 (1948).
[11] C. S. Barrett and O. R. Trautz, Trans. Am. Inst. Mining Met. Engrs. **175**, 579 (1948).
[12] C. S. Barrett, Am. Mineralogist **33**, 749 (1948).

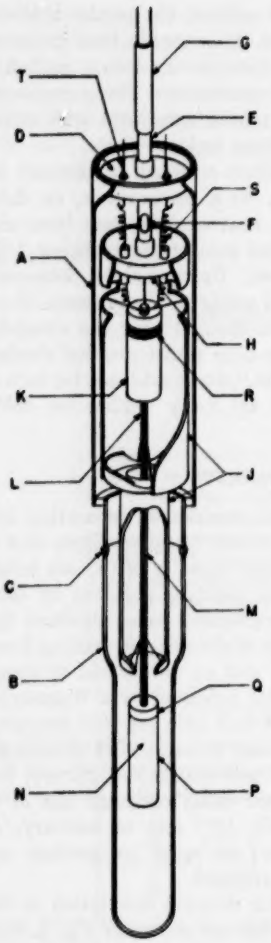

FIG. 1. Details of calorimeter.

of the tube and by covering the glass parts of the can with opaque cloth. The end of the pumping tube is blocked off by the brass plate H, which supports the fiber cage J. This is made in two parts so as to permit easy assembly of the system.

Within the cage, and supported from it by nylon threads, is the actual specimen. The metal under test is in the form of a cylinder K, to which is soldered a thick copper wire L. At its lower end the wire, which is stiffened by a glass rod M, is connected to the salt pill N. The resulting geometry prevents eddy currents from being induced in the metal and thereby affecting the measurements of the susceptibility of the salt.

The salt pill consists of about 20 grams of copper potassium sulfate molded (under a pressure of about 8 tons) into a cylinder $\frac{5}{8}$ inch in diameter and 2 inches in length. Embedded in the salt is a copper vane system[13] which, being joined to the copper wire, insures adequate thermal contact between the salt and the metal. A Lucite case P, sealed at the end Q by cold-setting Araldite, covers the salt pill and serves to minimize adsorption of helium.

Heat is supplied to the system by means of the heater R. This is made of No. 45 gauge enameled manganin wire and is cemented with clear Glyptal directly onto the specimen K. Electrical connections to the heater are made through spirals S of tinned No. 40 gauge manganin wire. At helium temperatures these become super-conducting and so provide a path of high electrical conductivity and low thermal conductivity. Kovar seals T are used to bring out the heater connections to the exterior of the vacuum can. The remainder of the heating circuit is quite conventional and will not be described here.

TEMPERATURE MEASUREMENT

The temperature of the combined specimen was obtained by ballistic measurements[14] of the susceptibility of the paramagnetic salt. A short period (5 seconds) galvanometer was used in order to obtain temperature readings as quickly as possible. In the case of copper potassium sulfate, measurements by Garrett[15] have shown that it obeys a Curie-Weiss law down to 0.1°K. Thus the absolute temperature is readily obtained from the galvanometer deflection θ, using the relation

$$\theta=\frac{\alpha}{T-(\delta_1+\delta_2)}+\beta, \tag{4}$$

where α, β are constants depending on the coil geometry and δ_1 is the Curie-Weiss constant for the salt. The values of δ_1 for copper potassium sulfate, as quoted in the literature, vary considerably (see Table I). Here Garrett's value of 0.034°K has been used. The constant δ_2 is given by the formula

$$\delta_2=fC(4\pi/3-N), \tag{5}$$

where C is the Curie constant for the material, f is the filling factor, and N is the demagnetization factor for the shape of pill used. The latter cannot be calculated exactly in the case of a cylinder but a good estimate can be obtained on the assumption that the cylinder

TABLE I. Various determinations of the Curie-Weiss constant δ_1 and the quantity A in the relation $C=AT^{-2}+\gamma T$.

Worker	δ_1 (°K)	A ($10^{-4}R$ deg²/mole)
de Klerk[a]	0.052	6.8
Garrett[b]	0.034	6.1
Benzie and Cooke[c]	0.035	6.0

[a] D. de Klerk, Physica **12**, 513 (1946).
[b] See reference 15.
[c] R. J. Benzie and A. H. Cooke, Proc. Phys. Soc. (London) **63**, 213 (1950).

[13] E. Mendoza, *Ceromonies Langevin-Perrin* (Paris, 1948), p. 53.

[14] N. Kurti and F. Simon, Proc. Roy. Soc. (London) **149**, 152 (1935).

[15] C. G. B. Garrett, Proc. Roy. Soc. (London) **203**, 375 (1950).

can be replaced by an ellipsoid of equivalent dimensions. Using a value of 0.96 for the filling factor and Garrett's value for the constant C, δ_2 was calculated to be 0.006°K. This figure is so small that the above-mentioned assumptions have comparatively little effect on the accuracy of the temperature measurements.

Calibration of the system was effected against the vapor pressure of helium, using the 1949 temperature scale.[16]

SPECIMENS

The general form of the specimen has already been described. For most of the experiments, the mass of the salt pill was kept around 20 grams. This value was influenced principally by sensitivity requirements in the ballastic circuit. Thus, with a measuring field of about 30 gauss, it was possible to obtain a deflection of roughly 40 cm at 1°K. This was sufficient to give an accurate calibration in the liquid helium region. The mass of the metal was chosen so as to give a value of heat capacity at 0.5°K equal to that of the salt. All specimens were analyzed spectroscopically for impurities and, except for one platinum sample, proved to be 99.9 percent pure or better. Further details of the samples are given below.

Copper

This sample was in the form of a cylinder, 1.9 cm in diameter and 5.0 cm in length, turned from commercial stock. The total mass, including the copper vane system and connecting rod, was 141.2 grams.

Silver

Here the specimen consisted of a cylinder 3 cm in diameter and 5.0 cm in length, turned from an ingot of extra high purity stock. The total mass of silver was 485.0 grams, while that of the associated copper vane system was 5.7 grams.

Platinum

Two specimens of this metal were used. The first was melted down from scrap foil. Spectroscopic analysis showed it to have an unusually high (approximately 2 percent) impurity content, undoubtedly acquired during fabrication. The lattice constant as measured by x-rays was (3.9141±0.0004) A as compared with the accepted value 3.9237 A at 20° given by Barrett.[17] A second sample in the form of a cylinder 0.75 cm in diameter and 1.5 cm in length was obtained from Goldsmith Brothers Smelting and Refining Company. This analyzed 99.99 percent pure and gave a lattice constant 3.9236 A, in good agreement with the accepted value. The mass of the second sample was 36.8 grams, that of the copper vane system being 7.4 grams.

[16] H. van Dijk and D. Shoenberg, Nature **164**, 151 (1949).
[17] C. S. Barrett, *Structure of Metals* (McGraw-Hill Book Company, Inc., New York, 1952), p. 647.

Palladium

Here the specimen was a cylinder approximately 0.75 cm in diameter and 1.5 cm in length, also obtained from Goldsmith Brothers. Its mass was 21.6 grams and that of the copper vane system 7.2 grams.

Tungsten

This was obtained in the form of a sintered rod from Fansteel Metallurgical Company. It was machined into a cylinder 1.75 cm in diameter and 5.0 cm in length. To insure better thermal contact between the salt and the specimen itself, copper disks were soldered to either end. The mass of tungsten was 255.5 grams and that of the vane system 17.3 grams.

Molybdenum

The same company also supplied a sintered rod of this metal. It was turned down into a cylinder of about the same dimensions as the tungsten sample, copper disks being soldered to either end as before. The mass of molybdenum was 100.6 grams, that of the copper being 14.3 grams.

Sodium

Two forms of specimen were used in this case. In the first, metal was melted under vacuum into a glass envelope, thermal contact between the specimen and salt being obtained by a copper-glass seal at the bottom of the container. This was used only once, owing to the tendency of the glass envelope to crack. In the second specimen a thin copper container was used, the metal being melted in under vacuum as before. Before sealing, the dead space in the can was filled with nitrogen at one atmosphere pressure. A copper wire extended some distance into the container, so that on cooling the sodium would contract onto it, thereby insuring adequate thermal contact throughout the specimen. The mass of sodium was 21.8 grams and that of the copper 40.8 grams. Spectroscopic analysis showed that the principal impurity in the metal was about 0.02 percent potassium.

PROCEDURE

In making a run, the specimen was first cooled down to about 0.15°K. Details of the demagnetization procedure are well known and will not be described here. Temperature readings were then taken every 15 seconds to establish a warmup curve. At appropriate intervals, known heat inputs were applied, resulting in distinct breaks in the curve. No appreciable after periods were observed except at the lowest temperatures and then only in the poorer conductors like tungsten. This showed that thermal contact between the salt and metal was always quite good and also that the temperature difference between them was small. Thus, by extrapolating the sections of the curve to the midpoints

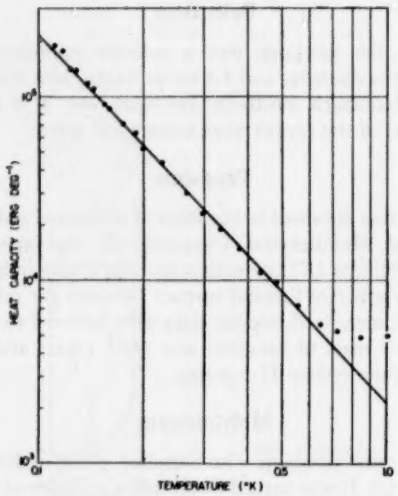

FIG. 2. Heat capacity of copper potassium sulfate.

of the heating periods, it was possible to calculate the resulting temperature rises of the combined system. From these it was a simple matter to calculate the combined heat capacity.

In analyzing the data, use was made of the fact that in the region of interest the total heat capacity can be represented by an equation

$$C=AT^{-2}+\gamma T, \tag{6}$$

provided that the lattice specific heats of both the salt and metal are negligible. In this expression the first term represents the heat capacity of the salt, the last representing the electronic heat capacity of the metal, assuming a linear temperature relation to hold. Rearranging the above equation, we have

$$CT^2=A+\gamma T^3. \tag{7}$$

Thus, if the above assumptions are true, a plot of CT^2 *versus* T^3 should give a straight line whose slope is γ and whose intercept on the vertical axis is the specific heat constant of the salt. The latter, of course, constitutes a check on the accuracy of the experiment, since the mass of the salt is known.

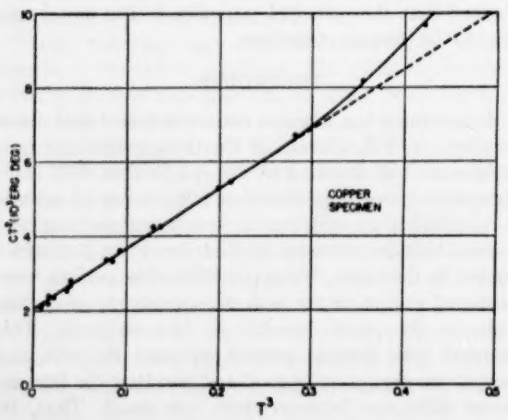

FIG. 3. Plot of CT^2 *versus* T^3 for copper specimen.

RESULTS

Considerable variation in the value of A for copper potassium sulfate exists in the literature. The various determinations are given in Table I.

In order to check on these determinations, an independent measurement was made using the above apparatus. The results for a salt pill of mass 19.8 grams are shown in Fig. 2. It will be seen that from 0.1°K to 0.65°K the experimental points lie quite well on a line of slope -2 corresponding to the postulated inverse square law. The resulting value of the constant A is $(5.8\pm0.2)\times10^{-4}R$ deg²/mole, in good agreement with the figures of Benzie and Cooke and of Barrett, so that it would appear that de Klerk's value is in error.

Beyond 0.65°K there is considerable deviation of the experimental points from the straight line. The deviation is too large to be attributed solely to the lattice specific heat. It is believed that the real cause is the adsorbed helium film on the surface of the salt. This adsorption has been minimized by covering the salt with a plastic container, but, even so, measurements above 0.65°K can hardly be expected to be reliable.

Similar adsorption effects are observed in the results for the metal specimens. For example, Fig. 3 shows a plot of CT^2 *versus* T^3 for the composite copper-salt sample. The initial part of the graph is a straight line, showing that the electronic specific heat of the metal is indeed a linear function of temperature. Beyond about $T^3=0.25$, however, the curvature is quite pronounced and cannot be explained by the effects of lattice heat capacity alone. Accordingly, in fitting a straight line to the experimental data, the points above 0.65°K have been given no weight. The intercept on the vertical axis corresponds within 2 percent to the value of A calculated from the mass of the salt. Figure 4 shows the results for copper plotted in a more usual form. The dotted curves give the specific heats of the salt and metal as obtained from the CT^2 *vs* T^3 plot and the full curve gives their resultant.

In all cases except sodium, it was found that the data below 0.65°K could be fitted quite well to a straight line on a CT^2 *vs* T^3 plot. As in the case of copper, the intercept on the vertical axis corresponded quite closely to that calculated from the mass of salt. The resulting values of γ are given in Table II.[18–25] In

[18] J. A. Kok and W. H. Keesom, Physica 3, 1035 (1936).
[19] Estermann, Friedberg, and Goldman, Phys. Rev. 87, 582 (1952).
[20] A. Wexler and W. S. Corak, Third International Conference on Low Temperature Physics and Chemistry, Houston, 1953 (unpublished).
[21] J. A. Kok and W. H. Keesom, Physica 1, 770 (1933).
[22] P. H. Keesom and N. Pearlman, Phys. Rev. 88, 140 (1952).

computing these, due allowance was made for the mass of the copper vane system.

In the case of sodium, extremely peculiar behavior was observed. Using copper potassium sulphate as a cooling agent, it was not possible to obtain appreciable demagnetization. Thus, final temperatures of the order of 0.85°K were reached instead of the expected value of 0.2°K. Allowing the specimen to remain overnight at liquid helium temperatures appeared to increase the cooling slightly on subsequent demagnetization.

In order to check these results, another experiment was carried out using iron ammonium alum as a refrigerant. This salt, having a much higher entropy of magnetization, produces a greater cooling effect. As expected, the final temperature of the system was considerably lower, being of the order of 0.3°K. The results for the combined heat capacity of the system,

TABLE II. Values of γ in the relation $C=AT^{-3}+\gamma T$.

Metal	γ 10^{-4} cal/mole deg^2 Present work	Previous work	Reference
Copper	1.73±0.08	1.78	a
		1.80	b
		1.60	c
Platinum	16.5 ±0.8	16.1	a
Silver	1.60±0.15	1.60	d
		...	e
		1.48	e
Palladium	25.6 ±1.3	31.0	f
Tungsten	3.53±0.18	50.0	g
		5.0	h
		1.8	i
Molybdenum	5.25±0.26	5.1	i

[a] See reference 18.
[b] See reference 19.
[c] See reference 20.
[d] See reference 21.
[e] See reference 22.
[f] See reference 10.
[g] See reference 23.
[h] See reference 24.
[i] See reference 25.

using this salt, are shown in Fig. 5. The curve for the salt pill alone is also shown. From these it can be seen that there is a pronounced maximum in the specific heat of sodium at about 0.87°K. Owing to the sharpness of the peak and the effects of exchange gas, the shape of the anomaly is not known with any great certainty. The entropy associated with the anomaly, as calculated from the curve, is less than 5×10^4 erg/deg. Another estimate of this entropy may be obtained from the final temperature reached after demagnetization. The resulting figure is 5×10^5 erg/deg, in marked disagreement with the value given above.

[23] A. A. Silvidi and J. G. Daunt, Phys. Rev. **77**, 125 (1950).
[24] M. Horowitz, Master of Science thesis, Ohio State University, 1950 (unpublished).
[25] M. Horowitz and J. G. Daunt, Phys. Rev. **91**, 1099 (1953).

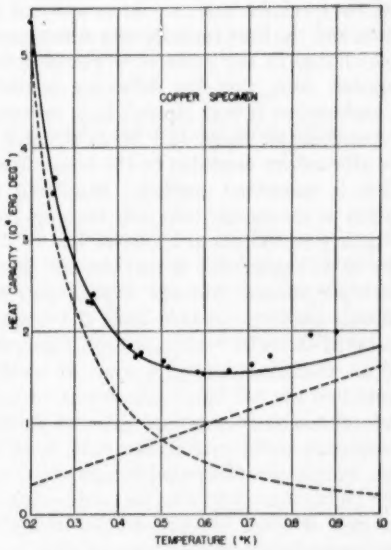

FIG. 4. Heat capacity of copper specimen.

DISCUSSION

Referring to Table II, it will be seen that the agreement between the two sets of values is quite good except for the case of tungsten. There is considerable variation in the values of γ for this metal as reported in the literature. Since the experimental error in the latest liquid helium determination[25] appears to be quite large, it is believed that the value obtained in the present work is more reliable.

Our figure for palladium is somewhat lower than that given by Simon.[10] To eliminate the possibility that could be due to the presence of hydrogen dissolved in

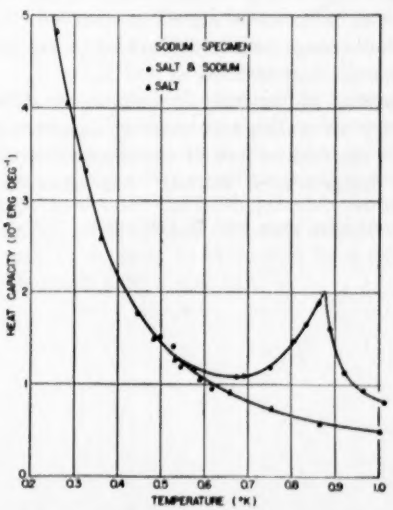

FIG. 5. Heat capacity of sodium specimen.

the metal, the specimen was vacuum annealed at 500°C for 8 hours, and the heat capacity was remeasured. No noticeable change in the value of γ was observed. It would appear, then, that the difference is real. One possible explanation is that Simon's data extends over a wider temperature range (1.5 to 20°K) and hence might be affected by variation in the Debye temperature. This is somewhat unlikely, since the lattice contribution to the specific heat only becomes equal to the electronic contribution at about 11°K.

A more likely explanation is that the two specimens had somewhat different purities. Experiments on the contaminated platinum sample gave the abnormally high γ value of 41.6×10^{-4} cal/mole deg^2. This specimen also had an anomalous lattice spacing. It would thus seem likely that the two effects are correlated and that the band structure is very sensitive to impurities. Such a situation could conceivably exist in all of the transition metals. The discrepancy between the two γ values for palladium would then be easily explicable.

In the case of silver, the present results are in fair agreement with those of Keesom and Kok,[18] and of Wexler and Corak.[20] The assumption of negligible lattice specific heat fails in this case. As a result, there is an increased curvature in the CT^2 *vs* T^3 plot, and hence it is difficult to obtain an accurate value of γ. It is fairly certain, however, that the present data are in disagreement with the results of Keesom and Pearlman.[22] As Clement[26] has pointed out, it is likely that the anomalous behavior reported by these workers is due to errors in thermometer calibration.

In general, therefore, the present work shows that the linear variation of electronic heat capacity with temperature holds down to 0.2°K. The present state of the theory does not permit any quantitative conclusions to be justifiably drawn from the data for the transition and noble metals. It is certain, however, that no such behavior as indicated by Eq. (3) is observed. The data for sodium cannot be analyzed owing to the presence of the specific heat anomaly at 0.87°K.

Concerning the anomaly in sodium, the differences in entropy on cooling and warming suggest that it is due to a martensitic-type of transformation occurring at low temperatures. Barrett[11] has observed x-ray evidence for the existence of such a transformation. Thus sodium, cold-worked at liquid hydrogen temperatures, showed a small diffraction peak in addition to that of the body-centered cubic pattern. This was taken as indicating the formation of a strain-induced face-centered cubic modification, similar to that found in lithium cold-worked at liquid nitrogen temperatures. Now in lithium a related structural change occurs spontaneously at liquid hydrogen temperatures. It is not unlikely, then, that a similar change occurs at low temperatures in the case of sodium.

Such a transformation as that described above could explain the behavior of sodium which is observed in these experiments. Thus the hysteresis associated with a martensitic transformation would account for the difference in entropy on cooling and warming. Again, the cusp-shaped nature of the anomaly could be explained by assuming that the steepest slope of the reverse transformation curve occurred in the vicinity of 0.87°K. This hypothesis would not prevent the possibility that the major part of the transition occupied an extended region above 1°K, thereby accounting for the large difference in the two entropy values.

A significant feature of the experimental curve of Fig. 5 is that the points were not all obtained on the same demagnetization. The shape of the anomaly would thus appear to be reproducible. To account for this fact, it is necessary to suppose that the thermal treatment prior to each demagnetization is able to restore the sample condition to its original position on the transformation curve.

It is clear, however, that the above explanation needs further confirmation from experiment. Such experimental data could be obtained by the x-ray analysis of sodium at liquid helium temperatures.

ACKNOWLEDGMENT

The author would like to express thanks to his sponsor, Professor A. W. Lawson, and to Professor E. A. Long for help and interest in this work. Thanks are also due Mr. Norman Phillips for his continued assistance in carrying out the experiments.

This research was supported by a Charles A. Coffin Fellowship and by a grant from the Commonwealth Scientific and Industrial Research Organisation, Australia.

[26] J. R. Clement, Phys. Rev. **93**, 1420 (1954).

Superconductivity of Nb_3Sn

B. T. MATTHIAS, T. H. GEBALLE, S. GELLER, AND E. CORENZWIT
Bell Telephone Laboratories, Murray Hill, New Jersey

(Received June 10, 1954)

Intermetallic compounds of niobium and tantalum with tin have been found. The superconducting transition temperature of Nb_3Sn at 18°K is the highest one known.

SOME intermetallic compounds crystallizing with the β-wolfram structure become superconducting, as was first pointed out by Hardy and Hulm.[1] In particular one of these, V_3Si, showed a remarkably high transition temperature between 16.9°K and 17.1°K. These authors made various attempts to raise this temperature by introducing a third component but were not successful.

The β-wolfram structure is a very peculiar structure with rather varying interatomic distances,[2] a fact which may render the addition of a third component rather difficult. It seemed therefore more favorable to look for another β-W compound with a large volume and a favorable electron/atom ratio[3] in order to raise the superconducting transition temperature. There is very little known about the systematic occurrence of intermetallic compounds in this β-W structure. The fact that thus far no niobium compounds have been reported seemed therefore not significant.

It was expected that in the Nb-Sn and Ta-Sn this crystal form would be found, an assumption which was verified. We have determined that Nb_3Sn and Ta_3Sn both crystallize in a β-W structure with a lattice constant of about 5.3A. The Ta_3Sn was measured in the apparatus previously described,[4] and became superconducting near 6°K. The transition temperature of the Nb_3Sn was determined by immersing the sample surrounded by a copper coil in liquid hydrogen. The self-inductance of the coil was measured on a General Radio Model 650A Bridge at 1 kc/sec as the sample was slowly cooled. Figure 1 shows the results for two different samples made under somewhat different conditions which were cooled from 18.5°K to 17.5°K during a period of about 30 minutes. The sharpness of the transition together with the reproducibility between samples indicates that these samples are indeed well-defined compounds. The onset of superconductivity at $18.05°K \pm 0.1°$ is determined by extrapolating the line of steepest slope to the high temperature line. Temperatures were measured by a copper constantan thermocouple secured to the measuring coil and independently checked with the vapor pressure of hydrogen.

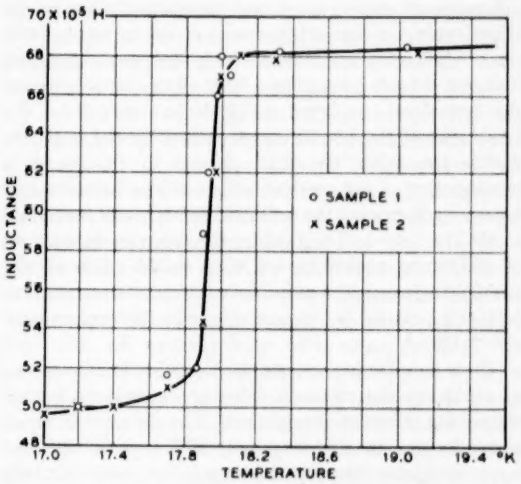

FIG. 1. Variation of susceptibility with temperature of Nb_3Sn.

APPENDIX

While the synthesis of an intermetallic compound is generally a rather straightforward process, it may be necessary to describe briefly the formation of these compounds. No reference to Nb-Sn or Ta-Sn was found in the literature. The melting point of niobium is nearly 400° above the boiling point of tin, and an arc furnace is therefore out of place. A complete reaction can, however, easily be obtained by having molten tin run over Nb or Ta powder in a closed-off quartz tube at 1200°C. Nb_3Sn and Ta_3Sn seem to be formed by a peritectic reaction between 1200°C and 1550°C.

[1] G. Hardy and J. K. Hulm, Phys. Rev. **89**, 884 (1953).
[2] H. I. Wallbaum, Z. Metallkunde **31**, 362 (1939).
[3] B. T. Matthias, Phys. Rev. **92**, 874 (1953).
[4] B. T. Matthias and J. K. Hulm, Phys. Rev. **87**, 799 (1952).

Theory of Scattering in Solids*

G. F. KOSTER†
Massachusetts Institute of Technology, Cambridge, Massachusetts
(Received May 17, 1954)

The scattering of an electron by an imperfection in a lattice is set up in terms of a linear combination of the Wannier functions associated with the lattice. The difference equations which the coefficients of the Wannier functions satisfy are discussed in the light of simple examples. A Green's function formulation of the difference equations is then introduced which leads to the proper asymptotic behavior of the scattered wave. This approach avoids many of the unwarranted assumptions usually made in the discussion of scattering in solids.

I. INTRODUCTION

IN a previous paper, the author and J. C. Slater treated the problem of impurity levels in a solid.[1] [We shall refer to this paper as (I)]. In that paper we used a linear expansion of the impurity wave function in terms of the complete set of Wannier[2] functions for the unperturbed periodic solid. It was shown that the coefficients in this linear expansion satisfied a set of difference equations involving the perturbation to the Hamiltonian. A formalism was derived for solving this set of difference equations which had some desirable features. As will be seen in a later section of this paper, the formalism employed in (I) is best suited for the treatment of the bound states caused by the impurity within the solid. We shall present in this paper a modification of the method which will be better suited for use in discussing the unbound levels of the perturbed solid. The hope will be that by treating the rigorous set of difference equations we shall avoid some of the simplifying assumptions made in the usual treatments of scattering caused by imperfections in the perfect periodic lattice.[3]

These simplifying assumptions consist, in most cases, of replacing the rigorous difference equations by approximate differential equations. The differential equations derived in this way generally is a Schrödinger equation where the potential term is the potential of the imperfections and the effect of the band structure of the periodic lattice is condensed into an effective mass which replaces the electron mass in the Schrödinger equation. In many cases, this simplification is not justified and we would be much safer in using the difference equations for doing our scattering theory.

Following the methods of the previous paper (I), we shall first set up the general difference equations for the scattering problem, and then use them to solve a simple linear chain scattering problem in order to illustrate the use of the difference equations. The method of the last paper (I) will then be used to solve a simple three-dimensional scattering problem. A modification of this method will be seen, in light of this three-dimensional example, to be advantageous. This modification will allow us to derive an asymptotic form for the scattered wave.

II. DIFFERENCE EQUATIONS FOR THE SCATTERING PROBLEM IN A SOLID

We shall assume that the reader is familiar with the notations and contents of (I). We expand the solution to our perturbed Hamiltonian H_0+H_1 in terms of Wannier functions belonging to different bands and lattice sites,

$$\psi(\mathbf{r})=\sum(n)\sum(\mathbf{R}_j)U_n(\mathbf{R}_j)a_n(\mathbf{r}-\mathbf{R}_j). \quad (1)$$

The unknown coefficients $U_n(\mathbf{R}_j)$ can be shown to satisfy a set of difference equations,

$$\sum(m,\mathbf{R}_j)[\mathcal{E}_m(\mathbf{R}_i-\mathbf{R}_j)\delta_{nm} + V_{nm}(\mathbf{R}_i,\mathbf{R}_j)]U_m(\mathbf{R}_j)=EU_n(\mathbf{R}_i). \quad (2)$$

These equations are Eq. (8) of (I) and are no different whether we are doing bound perturbed states or the scattering problem. The difference between these problems comes in the choice of the energy E. If E lies in the band, we know that there are propagating solutions to the unperturbed problem. Since this is the case, for those difference equations beyond the point where the perturbation vanishes, it is possible to find solutions which extend out to infinity. We noted in (I) that for this case (E lying in a band) there would be a solution to our impurity problem for every energy in the bands.

Since this is the case we might pose the following problem. We wish to find the solution to our difference equations assuming that at very large distances from the perturbation the wave function consists of an incident unperturbed solution to our problem and outgoing waves. The unperturbed solutions to the periodic potential problem for energies lying in the band are the Bloch functions. When expressed in terms of solutions to the difference equations these are the functions $U(\mathbf{R}_j)=\exp(i\mathbf{k}\cdot\mathbf{R}_j)$, where $E(\mathbf{k})$ is equal to E, the energy at which the scattering takes place. We therefore look for

* The research in this paper was supported jointly by the Army, Navy, and Air Force under contract with the Massachusetts Institute of Technology.
† Staff Member, Lincoln Laboratory, Massachusetts Institute of Technology, Cambridge, Massachusetts.
[1] G. F. Koster and J. C. Slater, Phys. Rev. **95**, 1167 (1954).
[2] G. H. Wannier, Phys. Rev. **52**, 191 (1937).
[3] E. Conwell and V. F. Weisskopf, Phys. Rev. **77**, 388 (1949) and various other papers. The general method of replacing difference equations by differential equations is treated in reference 2 and in J. C. Slater, Phys. Rev. **76**, 1592 (1949).

solutions to the difference equations $[U(\mathbf{R}_j)]$ which consist of $\exp(i\mathbf{k}\cdot\mathbf{R}_j)$ plus some function of $\mathbf{R}_j$ which represents the outgoing scattered wave.

III. A SIMPLE LINEAR PROBLEM

In order to examine the case of impurity levels in the band, let us treat a simplified one-dimensional crystal. We will use the same example as we did in (I). This is the case of a linear chain with nearest neighbor interactions. The difference equations for this case take the form:

$$\mathcal{E}(0)U(p)+\mathcal{E}(1)[U(p+1)+U(p-1)]=EU(p), \quad (3)$$

$$\mathcal{E}(0)U(0)+\mathcal{E}(1)[U(1)+U(-1)] =[E-V(0)]U(0). \quad (4)$$

The impurity only has matrix elements between Wannier functions located at the central atom. In (I) the energy band for this case was shown to contain the energies,

$$E=\mathcal{E}(0)+2\mathcal{E}(1)\cos kR. \quad (5)$$

Following the method outlined in the last section, we will look for a solution to our impurity problem for an energy in the band which consists of an incoming wave and outgoing scattered waves. We know that the only solutions to our general difference equations (3) are $\exp(\pm ikRp)$. The solution to our scattering problem must be made up of linear combinations of these two functions. We let our incident wave be described by $\exp(-ikRp)$. The scattered waves are outgoing waves. We have, therefore, that for

$$p\geqslant 0: \quad U_p=\exp(-ikRp)+A\exp(ikRp); \quad (6)$$

$$p\leqslant 0: \quad U_p=\exp(-ikRp)+B\exp(-ikRp). \quad (7)$$

(For $p<0$ we could lump the two terms together since they both depend on p in the same manner, but writing the solution in this form is nearest to what is done in three dimensions.) The constants A and B which represent the reflected and part of the transmitted wave must be determined from the special Eq. (4). First we notice that in order for both solutions to give the same value at the origin, A must equal B. Substituting these solutions into Eq. (4) we arrive at the result that

$$[\mathcal{E}(0)+V(0)](1+A) +\mathcal{E}(1)[2\cos kR+2Ae^{ikR}]=E(1+A). \quad (8)$$

Expressing the cos in terms of the energy by use of (5), we can simplify this to yield

$$V(0)(1+A)+2A\mathcal{E}(1)e^{ikR}=[E-\mathcal{E}(0)]A. \quad (9)$$

This can be further simplified by use of (5), giving finally:

$$V(0)(1/A)=-i2\mathcal{E}(1)\sin kR-V(0). \quad (10)$$

This is the desired equation for A. If A is expressed in the form $R\exp(-i\phi)$, where R is positive and real, we can readily show that

$$R=\left(\frac{[2\mathcal{E}(1)]^2-E'^2}{V^2}+1\right)^{\frac{1}{2}}, \qquad \phi=\tan^{-1}\frac{\{[2\mathcal{E}(1)]^2-E'^2\}^{\frac{1}{2}}}{V}, \quad (11)$$

where $E'=E-\mathcal{E}(0)$. We have now found the amplitude of the wave scattered from the impurity. [This result should be compared with (21) of (I).]

In this simple case, the solutions to the general difference equations (3) could be easily found. They consist solely of the propagating band solutions. In (I) we noted that even in more complex linear chain problems there are other solutions to the general difference equations (equations not involving the perturbation) for energies in the band besides the propagating ones. The presence of these additional nonpropagating solutions was what made the method used above impractical for more complex cases in (I). The same problem arises here.

The knowledge of the presence of these nonpropagating solutions for energies in the band allows us to say more of the nature of the scattered waves. If we demand that our scattered wave remains finite for large distances, the scattered wave must contain no behavior involving complex propagation constants $\mathbf{k}$, which gives rise to an exponential increase of $U(\mathbf{R}_j)$ with distance. Therefore that portion of the scattered wave which comes from the nonpropagating states ($\mathbf{k}$ complex or pure imaginary) must fall off exponentially with distance from the scattering center. This means, of course, that at very large distances, the scattered wave consists of only a linear combination of those states in the band which have the energy E of the incident wave. As we come close to the scattering center, there will be in addition to the asymptotic form a more rapidly varying dependence with distance which arises from the complex propagation constants which are solutions to the equations:

$$E(\mathbf{k})=E. \quad (12)$$

It would be convenient to ignore these complex propagation constants. We unfortunately are not at liberty to do so since they may form an important part of our scattering problem.

The presence of these nonpropagating parts of the scattered wave forms the essential difference between scattering in a solid and that in free space. In free space, the energy depends quadratically on the propagation constant $|\mathbf{k}|$. For positive energies (energies "in the band") there are only real propagation constants which are a solution to (12) and consequently there are no exponentially damped solutions to our unperturbed problem. In a solid, this is not the case. It may be true that scattering theory may be done in certain cases in a

solid ignoring the nonpropagating solutions to the difference equations but this will involve a certain approximation. (For instance assuming that E depends on $\mathbf{k}$ quadratically.) It is safer not to make this assumption and deal directly with the difference equations trying to include all the propagating and nonpropagating solutions to the unperturbed equations.

IV. GREEN'S FUNCTION FORMULATION OF THE SCATTERING PROBLEM

We remember that in (I) we were able to avoid the knowledge of the nonpropagating solutions to our difference equations with the energy E by the use of what turned out to be equivalent to a Green's function formulation to the problem. We can use the same method used in that paper to solve the scattering problem. We notice that in Eq. (38) of (I) the quantity

$$\sum(\mathbf{k})e^{i\mathbf{k}\cdot(\mathbf{R}_j-\mathbf{R}_l)}/[E-E_m(\mathbf{k})] \tag{13}$$

plays the role of a Green's function giving the effect at the lattice site $\mathbf{R}_j$ of a disturbance at the lattice site $\mathbf{R}_l$ for the mth band. Let us try to make use of this same quantity to satisfy our difference equations for the scattering problem.

We imagine that we have an incident wave of energy E and propagation constant $\mathbf{k}$. Since we are doing the scattering problem, it is assumed that this energy is contained in one of the bands. Let us call this the qth band. By the general method indicated in Sec. II, we can try as our wave function a sum of the incident wave and outgoing waves.

$$U_m(\mathbf{R}_j)=\delta_{q,m}e^{i\mathbf{k}\cdot\mathbf{R}_j} +\sum(\mathbf{R}_l)c_m(\mathbf{R}_l)\sum(\mathbf{k})\frac{e^{i\mathbf{k}\cdot(\mathbf{R}_j-\mathbf{R}_l)}}{E-E_m(\mathbf{k})}. \tag{14}$$

The only propagating parts to this solution come from the qth band and for those $\mathbf{k}$ values in that band which have the energy E. All other contributions to the sum over $\mathbf{k}$ for each band must contribute only to the nonpropagating part of the solution. The sum over $\mathbf{R}_l$ in (14) is to extend over only those lattice sites at which the perturbation does not vanish, that is, over those lattice sites for which $V_{nm}(\mathbf{R}_i,\mathbf{R}_j)$ is not zero. The unknown quantities $c_m(\mathbf{R}_l)$ are to be determined in order to satisfy the difference equations (2). We may substitute (14) into (2) in order to get the desired set of simultaneous equations for the c's.

$$\sum(m,\mathbf{R}_j)\{[\mathcal{E}_m(\mathbf{R}_i-\mathbf{R}_j)-E\delta(\mathbf{R}_i-\mathbf{R}_j)]\delta_{n,m} \times\sum(\mathbf{R}_l)c_m(\mathbf{R}_l)K_{E,m}(\mathbf{R}_j-\mathbf{R}_l) +V_{n,m}(\mathbf{R}_i,\mathbf{R}_j)\sum(\mathbf{R}_l)c_m(\mathbf{R}_l)K_{E,m}(\mathbf{R}_j-\mathbf{R}_l)\} =-\sum(m,\mathbf{R}_j)V_{n,m}(\mathbf{R}_i,\mathbf{R}_j)\delta_{q,m}e^{i\mathbf{k}\cdot\mathbf{R}_j}. \tag{15}$$

In Eq. (15) we have introduced the notation $K_{E,m}(\mathbf{R}_j-\mathbf{R}_l)$ for the kernel or Green's function of (13). We have also made one simplification by making use of the fact that the incident wave satisfies the equations with the perturbation set equal to zero.

A further simplification can be made in the first term inside the curly brackets in (15). There appears in this term the following:

$$\sum(\mathbf{R}_j)[\mathcal{E}_m(\mathbf{R}_i-\mathbf{R}_j)-E\delta(\mathbf{R}_i-\mathbf{R}_j)]K_{E,m}(\mathbf{R}_j-\mathbf{R}_l) =\sum(\mathbf{k},\mathbf{R}_j)[\mathcal{E}_m(\mathbf{R}_i-\mathbf{R}_j) -E\delta(\mathbf{R}_i-\mathbf{R}_j)]\frac{e^{i\mathbf{k}\cdot(\mathbf{R}_j-\mathbf{R}_l)}}{E-E_m(\mathbf{k})}. \tag{16}$$

Making use of the expansion of the energy $E_m(\mathbf{k})$ in a Fourier series,

$$E_m(k)=\sum(\mathbf{R}_s)\mathcal{E}(\mathbf{R}_s)e^{-i\mathbf{k}\cdot\mathbf{R}_s}, \tag{17}$$

we can eliminate the sum over $\mathbf{R}_j$, and arrive at the result that (16) equals

$$\sum(\mathbf{k})\frac{E_m(\mathbf{k})-E}{E-E_m(\mathbf{k})}e^{i\mathbf{k}\cdot(\mathbf{R}_i-\mathbf{R}_l)}=-N\delta(\mathbf{R}_i-\mathbf{R}_l). \tag{18}$$

We have made use of the well-known delta-function property of the sum over $\mathbf{k}$ of $\exp[i\mathbf{k}\cdot(\mathbf{R}_i-\mathbf{R}_l)]$. Substituting this result back into (15), we find as the set of simultaneous equations for the c's,

$$\sum(m,\mathbf{R}_j,\mathbf{R}_l)[-N\delta(\mathbf{R}_i-\mathbf{R}_l)\delta_{n,m} +V_{n,m}(\mathbf{R}_i,\mathbf{R}_j)K_{E,m}(\mathbf{R}_j-\mathbf{R}_l)]c_m(\mathbf{R}_l) =-\sum(\mathbf{R}_j)V_{n,q}(\mathbf{R}_i,\mathbf{R}_j)e^{i\mathbf{k}\cdot\mathbf{R}_j}. \tag{19}$$

We notice that the incident wave contributes the inhomogeneous term to these equations. We have therefore reduced the scattering problem to the solution of a set of linear simultaneous inhomogeneous equations for the c's. This set of equations extends over those bands and lattice sites for which the perturbation has nonvanishing matrix components. We have not shown this fact in a rigorous manner here but we could have carried out an argument similar to the one which we carried out in (I) in order to deduce the size of the secular equation rigorously.

There is, of course, another point which we glossed over in the foregoing derivation which we should discuss. We have correctly introduced the incident plane wave but we have not shown that the Green's function (13) corresponds to an outgoing wave. We know that the contribution to the wave function for other bands than the qth (the band in which the energy E lies) will contribute only an exponentially damped term from our experience in the last paper. The outgoing wave must therefore come from the qth band and in particular for those propagation vectors which give rise to the energy E. These are just the energies for which $E_q(\mathbf{k})=E$. This causes the denominator in (13) to vanish, giving rise to a

singularity in the sum (or integral) over $\mathbf{k}$. This is a familiar state of affairs. The manner in which we integrate around this singularity will determine whether our solution corresponds to incoming, outgoing, or standing waves. This is best illustrated by a simple example. This example will also tend to illustrate the difficulties involved in the method presented above and in a later section we shall show how these difficulties can be overcome by a modified definition of the Green's function.

Let us imagine that we have a situation where the energy falls near the bottom of a band which has its minimum near $\mathbf{k}=0$ and which is spherically symmetric about this point. If we choose the zero of energy at $\mathbf{k}=0$, the energy of the band can be expressed in the following form for small propagation vectors:

$$E=\alpha|\mathbf{k}|^2. \tag{20}$$

We now substitute this expression into the Green's function and assume that the principal contribution to the integral comes from the region around $k=0$. In this case we have that

$$K_E(\mathbf{R}_j-\mathbf{R}_l)=\int \frac{e^{i\mathbf{k}\cdot(\mathbf{R}_j-\mathbf{R}_l)}}{E-\alpha|\mathbf{k}|^2}(d\mathbf{k}). \tag{21}$$

We can easily perform the integration over angles, giving us one of the spherical Bessel functions:

$$K_E(\mathbf{R}_j-\mathbf{R}_l)=\int_0^\infty \frac{\{\sin k|\mathbf{R}_j-\mathbf{R}_l|\}2\pi k^2dk}{(E-\alpha k^2)k|R_j-R_l|}$$
$$=\int_{-\infty}^{\infty}\pi\frac{e^{ik|\mathbf{R}_j-\mathbf{R}_l|}kdk}{(E-\alpha k^2)|\mathbf{R}_j-\mathbf{R}_l|}. \tag{22}$$

This is, of course, nothing more than the familiar Green's function for scattering in free space. We notice that this integral has simple poles at $k=\pm(E/\alpha)^{\frac{1}{2}}$ along the real axis. We can get a variety of Green's functions depending on how we choose to integrate around these singularities in the complex plane. We can arrive at the results (ignoring constant multipliers)

$$K_E(\mathbf{R}_j-\mathbf{R}_l)\sim\frac{\sin[(E/\alpha)^{\frac{1}{2}}|\mathbf{R}_j-\mathbf{R}_l|]}{|\mathbf{R}_j-\mathbf{R}_l|}$$
$$\frac{\cos[(E/\alpha)^{\frac{1}{2}}|\mathbf{R}_j-\mathbf{R}_l|]}{|\mathbf{R}_j-\mathbf{R}_l|}$$
$$\frac{\exp[i(E/\alpha)^{\frac{1}{2}}|\mathbf{R}_j-\mathbf{R}_l|]}{|\mathbf{R}_j-\mathbf{R}_l|}$$
$$\frac{\exp[-i(E/\alpha)^{\frac{1}{2}}|\mathbf{R}_j-\mathbf{R}_l|]}{|\mathbf{R}_j-\mathbf{R}_l|}. \tag{23}$$

The first two represent standing waves and the third and fourth represent outgoing and incoming waves, respectively. Since we are looking for a Green's function which represents an outgoing wave, we would, of course, choose the third path of integration. We notice that (21) or (13) is not sufficient to determine the Green's function. In addition, a path of integration around the singularity must be specified.

In this simple example, the integration generating the Green's function could be reduced to a one-dimensional integration in the complex plane. In the case of more complicated dependence of $E(\mathbf{k})$ on $\mathbf{k}$, this reduction to a one-dimensional integral may not be so trivial. In this event, we should have difficulty in knowing what we meant by choosing a path of integration which gave rise to an outgoing Green's function. In the next section, we shall give a method of overcoming this difficulty so that we shall more easily restrict ourselves to outgoing waves.

V. IMPROVED GREEN'S FUNCTION FORMULATION

In the last section, (13) was used as the Green's function for the solution of the difference equations which expressed the scattering problem in a periodic structure. In this section we shall introduce a Green's function which will also satisfy the perturbed difference equations; but in addition, have the advantage of giving explicitly outgoing waves.

Let us try as a Green's function the quantity

$$K_{E,m}(\mathbf{R}_j-\mathbf{R}_l)=(1/i)\sum(\mathbf{k})$$
$$\times\int_0^\infty dt e^{i[E-E_m(\mathbf{k})]t}e^{i\mathbf{k}\cdot(\mathbf{R}_j-\mathbf{R}_l)}. \tag{24}$$

The sum over $\mathbf{k}$ values once again goes over the first Brillouin zone. The integration over t can be carried out at once and, when evaluated at the lower limit, will give rise to the Green's function (13). The evaluation of the integral over t is of course ambiguous when evaluated at the upper limit. It will be seen however that this does not influence the validity of the use of this Green's function. We must now substitute this Green's function into the difference equations and see if we can solve them.

We assume once again that the form of the solution to the difference equations is given by

$$U_m(\mathbf{R}_j)=\delta_{q,m}e^{i\mathbf{k}\cdot\mathbf{R}_j}$$
$$+\sum(\mathbf{R}_l)c_m(\mathbf{R}_l)\sum(\mathbf{k})K_{E,m}(\mathbf{R}_j-\mathbf{R}_l). \tag{25}$$

The energy E is assumed to lie in the qth band. The first term represents the incoming Bloch wave. The sum extends over only those lattice sites over which the perturbation extends. As before, we substitute (25) into (2). The proof that this form of the Green's function satisfies the difference equations runs exactly as the proof that (13) is a Green's function which allows us to satisfy the difference equations. We can make essentially the same simplification in the first term in the curly brackets in (15) that we did before. The only difference

will come in (18). This relation will be replaced by

$$\sum(\mathbf{k})(1/i)\int_0^\infty dt[E_m(\mathbf{k})-E]e^{i[E-E_m(\mathbf{k})]t}e^{i\mathbf{k}\cdot(\mathbf{R}_j-\mathbf{R}_l)}. \quad (26)$$

We shall now carry out the integral over t and replace the upper infinite limit by some large number A. This yields

$$\sum(\mathbf{k})(-1)\left\{\frac{E_m(\mathbf{k})-E}{E-E_m(\mathbf{k})}e^{i[E-E_m(\mathbf{k})]A} - \frac{E_m(\mathbf{k})-E}{E-E_m(\mathbf{k})}\right\}e^{i\mathbf{k}\cdot(\mathbf{R}_j-\mathbf{R}_l)}. \quad (27)$$

The first term in the summation we can make as small as we please by choosing A large enough. The rapid oscillation of the exponential will insure this. The second term is exactly the term which we had in (18). Thus we see that (26) will give the same value as (18) in the limit as A approaches infinity. That is, (26) will have the value $-N\delta(\mathbf{R}_j-\mathbf{R}_l)$. We are then justified in using the set of simultaneous equations (19) as the condition for the solution to the scattering problem. The only change that will take place is that we use the new definition (24) of the Green's function.

In order to complete the discussion of this Green's function, we must show that for large distances from the scattering center it represents an outgoing wave. The only term in (25) which contributes to the asymptotic form of the scattered wave is that portion of the wave function which comes from the qth band. The contribution from all other bands will give coefficients of the Wannier function which are exponentially damped. Let us therefore study $K_{E,q}(\mathbf{R}_n)$ for large $\mathbf{R}_n$. For convenience we shall drop the index q throughout the following remembering that we shall throughout be discussing the band in which the energy E lies. We have that

$$K(\mathbf{R}_n)=(1/i)\int(d\mathbf{k}) \times\int_0^\infty dt\exp\{i[E-E(\mathbf{k})]t+i\mathbf{k}\cdot\mathbf{R}_n\}. \quad (28)$$

Here we have assumed that we can replace the summation over $\mathbf{k}$ by an integral over the first Brillouin zone. $\mathbf{R}_n$ is assumed to be very large. This will cause rapid oscillations in the value of the exponential. We shall follow the method of stationary phases and assume that the principal contribution to the integral comes from that region where the variation of the exponent is small. This means that we shall set the gradient of the exponent in $\mathbf{k}$ space equal to zero as well as the derivative of the exponent with respect to t. This gives the conditions that

$$E=E(\mathbf{k}); \quad -[\nabla E(\mathbf{k})]t+\mathbf{R}_n=0. \quad (29)$$

The gradient in (29) is, of course, the gradient in $\mathbf{k}$ space. These equations determine the values of t and $\mathbf{k}$ around which the principal contributions to the integral (28) arise. The first of the two relations says that the contributions come from the surface of constant energy with energy E. This is not surprising since we know that the only propagating solutions of the difference equations with the energy E come from that portion of the energy band which has the energy E. The second of the relations embodied in (29) says that the portion of the constant energy surface which contributes to the integral is the portion near the point on this energy surface where the gradient is parallel to the vector $\mathbf{R}_n$. Let the values of the variables which satisfy these relations be $t=t_0$ and $\mathbf{k}=\mathbf{k}_0$. We can now introduce new variables which represent the change in the values of $\mathbf{k}$ and t as we depart from $\mathbf{k}_0$ and t_0: $\mathbf{k}=\mathbf{k}_0+\boldsymbol{\kappa}$; $t=t_0+\tau$. We shall now carry out the integral (28) over the variables τ and $\boldsymbol{\kappa}$ allowing these to range from plus to minus infinity assuming that the major contribution comes from the region where these variables are zero.

We start by expanding the exponent in a Taylor series keeping only terms up to the second order. [We have already assured the vanishing of the first order terms by the conditions (29).]

$$[E-E(\mathbf{k})]t+\mathbf{k}\cdot\mathbf{R}_n = \mathbf{k}_0\cdot\mathbf{R}_n-[\nabla E(\mathbf{k}_0)]\cdot\boldsymbol{\kappa}\tau-\tfrac{1}{2}t_0\left\{\frac{\partial^2E(\mathbf{k}_0)}{\partial\kappa_x^2}\kappa_x^2 + \frac{\partial^2E(\mathbf{k}_0)}{\partial\kappa_x\partial\kappa_y}\kappa_x\kappa_y+\cdots\frac{\partial^2E(\mathbf{k}_0)}{\partial\kappa_z^2}\kappa_z^2\right\}. \quad (30)$$

Substituting this into (28) gives

$$K(\mathbf{R}_n)\approx(1/i)e^{i\mathbf{k}_0\cdot\mathbf{R}_n} \times\int_{-\infty}^{\infty}\int\int\int\int d\tau(d\boldsymbol{\kappa})e^{-i[E(\mathbf{k}_0)\cdot\boldsymbol{\kappa}]\tau}e^{-\frac{1}{2}t_0[\cdots]}. \quad (31)$$

The second brackets in the exponent contain the expression contained in the curly brackets in (30). We shall now choose a coordinate system for $\boldsymbol{\kappa}$ one coordinate of which is perpendicular to the $E(\mathbf{k})=E$ surface at the point $\mathbf{k}_0$ and therefore parallel to the gradient of $E(\mathbf{k})$ at this point. The coordinates in the plane tangent to the constant energy surface we shall orient in such a way that we eliminate all cross derivative terms between these two coordinates in (30). If we call the coordinate perpendicular to the constant energy surface κ_1 and the two coordinates in the plane tangent to the energy surface κ_2 and κ_3, then the integral over τ from minus to plus infinity will be equal to $[2\pi/|\nabla E(\mathbf{k}_0)|]\delta(\kappa_1)$. This means that in the integral over κ_1 we must set $\kappa_1=0$. The

integral (31) is thereby reduced to

$$K(\mathbf{R}_n)\approx(1/i)\frac{2\pi}{|\nabla E(\mathbf{k}_0)|}e^{i\mathbf{k}_0\cdot\mathbf{R}_n}\int_{-\infty}^{\infty}d\kappa_2\int_{-\infty}^{\infty}d\kappa_3$$

$$\times\exp(-\tfrac{1}{2}it_0)\left\{\frac{\partial^2E(\mathbf{k}_0)}{\partial\kappa_2{}^2}\kappa_2{}^2+\frac{\partial^2E(\mathbf{k}_0)}{\partial\kappa_3{}^2}\kappa_3{}^2\right\}. \quad (32)$$

The integrals over κ_2 and κ_3 are elementary integrals. They are proportional to $\int_0^\infty(dx)\,\sin x^2=\frac{1}{2}(\pi/2)^{\frac{1}{2}}$. If we make use of this fact and substitute the value of t_0 which we obtain from (29), $[t_0=|R_n|/|\nabla E(\mathbf{k}_0)|]$, we obtain as a final result for the asymptotic form of the scattered wave:

$$K(\mathbf{R}_n)\approx-\frac{4\pi^2}{|\mathbf{R}_n|}e^{i\mathbf{k}_0\cdot\mathbf{R}_n}$$

$$\Big/\left[\left(\frac{\partial^2E(\mathbf{k}_0)}{\partial\kappa_2{}^2}\right)\left(\frac{\partial^2E(\mathbf{k}_0)}{\partial\kappa_3{}^2}\right)\right]^{\frac{1}{2}}. \quad (33)$$

We have still to show that this corresponds to an outgoing wave. We can indicate this best by Fig. 1. In this figure we show a two-dimensional surface of constant energy. In addition, we show the vector $\mathbf{R}_n$. The vector $\mathbf{k}_0$ is determined by the points of tangency of planes perpendicular to the vector $\mathbf{R}_n$ with the surface of constant energy. This, of course, satisfies the condition that the gradient of $E(\mathbf{k})$ be parallel to $\mathbf{R}_n$, since the gradient is normal to the surface of constant energy. We notice at once that in general there will be two points where the gradient is parallel to $\mathbf{R}_n$. Only one of these values of $\mathbf{k}_0$ will satisfy the second of the conditions (29). The reason is that the value of $t(t_0)$ determined from this relation must be positive. This means that the vectors $\mathbf{R}_n$ and $\nabla E(\mathbf{k}_0)$ must point in the same direction as well as being parallel. As we can see from the diagram, this means that the dot product of $\mathbf{R}_n$ and $\mathbf{k}_0$ will be positive. This corresponds to an outgoing wave in (33). We can see at once that there could be a somewhat different situation. In the preceding discussion, we have assumed that the gradient of $E(\mathbf{k})$ points outward. The reverse situation might also occur. This would mean that a surface of slightly higher energy would lie inside the surface of constant energy which we have drawn. In this case, the dot product of $\mathbf{R}_n$ and $\mathbf{k}_0$ would be negative which would not correspond to an outgoing wave. This situation can be easily remedied however by taking the complex conjugate of the first exponential term in (24). This will replace the negative sign in (29) by a plus sign and we shall once again be forced to get outgoing waves. From this discussion, we can see what it is in the Green's function (24) which gives us the outgoing rather than the incoming waves. It is merely whether we take $e^{-i[E-E(\mathbf{k})]t}$ or $e^{+i[E-E(\mathbf{k})]t}$ in the Green's function (24).

We see now what it is that corresponds to the third and fourth Green's functions in (23) (case of spherical

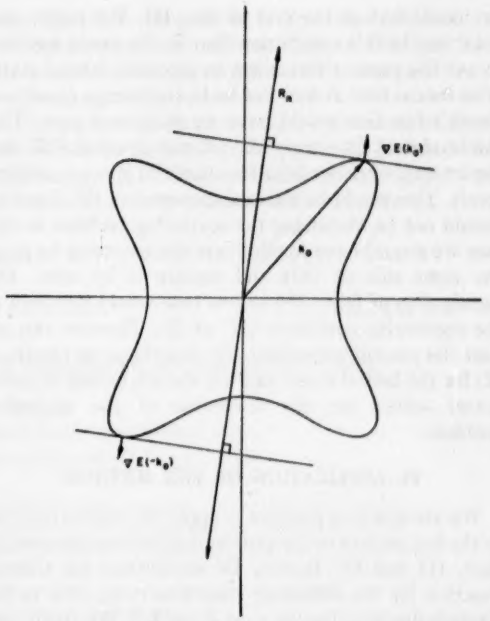

FIG. 1. A contour of constant energy (E) showing the relations between $\mathbf{k}_0$, the wave vector of the wave observed at $\mathbf{R}_n$ a point a large distance from the scattering center, and the vector representing the position of this lattice site ($\mathbf{R}_n$).

energy surfaces). We can also see that if we take the real and imaginary parts of the Green's function (24) we shall get the first and second style Green's functions in (23). It is rather instructive to take the imaginary part of the Green's function (24) explicitly. The imaginary part of (24) is given by

$$\mathrm{Im}K(\mathbf{R}_n)=\tfrac{1}{2}\int_{-\infty}^{\infty}dt\int(d\mathbf{k})e^{i\{[E-E(\mathbf{k})]t}e^{i\mathbf{k}\cdot\mathbf{R}_n}. \quad (34)$$

We have made use of the fact that $E(\mathbf{k})=E(-\mathbf{k})$. The integral over t just gives us a delta function,

$$\mathrm{Im}K(\mathbf{R}_n)=\pi\int d\mathbf{k}\delta(E-E(\mathbf{k}))e^{i\mathbf{k}\cdot\mathbf{R}_n}. \quad (35)$$

By introducing coordinate surfaces one of which is the surface of constant energy, we could actually carry out the integration over the delta function explicitly. This is quite straightforward and we shall not do this here. We shall content ourselves with pointing out that only propagating solutions of the unperturbed difference equations contribute to the imaginary part of the Green's function. This means that the imaginary part of (24) contributes only to the asymptotic form of the scattered wave. The remaining part of the asymptotic form comes from the real part of (24). This real part, in addition, is what makes up the rapidly varying exponentially damped part of the scattered wave which

we mentioned at the end of Sec. III. We might also point out in this connection that in the event we were to use the present formalism to calculate bound states (this means that E does not lie in any energy band) our Green's function would have no imaginary part. This can be seen at once from (35); E cannot equal $E(\mathbf{k})$ and the integral over the delta function will give a vanishing result. This would be the case discussed in (I). Since we should not be discussing the scattering problem in this case we should have to eliminate the incoming wave on the right side of (19) and replace it by zero. The satisfaction of Eqs. (19) in this case would just lead to the eigenvalue condition (41) of (I). Thus we can see that the present formalism will give the same results as (I) for the bound states but has the advantage of being better suited for the discussion of the scattering problem.

VI. APPLICATION OF THE METHOD

We are now in a position to apply the method outline in the last section to the problems which we discussed in Secs. III and IV. In Sec. IV we derived the Green's function for the difference equations using (13) as the Green's function for the case $E=\alpha|\mathbf{k}|^2$. We could now derive the Green's function using the definition (24). This can be done in a straightforward manner which we shall not reproduce here. The integrations over $\mathbf{k}$ and t can be carried out; all the integrals which appear being well known. The result is that we get the third of the Green's functions in (23). This is correct since it is the one which corresponds to an outgoing wave. We also can derive the asymptotic form of the Green's function for this case using (33). It turns out, as one might expect, that we get the same result doing this as we get from (24). This is not surprising for in the case of a quadratic dependence of E on $\mathbf{k}$ the asymptotic form of the Green's function holds all the way in to small values of $\mathbf{R}_n$.

The other simplified case which we treated in this paper was the case of a linear chain with nearest neighbor interactions with an impurity which extends over only one lattice site. For this case (using the notation of Sec. III), Eq. (19) reduces to

$$[-N+V(0)K_E(0)]c(0)=-V(0). \tag{36}$$

The solution to the difference equations is given by

$$U_p=\exp(-ikRp)+c(0)K_E(p). \tag{37}$$

In order to solve Eq. (36) for $c(0)$, we must first evaluate (24) for this case,

$$K_E(p)=\frac{N}{2\pi}(1/i)\int_{-\pi}^{\pi}d\alpha\int_0^{\infty}dt \times\exp\{it[E'-2\mathcal{E}(1)\cos\alpha]\}e^{i\alpha p}. \tag{38}$$

Here we have replaced the sum over k by an integral over the first Brillouin zone and have introduced the notation $\alpha=kR$. The integral over α is just an integral representation for the Bessel function. Carrying out this integral gives

$$K_E(p)=\frac{N}{i}e^{+i\pi p/2}\int_0^{\infty}e^{itE'}J_p[-2\mathcal{E}(1)t]dt. \tag{39}$$

The integral over t is a special case of an integral discussed in Watson[4] and gives $p\gtrless 0$.

$$\begin{aligned}K_E(p)&=\frac{N}{i}e^{+i\pi p/2}\frac{1}{\{[2\mathcal{E}(1)]^2-E'^2\}^{\frac{1}{2}}}\\&\times\left\{\cos\left[p\sin^{-1}\left(\frac{E'}{2\mathcal{E}(1)}\right)\right]\right.\\&\left.-i\sin\left[p\sin^{-1}\left(\frac{E'}{2\mathcal{E}(1)}\right)\right]\right\}\\&=\frac{Ne^{-i\pi p/2}(1/i)}{\{[2\mathcal{E}(1)]^2-E'^2\}^{\frac{1}{2}}}\left\{\cos p\left(\frac{\pi}{2}-\alpha\right)\right.\\&\left.-i\sin p\left(\frac{\pi}{2}-\alpha\right)\right\}=\frac{Ne^{+ip\alpha}}{i\{[2\mathcal{E}(1)]^2-E'^2\}^{\frac{1}{2}}}\\&=\frac{Ne^{+ikRp}}{i\{[2\mathcal{E}(1)]^2-E'^2\}^{\frac{1}{2}}}.\end{aligned} \tag{40}$$

For $p\lesseqgtr 0$, following Watson, we get the result:

$$K_E(p)=\frac{-Ne^{-ikRp}}{i\{[2\mathcal{E}(1)]^2-E'^2\}^{\frac{1}{2}}}. \tag{41}$$

We notice then that the Green's function does correspond to outgoing waves. We must now go on and determine the value of $c(0)$.

$$\begin{aligned}&\left\{-N+\frac{V(0)Ni}{\{[2\mathcal{E}(1)]^2-E'^2\}^{\frac{1}{2}}}\right\}c(0)=-V(0),\\&\frac{1}{c(0)}=+\frac{N}{V(0)}-\frac{Ni}{\{[2\mathcal{E}(1)]^2-E'^2\}^{\frac{1}{2}}}.\end{aligned} \tag{42}$$

If we multiply this relation by $1/K_E(0)$, we find that

$$\frac{1}{c(0)K_E(0)}=\frac{-i}{V(0)}\{[2\mathcal{E}(1)]^2-E'^2\}^{\frac{1}{2}}-1. \tag{43}$$

This is, however, just the same as the relation (10) if we identify $c(0)K_E(0)$ with A. If we make this identifica-

[4] G. N. Watson, *Theory of Bessel Functions* (Cambridge University Press, Cambridge, 1952), p. 405.

tion, the solution to the scattering problem will be given once again by (6) if we substitute the value of $c(0)$ into (37).

Thus we see that this method gives the same results as the direct solution of the difference equations for a simple case. The method also includes free electron scattering as we have seen earlier in this section. It is hoped that this method can be used to overcome some of the difficulties encountered in the direct solution of the difference equations without making the approximations inherent in replacing these difference equations by approximate differential equations.

The author wishes to express his gratitude to Dr. W. H. Kleiner for his helpful discussions. He is also indebted to Professor J. C. Slater for his stimulating encouragement and for his comments on the manuscript.

PHYSICAL REVIEW VOLUME 95, NUMBER 6 SEPTEMBER 15, 1954

Calculation of Wave Functions in a Symmetrical Crystalline Field

PAUL H. E. MEIJER
Department of Physics, Case Institute of Technology, Cleveland, Ohio
(Received April 5, 1954; revised manuscript received June 21, 1954)

It is possible to calculate the splitting of the energy levels of an ion caused by a crystalline field of a certain symmetry in a more systematic way. Instead of solving the secular equation, certain algebraic quantities, i.e., the idempotent elements of the ring of the group, are introduced which contain all the information that can be obtained from the symmetry. This makes it possible to state, before other physical arguments are introduced, how many parameters enter a particular problem. In order to make the method easy to handle, some tables have been added, and a special case has been worked out.

I. BETHE-KRAMERS METHOD[1,2]

WHEN an ion is subject to the influence of a crystalline environment, the allowed rotations of the ion are considerably reduced in number. Instead of the full rotation group, we deal with a subgroup consisting of 24, or fewer, transformations. By picking those representation matrices which correspond to the elements of the subgroup, we obtain a representation of this subgroup. This representation is however, in general, reducible. Now Wigner's theorem[3] states that those wavefunctions which transform according to one irreducible representation belong to the same eigenvalue, and in order to apply this theorem to the finite group mentioned above, the representation has to be reduced.

Bethe[1] showed that, by means of the properties of the characters, one can determine how many and which irreducible representations are contained in the reducible one. He gave the answer for most of the subgroups which occur in practice; a supplement and a correction of one of Bethe's statements are given by Opechowski.[4] The actual computation of the wave functions is usually carried out by conventional procedures without the use of group theory. The secular matrix,

$$\langle m_l,l|V_{el}|m_l',l\rangle=\lambda\langle m_l|\delta|m_l'\rangle,$$

is calculated, and using the roots of its eigenvalue equation one tries to find the unitary matrix which diagonalizes the V_{el} matrix. Unfortunately, the eigenvalue equation is of degree $2l+1$, although sometimes a factorization into equations of the first and second degree can easily be found (e.g., a cubical field on an adapted coordinate system).

To summarize, we can say that no use is made in the usual method of our knowledge of the characters of the representation. This fact, as well as the simplification in the secular determinant often found at the end of the calculation, led us to look for a method in which the reduction is performed in a direct way. We found such a method in a paper by Schoeneberg.[5] Essentially the same method is used for permutation degeneracy by Heitler[6] and Serber.[7] Wigner[8] comes still closer to our problem in a treatment of proper vibrations of symmetrical systems, but in none of these are explicit results given for the transformation matrices which perform the reduction.

II. REDUCTION OF A REPRESENTATION BY IDEMPOTENT ELEMENTS

The reduction of a representation consists of: (a) looking for a unitary transformation T which brings all the representation matrices G_k into the "box-form," and (b) of considering these boxes as separate representations of the group $\mathfrak{G}$.

The essential idea of the method is that instead of first transforming by T and then considering the "boxes" separately, these two steps are taken in the reverse

[1] H. Bethe, Ann. Physik (5) 3, 133 (1929).
[2] H. A. Kramers, Proc. Acad. Sci. Amsterdam 32, 1176 (1929).
[3] E. Wigner, Z. Physik 43, 624 (1927).
[4] W. Opechowski, Physica 7, 552 (1940).
[5] B. Schoeneberg, Abhandl. Math. Sem. Hamburg 9, 1 (1933).
[6] W. Heitler, Z. Physik 46, 47 (1927).
[7] R. Serber, J. Chem. Phys. 2, 706 (1934).
[8] E. Wigner, Gött. Nachr., p. 142 (1930).

order. This can be performed with the idempotent elements $e^{(\mu)}$ of the ring associated to the group. Multiplication of these elements with the matrices G_k generates the representation μ.[9] In case the representation matrices G_k were already in the "box" shape, this mapping of G_k on $e^{(\mu)}G_k$ has the result that all boxes, except that one which is designated by μ, are replaced by sets of zeros. In this particular representation of the group, the representation of the elements $e^{(\mu)}$ would have the number 1 in those places of its diagonal which correspond to the interior of the box with label μ, and zeros in all other places. Apart from the fact that we have a number of superfluous rows and columns containing only zeros in our representation matrix, this projection operator has the same effect as the second step mentioned above.

In case the representation matrices G_k are not in the box form, the generating elements can be defined by the following invariant properties:

$$e^{(\mu)}\cdot e^{(\nu)}=\delta_{\mu\nu}e^{(\mu)};\quad \sum_\mu e^{(\mu)}=E, \qquad (1)$$

where E is the unit element.[9] Moreover they commute with all elements G_k.

An explicit expression which fulfills these conditions is found by van der Waerden:[10]

$$e^{(\mu)}=\frac{n_\mu}{h}\sum \chi_\mu^*(i)C_i, \qquad (2)$$

where h is the order of the group, C_i the sum

$$C_i=G_1^{(i)}+G_2^{(i)}+\cdots+Gh_i^{(i)}$$

of the matrices all belonging to the same class i, $\chi_\mu(i)$ the character of these matrices in the irreducible representation μ, and n_μ or $\chi_\mu(e)$ the dimension of this particular representation. It can be shown that the expression (2) obeys the definition (1) (Appendix A).

After the mapping, however, the first step is reduced to a straightforward calculation. The matrix $G\cdot e^{(\mu)}$ operating on the state vector ψ gives the same result as the matrix G operating on the state vector $e^{(\mu)}\psi$. So the $e^{(\mu)}\psi_i$, for fixed μ, transform mutually into each other in an irreducible way under the operations of all G_k, which is the result wanted. Instead of performing the transformation T we only have to orthogonalize the wave functions $e^{(\mu)}\psi_i$, which can be done by a well-done procedure.[11]

It may occur that the original representation contains r_μ times the irreducible representation μ. The projection operator creates, in this case, a representation $G_k'=e^{(\mu)}\cdot G_k$, which has $r_\mu\cdot n_\mu$ independent basis elements, out of the original $\sum_\mu r_\mu\cdot n_\mu$. This invariant subspace can be split up into r_μ invariant spaces of dimension n_μ. We will outline a procedure by which this can be done. In this decomposition, r_μ coefficients remain undetermined.

Suppose the result is obtained and that the basis elements (we drop the index μ)

$$\varphi_1^{(i)},\quad \varphi_2^{(i)},\quad \cdots,\quad \varphi_n^{(i)}\quad (i=1,2,\cdots r)$$

are determined in such a way that a certain (i.e., arbitrary k, but fixed μ) representation matrix G_k^{irr} has diagonal form. As each element of a finite group has the property $g^n=E$ (n is called the order of the element), it is obvious that the relation

$$G_k'\varphi_\nu^{(i)}=\epsilon^{p_\nu}\varphi_\nu^{(i)}$$

holds, where ϵ is a root of unity: $\epsilon=\exp(2\pi i/n)$. We make the restriction, which holds in our case of the cubical and hexagonal groups, that there exists in every irreducible representation an element for which all p_ν's are different. This property can be used to find our new basis.

The element G_k', for which we take not a trivial matrix like E, can be diagonalized with a transformation matrix U. Suppose we have done this. Then we are able to find from our $r\cdot n$-dimensional basis all the $\varphi_\nu^{(i)}$'s belonging to a certain $\nu=\nu_1$ just by looking at the corresponding diagonal element in $UG'U^{-1}$. The general expression which has this property is a linear combination with r arbitrary coefficients b,

$$\varphi_\nu=\sum_i b_i\varphi_\nu^{(i)}, \qquad (3)$$

with $\nu=\nu_1$. This is done for $\nu=\nu_2$, $\nu=\nu_3$, $\cdots$ $\nu=\nu_n$. Finally all linear combinations (3) are made orthogonal, leaving only r coefficients arbitrary.

III. CALCULATION OF THE "SUM OF A CLASS"

The elements of the representation of the rotational group as functions of the eulerian angles $\langle m|D(\psi,\vartheta,\varphi)|m'\rangle$ can be found by a well-known method originally introduced by Weyl.[12] The $2j+1$ components $\langle m|$ of the state vector, which transform under a rotation of space D as the $2j+1$ monomials:

$$\langle m|\sim[(j+m)!(j-m)!]^{-\frac{1}{2}}\xi^{j+m}\eta^{j-m},\quad (m=j,\cdots,-j),$$

are related to the transformation properties of ξ and η:

$$\xi=\alpha\xi'-\beta^*\eta', \qquad \alpha=\cos\tfrac{1}{2}\vartheta\exp[\tfrac{1}{2}i(\varphi+\psi)],$$

$$\eta=\beta\xi'+\alpha^*\eta', \qquad \beta=i\sin\tfrac{1}{2}\vartheta\exp[\tfrac{1}{2}i(\varphi-\psi)],$$

[9] H. Weyl, *Theory of Groups and Quantum Mechanics* (Dover Publ. Inc., New York, n. d.), Chap. 5, Sec. 3.

[10] B. L. v. d. Waerden, *Moderne Algebra* (Springer, Berlin, 1940), second edition, Sec. 118.

[11] H. A. Kramers, *Die Grundlagen der Quantentheorie* (Akademische Verlagsgesellschaft, Book Review Dept., Leipzig, 1938), Vol. 1, p. 69.

[12] See, e.g., H. A. Kramers, *Die Grundlagen der Quantentheorie* (Akademische Verlagsgesellschaft, Book Review Dept., Leipzig, 1938), Part II, Sec. 61; or E. Wigner, *Gruppentheorie und ihre Anwendung auf die Quantenmechanik der Atomspektren* (Edwards Brothers, Inc., Ann Arbor, 1944), Chap. 15.

in the following way:

$$\langle m|=D\langle m'|=\sum_{m'}\langle m|D|m'\rangle\langle m'|$$
$$=[(j+m)!(j-m)!]^{-\frac{1}{2}}(\alpha\xi'+\beta^*\eta')^{j+m}(\beta\xi'-\alpha^*\eta')^{j-m},$$

from which we can find the matrix elements:

$$\langle m|D|m'\rangle=\sum_{k=0}^{j+m}\frac{[(j+m)!(j-m)!(j+m')!(j-m')!]^{\frac{1}{2}}}{k!(j-m'-k)!(j+m-k)!(m'-m+k)!}$$
$$\times\alpha^{j+m-k}(-\beta^*)^k\beta^{m'-m+k}(\alpha^*)^{j-m'-k}. \quad (4)$$

The values of α and β for the elements of the different groups under consideration are assembled in Table I. The signs of the α's and β's are chosen in such a way that, when the group is extended to a double group,[1,4] they all belong to the same class. We deal with three types of elements: those with $\vartheta=0$, $\pm\frac{1}{2}\pi$ and π which can be partially written out in advance:

$$\langle m|D(\psi,0,\varphi)|m'\rangle=\langle m|\delta|m'\rangle\alpha^{2m}, \quad (5a)$$

$$\langle m|D(\psi,\pi,\varphi)|m'\rangle=\langle m|\delta|-m'\rangle(-1)^{j+m}\beta^{-2m}, \quad (5b)$$

$$\langle m|D(\psi,\pm\tfrac{1}{2}\pi,\varphi)|m'\rangle=2^{-j}\langle m|\tfrac{1}{2}\pi|m'\rangle 2\alpha^{m+m'}\beta^{m-m'}. \quad (5c)$$

The numerical value of the matrix $\langle m|\frac{1}{2}\pi|m'\rangle$ can be found in Appendix B. For the calculation of the "sum over a class" we need to specify the group. (The notations are adapted to Bethe's paper.)

(a) *Cubical group:*

$$\langle m|E|m'\rangle=\langle m|\delta|m'\rangle,$$
$$\langle m|C_2|m'\rangle=(-1)^m\langle m|\delta|m'\rangle+(-1)^lA\langle m|\delta|-m'\rangle,$$
$$\langle m|C_3|m'\rangle=B(2m)\langle m|\delta|m'\rangle+2^{-j}F\langle m|\tfrac{1}{2}\pi|m'\rangle,$$
$$\langle m|C_4|m'\rangle=(-1)^{l+m}B'(2m)\langle m|\delta|-m'\rangle$$
$$+2^{-l}(i^{2m'}+i^{2m})(1+i^{m-m'})\langle m|\tfrac{1}{2}\pi|m'\rangle,$$
$$\langle m|C_5|m'\rangle=2^{-j}B(m+m')G\langle m|\tfrac{1}{2}\pi|m'\rangle,$$
$$\langle m|C_i'|m\rangle=-\langle m|C_i|m'\rangle \quad \text{for} \quad i=1,3,5.$$

If $2j$ is odd, C_2 and C_4 are multiplied by zero and are moreover zero by themselves. The exponents in the first three expressions are integers to avoid the ambiguity in sign of $(-1)^{\frac{1}{2}}$. The functions A, B, B', F, and G are given by:

$$A=2;\ m\equiv 0 \pmod 2,$$
$$F=4;\ m-m'\equiv 0 \pmod 4,$$
$$G=\begin{cases}4;\ m-m'\equiv 0 \pmod 8,\\ -4;\ m-m'\equiv 4 \pmod 8,\end{cases}$$
$$B=B'=\begin{cases}2;\ m+m'\equiv 0 \pmod 8,\\ -2;\ m+m'\equiv 4 \pmod 8,\end{cases}$$
$$B=\begin{cases}\sqrt{2};\ m+m'\equiv 1,7 \pmod 8,\\ -\sqrt{2};\ m+m'\equiv 3,5 \pmod 8,\end{cases}$$

and are zero for the values not indicated, apart from those which do not occur in the calculation.

(b) *Hexagonal group* or "Dieder"-group D_6 in the notation of Speiser:[13]

$$\langle m|E|m\rangle=1, \qquad \langle m|C_2|m\rangle=(-1)^m,$$
$$\langle m|C_3|m\rangle=\begin{cases}2;\ 2m\equiv 0 \pmod 6,\\ 1;\ 2m\equiv 1,5 \pmod 6,\\ -1;\ 2m\equiv 2,4 \pmod 6,\\ -2;\ 2m\equiv 3 \pmod 6,\end{cases}$$
$$\langle m|C_4|m\rangle=\begin{cases}2;\ 2m\equiv 0 \pmod{12},\\ 1;\ 2m\equiv 2,10 \pmod{12},\\ -1;\ 2m\equiv 4,8 \pmod{12},\\ -2;\ 2m\equiv 6 \pmod{12},\end{cases}$$

or

$$\begin{cases}\sqrt{3};\ 2m\equiv 1,11 \pmod{12},\\ 0;\ 2m\equiv 3,9 \pmod{12},\\ -\sqrt{3};\ 2m\equiv 5,7 \pmod{12},\end{cases}$$

$$\langle m|C_5|-m\rangle=(-1)^l\begin{cases}3;\ m\equiv 0 \pmod 3,\\ 0;\ m\equiv 1,2 \pmod 3,\end{cases}$$

$$\langle m|C_6|-m\rangle=(-1)^l\begin{cases}3;\ m\equiv 0 \pmod 6,\\ 0;\ m\equiv 1,2,4,5 \pmod 6,\\ -3;\ m\equiv 3 \pmod 6,\end{cases}$$

$$\langle m|C_i'|m\rangle=-\langle m|C_i|m\rangle \quad \text{for} \quad i=1,3,4.$$

For $2j$ odd, the $e^{(\mu)}$'s are always diagonal and symmetric with regard to the other diagonal, as we can see from the expressions above. So each two dimensional representation (Kramers-pair) always has the wave functions ψ_m and ψ_{-m}.

The calculation of the characters is found in Bethe (reference 1, pp. 143–46), that for the trigonal (rhombohedral) and tetrahedral group in Opechowski.[4]

IV. EXAMPLES

In this section, we will give some examples, which at the same time give the bases for the different irreducible representations. The latter are also convenient for the case that a given representation occurs several times as discussed in Sec. II.

1. First we deal with the case of the decomposition of an $L=2$ state in a cubical field: ${}^5D_2=\Gamma_3^e+\Gamma_5^e$ in cubical symmetry. Using the value of $\langle m|\frac{1}{2}\pi|m'\rangle$ from the appendix and the formulas of Sec. III(a) we find the matrices C_i. Using these in (2), we have for $\mu=3,5$ (all others give zero matrices)

$$\langle\pm 2|e^{(3)}|\pm 2\rangle=\langle\mp 2|e^{(3)}|\pm 2\rangle=\tfrac{1}{2}; \quad \langle 0|e^{(3)}|0\rangle=1;$$
$$\langle\pm 2|e^{(5)}|\pm 2\rangle=-\langle\mp 2|e^{(5)}|\pm 2\rangle=\tfrac{1}{2};$$
$$\langle\pm 1|e^{(5)}|\pm 1\rangle=1.$$

In this simple case, the state vectors are already orthogonal and only normalization is necessary. Denoting these components by $|\mu,i\rangle$, where i is just a label,

[13] A. Speiser, *Theorie der Gruppen von endlicher Ordnung* (Springer, Berlin, 1927), third edition.

TABLE I. Eulerian angles and values of α and β for the elements of the cubical and hexagonal double group.

Cubical								Hexagonal Set 1: $\beta=0$, $\alpha=\exp(i\pi n/6)$		
No.	Element	$\frac{\psi}{\pi}$	$\frac{\vartheta}{\pi}$	$\frac{\varphi}{\pi}$	α	β	Class	Element		n
1	xyz	0	0	0	1	0	$E(R=-E)$	E	1	0
2,2′	$x\bar{y}\bar{z}$	0	1	0	0	$\pm i$		R	1′	6
3,3′	$\bar{x}y\bar{z}$	1	1	0	0	± 1	C_2	C_2	2,2′	3,9
4,4′	$\bar{x}\bar{y}z$	1	0	0	± 1	0		C_3	3	2
5	xzy	0	$\frac{1}{2}$	0	$1/\sqrt{2}$	$i/\sqrt{2}$			4	10
6	$xy\bar{z}$	$\frac{1}{2}$	$\frac{1}{2}$	$-\frac{1}{2}$	$1/\sqrt{2}$	$1/\sqrt{2}$		C_3'	3′	8
7	$\bar{y}xz$	$\frac{1}{2}$	0	0	$(1+i)/\sqrt{2}$	0	C_3		4′	4
8	$xz\bar{y}$	0	$-\frac{1}{2}$	0	$1/\sqrt{2}$	$-i/\sqrt{2}$	$(C_3'=-C_3)$	C_4	5	1
9	$\bar{z}yx$	$-\frac{1}{2}$	$\frac{1}{2}$	$\frac{1}{2}$	$1/\sqrt{2}$	$-1/\sqrt{2}$			6	11
10	$yz\bar{x}$	$-\frac{1}{2}$	0	0	$(1-i)/\sqrt{2}$	0		C_4'	5′	7
11,11′	$z\bar{z}\bar{y}$	0	$\frac{1}{2}$	1	$\mp i/\sqrt{2}$	$\pm 1/\sqrt{2}$			6′	5
12,12′	$\bar{z}\bar{y}z$	$-\frac{1}{2}$	$\frac{1}{2}$	$-\frac{1}{2}$	$\mp i/\sqrt{2}$	$\pm i/\sqrt{2}$		Set 2: $\alpha=0$, $\beta=\exp(i\pi n/6)$		
13,13′	$\bar{y}z\bar{z}$	$\frac{1}{2}$	1	1	0	$\mp(1-i)/\sqrt{2}$	C_4	Element		n
14,14′	$\bar{z}zy$	0	$-\frac{1}{2}$	1	$\pm i/\sqrt{2}$	$\pm 1/\sqrt{2}$			7,7′	3,9
15,15′	$z\bar{y}x$	$\frac{1}{2}$	$\frac{1}{2}$	$\frac{1}{2}$	$\pm i/\sqrt{2}$	$\pm i/\sqrt{2}$		C_6	8,8′	1,7
16,16′	yxz	$\frac{1}{2}$	1	0	0	$\pm(1+i)/\sqrt{2}$			9,9′	5,11
17	zxy	$\frac{1}{2}$	$\frac{1}{2}$	0	$\frac{1}{2}(1+i)$	$\frac{1}{2}(1+i)$			10,10′	0,6
18	$z\bar{x}\bar{y}$	$\frac{1}{2}$	$\frac{1}{2}$	1	$\frac{1}{2}(1-i)$	$\frac{1}{2}(1-i)$		C_6	11,11′	2,8
19	$\bar{z}x\bar{y}$	$-\frac{1}{2}$	$\frac{1}{2}$	1	$\frac{1}{2}(1+i)$	$-\frac{1}{2}(1+i)$			12,12′	4,10
20	$\bar{z}\bar{z}y$	$-\frac{1}{2}$	$\frac{1}{2}$	0	$\frac{1}{2}(1-i)$	$-\frac{1}{2}(1-i)$	C_3			
21	yzx	0	$-\frac{1}{2}$	$-\frac{1}{2}$	$\frac{1}{2}(1-i)$	$-\frac{1}{2}(1+i)$	$(C_3'=-C_3)$			
22	$\bar{y}\bar{z}x$	1	$-\frac{1}{2}$	$-\frac{1}{2}$	$\frac{1}{2}(1+i)$	$-\frac{1}{2}(1-i)$				
23	$y\bar{z}\bar{z}$	1	$-\frac{1}{2}$	$\frac{1}{2}$	$\frac{1}{2}(1-i)$	$-\frac{1}{2}(1+i)$				
24	$\bar{y}z\bar{z}$	0	$-\frac{1}{2}$	$\frac{1}{2}$	$\frac{1}{2}(1+i)$	$\frac{1}{2}(1-i)$				

we find:

$$|5,1\rangle=(|2\rangle-|-2\rangle)/\sqrt{2},$$
$$|3,1\rangle=(|2\rangle+|-2\rangle)/\sqrt{2}, \quad |5,2\rangle=|1\rangle,$$
$$|3,2\rangle=|0\rangle, \quad |5,3\rangle=|-1\rangle.$$

2. In the case $2j$ odd, we have to mention now that $h=48$ in the case of the cubical double group. We consider ${}^5D_{\frac{1}{2}}={}^2\Gamma_7{}^e+{}^2\Gamma_8{}^e$, giving the "odd" representations apart from ${}^2\Gamma_6$ which is directly known from Table I:

$$\langle\pm 5/2|e^{(7)}|\pm 5/2\rangle=1/6; \quad \langle\pm 3/2|e^{(7)}|\pm 3/2\rangle=5/6;$$
$$\langle\pm 5/2|e^{(7)}|\mp 3/2\rangle=\langle\pm 3/2|e^{(7)}|\mp 5/2\rangle=-\tfrac{1}{6}\sqrt{5};$$
$$\langle\pm 5/2|e^{(8)}|\pm 5/2\rangle=5/6; \quad \langle\pm 3/2|e^{(8)}|\pm 3/2\rangle=1/6;$$
$$\langle\pm 5/2|e^{(8)}|\mp 5/2\rangle=\langle\pm 3/2|e^{(8)}|\mp 5/2\rangle=\tfrac{1}{6}\sqrt{5}.$$

In both cases, we have two state vectors which are dependent in a simple manner on the others. Dropping them, we have only to normalize, with the result

$$|7,1\rangle=(|5/2\rangle-\sqrt{5}|-3/2\rangle)/\sqrt{6};$$
$$|7,2\rangle=(\sqrt{5}|3/2\rangle-|-5/2\rangle)/\sqrt{6};$$
$$|8,1\rangle=(\sqrt{5}|5/2\rangle+|-3/2\rangle)/\sqrt{6};$$
$$|8,2\rangle=(|3/2\rangle+\sqrt{5}|-5/2\rangle)/\sqrt{6};$$
$$|8,3\rangle=|\tfrac{1}{2}\rangle; \quad |8,4\rangle=|-\tfrac{1}{2}\rangle.$$

3. The decomposition ${}^5D_2={}^1\Gamma_1{}^h+{}^2\Gamma_6{}^h+{}^3\Gamma_6{}^h$ in the hexagonal case is relatively simple as

$$\langle 0|e^{(1)}|0\rangle=1; \quad \langle\pm 2|e^{(3)}|\pm 2\rangle=1; \quad \langle\pm 1|e^{(3)}|\pm 1\rangle=1,$$

all others being zero, from which the components of the state vector follow immediately. Off-diagonal elements unequal to zero occur only in $l>2$; if $2j$ is odd, they never occur.

V. INTERNAL INTERACTION

In calculations on two coupled systems (e.g., orbit, electron spin, or nuclear spin) which are allowed only the transformations of a certain symmetry group, one also has to perform a reduction, viz., of the product-representation of the representations induced by the states of each system. In the case of spin-orbit interaction, we deal with $\Gamma_i\times D_j$ (Schlapp and Penney[14]) and in the case of the "mixture" of wave functions of different energy levels with $\Gamma_i\times\Gamma_j$.

In order to calculate the sum of a class:

$$\langle n,m|C_i|n',m'\rangle=\sum_{i=1}^{h_i}\langle m|C_i|m'\rangle\langle n|C_i|n'\rangle, \qquad (6)$$

we need a representation of the symmetry group, which can be generated through an appropriate base by Weyl's method described in Sec. III. In the case of the cubical group, to which we will restrict ourselves in this section, the representations are found in the following way. $\Gamma_1{}^e$ and $\Gamma_2{}^e$ are already given by their characters, $\Gamma_4{}^e$ is the representation we used in the first column of Table I for the labeling of our elements, and $\Gamma_5{}^e$ can be found from it by applying these transformations on yz, xz, xy, or by multiplication of the elements in class i from the representation Γ_4 with $\chi_3{}^e$. A base for Γ_3 is already known from Sec. IV $((\xi^4+\eta^4)/4\sqrt{3}$ and $\frac{1}{2}\xi^2\eta^2)$

[14] R. Schlapp and W. G. Penny, Phys. Rev. 42, 666 (1932).

TABLE II. Decomposition of the representations $\Gamma_i \times \Gamma_{i'}$ and $D_j \times \Gamma_i$ into $\sum_k n_k \Gamma_k$. (k) stands for Γ_k.

(a): $(\Gamma_{i'} \times \Gamma_{j'})$

	Γ_1	Γ_2	Γ_3	Γ_4	Γ_5	Γ_6	Γ_7	Γ_8
Γ_1	(1)	(2)	(3)	(4)	(5)	(6)	(7)	(8)
Γ_2		(1)	(3)	(5)	(4)	(7)	(6)	(8)
Γ_3			(1)+(2)+(3)	(4)+(5)	(4)+(5)	(8)	(8)	(6)+(7)+(8)
Γ_4				(1)+(3)+(4)+(5)	(2)+(3)+(4)+(5)	(6)+(8)	(7)+(8)	(6)+(7)+2(8)
Γ_5					(1)+(3)+(4)+(5)	(7)+(8)	(6)+(8)	(6)+(7)+2(8)
Γ_6						(1)+(4)	(2)+(5)	(3)+(4)+(5)
Γ_7							(1)+(4)	(3)+(4)+(5)
Γ_8								(1)+(2)+(3)+2(4)+2(5)

(b): $(D_j \times \Gamma_{i'})$

	Γ_1	Γ_2	Γ_3	Γ_4	Γ_5	Γ_6	Γ_7	Γ_8
D_0	(1)	(2)	(3)	(4)	(5)	(6)	(7)	(8)
$D_{\frac{1}{2}}$	(6)	(7)	(8)	(6)+(8)	(7)+(8)	(1)+(4)	(2)+(5)	(3)+(4)+(5)
D_1	(4)	(5)	(4)+(5)	(1)+(3)+(4)+(5)	(2)+(3)+(4)+(5)	(6)+(8)	(7)+(8)	(6)+(7)+2(8)
$D_{1\frac{1}{2}}$	(8)	(8)	(6)+(7)+(8)	(6)+(7)+2(8)	(6)+(7)+2(8)	(3)+(4)+(5)	(3)+(4)+(5)	(1)+(2)+(3)+2(4)+2(5)
D_2	(3)+(5)	(3)+(4)	(1)+(2)+(3)+(4)+(5)	(2)+(3)+2(4)+2(5)	(1)+(3)+2(4)+2(5)	(7)+2(8)	(6)+2(8)	2(6)+2(7)+3(8)
$D_{2\frac{1}{2}}$	(7)+(8)	(6)+(8)	(6)+(7)+2(8)	(6)+2(7)+3(8)	(6)+(7)+3(8)	(2)+(3)+(4)+2(5)	(1)+(3)+2(4)+(5)	(1)+(2)+2(3)+3(4)+3(5)
D_3	(2)+(4)+(5)	(1)+(4)+(5)	(3)+2(4)+2(5)	(1)+(2)+2(3)+2(4)+3(5)	(1)+(2)+2(3)+3(4)+2(5)	(6)+2(7)+2(8)	2(6)+(7)+2(8)	2(6)+2(7)+5(8)

which means that they transform like x^2+y^2 and z^2 under the condition $x^2+y^2+z^2=0$. Applying Γ_4 again on the two polynomials, we find easily the 2-dimensional single valued representation. Γ_6 and Γ_8 are identical with $D_{\frac{1}{2}}$ and $D_{1\frac{1}{2}}$ respectively, and Γ_7 is found by multiplying with χ_2.

In the case we deal with $\Gamma_i \times \Gamma_j$, Table II(a) gives the irreducible representations we can expect. The product representation $\Gamma_i \times D_j$ can be deduced from it by replacing D_j by its "components" [Table II(b)].

A simple nontrivial application is the reduction of $\Gamma_3 \times \Gamma_3$. The representation Γ_3 of $\mathfrak{H}$ as mentioned above is

$$E = G_2 = G_3 = G_4 = \begin{pmatrix} 1 & 0 \\ 0 & 1 \end{pmatrix};$$

$$G_5 = G_8 = G_{11} = G_{14} = \begin{pmatrix} 1 & 0 \\ -1 & -1 \end{pmatrix};$$

$$G_6 = G_9 = G_{12} = G_{15} = \begin{pmatrix} -1 & -1 \\ 0 & 1 \end{pmatrix};$$

$$G_7 = G_{10} = G_{13} = G_{16} = \begin{pmatrix} 0 & 1 \\ 1 & 0 \end{pmatrix};$$

$$G_{17} = G_{18} = G_{19} = G_{20} = \begin{pmatrix} -1 & -1 \\ 1 & 0 \end{pmatrix};$$

$$G_{21} = G_{22} = G_{23} = G_{24} = \begin{pmatrix} 0 & 1 \\ -1 & -1 \end{pmatrix}.$$

The three nonzero idempotent elements are:

$$e^{(1)} = \tfrac{1}{6} \begin{pmatrix} 4 & 2 & 2 & 4 \\ -2 & -1 & -1 & -2 \\ -2 & -1 & -1 & -2 \\ 4 & 2 & 2 & 4 \end{pmatrix}; \quad e^{(2)} = \tfrac{1}{2} \begin{pmatrix} 0 & 0 & 0 & 0 \\ 0 & 1 & -1 & 0 \\ 0 & -1 & 1 & 0 \\ 0 & 0 & 0 & 0 \end{pmatrix};$$

$$e^{(3)} = \tfrac{1}{3} \begin{pmatrix} 1 & -1 & -1 & -2 \\ 1 & 2 & 2 & 1 \\ 1 & 2 & 2 & 1 \\ -2 & -1 & -1 & 1 \end{pmatrix}.$$

Using these three matrices as projection operators on

$$\psi_1 = \varphi_1^{(1)} \varphi_1^{(2)}, \qquad \psi_3 = \varphi_2^{(1)} \varphi_1^{(2)},$$
$$\psi_2 = \varphi_1^{(1)} \varphi_2^{(2)}, \qquad \psi_4 = \varphi_2^{(1)} \varphi_2^{(2)},$$

we find 12 linear combinations of ψ_i's of which only 4 are independent. These four can be orthonormalized,[11] with the final result

$$\begin{aligned} &\Gamma_1: \quad (2\psi_1+\psi_2+\psi_3+2\psi_4)/\sqrt{10}, \\ &\Gamma_2: \quad (\psi_2-\psi_3)/\sqrt{2}, \\ &\Gamma_3: \quad \begin{cases} (3\psi_1-\psi_2-\psi_3-2\psi_4)/\sqrt{15}, \\ (\psi_2+\psi_3-\psi_4)/\sqrt{3}. \end{cases} \end{aligned} \tag{7}$$

As no closed formula can be given for the general treatment, other applications may be worked out along the same lines for each case separately.

VI. CONCLUSIONS

A practical advantage of the reduction method outlined is its straightforwardness and the possibility of checking the $e^{(\mu)}$'s in the relations (1). The main point, however, is the knowledge of the wave function from the symmetry only, which makes it possible to state, before other physical arguments are introduced, how many parameters enter the problem.

I would like to express my thanks to Professor J. Korringa for his stimulating discussions and to him and to Dr. T. A. Springer for valuable suggestions, the latter especially with regard to the mathematical part.

This work was a part of the research program of the *Stichting Fundamenteel Onderzoek op het gebied van de Materie* and was made possible by financial support of the *Organisatie voor Zuiver Wetenschappelijk Onderzoek*.

I am also very grateful for the hospitality of the Case Institute of Technology, for the opportunity to finish this work, and for assistance from a National Science Foundation grant at Case. My stay in the U. S. A. was made possible by a Fulbright travel grant.

APPENDIX A

We have to prove the expression (2) has the properties (1). In order to obtain the first relation, we rewrite (2) in the following way, which is merely a rearrangement of the sum

$$e^{(\mu)}=\frac{n_\mu}{h}\sum_{g\in\mathfrak{G}}\chi_\mu(g^{-1})\cdot G$$

$$=\frac{n_\mu}{h}\sum_{f\in\mathfrak{G}}\chi_\mu(f\cdot g)G^{-1}\cdot F^{-1}\quad\text{for}\quad g\in\mathfrak{G}.$$

The product is

$$e^{(\mu)}\cdot e^{(\nu)}=\frac{n_\nu}{h}\sum_{f\in\mathfrak{G}}F^{-1}\left[\frac{n_\mu}{h}\sum_{g\in\mathfrak{G}}\chi_\mu(g^{-1})\chi_\nu(f\cdot g)\right]. \quad \text{(A1)}$$

We will show that the expression in brackets equals $\delta_{\mu\nu}\cdot\chi_\mu(f)$, which allows us to substitute (2).

As the character is a linear function: $\chi(g)+\chi(f)=\chi(g+f)$ and $\chi(ag)=a\chi(g)$, where a is a number, the expression in brackets can be written as

$$\frac{n_\mu}{h}\sum_{g\in\mathfrak{G}}\chi_\mu(g^{-1})\chi_\nu(f\cdot g)=\chi_\nu\left(\frac{n_\mu}{h}\sum_g\chi(g^{-1})\cdot fg\right).$$

The coefficient of f inside the brackets equals $e^{(\mu)}$ so the result is:

$$\chi_\nu(f\cdot e^{(\mu)})=\chi_\mu(f)\delta_{\mu\nu},$$

as we may use the representation after transformation with T, the character being an invariant.

The second property of (1) is easily shown (compare van der Waerden, reference 10, Sec. 128).

$$\sum_\mu e^{(\mu)}=\frac{1}{h}\sum_i C(i)\cdot\sum n_\mu\chi_\mu{}^*(i)$$

$$=\frac{1}{h}\sum_i C(i)\cdot\begin{Bmatrix}h\text{ for }i=1\\0\text{ for }i\neq1\end{Bmatrix}=C(1)=E.$$

APPENDIX B

We want to calculate the following sum

$$\langle m|\tfrac{1}{2}\pi|m'\rangle=\sum_{k=0}^{l+m}(-1)^k\frac{[(j+m)!(j-m)!(j+m')!(j-m')!]^{\frac{1}{2}}}{k!(j+m-k)!(j-m'+k)!(m'-m+k)!}$$

$$=\sqrt{\frac{(j+m')!(j-m')!}{(j+m)!(j-m)!}}\sum_{k=0}^{l+m}(-1)^k\binom{j+m}{k}\binom{j-m}{j-m'-k}. \quad \text{(B1)}$$

TABLE III. Values of $\langle m|\frac{1}{2}\pi|m'\rangle$ for $m>0$ and $m'>0$. The other values can be found by the symmetry relations (B3) and (B4).

$j=\frac{1}{2}$

m \ m'	1
1	1

$j=1$

m \ m'	1	0
1	1	$-\sqrt{2}$
0	$\sqrt{2}$	0

$j=1\frac{1}{2}$

m \ m'	$\frac{3}{2}$	$\frac{1}{2}$
$\frac{3}{2}$	1	$-\sqrt{3}$
$\frac{1}{2}$	$\sqrt{3}$	-1

$j=2$

m \ m'	2	1	0
2	1	-2	$\sqrt{6}$
1	2	-2	0
0	$\sqrt{6}$	0	-2

$j=2\frac{1}{2}$

m \ m'	5/2	3/2	1/2
5/2	1	$-\sqrt{5}$	$\sqrt{10}$
3/2	$\sqrt{5}$	-3	$\sqrt{2}$
1/2	$\sqrt{10}$	$-\sqrt{2}$	-2

$j=3$

m \ m'	3	2	1	0
3	1	$-\sqrt{6}$	$\sqrt{15}$	$-2\sqrt{5}$
2	$\sqrt{6}$	-4	$2\sqrt{5}$	0
1	$\sqrt{15}$	$-2\sqrt{5}$	-1	6
0	$2\sqrt{5}$	0	-6	0

$j=3\frac{1}{2}$

m \ m'	7/2	5/1	3/2	1/2
7/2	1	$-\sqrt{7}$	$\sqrt{21}$	$-\sqrt{35}$
5/2	$\sqrt{7}$	-5	$3\sqrt{3}$	$-\sqrt{5}$
3/2	$\sqrt{21}$	$-3\sqrt{3}$	1	$\frac{3}{5}\sqrt{15}$
1/2	$\sqrt{35}$	$-\sqrt{5}$	$-\frac{3}{5}\sqrt{15}$	3

$j=4$

m \ m'	4	3	2	1	0
4	1	$-2\sqrt{2}$	$2\sqrt{7}$	$-2\sqrt{14}$	$\sqrt{70}$
3	$2\sqrt{2}$	-6	$2\sqrt{14}$	$-2\sqrt{7}$	0
2	$2\sqrt{7}$	$-2\sqrt{14}$	4	$2\sqrt{2}$	$-2\sqrt{10}$
1	$2\sqrt{14}$	$-2\sqrt{7}$	$-2\sqrt{2}$	6	0
6	$\sqrt{70}$	0	$-2\sqrt{10}$	0	6

$j=4\frac{1}{2}$

m \ m'	9/2	7/2	5/2	3/2	1/2
9/2	1	-3	6	$-2\sqrt{21}$	$3\sqrt{14}$
7/2	3	-7	10	$-2\sqrt{21}$	$-\sqrt{14}$
5/2	6	-10	8	0	$-2\sqrt{14}$
3/2	$2\sqrt{21}$	$-2\sqrt{21}$	0	8	$-2\sqrt{6}$
1/2	$3\sqrt{14}$	$\sqrt{14}$	$-2\sqrt{14}$	$2\sqrt{6}$	6

This can be done for the case $m=0$, which occurs only for integral j ($j=l$). From

$$(1+b)^l(1-b)^l=(1-b^2)^l,$$

we get

$$\sum_{k=0}^{l}(-1)^k\binom{l}{k}b^k\sum_{t=0}^{l}\binom{l}{t}b^t=\sum_{u=0}^{l}(-1)^u\binom{l}{u}b^{2u};$$

comparing the coefficient of b^{2u} gives

$$\sum_{k=0}^{l}(-1)^k\binom{l}{k}\binom{l}{2u-k}=(-1)^u\binom{l}{u}. \quad \text{(B2)}$$

So, by putting $2u=l-m'$, we find the summation for $l-m'$ even. If $l-m'$ is odd the sum equals zero, as can be proved from the following symmetry relations:

$$\langle m|\tfrac{1}{2}\pi|m'\rangle=(-1)^{l+m}\langle m|\tfrac{1}{2}\pi|-m'\rangle, \quad \text{(B3)}$$

by replacing k by $l+m-k'$, and

$$\langle m|\tfrac{1}{2}\pi|m'\rangle=(-1)^{m-m'}\langle m'|\tfrac{1}{2}\pi|m\rangle, \quad \text{(B4)}$$

by replacing k by $k''-m'+m$ in the first expression of (B1). In the latter case, we may extend the summation to begin with zero, the extra-terms being zero by definition.

In order to find the result for $m\neq 0$, one can take the coefficients from: $(1+b)^{l+m}\cdot(1-b)^{l-m}=(1-b^2)^{l-m}\cdot(1+b)^{2m}$ if $m>0$, but no expression in closed form has been obtained. The number of elements that actually need to be calculated is further reduced by the following results for the sum in the second expression (B1):

$$m'=j \quad : \quad 1; \quad m'=j-2 : 2m^2-j;$$
$$m'=j-1 : -2m; \quad m'=j-3 : -(2m/3)(2m^2-3j+1).$$

The final results for $j=\frac{1}{2}, \cdots, 4\frac{1}{2}$ are given in Table III. Actually, we only need the matrix elements for which $m=m'+4p$ ($p=0, \pm 1, \pm 2\cdots$).

PHYSICAL REVIEW VOLUME 95, NUMBER 6 SEPTEMBER 15, 1954

Strong Field Induced Paramagnetic Anomaly in $NiSiF_6\cdot 6H_2O$

WARREN E. HENRY
Naval Research Laboratory, Washington, D. C.

(Received May 3, 1954)

A non-Brillouin dependence of the magnetic moment (M) of nickel fluosilicate hexahydrate has been shown from experimental magnetization studies in the temperature (T) range 1.3–4.2°K and in magnetic fields (H) up to 58 000 gauss. A branching of magnetic moment isotherms, when M is plotted against H/T, not only indicates non-Brillouin dependence but also eliminates the possibility of using simple exchange interaction to explain the results. The characteristic pattern of magnetic moment dependence on H/T can be reproduced by the use of energy levels quadratic in the magnetic field, where the coefficient of the quadratic term is about 0.7×10^{-26} erg gauss^{-2}.

MAGNETIZATION of nickel fluosilicate hexahydrate and analysis of the results have been carried out through comparison with simple paramagnetics and with substances exhibiting exchange interaction. Previous investigations[1] have shown that ions in an S-state, whether it be natural, as in the cases of Fe^{+++} and Gd^{+++} or S-state by quenching, as in the case of Cr^{+++}, follow the Brillouin function up to over 99.5 percent saturation in magnetically dilute assemblies.

In the cases of manganous chloride tetrahydrate and manganous bromide tetrahydrate, magnetization up to practical saturation[2] has shown a separation of magnetic moment isotherms at small H/T but a convergence at high H/T. Here exchange interaction is exhibited. A quantitative correlation of moments with H/T has been achieved through the application of Van Vleck's treatment[3] of simple antiferromagnetics in which the departure from Brillouin's function depends on the magnetization.

In the case of nickel fluosilicate hexahydrate, when the magnetization is plotted against H/T (Fig. 1) there is very little separation of magnetic moment isotherms for low values of H/T. However, an anomaly, in the form of a branching at high values of H/T occurs, the percentage separation increasing with H/T. By elimination, it may be concluded that the anomaly is probably associated with the crystalline electric field acting through the medium of a little spin-orbit coupling.

If the energy levels of the Ni^{++} are linear in H, the magnetic moment would be dependent on H/T. Now, energy levels calculated[4] by Ollum and Van Vleck, and by Kambe, for this substance contain nonlinear terms, but these terms involve fractional powers of H with

[1] W. E. Henry, Phys. Rev. **88**, 559 (1952).
[2] W. E. Henry, Phys. Rev. **94**, 1146 (1954).
[3] J. H. Van Vleck, J. phys. radium **12**, 282 (1951).
[4] J. F. Ollum and J. H. Van Vleck, Physica **17**, 205 (1951); K. Kambe (private communication); see also Ishigure, Kambe, and Usui, Physica **17**, 310 (1951).

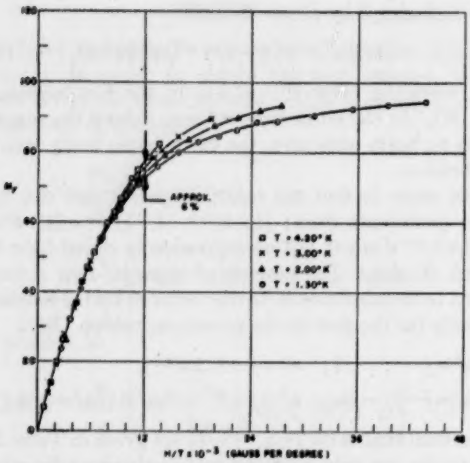

FIG. 1. Plot of relative moment (M_r) against H/T for nickel fluosilicate hexahydrate.

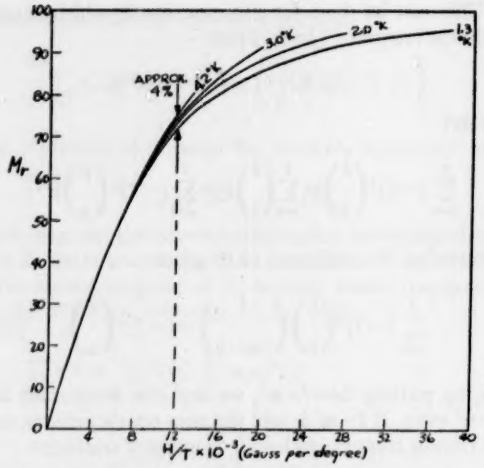

FIG. 2. Calculated magnetic moment curves on quadratic dependence of energy levels on fields.

exponents less than unity. However, the observation of the departure of moment from H/T dependence (Fig. 1) and analysis show not only that there are nonlinear terms in the energy levels but also that there must be terms higher than the first degree. To investigate this, we neglect terms lower than H and put in the first and second powers of H in the energies, as follows:

$$E_{1,3}=\pm(\mu H+CH^2); \quad E_2=0, \tag{1}$$

where μ is the atomic moment, H the magnetic field, and C a constant. If C is set equal to 0.7×10^{-26} erg-gauss^{-2}, one obtains curves of the type shown in Fig. 2. While magnetic moment curves calculated from the energy levels in the usual way give a total separation of about 4 percent at 12 000 gauss per degree as compared with about 6 percent for the experimental curves, it can be seen that through the employment of quadratic terms, the desired character of variation of moment with H/T is obtained. That is, the isotherms branch, they occur in the correct order, and the percentage separation of isotherms increases with H/T.

Published energy levels[4] deduced from crystalline splitting and exchange are inadequate for the high-field range because the total calculated isotherm separation (2 percent at 12 000 gauss per degree) is too small and because the separation is decreasing with H/T. Introduction of a quadratic dependence of energy levels on field as illustrated in Fig. 2, leads to characteristic isotherm branching of an appropriate form. A similar high field anomaly has been observed in $CoSO_4\cdot7H_2O$. Further work is being done.

Hyperfine Structure of Helium-3 in the Metastable Triplet State*†

GABRIEL WEINREICH,‡ *Columbia University, New York, New York*

AND

VERNON W. HUGHES, *University of Pennsylvania, Philadelphia, Pennsylvania*

(Received April 28, 1954)

The He^3 atom in the $^3S_1$ metastable state represents a system simple enough to be calculable by modern computing methods. For this reason a measurement of the hyperfine splitting of this state is of particular interest, since it is expected that a comparison with theory will reveal some effects of relativity, quantum electrodynamics, and nuclear structure.

The measurement reported here was made by the atomic-beam magnetic resonance method. Three cubic centimeters NTP of He^3 gas was continuously circulated and purified in a closed vacuum system. Frequencies of transitions between hyperfine levels were measured in a magnetic field of about $\frac{1}{2}$ gauss, with the final precision limited by inhomogeneity of the magnetic field. The value thus obtained for the (inverted) hfs splitting is 6739.71 ± 0.05 Mc/sec.

The best theoretical value currently available is 6735.9 ± 4.7 Mc/sec, as calculated by Teutsch and Hughes from the six-term Hylleraas function (see following paper). A more informative comparison with theory awaits the calculation of a more accurate electronic wave function.

1. INTRODUCTION

THE present experiment was prompted by the extraordinary fruitfulness of measurements of the hyperfine splitting of the hydrogen isotopes.[1–3] The effects of major significance shown up by those experiment were:

(a) Relativistic effects, of order $(\alpha Z)^2$; these are predicted by the Dirac equation.[4]

(b) Quantum-electrodynamic effects. These include a correction of order α to the magnetic moment of the electron[5] and corrections of order α^2 from polarization and fluctuation energy effects.[6,7] There are also relativistic reduced-mass effects of order $\alpha m/M$ involving photon exchanges between electron and proton.[8]

(c) Effects relating to the finite size of the nucleus and the consequent error of considering it a point dipole.[8–10] The estimated[11] magnitude of the effect of possible proton structure on the hfs of hydrogen is about a part in 10^5. Whereas the experimental determination[3] is considerably better than that, present knowledge of the fundamental physical constants does not allow the calculation of the hydrogen hfs to an accuracy better than a part in 10^5. In deuterium, on the other hand, the nuclear structure effect is of relative order 10^{-4} and has been definitely observed.[3]

Similar effects are to be expected in the case of helium. The relativistic effects have been calculated,[12] and the quantum-electrodynamic effects are expected to be the same as in hydrogen.[7] Thus the nuclear structure effect, which has been estimated[12,14] to be more than a part in 10^4, is directly determined by a measurement of the hfs splitting.

Sessler[12] has calculated this effect in detail and has given numerical values for various assumed nuclear wave functions. These values vary by about 25 percent, depending on the nuclear wave function used. An experimental hfs measurement good to a part in 10^5 would give the nuclear structure effect to about 5 percent and would thus distinguish strongly between the various models of the He^3 nucleus.

The ability to produce and detect a beam of helium atoms in the $^3S_1$ metastable state[15] suggested the measurement of the hyperfine splitting of the He^3 atom in this state by the atomic-beam magnetic resonance method. Such a measurement, to an accuracy somewhat better than 1 part in 10^5, will be described in this paper. The only previous determination was an optical one[16] which yielded the result 0.221 ± 0.005 cm^{-1}, or $\Delta\nu = 6630 \pm 150$ Mc/sec.

The apparatus adapted for this experiment was that used for measurements of the electronic magnetic moment of the metastable triplet state of helium-4,

* Submitted by Gabriel Weinreich in partial fulfillment of the requirements for the degree of Doctor of Philosophy in the Faculty of Pure Science, Columbia University.

† Research supported in part by the Office of Naval Research.

‡ U. S. Atomic Energy Commission Predoctoral Fellow, 1951–1952; now at Bell Telephone Laboratories, Murray Hill, New Jersey.

[1] J. E. Nafe and E. B. Nelson, Phys. Rev. **73**, 718 (1948); Nagel, Julian, and Zacharias, Phys. Rev. **72**, 971 (1947).

[2] E. B. Nelson and J. E. Nafe, Phys. Rev. **75**, 1194 (1949).

[3] A. G. Prodell and P. Kusch, Phys. Rev. **88**, 184 (1952).

[4] G. Breit, Phys. Rev. **35**, 1447 (1930).

[5] J. Schwinger, Phys. Rev. **73**, 416 (1948).

[6] R. Karplus and A. Klein, Phys. Rev. **85**, 972 (1952).

[7] N. M. Kroll and F. Pollock, Phys. Rev. **86**, 876 (1952).

[8] E. E. Salpeter and W. A. Newcomb, Phys. Rev. **87**, 150 (1952).

[9] A. Bohr, Phys. Rev. **73**, 1109 (1948); F. Low, Phys. Rev. **77**, 361 (1950); F. Low and E. E. Salpeter, Phys. Rev. **83**, 478 (1951).

[10] E. N. Adams II, Phys. Rev. **81**, 1 (1951).

[11] H. A. Bethe and C. Longmire, Phys. Rev. **75**, 306 (1949).

[12] A. M. Sessler, Ph.D. dissertation, Columbia, 1953 (unpublished).

[13] V. Hughes and G. Weinreich, Phys. Rev. **91**, 196 (1953).

[14] A. M. Sessler and H. M. Foley, Phys. Rev. **91**, 444 (1953).

[15] Hughes, Tucker, Rhoderick, and Weinreich, Phys. Rev. **91**, 828 (1953).

[16] Fred, Tomkins, Brody, and Hamermesh, Phys. Rev. **82**, 406 (1951).

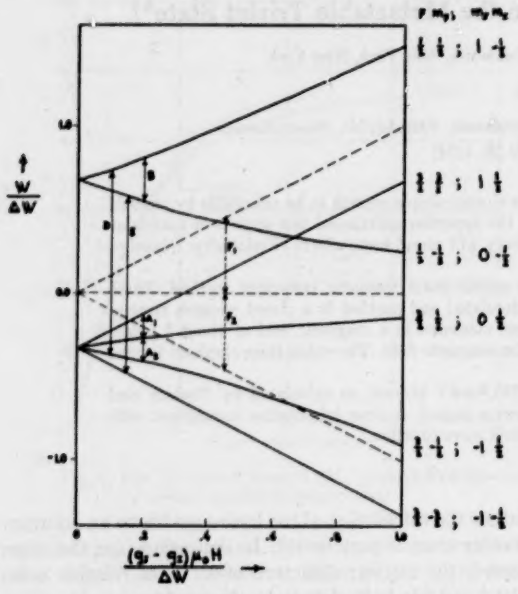

FIG. 1. Sublevels of the $^3S_1$ state in a magnetic field for He^3 and He^4.

and reference is made to the report of that experiment[15] for a description of the vacuum system, magnets, discharge tube beam source, detector, and other major features of the machine. The dimensions of the slits, magnets, and beam have not been changed. Additions to and modifications of the apparatus peculiar to the present experiment, notably a circulation system for continual re-use of the gas and a radio-frequency system for the region of 7000 Mc/sec, are described in later sections of this paper.

Unlike the case of hydrogen, the electronic wave function for helium is not known exactly, and such approximate forms as have been published in the past are much too rough to allow an adequate comparison of the present experiment with theory (see Sec. 7.5). However, it appears that the calculation of such a wave function to the required accuracy is within the possibility of present-day computing techniques.[17]

A preliminary report of the present experiment has been made.[18]

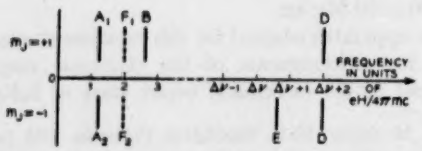

FIG. 2. Low-field transition frequencies in Lorentz units for He^3 and He^4, classified by initial m_J state.

[17] Meyerott, Luke, Clendenin, and Geltman, Phys. Rev. 85, 393 (1952); Luke, Meyerott, and Clendenin, Phys. Rev. 85, 401 (1952); L. H. Thomas (private communication).

[18] Weinreich, Grosof, and Hughes, Phys. Rev. 91, 195 (1953).

2. DESIGN OF THE EXPERIMENT

2.1 Structure of the $^3S_1$ State

The Hamiltonian for the hyperfine energy levels of an atom in a magnetic field is

$$\mathcal{H}=g_J\mu_0\mathbf{J}\cdot\mathbf{H}+g_I\mu_0\mathbf{I}\cdot\mathbf{H}+a\mathbf{I}\cdot\mathbf{J},$$

where $\mathbf{J}\hbar$ and $\mathbf{I}\hbar$ are, respectively, the electronic and nuclear angular momenta, g_J and g_I the corresponding gyromagnetic ratios, μ_0 the Bohr magneton, $\mathbf{H}$ the magnetic field, and a the hyperfine interaction constant.

For the metastable triplet state of helium, J is 1. In the case of helium-4, I is zero and there is no hfs. For helium-3, I has the value $\frac{1}{2}$, and thus at zero magnetic field the level becomes a doublet of energy separation $\Delta W=h\Delta\nu=\frac{3}{4}a$.

The solid lines of Fig. 1 show the further splitting which this level undergoes when subjected to an external magnetic field. Note that, in accordance with the optical data[16] which the present experiment further verified, the hfs is shown as inverted.

The dotted lines of Fig. 1 show the linear Zeeman effect of the corresponding state of helium-4.

Explicit solutions for the energies of the six He^3 sublevels and three He^4 sublevels are listed in Table I.

2.2 Observable Transitions

For an accurate measurement of hyperfine structure it is advantageous to measure transitions at low magnetic field, for then the major part of the energy splitting is due to the hyperfine interaction rather than to the interaction with the external field. The low-field selection rules for induced magnetic dipole transitions are

$$\Delta F=0,\pm1,\quad \Delta m_F=0,\pm1,$$

where $\mathbf{F}=\mathbf{I}+\mathbf{J}$, and m_F is the corresponding magnetic quantum number.

These selection rules allow ten transitions between the six levels. Of the ten, three are unobservable in our apparatus because the associated moment changes in the high A and B fields are too small to cause appreciable defocusing of the beam. Of the remaining seven, two are so-called σ lines, i.e., transitions with $\Delta m_F=0$. These require for their excitation an rf magnetic field parallel to the static field.

It will be seen from the description of the apparatus transition region, given in Sec. 5.1, that σ lines were not observable. Thus we were left with five observable transitions.

Figure 2 indicates these five lines, with low-field frequencies in units of $eH/4\pi mc$ (Lorentz units). Explicit solutions for arbitrary values of field are listed in Table II.

A wire stop was placed in the apparatus (Sec. 5.1) so as to pass either only the $m_J=+1$ or only the $m_J=-1$ atoms selected by the A field. The transitions in Fig. 2 are therefore also classified according to

which initial m_J state is involved. It is seen that for $m_J=+1$ there are two low-frequency transitions and one high-frequency transition, and for $m_J=-1$ there are one low-frequency transition and two high-frequency transitions.

If the hfs were not inverted, the roles of the two m_J states would be reversed; thus not only the magnitude but also the sign of $\Delta\nu$ is determined by the present experiment.

The dotted lines denoted by F_1 and F_2 are the two helium-4 transitions. They were, in fact, observable in our beam since the gas sample used contained about 30 percent helium-4.

2.3 Expected Line Shapes

The usual "natural" line shape for an atomic beam experiment is derived on the assumption that an atom sees the rf field as being suddenly applied and suddenly removed.[19] In our case, however, the atom experiences the rf field by traveling through a resonant cavity; and since the cavity is in its fundamental mode, the amplitude of the rf appears to the atom modulated by a factor $\sin(\pi t/\tau)$, where τ is the transit time through the cavity. Although the "natural" line width will remain of the order of $1/\tau$, an apparatus of sufficient resolving power would reveal a shape somewhat different[20] from that of reference 19.

Such resolving power was not, however, available in our experiment because of magnetic field inhomogeneity. From previous experience with the apparatus,[21] an inhomogeneity at low fields of about $\frac{1}{3}$ gauss was known to exist; using the last column of Table II, we see that this implies widths of about 900 kc/sec and 300 kc/sec for the D and E lines, respectively. The frequency $1/\tau$, on the other hand, when one uses 10^5 cm/sec as a typical velocity and 2.24 cm as the length of the cavity (Sec. 5.1), turns out to be only about 40 kc/sec. Thus the shape of the observed line will be that determined by the inhomogeneity pattern.

TABLE I. Energies of the sublevels of a $^3S_1$ state with $I=\frac{1}{2}$ (He^3) and $I=0$ (He^4) as a function of magnetic field. Energies W are given in units of ΔW, the (inverted) hyperfine splitting at zero field; $x=(g_J-g_I)\mu_0 H/\Delta W$, $y=g_I\mu_0 H/\Delta W$.

I	F, m_F	m_J, m_I	$W/\Delta W$
$\frac{1}{2}$	$\frac{1}{2}, \frac{1}{2}$	$1, \frac{1}{2}$	$-\frac{1}{4}(1-3x)+\frac{1}{2}y$
	$\frac{1}{2}, \frac{1}{2}$	$0, \frac{1}{2}$	$\frac{1}{4}(1+3x)-\frac{1}{4}[(1+3x)^2+8]^{\frac{1}{2}}+\frac{1}{4}y$
	$\frac{3}{2}, \frac{1}{2}$	$0, \frac{1}{2}$	$\frac{1}{4}(1-3x)-\frac{1}{4}[(1-3x)^2+8]^{\frac{1}{2}}-\frac{1}{4}y$
	$\frac{3}{2}, -\frac{1}{2}$	$-1, -\frac{1}{2}$	$-\frac{1}{4}(1+3x)-\frac{1}{4}y$
	$\frac{1}{2}, -\frac{1}{2}$	$1, -\frac{1}{2}$	$\frac{1}{4}(1+3x)+\frac{1}{4}[(1+3x)^2+8]^{\frac{1}{2}}+\frac{1}{4}y$
	$\frac{1}{2}, -\frac{1}{2}$	$0, -\frac{1}{2}$	$\frac{1}{4}(1-3x)+\frac{1}{4}[(1-3x)^2+8]^{\frac{1}{2}}-\frac{1}{4}y$
0		1	$x+y$
		0	0
		-1	$-x-y$

2.4 Radio-Frequency Power Required

The rf power required for inducing the high-frequency transitions can be estimated by the approximate requirement that the line width due to power broadening equal the line width caused by the field inhomogeneity. This requirement can be expressed as

$$\frac{1}{\hbar}g_J\mu_0(|J_x|)H_{rf}=\frac{\partial f}{\partial H}\cdot\Delta H,$$

where $(|J_x|)$ is the matrix element of J_x for the transition, f is the frequency of the transition, H_{rf} is the rf magnetic field, and ΔH the field inhomogeneity. When the appropriate numbers are substituted, the above equation becomes

$$\frac{H_{rf}}{\Delta H}\cong\begin{cases}3 \text{ for } D \text{ line}\\ 0.6 \text{ for } E \text{ line}\end{cases}.$$

On the other hand, using appropriate values for the Q and volume of the cavity (see Sec. 5.1) and an appropriate frequency, we find the power required for maintaining a given rf magnetic field in the cavity to be

$$\text{Power in milliwatts}\cong 2000(H_{rf})^2 \quad (H_{rf} \text{ in gauss}).$$

TABLE II. Frequencies of transitions between Zeeman levels of a $^3S_1$ state with $I=\frac{1}{2}$ (He^3) and $I=0$ (He^4) as a function of magnetic field. Frequencies ν are given in units of $\Delta\nu$, the hyperfine splitting at zero field; $x=(g_J-g_I)\mu_0 H/h\Delta\nu$, $y=g_I\mu_0 H/h\Delta\nu$.

I	Name	Transition	$\nu/\Delta\nu$	Approx. field-dep. at low fields, (Mc/sec)/gauss
$\frac{1}{2}$		$(F,m_F)\leftrightarrow(F',m_F')$		
	A_1	$\frac{1}{2}, \frac{1}{2}\leftrightarrow\frac{3}{2}, \frac{1}{2}$	$-\frac{1}{4}(1-x)+\frac{1}{2}[(1+3x)^2+8]^{\frac{1}{2}}+y$	1.9
	A_2	$\frac{1}{2}, \frac{1}{2}\leftrightarrow\frac{3}{2}, -\frac{1}{2}$	$x-\frac{1}{4}[(1+3x)^2+8]^{\frac{1}{2}}+\frac{1}{2}[(1-3x)^2+8]^{\frac{1}{2}}+y$	1.9
	B	$\frac{1}{2}, \frac{1}{2}\leftrightarrow\frac{1}{2}, -\frac{1}{2}$	$x+\frac{1}{4}[(1+3x)^2+8]^{\frac{1}{2}}-\frac{1}{2}[(1-3x)^2+8]^{\frac{1}{2}}+y$	3.7
	D	$\frac{1}{2}, \frac{1}{2}\leftrightarrow\frac{3}{2}, -\frac{1}{2}$	$x+\frac{1}{4}[(1+3x)^2+8]^{\frac{1}{2}}+\frac{1}{2}[(1-3x)^2+8]^{\frac{1}{2}}+y$	2.8
	E	$\frac{1}{2}, -\frac{1}{2}\leftrightarrow\frac{3}{2}, -\frac{1}{2}$	$\frac{1}{2}(1+x)+\frac{1}{2}[(1-3x)^2+8]^{\frac{1}{2}}+y$	0.93
0		$(m_J)\leftrightarrow(m_J')$		
	F_1	$1\leftrightarrow 0$	$x+y$	2.8
	F_2	$-1\leftrightarrow 0$	$x+y$	2.8

[19] I. I. Rabi, Phys. Rev. **51**, 652 (1937).
[20] See R. T. Daly, Jr. and J. R. Zacharias, Phys. Rev. **91**, 476 (1953).
[21] Weinreich, Tucker, and Hughes, Phys. Rev. **87**, 229 (1952).

With $\Delta H = \frac{1}{2}$ gauss, this then means

$$\text{Required power} \cong \begin{cases} 2000 \text{ milliwatts for } D \text{ line} \\ 80 \text{ milliwatts for } E \text{ line} \end{cases}.$$

The Sperry 2K44 klystron used in this experiment, is rated at 250 milliwatts; it is thus seen that, while one can hope to saturate the E line, the D line is bound to be only weakly excited.

2.5 Gas Purity Required[22]

The helium atoms in the discharge tube are excited to the metastable state by collision with electrons and return to the ground state primarily by collision with the walls. In our discharge tube, the average distance from a wall was $\sim$3 mm, and the pressure was such that the mean free path of an atom was $\sim$0.3 mm.

The presence in the discharge tube of impurity atoms adds another mechanism for the quenching of metastables. If we assume that a metastable atom is always quenched by collision with an impurity atom, our criterion for maximum allowable impurity concentration should be that within its mean lifetime a metastable atom does not collide with an impurity atom.

The expected number of collisions with other atoms which a given atom makes in diffusing a distance a is $(a/\lambda)^2$, where λ is the mean free path. Using $a=3$ mm, $\lambda=0.3$ mm, we find $(a/\lambda)^2=100$; and for none of the atoms collided with to be foreign atoms, we must have

$$\text{Maximum impurity fraction} \cong 10^{-2}.$$

The above calculation indicates (in agreement with observed facts) that a few percent of impurity atoms are sufficient to lower the metastable concentration very appreciably.

3. APPARATUS: GAS HANDLING SYSTEM

A total of 3 cc NTP of He^3 was available to us; we designed the gas handling system to work with half of that amount. The system, whose functions can be divided into circulation, storage, and purification, is diagrammed in Fig. 3.

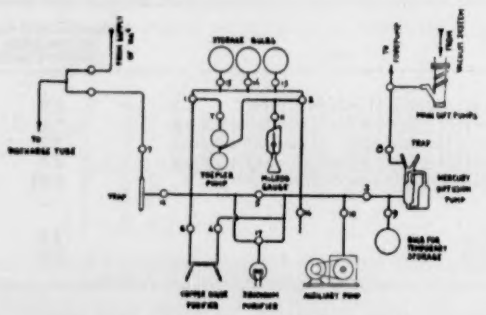

FIG. 3. Gas handling system for helium 3.

[22] See also Appendix I of reference 15.

3.1 Circulation and Storage

Circulation is effected by means of the mercury diffusion pump, which is a type GHG-15 made by Distillation Products, Inc. This pump removes the gas as it comes out of the main diffusion pumps and pumps it back into the discharge tube. The pressure in the return line varies from about 1.5 mm at the output of the mercury pump to a few tenths of a millimeter in the discharge tube. Liquid-nitrogen traps precede and follow the return path.

Alternative connections, labeled "from supply of He^4" and "to forepump" in the figure, were used when no recirculation was required, in particular when a helium-4 beam was run for the purpose of making adjustments on the machine.

Two completely separated storage spaces were available as shown. This was necessary in order to be able to let air into any one part of the system without running into the stored gas. Air had to be admitted for various purposes such as cleaning and greasing stopcocks, changing purifier material, minor glassblowing changes, and admitting and removing the gas.

The Toepler pump had a capacity of 500 cc. The McLeod gauge, with two ranges calibrated from 0.5 micron to 1.8 mm, was connected into the input arm of the Toepler pump.

3.2 Purification by Zirconium

During the planning stage, four substances were considered which would not be trapped on the liquid nitrogen traps and would thus contaminate the gas. These were nitrogen, oxygen, hydrogen, and methane. The first two were expected to present the major problem, since some leakage in the apparatus, notably in the metal system, is unavoidable, and air would thus continually be added to the circulating gas.

Zirconium was chosen as the purifying agent, since at a temperature of about 1300°C it combines with both oxygen and nitrogen, and at about 600°C it adsorbs hydrogen. The purifier was simply a glass bulb with a ground joint and two metal seals supporting a zirconium filament. It could be connected to the system and the impurities allowed to diffuse and combine (see Fig. 3).

It was thought originally that since hydrogen and methane, unlike oxygen and nitrogen, cannot leak into the system, contamination by these gases would present a minor problem at most.

3.3 Purification by Electrodes

The first test of the purification system was made with a sample of helium-4. It was planned to circulate it without purification in order to determine the length of time that it is possible to do so, and then to attempt to purify it. The size of the metastable beam was to be taken as an operational criterion of purity.

The surprising result of this test was that after about five hours of running no decrease in the beam was

observable; in fact, the beam had become somewhat larger. Considering that the idle leak-up rate in the system was of the order of 1 micron/hour and that the volume of the system was about 50 liters, one finds that 10^{-3} mm/hr$\times$50 l$\times$5 hr$=$0.25 mm-l of air should have accumulated during the above run, which amounts to about 20 percent of the total gas. That this amount of contamination (which would have been sufficient to have a strong effect on the color of the discharge, and considerably more than is required to quench the metastable beam) was not, in fact, observed showed that some unplanned but very efficient purifying mechanism was in operation.

This mechanism turned out to be the phenomenon known as "cathode cleanup": the cathode of the discharge tube, which was made of aluminum, was absorbing and/or combining chemically with the impurities. The process was so efficient that, as long as the discharge was on, all the air leakage into the system was continuously and automatically taken care of.

3.4 Purification by Copper Oxide

After twenty or thirty hours of running with He^3, the gas began to show symptoms of severe contamination. First, the metastable beam began to disappear; later the discharge began to take on a pronounced foreign color, and the total amount of gas, as measured by the McLeod gauge, showed a definite increase. Since the original tests with helium-4 indicated that all the impurities introduced in normal operation were removed by the electrodes, it was at first suspected that their cleanup mechanism had for some reason ceased to operate. Changing the cathode, however, produced no improvement.

A spectroscopic observation of the discharge showed the presence of hydrogen. Apparently the cathode was not very efficient in cleaning out this gas, if, indeed, it cleaned it out at all.

The source of this hydrogen, and the reason why it did not show up in the helium-4 trial runs, was not exhaustively investigated; however, two sources can be definitely identified.

(1) Whenever a new cathode was installed, it was first operated with helium-4. During the first five minutes or so the discharge was strongly blue, and the spectrum showed the hydrogen lines as well as a wealth of band structure This was presumably due to organic matter being removed from the cathode surface. With time, the foreign colorations disappeared; if, however, a slow evolution of such matter continued, it would accumulate and show up as contamination after some time.

(2) The other known source of hydrogen was the zirconium purifier. When operating at the high temperatures required for oxygen and nitrogen removal, it dissociated the traces of organic vapors evolved by the vacuum grease.

An electrically heated quartz U-tube of 10-mm o.d. was then filled with CuO and installed in the position shown in Fig. 3 so that, with stopcock No. 5 closed, the gas would pass through it in the course of circulation. The action of the CuO is to oxidize the hydrogen to water (methane to water and carbon dioxide), the product being frozen out on the traps. It was important never to heat the quartz to a high enough temperature to cause devitrification, for it was found that when the quartz became devitrified the purifier would give off hydrogen instead of removing it. At about 550°C, this purifier gave satisfactory service.

4. APPARATUS: DISCHARGE TUBE

In order to be able to work with a minimum amount of gas, it was considered necessary to make all volumes in the system as small as possible. In particular, this applied to the two bulbs around the discharge tube electrodes. The remainder of the discharge tube was the same as that described in reference 15.

The effects of cathode deterioration described below were of special importance in the present experiment because of the limited amount of available gas.

4.1 Anode

Since relatively little heating of the anode occurs in a glow discharge, there was no particular problem in making it reasonably small. It consisted of an aluminum disk $1\frac{1}{2}$ inches in diameter and $\frac{1}{8}$ inch thick, supported by a $\frac{1}{4}$-inch diameter threaded Kovar rod.

4.2 Cathode: Construction

The construction of the water-cooled cathode is shown in Fig. 4. Except for the smaller bulb, it is similar to that used in our previous experiments.

4.3 Cathode: Sputtering

In the experiments on helium-4,[15] the major cathode difficulty was that of sputtering. For a long time (say 30 hr) after a new electrode had been installed, no sputtering was seen. It would then suddenly start at a very rapid rate, so that the change from no visible sputtered film to a film too thick to show interference fringes took place sometimes in the order of minutes.

A few hours after the sputtering had begun, effects detrimental to the operation of the experiment began to appear. The minimum pressure at which a discharge could be maintained rose rapidly. The discharge would go out and, when re-ignited, would glow in quite a different mode, the electrode voltage being about 4000 volts instead of the usual 2500 or so. The power supply was not capable of supplying the customary 100 ma at this voltage, so that the yield of metastables became very low; but even if it had been so capable, the cathode dissipation would probably have been excessive. By

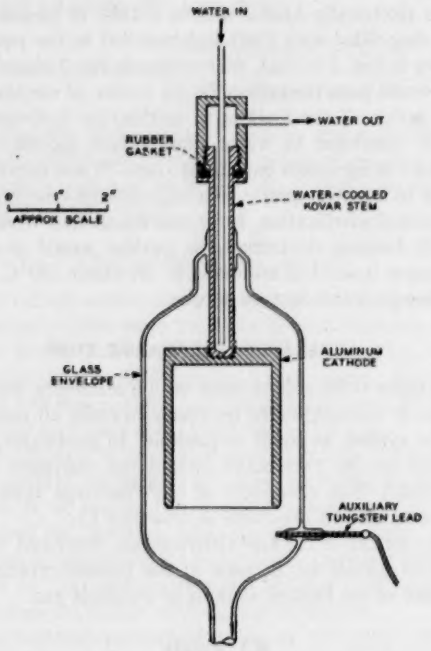

FIG. 4. Construction of cathode. The function of the "auxiliary tungsten lead" is discussed in Sec. 4.3.

increasing the gas pressure in the tube, a discontinuous transition to the usual mode could sometimes be effected; at this point, however, the pressure was so high that an adequate vacuum could not be maintained in the main chamber. In the case of helium-3, the more basic limitation due to the available amount of gas applied.

An explanation of the presence of the high-voltage mode was proposed in terms of the film of sputtered metal acting as a floating electrode. The discharge was thought to break up into two discharges in series, *viz.*, one from cathode to sputtered film, the other from sputtered film to anode. The presence of two cathode falls would qualitatively explain the higher total voltage.

To test this hypothesis, a tungsten lead was sealed into the glass at the point where the sputtered film was expected to appear, with the idea of shorting out one of the two discharges by connecting this lead to the main cathode (Fig. 4). This test gave some support to the two-discharge hypothesis. It was found that when the sputtered film became heavy, connecting the tungsten to the cathode did, in fact, return the discharge to its "normal" mode.

4.4 Cathode: Gas Absorption

The above method of avoiding the ill effects of sputtering did not, however, prove useful, for a more serious problem arose: the "cleanup," or absorption, by the cathode of the helium itself.[23–25] That such a process was taking place was unfortunately not realized in the beginning; thus, about 1 cc NTP of helium-3 was lost.

After the loss had been discovered, frequent checks of gas pressure were made in order to determine how and when the gas was disappearing. It was found that the gas pressure remained constant until the cathode had started to sputter. Some minutes later, the pressure suddenly started to drop at a rate corresponding to the loss of about 0.01 mm-l/min. The discharge was then immediately shut off and the run terminated.

Removing the electrode, scraping off a surface layer, and removing the sputtered film from the glass restored the system to its former nonabsorbing state. In order to prolong the possible running time, two identical electrodes were blown onto the tube. When the first one began to absorb, its electrical lead was disconnected and the second one placed in operation.

It was found that after repeated scrapings the useful life of the cathodes decreased, and the absorption began before any visible sputtering. Finally, a state was reached where scraping did no good at all: the cathode began to absorb as soon as it was placed in operation. Both cathodes were then replaced by new ones; these behaved properly. It thus seems that the absorption process depends on some sort of surface condition which, upon continued exposure, penetrates the body of the material.

There was no obvious relation observed between the purity of the helium and the amount of absorption. On the other hand, no sputtering was ever observed except in fairly pure helium.

5. APPARATUS: RF SYSTEM

5.1 "Hairpin" Design and Construction

The "hairpin," or assembly for impressing rf magnetic fields on the beam, is diagrammed in Fig. 5. It consists of two parts: a rectangular cavity with a fundamental resonant frequency in the vicinity of 7000 Mc/sec, and a loop of copper sheet, $\frac{1}{4}$ in. long along the beam, and terminated in a U-shaped foot near the cavity exit slit. The function of the loop was twofold: it could be used as a source of rf magnetic fields of relatively low frequency (0–1000 Mc/sec); it could also act, due to the placement of the foot, as a monitor of oscillations in the cavity.

The wire stop, also shown in Fig. 5, served to intercept the ultraviolet light from the discharge tube but pass the (deflected) atomic beam. Depending on the placement of the wire, either the $m_J=+1$ or the $m_J=-1$ component could be passed.

Figure 6 shows a cross section, as seen along the

[23] H. Alterthum, Lompe, and Seeliger, Z. tech. Phys. **17**, 407 (1936).
[24] H. Alterthum and A. Lompe, Z. tech. Phys. **19**, 113 (1938).
[25] M. J. Reddan and G. F. Rouse, Trans. Am. Inst. Elec. Engrs. **70**, 1924 (1951).

beam, of the cavity and mounting. The rf was brought in through a coaxial vacuum seal taken from a burned-out Sperry klystron (another such seal was used for connecting to the copper loop). The cavity was attached by six screws to a silver-plated block which contained a tapered coaxial line ending in a small loop which excited the cavity.

Since the gap of the C magnet was $\frac{1}{4}$ in., while the wavelength of the relevant radiation was about seven times that, it was not possible to design a cavity which would have a magnetic field component parallel to the static field. This is the reason why, as mentioned in Sec. 2.2, σ lines were not observable.

As pointed out in Sec. 2.2 (see Fig. 2), the high-frequency resonances observable in the beam, namely the lines D and E, have the frequency $\Delta\nu$ at zero magnetic field and both increase in frequency with an applied magnetic field. In order to be sure of finding the lines, it was therefore necessary to construct the cavity to a frequency high enough so that one could be sure that it was higher than $\Delta\nu$. The previously known optical determination[16] was $\Delta\nu=6630\pm150$ Mc/sec; the cavity was therefore build to have a frequency of 6850 Mc/sec. The inside dimensions of the cavity were 10.0 cm high$\times$2.24 cm long$\times$0.43 cm wide, and it had a Q somewhat greater than 1000.

After a high-frequency line had been observed at this frequency (method 2 of Sec. 6.2 below), it was required to lower the frequency of the cavity to the neighborhood of $\Delta\nu$ (method 3 of Sec. 6.3 below). This was accomplished by placing a strip of Teflon inside the cavity. The strip was of such dimensions as to jam fairly tightly against the sides of the cavity. By moving the Teflon into regions of weaker or stronger rf electric field, one could vary the effective capacitance of the cavity and thus its resonant frequency. It was thus fairly easy to tune it to the required 6740 Mc/sec.

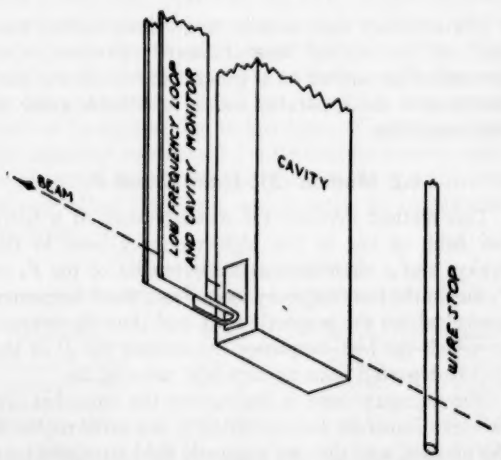

FIG. 5. Arrangement of transition region ("hairpin" assembly).

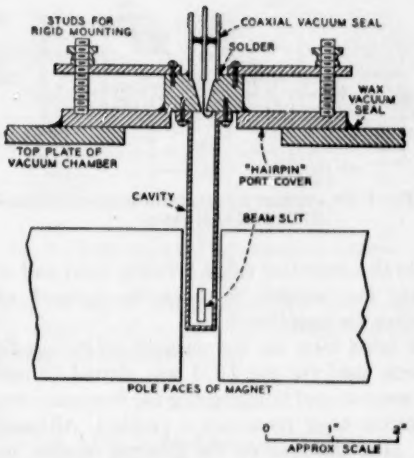

FIG. 6. Construction of cavity and mounting.

The Q of the cavity was not noticeably affected by the introduction of the Teflon.

In tuning the cavity, it was necessary to take into account the change in resonant frequency which occurs upon application of vacuum due to the nonzero dielectric susceptibility of air.

5.2 Radiofrequency Sources

For observing low-frequency resonances, a precision signal generator (General Radio type 805-C) was used up to 50 Mc/sec; a butterfly oscillator (General Radio type 857-A) from 90 to 350 Mc/sec; and a coaxial line lighthouse tube oscillator (radar jammer, APT-5/T-85) from 350 Mc/sec to 1000 Mc/sec.

The source of high-frequency power was a Sperry 2K44 klystron. The klystron was submerged in an oil bath, operated from a regulated power supply, and stabilized against a harmonic of the frequency standard by an automatic frequency control circuit.

5.3 Klystron Automatic Frequency Control

The automatic frequency control circuit was built on the general pattern of that of Lee and Dayhoff.[26] The beat frequency of, say, 50 Mc/sec produced between the klystron and the harmonic of the Columbia frequency standard was fed into an FM receiver (Hallicrafter type S-36). The output of the receiver discriminator was amplified by a dc amplifier and placed on the repeller of the klystron so as to provide negative feedback against frequency changes.

The dc amplifier, of which a circuit diagram is shown in Fig. 7, employed a General Electric 2B23 magnetic amplifier tube, which is a Hull magnetron[27] operating near cutoff. This kind of amplifier has the advantage

[26] C. A. Lee *et al.*, Phys. Rev. **91**, 1403 (1953). E. S. Dayhoff, Rev. Sci. Instr. **22**, 1025 (1951).
[27] A. W. Hull, Phys. Rev. **18**, 31 (1921).

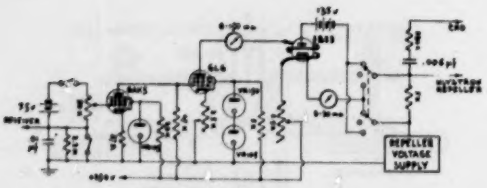

FIG. 7. Dc amplifier for automatic frequency control of 2K44 klystron.

that no dc connection exists between input and output, so that the repeller bias can be changed without adjusting the amplifier.[26]

The brass form for the solenoid which supplied the magnetic field for the 2B23 was slotted to minimize eddy currents and thus improve the frequency response.

Receiver noise presented a problem. Although this noise, as it appeared on the klystron repeller, was cut by a factor of about 20 when the feedback loop was completed, it was still sufficient to increase the band width of the klystron to about 500 kc/sec. It was therefore found necessary to sacrifice frequency response of the amplifier in favor of the decrease in noise obtained by smaller amplifier band width.

An *RC* filter with a time constant of 0.005 sec, placed on the grid of the first dc amplifier stage, cut the noise to a point where the klystron band width was some 15 kc/sec—as good as would be required for this experiment. The price paid for this was that the klystron would jump out of control on a very rapid voltage fluctuation. This was instantly recognizable by a large increase in repeller noise, as seen on a cathode-ray oscilloscope, and by the disappearance of the signal on the receiver *S* meter. Such rapid fluctuations did not occur very often and thus did not present a major problem.

5.4 Measurement of Frequency

Klystron frequencies were measured by tuning in another receiver (National type HRO-50) to the beat of the klystron with another harmonic of the standard. This beat was compared with the output of a crystal-calibrated variable frequency oscillator (General Radio Heterodyne Frequency Meter type 620-A) which was coupled into the same receiver.

It was not possible to use one receiver for both automatic frequency control and frequency measurement, since the signal from the frequency meter would interfere with the automatic frequency control action.

5.5 Cabling and Connections

Figure 8 shows a block diagram of the complete rf system. In order to conserve rf power, the output of the klystron was fed directly into the cavity through a length of RG-9/U cable. The cable from the copper pickup loop came out into a coaxial switch. For observing low-frequency resonances, the switch was connected to the appropriate low-frequency oscillator. For rough tuning of the klystron to the cavity frequency, the switch was connected, through a matching stub, to a crystal and dc meter and the loop thus used as a cavity oscillation monitor. For measurement and automatic frequency control, a third switch position led, again through a matching stub, to a mixer crystal where the signal picked up by the loop was mixed with the frequency standard harmonics. The mixed signal then passed into both receivers through a 100-Mc/sec low-pass filter.

6. METHODS OF MEASURING $\Delta\nu$

At least four methods are available for finding $\Delta\nu$ from measurement of transition frequencies. The first three are progressively more difficult and correspondingly more accurate. The fourth, the most accurate of all, requires an apparatus somewhat different from ours. At some future date, when theoretical advances make it interesting to know a more accurate value for $\Delta\nu$, a modification of the apparatus might be warranted which would make this fourth method possible.

6.1 Method (1): Lines A_1 and F_1

The ratio of the frequencies of transitions A_1 and F_1 (see Table II) at low fields is equal to

$$\tfrac{2}{3}+g_I/3g_J.$$

As the field is increased, however, the frequency A_1 begins to depart from its linear dependence on field, and from the amount of this departure $\Delta\nu$ may be calculated. This method is easy to apply, since one knows at what approximate frequencies to look for these transitions; but it is rather inaccurate, since it depends on the measurement of a small departure from a linear law.

At a field of about 150 gauss, this method was applied, yielding

$$\Delta\nu = 6754 \pm 50 \text{ Mc/sec.}$$

The accuracy here is only three times better than that of the optical measurement;[16] however, this determination served as a general check on the performance of the apparatus and as a valuable guide to later searching.

6.2 Method (2): Lines D and F_1

This method involves the measurement, at a fairly low field, of one of the high-frequency lines in the cavity, and a simultaneous measurement of the F_1 or F_2 line in the low-frequency loop. From the F frequency one calculates the magnetic field, and thus the amount by which the high-frequency line (either the D or the E) has departed from its zero-field value of $\Delta\nu$.

The accuracy here is limited by the fact that the two transitions are not occurring in the same region of the magnet, and the two magnetic field strengths may differ by as much as $\frac{1}{2}$ gauss.[21]

With the cavity tuned to 6850 Mc/sec, a high-frequency line was located by a systematic search. This was identified as the D line by the relative field-dependence of it and the F line. Measurement of both then yielded the result

$$\Delta\nu = 6739 \pm 2 \text{ Mc/sec.}$$

6.3 Method (3): Lines E and D

It can be seen from Fig. 2 that the D and E lines both have the frequency $\Delta\nu$ at zero field. It is not practicable to make atomic beam resonance measurements at zero field because of the loss of space quantization. The Q of the cavity was, however, low enough so that the two lines could be resolved by a small magnetic field ($\sim\frac{3}{4}$ gauss) and still both be within the cavity response, provided that the central frequency of the cavity was correctly adjusted.

In this method, the separation of the lines effectively gives the magnetic-field intensity; after it is known $\Delta\nu$ can be calculated from either frequency. Since both transitions occur in the same region of the magnetic field, the accuracy is limited only by line widths.

This method was the one used in the final measurements.

6.4 Method (4): σ Line

This method, potentially the most accurate one, could not be applied on our apparatus because of the inobservability of σ lines (see Sec. 5.1).

The method depends on the fact that one of the σ lines, *viz.*, the transition $(F, m_F) = (\frac{3}{2}, -\frac{1}{2})$ to $(\frac{1}{2}, -\frac{1}{2})$, has a minimum when the magnetic-field parameter x has a value of $\frac{1}{3}$ (see Fig. 1). This corresponds to a field of about 800 gauss, and the minimum frequency attained by this transition is exactly $\frac{3}{4}\sqrt{2}$ times $\Delta\nu$.

Because of the existence of this minimum, this particular transition is not strongly dependent on the field in this region, and the line width would be determined by the time that an atom spends in the transition region, i.e., the so-called "natural" line width. This width could be very much less than the width observed in our experiment. Since the correction that would need to be applied due to the field not having exactly the intensity necessary for minimum frequency would be of second order, a relatively inaccurate measurement of any other transition would serve to supply this correction.

TABLE III. Summary of data.

Date of observation	D-line, Mc/sec	E-line, Mc/sec	$\Delta\nu$, Mc/sec
February 7, 1953	6741.53	6740.33	6739.73
February 7, 1953	6741.87	6740.42	6739.70
March 7, 1953	6741.50	6740.33	6739.75
March 21, 1953	6741.06	6740.13	6739.67
Mean			6739.71

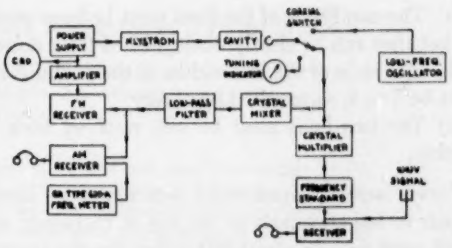

FIG. 8. Block diagram of radiofrequency system.

In order to apply this method, one would need to install a magnet with a gap of 3 or 4 cm and capable of supplying the requisite field.

7. RESULTS

7.1 Line Intensities and Widths

Under good conditions, the E line appeared as a galvanometer deflection of $\sim$7 cm, while the D line was barely more than 1 cm (a 1-cm deflection corresponds to a detector current of about 10^{-15} amp). This relative intensity is in accord with the considerations of Sec. 2.4.

The observed line widths were about $\frac{1}{3}$ Mc/sec for the E line and about 1 Mc/sec for the D line. This, too, agreed with expectations (Sec. 2.3).

7.2 Survey of Data

The result quoted in this paper is an average of four independent measurements (Table III). The range of magnetic fields covered by this data is approximately $\frac{1}{4}$ gauss, as large as could be conveniently encompassed by the response width of the cavity.

The reason why only four runs yielded reliable data, although considerably more than four attempts at obtaining data were made, is primarily the following. At the end of each run, the gas was returned to the storage space by use of the Toepler pump (Sec. 3.1). This operation took about 30 minutes, and any air which leaked into the system during this period was collected together with the helium, since the discharge was off and no purifying action was taking place (Sec. 3.3).

Thus each new run was begun with considerably contaminated helium and no data could be collected before the gas had purified sufficiently. Unfortunately, the time that elapsed during this purification also brought the cathode closer to its "poisoned," or absorbing, condition (Sec. 4.4). In many cases poisoning was reached before sufficient purification or very soon thereafter, and in such a case the run had to be terminated immediately.

7.3 Processing of Data

Three criteria were applied in accepting a given run as significant:

(a) The amplitude of the lines must be large enough so that they can be clearly distinguished from noise.

(b) The ratio of the line widths of the D and E lines must be 3 to 1, as required by theory.

(c) The two lines must be well resolved from one another.

Curves were obtained which represented an average of four to ten traversals of the line in frequency steps which were usually about 100 kc/sec for the (narrow) E line and 300 kc/sec for the (broad) D line; a sample curve, showing both lines, is shown in Fig. 9. The peaks of these curves were determined visually. No significant difference was obtained by three workers performing this determination independently.

7.4 Estimate of Error

The estimate of error quoted here is made on the basis of (a) the probable reliability of determining the peak of a line ($\sim\frac{1}{10}$ of the line width) and (b) the standard deviation of the group of four measurements (0.015 Mc/sec). On this basis, we quote for our final result:

$$\Delta\nu = 6739.71 \pm 0.05 \text{ Mc/sec.}$$

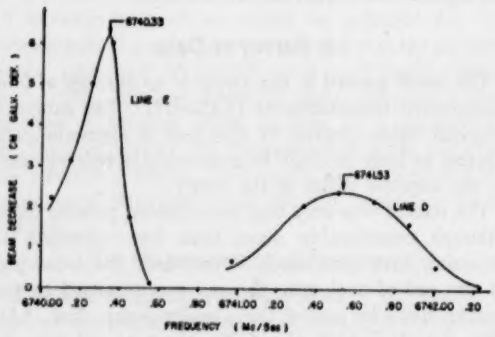

FIG. 9. Data of February 7, 1953, showing the two high-frequency resonances.

7.5 Comparison with Theory

As was pointed out in Sec. 1, the $^3S_1$ wave function for helium is not at present known with sufficient accuracy to make possible a precise calculation of $\Delta\nu$. Nevertheless, it may be of interest to compare our experimental value with such theoretical data as is today available.

Teutsch and Hughes[28] have calculated $\Delta\nu$ for this atomic state using a number of different published electronic wave functions and the value of the He^3 nuclear magnetic moment obtained by Anderson.[29] They have also obtained an estimate of maximum error by comparing the energy eigenvalue give by the particular wave function with the spectroscopically observed energy value.

The most reliable estimate they have obtained is the one from the six-term Hylleraas function. After correcting for reduced mass and for the anomalous electron moment, they obtain

$$\Delta\nu_{\text{theor}} = 6735.9 \pm 4.7 \text{ Mc/sec.}$$

Comparison of this number with the experimental value of the preceding section shows an encouraging agreement; however, the calculation is limited in accuracy by the wave function and necessarily misses all the fine points enumerated in Sec. 1. We are therefore gratified to learn that both Thomas[30] and Luke[31] are at present engaged in calculating a wave function with a precision adequate for a detailed interpretation of our experimental measurement.

8. ACKNOWLEDGMENTS

We wish to thank Professor I. I. Rabi for encouragement and stimulating discussions. Professor T. I. Taylor supplied us with useful advice on purifying methods. Mr. Gerard M. Grosof was of very considerable help in running the apparatus. We are grateful to Mr. Karl Schumann for some masterful glassblowing.

[28] W. R. Teutsch and V. W. Hughes, following paper [Phys. Rev. 94, 1461 (1954)].
[29] H. L. Anderson, Phys. Rev. 76, 1460 (1949).
[30] L. H. Thomas (private communication).
[31] P. J. Luke, quoted in reference 14.

Hyperfine Structure of Helium-3 in the Metastable Triplet State

WERNER B. TEUTSCH* AND VERNON W. HUGHES
University of Pennsylvania, Philadelphia, Pennsylvania
(Received April 29, 1954)

The hyperfine structure splitting in the metastable $^3S_1$ state of He^3 has been measured recently by the atomic beam magnetic resonance method. The Fermi value of the hfs splitting in this state is computed here using various available wave functions, including the six-term Hylleraas function of Huang. An error estimate for the hfs calculation can be made from a knowledge of the accuracy of the calculated binding energy. In all cases, the actual discrepancy between the computed value of the hfs and the experimental result is consistent with the estimated inaccuracy. In particular, the Hylleraas function yields a value of the negative binding energy of $0.087600\times 4/hcR_{He^4}$ (experimental value $0.087618\times 4/hcR_{He^4}$), and hence gives the hfs to about 0.1 percent. Thus the anomalous magnetic moment of the electron should be taken into account. The calculated result, including the order α anomalous moment of the electron and the order m/M reduced mass correction, is 6735.9 ± 4.7 Mc/sec as compared to the experimental value of 6739.71 ± 0.05 Mc/sec. Relativistic, higher order quantum electrodynamic, and nuclear structure effects are somewhat smaller than the uncertainty in our calculation.

THE hyperfine structure splitting in the metastable triplet state of He^3 has been measured recently by Weinreich and Hughes to 7 ppm.[1,2] Theoretical knowledge of this quantity is limited by the present knowledge of the electronic eigenfunction for this state. It is the purpose of this note to summarize the results obtained by using various approximate eigenfunctions given in the literature, the best of which, a six-term Hylleraas function,[3] yields the hfs to about 1 part in 10^3.

The hyperfine structure due to two electrons in s states can be written as a simple extension of Fermi's formula[4,5] for the one electron problem. In the case of one electron in an s state, the magnetic hyperfine interaction gives rise to two levels separated by an energy ΔW, given by Fermi[4] as

$$\Delta W=\frac{8\pi}{3}\frac{2I+1}{I}\mu\mu_0|\psi(0)|^2,$$

where I is the spin of the nucleus in units of $\hbar$, μ is the magnetic moment of the nucleus in absolute units, μ_0 is the Bohr magneton (approximately the spin magnetic moment of the electron), and $\psi(\mathbf{r})$ is the normalized Schroedinger wave function for the state in question. For the metastable $^3S_1$ state of helium the total angular momentum quantum number of the two electrons is $J=1$ and for He^3 the nuclear spin is $I=\frac{1}{2}$. Two hyperfine levels result and are separated by an energy given by a similar formula, differing only in the replacements of

$$\frac{2I+1}{I} \text{ by } \frac{2J+1}{J},$$

and[6]

$$4\pi a_0^3|\psi(0)|^2 \text{ by } 4\pi a_0^3\left[\int_{\tau_1}|\Psi(\mathbf{r}_1,0)|^2d\tau_1+\int_{\tau_2}|\Psi(0,\mathbf{r}_2)|^2d\tau_2\right]\equiv D(0),$$

where $\Psi(\mathbf{r}_1,\mathbf{r}_2)$ is the normalized two-electron wave function, and a_0 is the radius of the first Bohr orbit in hydrogen. The energy separation in frequency units is

$$\nu=\Delta W/h=FD(0)$$

with

$$F=\frac{2}{3}\frac{2J+1}{J}\frac{\mu\mu_0}{ha_0^3}=\frac{1}{3}\frac{2J+1}{J}\frac{\mu}{\mu_0}\alpha^2cR_\infty=202.990 \text{ Mc/sec},$$

where α is the fine structure constant, R_∞ is the Rydberg for an infinitely heavy nucleus and c is the velocity of light. The quantity μ/μ_0 is obtained by combining Anderson's result[7] for the ratio of the He^3 magnetic moment to the proton magnetic moment, with the ratio of the Bohr magneton to the proton moment. For the latter value as well as the other atomic constants, Dumond and Cohen's 1952 values[8] have been used. A correction of 60 ppm[9] is made for the diamagnetic shielding in He^3.

Various approximate wave functions have been employed to calculate the dimensionless quantity $D(0)$. Table I lists the value of $D(0)$ and ν together with the binding energy obtained from each wave function, as well as the estimated and actual accuracy of the calculated hfs frequency. The accuracy of the calcula-

* National Science Foundation Pre-doctoral Fellow.

[1] G. Weinreich and V. W. Hughes preceding paper [Phys. Rev. **94**, 1451 (1954)]. Weinreich, Grosof, and Hughes, Phys. Rev. **91**, 195 (1953).

[2] Fred, Tomkins, Brody, and Hamermesh, Phys. Rev. **82**, 406 (1951), obtained the hfs to about 2 percent using optical methods, in agreement with their rough calculations.

[3] Su-Shu Huang, Astrophys. J. **108**, 354 (1948).

[4] E. Fermi, Z. Physik **60**, 320 (1930).

[5] G. Breit and F. W. Doermann, Phys. Rev. **36**, 1732 (1930).

[6] In the notation of Breit and Doermann,

$$D(0)=4\pi a_0^3|\varphi_{1s}^{(Z)}(0)|^2(1+\epsilon)=32(1+\epsilon)$$

for helium.

[7] H. L. Anderson, Phys. Rev. **76**, 1460 (1949).

[8] J. W. M. DuMond and E. R. Cohen, Revs. Modern Phys. **25**, 691 (1953).

[9] E. Hylleraas and S. Skavlem, Phys. Rev. **79**, 117 (1950).

TABLE I. The frequency of the hyperfine structure splitting in the metastable triplet state of He^3 as computed from various approximate wave functions for that state.

Wave function[a]	$-E$[b] (Units of $4hcR_{He^4}$)	$D(0)$[c]	ν[d] (Mc/sec)	$\frac{\nu_{cal}-\nu_{exp}}{\nu_{exp}}$ (%)	Estimated accuracy of ν_{cal} (%)
$\varphi_{1s}^{(2)}(r_1)$ only[e]		32.0	6496		
$\varphi_{1s}^{(2)}(r_1)\varphi_{2s}^{(1)}(r_2)$[e]		32.5	6597		
Hartree $\psi_1(r_1)\psi_2(r_2)$[e,f]		32.977	6694		
$\varphi_{1s}^{(2.61)}(r_1)\varphi_{2s}^{(1.44)}(r_2)-\varphi_{2s}^{(1.44)}(r_1)\varphi_{1s}^{(2.61)}(r_2)$[g,h]	0.0819	32.9	6678	−0.9	1.2
$\sum_{n=2}^{6} a_n[\varphi_{1s}^{(2)}(r_1)\varphi_{ns}^{(2)}(r_2)-\varphi_{ns}^{(2)}(r_1)\varphi_{1s}^{(2)}(r_2)]$[g,i]	0.0859	33.36	6772	0.5	0.7
$2kse^{-2kt}\sinh(2ckt)$[g,j]	0.0855	32.29	6555	−2.7	0.8
$[2ks+c_2(2kt)^2]e^{-2kt}\sinh(2ckt)$[g,j]	0.0871	33.28	6756	0.2	0.4
Six-term Hylleraas function[k]	0.087600	33.1630	6731.8	−0.12	0.07
Anomalous moment $\alpha/2\pi$			7.8		
Reduced mass $-3m/M_{He^4}$			−3.7		
Six-term Hylleraas function with corrections			6735.9	−0.06	
Experimental results	0.087618[l]		6739.71[m]		

[a] The following notation has been used: $\varphi_{ns}^{(Z)}$ is the hydrogenic wave function for the s state with principal quantum number n in the field of nuclear charge Z. The Hylleraas variables s, t, and u ($s=r_1+r_2$, $t=-r_1+r_2$, $u=r_{12}$) are in units of a_0.
[b] E is the binding energy. The zero of energy is chosen as the ground state of the singly ionized atom.
[c] See text.
[d] Frequency of hyperfine structure splitting.
[e] The error estimate is not applicable to these non-symmetrized functions.
[f] W. S. Wilson and R. B. Lindsay, Phys. Rev. 47, 681 (1935), give $r_1\psi_1$ and $r_2\psi_2$. The values for $\psi_1(0)$ and $\psi_2(0)$ were obtained by A. M. Sessler (private communication).
[g] These functions are not normalized as given.
[h] See reference 10.
[i] W. Perl and V. W. Hughes, Phys. Rev. 91, 842 (1953). $a_2=1$, $a_3=-0.523$, $a_4=-0.090$, $a_5=-0.052$, $a_6=-0.049$.
[j] See reference 11. Results taken from Breit and Doermann's value for $1+\epsilon$. For the one-term function $k=0.6870$, $c=0.60$; for the two-term function $k=0.6521$, $c=4/9$, $c_2=0.1$.
[k] Su-Shu Huang, reference 3, gives $\Psi(r_1,r_2)=\frac{1}{2}C[e^{-ar_1-br_2}(c_1+c_2us+c_3ut+c_4us+c_5u^2us+c_6u^2ut)-e^{-br_1-ar_2}(c_1+c_2us-c_3ut+c_4us+c_5u^2us-c_6u^2ut)]$. $C=0.16346$, $a=2.704$, $a=2.096$, $b=0.6085$, $c_1=1$, $c_2=-0.2865$, $c_3=-0.2842$, $c_4=-0.07978$, $c_5=-0.007053$, $c_6=0.011718$.
[l] National Bureau of Standards Circular 467, Atomic energy levels (U. S. Government Printing Office, Washington, D. C., 1949).
[m] See G. Weinreich and V. W. Hughes, reference 1.

tion of $D(0)$ from any particular wave function was related to the discrepancy of the binding energy as calculated with that wave function by the method of Eckart[10] as used by Breit and Doermann.[5] This indicates

$$\frac{\Delta\nu}{\nu}=\frac{\Delta D(0)}{D(0)}\cong 2\frac{\langle\Psi_1|H'|\Psi_0\rangle}{\langle\Psi_0|H'|\Psi_0\rangle}\left(\frac{E-E_0}{E_1-E_0}\right)^{\frac{1}{2}},$$

where $\Delta\nu$ and $\Delta D(0)$ are the maximum uncertainty in ν and $D(0)$, H' stands for the hfs interaction operator, Ψ_0 and Ψ_1 are the wave functions for the $1s2s$ and $1s3s$ triplet states, E_0 and E_1 being the corresponding binding energies, and E is the binding energy as calculated with the approximate wave function in question. Using

$$\Psi_0\cong\frac{1}{\sqrt{2}}[\varphi_{1s}^{(2)}(r_1)\varphi_{2s}^{(1)}(r_2)-\varphi_{2s}^{(1)}(r_1)\varphi_{1s}^{(2)}(r_2)],$$

$$\Psi_1\cong\frac{1}{\sqrt{2}}[\varphi_{1s}^{(2)}(r_1)\varphi_{3s}^{(1)}(r_2)-\varphi_{2s}^{(1)}(r_1)\varphi_{1s}^{(2)}(r_2)],$$

where $\varphi_{ns}^{(Z)}$ is the hydrogenic wave function for the s state with principal quantum number n in the field of nuclear charge Z, and noting that

$$E_1-E_0=0.05334hcR_{He^4},$$

we get

$$\Delta\nu/\nu\cong\tfrac{1}{6}(\Delta E)^{\frac{1}{2}},$$

where ΔE is the difference between calculated and observed binding energy in units of $4hcR_{He^4}$. It should be noted that while the hfs splitting is computed for He^3, the wave functions are tested by using the binding energy they yield for He^4. In obtaining ΔE, such effects as nuclear motion and relativity should be included, if pertinent. Thus the bulk of the reduced mass correction has been taken into account by using R_{He^4},[11] but the α^2Z^2 relativistic contribution[12] to the binding energy of the second electron has been omitted. The latter changes E by a factor of $1+5\alpha^2Z_{eff}^2/16\cong 1+3\times10^{-5}$, which is too small to change ΔE appreciably for any wave function considered here. It should be remarked that while in principle the maximum uncertainty in the calculated frequency could be determined, the above result must be considered as a crude estimate of this uncertainty, mainly because of the approximate nature of the Ψ_0 and Ψ_1 used. It is then seen that for the various wave functions used, the actual discrepancy between the computed value and the experimental result is consistent with this estimated inaccuracy. Comparison should not be made until effects omitted by the simple Fermi theory and of the order of magnitude of the estimated error or larger have been included in the calculation. Thus, in the case of the six-term Hylleraas

[10] C. Eckart, Phys. Rev. 36, 878 (1930).

[11] E. A. Hylleraas, Z. Physik 54, 347 (1929).

[12] Luke, Meyerott, and Clendenin, Phys. Rev. 85, 401 (1952). See particularly p. 407. A more careful calculation following the prescription of J. Sucher and H. M. Foley (to be published) yields a result not inconsistent with this rough estimate.

function, the order α anomalous magnetic moment[13] and the order m/M reduced mass correction[14] have been taken into account by a factor

$$\left(1+\frac{\alpha}{2\pi}\right)\left(1+\frac{m}{M}\right)^{-3}\cong 1+\frac{\alpha}{2\pi}-3\frac{m}{M}.$$

[13] J. Schwinger, Phys. Rev. **73**, 416 (1948).
[14] G. Breit and R. E. Meyerott, Phys. Rev. **72**, 1023 (1947).

Relativistic,[15,16] higher-order quantum-electrodynamic,[17] and nuclear structure[16,18] effects are estimated to make contributions of the order of 1 part in 10^4, so that their inclusion in this calculation is not warranted.

[15] G. Breit, Phys. Rev. **35**, 1447 (1930).
[16] A. M. Sessler and H. M. Foley (to be published); abstract in Phys. Rev. **91**, 444 (1953).
[17] N. M. Kroll and F. Pollock, Phys. Rev. **86**, 876 (1952).
[18] V. W. Hughes and G. Weinreich, Phys. Rev. **91**, 196 (1953).

PHYSICAL REVIEW VOLUME 95, NUMBER 6 SEPTEMBER 15, 1954

Precision Wavelength and Isotopic Shift Measurements of Germanium Arc Lines*

G. V. Deverall, K. W. Meissner, and G. J. Zissis
Physics Department, Purdue University, Lafayette, Indiana
(Received June 9, 1954)

The employment of an atomic beam light source and of interferometric equipment made it possible to obtain information about the line structure and precision wavelength of eight Ge I lines arising from transitions between the lowest even and odd energy levels of germanium. Despite the high resolving power employed, it was impossible to observe line splittings. By comparing the total width of the lines with that expected from the beam data one can estimate that the isotope shift between consecutive even Ge isotopes is smaller than 0.005 cm^{-1}. The wavelength of the center of gravity of the different lines however, could be determined within ± 0.00004 A. This limit of error is in agreement with the wave number deviations obtained by the application of the Ritz combination principle.

INTRODUCTION

THE present investigation was undertaken in order to obtain information about the isotopic shift of germanium lines by means of an atomic beam light source. Previous investigations of this spectrum by use of liquid air cooled Schüler lamps showed that the isotope shift must be smaller than the line width obtained with this light source.[1] The only source which permits a sufficient reduction of the line width is the atomic beam source. The appreciable amount of pure germanium which was available from the Purdue University solid state group made it possible to employ this method.

The experiments were conducted in such a way that the spectrograms obtained could be used also for precision wavelength measurements. These were desirable in connection with recent investigations of the Ge I spectrum carried out in this laboratory.[2]

I. Experimental Methods and Equipment

A. Atomic Beam Light Source

1. General assembly.—The atomic beam light source used in this investigation is a modified version of the atomic beam used by Mundie and Meissner,[3] by Meissner, Mundie, and Stelson,[4] and later by Deverall, Meissner, and Zissis[5] for work with magnesium, lithium, and indium, respectively. Figure 1 shows a schematic view of the general assembly. The germanium was evaporated from a graphite crucible, and the resulting vapor was collimated into a beam by the small aperture at the top of the upper furnace jacket. The beam was bombarded with electrons from two grid-filament assemblies and then condensed on the bottom of the liquid air container. The beam was viewed through a fused quartz window at the front of the upper vacuum chamber called "can" in the figure. A careful adjustment of the spectrograph is necessary to insure that the optic axis of the collimator passes through the center of the bombarded section of the beam and is perpendicular to the beam axis.

Large pump openings and high-speed pumps are essential in an atomic beam source. The upper and lower chambers are evacuated by two separate systems each consisting of a Distillation Products Inc. MC 275 diffusion pump and a fore pump. The pumping speed obtained was about 550 liter/sec at a pressure of 10^{-6} mm Hg.

2. Grid filament assemblies.—The grid filament assemblies are shown in place in Fig. 1. The grid consists of water-cooled nickel tubes and the filament of two strips of platinum foil covered with emission coating and supported by tungsten power leads sealed through

* Supported in part by the U. S. office of Naval Research.
[1] L. Sibaya, Current Sci. (India) **6**, 152 (1937); Hack Arroe, *Studier over Spektralliniers Struktur* (Kopenhagen, 1951).
[2] K. L. Andrew and K. W. Meissner, Phys. Rev. **85**, 716 (1952).
[3] L. G. Mundie and K. W. Meissner, Phys. Rev. **65**, 265 (1944).
[4] Meissner, Mundie, and Stelson, Phys. Rev. **74**, 932 (1948).
[5] Deverall, Meissner, and Zissis, Phys. Rev. **91**, 297 (1953).

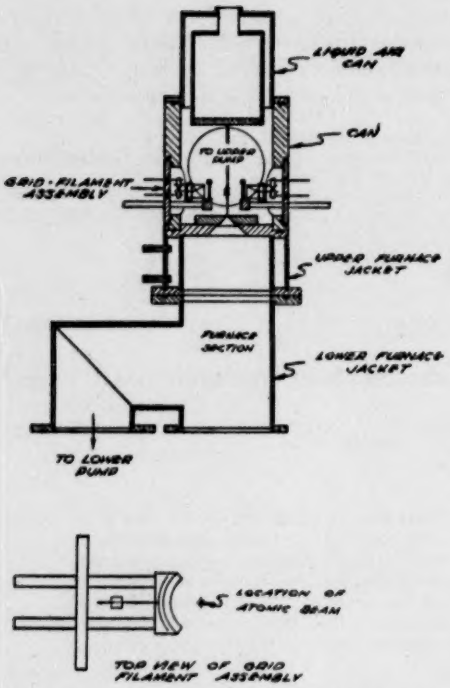

FIG. 1. Schematic drawing of the atomic beam light source.

a uranium glass press. To attach the platinum foil to the leads, the tungsten is first cleaned with sodium nitrite and then narrow strips of nickel foil are tacked to the front edges of the tungsten wires where the platinum filament strips are to be connected. The platinum foil is then wrapped once around the tungsten wire and spot-welded to it through the nickel foil. This technique results in good electrical contact and prevents the sputtering of the nickel in the vacuum.

3. Furnace.—The operating temperature necessary for a satisfactory germanium beam was about 1600°C. To attain this temperature a special graphite furnace was developed.[6] The design of this furnace was such that it produced a negligible magnetic field in the beam region in spite of the large operating currents used.

The graphite furnace containing a graphite crucible is shown in Fig. 2. This furnace permits operation at temperatures up to 1800°C. The heating section is a hollow graphite cylinder with a wall thickness of about 1 mm through which currents up to 500 amperes are passed. The conical form of the top part permits the upper water cooled power connection to be large and also assists in maintaining a favorable temperature distribution. The solid bottom part is provided with a screw thread for mounting.

The graphite crucible is suspended in the heating section from its conical flange. Short circuiting of the heating section is prevented by a narrow centering ridge. The crucible has a graphite lid containing an axial opening of about 1.5 mm diameter which acts as the beam source (oven aperture).

The graphite furnace is mounted in a support, Fig. 3, consisting in principle of two coaxial cylindrical tubes which serve both as current leads and as supports. The threaded bottom section of the furnace is screwed into the central copper cylinder. The rim of the conical section is clamped by the top flange of the outer cylinder which is split vertically on one side to permit tightening by means of a brass screw. The upper and lower connections to the furnace are cooled by circulating tap water and the water tubes leading to the lower connection serve as power leads. In order to prevent the furnace from being broken by mechanical and thermal stresses, the mechanical support of the lower part is furnished by a sylphon bellows shown in the figure.

The outer cylinder is at ground potential and is hard soldered to the brass base plate. The inner conductor is insulated from the outer one by Teflon sleeves on the fastening screws and a "linear o-ring" gasket which seals the joint between the base plate and the small flange to which the sylphon is soldered.

B. Spectroscopic Instruments

1. UV spectrograph.—The spectrograph used for this investigation was a Universal Steinheil Spectrograph. In order to make it applicable for interferometric work in the region between 2000 A and 11 000 A, it was equipped with quartz-fluorite optics. The collimator and camera lenses consisted of especially designed symmetric quartz-fluorite achromates of 750-mm focal length and free apertures of 60 mm and 65 mm, respectively. The lenses were designed and made by the Perkin-Elmer Corporation, Norwich, Connecticut and met all the desired specifications. With a calcium

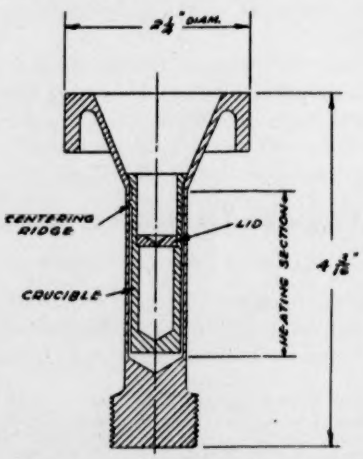

FIG. 2. Graphite furnace and crucible.

[6] H. Kopfermann and G. Wessel, Z. Physik. **130**, 100 (1951). This problem was discussed with G. Wessel during his visit at Purdue.

fluoride prism as dispersing element a practically plane focal surface was obtained. The materials used for the optical parts were Homosil fused quartz and synthetic calcium fluoride. The spectrograph was mounted on a special table which minimized vibration and permitted the spectrograph to be precisely aligned so that the axis of the collimator was perpendicular to the atomic beam.

2. Interferometer.—A Perot-Fabry interferometer was used to obtain the high resolution required for this investigation. It was mounted in parallel light between the collimator and the prism and was contained in a temperature and pressure controlled housing. This was provided with plane quartz windows which were sufficiently inclined to the axis of the interferometer to throw secondary images out of the principal spectrum. The temperature was maintained within $\pm 0.1°C$ during the time required for exposures. The interferometer consisted of crystalline quartz plates cut perpendicular to the optic axis and hollow cylindrical invar spacers, provided with three small flat projections at each end. This type of spacer has proved to be the most satisfactory of the various designs and has the added advantage that two or three spacers can be put together in series to form the various longer spacers required. Thus, a relatively small number of spacers can be combined to form a spacer of practically any length. Our experience with such combined spacers shows that the etalon thickness can be held constant during ten-hour exposures. The spring loading devices used to hold the quartz plates in contact with the spacers and to make the final adjustment for parallelism were orginally described by Hansen.[7] These springs were made of Elinvar to assure that the adjustment of the interferometer would not change with temperature.

Two sets of quartz plates were used during this investigation. The first pair was coated with aluminum to a reflectivity of 85 percent in green light. The second pair had a reflectivity of 92 percent in green light and was used only for the photographs taken with the 173-mm spacer. This second pair was kindly loaned by Professor M. Czerny, Physikalisches Institut der Universität Frankfurt Main.

3. Comparator and Densitometer.—The final analysis of the photographic plates was made from readings taken with a Zeiss Abbe comparator and from densitometer traces made with a Leeds and Northrup densitometer.

4. Standard.—The wavelengths were measured with respect to the Hg^{198} 5460 A line as standard. The standard source was a water cooled Hg^{198} Megger's Electrodeless Discharge Tube loaned by the National Bureau of Standards; the tube was excited by means of a 250-Mc oscillator.

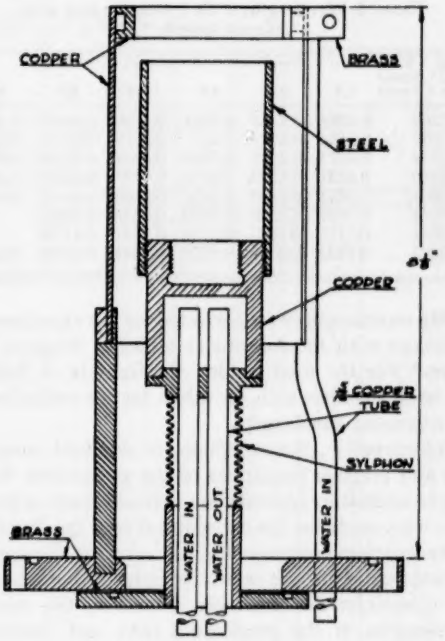

FIG. 3. Graphite furnace support.

II. Wavelength Measurements

A. Method of Evaluation

The method of evaluation was based upon the fundamental relation pertaining to the Perot-Fabry interferometer,

$$(p_x+\epsilon_x)=(p_s+\epsilon_s)=2t,$$

where $(p_x+\epsilon_x)$ and $(p_s+\epsilon_s)$ are the order numbers of the centers of the interference fringes of an unknown and a standard line of wavelengths λ_x and λ_s, respectively. The fractional order numbers, ϵ_x and ϵ_s, can be obtained from measurements of the diameters of the interference rings.

Plates taken with 1.2-, 2.0-, 4.9-, 6.0-, 6.4-, and 12.4-cm spacers were measured during the investigation. Since the patterns obtained with the 6.0- and 12.4-cm spacers were intended to be used for the final determination of the wavelengths they were separately measured with great care by each of the three authors.

In every case, the innermost eight fringes, if this many appeared, were used to obtain the fractional order number ϵ by the method of least squares.

For the preliminary determination of the etalon thickness the wavelength values of Burns and Adams[8] for the Hg^{198} lines were used. Since this spectrum extends over a large range of wavelengths the corrections due to the deviation of the actual air condition from standard air conditions cannot be neglected. Therefore,

[7] G. Hansen, Naturwiss. 15, 163 (1927).

[8] K. Burns and K. B. Adams, J. Opt. Soc. Am. 42, 56 (1952).

TABLE I. Wavelengths of Ge I lines obtained with different spacers.

Wavelength A \ Spacer t cm	1.2	2.0	4.9	6.4	6.0	12.4
3269	0.4885	0.4888	0.4885	0.4890	0.48887	0.48886
3039	0.0664	0.0673	0.0671	0.0673	0.06717	0.06712
2754	0.5871	0.5879	0.5879	0.5878	0.58788	0.58781
2709	0.6231	0.6239	0.6236	0.6237	0.62378	0.62372
2691	0.3403	0.3410	0.3408	0.3408	0.34112	0.34105
2651	0.5676	0.5683	0.5682	0.5678	0.56838	...
2651	0.1711	0.1717	0.1718	0.1721	0.17205	...
2592	0.5333	0.5339	0.5339	0.5341	0.53406	0.53402

the Hg wavelengths were corrected for the experimental conditions with the convenient tables of Meggers and Peters.[9] For the final results, the formula of Edlén[10] was used, together with his tables for the reduction of air to vacuum wavelengths.

Unfortunately, the corrections to standard temperature and pressure conditions of the germanium wavelengths ultimately obtained are in doubt since no provisions were made for the determination of the humidity in the interferometer housing, and since at the present no exact values of the refractive index of humid air in the ultraviolet are available. However, the relative wavelengths of the germanium lines and, therefore, the values of the levels, will be affected very little. In principle, the difficulty arising from air conditions could easily be overcome by evacuating the entire pressure tight housing of the interferometer and by direct determination of vacuum wavelengths and wave numbers.

C. Results

1. Wavelengths values.—The great variation in the wavelengths given by earlier investigators made it impossible unambiguously to determine the exact integer order number for large spacers. Therefore, the spectrogram obtained with the smallest spacer, 1.2 cm, was evaluated first. For this spacer the spectral range $\langle\Delta\lambda\rangle=\lambda^2/2t$ has values ranging from 0.0444 A at 3269 A to 0.0279 A at 2592 A and thus the wavelength values of the MIT tables,[11] and those independently measured during another investigation in this laboratory, were sufficiently accurate for obtaining the integer order numbers p of the germanium lines after the correct thickness t had been determined by means of mercury lines. Employing further the fractional order numbers ϵ, wavelengths of the germanium lines were obtained which were much more reliable than the grating values. The wavelength values resulting from the 1.2-cm spacer were then used to obtain the correct integer order numbers for the larger spacers. Since the spectral range decreases with increasing spacer thickness, the unknown wavelength has to be known within a few thousandths of an angstrom in order to find the correct integer order when working with the longest spacers employed. The smallest spectral range used in the present investigation for wavelength measurements was 0.0027 A for $\lambda=2592$ A and $t=12.4$ cm.

TABLE II. Final wavelength values wave numbers, and combinations.

Wavelength	Wave number	Combination
3269.48886	30 577.0065	$4p^2\,{}^1D_2-5s\,{}^3P_1^\circ$
3039.06712	32 895.2615	$4p^2\,{}^1D_2-5s\,{}^1P_1^\circ$
2754.58781	36 292.3447	$4p^2\,{}^3P_2-5s\,{}^3P_1^\circ$
2709.62372	36 894.5552	$4p^2\,{}^3P_1-5s\,{}^3P_0^\circ$
2691.34105	37 145.1713	$4p^2\,{}^3P_1-5s\,{}^3P_1^\circ$
2651.56833	37 702.3054	$4p^2\,{}^3P_0-5s\,{}^3P_1^\circ$
2651.17201	37 707.9412	$4p^2\,{}^3P_2-5s\,{}^3P_2^\circ$
2592.53402	38 560.7682	$4p^2\,{}^3P_1-5s\,{}^3P_2^\circ$

TABLE III. Low-energy levels of Ge I.

Config.	Design.	Level sep.	Present work	AEL[a]
$4s^24p^2$	$4p^2\,{}^3P_0$		0.0000	0.00
	$4p^2\,{}^3P_1$	557.1341	557.1341	557.10
even	$4p^2\,{}^3P_2$	852.8268	1 409.9609	1 409.90
levels	$4p^2\,{}^1D_2$	5 715.3380	7 125.2989	7 125.26
$4s^24p5s$	$5s\,{}^3P_0^\circ$		37 451.6893	37 451.53
	$5s\,{}^3P_1^\circ$	250.6161	37 702.3054	37 702.15
odd	$5s\,{}^3P_2^\circ$	1 415.5967	39 117.9021	39 117.77
levels	$5s\,{}^1P_1^\circ$	902.6583	40 020.5604	40 020.43

[a] See reference 12.

Table I gives a compilation of the germanium wavelengths obtained with the different spacers. This table shows that the corrections for the dispersion of the phase shift due to reflection at the aluminized interferometer plates is negligible. A possible small phase correction would affect the final wavelength values obtained from the 6.0-cm and 12.4-cm spacers only within the limit of accuracy.

Table II contains the final values together with the wave numbers σ in cm^{-1} and the transitions known from earlier investigations.[12] These values, except those of the lines at 2651 A, were obtained with respect to the green Hg^{198} line as primary standard, its value being assumed to be 5460.75320 A. Since the patterns of the two lines at 2651 A were not separated with the spacer of 12.4 cm, the wavelengths of these two lines were obtained from the data for the 6.0-cm spacer. The exact value of the spacer thickness used in this case was an average value obtained by means of the other germanium wavelengths resulting from the measurements with the 12.4-cm spacer. This manner of computing seemed to be the most consistent although the direct use of the primary Hg standard led to practically the same results.

From the agreement between the values obtained

[9] W. F. Meggers and C. G. Peters, Bull. Bur. Standards **14**, 697 (1919).

[10] B. Edlén, J. Opt. Soc. Am. **43**, 339 (1953).

[11] *MIT Wavelength Tables* (John Wiley and Sons, Inc., New York, 1939).

[12] For details see Charlotte E. Moore, *Atomic Energy Levels* National Bureau of Standards Circular No. 467 (U. S. Government Printing Office, Washington, D. C., 1953), Vol. 2, p. 135. We shall refer to these tables as AEL.

with the 6.0-cm and 12.4-cm spacers in Table I, and from the general error considerations, it can be deduced that the greatest possible error of the wavelengths given in Table II is ±0.00004 A.

During the measurements of the Perot-Fabry patterns it was found that the germanium fringes could be measured more accurately than those of the Hg^{198} as a result of greater sharpness of the lines produced in the atomic beam light source.

2. Energy levels of Ge I.—From the wave numbers and the knowledge of the transitions involved,[12] there follow immediately new precision values for the energy levels. The results are contained in Table III which also gives a comparison with the AEL values.[12] A level diagram is given in Fig. 4.

The application of the combination principle permits a check of the accuracy obtained, since the intervals 852 cm^{-1} and 1415 cm^{-1} appear twice, namely as 852.8266 and 852.8270 cm^{-1}, and 1415.5965 and 1415.5969 cm^{-1}. This agreement supports the previously given limit of relative accuracy of our results as ±0.00004 A.

Table IV gives a representation of all known combinations between the even and odd levels resulting from the configurations $4s^24p^2$ and $4s^24p5s$, respectively. It contains also six transitions which are very well known but have not been obtained with the atomic beam. Four of them can be calculated, however, and as Table V shows the calculated values are in good agreement with the MIT values and the preliminary values recently obtained interferometrically by Meissner and VanVeld of this laboratory using a liquid air cooled hollow cathode and Krypton standards. This table also shows that Richter's values[13] deviate greatly from those of the other observers. The two transitions involving the even $4p^2\ ^1S_0$ level were not obtained with the atomic beam and the values shown in Table IV are those of Meissner and VanVeld (unpublished). The wave number differences between these lines are in good agreement with the atomic beam values.

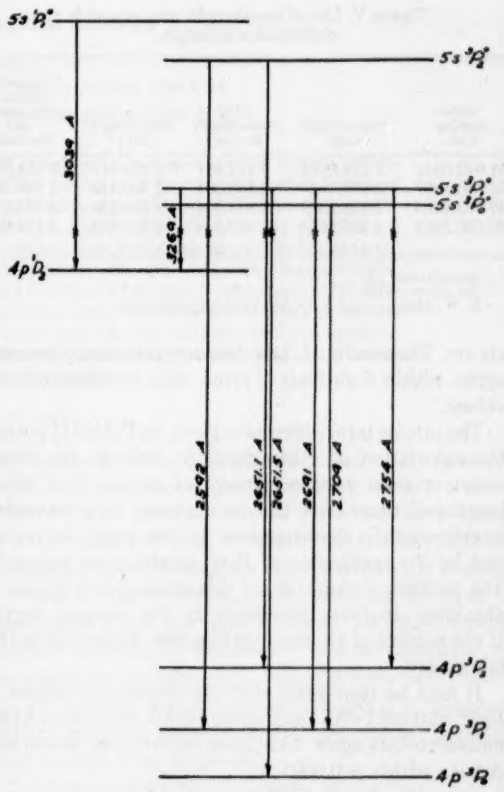

FIG. 4. Energy level diagram for transitions observed in the germanium beam.

The great accuracy, with which the wavelength of eight germanium lines were determined in this investigation, suggests that they may be used as secondary standards in as much as reliable standards in this wavelength region are sparse. Preliminary measurements of the wavelengths of these lines have been carried out in this laboratory with a hollow-cathode source and an

TABLE IV. Combination scheme of lines arising from transitions between the lowest even and odd levels of Ge I.

Even $4s^24p^2$ / Odd $4s^24p5s$	Levels	$4p^2\ ^3P_0$	$4p^2\ ^3P_1$	$4p^2\ ^3P_2$	$4p^2\ ^1D_2$	$4p^2\ ^1S_0$
	cm^{-1}	0.0000	557.1341	1 409.9609	7 125.2989	16 367.336
$5s\ ^3P_0°$	37 451.6893		36 894.5552 obs. .5552			
$5s\ ^3P_1°$	37 702.3054	37 702.3054 obs. .3054	37 145.1713 obs. .1713	36 292.3445 obs. .3447	30 577.0065 obs. .0065	21 334.969 obs. .969
$5s\ ^3P_2°$	39 117.9021		38 560.7680 obs. .7682	37 707.9412 obs. .9412	31 992.6032 calculated	
$5s\ ^1P_1°$	40 020.5604	40 020.5605 calculated	39 463.4264 calculated	38 610.5997 calculated	32 895.2615 obs. .2615	23 653.224 obs. .224

[13] C. Richter, Z. wiss. Phot. 25, 380 (1928).

TABLE V. List of wavelengths obtained with combination principle.

Wave number Calc.	Wavelength Calc.	Wavelength Richter[a]	Wavelength MIT[b]	Wavelength (Meissner and VanVeld)[c]
31 992.6032	3 124.8164	3 124.831	3 124.817	3 124.816
38 610.5997	2 589.1887	2 589.201	2 589.188	2 589.188
39 463.4263	2 533.2303	2 533.241	2 533.229	2 533.231
40 020.5605	2 497.9623	2 497.974	2 497.963	2 497.963

[a] See reference 13.
[b] See reference 12.
[c] K. W. Meissner and R. D. VanVeld (unpublished).

air arc. The results of these less accurate measurements agree, within their limit of error, with the atomic beam values.

The precise term differences given in Table III permit the calculation of other classified lines in the ultraviolet or even vacuum ultraviolet region. The wavelengths of these lines can be obtained from extended interferometric measurements in the near ultraviolet and by the application of Ritz' combination principle. The possible exploitation of this method as a means of obtaining auxiliary standards in the vacuum region is the subject of an investigation now underway in this laboratory.

It may be mentioned that the wavelength values of Hg^{198} obtained with the spacers used in the atomic beam measurements agree with those reported by Burns and Adams within ± 0.0001 A.

III. Isotopic Shift

As stated in the introduction this investigation was undertaken to study the isotopic shift of the germanium spectrum. Germanium possesses five isotopes of which four are of the even-even variety and one odd-even. The three principal isotopes (70, 72, 74) are of about equal abundance (26.6 percent, 27.4 percent, 36.4 percent, respectively). Isotope 76 has an abundance of 7.7 percent and isotope 73 of 7.8 percent. This distribution of abundances is favorable for measuring small line shifts. Theoretically one expects only small shifts due to the atomic number of germanium (32), and the fact that the terms, in the transitions observed, do not involve deeply penetrating orbits. However, by the use of an atomic beam light source and a high resolving power interferometer it was hoped to measure these small shifts.

The predicted normal shift is

$$\Delta\sigma = (\Delta M/M_1M_2)\times 5.49\times 10^{-4}\ \text{cm}^{-1}$$
$$= 0.0085\ \text{cm}^{-1} \text{ for } \lambda = 2592\ \text{A},$$

where $M_1 = 70$, $M_2 = 72$, $\Delta M = 2$, and σ = wave number of spectral line.

The specific and volume effects for this atom have not been calculated, but should be small for the electron configuration involved.

A careful microscopic study of the interferometer fringes showed no detectable splittings; therefore, densitometer traces were made of the patterns to determine whether any asymmetry could be found in the fringes of the lines. The intensity distribution was obtained from the densitometer traces by distorting the linear radius scale into a quadratic one. Since no intensity marks were provided on the plates, the replotting of the data was made under the reasonable assumption that the densities involved were in the linear section of the characteristic curve of the phtographic plates. The analysis of the traces showed that even with a large spacer (173 mm) and highly reflective coatings (92 percent in green light) no significant asymmetry could be detected. The only way to arrive at an estimation of the isotopic shifts involved was to compare the observed width of the lines with that expected from data concerning the atomic beam and the interferometer. As a result of these analyses it can be asserted that the isotope line shift between two consecutive even isotopes is less than 0.005 cm^{-1}. This is less than the expected normal shift and it implies that the volume shift must be small and in the opposite direction to the mass shift.

The germanium used in this investigation was prepared by Miss Louise Roth of the Purdue Physics Department's Solid State Group. We wish to thank her for her very able assistance.

The densitometer traces were made at the Argonne National Laboratory. We are grateful to Dr. Mark Fred and Dr. Frank Tomkins for helpful suggestions.

Isotope Shift in Neutral Carbon*

JAMES P. NICKLAS
Department of Physics, University of Buffalo, Buffalo, New York
(Received January 13, 1954; revised manuscript received June 8, 1954)

There is a possibility that the discrepancy between the experimental values of spectral isotope shift in light elements and the values calculated by including nuclear motion may be reduced by using improved one-electron wave functions. In order to investigate this possibility and at the same time to make a comparison with recently obtained experimental data, the shift of the transition $2p^2\,{}^1S-2p3s\,{}^1P$ ($\lambda=2478.5$A) of neutral carbon has been calculated using Hartree one-electron functions without exchange. The functions for the $2p3s$ configuration were calculated by the author for this purpose. The agreement with the experimental value is comparable to that obtained for other elements with this type of function. A comparison of the term shifts is made for both the ${}^3P$ and ${}^1S$ terms of the $2p^2$ configuration using Hartree functions with and without exchange and analytic functions of the Morse, Young, and Haurwitz type. The use of functions with exchange produced a significant change in the calculated term shifts which indicates that it may be possible to improve the agreement between calculated and observed transition shifts.

INTRODUCTION

EXPERIMENTAL measurements of the isotope shift of the spectral line $2p^2\,{}^1S_0-2p3s\,{}^1P_1$ ($\lambda=2478.5$A) in neutral carbon have been reported by two investigators.[1,2] Each reported a value of -0.156 ± 0.002 cm^{-1} for the shift from C^{12} to C^{13} and one[1] reported a value of -0.294 ± 0.002 cm^{-1} for the shift from C^{12} to C^{14}. A method has been published previously[3] for calculating a theoretical value for the difference of energy levels in light atoms due to nuclear motion. Application of the method to lithium,[4] boron,[5] neon,[3] and magnesium[6] has produced varying degrees of agreement with experimentally determined shifts. Before presenting the results obtained by calculating some shifts in neutral carbon, a brief review of the theory will be presented following the notation used by Vinti.[6]

It has been shown by Bartlett and Gibbons,[3] that the assumption of a finite nuclear mass adds a term to the Hamiltonian of an atom equal to

$$(2M)^{-1}\left(\sum_{i=1}^{p}\mathbf{p}_i\right)^2,$$

where $\mathbf{p}_i$ is the linear momentum of the ith electron relative to the nucleus and M is the nuclear mass. This term can be expressed as the sum of two terms,

$$N=(2M)^{-1}\sum_{i=1}^{p}\mathbf{p}_i^2 \quad \text{and} \quad \sigma=M^{-1}\sum\sum_{i>j}\mathbf{p}_i\cdot\mathbf{p}_j.$$

The quantity N is customarily called the "normal" shift. It can be shown that its effect is to add a term $-(m/M)E$ to the unperturbed eigenfunctions, where E is the observed total energy. This is equivalent to assuming a reduced mass for the electrons as is done in the case of the hydrogen atom. The second term is customarily called the "specific" shift. Its effect cannot be evaluated exactly but since it is small compared to the energy of the atom, first-order perturbation theory can be applied. Russell-Saunders coupling is assumed and the spin-orbit terms in the Hamiltonian are assumed small enough to be neglected.

In order to evaluate the effects of the term σ, it is necessary to obtain the diagonal elements $\bar{\sigma}$ of the corresponding operator with respect to the unperturbed wave functions. It is not necessary to calculate any off-diagonal elements since the Slater diagonal sum rule can be applied. If determinantal wave functions U are formed from an orthogonal set of one-electron functions of the form $R(n,l)(r)f(\theta,\phi)\alpha(s)$, expressions for evaluating the necessary diagonal elements can be derived.[6] These expressions are of the form:

$$(U|\sigma|U)=-M^{-1}\sum_{\mu>\rho}\sum|(n,l,m_l|\times\mathbf{p}|n',l-1,m_l')|^2\delta(m_s,m_s'),$$

where μ and ρ represent the sets of quantum numbers n, l, m_l, m_s, and n', l', m_l', m_s', respectively. The $\delta(m_s, m_s')$ indicates that the spins of the two orbits μ and ρ are the same. The sums are extended over all occupied orbits. The nonzero terms in the double sum can be expressed[6] as:

$$|(n,l,m_l|\mathbf{p}|n',l-1,m_l)|^2=C_l^2(l^2-m_l^2)(2mRy)J^2(n,l;n',l-1),$$

$$|(n,l,m_l|\mathbf{p}|n',l-1,m_l\mp1)|^2=\tfrac{1}{2}C_l^2(l\pm m_l-1)(l\pm m_l)(2mRy)J^2(n,l;n',l-1),$$

* Submitted in partial fulfillment of the degree of Doctor of Philosophy in the Department of Physics, University of Buffalo, Buffalo, New York.

[1] J. R. Holmes, Phys. Rev. **77**, 745 (1950); J. Opt. Soc. Am. **41**, 360 (1951).
[2] C. R. Burnett, Phys. Rev. **80**, 494 (1950).
[3] J. H. Bartlett and J. J. Gibbons, Jr., Phys. Rev. **44**, 538 (1933).
[4] D. S. Hughes and C. Eckart, Phys. Rev. **36**, 694 (1930).
[5] W. Opechowski and D. A. DeVries, Physica **6**, 913 (1939); J. P. Vinti, Phys. Rev. **58**, 879 (1940).
[6] J. P. Vinti, Phys. Rev. **56**, 1120 (1939).

where Ry is the Rydberg energy,

$$C_l=[(2l+1)(2l-1)]^{-1},$$

and

$$J(n,l;n',l-1)=\int_0^\infty R(nl)\times\left[\frac{dR(n',l-1)}{dr}-\frac{l-1}{r}R(n',l-1)\right]r^2dr.$$

In these integrals the radial parts of the one-electron functions $R(nl)$ are assumed to be so normalized that

$$\int_0^\infty R^2r^2dr=1.$$

The variable of integration r is expressed in units of the Bohr radius and the units of $\bar{\sigma}$ are cm^{-1}.

It is apparent that it is necessary to know the radial parts of the one-electron wave functions $R(nl)$ in order to evaluate the integrals. The sum of the two quantities $\bar{N}$ and $\bar{\sigma}$ mentioned before gives the energy shift from an atom of infinite nuclear mass to one of mass M. In order to calculate the shift between isotopes, it is necessary to calculate the shift from an infinite nuclear mass to each of the two isotopic masses and to take the difference between the two. In order to calculate the frequency shift in a given transition, it is necessary to calculate the shift of each of the energy levels of the transition and take their difference. It can be shown from the properties of the operators N and σ that to the approximation used, all the levels of a given multiplet have the same shift.

FORMULAS FOR SPECIFIC SHIFT IN CARBON

In evaluating the shift in the spectral line

$$2p^2\,{}^1S_0-2p3s\,{}^1P_1$$

of neutral carbon, it is necessary to obtain the shifts in the terms $2p^2\,{}^1S$ and $2p3s\,{}^1P$. There are three terms which arise from the configuration $2p^2$. These are ^1D, ^1S, and ^3P. An expression for the shift in the ^1S term can be found from Slater's diagonal sum rule. The shift for ^1D can be readily calculated by observing that the electronic state $2p(m_s=\frac{1}{2},\ m_l=1)2p(m_s=-\frac{1}{2},\ m_l=1)$ belongs only to this term. Evaluation of the double sum leads to

$$\bar{\sigma}=(M_1^{-1}-M_2^{-1})(\tfrac{2}{3}mRy)[2J^2(2p,1s)+2J^2(2p,2s)]. \quad (1)$$

TABLE I. Specific isotope shift of C^{13} relative to C^{12} in cm^{-1}.

Term	M.Y.H. functions	Hartree functions without exchange	Hartree-Fock functions with exchange
$2p^2\,{}^1S$	...	0.908	1.000
$2p^2\,{}^3P$	0.893	0.908	1.064
$2p3s\,{}^1P$	...	0.591	...

The electronic state $2p(m_s=\frac{1}{2},m_l=0)2p(m_s=\frac{1}{2},m_l=1)$ appears only in the ^3P term and the shift for this term can be shown to be the same as (1). There are three electronic states for which $\sum m_s=0$, $\sum m_l=0$, and according to the diagonal sum rule the sum of the shifts of all three electronic states, less the shift of the ^3P and ^1D gives the shift of the ^1S. The shift of the ^1S can also be shown to be the same as (1) and so the expressions for the shift of all three terms have the same form. The shift of the $2p3s\,{}^1P$ term may be found by applying the diagonal sum rule. The electronic state $3s(m_s=\frac{1}{2},\ m_l=0)2p(m_s=\frac{1}{2},\ m_l=1)$ is present in only the $2p3s\,{}^3P$ term and so the shift for this term is:

$$\bar{\sigma}=(M_1^{-1}-M_2^{-1})(\tfrac{2}{3}mRy)[J^2(2p,1s)+J^2(2p,2s)+J^2(2p,3s)].$$

There are two electronic states for which $\sum m_s=0$, $\sum m_l=0$ and the sum of the shifts for these two states is the same as (1). Therefore, the shift of the ^1P term is:

$$\bar{\sigma}=(M_1^{-1}-M_2^{-1})(\tfrac{2}{3}mRy)[J^2(2p,1s)+J^2(2p,2s)-J^2(2p,3s)].$$

TABLE II. Values of the J integrals calculated from radial functions.

Term		M.Y.H. functions	Hartree functions without exchange	Hartree-Fock functions with exchange
$2p^2\,{}^1S$	$J(2p,1s)$	...	−1.2301	−1.2949
	$J(2p,2s)$	...	0.5155	0.5297
$2p^2\,{}^3P$	$J(2p,1s)$	−1.1899	−1.2301	−1.3500
	$J(2p,2s)$	0.5766	0.5155	0.5105
$2p3s\,{}^1P$	$J(2p,1s)$	...	−1.4559	...
	$J(2p,2s)$	...	0.4715	...
	$J(2p,3s)$	...	0.1583	...

NUMERICAL CALCULATIONS

There are several types of one-electron radial functions available for the $2p^2$ configuration of neutral carbon. Torrance[7] has computed Hartree numerical functions without exchange and Jucys[8] has computed Hartree-Fock functions with exchange. Analytic functions of the Morse, Young, and Haurwitz type (M.Y.H.) have also been calculated[9] for the ^3P term only. The shifts for both the $2p^2\,{}^1S$ and $2p^2\,{}^3P$ terms have been calculated using these functions. The results are tabulated in Table I. As previously mentioned, the expressions for the $2p^2\,{}^3P$ and $2p^2\,{}^1S$ shifts are the same; the difference in numerical results in the case of the Hartree-Fock functions is due to a difference in the wave functions for the two terms. In the case of the Hartree functions without exchange, there is no distinction between terms of a given electron configuration. The Hartree-Fock and M.Y.H. functions are inherently

[7] C. C. Torrance, Phys. Rev. **46**, 388 (1934).
[8] A. Jucys, Proc. Roy. Soc. (London) **173**, 59 (1939).
[9] W. E. Duncanson and C. A. Coulson, Proc. Roy. Soc. (Edinburgh) **62**, 37 (1944).

orthonormal, but the Hartree functions without exchange must be orthogonalized by taking linear combinations as follows:

$$R_0(1s)=R(1s),$$
$$R_0(2s)=1.0006R(2s)-0.03552R(1s).$$

It is not necessary to modify $R(2p)$ since the angle functions produce orthogonality to the s electron functions.

There were no radial functions available for the $2p3s$ configuration so it was decided to calculate Hartree functions without exchange. It was also necessary to orthogonalize these functions as follows:

$$R_0(1s)=R(1s),$$
$$R_0(2s)=1.0007R(2s)-0.03703R(1s),$$
$$R_0(3s)=1.0050R(3s)-0.09879R(2s)-0.00623R(1s).$$

The calculated shift for the ^1P term is also given in Table I.

TABLE III. Specific isotope shift of C^{14} relative to C^{13} in cm^{-1}.

Term	M.Y.H. functions	Hartree functions without exchange	Hartree-Fock functions with exchange
$2p^2\,{}^1S$	...	1.686	1.857
$2p^2\,{}^3P$	1.658	1.686	1.976
$2p3s\,{}^1P$	...	1.098	...

The values of the J integrals calculated with the orthogonalized Hartree functions as well as with the Hartree-Fock and M.Y.H. functions are shown in Table II. Numerical integration was used in the calculations involving Hartree and Hartree-Fock functions.

It is possible to compute the shift of C^{14} relative to C^{12} merely by putting the appropriate masses in the formulas. The results obtained are listed in Table III.

From the term shifts computed above, with Hartree functions, the shift in the transition can be readily computed. The results are tabulated with experimental values, in Table IV.

TABLE IV. Comparison of experimental and calculated shifts for the transition $2p^2\,{}^1S-2p3s\,{}^1P$ ($\lambda=2478.5$A) in cm^{-1}.

	C^{13} relative to C^{14}	C^{14} relative to C^{12}
Experimental shift	-0.156 ± 0.002	-0.294 ± 0.002
Normal shift	0.141	0.261
Experimental specific shift	−0.297	−0.555
Calculated specific shift	−0.317	−0.588

The discrepancy between the experimental and calculated specific shifts is 0.020 cm^{-1} for the $C^{12}-C^{13}$ case. The effect of exchange on the shift of the $2p^2\,{}^1S$ term is 0.092 cm^{-1}, which is larger than the discrepancy and indicates that the inclusion of exchange in the calculations may improve the transition results. However, there are no Hartree-Fock functions available at present for the $2p3s\,{}^1P$ term. If the $2p^2\,{}^1S$ term shift calculated with Hartree-Fock function is used with the $2p3s\,{}^1P$ term shift calculated with Hartree functions, the transition specific shift is -0.409 cm^{-1}. This is in poorer agreement with the experimental value than when Hartree functions are used for both terms. It appears from this, that it is not advisable in such calculations to mix the types of functions used.

A calculation of the $C^{12}-C^{13}$ specific shift was made with the assumption that the $1s$ and $2s$ Hartree radial functions are the same for the $2p3s$ configuration as for the $2p^2$ configuration. The value of the transition shift obtained is -0.460 cm^{-1}. It is apparent that such an assumption is not justified in the case of these terms of carbon.

At present, work is proceeding on a calculation of Hartree-Fock functions for the $2p3s\,{}^1P$ term of carbon. It is hoped that the use of this type of function for both terms will improve the agreement between experimental and calculated shift for the $2p^2\,{}^1S-2p3s\,{}^1P$ transition.

The author wishes to express his appreciation to Dr. W. H. Davis for suggesting the problem.

Isotope Shift in Neutral Oxygen*

CHARLES E. TREANOR
Department of Physics, University of Buffalo, Buffalo, New York
(Received June 8, 1954)

Isotope shifts in levels of the first and second excited configurations of oxygen were calculated using Hartree one-electron wave functions, computed for $1s^22s^22p^33s$ and $1s^22s^22p^33p$. The suitability of the wave functions for this type of calculation can be checked with recent experiments in nine spectral lines of neutral oxygen. The discrepancies between calculated and observed shifts are from -0.09 cm^{-1} to $+0.09$ cm^{-1} for the shift between O^{18} and O^{16}. It appears that better one-electron wave functions (e.g., Hartree-Fock functions including exchange) could account for these discrepancies.

INTRODUCTION

RECENT spectroscopic measurements with oxygen enriched in O^{18} have resulted in the determination of the isotope shift in 20 lines of neutral oxygen.[1] Nine of these lines are transitions between the configurations $1s^22s^22p^33s$ and $1s^22s^22p^33p$, the first and second excited configurations. Parker and Holmes,[1] using the first order theory of Bartlett and Gibbons,[2] have shown that the shifts of the various states can be made consistent with the assumption that they are caused by nuclear motion. They fixed two parameters in the theory by using the experimental data from two lines (λ7772 and λ8820), assumed a third parameter to be negligibly small, and found that most remaining shifts could be calculated correctly from this. In the present paper Hartree one-electron wave functions without exchange were computed and used to calculate the isotope shift for these configurations.

The general theory required for calculation of the isotope shift due to nuclear motion is reviewed in the paper preceding this.[3] The same notation will be used here. The isotope shift of an energy level is divided into the "normal" shift ($\bar{N}$) and the "specific" shift ($\bar{\sigma}$). We will be concerned only with the specific shift, since the normal shift can be determined without knowledge of the wave functions.

FORMULAS FOR THE SPECIFIC SHIFT IN NEUTRAL OXYGEN

The first excited configuration of neutral oxygen, $1s^22s^22p^33s$, gives rise to 6 Russell-Saunders terms. The formulas for the specific shift for these terms can be obtained by using the diagonal sum rule, as described in the preceding paper on carbon.[3] The formulas listed below describe the shift of O^{18} relative to O^{16}.

$$\begin{aligned} &\bar{\sigma}(^3S)=3A+3B, \quad \bar{\sigma}(^1P)=3A \\ &\bar{\sigma}(^5S)=3A-B, \quad \bar{\sigma}(^3D)=3A+2B, \\ &\bar{\sigma}(^3P)=3A+2B, \quad \bar{\sigma}(^1D)=3A. \end{aligned} \tag{1}$$

The abbreviations introduced are

$$\begin{aligned} A&=(M_{16}^{-1}-M_{18}^{-1})(\tfrac{2}{3}mRy)[J^2(2p,2s)+J^2(2p,1s)] \\ B&=(M_{16}^{-1}-M_{18}^{-1})(\tfrac{2}{3}mRy)[J^2(2p,3s)] \end{aligned} \tag{2}$$

and, for example,

$$J(2p,3s)=\int_0^\infty R(2p)\frac{d}{dr}R(3s)r^2dr.$$

$\bar{\sigma}$ is expressed in cm^{-1}, while r is in units of the Bohr radius. The quantity $(M_{16}^{-1}-M_{18}^{-1})(\frac{2}{3}mRy)=0.2767$.

In the case of the $2p^33p$ configuration, the shifts are the same for all states of the configuration, namely $\bar{\sigma}$ (all $2p^33p$ states)$=3A'+C'$, with

$$\begin{aligned} A'&=(M_{16}^{-1}-M_{18}^{-1})(\tfrac{2}{3}mRy) \\ &\quad\times[J^2(2p',2s')+J^2(2p',1s')] \\ C'&=(M_{16}^{-1}-M_{18}^{-1})(\tfrac{2}{3}mRy) \\ &\quad\times[J^2(3p',2s')+J^2(3p',1s')]. \end{aligned} \tag{3}$$

The primes indicate the second excited configurations.

The shift in a spectral line of O^{18} relative to O^{16} is then obtained by subtracting the shift in the lower level from that of the upper level.

NUMERICAL CALCULATIONS

The formulas (1) for the quantities $\bar{\sigma}$ assume that the one-electron wave functions are orthogonal. Although this is not satisfied by Hartree wave functions with the same l but different n, the difficulty can be circumvented by using linear combinations of the original functions. The orthonormal combinations used in this calculation are

$$\begin{aligned} &R_0(1s)=R(1s), \\ &R_0(2s)=(1.0004)R(1s)-(0.0270)R(1s), \\ &R_0(3s)=(1.0052)R(3s)-(0.0723)R(2s)-(0.0038)R(1s), \\ &R_0(2p)=R(2p), \\ &R_0(3p)=(1.0123)R(3p)-(0.1571)R(2p), \end{aligned}$$

$$\int_0^\infty R_0(n,l)R_0(n',l)r^2dr=\delta_{n,n'}.$$

* Part of a dissertation to be submitted in partial fulfillment of the requirements for the degree of Doctor of Philosophy at the University of Buffalo.

[1] L. W. Parker and J. R. Holmes, J. Opt. Soc. Am. **43**, 103 (1953).
[2] J. H. Bartlett and J. J. Gibbons, Jr., Phys. Rev. **44**, 538 (1933).
[3] J. P. Nicklas, preceding paper [Phys. Rev. **95**, 1469 (1954)].

TABLE I. Specific shift of O^{18} relative to O^{16} in cm^{-1}.

λ	Transition	Formula for shift	Calculated specific shift	Experimental specific shift	Experimental minus calculated
7772	$3s\,^5S-3p\,^5P$	$3(A'-A)+C'-3B$	−0.0382	0.015→0.018	+0.055
8820	$3s\,^1D-3p\,^1F$	$3(A'-A)+C'$	−0.0194	0.064→0.068	+0.085
8446	$3s\,^3S-3p\,^3P$	$3(A'-A)+C'+B$	−0.0022	0.08→0.10	+0.09
3955	$3p\,^3P-3s\,^3P$	$3(A-A')-C'+2B$	+0.0292	0.0→−0.2	...
8222	$3s\,^3D-3p\,^3D$	$3(A'-A)+C'-2B$	−0.0292	0.034→0.040	+0.066
3823	$3s\,^3D-3p\,^3D$	$3(A'-A)+C'-2B$	−0.0292	0.03→0.05	+0.07
7157	$3s\,^1D-3p\,^1D$	$3(A'-A)+C'$	−0.0112	0.05→0.07	+0.07
7995	$3p\,^3P-3s\,^3D$	$3(A-A')-C'+2B$	+0.0292	−0.06→−0.07	−0.09
7476	$3s\,^3P-3p\,^3D$	$3(A'-A)+C'-2B$	−0.0292	−0.04→−0.06	−0.02

The required J integrals, calculated with these orthogonal wave functions, are

$$J(2p,1s)=-2.0771,\quad J(2p',1s')=-2.0721,$$
$$J(2p,2s)=0.6138,\quad J(2p',2s')=0.6160,$$
$$J(2p,3s)=0.1806,\quad J(3p',1s')=0.1253,$$
$$J(3p',2s')=0.0282,$$

so that the quantities defined by Eqs. (2) and (3) become

$$A=1.2634\ cm^{-1},\quad A'=1.2583\ cm^{-1},$$
$$B=0.0090\ cm^{-1},\quad C'=0.0041\ cm^{-1}.$$

The corresponding shifts in nine spectral lines were calculated from these and are given in Table I. Also listed are the experimental shifts observed by Parker and Holmes.

Parker and Holmes[1] have shown that all but two of the lines (λ7995 and λ7476) have shifts consistent with the assumption that $3(A'-A)=0$, $B=0.0165\pm0.0015$ cm^{-1}, and $C'=0.066\pm0.002$ cm^{-1}. They point out that λ7476 may be incorrectly classified. The only comparisons available for transitions between two excited levels are calculations in neon, where the configurations are the same as for oxygen (except for two more $2p$ electrons), and a single transition in ionized boron, where Morse, Young, Haurwitz (M.Y.H.) functions were used. In the case of ionized boron, the discrepancy is 0.168 cm^{-1}. In the calculation for neon, where Hartree wave functions were used, four transitions could be checked. The value of $5(A'-A)$ was assumed negligibly small, and experimental comparison indicates that the calculated value of C' is too small by about 0.03 cm^{-1}, which is in the same direction (and about half as large) as the discrepancy in oxygen. Although configuration interaction is certainly important in many of the levels of oxygen, it could be expected that the effect on λ7772 ($3s\,^5S-3p\,^5P$) would be small. The error of 0.055 cm^{-1} in this line is as bad as that in some of the other lines.

The effect on the isotope shift of including exchange in the one-electron wave functions has been investigated in a preliminary way in carbon.[3] Calculations show that the shift of the ground level is changed 0.170 cm^{-1} for ^1S and 0.290 cm^{-1} for $^3P(\Delta M=2)$ by including the effects of exchange in the calculation of the wave functions. The Hartree wave functions give equal shifts for the two levels, while Hartree-Fock wave functions give a difference of 0.120 cm^{-1}. It seems plausible then that the neglect of exchange could explain the discrepancy in λ7772. In fact, a discrepancy of the same magnitude in neutral boron (transition from first excited configuration to ground configuration) was removed by using M.Y.H. wave functions in place of Hartree functions.[4] To investigate this and other problems in neutral oxygen, it is planned to calculate the wave functions including exchange for the $3s\,^5S$ and $3p\,^5P$ configurations.

The author wishes to express his appreciation to Dr. W. H. Davis for suggesting this problem.

[4] J. P. Vinti, Phys. Rev. **58**, 879 (1940).

Electron Spin Magnetic Moment in Atomic Hydrogen*

ROBERT BERINGER AND MARK A. HEALD†
Sloane Physics Laboratory, Yale University, New Haven, Connecticut
(Received June 7, 1954)

The ratio of the electron-spin g factor to the proton g factor has been measured in atomic hydrogen by a precision microwave magnetic resonance absorption technique. The result obtained is

$$-g_s/g_p = 658.2277 \pm 0.0002,$$

where g_p refers to protons in molecular hydrogen. The ratio is in good agreement with the atomic-beam result of Koenig, Prodell, and Kusch, and verifies their conclusions concerning the magnitude of the quantum electrodynamical contribution to g_s.

INTRODUCTION

THE evidence for an anomaly in the magnetic moment associated with electron spin began with a discrepancy in the hyperfine splitting in atomic hydrogen.[1] Breit[2] interpreted this as due to a small electron spin moment in addition to that given by the Dirac theory. Schwinger[3] showed that radiation processes in quantum electrodynamics predicted this addition and calculated the correction to the electron spin g factor g_s to the first order in the fine-structure constant. Direct g-factor measurements in one-electron atomic states[4] confirmed the calculated correction.

Although a number of observations with atomic systems have checked these results, no precision measurement of g_s for "free" electrons has been successful thus far, and at the present time measurement of Zeeman level displacements in atoms is the most accurate method of determining g_s. The calculation of g_s from the measured g_J of an atomic state involves corrections due to the purity of the atomic state and relativistic and internal diamagnetic effects. For the hydrogen atom these corrections are known with considerable accuracy, and at the present time they do not limit the accuracy with which g_s is known.

Because of the limited accuracy of magnetic field measurements, g_s is not measured directly in the atomic hydrogen experiments, but rather the ratio $g_s(1s\,^2S_{\frac{1}{2}}$ hydrogen$)/g$(proton) is determined and combined with the result of another experiment which determines g(orbital electron)$/g$(proton). The atomic-beam experiment of the Columbia group[5] or the experiment reported here give the ratio g_s/g_p with an error of about one part per million. The Gardner-Purcell experiment[6] determines the ratio g_l/g_p with an error of 12 ppm so that g_s is known with the same error. With a tenfold increase in the accuracy of the Gardner-Purcell experiment, g_s will be known to one ppm, and the exactness of the quantum electrodynamical corrections to a second order in the fine-structure constant[7] can be assessed.

At the time the Columbia atomic hydrogen results were announced,[8] we had developed a microwave absorption experiment[9] for the same purpose. Work was continued and during the past year the experiments were completed. Our strongest reason for continuing with measurements which were not expected to improve significantly on the accuracy of the atomic-beam results was the desire to check an important constant by a different experimental method. At the same time, we could test our method against the highly developed techniques of atomic-beam magnetic resonance. The microwave absorption method developed in the course of this work promises to have general applicability in the

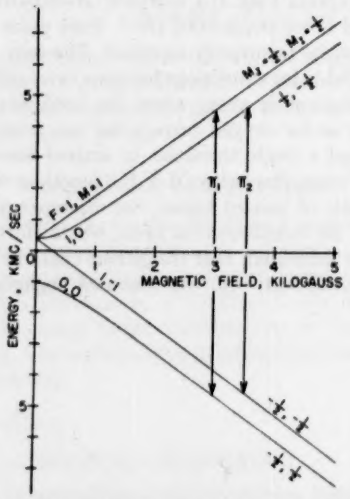

FIG. 1. Magnetic-field dependence of the hyperfine energy levels of the ground state of the hydrogen atom. The arrows indicating the microwave transitions are drawn to scale for the present experiment.

* Assisted by the U. S. Office of Naval Research.
† National Science Foundation Fellow, 1952–53; DuPont Company Fellow in Physics, 1953–54. This work is part of a dissertation presented to Yale University for the Ph.D. degree.
[1] Nafe, Nelson, and Rabi, Phys. Rev. **71**, 914 (1947); Phys. Rev. **73**, 718 (1948); Nagle, Julian, and Zacharias, Phys. Rev. **72**, 971 (1947).
[2] G. Breit, Phys. Rev. **72**, 984 (1947); **73**, 1410 (1948).
[3] J. Schwinger, Phys. Rev. **73**, 416 (1948).
[4] P. Kusch and H. M. Foley, Phys. Rev. **74**, 250 (1948); and summary in reference 5.
[5] Koenig, Prodell, and Kusch, Phys. Rev. **88**, 191 (1952).
[6] J. H. Gardner, Phys. Rev. **83**, 996 (1951).
[7] R. Karplus and N. M. Kroll, Phys. Rev. **77**, 536 (1950).
[8] Koenig, Prodell, and Kusch, Phys. Rev. **83**, 687 (1951).
[9] R. Beringer and E. B. Rawson, Phys. Rev. **87**, 228 (1952).

measurement of g factors and hyperfine coupling energies in atoms. By avoiding beam detection problems it makes such measurements relatively simple; and the present work shows the accuracy to be comparable with the best atomic beam work.

The theory of the atomic-hydrogen experiment is treated in reference 5; we briefly review the reasoning. Suppose hydrogen atoms to be in a strong magnetic field which splits the two states, $M_J=\pm\frac{1}{2}$, by an energy corresponding to microwave frequencies. Let the frequency for the microwave transitions $M_J=\frac{1}{2}\rightarrow-\frac{1}{2}$ and the frequency for proton resonance be measured in the same field. The ratio of these two frequencies essentially determines g_J/g_p, and the accuracy of this ratio is independent of the rather large uncertainty in the proton moment itself. In the actual experiment the deduction of g_J/g_p is complicated by atomic hyperfine-structure. With the assumption that the ground state of atomic hydrogen is pure $^2S_{\frac{1}{2}}$, the level energies W, including magnetic hyperfine interactions, are given by the Breit-Rabi formula:

$$W\left(F=\begin{matrix}1\\0\end{matrix},M_F\right)$$
$$=-\tfrac{1}{4}\Delta W+g_p\mu_0HM_F\pm\tfrac{1}{2}\Delta W(1+2M_Fx+x^2)^{\frac{1}{2}}$$
$$=-\tfrac{1}{4}h\nu_{\rm H}-h\nu_pM_F\pm\tfrac{1}{2}h\nu_{\rm H}(1+2M_Fx+x^2)^{\frac{1}{2}},$$

where

$$x=(g_J-g_p)\mu_0H/\Delta W=(1-g_J/g_p)\nu_p/\nu_{\rm H}.$$

$\Delta W=h\nu_{\rm H}$ is the zero-field hyperfine splitting of atomic hydrogen;[10] the field strength H is measured in units of proton resonance frequency where $h\nu_p=-g_p\mu_0H$, g_p refers to protons, and μ_0 is the Bohr magneton. The transitions $\Delta M_J=\pm1$, $\Delta M_I=0$ occur in the microwave region for moderate fields and are conventionally labeled π_1 and π_2, as shown in Fig. 1. Writing the transition energy as $h\nu$, one obtains the ratio g_J/g_p as a function of frequencies only. For the π_1 and π_2 transitions (upper and lower signs, respectively),

$$-\frac{g_J}{g_p}=\frac{\nu}{\nu_p}\left(\frac{\nu+\nu_p\mp\nu_{\rm H}\mp\frac{1}{2}\nu_p\nu_{\rm H}/\nu}{\nu+\nu_p\mp\frac{1}{2}\nu_{\rm H}}\right). \qquad (1)$$

There are several diamagnetic effects associated with the interpretation of ν_p and g_p in addition to the bulk demagnetization effects which are discussed later. The first concerns g_p which, in the Breit-Rabi formula written above, refers to protons in atomic hydrogen. That is, the internal diamagnetic corrections to the field at the proton are included in the definition of g_p. The second diamagnetic effect arises from the use of protons in mineral oil for field calibration. A correction for this can be made exactly by substituting into (1) for ν_p the quantity

$$\frac{g_p(\text{atomic hydrogen})}{g_p(\text{oil})}\nu_p(\text{oil}),$$

in which case the ratio calculated in (1) is g_J/g_p(atomic hydrogen). A sufficiently accurate procedure is to ignore the differences in the parenthesis of (1) and to calculate g_J/g_p(oil) using the observed ν_p(oil). The same procedure can be used for other proton-containing samples.

MICROWAVE EXPERIMENT

The determination of g_J/g_p consisted of two parts, a microwave resonance experiment with atomic hydrogen followed by a proton resonance experiment with mineral oil in the same magnetic field. In our apparatus the magnetic field was controlled by the frequency of a proton resonance unit called the *regulator* which was used to vary, reset, and regulate the field in the magnet gap. It did not, however, directly measure the field in the region where atomic hydrogen resonance occurred since its proton coil could not occupy this region. The measurement of proton resonance in this region was accomplished with a second proton unit whose proton coil could be inserted into the microwave cavity in place of the atomic-hydrogen vapor at the conclusion of the microwave experiment. This unit was called the *simulator*.

The experiment used the method of magnetic resonance which was first developed by Rabi, Zacharias, Millman, and Kusch[11] for molecular-beam spectroscopy. Our microwave version was similar to the nuclear magnetic-resonance absorption method of Purcell, Torrey, and Pound[12] in that it detects transitions by the absorption of electromagnetic energy rather than by the trajectories of reoriented atoms. The apparatus was originally developed for the study of stable paramagnetic molecules.[13]

Microwave energy at about 9000 Mc/sec is generated by a klystron oscillator and coupled through a resonant cavity to a detector. The cavity is in a uniform magnetic field of a few thousand gauss and contains the atoms being studied, which must be in states of nonzero total electronic angular momentum. Each atomic state is split into its Zeeman levels which, for the fields used, are separated by microwave frequencies. The magnetic field is then varied until a level separation coincides with the cavity frequency. Absorption and stimulated emission occur and a net lowering of the power at the microwave detector results. The oscillator, detection system, and general experimental details are described in references 13.

In the present work the atomic hydrogen was pro-

[10] A. G. Prodell and P. Kusch, Phys. Rev. **88**, 184 (1952), who obtained $\nu_{\rm H}=1420.4051\pm0.0002$ Mc/sec.

[11] Rabi, Zacharias, Millman, and Kusch, Phys. Rev. **53**, 318 (1938).

[12] Purcell, Torrey, and Pound, Phys. Rev. **69**, 37 (1946); Bloembergen, Purcell, and Pound, Phys. Rev. **73**, 679 (1948).

[13] R. Beringer, Annals N. Y. Acad. Sci. **55**, 814 (1952); R. Beringer and J. G. Castle, Jr., Phys. Rev. **78**, 581 (1950); **81**, 82 (1951); Beringer, Rawson, and Henry, Phys. Rev. **94**, 343 (1954).

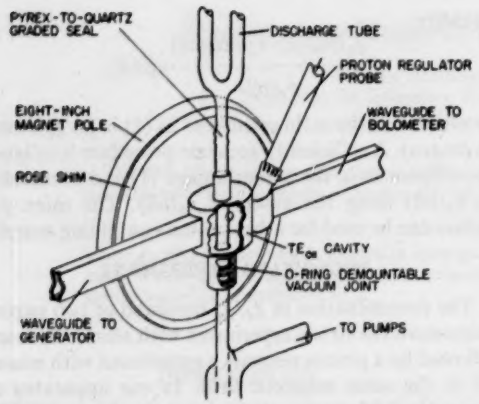

FIG. 2. Cutaway view of atom cavity in magnet gap. The wave guide to the bolometer is offset to permit centering of regulator proton-coil chamber in the magnet gap.

duced in an air-cooled Wood discharge tube.[14] The tube, of 15-mm o.d. Pyrex, was shaped like a narrow, upright U of total length 1.4 m with aluminum electrodes at each end. Tank hydrogen, bubbled through water, was passed through pressure dropping capillaries and led into the Wood tube near each electrode. From the bottom of the U a vertical tube of 13 mm o.d. passed down along the axis of the microwave cavity and coupled through a demountable O-ring vacuum joint to a liquid-air trap and the pumps. The essentials are shown in Fig. 2. The discharge with 20 000 Ω ballast resistance in series operated at a potential of about 2200 v at 50 ma.

The lower part of the discharge tube and the atom-vapor tube were coated with a layer of fused metaphosphoric acid[15] which inhibits wall recombination of atomic hydrogen. This coating did not extend into the cavity. With a model tube similarly treated we measured atomic concentrations of 50 percent in the atom-vapor tube 20 cm from its connection with the discharge tube with flow rates of 10^{-4} g/sec. A recombination bolometer of tungsten wire was used to determine the atom concentration.

The gas system was designed for fast pumping of the atomic vapor from discharge tube to cavity. A small oil diffusion pump of speed 5 l/sec (with air at our operating pressures), backed with a mechanical pump, was connected to the atom-vapor tube through a high-conductance line and liquid-air trap. Under typical conditions the gas transit time from the base of the U to the cavity was estimated to be 10^{-3} sec. It would be possible to reduce this transit time to 10^{-3} sec without major change of the pumping system. The pressure at the cavity was of the order of 50 microns.

The cavity resonated in the TE_{011} mode which permits concentric holes in the end plates without seriously imparing the Q or perturbing the fields. To lower dielectric losses the axial tube was of fused silica. With the tube in place a typical cavity had an unloaded Q of 15 000 at 9200 Mc/sec and a transmission factor of 3.5 db. Cutoff wave guides surrounding the silica tube at top and bottom suppressed leakage of the cavity fields. Several cavities differing in details were used in the course of the experiments. They were constructed of commercial copper or silver-plated brass.

The arrangement of a TE_{011} mode cavity with an axial atom-vapor tube is particularly suitable for the experiment. The microwave electric field is low in the axial region while the microwave magnetic field is large, being distributed in space much like the magnetic field of a solenoid of length about one-half the cavity height. This field configuration gives good coupling of the microwave radiation to transitions of the $\Delta M_J = \pm 1$ type. It also makes it possible to determine the dc magnetic field in the same region of space with a simulator proton coil the dimensions of which are chosen to yield approximately the same distribution of rf magnetic fields as those in the microwave cavity. This is very desirable since the sampling of inhomogeneities in the magnet field must be closely similar in the atomic hydrogen and simulator experiments. Sampling differences can contribute important systematic errors in the experiment and we have gone to considerable effort to minimize them.

MAGNETIC FIELD

The electromagnet which provided the uniform magnetic field had ribbon-wound coils with edge cooling provided by water-cooled fins. The yoke, winding, and conical poles were designed for high fields (20 000 gauss). The poles tapered to 8-inch diameter at the air gap which was 2 inches long. The pole tips were ground and lapped flat. They rested loosely on the main poles with an oil film between. Final adjustment of the gap was made with brass jacks in the air gap which pressed the tips apart and could rock them about 10^{-4} inch on the oil film.

The tips were flat and parallel, but a raised edge or Rose[16] shim was provided for each. These shims could be slid around to obtain improved homogeneity at the point in the gap selected for the experiment. The shims were held to the pole tips by magnetic forces. Small pieces of nickel sheet were used as local shims.

Except for preliminary mechanical alignment of the pole tips all of the shimming was empirical. The simulator proton coil was placed in the cavity and the shims adjusted until the narrowest and most symmetrical proton signal was observed on the oscilloscope. The field distribution varied somewhat from day to day and hour to hour, so that the magnet was reshimmed for each run. While tedious, this procedure had merit in providing a rather random set of field inhomogeneities

[14] R. W. Wood, Phil. Mag. **44**, 538 (1922).
[15] H. G. Poole, Proc. Roy. Soc. (London) **A163**, 404 (1937).
[16] M. E. Rose, Phys. Rev. **53**, 715 (1938).

for the various runs and hopefully a random error in g_J/g_p resulting from sampling differences between the microwave and the proton experiments.

The magnet was powered by 200-ampere-hour lead storage cells for the 3000-gauss range used in these measurements. The current was adjusted with a series-parallel combination of commercial slide-wire rheostats. In addition to the main coil, two high impedance pole-tip coils were provided. One supplied the magnetic-field modulation (30 cycles/sec) and the second was used for field regulation. The regulator unit provided a feedback signal for this second coil. The regulator proton coil was originally mounted close but not attached to the microwave cavity. In the later experiments the coil was contained in a shield which was rigidly attached to the cavity as close to the experimental region of the cavity as possible. The relative differential field between simulator and regulator proton coils was typically about 30 ppm.

The regulator and simulator units used a nuclear resonance circuit of our design. It is shown in Fig. 3. The chief point of interest is the separation of the oscillator and resonance-detector functions, with the proton coil appearing in the detector circuit. Most of the wide-frequency-coverage nuclear-resonance detectors which have been described put the proton coil in the oscillator tank. This leads to undesirable frequency modulation of the oscillator when resonances with "wiggles" are used. In our circuit the oscillator and detector tanks are tuned together with a dual condenser; small tracking errors are compensated with a trimmer capacitor C_1, and tracking is tested by a rotating capacitor C_2 which produces very slight frequency modulation of the oscillator. The trimmer is adjusted to give zero amplitude modulation output from this frequency modulation, thus assuring that the proton circuit is exactly tuned to the oscillator frequency. With this arrangement and alignment procedure we were assured that asymmetries in the proton resonance pattern were due to field inhomogeneities and we could take steps to reduce them. Other circuits tried were inferior in this respect and led to systematic errors in field measurement due to circuit unbalance. The

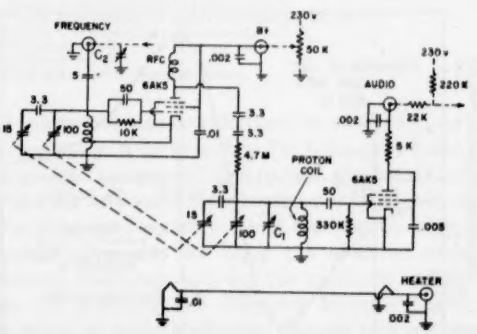

FIG. 3. Proton magnetic resonance absorption circuit with separated oscillator and detector stages.

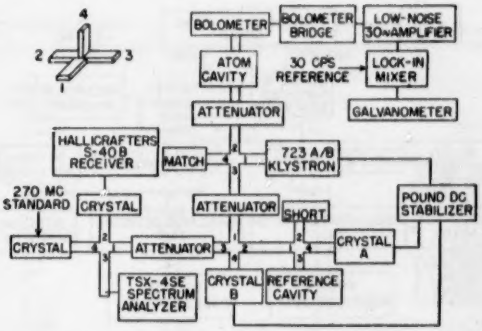

FIG. 4. Microwave magnetic resonance absorption spectrometer, showing frequency stabilization and measurement equipment, and detection system. The atom cavity is in a magnetic field, which is modulated at 30 cycles/sec.

circuit is quite dependable, easily constructed, and has a fairly good noise figure.

The regulator generated its field-control signal by mixing the amplified proton resonance signal with a 30-cycle/sec reference signal in a lock-in mixer. The mixer output drove a push-pull dc power amplifier with the pole-tip coil as a cathode load. Suitable low-pass filters in the loop prevented oscillation. The feedback gain (gauss per gauss) was about 300, giving short-time (1 sec) field excursions of less than 0.005 gauss and long-time stability at a drift rate determined by the lead storage cells. The current through the pole-tip coil was kept near zero by periodic readjustment of the main magnet current. The over-all field stability and setting accuracy was about equal to the accuracy of centering the simulator resonance with respect to the sweep which was 0.2 ppm (0.0007 gauss).

FREQUENCY SYSTEM

The regulator and simulator proton units were both locked to accurately known frequencies. These frequencies were generated in mixers using appropriate frequencies from a standard frequency system. The microwave frequency used in the atomic hydrogen experiment was measured with the same system. Reference to Eq. (1) shows that g_J/g_p is almost independent of the absolute value of the frequency provided that ν/ν_p is accurately known. However, we periodically standardized our frequencies against radio station WWV to less than half a part per million.

The local standard was a 100-kc/sec temperature-regulated crystal oscillator.[17] This frequency was multiplied to 270 Mc/sec in the usual way by a chain of amplifiers with plate tanks tuned to harmonics of the grid drive. The 270-Mc/sec harmonics from a silicon-tungsten crystal were used as standard microwave frequencies. The cavities were designed to resonate near a 270-Mc/sec harmonic so that a radio receiver could be used to measure the frequency difference between the

[17] Bliley model BCS-1A.

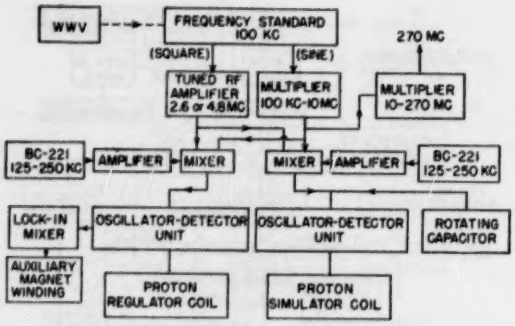

FIG. 5. Standard frequency and proton-resonance field-calibration systems. Both proton signals are displayed on oscilloscopes with coherent 30-cycle/sec sinusoidal sweep.

markers and the klystron oscillator. The receiver was calibrated with a BC-221 frequency meter. This microwave generating and frequency measuring equipment is shown in Fig. 4.

The proton regulator and simulator locking frequencies were generated by mixing the standard 10 Mc/sec with a suitable high-order harmonic of the 100-kc/sec standard and with the 125–250-kc/sec electron coupled oscillator output of a BC-221 frequency meter. Figure 5 shows this equipment. For best operation the line length from the rotating capacitor had to be adjusted so that its impedance variation at the oscillator was purely reactive. With other line lengths some undesirable amplitude modulation was introduced.

PROCEDURE AND RESULTS

An experiment involved the following steps. (a) The field homogeneity was adjusted using the mineral-oil simulator coil mounted in the cavity. Shims were moved until the best proton resonance pattern was obtained. (b) After suitable homogeneity was achieved, a "simulator run" was made. This consisted in setting the field with the proton regulator and tuning the simulator frequency until its pattern was centered on an oscilloscope. The oscilloscope was swept with the 30-cycle/sec field modulation signal. The simulator run consisted of about ten regulator settings, equally spaced in regulator proton frequency and centered at the resonance field for the microwave transition. (c) The simulator coil was then removed and the discharge tube put in place as shown in Fig. 2. Quick change vacuum and gas connections were made, the gas flow adjusted, and the discharge initiated. The microwave oscillator was tuned to the cavity resonance, its frequency measured, and a "microwave run" begun. This consisted in setting the regulator and noting the detected 30-cycle/sec signal output on a galvanometer. The magnetic field was varied point-by-point through the region of the atomic hydrogen resonance. A plot of a microwave run is shown in Fig. 6. (d) The discharge-tube system was quickly dismantled and another simulator run taken to verify step (b).

Throughout an experiment, including the time between the runs, the magnetic field was regulated and kept to values near the microwave resonance and was varied only enough to display the resonances. This control was maintained in order to minimize changes in the distribution of the field in the gap since we relied on the oscillator frequency of the regulator to reproduce magnetic field values in the experimental region of the cavity. Actually, there remained both systematic and random temporal drifts in this reproducibility, as indicated by changes in the frequency difference between regulator and simulator. Although these drifts were random in direction, their average value increased with time. Thus it was essential to take a set of runs, simulator, microwave, simulator, as rapidly as possible. With our apparatus the total elapsed time was at least 45 min.

In all, from the beginning of the experiments, forty-seven microwave runs and associated simulator runs were made. The three earliest runs used crude frequency and field control and were essentially exploratory. They are not included in this paper. The other forty-four runs began in December 1952, and extended through October 1953. During this period modifications were made in the cavities, simulator coils, regulator unit and its mounting, standard-frequency system, and the microwave-oscillator stabilization system. Three cavities were essentially as shown in Fig. 2 and one of these was used in runs which received ninety percent of the total weight; a fourth used reentrant metal tubes surrounding all but a short central region of the atom vapor tube in an attempt to reduce the volume of the experimental region and hence the total field inhomogeneity. Throughout the course of the experiments the data improved as judged by consistency and by the width of the microwave resonance line and the reproducibility of simulator runs. These improvements resulted from better mechanical design, more accurate field control, and reduced microwave power level. The latter largely eliminated saturation line-broadening which was present in the runs previous to June 4, 1953. In view of these improvements we adopted a set of weighting criteria for the data, but did not reject any data *a priori*. However, rejections were later made on statistical grounds.

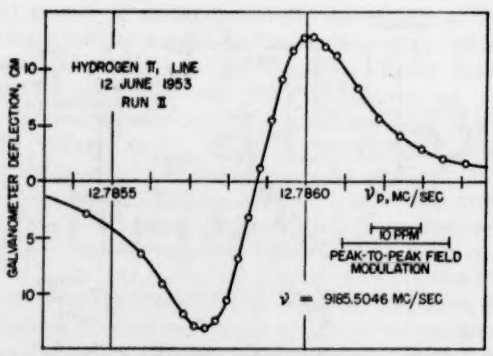

FIG. 6. Plot of the data of a good microwave run.

TABLE I. Summary of experimental data.

Run	Peak-to-peak field modulation (ppm)	Rf power at bolometer (mw)	Peak-to-peak microwave linewidth (ppm)	Assigned linewidth error (ppm)	Assigned simulator error (ppm)	Total normalized weight (%)	$-g_J/g_p$
			Hydrogen π_1 line				
1952							
[a]Dec. 19	50	0.5	68	5.5	4.9	0.1	658.2324[g]
20 I	50	0.5	79	3.6	6.4	0.1	.2256[g]
II	50	0.5	74	3.6	6.4	0.1	.2221[g]
22 I	50	0.5	77	4.1	3.0	0.3	.2252[g]
II	50	0.5	74	3.7	3.0	0.4	.2236[g]
1953							
[b]Jan. 20	55	0.3	50	3.16	1.52	0.6	.2166
22 I	33	0.5	33	2.36	1.20	1.1	.2145
II	33	0.5	44	2.87	1.04	0.8	.2157
23 I	33	0.5	37	1.90	2.40	0.8	.2201
II	33	0.5	37	2.20	1.04	1.3	.2166
28 I	33	0.5	46	2.38	2.36	0.7	.2212[g]
II	33	0.5	42	2.15	2.36	0.8	.2220[g]
29 I	33	0.5	42	2.46	1.64	0.9	.2176
II	33	0.5	44	2.70	1.56	0.8	.2173
[c]Mar. 25	36	0.5	29	1.43	2.28	1.1	.2209[g]
[d]May 4 I	37	1.0	40	1.99	1.55	1.2	.2191
II	37	0.5	40	1.92	0.51	2.0	.2187
22	37	0.7	34	2.87	1.84	0.7	.2251[g]
June 3 I	37	1.0	38	2.80	1.32	0.8	.2241[g]
II	37	1.4	38	2.02	1.10	1.5	.2167
III	37	1.4	38	1.81	0.68	2.1	.2194
IV	37	0.35	30	1.55	0.65	2.8	.2171
4 I	26	0.33	23	1.17	1.33	2.5	.2151
II	26	0.10	22	1.07	1.33	2.7	.2152
III	26	0.18	23	1.11	0.93	3.8	.2188
IV	26	0.15	23	1.15	0.48	5.1	.2181
5	26	0.20	20	1.08	0.72	4.6	.2186
12 I	27	0.09	24	1.21	0.60	4.3	.2161
II	21	0.16	20	0.98	0.50	6.4	.2171
III	21	0.09	21	1.04	1.58	2.2	.2195
IV	21	0.13	20	0.99	0.48	6.4	.2179
			Hydrogen π_2 line				
[e] 27	18	0.18	23	1.18	2.41	1.1	.2157
30	18	0.14	20	0.97	0.48	6.7	.2168
July 1	18	0.16	21	1.53	0.99	2.4	.2171
4	18	0.15	22	1.28	1.88	1.5	.2174
Sept. 1	27	0.07	26	1.27	1.11	2.8	.2172
2 I	27	0.20	26	1.28	0.91	3.2	.2162
II	27	0.20	27	1.31	0.35	4.3	.2170
9	27	0.23	27	1.32	1.76	1.6	.2168
17	27	0.17	23	1.09	1.26	2.8	.2175
22	23	0.17	20	1.04	1.36	2.7	.2184
26	23	0.17	21	1.03	0.77	4.7	.2175
29	23	0.17	22	1.09	0.73	4.6	.2171
[f]Oct. 3	24	0.17	21	1.03	1.40	2.6	.2172

[a] Cavity *A* (cylindrical) and matching simulator coil *A*.
[b] Cavity *A* modified, and simulator coil *B*.
[c] Cavity *B* (re-entrant sleeve) and simulator coil *C*.
[d] Cavity *C* (cylindrical) and simulator coil *D*.
[e] Simulator coil *E*.
[f] Simulator coil *F*.
[g] Data discarded in final calculation.

A microwave run was analyzed to yield g_J/g_p in the following way. A curve such as Fig. 6 was drawn and the line-center "cross-over" determined graphically. This yielded the field value for microwave resonance in units of the regulator frequency, which was then converted to simulator frequency by using the observed average difference frequency between the regulator and simulator. In obtaining this difference frequency account was taken of field-distribution changes between simulator runs and tracking errors of the two BC-221 meters. The simulator frequency thus obtained is ν_p. This, together with the measured microwave frequency ν was substituted into Eq. (1) to determine g_J/g_p where g_p refers to protons in the cylindrical mineral oil sample.

Table I gives the results for the forty-four runs. The observed line width was probably due primarily to inhomogeneity broadening. However, calculations indicated that the contributions due to wall and interatomic collisions and to Doppler effect were of nearly the same order of magnitude. Some saturation broadening was present in the early runs. The assigned errors appearing in Table I were based on two independent measures of

TABLE II. Summary of results by groups of runs.[a]

Group	Number of runs[b]	All data	Retained data
December	5(0)	658.2253±0.0015	...
January	9(7)	658.2177±0.0008	658.2168 ±0.0007
March	1(0)	658.2209±0.0018	...
May–June	6(4)	658.2196±0.0011	658.2186 ±0.0006
June	10	658.2175±0.0004	658.2175 ±0.0004
All π_1	31(21)	658.2180±0.0004	658.2175 ±0.0003
June–July	4	658.2168±0.0002	658.2168 ±0.0002
Sept.–Oct.	9	658.2172±0.0002	658.2172 ±0.0002
All π_2	13	658.2171±0.0002	658.2171 ±0.0002
All runs	44(34)	658.2176±0.0003	$658.2173_4+0.0001_9$

[a] The precision estimate shown is the statistical standard error in the weighted mean.
[b] The figure in parentheses is the number of runs retained in the final calculation.

precision. The first is a measure of the indeterminacy in the microwave resonance field contributed by the microwave run. This was computed from the observed line width, with additions from asymmetry in the line and from crossover indeterminacy caused by noise. A representative, symmetric line of 0.06 gauss "peak-to-peak" width (20 ppm in field, or the equivalent of 170 kc/sec in microwave frequency) was taken as an assigned error of 1.0 ppm. The second is a measure of the indeterminacy in the microwave resonance field contributed by the observed shift in the simulator-regulator field difference before and after a microwave run. This assigned error was increased for long time intervals between simulator runs; minor contributions were assigned from estimates of the mechanical stability of the apparatus in the magnet gap, the dependability of the alignment procedure for the proton-resonance circuits, and the care exerted in evaluating calibration errors and frequency drifts in the BC-221 frequency meters. In later runs, a typical observed shift in the regulator-simulator differential field of 0.004 gauss (1.3 ppm) for simulator runs one hour apart was taken as an error of 0.5 ppm. Suitable lower limits were imposed on the various assigned errors to prevent fortuitous runs from receiving undue weight. The weighting factors used were the reciprocals of the sum-of-squares of the two indices. The highest-weighted run contributed one-fifteenth of the total weight of the 44 runs. Measurement and control of the microwave frequency were sufficiently accurate to provide no contribution to the assigned error.

A summary of the weighted means and standard errors obtained from different groups of runs, representing major modifications in apparatus and procedure, is given in Table II. A weighted histogram of all runs appears in Fig. 7, together with the normal error curve of corresponding mean and standard deviation.

One immediately observes the large number of anomalously high values which were obtained. Generally these runs occurred among the earlier measurements, and consistently received low weights on the basis of the error indices just discussed. Nevertheless, we are unable to account for this obvious asymmetry of wide deviations. In view of the consistency of the more recent runs, we feel justified in rejecting these extreme values as statistically unacceptable, and further we believe that the effects which caused these extreme values were not present in the majority of the runs and do not influence the mean value of the remaining distribution. The value of g_J/g_p above which runs are rejected is somewhat arbitrary, but not very critical; we have chosen to discard the ten runs (5 percent of total weight) above the arrow in Fig. 7. A summary of the data remaining appears in the final column of Table II; the appropriate error curve is shown in Fig. 7.

We take as our best value,

$$-g_J/g_p(\text{mineral oil})=658.21734\pm0.00019,$$

where the proton resonance is observed in our finite-cylinder mineral oil samples. The error shown is the statistical standard error in the weighted mean.

DIAMAGNETIC AND RELATIVISTIC CORRECTIONS

In precision nuclear resonance experiments several corrections to the magnetic field at the nucleus must be considered if accurate values of nuclear moments are sought.[18] In this experiment, nuclear resonance is used as a magnetic field standard and the only relevant considerations are those of reproducibility of the standard. While mineral oil is a very convenient working standard, previous measurements have shown that there are significant variations in the diamagnetic shielding of the protons in different samples of mineral oil.[19] At

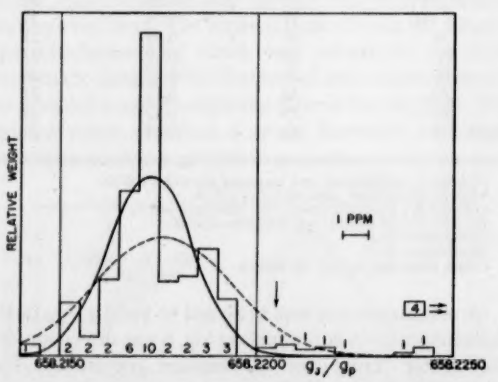

FIG. 7. Weighted histogram of g-factor ratio determinations. The number at the base of each column indicates the number of runs falling within that range. The dashed error curve is fitted before discarding data above the arrow; the solid curve, with maximum at 658.2173, after discarding.

[18] W. C. Dickinson, Phys. Rev. **81**, 717 (1951).
[19] H. A. Thomas, Phys. Rev. **80**, 901 (1950); H. S. Gutowsky and R. E. McClure, Phys. Rev. **81**, 276 (1951). They obtain shifts from H_2 of 1.6 and 3.7 ppm, respectively, for spherical samples.

present, molecular hydrogen is probably the most reproducible standard for field measurements. It is also a substance for which reliable diamagnetic corrections have been calculated.[20]

We compared the frequency of proton resonance in a finite-cylindrical sample of our mineral oil (Squibb Heavy Californian Liquid Petrolatum) with that in molecular hydrogen at about 70 atmospheres pressure. This comparison was made in a thick-walled brass chamber fitted with a plunger by means of which the mineral oil sample (in a polystyrene capsule) could be alternately inserted in the proton-detector coil or withdrawn, leaving only H_2 in the rf field of the coil. The oil samples were of the same size and shape as in our simulator coils (length/diameter = 3.1). Thus the proton frequency shift between oil and H_2 can be applied directly to give g_J/g_p(spherical H_2). We measured, for our sample and geometry, a relative field shift,

$$\Delta H/H = (2.1 \pm 0.1) \text{ ppm}.$$

The sign is such that the field at the protons in oil is lower than in H_2 for a given external field.

Table III summarizes the numerical values we obtain for various relevant corrections. The entries for proton resonance in a finite-cylinder of mineral oil and for a spherical H_2 sample are direct measurements from our experiments. The entry for a spherical mineral oil sample is included for comparison with the Columbia results[6] and uses their value for the susceptibility of oil in making the bulk demagnetization correction. This correction was not measured by us and the g_J/g_p(spherical oil) ratio is less reliable than other entries in this table.

TABLE III. Summary of results for particular proton samples.

Proton resonance environment	Magnitude of shift from spherical H_2 (ppm)	$-g_J/g_p$	$-g_s/g_p$
Finite-cylinder mineral oil	$+2.1 \pm 0.1$[a]	658.2173[a] ± 0.0002	
Spherical mineral oil	$+3.2 \pm 0.3$[b]	658.2181 ± 0.0003	658.2298 ± 0.0003
Spherical H_2	...	658.2160 ± 0.0002	658.2277 ± 0.0002
Unshielded protons	-26.6 ± 0.3[c]	658.1984 ± 0.0003	658.2101 ± 0.0003

[a] Primary experimental measurements.
[b] Directly comparable with the measurements cited in reference 19.
[c] Taken from Newell, reference 20.

[20] N. F. Ramsey, Phys. Rev. **78**, 699 (1950); G. F. Newell, Phys. Rev. **80**, 476 (1950).

The electron g-factor observed in this experiment is $g_J(^2S_{\frac{1}{2}}\,\mathrm{H})$. To obtain g_s for a free electron one must apply a relativistic correction on account of the binding of the electron in the hydrogen atom,[21]

$$\begin{aligned} g_J(^2S_{\frac{1}{2}}\,\mathrm{H})/g_s &= \tfrac{1}{2}[2(1-\alpha^2)^{\frac{1}{2}}+1], \\ &= 1-\alpha^2/3-\alpha^4/12-\cdots, \\ &= 1-17.75\times 10^{-6}. \end{aligned}$$

This modification is included in the final column of Table III. A thorough discussion of other considerations in reducing g_J to g_s is given in reference 5.

DISCUSSION

The primary quantity measured by Koenig, Prodell, and Kusch[5] is

$$-g_J/g_p(\text{spherical mineral oil}) = 658.2171 \pm 0.0004.$$

(The precision estimate shown here with their result is again the statistical standard error.) For this same quantity we obtain from Table III,

$$658.2181 \pm 0.0003.$$

The difference of 1.5 ppm is consistent with the estimated precision of the two measurements, especially when allowance is made for possible differences between mineral oil samples.

Gardner's measurement[6] of

$$-2g_l/g_p = 657.475 \pm 0.004$$

was made using proton samples of water and mineral oil of presumably spherical geometry. Our g_s/g_p result most comparable to Gardner's conditions is 658.2298. Combining the two results, we obtain

$$\begin{aligned} g_s &= 2(g_s/g_p)(g_p/2g_l) \\ &= 2(1.001148 \pm 0.000006), \end{aligned}$$

taking g_l as unity and again expressing precision as a standard error. The value obtained by Karplus and Kroll from quantum electrodynamical calculations was[7]

$$g_s = 2(1.00114536).$$

The agreement is remarkable although unchanged, of course, from the results of Koenig, Prodell, and Kusch on account of the limited precision of Gardner's measurement.

The authors wish to acknowledge the assistance of Dr. E. B. Rawson in the development of the apparatus and techniques used here.

[21] G. Breit, Nature **122**, 649 (1928); H. Margenau, Phys. Rev. **57**, 383 (1940); N. F. Mott and H. S. W. Massey, *Theory of Atomic Collisions* (Clarendon Press, Oxford, 1949), second edition, p. 72.

Energy Levels in Pb^{206} from the Decay of Bi^{206}

D. E. ALBURGER,*
Nobel Institute of Physics, Stockholm, Sweden, and Brookhaven National Laboratory,† Upton, New York

AND

M. H. L. PRYCE, *Clarendon Laboratory, Oxford, England*

(Received June 14, 1954)

The energies, spins, and parities of 10 excited states in Pb^{206} and the probable energies, spins, and parities of two additional states have been established by studies of 6.4-day Bi^{206} decay. The experiments include—intensity and precision energy measurements on the conversion lines in a double-focusing spectrometer; coincidences between pairs of K-conversion lines in a two-lens "spectrogoniometer"; coincidences between gamma rays and conversion electrons in a modified intermediate-image spectrometer; discovery of a 145 ± 15 microsecond isomeric state decaying by either of two $E3$ transitions; examination of the low-energy conversion spectrum; and relative gamma intensity measurements with a scintillation spectrometer. The adopted decay scheme contains 28 of the observed transitions and satisfies all of the conditions imposed by the energy and coincidence measurements. A few additional very weak transitions are unassigned. It is shown from a theoretical analysis based on the shell model that the observed levels are in agreement with the approximate calculations. Eleven gamma rays decaying with a half-life of 14 days are assigned to Bi^{205}.

I. INTRODUCTION

THE nucleus Pb^{206} differs from the double closed-shell Pb^{208} by two neutrons, and its level structure should thus be largely predictable[1] in terms of the shell model. It is a stable nucleus, which also occurs as the end point of three known radioactivities. Of these, the beta decay of Tl^{206} leads always to the ground state[2] so that no information concerning the level structure of Pb^{206} is obtained. The alpha decay of Po^{210} goes mainly to the ground state, but in a small fraction of the disintegrations leaves the Pb^{206} nucleus in its first excited state at 803 kev. The other activity is the 6.4-day electron capture of Bi^{206} which leaves the Pb^{206} in a highly excited state and is followed by a complex spectrum of gamma rays. Alburger and Friedlander[3] found fifteen gamma rays in Bi^{206} decay, including one whose energy agreed with the 803-kev radiation in the decay of Po^{210}.

Evidence on the excited levels of Pb^{206} can also be derived[4] from the reaction $Pb^{207}(d,t)Pb^{206}$, which indicates levels at 0.86, 1.37, 1.71, 2.22, and 3.03 Mev, but these are probably unresolved groups of levels.

The present paper reports a continuation of the investigation of the spectrum of Bi^{206}, using more precise and powerful techniques, in the course of which twenty-eight gamma rays have been established, all of which can be fitted into a term diagram, together with a number of radiations of very low energy whose precise interpretation is still uncertain. Except for four gamma rays and two energy levels, the assignment of energies, spins, and parities of the levels, and multipole character of the gamma rays, can be regarded as reasonably unambiguous. Twelve excited levels are involved in all, of which one (at 2200.3 kev, spin 7−) is isomeric with half-life 145 ± 15 microseconds.[5] Capture takes place almost entirely into two 5− levels at 3280.1 and 3403.5 kev.

Shortly after the publication of the earlier experimental work[3,4] a theory of the energy levels of Pb^{206} was proposed by Pryce,[1] based on the shell model and the supposedly known level scheme of the simpler nucleus Pb^{207}, and correlated with the experimental data. At that time it was not possible to establish an unambiguous level scheme and little progress was made in the correlation between theory and experiment. To unravel as complex a spectrum as that of Bi^{206} it is necessary to measure gamma-ray energies to very high precision, and detailed coincidence measurements are very desirable. The present work has been performed with this intention. As will be seen in Sec. X, the agreement between the predictions of the shell model and the observed level scheme is very good. In addition to the levels actually observed, the theory predicts many more, but their nonappearance can plausibly be explained in terms of low branching probabilities in the de-excitation process following electron capture.

II. Bi^{206} CONVERSION ELECTRON SPECTRUM ABOVE 90 KEV

Measurements on the internal conversion electrons above 90 kev occurring in the decay of Bi^{206} were made in the 50-cm radius double-focusing spectrometer[6] at the Nobel Institute. This instrument proved to be excellent for these investigations because of its high resolution and luminosity, low background of scattered electrons, and the ease with which precision determina-

* Research at the Nobel Institute of Physics was supported by a National Science Foundation Fellowship.
† Under contract with the U. S. Atomic Energy Commission.

[1] M. H. L. Pryce, Proc. Phys. Soc. (London) A65, 773 (1952).
[2] D. E. Alburger and G. Friedlander, Phys. Rev. 82, 977 (1951).
[3] D. E. Alburger and G. Friedlander, Phys. Rev. 81, 523 (1951).
[4] J. A. Harvey, Phys. Rev. 81, 353 (1951); Can. J. Phys. 31, 278 (1953).
[5] D. E. Alburger and M. H. L. Pryce, Phys. Rev. 92, 514 (1953).
[6] Hedgran, Siegbahn, and Svartholm, Proc. Phys. Soc. (London) A63, 960 (1950).

tions could be made. Many different runs were carried out under various conditions of source size and strength and spectrometer resolution. Sources were made in the Institute's large cyclotron by bombarding lead targets with an internal beam of deuterons. Carrier-free separations of the bismuth were then performed according to the chemical methods already described[3] and the activity was electroplated on copper foils using a strip of Pt as an anode. The copper foil forming the cathode was soldered to an enamel-coated wire and immersed into the solution. In order to define the area of the active deposit, all other parts of the foil and the solder connection to the lead-in wire were painted with zapon having nail polish added as a visual aid. A potential of 3 volts and plating times between 1 minute and 2 hours were used. Generally there was never any observable spreading of even the lowest energy lines as a result of source thickness.

The first survey run was made at a spectrometer resolution of 0.5 percent using a 6 mm×14 mm sample which had been prepared from activity produced by a 200 microampere-hour bombardment at 25 Mev. Many of the general features of the electron spectrum which had been observed earlier[3] were confirmed but quite a few new lines appeared. Subsequent study showed that many of these new lines decayed at a slower rate than 6-day Bi^{206}. Reduction of the beam energy to 16 Mev by moving in the cyclotron target to a smaller radius eliminated all of the more slowly decaying lines in later work. Further discussion of these lines will be given in the next section. Two new 6-day transitions found in this run were observed because of the improved resolution, together with two weak K lines corresponding to gamma rays of 386 and 1596 kev which had been missed in the earlier investigations. In view of the absence of gamma rays able to produce photo-neutrons[7] from deuterium when the detector was exposed to Bi^{206} sources, the search for new conversion lines was not continued above 2.2 Mev in the double-focusing spectrometer.

Certain portions of the spectrum were then examined in more detail using a 2 mm×14 mm source and a spectrometer resolution of 0.22 percent. One region of particular interest is shown in Fig. 1. It had already been established[3] that the 803.3-kev transition corresponds to the first excited state of Pb^{206} and that this gamma ray is the same as the one appearing in Po^{210} alpha decay to Pb^{206}. A K to $(L+M)$ ratio of 3.7 had been obtained for the Po^{210} internal conversion electrons but a determination of the corresponding ratio for Bi^{206} was not possible at 1.2 percent resolution owing to the presence of the two K lines masking the 803-kev L and M electrons. Alpha-gamma angular correlation experiments[8] on Po^{210} by DeBenedetti and Minton suggested that the 803-kev state is 2+, in agreement with the

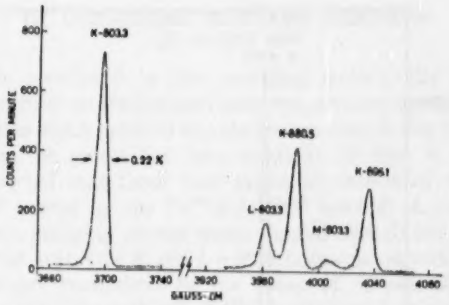

FIG. 1. Conversion electrons of the 803.3-kev transition measured in the double-focusing spectrometer showing the separation of the L and M lines from two other K lines at 0.22 percent resolution.

predicted character of the first excited state of an even-even nucleus.[9] However the K to $(L+M)$ ratio of Po^{210} conversion electrons seemed to be too low for an $E2$ transition. It was suggested[10] by Goldhaber and Hill that a weak gamma ray of about 880 kev might be present in Po^{210} decay and if so its K conversion line could make a contribution to the $(L+M)-803$ line thereby accounting for the low K to $(L+M)$ ratio observed for the 803 kev transition. In this case the $(L+M)$ line of the proposed 880-kev gamma would be resolved and might be visible. To test this hypothesis a new 500-Mc Po^{210} source was obtained through the U. S. Atomic Energy Commission by one of us (D.E.A.) and the conversion electron spectrum of Po^{210} was re-examined in April, 1952, with the Brookhaven lens spectrometer. A careful search failed to reveal the $(L+M)$ line of the suggested 880-kev transition. The upper limit placed on a possible 880-kev K-line intensity, assuming even the largest possible $K/(L+M)$ ratio, was far too small to affect appreciably the $K/(L+M)$ ratio of the 803-kev transition. This remeasurement was made at 2 percent resolution and yielded a transition energy of 804±3 kev and a K to $(L+M)$ ratio of 3.8±0.3 in agreement with the earlier results. It was concluded[11] that the empirical curves of $K/(L+M)$ as a function of Z^2/E may not be accurately valid at high Z.

Returning to the Bi^{206} data of Fig. 1 it may be seen that complete resolution of the L and M electrons of the 803.3 kev transition is achieved at 0.22 percent resolution. A K to L ratio of 4.8±0.3 and a K to $(L+M)$ ratio of 4.0±0.3 are obtained from this curve. The latter agrees with the Po^{210} results discussed above and further confirms that the same transition is involved in both the Po^{210} and Bi^{206} decay processes. It is shown in Sec. XI. that this K/L ratio agrees well with the theoretical value for $E2$ radiation.

Another part of the spectrum studied at 0.22 percent

[7] E. der Mateosian and M. Goldhaber, Phys. Rev. **78**, 326 (1950).
[8] S. DeBenedetti and G. H. Minton, Phys. Rev. **85**, 944 (1952).
[9] M. Goldhaber and A. W. Sunyar, Phys. Rev. **83**, 906 (1951).
[10] M. Goldhaber and R. D. Hill, Revs. Modern Phys. **24**, 179 (1952).
[11] D. E. Alburger, Phys. Rev. **92**, 1257 (1953).

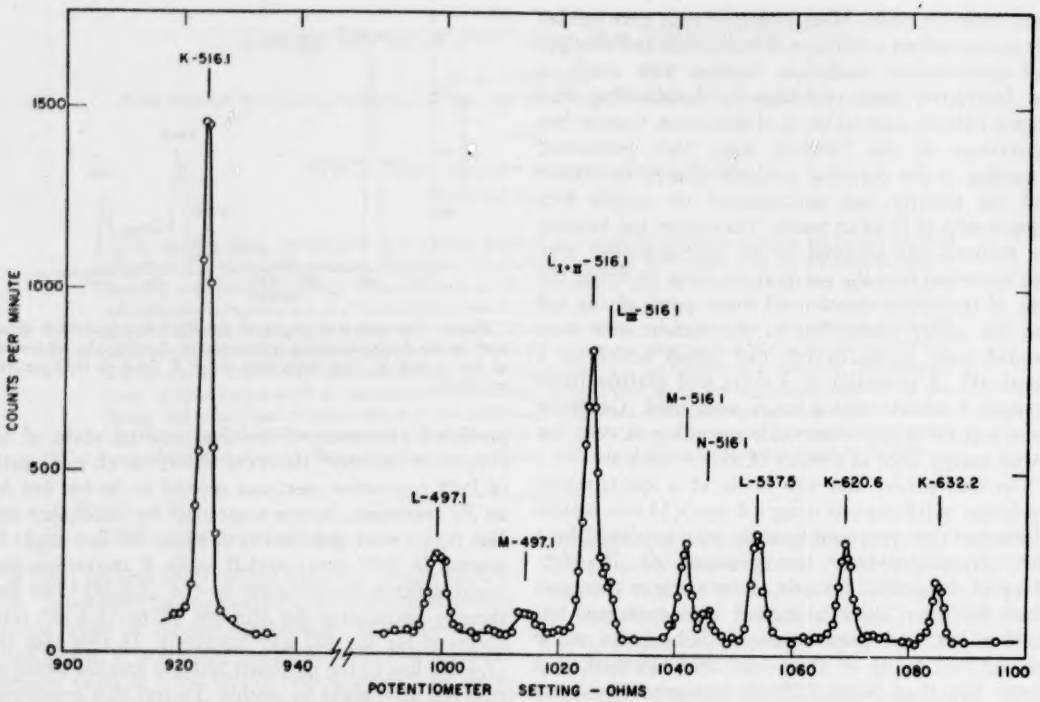

FIG. 2. Bi^{206} conversion spectrum at 0.22 percent resolution in the region of lines corresponding to the 516.1-kev 145-microsecond $E3$ transition.

resolution is given in Fig. 2. This shows a number of lines including the conversion electrons corresponding to the 516.1-kev $E3$ isomeric transition in Pb^{206}. Relative conversion intensities of this transition, given in a report already published,[5] were taken from this figure and are listed again in Table XII together with the theoretical K/L_{I+II} ratio.

Precision determinations were made on the 19 strongest K-conversion lines of Bi^{206} following techniques similar to those previously developed at the Nobel Institute. The procedure consisted of comparing the extrapolated high-energy momentum edges of the Bi^{206} K lines with those of standard sources in the double-focusing spectrometer. Three comparison standards were available whose momenta are known with an accuracy of better than 2 parts in 10^4 and which are well spaced with respect to the Bi^{206} spectrum. These were the ThF line at 1388.55±0.2 gauss-cm,[12] the Cs^{137} K-conversion line at 3381.28±0.5 gauss-cm,[13] and the K-conversion line of the 1.3325±0.0003-Mev gamma ray[14] of Co^{60} which lies at 5879.2 gauss-cm. After carefully demagnetizing the spectrometer magnet, the high-energy edges of all the Bi^{206} lines and the three standards were run in order of increasing momentum. This required changing sources at the proper point for inserting each standard. To ensure a fixed geometry each source was placed behind a 2-mm wide window whose position in the spectrometer could be reproduced accurately. ThF sources were made by electrostatic collection on copper strips from thorium-active deposit and the Co^{60} source was the same as that used in the precision determinations already reported.[14] Two complete sets of comparison runs were made at a resolution of 0.25 percent. Final values were taken from the second run in which the calibration constants of the spectrometer derived from the three standard lines were as follows:

ThF	2.80755 gauss-cm/ohm
Cs^{137}	2.80727 gauss-cm/ohm
Co^{60}	2.80790 gauss-cm/ohm

These figures indicate a surprisingly good linearity of the instrument over a factor of 4 variation of field setting. Because the spread of only 2 parts in 10^4 is well within the errors of the absolute values a fixed calibration constant of 2.80757 gauss-cm/ohm was adopted.

It is estimated that the errors of the 19 accurately determined Bi^{206} gamma rays given in Group A of Table I are about 5 parts in 10^4. These values were obtained by adding 88.0 kev to the energy of each K line. In the previous work[3] the conversion electrons had been measured in a lens spectrometer and the

[12] G. Lindström, Phys. Rev. 83, 465 (1951).
[13] Lindström, Siegbahn, and Wapstra, Proc. Phys. Soc. (London) B66, 54 (1953).
[14] Lindström, Hedgran, and Alburger, Phys. Rev. 89, 1303 (1953).

following transition energies in kev were reported: 182, 234, 260, 341, 396, 470, 505, 536, 590, 803, 880, 889, 1020, 1097, and 1720. Re-examination of the old data revealed that numerical errors had been made in obtaining the energies of the 470 and 505 kev gamma rays, which accounts for the large discrepancies with the values 497.1 and 516.1 kev in Table I. Otherwise the agreement is 1 percent or better for corresponding lines. The 590-kev gamma finds no counterpart in Table I because the strong conversion line from which it had been derived turned out, from the present experiments, to be the L line of a 516.1-kev isomeric transition rather than K 590. Of the remaining transitions in Group A of Table I, gammas 5 and 18 had been missed in the old work because of their low conversion intensities and 10 and 11 were in an unresolved region. The K line of number 12 had been observed but no interpretation was given.

In further work with the double-focusing spectrometer, a strong source was prepared from a sample made at 16-Mev bombarding energy. A number of new and very weak 6-day lines was observed, some of which were only 10 percent as strong as the background rate. Their transition energies which are given in Group B of Table I were determined, except for the 123.6-kev transition, from the positions of the K peaks referred to the neighboring and more accurately measured Bi^{206} lines listed in Group A of Table I. A resolution of about 0.5 percent was used and errors were estimated to be of the order of 0.15 percent. The 123.6-kev transition was determined by interpreting the observed electron line as L-123.6. Later the corresponding K line was found with the intermediate-image spectrometer. Among the gamma rays given in Group B of Table I, the K line of the 816.3-kev transition was barely visible making this the only doubtful gamma ray on the list. Relative conversion intensities and K/L ratios are discussed in Sec. XI. There was only one weak electron line observed in the double-focusing spectrometer, having an energy of 102.2 kev, to which no firm assignment has been made.

TABLE I. Bi^{206} transition energies in kev.

A. From *K*-line determinations accurate to 5 parts in 10^4.		
1. 184.1	8. 516.1	15. 895.1
2. 234.3	9. 537.5	16. 1018.8
3. 262.8	10. 620.6	17. 1098.6
4. 343.4	11. 632.2	18. 1596.3
5. 386.0	12. 657.3	19. 1719.7
6. 398.1	13. 803.3	
7. 497.1	14. 880.5	
B. From *K*-line determinations accurate to 1.5 parts in 10^3.		
20. 123.6	24. 753.9	27. 1405.2
21. 202.5	25. 816.3	
22. 313.6	26. 841.7	
23. 739.9		

III. CONVERSION ELECTRON SPECTRUM OF 14-DAY Bi^{206}

As mentioned in the preceding section, the first survey run on the bismuth spectrum revealed a number of lines which decayed at a slower rate than 6-day Bi^{206}. Since the source had been made at 25 Mev it was suspected that these lines might be associated with Bi^{205} formed by the $Pb^{206}(d,3n)Bi^{205}$ reaction. A study over a period of several weeks showed that all but one pair of lines, (the K and $L+M$ lines associated with the 1064-kev transition[11] in the decay of 50-year Bi^{207}) were decaying with a half-life approximately twice as long as that of Bi^{206} or consistent with the 14.5-day period[15] of Bi^{205}. It was reasoned that if the $(d,3n)$ reaction were responsible, the threshold would be high and production of this isotope would not occur at a lower bombarding energy. Later a bismuth source from a 16-Mev bombardment was examined and only very slight indications of even the strongest of these 14-day lines were detected. It was concluded that if the isotope and reaction assignments were correct, then the $Pb^{206}(d,3n)$ threshold must be in the neighborhood of 16 Mev.

Table II gives the energies, relative K-line intensities, and approximate K/L ratios of these transitions. The energies, which are accurate to about 0.2 percent, seem to have little, if any, correlation with the Bi^{205} gamma rays of 0.431, 0.527, 0.550, 0.746, and 1.84 Mev reported[16] by Karraker and Templeton. Of their values the last is close to k of Table II but it would then be difficult to understand why the much stronger 1766.3-kev transition had not been observed. More recently Wapstra has reported[17] a 1.77-Mev gamma ray in bismuth sources made by 27-Mev deuteron bombardment of lead and tentatively assigns this to Bi^{205} from its decay rate. His gamma ray probably corresponds to i of Table II.

The K/L ratios given in Table II cannot be considered as very satisfactory inasmuch as only one run

TABLE II. Data on 14-day lines assigned to Bi^{206}.

	E_γ (kev)	Relative K-line intensity	K/L
a.	284.4	100	
b.	703.7	87	~5
c.	911.6	8.9	
d.	988.6	22	
e.	1044.6	31	~4
f.	1074.1	2.9	
g.	1189.8	4.0	~4
h.	1615.4	2.4	~4
i.	1766.3	40	5.8
j.	1777.8	4.4	
k.	1864.2	1.6	~5

[15] Hollander, Perlman, and Seaborg, Revs. Modern Phys. **25**, 469 (1953).
[16] D. G. Karraker and D. H. Templeton, Phys. Rev. **81**, 510 (1951).
[17] A. H. Wapstra, thesis, Amsterdam, 1953 (unpublished).

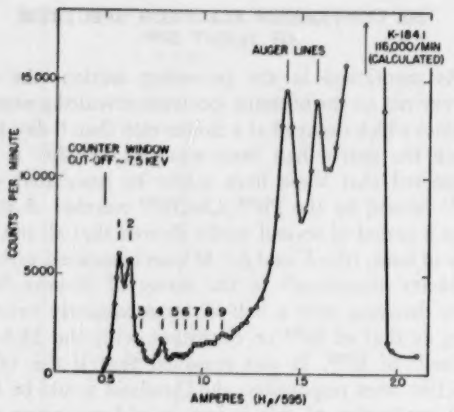

FIG. 3. The low-energy electron spectrum of Bi^{206} as observed in the intermediate-image spectrometer.

was made and furthermore the presence of many Bi^{206} lines made the measurements inaccurate. A possible isomeric transition in Pb^{205} is not suggested by the conversion data.

Although it is too early to propose a decay scheme for Bi^{205}, there are three cascade crossover relationships, given in Table III, which hold within the errors of measurement. From these several possibilities for the level scheme of Pb^{205} suggest themselves, one of which would include states at 703.7, 988.6, 1615.4, and 1777.8 kev. There may well be other 14-day lines which were too weak to be observed in the present investigation. A suggested way of studying the spectrum would be to make an intense bombardment of lead with deuterons ~25 Mev and then allow the target to decay before performing the chemical separation and spectrometer runs. Each month of decay would reduce the amount of Bi^{205} by a factor of 4 but at the same time the Bi^{205}/Bi^{206} ratio would increase by a factor of 4. After a suitable period the spectrum would be relatively free of Bi^{206} and there might be hope of making a more conclusive examination of the Bi^{205} conversion electrons and perhaps even doing coincidence experiments.

IV. LOW-ENERGY LINES OF Bi^{206} —AUGER INTENSITIES

In order to have more complete information on the entire conversion spectrum of Bi^{206}, the investigation of electron energies was extended below 96 kev by means of the Slätis-Siegbahn intermediate-image spectrometer[18] at the Nobel Institute. This instrument is more satisfactory than the double-focusing spectrometer at very low energies if only moderate resolution is desired. The spectrum was run according to standard procedures using a 0.5-cm diameter electroplated source, a spectrometer resolution of 4 percent, and a counter window with a 7.5-kev cutoff. Figure 3 shows the results obtained. Unfortunately the peaks labelled 5, 6, and 8 do not show up well in the drawing but these could be reproduced consistently in three separate studies which were made to establish that all of the lines were decaying with a half-life of 6 days. The energies of the lines and their intensities are listed in Table IV. It is estimated that the momentum values from which the energies were derived are accurate to 2–3 percent. This is consistent with the observed energies of the main Auger groups which, according to known binding energies, should be

$$(K-L)-L\cong 57 \text{ kev},$$
$$(K-L)-M\cong 69 \text{ kev}.$$

Intensities are given in electrons per 100 disintegrations, this normalization having been made by measuring the K-803.3 line and assigning the latter a value of 0.85 electron per 100 disintegrations as in Table XI. Since the peak heights were taken rather than areas the actual total K Auger intensity is probably greater than the 3 percent indicated by Table IV.

It is of interest to consider the K Auger intensity in relation to the decay scheme. K x-rays or Auger electrons can arise following either K electron capture or internal conversion in the K shell. According to the sum of numbers in column 4, Table XI, internal conversion produces K-shell vacancies in about 45 percent of the disintegrations. Massey and Burhop have calculated[19] the internal conversion probability of K_α x-rays and find this to be 5 percent at $Z=82$. Taking the gamma-ray data into account, the K Auger yield would be 7 percent if all of the primary excitations involved K electron capture, or 2 percent if only L capture occurs. Because of the large probable errors in the intensities of these low energy lines and the likelihood that the K Auger intensities given in Table IV are low, the experimental results cannot be used as an argument that there is only a small amount of K capture. Without more accurate data it is not possible to derive a meaningful value for the ratio of K to L capture or information about the disintegration energy which might be derived from such a ratio.

The only two low-energy lines to which definite assignments have been made, except for the Auger lines, are Nos. 4 and 9. No. 9 seems to fit as the K line of the 123.6-kev gamma ray whose L line was observed

TABLE III. Bi^{205} Cascade cross-over relations derived from the transitions listed in Table II.

Gamma	Sum (kev)	Possible crossover	Difference in energy (kev)
$a+b$	988.1	d	0.5
$b+c$	1615.3	h	0.1
$b+f$	1777.8	j	0.0

[18] H. Slätis and K. Siegbahn, Arkiv Fysik 1, 339 (1949).

[19] H. W. S. Massey and E. H. S. Burhop, Proc. Roy. Soc. (London) A153, 661 (1936).

as mentioned in Sec. II while No. 4 is the proposed K line of a 107.2-kev gamma. It is possible that No. 8 is the K line of a 117-kev gamma whose L line is the previously unassigned 102.2-kev electron found in the double-focusing spectrometer. On the other hand the 102.2-kev line may be an M line corresponding to the 107.2-kev transition proposed above. Energetically, lines 1, 2, and 3 could be Auger electrons arising from L-shell vacancies. There does not seem to be enough published information on L Auger effects to establish such assignments, particularly in regard to the intensities of such lines relative to the K Auger peaks. Judging from the appearance of Fig. 3 it is likely that other unresolved lines exist in Bi^{206} at these low energies and, if so, a study at higher resolution would be profitable.

TABLE IV. Low-energy electron lines of Bi^{206}. Numbers refer to peaks in Fig. 3.

Line	Energy (kev)	Intensity (electrons per 100 disintegrations)*
1	10.2	0.99
2	12.3	0.89
3	14.3	0.23
4	19.2	0.23
5	23.2	0.05
6	26.0	0.02
7	28.8	0.08
8	31.8	0.04
9	36.2	0.07
Auger 1	58.6	1.8
Auger 2	71.1	1.1

* Taken from peak height. No window corrections have been made.

V. SEARCH FOR POSITRONS FROM Bi^{206}

During the course of the low-energy conversion line measurements with the intermediate-image spectrometer described in the preceding section, an attempt was made to detect positrons emitted in the decay of Bi^{206}. A set of spiral baffles already present in the instrument served to reject positive or negative electrons as desired. Using the same source and apertures as in the preceding section, counts were taken at a number of current settings between 300 and 7500 gauss-cm (8 kev to 1.8 Mev). An upper limit of 10 counts per min could be placed on the yield of positrons at any point over this region. Considering the 4-percent spectrometer resolution any positron distribution whose maximum lay below 1.8 Mev could have been detected if the integrated spectrum contained more than 200 positrons per min. The yield of the K-803.3 line with the current reversed was 4460 counts per min. Since this transition occurs once per disintegration and is 0.85 percent converted in the K shell (see Sec. XI) one can conclude that the maximum number of positrons per disintegration is $200/(4450\times117)=1/2600$.

VI. SPECTROGONIOMETER COINCIDENCE EXPERIMENTS

With so many transitions occurring in Bi^{206} decay it became apparent that coincidence studies would be of great assistance in formulating a decay scheme. At first sight it appeared from the complexity of the conversion spectrum that reasonably good resolution would be required in both sections of the apparatus and that coincidences between K conversion electrons would be the most profitable thing to look for.

Available for this purpose was a two-lens spectrometer, or "spectrogoniometer," designed by Professor Kai Siegbahn[20] and located at the Royal Institute of Technology in Stockholm. This instrument can be used for studies of coincidences between electrons of separately selected energy and in addition the angular correlation of these electrons can be measured between 90° and 180°. The latter feature was not used in the present experiments which were always performed at 180°. Prior to this work the instrument had been modified by Professor Siegbahn to use anthracene crystal detectors in conjunction with magnetically shielded RCA 5819 photomultipliers, and to use a coincidence circuit of $\sim8\times10^{-8}$ sec resolving time. The crystals were located inside the vacuum chamber and were optically connected to the 5819's by Lucite end windows approximately 5 mm thick. At the lowest electron energy studied (96 kev) the pulses obtained were large enough to operate the coincidence circuit satisfactorily. Otherwise the performance features of the instrument such as the 0.3 percent transmission at 3 percent resolution of each section, were the same as those already given.[20] The effect of resolution is shown in Fig. 4 which compares the three neighboring K conversion lines of 497.1-, 516.1-, and 537.5-kev transitions as seen in the double-focusing spectrometer at 0.5 percent resolution, the spectrogoniometer at 3 percent, and the intermediate-image spectrometer at 5.5 percent resolution.

Mounting of the sources had to be considered carefully since one of the spectrometers detects electrons which have passed through the source backing. In order to retain the electroplating method a thin copper foil was to be preferred. Suitable foils were prepared by rolling copper sheet down to 7 mg/cm² and then dipping these in a weak solution of nitric acid until the thickness was reduced to 2.5–3 mg/cm². The presence of many pinholes was evidence of considerable nonuniformity of the foils. For mechanical support each foil was soldered to a 2.2-cm diameter brass ring fitting the spectrometer source holder. Electroplating of the activity was then carried out in the usual manner after painting the backing with a zapon nail-polish mixture except for a 0.5-cm diameter central area where the bismuth was deposited. When the plating was completed the zapon on the foil immediately behind the source spot was dissolved off in order to remove unnecessary material.

The effect of the backing on the electrons passing

[20] K. Siegbahn, Arkiv Fysik 4, 233 (1952).

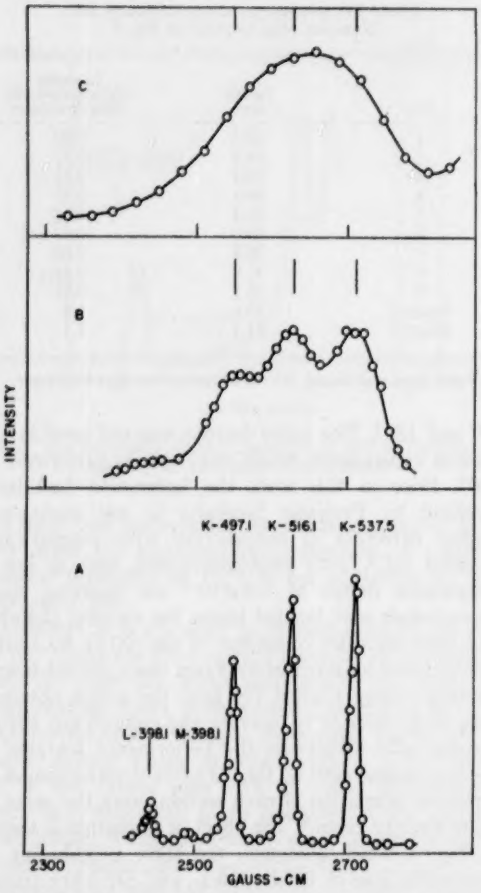

FIG. 4. Bi^{206} K-conversion electrons of the 497.1-, 516.1-, and 537.5-kev transitions as observed in the double-focusing spectrometer at 0.5 percent resolution, curve A; one section of the spectrogoniometer at 3 percent resolution, curve B; and the intermediate-image spectrometer at 5.5 percent resolution, curve C.

through it is shown in Fig. 5 for two K lines of 96-kev and 255-kev energy. Comparison with the curves taken when the activity side was facing the spectrometer shows that the backing causes a considerable distortion of the 96-kev peak but has relatively little effect on the 255-kev peak. In the latter case the line is shifted by about 3 kev consistent with the 2.5-mg/cm² average thickness of the copper. Coincidence studies involving the 184.1-kev transition were always made with its K line entering that spectrometer on the source side of the foil.

With each spectrometer set on the peak of a K line the coincidence rate was measured and compared with the random rate calculated from the singles and the known coincidence resolving time. In the region shown in Fig. 4 the momentum resolution was sufficient to establish separately the coincidence effects at each peak. However, many of the other K lines were not resolved well enough or were too weak to be accessible to this type of measurement. In the latter case the random rate proved to be a limitation. For example, although a net coincidence rate equal to the random rate between K-537.5 and K-803.3 could be observed, no definitive results could be obtained when K-803.3 and K-880.5 (with K-895.1 unresolved) were focused. It was concluded from later knowledge of the multipole orders of these gammas that the coincidence effect between two transitions whose conversion coefficients are both ≤ 1 percent is difficult to establish in this instrument. From the point of view of coincidence experiments the 6.4-day half-life of Bi^{206} is rather ideal, since it is long enough to allow good data to be taken and analyzed yet short enough to permit any given pair of lines to be studied under optimum conditions within a reasonable time.

The results of these experiments are given in Table V. It was not possible to reproduce the coincidence rate of a given pair to better than 50-percent accuracy in widely separated runs. The relative intensity figures given in Table V may therefore be in error as much as a factor of 2. Also listed in the table are the noncoincident pairs, those for which a yield might have been expected on the basis of the line intensities, but which showed no effect above the background rate. Evidently these cases impose equally important restrictions on the decay scheme.

It may be seen from a consideration of Fig. 1 that the K-880.5, K-895.1, L-803.3, and M-803.3 lines are unresolved in the spectrogoniometer because of the 3 percent resolution. While the 343.4–880.5 and 343.4–895.1 pairs have been listed under the "no coincidences" column of Table V, actually coincidences were observed in these runs. The ratio of the K-343.4–K-803.3 coincidences to the rate measured between K-343.4 and this unresolved group was 3.5 ± 1.5. Since this figure is consistent with the $K/(L+M)$ ratio of the 803.3-kev transition derived from Fig. 1, all coincidences with the unresolved group in this case could be attributed to the 803-kev L and M electrons. A similar situation arose when the K-537.5 line was studied together with the K-803.3 line and the unresolved group mentioned above, but in this case the ratio was about 2 and the

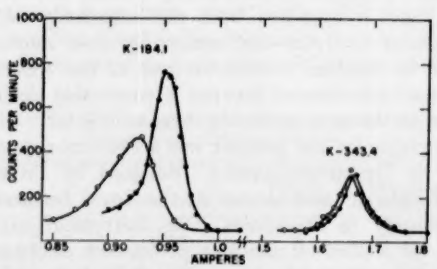

FIG. 5. Electron lines of 96 and 255 kev observed in the spectrogoniometer to study the effect of source backing. Solid points—direct observation. Open circles—electrons observed after passing through the backing.

statistical errors were relatively large. If the L and M electrons of the 803.3-kev transition had not been resolvable otherwise, measurements such as those described here would have been a way to obtain the $K/(L+M)$ ratio in spite of complete masking of the L and M lines.

VII. ELECTRON-GAMMA COINCIDENCE MEASUREMENTS

When it was first suspected that one or both of the highest energy transitions in the decay of Bi^{206} might be in coincidence with other gamma rays in the decay scheme, it was realized that a limited number of coincidence experiments could be done which would not require good resolution in both parts of the apparatus, such as the work described in preceding section. An examination of the strong transitions listed in Group A of Table I shows that gammas No. 18 and No. 19 are 50 percent higher in energy than their nearest neighbor. This suggested looking for coincidences between K-conversion lines and the output of a NaI gamma-ray detector biased so as to respond only to the more energetic radiation.

The equipment selected for this work was the Slätis-Siegbahn intermediate-image beta-ray spectrometer[18] which can be operated at 4 percent resolution when the transmission is 8 percent. Other experiments on Bi^{206} using this instrument have already been described in Secs. IV and V. A spare source-end pole piece of the spectrometer incorporating a NaI crystal and EMI photomultiplier detector was available and had been tested by Dr. J. Moreau. The photomultiplier was equipped with an iron shield and inserted into a large hole machined through the pole piece such that the NaI crystal, held in contact with the face of the tube, came to within several cm of the normal source position. Its location did not result in a very favorable solid angle subtended at the source (i.e., <10 percent) but further insertion would have had a serious effect on the gain of the photomultiplier. A light-piping arrangement had not been constructed at that time. In the photomultiplier position chosen, the variation of the magnetic field from zero to full current caused a pulse-height shift of about 10 percent when Co^{60} gamma rays were measured.

TABLE V. Bi^{206} coincident and noncoincident transitions from electron-electron measurements. Gamma energies in kev.

Coincident pair	Coin./min	No coincidences observed
184.1−262.8	4.0	184.1−343.4
184.1−398.1	10.0	184.1−516.1
184.1−497.1	2.5	184.1−537.5
184.1−880.5 and/or 895.1	0.74	184.1−803.3
184.1−1018.8	0.5	343.4−398.1
343.4−497.1	1.2	343.4−880.5
343.4−516.1	3.4	343.4−895.1
343.4−537.5	7.0	398.1−516.1
343.4−803.3	0.66	398.1−537.5
398.1−497.1	1.2	537.5−880.5
537.5−803.3	0.23	537.5−895.1

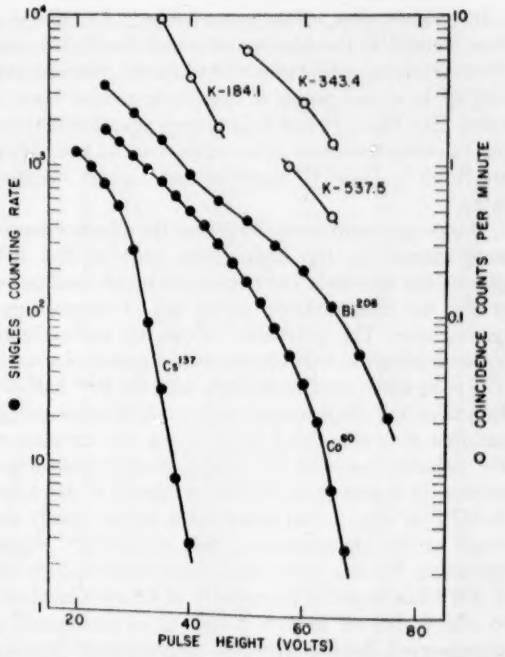

FIG. 6. Integral discriminator curves obtained with the NaI detector used in the electron-gamma coincidence measurements. Curves with solid points are for Cs^{137}, Co^{60}, and Bi^{206}. Open circles indicate the change of coincidence rate with discriminator setting when three different K lines were focused.

A decrease in the resolution of the intermediate-image spectrometer from 4 percent to 5.5 percent when using the largest aperture and a 5-mm diameter source was observed in going from the normal source-end pole piece to the modified one described above. Apparently this was the result of a less favorable magnetic field distribution caused by the large hole for the photomultiplier. Curve C of Fig. 4 shows how the 5.5 percent resolution affected one important region of the conversion electron spectrum.

The outputs of the spectrometer Geiger counter and the crystal detector discriminator were fed to a coincidence circuit having a resolving time of 0.4 microsecond. Bi^{206} sources which had been used in the spectrogoniometer measurements were of the proper size and had decayed to the point where they could be employed for these experiments.

Figure 6 shows the NaI detector integral pulse-height distributions taken with Cs^{137}, Co^{60}, and Bi^{206} sources. These have not been normalized as regards intensity since the main feature of importance here is the rate of falloff in a given pulse-height range. The Bi^{206} curve clearly shows the presence of gamma rays more energetic than the 1.3-Mev Co^{60} radiation and also gives some evidence of complexity.

In the first tests, coincidences between K-conversion lines focused in the spectrometer and the NaI crystal detector output were looked for when the discriminator was set to accept pulses of amplitude greater than 55 volts. (See Fig. 6.) Four K lines gave effects well above the calculated random rates while five did not. These are listed in Table VI together with the net counting rates.

It was important to establish that the effects observed were caused by the high-energy part of the Bi^{206} gamma-ray spectrum and not by pile up of small pulses or by the discriminator curve tail of lower-energy gamma rays. The possibility of pile up was excluded by measuring the coincidences over a period of a week. The rates were found to decrease with the Bi^{206} half-life. Effects of the discriminator curve tail of lower-energy gammas were eliminated by studying the variation of the coincidences with the discriminator pulse-height setting. It is seen from the curves labeled K-343.4 and K-537.5 in Fig. 6 that these rates follow closely the shape of the high-energy portion of the Bi^{206} singles spectrum. On the other hand, coincidences with the K-184.1 line found in the vicinity of 40 volts, as shown in Fig. 6, fall off in such a way as to correspond to gamma-rays having energies intermediate between those of Cs^{137} and Co^{60}. According to any reasonable extrapolation of the K-184.1 curve the coincidence rate at 55 volts would not be detectable above background in agreement with the measurements at this setting. The rates of change of the 803.3 and 880.5 coincidences with discriminator setting were not studied because of the low yield. These lines have been assigned as being in coincidence with the high-energy gammas since the yields of all 4 lines in Table VI at a pulse-height setting of 55 volts are in proportion to the relative K-line intensities.

One other possibility is the effect of pulse addition in the crystal. Thus two members of a triple cascade might give a large pulse which would account for the observed distribution of yield with discriminator setting indicated in Fig. 6. Because of the small solid angle for gamma detection and the low efficiency imposed by the size of the NaI crystal ($\sim\frac{1}{2}$ inch cube), it was not thought that pulse addition could have accounted for the yields observed.

TABLE VI. Coincidence effects between the 1596.3 and/or 1719.7-kev gamma rays and the K-lines of other transitions at a discriminator setting of 55 volts (see Fig. 6). Gamma energy in kev.

Coincidences observed	Counts per min	No detectable coincidences
343.4	3.2	184.1
537.5	0.96	262.8
803.3	0.35	497.1
880.5 and/or 895.1	0.21	516.1 1018.8

It might be questioned how the coincidence or noncoincidence effects listed in Table VI for the 497.1-, 516.1-, and 537.5-kev gamma rays could be established when their individual K lines were not resolved (see Fig. 4). The net coincidence rates when the spectrometer was set at the momenta corresponding to the three peaks were as follows: 537.5−0.96/min, 516.1−0.61/min, and 497.1−0.10/min. A plot of these rates shows that they are roughly consistent with the shape of a conversion line of 5.5 percent half-width centered at the K-537.5 position. While coincidences with the two lower-energy lines cannot be excluded entirely it seems improbable that they occur.

Several cases other than those listed in Table VI were examined but no conclusive results were obtained. The experiments were limited by the spectrometer resolution or by low yields. The K-398.1 line could not be studied because of the unresolved L and M electrons of the 343.4-kev transition, already known to be in coincidence from measurements on the K-343.4 line.

VIII. MEASUREMENT OF THE 145-MICROSECOND ISOMERIC LIFETIME

A report has already been given[5] on the discovery of a 145-microsecond isomeric state in Pb^{206} decaying by $E3$ transitions of 516.1 or 202.5 kev. Revised values of the relative conversion intensities are discussed in Sec. XI. The lifetime measurements were made at the Nobel Institute with a triggered oscilloscope (Tektronix-type 511AD synchroscope) connected through an amplifier and discriminator to the output of a NaI crystal and EMI photomultiplier. The detector was exposed to a weak source of Bi^{206} and the delayed pulse distribution was measured by counting the number of pulses appearing in a slot of fixed width placed over the face of the scope at various distances from the origin pulse. A 10-cm, 500-microsecond base line was used, while the slot width was 1.5 cm corresponding to an interval of 75 microseconds. Recording of the data was done electrically by focusing the image of the scope screen with a large lens onto a 931 photomultiplier whose circuit was designed to avoid spurious pulses from the decay of the scope screen phosphor. The resulting delayed pulse distribution, after subtraction of a calculated random rate, is given in Fig. 1 of reference 5. This shows the presence of a state having a half-life of 145±15 microseconds.

Several further details of these measurements might be worth mentioning. One difficulty in recording the data was caused by background light on the scope screen. An intensity blanking circuit was not available and at the low triggering rates (~25/sec) there was a tendency for the flickering of the background light to cause spurious counts from the 931 photomultiplier. This trouble was minimized as described in the following. The discriminator output pulses, all of equal size, were fed to the scope amplifier whose gain was set at

maximum. Saturation of the amplifier in this manner resulted in pulses whose light was concentrated mostly at the top giving the appearance of detached spots on the screen above the base line. The height of the 1.5-cm wide movable slot was narrowed down to 5 mm and its vertical position was adjusted to a height above the base line such that only these spots could be seen. In this way the ratio of the intensity of light associated with a pulse to the intensity of background light was increased to the point where reliable operation was achieved.

An important part of the measurements was the calibration of the base line. This was done by presenting on the scope screen a 200-kc/sec sine wave from a G. R.-type 805C signal generator. Without disturbing the optical lens, the 931 photomultiplier pulse-detector tube was removed and the image of the scope screen formed by the lens was observed with the aid of a low-power microscope borrowed from the Institute's large comparator. The number of cycles was then counted for each position of the same 1.5-cm wide cardboard mask as employed in taking the delayed pulse distribution. On the average 15 cycles appeared in the slot and these could be counted with an accuracy of about $\frac{1}{3}$ of a cycle. The calibration carried out in this way effectively eliminated all parallax errors inasmuch as the microscope saw closely the same sweep interval as the photomultiplier. It was found that the inherent nonlinearity of the scope sweep combined with the effect of curvature of the tube face required corrections of up to 20 percent near the ends of the trace. Unfortunately it could not be determined whether or not the sweep rate when the calibrating sine wave was impressed was slightly different than under the pulse conditions of the experiment. An accurate pulser time base would have been more suitable for calibration purposes. Actually a more satisfactory determination of the half-life could be made with a larger NaI crystal together with a pulse-time channel analyser.

IX. CONSTRUCTION OF THE TERM DIAGRAM OF Pb^{206}—ENERGIES

With the exception of the weak unassigned electron line of 102.2 kev mentioned in Sec. II and seven of the very low-energy lines discussed in the Sec. IV, the results described thus far all fit in with the Pb^{206} level scheme shown in Fig. 7. This has 10 excited states whose energies, spins, and parities can be assigned with fair certainty and two additional states whose energies, spins, and parities are probable.

Construction of the term diagram was started by assuming 0+ for the ground state and by assigning an energy of 803.3 kev and a spin and parity of 2+ to the first excited state because of the evidence previously discussed in Sec. II. All of the transitions listed in Table I were then considered for possible cascade crossovers involving three or more gamma rays.

TABLE VII. Double cascade crossover relationships involving sums less than 1720 kev. Gamma numbers from Table I.

	Gamma No.	Sum (kev)	Possible crossover gamma No.	Difference (kev)	Agreement with scheme
A. a.	2 +3	497.1	7	0.0	Yes
b.	2 +5	620.3	10	0.3	Yes
c.	2 +6	632.4	11	0.2	Yes
d.	3 +11	895.0	15	0.1	Yes
e.	4 +9	880.9	14	0.4	Yes
f.	5 +11	1018.2	16	0.6	Yes
g.	6 +7	895.2	15	0.1	Yes
h.	6 +10	1018.7	16	0.1	Yes
i.	7 +17	1595.7	18	0.6	Yes
j.	10 +17	1719.2	19	0.5	Yes
B. k.	1 +11	816.3	25	0.0	Yes
l.	1 +12	841.4	26	0.3	No
m.	1 +22	497.7	7	0.6	No
n.	3 +20	386.4	5	0.4	Yes
o.	4 +7	840.5	26	1.2	No
p.	4 +22	657.0	12	0.3	Yes
q.	4 +24	1097.3	17	1.3	No
r.	5 +16	1404.8	27	0.4	No
s.	7 +20	620.7	10	0.1	Yes
t.	9 +21	740.0	23	0.1	No
u.	15 +20	1018.7	16	0.1	Yes
v.	15 +21	1097.6	17	1.0	No
w.	18 +20	1719.9	19	0.2	Yes
x.	21 +22	516.1	8	0.0	Yes
y.	21 +25	1018.8	16	0.0	No
z.	22 +27	1718.8	19	0.9	Yes
aa.	24 +26	1595.6	18	0.7	Yes
C. bb.	107.2+11	739.4	23	0.5	Yes

Pairs of gamma rays whose sums were less than 1720 kev were examined first. These may be divided into two classes—those derived from the 19 accurately measured transitions (Group *A* of Table I) and others including all 27 gammas of Table I. In the first class there are 126 possible pairs of lines and of these the sum energies of the ten cases listed in Group *A* of Table VII agree with a third gamma-ray of Group *A* of Table I within the combined probable errors of the measurements. Every one of these is consistent with the level scheme. Three relations somewhat outside the errors, are the following:

$$1+10=804.7;\quad \Delta E=1.4,$$
$$3+10=883.4;\quad \Delta E=2.9,$$
$$5+7\ =883.1;\quad \Delta E=2.6.$$

The fact that cascade crossovers corresponding to these can be rejected illustrates the importance of precision measurements in the interpretation of this very complex spectrum.

When all 27 transitions of Table I are considered, there are 266 pairs of gammas having sums less then 1720 kev. Group *B* of Table VII lists 17 cases which fall within the errors and involve the less accurately measured gammas rays given in Group *B* of Table I. Nine of these agree with the scheme while 8 do not. If the level diagram is correct, then the latter are chance additions arising from the large number of possibilities and the lower accuracy of the measurements. In

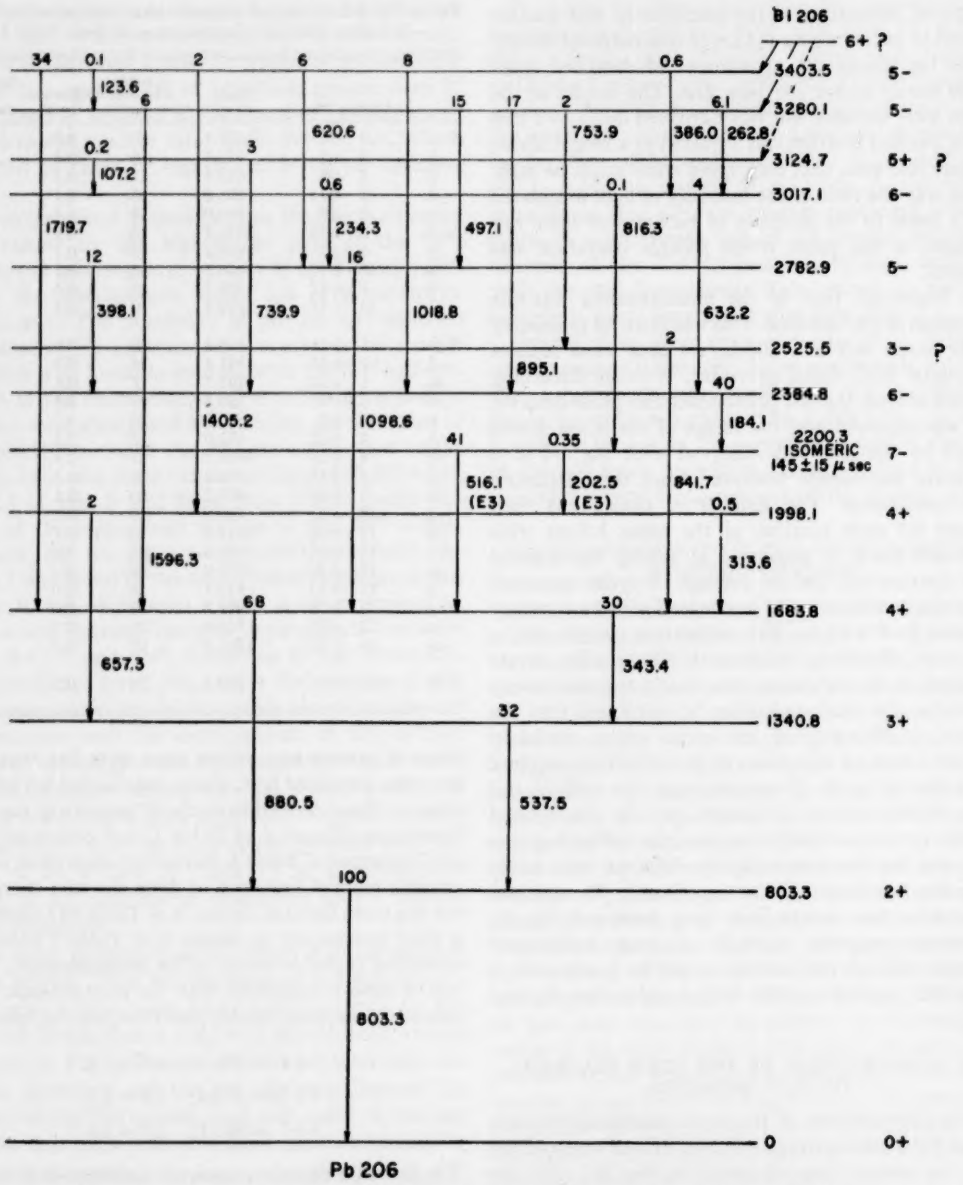

FIG. 7. Energy levels and transitions in Pb^{206}. The number at the head of each transition is its intensity in percent per disintegration.

addition, if line 4 of Table IV is interpreted as the K line of a 107.2-kev gamma ray, there is one further cascade crossover, which is listed as C of Table VII.

Triple cascades were also considered but here the analysis becomes more ambiguous because of the very large number of possibilities. For example, the 19 transitions listed in Group A of Table I can be combined in more than 300 ways to yield triple sums less than 1720 kev. Some triple sums can be derived directly from the double sums listed in Table VII. Aside from these there are three relations which agree with the scheme, while four do not agree and must be considered as chance additions. Triple sums involving all 27 transitions of Table I have not been analyzed.

Although the scheme does not necessarily have to follow all of the sum relationships, it must in every case be consistent with well-defined coincidence measurements. The coincidence results described in Secs.

VI and VII together with the isomer measurements discussed in Sec. VIII and the cascade crossover data cited in Table VII were largely responsible for the level arrangement adopted. Inspection shows that all 31 of the coincidence or noncoincidence results listed in Tables V and VI are in accordance with the decay scheme. While it has already been mentioned in Sec. VII that the relative gamma-electron coincidence rates are consistent with the scheme, no detailed analysis of the electron-electron coincidence rates given in Table V has been made.

X. CONSTRUCTION OF THE TERM DIAGRAM OF Pb^{206} —SPINS AND PARITIES—CORRELATION WITH THE SHELL MODEL

The energies of the levels in the term diagram can be deduced uniquely from the experimental material alone, except for the two doubtful levels at 2525.5 and 3124.7 kev. All the other levels are involved in at least three transitions, eight in at least four and one (1683.8) in as many as eight transitions. The ground state is involved in only the 803.3-kev transition, and it was fortunate that it was known at the outset that this transition was from the first excited state, although the coincidence measurements also fix its position unambiguously. The spins and parities of the well-established levels could probably also have been deduced from the experimental data alone by using the K/L ratios, the conversion line intensities, and the calculated conversion coefficients[21] to evolve a consistent scheme of multipole orders and transition intensities, but in practice this would have been difficult. Instead, the predictions of the shell model were used as a guide and were found to be very helpful. Later the intensities were employed to clear up doubtful points.

Those energy levels of Pb^{206} which do not involve the excitation of nucleons from the closed shells can be treated as arising from a system of two neutron holes. If one knows the energy levels for a single hole, the theory of reference 1 can be applied, the interaction energy between the two neutron holes being given by the same formulas as for two identical nucleons. For the purpose of calculating the energy levels, two holes in a closed shell behave in exactly the same way as two two nucleons outside a closed shell (this point was not clearly expressed in reference 1). The necessary starting point is furnished by the levels of Pb^{207}, which are the levels of a single hole. Since the publication of the earlier work[1] better information on the levels of Pb^{207} has been accumulated,[15,17,22,23] and we adopt the levels given in Table VIII. The present scheme differs from the older one by the disappearance of the $f_{7/2}$ level from 1.11 Mev and of the four levels above 2 Mev, which are not confirmed by the recent work. The $f_{7/2}$ level is probably somewhere close above 2.35 Mev, but there is no information concerning its position at present. The levels of Pb^{206} are derived by assigning one of the levels of Table VIII to each neutron hole. From each such pair of Pb^{207} levels (configuration) a number of energy levels of different spins can be constructed for Pb^{206}, according to the ordinary rules of vector coupling. As an example, the configuration $p_{1/2}f_{5/2}$ contains two levels (2+ and 3+). If there were no interaction between the holes the energy of the levels would be just the sum of the energies of the two Pb^{207} levels in the configuration, and all Pb^{206} levels from the same configuration would be degenerate, but because of the interaction the levels are split. According to the simplified form of the theory,[1] which assumes that the range of the nuclear forces is negligible compared with the diameter of the nucleus, some levels are not shifted at all, while others are depressed. The energy of the unshifted levels of a configuration will be called its "head;" referred to a nominal zero it is the sum of a pair of values from Table VIII.

The ground state of Pb^{206} corresponds to both holes being in the $p_{1/2}$ level, i.e., the configuration $p_{1/2}^2$. Because of the exclusion principle, there is only the state $I=0(+)$ in this configuration. Interaction depresses its energy below the nominal zero by an amount which we estimate, for reasons given later, to be 0.77 Mev. The head of a configuration, referred to the ground state of Pb^{206} as zero, is therefore obtained by adding 0.77 Mev to the sum of the two Pb^{207} energies. Table IX lists the lowest thirteen configurations, their

TABLE VIII. Energy levels of Pb^{207}.

Level	Parity	Energy (Mev)
$p_{1/2}$	−	0.00
$f_{5/2}$	−	0.570
$p_{3/2}$	−	0.87
$i_{13/2}$	+	1.634
$h_{9/2}$	−	2.35

TABLE IX. Pb^{206} configurations.

	Configuration	Head (Mev)	Spins	Parity	Approximate interaction parameter (Mev)
1	$p_{1/2}^2$	(0.77)	0	+	0.4
2	$p_{1/2}f_{5/2}$	1.34	2,3	+	0.3
3	$p_{1/2}p_{3/2}$	1.64	1,2	+	0.4
4	$f_{5/2}^2$	1.91	0,2,4	+	0.4
5	$f_{5/2}p_{3/2}$	2.21	1,2,3,4	+	0.3
6	$p_{1/2}i_{13/2}$	2.40	6,7	−	0.2
7	$p_{3/2}^2$	2.51	0,2	+	0.4
8	$f_{5/2}i_{13/2}$	2.97	4,5,6,7,8,9	−	0.2
9	$p_{1/2}h_{9/2}$	3.12	4,5	+	0.2
10	$p_{3/2}i_{13/2}$	3.27	5,6,7,8	−	0.2
11	$f_{5/2}h_{9/2}$	3.69	2,3,4,5,6,7	+	0.2
12	$p_{3/2}h_{9/2}$	3.99	3,4,5,6	+	0.2
13	$i_{13/2}^2$	4.04	0,2,4,6,8,10,12	+	0.5

[21] Rose, Goertzel, Spinrad, Harr, and Strong, Phys. Rev. 83, 79 (1951).

[22] D. E. Alburger (unpublished).

[23] J. R. Prescott, Proc. Phys. Soc. (London) 67, 540 (1954).

heads, the spins of the levels derived from them, and their parities. It should be noticed that if both holes occupy the same Pb^{207} level, only even values of I are allowed by the exclusion principle.

The amount by which the levels are depressed by the interaction between the holes is expressible in terms of a positive parameter ϵ (called—ϵ_s in reference 1) involving the strength of the singlet nuclear force and an integral over the radial wave functions of the single neutron levels. There is a different ϵ for each configuration, whose value can be calculated if one knows the wave functions. As the theory is at best approximate and is only used here as a guide, no attempt has been made at performing the calculation. Instead, rough values of ϵ have been estimated semi-empirically and are listed in Table IX.

In this way the theory can be used to predict the pattern of the energy levels of Pb^{206}. In Table X the energies of all levels up to about 3.7 Mev, expressed in terms of the parameters $\epsilon_1, \cdots \epsilon_{13}$, are arranged according to their spin and parity. It will be seen that except for the 0+ levels the coefficients of ϵ are not large, so that, with these exceptions, errors in estimating ϵ do not matter much.

When two levels of the same spin and parity are predicted to be close together the theory breaks down because configuration interaction becomes important. This is most likely to be a large effect for the 0+ levels, for which the matrix elements of configuration coupling are the largest, and for that reason, and the large coefficient of ϵ, their predicted position is liable to be in error by as much as 1 Mev. This large uncertainty in the 0+ levels is indicated in Table X by $\sim$. Other levels are probably reliable to 0.3 Mev or better if the coefficient of ϵ is less than 1 and no perturbing level is close.

In addition to these levels one must expect the presence of core excitation levels. Information on these may be obtained from the known excited levels of Pb^{208}. The first two are at 2.615 Mev ($I=3-$) and 3.198 Mev ($I=5-$).[24] Since they are not excited[5] in the reaction $Pb^{207}(d,p)Pb^{208}$, they presumably arise from an excited proton, the neutrons remaining effectively undisturbed. Similar levels at about the same energy may therefore be expected in Pb^{206}, and have been listed, marked with an a in Table X. More complex excited protons levels, in which the neutrons are also disturbed from the $p_{1/2}^{-2}$ configuration, must also be expected to start at around 2.6+0.803=3.4 Mev. Many spins are possible, with odd parity, but these levels are not listed, although they may well fall into the interesting energy range. According to Harvey[4] the lowest neutron excitation level in Pb^{208} is at 3.37 Mev. Since it probably corresponds to a neutron promoted from the $p_{1/2}$ level to the $2g_{9/2}$ level, in Pb^{206} the corresponding level will arise from the promotion of an $f_{5/2}$ neutron, the $p_{1/2}$ level being empty in the ground state, and so will be roughly 0.57 Mev higher (i.e., at 3.9 Mev). This is outside the present range of interest.

TABLE X. Predicted levels of Pb^{206}.

Spin and parity	Predicted energies (Mev) (neglecting configuration interaction)
0+	$\sim 0.77-\epsilon_1=0.00$, $\sim 1.91-3\epsilon_4$, $\sim 2.51-2\epsilon_7$, $\sim 4.04-7\epsilon_{13}\cdots$
1+	1.64, 2.21, $\cdots$
2+	$1.34-1.2\epsilon_1$, $1.64-0.8\epsilon_3$, $1.91-0.7\epsilon_4$, $2.21-0.35\epsilon_5$, $2.51-0.4\epsilon_7$, $3.69-2.9\epsilon_{11}$,
3+	1.34, 2.21, 3.69, $\cdots$
3−	2.6,[a] $\cdots$
4+	$1.91-0.3\epsilon_4$, $2.21-1.1\epsilon_5$, $3.12-1.1\epsilon_9$, $3.69-1.0\epsilon_{11}$, $\cdots$
4−	2.97, $\cdots$
5+	3.12, 3.69, $\cdots$
5−	$2.97-0.3\epsilon_6$, $3.27-1.8\epsilon_{10}$, 3.2[a], $\cdots$
6+	$3.69-0.5\epsilon_{11}$, $\cdots$
6−	2.40, 2.97, 3.29, $\cdots$
7+	3.69, $\cdots$
7−	$2.40-0.9\epsilon_6$, $2.97-0.6\epsilon_9$, $3.27-0.6\epsilon_{10}$, $\cdots$
8−	2.97, 3.27, $\cdots$
9−	$2.97-1.6\epsilon_6$, $\cdots$

[a] Proton excitation levels.

Inspection of Table X at once shows some of the characteristic features of the term diagram of Pb^{206} which proved useful in the interpretation of the spectrum. Particularly important is the prediction that the lowest level of spin $I=7$ is lower than any levels of spin $I=5$, 6, and ≥ 8. If this level is reached, therefore, it will de-excite by an $E3$ transition to a 4+ level, followed by a cascade via 3+ and 2+ levels to the 0+ ground state. When the 516.1-kev $E3$ transition was found experimentally, its place in the scheme could immediately be understood and be used firmly to anchor the other levels.

We now return to the reasons for taking 0.77 Mev for the shift of the ground state relative to the nominal zero. Having once obtained a reasonable identification of the observed levels, it was seen that two of them were levels in which the approximate theory predicts no shift from the configuration head, so that their position relative to the nominal zero is known. These are the $p_{1/2}f_{5/2}$ 3+ level at 0.57 Mev from the nominal zero, actually at 1.340 Mev, whence the shift is 1.34 −0.57=0.77 Mev, and the $p_{1/2}i_{13/2}$ 6− level at 1.635 Mev from the nominal zero, actually at 2.385 Mev, whence the shift is calculated to be 2.385−1.635=0.75 Mev. The agreement between these two values is better than could have been expected. The value 0.77 Mev was adopted because the 3+ level is less likely to

[24] Elliott, Graham, Walker, and Wolfson, Phys. Rev. **93**, 356 (1954).

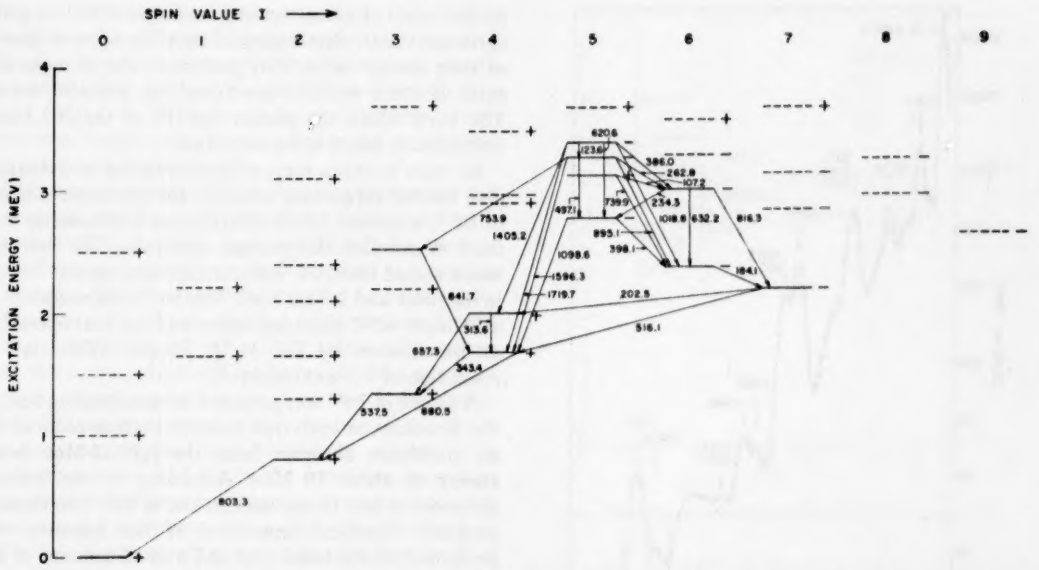

FIG. 8. The energy levels of Pb^{206} separated according to spin value. Solid lines—levels and transitions determined experimentally and theoretically predicted. Dashed lines—additional levels expected from the theory but not observed. Inaccuracies in positions of the theoretically calculated levels are 1 Mev for the spin-0 levels and 0.3 Mev for all others.

be perturbed (see Table X). If the very doubtful assignment of the 3124.7-kev level is correct, this also gives 0.77 Mev.

The doubtful level at 2525.5 kev, which is reached from the 3280.1 level and radiates to the 1683.8 level, has tentatively been assigned the spin 3− because such a level is predicted near 2.6 Mev, and as this is a proton excited level the $E2$ transition from the 5− level might be expected to compete to a measurable extent with the stronger $E1$ and $M1$ transitions; and there seems to be no other reasonable predicted level near. This assignment makes the relative intensities of the 753.9- and 841.7-kev gamma rays reasonable. One would expect this level also to be reached from the 3403.5 level, and to radiate to the 1340.8 and 803.3 levels, but unfortunately weak conversion lines from any of these transitions would be masked by conversion lines of stronger gamma rays. The possibility also remains that the two gamma rays are emitted in the inverse order, and that the level is at 2438 instead of 2525.5 kev.

The even more doubtful level at 3124.7 kev has been assigned on the grounds that a 5+ level is predicted at 3.12 Mev and, if it exists, it might be expected to show up. Its strongest radiation might be by $E1$ to the 6− level at 2384.8 kev, and this fits well with the previously unassigned 739.9-kev gamma-ray if the precise energy of the level is taken as 3124.7. The other expected transitions involving such a level are either in the high energy region where a very weak line would be missed, or masked by stronger conversion lines, except for the transition to the 3017.1 level, whose K-conversion line fits well with line 4 of Table IV (see also *bb* of Table VII).

XI. TRANSITION INTENSITIES AND K/L RATIOS

Table XI lists in column 4 the relative intensities of K-lines in Bi^{206} decay. These were taken mostly from the double-focusing spectrometer data discussed in Sec. II and include corrections for the 3.8 mg/cm² counter window according to curves published[25] by Saxon. The K-184.1 relative line intensity was derived from the earlier lens spectrometer data[3] corrected for a 2-mg/cm² counter window used while consistency checks between the two sets of data were made for other lines insofar as possible. Since it is fairly certain that the 803.3-kev gamma occurs once per disintegration this transition has been assigned a value of 100 in column 5. Based on the 803.3 being a pure $E2$, the normalization of values in column 4 gives the number of K-conversion electrons emitted per 100 disintegrations. Thus the ratio of a number in column 4 to the corresponding number in column 5 is an approximate value of the K conversion coefficient in those cases where the conversion is not large (i.e., <0.1). Errors in the intensities of K lines above 250 kev are probably no greater than 15 percent, but because of uncertainties in window corrections the lower-energy K lines may be in error by as much as 30 percent.

In deducing the relative transition intensities given in column 5 of Table XI consideration had to be given to the possibility of mixtures, particularly for the many $M1$ transitions. Only in the case of the 184.1-kev gamma is

[25] D. Saxon, Phys. Rev. **81**, 639 (1951).

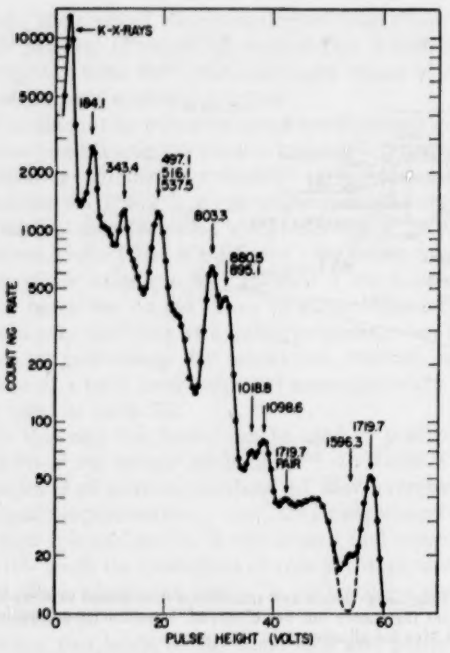

FIG. 9. Differential pulse-height spectrum of Bi^{206} gamma rays in a NaI scintillation spectrometer.

there definite evidence for a very pure $M1$. From photographic exposures made in a semicircular beta spectrograph, Michelich has found[26] no detectable L_{III} line in the 184.1-kev transition and thus has shown that there is at most a fraction of a percent of $E2$ present. If no allowance is made for mixtures, the transition intensities derived from the K-conversion line data and the theoretical conversion coefficients form a reasonably consistent scheme except for the intensity of the 537.5-kev gamma which comes out too low for proper balancing. The assumption that the 537.5-kev transition contains $M1+E2$ in the ratio of 5 to 3 will account correctly for the balance. As the admixture might, on general grounds, be expected to increase progressively with increasing energy the intensities calculated for the $M1(+E2)$ transitions have, rather arbitrarily, been increased by a factor of from 20 to 50 percent in column 5 of Table XI.

According to the analysis the primary excitation is shared about equally between the two top 5− levels. There is no direct evidence of other levels being appreciably excited although weak excitation of the doubtful 3124.7-kev level is suggested.

Relative intensities of conversion lines corresponding to the 516.1 and 202.5 kev $E3$ isomeric transitions have already been published,[8] but unfortunately the necessary counter window corrections to the 202.5 lines had been overlooked. The corrected ratio of the two $E3$ K-line intensities, as derived from Table XI, leads to a revised ratio of unconverted gammas of ~760, in good agreement with that expected from the seventh power of their energy ratio. This correction also changes the ratio of 516.1 to 202.5-kev transition probabilities to 120, from which the partial half-life of the 202.5-kev transition is found to be ~0.02 sec.

In order to check some of the intensities and thereby give further supporting evidence for the decay scheme of Bi^{206}, a sodium iodide scintillation spectrometer was used to examine the gamma spectrum. The detector was a sealed Harshaw unit containing a crystal 3.8 cm in diameter and 2.5 cm high. This had been mounted on a Dumont 6292 photomultiplier and set into operation at Brookhaven by Dr. B. J. Toppel. With Cs^{137} a resolution of 7.5 was observed.

A source of Bi^{206} was prepared by bombarding lead in the Brookhaven cyclotron using deuterons reduced by an aluminum absorber from the full 22-Mev beam energy to about 16 Mev. According to the findings discussed in Sec. II any background of Bi^{205} was thereby avoided. Chemical separation of the bismuth was performed in the usual way and a small amount of the activity was placed above the NaI crystal.

Figure 9 shows the differential pulse height spectrum using a channel width of 0.8 volt. The peaks are identified with Bi^{206} gamma energies from Table I.

Relative gamma-ray intensities were found by determining the number of electrons in each photopeak and correcting for the efficiency of the crystal. The

TABLE XI. Transitions and intensities in the decay of Bi^{206}.

Gamma	Energy (kev)	Multipole	K-line intensity (electrons per 100 disintegrations)	Transition intensity adopted from K-line intensities (803.3 = 100)	Transition intensity from gamma meas.
1	184.1	$M1$	28	40	45
2	234.3	$M1$	0.24	0.6	
3	262.8	$M1$	2.1	6.1	
4	343.4	$M1$	6.6	30	25
5	386.0	$M1$	0.13	0.6	
6	398.1	$M1(+E2)$	1.76	12	
7	497.1	$M1(+E2)$	1.37	15	
8	516.1	$E3$	1.95	41 = 88	76
9	537.5	$M1(+E2)$	2.08	32	
10	620.6	$M1(+E2)$	0.27	6	
11	632.2	$M1(+E2)$	0.21	4	
12	657.3	$M1(+E2)$	0.084	2	
13	803.3	$E2$	0.85	100	100
14	880.5	$E2$	0.48	68 = 85	65
15	895.1	$M1(+E2)$	0.32	17	
16	1018.8	$M1(+E2)$	0.11	8	8
17	1098.6	$E1$	0.029	16	14
18	1596.3	$E1$	0.0054	6	5.5
19	1719.7	$E1$	0.029	34	32
20	123.6	$M1$	0.069	0.1	
21	202.5	$E3$	0.020	0.35	
22	313.6	$M1$	0.14	0.5	
23	739.9	$E1$	0.011	3	
24	753.9	$E2$	0.0074	2	
25	816.3	$M1(+E2)$	0.0025	0.1	
26	841.7	$E1$	0.0050	2	
27	1405.2	$E1$	0.0020	2	
28	107.2	$E1$	0.23	0.2	

[26] J. W. Mihelich (private communication).

photoline intensities were measured using a nonoverload amplifier and a differential pulse-height analyzer, each photoline being run after adjusting the voltage on the photomultiplier so that the peak was centered at a pulse height of 35 volts. After subtraction of an estimated background the areas under the curves were measured with a planimeter.

The total detection efficiency *versus* energy for this size crystal has been calculated[27] by McGowan, while Heath, Bell, and Davis have measured[28] the ratio of the full energy loss peak to total intensity at a number of energies. By combining these data a curve of photopeak efficiency *versus* energy was derived. As expected, this was found to fall off a little faster with energy than the curve published[29] by Hornyak and Coor for a slightly larger crystal (4-cm diam by 3 cm high). Using this curve, extrapolated in the case of the 184.1-kev gamma, the line intensities were converted to gamma intensities and finally the transition intensities were obtained after correcting for internal conversion based on the multipole orders given in column 3 of Table XI. This correction was large only for the 184.1 and 343.4-kev transitions. The resulting transition intensities are given in the last column of Table XI. Within the estimated errors of approximately 30 percent, it is seen that the directly measured intensities of gamma rays accessible to the experiment are in agreement with those derived from the conversion line intensities. These data give strong support to a number of the spin and parity assignments which were made at first mostly on the basis of the theoretical analysis.

K/L ratios, plotted against Z^2/E in Fig. 10, were taken from the double-focusing spectrometer measurements described in Sec. II except for the 184.1-kev transition whose low energy made it more desirable to use the earlier lens spectrometer data where the window corrections were smaller. Peak heights were used as a measure of line intensity in all cases. An inspection of Fig. 2 shows that the L_{III} line of the 516.1-kev transition is almost resolved so that its contribution to the L_{I+II} peak height is not appreciable. Thus the

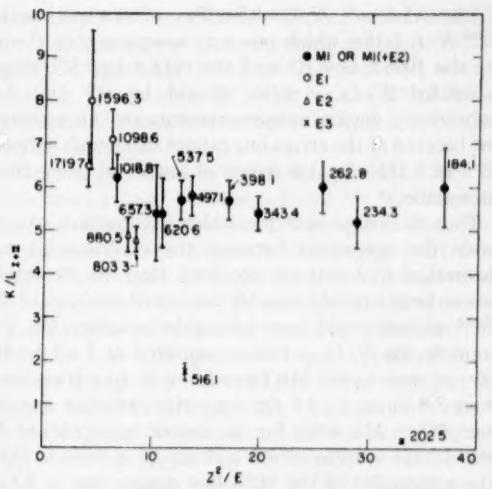

FIG. 10. K/L_{I+II} conversion ratios for Pb^{206} transitions.

K/L ratios in Fig. 10 represent K/L_{I+II} with the possible exception of higher energy lines where the L_{III} line is relatively closer to the L_{I+II} peak.

Many of these K/L ratios may be compared directly with theoretical values derived from the K-conversion coefficients already published[21] together with some L-conversion coefficients which have been privately distributed by Dr. M. E. Rose. Because the present set of L-conversion coefficients covers only a few values of Z it is not yet possible to interpolate for $Z=82$. Ratios have therefore been computed for $Z=85$ and it has been assumed that the ratios for $Z=82$ are not appreciably different. Although no L_{III} conversion coefficients are available as yet the lack of these is not serious in most cases owing to the probability that L_{III} lines did not contribute to the experimental ratios because of the high resolution used.

Table XII gives the experimental conversion line intensities of the two $E3$ isomeric transitions which have now been changed from the previously published values[5] so as to take counter window absorption into account. The last two columns indicate that the agreement between the experimental and theoretical K/L_{I+II} values is very good. For the 202.5-kev transition an extrapolation of the K-conversion $E3$ curve[21] was necessary in order to derive K/L_{I+II}.

Theoretical K/L_{I+II} ratios ($Z=85$) for a number of $E1$, $M1$, and $E2$ transitions in Pb^{206} may also be compared with Fig. 10. The calculations show that $M1$'s above $Z^2/E=6$ have a very nearly constant K/L_{I+II} ratio of about 5.9. According to Fig. 10 none of the $M1$ or $M1(+E2)$ transitions assigned in the scheme have ratios deviating from this value by more than the experimental error. The two $E2$ transitions of 803.3 and 880.5 kev have K/L_{I+II} ratios whose positions are consistent with a value of 4.55 calculated for a gamma of

TABLE XII. Conversion electrons and unconverted gamma rays per 100 Bi^{206} disintegrations of the two $E3$ isomeric transitions in Pb^{206}—experimental and theoretical K/L_{I+II} ratios.

E_γ (kev)	Estimated unconverted γ's	K	L_{I+II}	L_{III}	M	N	K/L_{I+II}	K/L_{I+II} (theoretical)
202.5	0.05	0.020	0.10	0.044	0.039	···	0.20	0.192[a]
516.1	38	1.95	1.09	~0.2	0.36	~0.07	1.78	1.58[b]

[a] Calculated for $k=0.4$ $mc^2=205$ kev.
[b] Calculated for $k=1.0$ $mc^2=511$ kev.

[27] F. K. McGowan (privately circulated tables). See Phys. Rev. 93, 163 (1954).
[28] Heath, Bell, and Davis, Oak Ridge National Laboratory Report ORNL 1415 (unpublished).
[29] W. F. Hornyak and T. Coor, Phys. Rev. 92, 675 (1953).

770 kev (1.5 mc^2, $Z^2/E=8.8$). Two other experimental Bi^{206} K/L ratios which one may compare with theory are the 1098.6 kev $E1$ and the 1018.8 kev $M1$ whose calculated K/L_{I+II} ratios should be 6.8 and 5.9, respectively. Again the measurements are in agreement, but because of the errors one cannot disinguish between $E1$'s and $M1$'s in this region of low Z^2/E using these data alone.

Thus in every case for which comparison can be made the agreement between the experimental and theoretical K/L ratios is excellent. Had the theoretical values been available earlier the initial analysis of the Pb^{206} scheme would have been aided considerably. For example the K/L_{I+II} ratios computed at $k=1.0=511$ kev, or close to the 516.1-kev isomeric transition, vary from 5.8 down to 2.1 for magnetic radiation ranging from $M1$ to $M5$, while for the electric multipoles an $E2$ would have a ratio of 3.4 and an $E4$ a ratio of 0.86. The assignment of the 516.1-kev gamma ray as $E3$ on the basis of the measured K/L_{I+II} ratio of 1.78 is unambiguous and gives another independent check on this transition.

XII. DISCUSSION

The agreement between the observed levels of Pb^{206} and the predictions of the shell model can be considered very satisfactory. The shell model can also be used to understand the nature and spin of the main capturing states, which, by fixing the starting point of the gamma-ray cascade, also contribute to the characteristic features of the Bi^{206} spectrum.

One first needs to estimate the spin of the ground state of Bi^{206}. This is a nucleus with one proton outside the closed shell and three holes in the closed neutron shell. We assume that the proton is in the $h_{9/2}$ level, by analogy with stable Bi^{209}, and that the neutron configuration is $p_{1/2}^{-2}f_{5/2}^{-1}$, i.e., an $f_{5/2}$ hole in a closed subshell. By a theorem due to Kurath,[30] the lowest state of a configuration with one proton in a level j and one neutron hole in a level j' is the one with $I=j+j'-1$, which in the present case is $9/2+5/2-1=6$. The parity is even. If this is true, electron capture will go preferentially to states of spin $I=5$, 6, 7 in Pb^{206}, if they are energetically accessible, these transitions being either allowed or first forbidden according to parity. Since in such a heavy nucleus first forbidden transitions which are not l forbidden are nearly as probable as allowed transitions, the parity is not very important. Capture to other spin states may be expected to be more highly forbidden.

The degree of forbiddenness is not the only relevant factor in capture, however, for if the shell model is a good approximation the nuclear matrix element for the capture in any of the two-hole levels of Pb^{206} must be very small, since such a transition involves not only a change of a proton into a neutron, but also a further neutron jump. The only exceptions to this limitation are the highly forbidden transitions in which the $h_{9/2}$ proton changes into a neutron in one of the available $p_{1/2}$ or $f_{5/2}$ states (i.e., $I=6\rightarrow I=0$, 2, or 3), or the energetically inaccessible states in which the newly formed neutron is in the next shell. This indicates that if a suitable proton excitation level of Pb^{206} is available this will be the main capture level. Such a level is furnished by the predicted 5− level at about 3.2 Mev, which is plausibly a mixture of the proton configurations $h_{9/2}s_{1/2}^{-1}$ and $h_{9/2}d_{3/2}^{-1}$, coupled to the ground neutron configuration $p_{1/2}^{-2}$. Electron capture can then take place with the conversion of a $d_{3/2}$ proton (from inside the 82-shell) in Bi^{206} into an $f_{5/2}$ neutron, filling that level in forming Pb^{206}. This satisfactorily explains why the main capture is observed to two 5− levels of high excitation (3.4035 and 3.2801 Mev). That there are two such levels, instead of one, can plausibly be explained either by the presence of the $p_{3/2}i_{13/2}$ 5− level very close to the proton excited level, so that the two levels perturb each other and share their characteristics, or be ascribed to one of the more complex proton excitation levels discussed in Sec. X. That this is essentially the mechanism of capture is supported by the short half-life of Bi^{206} (6.4 days), compared with the long half-life (50 years) of Bi^{207}, for which no excited proton level in Pb^{207} is available.

That capture takes place mainly into two highly excited 5− levels at once explains the unusual complexity of the spectrum. The main de-excitation of the capture levels occurs by $E1$ transitions to the 4+ level at 1683.8 kev, and by $M1$ transitions to the 2782.9 5− and the two 6− levels at 3017.1 and 2384.8 kev. Cascades through the odd levels lead either to the lower 6− level, and thence in two steps via the isomeric level to the lowest 4+ level, or else more directly to the 4+ level. After that, the nucleus cascades through the 1340.8 and 803.3 kev levels to ground. Other levels are only weakly excited. Since at each step the most probable transition tends to be the one involving the greatest energy with the least spin change, one readily understands why no 1+, and only the lowest 0+, 2+ and 3+ levels have been detected, and also why no 8−, 9− or higher 7− levels have been found.

A point which may be mentioned is that although the first excited level is 2+ as in most even-even nuclei, the explanation is here different. Usually the first excited state belongs to the same configuration as the ground state, while in Pb^{206} the ground configuration, $p_{1/2}^2$, contains only the one state 0+, and the first excited state belongs to $p_{1/2}f_{5/2}$. This serves to explain its unusually high energy for such a heavy nucleus.

In one way the outcome of the present investigation is disappointing. It had been hoped that by a study of the Bi^{206} spectrum one could gain enough information concerning all the levels of several configurations to put the theory to a quantitative test, and to learn something concerning the importance of configuration interaction. Unfortunately not more than two levels belonging to

[30] D. Kurath, Phys. Rev. 87, 528 (1952).

any one configuration have been observed, which is not enough to test the theory. This lack of information arises because the higher states of low spin are not reached by the gamma cascade. A more searching test of the theory must await the investigation of the low-spin levels of Pb^{206} by other means, such as (d,t) reactions employing improved resolution or excitation by inelastic scattering of neutrons.

The correlation between the Pb^{206} levels found in the decay of Bi^{206} and the levels found by Harvey[4] in the reaction $Pb^{207}(d,t)Pb^{206}$ is interesting. This is essentially a neutron pick-up reaction, and since in the ground state of Pb^{207} there is already a hole in the $p_{1/2}$ level, it is to be expected that those levels of Pb^{206} which are strongly excited are those with a $p_{1/2}$ hole. These are (*i*) the ground state (*ii*) the 2+ and 3+ states of $p_{1/2}f_{5/2}$ (803.3 and 1340.8 kev), (*iii*) the 1+ and 2+ states of $p_{1/2}p_{3/2}$ (not found in the present work, but predicted near 1.64 and 1.35 Mev, respectively), (*iv*) the 6− and 7− states of $p_{1/2}i_{13/2}$ (2384.8 and 2200.3 kev), and (*v*) the 4+ (predicted near 2.9 Mev) and 5+ (3124.7 kev?) levels of $p_{1/2}h_{9/2}$. In addition, because of strong configuration interaction in 0+ states, one might expect to find the next 0+ level (1 Mev?). The observed triton group indicating a level at 0.86 Mev can correspond to 803.3 kev unresolved from the 0+ level; that at 1.37 Mev the 1340.8 kev level unresolved from the second 2+ level; 1.71 Mev the 1+ level; 2.22 Mev the unresolved 6− and 7− levels; and 3.03 the unsolved $p_{1/2}h_{9/2}$ doublet. Better agreement can hardly be expected, for the triton groups are 300 kev wide and curve fitting was necessary to resolve them into the above groups.[4] Better resolution would certainly be rewarding.

Although the shell model appears to give reliable predictions concerning the energies of the levels and the selection rules for electron capture, it is unreliable about radiation intensities. In its crudest form it would predict very small transition probabilities for electric multipoles between any of the neutron levels, which is quite inconsistent with the observed speed of the *E*3 isomeric transitions. According to the Weisskopf formula[31] the lifetime for a 516-kev *E*3 proton transition is 13 microseconds, while the observed lifetime (145 microseconds) is only 11 times slower. Such speed for what is essentially a neutron transition cannot be explained by any simple configuration mixing and must be taken as indicating some kind of collective motion in which either the neutrons "convect" electric charge, or the nucleus as a whole is deformed as in the collective model.[32] The strong 880.5-kev *E*2 crossover, and the necessity of assuming $M1+E2$ for the 537.5 line to balance the intensities in Table XI also point in a similar direction.

The energy release in the disintegration of Bi^{206} can be estimated to lie between 3.4 and 3.7 Mev from the fact that the 3403.5-kev level is strongly excited, while no measurable excitation of any higher level takes place. The absence of positrons is easily understood. Although there is enough energy (>181 kev) for positron emission to the 7− state at 2200.3 kev, the calculated ratio of positrons to *K* captures[33] for a positron energy less than 300 kev is less than 1 in 10^4. As the number of *K* captures into this state can be estimated from the gamma-ray intensities at not more than about ten percent per disintegration the positron yield cannot much exceed 1 in 10^5. Transitions to energetically more favored states are at least second forbidden and cannot be expected to contribute appreciably to the positron yield.

XIII. ACKNOWLEDGMENTS

The authors would like to thank Professor Manne Siegbahn for making the facilities of the Nobel Institute of Physics available for the major part of the experimental work and Professor Kai Siegbahn for the use of equipment at the Royal Institute of Technology. Their kind hospitality to the first-named author during 1952–1953 is greatly appreciated. Experiments at the Nobel Institute were made possible by the generous assistance of a number of persons. Dr. H. Atterling and the crew of the large cyclotron carried out many target irradiations essential to this project. Dr. L. Melander arranged for the chemical separations, which were performed by Dr. W. Forsling and Mr. T. Karlsson of his group. Thanks are also due Mr. B. Åström who gave considerable assistance with various electronic equipments and scintillation detectors. Experiments at the Royal Institute of Technology were aided by the help of Dr. T. Gerholm and other members of Professor Kai Siegbahn's group. Professor H. Slätis and Dr. A. Hedgran gave much of their time in discussing the use of the double-focusing and intermediate-image spectrometers. The authors are also indebted to the crew of the Brookhaven cyclotron for bombardments and to Mrs. Elizabeth Wilson Baker for chemical separations.

[31] J. M. Blatt and V. F. Weisskopf, *Theoretical Nuclear Physics* (John Wiley and Sons Inc., New York, 1952), p. 627.

[32] A. Bohr, Kgl. Danske Videnskab. Selskab, Mat.-fys. Medd 26, No. 14, (1952).

[33] E. Feenberg and G. Trigg, Revs. Modern Phys. 22, 399 (1950).

Decay of Rb^{86}†

W. S. LYON AND J. E. STRAIN
Analytical Chemistry Division, Oak Ridge National Laboratory, Oak Ridge, Tennessee
(Received June 11, 1954)

The gamma-ray spectrum of Rb^{86} has been examined with a NaI(Tl) gamma-ray spectrometer. Only the gamma ray of energy 1.08 Mev has been found; the fraction of decay proceeding through the transition is 0.089±0.005.

RUBIDIUM-86 (19.5 day) has been reported as a negatron emitter having two beta groups with maximum energies of 1.82 and 0.72 Mev.[1] The presence of a 1.08-Mev gamma ray in coincidence with the 0.72-Mev beta has also been previously noted. The fraction of the total decay occurring through the 1.08-Mev gamma ray has been quite uncertain, however, with values reported ranging from 20 percent[2] to 12 percent.[3] It was therefore thought of interest to measure accurately the branching ratio of Rb^{86} by finding the fractional decay through the 1.08-Mev gamma ray.

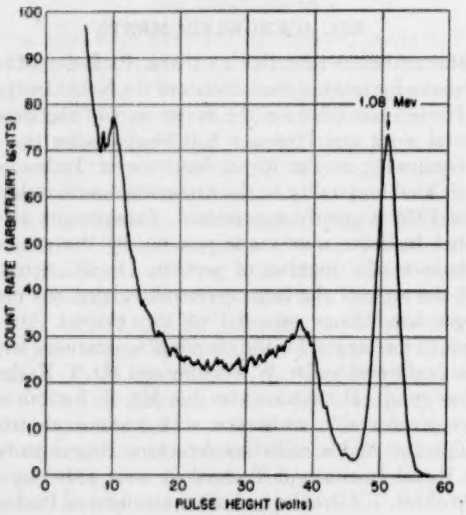

FIG. 1. Gamma-ray spectrum of Rb^{86}.

Chemically pure Rb_2CO_3 was irradiated in the Oak Ridge National Laboratory graphite reactor, removed, dissolved, and processed through an ion-exchange separation—similar to that described below—by the Operations Division, Oak Ridge National Laboratory. The gamma spectrum of this processed material showed only one gamma ray of energy 1.08 Mev. A portion of this solution was further purified, however, by making it 0.1*N* in HCl and passing it through an ion-exchange column containing *IR*-100 resin. A portion of the center cut of the main activity fraction (Rb) was used for the measurements. The only other activity observed from the ion exchange separation was a small amount of Cs^{134} which was removed, assayed, and found to correspond to 0.03 percent of the original Rb activity.

Aliquots of the repurified center-cut Rb solution were assayed by absolute beta counting, 4π counting, and 4π coincidence counting. Agreement between the three methods was excellent.

Aliquots were then measured by means of calibrated NaI(Tl) gamma-ray spectrometer.[4] Figure 1 is a typical spectrum obtained. The area beneath the 1.08-Mev photoelectron peak was obtained by integration; this area when divided by the efficiency of the counter for 1.08-Mev gamma rays yielded the number of 1.08-Mev gamma-ray transitions. The number of gamma-ray transitions divided by the absolute beta disintegration rate yielded the gamma branching ratio. In addition, aliquots of the Rb^{86} solution were read on a calibrated high-pressure ionization chamber,[5] and the number of gamma disintegrations calculated. This value was also used to calculate the gamma branching ratio. Agreement between the two methods was within experimental error. The average value for the gamma branching in Rb^{86} was thus found to be (8.9±0.5) percent.

† Based on work performed under contract to U. S. Atomic Energy Commission.

[1] Hollander, Perlman, and Seaborg, Revs. Modern Phys. **25**, 469 (1953).
[2] Zaffarano, Kern, and Mitchell, Phys. Rev. **74**, 682 (1948).
[3] C. E. Mandeville and E. Shapiro, Phys. Rev. **77**, 439 (1950).
[4] B. Kahn and W. S. Lyon, Nucleonics **11**, No. 11, 61 (1953).
[5] J. W. Jones and R. T. Overman, U. S. Atomic Energy Commission Report 2367, March 20, 1948 (unpublished).

Alpha Half-Lives of Cm^{244}, Cm^{245}, and Cm^{246}

A. M. Friedman, A. L. Harkness, P. R. Fields, M. H. Studier, and J. R. Huizenga
Argonne National Laboratory, Lemont, Illinois

(Received June 14, 1954)

The alpha half-lives of Cm^{244}, Cm^{245}, and Cm^{246} measured from mass spectrometric analyses of curium and its plutonium daughters are 18.4±0.5 years (weighted average of present results and those reported in reference 1), $1.15\pm0.5\times10^4$ years, and $4.0\pm0.6\times10^3$ years, respectively.

THE alpha half-lives of Cm^{244}, Cm^{245}, and Cm^{246} have been determined by a technique which depends on the growth of the plutonium daughters from a curium sample of known isotopic composition. The decays involved in this experiment are

$$Cm^{242} \xrightarrow[162.5\ \text{day}]{\alpha} Pu^{238} \xrightarrow[90\ \text{yr}]{\alpha}, \quad (1)$$

$$Cm^{244} \xrightarrow{\alpha} Pu^{240} \xrightarrow[6580\ \text{yr}]{\alpha}, \quad (2)$$

$$Cm^{245} \xrightarrow{\alpha} Pu^{241} \xrightarrow[13\ \text{yr}]{\beta^-}, \quad (3)$$

$$Cm^{246} \xrightarrow{\alpha} Pu^{242} \xrightarrow[\sim5\times10^5\ \text{yr}]{\alpha}. \quad (4)$$

The curium, produced by the irradiation of plutonium 239 in the Materials Testing Reactor (MTR), was initially chemically separated from plutonium by anion and cation resin columns.[1] After a two week interval, the plutonium daughters were separated from their curium parents. This plutonium sample was analyzed in a 12-inch, 60° mass spectrometer with multiple filament surface ionization source.[2] The possibility of nonradiogenic plutonium contamination of the curium at the beginning of the first growth period necessitated a second growth period of the plutonium daughters and their separation from the curium. The isotopic composition of this second plutonium sample measured in the same mass spectrometer is given in column 4 of Table I. Column 2 of Table I gives the mole percent of each curium isotope in the parent curium sample. Since the time necessary to complete the experiments was short in comparison to the half-lives involved (a correction was made in the mole percent of Cm^{242} due to decay) the following type expression can be written for the unknown half-lives.

$$T_{\frac{1}{2}}(Cm^{244}) = T_{\frac{1}{2}}(Cm^{242}) \frac{\text{mole percent } Cm^{244}}{\text{mole percent } Cm^{242}} \times \frac{\text{mole percent } Pu^{238}}{\text{mole percent } Pu^{240}}. \quad (5)$$

Substituting in Eq. (5), the values obtained from the mass spectrometer for the curium and plutonium isotopic ratios and the value of 162.5 days[3] for the Cm^{242} half-life gives a value of 17.9±0.5 years for the Cm^{244} half-life. Since the Cm^{242} isotopic content depends on a decay correction, the alpha half-lives of Cm^{245} and Cm^{246} are calculated relative to the alpha half-life of 18.4 years for Cm^{244} (this is a weighted average of the 17.9 years and earlier values reported in reference 1). Using an equation similar to Eq. (5), the calculated half-lives of Cm^{245} and Cm^{246} are $1.15\pm0.5\times10^4$ years and $4.0\pm0.6\times10^3$ years, respectively.

The amount of Pu^{242} formed by electron capture of Am^{242} [see footnotes (b) and (c) of Table I; this americium is 99.95 mole percent Am^{243}] is negligible compared to that formed by Cm^{246} alpha decay.

TABLE I. Mass spectrometric analyses in mole percent of a curium sample and its plutonium daughters.

Curium isotope	Mole percent[a]	Plutonium isotope	Mole percent
$_{96}Cm^{242}$	1.52 ±0.04	$_{94}Pu^{238}$	38.9 ±0.3
$_{96}Cm^{243}$	...[b]	$_{94}Pu^{239}$[c]	0.132 ±0.005
$_{96}Cm^{244}$	95.83 ±0.07	$_{94}Pu^{240}$	61.0 ±0.3
$_{96}Cm^{245}$	1.27 ±0.04	$_{94}Pu^{241}$	0.0013±0.0005
$_{96}Cm^{246}$	1.36 ±0.04	$_{94}Pu^{242}$	0.0040±0.0005
$_{96}Cm^{247}$	0.016±0.002		

[a] These data are the same as those published previously (reference 1) with a correction due to the Cm^{242} decay.
[b] Cm^{243} was not determined due to Am^{243} impurity in the curium.
[c] The presence of Pu^{239} is partially accounted for by the reactions

$$Am^{242} \xrightarrow{\alpha} Np^{238} \xrightarrow{\beta^-} Pu^{238}.$$

[1] Stevens, Studier, Fields, Mech, Sellers, Friedman, Diamond, and Huizenga, Phys. Rev. 94, 1083 (1954).
[2] M. G. Inghram and W. A. Chupka, Rev. Sci. Instr. 24, 518 (1953).
[3] Hanna, Harvey, and Moss, Phys. Rev. 78, 617 (1950).

Mass-Spectrometric Study of Deuteron-Induced Reactions in Iodine*

SILVIO J. BALESTRINI†
Department of Physics, University of California, Berkeley, California
(Received June 7, 1954)

Absolute cross sections for the $(d,2n)$, $(d,3n)$, and (d,p) plus (d,n) reactions in I^{127} have been measured for deuteron energies up to 18 Mev by the method of isotope dilution. The stable and long-lived isotopes of xenon produced by deuteron bombardment of stacked foils of KI were distilled from these foils, were mixed with known quantities of atmospheric xenon, and after purification were examined for isotopic composition in a mass spectrometer. For purposes of comparison, relative activation cross sections for the (d,p) reaction on I^{127} were measured by standard counting techniques. The cross section for the formation of the compound nucleus Xe^{129} is found to be in good agreement with theoretical calculations if the interaction radius is taken to be $(1.3A^{\frac{1}{3}}+1.21)10^{-13}$ cm. The curves for the yield of I^{128} and for the total production of Xe^{128} are of the same shape. It is argued that the (d,p) and (d,n) stripping reactions are the principal mechanism for the formation of this latter nuclide. A precise mass-spectrometric determination of the half-life of Xe^{127} yields a value of 36.406 ± 0.016 days.

I. INTRODUCTION

THERE have appeared detailed theoretical calculations of the cross sections for the formation of the compound nucleus by charged particles at moderate energies.[1–3] The sparseness of experimental data with which to compare these calculations in the case of deuterons may be explained as follows: Target elements which are monoisotopic are invariably of odd Z. Since the compound nucleus formed by deuterons on such targets is of even Z and decays principally by neutron emission, and since elements of even Z usually have several stable isotopes, many of the reaction products are likely to be stable. Moreover, when unstable, the reaction products are usually beta-active so that absolute counting is difficult. Consequently, the sum of all the cross sections of reactions proceeding by way of the compound nucleus is usually difficult if not impossible to obtain by radioactive methods. The only such investigation that has come to the attention of the author is that of Kelly and Segrè,[4] who obtained absolute cross sections for the (d,n), (d,p), $(d,2n)$, and $(d,3n)$ reactions on Bi^{209} from the alpha activities of the reaction products.

In recent years, the sensitivity of mass spectrometers for noble gasses has been developed to a high degree, and these instruments are now applicable to investigations of nuclear reactions leading to the production of stable or semi-long lived isotopes of noble gases.[5–9] In the present work, I^{127} was bombarded with deuterons at various energies up to 18 Mev, and a mass spectrometer was employed to measure the quantity and composition of the xenon isotopes that were produced, from which were computed the reaction cross sections involved. The xenon isotopes produced are stable with the exception of Xe^{127}, which decays by K capture with a half-life of more than a month.

II. EXPERIMENTAL PROCEDURE

In constructing the target, use was made of the well-known stacked-foil technique with the slight modification that the "foils" were in the form of evacuated and sealed aluminum packets, resembling ravioli, containing a uniform, thin layer of KI for a filling. The xenon formed in each packet was extracted and mixed with a known and comparable quantity of normal xenon, which will be referred to hereafter as the spike, and the mixture was analyzed with a mass spectrometer. This is known as the isotope-dilution technique.

Target Construction

A group of two-mil, 2S aluminum foils were cut to a size of $1\times2\frac{1}{2}$ inches and weighed. Half of these were then plated with a layer of KI over an area of $\frac{1}{2}\times1\frac{3}{4}$ inches. A successful plating was accomplished by spraying a saturated ethyl alcohol solution of KI from a Paasche H1 Airbrush onto a masked foil under a heat lamp, 50 cc of solution sufficing to deposit a layer one or two mils thick. To exclude moisture, the Airbrush was operated with high-purity nitrogen from a cylinder. Uniformity of thickness was obtained by moving the brush with a machine that combined two reciprocating, uniform motions at right angles and differing greatly in frequency. The resulting zig-zag trace can be visual-

* This work was supported by the U. S. Office of Naval Research.
† Now at the Los Alamos Scientific Laboratory, Los Alamos, New Mexico.
[1] V. F. Weisskopf, Lecture Series in Nuclear Physics, Atomic Energy Commission Declassified Document MDDC-1175, 1947 (unpublished).
[2] J. M. Blatt and V. F. Weisskopf, *Theoretical Nuclear Physics* (John Wiley and Sons, Inc., New York, 1952), Chap. 8.
[3] M. M. Shapiro, Phys. Rev. **90**, 171 (1953).
[4] E. L. Kelly and E. Segrè, Phys. Rev. **75**, 999 (1940); E. L. Kelly, Ph.D. thesis, University of California Radiation Laboratory Report UCRL-1044, 1950 (unpublished).
[5] Macnamara, Collins, and Thode, Phys. Rev. **78**, 129 (1950).
[6] J. H. Reynolds, Phys. Rev. **79**, 789 (1950).
[7] M. G. Inghram and J. H. Reynolds, Phys. Rev. **78**, 822 (1950).
[8] W. H. Fleming and H. G. Thode, Phys. Rev. **90**, 857 (1953).
[9] J. Hayden and M. G. Inghram, Circular No. 522 (U. S. Government National Bureau of Standards Printing Office, Washington, D. C., 1953), p. 189.

ized as many superposed sets of parallel lines about 1/20 inch apart. Since the spray pattern was about $\frac{3}{8}$ inch in diameter, this resulted in a uniform deposit. The area sprayed was about $4\frac{1}{2}\times 2\frac{1}{2}$ inches, considerably larger than the mask opening. To avoid their picking up moisture, the plated foils were kept until needed in an oven held at 110°C.

To form a packet, some natural color, stick form, type I Araldite adhesive was melted and applied sparingly around the edge of an unplated foil. This foil was put over a plated foil, and the pair was inserted in a clamping arrangement inside a bell jar. Evacuation of the bell jar was begun immediately with a mechanical pump, the time between removal of the plated foil from the oven and this evacuation being kept to a minimum. The unit inside the bell jar was then heated electrically and maintained at 180°C for one hour, using a Variac for current control, during which time the Araldite melted, flowed into contact with both foils completely around their periphery, and hardened by curing. This evacuation of the ravioli served a twofold purpose. First it served to exclude atmospheric xenon from the packet, which xenon would constitute a source of error in the isotopic dilution measurements. Second, after the completed packet was removed from the bell jar, the external atmospheric pressure served to clamp the KI layer mechanically between the aluminum foils.

In the assembled target, the packets were clamped between water-cooled spacers so as to keep the Araldite cool during bombardment. This part of the target was electrically insulated from ground so as to permit measurement of the deuteron beam current, and was filled with helium at a pressure only slightly in excess of atmospheric pressure to ensure the exclusion of oxygen and so prevent oxidation of the hot aluminum foils during bombardment. The helium filling also aided in cooling and provided the above-mentioned clamping action. To insure that the measured beam current passed through the KI layers and was not contributed to by ionization currents, the beam was collimated and passed through an evacuated space in front of the foils. The target was mounted externally against the cyclotron snout and in the magnetic field. This eliminated the possibility of error from secondary electrons.

Preparation of the Spikes

The spikes were prepared by a method similar to that used by Hayden and Inghram.[9] Volumes of Pyrex glass were constructed. Each had a break-off seal at the upper end and a one-mm capillary at the lower end with a flange near the bottom of the capillary. The volume of each, including the capillary, was determined by weighing when empty and when filled with mercury. These volumes were mounted on a manifold by means of their flanges, taking care not to disturb the capillary while joining the glass, such that the end of the capillary extended down into the manifold a short distance. The manifold was connected to a vacuum system communicating directly with a McLeod pressure gauge, an additional 300-cc backing volume, and a gas pipette to introduce small quantities of spectroscopically pure xenon gas. The mercury columns of the McLeod gauge were fitted with a pair of accurately engraved centimeter scales backed by a mirror to avoid parallax. The gauge was also provided with a vibrator to prevent any sticking of the mercury.

The manifold was evacuated using a mercury diffusion pump and baked for 15 hours at 390°C. It was allowed to cool slowly, and pumping was continued at room temperature for 12 hours more before filling. Normal xenon was admitted to a pressure of about 7×10^{-3} mm of Hg. The mercury in the manifold was raised to where it just closed off a capillary, and the pressure was measured. When all the volumes were closed off in this manner, the mercury in the manifold was raised half-way up the capillaries, and the volumes were sealed off at the capillaries with a torch flame. The hot glass caused the mercury to lower somewhat, but this entailed a very small correction to the quantity of trapped xenon. Each pressure determination required a correction for the small amount of gas introduced into the system by outgassing of the mercury of the gauge with each measurement. This successively increasing correction never reached one percent.

The quantity of trapped xenon in each spike could be computed knowing its volume, temperature, and pressure just as the mercury closed it off, provided that there are no significant surface occlusion effects at the temperature and pressure used. To test for this, a 60-cc bulb was filled with Pyrex glass wool such that it presented slightly more than 10^4 cm^2 of surface area. In preparing the bulb, its volume was determined by weighing both empty and full of distilled water before inserting the glass wool. The diameters of thirty strands of wool from the same supply were measured with a comparator to obtain an average value and a probable deviation. From this and the density of Pyrex glass, the volume and surface area of the wool in the bulb was computed from its weight. The bulb was connected, through a small mercury cutoff, to the McLeod gauge which formed a second volume. The two volumes, including their associated tubing, were accurately known. After assembly, the bulb was baked out during evacuation in the same manner as for the spike volumes. The evacuated bulb was closed off by its mercury cutoff, and xenon was admitted into the McLeod gauge and associated tubing to a pressure of about 7×10^{-3} mm of Hg. The pressure was determined accurately, the bulb was opened to the McLeod gauge, and the pressure was measured again. A discrepancy between the latter pressure and the value computed from the former, using the two volumes and the gas law, is a measure of surface occlusion to the glass wool. The results of this test show

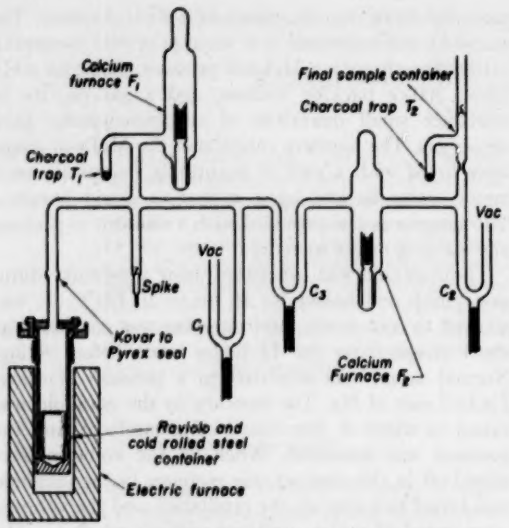

FIG. 1. System for the extraction, mixing, and purification of xenon gas sample and spike.

no occlusion to within a probable error of 1.8×10^{10} molecules per square centimeter at 6.5×10^{-3} mm Hg. This corresponds to an error due to surface occlusion in the contents of a spike of about 0.05 percent.

Purification of a Sample for Analysis

The assembled purification system is shown schematically in Fig. 1. The various parts of the system can be closed off by means of mercury cutoffs C_1, C_2, and C_3, and at no time does the sample come into contact with stopcock grease. The two electrically heated calcium furnaces F_1 and F_2 are replicas of that described by Arrol, *et al.*[10] The trap T_1 contained roughly 70 mg of activated charcoal, while trap T_2 contained about 10 mg. The system was recharged with fresh calcium turnings and fresh charcoal before each purification. When unused, the system was kept at diffusion pump vacuum to prevent the cold rolled steel sample container from absorbing gas, and the time during which air had to be admitted to prepare for a purification was kept to a minimum.

During evacuation of the system, both charcoal traps were maintained at 300°C, and the calcium in both furnaces was degassed by heating. After evacuation, the mercury cutoffs C_1 and C_3 were closed by raising their mercury levels, and the spike was opened to the system and flamed. Then while keeping traps T_1 and T_2 hot and C_2 open, the electric furnace was raised to 800°C (above the melting point of aluminum and KI) and maintained there for a few minutes before switching off the heating current. This step required about one hour during which time there evolved nearly 40 cc of gas at STP. This gas was consumed by heating F_1 until a mirror of calcium on the outer glass envelope could be maneuvered about with a torch. T_1 was then chilled with liquid nitrogen for 15 minutes to collect the xenon and reheated to release it for a good mixing of the xenon from the two sources. Next, the xenon was collected in the other half of the system by closing C_2, opening C_3, and freezing T_2. In all this time, the electric furnace was not allowed to cool below 300°C. Fifteen minutes later, C_3 was closed, the gas now contained in T_2 was released by warming, and the calcium furnace F_2 was used to clean up the remaining impurities by maneuvering its calcium mirror about for 20 minutes. In the final step, T_2 was chilled once more, and the final sample container was sealed off at its constriction and mounted on the spectrometer sample system for analysis.

Preliminary test purifications of unbombarded targets indicated that a double purification with calcium was necessary for a complete removal of impurities. A single purification, using only one calcium furnace, resulted in the survival of detectable impurities at masses 127 and 128. To test for the inclusion of normal xenon from sources other than the spike, such a purification was carried out on an unbombarded target without including a spike. No xenon was detected.

Spectrometric Analyses

The analyses were performed on a single-focusing, 9-in. radius, 60° magnetic-sector type mass spectrometer employing magnetic sweep. The ion currents were measured with a 1.5×10^{11} ohm resistor and a vibrating reed electrometer and recorded on a moving chart. Ionization of the gas sample was accomplished by electron bombardment in a source of standard design using a source magnet. Owing to the fact that the available source magnet was one of poor design, its fringing field extended significantly into the space where the ions were brought to focus onto the collimating slits. This produced a slight mass discrimination but one which could be determined and corrected for in each analysis. The collimating slits were opened as wide as the necessary resolution permitted.

The spectrometer sample system is constructed of Pyrex glass and employs mercury cutoffs where necessary. Three-quarters of its volume can be cut off and reduced from 300 to 30 cc by introducing mercury from an associated reservoir and thereby increasing the sample pressure behind the leak. The leak consists of a one-mil hole in a one-mil aluminum foil through which the sample is slowly passed into the source. With this arrangement, 10^{12} molecules of one isotope of xenon produce a signal of one mv at the electrometer which decreases to half-value in $4\frac{1}{2}$ hours. With the sample compressed as above, the signal is ten times this value but decreases correspondingly faster. The average noise amplitude is in the neighborhood of 1/20 mv. By baking

[10] Arrol, Chackett, and Epstein, Can. J. Research **27**, 757 (1949).

the spectrometer tube overnight before each sequence of analyses and by briefly lowering the liquid nitrogen level on the trap nearest the ion source between successive analyses within each sequence, the background at the xenon mass positions is kept to such a level that it is never observable over this noise signal.

An analysis consisted of from 8 to 10 slow sweeps of the mass spectrum, and if there was no need to save the sample, 4 more sweeps were taken with the sample compressed behind the leak. Figure 2 is a drawing of a typical sweep, prior to compression, from the analysis of the purified xenon from the packets for 16.6-Mev deuterons plus spike together with a comparison spectrum of normal xenon. Since the heavier xenon isotopes in the mixture are present only from the spike and should show the relative abundances of normal xenon, these peak heights are used to determine and correct for the slight and regular mass discrimination usually observed by comparing their ratios to those of Nier[11] and to compute the quantity of each of the lighter isotopes produced.

III. BOMBARDMENTS

All the deuteron bombardments for this work were made at the 60-in. Crocker Laboratory cyclotron of the University of California at Berkeley, California.

Preliminary Bombardment

A preliminary bombardment was made on a KI target sufficiently thick to stop the deuteron beam. The KI had been melted into a copper boat, covered with a 2-mil aluminum foil by the same method used to seal the packets, and introduced into the target chamber in place of the packets with the foil side facing the beam.

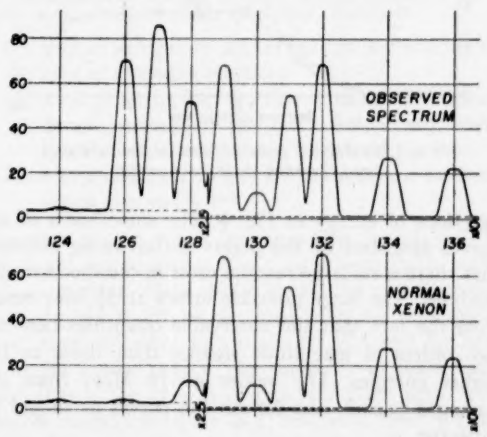

FIG. 2. Abundance spectra *vs* mass number of purified xenon from target for 16.6-Mev deuterons plus spike (above) and normal xenon for comparison (below). The observed intensities must be multiplied by the scale factors indicated below each trace, read from right to left.

[11] A. O. Nier, Phys. Rev. **79**, 450 (1950).

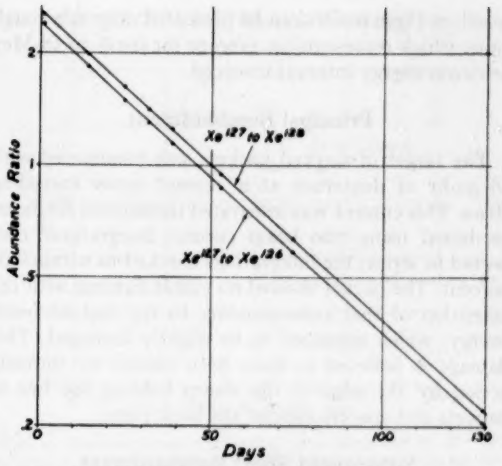

FIG. 3. Logarithmic plot of the abundance ratios *vs* time of radioactive Xe^{127} to the stable Xe^{126} and Xe^{128} isotopes.

Although the foil was cooled by a directed blast of air, it did not survive the bombardment, and the target was badly burned where the beam current density was greatest. After purification without adding a spike, the spectrometer analysis revealed comparatively large quantities of xenon at masses 126, 127, and 128, and in addition a minute trace of normal xenon introduced from the atmosphere during bombardment.

To observe the behavior of Xe^{127}, the major portion of this gas sample was reclaimed and introduced into a portable Pyrex glass manifold by freezing the charcoal trap with which the manifold was provided and sealing the manifold. The manifold contained some calcium turnings and was provided with a number of break-off seals, each with a constriction between it and the manifold. This sample was analyzed seven more times during the next few months; each time the calcium was volatilized, after warming the charcoal slightly, before admitting the sample into the spectrometer sample system through one of the break-off seals. After each analysis, the unused portion of the sample was reclaimed by freezing the charcoal trap and sealing off the sample manifold next to the break-off seal. In Fig. 3, the abundance ratios of Xe^{127} to Xe^{126} and to Xe^{128} are plotted on a logarithmic scale *vs* time. From these values, the least-squares solution for the half-life of Xe^{127}, subject to the condition that the abundance ratio between masses 126 and 128 is constant yields 36.406 ± 0.016 days. This latter abundance ratio fluctuated by about $\frac{1}{2}$ percent from run to run due to difficulty in reproducing a given mass discrimination in adjusting the source magnet for each analysis. However, this ratio shows no trend.

In this target, no Xe^{129} was detectable in excess of that from the atmospheric xenon, indicating the absence of the (d,γ) reaction. Since this target was damaged, the upper limit of 10^{-4} barn for this reaction

based on these results can be presented only as a rough value which represents an average for the 0- to 18-Mev deuteron energy interval involved.

Principal Bombardment

The target of stacked packets was bombarded with 48 μa-hr of deuterons at a current never exceeding 10 μa. This current was integrated throughout the bombardment using two beam current integrators[12] connected in series; the integrations checked to within 0.04 percent. The packet showed no visible damage with the exception of that corresponding to the highest beam energy, which appeared to be slightly damaged. This damage is believed to have been caused by shearing action by the edge of the clamp holding the tier of packets and spacers against the back plate.

Subsequent Short Bombardment

For reasons explained below, a function of relative yield *vs* deuteron energy was desired for the formation of I^{128}. This nuclide decays with a 24.99-min half-life principally by beta emission with which there is an associated 0.428-Mev gamma radiation.[13] To obtain this function, a new stack of packets was prepared with one-mil foils and additional foils in between to act as absorbers, and was bombarded with a 0.2 μa-hr. The activity of the 0.428-Mev radiation was followed in each packet by using a crystal scintillator, photomultiplier, and pulse-height analyzer. After subtracting activities with longer half-lives, the resulting 24.99-min activities were extrapolated back to some convenient time and an activation curve was constructed.

IV. BEAM ENERGY

The energy of the deuteron beam at the front and back of each KI layer of the assembled target was computed using the range-energy curves of Aron, Hoffman, and Williams;[14] the stopping power curve for KI was computed using 200 ev and 490 ev, respectively, for the mean excitation potentials of K and I and by setting up a ratio between this stopping power and that for aluminum. Since the KI layer thicknesses were considerably smaller than those of the intervening aluminum, the error from uncertainty in stopping power of the KI is believed small. In the curves that follow, the energy width of each plotted point refers to the energy of the deuteron beam between entrance and exit from the KI layer, and the ordinate refers to the average cross section between these energy limits.

As no direct measurement of the beam energy was made, and as the collimator opening was made large to reduce bombardment time at the expense of including a spread in energy, the energy of the beam is taken as 19.8 Mev with a spread of 0.15 Mev. These values are based on the results of previous experimenters who have made energy measurements at the 60-in. cyclotron. An initial energy spread or error in the beam increases by 50 percent at 12 Mev and by 150 percent at 6 Mev.

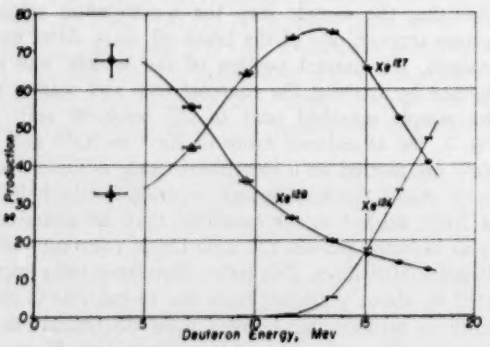

FIG. 4. Percent relative production of xenon isotopes *vs* deuteron energy.

V. EXPERIMENTAL RESULTS AND DISCUSSION

The percentage relative production of the three xenon isotopes from the principal bombardment are shown as functions of energy in Fig. 4. The smoothness of the curves described by the points is convincing evidence that there is no large random error in the spectrometer analyses. The large probable errors at 3½ Mev result from the fact that the observable quantities here are two orders of magnitude smaller than those at the higher energies. The values at 18 Mev, from the damaged packet, also fall on the curves as should be expected.

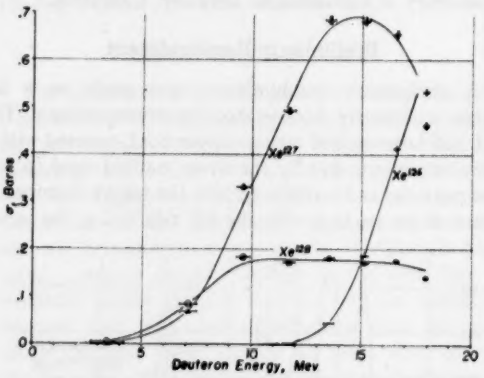

FIG. 5. Production cross sections for the indicated xenon isotopes *vs* deuteron energy.

The computed cross sections appear on an absolute scale of barns in Fig. 5 and in Table I. That the damaged

[12] K. D. Jenkins, University of California Crocker Laboratory Report 60–68, 1950 (unpublished).

[13] Holander, Perlman, and Seaborg, Revs. Modern Phys. **25**, 469 (1953).

[14] Aron, Hoffman, and Williams, Atomic Energy Commission Declassified Document AECU-663, 1949, second revision (unpublished).

packet, for 18 Mev, should show deviation, presumably from a partial loss of its xenon, was to be expected. Smooth curves have been drawn through the remaining points consistent with their percentage yields. While the percentage probable error for a measured cross section as computed statistically is less than 1.5 percent for all the larger cross sections, these points have a mean deviation of 4 percent from the smooth curves drawn to represent them. The cause for the latter deviations is attributed to the isotope dilution technique as applied here and is thought to be due to either imperfect extraction of the xenon from the packets or to loss of xenon from the spikes during their three-month storage, perhaps from surface effects not yet understood. These two effects produce error of opposite sign.

In this experiment, Xe^{127} and Xe^{126} were produced, respectively, by $(d,2n)$ and $(d,3n)$ reactions by way of the compound nucleus; other contributing reactions at these energies are insignificant. But Xe^{128} can in principle be produced by four reactions. They are:

(1) a (d,n) reaction by way of the compound nucleus,
(2) a (d,n) stripping reaction,
(3) a (d,p) stripping reaction yielding I^{128} which decays principally to Xe^{128} before any mass spectrometric analysis can be carried out, and
(4) a (d,p) reaction by way of the compound nucleus, which also yields I^{128}.

TABLE I. Reaction cross section in barns. The cross section for the formation of the compound nucleus Xe^{129} is obtained by adding those of Xe^{126} and Xe^{127}. The probable errors listed for the cross sections are determined statistically and exclude systematic errors.

Deuteron energy, Mev	Xe^{126}	Xe^{127}	Xe^{128}	Xe^{129}
3.4±0.6	$<2\times10^{-4}$	0.0021±1	0.0044±4	0.0021±1
7.1±0.4	$<2\times10^{-4}$	0.0684±8	0.085±1	0.684±8
9.6±0.3	0.00074±8	0.330±5	0.183±2	0.331±5
11.7±0.2	0.00279±9	0.491±6	0.172±2	0.494±6
13.5±0.2	0.0441±5	0.683±8	0.181±2	0.727±9
15.1±0.2	0.186±2	0.681±8	0.171±2	0.87±1
16.6±0.2	0.411±5	0.653±8	0.175±2	1.06±1
17.9±0.2	0.529±6	0.461±6	0.140±2	0.99±1

The cross section values for the production of Xe^{128} in Fig. 5 are reproduced in Fig. 6 on a logarithmic scale. For comparison, there is also shown the curve for the relative yield of I^{128}, as obtained from the subsequent short bombardment, with ordinates adjusted for best fit to the former points. The similarity in shape indicates that if the (d,n) reactions take place with comparable magnitude to the (d,p) reactions, their relative production curves at these energies are similar in shape. It is believed that Xe^{128} is formed to a greater extent by the stripping reactions (2) and (3) for the following reason: The threshold energy for the $(d,2n)$ reaction is estimated at 3.5 Mev by plotting the binding energy per nucleon against atomic mass for the xenon isotopes

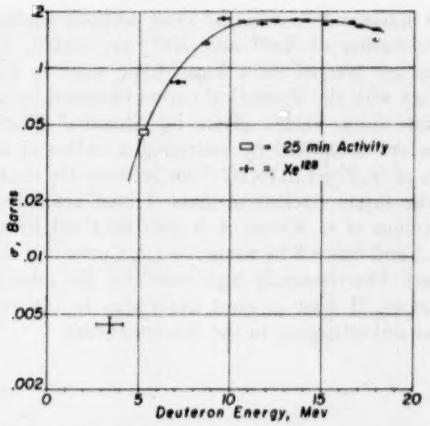

FIG. 6. Absolute cross section for total formation of Xe^{128} *vs* deuteron energy compared as to shape with relative cross section for the formation of 25-minute I^{128}.

and drawing parabolas through the points to obtain a value for Xe^{127}. At energies above 3.5 Mev, the probability for a single neutron evaporation from the compound nucleus, i.e., reaction (1), decreases rapidly; this fraction of the compound nucleus cross section can be estimated from theory[15] to rise to a maximum value of about 0.02 barns in the neighborhood of 9 Mev, whereas the cross section for the production of Xe^{128} is seen to rise to nine times this value. Reaction (4) is less to be expected than reaction (1) because of barrier discrimination against proton emission.

Accordingly, to compute the cross section for the formation of the compound nucleus Xe^{129} from the

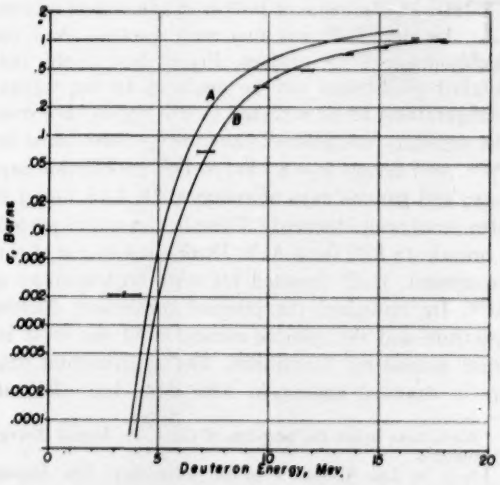

FIG. 7. Absolute cross sections for the formation of the compound nucleus Xe^{129} *vs* deuteron energy. The points are experimental values. Curves *A* and *B* are theoretical for two values of the interaction radius $(r_0A^{\frac{1}{3}}+1.21)\times10^{-13}$ cm. *A*: $r_0=1.5$; *B*: $r_0=1.3$.

[15] See reference 2, p. 377.

target nucleus I^{127}, only the cross sections leading to the formation of Xe^{126} and Xe^{127} are added. These results are plotted on a logarithmic scale in Fig. 7 together with the theoretical curves obtained by interpolation from values given by Shapiro.[3] Shapiro's values are computed by assuming a radius of interaction of $(r_0A^{\frac{1}{3}}+1.21)\times10^{-13}$ cm between the deuteron and the target nucleus of mass A, and are listed for two values of r_0. Curve A is that obtained by using $r_0=1.5$ and curve B by using $r_0=1.3$. Curve B is clearly favored. The unusually high value for the total cross section at $3\frac{1}{2}$ Mev is most likely due to the energy spread and straggling in the deuteron beam.

VI. ACKNOWLEDGMENT

I wish to express my gratitude to the personnel of Crocker Laboratory, at the University of California, for their technical advice and cooperation, to Professor A. C. Helmholz for helpful discussions in planning the experiment and for arranging the cyclotron bombardments, and to Mr. Karl G. Porges for the generous loan of his pulse-height analyzer.

Finally, I wish to express my warmest gratitude to Professor John H. Reynolds, who directed this research, for his continued interest, excellent advice, and encouragement.

PHYSICAL REVIEW VOLUME 95, NUMBER 6 SEPTEMBER 15, 1954

Energy Levels in Po^{210}*

J. W. MIHELICH, A. W. SCHARDT,† AND E. SEGRÈ‡
Brookhaven National Laboratory, Upton, New York
(Received June 3, 1954)

The K-capture decay of At^{210} to levels in Po^{210} has been investigated in detail using conversion electron and γ-ray spectroscopy, and coincidence techniques. Ten transitions of the following energies and indicated multipolarities have been observed: 0.047 ($E2$), 0.116 ($M1$), 0.246 ($E2$), 0.404, 1.185 ($E2$), 1.441 ($E1$), 1.487 ($E1$), 1.604 ($E1$), 2.23, and 2.6 Mev. On the basis of these measurements, a consistent decay scheme may be proposed. Tentative γ-γ angular correlation measurements confirm this scheme. The spin and parity of At^{210} are probably $4-$, $5-$, or $6\pm$. Some information has also been obtained on other At isotopes. A weak 671-kev γ ray not in coincidence (within 0.1 μsec) with K x-rays or α particles appeared in the decay of At^{211}. Gamma-ray transitions of 83.8, 91.1, 195, 548, and 784 kev were observed in the decay of At^{209}.

I. INTRODUCTION

THE level scheme of Po^{210} is of theoretical interest because Po^{210} has two more protons than the doubly-magic Pb^{208} nucleus. Pryce[1] has shown that detailed predictions can be made as to the nuclear configurations to be expected in this region; however, the necessary calculations have not yet been done for Po^{210}. At^{210} decays ($t_{\frac{1}{2}}=8.3$ hr) to Po^{210} by electron capture; and gamma rays of energy 0.25, 1.15, and 1.40 Mev have been observed.[2] There is also a 0.17 percent α branch[2] to Bi^{206} from At^{210}. During the course of this experiment, Hoff[3] reported his work on the decay of At^{210}. He measured the internal conversion electron spectrum and the relative intensities of the most intense gamma-ray transitions. The experimental data are in essential agreement with ours, but with our additional information a different and more definite decay scheme may be proposed.

The internal conversion lines of a carrier-free source were investigated with both high (0.2 percent) and intermediate (2.8 percent) resolution β-ray spectrometers. A scintillation spectrometer with a gray-wedge coincidence analyzer was used to identify gamma cascades, and to measure their relative intensities. Preliminary angular correlation data have been obtained. With this information it is possible to make definite multipolarity assignments for all prominent gamma transitions and to specify the spin and parity of several levels in Po^{210}.

The source was prepared by the $Bi^{209}(\alpha,3n)At^{210}$ reaction using the α beam of the BNL 60-in. cyclotron. The $(\alpha,2n)$ and $(\alpha,4n)$ reactions are in competition with $(\alpha,3n)$; thus, the source consists of a mixture of At^{211}, At^{210}, and At^{209}. The relative amount of the three activities can be varied by changing the bombarding energy.[4] The differences in half-life ($t_{\frac{1}{2}}=7.5$ hr, At^{211}; $t_{\frac{1}{2}}=8.3$ hr, At^{210}; $t_{\frac{1}{2}}=5.5$ hr, At^{209}) are another aid in assigning the gamma rays to a definite isotope. A short summary of the information obtained on At^{211} and At^{209} will be given at the end of the paper. In addition, a

* Work done under the auspices of the U. S. Atomic Energy Commission.
† Now at Los Alamos Scientific Laboratory, Los Alamos, New Mexico.
‡ Summer visitor at Brookhaven in 1953. Permanent address: University of California, Berkeley, California.
[1] M. H. L. Pryce, Proc. Phys. Soc. (London) **A65**, 773 (1952).
[2] Hollander, Perlman, and Seaborg, Revs. Modern Phys. **25**, 597 (1953).
[3] R. W. Hoff, University of California Radiation Laboratory Report UCRL-2325 (unpublished).
[4] E. L. Kelly and E. Segrè, Phys. Rev. **75**, 999 (1949).

barely detectable amount of 13-hr I^{122} activity was made by the $(\alpha,2n)$ reaction on antimony impurities in the bismuth target.

Carrier-free sources were made by distilling the astatine from the irradiated bismuth foil and collecting it on silver in the form of silver astatide.[5] Two types of sources were needed. One consisted of a thin layer of silver evaporated onto 5-mg/cm² Al foil for use with the lens beta spectrometer and the scintillation counters. The other was a line source as required for the 180° permanent magnet spectrograph. This was made by distilling the astatine onto an edge of a silver bar; the rest of the bar had been masked previously by copper plating.

II. INTERNAL CONVERSION ELECTRON SPECTRUM

Conversion electron studies were made with high resolution (0.2 percent) permanent magnet spectrographs. Magnets of 54, 109, 275, and 650 gauss were used to cover the energy range from 8 to 1700 kev. Details of the spectrograph, together with procedures for obtaining and interpreting data, have been described previously.[6] In general, two exposures were made with each source, and the relative decay rate of the conversion lines was used to determine whether they originated from At^{210} or At^{209}. Figure 1 shows the electron spectra obtained with 109- and 650-gauss magnets. The conversion electron data are summarized in Table I. Not included are the Auger lines due to the K and L x-ray series, since they have no bearing on the decay scheme.

The energy difference between electron lines caused by ejection of electrons from various shells and subshells is characteristic of the element in which the conversion takes place. The energy measurements are sufficiently accurate to ascertain that all conversion lines up to 500 kev originated in polonium. Intensity measurements of each of the three L conversion lines could be made for transitions below 300 kev. This information indicates[7] that the 46.7-kev (γ_3) and 246-kev (γ_2) transitions in At^{210} are predominantly $E2$; however, some $M1$ admixture cannot be ruled out. The 116-kev (γ_1) transition in At^{210} and the 195-kev transition in At^{209} are $M1$. The conversion lines of the 84-kev transition are too weak for definite assignment. This transition is an electric multipole ($E2$ or higher order), probably originating in the decay of At^{209}.

The intensities of the conversion lines from transitions between 246 kev and 1600 kev were measured with a lens beta spectrometer.[8] The instrument was equipped with a mica (nominally 2.2-mg/cm²) end-

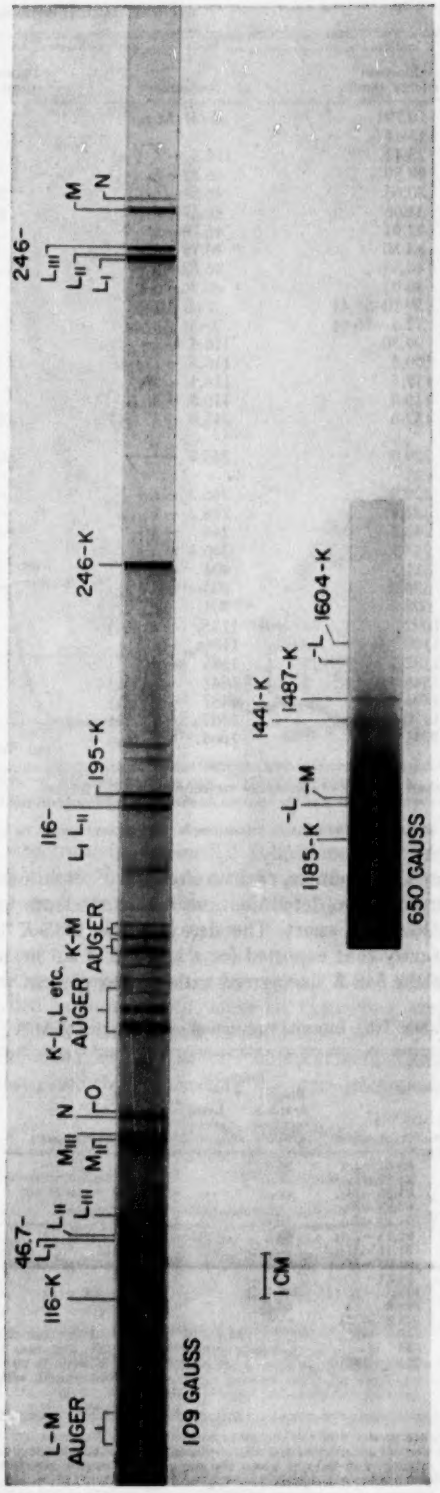

FIG. 1. Conversion electron spectra taken with permanent magnet spectrographs.

[5] Johnson, Leininger, and Segrè, J. Chem. Phys. **17**, 1 (1949).
[6] Gillon, Krishnan, de-Shalit, and Mihelich, Phys. Rev. **93**, 124 (1954).
[7] J. W. Mihelich, Phys. Rev. **87**, 646 (1953); Gellman, Griffith, and Stanley, Phys. Rev. **85**, 944 (1952); Rose, Goertzel, and Swift, privately circulated tables.
[8] Thanks are due Dr. D. E. Alburger for the use of his β spectrometer.

TABLE I(a). Internal conversion electron lines of At^{210}.

Electron energy (kev)[a]	Assignment	Intensity: Photographic spectrograph[b]	Intensity: Lens spectrometer[c]	Remarks
10.79 } 13.14	L–M Auger			
23.42	116.5 $-K$ (γ_7)	5.80		$K/L \geq 4$
29.89	46.82 $-L_I$ (γ_8)	0.55		
30.63	46.66 $-L_{II}$	16.9		
33.06	46.87 $-L_{III}$	14.3		
42.94	46.78 $-M_{II}$	5.7		
43.50	46.79 $-M_{III}$	6.2		
46.35	46.82 $-N_V$	3.7		
46.93	46.96 $-O_V$	0.8		
59.10–65.41	K–L Auger			
72.5 –76.64	L–M Auger			
99.50	116.4 $-L_I$	1.32		
100.3	116.5 $-L_{II}$	0.15		
112.5	116.4 $-M_I$	0.34		
115.8	116.5 $-M_{III}$			
152.6	245.8 $-K$ (γ_3)	12.53	12.53±2	Two sets of intensity data are normalized for γ_3-K
229.0	245.9 $-L_I$	~1.0		
229.9	246.2 $-L_{II}$	7.2	16.6	
332.4	246.2 $-L_{III}$	3.9		
242.5	246.3 $-M_{II}$	~3.7		
243.1	246.4 $-N_{III}$	1.0		
311	404 $-K$		23×10^{-3}	
386	403 $-L$		4.6×10^{-3}	
608	701 $-K$		5×10^{-3}	
1092	1185 $-K$ (γ_1)		68×10^{-3}	$K/(L+M)=3.9$
1168	1184 $-L$ }		17×10^{-3}	
1182	1186 $-M$ }			
1348	1441 $-K$ (γ_5)		6.2×10^{-3}	
1394	1487 $-K$ (γ_4)		8.2×10^{-3}	$K/(L+M)=3.6$
1470	1487 $-L$		$(2.3\pm0.5)\times10^{-3}$	
1511	1604 $-K$ (γ_6)		$(3.2\pm0.6)\times10^{-3}$	

[a] Absolute accuracy of the energy measurements is 0.3 percent.
[b] The overall accuracy of the relative intensities is ±20 percent, but the relative intensities of lines of about the same energy can be measured to ±5 percent.
[c] The accuracy of the relative intensities is ±20 percent except as noted.

window G-M counter, and was set for a resolution of 2.8 percent. Two determinations of the spectrum were made 16 hours apart. The decay of the 1185-K line was exactly that expected for a half-life of 8.3 hr, and that of the 548-K line agreed within a few percent with the 5.5-hr half-life of At^{209}. The 246-kev K and L conversion lines were measured only at the later time because with the original source strength the dead-time losses in the G-M tube were excessive. The conversion electron spectrum is shown in Figs. 2 and 3. The points have been corrected for decay during the experiment using the At^{210} half-life. The intensity measurement of the 153-kev electron line (246-K) required a 10 percent counter-window absorption correction.[9]

TABLE I(b). Internal conversion electron lines of At^{209}.

T (kev)[a]	Assignment	Intensity: Photographic spectrograph[b]	Intensity: Lens spectrometer[c]	Remarks
67.53	83.67 $-L_{II}$	36.4		
70.06	83.87 $-L_{III}$	29.3		
79.91	83.75 $-M_{II}$	...	...	
83.12	83.83 $-N_{III}$	...	...	
74.92	91.15 $-L_{II}$	75.6		
77.32	91.13 $-L_{III}$	68.7		
87.31	91.15 $-M_{II}$ }	35.4		
87.74	91.03 $-M_{III}$ }			
90.41	91.11 $-N_{II}$			
102.2	195.3 $-K$	265.0		$K/L=4.0\pm1.0$
178.9	195.8 $-L_I$	66.5		
191.6	195.8 $-M_I$	...		
455	548 $-K$		16.9×10^{-3}	The lens spectrometer intensities are not comparable with those from the photographic spectrograph
528	545 $-L$		6×10^{-3}	
691	784 $-K$		10×10^{-3}	

[a] Absolute accuracy of the energy measurements is 0.3 percent.
[b] The over-all accuracy of the relative intensities is ±20 percent, but the relative intensities of lines of about the same energy can be measured to ±5 percent.
[c] The accuracy of the relative intensities is ±20 percent except as noted.

TABLE I(c). Unassigned internal conversion electron lines.

Electron energy (kev)	Intensity estimate	Possible assignment
538	weak	542 $-M$ At^{209} (?)
700	weak	
727	medium strong	820 $-K$ At^{210} (?)
762	medium	855 $-K$
837	medium	854 $-L_I$
865	medium	958 $-K$
885	weak	
923	very weak	
939	very weak	956 $-L$

[9] The transmission of this G-M tube window has been calibrated against a counter with a 0.5-mg/cm² window.

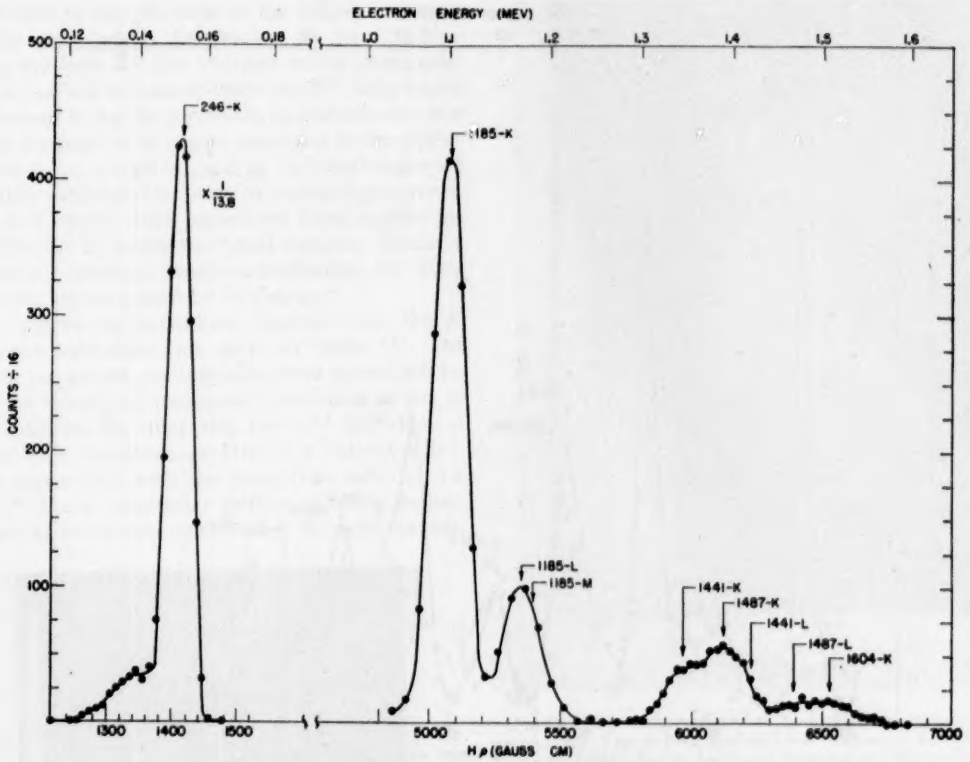

FIG. 2. Electron lines from 1.0 to 1.7 Mev and K conversion line of 246-kev gamma ray. Data were taken with a lens spectrometer having a resolution of 2.8 percent.

III. SCINTILLATION SPECTROMETER MEASUREMENTS

The electronic equipment used consisted of K1186 DuMont photomultipliers, Beva 1.5-kev power supplies, nonoverload amplifiers[10] with a gain of 1000, an Atomic Instrument single-channel analyzer, and a gray-wedge coincidence analyzer[11,12] (0.1-μsec coincidence time). NaI(Tl) (obtained from Harshaw Chemical Company) crystals 2 mm thick were used to detect x-rays. Gamma rays were detected with crystals $1\frac{1}{2}$ inches in diameter by 1 inch high. However, a 2×2 inch crystal had to be used to detect the weak 2.2- and 2.6-Mev transitions. The low-energy conversion and Auger electrons as well as alpha particles were detected with a 1-mm thick anthracene crystal.

Figure 4 shows the pulse-height spectrum obtained with a source of At^{209} and At^{210} held about 3 inches above the crystal. The curves were obtained by tracing isodensity lines on gray-wedge photographs processed by the technique described previously.[13] An almost identical spectrum is obtained if coincidences are required with either 76 kev (K x-rays) or 12 kev (L x-rays) photopeaks from a thin NaI(Tl) crystal. This shows that all the observed gamma rays are due to electron capture in a heavy element, presumably one of the astatine isotopes. The energy region 1.2 to 1.8 Mev was studied in more detail using an expanding amplifier, and the existence of γ_6 was confirmed.

Coincidences between the different transitions were investigated by channeling on one photopeak and

TABLE II. Coincidence data.

Transition triggering the analyzer		Gamma rays displayed	
γ	Energy (kev)	Coincidences observed	Definite absence of coincidences
γ_1	1185	γ_3, γ_4,[a] γ_4 and γ_5,[b] γ_8	
γ_3	246	γ_1, γ_5,[a] γ_4 and γ_5, γ_6, γ_8,[c]	
γ_4 and γ_5	1441 and 1487	γ_1, γ_5, γ_3	γ_6, γ_8, γ_9
γ_6	1604	γ_1, γ_3	γ_5,[d] γ_4 and γ_5
γ_8	2230±20	γ_1, γ_3	γ_4 and γ_5, γ_6, γ_9[e]
γ_9	2630	γ_1	

[a] L conversion electrons of γ_3 were observed.
[b] It is not possible to resolve γ_4 and γ_5 with a scintillation spectrometer.
[c] This coincidence is not certain because, with the detection efficiency used, the addition peak of the 1186-kev plus 1441-kev gammas could account for the lines at 2.6 Mev.
[d] The 1604- and 1441-kev gamma rays cannot be separated completely from each other. However, only 18 percent of the pulses falling in a 7 percent wide channel centered at 1.6 Mev are in coincidence with the 46-kev transition.
[e] γ_8 is not in coincidence with any of the gamma-ray transitions from 300 to 900 kev unless that transition is highly converted ($\alpha_{total} \gtrsim 5.0$).

[10] W. A. Higinbotham, Brookhaven National Laboratory Report BNL-234 (T-36) (unpublished).
[11] R. L. Chase, Brookhaven National Laboratory Report BNL-263 (T-42) (unpublished).
[12] Bernstein, Chase, Schardt, Rev. Sci. Instr. **24**, 437 (1953).
[13] A. W. Schardt, Brookhaven National Laboratory Report BNL-237 (T-37) (unpublished).

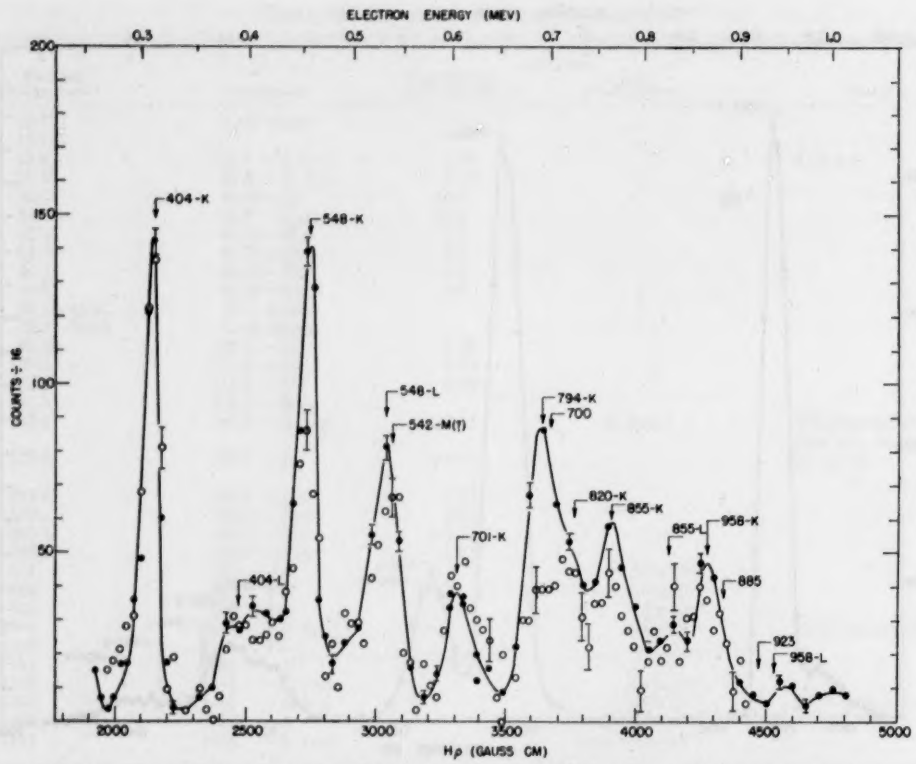

FIG. 3. Electron lines from 0.3 to 1.0 Mev as observed with a lens spectrometer. The points plotted with 0 were taken about 15 hours later and have been corrected for decay with 8.3-hr half-life.

photographing on the the gray-wedge analyzer the pulse-height distribution in time-coincidence with it. Typical spectra photographed on Polaroid film are shown in Figs. 5 and 6. A summary of the coincidence results is given in Table II. In interpreting the coincidence data, account was taken of scattering contributions, coincidences with the background on which the photolines are superimposed, and the appearance of addition peaks if a high detection efficiency is used.

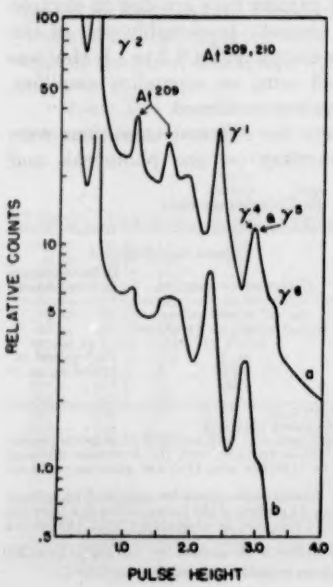

FIG. 4. Differential pulse-height spectrum of an At^{210}, At^{209} source. (a) Fresh source, (b) same source after several half-lives. Different crystals and gain settings were used in taking the two curves.

The energies of the gamma rays were measured with the scintillation counter. For those cases where the energies were also measured with the beta spectrometer, the agreement is better than 2 percent. Only the energy of γ_9 (2630 kev) is somewhat uncertain because its photopeak is superimposed on the addition peak due to the simultaneous detection in the same crystal of time-coincident gamma rays (γ_1 and γ_4). However, coincidences between γ_1 detected by a second crystal and pulses in this energy region were observed, and the photopeak of γ_9 was still present with the source 8 inches from the crystal, at which distance the addition peak should be negligible. At this distance the counting rate was too low for an accurate energy measurement.

The relative intensities of the At^{210} gamma rays were calculated from a single-channel pulse-height spectrum taken with the source 2 inches above the standard cylindrical $1\frac{1}{2}$-inch diameter by 1-inch high crystal. In order to evaluate the contribution of the higher

energy lines to the photoline of the 1185-kev gamma ray, the pulse-height distribution of the 1.51-Mev gamma ray from K^{42} was matched to the photopeaks of γ_4, γ_5, γ_6, and subtracted from the At^{210} pulse-height distribution. It was then possible to evaluate to a few percent the number of counts contained in the photopeaks of γ_1, γ_2, (γ_4 and γ_5), and γ_6. The relative gamma intensities were found by using the calibration curve of Kahn and Lyon,[14] small corrections being applied for the difference in source to crystal distance. Within a few percent identical results are obtained by using calibration curves quoted by McGowan.[15]

The gamma-ray intensities, together with the K conversion coefficients, are given in Table III. The electron and gamma ray intensities were normalized by using the theoretical conversion[16] coefficient of one of the transitions. By comparing the 1185 transition to the 246 ($E2$) transition, $\alpha_K(1185)=(4.74\pm0.9)\times10^{-3}$, which agrees well with the theoretical value of 4.8×10^{-3}.[16] The K conversion coefficients of the higher-energy transitions were computed in the same manner.

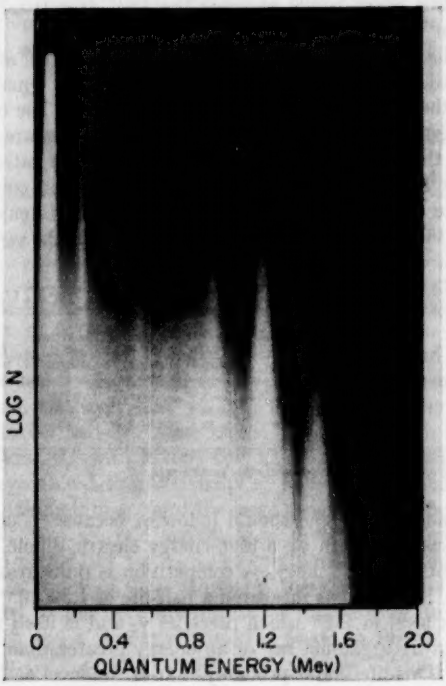

FIG. 5. Pulse-height spectrum in coincidence with a channel at 246 kev. The source was very close to the detector; therefore coincidence peaks are present at the gamma-ray energy plus K x-ray energy. Some scattering between the two detector crystals was present. Therefore a spurious peak is present at 0.94 Mev (1.18–0.24 Mev).

[14] B. Kahn and W. S. Lyon, Nucleonics **2**, No. 11, 61 (1953).
[15] F. K. McGowan, Phys. Rev. **93**, 163 (1954).
[16] Rose, Goertzel, Harr, Spinrad, and Strong, Phys. Rev. **83**, 79 (1951); Rose, Goertzel, and Swift, "L-Shell Coefficients" (privately circulated).

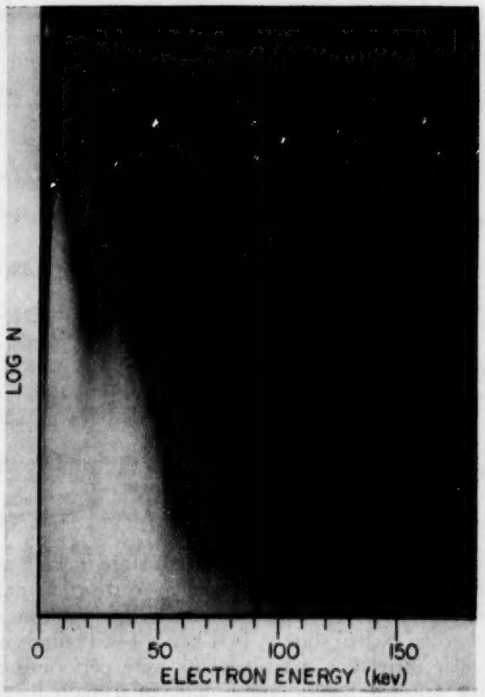

FIG. 6. Low-energy electrons in coincidence with 246-kev gamma ray. The $46.7-L$ and $46.7-M$ conversion lines are unresolved. Pulses due to L–Auger electrons are discernable just above noise.

IV. DECAY SCHEME AND DISCUSSION

The decay scheme shown in Fig. 7 has been constructed on the basis of the data summarized in Tables I–III. Some of the possible spin assignments were eliminated by making use of preliminary angular correlation data. A short account of the arguments involved in the construction of the level scheme follows.

The coincidence and relative intensity data show that γ_1 and γ_2 are in cascade proceeding from the first and second excited states in Po^{210}. The 1185-kev transition was placed at the bottom of the cascade to agree with the 2+ level at ~1 Mev predicted by systematics.[17] Some support for this sequence is given by the absence of gamma rays[18] in the RaE (Bi^{210}) beta decay. The logft value for the β decay to the ground state in Po^{210} is 8.1.[18] Regardless of any reasonable spin assigned to Bi^{210} a measurable competition to a 2+ level at 246 kev in Po^{210} might be expected if the sequence of γ_2 and γ_1 were inverted.

If pure $E2$ transitions, and spin assignments of 0+

[17] M. Goldhaber and A. W. Sunyar, Phys. Rev. **83**, 906 (1951); Horie, Umezawa, Yamaguchi, and Yoshida, Progr. Theoret. Phys. (Japan) **6**, 254 (1951); G. Scharff-Goldhaber, Phys. Rev. **90**, 587 (1953); P. Preiswerk and P. Staehlin, Helv. Phys. Acta **24**, 625 (1952).
[18] M. Goldhaber and R. D. Hill, Revs. Modern Phys. **24**, 179 (1952).

TABLE III. Transitions in the decay of At^{210}.

Transition No. and energy (kev)	Photon intensity	Transition intensity $N_\kappa+N_\gamma$	Experimental[a] ϵ_K	Theoretical K-conversion[a,b] coefficient α_1	α_2	β_1	β_2	β_3	Multipole order and criterion
γ_3 46.7	···	0.34±0.08[c]	···						$E2$ (L conv. ratio)
γ_7 116.5	···	0.05±0.01[c]	···			8.5[d]			$M1$ (K/L ratio, L conv. ratio)
γ_2 246.0	0.80±0.08	0.99±0.10[e]	···	4.6(−2)	1.06(−1)	1.2	3.5		$E2$ (K/L ratio, L conv. ratio)
γ_8 404.0	≤0.02		≥1(−1)	1.4(−2)	3.6(−2)	3.0(−1)	7.2(−1)	1.7	$E1+M2$ or $M3$ (K/L ratio, limit on conv. coeff.)
γ_1 1185.0	1.00	1.00[e]	4.74(−3)[f]	1.78(−3)	4.8(−3)	1.9(−1)	3.4(−1)		$E2$ (K conv. coeff., 2+→0+transition)
γ_5 1441	0.83±0.08	0.35±0.04[g]	1.2(−3)[f]	1.24(−3)	3.28(−3)	1.07(−2)	2.0(−1)		$E1$ (K conv. coeff.)
γ_4 1480		0.48±0.05[g]							$E1$ (K conv. coeff.)
γ_6 1604	0.19±0.03	0.19±0.03	1.1(−3)[f]	1.08(−3)	2.86(−3)	8.8(−2)	1.6(−1)		$E1$ (K conv. coeff.)
γ_8 2226	weak								
γ_9 2600	very weak								

[a] Number of parenthesis gives power of 10.
[b] Taken from reference 16 except where noted.
[c] The theoretical conversion coefficients were used to calculate the intensity of transitions γ_3, γ_5, and γ_7.
[d] See reference 23.
[e] Transition intensity of γ_1 is arbitrarily set equal to unity.
[f] Calculated relative to the theoretical α_2 of γ_2.
[g] The ratio of transition intensities of γ_4 and γ_5 is taken to be the same as the ratio of the K conversion lines.

and 2+ for ground and first excited state in Po^{210} are accepted, then even crude angular correlation data between γ_1 and γ_2 suffice to indicate that the spin of the second excited state at 1431 kev is 4+. Preliminary angular correlation measurements were performed at three selected angles using differential pulse-height selectors on both counters. Table IV lists the measured anisotropies together with the different theoretical values[19,20] to be expected for possible spin assignments. No correction has been made for the fact that the 1185 photopeak is superimposed on the Compton distribution from the higher-energy gamma rays. A correction for this effect would increase the 180° anisotropy to about +12 percent.

The composite conversion coefficient of the unresolved photopeaks of γ_4 and γ_5 (Table III) is equal to the theoretical minimum value (i.e., for $E1$). The only consistent conclusion is that both transitions are $E1$ and their relative intensities follow from the ratio of their K conversion lines. γ_3 (47-kev $E2$) is in coincidence with γ_4 or γ_5. γ_3 and γ_5 are of equal intensity, and their energies add up to that of γ_4. Thus the $\gamma_5-\gamma_3$ cascade is likely. γ_3 should follow γ_5 because γ_3 could not compete with γ_4, a high-energy electric dipole. On the other hand, the γ_4,γ_5 competition is quite reasonable. Sunyar[21] has measured a half-life of 1.5×10^{-9} sec for a level in Po^{210} which precedes γ_2 and is itself preceded by a gamma ray of an energy greater than 660 kev. This lifetime is probably that of the level at 1478 kev shown in Fig. 7.

TABLE IV. Anisotropy of the angular correlation $\gamma_1-\gamma_2$.

θ	Experimental[a] percent	Theoretical 4-2-0 percent	Theoretical 3-2-0 percent	Theoretical 2-2-0 percent	Theoretical 1-2-0 percent	0-2-0 percent
135°	+12±8	+7.3	−8	−28	+115	−50
157.5°	+3±9	+13.7	−24	−10	+40	+30
180°	+9±5	+16.8	−33	+8	−33	+100

[a] Not corrected for contribution of other gamma rays.

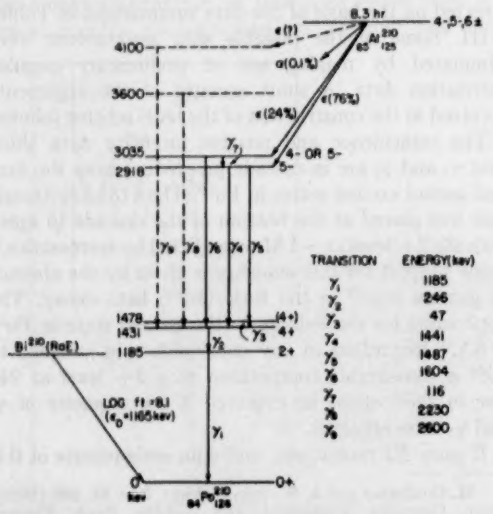

FIG. 7. Energy-level diagram of Po^{210}.

The ratio of transition intensities of γ_4 and γ_5 is taken to be the same as the ratio of the K conversion lines.

Some angular correlation data were obtained with channels set on the photopeaks of the 246-kev and (1441 and 1484)-kev gamma rays. Preliminary results are listed in Table V. The observed anisotropy is the sum of two independent angular correlations; one the double cascade $\gamma_4-\gamma_2$, and the other the triple cascade $\gamma_5-\gamma_3-\gamma_2$ with γ_3 unobserved (Fig 8). The correlation

[19] S. P. Lloyd, Phys. Rev. 83, 716 (1951).
[20] L. C. Biedenharn and M. E. Rose, Revs. Modern Phys. 25, 729 (1953).
[21] A. W. Sunyar (private communication).

function is therefore as follows:

$$W(\theta)=1+(0.57A_2+0.43ba_2)P_2(\cos\theta),$$

where A_2 and a_2 are the correlation coefficients for the $\gamma_4-\gamma_2$ and $\gamma_5(\gamma_3)-\gamma_2$ cascades, respectively,[20] and b (less than unity) takes account of the loss of correlation which is possible since the 1478-kev level probably has a half-life of 1.5×10^{-9} sec.[21] Loss of angular correlation in 10^{-9} sec was probably small since the source consisted of At^- ions in a solution of 6N nitric acid, saturated with sulfur dioxide. For pure dipole and quadrupole transitions, the theoretical values[19,20] of these coefficients are listed in Table VI together with the anisotropy at 180° for extreme values of b. The data of Table V agree only with $j_0=5$ and $j_1=4$ (see Fig. 8); however, $j_1=5$ or 6 cannot be ruled out until a more accurate estimate of b can be made. Small admixtures of higher multipoles to the transitions would change appreciably the theoretical correlation coefficients. However, our preliminary data do not warrant a detailed analysis.

γ_6 (1604 kev) is in coincidence only with γ_1 and γ_2; therefore, it originates from a 3035-kev level. The spin and parity of this level should be either 4− or 5− in order to be consistent with γ_6 being $E1$, and the absence of a crossover to the 1185-kev 2+ level. The difference in energy between the 3035-kev and the 2918-kev levels, as well as the spin and parity assignments, are such that γ_7 (116 kev $M1$) may be the transition between these levels. The competition of a 116-kev $M1$ with a 1604-kev $E1$ transition should be unfavorable. Using Weisskopf's[22] half-life relationships, and taking into account the large conversion coefficient ($\sim$11)[23] of γ_7, one arrives at a theoretical intensity ratio of 5×10^{-4} for γ_7/γ_6 as compared to the experimental value of 0.25. However, the theory is not expected to give accurate results for these highly excited levels, and a similar situation is found in Pb^{206}.[24] Unfortunately, no coincidence data could be obtained for γ_7.

With the available data, the less intense transitions cannot be placed uniquely in the decay scheme. However, the 2230- and 2630-kev gamma rays are in coincidence with γ_1 and γ_2 (Table III). Hence they arise from high-lying levels. The other weak transitions of 404 kev, etc., cannot be placed in the decay scheme, particularly since the interpretation of the conversion electron spectrum is not unique.

TABLE V. Experimental anisotropy of the angular correlation (γ_4 and γ_5)—γ_2.

θ	$\epsilon(\theta)$ percent
135°	−2.5±6
180°	−7.3±4

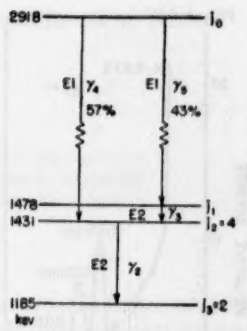

FIG. 8. Detail of Fig. 7 showing level designations referred to in Table VI.

With the proposed decay scheme, the small amount of branching to the 4.1-Mev level can be accounted for if an energy of 0.1 Mev is available for the decay in this branch. Therefore the energy difference between the At^{210} and Po^{210} ground states is probably not much greater than 4.2 Mev. The energy available for the most intense K-capture branch to the 5− level at 1918 kev is approximately 1.3 Mev; hence $\log ft\simeq6.2$. An experimental upper limit of 10 percent may be placed on K capture to the levels at 1431 kev and 1478 kev, thus $\log ft>7.7$. In the absence of any abnormal behavior these $\log ft$ values limit the possible spins of At^{210} to 4−, 5−, or 6±. However, $\log ft$ values are not necessarily conclusive for nuclei near Pb^{208}.[25]

V. At^{211}

Sources of At^{211} were produced by bombarding Bi with alpha particles having an energy below the $Bi(\alpha,3n)At^{210}$ threshold.[4] The conversion electrons between 10 and 300 kev were studied with the permanent magnet spectrograph; only Auger lines were found. In addition to the K and L x-rays the three photolines shown in Fig. 9 were observed with a NaI(Tl) scintillation counter. The lines with an energy of 880±8 kev and 562±5 kev are transitions in Pb^{206} associated with the Po^{211} alpha decay[1,3] (Fig. 10). Coincidences between them and the Po^{211} alpha groups were observed.

TABLE VI. Theoretical angular correlation coefficient for cascade (γ_4 and γ_5)—γ_2.

j_0	j_1[a]	A_2[b]	a_2[b]	Anisotropy[b] $b=1$	Anisotropy[b] $b=0$
4	4	+0.196	+0.167	+30.5%	+19%
4	5	+0.196	−0.171	+5.7%	
5	4	−0.0714	−0.0357	−8.6%	−6.4%
5	5	−0.0714	+0.186	+6.0%	
5	6	−0.0714	−0.250	−24.2%	

[a] See Fig. 8 for quotation.
[b] See formula in text for notation.

[22] J. Blatt and V. F. Weisskopf, *Theoretical Nuclear Physics* (John Wiley and Sons, Inc., New York, 1951).
[23] J. R. Reitz, Phys. Rev. **77**, 10 (1950).
[24] D. E. Alburger (private communication).
[25] A. de-Shalit and M. Goldhaber, Phys. Rev. **92**, 1211 (1953).

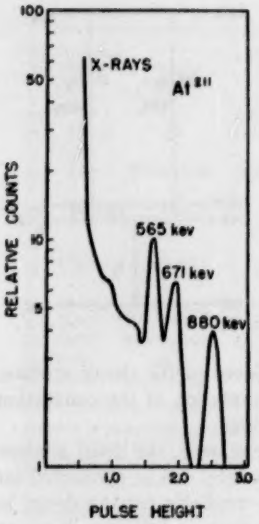

FIG. 9. Pulse-height spectrum of an At^{211} source.

The 671±5 kev gamma ray is not in coincidence (0.1 μsec) with either alpha particles or K x-rays. However, this line is in all probability associated with the At^{211} decay because its intensity relative to the other two gamma rays was constant over a period of 9 half-lives of At^{211}. The ratio of the 671- to 565-kev gamma intensities is 0.73±0.1. The alpha spectrum of an At^{211} source in equilibrium with Po^{211} has been investigated.[2] No alpha group was found which could account for the 671-kev transition. Therefore, it is probable that this gamma ray originates from an isomeric state in Po^{211} which is reached by K capture of At^{211}, unless it is a prompt gamma ray following L capture of At^{211}. Since the 562-kev branch has an abundance of 0.5 percent,[3] the branching in the At^{211} electron capture would be 0.37 percent to this state in Po^{211}. Spiess[26] has reported two levels in Po^{211} with half-lives against α decay of 0.52 sec and 25 sec. He concluded that the 0.52-sec level is approximately 0.3 Mev above the 25-sec level. He also has shown that the 25-sec level is formed to less than one part in 10^4 in the electron capture decay of At^{211}. Therefore, the intensity of the 671-kev transition is too great for it to be associated with the 25-sec level.

An alternate possibility is that the 671-kev transition proceeds between levels in At^{211}. However, this would require that (a) this hypothetical lower level in At^{211} has a half-life either very short or very long compared to 7.3 hr, since only one half-life (7.3 hr) has been observed, and that (b) this level is not formed in appreciable quantity by the $Bi(\alpha,2n)At^{211}$ reaction.

VI. At^{209}

The conversion electron lines are listed in Table I(b). The following gamma rays could be identified: 83.8 (electric) 91.1 (electric), 195 ($M1$), 548, 784 kev. In the scintillation counter spectrum the photopeaks were superimposed on the At^{210} continuum; therefore no relative yields were measured.

We wish to thank Dr. J. Hudis in particular for performing many chemical separations and source preparations. Dr. J. Miskel helped in one run. We are indebted to the BNL 60-inch cyclotron group for the irradiations of bismuth. Thanks are due to Dr. M. Goldhaber for discussion, and to Dr. J. B. H. Kuper for his continued interest in this problem.

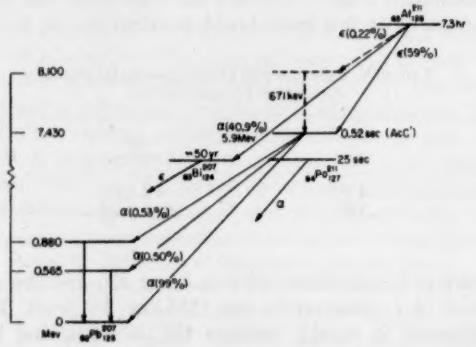

FIG. 10. Decay scheme of At^{211}, Po^{211}.

[26] F. N. Spiess, University of California Radiation Laboratory Report UCRL-1494, 1951 (unpublished).

Energy and Angular Distribution of Protons from Deuteron Bombardment of Nickel*

WILLIAM W. PRATT†
Department of Physics, State University of Iowa, Iowa City, Iowa
(Received June 11, 1954)

The energy spectrum and angular distribution of protons resulting from 3.03-Mev deuteron bombardment of Ni^{58} and Ni^{60} have been studied by means of a nuclear emulsion technique. Three previously unreported energy levels in Ni^{60} have been found. The angular distribution of the protons indicates that the reaction is primarily due to compound nucleus formation.

I. INTRODUCTION

THE energy of proton groups resulting from deuteron bombardment of nickel has been studied by several investigators[1–3] for the purpose of determining neutron binding energies and the distribution of energy levels in the residual nucleus. The angular distribution of protons resulting from the bombardment of nickel with 14-Mev deuterons has been studied by Gove,[4] who concluded that, for this value of deuteron energy, the (d,p) reaction is primarily due to a stripping process. The present work, using 3.03-Mev deuterons, was undertaken in order to make a further study of energy levels in the nickel isotopes and to determine whether the stripping mechanism still predominates at this value of deuteron energy.

II. APPARATUS AND EXPERIMENTAL PROCEDURE

A deuteron beam of energy 3.07 ± 0.05 Mev was obtained from the University of Iowa Van de Graaff generator. After passing through a suitable collimating system the beam was allowed to enter the target chamber, a schematic diagram of which is shown in Fig. 1. The target consisted of either a thin nickel foil or of a thin nickel deposit on a silver backing. The face of the target was, in all cases, mounted at an angle of 45° with respect to the direction of the deuteron beam. The angular divergence of the beam is less than 1° and the target spot is 2 mm (in the plane of observation) $\times 1$ mm.

Protons emerging from the target are detected in Eastman NTA, 100-micron emulsion nuclear track plates. The plates are tilted so that the protons dip into the emulsion at an angle of 5° with respect to the surface. Protons emerging at angles between 0° and 80°, with respect to the deuteron beam, pass through the target backing (if any) and are detected in the forward plate. Protons emerging at angles between 80° and 160° are detected in the rear plate. Shields of silver and aluminum are inserted between the target and each of the plates. A thickness of silver sufficient to stop elastically scattered deuterons as well as the direct beam is employed. The use of silver for this purpose has been found to give rise to negligible background due to (d,p) reactions in the shield. In addition to the silver shield, it is sometimes found to be advantageous to insert additional shields of aluminum in order to reduce the track length of the protons in the emulsion to a convenient value (20–200 microns) for range measurements with the calibrated eyepiece scale in the microscope. Aluminum is used for this purpose since it gives less scattering of the protons (for a given energy loss) than silver.

After exposure the plates are developed; and scribe marks are placed on the emulsion to divide the surface of the emulsion into regions characteristic of the same angle of emergence of the protons with respect to the deuteron beam. The angular width of these regions would be 3° if the target spot were a point. If the finite size of the target spot is taken into account, the maximum angular width is about 6°. A Spencer monocular microscope with a 4-mm achromatic objective and a $10\times$ eyepiece is used to scan the plates.

III. PROTON ENERGY MEASUREMENTS

Proton energy spectra were obtained at several angles using a target foil of natural nickel of surface density 0.5 mg/cm². The spectrum of protons emerging at an angle of 45° with respect to the deuteron beam is shown in Fig. 2(a). The horizontal scale, giving proton track length in the emulsion, was converted to proton energy using the range-energy relation for NTA emulsions given by Richards *et al.*[5] Corrections for the proton

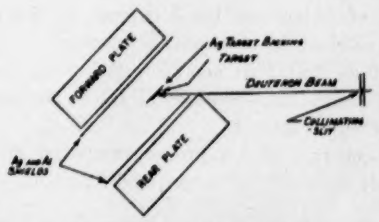

FIG. 1. Diagram of apparatus.

* This work was supported in part by the U. S. Atomic Energy Commission.
† Now at the Pennsylvania State University, State College, Pennsylvania.
[1] J. A. Harvey, Phys. Rev. **81**, 353 (1951).
[2] D. C. Hoesterey, Phys. Rev. **87**, 216 (1952); verbal report quoted in Nuclear Science Abstracts **6**, 24B (1952).
[3] McFarland, Bretscher, and Shull, Phys. Rev. **89**, 892 (1953).
[4] H. E. Gove, Phys. Rev. **81**, 364 (1951).
[5] Richards, Johnson, Ajzenberg, and Laubenstein, Phys. Rev. **83**, 994 (1951).

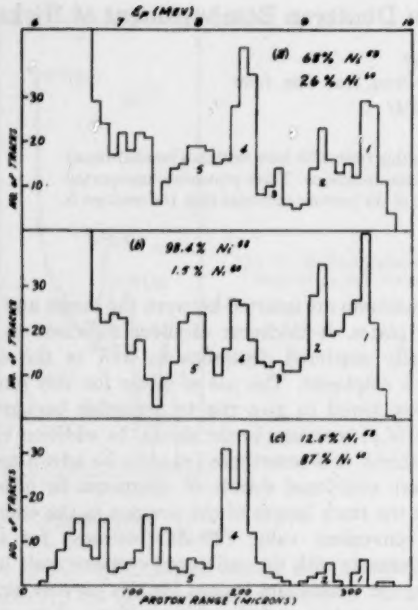

FIG. 2. Proton spectra at 45° angle of proton emission, (a) normal Ni, (b) enriched Ni^{58}, (c) enriched Ni^{60}.

energy loss in the silver and aluminum shields were made using the range-energy relations given by Aron, Hoffman, and Williams.[6]

It is seen from Fig. 2(a) that five groups of protons are reasonably well resolved. All of these groups appear consistently in the data taken at each angle of proton emergence. In order to identify the origin of each of these groups, measurements were made using separated isotopes obtained from the Oak Ridge National Laboratory. Natural nickel contains 68 percent Ni^{58} and 26 percent Ni^{60}; and it has been assumed that all of the proton groups observed here originate in a (d,p) reaction in one of these isotopes. Accordingly measurements were made with a target consisting of 98.4 percent Ni^{58}, 1.5 percent Ni^{60} and a target consisting of 87 percent Ni^{60}, 12.5 percent Ni^{58}. These targets were electrodeposited[7] on a silver backing.

The proton energy spectra obtained using the separated isotopes are shown in Figs. 2(b) and 2(c). The product of (integrated beam current)×(target thickness)×(solid angle observed) is roughly the same in each of Figs. 2(a), 2(b), and 2(c). Background measurements indicate that essentially all tracks observed arise from the nickel targets.

It is seen that all five proton groups are present in the highly enriched Ni^{58} target, and that Group 4 alone appears in strength in the Ni^{60} target. There is also evidence for a group at about 7.5 Mev in the Ni^{60} target which is not apparent in the Ni^{58} target. An analysis of the relative intensities indicates that Groups 1, 2, 3, and 5 are essentially all due to reactions in Ni^{58} and that Group 4 is due to reactions in both Ni^{58} and Ni^{60}. For the ratio of isotopic cross sections for the reactions contributing to Group 4, the value

$$\sigma(Ni^{60}(d,p)Ni^{61})/\sigma(Ni^{58}(d,p)Ni^{59})=1.6$$

is obtained. This implies that the protons in Group 4 observed with the normal nickel target are about 60 percent due to Ni^{58} and 40 percent due to Ni^{60}.

After correcting for the energy loss of the deuterons in the target,[6] the mean deuteron energy is found to be 3.03 Mev. From this and the measured proton energies the Q value (energy released) corresponding to each of the observed proton groups may be computed. The Q values obtained, averaged over all angles for which measurements were made, are given in Table I.

These results may be compared with data observed by several other investigators.

(1) Stelson and Preston[8] have studied the (p,n) reaction in Co^{59}, leading to the ground state of Ni^{59} and to an excited state in Ni^{59}. The result for the excitation energy of the excited state is 0.33±0.05 Mev.

(2) McFarland, Bretscher, and Shull[3] have studied the (d,p) reaction in Ni^{58} using 10.2-Mev deuterons and magnetic analysis of the emerging protons, which should give rather precise energy values. They find proton groups corresponding to Q values of 6.77 Mev, 6.35 Mev, and other groups with Q values below 4 Mev. No groups are reported with Q values between 4 Mev and 6.35 Mev.

(3) Harvey[1] has studied the (d,p) reaction in Ni^{58} using 14-Mev deuterons and range measurement of the emerging protons. His result for the Q value of the ground state in Ni^{59} is 6.78±0.10.

(4) Kinsey and Bartholomew[9] have studied the gamma-ray energy spectrum resulting from thermal-neutron capture in normal nickel. Their results for the six highesten-ergy gamma rays are given in Table II. These values may be converted to the Q value of the corresponding (d,p) reaction if it is assumed that the

TABLE I. Energy released (Q) in the (d,p) reaction in nickel.

Target	Proton group	Q (Mev)
Ni^{58}	1	6.70±0.1
Ni^{58}	2	6.37±0.1
Ni^{58}	3	5.96±0.1
Ni^{58}	4	5.55±0.1
Ni^{60}	4	5.55±0.1
Ni^{58}	5	5.08±0.1

[6] Aron, Hoffman, and Williams, Atomic Energy Commission Report AECU-663, May 28, 1951 (unpublished).

[7] The writer is indebted to Professor W. E. Bennett of the Department of Chemistry for advice on the electrodeposition of nickel.

[8] P. H. Stelson and W. M. Preston, Phys. Rev. **86**, 807 (1952).

[9] B. B. Kinsey and G. A. Bartholomew, Phys. Rev. **89**, 375 (1953).

gamma ray originates in the compound nuclear state in which the neutron is captured. The Q values obtained in this way are also indicated in Table II.

(5) Hoesterey[2] has studied the (d,p) reaction in Ni^{60}, finding a ground state Q value of 6.30 Mev and an excited-state Q value of 5.69 Mev.

(6) Owen, Cook, and Owen[10] have studied the beta decay of Cu^{61} and the resulting gamma-ray spectrum in Ni^{61} to obtain energy levels in Ni^{61} corresponding to the ground state and to excited states at 0.655 Mev, 0.939 Mev, and 1.015 Mev.

All of these data are collected in Fig. 3 in a series of energy level diagrams in terms of the Q value for the (d,p) reaction leading to each level observed. The level diagrams are divided into three columns. The left-hand column contains results for the reaction $Ni^{58}(d,p)Ni^{59}$. The center column contains the (n,γ) data obtained with normal nickel. The right-hand column contains results for the reaction $Ni^{60}(d,p)Ni^{61}$. The data of Stelson and Preston,[8] where energy-level differences rather than Q values were determined, have been normalized to the ground-state Q value obtained by McFarland *et al.*[3] The data of Owen *et al.*,[10] where a similar situation exists, have been normalized to the ground-state Q value obtained by Hoesterey.[2] These normalizations have been indicated by using dotted lines to represent the ground states.

It will be of interest to attempt to identify the precise (n,γ) data of Kinsey and Bartholomew[9] with specific levels in the isotopes.

(1) The first level (A) obtained in the (n,γ) measurements (highest Q value) clearly corresponds to the ground state of Ni^{59}.

(2) The second level (B) in the (n,γ) data differs by 50 kev from the value obtained by McFarland *et al.* for the first excited state of Ni^{59}. Since both of these values are presumably more precise than this discrepancy would imply, it appears that this level should be associated with the ground-state transition in Ni^{61}. The agreement with Hoesterey's value in this case is very good. Furthermore, if the beta-gamma decay data of Owen *et al.* are normalized to this level there is excellent agreement between level E in the (n,γ) data and the third excited state in Ni^{61} obtained by Owen *et al.* There is no indication of any level in Ni^{59} corresponding to level E in the (n,γ) data. Thus levels B and E in the (n,γ) data are assigned to the ground state and third excited state, respectively, in Ni^{61}.

TABLE II. Gamma rays from neutron capture in nickel.[a]

Gamma ray	Gamma-ray energy E (Mev)	Corresponding Q value for (d,p) reactions. $Q=E-2.23$ Mev
A	8.997±0.005	6.77
B	8.532±0.008	6.30
C	8.119±0.010	5.89
D	7.817±0.008	5.59
E	7.528±0.011	5.30
F	7.22 ±0.02	4.99

[a] See reference 9.

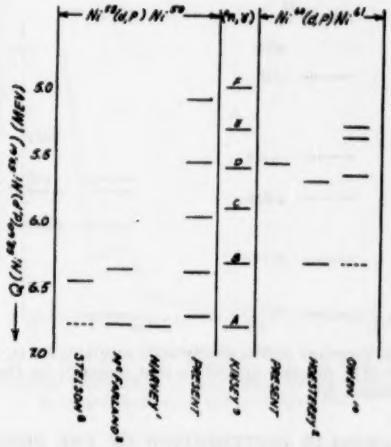

FIG. 3. Energy levels in Ni^{59} and Ni^{61} as observed by various investigators.

(3) Level C in the (n,γ) data is not near any proposed level in Ni^{61} but is close to the second excited state in Ni^{59} as found in the present work. It is therefore assigned to this state in Ni^{59}.

(4) Level D in the (n,γ) data is not in good agreement with the first excited state in Ni^{61} as obtained by Owen *et al.* or by Hoesterey. It is however in agreement with the third excited state in Ni^{59} as obtained in the present work. Furthermore, it is unlikely from intensity considerations[9] that it can be attributed to any level in Ni^{61}. It is therefore assigned to the third excited state of Ni^{59}.

(5) Level F in the (n,γ) data is within experimental error of the fourth excited state in Ni^{59} as found in the present work, and is tentatively assigned to this state.

Kinsey and Bartholomew[9] have assigned levels A, D, and E to Ni^{59} and level B to Ni^{61}. Our conclusions are in agreement with these assignments with the exception of level E, which we prefer to associate with Ni^{61}.

This section may be concluded by assigning partial energy level diagrams to Ni^{59} and Ni^{61}. These are indicated in Fig. 4. The diagram for Ni^{61} is that proposed by Owen *et al.* In the diagram for Ni^{59}, three new levels have been added by the present work. The (p,n) measurements of Stelson and Preston give faint indications of levels in Ni^{59} at 0.58 and 0.83 Mev. The higher of these is close to the second excited state indicated in Fig. 4. It is, however, difficult to understand why the (d,p) measurements of McFarland *et al.*[3] do not give any indication of the three higher levels in Ni^{59}.

[10] Owen, Cook, and Owen, Phys. Rev. **78**, 686 (1950).

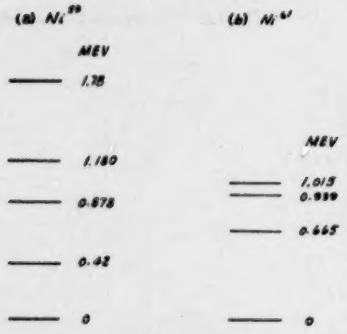

FIG. 4. Proposed partial energy level diagrams for (a) Ni^{59} and (b) Ni^{61}. The diagram for Ni^{61} is that proposed by Owen *et al.* (see reference 10).

IV. ANGULAR DISTRIBUTION OF THE PROTONS

Measurements similar to those shown in Fig. 2 were made at several different angles of proton emission, using a natural nickel target. From these measurements it is possible to obtain the angular distribution of proton groups 1, 2, 4, and 5. These results, some of which have been reported in a previous communication,[11] are shown in Figs. 5 and 6. It is seen that all of the angular distributions are symmetrical about 90°, giving no indication of the peak in the forward direction normally associated with a stripping process.[12] Measurements by Gove,[4] using 14-Mev deuterons, have, on the other hand, indicated a very strong forward maximum in the angular distribution of the protons. The result of one of Gove's measurements is reproduced in Fig. 7.

In the absence of any evidence of the stripping process, it is of interest to consider the predictions of the compound nucleus theory concerning the angular distributions to be expected. A rough estimate of the width and spacing of energy levels in the compound nucleus indicates that the capture of a deuteron will give rise to the simultaneous excitation of a large

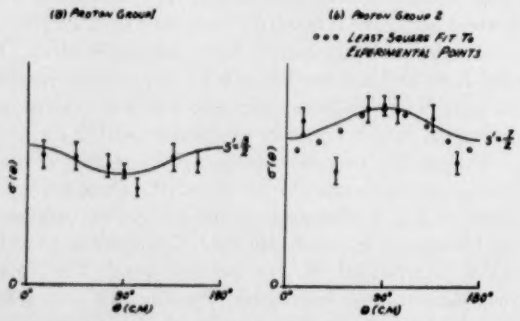

FIG. 5. (a) Angular distribution of proton group 1, (b) angular distribution of proton Group 2. Experimental errors indicated are statistical standard deviations.

number of compound nuclear levels. Under these conditions, the statistical theory proposed by Wolfenstein[13] may be expected to apply. The differential cross section predicted by this theory may be expressed in the form

$$\sigma(\theta)=\sum_{l,l',n,J}\frac{C_{s,s',\pi,\pi'}(l,l',n,J)}{F(J)}P_lP_{l'}\cos^{2n}\theta,$$

where θ is the angle of emission of the proton with respect to the deuteron beam; s, s', π, π' are spins and parities of the initial and final nucleus, respectively; l and l' are the orbital angular momentum of the incoming deuteron and the outgoing proton, respectively; n takes on all integral values from zero to infinity; P_l and $P_{l'}$ are the corresponding barrier penetrabilities; and $F(J)$ represents the density of states of angular momentum J in the compound nucleus. The coefficient C is, aside from a constant factor, a known function of all of its arguments and subscripts.[14,15] For a given

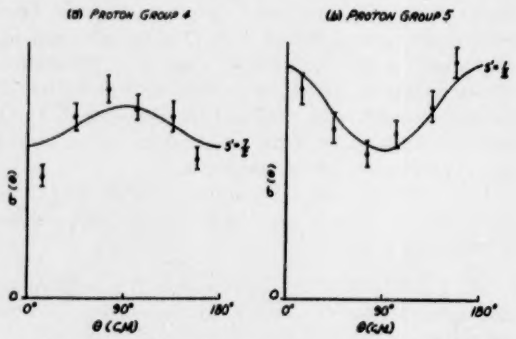

FIG. 6. (a) Angular distribution of proton group 4, (b) angular distribution of proton Group 5. Experimental errors indicated are statistical standard deviations.

reaction, the barrier penetrabilities may be estimated using the W.K.B. approximation.[16] Wolfenstein[13] has proposed two possible forms for the function $F(J)$. If it is assumed that all of the excitation in the compound nucleus is carried by a single particle, then $F(J)$ is taken as independent of J except that $F(0)=\frac{1}{2}F(1)$. If, on the other hand, the excitation is assumed to be distributed among several nucleons, then $F(J)$ is taken as proportional to $2J+1$.

In comparing experimental data from the reactions $Ni^{58}(d,p)Ni^{59}$ and $Ni^{60}(d,p)Ni^{61}$ with the statistical theory, we have employed shell model considerations in order to limit the number of combinations of initial and final spins and parities which must be considered. Both Ni^{58} and Ni^{60}, being even-even nuclei, are assumed to

[11] William W. Pratt, Phys. Rev. **94**, 1086 (1954).
[12] S. T. Butler, Proc. Roy. Soc. (London) **A208**, 559 (1951).
[13] L. Wolfenstein, Phys. Rev. **82**, 690 (1951).
[14] The writer is indebted to Dr. D. L. Falkoff for supplying him with a reprint of a paper (see reference 15) which greatly facilitated the evaluation of some of these coefficients.
[15] Falkoff, Colladay, and Sells, Can. J. Phys. **30**, 253 (1952).
[16] J. M. Blatt and V. F. Weisskopf, *Theoretical Nuclear Physics* (John Wiley and Sons, Inc., New York, 1952), p. 362.

have zero spin and even parity. For the ground state of either Ni^{59} or Ni^{61}, the shell model[17] implies a spin 3/2 (in units of $\hbar$) and odd parity. Furthermore the lowest three odd-neutron orbitals, outside of the closed $f_{7/2}$ shell, are believed[17] to be $p_{3/2}$, $f_{5/2}$, and $p_{1/2}$, all of which have odd parity. We have therefore calculated angular distributions only for transitions from a 0^+ state to a state of odd parity. Calculations for the transition to states of the type $1/2^-$, $3/2^-$, $5/2^-$, $7/2^-$, and $9/2^-$ have been carried out. The calculations have been performed neglecting the contribution of deuteron orbital angular momenta $\geqslant 3$ and of proton orbital angular momenta $\geqslant 6$. It is estimated that 90 percent of each reaction is due to l values within these limits. In the case of the $0^+ \rightarrow 9/2^-$ transition, certain contributions from protons with $l=5$ were also neglected, leading to an error which is believed to be no greater than 3 percent.

The result of the calculations for the case $E_d=2.94$ Mev, $Q=6.70$ Mev, corresponding to the ground-state transition in Ni^{59}, is presented in Fig. 8.

In Figs. 5 and 6 the experimental results are compared with the predictions of the statistical model. In each case the theoretical curve which can most easily be fitted to the data is shown;[18] and the assumption of single-particle excitation, which appears to give somewhat better agreement than the other assumption,[11] is used.

(1) Proton group 1 [Fig. 5(a)], representing the transition to the ground state of Ni^{59}, is in good agreement with the theoretical curve for a final $3/2^-$ state. This also is the ground state of Ni^{59} implied by the shell model.

(2) Proton group 2 [Fig. 5(b)], representing the transition to the first excited state of Ni^{59}, shows an unduly large spread in the experimental points. However, a least-squares fit of a curve of the form $a+b\cos^2\theta$ is indicated by the open circles, and is in agreement with the theoretical curve for a final $7/2^-$ state.

(3) Proton group 3 is too weak for a measurement of the angular distribution to be attempted.

(4) Proton group 4 [Fig. 6(a)], representing roughly equal contributions from transitions in Ni^{59} and Ni^{60}, is in fair agreement with the theoretical curve for a final $7/2^-$ state.[19] The significance of any such agreement in this case is, of course, open to question in view of the double transition involved.

(5) Proton group 5 [Fig. 6(b)], representing a transition to the fourth excited state in Ni^{59}, is in good agreement with the theoretical curve for a final $1/2^-$ state.

It may be concluded from these results that the reaction in which a compound nucleus is formed predominates over the stripping process in this case, and that the angular distribution of the emerging protons is well represented by Wolfenstein's theory.

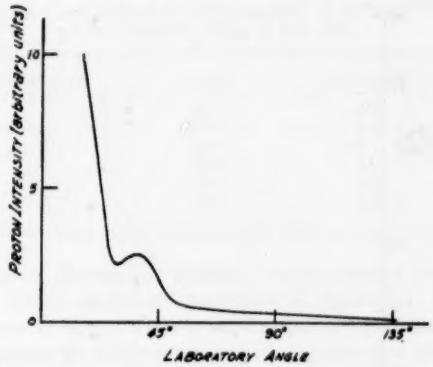

FIG. 7. Angular distribution of long range protons from 14-Mev bombardment of Ni (from reference 4).

In this connection it is of interest to consider the relative effectiveness of compound nucleus formation and stripping in the general case. It has previously been shown[12,20] that, for bombarding energies well above the Coulomb barrier of the target nucleus, the (d,p) reaction appears to proceed mainly by the stripping process. For bombarding energies below the barrier, however, the results which have been obtained to date are not definitive on this point. If it may be assumed, as indicated by the Butler theory,[12] that the angular distribution of protons associated with the stripping process is characterized at all energies by a forward maximum in the cross section which is large compared to the cross section in the backward direction, then the ratio $\sigma(\theta_m)/\sigma(\theta_0)$ may be considered as giving a rough measure of the relative importance of stripping and compound nucleus formation. Here θ_m is the angle in the forward direction corresponding to the maximum value of the cross section, and θ_0 is some angle in the backward direction, where the cross section is usually

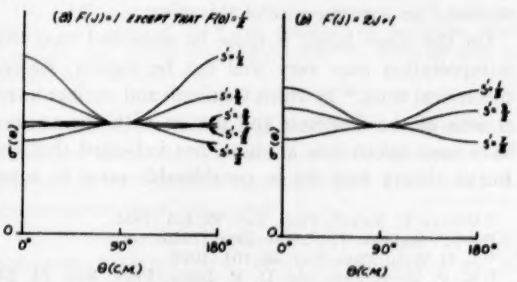

FIG. 8. Angular distribution of protons in a transition from a 0^+ state to an odd-parity state, $Q=6.7$ Mev, deuteron energy $=2.94$ Mev. (a) Single-particle excitation, (b) multiple-particle excitation. All curves are symmetrical about 90°.

[17] P. F. A. Klinkenberg, Revs. Modern Phys. 24, 63 (1952).

[18] Since the theoretical curves are not very sensitive to Q, the fit for other cases may be estimated from Fig. 8.

[19] This group was erroneously attributed entirely to the transition in Ni^{61} in our previous communication (reference 11).

[20] D. C. Peaslee, Phys. Rev. 74, 1001 (1948).

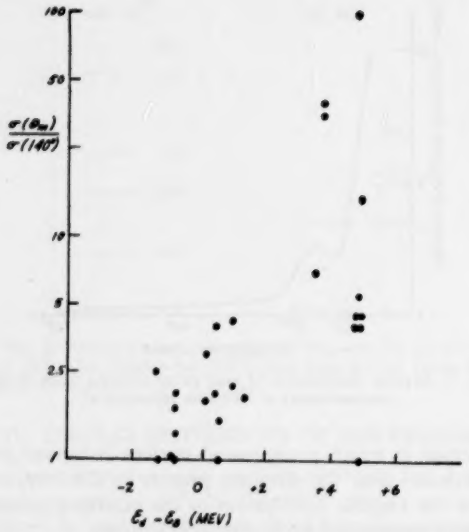

FIG. 9. Ratio of (d,p) cross section in forward direction to that in backward direction as a function of (deuteron energy) − (barrier height).

found to have a relatively small variation with angle. In Fig. 9 this ratio has been plotted as a function of the difference between deuteron bombarding energy (E_d) and Coulomb barrier height (E_B). The data[21–26] from which this figure has been constructed represent transitions in various isotopes leading to various states in the final nucleus.

It is seen that there is a systematic trend for the ratio $\sigma(\theta_m)/\sigma(140°)$ to decrease from a value large compared with unity at bombarding energies above the barrier to a value of the order of unity at bombarding energies below the barrier. This behavior is suggestive of a situation in which stripping predominates for high bombarding energies and compound nucleus formation predominates for low bombarding energies. If this is the correct interpretation of the data, then it is clear that the present results with nickel ($E_B \approx 7$ Mev) represent an extreme case of this effect.

On the other hand, it must be remarked that this interpretation may very well not be correct. Recent theoretical work,[27] in which Coulomb and nuclear interactions of the deuteron and proton with the nucleus have been taken into account, has indicated that the Butler theory may be in considerable error in some cases. In particular, the Coulomb effects appear to result in a broadening of the peak in the angular distribution and in shifting it to larger angles. Since these effects may be expected to increase as the deuteron energy is reduced, it is quite possible that the behavior of the ratio $\sigma(\theta_m)/\sigma(\theta_0)$ indicated in Fig. 9 may be accounted for without resorting to any contribution from compound nuclear formation. Thus, although the data of Fig. 9 are consistent with the suggestion that compound nucleus formation becomes relatively more important for low deuteron energies, they do not furnish a compelling argument that this is the case.

We may conclude this section with a discussion (of a highly speculative nature) of possible spin values for some of the states in Ni^{59} and Ni^{61}. In Fig. 10 the proposed partial energy level diagrams for these nuclei have been reproduced, together with the spin values implied by the angular distribution measurements (the spin $3/2^-$ for the ground states of Ni^{61} and Cu^{61} are taken from the shell model[17]). In addition the gamma rays observed[9] subsequent to thermal neutron capture in Ni^{58} and Ni^{60} have been indicated, as well as the beta rays observed[10] in the positron decay of Cu^{61}.

Most of these observations are seen to be consistent with the spin assignments. The capture of thermal neutrons by the (even-even) nuclei Ni^{58} and Ni^{60} will presumably lead to states in the excited nuclei Ni^{59} and Ni^{61} of spin 1/2 and even parity. Dipole emission of gamma radiation will then be expected to states of spin 1/2 or 3/2, and all of these transitions are indeed observed. The remaining states where spin assignments have been made are all $7/2^-$ states, requiring octupole emission of gamma radiation; in two of these three cases the gamma radiation is not observed. The emission of a positron from the $3/2^-$ state in Cu^{61} to the $3/2^-$ state in Ni^{61} is expected to be allowed, and this is in agreement with experimental observation.[10] The only discrepancies involve the third excited state in Ni^{59} and

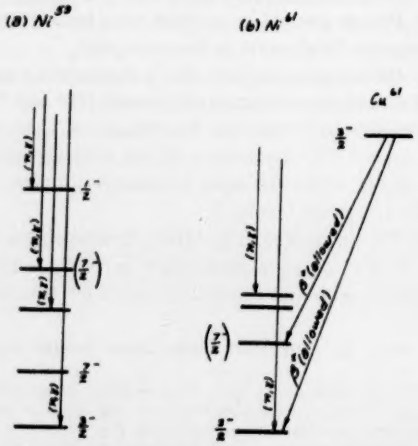

FIG. 10. Possible spin values in (a) Ni^{59} and (b) Ni^{61}.

[21] William E. Nickell, Phys. Rev. **95**, 426 (1954).
[22] W. C. Redman, Phys. Rev. **79**, 6 (1950).
[23] L. D. Wyly, Phys. Rev. **76**, 104 (1949).
[24] N. P. Heydenberg and D. R. Inglis, Phys. Rev. **73**, 230 (1948).
[25] W. M. Gibson and E. E. Thomas, Proc. Roy. Soc. (London) **A210**, 543 (1952).
[26] Burge, Burrows, Gibson, and Rotblat, Proc. Roy. Soc. (London) **A210**, 534 (1952).
[27] W. Tobocman and M. Kalos, Phys. Rev. **95**, 605 (1954); and verbal report.

the first excited state in Ni^{61}, both of which have been tentatively assigned a spin $7/2^-$ on the questionable basis of the angular distribution of proton group 4. The (n,γ) measurements show a strong transition to one of these states and the positron decay from Cu^{61} to the other is believed[10] to be allowed. Both of these observations are in disagreement with the 7/2 spin assignments. Whether these discrepancies can be attributed to the presence of one or more states which have not as yet been observed, to the presence of cascade gamma rays in the (n,γ) measurements, or to some other defect in our analysis, is not known at this time.

V. CROSS SECTIONS

From the known values of integrated deuteron beam current, target thickness, and solid angle subtended by the detecting plates, it is possible to obtain the cross section for the reaction leading to each observed transition. These results are presented in Table III. The absolute values of these cross sections are believed to be accurate to within about a factor of two. The errors in relative value are considerably less than this.

TABLE III. Cross sections for (d,p) reactions in Ni^{58} and Ni^{60} at a mean deuteron energy of 3.03 Mev.

Proton group	Target	$\sigma \times 10^{28}$ (cm^2)
1	Ni^{58}	6.6
2	Ni^{58}	8.8
3	Ni^{58}	2
4	Ni^{58}	6.0
	Ni^{60}	9.6
5	Ni^{58}	9.6

The writer wishes to express his appreciation to Professor James A. Jacobs and Mr. Philip R. Malmberg for valuable assistance with this work.

PHYSICAL REVIEW VOLUME 95, NUMBER 6 SEPTEMBER 15, 1954

Beta Spectra of Pr^{142}, Tm^{170}, and Rb^{86}†

A. V. POHM, W. E. LEWIS,* J. H. TALBOY, JR., AND E. N. JENSEN
Institute for Atomic Research and Department of Physics, Iowa State College, Ames, Iowa

(Received April 21, 1954)

The beta spectra and gamma rays of the isotopes Tm^{170}, Pr^{142}, and Rb^{86} have been examined with various types of spectrometers. An intermediate-image beta-ray spectrometer with a 10 percent transmission and a 5.5 percent resolution was used to examine the total and coincidence beta spectra. Total beta spectra were also studied with a thin-lens spectrometer set to about two percent resolution. Gamma rays were also studied with a scintillation spectrometer.

The results of the investigation indicate that the 125-day activity of Tm^{170} has two beta groups with maximum energies of 970±2 kev and 886±9 kev. Their respective intensities are about 78 percent and 22 percent, and their respective log ft values are approximately 9.0 and 9.1. Both beta groups are assigned as first forbidden transitions with $\Delta I = \pm 1$, "yes." The single observed gamma ray of Tm^{170} is assigned as an $E2$ transition with an energy of 84.1±0.4 kev.

The 19.2-hr activity of Pr^{142} has two beta groups with maximum energies of 2166±6 kev and 586±15 kev. The 2166-kev beta group has a log ft value of about 7.8 and the 586-kev beta group has a log ft value of about 7.1. The log$[(W_0^2-1)ft]$ value of the 2166-kev beta group is 10.2. The intensities for the 2166-kev and 586-kev beta groups were found to be, respectively, 90–95 percent and 5–10 percent.

The 2166-kev beta group is assigned as first forbidden with $\Delta I = 2$, "yes" and the 586-kev beta group as first forbidden with $\Delta I = 0$ or ± 1, "yes." The single observed gamma ray, having an energy of 1572±8 kev, is tentatively assigned as an $E2$ or $M1$ transition. The $E2$ and $\Delta I = 0$, "yes" choices are probably correct.

The 19.5-day activity of Rb^{86} has two beta groups with maximum energies of 1770±4 kev and 680±6 kev. Their intensities are about 88 percent and 12 percent, respectively. The log ft value for the 1770-kev beta group is about 8.5 and for the 680-kev beta group 7.8. The log $[(W_0^2-1)ft]$ value for the 1770-kev beta group is 9.7. This beta group is assigned as a first forbidden transition with $\Delta I = 2$, "yes," and the 680-kev beta group is tentatively assigned as first forbidden with $\Delta I = 0$, "yes." The single gamma ray has an energy of 1080±6 kev and is tentatively assigned as an $E2$ transition.

The Kurie plots of the 680-kev beta group of Rb^{86} and the 886-kev beta group of Tm^{170} were examined for deviations from a straight line. Within experimental error no deviation from a straight line was observed.

INTRODUCTION

IN this work an attempt was made to examine primarily the beta decays of Pr^{142}, Tm^{170}, and Rb^{86} using a coincidence technique. An intermediate-image spectrometer[1] which has a transmission of 10 percent at 5.5 percent resolution was used for the coincidence work. For conventional spectra, a thin-lens spectrometer set to two percent resolution and a scintillation spectrometer were also used.

In the intermediate-image spectrometer, the gamma rays were detected by a 5819 photomultiplier and a Lucite-covered NaI(Tl) crystal placed far enough behind the source to prevent distortion of the beta spectra by scattering (6292 phototubes are being used at present for the beta and gamma detectors). The focused beta particles were detected by an anthracene crystal and a

† Contribution No. 328 from the Institute for Atomic Research and Department of Physics, Iowa State College, Ames, Iowa. Work was performed in the Ames Laboratory of the U. S. Atomic Energy Commission.

* Now at the Minneapolis-Honeywell Regulator Company, Minneapolis, Minnesota.

[1] Nichols, Pohm, Talboy, and Jensen, U. S. Atomic Energy Commission Report No. ISC-345, 1953 (to be published).

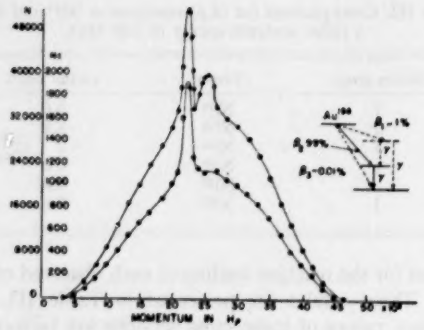

FIG. 1. Total and coincidence spectra of Au^{198}.

cooled (−40°C) 5819 photomultiplier. The scintillation pulses in the crystals were transmitted to the photomultiplier tubes by means of Lucite light pipes about 1.2 inches in diameter and 15 inches long.

To check the operation of the instrument, the activity of Au^{198} was examined; the coincidence and total beta spectra agreed well (Fig. 1). The Kurie plots of the total and coincidence spectra are indicated in Fig. 2. The end-point energy of 967±5 kev agrees with the value of 963 kev given by Hollander, Perlman, and Seaborg.[2] The Kurie plots deviate from a straight line below the conversion electron energy because of the presence of Au^{199} and the lower-energy beta group of Au^{198}. A detailed study of the contamination of Au^{198} by Au^{199} and its effect on the Au^{198} Kurie plot was made by Fan.[3] A very satisfactory coincidence counting rate of over 1000 counts per minute was obtained at the peak of the beta spectrum with about a five-microcurie source.

The coincidence circuit had a resolving time of about 0.5 microsecond. For most points the accidental coincidence counting rates were less than 40 percent of the true coincidence counting rates.

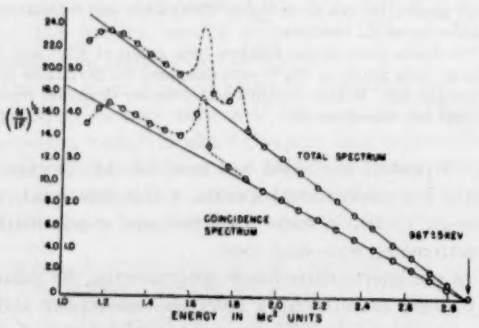

FIG. 2. Kurie plots of Au^{198} total and coincidence spectra.

[2] Hollander, Perlman, and Seaborg, Revs. Modern Phys. **25**, 469 (1953).
[3] Chan-Yun Fan, Phys. Rev. **87**, 252 (1952).

Reported work[4–10] on the 19.2-hour decay of Pr^{142} reveal that it has a complex decay. The investigations indicate that the decay of Pr^{142} has two beta groups with average energies of about 2.18 Mev and 0.65 Mev, and one gamma ray of about 1.58 Mev. The 0.65-Mev beta group was assigned an intensity ranging from 4 to 20 percent. The values of the maximum energy for the lower-energy beta group were determined by the subtraction method. Jensen *et al.*[9] ascribed a spin of two and odd parity to the ground state of Pr^{142} and a spin of one or two with even parity for the excited state of Nd^{142}. The 2+ assignment is probably correct because of the preponderance of 2+ first excited states for even-even nuclei.[11] Cork, Shreffler, and Fowler[5] also found additional gamma rays of 133.7, 328.9, 489.6, and 623.6 kev using a magnetic spectrograph.

Most investigators[2,12–27] of the 125-day activity of Tm^{170} found two beta groups with maximum energies of about 885 kev and 970 kev and one gamma ray at about 84.1 kev. Graham *et al.*[15] have made a thorough investigation of the radiations from Tm^{170}. They found the beta-ray spectrum to consist of two components with maximum energies of 968±4 kev and 884±4 kev and having relative intensities of 76 percent and 24 percent, respectively. The low-energy beta group was followed by a gamma ray having an energy of 84.1±0.1 kev. From the internal conversion coefficients the gamma ray was assigned as an *E2* transition.

Published work[10,28–35] on the 19.5-day activity of Rb^{86} indicates that it has two beta groups with maxi-

[4] DeWire, Pool, and Kurbatov, Phys. Rev. **61**, 564 (1942).
[5] Cork, Shreffler, and Fowler, Phys. Rev. **74**, 1657 (1948).
[6] C. E. Mandeville, Phys. Rev. **75**, 1287 (1949).
[7] E. T. Jurney, Phys. Rev. **76**, 290 (1949).
[8] E. R. Rae, Proc. Phys. Soc. (London) **A63**, 292 (1950).
[9] Jensen, Laslett, and Zaffarano, Phys. Rev. **80**, 862 (1950); Phys. Rev. **86**, 1047 (1952).
[10] J. Moreau and J. Perez y Jorba, Compt. rend. **235**, 38 (1952).
[11] G. Scharff-Goldhaber, Phys. Rev. **90**, 587 (1953).
[12] P. J. Grant, Nature **165**, 1018 (1950).
[13] R. L. Caldwell, Phys. Rev. **78**, 407 (1950).
[14] H. M. Agnew, Phys. Rev. **77**, 655 (1950).
[15] Graham, Wolfson, and Bell, Can. J. Phys. **30**, 459 (1952).
[16] J. S. Fraser, Phys. Rev. **76**, 1540 (1949).
[17] F. K. McGowan, Phys. Rev. **85**, 151 (1952).
[18] T. B. Novey, Phys. Rev. **78**, 66 (1950).
[19] K. Siegbahn, Arkiv. Fysik **4**, 250 (1952).
[20] R. Richmond and H. Rose, Phil. Mag. **43**, 367 (1952).
[21] M. Goldhaber and R. D. Hill, Revs. Modern Phys. **24**, 179 (1952).
[22] J. W. Mihelich and E. L. Church, Phys. Rev. **85**, 690 (1952).
[23] R. Bell and R. Graham, Phys. Rev. **78**, 490 (1950).
[24] H. Rose, Phil. Mag. **43**, 1146 (1952).
[25] D. Saxon and J. Richards, Phys. Rev. **76**, 186 (1949).
[26] R. L. Graham and D. H. Tomlin, Nature **164**, 278 (1949).
[27] Nakamura, Umezawa, and Takebe, Phys. Rev. **84**, 865 (1951).
[28] Macklin, Lidofsky, and Wu, Phys. Rev. **82**, 334 (1951).
[29] Zaffarano, Kern, and Mitchell, Phys. Rev. **74**, 682 (1948).
[30] H. R. Muether and S. L. Ridgway, Phys. Rev. **80**, 750 (1950).
[31] C. E. Mandeville and E. Shapiro, Phys. Rev. **77**, 439 (1950).
[32] E. T. Jurney, Phys. Rev. **74**, 1049 (1948).
[33] J. P. Palmer and L. J. Laslett, U. S. Atomic Energy Commission Report ISC-174, 1950 (unpublished).
[34] E. Haggstrom, Phys. Rev. **62**, 144 (1942).
[35] Hamilton, Lemonick, and Pipkin, Phys. Rev. **92**, 1191 (1953).

mum energies of about 1770 kev and 700 kev and one gamma ray of 1080 kev.

The 1770-kev beta group is found to have a shape characteristic of a $\Delta I=\pm 2$, "yes" transition.[28,30] The 700-kev beta group is generally reported as having an allowed shape.[30] Angular correlation measurements indicate an $E2$ transition for the gamma ray.[35,36]

Pr^{142}

The Pr^{142} activity was obtained by neutron bombardment of spectrographically pure Pr_6O_{11} at the Oak Ridge pile. (The Pr_6O_{11} and the Tm_2O_3 used in this work were made available through the courtesy of Dr. F. H. Spedding and Dr. J. E. Powell of this laboratory.) The source material had an estimated surface density of about 2 or 3 mg/cm² and was supported by a 40-μg/cm² Formvar-polystyrene film.

The investigation of the beta spectra of Pr^{142} revealed it has two beta groups. The higher-energy group

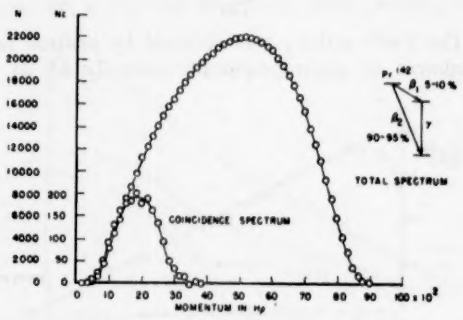

FIG. 3. Total and coincidence spectra of Pr^{142}.

has a maximum beta energy of 2166±6 kev. This beta group was examined with an intermediate image spectrometer set to 5.5 percent resolution and a thin-lens spectrometer set to 2 percent resolution. The values for the maximum beta energy of this group determined by the two instruments agreed within experimental error. In order to obtain a linear Kurie plot, it was necessary to apply the a correction factor. The correction factor is given by $a=(W_0-W)^2+\Lambda(W^2-1)$, where W is the total electron energy, W_0 is the total maximum electron energy, and the coefficient Λ is a function of electron energy and atomic number.[37] The total and coincidence spectra are shown in Fig. 3. The Kurie plots of the total spectrum are illustrated in Fig. 4, the lower-energy beta group being obtained by subtraction. The data shown in Fig. 4 were obtained with the thin-lens spectrometer. The Kurie plot of the coincidence beta spectrum is illustrated in Fig. 5.

The coincidence spectrum yields a maximum beta energy of 586±15 kev and has an allowed shape within

[36] D. T. Stevenson and M. Deutsch, Phys. Rev. **83**, 1202 (1951).
[37] Laslett, Jensen, and Paskin, Phys. Rev. **79**, 412 (1950).

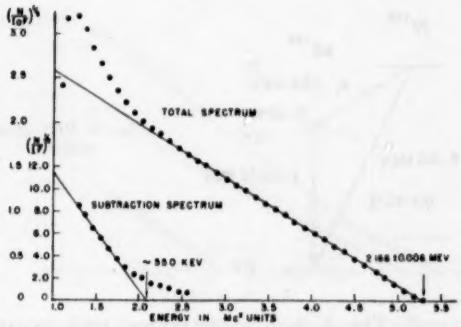

FIG. 4. Kurie plots of Pr^{142} total and subtraction spectra.

experimental error. The Kurie plot for the lower-energy beta group obtained by the conventional subtraction method, Fig. 4, shows considerable curvature near the maximum energy, apparently resulting from source thickness effects. Because of this, only a rough estimate could be made of the ratio of intensities of the two beta groups and of the maximum energy of the lower-energy beta group.

The scattering from the higher-energy beta group into the low-intensity, lower-energy beta group is probably responsible for most of the deviation of the subtracted Kurie plot near the maximum energy. This effect was not noticeable on the coincidence spectrum because scattered beta particles from the higher-energy group were not in coincidence with the gamma ray. From the subtraction data, the estimated intensities are 5–10 percent and 90–95 percent for the 586-kev and 2166-kev beta groups, respectively.

The log ft values were calculated using the average value of these estimated intensities, 7.5 percent and 92.5 percent. The 2166-kev beta group has a log ft value of 7.8 and a log $(W_0^2-1)ft$ value of 10.2. The 586-kev group has a log ft value of 7.1.

The gamma-ray spectrum of Pr^{142} was examined with an intermediate image spectrometer and a scintillation spectrometer. Using a lead radiator with a surface density of 23.2 mg/cm², a single gamma ray was

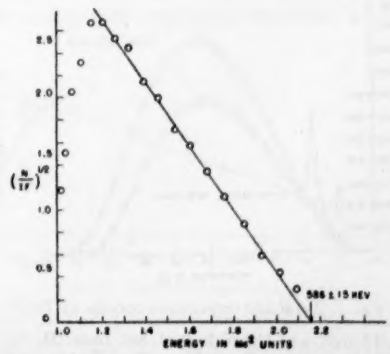

FIG. 5. Kurie plot of coincidence spectrum of Pr^{142}.

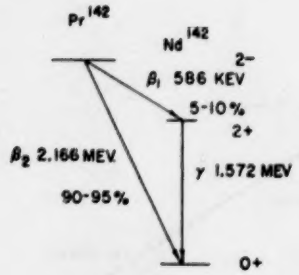

FIG. 6. Pr^{142} decay scheme.

observed. The K-shell photoelectron peak occurred at an energy of 1477 kev. When the K binding energy of 88 kev[38] and the correction for energy loss in the foil of 7 kev[39] were added to the electron energy, the gamma-ray energy was found to be 1572 ± 8 kev.

The scintillation spectrometer also indicated only one gamma ray with an energy of about 1600 kev. The additional gamma rays reported by Cork[5] were not observed. There appeared to be a slight peak at about 350 kev.

It is seen that the difference (1580 kev) between the maximum energy of the higher-energy beta group (2166 kev) and the maximum energy of the lower-energy beta group as obtained from the coincidence spectrum (586 kev) is in good agreement with the gamma-ray energy of 1572 kev.

Because it was necessary to plot the 2166-kev beta group of Pr^{142} with an a correction factor to obtain a linear Kurie plot, this transition is assigned as first forbidden with $\Delta I=2$, "yes." The log ft value is 7.8, which falls in the range of values for this type of transition.[40] The lower-energy beta group, within experimental error, appears to have an allowed shape as shown in Fig. 5. This information and its log ft value of 7.1 indicate that the transition is probably first forbidden with $\Delta I=0$ or ±1, "yes."

G. Scharff-Goldhaber[41] has surveyed the excited states of even-even nuclei and has found that in 66 out of 68 nuclei investigated an assignment of $I=2+$ for the first excited state is compatible with experimental results obtained on these isotopes. Taking the ground state of the even-even Nd^{142} nucleus to be 0+, the ground state of Pr^{142} is a 2− state. This is compatible with the predictions of the nuclear shell model[41] in regard to parity and spin in accordance with the rule proposed by Nordheim[40] for the beta decay of odd-odd nuclei. If the first excited state of Nd^{142} is a 2+ state, then the transition from the 2− ground state of Pr^{142} to the 2+ excited state of Nd^{142} would correspond to a $\Delta I=0$, "yes" transition. The possibility exists that this lower-energy transition could also correspond to a $\Delta I=\pm1$, "yes" transition to a 1+ state of Nd^{142}. However, because of the preponderance of 2+ first excited states for even-even nuclei, the 2+ choice is tentatively made for Nd^{142}. The resultant decay scheme is shown in Fig. 6. If the 2+ choice is correct, the gamma radiation corresponds to an $E2$ transition.

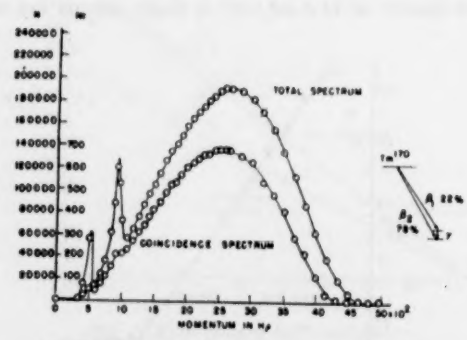

FIG. 7. Total and coincidence spectra of Tm^{170}.

[38] Hill, Church, and Mihelich, Rev. Sci. Instr. **23**, 523 (1952).
[39] Jensen, Laslett, and Pratt, Phys. Rev. **75**, 458 (1949).
[40] L. W. Nordheim, Revs. Modern Phys. **23**, 322 (1951).

Tm^{170}

The Tm^{170} activity was obtained by neutron bombardment of spectrographically pure Tm_2O_3 at the Oak Ridge pile. The sources were estimated to have an average thickness of about 1 mg/cm². The backing was a 40-μg/cm² Formvar-polystyrene film.

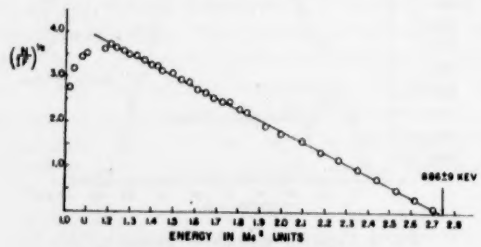

FIG. 8. Kurie plot of Tm^{170} coincidence spectrum.

It was found that Tm^{170} has two beta groups. The higher-energy group has a maximum beta energy of 970 ± 2 kev. This maximum energy was determined both with a thin lens and an intermediate-image spectrometer, and both values agreed within experimental error. The total and coincidence beta spectra are indicated in Fig. 7. The Kurie plot of the coincidence spectrum is illustrated in Fig. 8. Within experimental error, it has an allowed shape. The best coincidence values indicate a maximum energy of 886 ± 9 kev. This is an average of several determinations and is the value given in Fig. 8. The lower-energy beta group was also obtained by the conventional subtraction method on the total spectrum. The maximum energy obtained for the lower-energy group by this method was about 875 kev when the higher-energy group was assigned either as having an allowed or first forbidden shape with

[41] M. G. Mayer and S. A. Moszkowski, Revs. Modern Phys. **23**, 315 (1951).

$\Delta I=2$, "yes." In both cases, the subtraction group has an allowed shape. The Kurie plots are indicated in Figs. 9 and 10. Not all of the 25 points beyond the maximum energy of the lower-energy (886-kev) beta group used to perform the subtraction are indicated on the graphs. These data were obtained on a thin-lens spectrometer.

In Figs. 9 and 10 what appears to be a third low-energy beta group when a second subtraction is performed has been reported by others.[15,16] The work of Graham *et al.*[15] indicated that this distribution results from scattering. It was not detected in the coincidence spectrum probably because a thinner source was used in making the coincidence measurements.

Considering the 970-kev beta group and the 886-kev beta group as having allowed shapes, their respective intensities are 78 percent and 22 percent and their respective log *ft* values are 9.0 and 9.1.

Using values for the intensities of the two beta groups obtained by averaging the results of this work and that of Graham *et al.*,[15] the coincidence beta spectrum was

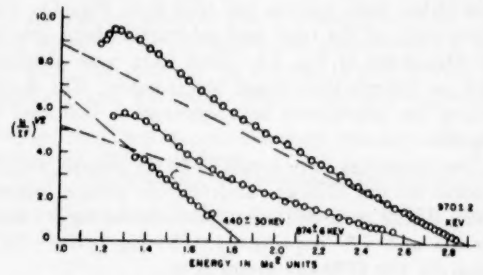

FIG. 9. Total and subtraction spectra of Tm^{170} (all groups plotted as allowed).

subtracted from the total spectrum. The Kurie plot of the resulting spectrum is illustrated in Fig. 11. These data were obtained with an intermediate image spectrometer and with a thinner source than that used in obtaining the data for Fig. 9. Within experimental error the Kurie plot is straight until the source thickness effect causes a deviation below 300 kev. The intensities used for the 886-kev and 970-kev beta groups were 23 percent and 77 percent, respectively.

The energy of the single gamma ray present in the decay of Tm^{170} was determined primarily from the composite L conversion line. The K conversion electron energy was near counter cutoff, and accordingly was unreliable. The energy correction for the composite L line was determined from relative intensities of the L_{I}, L_{II}, and L_{III} lines determined by Mihelich and Church.[22] The gamma-ray energy was measured to be 84.1 ± 0.4 kev.

It is seen that the difference between the maximum energy of the higher-energy beta group (970-kev) and the maximum energy of the lower-energy beta group as obtained from the coincidence spectrum (886 kev)

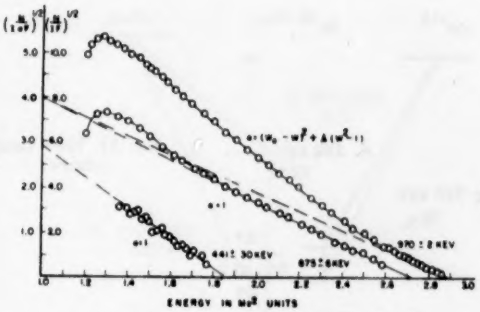

FIG. 10. Total and subtraction spectra of Tm^{170}.

is in good agreement with the 84.1-kev gamma-ray energy. These results on Tm^{170} are in good agreement with those of Graham *et al.*[15]

From the internal conversion data of Axel and Goodrich[42] and those of Hebb and Nelson,[43] it is found that the 84.1-kev gamma ray of Tm^{170}, which was determined to be an $E2$ transition,[17] should be highly converted. The Axel and Goodrich data were computed from the accurate relativistic calculations of Rose *et al.*[44]

The measurements of Fraser[16] and McGowan[17] also indicate that the gamma ray is converted more than 80 percent. The measurements of this work and those of Siegbahn[19] and Fraser[16] indicate that the number of conversion electrons is about 20 percent of the total number of beta particles.

If the 970-kev beta group of Tm^{170} is plotted with an a correction factor in the Kurie plot and a subtraction performed, Fig. 10, the intensities for the 970-kev and 886-kev beta groups are about 50 percent and 50 percent, respectively. This is in disagreement with the intensities expected from conversion electron measurements.

Because of the high conversion coefficient, the number of particles in the lower-energy 886-kev beta group should approximately equal the number of conversion electrons. If the 970-kev group is plotted as an allowed spectrum and a subtraction performed, Fig. 9, then the relative intensities are in agreement with the data on the number of conversion electrons, which indicates that the number of conversion electrons is equal to

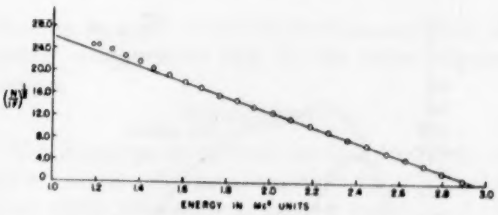

FIG. 11. Tm^{170} 970-kev beta group.

[42] P. Axel and R. F. Goodrich, Office of Naval Research Report, University of Illinois (unpublished).
[43] M. H. Hebb and E. Nelson, Phys. Rev. **58**, 486 (1940).
[44] Rose, Goertzel, and Perry, Phys. Rev. **83**, 79 (1951).

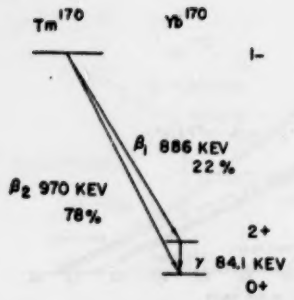

FIG. 12. Tm^{170} decay scheme.

about 20 percent of the total number of beta particles. Therefore, the 970-kev group is assigned an allowed shape.

From the coincidence spectrum, the 886-kev beta group was observed to have an allowed shape.

Using the measured K and L ratios and half-life measurements, McGowan[17] and others[22,23] determined the gamma ray to be an $E2$ transition. Therefore the excited state of Yb^{170} is assigned a 2+ state because of the $E2$ transition and the 0+ ground state for the even-even nucleus of Yb^{170}. From experimental evidence, both beta groups are found to have allowed shapes and log ft values of about 9. This suggests $\Delta I=0$ or ± 1, "yes" transitions. A consistent decay scheme can then be obtained by assigning the ground state of Tm^{170} as a 1− state. The resultant decay scheme consistent with experimental data is given in Fig. 12. Both beta groups are assigned as $\Delta I=\pm 1$, "yes" transitions.

Rb^{86}

The Rb^{86} sample was obtained from the Oak Ridge Isotope Division. The average source thickness was less than 2 mg/cm². The backing was a 40-μg/cm² Formvar-polystyrene film.

Two beta groups were found in the activity of Rb^{86}. The higher-energy group has a maximum energy of 1770±4 kev and the lower-energy group has a maximum energy of 680±6 kev which was determined by coincidence measurements. The maximum energy of the lower-energy beta group was also obtained by the conventional subtraction method. This yielded a maximum energy of 718±8 kev. The maximum energy of the higher-energy beta group was determined both with a thin-lens spectrometer and an intermediate image spectrometer. The values for both spectrometers agreed within experimental error. To obtain a linear Kurie plot, it was necessary to use the a correction factor on the higher-energy beta group. Both the coincidence and subtraction spectra of the lower-energy beta group indicate that it has an allowed shape. The total and coincidence beta spectra are shown in Fig. 13. The Kurie plots of the total and subtraction beta spectra are illustrated in Fig. 14. These data were obtained with an intermediate image spectrometer. The Kurie plot of the coincidence beta spectrum is indicated in Fig. 15.

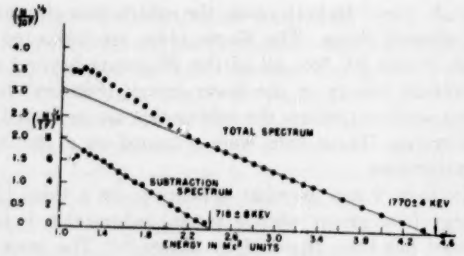

FIG. 14. Kurie plots of Rb^{86} total and subtraction spectra.

The intensities were found to be 88 percent and 12 percent for the 1770-kev and 680-kev groups, respectively. Using these relative intensities, the log ft values are 8.5 and 7.8, respectively. The log $[(Wo^2-1)ft]$ value for the 1770-kev group is 9.7.

The gamma radiation of Rb^{86} was examined by means of an intermediate image spectrometer and a lead radiator with a thickness of 16.7 mg/cm². When the correction for the K binding energy and the average energy loss in the foil was made,[39] the gamma-ray energy was found to be 1080±6 kev.

The 1770-kev beta group of Rb^{86} is considered as a $\Delta I=\pm 2$, "yes" transition because the a correction factor is necessary to obtain a linear Kurie plot and because of the log $[(Wo^2-1)ft]$ value of 9.7. From this information and the 0+ assignment to the ground state of the even-even nucleus Sr^{86}, the ground state of Rb^{86} can be assigned as a 2− state. The lower-energy beta group (680 kev) was found to have an allowed shape

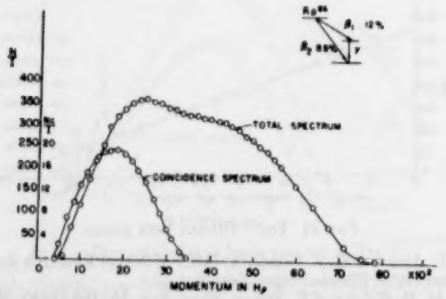

FIG. 13. Total and coincidence spectra of Rb^{86}.

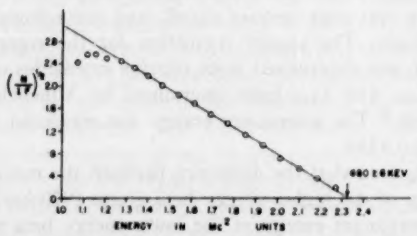

FIG. 15. Kurie plot of Rb^{86} coincidence spectrum.

and a log *ft* value of 7.8. This suggests a first forbidden transition with $\Delta I=0$ or ± 1, "yes" for the 680-kev group. The first excited state of Sr^{86} is tentatively assigned as a 2+ state because of the probable *E2* assignment[35] to the 1.080-Mev gamma ray. This is consistent with the beta-gamma polarization correlations made by Hamilton, Lemonick, and Pipkin.[35] A consistent decay scheme is then obtained by assigning the lower-energy beta group as a $\Delta I=0$, "yes" transition. This decay scheme is indicated in Fig. 16.

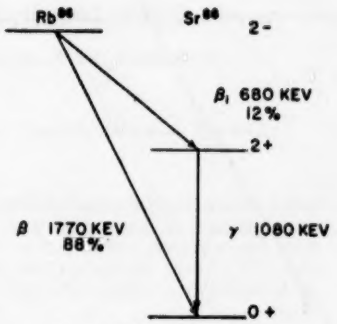

FIG. 16. Rb^{86} decay scheme.

DISCUSSION

The correction for the effect of the finite DeBroglie[45] wavelength was applied to the spectrum of Rb^{86}. This correction made no significant difference in the end points or shape of the subtraction or total spectra.

The Kurie plots of the 680-kev beta group of Rb^{86} and the 886-kev beta group of Tm^{170} were examined for deviation from a straight line. Limits on the value of the quantity ϕ defined by Mahmoud and Konopinski[46] for the Fierz interference effect were determined. For the 680-kev group of Rb^{86}, ϕ was -0.05 ± 0.10. For the 886-kev group of Tm^{170}, ϕ was 0.05 ± 0.08. The error given is the probable error determined by the statistics. The quantity 2ϕ is equal to r as defined by Davidson and Peaslee.[47] Within experimental error, there appears to be no deviation from a straight line.

It was found in general that the maximum energies obtained by coincidence methods are in better agreement with the energy differences between high-energy beta end points and gamma-ray energies than those obtained from subtraction spectra.

ACKNOWLEDGMENTS

The authors wish to express their appreciation to Mr. E. H. Dewell, Mr. J. Crook, and Mr. J. Phillips for preparation of sources, and to Mr. W. Rhinehart, Mr. A. A. Read, and the staff of the electronics shop for the design and construction of equipment. The authors would also like to express their appreciation to Mr. J. T. Jones, Jr., and Mr. E. W. McMurry for their aid in obtaining data.

[45] Rose, Perry, and Dismuke, Oak Ridge National Laboratory ORNL-1459, 1953 (unpublished).
[46] H. M. Mahmoud and E. J. Konopinski, Phys. Rev. **88**, 1266 (1952).
[47] J. P. Davidson and D. C. Peaslee, Phys. Rev. **91**, 1232 (1953).

PHYSICAL REVIEW VOLUME 95, NUMBER 6 SEPTEMBER 15, 1954

$A^{40}(\gamma,n)$ Threshold and the Mass of A^{39}†

J. HALPERN, R. NATHANS, AND P. F. YERGIN
University of Pennsylvania, Philadelphia, Pennsylvania
(Received June 11, 1954)

The $A^{40}(\gamma,n)A^{39}$ reaction is found to have a threshold at 9.85 ± 0.15 Mev. Using the most recent mass spectrograph measurements for the mass of A^{40}, the mass of A^{39} is calculated to have a value of 38.97681 ±0.00020. The relationship of this measurement to other reaction energy data is discussed.

INTRODUCTION

THE recent modification of the neutron detection apparatus used in this laboratory for the study of photonuclear reactions to accommodate gaseous targets[1] has permitted a determination of the $A^{40}(\gamma,n)$ threshold. Using the accurate mass spectrographic data for the mass of A^{40}, the measurement yields a precise value for the mass of A^{39} and an important check on nuclear transmutation data in this region of mass number.

EXPERIMENT

The apparatus is identical to that previously reported[1] for the study of the properties of the giant (γ,n) dipole resonances in gaseous targets, and the entire operational procedure is identical except that neutron yields in the vicinity of threshold are taken with greater statistical precision and are more closely spaced in betatron energy.

† Supported in part by the U. S. Air Research and Development Command and the joint program of the U. S. Office of Naval Research and the U. S. Atomic Energy Commission.
[1] Ferguson, Halpern, Nathans, and Yergin, Phys. Rev. **95**, 659 (1954).

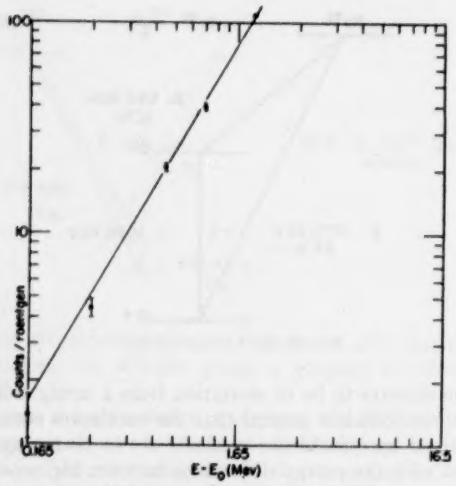

FIG. 1. Log-log plot of argon yield near threshold as a function of $E-E_0$. The assumed value of the threshold E_0 is 9.85 Mev.

The data appear in the form of neutron yields per roentgen for varying betatron energies and extrapolation to threshold is achieved in the manner previously used[2] for the measurement of photoneutron thresholds.

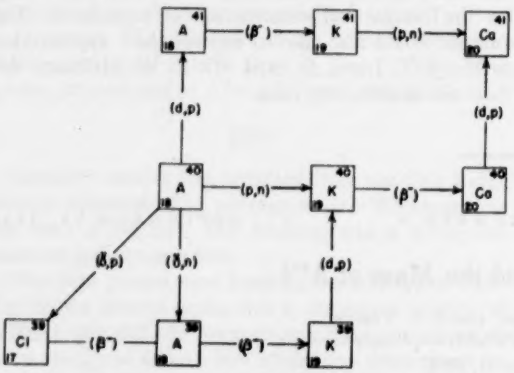

FIG. 2. Transmutations connecting the mass of A^{39} with the masses of neighboring isotopes.

[2] Sher, Halpern, and Mann, Phys. Rev. **84**, 387 (1951).

The data are assumed to be represented by the relation $Y=(E-E_0)^m$, where Y is the yield, E is the maximum bremsstrahlung energy, m is a constant for a given isotope, and E_0 is taken to be the threshold energy. E_0 and m are determined graphically by trial as shown by the log-log plot of Fig. 1 representing the data of this paper for an argon target at 100 atmosphere pressure. E_0 is found to be 9.85 Mev, and if a value of E_0 differing from this by 0.1 Mev is chosen the plot deviates strongly from a straight line. The absolute scale of energy of the betatron is calibrated in terms of the known (γ,n) thresholds of Bi, Mn, and C^{12}, and the over-all error in the threshold determination is estimated to be 0.15 Mev. Taking the value 39.97524 ± 3 for the mass of A^{40} as given by Nier,[3] this yields for the mass of A^{39} the value 38.97681 ± 0.00020.

DISCUSSION

Figure 2 shows the connection between the mass of A^{39} and neighboring isotopes as determined by available transmutation data. As can be seen, there are other reactions, though less direct than the $A^{40}(\gamma,n)A^{39}$ threshold, for deriving the mass of A^{39} from that of A^{40}. The $A^{40}(\gamma,p)Cl^{39}$ threshold coupled with the β-ray decay scheme of Cl^{39} to A^{39} is a simple chain. Haslam *et al.*,[4] report a total disintegration energy of 3.3 Mev for the decay of Cl^{39}, which in turn was produced from A^{40} by a (γ,p) reaction with a measured threshold of 14.2 ± 0.2 Mev. This would lead to an A^{39} mass of 38.97877 Mev in contradiction to the results of this paper. Wilkinson and Carver,[5] on the other hand, quote the $A^{40}(\gamma,p)$ threshold at 10.8 ± 0.1 Mev which, with the above disintegration energy of Cl^{39}, leads to an A^{39} mass of 38.97512.

Using data pertaining to the other chains[6] illustrated in Fig. 2, i.e., A^{40} to K^{40} to K^{39} to A^{39}, one arrives at a value of 38.97686 ± 0.00030 for the mass of A^{39}, in excellent agreement with our data.

[3] A. O. Nier, Phys. Rev. **81**, 624 (1952).
[4] Haslam, Katz, Moody, and Skarsgard, Phys. Rev. **80**, 318 (1950).
[5] D. H. Wilkinson and J. H. Carver, Phys. Rev. **83**, 466 (1951).
[6] See W. Low and C. H. Townes, Phys. Rev. **80**, 608 (1950) for a complete list of references.

Neutrons from the Proton Bombardment of B^{10}†

FAY AJZENBERG, *Department of Physics, Boston University, Boston, Massachusetts*

AND

WOLFGANG FRANZEN,* *Palmer Physical Laboratory, Princeton University, Princeton, New Jersey*

(Received June 3, 1954)

The $B^{10}(p,n)C^{10}$ reaction has been investigated at 30, 60, 90, 120, and 150 degrees in the laboratory system by the method of proton recoils in thick photographic emulsions. The mean energy of the incident protons was 17.2±0.15 Mev. The results indicate a ground-state Q value of −4.35±0.2 Mev, yielding a mass defect of 18.6 Mev for C^{10} in good agreement with beta decay results. The data also indicate a level in C^{10} at 3.34 ±0.2 Mev and partly resolved levels at excitation energies ≳5 Mev. The angular distributions of the neutrons to the ground state and to the 3.34-Mev state are shown.

UNTIL recently no information was available on the level structure of nuclei with $T_z=-1$, where $T_z\equiv(N-Z)/2$. Such information is of importance in the study of isobaric triads, and thus in the investigation of the validity of the hypotheses of charge symmetry and charge independence of nuclear forces. In a first investigation[1] an attempt was made to study the level structure of O^{14}. In this paper the level structure of C^{10} will be discussed.

Neutrons from the bombardment of an enriched boron target[2] by 17.3±0.15 Mev protons from the Princeton cyclotron were detected by means of Ilford C-2 nuclear emulsions 400 microns thick, placed at 30, 60, 90, 120, and 150 degrees to the incident beam. The experimental setup, the plate processing procedure, and the handling of the proton recoil data have been discussed in the O^{14} paper.[1] The enriched boron target was prepared as follows: a solution of polystyrene in benzene was added to the enriched boron powder. The slurry of elemental boron was then thoroughly mixed and dropped gently on a water surface. When the benzene evaporated, a thin film of polystyrene holding elemental boron in a fine suspension was lifted from the water and was ready to be used. The weight of the (boron) polystyrene film was found to be 7.2 mg/cm² which corresponds to an energy loss of 0.2 Mev for 17-Mev protons.[3]

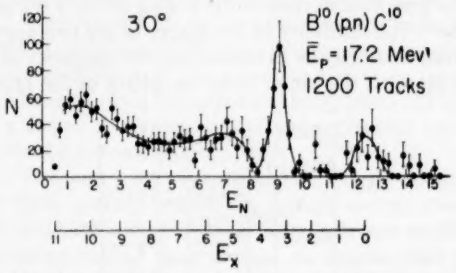

FIG. 1. 30° data. N is the relative number of neutrons per 200-kev interval; $\bar{E}_p$ is the average proton energy; E_n is the neutron energy; E_x is the excitation energy in C^{10}.

Figures 1 through 5 show the data at the five angles. A total of 4310 proton recoil tracks were measured. The data shown have been corrected for variation of the neutron-proton scattering cross section with energy, and for the finite thickness of the emulsion. The ground-state Q value derived from the results at the five angles is −4.35±0.2 Mev. The data also indicate, on the basis of 496 proton recoil tracks, an excited state in C^{10} with a Q value of −7.69±0.2 Mev, corresponding to an excitation energy of 3.34 Mev. We did not observe any neutron groups corresponding to levels in C^{10} below 3.34 Mev, although a level with low neutron yield at the five angles would not have been detected. It would seem improbable, however, that the formation of any low-lying state would be less likely than the formation of the ground state of C^{10} with its $J=0$ characteristic which involves emission of neutrons of high angular momentum.

At higher excitation energies, the data indicate either very wide levels or a number of unresolved levels in C^{10} except in the vicinity of $E_x\sim5$ Mev where discrete level

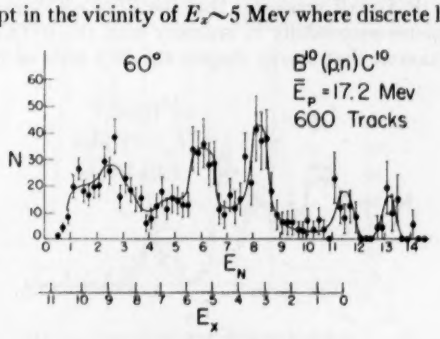

FIG. 2. 60° data.

† This work has been supported in part by the U. S. Air Force through the Office of Scientific Research and in part by the U. S. Atomic Energy Commission.

* Now at the University of Rochester, Rochester, New York.

[1] F. Ajzenberg and W. Franzen, Phys. Rev. **94**, 409 (1954).

[2] The loan of the enriched boron (98 percent B^{10}) was made by the Stable Isotopes Division of the U. S. Atomic Energy Commission, Oak Ridge, Tennessee.

[3] We are indebted to N. S. Wall and J. W. Irvine of the Massachusetts Institute of Technology for suggesting this method. See also N. S. Wall and J. W. Irvine, Rev. Sci. Instr. **24**, 1146 (1953).

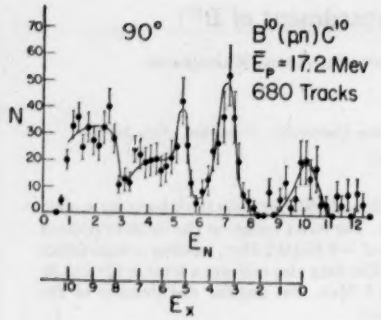

FIG. 3. 90° data.

structure is perhaps observed at some of the angles of observation. For instance, at 60 degrees, a wide group at a neutron energy of 6.1 Mev corresponds to level(s) at $E_x \sim 5.5$ Mev. At 90 degrees, a group at $E_n \sim 5.3$ Mev corresponds to level(s) at $E_x \sim 5.1$ Mev, and at 120 degrees there is some indication of level(s) at $E_x \sim 5.2$ Mev. The neutron groups at 13.2 Mev (60°) and at 10.8

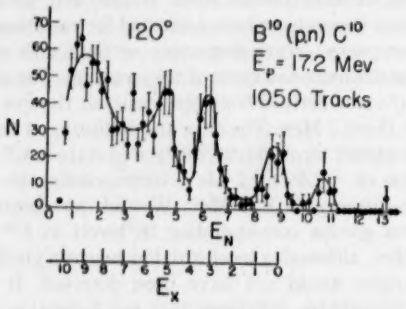

FIG. 4. 120° data.

Mev (120°) may be caused by either or both of the reactions $B^{11}(p,n)C^{11}$ ($Q=-2.762$ Mev)[4] and $C^{13}(p,n)N^{13}$ ($Q=-3.003$ Mev).[4] There is some indication from an exposure at 6.01 Mev with the M.I.T.-O.N.R. Van de Graaff generator that the $B^{11}(p,n)C^{11}$ reaction competes successfully in intensity with the $B^{10}(p,n)C^{10}$ reaction at that energy despite the 49:1 ratio of B^{10} to

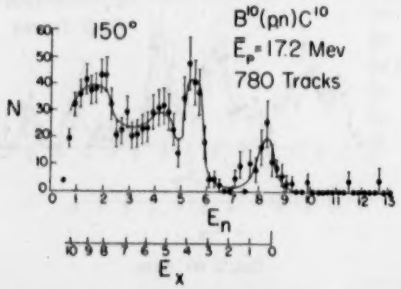

FIG. 5. 150° data.

[4] Richards, Smith, and Browne, Phys. Rev. **80**, 524 (1950).

B^{11} nuclei.[5] This can be qualitatively understood in terms of the relative J changes in the two reactions ($J=3\rightarrow 0$ for C^{10}; $J=\frac{3}{2}\rightarrow\frac{3}{2}$ for C^{11}).

The angular distributions of the neutrons to the ground state and to the 3.34-Mev state of C^{10} are shown in Fig. 6. The total number of neutrons in a given group at a given laboratory angle, was converted to center-of-mass values by means of Moskow's tables.[6] The relative number of neutrons was then corrected for the different areas scanned at the various angles. The uncertainties indicated for the angular distribution points are statis-

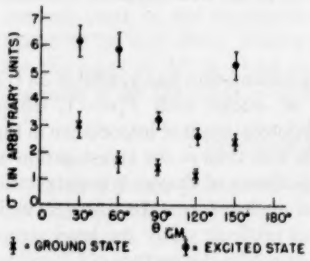

FIG. 6. Angular distribution in the center-of-mass system of the neutrons to the ground state and to the 3.34-Mev state of C^{10}.

tical uncertainties only. They do not include possible errors in the assignments of the neutrons to the group. The larger cross section for the formation of the first excited state than for the formation of the ground state of C^{10} is consistent with the smaller J change involved if the first excited state is the analog to the $J=2$ state in Be^{10}. The similarity in the shapes of the two angular distributions may be an indication that the parity of the two states is the same. Since the parity of the ground

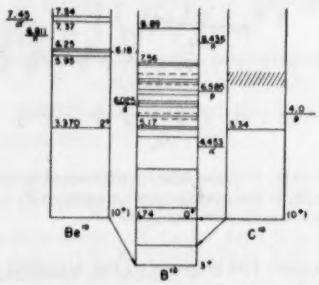

FIG. 7. The mass-10 isobaric triad. The levels whose energies are indicated are believed to be $T=1$ states.

state of C^{10} is even, this would indicate the even parity for the 3.34-Mev state expected from charge symmetry.

The mass defect of C^{10} derived from our data is 18.6 ± 0.2 Mev, which is in good agreement with the value of 18.84 ± 0.1 Mev obtained from beta decay results.[7] Figure 7 shows how the information derived from this work fits into the known picture of the mass-

[5] Ajzenberg, Mazari, and Rubin, 1954 (unpublished).
[6] M. Moskow, Master's essay, The Johns Hopkins University, 1948 (unpublished).
[7] R. Sherr and J. B. Gerhart, Phys. Rev. **91**, 909 (1953).

10 triad.[8,9] If we assume that the state at 3.34 Mev in C^{10} is formed by the same nucleon configuration as the 2^+ state at 3.37 Mev in Be^{10}, then there is essentially no energy shift for this state.[10] On the other hand, the 5-Mev level(s) in C^{10} seem to indicate an appreciable energy shift of one or more of the 6-Mev levels in Be^{10}. This energy difference can perhaps be explained as a Thomas-Ehrmann shift.[11,12]

We are very grateful to J. G. Likely and to F. C. Shoemaker for their assistance in the exposure of the plates, and to F. L. Friedman for several helpful discussions. The interest and support of P. T. Demos and of M. G. White rendered this experiment possible.

[8] F. Ajzenberg and T. Lauritsen, Revs. Modern Phys. **24**, 321 (1952).
[9] Bockelman, Jung, and Wilkinson (private communications).
[10] I. Talmi and Professor Wigner point out that this is not surprising despite the difference in the amount of binding of the 3.4-Mev states in Be^{10} and in C^{10}, since the presumed 2^+ character of the levels would mean a sufficiently high centrifugal barrier in the case of C^{10} to outweigh the fact that the state is energetically almost proton-unbound.
[11] R. G. Thomas, Phys. Rev. **88**, 1109 (1952).
[12] J. B. Ehrmann, Phys. Rev. **81**, 412 (1951).

PHYSICAL REVIEW VOLUME 95, NUMBER 6 SEPTEMBER 15, 1954

Gamma-Ray Spectra Following the β Decay of Br^{82}, Sb^{124}, and I^{131}†

D. C. Lu, W. H. Kelly, and M. L. Wiedenbeck
Randall Laboratory of Physics, University of Michigan, Ann Arbor, Michigan
(Received May 24, 1954)

Coincidences between the gamma rays following the β decay of Br^{82}, Sb^{124}, and I^{131} have been studied using the single scintillation crystal summing technique. A decay scheme for Br^{82} is proposed. The decay scheme of Sb^{124} proposed by Langer *et al.* is found to be consistent with our data as is the decay scheme of I^{131} proposed by Metzger and Deutsch and augmented by Emery.

Br^{82} [1]

THE gamma rays following the beta decay of Br^{82} were studied by the gamma-summing technique described previously.[2] The normal gamma spectrum (source outside) and the summing spectrum (source inside) are shown in the upper and lower parts of Fig. 1, respectively. A comparison between the two curves reveals the following information.

(1) The sum peak with the highest energy occurs at 2.62 Mev, indicating that the highest excited energy level involved is at 2.62 Mev. Since only one mode of beta decay exists,[3] it is natural to assume that the 2.62-Mev level is fed by this beta activity. This greatly simplifies the task of deducing the decay scheme. Thus, any selected gamma transition must be in cascade with other gamma transitions such that their energy sum is 2.62 Mev. This leads to the following.

(2) The 1.455-Mev gamma ray must be in cascade with other gamma rays whose energies sum up to 1.16 Mev (=2.62−1.46). This is confirmed by the evidence that a sum peak does occur at 1.16 Mev. The only manner to fulfill this requirement is to put the 1.455-, 0.608-, and 0.545-Mev transitions in triple cascade. This is further evidenced by the fact that summing does appear between 2.0 and 2.1 Mev (=1.455+0.608 or 0.545 Mev).

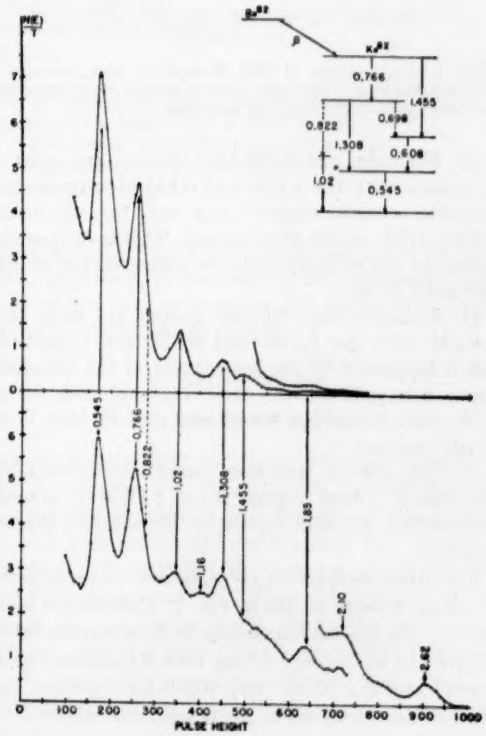

FIG. 1. γ-ray spectra of Br^{82}. Energies in Mev indicated at the top of the peaks. The upper curve is the normal spectrum and the lower curve is the summing spectrum. The counting time intervals on the upper ends of these curves were doubled.

† This investigation was supported in part by the Michigan-Memorial Phoenix Project, University of Michigan.
[1] Obtained from deuteron bombardment of bromine in the cyclotron.
[2] D. C. Lu and M. L. Wiedenbeck, Phys. Rev. **94**, 501 (1954).
[3] M. Deutsch, Phys. Rev. **61**, 672 (1942).

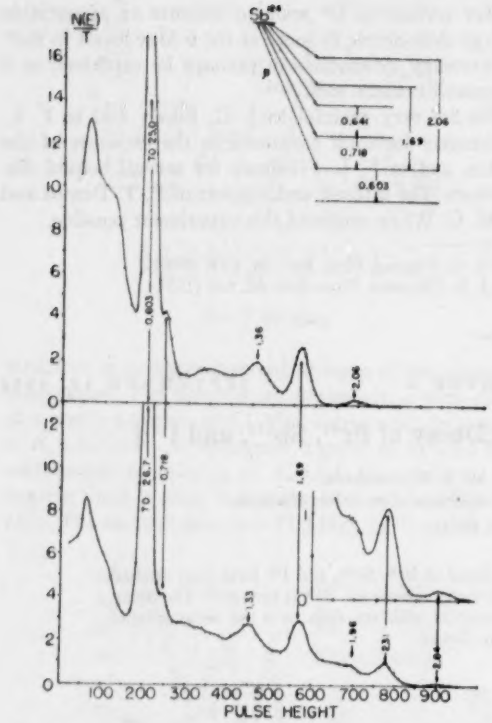

FIG. 2. γ-ray spectra of Sb^{124}. Energies in Mev indicated at the top of the peaks. The upper curve is the normal spectrum and the lower curve is the summing spectrum.

(3) Similarly, the 1.308-Mev gamma ray must be in cascade with the 0.766- and 0.545-Mev transitions. Intensity considerations[4,5] rule out the alternative 1.308+0.698+0.608-Mev cascade. This is further supported by the evidences that summing occurs at 2.10, 1.85 and 1.31 Mev.

(4) Similarly, the 1.02-Mev gamma ray must be in cascade with the 0.766- and 0.822-Mev transitions; this is supported by the appearance of the broadened strong sum peak at 1.85 Mev. The sum peak for the 0.766- and 0.822-Mev transitions at 1.59 Mev is not clearly resolved.

(5) The normal spectrum shows some possible indications of a weak gamma ray at 1.85 Mev, in agreement with a previous report by Meyers and Wattenberg.[6]

The above indications are sufficient for constructing the decay scheme shown in Fig. 1. The relative placement of the gamma transitions is, to a certain extent, dictated by the energy fitting that is necessary to accommodate the 0.822- and 0.698-Mev gamma rays which are not resolved in the present investigation but reported by previous investigators.[3–5] This decay scheme appears to be the only reasonable one that does not in one way or another contradict the accumulated evidences.

Sb^{124} [7]

Until quite recently, an uncertainty existed involving two alternative decay schemes of Sb^{124}. One of these, proposed by Langer, Lazar and Moffat,[8] is shown in Fig. 2. It contains gamma rays of 0.603, 0.64, 0.72, 1.69, and 2.06 Mev, and includes a triple cascade comprised of the 0.64-, 0.72-, and 0.60-Mev gamma rays. An alternative scheme proposed by Tomlinson[9] differs from the first one in that the 0.64-Mev transition is placed in cascade with the 0.603-Mev transition alone, and an additional weak 0.71-Mev transition is placed in triple cascade with the 0.72- and 0.603-Mev transitions. The existence of this 0.71-Mev transition was supported by the coincidence work of Metzger.[10] The existence of the 0.64- to 0.72- to 0.603-Mev triple cascade

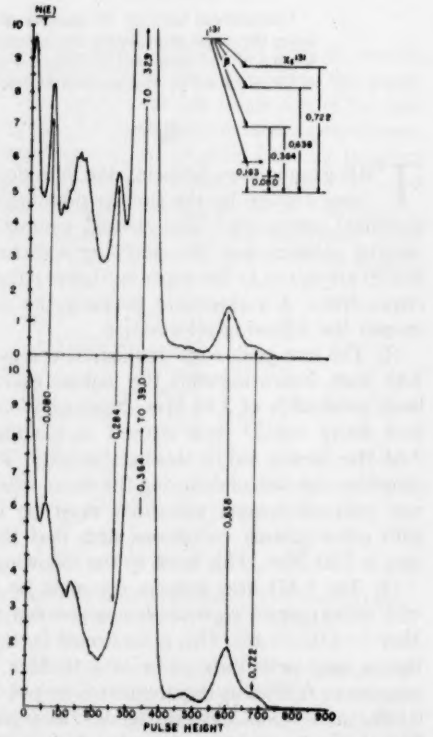

FIG. 3. γ-ray spectra of I^{131}. Energies in Mev indicated at the top of the peaks. The upper curve is the normal spectrum and the lower curve is the summing spectrum.

[4] Siegbahn, Hedgran, and Deutsch, Phys. Rev. **76**, 1263 (1949)
[5] B. Dzhelepov and A. Silantov, Doklady Akad. Nauk. S.S.S.R. **85**, 533 (1952).
[6] V. Myers and A. Wattenberg, Phys. Rev. **75**, 992 (1949).
[7] Obtained from Oak Ridge.
[8] Langer, Lazar, and Moffat, Phys. Rev. **91**, 338 (1953).
[9] E. P. Tomlinson, Indiana Conference on Nuclear Spectroscopy and the Shell Model, Technical Report, 1953 (unpublished), p. 31.
[10] F. R. Metzger, Indiana Conference on Nuclear Spectroscopy and the Shell Model, Technical Report, 1953 (unpublished), p. 32.

in the first scheme has since been established by Langer and Starner[11] through triple coincidence studies.

The present investigation using the summing technique was conducted shortly before the result of the triple coincidence measurements was published. It was hoped that the high efficiency of the summing technique for multiple coincidences might show whether the triple sum peak appears at 0.64+0.72+0.603=1.96 Mev or at 0.71+0.72+0.60=2.04 Mev. However, the normal spectrum shows the possible existence of a gamma ray at 1.36 Mev. This peak, when summed with the 0.603-Mev gamma ray, falls at 1.96 Mev and interferes with the observation of the triple sum peak. It is conceivable that when a larger crystal is used the present method will furnish independent information in this respect. The summing spectrum shown in Fig. 2 does show, however, a positive indication of the coincidence between the 2.06-Mev and the 0.603-Mev gamma rays.

[11] L. M. Langer and J. W. Starner, Phys. Rev. **93**, 253 (1954).

I^{131} [7]

The summing spectrum of the gamma rays following the beta decay of I^{131} is shown in the lower part of Fig. 3. The spectrum clearly indicates that the 0.284-Mev transition is in cascade with the 0.080-Mev transition. Because of the high efficiency of the crystal for detecting the 0.080-Mev gamma ray, the 0.286-Mev peak is greatly diminished through the summing effect. However, no such summing effect is observed for the 0.638-Mev or the 0.722-Mev gamma rays. This is a further confirmation of the decay scheme proposed originally by Metzger and Deutsch[12] and augmented by Emery.[13]

[12] F. Metzger and M. Deutsch, Phys. Rev. **74**, 1640 (1948).
[13] E. W. Emery, Phys. Rev. **83**, 679 (1951).

PHYSICAL REVIEW VOLUME 95, NUMBER 6 SEPTEMBER 15, 1954

Nuclear Levels in Ca^{43}†

TORSTEN LINDQVIST* AND ALLEN C. G. MITCHELL
Physics Department, Indiana University, Bloomington, Indiana
(Received June 9, 1954)

The nuclear levels in Ca^{43} have been studied in the decay of Sc^{43} by positron emission to Ca^{43}. Levels have been found at 0.369, 0.627, and 0.81 Mev. In an earlier experiment, the decay of K^{43} by negatron emission was studied by the authors and nuclear levels were found in Ca^{43} at 0.627, 1.00, 1.39, and 1.61 Mev. The levels have been given configuration assignments. Theoretical discussion of the $(f_{7/2})^3$ configuration is compared with experimental results.

I. INTRODUCTION

RECENTLY, the decay of K^{43} has been studied by the authors.[1] K^{43} decays by negatron emission to Ca^{43} and nuclear levels were found at 0.627, 1.00, 1.39, and 1.61 Mev. The spin of the ground state of Ca^{43} has been measured by Jeffries[2] and has been found to be 7/2 and of odd parity. Of the levels of Ca^{43} measured in the experiments on K^{43}, the ground state and that at 0.627 Mev were found to have odd parity, while those at 1.00, 1.39, and 1.61 Mev were shown to have even parity. Ca^{43} can be reached by the negatron decay of K^{43} or the positron decay of Sc^{43}. Since K^{43} has 19 protons and Sc^{43} 21 protons, the shell model predicts that the parity of the ground state of K^{43} will be even $(d_{3/2})$ and that of Sc^{43} odd $(f_{7/2})$. For this reason, and also since the spins of the two nuclei differ considerably, it is expected that different levels of Ca^{43} will be observed depending on which parent nucleus is investigated. Therefore, it was decided to reinvestigate the decay of Sc^{43} and to compare the results with those obtained from the decay of K^{43}.

† Supported by the joint program of the U. S. Office of Naval Research and the U. S. Atomic Energy Commission.
* On leave from the University of Uppsala, Uppsala, Sweden.
[1] T. Lindqvist and A. C. G. Mitchell, Phys. Rev. **95**, 444 (1954); **95**, 612A (1954).
[2] C. D. Jeffries, Phys. Rev. **90**, 1130 (1953).

II. DECAY OF Sc^{43}

(a) Previous Results

The radiations from Sc^{43} have been investigated by various authors. The most recent investigation by Haskins, Duval, Cheng, and Kurbatov[3] was carried out with a magnetic lens spectrometer and showed a half-life of 3.92±0.02 hr, two positron groups of 1.18. Mev (72 percent) and 0.77 Mev (28 percent), and a gamma ray of energy 0.375 Mev. Nussbaum, van Lieshout, and Wapstra,[4] using a scintillation counter, found a gamma ray of energy 0.375 Mev and a half-life of 4.0 hr.

[3] Haskins, Duval, Cheng, and Kurbatov, Phys. Rev. **88**, 876 (1952).
[4] Nussbaum, van Lieshout, and Wapstra, Phys. Rev. **92**, 207 (1953).

TABLE I. Ca isotopes and reactions.

Ca isotopes	Ca^{40}	Ca^{42}	Ca^{43}	Ca^{44}	Ca^{46}	Ca^{48}
Rel. abund. %	96.9	0.64	0.14	2.1	0.0032	0.18
Sc isotopes	Sc^{43}	...	Sc^{46}	Sc^{47}	Sc^{49}	...
	β^+		β^-	β^-	β^-	
from $Ca(\alpha,p)Sc$	3.9 hr	...	85 days	3.43 days	57 min	...
Sc isotopes	...	Sc^{44}	...	Sc^{46}	Sc^{48}	...
		β^+		β^-	β^-	
from $Ca(\alpha p,n)Sc$	...	4.0 hr	...	85 days	44 hr	...

(b) Preparation of Sources

The isotope Sc^{43} was prepared by the reaction $Ca^{40}(\alpha,p)Sc^{43}$. Purified CaO was bombarded for an hour with 40 μa of 18–22 Mev alpha particles. Table I shows the relative abundance of the various calcium isotopes and the possible reactions.

Considering the half-lives as well as the relative abundances of the isotopes, the most likely products to appear, besides the dominating Sc^{43}, are Sc^{44} and Sc^{47}. By reducing the beam energy to 17–18 Mev it was possible to suppress the Sc^{44} activity, since the $(\alpha,p n)$ reaction decreases more rapidly with alpha-particle energy than does the (α,p) reaction.

There was a small amount of Sc^{47} produced. During the first 24 hours, when Sc^{43} was measured, the activity from any Sc^{47} was too low to be detected, but after 5 days it was possible to measure the radiation in a scintillation spectrometer. A gamma ray of energy 180 kev was found and believed to belong to Sc^{47} since it had the same half-life. The half-life for Sc^{47} was checked over a two-week period giving $T_{1/2}=82.3$ hr (3.44 days) in agreement with earlier experiments.

The half-life of Sc^{43} was measured in the same run, and after subtraction of the 82.3-hr activity a half-life of 3.8 ± 0.1 hr was obtained for Sc^{43}.

(c) Gamma-Ray Spectrum

The gamma rays were investigated by measuring the photoelectron spectrum from various radiators with the help of a magnetic lens spectrometer. A scintillation spectrometer was also used. Figure 1 shows the photoelectron spectrum from a lead radiator of thickness 8 mg/cm^2. Photoelectron lines corresponding to three gamma rays and the annihilation radiation were found. In the scintillation spectrometer, there was also found a weak gamma ray of higher energy. Table II gives the energies and relative intensities for the gamma rays. In order to confirm that the photoelectron line at "0.627K" really was a K line and not an L line with the corresponding K line hidden under the annihilation radiation, various radiators were used. Uranium as well as indium radiators confirmed the result obtained with a lead radiator. The half-life for the γ rays was checked, and each had a half-life corresponding to the decay of Sc^{43}.

TABLE II. Gamma rays from Sc^{43}.

Energy Mev	Rel. abund.	Measured in
0.25 $\pm$0.01	0.5	magn. lens
0.369$\pm$0.005	8	magn. lens
0.511	100	magn. lens
0.627$\pm$0.005	2	magn. lens
0.84 $\pm$0.02	weak	scint. spectr.

(d) Positron Spectrum

The positron distribution was measured in the magnetic lens and was analyzed by making a Fermi plot of the data. The results are shown in Fig. 2. The spectrum can be analyzed into three groups as shown in the figure and in Table III.

Internal conversion lines were also looked for but none were found, implying that the gamma rays are of low multipole order.

(e) Disintegration Scheme of Sc^{43}

The results of the investigation are embodied in the disintegration scheme shown in Fig. 3. The three positron groups establish levels at 0.38 and 0.81 Mev, together with the ground state, and all three groups are of an allowed character. The gamma rays of energies 0.369, 0.627, and 0.25 Mev establish an additional level at 0.627 Mev. The positron transition leading to the 0.627-Mev level is so weak that it has not been found. The weak gamma ray of 0.84 Mev, seen only in a scintillation spectrometer, comes from the level populated by the lowest-energy positron group.

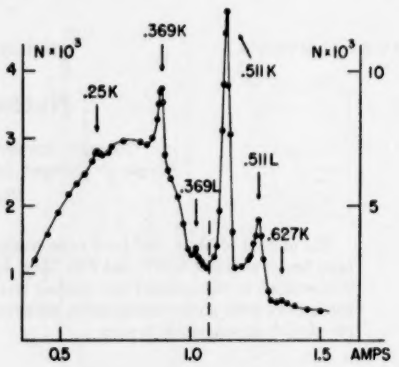

FIG. 1. Photoelectron spectrum from Sc^{43}.

In order to establish the position of the gamma ray at 0.369 Mev, coincidence experiments were performed in which positrons were detected in a scintillation spectrometer using an anthracene crystal and gamma rays in a similar apparatus using a NaI(Tl) crystal. With the scintillation spectrometer detecting gamma rays set on the 0.369-Mev line, the differential pulse-height analyzer of the scintillation spectrometer measuring positrons was swept through the spectrum. No coincidences were obtained for positron energies greater than 0.82 Mev, while coincidences were obtained for energies less than this. This shows that the line at

0.369 Mev is in coincidence with the positron group of 0.82-Mev energy. This experiment has additional importance since, in the decay of K^{43} there is a gamma ray of energy 0.369 Mev which appears to be in a different place in the level scheme.

The assignment of spins and parities to the levels of Ca^{43} was determined essentially by the values of log *ft* for the positron groups, the measured spin of the ground state of Ca^{43}, and the shell model configuration for the ground state of Sc^{43}. Sc^{43} has 21 protons and 20 neutrons and the shell model predicts unambigously a spin of 7/2 and odd parity for the ground state. The ground state of Ca^{43} has been measured and found to have a spin of 7/2 and odd parity. The positron transitions connecting the ground states of parent and daughter are allowed and are therefore consistent with $\Delta j=0$,no. The states established by the other two allowed positron groups, namely those of energy 0.369 Mev and 0.81 Mev, must have odd parity and spins of 5/2, 7/2, or 9/2. Ca^{43} has the configuration $(f_{7/2})^3$ and according to Kurath[5] the level order is 7/2 (ground state), 5/2, 3/2, 9/2, 11/2 . . ., all of odd parity. The first excited level at 0.369 Mev has therefore been given a spin of 5/2 and the third excited level at 0.81 Mev

TABLE III. Positron groups of Sc^{43}.

Group	*E* Mev	Relative abundance %	log(*ft*)	Spin and parity	Transition
I	1.20±0.01	79	5.0	$\Delta j=\pm1,0$,no	Allowed
II	0.82±0.02	17	5.1	$\Delta j=\pm1,0$,no	Allowed
III	0.39±0.03	4	4.9	$\Delta j=\pm1,0$,no	Allowed

a spin of 9/2, both consistent with *ft* values. Further, the second excited level at 0.627 Mev has been given a spin of 3/2, in agreement with the result obtained on K^{43} decay. This will account for the low intensity of the gamma ray at 0.627 Mev and the fact that no positron transition to this level is seen, since the latter would be characterized by $\Delta j=2$,no and would be very weak compared to the allowed transitions to the other states.

III. LEVELS OF Ca^{43}

The levels of Ca^{43} have been determined from three separate experiments: the disintegration of K^{43}, the reaction[6] $Ca^{42}(d,p)Ca^{43}$, and the present experiments on Sc^{43}. In addition the relative spacing and order of occurrence of the levels of Ca^{43} have been calculated according to the $(j-j)$ coupling model by Kurath.[5] The effects of surface coupling for this nucleus have been discussed by Bohr and Mottelson[7] and have been calculated in a weak-coupling approximation by Ford.[8]

[5] D. Kurath, Phys. Rev. **91**, 1430 (1953).
[6] C. M. Braams, Phys. Rev. **95**, 650 (1954).
[7] A. Bohr and B. R. Mottelson, Kgl. Danske Videnskal. Selskab, Mat.-fys. Medd **27**, No. 16 (1953).
[8] K. W. Ford (private communication).

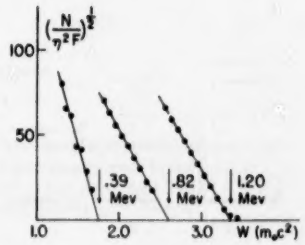

FIG. 2. Fermi plot for Sc^{43}.

It is, therefore, of interest to discuss the experiments in the light of the theory.

Figure 4 shows the levels obtained from the three experiments separately, together with the combined level scheme. No one method gives all the levels of Ca^{43}, but this is to be expected on account of selection rules. The experiment of Braams gives all of the levels up to 1.40 Mev, with the exception of that at 0.81 Mev, and, as shown in Fig. 4(*b*), the energies are in reasonably good agreement with those determined spectroscopically from radioactive nuclei. In this experiment, no assignments of spin and parity were given.

The work on K^{43} confirmed the shell model prediction for the ground state of K^{43}, spin 3/2 and even parity. Therefore the allowed beta transitions found there lead to the levels of even parity in Ca^{43}, shown in Fig. 4(*a*). On the basis of *ft* values and internal conversion coefficients, the 0.627-Mev level was given the assignment 5/2− or 3/2−.

The present experiment on Sc^{43} gives the levels shown in Fig. 4(*c*). The assignments of the levels have been discussed in the foregoing. The absence of transitions from Sc^{43} to the even parity states of Ca^{43} is accounted for both on energy and parity considerations.

No beta ray corresponding to a state at 0.369 Mev in Ca^{43} was found in the decay of K^{43}, although such a transition should have a character $\Delta j=\pm1,0$ yes and should easily compete with the transition to the 0.627-Mev state. This might have been missed on account of the low intensity of the transitions to all odd states.

In Fig. 4(*d*) is shown the level scheme obtained by combining the results of the two decay experiments. It is reasonable to consider that the low-lying, odd levels

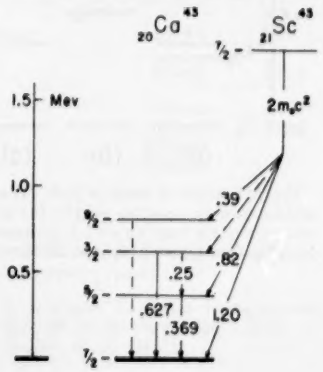

FIG. 3. Disintegration scheme of Sc^{43}.

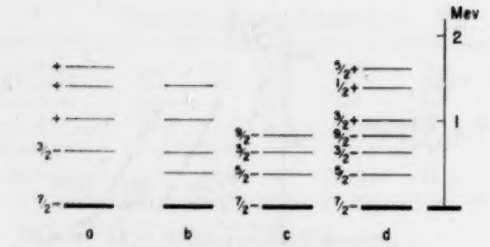

FIG. 4. Nuclear levels in Ca^{43}: (*a*) from K^{43} decay, (*b*) from Ca^{42} (d,p) Ca^{43}, (*c*) from Sc^{43} decay, (*d*) combined from (*a*) and (*c*).

arise from the $(f_{7/2})^3$ configuration. The even states of higher energy can be explained only by assuming a neutron from a lower shell being excited, thus giving a $(f_{7/2})^4$ configuration+a neutron hole in the preceeding shell. Therefore the even states have been given the spins 3/2, 1/2, and 5/2, in order of energy, as is shown in Fig. 4(*d*). This level order was chosen as the inverse of the observed order of filling of the states in the previous shell ($d_{5/2}$, $s_{1/2}$, $d_{3/2}$). There is, however, some possibility of inversions in the level order.

The results for the lower-energy states of odd parity can be compared with the theoretical calculations for the level energies of the configuration $(f_{7/2})^3$ obtained by Kurath.[5] His calculations are based on the "Majorana plus Bartlett" interaction and a strong spin-orbit coupling is assumed. In his calculations, no surface effects are considered. The energies of the states are given in units proportional to A_0, the Gaussian well-depth for the "Majorana plus Bartlett" interaction, and, as a function of ρ, the ratio of the nuclear size parameter to the range of nuclear forces. The experimental data were fitted to the theoretical curves by normalizing to the 0.81-Mev energy difference (7/2 to 9/2) in Ca^{43}, i.e., the largest energy difference determined experimentally. Table IV and Fig. 5 give this comparison for several values of ρ. It will be seen that the spacing between the 5/2 and 3/2 states is small for any of the values of ρ chosen, while the experimental value is large. A fit can be obtained for the 7/2–5/2 difference for $\rho=1.0$ or for the 3/2–9/2 difference for $\rho=1.3$, but no fit can be found for all four levels for any value of ρ.

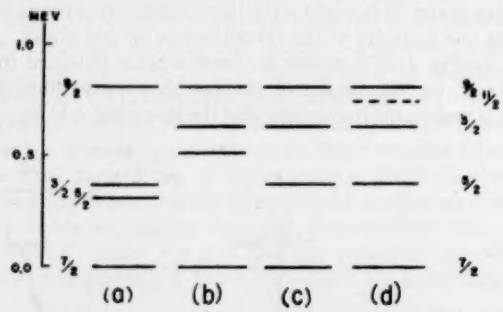

FIG. 5. Position of levels of Ca^{43}: (*a*) according to Kurath $(f_{7/2})^3$ without surface coupling $\rho=1.0$, (*b*) according to Kurath $(f_{7/2})^3$ without surface coupling $\rho=1.3$, (*c*) experimental, (*d*) with surface coupling (Ford); $\rho=1.35$, $A_0=28$ Mev, $\hbar\omega=15$ Mev.

The discrepancy between the observed level spacing and the predictions of Kurath can be explained in terms of an additional weak coupling of the particles to the nuclear surface. The surface interaction depresses the 5/2 state relative to the 3/2. For sufficiently strong coupling, this may result in spin 5/2 for the ground state of the $(f_{7/2})^3$ configuration[7] (e.g., Mn^{55}). In the present example, only a weak coupling is expected because of the double-closed-shell core, and indeed only a very weak surface coupling is required to fit the observed level spacing. Ford[8] fits the observed levels with

TABLE IV. Comparison of experimental energy level spacings.

	Without surface coupling Kurath $(f_{7/2})^3$		Experimental	With surface coupling Ford	
	$\rho=1.0$	$\rho=1.3$	···	$\rho=1.35$	$\hbar\omega=15$ Mev
7/2	0	0	0	0	7/2
5/2	0.31	0.51	0.369	0.369	5/2
3/2	0.37	0.63	0.625	0.625	3/2
				0.74	11/2
9/2	0.81	0.81	0.81	0.81	9/2
				1.07	15/2
	$A_0=29$ Mev	$A_0=39$ Mev		$A_0=28$ Mev	

Kurath's potential depth $A_0=28$ Mev, range parameter $\rho=1.35$, and surface vibration energy $\hbar\omega=15$ Mev. The theoretical level diagram corresponding to this choice of parameters is shown in Fig. 5. Since three parameters are used to fit three excited states, it is not surprising that the theoretical diagram fits the observed levels exactly. A test of the model could be made, however, if the remaining two states of spins 11/2 and 15/2 could be observed. It should be noted that, since the coupling to the surface causes considerable shifts in the levels, the normalization to the experimental data was made using the 7/2–5/2 difference (0.375 Mev) rather than the 7/2–9/2 difference (0.81 Mev) employed in the comparison of the experiments with Kurath's theory.

The authors are indebted to Dr. M. B. Sampson and the cyclotron group for making the irradiations, Mr. A. E. Lessor for performing the chemical separations, Miss Elizabeth Hebb for help with the coincidence experiments, and Dr. K. W. Ford for helpful theoretical discussion. One of us (TL) wishes to acknowledge a grant from the Swedish Atomic Committee and a fellowship from the Sweden-America Foundation.

The Decay of Cs^{136}†

J. L. Olsen* and G. D. O'Kelley‡
California Research and Development Company, Livermore, California

(Received January 5, 1954)

The radiations from Cs^{136} have been investigated with beta spectrometers, scintillation spectrometers, and a proportional counter spectrometer. Beta-particle groups of 341-kev and 657-kev energy were found, together with gamma-ray groups of energy 67.2, 153, 162, 265, 335, 822, 1041, 1245, 1410, 2350, and 2490 kev. A decay scheme is proposed on the basis of gamma-ray intensities and gamma-gamma coincidences.

THE nuclide Cs^{136} was discovered by Glendenin[1] in slow-neutron fission. Subsequent experiments by Finkle, Engelkemeir, and Sugarman[2] characterized the radiations by absorption techniques. Glendenin[3] was later able to assign this cesium isotope to mass 136 from the (n,α) reaction on La^{139}, and obtained a half-life of 13.7 days. Absorption experiments yielded a value of 0.35 Mev for the beta-particle energy, and 1.1 Mev for the gamma radiation.

Since Cs^{136} is a shielded nuclide, it is of special interest in the study of the fission process. Rather complex mixtures of cesium isotopes result from high-energy fission of uranium, and so a detailed study of the radiations from Cs^{136} was undertaken in the hope that some characteristic radiation would be discovered which could be used to unambiguously assign yields to Cs^{136} formed in high-energy fission.

For the present experiments carrier-free cesium fractions were obtained from uranium targets irradiated with 190-Mev deuterons in the 184-inch cyclotron of the University of California Radiation Laboratory. Early measurements of the radiations from such fractions showed that although Cs^{136} was the most prominent activity, the presence of other nuclides made the data rather questionable. Consequently, an intense source of the carrier-free, fission product cesium was deposited on the filament of a time-of-flight mass separator,[4] and the mass-136 fraction was collected. All measurements described below were performed on the mass-separated Cs^{136} sample.

The decay of a small portion of the mass-separated sample was followed with an end-window Geiger counter, and after six half-lives no deviation from a half-life of 12.9 days has been observed.

The radiations from Cs^{136} were studied on several instruments. A ring-focused, long magnetic lens beta spectrometer[5] was used to examine the electron spectrum in the energy range 100 to 2000 kev. For the energies below 200 kev a 25-cm radius, double-focusing beta spectrometer was employed. Gamma-ray energies were measured on sodium iodide scintillation spectrometers having a resolution for the Cs^{137} gamma ray of 7.5 to 9.0 percent full width at half-maximum, depending upon the application. Recording of the data was accomplished either by an automatically swept single-channel pulse-height analyzer, or a 50-channel analyzer for low counting rates. The low-energy electromagnetic radiation was also studied on a xenon-filled proportional counter, connected to the 50-channel analyzer.

Fermi analysis of the beta-particle spectrum shows the energies and intensities of the beta-particle transitions to be 341 ± 2 kev (92.6 percent) and 657 ± 3 kev (7.4 percent). From the Moszkowski nomographs,[6] $\log ft$ for the low-energy transition is 6.0, while that of the higher-energy beta group is 8.0.

Internal conversion lines from six gamma-rays were observed on the lens spectrometer, with the results shown in Table I. The K/L ratio for the 67.2-kev

Table I. Gamma-radiation from Cs^{136}.

Gamma ray	γ-ray energy, kev: Scintillation spectrometer	Proportional counter spectrometer	Beta spectrometer	K/L: Beta spectrometer
γ_1	67 ± 2	67.2 ± 0.5		3.5
γ_2	160 ± 2 (unresolved γ_2 and γ_3)		153 ± 1	5.9
γ_3			162 ± 1	1.0
γ_4	265 ± 3			
γ_5	334 ± 3		335 ± 2	5.2
γ_6	820 ± 8		822 ± 2	3.0
γ_7	1040 ± 10		1041 ± 5	
γ_8	1245 ± 13		1245 ± 6	
γ_9	1410 ± 28			
γ_{10}	2350 ± 45[a]			
γ_{11}	2490 ± 50[a]			

[a] Gamma-ray energies calculated from pair peaks.

† This work was performed under the auspices of the U. S. Atomic Energy Commission.

* Now at University of California Radiation Laboratory, Livermore, California.

‡ Now at Oak Ridge National Laboratory, Oak Ridge, Tennessee.

[1] E. Glendenin (unpublished) and *Radiochemical Studies: The Fission Products* (McGraw-Hill Book Company, Inc., New York, 1951) Paper No. 159, National Nuclear Energy Series, Plutonium Project Record, Vol. 9.

[2] Finkle, Engelkemeir, and Sugarman, *Radiochemical Studies: The Fission Products* (McGraw-Hill Book Company, Inc., New York, 1951). Paper No. 158, National Nuclear Energy Series, Plutonium Project Record, Vol. 9.

[3] L. E. Glendenin, Ph.D. thesis, Massachusetts Institute of Technology Report NP-1242, 1949 (unpublished).

[4] M. C. Michel, University of California Radiation Laboratory Report UCRL-2267, 1953 (unpublished).

[5] G. D. O'Kelley and J. L. Olsen, California Research and Development Company Report MTA-38, 1953 (unpublished).

[6] S. A. Moszkowski, Phys. Rev. 82, 35 (1951).

transition was determined on the double-focusing spectrometer.

Photoelectric peaks from eight gamma rays were identified on the scintillation spectrometers. Two additional peaks have been interpreted as pair production peaks from the two highest-energy gamma rays. The gamma-ray energies are also shown in Table I.

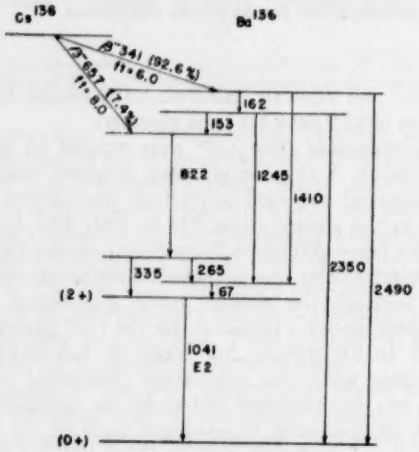

FIG. 1. Proposed decay scheme for Cs^{136}. Energy values are in kev.

No radiation was seen on the proportional counter besides the 67.2-kev transition, its xenon escape peak, and the K and L x-rays.

The decay scheme of Fig. 1 is proposed on the basis of gamma-ray intensities and gamma-gamma coincidence spectroscopy. The K-shell internal conversion coefficient for the 1.041-Mev gamma ray indicates an $E2$ transition, which leads to the assignment of a spin of two and even parity to the first excited state, as would be expected for an even-even nucleus.[7] A 1.041-Mev first excited state is consistent with other even-even nuclides in the region of mass 136. Work is continuing on the assignment of spins and parities to the other levels of Ba^{136}.

The authors wish to thank Mrs. P. W. McLaughlin, Dr. M. C. Michel, Mr. A. E. Larsh, and Mr. F. Stevens for their assistance in taking some of the data, and for the use of some of their experimental facilities. The chemical isolation of cesium was carried out by Mr. R. S. Gilbert.

Note added in proof.—Recent coincidence measurements show the 153-kev gamma ray to be in cascade with the 1245- and 162-kev gamma rays. This reverses the order of the 153–162 kev cascade from that shown in Fig. 1. The 153-kev transition is a crossover for a 65–88 kev cascade not shown in Fig. 1.

[7] M. Goldhaber and A. W. Sunyar, Phys. Rev. 83, 917 (1951).

PHYSICAL REVIEW VOLUME 95, NUMBER 6 SEPTEMBER 15, 1954

Yield of Alpha Particles from Photonuclear Reactions at 23-Mev Bremsstrahlung

L. H. GREENBERG, J. G. V. TAYLOR,* AND R. N. H. HASLAM
University of Saskatchewan, Saskatoon, Saskatchewan, Canada

(Received June 1, 1954)

The yield of alpha particles from (γ,α) reactions and other photoreactions involving alpha-particle emission from 9 elements up to atomic number 58 is given. Much of the data used have been previously published but further information has been obtained on the reactions in carbon, oxygen, and bromine. Original measurements have been made for the (γ,α) reactions in vanadium and silver. The yield is a maximum in the region of copper and drops rapidly with increasing atomic number. There is evidence that at high atomic numbers, reactions involving the emission of another particle as well as the alpha particle predominate over just single alpha-particle emission.

INTRODUCTION

THE study of the yield of neutrons and of protons from nuclei excited by photon absorption has received considerable attention. Sufficient data are now available for a preliminary examination of the dependence of alpha-particle yield on atomic number. The following is a report on the yield of alpha particles from the (γ,α) reaction produced by the bombardment of several medium weight nuclei with 23-Mev bremsstrahlung.

Figure 1 shows the (γ,α) yield points for betatron radiation having a maximum energy of 23 Mev. Some of the points shown are taken from previously described work, and some have been determined recently in this laboratory. A brief discussion of each point follows:

1. $C^{12}(\gamma,\alpha)Be^8$

This reaction has been examined by several workers,[1–4] some using bremsstrahlung and some using

* Now at McMaster University, Hamilton, Ontario.

[1] F. K. Goward and J. J. Wilkins, Proc. Roy. Soc. (London) A217, 357 (1953).
[2] Glättli, Seippel, and Stoll, Helv. Phys. Acta 25, 491 (1952).
[3] M. Eder and V. L. Telegdi, Helv. Phys. Acta 25, 55 (1952).
[4] H. Wäffler, and S. Younis, Helv. Phys. Acta 22, 614 (1949).

lithium gamma rays to produce the reaction. The reported cross sections at an energy of 17.6 Mev varies over a fairly wide range, namely from 1.1 to 2.4×10^{-28} cm²/atom. It was thought worth while to make a redetermination of the yield of this reaction.

The Be^8 nucleus resulting from the emission of an alpha particle from C^{12} may be in either the ground state or in an excited state. In either case the Be^8 is unstable and breaks into two alpha particles. If this has occurred in a nuclear emulsion, the event is seen as a three-pronged alpha-particle star which exhibits a momentum sum of practically zero.

A 100-micron Ilford E_1 emulsion was exposed to 196 r of 23-Mev bremsstrahlung from the University of Saskatchewan betatron and 1.3 cm² was searched. Of the stars located, 169 with three prongs showed the proper momentum balance. Correcting for the probable number whose tracks did not end in the emulsion there were 195 such events. The manufacturer's analysis gave 0.27 gram of carbon per cubic centimeter of emulsion. An analysis of these data gives 3570 events per mole of carbon per roentgen.

To compare this result with the results already published for 17.6-Mev radiation the cross section was calculated as a function of the photon energy. The energy of the photon which caused the event was assumed to be the sum of the energies of the three alpha particles and the binding energy of 7.15 Mev. On a series of plates (from which the above data were taken) exposed at betatron energies from 16 to 26.6 Mev the energy associated with 738 stars was calculated. Assuming a modified Schiff type bremsstrahlung spectrum as tabulated in the photon difference paper by Katz and Cameron,[5] the cross section curve was calculated. At 17.6 Mev the cross section was 1.7×10^{-28} cm²/atom, which is in the range of the previously published values. The yield point at 23 Mev is therefore assumed to be not inconsistent with the other data on this reaction.

2. $N^{14}(\gamma,\alpha)B^{10}$

This yield point was taken directly from the data of Millar and Cameron[6] and is 580 events/mole r at 24-Mev bremsstrahlung. At 23-Mev bremsstrahlung one would expect no more than 400 events/mole r. This is based on only 8 events but does serve to verify the dip in the yield curve.

3. $O^{16}(\gamma,\alpha)C^{12}$

This point has been obtained by combining the results of Millar and Cameron[6,7] with more recent observations of the authors. The cross section curve of Millar and Cameron[7] multiplied by the appropriate Schiff bremsstrahlung spectrum[5] gave an activation point. The cross section curve of Millar and Cameron was obtained from the number of "recoil events" identified in a nuclear emulsion. The authors have repeated this and obtained only a slightly different value. However, the method is very uncertain for low-energy alphas. There is some evidence that the oxygen may be very strongly excited to the levels around 13 Mev, and then, on decay to the ground state of carbon, there is a release of about 6 Mev. The observed alpha-particle energy would be about 4.5 Mev with the remainder going to the recoiling carbon. This recoiling nucleus would have a track about a micron in length and would only slightly raise the alpha-particle energy as measured by the track length. A large number of the observed recoil events do fit this transition and there were also a large number classified as single alpha particles but which have an energy appropriate for this reaction. The method by which Cameron obtained the cross section for the reaction assumed that the kinetic energy of the alpha particle plus recoil nucleus and the binding energy was the total energy involved in the reaction. It is almost certain, however, that in many cases when the high-energy oxygen levels are excited the recoiling carbon nucleus is in an excited state. The oxygen point therefore has the greatest uncertainty of all shown on the graph.

4. $V^{51}(\gamma,\alpha)Sc^{47}$

A yield point for 23-Mev bremsstrahlung was obtained for the (γ,α) reaction in V^{51} by the method of residual activity. A mass of 15.6 grams of sodium orthovanadate ($Na_3VO_4\cdot16H_2O$) was irradiated in the geometry used in the (γ,α) reaction in copper.[8] The sample

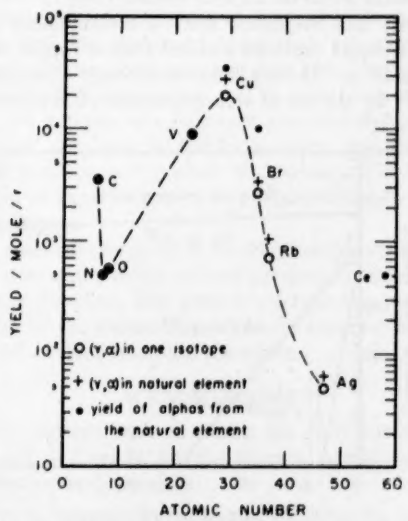

FIG. 1. The yield of alpha particles from photonuclear reactions as a function of atomic number. The (γ,α) yield from the heavy isotope, where one exists, as well as the yield corrected for the natural element is given. In cases where it has been measured the total yield of alpha particles from all reactions is also shown.

[5] L. Katz and A. G. W. Cameron, Can. J. Phys. **29**, 518 (1951).
[6] C. H. Millar and A. G. W. Cameron, Phys. Rev. **78**, 78 (1950).
[7] C. H. Millar and A. G. W. Cameron, Can. J. Phys. **31**, 723 (1953).
[8] Haslam, Smith, and Taylor, Phys. Rev. **84**, 840 (1951).

was dissolved in 100 ml of water with about 10-mg Sc^{+++} carrier and 2-mg Fe^{+++} carrier. An excess of NaOH was added to precipitate Sc and Fe as hydroxides. The solution was filtered through No. 40 filter paper. The precipitate was dried and counted between two RCL end-window counting tubes.

Counting corrections were based on the assumption of a 0.6-Mev beta.[9] The dose received by the sample was 46 400 roentgens in 40 minutes and was measured by the activity induced in tantalum strips irradiated simultaneously with the sodium orthovanadate. The activity of the sample was followed for 31 days, previous trial irradiations having shown a pure 72-day activity after this time. Subtraction of the 72-day titanium activity caused by the (n,p) reactions left the activity caused by 3.43-day Sc^{47} and a small amount due to 15-hour Na^{24}. The decay curves are shown in Fig. 2.

Correcting for attenuation of the beam in the sample, counting losses, etc., the yield was determined to be 9×10^3 disintegrations/mole r for 23-Mev bremsstrahlung. Natural vanadium is practically 100 percent V^{51} so there is no correction for the naturally occurring element.

5. $Cu^{65}(\gamma,\alpha)Co^{61}$ and $Cu(\gamma,\alpha)Co$

The yield point for the $Cu^{65}(\gamma,\alpha)Co^{61}$ reaction was taken from the published data of Haslam, Smith, and Taylor[8] and is 2.0×10^4 events/mole r of Cu^{65}. The yield from Cu^{63} was estimated from this on the basis of the statistical theory of nuclear reactions. By using the result of this calculation and correcting for isotopic abundance, the yield from naturally occurring copper was estimated to be 2.8×10^4 events/mole r.

Byerly and Stephens[10] made a measurement of the yield of alpha particles emitted from a copper sample irradiated at 24-Mev bremsstrahlung. Corrected to 23 Mev by the use of an approximate yield curve their data give 3.5×10^4 events/mole r. Because their method involved the detection of emitted alpha particles, reactions involving the emission of a neutron or proton as well as an alpha particle were included. The method used by Haslam, Smith, and Taylor detected only the events in which an alpha and no other particle was emitted. The yield point of Byerly and Stephens is expected to be higher than that of Haslam and the agreement is therefore excellent.

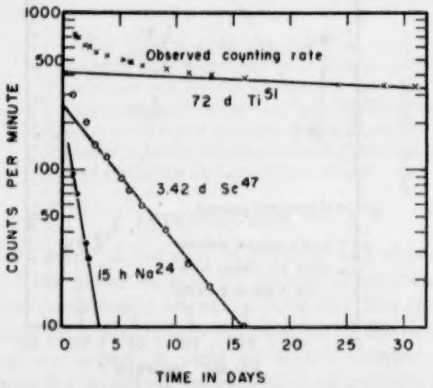

FIG. 2. The decay curve of the scandium separated from irradiated vanadium. Some 72-day Ti and 15-hour Na were also present but could be subtracted out.

[9] N. L. Krisberg and M. L. Pool, Phys. Rev. **75**, 1693 (1949).
[10] P. R. Byerly, Jr., and W. E. Stephens, Phys. Rev. **83**, 54 (1951).

6. $Br^{81}(\gamma,\alpha)As^{77}$ and $Br(\gamma,\alpha)As$

The yield for the reaction $Br^{81}(\gamma,\alpha)As^{77}$ was taken from the paper of Taylor and Haslam.[11] As for copper, a correction was made in order to obtain the yield from Br^{79} and the natural element. Taylor and Haslam had carried out a similar calculation at 17.6 Mev to compare their results with those obtained by Nabholtz *et al.*[12] using lithium gamma rays. The agreement at 17.6 Mev was good.

The yield at 23 Mev was 2.7×10^3 events/mole r in Br^{81} and 3.4×10^3 events/mole r in natural bromine.

The total yield of alpha particles from natural bromine can be estimated from the work of Haslam *et al.*[13] with nuclear emulsions. One may assume that the alpha particles in their high-energy peak were caused practically entirely by the reaction in bromine rather than both in bromine and silver as they assumed. Using their data and also more recent data of the authors, which are in excellent agreement, the yield of alpha particles from natural bromine was calculated to be 1.0×10^4 alphas/mole r. This would include many reactions in which other particles were also emitted and is, as expected, considerably higher than the yield measured by Taylor.

7. $Rb^{87}(\gamma,\alpha)Br^{83}$ and $Rb(\gamma,\alpha)Br$

The yield point for $Rb^{87}(\gamma,\alpha)Br^{83}$ was obtained by Haslam and Skarsgard[14] and was 7×10^2 events/mole r for 23-Mev bremsstrahlung. Correcting for the natural element one obtains 10.3×10^2 events/mole r.

8. $Ag^{109}(\gamma,\alpha)Rh^{105}$ and $Ag(\gamma,\alpha)Rh$

This reaction was of special interest because of the presence of Ag in a nuclear emulsion. The contribution of the silver atoms to the particle tracks observed in a nuclear emulsion bombarded with x- or gamma rays could be definitely established only by direct measurement of the cross section for the reaction.

The reaction $Ag^{109}(\gamma,\alpha)Rh^{105}$ may be detected by irradiating silver in the betatron beam and examining it for 37-hour Rh^{105} beta activity. Because of the high

[11] J. G. V. Taylor and R. N. H. Haslam, Phys. Rev. **87**, 1138 (1952).
[12] Nabholtz, Stoll, and Wäffler, Phys. Rev. **86**, 1043 (1952).
[13] Haslam, Cameron, Cooke, and Crosby, Can. J. Phys. **30**, 349 (1952).
[14] R. N. H. Haslam and H. M. Skarsgard, Phys. Rev. **81**, 479 (1951).

Coulomb barrier for alpha-particle emission, the cross sections for emission of neutrons or protons are much higher than the cross section for alpha emission. Reactions other than the (γ,α) would then lead to large interfering activities which would mask the low activity of the Rh^{105}. Also, to count the rhodium-105 it would be necessary to obtain a concentrated sample to avoid large self-absorption effects and poor geometry. For these two reasons it was necessary to separate the rhodium from the irradiated silver sample by a chemical method. The literature contains no method to separate small amounts of rhodium from large amounts of silver and a great deal of time was spent in developing a process.

The irradiated samples consisted of 50 g of $AgNO_3$. After irradiation they were dissolved in 150 ml of H_2O, and a rhodium carrier in the form of $RhCl_3$ solution was added. 20 mg of KCl as a 1-mg/ml solution was added, and the solution boiled for 3 minutes. The addition of concentrated NH_4OH to the hot solution yielded a heavy precipitate. On addition of excess concentrated NH_4OH, the major part of the precipitate dissolved, leaving a small amount of dark brown precipitate. The solution was then filtered in a Büchner funnel onto a 1-inch diameter filter paper. The precipitate was washed with NH_4OH and alcohol, dried, and counted between two end-window RCL counting tubes which gave a geometry factor of 0.6. The samples exhibited the 37-hour Rh^{105} activity with small amounts of 8-day Ag^{106} and 14-hour Pd^{109} in some samples.

The yield of the rhodium extraction was assumed to be 100 percent. It could not be measured because the composition of the precipitate was not known. However, the yield of precipitate was proportional within 5 percent to the amount of rhodium carrier added. It was then not illogical to assume that practically all of the rhodium was precipitated.

Samples were irradiated at 22 and 24 Mev. The radiation time for each was approximately one-half hour and the dosages up to 50 000 roentgens.

The dosage given to each sample was determined by measuring the activity induced in tantalum disks inserted in the end of the $AgNO_3$ sample holder. The conversion to roentgens was done in the same manner as outlined in the paper on the (γ,α) reaction in copper.[8] Appropriate corrections were also made for inverse square attenuation and absorption of the x-rays in the sample. The mean of the 22- and 24-Mev values was used to obtain the yield at 23 Mev which was 50 disintegrations/mole r. This is not the general procedure to obtain a yield point at 23 Mev but the 22- and 24-Mev yield points were part of an attempt to obtain a complete yield curve for the reaction.

Correcting for the isotopic abundance and the expected yield from the lighter isotope, natural silver would give 67 events/mole r. The errors are very large, and the correction is insignificant.

9. $Ce(\gamma,\alpha)Ba$

Toms and Stephens[15] measured the yield of alpha particles from a cerium sample bombarded with bremsstrahlung of 24-Mev maximum energy. The yield at 23 Mev would be lower by a factor of 0.7 to 0.9. The emitted alpha particles were observed and hence reactions other than those in which just a single alpha particle was emitted were included. For 24-Mev bremsstrahlung Toms and Stephens report a yield of 800 alphas/mole r from cerium. At 23 Mev this could be as low as 500 alphas/mole r.

This point as shown on the graph (Fig. 1) does not verify the downward trend toward higher atomic number. It could be either that, for the higher elements, reactions in which a neutron is also emitted are more predominant, or that a mechanism such as the direct photoelectric effect becomes more important.

DISCUSSION

This is only a preliminary survey to indicate the approximate value of the yield from the (γ,α) reactions in the various elements. The shape of the yield curve is similar to that of the curve for the proton yield as a function of atomic number presented by Mann and Halpern.[16] The alpha-particle yield is lower by a factor varying from 10^2 to 10^4.

It is obvious that more points at higher atomic number are required. The work of Toms and Stephens suggests that the downward trend may not continue as steeply becuase they calculate that from bismuth there would be 100 alphas/mole r. The absorption cross section for gamma rays increases with increasing atomic number, the potential barrier increases, and the photoelectric effect is expected to increase. The relative effects of these factors must be determined by further experiments.

It must also be pointed out that a yield curve such as this does not give the relative integrated cross sections for the reactions. The yield is a strong function of the energy at the resonance peak in the cross-section curve as well as the area under the curve.

ACKNOWLEDGMENT

The authors wish to thank the National Research Council of Canada for the financial assistance which made this work possible.

[15] M. E. Toms and W. E. Stephens, Phys. Rev. **92**, 362 (1953).
[16] A. K. Mann and J. Halpern, Phys. Rev. **82**, 733 (1951).

Differential Cross Sections for the $C^{12}(d,p)C^{13}$ and $C^{13}(d,t)C^{12}$ Reactions*

H. D. Holmgren,† J. M. Blair, B. E. Simmons, T. F. Stratton, and R. V. Stuart
University of Minnesota, Minneapolis, Minnesota

(Received June 14, 1954)

The differential cross section for the $C^{12}(d,p)C^{13}$ reaction has been measured for 3.29-Mev deuterons over an angular range from 5° to 140°. It was found to have a maximum near 25°, a minimum near 80°, and another increase at higher angles. Over the same angular range, the $C^{13}(d,t)C^{12}$ reaction has a differential cross section for 3.29-Mev deuterons which shows a maximum at 12°, a minimum at 57°, and a small rise at higher angles. For 2.19-Mev deuterons the structure of $C^{13}(d,t)C^{12}$ differential cross section is broader, with the maximum occurring at 17°. The experimental results have been compared with the results theoretically expected for stripping reactions.

INTRODUCTION

THE deuteron stripping theory developed by Butler[1] has recently been extended to (d,t) and (t,d) reactions by Butler and Salpeter[2] and Newns.[3] On the basis of this theory, the differential cross sections for the (d,t) and (t,d) reactions may be expressed in terms of l, the angular momentum carried into or out of the target nucleus by the neutron involved; R, an effective nuclear radius; and the momentum distribution of the neutron in the triton, considering the triton as a neutron bound to a deuteron-like core. Butler and Salpeter have suggested the possibility of obtaining information about the triton wave function by measuring the differential cross sections for the following reactions:

$$(A+1)+d\rightarrow A+t \quad (1)$$

and

$$A+d\rightarrow(A+1)+p \quad (2)$$

or

$$(A+1)+p\rightarrow A+d. \quad (3)$$

From the (d,p) or (p,d) observations one can, in principal, determine l and R. According to Butler and Salpeter, it is expected that these same values of l and R should be applicable for the (d,t) reaction. A measurement of the differential cross sections for reactions (1) and (2) or (3) should enable one to determine the form of the momentum distribution of the neutron in the triton. Newns has shown that the angular distribution for a (d,t) reaction is rather insensitive to the form of the space wave function of the triton. It is also somewhat questionable whether one should expect the same value of R to be applicable to both reactions on the basis of the Born approximation theory of stripping reactions.[4,5] In addition, Horowitz and Messiah[6] have shown that by taking into account the interaction of the outgoing proton with the final nucleus in a (d,p) reaction the absolute magnitude of the differential cross section may change by as much as a factor of 6 from that predicted by Butler's original formula. It was thus uncertain as to the amount of information which might be obtained from such a series of experiments, considering the present state of the theory. However, in the interest of stimulating theoretical work towards the improvement of the deuteron stripping theory and the extension of this theory to triton reactions, it was felt a study of reactions (1) and (2) would be justified.

With the limited energy available from the Minnesota electrostatic generator, it was necessary for the atomic number of the target nucleus to be less than 10 in order to satisfy the assumption of the theory that Coulomb effects may be neglected. In addition, it was desirable for the Q's of the reactions to be greater than zero. On the basis of these restrictions, the only reactions which could be studied were the following:

$$Be^9(p,d)Be^8 \quad \text{and} \quad Be^9(d,t)Be^8, \quad (4)$$

$$C^{12}(d,p)C^{13} \quad \text{and} \quad C^{13}(d,t)C^{12}, \quad (5)$$

$$O^{16}(d,p)O^{17} \quad \text{and} \quad O^{17}(d,t)O^{16}. \quad (6)$$

The $Be^9(d,t)Be^8$ reaction has already been rather thoroughly investigated.[7–10] The investigation of reactions (6) would have been very difficult since the highest enrichment of O^{17} available was less than one percent. Therefore the carbon reactions were studied.

The M.I.T. group first reported the $C^{13}(d,t)C^{12}$ reaction.[11] Their measurements gave a Q value of 1.310 $\pm$0.006 Mev for the $C^{13}(d,t)C^{12}$ reaction and a Q value of 2.716$\pm$0.005 Mev for the $C^{12}(d,p)C^{13}$ reaction. The differential cross sections for the $C^{12}(d,p)C^{13}$ reaction have been measured by Phillips[12] at 8 energies over the energy range extending from 0.75 Mev to 1.32 Mev and

* Supported in part by the joint program of the U. S. Office of Naval Research and the U. S. Atomic Energy Commission.

† Atomic Energy Commission Fellow during the preliminary parts of this work. Present address: Naval Research Laboratory, Washington 25, D. C.

[1] S. T. Butler, Proc. Roy. Soc. (London) **A208**, 559 (1951).
[2] S. T. Butler and E. E. Salpeter, Phys. Rev. **88**, 133 (1952).
[3] H. C. Newns, Proc. Phys. Soc. (London) **A65**, 916 (1952).
[4] Bhatia, Huang, Huby, and Newns, Phil. Mag. **43**, 485 (1952).
[5] P. B. Daitch and J. B. French, Phys. Rev. **87**, 900 (1952).
[6] J. Horowitz and A. M. L. Messiah, Phys. Rev. **92**, 1326 (1953).
[7] F. A. El-Bedewi, Proc. Phys. Soc. (London) **A64**, 947 (1951).
[8] Fulbright, Bruner, Bromley, and Goldman, Phys. Rev. **88**, 700 (1952).
[9] P. Cuer and J. J. Jung, Phys. Rev. **89**, 1151 (1953).
[10] D. R. Bach and P. V. C. Hough, Phys. Rev. **91**, 463 (1953).
[11] Strait, Van Patter, Buechner, and Sperduto, Phys. Rev. **81**, 747 (1951).
[12] G. C. Phillips, Phys. Rev. **80**, 164 (1950).

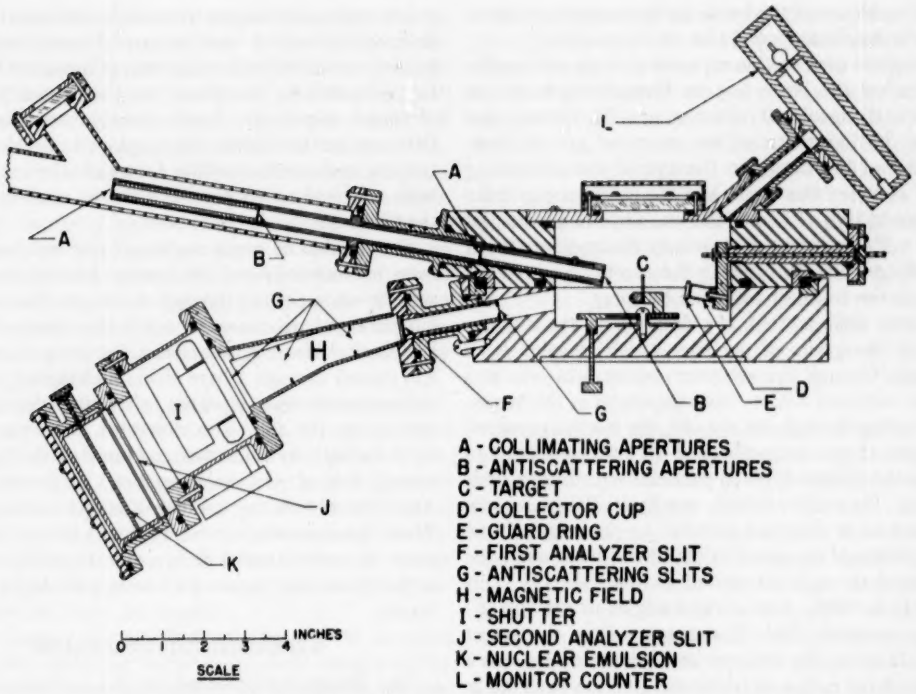

FIG. 1. Sectional drawing of the reaction chamber. The section is through the center of the chamber with the analyzer in the 160° position.

at 7.8 Mev by Rotblat.[13] The angular distributions of the protons emitted in this reaction have also been studied for 3.89-Mev,[14] 4.0-Mev[15] and 14.5-Mev[16] incident deuterons. The experimental data at all energies above 3 Mev indicated that the neutron carries one unit of angular momentum into the target nucleus.

The highest energy at which it was feasible to make the present study of the $C^{13}(d,t)C^{12}$ reaction was 3.29 Mev. The differential cross section of the $C^{12}(d,p)C^{13}$ reaction had not been determined previously at this energy, so it also was measured at this time. For purposes of studying the influence of the Coulomb interaction the $C^{13}(d,t)C^{12}$ differential cross section also was measured at a lower energy, 2.19 Mev.

REACTION CHAMBER

In the study of the $C^{13}(d,t)C^{12}$ reaction, it was necessary to employ a combination of momentum analysis in a magnetic field and range measurements in nuclear emulsions in order to distinguish the tritons from the other reaction products or the scattered deuterons. The reaction chamber which was used to observe this reaction is shown in Fig. 1.

The chamber consisted of two circular aluminum sections, each 9 in. in diameter. The upper section in Fig. 1 contained the diaphragms for collimating the incident ion beam from the electrostatic generator. The lower section, which could be rotated with respect to the upper section, contained the analyzer system. Proper alignment between the two was maintained by a ring of steel balls trapped between steel races. The rotating vacuum seal between the two sections was formed by an "O-ring." The axes of both the collimating system and the analyzer system were at angles of 10° with respect to the plane of the chamber. These axes intersected the axis of rotation of the chamber at the same point; thus, the angle between the axes of the two systems could be continuously varied from 0° to 160°.

The collimating system consisted of two beam-defining apertures (A), 9 in. apart, each with an antiscattering aperture (B) 3 in. behind it. The diameters of the collimating apertures were 0.058 in. The first antiscattering aperture was 0.065 in. in diameter, and the second was 0.100 in. in diameter.

The target assembly was mounted in the lower section of the chamber in such a manner that it could be rotated about the axis of the chamber. The plane of the target contained the axis of the chamber and the intersection of this axis with the axes of the collimating and analyzer systems. It was thus possible to vary the

[13] J. Rotblat, Nature **167**, 1027 (1951).
[14] R. E. Benenson, Phys. Rev. **90**, 420 (1953).
[15] D. A. Bomley and L. M. Goldman, Phys. Rev. **86**, 790 (1952).
[16] C. L. Black, Phys. Rev. **87**, 205 (1952).

angle of incidence of the beam on the target in order to obtain the maximum resolution of the analyzer.

The targets used in this experiment were sufficiently thin to allow the beam to pass through them and be stopped in the insulated collector cup (D). The cup was 0.350 in. in diameter and was mounted one in. from the center of the target on the axis of the collimating system. Between the target and the collector cup there was a guard ring (E) to which was applied a potential of -90 volts to repel the secondary electrons produced in the target and to prevent the secondary electrons formed in the collector cup from escaping.

The first analyzer slit (F) determined the angular spread of the group of particles which traveled from the target through the analyzer system. This slit was 0.032 in. wide and 5.92 in. from the center of the target. After passing through the slit (F), the particles entered the region of the magnetic field (H) which served to separate the various types of particles according to their momenta. The magnetic field, usually 10 500 gauss, was impressed in a direction parallel to the edge of the slit (F). Some of the particles deflected by the magnetic field passed through the second analyzer slit (J). This slit, 0.140 in. wide, was at right angles to the slit (F) and the magnetic field. The distance from the target to slit (J) along the trajectories of the particles was a function of the radius of curvature ρ of the particles in the magnetic field; thus, the solid angle subtended by the detector at the target was also a function of ρ. However, it was shown that, for values of ρ of interest in this experiment, the solid angle varied by less than $\frac{1}{2}$ percent from its average value of 5.58×10^{-5} steradian.

Directly behind the slit (J) there was located an Ilford C2 nuclear emulsion plate (K). This plate was in such a position that all the particles which passed through the slit (J) struck the surface of the emulsion at an angle of 10°. The amount of deflection of the particles by the magnetic field could be determined from the positions of the particle tracks in the emulsion. The plate holder contained six plates which could be positioned, one at a time, behind the second analyzer slit without opening the plate holder to the atmosphere.

Since the radius of the collector cup subtended an angle of 11° from the center of the target, it was necessary to remove the cup and monitor the beam with the proportional counter (L) when making observations at small angles. The axis of the slit system for the counter (L) was at an angle of 55° to the axis of the beam collimating system and intersected this axis at the center of the target.

TARGETS

During the course of this experiment, it was found that targets in which the incident deuterons lost 100 to 200 kev provided a practical compromise between the incompatible goals of maximizing the yield of particles from the reactions and minimizing their spread in energy. To make possible observation of the reactions at low angles, the targets were made with thin backings. Satisfactory targets were prepared by cracking methyl iodide[17] onto 0.005-mil nickel foils (Chromium Corporation of America, Waterbury 20, Connecticut). Details of target preparation have recently been described.[18] Ordinary methyl iodide was employed to make the C^{12} targets, and methyl iodide in which the carbon had been enriched to 63 percent C^{13} was used to prepare the C^{13} targets.

The number of target nuclei per cm² was determined from measurements of the energy loss which protons suffered upon passing through the target. The accelerating potential necessary to reach the threshold of the $Li^7(p,n)Be^7$ reaction was measured for protons which had passed through a bare nickel backing foil; then the measurement was repeated after the deposition of carbon on the foil. The difference between the two accelerating potentials was combined with the rate of energy loss of protons in carbon, as determined by Aron,[19] to obtain the number of target nuclei per cm². These measurements were repeated on at least four parts of each target foil in order to study the nonuniformities and obtain an average thickness of each target.

EXPERIMENTAL PROCEDURE

The charge accumulated by the collector cup was measured by a current integrator designed by Brown.[20] This current integrator was found to be accurate to within $\frac{1}{2}$ percent for currents in the range from 0.001 to 1 microampere.

The charge collection efficiency of the collector cup was determined by placing a one-inch diameter annular cup around the collector cup and then measuring the charge accumulated by this annular cup relative to that received by the collector cup. In this manner, it was found the smaller cup collected more than 98 percent of the incident deuterons.

For angles less than 15° the collector cup was removed, and the beam strength was monitored with the proportional counter mentioned above. The amplified pulses from this counter were analyzed by means of a 10-channel pulse-height analyzer so that it was possible to count only the deuterons elastically scattered from the target. The monitor sensitivity was calibrated with the current integrator for each target at the energy used for the plate exposure.

At low observation angles and a bombarding energy of 3.29 Mev, the protons from the $C^{12}(d,p)C^{13}$ reaction had about the same momentum as the elastically scattered deuterons. Since the flux of scattered deuterons was several orders of magnitude larger than the

[17] G. C. Phillips and J. E. Richardson, Rev. Sci. Instr. 21, 885 (1950).
[18] Holmgren, Blair, Famularo, Stratton, and Stuart, Rev. Sci. Instr. (to be published).
[19] W. A. Aron, University of California Radiation Laboratory Report UCRL-1325, 1951 (unpublished).
[20] R. J. S. Brown, Rev. Sci. Instr. (to be published).

flux of reaction protons, it was necessary to prevent these deuterons from reaching the nuclear emulsion plate. The range of protons was about four times the range of the deuterons; thus it was possible to stop all the deuterons without losing a significant number of protons by placing an aluminum foil of suitable thickness between the second analyzer slit and the nuclear emulsion plate. However, to prevent some protons from missing the plate, because of small-angle scattering in the aluminum foil, it was necessary to tip the plates so that the particles entered the emulsion at an angle of 45°. It was also found that by wrapping the plates in 2.5-mil aluminum foil the scattered deuterons could be completely removed without appreciably broadening the group of protons.

A group of particles, having a given momentum, produced tracks in the emulsion in a narrow band parallel to the one-in. dimension of the 1- ×3-in. plates. The slit (J) defined the region across the plate which could be struck by the particles so that small variations in the position of the plates would be unimportant. The bands varied from 3 mm to 6 mm in width, depending upon the energy spread of the particles emitted from the target.

The number of particle tracks having the required length in a particular band was counted using a microscope having a net micrometer disk inserted in one eyepiece. For all of the plates exposed with the 45° plateholder and for 6 of the plates obtained with the 10° plateholder, the total number of particle tracks having the required length in the band was counted. However, to facilitate the more rapid accumulation of data, the remainder of the plates were analyzed by counting all tracks having the required length in a measured fraction of the area of the band. A comparison of the two methods showed satisfactory agreement.

The entire experimental procedure was tested by measuring the differential cross sections for the elastic scattering of 3.10-Mev incident deuterons by gold and nickel foils. These measurements agreed with the calculated values of the Coulomb cross sections to within 3 percent, which is less than the estimated errors.

In order to obtain the minimum spread in energy of the particles entering the analyzer, it was necessary to rotate the target as the angle of the analyzer was changed. Because of this, the apparent thickness of the target and the number of target nuclei per cm² were a function of the analyzer angle. The angle of incidence of the beam on the targets increased from a minimum of 10° for low angles to 47° for analyzer angles in the region of 90°. The number of target nuclei per cm² can be expressed as $N_0/\cos\alpha$, where N_0 is the number of target nuclei per cm² observed for normal incidence, and α is the angle of the incidence. The surfaces of the targets were observed to be slightly wrinkled. Because of these wrinkles, it was necessary to express the angle of incidence as $\alpha=\alpha_0+\delta$, where α_0 is the angle of incidence calculated from the rotation of the target assembly, and δ is the correction due to the wrinkles. The corrections δ were determined for each target by measuring the yield of reaction particles at a fixed analyzer angle as a function of the calculated angle of incidence α_0 and then fitting the experimental points with a curve of the form $1/\cos(\alpha_0+\delta)$. These corrections δ were found to be of the order of 5°. It was believed, on the basis of this work, that the angle of incidence α could be determined to less than 1°.

Because the angular distribution at low angles was of particular interest, four to ten plates were exposed for each angle in the region from 5° to 40° to provide a check on the consistency of the results. At least 2 exposures were taken for each angle greater than 40° for the $C^{13}(d,t)C^{12}$ reaction.

It was found that observations could not be made for angles less than 5° because of the presence, in this region, of large numbers of deuterons scattered by the edges of the analyzer slit (F). In the case of the $C^{13}(d,t)C^{12}$ reaction at these angles, the tritons could not be separated from the scattered deuterons by the use of absorbers, since their ranges were nearly the same. The protons from the $C^{12}(d,p)C^{13}$ reaction could pass through an absorber foil sufficiently thick to stop the scattered deuterons, but the nuclear emulsions were completely blackened in the region reached by the protons because of the x-rays produced when the deuterons were stopped in the foil.

ERRORS AND RESULTS

Since the theory is more sensitive to the angular distributions than to the absolute magnitude of the differential cross sections, the errors in this experiment were divided into two groups. This allows the theoretical predictions to be compared more critically with the experimental results. The first group of errors included those which affected only the angular distributions. These errors consisted of the statistical errors, the plate reading errors, the errors in the relative calibration of the current integrator scales, and the errors in the determination of the angle of incidence of the beam on the targets. At low angles, where a number of exposures had been taken, the errors due to the combination of the statistical errors and the plate reading errors were replaced by the errors determined from the reproducibility of the data. From this, it could be estimated that the plate reading errors were in the order of 1 percent. For angles greater than 40°, the statistical errors were about 3 percent. The relative current integrator error was less than ½ percent and was thus negligible. The errors in the angle of incidence were believed to be 1°. On this basis, it was necessary to assign 2- to 3-percent relative errors at low angles and errors of the order of 5 or 6 percent in the region of 90°. The second group of errors was composed of the errors in the quantities which entered into the calculation of

TABLE I. The center-of-mass differential cross sections σ for the $C^{13}(d,p)C^{13}$ reaction for 3.29-Mev incident deuterons as a function of the center-of-mass angle θ. The cross sections are in millibarns (10^{-27} cm^2).

θ (deg)	σ (mb)
5.4	11.6±0.3
10.8	13.9±0.4
16.2	17.8±0.4
21.6	19.3±0.4
27.0	21.1±0.5
32.3	18.5±0.7
43.0	14.1±0.4
53.6	9.4±0.3
64.0	6.9±0.3
74.4	5.9±0.2
84.6	5.9±0.3
94.6	6.2±0.3
109.5	9.1±0.6
124.0	10.9±0.5
138.3	11.9±0.6

the absolute differential cross section. In addition to the relative errors, this group consisted of the absolute current integrator calibration error, the errors in the measurement of the solid angle of the analyzer system, and the errors in the determination of the number of target nuclei per cm^2. On the basis of the measurement of the elastic scattering differential cross sections for gold and nickel, it was assumed that the combination of the first two errors was less than 3 percent. The errors in the determination of the number of target nuclei per cm^2 consisted of a 3 percent error in the value of the rate of energy loss of protons in carbon and about an 8 percent error in the measurement of the thickness of the targets. The errors in the thickness measurements were estimated by comparing the yields for three targets. On this basis, it was necessary to assign an absolute error of the order of 9 percent at low angles and about 10 percent at higher angles.

The center-of-mass differential cross section for the $C^{12}(d,p)C^{13}$ reaction for 3.29-Mev incident deuterons is presented in Table I and is plotted in Fig. 2 as a function of the center-of-mass angle. The error bars represent only the relative errors. The center-of-mass differential cross sections for the $C^{13}(d,t)C^{12}$ reaction are plotted as a function of the center-of-mass angle for 3.29-Mev incident deuterons in Fig. 3 and for 2.19-Mev incident deuterons in Fig. 4. The values of the cross sections for the $C^{13}(d,t)C^{12}$ reaction are presented in Tables II and III.

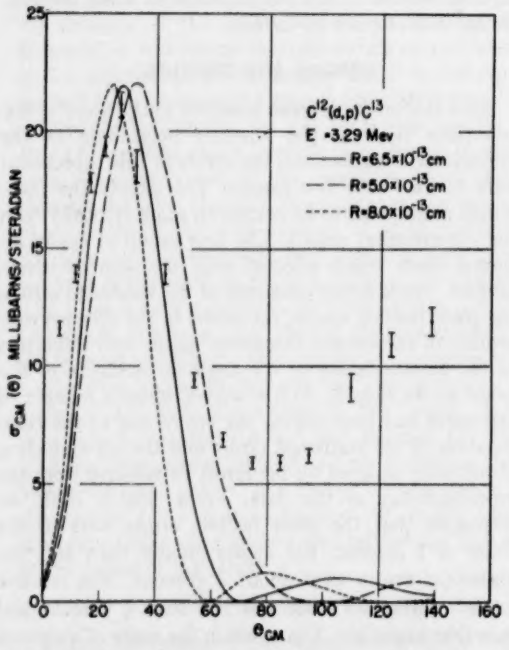

FIG. 2. Center-of-mass differential cross sections for the $C^{13}(d,p)C^{13}$ reaction *vs* center-of-mass angle, for incident deuterons of 3.29-Mev energy. Points represent experimental determinations. Curves are theoretical angular distributions on the basis of Butler's formula for $l=1$ and $R=5.0\times10^{-13}$, 6.5×10^{-13}, and 8.0×10^{-13} cm. The curves were normalized to the observations at their maximum values.

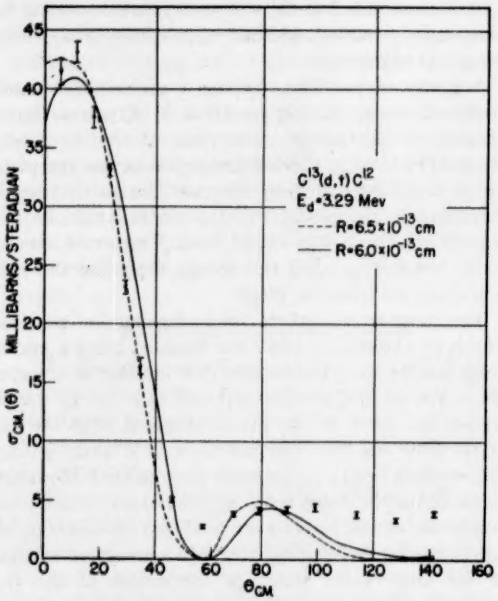

FIG. 3. Center-of-mass differential cross sections for the $C^{13}(d,t)C^{13}$ reaction *vs* center-of-mass angles, for incident deuterons of 3.29-Mev energy. Points represent experimental determinations. Curves are theoretical angular distributions on the basis of Butler's formula modified for the $C^{13}(d,t)C^{13}$ reaction for $l=1$ and $R=6.0\times10^{-13}$ and 6.5×10^{-13} cm, assuming Irving's internal wave function for the triton. Curves were normalized to the observations at their maximum values.

DISCUSSION OF RESULTS

In Fig. 2 the theoretical angular distributions determined on the basis of Butler's formula with $l=1$ for three values of the parameter R are compared with the experimentally observed center-of-mass differential cross

section of the $C^{12}(d,p)C^{13}$ reaction for 3.29-Mev incident deuterons. The theoretical curves in Fig. 2 are normalized at the first maximum to the maximum value of the observed cross sections. Only curves for $l=1$ are shown in Fig. 2, since this is the only value of l for which the theoretical angular distribution has a maximum in the region of the observed maximum.[13–16] The theoretical curve for $R=6.5\times10^{-13}$ cm has a maximum at about the same position as the observed differential cross sections; however, this theoretical curve does not agree with the experimental points for either higher or lower angles. The disagreement is particularly noticeable for angles greater than 80°.

Theoretical angular distributions for the $C^{13}(d,t)C^{12}$ reaction at 3.29 Mev are compared with the experimental differential cross section in Fig. 3. The curves are calculated from Butler's formula modified for (d,t)

TABLE II. The center-of-mass differential cross sections σ for the $C^{13}(d,t)C^{12}$ reaction for 3.29-Mev incident deuterons as a function of the center-of-mass angle θ. The cross sections are in millibarns (10^{-27} cm²).

θ (deg)	σ (mb)
5.8	41.5 ±1.1
11.6	43.1 ±0.9
17.4	37.6 ±0.9
23.2	33.1 ±0.5
28.8	23.1 ±0.6
34.7	16.4 ±0.6
46.0	5.10±0.15
57.1	2.80±0.10
68.1	3.84±0.16
78.8	4.12±0.20
89.2	4.36±0.20
99.3	4.45±0.27
114.0	3.82±0.19
128.1	3.35±0.15
141.6	3.91±0.15

reactions and employing Irving's internal space wave function for the triton.[3] Two values of the parameter R are used with $l=1$. It may be seen that a value of R in the region of 6.25×10^{-13} cm would produce excellent agreement between the theoretical curve and the experimental points. The agreement between this value of R and the one obtained from the $C^{12}(d,p)C^{13}$ reaction may be only fortuitous.

In Fig. 4 the theoretical angular distributions for three values of the parameter R with $l=1$ for the $C^{13}(d,t)C^{12}$ reaction at 2.19 Mev are compared with the experimental observations. It may be seen that $R=5.5\times10^{-13}$ cm produces about the best agreement; however, it is not possible to obtain as good agreement at this energy as at the higher energy. The experimental results are in qualitative agreement with results of Butler and Austern,[21] who have attempted to take into account the Coulomb effects for a (d,n) reaction. Their results indicate that the increased importance of the

[21] S. T. Butler and N. Austern, Phys. Rev. **93**, 355 (1954).

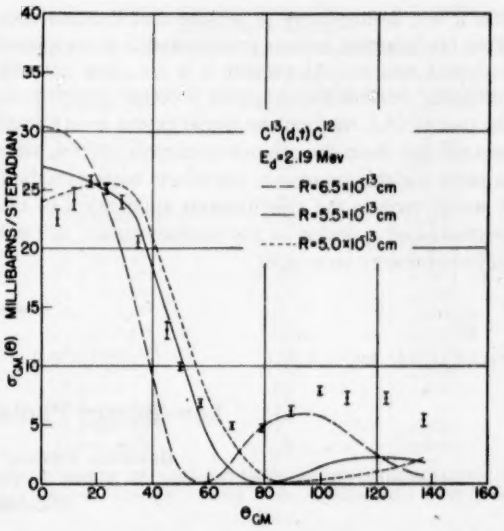

FIG. 4. Center-of-mass differential cross sections for the $C^{13}(d,t)C^{12}$ reaction *vs* center-of-mass angle, for incident deuterons of 2.19-Mev energy. Points represent experimental determinations. Curves are theoretical angular distributions on the basis of Butler's formula modified for the $C^{13}(d,t)C^{12}$ reaction for $l=1$ and $R=5.0\times10^{-13}$, 5.5×10^{-13}, and 6.5×10^{-13} cm, assuming Irving's internal wave function for the triton. Curves were normalized to the observations at their maximum values.

Coulomb effect at the lower energy causes the distribution to broaden and shift to higher angles if the same R is used as at the higher energy.

The observed discrepancies between the experimental points and the theoretical curves for the $C^{13}(d,t)C^{12}$ reaction may be expected to be eliminated by refinements in the theoretical calculations for the pick-up process. However, it appears that it will be impossible to account for the observed discrepancies in the $C^{12}(d,p)C^{13}$ reaction merely with refinements in the calculations based on a stripping process alone, and

TABLE III. The center-of-mass differential cross sections σ for the $C^{13}(d,t)C^{12}$ reactions for 2.19-Mev incident deuterons as a function of the center-of-mass angle θ. The cross sections are in millibarns (10^{-27} cm²).

θ (deg)	σ (mb)
5.8	22.6±0.7
11.6	24.2±0.9
17.4	25.7±0.5
23.2	25.0±0.4
29.0	23.9±0.6
34.7	20.5±0.5
45.1	13.0±0.7
49.9	9.9±0.3
57.2	6.8±0.2
68.2	4.9±0.2
78.9	4.7±0.3
89.3	6.2±0.4
99.4	7.8±0.3
109.3	7.3±0.5
123.5	7.3±0.5
137.2	5.5±0.3

that it will be necessary to include contributions from other fundamental nuclear processes such as compound nucleus formation. At present it is not clear how the compound-nucleus and stripping processes interfere. In the case of (d,t) reaction one would expect a very small contribution from the compound-nucleus process, since in order for this process to contribute to the reaction, it would require the simultaneous appearance of two neutrons and a proton at the nuclear surface, all with sufficient energy to escape.

ACKNOWLEDGMENTS

We would like to express our appreciation to Professor J. H. Williams for his advice and encouragement throughout the course of the experiment. We should also like to thank Dr. K. Famularo, Dr. D. M. Van Patter, and Dr. W. B. Cheston for their help and suggestions. Finally, we wish to thank Mr. R. B. Thorness for his supervision of the construction of the reaction chamber and Mr. D. Schifferl for his exceptionally accurate work in the construction of the chamber.

PHYSICAL REVIEW VOLUME 95, NUMBER 6 SEPTEMBER 15, 1954

Low-Energy Photofission Yields for U^{238}†

HAROLD G. RICHTER* AND CHARLES D. CORYELL
Department of Chemistry and Laboratory for Nuclear Science, Massachusetts Institute of Technology, Cambridge, Massachusetts
(Received June 9, 1954)

The pattern of mass number dependence of fission yield has been determined in the photofission of natural uranium (U^{238}) by 16-Mev electrons from the linear accelerator. The effective photon energies were principally 9–14 Mev. Yields were determined by quantitative radiochemical isolation and close approximation to absolute β counting for 19 chains. The peak-to-valley ratio is 110, the highest found yet outside of low-energy neutron studies. A spike in fission yields was found near mass number 133. Yields were also obtained for a number of chains in photofission with 10-Mev electrons.

I. INTRODUCTION

As part of an extended study of the pattern of fission yields as a function of energy and nature of the nucleus undergoing fission, a detailed study has been made of the yields in the photofission of natural uranium (essentially the photofission of U^{238}). It is well known that low-energy fission gives principally asymmetric mass division, with peak yields near mass numbers 97 and 138, and a deep valley for masses near symmetric division (~117). The dependence of the peak-to-valley yields on the energy available to the fissioning nucleus has been the subject of considerable interest. An attempt was made to determine the energy dependence of the very low yields of symmetrical fission using the photons produced by electrons of 10 Mev and 16 Mev impinging on a cylinder of uranium salt. In addition, interest is attached to fission yields in the mass region 131-138 where a fission yield spike occurs, presumably related to closed-shell effects in the primary fission products.[1–4] Photofission yields for masses 132, 133, and 134 are correlated with yield for other fission processes.

II. EXPERIMENTAL PROCEDURE

A. Irradiation Procedure

The M.I.T. linear accelerator[5] accelerates electrons to a maximum energy of about 16 Mev, with those electrons reaching the end of the machine having a spread of energy of about ±0.6 Mev. The machine terminates, in the target chamber, in a thin aluminum window through which the electrons can be passed essentially unimpeded. On rapid deceleration in a heavy metal target, the electrons give rise to a spectrum of photons ranging in energy from zero to the maximum electron energy. This diverging beam of x-rays is customarily the source of photons for irradiations.

Since the sample irradiated in this study was the salt of a heavy metal, it seemed more conservative of the photons to produce them in the immediate vicinity of the target nuclei by absorbing the electrons directly in the 20-gram uranium salt sample in a cylinder 10 cm long and 1.4 cm in diameter. The fission rate was increased by more than an order of magnitude employing this method over that of placing the sample in a lead-produced photon beam. Such an increase of

† This research was supported in part by the U. S. Atomic Energy Commission.

* Presented in partial fulfillment for the Ph.D. degree in the Department of Chemistry, Massachusetts Institute of Technology, Cambridge, Massachusetts. Present address: Department of Chemistry, University of Oregon, Eugene, Oregon.

[1] L. E. Glendenin, Massachusetts Institute of Technology Laboratory for Nuclear Science and Engineering, Technical Report No. 35, December, 1949 (unpublished).

[2] Wiles, Smith, Horsely, and Thode, Can. J. Phys. 31, 419 (1953).

[3] A. C. Pappas, Massachusetts Institute of Technology Laboratory for Nuclear Science, Technical Report No. 63, September, 1953 (unpublished).

[4] D. R. Wiles, Ph.D. thesis in Chemistry, Massachusetts Institute of Technology, November, 1953 (unpublished); D. R. Wiles and C. D. Coryell (to be published).

[5] P. T. Demos, Massachusetts Institute of Technology Laboratory for Nuclear Science and Engineering, Technical Report No. 50, May, 1951 (unpublished).

activity was necessary to carry out the study. Either uranyl nitrate hexahydrate or uranyl chloride was used as target. Irradiation times were usually one hour in length.

The linear accelerator was also run at approximately 10 Mev by disconnecting the last three sections. The machine was less reproducible in operation than at 16 Mev, and because of low intensity and low photofission cross section, much smaller amounts of fission products were produced.

Electron-induced fission is considered negligible compared to the fission from the x-rays (bremsstrahlung) produced as the electrons are slowed down.

B. Absence of Appreciable Photoneutron Fission

That neutrons from the photoneutron effect were not contributing to the observed fissions was shown by the following experiments using Si^{31} from the $P^{31}(n,p)$ reaction to show the presence of fast neutrons. Identical "sandwiches," consisting of a small disk of red phosphorus between two disks of uranyl chloride, were irradiated, one in the linear accelerator, one in the fast-neutron beam of the cyclotron (14-Mev deuterons impinging on beryllium), and one in partially thermalized neutrons from the same source (the latter two samples being wrapped well with cadmium foil to minimize thermal fission of U^{235}). After irradiation, the phosphorus samples were counted directly, while the uranium samples were analyzed radiochemically for Ba^{139}. If the fast neutron spectrum for the cyclotron is the same as that from the $U^{238}(\gamma,n)U^{237}$ reaction at the linear accelerator, the activity induced in the P^{31} samples should be comparable after normalizing to a given fission rate by means of the Ba^{139} activities. Since the fast-neutron spectrum of the cyclotron probably contained many more neutrons of high energy than did the linear accelerator neutron spectrum, the cyclotron spectrum was changed drastically by surrounding the sample with 10 cm of paraffin, in order to bracket the actual spectrum. Table I summarizes the data from the experiments.

From the ratios of activities of Si^{31} to Ba^{139} it appears that very little Si^{31} activity was produced from $U^{238} \times(\gamma,n)U^{237}$ neutrons, and consequently few fissions (less than 0.8 percent) could be caused by neutrons from this source.

C. Analytical and Counting Procedure

After irradiation, the uranium samples were dissolved in a suitable quantity of water, and aliquots were analyzed radiochemically for the various fission products. Standard analytical procedures[6] were modified when necessary to provide for the large quantities of uranyl ion present. Barium analyses were performed on an aliquot of each irradiated sample in order to normalize the yields to that of 85-min Ba^{139} and to compare the individual irradiations.

Final precipitates were filtered on tared filter papers, weighed, and then mounted on Scotch tape for counting. Victoreen Geiger-Mueller counters with thin mica end windows were used, and all counting was done at second shelf geometry.[7]

In order to correct the observed counting rates for absorption in the sample covering, air, and tube window, and for the many kinds of scattering exhibited by β rays, the data of Zumwalt[8] and Engelkemeir and co-workers[9] were used. It is estimated that the corrected activities are reliable to within ± 10 percent with the use of such corrections. The corrected activities were computed over to saturation activities taking into account the chain relations, irradiation and decay times, and chemical yield, and then expressed in terms of the saturation activity of 85-min Ba^{139}.

TABLE I. Comparison of fast neutron effects with fission.

Irradiation	Ratio Si^{31}/Ba^{139}(counts/sec)
Cyclotron, fast neutrons	1680/1035=1.6
Cyclotron, slower neutrons	42.0/32.0=1.3
Linear accelerator	50/5500=0.009
Limit for photoneutron fission	<0.009/1.3

TABLE II. Summary of high-energy fission yield experiments (x-rays up to 16 Mev).

Nuclide	Fission yield, %	Reliability
2.40-hr Br^{83}	0.288	±0.056
31-min Br^{84}	0.511	±0.10
53-day Sr^{89}	3.67	±0.60
9.7-hr Sr^{91}	4.22	±0.48
2.7-hr Sr^{92}	3.46	±0.35
10.0-hr Y^{93}	5.29	±0.36
17.0-hr Zr^{97}	6.31	±0.23
68.1-hr Mo^{99}	6.06	±0.16
4.5-hr Ru^{105}	3.61	±0.17
13.0-hr Pd^{109}	0.224	±0.04
21.0-hr Pd^{112}	0.110	±0.01
5.0-hr Ag^{113}	0.0627	±0.0041
21-min Ag^{115}	0.0522	±0.0036
8.00-day I^{131}	4.43	±0.38
77-hr Te^{132}	5.78	±0.40
22.4-hr I^{133}	7.06	±0.40
85.0-min Ba^{139}	5.97[a]	...
12.8-day Ba^{140}	5.77	±0.33
33.0-hr Ce^{143}	5.32	±0.34

[a] Reference value to give integral of the yield-mass curve of 200 percent.

III. RESULTS

The saturation activities are directly proportional to the fission yields. The spread of masses (83 to 143) is great enough that the data can be used to estimate the normalizing constant necessary to give summation of the yield-mass curve to 200 percent. To define the mass

[6] C. D. Coryell and N. Sugarman, *Radiochemical Studies: The Fission Products* (McGraw-Hill Book Company, Inc., New York, 1951), National Nuclear Energy Series, Plutonium Project Record, Vol. 9, Div. IV.

[7] See reference 6, Introduction to Part I, p. 4.

[8] L. R. Zumwalt, Oak Ridge National Laboratory Unclassified Report Mon C-397, September 14, 1949 (unpublished).

[9] Engelkemeir, Seiler, Steinberg, and Winsberg, reference 6, Paper 4.

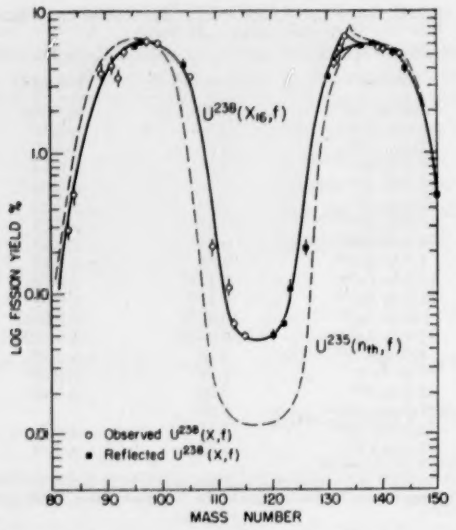

FIG. 1. Yield-mass curve for the fission of U^{238} by photons of 16-Mev maximum energy. Curve for thermal fission of U^{235} for comparison.

yield curve more sharply for this purpose, it was convenient to assume arbitrarily that an average of 3 neutrons is emitted per fission, so that for the relative yield of each mass number A, a reflected point could be plotted of the same yield at mass number 238-A-3. Normalization to 200 percent total yield was achieved by assigning 85-min Ba^{139} the fission yield of 5.97 percent for the 16-Mev experiments and the yield of 5.87 percent for the 10-Mev experiments.

Table II and Fig. 1 summarize the experimental yields of 19 species from the fission of U^{238} by x-rays of maximum energy approximately 16 Mev. The values reported represent an average of at least three individual determinations of each species. In the last column of the table is an estimate (the standard deviation) of the reliability of the separate fission yields. For reference purposes, the smoothed, yield-mass curve for thermal fission of U^{235} taken from Manhattan Project data[6] is also plotted in Fig. 1 as a broken line.

Intensities were not high enough to get the yield of 2.3-day Cd^{115}. Experiments were directed to 3-hr Cd^{117} but trouble was encountered with a 40-min isomer and isomeric indium daughters,[10] so useful yield data were not obtained.

Table III presents the experimental yields of 13 species from the fission of U^{238} by x-rays of maximum energy approximately 10 Mev. The estimated errors of these yields are somewhat greater than those of the higher energy irradiations because of the very low activity obtained from the samples. Those yields for which no estimate of error is given were single observations.

[10] Coryell, Lévêque, and Richter, Phys. Rev. **89**, 903 (1953).

It was of interest to establish the distribution of photon energies producing the fissions. This can be obtained as the product of the photon spectrum $N(E)$ and the fission cross-section function $\sigma(E)$. The thin-target photon energy distribution function of Schiff[11] is used as a starting point. Production of x-rays by degraded electrons in the target leads to a considerable softening of the spectrum from the thin target spectrum. Dr. I. Halpern helped us treat the case of axial incidence of an electron beam on a narrow cylinder, for which it was shown that the correction factor on a $1/E$ spectrum is $1+\ln[7(E_0-E)/4]$, where (1/7) g/cm² is the target thickness before electrons and thus potential hard x-rays are lost from the cylinder, and 4 Mev cm²/g is the effective stopping power of the uranium salt. It is assumed that the Schiff spectrum should be corrected by the same factor.

Figure 2 shows in curve A (broken line) the Schiff thin-target spectrum for 16-Mev electrons, in arbitrary units. Curve B is the spectrum corrected to cylindrical thick target by the factor given above. Curve C is the fission cross-section function determined by Ogle and McElhinney[12] for x-rays on U^{238}. Curve D (again in arbitrary units) is the product of curves B and C and represents the relative number of fissions caused by photons of energy E. It is seen that there is a broad maximum from 9 to 14 Mev, and the effective x-ray energy might be called 12 Mev.

A similar treatment cannot be applied easily to the data for 10-Mev electrons because of the poorer control of the beam energy and the closeness to the threshold of the fission reaction. The effective energy is certainly below 10 Mev, and perhaps about 8.5 Mev.

IV. DISCUSSION

The most prominent feature of the curve for the fission of U^{238} by x-rays up to 16 Mev (Fig. 1) is the fact that the valley for symmetrical fission has risen only about sixfold over the very low value observed for

TABLE III. Summary of low-energy fission yield experiments (x-rays up to 10 Mev).

Nuclide	Fission yields, %	Reliability
2.40-hr Br^{83}	0.300	±0.045
31-min Br^{84}	0.411	±0.074
9.7-hr Sr^{91}	4.44	
17.0-hr Zr^{97}	5.11	
68.1-hr Mo^{99}	4.94	
13.0-hr Pd^{109}	0.0854	±0.020
21.0-hr Pd^{112}	0.042	±0.002
8.00-day I^{131}	3.76	±0.16
77-hr Te^{132}	5.58	±0.80
22.4-hr I^{133}	6.80	±0.60
85.0-min Ba^{139}	5.87*	...
12.8-day Ba^{140}	5.77	±0.47
33.0-hr Ce^{143}	5.94	

* Reference value to give integral of the yield-mass curve of 200 percent.

[11] L. I. Schiff, Phys. Rev. **83**, 252 (1951).
[12] W. E. Ogle and J. McElhinney, Phys. Rev. **81**, 344 (1951).

thermal fission of U^{235}. Indeed, the ratio of the peak-to-valley yields is 110 (6.3/0.052) in $U^{238}(x_{16}f)$ compared to 600 in $U^{235}(n_{th}f)$. Low intensities precluded determination of the yields of silver and cadmium activities in the experiments with low energy (up to 10 Mev) x-rays, but Table III shows that the yields of Pd^{109} and Pd^{112} are lower by a factor of 2.5 than for the higher-energy x-rays.

Previous work on photofission has taken place only at higher beam energies. Spence[13] reports a peak-to-valley ratio of ~24 for U^{235} irradiated with x-rays from a betatron operating at 22-Mev maximum energy. Schmitt and Sugarman[14] obtained a peak-to-valley ratio, defined by 17-hr Zr^{97}/(2.3-day Cd^{115m}+43-day Cd^{115}), of 20 for U^{238} in the x-ray beam of a betatron operating at 22 Mev, a ratio of 10 at 48 Mev, and a ratio of 7 at 100 Mev. The peak-to-valley ratio of 110 in this work lies far above any simple extrapolation of the betatron data to lower energies. It appears, therefore, that an increase in yield of symmetrical fission sets in just above 16 Mev, a small amount of which lowers the ratio greatly. Cross-section measurements[12,15] show that most of the photofission for bremsstrahlung of maximum energy above 20 Mev occurs in the giant resonance of about 18 Mev. Schmitt and Sugarman[14] have pointed out that a high-energy cross-section tail extends above 48 Mev, giving symmetric fission.

Turkevich and co-workers[16] have presented a rough empirical correlation of peak-to-valley ratio against the excitation of the compound nucleus undergoing fission, irrespective of the nature of this nucleus. The ratio for low-energy photofission of U^{238} does not fit well on this curve.

There is considerable interest in fine structure in fission yields, in particular in the spike around mass 134 discovered in thermal neutron fission by Thode and Graham,[17] and its change with fissioning nucleus and energy. Two sources are credited for this spike: enhanced neutron emission[1,3] from primary fission fragments with a few neutrons (odd number) above 82, and *a priori* selectivity[2–4,18] in fission for closed shell structures (nuclei with 82 neutrons or 50 protons). The analysis of Pappas[3] indicates that for thermal neutron fission of U^{235}, the two sources contribute approximately equally. It is generally considered that increasing the energy of fission should lower the selectivity for closed-shell structures.

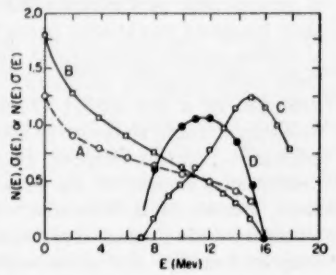

FIG. 2. Photon intensity, cross section, and photofission yield, dependence on energy. *A*, Schiff thin-target spectrum; *B*, photon spectrum corrected for target shape (see text); *C*, Ogle-Mc-Elhinney cross-section curve; *D*, product of *B* and *C*, representing photofission energy distribution.

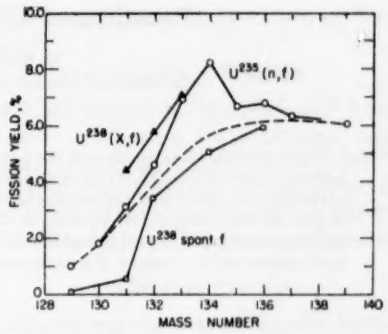

FIG. 3. Comparisons of fine structure in fission yields for different types of fission. Broken line, hypothetical smooth curve for $U^{235}(n,f)$.

Evidence for the spike is still present in the photofission data for 8.0-day I^{131}, 77-hr Te^{132}, and 22.4-hr I^{133} as shown in Fig. 1, and exhibited in more detail in Fig. 3, in comparison with other results. The broken line in Fig. 3 is the smoother curve for U^{235} thermal neutron fission,[6] a hypothetical shell-independent line. The circles represent mass-spectrometric data of Thode and co-workers[2] for xenon and cesium thermal fission products of U^{235}, normalized to 3.1 percent for chain 131, with Ba^{139} added. The squares represent Wetherill's data[19] for spontaneous fission of U^{238} based on a yield of 6.0 percent for Xe^{136}. The triangles represent the data from this work.

The spontaneous fission reaction represents tunnelling through the barrier without excess energy, and shows narrower peaks. A pronounced shoulder is apparent at mass 132. The curve for $U^{235}(n,f)$ shows the spike at mass 134. The more fragmentary data for photofission show that a spike occurs for it at or beyond mass 133, and in addition, that the peaks are wider, as seen also from Fig. 1. Data for the complimentary peak around mass number 101 would be helpful in determining how much of the selectivity effect remains.

It is a pleasure to acknowledge the assistance of the Linear Accelerator Group, Mr. Arthur Vash, Mr. Melvin Labitt, and Dr. John Winhold. The authors are indebted to Drs. Peter Demos and I. Halpern for many helpful and stimulating discussions.

[13] R. W. Spence, Unclassified Brookhaven National Laboratory Conference Report BNL-C-9, July, 1949 (unpublished).
[14] R. A. Schmitt and N. Sugarman, Phys. Rev. **89**, 1155 (1953).
[15] G. C. Baldwin and G. S. Klaiber, Phys. Rev. **71**, 3 (1947).
[16] Turkevich, Niday, and Tompkins, Phys. Rev. **89**, 553 (1953).
[17] H. G. Thode and R. L. Graham, Can. J. Research **A25**, 1 (1947).
[18] Glendenin, Steinberg, Inghram, and Hess, Phys. Rev. **84**, 860 (1951).
[19] G. W. Wetherill, Phys. Rev. **92**, 907 (1953).

Reactions of 370-Mev Protons with Cobalt*†

E. BELMONT‡ AND J. M. MILLER
Department of Chemistry, Columbia University, New York, New York
(Received June 7, 1954)

The individual cross sections for the formation of 37 different radioactive products that result from the inelastic interaction of 370-Mev protons with cobalt nuclei have been determined. The results are interpreted in the light of a model that emphasizes the importance of the evaporation of particles from an excited nucleus to give the final products of the collision. By the interpolation of the formation cross sections of the undetected product nuclei, an estimation is made of the total inelastic interaction cross section and the differential cross section for the transfer of a given excitation energy to the target nucleus in an inelastic collision.

INTRODUCTION

TWO related questions of interest in the study of the inelastic interaction of high-energy nucleons with nuclei are

(1) the differential cross section for a given energy transfer, and

(2) the subsequent behavior of the struck target nucleus.

Information on these points may be obtained from two different kinds of experiments: those, such as cloud chamber, nuclear emulsion, and counter experiments that focus attention on the particles emitted as a result of an inelastic interaction; and those, such as radiochemical studies, that focus attention on the nuclei remaining after the inelastic interaction. The work to be reported here is concerned with the investigation of the interaction of 370-Mev protons with Co^{59} nuclei by means of the latter method. The information obtained in this manner complements the studies of the emitted particles because it is sensitive to the emission of neutral particles and because it is capable of detecting events that occur in only one in 10^5 or 10^6 inelastic interactions.

Other studies on the formation cross sections of specific radioactive products in high-energy nuclear reactions are discussed in a recent review article.[1] The examination of the nuclear reactions of cobalt with 240-Mev protons has been carried out by Wagner and Wiig.[2]

METHOD

Irradiation

Metallic cobalt targets, prepared by powder metallurgical techniques from Johnson-Matthey spectroscopically pure cobalt sponge, approximately 1 gram per square centimeter thick (*ca* 2 Mev thick), were irradiated in the circulating proton beam of the Nevis cyclotron at a radius corresponding to an energy of 370 Mev. In several of the irradiations, the cobalt target was sandwiched between two sets of three 7-mil aluminum foils; the Na^{24} activity produced in the center member of each set was a measure of the effective beam current during the irradiation.

Chemical Separations

After irradiation, the targets were dissolved in nitric acid to which had been added known quantities of inactive carrier (*ca* 2 mg) for each of the elements which were to be isolated. The elements of interest were then separated from the resulting solution by procedures that entailed some modification of well known schemes of qualitative and quantitative analysis for the elements in this region of the periodic system.[3] The fraction of the inactive carrier that had been recovered was determined by a quantitative analysis of each sample performed after the sample had been counted for a suitable length of time.

Counting Techniques

The isolated chemical fractions were filtered onto disks of filter paper, mounted on cardboard cards, and then counted with suitable detectors under conditions of reproducible geometrical efficiency. In most cases, since the decay was at least partly by particle emission, a helium-organic-quench-filled Geiger tube,[4] with a brass baffle to define geometry, was employed as the detector. In a few rather crucial instances, it was necessary to count x-rays in the 5-kev region with known efficiency. For this purpose, an argon-methane filled proportional counter of the type described by Bernstein, Brewer, and Rubinson,[5] was employed. The pulses from the proportional counter were put through a linear amplifier and pulse-height analyzer so as to provide additional evidence on the radiochemical purity of the sample. The relative efficiencies of the Geiger and proportional counters were determined by counting

* This paper is based on a thesis submitted by E. Belmont in partial fulfillment of the requirements for the degree of Doctor of Philosophy at Columbia University.

† Assisted by the U. S. Atomic Energy Commission.

‡ An Atomic Energy Commission Predoctoral Fellow from 1950 to 1952. Now at Bendix Aviation, Eatontown, New Jersey.

[1] D. H. Templeton, Ann. Rev. Nuc. Sci. **2**, 93–104 (1953).

[2] G. Wagner and E. O. Wiig, J. Am. Chem. Soc. **74**, 1101 (1952).

[3] Detailed procedures are reported by E. Belmont in Atomic Energy Commission Report NYO–3198 (unpublished).

[4] Nucleonic Corporation of America, Model GM1WAA.

[5] Bernstein, Brewer, and Rubinson, Nucleonics **6**, No. 2, 39 (1950).

a sample that has a known branching ratio of positron emission to electron capture, e.g., Mn^{52}, on both tubes.

The relative formation cross sections were obtained by correcting the observed counting rates for absorption by the counter window, absorption and scattering by air, absorption and scattering by sample and mounting structure, the decay scheme of the active sample, decay from end of bombardment, the finite time of irradiation, and the chemical yield in the separation procedure. The scattering and absorption correction factors were either determined experimentally or estimated from literature values.[6] The corrections for the scattering and absorption of the particles, except for weak beta emitters such as Ca^{45}, did not exceed 10 to 15 percent. In nearly all bombardments the time of irradiation was short compared to the half-life of the active species investigated, so that errors due to fluctuation of beam current during the run were held to a minimum.

INTERPRETATION OF DECAY DATA

The determination of cross sections from the counting data of each chemical fraction requires analysis of a composite decay curve into its component parts, and correction of the activity of each component for the sensitivity of the detector to the radiation emitted by that component. In most cases, because of a convenient spread in half-life, the decay curve analysis presented no problem. Also, in most cases, the decay scheme, which must be known for the detection efficiency correction, has been examined and the data made available in recent compilations.[7] In a few cases, however, because of an unfortunate combination of half lives, or because of an unknown decay scheme, it was necessary to introduce some arbitrary assumptions into the analysis of the data. These assumptions will be presented in the following paragraphs of this section.

Cobalt Fraction

The similarity of the half-lives of Co^{56} and Co^{58} makes it impossible to differentiate between the two by decay curve analysis. Owing to the substantial difference in the energy of the particles from these two isotopes, however, an estimate of their relative activities, good to about 50 percent, can be made by means of an aluminum absorption curve. Further difficulties arise from the unknown, but obviously complicated, decay scheme of Co^{56}. In the results reported here, Co^{56} was taken to decay 25 percent by positron emission.[8]

Scandium Fraction

It was not possible to distinguish Sc^{43} from Sc^{44} by decay-curve analysis or by absorption experiments since these two isotopes have identical half-lives and rather similar particle energies. In this report, therefore, we will give only the sum of these two yields without any correction for electron capture contribution.

Chlorine Fraction

No attempt was made to distinguish between 33.2-minute Cl^{34} and 37.3-minute Cl^{38}; the sum of the two yields is reported.

Unknown Branching Ratios

The small contribution of electron capture to the decay of Fe^{53}, Mn^{51}, Cr^{49}, V^{47}, Ti^{45}, K^{38}, F^{18}, and C^{11} was estimated by the method of Feenberg and Trigg[9] under the assumption that they are all allowed transitions.

RESULTS AND DISCUSSION

The cross sections in millibarns for the formation of 37 different product nuclei that result from the inelastic interaction of 370-Mev protons with the Co^{59} nucleus are listed in Table I. The precision estimate is either based upon multiple determinations, or in the event of a single determination, it is based upon a precision estimate of each factor involved in the cross-section determination. These cross sections are all based upon a cross section of 44 millibarns for the $C^{12}(p,pn)C^{11}$ reaction interpolated from the data of Warshaw, Swanson, and Rosenfeld.[10,11] These data are also presented in summary form in Figs. 1 and 2.[12] In Fig. 1, the sum of the cross sections for the formation of products of a given atomic number is plotted against the atomic number. In Fig. 2, the sum of the cross sections for a given mass number is plotted against the mass number.

The evaluation of the total inelastic cross section, and of the complete distribution of product nuclei that results from an inelastic collision, requires the interpolation of the unmeasured formation cross sections of the

[6] L. Zumwalt, Atomic Energy Commission Report MDDC-1346, 1947 (unpublished); B. Burtt, Nucleonics **5**, No. 2, 38 (1949). Engelkemeir, Seiler, Steinberg, and Winsberg, *Radiochemical Studies: The Fission Products* (McGraw-Hill Book Company, New York, 1951), Paper No. 4, National Nuclear Energy Series, Plutonium Project Record, Vol. 9, Div. IV.

[7] *Nuclear Data*, National Bureau of Standards Circular No. 499 (U. S. Government Printing Office, Washington, D. C., 1950). Hollander, Perlman, and Seaborg, Revs. Modern Phys. **25**, 469 (1951).

[8] King, Dismuke, and Way, Oak Ridge National Laboratory Report ORNL-1450 (unpublished).

[9] E. Feenberg and G. Trigg, Revs. Modern Phys. **22**, 402 (1950).

[10] Warshaw, Swanson, and Rosenfeld, Phys. Rev. **95**, 649(A) (1954).

[11] Because of the short half-life of C^{11}, the $C^{12}(p,pn)$ reaction was not directly used as a beam monitor in these runs; but rather, the cross section for the $Al^{27}(p,3pn)Na^{24}$ reaction was determined relative to the carbon cross section, and the aluminum reaction was then employed to monitor the beam. Unfortunately, the cross section for the formation of Na^{24} from aluminum determined in this manner gave a value of 15.5 millibarns; a result that is in disagreement both with the value of 10.8 millibarns determined absolutely by Marquez [L. Marquez, Phys. Rev. **86**, 405 (1952)] and an unpublished value of approximately 10–11 millibarn by R. Folger and P. Stevenson.

[12] The result for mass number 58 is not included in these figures.

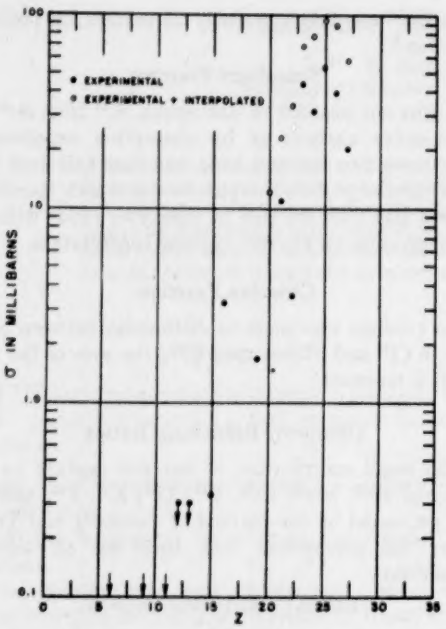

FIG. 1. Cross section in millibarns for the formation of given atomic-number products from the bombardment of cobalt with 370-Mev protons. The solid circles represent experimental values; the open circles give the sum of experimental and interpolated values.

stable, very short-lived, and very long-lived products. Since it is not possible at this time to make that interpolation in a satisfyingly unambiguous manner, we shall first examine some of the gross features of high-energy reactions that can be derived from the experimental results, and then attempt to infer the unmeasured cross sections.

General Features

Figures 1 and 2 indicate that the measured cross sections, within the fluctuations to be expected because of the contribution of stable and long-lived products, do not diminish appreciably within four atomic numbers or ten mass numbers of the target. We may conclude that an inelastic interaction has essentially equal probability of ejecting up to at least ten nucleons from the struck nucleus.

Figure 3, where the cross sections for the formation of a product nucleus of given atomic number is plotted against mass number, illustrates a second attribute of these reactions: the strong correlation between the number of neutrons and protons lost from a struck nucleus. For example, the loss of one proton and three neutrons (excluding the incident proton) is 130 times more probable than the loss of one proton and five neutrons; this factor, on the other hand, would be approximately 2.5 if random emission of neutrons and protons occurred. A more satisfying demonstration of this point would be afforded by a comparison of the relative yields within an isobaric set of products; the usefulness of that comparison in this work, though, is lessened since we were unable to measure more than two cross sections in any isobaric set. If, however, the most probable charge, Z_A, for a given mass number product is chosen, and if the cross sections for the various products are plotted against the displacement from this most probable atomic number as is done in Fig. 4 for odd mass-number products, then the correlation in the relative number of neutrons and protons emitted is seen more clearly. Further, this plot suggests that the atomic

TABLE I. Cross sections for the formation of nuclides from the bombardment of cobalt with 370-Mev protons.

Nuclide Z		A	Cross section in millibarns
28	Ni	57	0.34± 0.08
27	Co	58	121 ±60
		56	15.2 ± 3.8
		55	5.2 ± 1.3
26	Fe	55	37.0 ± 9.0
		53	1.7 ± 0.6
		52	0.28± 0.07
32	Mn	56	3.8 ± 1.0
		54	25.4 ± 7.0
		52	14.1 ± 3.5
		52*m*	5.6 ± 2.2
		51	4.1 ± 1.4
24	Cr	51	27.5 ± 2.0
		49	4.1 ± 1.0
23	V	49	31.1 ± 9.0
		48	10.6 ± 2.8
		47	2.1 ± 1.0
22	Ti	45	3.5 ± 0.9
21	Sc	46	2.2 ± 0.3
		44*m*	3.5 ± 1.4
		43+44	5.0 ± 1.7
20	Ca	47	0.06± 0.03
		45	0.66± 0.33
19	K	43	0.50± 0.23
		42	0.85± 0.28
		38	0.31± 0.14
17	Cl	39	0.50± 0.40
		38+34	2.8 ± 1.4
15	p	33	0.03± 0.02
		32	0.30± 0.1
13	Al	29	<0.30
12	Mg	27	<0.30
11	Na	24	0.07± 0.03
9	F	18	0.07± 0.03
6	C	11	0.05
	Total		330 ±65

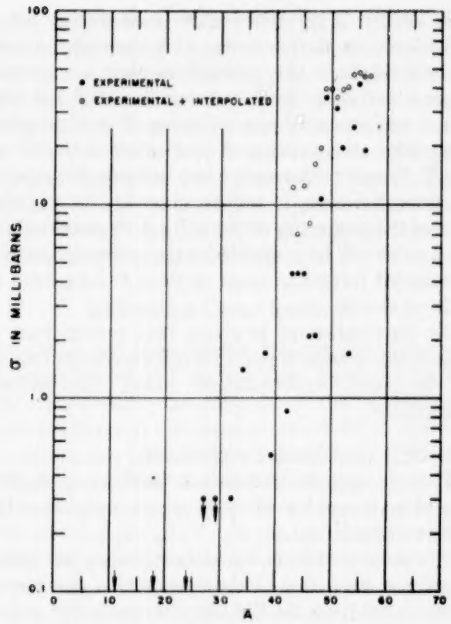

FIG. 2. Cross section in millibarns for the formation of given mass-number products from the bombardment of cobalt with 370-Mev protons. The solid circles represent experimental values; the open circles give the sum of experimental and interpolated values.

number distribution function for a given odd mass-number product is nearly independent of mass number in the region of mass number 49 to 55, except, of course, for a linear shift in the peak position. If this is the case, then we would again conclude that the formation cross sections for mass numbers 55, 51, and 49 are essentially the same.

Comparison with Nucleon-Induced Stars in Photographic Emulsion

Bernardini, Booth, and Lindenbaum[13] found equal probabilities for one, two, or three black prongs from stars induced by 300–350 Mev protons incident upon the nuclei in photographic emulsion; they also observed that these numbers of black prongs are usually accompanied by one sparse black or gray prong ($E \gtrsim 30$ Mev). From their work, it is also seen that the probability of stars with more than three black prongs falls off rather rapidly with increasing prong number until it has effectively vanished for about eight or nine black prongs. If it is assumed that about $\frac{1}{4}$ of the observed black prongs are alpha particles, and that $\frac{3}{4}$ of them are protons,[14,15] the star data correspond to an equal probability for the loss of from one to about four charges from the target nucleus; a conclusion that is consistent with the data illustrated in Fig. 1.

Model for High-Energy Reactions

The results of this experiment are in agreement with the consequences of the model set forth by Serber[16] for high-energy reactions: the interaction of a high-energy nucleon with a nucleus is best described as a series of interactions of the incident nucleon with individual nucleons in the nucleus; a nucleonic cascade is generated and a variable fraction of the incident energy is deposited in the struck nucleus. This model has been given quantitative treatment by means of the Monte Carlo formalism by Goldberger[17] and by Bernardini, Booth, and Lindenbaum.[18] In both of these treatments, the notion of nucleon-nucleon interactions was extended down to include the low-energy components of the nucleonic cascade; and, with the increasing assistance of the exclusion principle, they both thus reproduce the observed asymmetry in the angular distribution of the black prongs in nucleon-induced emulsion stars. The results described here can throw some light on the relative importance of "knock-on," as opposed to "evaporated," low-energy particle emission. The data demonstrate the decisive importance of the final evaporation phase of the process in giving the

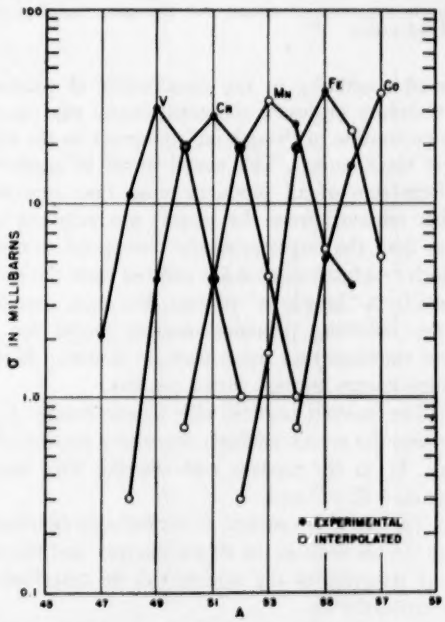

FIG. 3. The variation of the cross section for the formation of a given atomic-number product with mass number. The points for a given atomic-number product are connected by tie lines. The solid circles represent experimental values, and the open circles give the interpolated values.

[13] Bernardini, Booth, and Lindenbaum, Phys. Rev. **85**, 826 (1952); **88**, 1017 (1952).
[14] R. J. Le Couteur, Proc. Phys. Soc. (London) **A63**, 259 (1950).
[15] R. W. Deutsch, University of California Radiation Laboratory Report UCRL-2258 (unpublished).
[16] R. Serber, Phys. Rev. **72**, 1114 (1947).
[17] M. Goldberger, Phys. Rev. **74**, 1269 (1948).

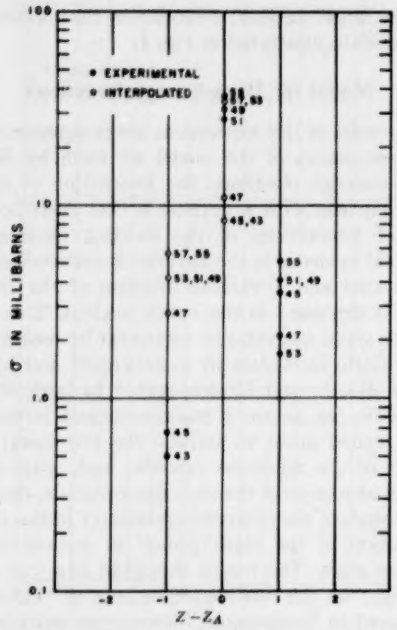

FIG. 4. Cross section for the formation of a given odd mass-number product, A, plotted against the difference between the atomic number of that product, Z, and the atomic number, Z_A, of the most probable product of that mass number. The solid circles are experimental values, and the open circles give interpolated values.

observed specificity in the distribution of products, and therefore suggest a simplified model that ignores the contribution of "knock-on" processes to the emission of black prongs. This model would be applied to the formation of all products more than one mass number removed from the target; products one unit lighter than the target probably correspond to events in which two fast nucleons are emitted from the struck nucleus by a "knock-on" process. We may, therefore, try the following phenomenological model for the nuclear reactions that result from an inelastic collision of a high-energy nucleon with a nucleus:

(a) The incident particle with kinetic energy E_i, in traversing the struck nucleus, deposits a portion of its energy, U, in the nucleus and emerges with kinetic energy $E_f = E_i - U$ and

(b) The excitation energy, U, is randomly distributed among the nucleons in the struck nucleus, and the subsequent behavior of the system can be described by evaporation theory.

This model leads to the following expression for the formation cross section of a product nucleus characterized by mass number A and atomic number Z:

$$\sigma_{A,Z} = \int_0^\infty \frac{d\sigma}{dU} \eta(U; A,Z) dU,$$

where $d\sigma/dU$ is the differential cross section for the deposition of excitation energy U in the struck nucleus, and $\eta(U; A,Z)$ is the probability that a nucleus of charge Z and mass number A remains after the target nucleus has expended the excitation U in the emission of particles and photons. A discussion of $d\sigma/dU$ and $\eta(U; A,Z)$ will be presented in a subsequent paper; at this time, however, it will be necessary to anticipate a few of the properties of the $\eta(U; A,Z)$ distribution so that a guide will be available for the interpolation of the unmeasured formation cross sections of long-lived and stable products.

The distribution of products that results from the evaporation of several particles from an excited nucleus can be easily approximated under the following assumptions:

(1) Only nucleons are evaporated,

(2) each nucleon evaporated from an excited nucleus of mass number 45 to 60 carries away from 15 to 20 Mev of excitation,

(3) the probabilities of either proton or neutron emission at each step in the evaporation cascade may be calculated from the Weisskopf formalism,[18] and

(4) the density of energy levels of a nucleus excited to U Mev above the ground state is given by $C \exp[2a^{\frac{1}{2}}(U+d)^{\frac{1}{2}}]$, where C and a are constants, and d has the value of 1.5 Mev for odd-odd nuclei, 0 Mev for odd-even or even-odd nuclei, and -1.5 Mev for even-even nuclei. The quantity d is a correction applied to the simple level density formula in a manner suggested by Hurwitz and Bethe,[19] and arises from their analysis of the effect upon neutron capture cross sections of the oddness or evenness of neutron and proton number of the target nucleus.

As an indication of the predictive value of this approximate method for the analysis of an evaporation cascade, we may compare the ratio of peak cross sections for the $Cu^{63}(p,pn)Cu^{62}$ and the $Cu^{63}(p,2n)Zn^{62}$ reactions calculated by this approximate method with the ratio observed by Ghoshal:[20] the computed ratio is 3.6, and the observed ratio is 4.0. If a correction is not made for the difference in level densities of odd-odd and even-even nuclei, the calculated value decreases to 0.7; this symmetry correction, as was pointed out by Ghoshal, improves matters considerably.

The application of this calculation to the relative yields of the odd mass-number isobars resulting from evaporation of nucleons from an excited Co^{59} nucleus indicate that for each mass number, the peak does indeed occur at the Z_A value used in Fig. 4, and that the cross section for the formation of odd mass-number isobaric products two atomic numbers on either side of the peak contribute, at most, only a few percent to

[18] J. Blatt and V. Weisskopf, *Theoretical Nuclear Physics* (John Wiley and Sons, Inc., New York, 1952).
[19] H. Hurwitz and H. Bethe, Phys. Rev. **81**, 898 (1951).
[20] S. N. Ghoshal, Phys. Rev. **80**, 939 (1950).

the total cross section of that mass number. The estimation of the relative yields of even mass-number isobaric products does not give a peak, but rather there are two nearly equal "peak yields" that arise because of the symmetry effect on the density of nuclear energy levels. The double peak corresponds to the Group II products of Rudstam, Stevenson, and Folger.[21] These conclusions will be incorporated into the next section where an attempt will be made to evaluate the total inelastic interaction cross section.

Absorption Cross Section

The values for some of the unmeasured cross sections, interpolated and extrapolated from the experimental results under the guidance of the approximate evaporation cascade calculations described in the previous section, are presented in Table II and Figs. 1 to 4.[22] The sole exception to this method of interpolation and extrapolation occurs at mass number 58; there, in view of the finite probability for the emission of two fast ($E \geqslant 50$ Mev) particles observed in photographic emulsion studies,[13] it was assumed that the distribution of products was governed by "knock-on" rather than "evaporation" processes.

No attempt was made to estimate the unmeasured yields of products with mass number less than 43 because of the sparsity of measured cross sections in that mass number region, the probable inadequacy of the assumed model in explaining the production of light nuclei, and finally because it seems that only a small fraction of the inelastic interactions produce these light products and therefore this omission will have but little consequence upon the estimation of the absorption cross section.

The sum of the measured and estimated cross sections listed in Tables I and II gives 700 ± 155 millibarns as an estimate of the absorption cross section of the cobalt nucleus for 370-Mev protons. Since only about half of this figure is made up of experimental values, and since there are some doubts about the absolute value upon which it is based, it would be surprising if this value were not in considerable error. It is clear that this is a rather unsatisfactory method for determining an absorption cross section; it is of interest, nevertheless, to compare this estimate with similar values obtained in other ways in order to provide some external check on the approximate validity of the interpolated values so that they may be employed in an estimation of $d\sigma/dU$.

The total cross section for 410-Mev neutrons on copper, as measured by Nedzel,[23] has been found to be 1187 millibarns. If the inelastic contribution to this cross section is still at least one-half, as it was at 270 Mev,[24] then the absorption cross section would be at least 593 millibarns. Ball[25] has found an inelastic interaction cross section of 755 millibarns for 300-Mev neutrons on copper by a "poor geometry" attenuation experiment; a value that is in excellent agreement with the 700-millibarn absorption cross section for 340-Mev protons on copper determined by Batzel, Miller, and Seaborg[26] through a radiochemical study similar to the one described in this paper. Also employing the radiochemical technique, Rudstam, Stevenson, and Folger[21] estimate an inelastic cross section of 350 millibarns for 340-Mev protons on iron, which is a much lower result than any of the others quoted and which seems to be based upon a 10–11 millibarn cross section for the $Al^{27}(p,3pn)Na^{24}$ reaction, although the value employed is not explicitly stated in their paper.

The expected value of the absorption cross section may also be computed from the "optical model,"[27]

TABLE II. Interpolated cross sections for the formation of nuclides from the bombardment of cobalt with 370-Mev protons.

Nuclide Z		A	Cross section in millibarns
27	Co	57	37
		54	1.7
26	Fe	58	120
		57	6.7
		56	24
		54	20
25	Mn	55	6
		53	34
		50	1.7
24	Cr	54	1
		53	4
		52	20
		50	20
		48	0.3
23	V	52	1
		51	4
		50	20
22	Ti	50	1
		49	4
		48	9
		47	11
		46	6
21	Sc	48	0.5
		47	2.8
		46	6.0
		45	8.5
20	Ca	46	0.1
		44	2.8
		43	8.5
Total			375 ± 140

[21] Rudstam, Stevenson, and Folger, Phys. Rev. **87**, 358 (1952).
[22] The estimated error assumes a variance for each interpolated value that is equal to the square of the interpolated value.
[23] V. A. Nedzel, Phys. Rev. **94**, 174 (1954).
[24] J. De Juren, Phys. Rev. **80**, 27 (1950).
[25] W. P. Ball, University of California Radiation Laboratory Report UCRL-1938 (unpublished).
[26] Batzel, Seaborg, and Miller, Phys. Rev. **84**, 671 (1951).
[27] Fernbach, Serber, and Taylor, Phys. Rev. **75**, 1352 (1949).

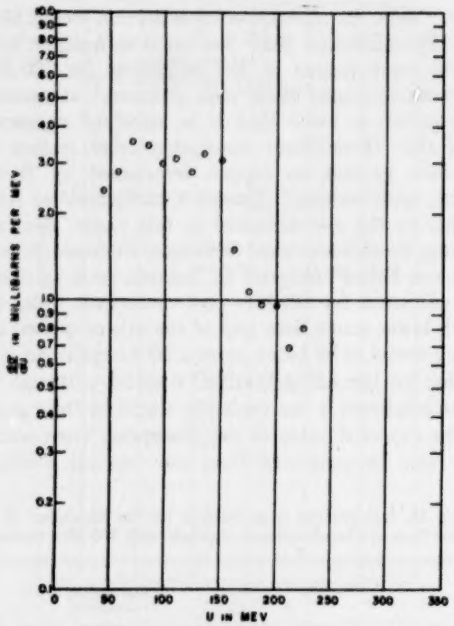

FIG. 5. Differential cross section for the deposition of excitation energy U in the inelastic interaction of 370-Mev protons with cobalt.

which gives

$$\sigma_a=\pi R^2\left[1-\frac{1-(1+2KR)\exp-2KR}{2K^2R^2}\right],$$

where K is the absorption coefficient for protons in nuclear matter and R is the nuclear radius. If the values of $K=0.485\times10^{13}$ cm^{-1} and $R=1.23\times10^{-13}A^{\frac{1}{3}}$ cm, found by Nedzel[28] to give the best fit to the 410-Mev neutron total cross sections, are used, then $\sigma_a=650$ millibarns for Co^{59}. The parameter K may also be evaluated from the free-nucleon total cross section if the impulse approximation is used:

$$K=3[Z^a\alpha(r_0)\sigma_{pp}+N\beta(r_0)\sigma_{pn}]/4\pi r_0^3A,$$

where $\alpha(r_0)$ and $\beta(r_0)$ serve to correct the free-nucleon cross sections, σ_{pp} and σ_{pn}, for scatterings into inaccessible states.[17] If σ_{pp} is taken as 27 millibarns, σ_{pn} as 34 millibarns,[28] $\alpha(r_0)$ evaluated for a Fermi gas model and for p-p scattering spherically symmetric in the center-of-mass system, and $\beta(r_0)$ approximated under the assumption that the p-n scattering angular distribution is roughly the same at 400 Mev as it is at 270 Mev,[28] then the dependence of σ_a upon r_0 for Co^{59} is as presented in Table III. It is seen that the σ_a estimated from the present work corresponds to an $r_0=1.44\times10^{-13}$ cm.

TABLE III. The absorption cross section of cobalt for 370-Mev protons calculated by means of the optical model as a function of r_0.

$r_0\times10^{13}$ cm	$\sigma_a/\pi r_0^2\times10^{-26}A^{\frac{1}{3}}$	$\sigma_a\times10^{24}$ cm^2
1.0	0.89	0.42
1.1	0.86	0.49
1.2	0.83	0.56
1.3	0.78	0.62
1.4	0.75	0.69
1.5	0.72	0.77
1.6	0.68	0.84

From these various comparisons we may conclude that the interpolated cross sections are sufficiently reliable to be used in the estimate of the relative formation cross section of each mass-number product as will be done in the following section.

$d\sigma/dU$: Although the absolute values of the measured cross sections are in some doubt owing to the conflicting results for the only observed activation cross sections measured in this energy region that might be used in beam monitoring, the relative values of the cross sections listed in Tables I and II are clearly unaffected by this dilemma and may be used, in the spirit of the proposed model, to infer the probability of an inelastic interaction resulting in a given energy transfer. To accomplish this, we must estimate how much excitation energy each product represents. For this purpose we can employ the extensive calculations made by Le Couteur[29] on the number and kind of particles emitted from an excited nucleus as a function of its excitation energy, with approximate corrections to make the results applicable to an excited Co^{59} nucleus. The results of this analysis, which indicate an excitation of from 14 to 17 Mev per mass number lost from the target, is presented in Fig. 5 where the differential cross section per unit of excitation energy in millibarns per Mev is plotted against the excitation in Mev.

The results for mass number 58 are not included in this analysis since that product, as has been previously stated, is undoubtedly largely formed by a "knock-on" process and represents an energy transfer that is certainly greater than that required to evaporate one nucleon from a cobalt nucleus.

CONCLUSIONS

The distribution of products resulting from the inelastic interaction of 370-Mev protons with cobalt nuclei demonstrates the decisive importance of the evaporation process in dissipating the energy transferred to the struck nucleus. The data, interpreted in the light of product formation through evaporation processes, indicate a rather uniform (within 30 percent) differential cross section for transferring up to about 40 percent of the incident energy of the proton to the target nucleus as a whole. The cross section shows a rapid drop for energy transfers in excess of about one half of the incident energy.

[28] Kelley, Leith, Segrè, and Wiegand, Phys. Rev. **79**, 96 (1950).
[29] R. J. Le Couteur, Proc. Phys. Soc. (London) **A65**, 718 (1952).

ACKNOWLEDGMENTS

We wish to thank Dr. D. H. Greenberg and Dr. J. B. Cumming for their assistance and many stimulating conversations.

It is a pleasure to record our indebtedness to the Brookhaven National Laboratory for the use of counting equipment, and in particular to Dr. G. Friedlander for his many helpful suggestions and criticisms.

We are also very grateful to the operating staff of the Nevis cyclotron.

We wish to thank the U. S. Atomic Energy Commission for their generous support of this work and for a predoctoral fellowship awarded to one of us (E.B.).

PHYSICAL REVIEW VOLUME 95, NUMBER 6 SEPTEMBER 15, 1954

Absorption of Negative Pions in Deuterium: Parity of the Pion*

W. CHINOWSKY AND J. STEINBERGER
Columbia University, New York, New York

(Received June 8, 1954)

The reaction $\pi^-+d\rightarrow 2n$ has been observed by detecting the two neutrons in coincidence with slow negative mesons incident on a liquid deuterium target. The observed angular correlation of the two neutrons confirms the identification of the process. The process is therefore not forbidden, and this fact may be used to establish the odd relative parity of the pion and the nucleon.

I. INTRODUCTION

IT was first pointed out by Ferretti[1] that the capture in deuterium of negative mesons at rest might furnish a means of distinguishing between scalar and pseudoscalar pions. The reaction,

$$\pi^-+d\rightarrow 2n, \qquad (1)$$

is forbidden for scalar mesons in S states since requirements of angular momentum and parity conservation and the Pauli principle cannot simultaneously be satisfied. The argument is independent of the theoretical model for the process. If the reaction is observed, then to rule out scalar parity for the pion, it is only necessary to show that the reaction proceeds indeed from an S state. Brueckner, Serber, and Watson[2] have shown, using the measured cross section for the process $\pi^++d\rightarrow 2p$, extrapolated to lower energy, that capture from the excited states of the meson-deuteron atom does not compete favorably with electromagnetic de-excitation. At most, one in thirty mesons is expected to be captured before reaching the ground state. Therefore, if more than one-thirtieth of the stopped mesons are captured according to process (1), the meson cannot be scalar. Since it has already been shown that the pion has zero spin,[3,4] the pion is then pseudoscalar.

The only previous evidence for reaction (1) is furnished by the experiments of Panofsky, Aamodt, and Hadley.[5] In these experiments measurements were made on the energy spectra of γ rays from hydrogen and deuterium gases at 3000 lb/sq. in. pressure and 78°K in which mesons had come to rest. All reactions in hydrogen give γ rays, either directly or through π^0 decay. The γ-ray yield from deuterium was lower and left 70 percent of the capture processes unaccounted for. This was interpreted to mean that 70 percent of the captures proceed through reaction (1).

In view of the important consequences of this result, we have performed an experiment in which the two neutrons are observed in coincidence and in coincidence with incident mesons some of which come to rest in a container of liquid deuterium. This provides a direct observation of the process (1) and confirms the conclusions of Panofsky *et al.*

II. EXPERIMENTAL ARRANGEMENT

Negative mesons produced at the internal target of the Columbia University 390-Mev cyclotron are collimated in a channel of the 8-foot iron shielding wall and further analyzed by a double focusing magnet and the beam defining counters No. 1 and No. 2. (See Fig. 1.) Counter No. 1 is a liquid scintillator $4\frac{1}{2}$ inches in diameter and $\frac{5}{8}$ inch thick; counter No. 2 is a stilbene crystal $2\frac{1}{4}$ inches horizontally, $2\frac{3}{4}$ inches vertically, and $\frac{1}{8}$ inch in thickness. Between counters No. 1 and No. 2 a 2 g/cm² carbon absorber is inserted, with 5 g/cm² of LiH and 2.7 g/cm² of polyethylene between counter No. 2 and the deuterium target. The absorber thickness is chosen to maximize the number of mesons which stop in the deuterium; the type of material to minimize Coulomb scattering, consistent with convenience.

* This research was supported by the joint program of the U. S. Office of Naval Research and the U. S. Atomic Energy Commission.

[1] B. Ferretti, in Report of an International Conference on Low Temperatures and Fundamental Particles (The Physical Society, London, 1946), Vol. 1, p. 75.

[2] Brueckner, Serber, and Watson, Phys. Rev. **81**, 575 (1951).

[3] Durbin, Loar, and Steinberger, Phys. Rev. **83**, 646 (1951).

[4] Clark, Roberts, and Wilson, Phys. Rev. **83**, 649 (1951).

[5] Panofsky, Aamodt, and Hadley, Phys. Rev. **81**, 565 (1951).

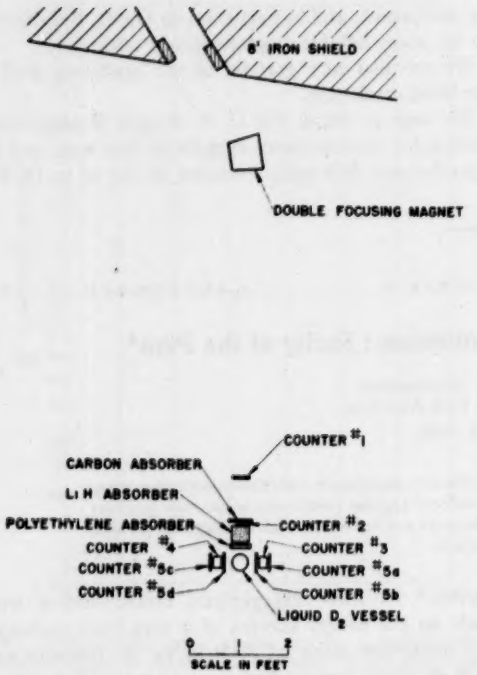

FIG. 1. Experimental arrangement used to detect neutron-neutron coincidences.

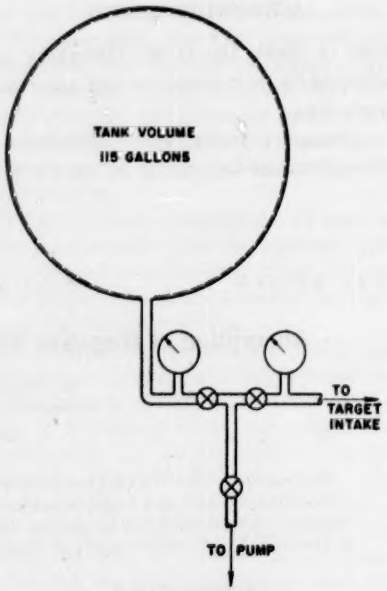

FIG. 2. Gaseous-deuterium filling system.

The hydrogen target previously described[6] is used here with liquid deuterium in the scattering chamber. The only modification required is the insertion of a plug to prevent communication between the hydrogen and deuterium reservoirs. The D_2 intake is connected to the gaseous-deuterium filling system shown in Fig. 2. Before liquefaction the pressure of the gas in the 115 gallon reservoir is 21 lb/sq. in. On admission to the target the gas is cooled by passing successively through copper coils in the liquid nitrogen and hydrogen reser-

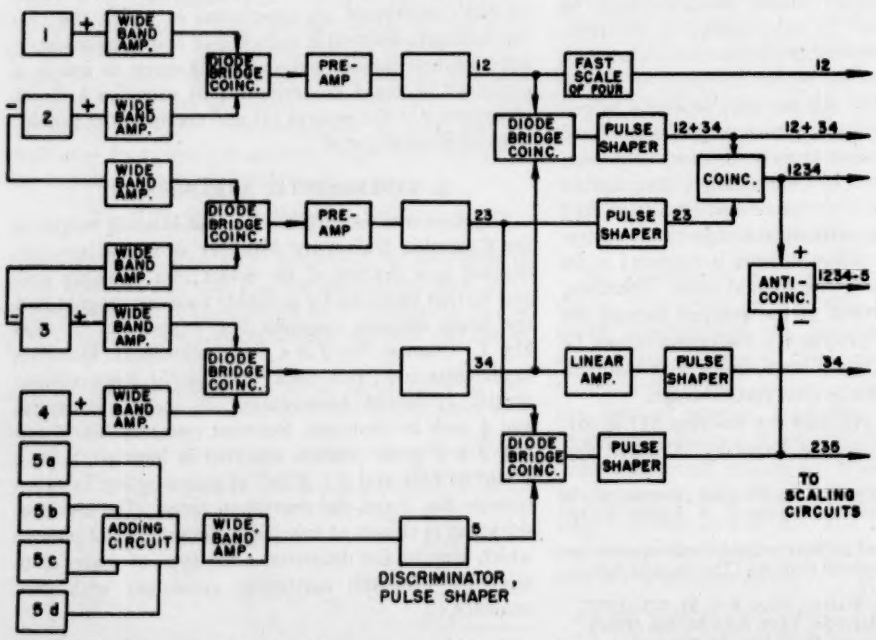

FIG. 3. Block diagram of electronics.

[6] Bodansky, Sachs, and Steinberger, Phys. Rev. 93, 1367 (1954).

voirs. When equilibrium is reached, approximately ½ liter of liquid has accumulated and the pressure of the deuterium system is 5 lb/sq. in. The liquid deuterium in the reservoir can be admitted to the target cup and returned in the manner previously described. At the conclusion of the experiment, the hydrogen is allowed to evaporate and the deuterium returns to the gas reservoir.

Counters No. 3 and No. 4, the neutron detectors, are liquid scintillators 2½ inches in diameter and 2 inches thick along the direction of motion of the neutrons. Counters 5 *a*, *b*, *c*, and *d* are plastic scintillators 4½ inches in diameter and ½ inch thick. The center of each neutron counter is 5⅜ inches from the center of the target cup. The six counters of the detection system have a common axis passing through the center of the target cup.

An "event" constitutes a coincidence 1234 in anticoincidence with the parallel connection of the set of four counters No. 5. (See Fig. 3.) The neutrons are detected by means of stars or proton recoils made in No. 3 and No. 4. The discriminator on the 34 coincidence is adjusted so that pulses in No. 3 and No. 4 are rejected if the energy loss due to ionization is less than

TABLE I. *n-n* coincidences observed with geometry of Fig. 1. Rates are per 10^6 incident mesons as measured in 12 coincidence.

	Counts with D_2 in cup	Counts with cup empty	Net due to D_2
1234	1.02±0.19	0.08±0.1	0.94±0.20
1234−5	0.70±0.16	0.08±0.1	0.62±0.19

roughly 10 Mev. Charged particles are rejected in counters No. 5*b* and No. 5*d*. Low-energy γ rays are rejected by the pulse-height requirement and high-energy γ rays converted in No. 3 and No. 4 are rejected in counters No. 5*a* and No. 5*c*. The system is specific for the detection of *n-n* coincidences with neutron energy greater than approximately 10–20 Mev. The efficiency for detection can be estimated from information on the *n-p* cross section[7] and star formation in carbon.[8] These experimental results yield a probability $\epsilon_n = 0.065 \pm 0.015$ for the formation by 70-Mev neutrons, of charged secondaries with energy sufficient to register a 34 coincidence.

III. EXPERIMENTAL RESULTS

A. The Process $\pi^- + d \rightarrow 2n + \gamma$[9]

We have used the γ rays of this reaction in order: (1) to determine the thickness of the absorber in the incident beam which maximizes the number of mesons which come to rest in the target, and (2) to permit an estimate

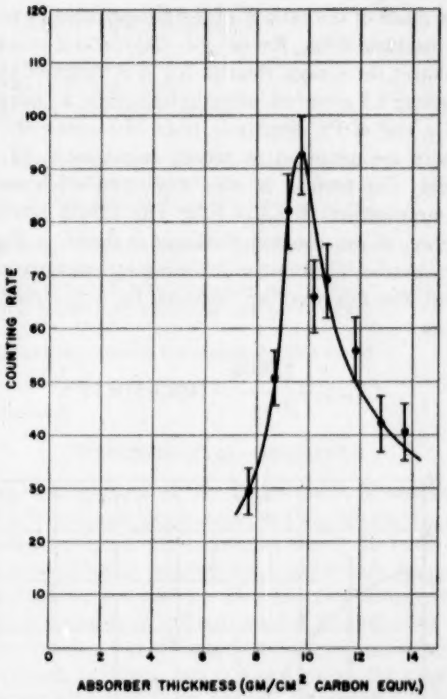

FIG. 4. Counting rate of γ rays from the reaction $\pi^- + d \rightarrow 2n + \gamma$ *vs* thickness of absorber in the incident beam.

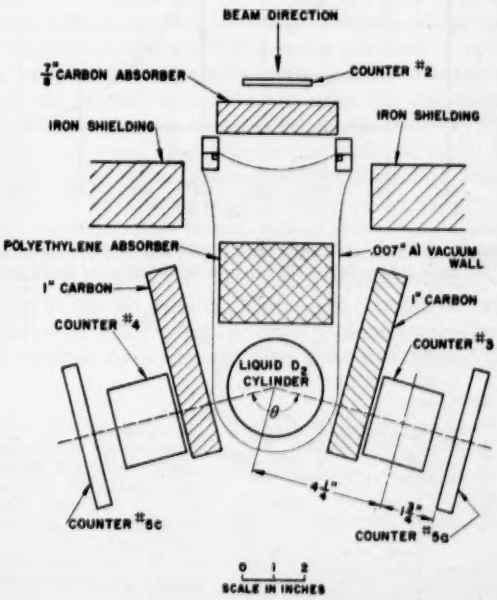

FIG. 5. Experimental geometry used to measure *n-n* coincidence rate as a function of the angle θ between the neutron detectors.

[7] Hadley, Kelly, Leith, Segrè, Wiegand, and York, Phys. Rev. **75**, 351 (1949).
[8] D. A. Kellogg, Phys. Rev. **90**, 224 (1953).
[9] The reaction $\pi^- + d \rightarrow 2n + \pi^0 \rightarrow 2n + 2\gamma$ is improbable (reference 5). In an experiment which will be reported at a later time we have shown that this process occurs in less than 0.1 percent of the cases of absorption.

to be made of the ratio R of the nonradiative to radiative capture rates, $R=(\pi^-+d\rightarrow 2n)/(\pi^-+d\rightarrow 2n+\gamma)$. To detect the γ rays, counter No. 3 is replaced by an absorber, 1.8 g/cm² of polyethylene, with a converter of 7 g/cm² of Pb directly in front of counter 5*b*. The circuits are arranged to record coincidences 12 and 125*a*5*b*. The product of solid angle and efficiency for this arrangement is $\epsilon_\gamma\Omega_\gamma=0.20$. The 125*a*5*b* rate as a function of the absorber thickness is shown in Fig. 4. The absorber used in the following experiments is 9.7 g/cm². For this absorber thickness the γ ray counting rate is

$$CR_{2n+\gamma}=\frac{125a5b}{12}=(488\pm 5)\times 10^{-6}.$$

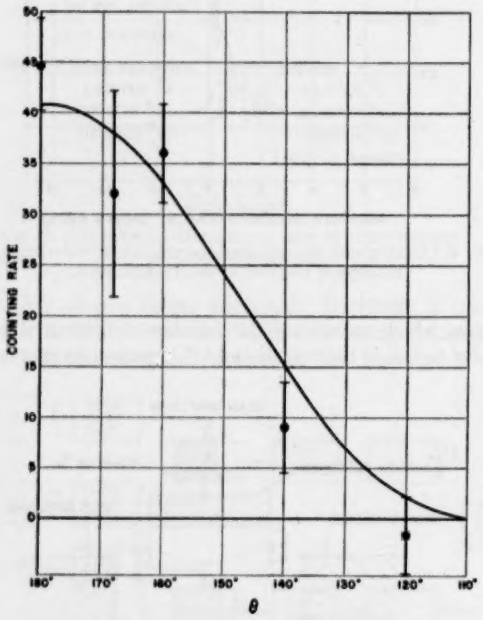

FIG. 6. Observed and calculated n-n coincidence counting rates vs the angle subtended by the two neutron detectors at the target.

B. n-n Coincidences

The results of the search for n-n coincidences with the geometry of Fig. 1 and the electronic arrangement of Fig. 3 are given in Table I. The observed $2n$ rate

$$CR_{2n}=\frac{(1234)_{\gamma}-5}{12}=(0.62\pm 0.19)\times 10^{-6}.$$

The ratio R is

$$\frac{CR_{2n}}{CR_{2n+\gamma}}\times\frac{\epsilon_\gamma}{(\epsilon_n)^2}\times\frac{\Omega_\gamma/4\pi}{(\Omega_n/2\pi)g}.$$

The quantity g is a geometrical factor; it is the probability that one of the two neutrons traverse counter No. 3 if it is known that the other has traversed counter No. 4 and that the two neutrons were emitted at 180° to each other. The quantity g was computed numerically to be 0.12. With the values $\epsilon_\gamma\Omega_\gamma=0.20$, $\epsilon_n=0.065\pm 0.015$, and $\Omega_n=0.17$, then $R=1.5\pm 0.8$. This is quite similar to the value $R=2.4\pm 0.5$ obtained by Panofsky *et al.* from a comparison of the γ-ray yields in hydrogen and deuterium. The discrepancy is within the experimental uncertainties.

C. n-n Angular Correlation

To test the identification of the observed events, we have measured the coincidence rate as a function of the angle subtended by the two neutron detectors at the target. This was, however, physically impossible with the arrangement of Fig. 1. It was necessary to sacrifice the anticoincidence counters 5*b* and 5*d* to obtain the required mobility without reducing the counting rate to an impossible value. The new geometry is shown in Fig. 5. The additional absorber serves to make the system insensitive to low-energy charged particles and the remaining anticoincidence counters reject high-energy γ rays. The results are shown in Fig. 6. The theoretical curve represents the response of the detection system to particles emerging with equal probability from the various volume elements of the deuterium and at 180° to each other. The consistency of the experimental points with the calculated function confirms the identification of the events as n-n coincidences.

Mass Measurements of Slow Cosmic-Ray Mesons

M. INOKI, T. YASAKI, AND Y. MATSUKAWA
Physics Institute, Yamanashi University, Kofu City, Japan
(Received May 18, 1953; revised manuscript received May 6, 1954)

By observing the ionization and subsequent range of individual charged slow particles, using two cloud chambers set one upon another, we have determined the mass of 36 slow particles in the soft component whose ranges are less than 2.5 mm in aluminum and the mass of 12 particles in the hard component at 300 meters altitude.

With regard to the measured masses, we observed a significant difference between the results in the soft component and those in the hard component. In the latter, the 21 masses can be interpreted as representing 4 proton and 8 μ-meson masses. In the former, 11 masses are consistent with the proton mass, whereas the remaining 25, ranging over values from 54 to 649 electron masses, can hardly be interpreted as the observation of μ mesons only.

The results seem to indicate the possible existence of at least two new mesons, the masses of which would be about 100 and 600 electron masses, respectively.

INTRODUCTION

SEVERAL experimental studies[1] which have been recently made on the mass of cosmic-ray particles at sea level, have made it clear that they are composed of protons, μ mesons, and electrons. However, these studies have determined the masses of particles within a limited range region where the μ-meson intensity is near maximum, and the particles in extremely low and extremely high energy regions escaped these mass determinations. Merkle *et al.*[2] have measured the masses of particles in a comparatively short range region from 4 to 13 cm of lead; however, there are no data for the particles of shorter ranges, except for a few early ones, some of which[3] appeared to be inconsistent with the μ-meson mass.

Considering the complexity and variety of cosmic-ray phenomena in the atmosphere which have not yet been surveyed completely by experimental studies, we decided to test whether new hitherto unknown mesons exist among the slow particles in the soft component near sea level.

In our previous study,[4] we measured the β-decay probability of the slow mesons which stopped within a 2-mm carbon plate. It appeared that the result gives evidence for the existence of new mesons stable against β decay. On the basis of that result, this study has been carried out to determine their mass. To give a confirmation of the above view[5] that the new mesons exist only in the extremely low-energy region, we have also made mass determination for the particles in the hard component, filtering out the soft radiation with 30 cm of lead, using the same apparatus and the same method, and have made a comparison between the results.

[1] W. B. Fretter, Phys. Rev. **70**, 625 (1946); J. G. Retallack and R. B. Brode, Phys. Rev. **75**, 1716 (1949).
[2] Merkle, Goldwasser, and Brode, Phys. Rev. **79**, 926 (1950).
[3] A. J. Ruhling and H. R. Crane, Phys. Rev. **53**, 266 (1938).
[4] Inoki, Yasaki, and Matsukawa, Phys. Rev. **86**, 129 (1952).
[5] Yasaki, Inoki, and Matsukawa, Proc. of Faculty of Liberal Arts and Education (Yamanashi University Press, Kofu, 1952), No. 1.

EXPERIMENTAL APPARATUS

The arrangement of the apparatus is illustrated in Fig. 1. The upper cloud chamber CH_1, which is a rear illumination type, was expanded slowly in both side directions by using two bellows B of 150-mm diameter. This chamber was used for the ionization measurement by drop counting of diffused tracks. The effective size of the chamber was 300 mm in length, 80 mm in width, and 50 mm in depth, and it was set with the 300-mm $\times$80-mm effective faces vertical. A clearing field of 200 volts was supplied between two drilled plates E which produce a uniform electric field between them with the aid of two potential dividers R made of series resistance.

This field voltage was reduced from 200 to 60 volts as soon as possible after the passage of a slow particle through the proportional counters C_1 and C_2. A window of dimensions 400 mm$\times$30 mm was provided in each of the upper and lower walls of the chamber; the upper wall was packed against air with a 0.1-mm aluminum foil F_1 and the lower with a 0.2-mm aluminum foil F_2. The chamber was filled with air and saturated vapor of a 3:1 mixture of propyl and ethyl alcohol to a total pressure of 380 mm Hg at 15°C. Illumination was given with two argon flash lamps, each of which was excited by the discharge of a condenser of 20-μf capacity charged to 5000 volts. The tracks were photographed using a Serenar lens of 50-mm focal length at an aperture of $f/8$. During the cloud chamber expansion, the width of a counter-controlled track was diffused to

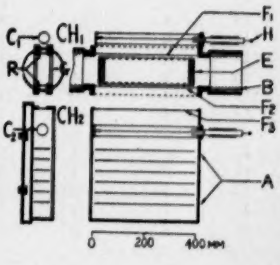

FIG. 1. Schematic arrangement of the apparatus showing the cloud chambers, CH_1, CH_2; the proportional counters, C_1, C_2; the plates, A; the aluminum foils, F_1, F_2, F_3; the bellows, B; the drilled plates, E; the resistance series, R; and the glass G.

about 6 mm and it was separated simultaneously into two parallel columns of positive and negative ions about 16 mm apart.

The lower multiplate cloud chamber CH_2 contained the proportional counter C_2 and 6 aluminum plates A each 0.3-mm thick, or 8 stylon plates (an organic compound of carbon and hydrogen); each of the 4 top stylon plates was 0.36-mm aluminum equivalent in thickness, and each of the remaining four was 0.73-mm aluminum equivalent. The chamber was 400 mm square by 80 mm deep. A window of dimensions 400 mm $\times$30 mm, which was packed against air with a 0.05-mm aluminum foil F_3, was provided in the upper wall of the chamber. The chamber was filled with air and saturated vapor of ethyl alcohol to a total pressure of 710 mm Hg at 15°C. Stereoscopic multiplate cloud chamber photographs were taken, using a front camera and a side camera 55 cm apart.

The proportional counters C_1 and C_2 were used not only to define the solid angle of incident particles but also to select them as to ionization. Each of the counter tubes, which are 40 mm in diameter, 340 mm in effective length, and 0.2 mm in wall thickness of aluminum, was filled with methane gas of 660-mm Hg pressure at 15°C. A stabilized voltage of 5000 volts was supplied to the terminal H of the central wire, 0.3 mm in diameter, through a high resistance of 50 megohms. All the apparatus was enclosed in a box inside which the temperature was kept at 15°$\pm$0.2°C during the winter and at 35°$\pm$0.4°C during the summer. The measured ionization at the latter temperature was corrected to the ionization at 15°C.

OBSERVATIONS

A set of preliminary observations was made for 50 fast cosmic-ray particles, penetrating 5 cm of lead. Their average ionization was 50.7 drops per cm in air of 700-mm Hg pressure at 15°C, when clusters larger than 40 drops were excluded. The probable error of the ionization for an individual track was 11 percent, provided that the 50 fast particles had the same ionization. By the relation of energy to ionization, their

TABLE I. Mass measurement for particles in the soft component, carried out in the first experiment. In the first column, track numbers followed by an asterisk refer to particles which emit a decay particle, and those enclosed with parentheses probably have systematic errors in either ionization or range. The plate number zero means that the particle stopped in the lower wall of the counter inside the lower chamber.

Track number	Plate number in which particle stopped	Deviation from the center line (mm) X_0	X_1	X_3	Range in aluminum R(mm)	Probable error in range ΔR(mm)	Total number of drops N	Length of track measured L(cm)	Ionization in minimum ionization units I	Probable error in ionization ΔI	Mass in electron mass units M	Probable error in the mass ΔM
1*	5	−4	−7	−10	2.49	0.08	644	6.7	4.8	0.2	234	21
2	6	4	1	−1	2.75	0.08	376	5.3	3.6	0.2	135	15
3	6	18	19	19								
4	6	−13	−13	−12	2.77	0.08	1045	7.4	7.2	0.2	649	45
5	2	8	12	15	1.48	0.08	888	6.4	7.0	0.2	318	29
(8)	2	−1	−1	−1	1.29	0.08	583	6.7	4.3	0.2	93	11
9	6	10	10	11	2.65	0.08	701	5.5	6.5	0.3	465	41
11	3	−12	−10	−9	1.66	0.08	608	5.8	5.2	0.2	189	18
13	1	−12	−14	−16	1.32	0.10	1250	6.9	9.2	0.3	583	60
14	3	2	2	1	1.59	0.08	858	5.0	8.6	0.3	600	55
15	2	−20	−18	−17								
16	3	−3	−10	−13	1.86	0.09	349	4.6	3.8	0.2	103	14
17	3	0	−3	−5	1.66	0.08	575	7.4	4.0	0.2	105	11
(19)	1	24	14	6	1.05	0.09	386	3.4	5.7	0.3	141	21
20	6	0	−2	−3	2.55	0.08	531	6.1	4.3	0.2	194	19
21	2	0	10	19	1.93	0.09	1012	7.7	6.6	0.2	364	31
(22)	2	16	9	2	1.30	0.08	754	5.8	6.5	0.3	236	25
23	1	−2	−2	−2	1.07	0.09	2767	8.0	18.2	0.4	2120	226
25	2	−11	−8	−5	1.44	0.10	1822	6.3	15.1	0.4	1870	173
26	2	12	13	14	1.42	0.08	1639	5.2	16.5	0.4	2260	188
27	4	2	3	7	1.97	0.08	1716	6.4	13.6	0.4	2020	140
28	5	−6	−7	−8	2.30	0.08	1175	5.0	11.8	0.4	1730	129
29	3	0	−6	−10	1.96	0.10	2165	8.8	12.6	0.3	1700	126
30	3	−4	−8	−13	1.59	0.08	814	7.4	5.5	0.2	200	18
31	2	−15	−15	−15	1.50	0.08	653	4.7	7.0	0.3	323	33
32	4	−5	−8	−11	1.99	0.08	1092	7.1	7.8	0.3	574	45
33	4	12	8	4	1.95	0.08	1772	7.2	12.5	0.3	1650	113
34	0	8	12	15	0.81	0.09	682	8.5	4.1	0.2	54	8
35	4	−4	1	6	2.04	0.08	904	7.2	6.3	0.2	337	28
36	4	4	8	12	2.01	0.08	890	5.6	8.0	0.3	628	52
(37)	4	−19	−11	−4	2.01	0.08	465	7.7	2.9	0.2	60	8
38	1	6	7	8	1.11	0.09	2319	7.2	16.6	0.4	1790	189
39	6	0	5	8	2.77	0.09	1585	7.7	10.5	0.3	1630	108
40	air	−8	−9	−10	1.20	0.00	637	7.4	4.2	0.2	82	10
41	2	1	−2	−6	1.41	0.08	1337	4.5	15.2	0.4	1850	165
42	2	10	2	−6	1.55	0.09	855	6.3	6.9	0.2	323	32
43	1	9	7	6	1.01	0.08	1207	5.7	10.8	0.3	645	72
44	2	2	−4	−8	1.63	0.09	2246	8.0	14.4	0.3	1880	157

TABLE II. Mass measurement for particles in the hard component, carried out in the second experiment. In the first column, track numbers followed by an asterisk refer to particles which emit a decay particle, and those enclosed with parentheses probably have systematic errors in either ionization or range.

Track number	Plate number in which particle stopped	Deviation from the center line (mm) X_0	X_1	X_2	Range in aluminum equivalent R(mm)	Probable error in range ΔR(mm)	Total number of drops N	Length of track measured L(cm)	Ionization in minimum ionization units I	Probable error in ionization ΔI	Mass in electron mass units M	Probable error in the mass ΔM
1*	2	−1	−2	−3	1.36	0.09	829	7.2	5.7	0.2	186	18
(2)	7	12	14	16	5.51	0.16	820	6.4	5.6	0.2	775	60
3*	2	12	12	12	1.95	0.16	779	7.1	5.1	0.2	191	23
4*	1	14	4	−4	1.19	0.18	961	7.2	6.2	0.2	192	37
(5)	4	−17	−9	−1	2.12	0.09	1651	5.8	13.1	0.3	1970	137
6	2	10	6	2	1.38	0.09	1708	5.6	13.6	0.3	1410	129
(7*)	4	3	−1	−5	2.19	0.09	571	6.9	3.7	0.2	112	12
8	7	−6	−7	−9	4.00	0.20	636	6.9	4.0	0.2	250	43
(9)	5	−19	−10	−2	2.70	0.16	511	6.9	3.2	0.1	100	11
10	1	0	−5	−10	1.05	0.09	2032	5.6	16.2	0.4	1600	177
11	5	−3	−5	−5	2.62	0.16	713	6.9	4.4	0.2	206	22
12	6	0	−6	−11	3.30	0.16	747	6.7	4.8	0.2	308	27

ionization is not the same and show a slight relativistic increase.

The ratio of positive to negative drops in all tracks was smaller than 3:1. When the ratio was decreased to about 1:1, no appreciable increase of the average ionization of positive ion tracks was observed. That means the condensation efficiency on positive ions is about 100 percent in the ratio of 3:1. However, to be on the safe side, the ratio was kept smaller than 2:1 throughout the whole period of the observations. Clusters larger than 40 drops were also excluded in the measurements.

As the criterion for exclusion of these clusters, discrimination of which in dense tracks was somewhat difficult by their appearance alone, the following procedure was applied. Each of the diffused tracks was printed in an enlargement to 3.2 times the full size. Then, dividing the positive ion track into small sections, each of 5-mm length, the drop number per section and their mean value n were obtained by drop counting. Any two successive sections whose total number of drops was larger than $2n+40$ were excluded from the measurement, as they were considered to show the fluctuation caused by the presence of clusters larger than 40 drops in about 1 cm square on the photograph, because the Gaussian fluctuation of $2n$ drops should be far smaller than 40. The total number of drops N of the individual track was obtained by subtracting background drops neighboring it from the total number of drops of all sections which passed the above excluding criterion. We used the minimum ionization, 20.7 ion pairs per cm in air and alcohol vapor mixture of 380-mm Hg pressure at 15°C, which is converted into 40 ion pairs at N.T.P. in dry air. The minimum ionization was determined from the measured ionization of 13 protons, described later. We neglected the overlapping correction for ionization measurement, since the computed value[6] of it was $0.0004I^2$. Following the method of Hazen,[7] the statistical error in the ionization was estimated by the assumption that it is caused essentially by the statistical fluctuation of the number of primary ions which was assumed to be 40 percent of the measured ionization. The probable error ΔI, therefore, was computed by a relation, $\Delta I/I=0.67/(0.4N)^{\frac{1}{2}}$, where I is the ionization in units of the minimum ionization. The value of N, I, and ΔI are shown in Tables I and II.

In Fig. 2, the ZZ' axis is a vertical line passing through the center of the two 30-mm×400-mm windows. The deviation of each individual track from the ZZ' axis, projected on the plane, at the counter wall X_2 and at the window of the lower chamber X_1, was determined from the stereoscopic photographs of the track. Its deviation at the window of the upper chamber X_0 was estimated by an extension of the path of the particle PN, assuming that all particles penetrated the aluminum foil F_3 without any scattering. In Table I and Table II, the values of X_0, X_1, and X_2 for the individual tracks are shown. A minus sign before a value of X indicates backward deviation.

The range of an individual particle was computed as the sum of the path lengths in the foils, the counter

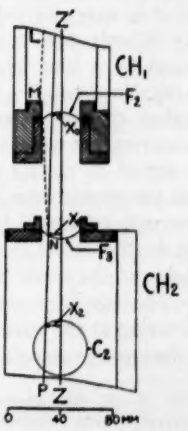

FIG. 2. A cross section of the windows of the upper and the lower chamber, illustrating the path of a particle between them. The dotted line LMN shows the path of a particle scattered at the window frame.

[6] R. H. Frost and C. E. Nielsen, Phys. Rev. **91**, 864 (1953).
[7] W. E. Hazen, Phys. Rev. **65**, 259 (1944).

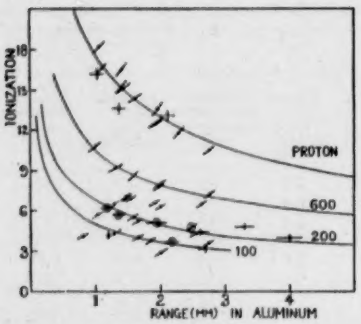

FIG. 3. Curves of ionization *versus* range, and the experimental observations. The projections of the line extending to both sides of each point show on the coordinate axes the probable errors, $\pm\Delta I$ and $\pm\Delta R$. The observations in the first experiment are represented by the points having extended diagonal lines and those in the second experiment are represented by the points having extended horizontal and vertical lines. In both cases, each observation with uncertain error is represented by points having extended dotted lines, and each point enclosed with a small circle represents the observation of a decaying meson.

wall, the plates, and the air traversed by the particle, assuming that it was stopped in the middle of the thickness of the stopping plate. As the probable error in range, we used one-fourth the thickness of the plate, divided by the cosine of the angle between the normal to the surface of the plate and the direction of the track.

On the assumption that the charge of the individual particle is identical with that of the electron, each mass was computed with the aid of the curves relating range to ionization;[8] the results are shown in Fig. 3. The probable error in the mass was computed by using the relation $M \propto RI^2$.

In the first experiment, the apparatus was operated without any absorber above it except a thin roof whose thickness was about 5-mm lead equivalent, and with 6 aluminum plates inside the lower chamber. During an effective working period of 400 hours, 262 slow particles of ionization larger than 3 times minimum were observed by both chambers, and 44 of these were stopped in the plates. 6 tracks, probably proton tracks, out of 44 were omitted since the drop counting of these was difficult due to a dimness of their drop figures caused by a blur in the glass of the chamber. Two tracks, No. 3 and No. 15 in Table I, passing outside the window of the lower chamber, were also omitted. Measurements were made on the remaining 36 tracks. 11 out of 36 masses are consistent, within the error, with the proton mass, whereas the remaining 25 spread over values from 54 to 649, as seen in Table I and in Fig. 4. Among the 25 tracks, No. 8 lacks a negative ion track and the other three tracks, No. 19, No. 22, and No. 37, may have entered into the lower chamber by scattering at the window frame of the upper chamber, as the passage along *LMNP* in Fig. 2 did, for instance. Therefore they probably have systematic errors in either ionization or range, causing uncertain masses smaller than the true one. However, by an estimation of their track densities in the lower chamber, they are probably mesons.

In the second experiment, the apparatus was operated by placing 30 cm of lead immediately above the proportional counter C_1, and using 8 stylon plates, or 6 stylon plates during first 20 hours, inside the lower chamber. During the effective working period of 370 hours, 59 slow particles of ionizations larger than 3 times minimum were observed and 13 of them were stopped in the plates. One track, probably that of a proton, was omitted due to a dimness of the drop figure. Measurement were made on the remaining 12. Among the 12 tracks, 6 masses were obtained whose average, 222 ± 14, is consistent, within the error, with the μ meson mass. Two tracks, No. 5 and No. 9, have the same kind of error as No. 19 in Table I. Two other tracks, No. 7 and No. 2, show diffused tracks, in which the number of negative ion drops is less than $\frac{1}{3}$ of the positive ones. Therefore these 4 also have uncertain masses. However, two of the above tracks, No. 7 and No. 9, should represent μ mesons, because one of these shows a decay particle and the other is not dense enough for protons in the lower chamber. The average mass of the 13 protons in Tables I and II is 1810 ± 39. The probable error in the mass of an individual proton, estimated from the mass distribution, is 142 which is consistent, within the error, with the mean value, 153, of $|\Delta M|$ of the 13 protons.

INTERPRETATION

Concerning not only the mass but also the intensity, there is a significant difference between the results of the first experiment and those of the second, the latter being consistent with the results of other investigators. By a statistical analysis, rejecting the uncertain masses, the two results do not represent two groups of measured values for the same set of events, with a level of signif-

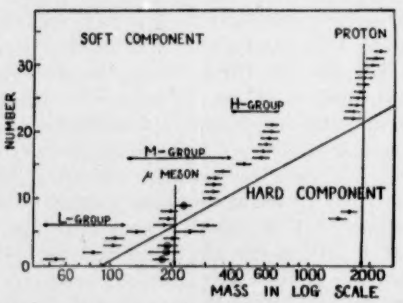

FIG. 4. Integral mass spectra showing the measured masses, arranged in order of increasing mass, obtained in the first and second experiments. Each point represents the measured mass on a logarithmic scale and the length of the lines extended on both sides of each point represents the probable error of the measured mass, $\pm\Delta M$. Each point enclosed with a small circle represents the measured mass of a decaying meson.

[8] D. J. X. Montgomery, *Cosmic Ray Physics* (Princeton University Press, Princeton, 1949), Appendix E.

TABLE III. The observed intensities of the particles. The number of fast particles in the second column is a roughly estimated number of all fast particles penetrating the effective space of both chambers during the effective working period. The actual intensities of the slow particles in the ionization region, $3<I<6$, are about twice the observed ones, because the selection efficiency of these particles out of the fast ones, obtained by twofold coincidence of the proportional counters, was about 0.5.

	Effective working period (hours)	Number of fast particles penetrating the plates	Number of slow particles penetrating the plates $3<I$	Effective g/cm² of the plates used	Number of slow particles stopped in the plates		Observed number of decaying mesons	Expected number of according to the meson data of Merkle *et al.*
					Protons	Mesons		
1st exp.	400	96 000	220	0.49(aluminum)	17	25	1	2
2nd exp.	370	62 000	46	1.18(stylon)	5	8	4	

icance of one percent. In addition to this discrepancy, a great discrepancy exists in the first experiment between the observed meson intensity and the estimated μ-meson intensity, as is shown in Table III. Therefore, the observation of 25 "mesons" seems to imply the existence of new mesons as a necessary consequence. However, the foregoing view rests on the assumption that the errors of measurement are entirely statistical. There are a number of possible errors other than the statistical ones, as described below (see Figs. 5 and 6).

(1) If a proton or a μ meson is scattered at the window frame of the upper chamber and enters into the lower chamber, scattering again in the 0.05-mm aluminum foil at its top window, then the estimated range is too small by the amount of the path length inside the frame, and this results in too low a value of the mass. The deviations from the center line X_0 in Tables I and II, were obtained by assuming zero scattering angle of the incident particles in the 0.05-mm foil mentioned previously. The theoretical scattering angle in the foil for a proton or a μ meson which is to be stopped in the bottom plate, is 0.6° or 1.4°, respectively, by a relation of Annis *et al.*[9] However, these values are smaller than one-tenth of the angle which is needed in order to attribute the 25 subproton masses to the tracks of scattered protons and μ mesons.

(2) If a section of the multiplate chamber does not work properly and a proton or a μ meson which actually goes through a plate appears to be stopped, then it also simulates a lower mass. The increasing ratio of ionization in two successive sections immediately above the stopping plate can be used as an indirect identification for ending of the particles. On 16 tracks out of 25, the increases in ionization were seen on the photographs; however, the increases were not seen on the remaining 9. We think that the nonincrease of ionization of the tracks on the photographs was caused by the following reasons. (a) In our multiplate chamber, containing the 0.3-mm plates, the increasing ratio is small. The estimated ratio from the curve in Fig. 3, is between 1.3 and 1.7 for half of the stopped μ mesons. (b) The illumination intensity was not sufficient, and therefore we used a strong contrast developer which may have failed to reproduce the slight increases of ionization, mentioned above, on the film. (c) The illumination intensity and the condensation efficiency of vapor on ions were not perfectly uniform for each section. The illumination intensity was particularly weak at the top space. The majority of the 2700 multiplate chamber photographs, taken during the 400-hour period, recorded cosmic-ray showers or β rays produced by γ rays from earth. By examination of these, especially on the 9 photographs taken by the side camera, it was certain that all sections of the multiplate chamber were sensitive for fast particles during the operations.

If the 25 meson masses were simulated masses of slow protons caused by the errors previously described, then we find it hard to interpret the presence of the clearly isolated group of 11 protons in the first experiment and the disappearance of the unusual masses in the second experiment.

(3) If some particle experiences energy losses other than those due to ionization inside the counter wall or plates, then it appears to have a lower mass than it actually is. For example, if a meson is captured in flight by a nucleus in a plate, then the apparent range is smaller by the amount of the residual range at the place where it was captured. However, such energy losses by known particles are not frequent enough for the 25 mass distributions to be interpreted in this way.

(4) If there exist τ and π mesons at sea level, the 25 masses, except for the six smaller than 105 electron masses, might be explained as representing τ, π, and μ mesons, so far as mass is concerned, assuming some systematic error in measurement. However, in that case about 6 decaying mesons should be observed, contrary to the result which shows only one, provided that half of them are positively charged and the geometrically computed detection efficiency of the decay particle emitted isotropically from the plate is 0.6. This value is consistent within the error with 0.5, which is obtained by the second experiment, showing 4 decaying mesons out of 8.

It seems to us that interpretation of the result in terms of the errors or of known mesons is hardly possible. To give a decisive conclusion for the existence of new mesons, accumulation of more exact data may perhaps be needed;[10] however, at the present stage, we propose the existence of new mesons of a new type as the most probable interpretation of our results.

We temporarily classified the 25 masses, rejecting 4

[9] Annis, Bridge, and Olbert, Phys. Rev. 89, 1216 (1953).

[10] For that purpose, a magnetic cloud chamber is under construction.

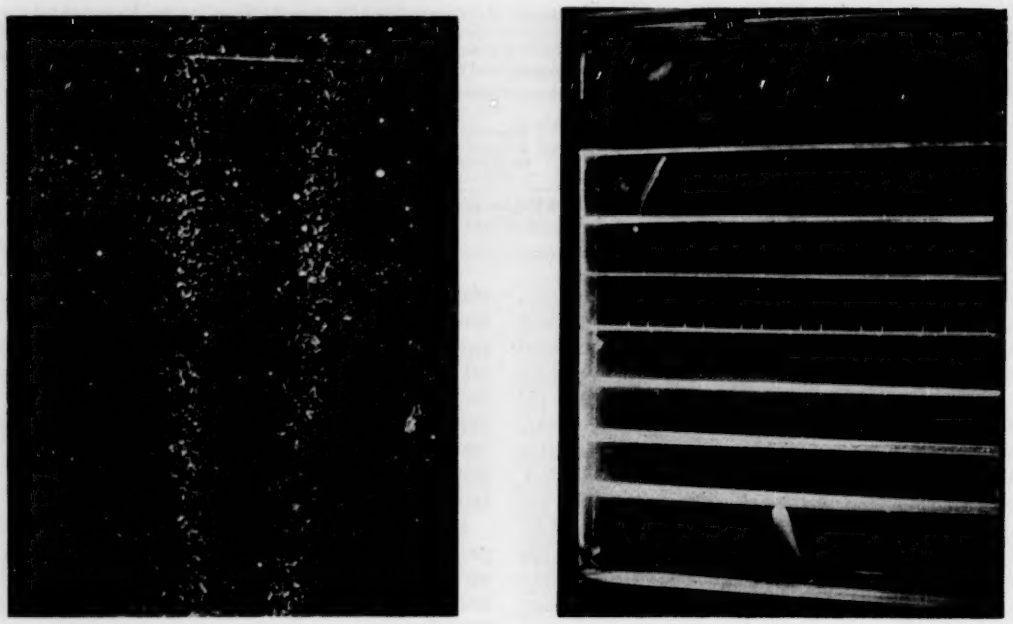

(a) (b)

FIG. 5. Typical cloud-chamber photograph of the meson, No. 40 in Table I, in the L group, showing the diffused tracks of positive and negative ions in the upper chamber, and the photograph of the track of the same meson stopped in air between the first and the second plate in the lower chamber, taken by the side camera.

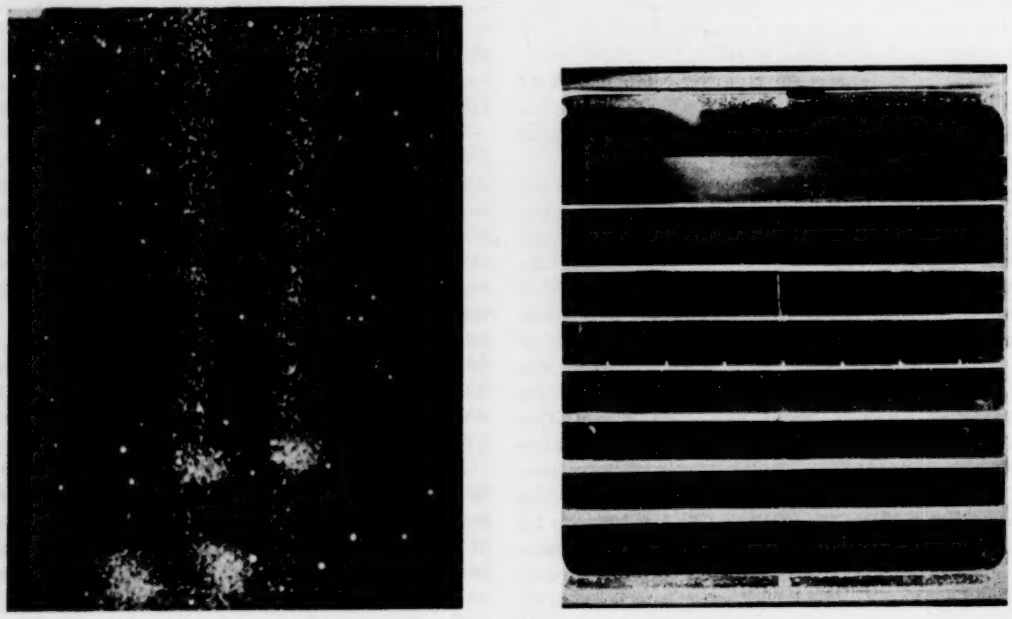

(a) (b)

FIG. 6. Typical cloud-chamber photograph of the μ meson, No. 1 in Table II, showing the diffused tracks in the upper chamber, and the photograph of the track of the same meson emitting the decay electron at the second plate in the lower chamber, taken by the front camera.

uncertain ones, into 3 groups, namely L, M, and H groups, which represent 4 masses from 54 to $105m_e$, 10 masses from 135 to $364m_e$, and 7 masses from 465 to $649m_e$, respectively. The M group contains μ mesons, for which the number estimated by using the data of Merkle *et al.* is about 2, that estimated from the number of decay electron is about 3, and that expected from the measured mass is about 5. It is uncertain whether the remaining particles in the M group are π mesons or mesons of a new type. The L and H groups, in which the average masses are 86 and 592, respectively, are free from π and μ mesons, thus implying mesons of a new type. Concerning the decay of the new mesons, there is doubt whether they are a "non-decaying type" or a "long-lived type," or whether they produce a decay particle of such short range as to be undetectable, or whether they are negatively charged particles and are captured by nuclei before their spontaneous decay.

PHYSICAL REVIEW VOLUME 95, NUMBER 6 SEPTEMBER 15, 1954

Diurnal Variations of the Intensity of Cosmic Rays Far Underground*

P. BARRETT,† G. COCCONI, Y. EISENBERG, AND K. GREISEN
Cornell University, Ithaca, New York

(Received June 9, 1954)

In the analysis of 249 762 coincidences due to cosmic rays at a depth of 1600 m.w.e. underground, no diurnal variation of the rate with respect to solar or sidereal time was found. With high confidence the amplitudes of such variations may be said to be less than one percent of the average intensity. The average energy of the primary cosmic rays responsible for the particles recorded was about 4×10^{13} ev.

IN 1950 a series of measurements of the intensity of cosmic rays reaching a depth of 1600 meters water equivalent (m.w.e.) was begun in a salt mine near Ithaca, New York (geographical latitude $\lambda=42.5°$N). Analyses of the intensity-time variations, based on part of the results, have already been published.[1,2] Now these measurements have been completed, and the results we publish here supersede the previous ones.

Other experiments performed in the same mine[3] have shown that the observed particles are mu mesons created with an average energy of about 10^{12} ev by primary cosmic rays having an average energy of about 4×10^{13} ev.

The intensity was measured by several vertical telescopes, each containing two trays of G.M. counters (30 in.×40 in.) separated by four inches of lead, and shielded above and below by two inches of lead. The number of coincidences in each telescope was recorded hourly. A total of 249 762 coincidences have been recorded during the period July, 1951 to August, 1953, with an average rate per telescope of 10.7 per hour. The accidental coincidences, which have not been subtracted, were about five percent of the total.

The data have been assembled according to the hour of solar time (Eastern Standard Time), or of local sidereal time in which the counts were recorded. Small corrections were applied for slight differences of running time in the different intervals. The results are plotted in Fig. 1, showing the apparent variation of intensity as a function of the solar time and as a function of the sidereal time. The errors indicated are standard errors.

On the solar time scale, the deviations from the mean have a quite normal distribution, with an rms value just equal to that which is expected from statistical fluctuations of the numbers of counts recorded. Fitting these data to a sinusoidal diurnal intensity variation can reduce the residual mean square deviation, the best fit occurring for an assumed amplitude equal to 0.5 percent of the mean counting rate, with 5.9 hours E.S.T. as the time of the maximum. However, the fit is

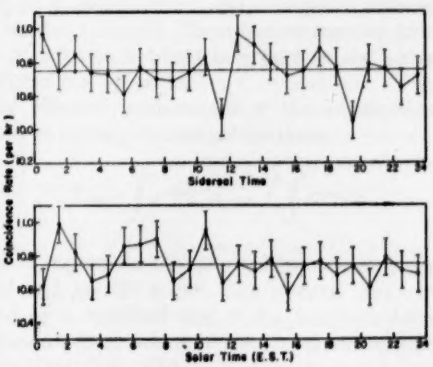

FIG. 1. Average coincidence rate of the three counter telescopes, as a function of local sidereal time and Eastern Standard solar time. The indicated errors are standard errors.

* The research reported in this paper has been sponsored by the Geophysics Research Directorate of the Air Force Cambridge Research Center, Air Research and Development Command.

† Now at Syracuse University, Syracuse, New York.

[1] G. Cocconi, Phys. Rev. **83**, 1193 (1951).

[2] P. H. Barrett and Y. Eisenberg, Phys. Rev. **85**, 674 (1952).

[3] Barrett, Bollinger, Cocconi, Eisenberg, and Greisen, Revs. Modern Phys. **24**, 133 (1952).

hardly better than that which is expected from normal data involving the same number of counts in the absence of any real intensity variation. With high confidence, the true amplitude can be said to be less than one percent of the average intensity.

On the sidereal time scale, several of the deviations are a little large for a normal distribution, the mean square deviation being 1.4 times the most probable value. But in view of the angular resolution of the apparatus (effective aperture $\approx 60°$, determined mainly by the zenith-angle distribution of the mesons), and the fact that neighboring points on the graph do not show similar deviations in the same direction, we infer that the large deviations were more probably caused by random flucutations than real intensity changes. Indeed, fitting the data to a sinusoidal intensity variation hardly reduces the residual deviations at all, the fit being poorer than that expected on the average if the deviations are random. One may confidently infer that the amplitude of any sinusoidal diurnal intensity variation with respect to sidereal time is less than 0.7 percent of the average intensity. The best fit is for an amplitude of 0.1 percent, with maximum at 16.5 hours local sidereal time, but there is no evidence that the effect is real.

Our results contradict those of Sekido *et al.*[4] who, at a similar latitude and similar energy, seemed to observe a large intensity variation with respect to sidereal time. However, our analysis of their data indicates that their results were not significant statistically. On the other hand, our results are in good agreement with those of Sherman[5] who, at 846 m.w.e. underground, found diurnal amplitudes less than one percent, the data being consistent with zero amplitude.

Our results are not inconsistent with those of Daudin and Daudin,[6] who at a similar latitude, but at a higher primary energy (by detecting air showers of energy $\sim 2\times 10^{15}$ ev) and with better statistics than ours, found a sidereal variation with amplitude a few tenths of a percent, barely significant statistically; the maximum occurring at 22 hours local sidereal time.

In sharp contrast to the measurements at northern latitudes stand the results of Farley and Storey[7] obtained in Auckland, New Zealand, where the central region of the galaxy passes overhead at 18 hours local sidereal time. A very significant maximum was found to occur at this time in the air shower intensity (primary energy $\sim 10^{15}$ ev); on the assumption of a sinusoidal variation, the amplitude was about 1.5 percent.

It may be mentioned that these results, both the positive and the negative ones, have a bearing on theories of the origin of cosmic rays.[8] The positive results from New Zealand lend encouragement to a continuation of these studies. In retrospect, however, it is clear that it is better to look for the primary asymmetries by measuring variations of air shower intensities than by measuring variations in the meson intensity far underground. It is true that the latter method has an advantage, in that the meson intensity is comparatively insensitive to atmospheric changes, and therefore would not contain a spurious sidereal time variation due to solar and seasonal effects. But this is more than compensated for by the improved statistics that are obtainable in the air shower measurements, owing to the large effective area over which the showers can be detected. Thus, one can count events of primary energy around 10^{15} ev, as air showers at ground level, with about the same frequency as one can count primary events of 10^{13} ev by detection of the mesons underground. If events of equal primary energy are selected, the air shower counting rates can exceed the underground rates by a factor of about 1000.

[4] Sekido, Masuda, Yoshida, and Wada, Phys. Rev. **83**, 658 (1951).
[5] N. Sherman, Phys. Rev. **89**, 25 (1953).
[6] A. Daudin and J. Daudin, Compt. rend. **234**, 1551 (1953); and private communication from A. Daudin.
[7] F. J. M. Farley and J. R. Storey, Nature **177**, 445 (1954); and private communication from F. J. M. Farley.
[8] See, e.g., Morrison, Olbert, and Rossi, Phys. Rev. **94**, 440 (1954).

Atmospheric Temperature Effect for Mesons Far Underground*

P. Barrett,† G. Cocconi, Y. Eisenberg, and K. Greisen
Cornell University, Ithaca, New York

(Received June 4, 1954)

A continuation of measurements previously reported has led to verification of the positive temperature effect for μ mesons detected at 1574 m.w.e. underground, which are created in the atmosphere with an average energy of about 8×10^{11} ev. The new result for the temperature coefficient at this depth is 0.33 ± 0.13 percent per deg C; and this value combined with the previous measurement yields an average of 0.46 ± 0.11 percent per degree, agreeing with the value expected if the $\pi-\mu$ decay process is responsible for all, or most, of these μ mesons.

THE effect of atmospheric temperature on the intensity of cosmic-ray mesons far underground has been discussed in previous publications,[1,2] in which experimental values of the temperature coefficient, $\alpha=(1/I)(\partial I/\partial T_{eff})$ were reported for depths of 1574 and 846 meters water equivalent (m.w.e.) underground. The measurements in a salt mine at 1574 m.w.e. have been continued, with modified recording apparatus, in order to verify the existence of the effect and to reduce the rather large statistical error in the determination of α. It is the purpose of this article to report the results obtained.

The apparatus consisted of three independent telescopes, each containing two broad trays of counters (30 in.$\times$40 in.) separated by four inches of lead, and shielded above and below by two inches of lead as in reference 1. Steps taken to ensure reliability of the record coincidence rates were the following:

1. Quenching circuits were used with the counters in order to prolong their lives and improve the constancy of their efficiency. The dead times imposed by the quenching circuits were measured periodically, and the indicated corrections for dead-time inefficiency (about one percent) were made. In the course of the experiment, the maximum variation of this correction was ±0.1 percent of the mean counting rate.

2. The coincidence resolving time was measured periodically, to prevent slow variations of the accidental coincidence rate from indicating a spurious seasonal variation of intensity. The indicated corrections, averaging six percent, were made; and the variations of these corrections affected the results appreciably, the standard deviation of the correction being one percent of the average counting rate, which is 0.7 times the statistical standard error of the monthly counting rates to which the corrections were applied.

3. The numbers of single pulses registered by the counter trays (mostly due to local radioactivity) were monitored continually. The statistical accuracy of this count was so high that failure of a counter would be indicated clearly without much delay. In addition, the plateaus of the counter trays were tested twice per week; and time intervals of doubtful reliability were discarded.

4. The two-fold coincidences in each telescope (about 10 per hour) were totalled on mechanical registers, and in addition were displayed (after passing through a scale of 4) on a clock-driven pen recording instrument. On the latter record, any spurious counts due to electrical disturbances were distinguishable.

The temperature information was obtained from the U. S. Weather Bureau, and consisted of radiosonde observations made at three Air Force stations: Rome, New York, about 75 miles northeast of the salt mine; Buffalo, New York, 120 miles WNW of the mine; and Hempstead, Long Island, about 240 miles southeast of the mine.

The radiosonde balloon flights are not uniformly successful, attaining a maximum elevation that varies greatly from one flight to another. It has been suggested[3] that correlations of intensity variations with changes of upper air temperature may be unreliable, because of the temperature measurements being nonrepresentative owing to a correlation between weather conditions and success of the flights. However, in the present case there seemed to exist other factors, entirely uncorrelated with air temperature, which exerted a much stronger influence on success of the flights (e.g., variations in the type of balloon used, and changes in personnel at the weather stations). These factors were so dominant that no relation between temperature and success of the flights was apparent.

The effective temperature of the atmosphere was defined as in the previous publications:

$$T_{eff}=\int e^{-\lambda x}T(x)dx \Big/ \int e^{-\lambda x}dx,$$

where x represents the atmospheric pressure level in g/cm^2 and $\lambda=120$ g/cm^2. The integral was approximated by a weighted sum of the temperatures at all the pressure levels where temperatures were reported in the weather data. This is in contrast to the previous

* The research reported in this paper has been sponsored by the Geophysics Research Directorate of the Air Force Cambridge Research Center, Air Research and Development Command.

† Now at Syracuse University, Syracuse, New York.

[1] Barrett, Bollinger, Cocconi, Eisenberg, and Greisen, Revs. Modern Phys. 24, 133 (1952).

[2] N. Sherman, Phys. Rev. 93, 208 (1954).

[3] H. O. Curtis, Proceedings of the Duke University Cosmic Ray Conference, 1953 (unpublished), Sec. IV, p. 14.

TABLE I. Average temperatures, running times, and numbers of counts recorded each month, corrected for accidental coincidences and dead-time inefficiency. (In calculating the results marked with an asterisk, the data in parentheses have been omitted.)

Month	$(T_{eff})_M$	Telescope 1 t_i(hr)	Telescope 1 n_i	Telescope 2 t_i(hr)	Telescope 2 n_i	Telescope 3 t_i(hr)	Telescope 3 n_i
Nov. '52	−55.3°C	216	2060	99	1074	260	2509
Dec.	−55.9	623	6177	623	6795	419	4162
Jan. '53	−55.95	684	6834	734	8121	740	7345
Feb.	−55.05	364	3595	381	4209	197	1920
Mar.	−52.2	590	5849	609	6820	21	222
Apr.	−51.6	814	8310	810	8937	508	4965
May	−52.1	512	5094	580	6583	136	1332
June	−51.6	605	6064	441	4878	595	5826
July	−50.5	494	4914	494	5463	367	3678
Aug.	−50.5	(586)	(5560)	455	5262	526	5394
Totals		4902*	48 897*	5226	58 142	3769	37 353
Average rate (hr^{-1}):		9.975*		11.126		9.911	
Average of T_{eff}:		−53.2°C*		−53.0°C		−53.1°C	
Temperature coeff., α:		+0.29±0.22*		+0.42±0.20		+0.26 ±0.23%/ deg C	
Correlation coeff., r:		+0.43*		+0.54		+0.34	

analyses,[1,2] where the temperatures at only six levels were used in approximating the integral. At altitudes above $x=20$ g/cm² the temperature was assumed to be the same as at 20 g/cm², for lack of other information.

Two independent methods of analysis of the data were used, the first depending only on the seasonal variations of temperature and counting rate (as in references 1 and 2), and the second depending only on short-period fluctuations of temperature and intensity.

For the first method, monthly averages were computed of the temperature at each of the pressure levels, and from the monthly averages, values of T_{eff} for the month were computed. Because of the different distances of the weather stations from Ithaca, the measurements at Rome, Buffalo, and Hempstead were combined with weighting factors in the ratio 3:2:1.

For each telescope, an over-all average temperature was computed from the relation $\langle T_j\rangle_M=\Sigma_i t_{ij}T_{eff}/\Sigma_i t_{ij}$ and an average rate from the relation $\langle R_j\rangle_M=\Sigma_i n_{ij}/\Sigma_i t_{ij}$; where t_{ij} represents the running time of telescope j in the ith month, and n_{ij} the number of counts recorded. ΔT_{ij} and Δn_{ij} represent the deviations of T_{eff} and n_{ij} from $\langle T_j\rangle_M$ and from $\langle R_j\rangle_M t_{ij}$, respectively. The pertinent data are given in Table I.

The temperature coefficient α is computed from the relation $\alpha=\Sigma(\Delta n\Delta T)/\Sigma(\langle R_j\rangle_M t\Delta T^2)$, and the correlation coefficient is defined by

$$r=\Sigma(\Delta n\Delta T)\{\Sigma\Delta n^2/(\langle R_j\rangle_M t)\cdot\Sigma(\langle R_j\rangle_M t\Delta T^2)\}^{-\frac{1}{2}}.$$

In this form, the relations may be applied either to the data of a single telescope, by summing only over the index i for constant j, or to all of the data by summing over both i and j. These relations are based on the assumption that the only significant errors are the random statistical fluctuations of the (corrected) numbers of counts. Following that assumption, the standard errors are given by $\epsilon_\alpha=\{\sum(\langle R_j\rangle_M t\Delta T^2)\}^{-\frac{1}{2}}$.

Of the thirty entries in Table I, one of them (in parentheses) exhibits a very improbable fluctuation: 3.5 standard errors even if there is no temperature effect, and 4.3 standard errors in view of the likely value of α. The probability of obtaining such a point among thirty samples is very small. It is not clear whether the entry represents an instrumental fault or a rare statistical fluctuation; but in either case, the point would exert abnormal influence on the calculated results if it were included. Including this point, the value of α obtained from all the data in Table I is $\alpha=0.22\pm0.12$ percent per deg C, and the correlation coefficient is $r=0.26$; excluding this point, which we consider gives a more probable result, $\alpha=0.33\pm0.12$ percent per deg C, and $r=0.44$.

In Fig. 1, the data obtained in months of nearly equal mean temperature have been combined, and summed over the three telescopes; the deviations of the counting rates from the 10-month average being plotted against the deviations of the temperature.

An estimate of the accuracy of the monthly averages of T_{eff} has been made on the basis of the differences between the values of T_{eff} obtained from measurements at the three stations, Rome, Buffalo, and Hempstead. On this basis, the rms error in the values of T_{eff} for single months, using the data of a single station, is is 0.58°C, and the expected rms error in the weighted average of the three stations is 0.35°C. The deviations included in this computation arise not only from errors of measurement during the balloon flights, but from sampling different days of the month at the different stations, and from real variations of temperature over the distance (about 350 miles) between the most distant stations. All of these factors enter also into the possible error in the assumed temperatures of

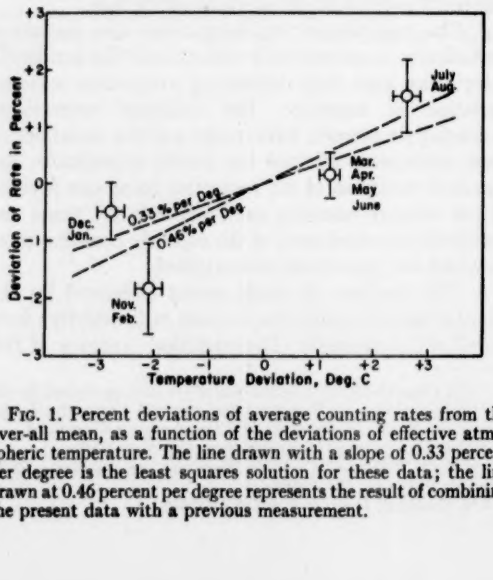

FIG. 1. Percent deviations of average counting rates from the over-all mean, as a function of the deviations of effective atmospheric temperature. The line drawn with a slope of 0.33 percent per degree is the least squares solution for these data; the line drawn at 0.46 percent per degree represents the result of combining the present data with a previous measurement.

the atmosphere over the salt mine. Because of the central location of the mine between the weather stations, the estimate of 0.35°C. for the rms error in T_{eff} is probably generous. Inclusion of this in the error calculation raises the standard error in α by only four percent.

The subtraction of accidental coincidences leads to another small increase of the statistical error in α, namely, by a factor 1.03. With these considerations, the result of the analysis based on the seasonal temperature variation is given as $\alpha=0.33\pm0.13$ percent per degree.

A test for the existence of deviations due to other causes than random statistical fluctuations and the temperature effect is given by the sum of the squares of the residual deviations relative to their statistical standard errors. Excluding the one entry discussed above, the 29 remaining entries in Table I yield 28 for the sum, in good agreement with the expected value 26 ± 7. This agreement suggests that the deviations not due to the simple statistical errors are comparatively small.

The above discussion relates entirely to the determination of α based on the seasonal temperature variation. In addition, the following method, based on short-term fluctuations, was applied. Each time there was a successful balloon flight reaching at least the 30 millibar level, the temperature measurement was assumed to be correct for a six-hour interval centered about the time of the balloon flight; and the numbers of counts recorded in that period were tabulated. The data for such periods were arranged in time sequence, and α was computed from the relation $\alpha=\sum(\Delta n\Delta T)/\sum(\langle n\rangle_{Av}\Delta T^2)$, where Δn is the difference between the numbers of counts recorded in two successive periods, and ΔT the corresponding difference in temperature.

In this method of analysis, the seasonal variation of temperature has practically no effect; and a slow drift of the efficiency of the apparatus or the resolving time for chance coincidences is of no importance. However, the periods were such as to include only 45 percent of all the coincidences that were usable in the analysis of the seasonal temperature effect; and the rms temperature variation between successive intervals was smaller than the seasonal temperature variation; hence the statistical error obtained by the use of short-term fluctuations is comparatively large.

The result obtained by this method is $\alpha=0.42\pm0.46$ percent per deg C. This determination would not be significant in itself, but by agreeing well with the result of the first analysis it adds a little weight to the latter.

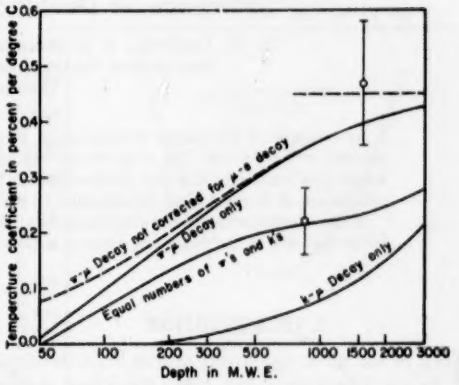

FIG. 2. Temperature coefficients measured at 1574 m.w.e. and 846 m.w.e. (Sherman, reference 2), compared with predicted variations of the coefficient with depth, calculated under different assumptions as to the mode of origin of the mesons (see reference 1).

There have thus been three independent measurements of the temperature coefficient at 1574 m.w.e.: the results being 0.79 ± 0.20,[1] 0.33 ± 0.13, and 0.42 ± 0.46 percent per deg C. The weighted average of these is: $\alpha=0.46\pm0.11$ percent per degree. This value is represented in Fig. 2 along with calculated curves of α *vs* depth underground, taken from reference 1. Also shown on the graph is the point obtained by Sherman[2] at 846 m.w.e.

It may be observed that the measurements at 846 and 1574 m.w.e. are in reasonable agreement with each other, considering the standard errors; and that both could be consistent with μ mesons of high energy ($3\times10^{11}-10^{12}$ ev) being generated only by decay of π mesons. They could also be consistent with generation by $\pi-\mu$ and $\kappa-\mu$ decay involving roughly equal numbers of π's and κ's; but not with an origin entirely by $\kappa-\mu$ decay unless the lifetime assumed for this process (2×10^{-9} sec) was too short. The uncertainty of the parameters of the $\kappa-\mu$ decay process at the present time must be emphasized, however; and the only definite conclusion that can yet be drawn from these experiments is that production of μ mesons of $\sim10^{12}$ ev still involves a decay process as it does at lower energy, the average ratio of lifetime to mass of the parent particles being not very different from that of the π meson.

Evidence for Double Production of V^0 Particles*†

R. W. THOMPSON, J. R. BURWELL, R. W. HUGGETT, AND C. J. KARZMARK
Department of Physics, Indiana University, Bloomington, Indiana
(Received June 7, 1954)

An example of the double production of V^0 particles is described and interpreted as evidence for the process: $\pi^-+p\rightarrow\Lambda^0+\theta^0$. The Λ^0 and θ^0 are well identified from analysis of their decays in the chamber, from which $Q(\Lambda^0)=37\pm4$ Mev and $Q(\theta^0)=223\pm10$ Mev. The nature of the incident particle is suggested by calculation of its mass from the observed V^0-particle momenta.

If the interpretation of the event is correct, the spin of the θ^0 is determined to be integral and the possibility that one of the decay fragments is a muon is excluded. We therefore have $\theta^0\rightarrow\pi^++\pi^-$.

I. INTRODUCTION

ONE of the most significant results from the Brookhaven Cosmotron has been the clear evidence obtained by Shutt and his collaborators for the production of heavy unstable particles in pairs. Working with a pressurized hydrogen diffusion magnet chamber exposed to the 1.5-Bev π^- beam, these authors have found four examples indicating, directly or indirectly, the simultaneous production of a V^0 particle and a K^0 particle in an elementary (π^-,p) collision. In case D,[1] the entire process, including the decay of both neutral particles, is seen in the gas of the chamber. In cases A and B,[2] the (π^-,p) collision and the V^0 decay are seen, and the simultaneous production of a K^0 is inferred by application of the conservation laws. In case C,[1] a V^0 decay and a K^0 decay are seen in the same photograph, and their simultaneous production in the bottom wall of the chamber is strongly suggested.

The argument that one of the products is a neutral hyperon is based on mass determination of the positive decay fragment which is distinctly heavily ionizing in all four cases. The mass values derived from momentum and ionization estimates are consistent with the proton mass. Furthermore, the $Q(p,\pi)$ values, when they can be directly determined from measured momenta (cases A and C give $Q=51$ and 54 ± 20 Mev, respectively), are compatible with the cosmic-ray mean value of 37 ± 1 Mev[3] for the normal Λ^0. Thus, although the quoted errors do not entirely exclude the possibility that the heavy neutral product is one of the types reported by Leighton *et al.*,[4] the most likely possibility is that it is, in fact, a normal Λ^0, as observed in cosmic radiation.

The identification of the K^0 meson is perhaps less unambiguous. In cases A and B, in which the K^0 decay is not observed, the best estimate of the K^0 mass is indirectly obtained from the known π^- beam energy and from the angular orientation of the V^0 fragments, with the assumptions that the V^0 is a normal Λ^0 and that the K^0 and the Λ^0 are the only particles produced in the process. The resulting masses in the two cases are $(1350\pm70)m_e$ and $(1280\pm80)m_e$, respectively. Both are somewhat higher than, although perhaps not entirely incompatible with, the θ^0 mass of $(966\pm10)m_e$ determined from cosmic-ray observations.[3,5] However, in both events, as these authors are careful to point out,[2] it is possible to balance energies and momenta if it is assumed that two neutral particles (one of which may be a π^0) are produced in addition to the Λ^0.

In case C, low upper limits for the masses of both K^0 decay fragments can be set. The directly determined $Q(\pi,\pi)$ value is 271 ± 30 Mev; again somewhat higher than the cosmic-ray value of 214 ± 5 Mev, although much lower than the results for cases A and B which correspond to $Q(\pi,\pi)$ values of 410 ± 35 Mev and 375 ± 40 Mev, respectively.[6] In case D, none of the tracks permits good direct measurement, so the momenta are indirectly derived from the π^- beam energy and the angles, again under the assumptions that the only products of the reaction are the two V^0 particles which are observed to decay, etc. The result is $Q(p,\pi)=27\pm11$ Mev for the V^0 and $Q(\pi,\pi)=258\pm41$ Mev for the K^0. Again the $Q(\pi,\pi)$ is a little high, and in this case the $Q(p,\pi)$ is a little low; but in view of the quoted errors, both are compatible with the cosmic-ray results for the Λ^0 and θ^0.

II. DESCRIPTION OF EVENT *R*-530

In the experiment with the large magnetic chamber,[3] triggered by cosmic-ray penetrating showers, we have obtained a photograph showing two V^0 events, which is similar to the Brookhaven examples described above. If that identification is correct, the event confirms the Brookhaven work and in addition provides clarification as to the specific nature of the neutral unstable particles which are produced.[7]

* Assisted by the U. S. Office of Ordnance Research and by grant of the Frederick Gardner Cottrell Fund of the Research Corporation.

† A report of this work was given at the Washington meeting of the American Physical Society, 1954 [Phys. Rev. 95, 661(A) (1954)].

[1] Fowler, Shutt, Thorndike, and Whittemore, Phys. Rev. **93**, 861 (1954).

[2] Fowler, Shutt, Thorndike, and Whittemore, Phys. Rev. **91**, 1287 (1953).

[3] Thompson, Buskirk, Etter, Karzmark, and Rediker, Phys. Rev. **90**, 329 (1953).

[4] Leighton, Wanlass, and Anderson, Phys. Rev. **89**, 148 (1953).

[5] See the report of the Indiana group at the Fourth Rochester Conference on High Energy Physics (University of Rochester Press, Rochester, to be published).

[6] These Q values were computed from the K^0 masses given in reference 2, assuming $m_\pi c^2=139.7$ Mev.

[7] Since event *R*-530 was reported at the Washington meeting, we have learned from Dr. Thorndike that the estimate of the

The photograph (film No. *R*-530) is shown in Fig. 1. The two decay apexes, (1,2) and (3,4), are well-illuminated although near the top of the chamber. The tracks of the four decay fragments are the only tracks in the photograph, except for track 5 which is spatially unrelated. Tracks 2 and 3 pass out of the illuminated region at the front, and track 1 passes out to the rear. Fortuitously, all four curvatures can be fairly well determined as may be judged from the comparator plots in Fig. 2 and Fig. 3. The curvature and angle data have been reduced by the new least-squares methods developed for this large chamber,[8] and the results for the two V^0 events are given in Table I.

In addition to the data in Table I, the observed ionizations provide information as to the nature of the

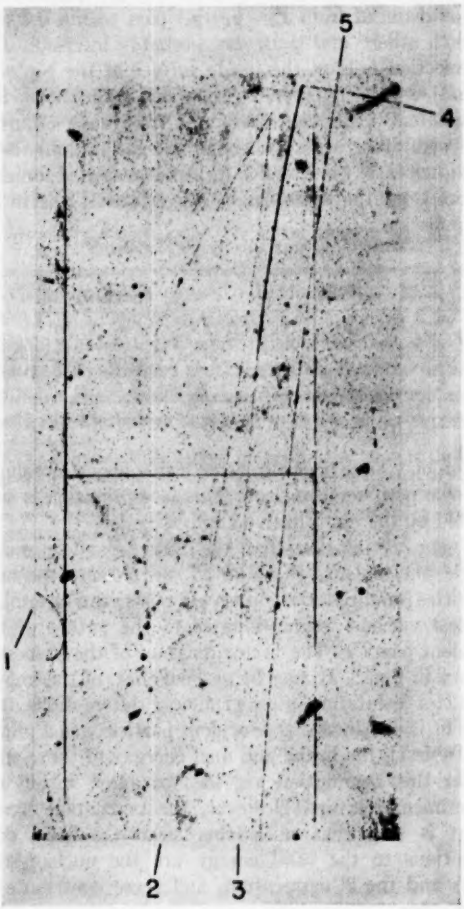

FIG. 1. Right eye view of *R*-530.

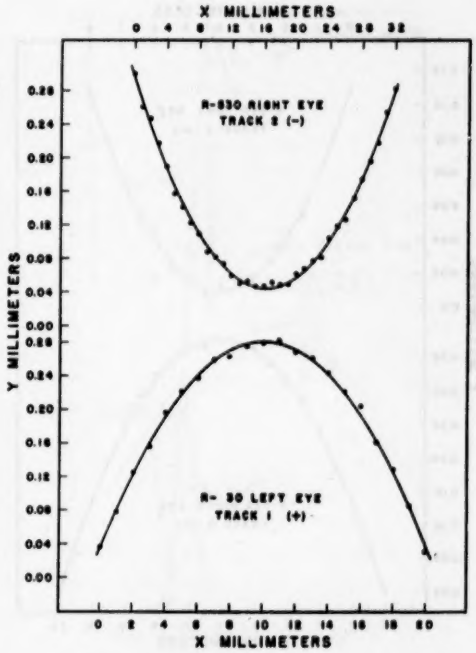

FIG. 2. Comparator plot of positive and negative fragments from decay (1,2) in *R*-530.

fragments. The estimated ionization of track 3 is from 6 to 10 times the minimum value, to be compared with factors of 7 and 2.8 to be expected for a proton and a K meson ($970m_e$) of this momentum, respectively. Thus the ionization of track 3 is consistent with the proton mass, but is a little too heavy to favor the K-meson mass. The ionization of track 4 appears to be a little more than, but certainly less than 3 times, the minimum value. A pion of this momentum would be heavily ionizing by a factor 2. Thus the estimated ionizations of tracks 3 and 4 together with the $Q(p,\pi)$ value given in Table I fairly well identify the decay (3,4) to be that of a Λ^0 where the Q of 37 ± 4 Mev is limited in this case to a sufficiently narrow interval that anomalous values of 10 or 75 Mev[4] are probably excluded.

The ionizations of tracks 1 and 2 are apparently at or near the minimum value and thus are less informative. The identification of decay (1,2) is therefore based

TABLE I. Basic data on the two V^0 events.

Track	Event (1,2) 1	Event (1,2) 2	Event (3,4) 3	Event (3,4) 4
Charge	+	−	+	−
Momentum (Bev/c)	0.35 ± 0.01	0.94 ± 0.04	0.30 ± 0.02	0.106 ± 0.008
Angle between tracks	$40.4\pm0.2°$		$88.1\pm0.2°$	
V^0 momentum (Bev/c)	1.23 ± 0.05		0.32 ± 0.02	
α	-0.512		$+0.758$	
p_T (Bev/c)	0.172		0.099	
Q value (Mev)	$Q(\pi,\pi)=223\pm10$		$Q(p,\pi)=37\pm4$	
V^0 identity	K^0		Λ^0	

π^--beam kinetic energy at Brookhaven has been revised from 1.5 Bev down to 1.37 Bev. The effect of this revision is to reduce the $Q(\pi,\pi)$ values of the K^0 in Cases *A*, *B*, and *D* to 375, 330, and 233 Mev, respectively.

[8] Thompson, Buskirk, Cohn, and Karzmark, Proceedings of the Bagnères Conference, Report No. *A*-3, 1953 (unpublished).

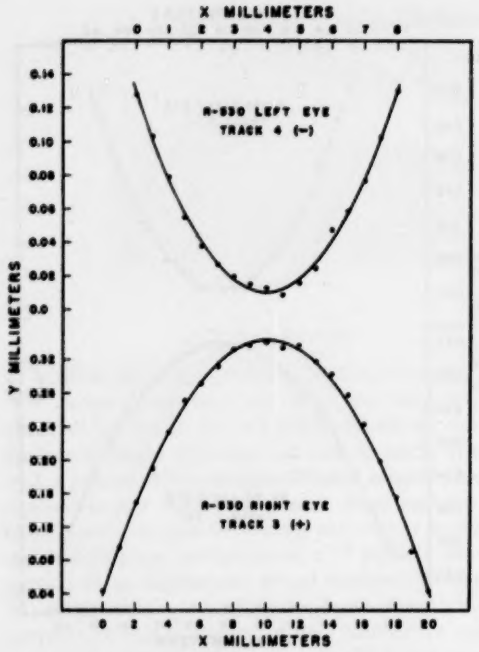

FIG. 3. Comparator plot of positive and negative fragments from decay (3,4) in *R*-530.

on the dynamics of the decay. The fact that the $Q(\pi,\pi)$ value of 223±10 Mev, from Table I, is very near the mean value of 214±5 Mev for the θ^0 is a necessary but not a sufficient condition that decay (1,2) be a θ^0. The possibility of identification with various other decay schemes may be tested by computation of Q values for the various appropriate fragment masses.

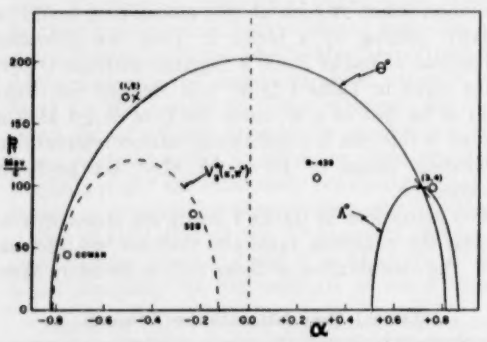

FIG. 4. Q-curve plot (for $\beta=1$) showing the relationship of decays (1,2) and (3,4) to various decay schemes. The solid curves are drawn for $\Lambda^0\rightarrow p+\pi^-+37$ Mev and $\theta^0\rightarrow\pi^++\pi^-+214$ Mev. The dashed curve is drawn for $V_2^0\rightarrow K^-+\pi^++60$ Mev (see reference 4). The coordinates of the circles are the observed values of p_T and α. In addition, for decays (1,2) and (3,4), crosses are plotted showing the computed displacement of the circles for $\beta\rightarrow 1$. Events No. 328 and *R*-439 are the anomalous events reported by the Indiana group (see references 3 and 5). The point at the lower left-hand corner of the plot is the event found by E. W. Cowan [Phys. Rev. 94, 161 (1954)].

A more revealing procedure is to make the comparison in terms of the Q-curve plot[3] as shown in Fig. 4. It is seen that decay (1,2) falls very near the θ^0 curve,[9] in a position which corresponds to a relatively probable angle of emission in the center-of-mass system. However, the position is such that identification of decay (1,2) with other decay schemes or isolated anomalous points is not suggested by the data.

III. ANALYSIS AS DOUBLE PRODUCTION

The relative orientation of the two neutral decays suggests that the Λ^0 and θ^0 were produced in the same interaction. A copunctuality test may be applied here since all four decay fragment momenta are directly measured. The result is that the lines of flight of the θ^0 (as deduced from the vector sum $\mathbf{P}_\theta=\mathbf{p}_1+\mathbf{p}_2$) and the Λ^0 (as deduced from $\mathbf{P}_\Lambda=\mathbf{p}_3+\mathbf{p}_4$) pass within 0.2 mm of each other[10] and thus very probably intersect. The intersection falls at the inside surface of the top wall (brass) of the chamber, with an uncertainty of a few millimeters. Thus the interaction may have occurred just within the brass wall or in the gas (argon) itself. In either case, the absence in the chamber of ionizing tracks from the same origin suggests that the interaction may have been a relatively simple one, involving a single peripheral nucleon. This interpretation is supported by the quantitative analysis below.

TABLE II. Energy balance for pion incidence.

Initial energy (Bev)	Final energy (Bev)
$E_\pi=1.53$[a]	$E_\Lambda=1.16$
$m_pc^2=0.94$	$E_\theta=1.32$
$E_\pi+m_pc^2=2.47\pm0.05$	$E_\Lambda+E_\theta=2.48\pm0.05$

[a] This figure is the total energy of a pion of momentum $\mathbf{P}=\mathbf{P}_\Lambda+\mathbf{P}_\theta$.

Under assumption that the target particle was a single nucleon and that the Λ^0 and θ^0 were the only particles produced, the conservation laws can be applied to test various assumptions as to the nature of the incident particle. The vector diagram of the process is shown in Fig. 5. It may be verified that, of the known particles exhibiting strong nuclear interactions, the best fit is obtained if the incident particle was a pion.[11] In Table II, the initial and final energies of the system under this assumption are seen to agree within the experimental errors. However, the percentage agreement is somewhat misleading since the main contributions to the total energy are the nucleon rest mass and the θ^0 momentum, and these contribute to

[9] This is anticipated since the Q value is close to the mean of 214 Mev, for which the θ^0 curve in Fig. 4 is drawn.

[10] The figure of 0.2 mm is fortuitously small since the errors from the momenta and the reconstruction process are several times as large.

[11] The incident pion may easily have been produced in a nuclear interaction in the absorber (8 in. of copper) immediately above the chamber without other products of that interaction being visible in the chamber.

both the initial and final energies in essentially the same way. Also, for the same reason, the errors in the initial and final energies given in Table II are not independent.

An alternate method which is considerably more sensitive is to compute the mass of the incident particle, although it is clear that the value so obtained will be rough since the incident particle is quite relativistic. From the equation

$$mc^2=\{[(P_\Lambda^2c^2+M_\Lambda^2c^4)^{\frac{1}{2}}+(P_\theta^2c^2+M_\theta^2c^4)^{\frac{1}{2}}-m_pc^2]^2 - |\mathbf{P}_\Lambda+\mathbf{P}_\theta|^2c^2\}^{\frac{1}{2}},$$

and from the data in Table I and Fig. 5, we find $mc^2=0.27\pm0.13$ Bev,[12] which is easily compatible with the pion rest energy.

Thus, with the reservations stated above, the most likely interpretation of the event is the double-production process:

$$\pi^-+p\rightarrow\Lambda^0+\theta^0. \quad (1)$$

In the center-of-mass system, the Λ^0 was emitted in the backward direction at an angle of 168° with the direction of the incident pion. In the laboratory system, the decay planes of the Λ^0 and θ^0 make angles of 26.5° and 10.6°, respectively, with the production plane.

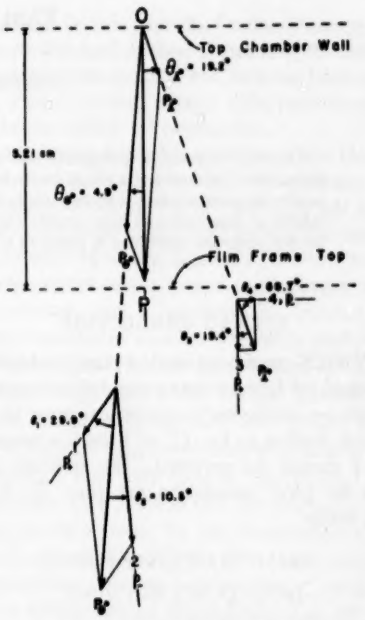

FIG. 5. Vector diagram of *R*-530.

IV. THE SPIN AND DECAY SCHEME OF THE θ^0 MESON

Although it has generally been assumed that the θ^0 decays into two pions (instead of a π and a μ) and therefore has integral spin, neither fact has ever been proved. The Indiana work based on dynamic analysis indicates that the θ^0 decay is a two-body process in which both fragments are L mesons (π or μ).[13] Actually, the dynamic data favor the pion mass for both fragments but this conclusion is not entirely firm. However, there is good evidence that one of the fragments is a pion. For example, the Paris group[14] reports 3 nuclear interactions induced by θ^0 secondaries. Also there is one Indiana event in which the positive fragment undergoes π-μ decay. We have therefore $\theta^0\rightarrow\pi^\pm+(\pi^\mp$ or $\mu^\mp)$.

However, if Eq. (1) is correct, the spin of the θ^0 must be integral and therefore both decay fragments must be pions, $\theta^0\rightarrow\pi^++\pi^-$.

[12] The motion of the target nucleon in the nucleus (brass or argon) introduces additional uncertainty in the value of mc^2 so derived, although the most likely situation is that the nucleon is moving at right angles to the incident pion in which case the effect is inappreciable.

[13] Thompson, Buskirk, Cohn, and Karzmark, Proceedings of the Bagnères Conference, Report No. *B*-2, 1953 (unpublished).

[14] Gregory *et al.*, Proceedings of the Bagnères Conference, p. 35, 1953 (unpublished).

Pion Production Ratios. II

D. C. PEASLEE
Columbia University, New York, New York
(Received June 7, 1954)

The ratio of positive to negative pion production is considered for protons of ~0.35-Bev energy incident on nuclei. The model of a single excited nucleon is used. It is argued that (i) at these energies the meson-producing nucleon state is about equally likely to be $T=\frac{1}{2}$ or $T=\frac{3}{2}$; (ii) structural effects in the final nucleus inhibit π^- production in light nuclei, where isotopic spin is conserved. Effect (ii) may be partly responsible for the observed difference in shape of π^+ and π^- production curves as a function of A.

I. $T=3/2$ PRODUCTION

PREVIOUS considerations[1] of pion production ratios around 1.5 Bev are here extended to lower energies. We begin by correcting[2] a numerical error in I: in the paragraph leading to Eq. (1) of I the fractional weights $\frac{3}{4}$ and $\frac{1}{4}$ should be reversed. The over-all fractional weights for pion production are then ($\frac{3}{8}$, $\frac{1}{8}$, 0), and Eq. (1) reads

$$\begin{aligned}(\pi^+):&\quad (1/15)[26\sigma_2{}^s+25\sigma_1{}^s],\\ (\pi^0):&\quad (1/15)[28\sigma_2{}^s+5\sigma_1{}^s],\\ (\pi^-):&\quad (1/15)[6\sigma_2{}^s].\end{aligned}\tag{C1}$$

Equation (2) is unchanged, but the corrected Eq. (3) reads

$$\begin{aligned}(\pi^+):&\quad [1.28\sigma_2{}^s+0.83\sigma_1{}^s+0.37\sigma_2{}^a],\\ (\pi^0):&\quad [0.90\sigma_2{}^s+0.52\sigma_1{}^s+0.37\sigma_2{}^a],\\ (\pi^-):&\quad [0.70\sigma_2{}^s+0.09\sigma_1{}^s+0.37\sigma_2{}^a].\end{aligned}\tag{C3}$$

These changes do not alter the essential conclusions of I: ρ is unchanged for $\sigma_2 \gg \sigma_1$ and is increased from 6 to 9 when $\sigma_1 \gg \sigma_2$. The remarks about π^0 production should be deleted.

II. $T=1/2$ PRODUCTION

A number of measurements have been made[3-7] of the ratio $\rho=\pi^+/\pi^-$ at a specific angle of production, using incident protons of 340–380 Mev. For light target nuclei (Be excepted) the values of ρ are large, of order 10 for C and Al, and even larger for D. Among heavy nuclei (Pb, Ag, Cu), ρ drops to around 5, even for $E_p=40$ Mev[5] where the pion emission should not be appreciably affected by nuclear Coulomb barriers. Among the light targets Be is exceptional in having $\rho \sim 5$ like the heavy nuclei.

The part of the pion production that occurs through the resonant $T=\frac{3}{2}$ state is predominantly due to single-nucleon excitation at $E^p \sim 1$ Bev,[1] and should be even more so at $E^p \sim 0.35$ Bev. This type of production has $\rho(3/2) \approx 10$, which is appreciably larger than the value observed for heavy nuclei. The simplest modification of the model is to assume that some production occurs through a $T=\frac{1}{2}$ excited nucleon state; such production has $\rho(1/2) \approx 3$. Let $\bar{\rho} \approx 5$ be the measured ratio for a heavy nucleus, and $\pi(3/2)$, $\pi(1/2)$ the total pion production (all charges) proceeding through single excitation of a nucleon to a $T=\frac{3}{2}$ or $T=\frac{1}{2}$ state. For proton bombardment of a nucleus with Z protons and N neutrons, the procedure of reference 1 yields

$$\frac{\pi(3/2)}{\pi(1/2)}=\left\{\frac{2Z+N}{\lambda Z+N}\right\}\left\{\frac{\bar{\rho}-\rho(1/2)}{\rho(3/2)-\bar{\rho}}\right\},\tag{1}$$

$$\lambda=2\sigma_1{}^{s\prime}/(\sigma_1{}^{s\prime}+\sigma_1{}^{a\prime}).$$

Here the $\sigma_1{}'$ are cross sections for single excitation of a nucleon to a $T=\frac{1}{2}$ state in an $n-p$ collision; the superscripts s, a denote respective compound states of $T=1, 0$.

In lieu of any information on the subject, we assume $\lambda \approx 1$. Then for a heavy nucleus with $Z=0.8N$, $\rho(1/2)=2.6$, and by Eq. (C3) $\rho(3/2)=9.2$. Substitution of these values with $\bar{\rho}=5$ into (1) yields

$$\pi(3/2)/\pi(1/2) \approx 0.8.\tag{2}$$

Result (2) is compatible with the high-energy results indicating $\pi(3/2) \gg \pi(1/2)$, if the $\pi(3/2)$ excitation is assumed to be resonant at some energy above that generally reached by $E_p \approx 0.35$-Mev protons, while the $\pi(1/2)$ excitation is not. This is in accord with the observations on π-nucleon scattering.

III. LIGHT NUCLEI

The enhancement of ρ for light nuclei at the same E_p must now be attributed to structural effects in these nuclei: in particular, to the validity of isotopic spin as a quantum number for initial and final states, and the strong dependence of nuclear binding energy on this quantum number. Pion production increases rapidly with proton energy around $E_p=0.35$ Bev.[8] This implies that the initial production process (regardless of subsequent meson scattering or absorption in the nucleus)

[1] D. C. Peaslee, Phys. Rev. **94**, 1085 (1954); hereafter referred to as I.
[2] H. A. Bethe (private communication).
[3] Block, Passman, and Havens, Phys. Rev. **88**, 1239 (1952).
[4] J. Carothers and C. G. Andre, Phys. Rev. **88**, 1426 (1952).
[5] R. Sagane, Phys. Rev. **90**, 1003 (1953).
[6] S. L. Leonard, Phys. Rev. **93**, 1380 (1954).
[7] W. F. Dudziak, Phys. Rev. **94**, 756 (1954).
[8] Passman, Block, and Havens, Phys. Rev. **88**, 1247 (1952).

tends to concentrate most of the available energy in the meson and leave the residual nucleus in a state of low excitation. Consider the final state of the nucleus (bound or unbound) after emitting the π but no nucleons. If the initial light nucleus had $T=0$ in its ground state ($N=Z$), the final nuclear state will have $T=\frac{1}{2}, \frac{3}{2}$ for π^+ emission, but $T=\frac{3}{2}$ only for π^- emission. For light, odd-A nuclei, however, the lowest $T=\frac{3}{2}$ state lies above the lowest $T=\frac{1}{2}$ state by $\Delta(\frac{3}{2}, \frac{1}{2})\approx 10$ Mev.[9] Thus the low-lying residual states have a preponderance of $T=\frac{1}{2}$ levels, which will tend to inhibit π^- production and increase the value of ρ.

This mechanism of π^- inhibition should be most effective for production from deuterium: here $\Delta(\frac{3}{2}, \frac{1}{2})$ presumably has a maximum value, and the center-of-gravity energy is the lowest for a given E_p. The observations agree with this expectation: ρ achieves its largest values for D; and, even more satisfactory, it increases rapidly with E_π for fixed E_p.[4]

The above argument for light nuclei is special to targets with $T=0$. For light, odd-A targets with $N=Z+1$, both π^+ and π^- emission lead to nuclear states with $T=1, 2$ that differ only by Coulomb energy. For a light nucleus the Coulomb difference should be small, so that ρ would approach the uninhibited value. This is in agreement with the observations on Be.

An Al target, on the other hand, shows a relatively high value of ρ. In this case the Coulomb energy difference between the final nuclear states is $\gtrsim 10$ Mev, even though isotopic spin appears not to have broken down seriously. This Coulomb energy difference is again in the direction to inhibit π^- production.

These arguments for light nuclei indicate that with protons on $N=Z+1$ target nuclei π^0 production should be considerably enhanced for $A=4n-1$ target but not for $A=4n+1$, because[9] the $\Delta(1, 0)$ of the final nuclei are of order 15 and 0 Mev, respectively.

For heavy nuclei isotopic spin is no longer a good quantum number, and a tendency to balance exists between the energies of nuclear symmetry and of Coulomb repulsion. The residual nuclei from π^+ and π^- emission have relatively small energy differences in their ground states—of order 4, 3, and 2 Mev for Cu, Ag, and Pb targets. Structural effects of heavy nuclei therefore provide relatively little π^- inhibition.

The inhibition of π^- production by protons on light nuclei may partly account for the observation that π^- production increases more steeply with target number A than π^+ production. Among light nuclei, π^- production should show strong isotope dependence (e.g., B^{10}, B^{11}); no such dependence is expected for π^+ production, and none has been found.[10]

[9] For notation see D. C. Peaslee, Phys. Rev. **95**, 717 (1954).

[10] J. Merritt, University of California Radiation Laboratory Report UCRL-2424, 1953 (unpublished).

PHYSICAL REVIEW VOLUME 95, NUMBER 6 SEPTEMBER 15, 1954

Phase Shift Analysis of the Scattering of Negative Pions by Hydrogen*

E. FERMI, *Institute of Nuclear Studies, University of Chicago, Chicago, Illinois*

AND

N. METROPOLIS AND E. FELIX ALEI, *Los Alamos Scientific Laboratory, Los Alamos, New Mexico*

(Received May 6, 1954)

A phase shift analysis of the scattering of negative pions by hydrogen in the range 115 to 215 Mev is presented. In the present paper two solutions are given that represent the data within the experimental error by two rather different sets of phase shifts. One of these solutions is excluded on the basis of some information on the scattering of positive pions. The other solution is compatible with all the experimental data known at present. It is pointed out, however, that this is not the only solution that has such properties. In addition, calculations carried out on scattering of positive and negative pions at 61.5 Mev are presented.

I. INTRODUCTION

THIS paper describes some systematic attempts to analyze in terms of phase shifts the experimental data on pion-hydrogen scattering.[1,2] Two essentially independent calculations are described. Part 1 is concerned with the analysis of the experimental results of B[1] on the scattering of negative pions in the energy range 115 to 215 Mev. These calculations that are now being published have been completed during the spring and summer of 1953 and have been circulated privately. In the intervening period there have been a number of other attempts at interpreting essentially the same data.[3]

* Research supported by a joint program of the U. S. Office of Naval Research and the U. S. Atomic Energy Commission.

[1] Anderson, Fermi, Martin, and Nagle, Phys. Rev. **91**, 155 (1953), quoted as A; Fermi, Glicksman, Martin, and Nagle, Phys. Rev. **92**, 161 (1953), quoted as B.

[2] Bodansky, Sachs, and Steinberger, Phys. Rev. **90**, 997 (1953); **93**, 918, 1367 (1954).

[3] M. Glicksman, Phys. Rev. **94**, 1335 (1954); R. Martin, this issue [Phys. Rev. **95**, 1583 (1954)]; and in particular de Hoffmann, Metropolis, Alei, and Bethe, following paper [Phys. Rev. **95**, 1563 (1954)], where the calculations presented in this paper are extended and attempts are made to choose one out of several possible solutions.

We refer to Fig. 1 of B where the experimental results are summarized. From this figure one can see that the charge exchange scattering apparently goes through a maximum somewhat below 200 Mev, and also that at about the same energy the angular distribution of this process changes from being mostly backward to being mostly forward. It has been suggested[4] that some features of the pion-nucleon scattering and of the pion photoeffect may indicate the existence of a resonance level in a state of isotopic spin $\frac{3}{2}$ and ordinary spin $\frac{3}{2}$ at approximately this energy. The features of the negative pion scattering in the vicinity of 200 Mev might be due to the effect of this hypothetical resonance level. For this reason it appeared worthwhile to see whether a phase shift analysis of the data would support the hypothesis of the existence of such a level. The solutions obtained in the present paper do not show this resonance level; however, solutions that are compatible with the existence of such a resonance are quoted in reference 3.

In Sec. IV we describe the phase shift calculations carried out on the experimental data of Bodansky, Sachs, and Steinberger[2] at 61.5 Mev. These authors suggested that we analyze their data to confirm their earlier calculations and to search for other solutions, as well as to determine the sensitivity of the analysis to small deviations in the phase shifts. We are indebted to them for the preparation of the data and for several useful discussions. For these relatively low pion energies, it is necessary to include a term corresponding to the Coulomb scattering.

After this work was completed, a preprint of a paper by Homa, Goldhaber, and Lederman[5] was received. In this work some results on the scattering of positive pions by hydrogen at 151 and 188 Mev are given. Other results on total cross sections of positive pions have been reported by Ashkin, Blaser, Stern, Gorman, and Feiner.[6] The relationship of these results with the results of the present calculation will be discussed at the end of this paper.

There are two reasons why a phase shift analysis of the experimental data presented in B is not very reliable. One is that only experimental results on the scattering of negative pions were available when this calculation was undertaken. Therefore there is no check of a set of phase shifts on the joint behavior of positive and negative pions. The second is that with our present experimental information it is impossible to include in the phase shift analysis any contribution of the d levels. Neglecting the d-level phase shifts is probably allowable at low energies, but becomes less plausible at higher energies where the relative de Broglie wavelength of the pion-nucleon system becomes appreciably smaller than the Yukawa radius.

For these reasons, the phase shift analysis of the Chicago data here presented may be seriously in error. It should be noted that the ambiguity is somewhat reduced by the fact that some results on the positive pion cross section have now become available, but even when these data are included some considerable ambiguity remains in the interpretation. These ambiguities are discussed in the following paper[3] where an attempt is made to arrive at the choice between the various possibilities on the basis of certain theoretical hypotheses.

II. THE MATHEMATICAL PROBLEM

The general procedure followed in the computation of the phase shifts for the s- and p-waves has already been described in A.[1] We elaborate on that discussion and remark on two variants in the method; the simplification for the analysis of the Columbia data[2] at lower energy is also discussed. At a given energy the differential cross sections for all the scattering processes,

$$\pi^+\rightarrow\pi^+, \quad \pi^-\rightarrow\pi^-, \quad \text{and} \quad \pi^-\rightarrow\pi^0\rightarrow 2\gamma, \tag{1}$$

are expressed in terms of the six phase shift angles of the s- and p-waves of isotopic spins $\frac{3}{2}$ and $\frac{1}{2}$. For these six angles, we use the same notation of A and we indicate them by α_3, α_1, α_{33}, α_{31}, α_{13}, α_{11}. In the phase shift calculations described in A, differential cross sections were available for the three processes (1), each measured at three different angles.

At a point in the six-dimensional space of the phase shifts, one can compute the above-mentioned nine cross sections using the formulas given in A (Sec. X). Then one can evaluate the function

$$M(\alpha_3, \alpha_1, \alpha_{33}, \alpha_{31}, \alpha_{13}, \alpha_{11}) = \sum_{i=1}^{9} (\Delta i/\epsilon_i)^2, \tag{2}$$

where Δ_i is the difference between the experimentally measured and the computed cross section, and ϵ_i is the corresponding experimental error. The value of M is a measure of the approximation to the nine experimental data. The mathematical problem then is to explore the six-dimensional space for the minimum (or minima) of the function M.

With the use of the Los Alamos electronic computer, the MANIAC, two methods were used. In the first, one starts at some point and proceeds along the first coordinate axis, α_3, in steps of, say, $\frac{1}{2}°$ until a minimum is reached. Then one moves along the second axis, and so on, until no further improvement is found. The completed procedure is refined by using a smaller step of $\frac{1}{16}°$. In the second method, one first computes the gradient and then proceeds along that direction until a minimum is found. There the gradient is again computed and the process repeated until a (relative) minimum is found. In general, the second method is faster, although in certain instances this was not so, simply because the

[4] K. A. Brueckner, Phys. Rev. **86**, 106 (1952).
[5] Homa, Goldhaber, and Lederman, Phys. Rev. **93**, 554 (1954).
[6] Ashkin, Blaser, Stern, Gorman, and Feiner, quoted by Ashkin at the Fourth Annual Rochester Conference on High Energy Nuclear Physics, January, 1954 (University of Rochester Press, Rochester, to be published).

computation of the gradient is relatively time-consuming.

Under the assumptions stated in A, the differential cross sections may be written

$$d\sigma_n/d\omega = a_n + b_n \cos\chi + c_n \cos^2\chi, \qquad (3)$$

where n corresponds to the three processes (1), and χ is the scattering angle in the center-of-mass system. The coefficients a_n, b_n, c_n are the quantities that are first evaluated for a set of phase shifts. By means of Eq. (3) one finds then the cross section for the various values of χ. An alternate procedure, therefore, is to find a least-squares solution of the coefficients instead of the cross sections. The former may be regarded as the more fundamental quantities, but the experimental errors on them are larger.

For energies up to 135 Mev, experimental results were used for all three processes (1). However, for higher energies, only measurements for the scattering of negative pions were available. The differential cross sections for each of the two processes are measured at three angles. In this case, therefore, the six phase shift angles α_i are determined from six cross sections only, with no internal checking of the procedure being possible. However, for each solution, one can compute the total cross section for the scattering of positive pions and compare with the corresponding experimental value.

At each energy where a computation is made, it is found that, in general, more than one solution exists; i.e., several relative minima of Eq. (2) are reached. In order to correlate a solution at one energy with that at another, use may be made of a continuity principle. One may make a graphical interpolation of the experimental cross sections (or coefficients) and then find a set of solutions to the minimum problem at rather close intervals of energy. The starting point for the search of a minimum at each energy step may conveniently be taken as the solution in the preceding energy step. In this way one chooses a solution that is near the one obtained immediately before. This "tracking" procedure may enable one to select a set of solutions that

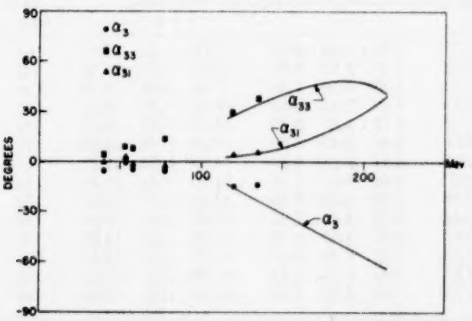

FIG. 1. Phase shifts of the states of isotopic spin $\frac{3}{2}$ plotted *versus* the energy of the primary pion for solution 1. For comparison, values of the same phase shifts at lower energies are also plotted.

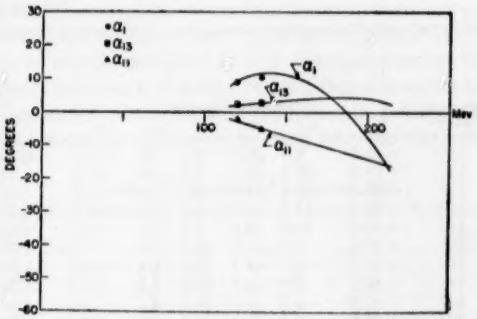

FIG. 2. Phase shifts of the states of isotopic spin $\frac{1}{2}$ plotted *versus* the energy of the primary pion for solution 1. Values previously obtained at 120 and 135 Mev are also plotted.

represents the data within the experimental errors and is consistent with the total positive pion cross sections. It has the advantage to average out in part the very sizable experimental errors.

III. CALCULATIONAL RESULTS FOR THE ENERGY RANGE 115 TO 215 MEV

Results on the phase shifts for the energies of 120 and 135 Mev were given in A. Both positive- and negative-pion measurements were used there. It was found that two sets of almost equivalent solutions, the "first solution" and the "Yang solution" existed.[7] A third minimum was found with a very large value of M, hence a very poor least-squares solution of the problem.

For the higher energies, where only negative-pion cross sections were used, two rather different solutions have been found that correspond to two somewhat different interpolations of the experimental results.

In both calculations we have chosen for the lowest energy a solution close to the "first solution" obtained in A. No attempt has been made in the work described in this paper to investigate the high-energy behavior of the Yang solution. This point is discussed, among others, in the next paper.[3]

The two sets of solutions obtained are presented in Tables I and II, and the first set is shown graphically in Figs. 1 and 2. The first of these solutions actually was obtained by following a somewhat mixed procedure. First, two sets were computed starting from two different graphic interpolations of the experimental data. The corresponding phase shifts were rather similar. They were combined and smoothed out in order to obtain the phase shifts and it was verified that they represent the experimental cross sections within the experimental error.

The second set was obtained from a different interpolation of the experimental data. In this case an analytical interpolation formula was used. This calculation was carried out twice with different analytic interpola-

[7] E. Fermi and N. Metropolis, Los Alamos unclassified report LA-1492, 1952 (unpublished).

TABLE I. First solution.

Energy (Mev)	Phase shifts (degrees) α_{31}	α_{33}	α_{13}	α_{11}	Computed cross sections in the c. m. system corresponding to the laboratory scattering angles 45°, 90°, 135° (10^{-27} cm²/sterad) $-\to-$			$-\to\gamma$			$+\to+$			Total cross section of π^+(10^{-27} cm²)
115	−13.4	8.2	26.0	2.7	1.6	−2.1	0.90	0.41	0.85	1.69	2.86	5.01	3.34	4.42	12.69	75
125	−18.4	10.3	30.6	3.7	2.0	−3.5	1.13	0.53	0.98	2.20	3.74	6.59	4.29	5.70	15.89	95
135	−23.5	11.3	34.9	5.0	2.4	−4.9	1.35	0.65	1.15	2.79	4.50	7.88	5.57	6.84	18.59	115
145	−28.5	11.3	38.9	6.7	2.8	−6.3	1.52	0.76	1.32	3.44	5.03	8.70	7.10	7.67	20.46	133
155	−33.6	10.3	42.6	9.2	3.2	−7.7	1.66	0.85	1.53	4.17	5.35	9.13	8.84	8.16	21.73	149
165	−38.6	8.2	45.8	12.3	3.6	−9.1	1.78	0.92	1.76	4.96	5.48	9.16	10.72	8.36	22.38	163
175	−43.7	5.1	48.3	16.0	4.0	−10.5	1.86	1.00	2.01	5.70	5.36	8.73	12.45	8.16	22.23	173
185	−48.7	0.9	49.8	20.8	4.2	−12.0	1.94	1.09	2.30	6.47	5.12	8.16	14.10	7.72	21.92	181
195	−53.8	−4.2	49.4	26.5	4.2	−13.4	2.05	1.22	4.68	7.02	4.68	7.37	15.19	7.01	21.16	184
205	−58.8	−10.5	46.9	32.6	3.6	−14.8	2.23	1.43	2.74	7.31	4.11	6.45	15.65	6.25	19.81	181
215	−63.9	−17.7	41.0	39.8	2.0	−16.2	2.53	1.70	2.66	7.20	3.46	5.44	15.21	5.68	17.60	170

tion and gave in both cases rather similar results. Only one of them is reported here in detail.

IV. ANALYSIS OF COLUMBIA EXPERIMENT AT 61.5 MEV

Bodansky, Sachs, and Steinberger[2] provided us with the experimental measurements given in Table III. The data represent extrapolations of their measured values to 61.5 Mev from 58 Mev for the positive pions and from 65 Mev for the negative pions. This extrapolation was done in order to have a complete set for both positive and negative pions at a single energy. Thus a least-squares procedure was used for fourteen cross sections. At this relatively low energy it is possible to use somewhat simpler expressions for the cross sections obtained by expanding the exponentials of A, formula (10), and keeping first-order terms. This expansion is permissible because all phase shifts should be small at this energy. It is necessary, however, to include a term for the Coulomb scattering, that is important at low energy.

Two computations were made starting at two points corresponding to approximate solutions of the problem previously obtained by Bodansky, Sachs, and Steinberger. In addition to these, twenty-two computations were made starting at randomly selected points. Seven different solutions were found. These are given in Table IV. The first two are similar to those found by Bodansky, Sachs, and Steinberger.

It is known from purely algebraic considerations that the multiplicity of solutions may be large. With our assumption of small phase shifts, whenever the p-phase shifts for one of the two isotopic spin states, say $T=\frac{1}{2}$, are approximately equal, there exists a twofold multiplicity of p-phase shifts for $T=\frac{3}{2}$.[8] These latter are related as follows:

$$\begin{aligned} 2\alpha_{33}+\alpha_{31}&=2\alpha_{33}'+\alpha_{31}', \\ \alpha_{33}-\alpha_{31}&=\alpha_{31}'-\alpha_{33}', \end{aligned} \tag{4}$$

corresponding to the two multiple sets. These conditions hold approximately for minima 1,2; and 6,7 of Table IV for $T=\frac{3}{2}$; and for 3,4 for $T=\frac{1}{2}$. Minimum 5 shows no

TABLE II. Second solution.

Energy (Mev)	Phase shifts (degrees) α_{31}	α_{33}	α_{13}	α_{11}	Computed cross sections in the c. m. system corresponding to the laboratory scattering angles 45°, 90°, 135° (10^{-27} cm²/sterad) $-\to-$			$-\to\gamma$			$+\to+$			Total cross section of π^+(10^{-27} cm²)
115	−10.9	8.5	23.2	9.8	3.0	−8.2	0.99	0.50	0.73	1.39	2.49	5.03	2.69	2.82	12.26	64
125	−14.0	9.7	33.1	5.1	1.3	−2.8	1.21	0.47	1.04	2.47	3.76	6.76	5.19	5.36	16.62	102
135	−16.5	10.5	39.7	3.8	1.0	−0.4	1.42	0.50	1.32	3.38	4.66	7.86	7.08	6.88	19.29	126
143	−18.5	10.8	44.3	2.8	1.1	0.9	1.56	0.55	1.52	3.99	5.14	8.33	8.40	7.80	20.53	141
155	−17.9	10.7	51.8	1.9	1.5	1.4	1.74	0.66	1.78	4.77	5.47	8.70	10.32	8.53	21.61	159
167	−8.9	10.0	61.6	0.3	1.6	1.4	1.91	0.81	2.01	5.46	5.47	8.50	12.26	8.78	22.00	173
173	−3.3	9.4	66.6	−0.2	1.8	1.1	1.98	0.89	2.11	5.73	5.34	8.27	13.09	8.76	21.81	177
184	6.9	7.3	74.8	3.2	3.3	−3.4	2.11	1.06	2.29	6.22	5.01	7.74	14.60	8.42	21.25	184
188	9.4	6.6	69.6	10.6	4.0	−14.9	2.16	1.13	2.36	6.38	4.86	7.50	13.48	6.87	19.93	174
192	11.0	6.4	61.7	15.1	3.1	−25.5	2.21	1.20	2.43	6.57	4.80	7.27	13.47	5.03	17.66	156
196	12.7	5.9	51.3	22.2	1.3	−35.9	2.24	1.26	2.47	6.67	4.48	6.94	11.87	2.56	14.60	128
200	14.4	5.3	46.9	25.6	0.0	−40.5	2.28	1.34	2.53	6.81	4.26	6.62	11.37	1.62	12.87	117
208	18.1	3.7	40.3	31.5	−3.1	−46.7	2.35	1.48	2.63	7.05	3.78	5.93	10.89	0.57	10.03	103
216	20.7	0.3	35.4	38.6	−5.5	−49.7	2.42	1.63	2.73	7.27	3.26	5.17	10.74	0.28	8.49	97

[8] This is exactly the multiplicity of p-phase shifts found in an analysis of p-He[4] elastic scattering angular distribution by C. L. Critchfield and D. C. Dodder, Phys. Rev. **76**, 602 (1949).

multiplicity because for both isotopic spins, the p-wave shifts are neither small nor equal.

Finally, we took minimum 1 of Table IV and varied separately each of the phase shifts in turn until the value of M of Eq. (2) increased from its minimum value of 86 to 128. The results are summarized in Table V. This gives a measure of the sensitivity of the solution to small changes in the phase shifts. Both positive and negative changes are shown.

TABLE III. Extrapolated data of Columbia experiments.

$\pi^+ \longrightarrow \pi^+$	
θ	$d\sigma/d\omega$
36°	0.27±0.12
47	0.53±0.09
64	0.74±0.07
101	1.39±0.08
129	2.36±0.12
155	3.13±0.17
$\pi^- \longrightarrow \pi^-$	
θ	$d\sigma/d\omega$
42°	0.83±0.12
53	0.47±0.07
70	0.28±0.05
101	0.21±0.05
151	−0.01±0.10
$\pi^- \longrightarrow 2\gamma$	
θ	$d\sigma/d\omega$
50°	0.69±0.05
97	1.76±0.07
150	2.88±0.16

V. CONCLUSIONS

We first observed that solution 2 is almost certainly to be discarded. This was not evident when the solution was first obtained in the summer of 1953 but appears now well established because it seems to be incompatible with the data on positive-pion cross sections that have since become available.[5,6,9] This, of course, does not prove that solution 1 is correct, because there are other solutions that have been found subsequently[3] that are about equally compatible with the experimental data. About solution 1, one may remark that it does not show a resonance of the state of isotopic spin $\frac{3}{2}$ and angular momentum $\frac{3}{2}$. This can be seen because the corresponding phase shift α_{33} does not reach 90° but starts decreasing after going through a maximum of approximately 50°. It has already been pointed out that other solutions quoted in reference 3 show the resonance feature. Otherwise they are about equivalent to solution 1 in accuracy in which they represent the experimental data, so that a decision between them on this basis does not appear possible at the present time. A decision can be obtained only by introducing theoretical arguments as has been done, for example, in the following paper. At the present status of the theory, such arguments must of necessity be somewhat hypothetical.

TABLE IV. Analysis of Columbia data.

	α_3	α_1	α_{33}	α_{31}	α_{13}	α_{11}	Relative minimum
1	−5.4	9.4	8.3	−1.8	−2.0	0.1	86
2	−5.4	9.4	1.6	11.6	−0.7	−2.7	86
3	13.0	−3.6	−2.7	−1.1	6.3	−1.2	143
4	13.0	−3.6	−1.6	−3.1	1.3	9.0	143
5	−11.2	0.9	4.0	0.4	−8.3	0.5	250
6	8.5	−2.5	−0.7	−10.3	5.9	5.2	324
7	8.5	−2.5	−6.9	2.7	5.4	5.8	324

TABLE V. Change in phase angles separately to produce a given change in the minimum function M.

	$+\delta$	$-\delta$
α_3	1.1°	−1.4°
α_1	0.9	−1.0
α_{33}	0.6	−0.8
α_{31}	0.9	−1.1
α_{13}	0.9	−0.8
α_{11}	1.7	−1.7

[9] Fowler, Lea, Shephard, Shutt, Thorndike, and Whittemore, Phys. Rev. 92, 832 (1953).

Pion-Hydrogen Phase Shift Analysis between 120 and 217 Mev

F. DE HOFFMANN, N. METROPOLIS, AND E. F. ALEI, *Los Alamos Scientific Laboratory, Los Alamos, New Mexico*

AND

H. A. BETHE, *Cornell University, Ithaca, New York*

(Received May 6, 1954)

An analysis has been made of the experimental angular distributions of negative pion—hydrogen scattering between 120 and 217 Mev. The usual assumptions of charge independence, and contributions from S and P waves only, are used and the six phase shifts determined as a function of energy by means of the Los Alamos MANIAC. The resulting phase shifts are used to predict positive pion—hydrogen scattering in this energy region. Comparison with the experimental data on positive pions enables one to exclude some of the sets of solutions obtained from the negative pion data.

Essentially three acceptable sets of solutions are found. Arguments are given why one of these is likely to be the physically correct one. Its characteristics are that the predominant phase angle with $T=3/2, j=3/2$ passes through 90° at about 195 Mev, that none of the other phase angles shows a resonance in our energy region, and that the $T=1/2$ phase angles are all small.

1. INTRODUCTION

IN the preceding paper Fermi and Metropolis[1] reported on an analysis of π meson-hydrogen scattering data in terms of phase shifts. The present paper continues to make the basic assumptions[2] used by Fermi and Metropolis that (a) nuclear forces are charge-independent and (b) only S and P waves contribute to the scattering. While the latter assumption is in some doubt[3] we shall still make it for the sake of simplicity. Our analysis concerns the energy region between 120- and 217-Mev meson energy.

The experimental data (which are discussed more fully in Sec. 2, where references may also be found) consist of both transmission and angular distribution measurements. The total negative cross section (sum of the direct and charge exchange scattering[4]), $\sigma_T(\pi^-)$, is very well known from transmission measurements in our energy region. It shows a broad maximum from about 150 to 200 Mev (Fig. 1). The most recent transmission measurements of $\sigma_T(\pi^+)$ by the Carnegie Institute of Technology group also show a definite maximum in the same energy region and of the same shape but much higher in magnitude (Fig. 2). Older measurements, by both the Columbia and the Brookhaven groups, indicated considerably lower cross sections. However, the Carnegie transmission measurements are far superior in energy resolution and in statistical accuracy so that we propose to use them to the exclusion of the older measurements. The angular distributions for direct π^- and charge exchange scattering are fairly well established between 120 and 217 Mev. On the other hand, the angular distribution of π^+ scattering is not known very well and we prefer to use it merely as confirmatory evidence, while considering the $\pi^-\rightarrow\pi^-$ and $\pi^-\rightarrow\pi^0$ angular distributions as primary data.

In principle the knowledge, at a given energy, of any two angular distributions (in our case $\pi^-\rightarrow\pi^-$ and $\pi^-\rightarrow\pi^0$) of the three scattering processes involved enables us to solve for the six phase shifts,[5] α_3, α_1, α_{33}, α_{31}, α_{13}, α_{11}. However, as was anticipated, particularly by Ashkin and Vosko,[6] and as we shall verify presently, there is actually a multiplicity of such sets of phase angles in our high-energy region. We shall find that some decision between solutions is possible on experimental grounds, but to a large extent we have to rely on theoretical discussions concerned with the physics of the situation.

The simplest physical argument concerns total cross sections. Both $\sigma_T(\pi^+)$ and $\sigma_T(\pi^-)$ show a maximum; of these, $\sigma_T(\pi^+)$ is especially suggestive of a resonance. Hence a solution which shows a resonance in the predominant phase angle would look more plausible than one that does not. Moreover, comparison of the recently

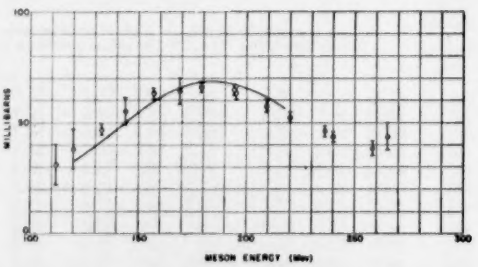

FIG. 1. The variation of $\sigma_T(\pi^-)$—the sum of the total cross sections for direct and charge-exchange scattering of π^- from protons—*versus* energy. Only transmission measurements are shown. The curve is from interpolation (b) of Sec. 7.

[1] Fermi, Metropolis, and Alei, preceding paper [Phys. Rev. 95, 1581 (1954)].

[2] H. L. Anderson *et al.*, Phys. Rev. 91, 155 (1953).

[3] M. Glicksman, Phys. Rev. 94, 1335 (1954) has recently found that the angular distribution for $\pi^-\rightarrow\pi^-$ scattering at 217 Mev can best be fitted by including a fair amount of D wave in addition to S and P, although a reasonable fit is still obtained by S and P waves only.

[4] The radiative absorption correction is negligible at our high energies.

[5] Our phase shift designation is identical to that employed by Fermi and Metropolis in the preceding paper.

[6] J. Ashkin and S. H. Vosko, Phys. Rev. 91, 1248 (1953).

obtained $\sigma_T(\pi^+)$ transmission data by the Carnegie group with $\sigma_T(\pi^-)$ shows that $\sigma_T(\pi^+) \approx 3\sigma_T(\pi^-)$ between 130 and 200 Mev; this suggests strongly, just as at the lower energy, that there is little contribution from the $T=\frac{1}{2}$ states. Next we argue that phase shifts which were small and well behaved at low energy will not suddenly become very large at higher energy; then α_{33} is the natural candidate for a resonance, and it also gives the correct magnitude for the resonance cross section.

Apart from the considerations just mentioned, we naturally prefer a solution which shows the smoothest and least steep variation of phase shifts. If necessary, in order to make a decision between solutions, we can also ask which of them resembles more closely the behavior to be expected from a purely theoretical strong-coupling calculation of phase shifts along the lines of the Tamm-Dancoff method.[7]

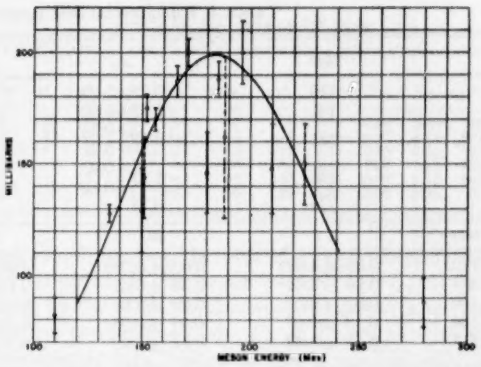

FIG. 2. The variation of $\sigma_T(\pi^+)$—the total cross section of the scattering of π^+ from protons—*versus* energy. Experimental points shown by a solid line are transmission measurements, those shown by a dotted line are integration measurements. The curve is from interpolation (b) of Sec. 7.

2. EXPERIMENTAL DATA[8]

a. Total Cross Section

The quantity $\sigma_T(\pi^-)$ has been well established, to about ± 2–3 mb, between 133 and 258 Mev by transmission measurements at the Carnegie Institute of Technology.[9] We show their values at 133, 157, 179, 194, 195, 215, 236, 240, and 258 Mev in Fig. 1. Also shown are selected transmission measurements of $\sigma_T(\pi^-)$ of the Chicago and Brookhaven groups. In particular the values are due to the following authors. At 112 Mev: Anderson *et al.*;[10] 120 and 144 Mev: Anderson *et al.*;[2] 169 Mev: Fermi *et al.*;[11] 209 and 220 Mev: Glicksman;[12] 265 Mev: Yuan *et al.*[13] It will be noted that the Brookhaven 265-Mev point appears somewhat out of line with the lower-energy data.

Good values for the positive cross section $\sigma_T(\pi^+)$ are available only from transmission measurements. Figure 2 indicates transmission measurements by means of a solid line and integration measurements by means of a broken line for the individual limits of errors. The transmission measurements are due to the following authors: at 110 Mev: Anderson *et al.*;[2] at 135, 152, 156, 166, 171, 185, and 196 Mev: Ashkin *et al.*;[9] at 150, 180, 210, and 280 Mev: Yuan *et al.*[13]

Integration values are shown at 151, 188, and 225 Mev in Fig. 2. Those at 151 and 188 Mev are from photographic plate work; the 225-Mev measurement was by means of a diffusion cloud chamber. The value at 151 Mev was obtained by Grandey and Clark[14] by combining their data with those of Homa *et al.*,[15] at that energy (a total of about 100 tracks). That at 188 Mev is due to Homa *et al.*[15] (a total of about 40 tracks). The 225-Mev point, measured at Brookhaven, is due to Fowler *et al.*,[16] and is based on 116 tracks.

Examining the $\sigma_T(\pi^+)$ measurements due to different experimenters we note that the results of Ashkin *et al.* have the greatest experimental accuracy. Not only is the statistical accuracy superior to the Brookhaven results, but also the energy definition is much better. In particular, it is about ± 6 Mev for the Carnegie experiments whereas it is about ± 25 Mev for the Brookhaven experiments. Thus, it is perhaps not too surprising that the Brookhaven transmission measurements miss the rather sharp maximum in $\sigma_T(\pi^+)$.[17]

An interesting comparison may be made between $\sigma_T(\pi^+)$ and $\sigma_T(\pi^-)$ as follows. It can easily be verified[18] that

$$3\sigma_T(\pi^-) = \sigma_T(\pi^+) + 2\sigma_T(T=\tfrac{1}{2}), \qquad (1)$$

where the last quantity in Eq. (1) denotes the scattering due to a pure state of isotopic spin $\frac{1}{2}$. Thus $3\sigma_T(\pi^-)$ is an upper limit to the value $\sigma_T(\pi^+)$ may reach. In actual fact, we see that the measured values of Ashkin reach this upper limit within experimental error. The Brookhaven measurement for $\sigma_T(\pi^+)$ is again exactly three times the value of $\sigma_T(\pi^-)$ as read off from Fig. 2. Thus we believe that $\sigma_T(T=\frac{1}{2})$ and hence α_1, α_{13}, and α_{11}

[7] G. F. Chew, Phys. Rev. **89**, 591 (1953); and Dyson, Ross, Salpeter, Schweber, Sundaresan, Visscher, and Bethe, Phys. Rev. (to be published).

[8] This section is not a complete survey of experimental data. In general only the most recent and more accurate results are quoted here.

[9] Ashkin, Blaser, Feiner, Gorman, and Stern, private communication from J. Ashkin.

[10] H. L. Anderson *et al.*, Phys. Rev. **85**, 934 (1952).

[11] E. Fermi *et al.*, Phys. Rev. **92**, 161 (1953).

[12] M. Glicksman, Phys. Rev. **94**, 1335 (1954).

[13] L. C. Yuan and S. J. Lindenbaum, Proceedings of the Fourth Annual Conference on High Energy Physics, Rochester (University of Rochester Press, Rochester, to be published).

[14] R. A. Grandey and A. F. Clark, Phys. Rev. **94**, 766 (1954).

[15] Homa, Goldhaber, and Lederman, Phys. Rev. **93**, 554 (1954), as corrected in a private communication to the authors.

[16] W. B. Fowler *et al.*, Phys. Rev. **92**, 832 (1953). The authors have recently corrected their reported mean energy from 260 Mev to 225 Mev.

[17] L. C. L. Yuan, remark at the Fourth Annual Conference on High Energy Physics, Rochester (University of Rochester Press, Rochester, to be published).

[18] See Eqs. (5)–(13).

TABLE I. Experimental data concerning the nine coefficients in Eqs. (2)–(4).

Mev	A_+	B_+	C_+
110	0.25 ± 0.05	-0.34 ± 0.06	0.53 ± 0.14
135	0.35 ± 0.20	-0.63 ± 0.25	1.60 ± 0.60
151	$0.72^{+0.34}_{-0.27}$	$-0.36^{+0.28}_{-0.35}$	$1.46^{+0.93}_{-0.73}$
188	$1.32^{+0.93}_{-0.76}$	$-0.54^{+0.33}_{-0.44}$	$1.15^{+1.38}_{-0.56}$
225	0.78	0.44	3.8

Mev	A_-	B_-	C_-	A_0	B_0	C_0
120	0.038 ± 0.009	0.026 ± 0.013	0.09 ± 0.03	0.05 ± 0.03	-0.15 ± 0.04	0.25 ± 0.13
144	0.09 ± 0.02	0.08 ± 0.03	0.17 ± 0.05	0.12 ± 0.05	-0.21 ± 0.05	0.43 ± 0.22
169	0.07 ± 0.02	0.05 ± 0.03	0.35 ± 0.07	0.21 ± 0.08	-0.07 ± 0.07	0.49 ± 0.26
194	0.15 ± 0.03	0.09 ± 0.05	0.39 ± 0.11	0.23 ± 0.11	-0.01 ± 0.10	0.79 ± 0.35
217	0.13 ± 0.02	0.12 ± 0.03	0.37 ± 0.06	0.20 ± 0.03	0.19 ± 0.04	0.75 ± 0.11

are small in our energy region, a fact we have already stressed in the introduction.

The Carnegie data enable one to draw a smooth curve from the maximum around 200 Mev to the Brookhaven values[13,16] at 225 and 280 Mev and beyond. We have made use of this situation in our analysis.

b. Angular Distribution

Turning now to the differential cross section, we may write it, assuming only S and P waves, as[19]

$$\lambda^{-2}d\sigma(\pi^+\to\pi^+)/d\omega = A_+ + B_+\cos\theta + C_+\cos^2\theta, \quad (2)$$

$$\lambda^{-2}d\sigma(\pi^-\to\pi^-)/d\omega = A_- + B_-\cos\theta + C_-\cos^2\theta, \quad (3)$$

$$\lambda^{-2}d\sigma(\pi^-\to\pi^0)/d\omega = A_0 + B_0\cos\theta + C_0\cos^2\theta. \quad (4)$$

The available experimental data concerning the nine coefficients in Eqs. (2) through (4) are shown in Table I. The positive coefficients, A_+, B_+, C_+, have been measured at 110 and 135 Mev by counter work at Chicago,[2] the measurements at 151 Mev,[20] 188 Mev[16] are from photographic plate work, and that at 225 Mev[21] was obtained by means of a diffusion cloud chamber. While the reported spread in energies is only ±7 Mev at 151 Mev and ±8 Mev at 188 Mev, the last point has an energy spread of ±45 Mev. In addition, the Brookhaven data are not very well fitted by a formula of the type (2): either the point at 135° will fall below or that at 165° above the curve. If the latter is disregarded, a larger value of B_+ is indicated. In any case, the error in A_+, B_+, and C_+ at 225 Mev is quite large, just how large is difficult to estimate. Therefore, we give the 225-Mev values in Table I (and on Fig. 6) without showing limits of error.

The negative and zero coefficients of Eqs. (3) and (4) have been measured by counter work at Chicago. In particular the authors are, at 120 and 144 Mev: Anderson *et al.*;[2] 169 and 194 Mev: Fermi *et al.*;[11] 217 Mev: Glicksman.[12] Of these, the 217-Mev point is the most recent and accurate one. One check on the accuracy is a comparison of the total cross sections: at 217 Mev one finds that integration of the Chicago differential measurements yields a total cross section for π^- of 56 mb, in excellent agreement with the Carnegie transmission value of 55.5 mb at 215 Mev. At 169 and 194 Mev on the other hand, the agreement between integration and transmission value is only good to about 10 percent.

3. METHOD

As noted in Sec. 2, the direct negative and charge exchange data are better known than the $\pi^+\to\pi^+$ data in our energy region. This has led us to a phase shift analysis in which we regard A_-, B_-, C_-, A_0, B_0, and C_0 as primary data; the six phase shifts are deduced and the resultant A_+, B_+, and C_+ are checked against the available positive pion data.

Before discussing the method proper, we list the formulas for the coefficients in terms of phase shifts for easy reference.[22]

$$A_+ = \tfrac{1}{4}(|a|^2+|c|^2), \quad (5)$$

$$B_+ = \tfrac{1}{4}(ab^*+a^*b), \quad (6)$$

$$C_+ = \tfrac{1}{4}(|b|^2-|c|^2), \quad (7)$$

$$A_- = (1/9)\cdot\tfrac{1}{4}(|x|^2+|z|^2), \quad (8)$$

$$B_- = (1/9)\cdot\tfrac{1}{4}(xy^*+x^*y), \quad (9)$$

$$C_- = (1/9)\cdot\tfrac{1}{4}(|y|^2-|z|^2), \quad (10)$$

$$A_0 = (2/9)\cdot\tfrac{1}{4}(|p|^2+|r|^2), \quad (11)$$

$$B_0 = (2/9)\cdot\tfrac{1}{4}(pq^*+p^*q), \quad (12)$$

$$C_0 = (2/9)\cdot\tfrac{1}{4}(|q|^2-|r|^2), \quad (13)$$

[19] In Eqs. (2) through (4) λ is the wavelength of the incident meson in the center-of-mass system.

[20] Combined results of Grandey and Clark (reference 14), and Homa *et al.* (reference 15).

[21] W. B. Fowler *et al.* (reference 16). The resolution into A_+, B_+, C_+ was not performed by the Brookhaven group; therefore, the numbers quoted in Table I are our fit of Eq. (2) to the data.

[22] In our notation the scattered amplitudes a, b, c, x, y, z, p, q, and r are lower case letters where Ashkin and Vosko (reference 6) use upper case letters. Conversely our coefficients in the angular distribution are denoted by upper case letters where they use lower case letters. Some authors (including the following paper by Martin) use a, b, c to denote λ^3A_+, λ^3B_+, and λ^2C_+; we do not follow this practice but reserve these symbols for use as shown in Eqs. (5)–(7).

where[22]

$$a=e^{2ia_{33}}-1, \tag{14}$$

$$b=2e^{2ia_{33}}+e^{2ia_{31}}-3, \tag{15}$$

$$c=e^{2ia_{33}}-e^{2ia_{31}}, \tag{16}$$

$$x=a+2e^{2ia_1}-2, \tag{17}$$

$$y=b+4e^{2ia_{13}}+2e^{2ia_{11}}-6, \tag{18}$$

$$z=c+2e^{2ia_{13}}-2e^{2ia_{11}}, \tag{19}$$

$$p=\tfrac{3}{2}a-\tfrac{1}{2}x, \tag{20}$$

$$q=\tfrac{3}{2}b-\tfrac{1}{2}y, \tag{21}$$

$$r=\tfrac{3}{2}c-\tfrac{1}{2}z. \tag{22}$$

Our method is in general similar to that used by Fermi and Metropolis for the work reported in the preceding paper. However, while they operate with nine differential cross sections (three for each of the three processes) we use the nine coefficients A, B, C in Eqs. (2)–(4). For details of the computer method we refer to the preceding paper.

In the present calculation the MANIAC is provided with the six input data A_-, B_-, C_-, A_0, B_0 and C_0 at a given energy, including the errors as shown in Table I. Each of these coefficients is dependent upon the six phase shifts as given in Eqs. (8)–(13). A given set of six starting phase angles is then varied by the MANIAC so as to minimize the least squares quantity,

$$M=\sum_{x=A-,B-,C-,A_0,B_0,C_0}\left(\frac{x(\text{exp})-x(\text{theor})}{\epsilon(x)}\right)^2. \tag{23}$$

Explicitly, in the first term in Eq. (23), A_-(exp) is the mean value of A_- as given in Table I, A_-(theor) the value obtained from Eq. (8) with a particular set of six phase angles, and $\epsilon(A_-)$ the experimental limit of error on A_- as given in Table I. If the result is $M=0$, then the corresponding phase angles solve our six equations exactly.

As has been pointed out repeatedly, particularly by Ashkin and Vosko,[6] the system of Eqs. (8) through (13) has in general far more than one solution for one and the same set of six coefficients at a given energy. Thus the first task is to find all the solutions at a given energy resulting from the mean values of the six coefficients given in Table I. This is done by picking a random set of six phase angles (generated by the MANIAC) and asking the computer to minimize Eq. (23). Repeating this procedure many times will lead to a number of different solutions with M so close to zero that in essence these are the different solutions for one and the same set of A_-, B_-, C_-, A_0, B_0, and C_0.

After the different solutions at various energies have been found, we face the task of proper selection. The first criterion is the $\sigma_T(\pi^+)=4\pi\lambda^2(A_++C_+/3)$ predicted by the solution. The second criterion is to compare the predicted A_+, B_+, C_+ of a solution with the experimental data, insofar as this is possible with the poorly known $\pi^+\to\pi^+$ angular distributions.

[22] For $\pi^+\to\pi^+$ scattering the nonspin flip amplitude is proportional to $(a+b\cos\theta)$, the spin flip amplitude to $c\sin\theta$. The other quantities are similarly the appropriate ones for $\pi^-\to\pi^-$ and $\pi^-\to\pi^0$ scattering.

TABLE II. Solutions at 217 Mev.

Solution	a_{33}	a_{31}	a_{33}	a_{31}	a_{13}	a_{11}	A_+	B_+	C_+	$\sigma_T(\pi^+)$
1	20	4	73	14	−7	7	0.86	0.96	3.46	160
2	21	2	50	117	1	−1	0.98	0.92	3.35	167
3	−67	0	40	37	4	−11	0.85	0.93	3.51	161
4	19	6	35	73	−16	12	0.47	1.07	3.52	131
5	−2	15	125	−3	11	30	0.64	0.06	2.13	107
6	−65	0	165	−15	19	36	0.82	0.90	0.60	81

4. SOLUTIONS AT INDIVIDUAL ENERGIES

a. Multiple Solutions at 217 Mev

Let us pick the 217-Mev point and examine the different solutions found. In Table II we exhibit the six solutions, and the resultant values of A_+, B_+, C_+, and $\sigma_T(\pi^+)$. In all cases M [Eq. (23)] is low, so that all solutions arise from the same set of input coefficients, namely that given as the mean in Table I.[24]

It should be pointed out that while the relative signs of the six phase shifts are fixed within each solution, all signs of a given solution can be reversed and the resulting solution will still satisfy Eqs. (8) through (13) and lead to identical values for A_+, B_+, and C_+. Moreover, any integral multiple of 180° can be added to any particular phase shift.

We should now like to make a selection between the solutions in Table II on the basis of the π^+ data. It is noted immediately that the first three solutions give nearly identical results also for π^+ scattering so that with any experimental accuracy now foreseeable for π^+ scattering, a distinction between these three will not be possible. The solutions 4, 5, and 6 differ substantially from solutions 1, 2, and 3 in the predicted π^+ scattering, both in total cross section and in angular distribution. From the available data on $\sigma_T(\pi^+)$ we can definitely exclude solutions 5 and 6 as giving too low values for $\sigma_T(\pi^+)$. We cannot be quite so definite about solution 4 because the lower limit of the experimental cross section at 225 Mev is just about 130 mb, the predicted cross section from solution 4. However, a smooth interpolation between the measured cross sections up to 200 and at 225 and 280 Mev indicates a value of about 160 mb at 217 Mev and thus makes solution 4 rather unlikely.

We now turn to the π^+ angular distributions predicted by our solutions 1 through 4. The resulting A_+, B_+, and C_+ of solutions 1 through 3 are very close to each other. The comparison with the experimentally measured values may be seen by inspection of Table I

[24] In Sec. 6 we discuss to what extent the solutions are sensitive to changes of the input coefficients, within the limits of the experimental error on each listed in Table I.

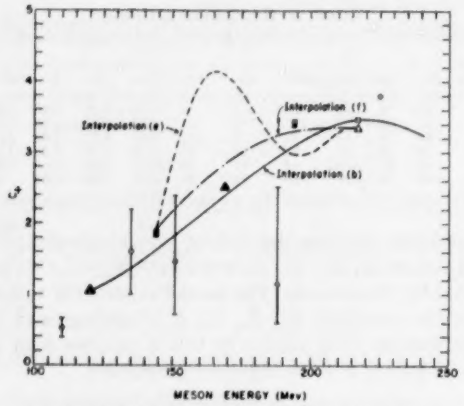

FIG. 3. The coefficient C_+ of Eq. (2) as a function of energy. The curves are interpolations discussed in Sec. 7.

and Fig. 3. A_+ of solutions 1 through 3 fits reasonably well with the experimental values of Table I. C_+ agrees within experimental error with the Brookhaven 225-Mev measurement, but the mean of the 188-Mev Columbia measurements is far out of line with any reasonable interpolation between our theoretical point (solutions 1 through 3) at 217 Mev and the lower-energy points. However, the very large limit of error of the 188-Mev Columbia point should be noted. The value of B_+ in solutions 1 to 3 seems high compared with the Brookhaven point at 225 Mev, and very high compared with the Columbia point at 188 Mev. However, it should be noted that if the 165° value of the Brookhaven data is disregarded, a larger value of B_+ is indicated at 225 Mev than we have chosen to give in Table I.

Note that solution 4 has a distinctly lower value of A_+ than solutions 1 through 3. In fact it seems quite low compared to the experimental evidence of Table I. We have already noted that solution 4 gives rather too low a value for $\sigma_T(\pi^+)$. Thus, while we cannot definitely exclude solution 4, we shall nevertheless choose to exclude it from our discussion because of its π^+ predictions.

The fact that A_+, B_+, and C_+ of solutions 1 through 3 are very close is a phenomenon which we shall find to be true of the groups of acceptable solutions at energies other than 217 Mev as well. This is confirmatory evidence for the statement made in the introduction that the $T=1/2$ contributions are not very important compared to the $T=3/2$ ones. Therefore, we believe that one can carry through much of the analysis by using the resulting A_+, B_+, and C_+ only. As a case in point, let us examine first why there are three acceptable solutions at 217 Mev.

For this purpose, it is very convenient to use the graphical method of Ashkin and Vosko[25] as applied to the π^+ angular distribution. In particular, we choose A_+, B_+, and C_+ of solution 1 and plot the Ashkin diagram. Then, as Ashkin and Vosko have pointed out, we find two complex points a [Eq. (14)], which we denote by a_1 and a_2. Ashkin has pointed out that in certain energy regions a_2 is excluded. The condition that a_2 is acceptable is that

$$|(a+b+3)-a| \leqslant 3. \tag{24}$$

The quantity $(a+b)$ is given by experiment. At 217 Mev one finds both a_1 and a_2 acceptable. Each of these points a leads both to a Fermi and a Yang solution (see Sec. 8, and Ashkin and Vosko[6]). By construction the point a_1 corresponds to $|\alpha_3|=20°$. One of the sets of α_{33} and α_{31} resulting from point a_1 is, again by *a priori* construction, solution 1. The other is roughly solution 2, as far as the $T=\frac{3}{2}$ phase shifts go. That it should not be exactly solution 2 is not surprising; after all, A_+ and C_+ of solution 2 do in fact differ slightly from that of solution 1. Putting it another way, solutions 1 and 2 could only be expected to be exactly corresponding Fermi and Yang type solutions if $\alpha_{13}=\alpha_{11}=0$.[26]

In the present case a_2 is exactly three units away from the point $(a+b+3)$; hence it just barely satisfies Eq. (24) and consequently leads to one and not two sets of α_{33} and α_{31} and thus to only one extra solution. In fact the solution it gives is very closely solution 3 of Table II as far as the $T=\frac{3}{2}$ phase shifts are concerned. Solution 3, it should be noted, is the same as the "first solution" found at 216 Mev by Fermi and Metropolis[1] during the summer of 1953.

b. Solutions at 120 and 144 Mev

At 144 Mev the computer found a total of seven distinct solutions. However, four of these resulted in values of $\sigma_T(\pi^+)$ in the range from 38 to 103 mb; we feel that these are excluded by the experimental data shown in Fig. 2. The other three solutions are given in Table III. Their $\sigma_T(\pi^+)$ seem acceptable, although that of solution 3 seems rather low. Of these solutions, 1 is of the Fermi type, and 2 and 3 are of the Yang type.

The question now arises how the solutions at 144 Mev are connected to solutions at another energy. In particular, we would like to connect the 144-Mev solutions with those at 120 Mev and those at 217 Mev (just discussed in Sec. 4a). One way of establishing some connection between solutions at different energies is the method of "tracking." By tracking between, say, 144 and 120 Mev we mean the following procedure: interpolate the six input coefficients *linearly* between 144 and 120 Mev in small energy steps (3 Mev in this

TABLE III. Solutions at 144 Mev.

Solution	α_{31}	α_{11}	α_{33}	α_{31}	α_{13}	α_{11}	A_+	B_+	C_+	$\sigma_T(\pi^+)$
1	−13	14	46	5	3	−5	0.49	−0.38	1.84	143
2	−12	12	21	60	−6	9	0.42	−0.36	1.91	136
3	−9	12	23	54	5	−16	0.29	−0.33	2.02	124

[25] See reference 6, and also Sec. 9 of this paper.

[26] This has been shown by H. A. Bethe (unpublished).

case). Then start the computer at 144 Mev with a particular set of angles corresponding to one of the solutions. The computer then finds a new set of phase angles at the energy (144-ΔE) Mev to fit the six linearly interpolated input coefficients. Eventually 120 Mev is reached in this fashion. We are fully aware that physically a linear interpolation of the input coefficients need not be correct. In actual fact, however, it is likely to be not too far from the truth in the energy region from 120 to 144 Mev since the experimental data seem rather smooth. In any case we believe that, while intermediate energy results should not be trusted, the procedure of "tracking" does provide an insight into which solutions are related at 120 and 144 Mev. The tracking procedure is not likely to be as good when applied from 144 Mev upward in energy since there is little reason to believe that the six input coefficients vary linearly over energy intervals as large as 25 Mev in this region.

As to actual results of the tracking between 144 and 120 Mev, we find that all three solutions of Table III track vary smoothly, with M very small at all intermediate energies, down to 120 Mev. The resulting values at 120 Mev are shown in Table IV. It is seen that the π^+ data deduced from solution 3 are significantly different from those obtained from solutions 1 and 2 which agree between themselves. In the first place, solution 3 gives a value for $\sigma_T(\pi^+)$ which appears too low in comparison with Fig. 2. But much more striking is the discrepancy of A_+; the directly measured values at 110 and 135 Mev interpolate to give $A_+ \approx 0.27$ at 120 Mev which is compatible with $A_+ = 0.20$ as deduced from solutions 1 and 2 but certainly not with $A_+ = 0.04$ deduced from solution 3. Hence solution 3 is excluded at 120 Mev and by continuity, therefore, we also reject solution 3 at 144 Mev. Solutions 1 and 2 at 120 Mev are both acceptable in terms of the resulting π^+ data; solution 1 is the Fermi and 2 the Yang type. Note that we have assigned the over-all signs of the phase shifts such that α_3 is negative and α_1 is positive. This agrees with the choice of sign necessitated by the extensive low-energy experiments between 40 and 78 Mev.[27] Hence there is no ambiguity in over-all sign at 120 or 144 Mev.

Thus we are led to believe that at 144 Mev only solutions 1 and 2 of Table III are acceptable. Just as at 217 Mev, the two solutions which we accept at 144 Mev have almost identical A_+, B_+, and C_+. To understand this more fully, it is advisable to draw an Ashkin diagram from the A_+, B_+, C_+ of, say, solution 1. We then find that now only one of the complex points a [Eq. (14)] is acceptable, *viz.*, a_1. The other, as Ashkin and Vosko have pointed out, is unacceptable because the inequality Eq. (24) is violated. The acceptable a leads to two sets of P phase shifts for $T = \frac{3}{2}$, one of which is by construction identical to solution 1 (Fermi solution) while the other is very close to solution 2 (Yang solution).

TABLE IV. Solutions at 120 Mev.

Solution	α_3	α_1	α_{33}	α_{31}	α_{13}	α_{11}	A_+	B_+	C_+	$\sigma_T(\pi^+)$
1	−12	8	30	6	2	−4	0.20	−0.36	1.04	87
2	−12	8	14	37	−3	4	0.20	−0.36	1.05	87
3	−11	8	20	24	5	−13	0.04	−0.35	1.19	69

[27] For a detailed discussion of these see the forthcoming book, *Mesons and Fields*, Vol. II, by H. A. Bethe and F. de Hoffmann.

TABLE V. Solutions at 169 Mev.

Solution	α_3	α_1	α_{33}	α_{31}	α_{13}	α_{11}	A_+	B_+	C_+	$\sigma_T(\pi^+)$
1	−4	7	64	3	−1	7	0.77	−0.11	2.53	177
2	−4	7	32	96	0	6	0.78	−0.11	2.52	174
3	−42	7	49	12	1	2	0.81	−0.12	2.50	176
4	−3	9	32	88	−4	10	0.69	−0.08	2.64	168
5	−2	6	58	10	−8	14	0.54	−0.04	2.78	156

c. Solutions at 169 and 194 Mev

The solutions at 169 and 194 Mev were again obtained by starting from different random sets of angles, as described in Sec. b. The method of "tracking" described in Sec. 4b was used to obtain the connection of sets at different energies, and also turned up some additional solutions.[28] For instance, solution 3 of Table II was tracked starting at 217 Mev and led to a solution at 194 Mev not previously found by the random angle method.

By these means solutions at 169 Mev were found; the acceptable one as far as π^+ predictions are concerned are tabulated in Table V. At 169 Mev we rejected the three other solutions found which yielded $\sigma_T(\pi^+)$ between 77 and 126 mb.[29] All solutions given in Table V have an M value close to zero. As explained in Sec. 3, the MANIAC computes A_-, B_-, C_-, A_0, B_0, and C_0 from the six phase angles of the particular solution and compares them with the mean experimental values quoted in Table I. Hence, M close to zero means that A_-, B_-, C_-, A_0, B_0, and C_0 given by the solution are essentially identical with the mean experimental values.

Table VI gives the "acceptable" solutions at 194 Mev. We rejected one solution which yielded $\sigma_T(\pi^+) = 124$ mb. We might also reject solutions 7 and 8 as giving too low $\sigma_T(\pi^+)$. This time it should be noted that all but solutions 2 and 3 have M values not close to zero; in particular all other solutions give C_0 about 0.76 instead of 0.79 as given in Table I (of course, this is well within the experimental error) while the other input coefficients do correspond to the mean values of

[28] This method was also used at 144 and 217 Mev to ascertain that the maximum acceptable solutions are found.

[29] Even the accepted five solutions give lower values for $\sigma_T(\pi^+)$ than the transmission values, 190–200 mb, of the Carnegie Institute of Technology group. Also the $\sigma_T(\pi^-)$ obtained by integration of the 169-Mev differential cross sections is too low. This may throw some doubt on the accuracy of the 169-Mev results at least as far as absolute values are concerned.

TABLE VI. Solutions at 194 Mev.

Solution	α_3	α_1	α_{33}	α_{31}	α_{13}	α_{11}	A_+	B_+	C_+	$\sigma_T(\pi^+)$
1	−13	−14	94	−14	1	8	0.96	0.39	3.43	191
2	−22	7	67	143	−4	−11	1.08	0.40	3.31	199
3	−43	1	58	23	5	−19	0.80	0.25	3.81	189
4	−13	−14	82	−22	−1	2	0.99	0.23	3.46	195
5	−13	−14	86	−18	0	3	0.99	0.28	3.46	195
6	14	15	60	133	−4	−2	0.97	0.43	3.39	192
7	16	17	30	74	−22	4	0.55	0.84	2.92	139
8	13	14	33	72	−22	9	0.46	0.67	3.19	140

Table I. Note how many acceptable solutions exist at 194 Mev; we shall have occasion to understand how critical an energy region this is in Sec. 5. This leads us to believe, for instance, that the differences between solutions 7 and 8 are not truly significant, and also those between solutions 1, 4, and 5.

5. CONNECTION OF SOLUTIONS AT DIFFERENT ENERGIES

The most difficult task is to decide which solutions at a certain energy are in reality connected to solutions at another energy. The first attempt in this direction is our method of "tracking" (Sec. 4b) with the input coefficients linearly interpolated between two energies at which measurements have been made. We should emphasize again that in fact there is no reason for the coefficients to vary linearly between, say, 169 and 194 Mev. However, if the phase shifts vary smoothly on a track from one energy to another, then we believe this to give an indication of a likely connection. This linear tracking indicates the existence of the following apparent tracks:

Track T1: Solution 1 at all energies.
Track T1a: Same as Track T1, except Solution 5 at 194 Mev.
Track T2: Solution 3 at 120 Mev and 144 Mev, Solution 2 at 169 Mev, Solution 6 at 194 Mev, Solution 2 at 217 Mev.
Track T3: Solution 3 at 169 Mev, 194 Mev, and 217 Mev.
Track T4: Solution 2 at 120 Mev and 144 Mev, Solution 4 at 169 Mev, Solution 7 at 194 Mev, Solution 4 at 217 Mev.

Let us now examine the behavior of the phase angles as a function of energy for Track T1. In particular we focus our attention on the biggest phase shift, namely, α_{33}. We notice that between 120 and 194 Mev α_{33} rises smoothly from 30° to 94°. However, at 217 Mev solution 1 of Table II gives $\alpha_{33}=73°$, which reverses the smooth upward trend of the curve. However, we are at liberty to reverse the sign of all angles in solution 1 at 217 Mev and to add 180° where desirable. In this way, we can replace α_{33} by $\alpha_{33}'=180-73=107°$, so that now α_{33} continues to rise smoothly up to 217 Mev. This modification has the advantage that the reversal of sign of the other angles also makes them fit better to the lower energy results.

There is, however, one difficulty; if we actually track from solution 1 at 194 Mev to solution 1 at 217 Mev by the method described, then the relative signs as given in Tables II and VI are definitely specified; in particular, α_3 which starts at a negative value goes through zero and then becomes positive. The question arises why the solution of opposite sign is not found by the MANIAC. The explanation may be given most easily in terms of the behavior of the point a on an Ashkin graph of the positive coefficients.

The first steps in construction of the Ashkin diagram are the determination of $|a+b|$ from the forward scattering and $\mathrm{Re}(a+b)$ from the total cross section. This means that the point $(a+b)$ is determined in the complex plane except for the sign of its imaginary part. Now it can easily be verified from Eqs. (14) and (15) that

$$\mathrm{Im}(a+b)=\sin 2\alpha_3+2\sin 2\alpha_{33}+\sin 2\alpha_{31}. \tag{25}$$

Thus, at energies below 120 Mev the quantity $\mathrm{Im}(a+b)$ is seen to be positive and the point $(a+b)$ must be chosen in the upper half of the complex plane. (This in turn determines the sign of α_3 which will result from the construction of the Ashkin diagram.[30]) Now assume that there is in fact a resonance in α_{33}, i.e., this quantity passes through 90°, and assume further that the other two phase shifts are small (as indeed they are for Track T1). Then expression (25) has to change sign and becomes negative above the resonance; the imaginary part of $(a+b)$ has to go through zero at some energy. Now, experimentally, this imaginary part is determined from the difference, D, of the squares of $|a+b|$ and $\mathrm{Re}(a+b)$,

$$D=\mathrm{Im}^2(a+b)=|a+b|^2-[\mathrm{Re}(a+b)]^2, \tag{26}$$

or

$$\tfrac{1}{4}D=(A_++B_++C_+)-(A_++\tfrac{1}{3}C_+)^2. \tag{27}$$

Both terms on the right of Eq. (27) are large quantities compared to D near the point where D itself is close to zero. Now the two quantities on the right are obtained from interpolation of inaccurate experimental data at any given energy. Hence, it is very unlikely that D goes *exactly* to zero at a given energy with input values used in the MANIAC. It is possible that D will either go negative when the energy is increased by a certain energy step and remain negative for a certain energy range or else D remains positive all the time. In the former case there is then no solution at all in the interval in which D is negative; in the latter case the imaginary part never goes exactly through zero. With the actual observations (interpolated) the latter is realized; in fact, the lowest value of D is about

$$D\approx 0.006(a+b)^2. \tag{28}$$

The computer following the experimental values of D

[30] Choosing the other point $(a+b)$ thus simply reverses the sign of α_3 as obtained from the graph.

has no opportunity to reverse the sign of $\mathrm{Im}(a+b)$ and therefore keeps this imaginary part positive.

A "mistake" in the imaginary part of $(a+b)$ is equivalent to a reversal of sign of all phase shifts. Hence, above the resonance the computer will give the incorrect sign for all α's.

Now in actual fact the primary input data into the MANIAC are not the positive but the negative and zero coefficients. The argument can be rephrased easily in terms of these. The relevant Ashkin diagram then involves x [Eq. (17)] and y [Eq. (18)]. The quantity which is analogous to D is then given by

$$D' = |x+y|^2 - [\mathrm{Re}(x+y)]^2. \qquad (29)$$

Since we find that in our energy region the $T=\frac{1}{2}$ phase shifts are small, the quantities x and y are not very different from a and b. Therefore, just as in the positive case, Eq. (29) has difficulty in going through zero and the argument carries through in the same way.

These considerations show that the phase shifts near 194 Mev are extremely sensitive to the experimental data. The sensitivity is further increased if α_{11} and α_{13} are also permitted to be different from zero. Thus, the multiplicity of solutions found in this critical energy region is not very surprising.

Based on this sensitivity at 194 Mev, we decided in particular not to distinguish between Track T1 and T1a, which are identical except for a small difference around 194 Mev. Instead we shall henceforth speak of a Track I, where an average of solutions 1 and 5 of Table VI is chosen at 194 Mev and where the signs at 217 Mev are reversed as discussed and as indicated in Table VII. A track of type T1 has been found independently by Glicksman[12] who made an analysis under the assumption that $\alpha_{31}=\alpha_{13}=\alpha_{11}=0$.

Examining Tracks T2 and T4 with respect to overall consistency, we note that Track T2 starts with an unacceptably low $\sigma_T(\pi^+)$ at 144 Mev and ends up with a very acceptable $\sigma_T(\pi^+)$ at 217 Mev. On the contrary, Track T4 starts with a very acceptable solution at 144 Mev and ends up with a somewhat low cross section at 217 Mev. Closer examination of the entire behavior of the two tracks shows that the respective phase angles come very close together in the intermediate energy region. Therefore the connection between the high and low energy end is not clearly established and a slightly different interpolation of A_-, B_-, C_-, A_0, B_0, and C_0 may easily lead to a different result.

TABLE VII. Track I.

Energy (Mev)	α_3	α_1	α_{33}	α_{31}	α_{13}	α_{11}
217	−20	−4	107	−14	7	−7
194	−13	−14	90	−16	0	5
169	−4	7	64	3	−1	7
144	−13	14	46	5	3	−5
120	−12	8	30	6	2	−4

TABLE VIII. Tracks II and IIa.

Track II						
Energy (Mev)	α_3	α_1	α_{33}	α_{31}	α_{13}	α_{11}
217	−21	−2	130	243	−1	1
194	−22	7	67	143	−4	−11
169	−4	7	32	96	0	6
144	−12	12	21	60	−6	9
120	−12	8	14	37	−3	4
Track IIa						
Energy (Mev)	α_3	α_1	α_{33}	α_{31}	α_{13}	α_{11}
217	21	2	50	117	1	−1
194	14	15	60	133	−4	−2

We have, therefore, switched the connection at 169 Mev. Furthermore, at 194 Mev solutions 2 and 6 are very similar with regard to the large phase shifts α_{33} and α_{31} and with regard to A_+, B_+, C_+. Hence we consider solution 2 equally acceptable as solution 6. We therefore adopt a Track II which uses solution 2 at all energies except that at 194 Mev it may use either solution 2 or 6.

At low energies Track II is the Yang solution. As will be shown in Sec. 8, the Yang solution which is the counterpart of the Fermi solution represented by Track I is characterized by a very rapid increase of the phase shifts, particularly of α_{31} in the neighborhood of 200 Mev. Being the counterpart of Track I, it yields an α_3 whose behavior is essentially the same as for Track I. Therefore we choose at 217 Mev to reverse the signs of all phase shifts of solution 2 in Table II. Since this makes $\alpha_3=-21$ at 217 Mev and $\alpha_3=-4$ at 169 Mev, we find that now solution 2 at 194 Mev fits in better than solution 6, and we therefore select it. Then, in order to maintain a monotonic increase of α_{33} and α_{31}, we add 180° to the former and 360° to the latter to the values quoted in Table II with signs reversed. This yields the data listed in Table VIII for Track II.

The very rapid increase of α_{33} from 169 to 217 Mev is apparent, and the increase of α_{31} is even more rapid. It is evident, however, that the interpolation from 169 Mev up and the choice of signs and multiples of 180° is to a large extent arbitrary for Track II. It would be entirely possible to choose a less rapid increase of the phase shifts, for instance as shown in Track IIa in Table VIII in which we have chosen solution 6 at 194 Mev, chosen the signs at 217 Mev as in solution 2 of Table II, and omitted the addition of multiples of 180°. From 169 Mev down, Track IIa agrees with Track II. Unlike II, Track IIa shows a maximum in both α_{33} and α_{31} instead of a monotonic increase.

It will be noted that T3 "disappears" below 169 Mev. In fact, performing the linear tracking between 169 and 144 Mev, the track seems to disappear at about 146 Mev. The detailed behavior is indicated in Table IX. At 169 Mev Track T3 has a value $M=1\times10^{-5}$, i.e., the solution reproduces the mean input

TABLE IX. Disappearance of track T3.

Mev	A_-	A_0	B_-	B_0	C_-	C_0	α_3	α_1	α_{33}	α_{31}	α_{13}	α_{11}
149	0.086	0.174	0.069	−0.191	0.210	0.462	49	−10	−36	−19	−3	8
147	0.088	0.173	0.069	−0.204	0.197	0.453	47	−10	−36	−17	−3	8
145	0.089	0.124	0.079	−0.205	0.177	0.431	14	−12	−47	−5	−2	5
144	0.090	0.120	0.080	−0.210	0.170	0.430	14	−12	−46	−5	−2	6

Mev	A_+	B_+	C_+	M	$\sigma_T(\pi^+)$	$\sigma_T(\pi^-)$
149	0.645	−0.365	2.10	3×10^{-2}	167	60
147	0.636	−0.403	2.04	5×10^{-2}	165	60
145	0.512	−0.372	1.87	1×10^{-4}	145	53
144	0.494	−0.380	1.83	4×10^{-7}	142	53

coefficients essentially exactly. As the energy is lowered, all six phase angles vary smoothly towards their values at 147 Mev shown in Table IX. However, the value of M rises very sharply until it reaches a value of 5×10^{-2} at 147 Mev. Between 147 and 145 Mev there is a sharply discontinuous behavior. This is evidenced most strikingly in the phase angles. At the same time, the value of M has become very much lower again and at 144 Mev essentially solution 1 of Table III is reached. We believe that this behavior indicates that in actual fact Track T3 disappears. What seems to happen as we approach 147 Mev from above is that the computer has to use a set of A_-, B_-, C_-, A_0, B_0, and C_0 more and more different from the interpolated input coefficients in order to find a solution of type T3. Finally the M becomes so high that the minimum disappears and then the computer is forced to look for another "type" of solution at that energy. It searches around for a considerable length of time (this is physically indicated by the comparative length of time it takes to go from 147 to 145 Mev as compared to from 149 to 147 Mev) and finally falls into another track, namely, Track T1.[31]

The variation with energy of the principal phase shifts is seen to be reasonably smooth. We therefore assign the name Track III to it and exhibit it as the third principal track in Table X.

That this track disappears somewhere near 146 Mev can again be understood from Ashkin diagrams using positive pions alone: As we have seen Track III corresponds to essentially the same π^+ scattering as Track I and therefore to the same (positive) Ashkin diagram. However, as we discussed in connection with the 217-Mev analysis, solution III arises from the point a_2 on the Ashkin diagram whereas solutions I and II arise from the point a_1. As will be discussed in Sec. 9, the Ashkin solution a_2 exists only when the total cross section is reasonably close to the resonance cross section $8\pi\lambda^2$ which is the case only in a limited energy region approximately from 150 Mev to 200 Mev. At 120 Mev, a_2 is definitely excluded and, since the $T=\frac{1}{2}$ phase shifts are small, only two solutions are present. Therefore, since Track III is associated with the point a_2 it must disappear somewhere above 120 Mev, namely, at the point where a_2 is no longer admissible. Whether this point be 146 Mev or another energy is not pertinent to our argument.

TABLE X. Track III.

Energy (Mev)	α_3	α_1	α_{33}	α_{31}	α_{13}	α_{11}
217	−67	0	40	37	4	−11
194	−43	1	58	23	5	−19
169	−42	7	49	12	1	2

[31] Or T1a since at this energy Tracks T1 and T1a are indistinguishable.

The "first" solution of Fermi and Metropolis reported in the preceding paper follows essentially Track III at high energies and Track I at low energies. It can again be shown by use of Ashkin diagrams (Sec. 9) that the solutions of Tracks I and III become identical at some energy if only positive mesons are considered; in other words, that Tracks I and III cross. One is therefore free to go from one track to the other without a discontinuity in phase shifts; but there will, of course, be a discontinuity in first derivative. If data for π^+ scattering existed and if they were very accurate, then the decision between these tracks could be made on this basis: If the Track I solution were correct, then the solution using Track I at low and Track III at high energy would show a definite break in the curve of phase shifts *vs* energy, particularly for α_3. However, the availability of only negative-pion data with rather large experimental error, plus the possibility of taking up slack in the phase shifts α_{11} and α_{13}, made it possible for Fermi and Metropolis to obtain a rather smooth curve for all six phase shifts *vs* energy using a combination of Tracks I and III.

There is at present no experimental argument to disprove the Fermi-Metropolis set. However, since Ashkin's point a_2 nearly disappears at 217 Mev, we expect that accurate angular distribution measurements at slightly higher energies (260–300 Mev) will definitely discriminate between Tracks I and II on the one hand and Track III on the other. Because of the physical arguments which we shall give later (Sec. 10), we believe that the combination of Tracks I and III is not the correct solution.

We are thus left with Tracks I and II. The coefficients A_-, B_-, C_-, A_0, B_0, and C_0 of Tracks I and II

coincide with the mean input coefficients by construction.

The π^+ predictions of Tracks I and II for C_+ are shown in Fig. 3. Track I points are shown as little squares and Track II points as little triangles. It will be noted that neither set of points is in sharp disagreement with experiment except for C_+ as deduced from measurements at 188 Mev. For the time being the reader should ignore the curves; we shall discuss their meaning in Sec. 7. The calculated values for A_+ are in good agreement with experiment but for B_+ the calculated value is generally higher than the observed. The most apparent discrepancy is in the predicted B_+ at 217 Mev compared to the measured Brookhaven value at 225 Mev, We shall discuss in Sec. 7 why this is probably not too serious.

The predicted total π^+ cross section of Track I seem to be in very good agreement with the Carnegie experimental data as plotted in Fig. 2. Since these are much better than the angular distributions of π^+, we regard the disagreements with the latter as not serious.

6. SENSITIVITY OF RESULTS

So far the solutions have been obtained with the mean values of the input data as given in Table I. To test the sensitivity of the results to the changes in the input coefficients it was decided to adopt the following procedure at 144, 194, and 217 Mev.

The MANIAC was started off with the solution of Track I at 217 Mev. Then each input coefficient was varied upward and downward roughly to the limit of the experimental error shown in Table I. At the same time the other five input coefficients were kept at their mean value. A new solution was thereby found, showing the effect of changing this one input coefficient. The results of this operation are shown in Tables XI(a) and XI(b).

In Table XI(a) we show first the original solution for ease of reference. In the next line the case where A_- was varied so as to be a smaller number is shown. By leaving blank the values in the columns A_0 through C_0 we mean to imply that these values are essentially unchanged from the original (occasionally one of the other coefficients also varies by 1–2 percent of its original value). We repeat this procedure, varying A_- upward, and then do it in turn for the other coefficients. In Table XI(b) we show the resultant values of A_+, B_+, and C_+ and also list $\sigma_T(\pi^+)$ and $\sigma_T(\pi^-)$ for easy reference. In a few cases the variation of $\sigma_T(\pi^-)$ is more than the ± 2 mb permitted by the transmission experiments. More significant are the variations of the resultant $\sigma_T(\pi^+)$: the interpolation between the better measurements of $\sigma_T(\pi^+)$ on Fig. 2 exclude variations of "A_0 down" and "C_0 down" to the full limit of error for these quantities. The most striking feature of Table XI(a) is that it shows the sensitivity of the coefficients α_{13} and α_{11}: their values apparently cannot be determined with any reliability. On the other hand, the principal phase shifts seem to be rather insensitive to permissible changes of the input coefficients.

Next it was thought desirable to investigate the variation of more than one coefficient at a time. Natu-

TABLE XI. Input variation. 217 Mev, Track I.

(a)

	A_-	A_0	B_-	B_0	C_-	C_0	α_1	α_3	α_{33}	α_{31}	α_{13}	α_{11}
Original	0.13	0.20	0.12	0.19	0.37	0.75	−20	−4	107	−14	7	−7
A_- down	0.110						−21	−3	105	−12	−1	−2
A_- up	0.148						−21	−5	106	−11	9	−8
A_0 down		0.169					−17	−4	120	−20	12	−14
A_0 up		0.229					−23	−3	95	−12	−1	0
B_- down			0.089				−18	−2	108	−15	9	−9
B_- up			0.151				−22	−6	105	−13	3	−3
B_0 down				0.155			−19	−5	104	−13	4	−5
B_0 up				0.228			−21	−3	110	−15	8	−9
C_- down					0.312		−22	−7	108	−9	4	1
C_- up					0.433		−19	−2	107	−10	7	−12
C_0 down						0.626	−17	−3	122	−18	13	−16
C_0 up						0.854	−22	−8	105	−16	3	10

(b)

	A_+	B_+	C_+	$\sigma_T(\pi^+)$	$\sigma_T(\pi^-)$
Original	0.855	0.956	3.46	160	56.0
A_- down	0.916	0.931	3.35	162	54.4
A_- up	0.869	0.980	3.47	161	57.6
A_0 down	0.500	0.983	3.62	136	53.6
A_0 up	1.07	0.927	3.34	174	58.4
B_- down	0.791	0.859	3.49	156	56.1
B_- up	0.941	1.03	3.37	165	55.9
B_0 down	0.909	0.845	3.40	163	56.0
B_0 up	0.797	1.08	3.49	156	56.1
C_- down	0.942	1.01	3.10	157	53.9
C_- up	0.785	0.933	3.73	161	57.7
C_0 down	0.497	0.966	3.35	129	52.7
C_0 up	0.893	1.08	3.61	167	58.7

TABLE XII. Input variation. 217 Mev, Track I.

(a)

	A_-	A_0	B_-	B_0	C_-	C_0	α_3	α_1	α_{33}	α_{31}	α_{13}	α_{11}
Original	0.13	0.20	0.12	0.19	0.37	0.75	−20	−5	107	−14	7	−8
Case 1	0.109	0.168			0.433	0.874	−19	−3	104	−20	4	−6
2	0.148	0.232			0.306	0.630	−23	−8	111	−5	10	−6
3	0.110				0.433		−20	−1	105	−16	3	−9
4	0.148				0.310		−23	−9	107	−8	7	1
5		0.168				0.873	−21	−6	106	−18	6	−3
6			0.151	0.229			−23	−5	108	−14	6	−7
7			0.0892	0.154			−18	−4	105	−14	7	−8
8			0.0891	0.228			−19	−1	112	−17	11	−11
9	0.110		0.0891	0.228	0.433		−19	2	111	−19	7	−12
10		0.232	0.0891	0.228		0.626	−19	0	116	−15	12	−15
21	0.122	0.207	0.136	0.243	0.361	0.776	−25	−4	103	−12	1	3
22	0.152	0.183	0.147	0.155	0.339	0.814	−23	−12	107	−13	2	8
23	0.152	0.215	0.147	0.155	0.404	0.807	−23	−12	98	−17	0	8

(b)

	A_+	B_+	C_+	$\sigma_T(\pi^+)$	$\sigma_T(\pi^-)$
Original	0.855	0.959	3.456	160	56.0
Case 1	0.777	0.934	3.968	168	56.9
2	0.957	1.053	2.842	152	55.2
3	0.831	0.925	3.635	163	56.1
4	0.965	1.078	3.072	159	55.9
5	0.812	1.004	3.725	164	56.8
6	0.867	1.169	3.443	161	56.0
7	0.855	0.756	3.456	160	56.0
8	0.709	0.961	3.546	151	56.0
9	0.691	0.945	3.763	155	56.1
10	0.664	0.952	3.290	141	55.3
21	0.978	1.157	3.404	168	56.5
22	0.899	1.091	3.366	161	57.4
23	0.979	1.021	3.631	175	61.6

rally a great many variations are possible. However, of these, certain ones play havoc with the resultant $\sigma_T(\pi^-)$ and $\sigma_T(\pi^+)$ cross sections and were, therefore, excluded. Certain other variations merely change $\sigma_T(\pi^-)$ a little more than the allowable ± 2 mb. Of the combined variations, cases 21, 22, and 23 were devised with the intent to maximize the change of one or the other of the phase angles.

All the results are shown in Tables XII(a) and XII(b), with the same conventions as those adopted for Tables XI(a) and XI(b). It will be noted that in first approximation the effect of varying more than one coefficient at a time is additive in terms of the effect on the angles, except insofar as α_{11} and α_{13} are concerned.

Table XII(a) and XII(b) show several features. First, it does not seem possible to make α_{31} change sign. This is relevant because there is some evidence that α_{31} is positive around 100 Mev. The same seems to be true of α_1. The phase angle α_3 is rather well established and not very sensitive. The phases α_{13} and α_{11} cannot both be simultaneously made zero, judging from the variations we tried. Changes of α_{33} up to $\pm 9°$ are possible but in these cases [Eqs. (10) and (23)] the total cross section $\sigma_T(\pi^+)$ changes substantially so that the Carnegie measurements of $\sigma_T(\pi^+)$ determine α_{33} very accurately.

Variations of single coefficients for Track I at 144 Mev are shown in Tables XIII(a) and XIII(b). From Table XIII(b) we see that probably the full variations of A_0 down, C_0 down, and C_0 up can be excluded on the basis of $\sigma_T(\pi^+)$. The most interesting result of Table XIII(a) is the instability of α_3 at this energy, and the high stability of α_{33}, especially when large changes of $\sigma_T(\pi^+)$ are excluded.

Variations of more than one coefficient at a time were also carried out for Track I at 144 Mev. The results are given in Tables XIV(a) and XIV(b). Of these, case 34 was set up with the specific intention to lower the somewhat high value of α_1. It will be seen that indeed α_1 can be lowered quite markedly, namely from 13 to 9°. While the values of α_{11} and α_{13} are not too big we still did not find a variation which gave $\alpha_{11}=\alpha_{13}\approx 0$ and α_1 less than 12°.

Input variations of one coefficient at a time were also carried out at 194 Mev for Track I. The phase shifts showed appreciably greater sensitivity but not quite as great as we anticipated for this critical energy region. However, in a few of these variations the resulting solutions had a very large M value [Eq. (23)]. This meant that the phase angles, which the computer obtained as a solution, led to A_-, B_-, C_-, A_0, B_0, and C_0 different from the mean input values, apart from the one that was purposely changed. We believe this to indicate that these particular input changes do not permit a solution in the neighborhood of Track I. This was in particular the case when B_0 or C_0 was increased to its experimental limit. In both cases a solution could be found only if at the same time C_- was increased even

TABLE XIII. Input variation. 144 Mev, Track I.

(a)

	A_-	A_0	B_-	B_0	C_-	C_0	α_3	α_1	α_{33}	α_{31}	α_{13}	α_{11}
Original	0.0900	0.120	0.0800	−0.210	0.170	0.430	−13	14	46	5	3	−5
A_- down	0.0704						−12	13	46	5	1	−4
A_- up	0.109						−15	13	47	5	4	−8
A_0 down		0.0774					−12	12	41	10	5	−10
A_0 up		0.170					−19	13	50	1	1	−4
B_- down			0.0488				−9	14	47	4	2	−5
B_- up			0.107				−20	10	45	7	4	−8
B_0 down				−0.250			−8	11	49	3	2	−4
B_0 up				−0.159			−20	13	44	8	4	−8
C_- down					0.119		−11	13	46	3	1	−7
C_- up					0.220		−16	12	47	7	4	−5
C_0 down						0.244	−23	14	37	4	6	−4
C_0 up						0.617	−7	13	57	8	−1	−10

(b)

	A_+	B_+	C_+	$\sigma_T(\pi^+)$	$\sigma_T(\pi^-)$
Original	0.494	−0.381	1.843	143	52.9
A_- down	0.465	−0.362	1.805	138	50.3
A_- up	0.435	−0.396	1.882	138	55.4
A_0 down	0.307	−0.390	1.907	122	47.4
A_0 up	0.669	−0.364	1.805	165	59.3
B_- down	0.500	−0.480	1.869	146	52.9
B_- up	0.483	−0.288	1.818	141	52.9
B_0 down	0.449	−0.504	1.882	148	52.9
B_0 up	0.532	−0.219	1.818	140	52.9
C_- down	0.498	−0.305	1.651	136	50.7
C_- up	0.485	−0.438	1.997	149	55.0
C_0 down	0.444	−0.521	1.267	120	44.9
C_0 up	0.492	−0.232	2.330	165	60.9

beyond its experimental limit. Thus if a more accurate measurement gave values of B_0 and C_0 near the present upper experimental limit, and if at the same time C_- were left unchanged, then there would probably be no solution near Track I. Apart from this, an exact phase shift determination at this energy would require particularly precise knowledge of the experimental angular distributions.

For the Yang track, Track II, the variation was carried out for single coefficients only and only at 144 Mev. Again (as in the case of Track I) α_3 is very sensitive, while α_{33} and α_{31} are not.

7. INTERPOLATION OF PHASE ANGLES

From the discussion so far, it is evident that we have more reason to believe the results of Tracks I and II at 120 Mev, 144 Mev, and 217 Mev than at the intermediate energies between 144 and 217 Mev. The experimental data are more accurate at the lowest and highest energy; on the other hand, the phase shifts are less sensitive to the experimental data than at the intermediate energies. It is, therefore, perhaps more reasonable to obtain the phase shifts at the intermediate energies by interpolation of the phase shifts between 120 (or 144) and 217 Mev rather than by actual analysis

TABLE XIV. Input variation. 144 Mev, Track I.

(a)

	A_-	A_0	B_-	B_0	C_-	C_0	α_3	α_1	α_{33}	α_{31}	α_{13}	α_{11}
Original	0.0900	0.120	0.0800	−0.210	0.170	0.430	−14	13	47	5	3	−6
Case 11		0.0699				0.678	−6	12	44	19	2	−1
12		0.143				0.307	−19	14	42	2	4	−4
31		0.169	0.111	−0.160	0.121	0.415	5	18	46	−1	−9	1
32		0.0684	0.111	−0.160	0.120	0.675	5	17	44	12	−5	−11
34			0.0488	−0.159			−12	9	48	3	2	−6
35		0.170	0.0486	−0.159	0.119		−9	11	51	−5	−3	−5

(b)

	A_+	B_+	C_+	$\sigma_T(\pi^+)$	$\sigma_T(\pi^-)$
Original	0.494	−0.381	1.843	143	52.9
Case 11	0.192	−0.224	2.637	138	57.1
12	0.554	−0.465	1.459	134	50.6
31	0.520	0.171	1.507	132	56.4
32	0.298	0.214	2.159	132	54.6
34	0.546	−0.322	1.834	149	52.9
35	0.715	−0.210	1.587	125	57.1

TABLE XV. Values of α_{33} for interpolation (b) of Sec. 7.

Mev	α_{33}
120	30.0°
127	34.0°
133	38.1°
139	42.5°
144	46.0°
151	51.5°
160	58.8°
169	66.5°
178	73.9°
184	78.9°
188	82.5°
194	87.5°
202	94.3°
208	99.4°
217	107.0°

of the experimental data. It is encouraging for such interpolation that Track I shows already an almost linear behavior for α_{33} between 120 and 217 Mev. Similarly, if the values of α_3 are plotted against the momentum of the meson (in the center-of-mass system) and if a straight line is drawn on this plot between the values (Track I) of α_3 at 120 and 217 Mev, then this line will also fit the experimental data at energies below 120 Mev down to 60 Mev.

In view of the above, we tried the following interpolations:

(a) All phase angles linearly interpolated between the Track I values at 120 and 217 Mev.

(b) Between 120 and 217 Mev, Track I values, α_1 parabolically interpolated with zero slope at 120 Mev,[32] α_{33} read off from a smooth plot of Track I points as given in Table XV, other 4 phase angles linearly interpolated.

(c) Between 144 and 217 Mev, Track I, all phase angles linearly interpolated.

(d) Between 144 and 217 Mev, case 34 phase angles (table 14a) at 144 Mev and Track I phase angles at 217 Mev, all phase angles linearly interpolated.

(e) Between 144 and 217 Mev, Track II, all phase angles linearly interpolated.

(f) Between 144 and 217 Mev, Track IIa, all phase angles linearly interpolated.

Of these interpolations, we consider (b) the most useful one in that it comes closest to reproducing the experimental data. The more straightforward interpolation (a) gave values for B_- which were extremely low at all intermediate energies between 120 and 217 Mev; this was the reason for choosing interpolation (b). The results of interpolation (b) for the coefficients A, B, C are shown in Table XVI. For the $T=\frac{3}{2}$ phase shifts we have also extrapolated their behavior beyond 217 Mev by means of straight lines and computed A_+, B_+, and C_+. These are also shown in Table XVI. The extrapolation to higher energies was not carried out for the coefficients involving $T=\frac{1}{2}$ phase shifts since α_1 is changing so rapidly in the region around 200 Mev, and it is difficult to predict its behavior beyond 200 Mev. The results of interpolation (b) are also shown graphically by means of a solid curve in Figs. 3 through 6. Furthermore, the total cross sections have been computed for interpolation (b) and are shown as solid curves on Figs. 1 and 2.

The coefficients A_0, A_+, C_0, and C_- are given very well by interpolation (b) except for C_- at 169 Mev which is slightly outside experimental error. All other points for A_0, A_+, C_0, and C_- are well within the experimental error. The calculated values for B_0 tend to be slightly too high, those for B_- appreciably too low; the latter quantity will be discussed in more detail below. The erratic behavior of A_- which is found experimentally is not reproduced by interpolation (b). This discrepancy of A_- at 169 Mev and B_- at 144 Mev are the only disagreements with the negative pion scattering data worth considering; at other energies A_- agrees well within and B_- is just at the limit of the experimental error.

TABLE XVI. Phase angle interpolation (b) of Sec. 7.

Mev	A_-	A_0	A_+	B_-	B_0	B_+	C_-	C_0	C_+
120	0.038	0.050	0.200	0.026	−0.150	−0.360	0.090	0.250	1.040
127	0.055	0.064	0.289	0.027	−0.147	−0.366	0.110	0.270	1.167
133	0.066	0.081	0.371	0.029	−0.152	−0.375	0.126	0.306	1.322
139	0.082	0.100	0.476	0.026	−0.144	−0.368	0.148	0.334	1.477
144	0.094	0.115	0.559	0.022	−0.138	−0.356	0.155	0.367	1.606
151	0.111	0.140	0.684	0.021	−0.120	−0.315	0.184	0.406	1.812
160	0.132	0.172	0.836	0.021	−0.090	−0.227	0.219	0.470	2.117
169	0.149	0.200	0.965	0.020	−0.045	−0.094	0.252	0.526	2.395
178	0.158	0.221	1.055	0.020	0.013	0.080	0.287	0.581	2.667
184	0.159	0.231	1.086	0.025	0.047	0.206	0.306	0.617	2.841
188	0.160	0.233	1.090	0.029	0.071	0.290	0.321	0.640	2.956
194	0.155	0.235	1.083	0.039	0.104	0.426	0.337	0.672	3.100
202	0.149	0.230	1.034	0.063	0.149	0.641	0.357	0.711	3.287
208	0.143	0.220	0.977	0.082	0.171	0.776	0.364	0.731	3.369
217	0.130	0.200	0.860	0.120	0.190	0.960	0.370	0.750	3.460
225			0.731			1.097			3.456
232			0.617			1.194			3.402
241			0.472			1.277			3.245

[32] This horizontal tangent is indicated from our own analysis and also fits well with the values of α_1 known between 60 and 120 Mev.

For the positive pion scattering, disagreement at 151 Mev is not too bad. At 188 Mev the predicted values of both B_+ and C_+ are very much higher than the center of the observations but if the angular distribution is computed from our A_+, B_+, and C_+ of interpolation (b) and compared with the experimental points the agreement is well within the limits of error except at 45°. At 225 Mev the predicted value for C_+, 3.46, agrees very well with the measured value of 3.8, the measured value now lying above the prediction. The predicted value for B_+, 1.10, is considerably higher than the measured 0.44 but this discrepancy is probably not serious for two reasons. First, it is more difficult to deduce B_+ from the measurements than any other coefficient because the measured distribution does not

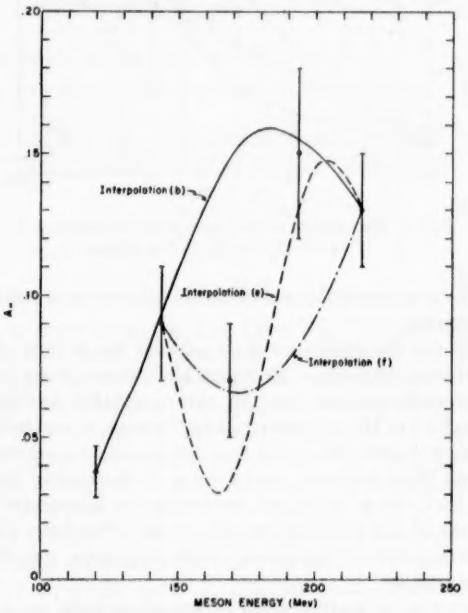

FIG. 4. The coefficient A_- of Eq. (3) as a function of energy. The curves are interpolations discussed in Sec. 7.

fit an expression of the form (2) very well. Second, the coefficient B_+, in contrast to A_+ and C_+, varies in a complicated way with energy; in fact, it must go through a maximum at some energy not far above 225 Mev (see, e.g., Fig. 11). Indeed, B_+ is given by

$$\tfrac{1}{2}B_+ = \sin\alpha_3[2\sin\alpha_{33}\cos(\alpha_{33}-\alpha_3) + \sin\alpha_{31}\cos(\alpha_{31}-\alpha_3)]. \quad (30)$$

If α_{31} is small, only the first term matters, and with $\alpha_3 \approx -20°$, this term has a maximum for $\alpha_{33} \approx 125°$. This behavior is shown by our extrapolation of B_+: while B_+ decreases very much when the energy is decreased below 225 Mev, it does not increase much when it is raised. Hence, due to the wide energy spread of the mesons used in the Brookhaven experiments the average of B_+ should be lower than the value at 225 Mev.

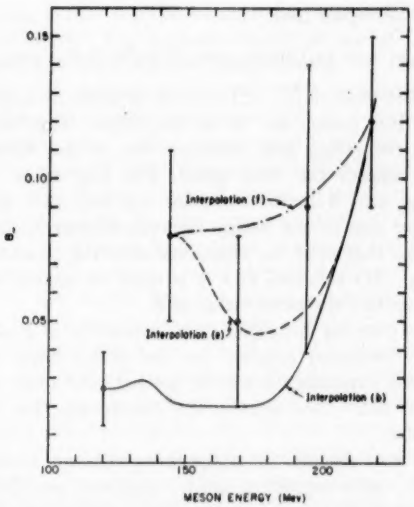

FIG. 5. The coefficient B_- of Eq. (3) as a function of energy. The curves are interpolations discussed in Sec. 7.

Perhaps the most striking behavior is exhibited by the coefficient B_-. In contrast to B_0 and B_+, which change sign from negative at low to positive at high energies, B_- stays positive all the time. This is accomplished by the fact that the S scattering amplitude which is proportional to $(2\alpha_1+\alpha_3)$ for π^- scattering itself changes sign from positive to negative. In fact, it is precisely the positive sign of B_- at 217 Mev which forces us to make α_1 zero or negative at this energy.

The tendency of the B coefficients to go through zero, however, still manifests itself in our predicted B_- by the fact that the predicted values stay small and almost constant over a large energy interval from about 100 to 180 Mev. To investigate this more closely, we note that the coefficient B_- is given by Eqs. (9), (17), and (18). In particular, if in first approximation we set $\alpha_{31}=\alpha_{13}=\alpha_{11}=0$, then $y=b$. Furthermore, since α_3 and α_1 are small, we shall set $\sin\alpha_3=\alpha_3$ and $\sin\alpha_1=\alpha_1$. Then

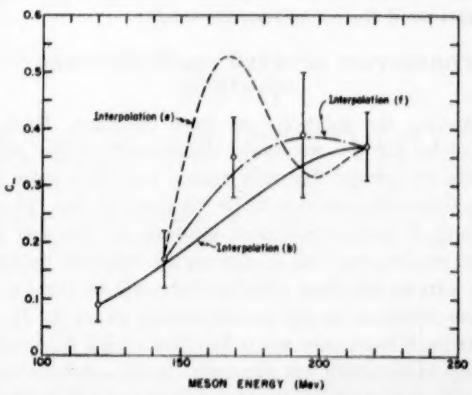

FIG. 6. The coefficient C_- of Eq. (3) as a function of energy. The curves are interpolations discussed in Sec. 7.

it can be shown that

$$B_- \approx (\alpha_3+2\alpha_1)\sin\alpha_{33}\cos\alpha_{33}+(\alpha_3^2+2\alpha_1^2)\sin^2\alpha_{33}. \quad (31)$$

The first term in Eq. (31), which is linear in α_3 and α_1, is for this reason apt to be the larger. However, the coefficient $\cos\alpha_{33}$ goes through zero at the resonance which makes the term small. The first term would change sign if it were not for the fact that α_1 also changes sign in our energy interval. However, the fact remains that near the resonance only the second term in Eq. (31) survives and it is small of second order; this explains the small value of B_-.

The peculiar behavior of B_- would be a good test of our proposed solution for the phase shifts. More accurate experiments will be needed, and these might at the same time resolve the discrepancy for A_- at 169 Mev.

We now discuss our other interpolations: interpolation (c) gave somewhat similar results as interpolation (b) except that B_- has in this case a sharp peak at 145 Mev. The latter seems to be impossible because it is then very hard to connect with the 120-Mev point. Interpolation (d) gave essentially the same result as interpolation (c) but, because of the extreme phase angles chosen at 144 Mev, B_- started lower than for case (c) at 144 Mev; hence (d) is more similar to interpolation (b).

As to interpolations (e) and (f) we found the following: the true Yang Track II gives rather pronounced maxima and minima in the coefficients, A, B, C, as might be expected because of the very rapid variation of the Yang phase shifts. Track IIa gives quite smooth results for the coefficients and some of them are shown in Figs. 3 through 6. It is seen that a better experimental determination of A_- and B_- could well decide between Tracks IIa and I. The interpolated Track II phase shifts are shown to be unreasonable by the erratic curves for the A, B, C; indeed, linear interpolation of the Yang phase shifts is not appropriate and does not, of course, rule out the Yang phase shifts as such because we know there is always a Yang set to every Fermi set if the α_{11} and α_{13} are small.

8. CONNECTION BETWEEN FERMI AND YANG SOLUTIONS

Among the solutions we have obtained, Track I gives by far the smoothest dependence of the phase shifts on energy. For this reason, and even more for the theoretical reasons to be discussed in Sec. 10, we believe it to be the correct solution. In this and the next section, we wish to discuss the relations between the various solutions. Further light will be thrown on these relations by the accompanying paper by R. L. Martin. We are very much indebted to Dr. Martin for many ideas which are presented in this and the next section; he pointed out to us first that the Fermi and Yang tracks for α_{33} must cross as shown in Fig. 7, and

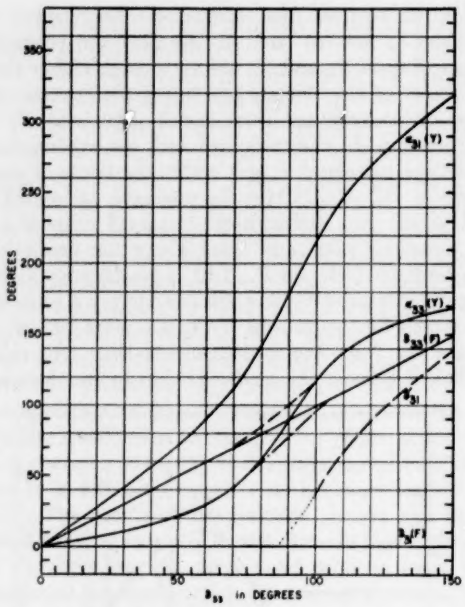

FIG. 7. The relation of the phase angles of Solutions I′ (Fermi type) and II′ (Yang type).

he gave us invaluable aid on the interpretation of Ashkin diagrams.

In our discussion, we shall consider the *positive* pion scattering as given. This is possible because, as we have repeatedly pointed out, all the acceptable solutions, Tracks I to III, give very nearly the *same* π^+ scattering. This in turn is due to the fact that α_{11} and α_{13} are small in all these solutions, and even α_1 is moderately small so that the π^- data can essentially be interpreted in terms of $T=\frac{3}{2}$ scattering with small corrections. Considering the π^+ scattering as given greatly simplifies the analysis.

Instead of starting from experimental data, we shall in this and the next section take the point of view that there is a "true" set of phase shifts very similar to Track I. We shall call it Track I′. Then from this true set we can calculate a π^+ angular distribution which we shall call the *theoretical distribution*. We shall then determine what other sets of phase shifts, if any, will also be compatible with the theoretical angular distribution; these we shall call "supplementary solutions."

We denote phase shifts in the "true solution" Track I′ by δ instead of α and define them as follows: δ_{31} shall be zero for all energies, δ_{33} shall increase monotonically and fairly rapidly with energy, and δ_3 shall be negative and decrease slowly with energy. We shall not specify the relation between energy and phase shifts but merely the relation between the two nonvanishing phase angles, which we shall take to be

$$\delta_3=-10^\circ-0.1\delta_{33}. \quad (32)$$

This is rather well fulfilled by the original Track I in our energy range.

The "true solution" is of the Fermi type and we shall first investigate the Yang solution corresponding to it; the Yang phase shifts will be denoted by α. By definition the Yang solution has the same S phase as the Fermi solution, hence

$$\alpha_3=\delta_3. \tag{33}$$

The difference between the P_1 and P_3 phase shifts is reversed, so that

$$\alpha_{31}-\alpha_{33}=\delta_{33}-\delta_{31}=\delta_{33}. \tag{34}$$

Finally the amplitude for P scattering without spin flip is preserved, i.e., [see Eq. (15)]

$$b\equiv 2(e^{2i\alpha_{33}}-1)+e^{2i\alpha_{31}}-1=2(e^{2i\delta_{33}}-1). \tag{35}$$

Together with Eq. (34), this yields

$$e^{2i\alpha_{33}}=(2e^{i\delta_{33}}+e^{-i\delta_{33}})/(2e^{-i\delta_{33}}+e^{i\delta_{33}}). \tag{36}$$

It is obvious that the right-hand side has absolute value unity so that a solution α_{33} exists, and it is easily seen that

$$\tan\alpha_{33}=\tfrac{1}{3}\tan\delta_{33}. \tag{37}$$

For small δ_{33}, Eq. (37) gives

$$\alpha_{33}\approx\tfrac{1}{3}\delta_{33}, \tag{38}$$

i.e., a small 33-phase, and then Eq. (34) yields $\alpha_{31}=(4/3)\delta_{33}$. As δ_{33} approaches 90°, however, α_{33} will also approach 90°: With our particular choice of the "true" Fermi solution, the Yang solution will have a P_1 resonance at exactly the same energy as the Fermi solution. The only difference is that the Yang phase passes through 90° much faster than the Fermi phase. This is illustrated in Fig. 7 which shows the Yang phase shifts α_{33} and α_{31} as functions of the Fermi phase δ_{33}. As δ_{33} approaches 180°, so does α_{33}, only faster.

The P_1 phase shift α_{31} changes much faster still. We have

$\alpha_{31}=(4/3)\delta_{33}$	90°	180°	270°	360°
when δ_{33}=small	60°	90°	120°	180°.

This is also given in Fig. 7. Thus, where the Fermi phase shifts show one resonance only, $\delta_{33}=90°$, the Yang shifts show three, one in α_{33} and two in α_{31} (90° and 270°). Somewhat surprisingly, these three resonances give exactly the same angular distribution at every energy as the one Fermi resonance so that the two solutions cannot be distinguished by experiment. However, the Fermi solution is far simpler and hence preferable unless there are strong theoretical arguments to the contrary. The similarity of the Yang solution to Track II is obvious. In particular, when $\delta_{33}=107°$ (which corresponds to 217 Mev on Track I) then Fig. 7 gives $\alpha_{33}=133°$ and $\alpha_{31}=240°$ which agree closely with the Track II values (Table VIII).

One important feature of our two solutions, Fermi and Yang, is that the curves α_{33} and δ_{33} cross. With our choice of $\delta_{31}=0$, this happens exactly at $\delta_{33}=90°$, and thus at $b=-2$, Eq. (35). In other words, for crossing to occur, the real past of b must have a specific value, -2, when the imaginary part vanishes. If b is derived from experimental data, rather than from our "true solution," this will in general not be fulfilled, and then the crossing will not occur. Therefore, if we start from experimental data, it may appear more natural to join the curve α_{33} at large phase angles to the curve δ_{33} at small phase angles, and vice versa. This is indicated by the dashed and dot-dashed connecting lines on Fig. 7. In other words, what we call the Yang solution at high energies is then joined to the Fermi solution at low ones (dashed connection). We shall denote this combination as Track I′–II′ and its phase angles by δ'. The δ_{31}' corresponding to this solution is zero at low energy and it is easy to see that continuity requires us to choose $\delta_{31}'=\alpha_{31}-\pi$ at high energies; then $\delta_{31}'<\delta_{33}'$, throughout as for a Fermi solution. The curve for δ_{31}' is also shown in Fig. 7, by a dashed line. It rises suddenly and rapidly from zero to high values. The exact behavior of δ_{31}' at the start from zero depends on the precise way how the lower and upper parts of the δ_{33}' curve are joined; to indicate the uncertainty of this beginning, it is shown dotted on Fig. 7. The behavior of δ_{31}' is of course physically very unreasonable. However, on purely experimental grounds, the primed solution cannot be excluded. The δ' solution will be further discussed in the accompanying paper by Martin.

9. THE FERMI-METROPOLIS SOLUTION

Ashkin and Vosko[6] have pointed out that there are in general four solutions to the π^+ phase shifts rather than merely the Fermi and Yang solutions. To understand the other two solutions, we use Ashkin diagrams explicitly. We again consider positive pions only, and assume that there is a "true solution," defined as in the last section.

In the Ashkin-Vosko theory, we start from the amplitude for scattering without spin flip,

$$a+b\cos\theta, \tag{39}$$

where b is given by Eq. (35) and

$$a=e^{2i\alpha_3}-1 \tag{40}$$

from Eq. (14). Ashkin and Vosko show that the experimental data on π^+ give (1) the quantity $|a+b|$, (2) the real part of $a+b$, and (3) the quantity $|a-b|$. The analysis then proceeds in four steps (see Fig. 8), *viz.*,

1. $a+b$ is determined by the experimental data (except for the sign of its imaginary part). The point $\frac{1}{2}(a+b)$ is plotted on a graph; we shall call it point P.

2. A circle is drawn around point P with radius $\frac{1}{2}|a-b|$. A fixed circle is also drawn around the point -1 with radius 1; we shall call it the a circle. The intersection of the two circles determines the point a. There are in general two intersections, a_1 and a_2.

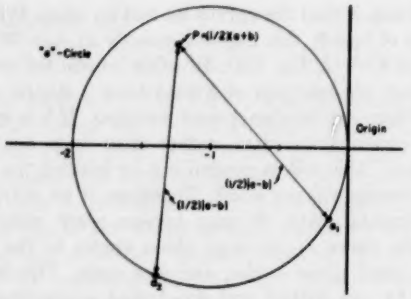

FIG. 8. Typical Ashkin diagram constructed from positive scattering coefficients A_+, B_+, and C_+.

3. From $a+b$ and a, b is determined. By Eqs. (15) and (24), b must satisfy the inequality

$$|b+3|<3. \tag{41}$$

Sometimes one of the solutions, a_2, is ruled out by this inequality. We must also have from Eqs. (15) and (24):

$$|b+3|>1. \tag{41a}$$

4. From b, the phase shifts α_{31} and α_{33} are found, using Eq. (15).

We shall construct the point $\frac{1}{2}(a+b)$ and determine $|a-b|$, not from experimental data, but from our "true solution." Thus we set

$$a=e^{2i\delta_3}-1, \tag{42}$$

$$b=2(e^{2i\delta_{33}}-1) \tag{43}$$

where δ_3 and δ_{33} are considered *known* quantities. We then proceed with the Ashkin and Vosko method to find *all* solutions corresponding to the same "experimental data." Clearly, as we proceed to find the intersections of the two circles according to step 2 of the Ashkin and Vosko procedure, one of the intersections will be exactly the "input a" of Eq. (42); we shall call it a_1 and thus have the first solution,

$$a_1=a, \quad b_1=b. \tag{44}$$

This solution satisfies condition (41) by construction, and leads to the Fermi and Yang solutions discussed in the last section.

The other solution, a_2, can then be found and examined as to whether it satisfies the inequality (41). To facilitate this, we shall for the moment simplify our assumed "true solution" still further by assuming $\delta_3=0$. Then the point P will lie on the a circle itself, at an angle $2\delta_{33}$ from the center. The point a_1 is now at the origin, and hence, as can be seen by suitable modification of Fig. 8, the point a_2 is by symmetry at the angle $4\delta_{33}$ on the a circle. Therefore,

$$a_2=e^{4i\delta_{33}}-1, \tag{45}$$

and the corresponding phase shift is

$$\alpha_3=2\delta_{33}. \tag{46}$$

Further,

$$b_2=a+b-a_2=2e^{2i\delta_{33}}-e^{4i\delta_{33}}-1, \tag{47}$$

and

$$|b_2+3|^2=9+4(\cos2\delta_{33}-\cos4\delta_{33})\leqslant 9. \tag{48}$$

Thus we must have

$$\cos2\delta_{33}<\cos4\delta_{33}, \tag{49}$$

which is satisfied if and only if

$$60°<\delta_{33}<120°. \tag{50}$$

In other words, the solution a_2, b_2 is not admissible if the "true" phase shift δ_{33} is small; in this region, there are only two solutions to our artificial problem, the Fermi and the Yang. When the true δ_{33} exceeds 60°, a new solution a_2 appears which is characterized by the large and rapidly varying phase shift α_3 given by Eq. (46). This solution will disappear again when δ_{33} reaches 120°. Thus the new solution can exist only if the cross section is large, in fact fairly close to the resonance cross section. Trouble with the phase shift analysis is, therefore, expected to arise, and in practice does arise, only in the region of large cross section. This fact has been mentioned already in Sec. 5.

In general, for any given value of δ_{33}, there will be two solutions belonging to a_2, of the Fermi and the Yang types, but at the points where the solution a_2 just appears or disappears, there will be only one set α_{33}, α_{31} because $|b+3|$ is exactly 3. This is the reason why there is only one solution of this type at 217 Mev, as shown in Sec. 4a.

If we start from low energies and thus from low δ_{33}, the solution a_2, b_2 will at first not exist, and when it first appears it has completely different values of all phase shifts, *viz.*,

$$\alpha_3=120°, \quad \alpha_{33}=30°, \quad \alpha_{31}=30°,$$

as compared with the "true" solution,

$$\delta_3=0, \quad \delta_{33}=60°, \quad \delta_{31}=0.$$

Therefore, no transition can be made at this point from the δ solution to the α solution. However, as δ_{33} (and the energy) increases, the point a_2 moves around the a circle and finally reaches the origin when $\alpha_3=180°$. This suggests a change in the definition to

$$\alpha_3'=\alpha_3-\pi=2\delta_{33}-\pi. \tag{51}$$

Then $\alpha_3'=\delta_3=0$ when $\delta_{33}=90°$. In fact, at this point *all* phase shifts of solution a_2 will agree with those of solution a_1. Therefore, we may use the "true" solution a_1 up to this point, and then switch to solution a_2, *without any discontinuity* in any of the phase shifts. This can be done either with the Fermi or the Yang set. After the switch is made, the phase α_3' will go from 0 to 60°.

We have still another alternative: it has been pointed out that the imaginary part of $a+b$ cannot be determined experimentally. It is, therefore, always possible

to replace the point P by its mirror image P' with respect to the real axis, this replaces δ_{33} by $\pi-\delta_{33}$, and changes the sign of all other phase shifts; α_3' is replaced by

$$\alpha_3''=-\alpha_3'=\pi-2\delta_{33}. \tag{52}$$

We can thus use the following solution: $\alpha_3=0$ for δ_{33} up to 90°, and α_3'' thereafter. The transition again involves no discontinuity in phase shifts. After the transition, the phase α_3'' goes from 0 to $-60°$; then the solution disappears. The behavior of α_3 follows essentially our previous Track I at low energies and switches to Track III afterwards, as will become still clearer in the rest of this section. We shall, therefore, call this solution Track I′–III′.

We now make our discussion more realistic by returning to the original choice (32) for our "true" solution. For this case, we have calculated numerically the phase shifts corresponding to the a_2 solution and shown them in Fig. 9. Both the solutions α_3' and α_3'' are shown.[33] Their similarity with the simpler case discussed above will be clear. It is possible either to go from solution δ_3 at low energies to α_3' at high; then the transition occurs at the point $\delta_{33}=66°$ and α_3' goes to high *positive* values afterwards. Or the transition can be made from α_3 to α_3''; this transition occurs at $\delta_{32}=81°$ and α_3'' then goes to large negative values. *This is essentially the behavior of the Fermi-Metropolis solution.*

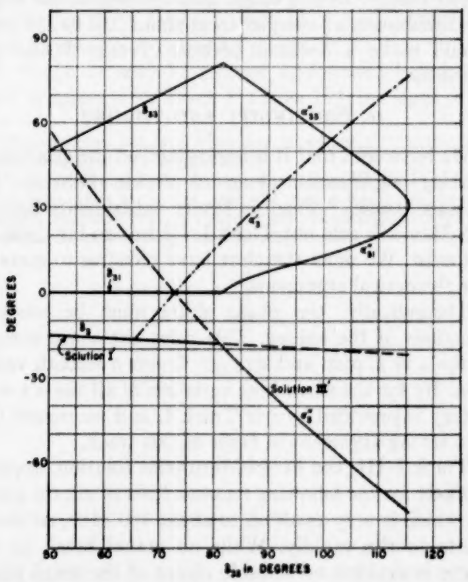

FIG. 9. The relation between the phase angles of Solution I′ (Fermi type) arising out of the point a_1 and Solution III′ (Fermi type) arising out of the point a_2.

[33] Actually there is a very small region around $\delta_{33}=75°$ where the a_2 solution does not exist even through $|b+3|>3$; in this region there is no solution because $|b+3|<1$, which violates Eq. (41a).

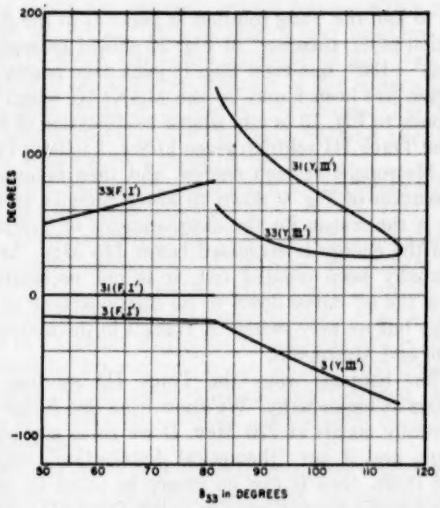

FIG. 10. Solution IV′; i.e., Solution I′ (Fermi type) arises out of the point a_1 until $\delta_{33}=81°$ and Solution III′ (Yang type) arises out of the point a_2 from then on.

We also give in Fig. 9 the calculated values of α_{33}'' and α_{31}'' which are derived from our "theoretical distribution" by taking the S phase shift to be α_3''. Figure 9 gives the Fermi type phases, Fig. 10 the Yang type. The Fermi type phases are again very similar to those of the Fermi-Metropolis solution: α_{33} goes up to a high value (in our case 81°) then decreases to about 32°. The phase α_{31} is zero until α_{33} reaches its maximum, then it increases rapidly and becomes finally equal to α_{33}. At this point, the solution disappears.

The solutions of Fig. 9 have continuous phase shifts but discontinuities in the derivatives of the phase shifts with respect to energy. If the experimental data were infinitely accurate, and if they were to agree with our "theoretical distribution," then these discontinuities in derivative would show up and could be used to rule out the a_2 type solutions. At present, the inaccuracy of the experimental data smooths out the plot of phase shift *vs* energy, and this tendency is further helped if also the phase shifts α_1, α_{13}, and α_{11} are available to fit the experimental data. Therefore, the Fermi-Metropolis solution was much smoother than our solution on Fig. 9 and did not show an actual discontinuity in derivative.

The Yang solution, Fig. 10, does not join to the low-energy *Fermi* solution at the transition point, $\delta_{33}=81°$, but there is in this case a discontinuity in value as well as derivative. The Yang solution corresponding to point a_2 would join smoothly to the low-energy *Yang* solution, Fig. 7. It is interesting that for the Yang solution given in Fig. 10, both α_{31}'' and α_{33}'' *decrease* with increasing energy (i.e., δ_{33}); they become equal to each other and to the phases of the Fermi solution, Fig. 9, when the solution a_2 disappears at $\delta_{33}=115.5°$. If one

tries to join the Yang solution of point a_2 to the *Fermi* solution of a_1, then α_{31}'' of Fig. 10 should be replaced by $\alpha_{31}''-180°$, but even then it joins very poorly. No solution has been found by the MANIAC which corresponds to Fig. 10 or any simple modification of it.

The Track III solution given in Sec. 5 follows Fermi and Metropolis at high energy, and then follows the a'' solution of Fig. 9 down to lower energies as well. This is the reason for the disappearance of Track III when the energy is decreased below 146 Mev. As has repeatedly been pointed out, it is not necessary to follow the a'' curve down to its disappearance at low energy but we may switch to Track I in the manner of Fermi and Metropolis.

What happens when the Track III solution disappears at high energy? We know from Sec. 5 that this essentially occurs at 220 Mev. If we go to any higher energy, and if our "theoretical distribution" remains valid there, then it can no longer be fitted by phase shifts which join continuously to the Track III solution at 220 Mev. Because of experimental errors, an approximate fit to the experimental data will remain possible for some time but ultimately the Track III solution will break down. This prediction is, of course, true only if our theoretical distribution really agrees with the experimental angular distributions of the future.

If we are correct in saying that Track III disappears at 220 Mev, then the near-equality of α_{31} and α_{33} at 217 Mev should be considered a danger sign. For the equality $\alpha_{31}=\alpha_{33}$ represents an extremum: $|b+3|$ has then its maximum value 3. To let α_{31} increase beyond α_{33} does not help, but merely brings us into the domain of Yang solutions. The condition $\alpha_{31}=\alpha_{33}$ eliminates the spin flip term and thus helps to increase the anisotropy of the angular distribution: this is necessary in the Track III solution because the large α_3 provides a very large isotropic term by itself.

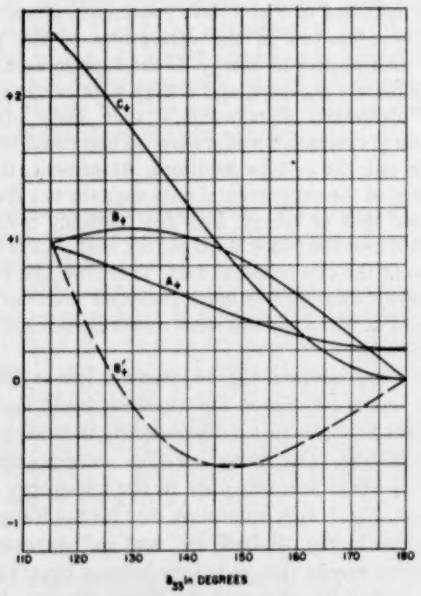

FIG. 11. The manner in which the breakdown of Track III might occur.

In Fig. 11, we illustrate the manner in which the breakdown of Track III might manifest itself. The figure is constructed as follows: we still assume that the "theoretical distribution" is the correct one. On the basis of the behavior of the phases when Track III disappears, we surmise that a Type III solution will approximate the angular distribution most closely if we assume $\alpha_{31}=\alpha_{33}$. With this assumption, we can then determine α_3 and α_{33} for an "extrapolated Track III" by requiring that A_+ and C_+ be correctly given thus:

$$\sin^2\alpha_3=A_+, \tag{53}$$

$$\sin^2\alpha_{33}=C_+/9. \tag{54}$$

Then we can calculate B_+; it is

$$B_+'=6\sin\delta_3\sin\delta_{33}\cos(\delta_{33}-\delta_3). \tag{55}$$

This "Track III value" of B_+' can then be compared with the correct value, B_+ of the theoretical distribution. The result is shown in Fig. 11: there is evidently no similarity at all between B_+ and B_+'. While B_+ still rises beyond the critical point, $\delta_{33}=115°$, B_+' falls sharply and even becomes negative at a somewhat higher energy. Even a rough measurement of the angular distribution at energies from about 250 to 350 Mev should make a decision between Tracks I and III possible.

10. CONTINUITY AND THEORY

We have seen that it is impossible, on the grounds of existing experiment alone to decide between the various "tracks." Possibly future experiments beyond 225 Mev will rule out Track I–III but so far these do not exist. We must therefore have recourse to more or less theoretical arguments.

Theoretically, the phase shifts must be analytic functions of the energy. This rules out sharp corners in the α *vs* E plot, and strongly favors a smooth variation. By far the smoothest variation of all the α's with energy is provided by our Track I, and we regard this as a strong argument in favor of this track.

Track I–III, the Fermi-Metropolis solution, appears unlikely for the following reasons. First of all, the phase α_{31} which is very small up to about 160 Mev, suddenly starts to rise rapidly. While an actual break in the curve is avoided by suitable choice of the small phase shifts α_{11}, α_{13}, we still believe that it would be almost impossible to devise a theory to give just this behavior of α_{31}.

Stranger still is the behavior of α_3. Apart from a complicated behavior at low energies,[34] this quantity up to

[34] R. E. Marshak, Phys. Rev. 88, 1208 (1952).

about 150 Mev behaves very regularly, being represented quite well by a straight line; in degrees, we have

$$\alpha_3 = 9.6° - 17.1°\eta, \tag{56}$$

where η is the meson momentum in units of μc in the center-of-mass system. Now this is what should be expected from a strong repulsive potential of short range (about $2\hbar/Mc$). Indeed, available theory, either using the Tamm-Dancoff method[35] or a contact transformation,[36] predicts just such a repulsion, arising from the virtual production of a nucleon pair. If this is correct, then a behavior like Eq. (56) should remain valid up to energies of the order Mc^2. Quite generally, *any* strong repulsive potential will give a negative phase shift proportional to the momentum, and when the energy gets high enough to penetrate the repulsive core, the slope of the curve α *vs* η will become *smaller*. It seems almost impossible to construct a repulsive interaction in an S state which would make the α *vs* η curve suddenly much steeper at high energies.[37]

The rather sharp peak of α_{33} in Solutions I–III also makes a theoretical explanation difficult, and in particular a close approach to 90° followed by a rapid decrease looks suspicious.

In Track II, α_3 is well-behaved, and also the monotonic increase of α_{33} and α_{31} with energy is reasonable. However, the extremely rapid increase of α_{33} and α_{31}, and the need to explain 3 resonances rather than 1, make this track also very unlikely.

The combination Track I and IIa or I′–II′ (dashed line in Fig. 7) is rejected because of the sudden and rapid increase of α_{31} after δ_{33} passes 90°.

A Track Ia may be defined as follows: Below 194 Mev, it agrees with Track I; above 194, the signs of all phase shifts are reversed, except for α_{33} which is replaced by $\pi - \alpha_{33}$. This in fact is the solution 1 of Table II which was found originally at 217 Mev. We reject this track mainly because of the sudden jump of α_3 from negative to positive values near 194 Mev, and also because α_{33} goes close to 90° and then falls again, with almost a break at the top.

Track I has no such faults and we therefore believe it to be the correct solution.

A further argument for Track I is the behavior of photomeson production, as analyzed by Ross.[38] Particularly the fact that the experimental angular distribution of positive photomesons shifts from a backward to a forward maximum at high energies, is strong evidence for a resonance in α_{33}. Watson[39] has given an argument for the same conclusion on the basis of the (less well measured) angular distribution of neutral photomesons.

As to the *theory* of meson scattering, the quantitative results of the Tamm-Dancoff theory are still very incomplete, and many points in the method are not yet well understood. However, some qualitative features seem clear, both from the nonrelativistic formulation of Chew[7] and from the relativistic one of Dyson *et al.*[7] These are: (1) only the phase α_{33} is large, due to an attractive interaction in this state; (2) α_{33} may (but does not need to) have a resonance; (3) α_{31}, α_{11} and α_{13} are small and slowly varying; and (4) α_3 behaves as if there were a strong repulsive potential of short range. Calculations of α_1 are complicated by renormalization problems, but a positive value is likely.

Track I or rather an interpolation like (b) in Sec. 7 is the only one which agrees with these theoretical predictions. Together with its smoothness, we believe this makes it almost certain that it is the correct one.

We should like to thank Josephine Powers for helping with the hand computing.

[35] Dyson, Ross, Salpeter, Schweber, Sundaresan, Visscher, and Bethe, Phys. Rev. (to be published).
[36] S. D. Drell and E. M. Henley, Phys. Rev. **89**, 1053 (1952).
[37] A long-range attractive potential plus a strong short-range repulsion will make the α *vs* η curve bend downwards, but this will occur mostly at low energy and certainly not set in suddenly.
[38] M. Ross, Phys. Rev. **94**, 454 (1954).
[39] K. M. Watson (private communication).

Phase-Shift Analysis of the Scattering of Negative Pions on Hydrogen*

RONALD L. MARTIN
Laboratory of Nuclear Studies, Cornell University, Ithaca, New York
(Received May 6, 1954)

A phase-shift analysis of the scattering of negative pions on hydrogen in the energy range 120 to 217 Mev is presented. The usual assumptions that the scattering is charge-independent and that scattering in S and P states only is important are made and in addition the P-wave phase shifts of isotopic spin $\frac{1}{2}$ assumed to be zero. Of many approximate solutions obtained a solution showing a resonance in the P state of ordinary spin $\frac{3}{2}$ and isotopic spin $\frac{3}{2}$ in the neighborhood of 195 Mev is considered to have the highest probability of being correct.

I. INTRODUCTION

WITH the assumption that only S and P states are important in pion-proton scattering in the energy range analyzed, 120–217 Mev, and that the interaction is charge independent, the reactions

$$\pi^+ + p \rightarrow \pi^+ + p, \quad (1)$$

$$\pi^- + p \rightarrow \pi^- + p, \quad (2)$$

$$\pi^- + p \rightarrow \pi^0 + n, \quad (3)$$

can be described by a set of six phase shifts[1] α_3, α_1, α_{33}, α_{31}, α_{13}, and α_{11}. Reaction (1) is then described by the three phase shifts of isotopic spin $\frac{3}{2}$ while reactions (2) and (3) require all six of the phase shifts to describe the interaction.

The angular distributions of reactions (2) and (3) have been investigated[2–4] at several energies in the energy region being considered. The angular distribution of reaction (1) has been investigated[2,5,6] at several energies in this interval but presents some difficulties in interpretation under the above assumptions. In particular, the distribution measured by Homa, Goldhaber, and Lederman[6] at 188 Mev requires D-wave scattering for the best fit and if this is substantiated by further investigation would render the phase-shift analysis presented here invalid. However, within the errors of the experiment the distribution can be fitted with S- and P-wave scattering.

Recently Ashkin and Vosko[7] have presented a geometrical method for obtaining the six phase shifts from the experimental angular distribution of the 3 reactions. Using the scattering data of negative pions alone, however, only 5 of the 6 independent parameters are related to the geometrical plot so that the six phase shifts are not directly determined by this method. If one assumes that the two P-wave phase shifts of isotopic spin $\frac{1}{2}$, α_{13} and α_{11}, are zero one can use the geometrical diagrams to solve for the remaining four phase shifts and this procedure was followed in the present analysis.

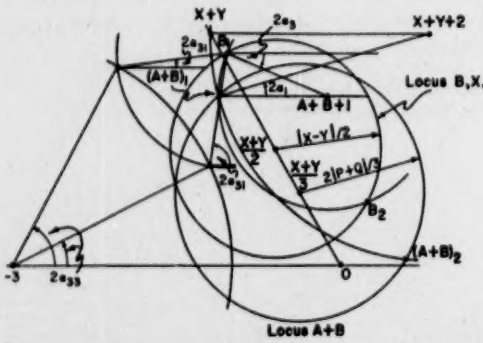

FIG. 1. Phase shift solution at 125 Mev by the goemetrical method of Ashkin and Vosko.

II. EXPLANATION OF METHOD

Following Ashkin and Vosko, but assuming $\alpha_{11}=\alpha_{13}=0$, leads to the following scattering formulas:[8]

$$\frac{d\sigma(+)}{d\Omega}=\frac{1}{4k^2}[|A+B\cos\theta|^2+|C\sin\theta|^2]$$
$$=a_+ + b_+\cos\theta + c_+\cos^2\theta, \quad (4)$$

$$\frac{d\sigma(-)}{d\Omega}=\frac{1}{36k^2}[|X+Y\cos\theta|^2+|Z\sin\theta|^2]$$
$$=a_- + b_-\cos\theta + c_-\cos^2\theta, \quad (5)$$

$$\frac{d\sigma(0)}{d\Omega}=\frac{1}{18k^2}[|P+Q\cos\theta|^2+|R\sin\theta|^2]$$
$$=a_0 + b_0\cos\theta + c_0\cos^2\theta, \quad (6)$$

* Assisted by the joint program of the U. S. Office of Naval Research and the U. S. Atomic Energy Commission.

[1] The notation is that of reference 2.

[2] Anderson, Fermi, Martin, and Nagle, Phys. Rev. 91, 155 (1953).

[3] Fermi, Glicksman, Martin, and Nagle, Phys. Rev. 92, 161 (1953).

[4] M. Glicksman, Phys. Rev. 94, 1335 (1954).

[5] Homa, Goldhaber, and Lederman, Phys. Rev. 93, 554 (1954).

[6] R. A. Grandey and A. F. Clark, Phys. Rev. 94, 766 (1954).

[7] J. Ashkin and S. H. Vosko, Phys. Rev. 91, 1248 (1953).

[8] Our notation differs from that used in the preceding paper by de Hoffmann *et al.* as follows: Our lower case letters, in equations (4), (5), and (6), are related to the notation of de Hoffmann *et al.* by $a_+ \rightarrow X^3 A_+$, etc. Our upper case letters in (7) through (13) are written as lower case letters by de Hoffmann *et al.*

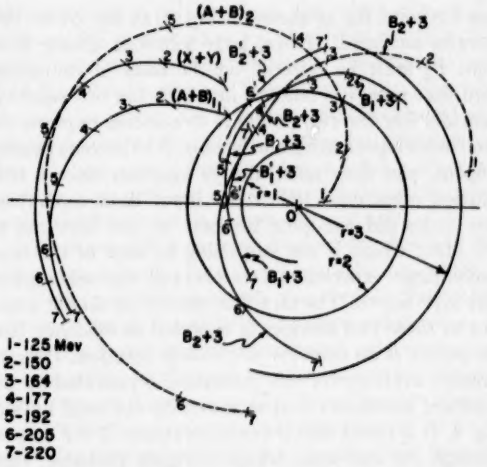

FIG. 2. Pertinent points of the geometrical solutions at different energies for an interpolation of the negative pion-proton scattering data.

where k is the wave number in the c.m. system.

$$A=\exp(2i\alpha_3)-1, \tag{7}$$

$$B=2\exp(2i\alpha_{33})+\exp(2i\alpha_{31})-3, \tag{8}$$

$$C=\exp(2i\alpha_{33})-\exp(2i\alpha_{31}), \tag{9}$$

$$X=A+2\exp(2i\alpha_1)-2, \tag{10}$$

$$Y=Q=B, \tag{11}$$

$$Z=R=C, \tag{12}$$

$$P=3A/2-X/2, \tag{13}$$

$$|X+Y|^2=36k^3(a_-+b_-+c_-), \tag{14}$$

$$|X-Y|^2=36k^3(a_--b_-+c_-), \tag{15}$$

$$\mathrm{Re}(X+Y)=-6k^3(a_-+\tfrac{1}{3}c_-+a_0+\tfrac{1}{3}c_0), \tag{16}$$

$$|P+Q|^2=18k^3(a_0+b_0+c_0), \tag{17}$$

$$|P-Q|^2=18k^3(a_0-b_0+c_0), \tag{18}$$

$$(A+B)=2(P+Q)/3+(X+Y)/3, \tag{19}$$

$$(A+B)=(X+Y)+2-2\exp(2i\alpha_1), \tag{20}$$

$$\mathrm{Re}(A+B)=-2k^2\sigma_+(\mathrm{total})/4\pi. \tag{21}$$

Figure 1 shows a representative solution by the method applied. The point $X+Y$ is located from the experimental data through (14) and (16). A circle with center at $(X+Y)/2$ and radius $|X-Y|/2$, given by (15), is the locus of both points X and Y on opposite sides of a diagonal. This same circle is also the locus of points B and Q from (11) (this is true only for $\alpha_{11}=\alpha_{13}=0$). Two circles are obtained from (19) and (20) as the locus of point $(A+B)$, namely a circle of radius 2 from center $X+Y+2$ and a circle of radius $2|P+Q|/3$, given by (17), from center $(X+Y)/3$. Two points $A+B$ are obtained by the intersections of these circles and each defines a value of α_1 through (20). One of these points $(A+B)$ can always be excluded as will be seen later. A is a vector from the origin to a circle of radius 1 and center -1 as given by (7) so that a second locus of point B is obtained from $B=(A+B)-A$ as a circle of radius 1 with center at point $A+B+1$. Therefore two points B are located, each defining an angle α_3 as shown. Angles α_{33} and α_{31} are determined from (8) as shown and exist as two sets for each point B. The set of α_{33} and α_{31} with the larger value of α_{33} is commonly called the Fermi type solution and the other the Yang type solution. At a given energy then one finds two values of α_3 with the same value of α_1, and for each value of α_3 a Fermi and a Yang set of α_{33} and α_{31}, a total of four sets of phase shifts.

III. PHASE-SHIFT SOLUTIONS

In order to determine the continuity of solutions a smooth interpolation of the experimental cross sections of the scattering of negative pions on hydrogen in the energy interval 120–217 Mev was chosen as the input data for the graphical solutions. The pertinent points of the Ashkin diagrams at different energies are shown in Fig. 2. In locating these points many ambiguities exist to give rise to numerous solutions and each must be considered. One could as well have chosen the initial point $X+Y$ in the opposite imaginary plane. This would have the effect of reflecting all points on Fig. 2 through the real axis which would correspond to a change of sign of all phase shifts. However, at 125 Mev the point $X+Y$ was chosen in the positive imaginary plane to make the value of α_3 negative[9] at this energy, so that the signs of the phase shifts are then determined from continuity. With increasing energy the point $X+Y$ moves toward the real axis and may or may not cross the real axis, as shown by Fig. 3, so that both possibilities must be considered.

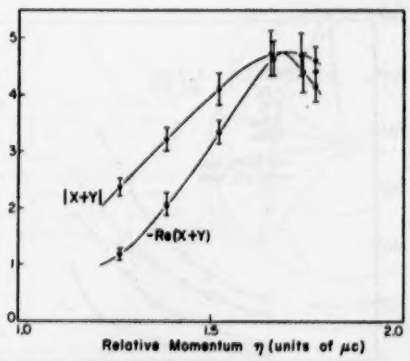

FIG. 3. Graph indicating possibility that $X+Y$ becomes real.

[9] Bodansky, Sachs, and Steinberger, Phys. Rev. **90**, 997 (1953); Phys. Rev. **93**, 918 (1954); J. Orear, Phys. Rev. **93**, 918 (1954). Barnes, Angell, Perry, Miller, Ring, and Nelson, Phys. Rev. **92**, 3128 (1953).

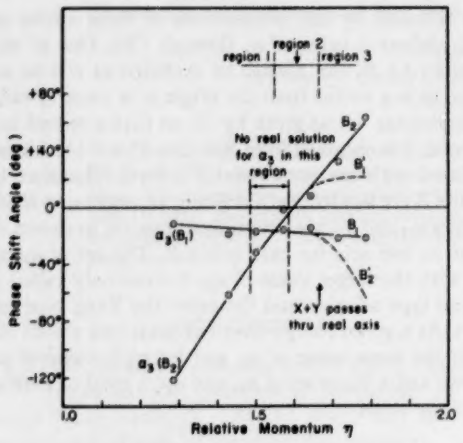

FIG. 4. Possible behavior of α_3.

The point labeled $(A+B)_2$ can be rejected at each energy by one or more arguments. At low energies the point is rejected by its representation of a negative total cross section through (21). In addition, at all energies except those represented by points 5 and 6 it does not give rise to acceptable solutions in that the circle for the locus of B derived from $(A+B)_2$ does not intersect the other circle of locus B. Both arguments are valid at 125 Mev as shown in Fig. 1. The point $(A+B)_2$ does give acceptable solutions at energies represented by points 5 and 6 but these are rejected on the basis of continuity and the points B derived from this $A+B$ are not included on Fig. 2. The acceptable point $(A+B)_1$ follows closely the point $X+Y$ and so crosses or does not cross the real axis with $X+Y$.

As pointed out by Ashkin and Vosko[7] some points A (here the corresponding point B) do not give rise to acceptable solutions because the point $B+3$ is more than 3 units from the origin, violating (8). This is the case for point B_2, as shown in Fig. 2. at the lowest two energies analyzed. Hence, later solutions arising from point B_2 must be rejected on the basis of continuity until that energy is reached at which the two points B coincide. For the two points B to coincide requires the two circles representing the locus of B to become exactly tangent, and they must always intersect since a true solution must exist. With the input data used these two circles did not quite intersect at 164 Mev nor at 177 Mev, which is not surprising in view of the relatively large experimental errors and the assumption that $\alpha_{11}=\alpha_{13}=0$. The fact that the circles do not intersect at these two energies is regarded as evidence that the points B do coincide in the true solution. Perhaps stronger evidence for this conclusion is provided by the resultant solutions for α_3 as shown by the solid lines of Fig. 4. It is noted that if one allows point $X+Y$ to pass through the real axis, which is highly probable, then one can draw nearly straight lines to connect each set of

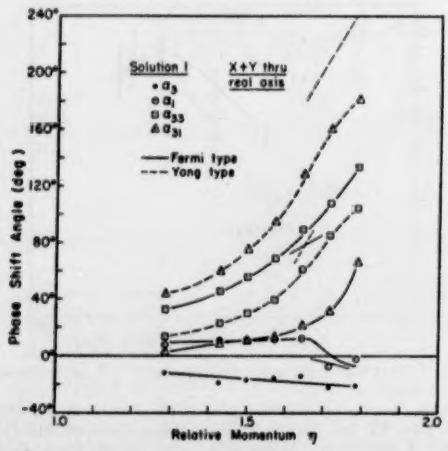

FIG. 5. Phase-shift solution 1.

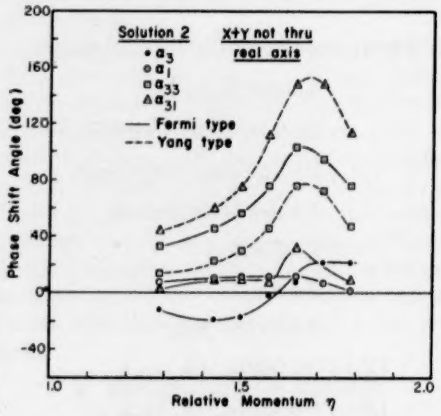

FIG. 6. Phase-shift solution 2.

values of α_3 at high and low energies, indicating a very regular behavior of the α_3 which is the only solution at lower energies. To find the solutions at 164 and 177 Mev, points B_1 and B_2 were chosen to be equidistant from the point of closest approach of the two circles defining the locus of B and giving values of α_3 which best fit the solid lines of Fig. 4. These points B gave real solutions of α_{33} and α_{31}. The procedure is justified in that cross sections predicted by the phase shifts with these assumed values of α_3 give reasonable agreement with the experimental data.

For the case that point $X+Y$ is not allowed to cross the real axis the points of Fig. 2 obtained at the last two energies should be reflected through the real axis. The continuity of points then requires that B_1 be continuous with the reflected points of B_2, which will be called B_2', and *vice versa*. The resultant continuous curves of $B+3$ are shown on Fig. 2. One can easily see by constructing α_{33} and α_{31} through (8) from points $B+3$ that

this reflection of points reflects the values of α_{33} and α_{31} through 90° so that what was the Fermi solution of one point becomes the Yang solution of the reflected point, and that this involves no loss of continuity. The labels 1 and 2 on points $A+B$ cannot be interchanged when these points are reflected through the real axis since only one of these points (here labeled $A+B_1$) is acceptable at both high and low energies and so must be continuous whether or not it crosses the real axis.

The phase shift solutions obtained are shown in Figs. 5 through 8. Each figure shows two solutions which are the Fermi and Yang type sets of α_{33} and α_{31} derived from the same point B and with the same values of α_3 and α_1. At the lowest energy investigated only one point B is acceptable so that all solutions arise continuously from the two solutions at 125 Mev. The two solutions at this energy are very close to those reported by Anderson.[2] The various solutions may be identified from Fig.

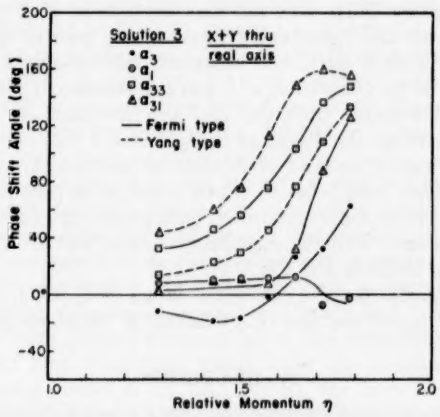

FIG. 7. Phase-shift solution 3.

2 by their relation to curves $B+3$, which is labeled in 3 intervals for this reason. All solutions arise from point B_1 from the lowest energy investigated to the point of intersection of B_1 and B_2, and from this point continue as follows: Solution 1 arises from B_1 and B_1, solution 2 from B_2 and B_1', solution 3 from B_2 and B_2, and solution 4 from B_1 and B_2'. Here the first letter indicates the curve followed in the energy interval from the energy at which points B intersect to the energy at which point $X+Y$ either crosses the real axis or turns back into the positive imaginary plane, and the second letter indicates the curve followed in the higher energy interval.

The Fermi-type solution 4 is similar in characteristics to a solution found by Fermi and Metropolis.[10] Although the phase shifts are considerably different in the neighborhood of 190 Mev, it will be seen later that the data allow large ranges of phase shifts in this energy region.

[10] Fermi, Metropolis, and Alei, this issue [Phys. Rev. **95**, 1581 (1954)].

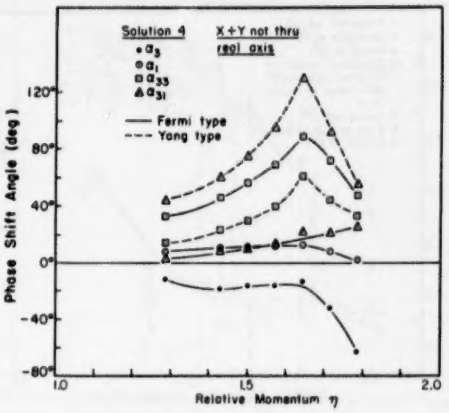

FIG. 8. Phase-shift solution 4.

The Yang-type solution 2 is similar to that reported by de Hoffmann *et al.*[11] In addition, by their tracking method, they obtained the solution corresponding to the Fermi-type solution 2, but chose to reverse signs at the higher energies and thereby obtained an entirely new solution.

The author was aware of this solution proposed by de Hoffmann *et al.*, and also independently by Glicksman[4] when it was realized that within the errors of the experimental data the points $B+3$ on Fig. 2 could be shifted to the extent that the line $B+3$ becomes tangent to the unit circle. When the point $B+3$ lies on the unit circle, the two values of α_{33} of the Fermi and Yang type solutions become equal and the two values of α_{31} differ by 180° (they must differ by this amount because of continuity although the vectors representing these phase shifts are equal). The construction shown in Fig. 9 indicates that it then becomes possible at higher energies to interchange the values of α_{33} between the Fermi and Yang type solutions in Figs. 5 through 8. This re-

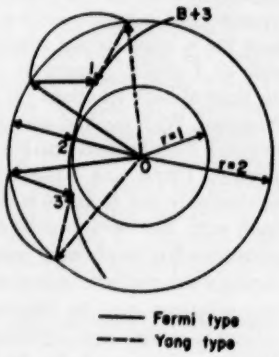

FIG. 9. Construction to show possibility of interchange of Fermi and Yang type solutions for α_{33}. Vectors with magnitude 2 have phase angles $2\alpha_{33}$ and vectors with magnitude 1 have phase angles $2\alpha_{31}$.

[11] See accompanying paper by de Hoffmann, Metropolis, Alei, and Bethe. Their track IIa, Table IX, corresponds to the Yang solution 2 presented here. Their solution 1 corresponds to the Fermi-type solution 2 presented here while this solution with signs reversed at 217 Mev is reported as Track I, Table VIII, and is the new solution spoken of above.

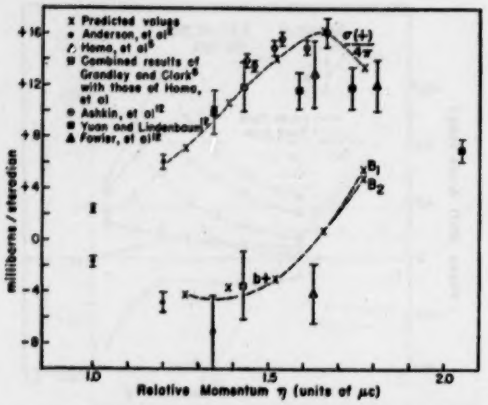

FIG. 10. Positive pion-proton scattering. Observed and predicted values of $\sigma(+)/4\pi$ and b.

quires also the interchange of the values of α_{31} with addition or subtraction of 180° to make this phase shift continuous. The interchange is indicated in Fig. 5 by the short lines and the resultant Fermi-type solution with α_{31} small is that solution found by de Hoffmann *et al.*, and by Glicksman. The interchange is possible in all of the other pairs of solutions but is not shown for the sake of clarity.

In order to check the accuracy of the method, solutions were also obtained using the experimental data[2-4] at 120, 144, 169, 194, and 217 Mev. These solutions are listed in Table I along with a criterion of fit to the data in the last column through the relation

$$M=\sum_{i=1}^{6}\left(\frac{\Delta_i}{\epsilon_i}\right)^2 \tag{22}$$

where Δ_i is the difference between the measured and predicted cross sections, ϵ_i is the error quoted for the measured cross sections, and the summation is over the cross-section measurements at 3 angles for reaction (2), and the γ cross-section measurements of reaction (3), also at 3 angles (except at 217 Mev where the cross sections of both reactions (2) and (3) were measured at 6 angles). With α_{11} and α_{13} equal to zero, the predicted angular distributions for reactions 1–3 of the corresponding Fermi and Yang type solutions are identical so that only one M value is listed in the last column for both sets. The solutions listed in this table are those corresponding to allowing point $X+Y$ of Fig. 2 to pass through the real axis (solutions 1 and 3) but the other two solutions may be obtained as before by suitable reversals of sign and addition of 180°. Here again, at 169 Mev, the two circles for locus of point B did not intersect so that the phase shifts listed at 169 Mev are those derived from assumed values of α_3 in the same manner as the solutions at 164 and 177 Mev from the interpolated data as previously discussed.

The phase-shift solutions given in Table I are not very different from the solutions obtained from the interpolated data, except at 194 Mev. The solution from the interpolated data at 194 Mev is also listed in Table I for comparison. It is noted that while the two solutions are reasonably different at 194 Mev they give about the same fit to the experimental data, and this energy region can be seen to be very critical in that a small change in data results in a relatively large change in phase shifts. This is mainly due to the relative insensitivity of the largest contributions to the predicted cross sections, such as $\sin^2\alpha_{33}$ and $\sin^2(\alpha_{33}-\alpha_3)$, when α_{33} is near 90°. It is also evident from the Ashkin diagrams, since point $X+Y$ is very close to the real axis at this energy so that any change of either $|X+Y|$ or $\mathrm{Re}(X+Y)$ makes a relatively large change in point $X+Y$.

Also at this energy the solutions obtained directly from the diagrams from point B_2 were very poor in that the phase shifts were not very continuous with those at lower and higher energy, gave a very poor fit to the experimental data, and predicted unreasonable structure in the parameters a, b, and c of reaction (1). They were therefore discarded and another point B_2 constructed on the diagrams (from points $A+B_1$ and B_1) which gave the same predictions for reaction (1) as did solutions from point B_1. These phase shifts were found to be much more acceptable, gave predictions in better agreement with the experimental data, and are those listed in Table I at 194 Mev.

Figures 10 and 11 show the values of a_+, b_+, c_+, and $\sigma(+)_{\text{total}}$ of reaction (1) predicted by the above phase shifts.

IV. DISCUSSION

The phase shifts presented here are only approximate solutions to the data due to graphical inaccuracies and the assumption that $\alpha_{11}=\alpha_{13}=0$, which latter implies the use of only four out of the six independent data. No attempt has been made to refine the values of the phase shifts obtained from the diagrams to give a better fit to the data, except as previously discussed at 194 Mev. To do this with any confidence requires a somewhat better knowledge of the angular distribution of reaction (1) than is presently available. While the actual

TABLE I. Approximate phase-shift solutions of experimental data.

E (Mev)	Rel. mom. η	Solution from point	α_3	α_1	Fermi solution α_{33}	Fermi solution α_{31}	Yang solution α_{33}	Yang solution α_{31}	M
120	1.26	B_1	−11.6	+8.0	30.3	4.3	13.6	39.7	5.1
144	1.39	B_1	−12.8	11.5	43.4	1.3	18.1	60.2	6.7
169	1.52	B_1	−16.0	11.4	59.3	11.5	31.7	79.3	6.4
194	1.66	B_1	−9.2	16.3	101.4	29.1	75.7	148.0	1.9
		B_1[b]	−16	10	92	23	66	135	2.3
		B_2	+14.6	16.3	119.2	50.6	91.0	159.6	3.9
217[a]	1.77	B_1	−19.8	−2.7	132.0	66.7	102.8	168.2	6.8
		B_2	+59.1	−2.7	145.6	123.2	131.2	153.6	12.4

[a] M values summed over 12 measurements.
[b] Solution from interpolated data.

values of the phase shifts presented here are not considered accurate it is felt that accurate solutions could be found with the characteristic behavior of all of the solutions 1–4.

It is possible that solutions to the negative pion scattering data alone could exist in which point $X+Y$ of Fig. 2 were on one side of the real axis and point $A+B$ on the other. Such solutions would give large values of one or more of α_1, α_{13}, and α_{11} and would not be detected in this analysis. If these solutions did exist they would be excluded by an examination of the total cross sections[12] which are related by

$$3\sigma(-)=\sigma(+)+8\pi\lambda^2(\sin^2\alpha_1+2\sin^2\alpha_{13}+\sin^2\alpha_{11}), \quad (23)$$

where $\sigma(-)$ represents the total π^- scattering cross section including charge exchange. The experimental values are such that these 3 phase shifts must be small in the energy region investigated.

An exact solution with α_{13} and α_{11} not equal to zero may cause an additional multiplicity of solutions because of the multiplicity involved in selecting α_{11} and α_{13}, but since the values of these two phase shifts are required to be small by (23) such additional solutions will not be very different from those shown. It can be seen that the discussion of Fig. 2 would be highly confused for an exact solution, including α_{11} and α_{13}, since in this case the Fermi and Yang type solutions would not give identical cross section predictions, would not be derived from the same point B, and would not have identical values of α_3 and α_1. However, a similar discussion of points of Fig. 2 obtained from positive pion scattering data would be valid and would lead to solutions with characteristics of all of the solutions presented here. One then would have the freedom of choosing values of α_1, α_{11}, and α_{13} for each of the solutions in order to best fit the negative pion scattering data. That a good fit could be obtained for each solution seems certainly possible in view of the results obtained here of almost identical fits without using any of the freedom of choice of these 3 phase shifts.

It is quite possible that solutions 3 and 4 may disappear at a slightly higher energy than the highest energy investigated. This would occur if point B_2+3 of Fig. 2 were to become more than three units from the origin, which violates (8). At the energy at which these solutions disappear α_{31} would be equal to α_{33} and the Fermi and Yang solutions would be identical. It is seen from Figs. 7 and 8 that these phase shifts appear to be converging, so that the disappearance of these 2 sets of solutions at higher energy is considered probable.

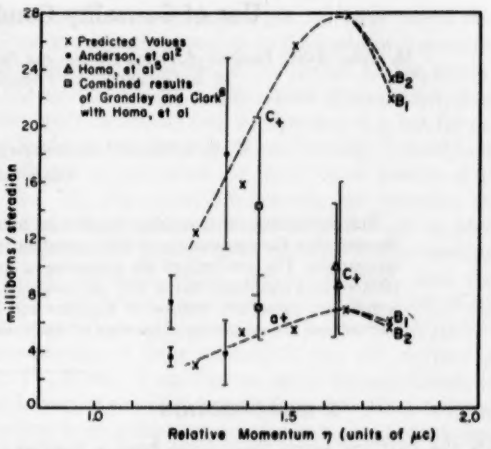

FIG. 11. Positive pion-proton scattering. Observed and predicted values of a and c.

It appears that it may be impossible to decide experimentally between the resonance solution 1 and the nonresonance solution 2 since cross sections predicted by these sets of solutions differ only in the narrow energy region of about 170–200 Mev, and here only by such small amounts as to be indetectable experimentally. In addition it is this energy region in which the errors on the phase shifts are largest for a given experimental error. The resonance solution 1 implies that the two points B coincide and that points $X+Y$ and $A+B$ each pass through the real axis, all of which appear probable from the existing data. It is, therefore, felt that the resonance solution is the correct choice since it would involve less abrupt changes of the phase shifts.

There are strong theoretical arguments[13] in favor of the resonance solution proposed by de Hoffmann *et al.*, and by Glicksman. In addition to the above conditions required by the resonance solution, their solution requires that, at some energy in the neighborhood of 190 Mev, point B_1+3 be exactly one unit from the origin. In view of the large uncertainty in the phase shifts at this energy, such a behavior of point B_1 is certainly allowed and this solution is probably the true solution.

I am indebted to Professor H. A. Bethe for many informative discussions on this subject, and I am grateful to Dr. F. de Hoffmann, Dr. N. Metropolis, Dr. E. F. Alei, and Dr. H. A. Bethe and to Dr. M. Glicksman for making their analysis of the phase shifts available to me before publication.

[12] References 2, 3, 4, 5, and 6; Fowler, Lea, Shephard, Shutt, Thorndike, and Whittemore, Phys. Rev. **92**, 832 (1953) (their pion energy is now stated as 225 Mev); Ashkin, Blaser, Fiener, Gorman, and Stern, post-deadline paper at the New York meeting of the American Physical Society, 1954; L. C. L. Yuan and S. J. Lindenbaum (private communication).

[13] de Hoffmann, Metropolis, Alei, and Bethe, preceding paper [Phys. Rev. **95**, 1586 (1954)].

Use of Causality Conditions in Quantum Theory

M. GELL-MANN, *Institute of Nuclear Studies and Department of Physics, University of Chicago, Chicago, Illinois*
M. L. GOLDBERGER,* *Princeton University, Princeton, New Jersey*

AND

W. E. THIRRING,† *Institute for Advanced Study, Princeton, New Jersey*
(Received May 24, 1954)

The limitations on scattering amplitudes imposed by causality requirements are deduced from the demand that the commutator of field operators vanish if the operators are taken at points with space-like separations. The problems of the scattering of spin-zero particles by a force center and the scattering of photons by a quantized matter field are discussed. The causality requirements lead in a natural way to the well-known dispersion relation of Kramers and Kronig. A new sum rule for the nuclear photoeffect is derived and the scattering of photons by nucleons is discussed.

I. INTRODUCTION

IN the past few years there have been a number of papers which consider the question of deducing general conditions on scattering amplitudes on the basis of causality requirements. This has been a revival of the original work of Kronig[1] and Kramers[2] and followed for the most part a suggestion by Kronig[3] that causality requirements should be added to the usual conditions on the S matrix, namely, Lorentz invariance and unitarity. The actual requirements imposed by causality have been stated in various ways. Tiomno and Schutzer,[4] discussing the scattering of nonrelativistic particles, impose the condition that the scattered wave should be zero before the incident wave hit the scatterer. This work has been criticised by van Kampen[5] who discusses the same problem. He demands that the total probability outside the scatterer never exceed its initial value. In the case of photons, a different approach has been made. In several of the papers the problem is treated from the standpoint of the classical electrodynamics description of the propagation of light through a medium with an index of refraction where one imposes the condition that signals should not propagate faster than the velocity of light. This was, in fact, the original approach to Kronig and Kramers, and has been developed most rigorously by Toll.[6] The connection between the index of refraction and the scattering amplitude is then made by means of the optical relation:

$$n(\nu)=1+(2\pi c^2/\nu^2)\rho F(\nu), \tag{1.1}$$

where ρ is the density of scattering centers and $F(\nu)$ is the coherent forward scattering amplitude. This approach does not seem too satisfactory in that it is based on classical electrodynamics and further that the relationship to individual scatterers is established only in a circuitous way via Eq. (1.1). A more direct treatment has been given by van Kampen[7] who considers the scattering of photons by a spherically symmetric scatterer outside of which the interaction is exactly zero. His treatment, however, is still based on classical electrodynamics. The causality condition in this paper is that of Tiomno and Schutzer.

With a single exception, no one has to our knowledge discussed the problem of relativistic particles with mass. The exception is the work of Moshinsky[8] who has treated the special case of particles interacting with a zero-range force.

The causality requirement in the present paper is as follows: The quantum-mechanical formulation of the demand that waves do not propagate faster than the velocity of light is, as is well known, the condition that the measurements of two observable quantities should not interfere if the points of measurement are space-like to each other. In the case of the propagation of bosons to which we limit ourselves in this paper, our formal statement is that the commutator of two Heisenberg operators for the field in question shall vanish if the operators are taken at space-like points. This condition is sufficient to enable us to discuss the case of particles with mass, as well as photons. Our demand is a much more stringent one than that of Tiomno and Schutzer; not only can waves not be scattered before the incident wave arrives, but even after the arrival one must wait the appropriate time to receive a signal.

The principle object of the work of van Kampen and Schutzer and Tiomno was to obtain detailed information on the analytic behavior of the S matrix in the complex energy plane. In these treatments, the behavior of phase shifts for individual angular momenta are

* On leave of absence from the University of Chicago, Chicago, Illinois.

† Present address, Physikalisches Institute, Universitat Bern, Bern, Switzerland.

[1] R. Kronig, J. Opt. Soc. Am. **12**, 547 (1926).
[2] H. A. Kramers, Atti. congr. intern. fisici, Como, **2**, 545 (1927).
[3] R. Kronig, Physica **12**, 543 (1946).
[4] W. Schutzer and J. Tiomno, Phys. Rev. **83**, 249 (1951).
[5] N. G. van Kampen, Phys. Rev. **91**, 1267 (1953).
[6] J. S. Toll, Princeton thesis (unpublished). In this paper, one finds complete references, and numerous very interesting applications of the dispersion relations for light.
[7] N. G. van Kampen, Phys. Rev. **89**, 1072 (1953).
[8] M. Moshinsky (unpublished). We are indebted to Professor A. S. Wightman for showing us Dr. Moshinsky's paper.

studied. An entirely different and very powerful approach to this specific problem has been made by Wigner (unpublished lectures at Princeton, 1953) whose method unfortunately cannot be directly applied to the case of photons. In all of these treatments, it is essential to assume that the interaction vanishes exactly (or is completely known) outside some finite region in configuration space. This limitation has not been completely overcome in our work. In the case of the interaction between photons and a matter field we are forced to rely on the familiar field theoretic device of adiabatic switching on and off of interactions. We shall not discuss the implications of this procedure, but shall simply accept it, as is conventionally done, as one of the apparently necessary shortcomings of the present formalism.

In this paper we shall use our quantum-mechanical causality requirement, as described above, to discuss the scattering of spin-zero particles and of photons. We shall deduce results essentially equivalent to the Kramers-Kronig dispersion relations and which are independent of the size of a region of interaction. Wigner and van Kampen demonstrate that the scattering amplitudes for individual angular momenta are analytic in the upper half-plane, if regarded as functions of the energy. If one wants relations between real and imaginary parts of the amplitudes for real values of the energy (i.e., a dispersion relation), one needs not only analytically but also certain boundedness of the amplitudes. It turns out that one must supply an exponential factor depending on the size of the scattering region to secure the desired boundedness of the individual scattering amplitudes. This greatly complicates the dispersion relations and makes them essentially useless for our purposes. One finds, however, that certain combinations of the phase shifts, for example, the forward scattering amplitude, have boundedness properties of such a nature that any reference to the size of the region of interaction may be avoided. The dispersion relations deduced in connection with the forward amplitude are the classical ones of Kramers and Kronig and many applications have been made of them in the past. (See reference 6.) There are other combinations of phase shifts for which the size of the region plays no role; these are essentially the derivatives of the scattering amplitude evaluated in the forward direction. The boundedness conditions on these are more obscure and we have made no applications of them. Whereas all of the previous dispersion relations have been confined to completely coherent forward scattering amplitudes, our results allow a consideration of processes in which there are spin flips and polarization changes.

In Sec. II we shall discuss first the simple case of a spin-zero particle interacting with a spherically symmetric force center; the interaction is assumed to vanish exactly outside a finite radius. The possibility of bound states and particle absorption are included. The more realistic case of photons interacting with a quantized matter field is treated in Sec. III. We have used a perturbation theoretic approach to the problem, expanding the Heisenberg operators of the photon field in powers of the electric charge, e. The results obtained are in all probability rigorously true to all orders of e, but for our applications only the order e^2 was needed; it should not be difficult to generalize our result to all powers of e^2. In Sec. IV, the connection between the causality requirement on the forward amplitude deduced in Secs. III and IV and the dispersion relations is discussed. In all cases causality yields the information that the forward scattering amplitude has certain analyticity and boundedness properties and it is the mathematical consequences of these conditions that are explore in Sec. IV. In Sec. V we treat in detail the application of the dispersion relations to two cases of physical interest. The first is the deduction of a sum rule for photonuclear reactions in which the integrated photonuclear cross section (integrated up to the meson threshold) is related to the observed photomeson cross section. It is a generalization of the dipole sum rule given by Bethe and Levinger.[9] The second application is to the problem of the scattering of γ rays by protons. We use the dispersion relation to put limits on the forward scattering amplitude and in the case of low frequencies we get a limit on the phase shifts for the low multipoles. Since this case is of considerable experimental interest, we have gone beyond the results obtainable from our dispersion relations, mentioned above, to discuss the general features of γ-p scattering on the basis of some additional assumptions. Finally, in Appendix B we collect the relevant formulas for a phase shift analysis of this process.

II. SPIN-ZERO FIELD IN AN EXTERNAL POTENTIAL

Note added in proof.—It has been pointed out to us by Professor N. G. van Kampen that in this section the arguments pertaining to particles with mass are lacking in rigor. In the following sections, however, we use only results pertaining to massless fields. See reference 12.

In order to explain our procedure most simply, we shall consider first the rather academic case of a neutral spin-zero field interacting with a time-independent spherically symmetric external potential which vanishes outside a region of radius $a/2$. We shall assume for the time being that there are no bound states and that there is no particle absorption and later indicate the manner in which the results are modified if these complications are included. In this simple problem we may imagine that the solutions to the field equations are obtained; in terms of these normal modes we may confine our attention to one-particle states. It is perhaps worth noting that our problem is quite similar to that treated by van Kampen; it is simpler in that we deal with a scalar rather than a vector field (which difference is

[9] J. Levinger and H. A. Bethe, Phys. Rev. 78, 115 (1950).

trivial) but more complicated because we consider a nonvanishing rest mass.

We now make use of the fact that the vacuum expectation value of the commutator of two field operators, $\phi(x)$ and $\phi(x')$, vanishes if the points x, x' are space-like to each other. (Obviously any matrix element of such a commutator vanishes under these circumstances since the commutator itself vanishes.) $\phi(x)$ is the Heisenberg operator of our scalar field. Since such a commutator vanishes outside the light cone and is zero for $t_0=t_0'$, it must be an odd function of time. We may therefore confine our attention to positive values of the time difference t_0-t_0'. We may then define a retarded Green's function, $G_{\rm ret}(x,x')$, as follows:

$$i\langle 0|[\phi(x),\phi(x')]|0\rangle\eta(x-x')\equiv G_{\rm ret}(x,x'), \quad (2.1)$$

where $\eta(x-x')$ is zero if $x_0'>x_0$, and is unity of $x_0>x_0'$. The properties of $G_{\rm ret}(x,x')$ which we shall exploit are

$$\begin{aligned} G_{\rm ret}(x,x')&=0 \quad \text{if} \quad (x-x')^2>0 \\ &=0 \quad \text{if} \quad x_0<x_0'. \end{aligned} \quad (2.2)$$

By hypothesis we need consider only one-particle states which we may choose to be continuum states corresponding to plane waves plus outgoing spherical waves. If such states be characterized by the momentum vector $\mathbf{k}$ of the incident plane wave, we may write

$$\langle 0|\phi(x)|\mathbf{k}\rangle=(2w)^{-\frac{1}{2}}U_{\mathbf{k}}(\mathbf{r})e^{-iwx_0}, \quad (2.3)$$

where $w=+(k^2+\mu^2)^{\frac{1}{2}}$, with μ the particle ($\hbar=c=1$ throughout this paper). We choose a unit quantization volume and normalize the $U_{\mathbf{k}}$ to plane waves of unit amplitude. The factor $1/(2w)^{\frac{1}{2}}$ insures that $G_{\rm ret}(x,x')$ reduces to the conventional retarded Green's function for a free field.

We may now rewrite Eq. (2.1) in the form:

$$\begin{aligned} G_{\rm ret}(x,x')&=i\eta(x-x')\int\frac{d^3k}{(2\pi)^3}\{\langle 0|\phi(x)|\mathbf{k}\rangle\langle\mathbf{k}|\phi(x')|0\rangle \\ &\quad -\langle 0|\phi(x')|\mathbf{k}\rangle\langle\mathbf{k}|\phi(x)|0\rangle\} \\ &=i\eta(x-x')\int\frac{d^3k}{(2\pi)^3}\frac{1}{2w}\{U_{\mathbf{k}}(\mathbf{r})U_{\mathbf{k}}^*(\mathbf{r}) \\ &\quad\times e^{-iw(x_0-x_0')}-U_{\mathbf{k}}(\mathbf{r}')U_{\mathbf{k}}^*(\mathbf{r})e^{iw(x_0-x_0')}\}. \end{aligned} \quad (2.4)$$

Outside the region of interaction ($r,r'>a/2$) we may write the eigenfunctions $U_{\mathbf{k}}(\mathbf{r})$ as

$$\begin{aligned} U_{\mathbf{k}}(\mathbf{r})&=\sum_{l=0}^{\infty}\frac{(2l+1)i^l}{2kr}[h_l^{(1)}(kr)+h_l^{(1)*}(kr)]P_l(\mathbf{k},\mathbf{r}) \\ &\quad+\sum_{l=0}^{\infty}\frac{(2l+1)i^l}{2kr}[e^{2i\delta_l}-1]h_l^{(1)}(kr)P_l(\mathbf{k},\mathbf{r}), \end{aligned} \quad (2.5)$$

where $h_l^{(1)}(x)=(\pi x/2)^{\frac{1}{2}}H_{l+\frac{1}{2}}^{(1)}(x)$ and $H_{l+\frac{1}{2}}^{(1)}(x)$ is the customary Hankel function.[10] These functions are conveniently defined for our purposes as follows:

$$\begin{aligned} h_l^{(1)}(x)&=(-i)\exp[i(kr-\pi/2)]q_l(x), \\ q_l(x)&=\sum_{s=0}^{l}\frac{i^s(l+s)!}{s!(l-s)!(2x)^s}. \end{aligned} \quad (2.6)$$

The δ_l are the usual (real) phase shifts and the $P_l(\mathbf{k},\mathbf{r})$ are Legendre polynomials of the angle between $\mathbf{k}$ and $\mathbf{r}$. If we substitute the eigenfunctions (2.5) into (2.4), the angular integrations are easily carried out with the aid of the spherical harmonic addition theorem. Setting $|\mathbf{r}|=|\mathbf{r}'|$, and $x_0-x_0'=T$, we find for $G_{\rm ret}(x,x')$ the expression:

$$\begin{aligned} G_{\rm ret}(\mathbf{r},\mathbf{r}',T)&=\Delta_{\rm ret}(x-x')+\eta(T)\frac{\pi i}{r^2}\int_0^{\infty}\frac{dk}{2w(2\pi)^3} \\ &\quad\times\sum_{l=0}^{\infty}(2l+1)[(e^{2i\delta_l}-1)\{h_l^{(1)}(r)\}^2+(e^{-2i\delta_l}-1) \\ &\quad\times\{h_l^{(1)*}(kr)\}^2]P_l(\mathbf{r},\mathbf{r}')[e^{-iwt}-e^{iwt}], \end{aligned} \quad (2.7)$$

where $\Delta_{\rm ret}(x)$ is defined as $-\eta(x)\Delta(x)$ with $\Delta(x)$ as given by Schwinger.[11] We now define the scattering amplitude for individual angular momenta $f_l(k)$ by

$$f_l(k)=(e^{2i\delta_l(k)}-1)/2ik, \quad (2.8)$$

and furthermore *define* them for negative values of k as

$$f_l(-k)\equiv f_l^*(k). \quad (2.9)$$

Then using the elementary relation,

$$h_l^{(1)}(-x)=(-1)^{l+1}h_l^{(1)*}(x),$$

we find

$$\begin{aligned} G_{\rm ret}(r,r',T)&=\Delta_{\rm ret}(x-x')+\frac{\eta(T)}{(2\pi)^2r^2}\int_0^{\infty}\frac{kdk}{2w} \\ &\quad\times\left[\sum(2l+1)f_l(k)q_l^2\left(\frac{kR}{2}\right)(-1)^lP(\mathbf{r},\mathbf{r}')\right] \\ &\quad\times e^{ikR}(e^{-iwT}-e^{iwT}), \end{aligned} \quad (2.10)$$

where we have set $2r=R$. The conditions to be imposed on $G_{\rm ret}$, Eq. (2.2), are of course satisfied by $\Delta_{\rm ret}(x-x')$; to insure their being satisfied by the entire function $G_{\rm ret}(r,r',T)$ we must demand that the function $G(R,\vartheta T)$ defined by

$$\begin{aligned} G(R,\vartheta,T)&=\eta(T)\int_{-\infty}^{\infty}dk\frac{k}{2w}\left[\sum_{l=0}^{\infty}(2l+1)f_l(k)(-1)^l\right. \\ &\quad\left.\times P_l(\cos\vartheta)q_l^2\left(\frac{kR}{2}\right)\right]e^{ikR}(e^{-iwT}-e^{iwT}) \end{aligned} \quad (2.11)$$

[10] G. N. Watson, *Bessel Functions* (Cambridge University Press, New York, 1944), p. 73.

[11] J. Schwinger, Phys. Rev. **75**, 651 (1949).

(where ϑ is the angle between $\mathbf{r}$, $\mathbf{r}'$), vanish for

$$R\sin(\vartheta/2)>T, \quad R>a. \tag{2.12}$$

The restrictions on the $f_l(k)$ which are required to make G vanish under the conditions (2.12) are exceedingly complicated and we have not studied the problem in this form. One obtains considerable simplifications by choosing $\vartheta=\pi$ which corresponds to putting $\mathbf{r}'=-\mathbf{r}$. As we shall see below, the restriction to the forward direction may be relaxed somewhat and we can obtain information about scattering at other angles. Observing that $P_l(-1)=(-1)^l$ and writing $G(R,0,T)$ simply $G(R,T)$ we find that (2.11) and (2.12) may be replaced by

$$\begin{aligned}G(R,T)=\eta(T)\int_\infty^\infty dk\frac{k}{2w}\sum_{l=0}^\infty (2l+1)f_l(k)q_l^2(kR/2)\\ \times e^{ikR}(e^{-iwT}-e^{iwT})\\ =0 \quad \text{for} \quad R>T, \quad R>a.\end{aligned} \tag{2.13}$$

We shall drop the $\eta(T)$ factor and simply restrict our attention to positive values of T. It is convenient to rewrite (2.13) in the form

$$\begin{aligned}G(R,T)=\int_{-\infty}^\infty d\nu\epsilon(\nu)\int_{-\infty}^\infty dk\cdot k\delta(\nu^2-w^2)\\ \times M(k,R)e^{ikR-i\nu T}\\ =0, \quad R>T, \quad R>a,\end{aligned} \tag{2.14}$$

where

$$M(k,R)=\sum_{l=0}^\infty (2l+1)f_l(k)q_l^2(kR/2). \tag{2.15}$$

Using the δ function to carry out the integration over k, one finds, writing $k_l=+(\nu^2-\mu^2)^{\frac{1}{2}}$, that $G(R,T)$ may be written as

$$\begin{aligned}G(R,T)=\int_\mu^\infty \frac{d\nu}{2}M(k_\nu,R)e^{+ik_\nu R-i\nu T}\\ +\int_\infty^\mu \frac{d\nu}{2}M(-k_\nu,R)e^{-ik_\nu R-i\nu T}\\ +\int_{-\infty}^{-\mu}\frac{d\nu}{2}M(-k_\nu,R)e^{-ik_\nu R-i\nu T}\\ +\int_{-\mu}^\infty \frac{d\nu}{2}M(k_\nu,R)e^{ik_\nu R-i\nu T}.\end{aligned} \tag{2.16}$$

Let us now consider the function $(\nu^2-\mu^2)^{\frac{1}{2}}$ in the complex ν plane, and introduce cuts from $-\infty$ to $-\mu$ and from μ to ∞. If we choose the branch of $(\nu^2-\mu^2)^{\frac{1}{2}}$ which is real and positive when $\nu>\mu$, we find that (2.16) may be written as

$$\begin{aligned}G(R,T)=\int_C \frac{d\nu}{2}M((\nu^2-\mu^2)^{\frac{1}{2}},R)\\ \times\exp\{i[(\nu^2-\mu^2)^{\frac{1}{2}}R-\nu T]\},\end{aligned} \tag{2.17}$$

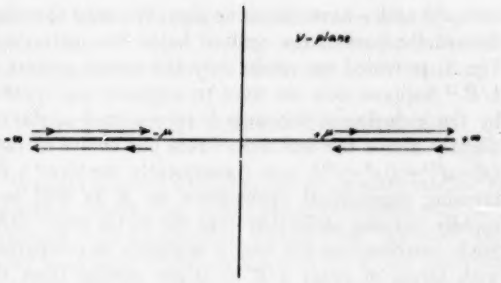

FIG. 1. The contour of integration C for the integral in Eq. (2.16). The heavy lines running from $-\infty$ to $-\mu$ and from μ to $+\infty$ are the branch lines of the function $(\nu^2-\mu^2)^{\frac{1}{2}}$.

where C is the contour shown in Fig. 1. In the strip between $-\mu$ and $+\mu$, $(\nu^2-\mu^2)^{\frac{1}{2}}=+i(\mu^2-\nu^2)^{\frac{1}{2}}$.

In place of the time interval T we shall introduce the variable $z=R-T$ so that $G(R,T)$ becomes a function of R and z; our requirement is that $G(R,z)$ shall vanish for $R>a$, $z>0$. There is every reason to believe that $G(R,z)$ is a well-behaved function of z so long as z is greater than zero; there is, however, a distinct possibility in many cases of physical interest that G involve terms proportional to $\delta(z)$ and $\delta'(z)$. This would in fact be the case if the total cross section were to approach a constant for large ν. It is perhaps worth noting that these singularities are not unexpected; the original commutator is certainly singular on the light cone. In order to obtain a formula valid even for $z=0$, we first first multiply G by e^{-iq_1z} and integrate over z from z to infinity (which cannot change the value since G is zero over this range) giving q_1, a negative imaginary part to insure convergence, and then multiply by e^{-iq_2z} and again integrate from z to infinity. We obtain then

$$H(R,z)=\int_z^\infty dz'\int_{z'}^\infty dz''e^{i(q_1z'+q_2z'')}G(R,z''),$$

$$\begin{aligned}H(R,z)=-e^{-i(q_1+q_2)z}\int_C \frac{d\nu}{2}\frac{M\{(\nu^2-\mu^2)^{\frac{1}{2}},R\}}{(\nu-q_1)(\nu-q_2)}\\ \times\exp\{i[(\nu^2-\mu^2)^{\frac{1}{2}}-\nu]R+i\nu Z\}.\end{aligned} \tag{2.18}$$

Strictly speaking, the upper limits of the z integrations should be R, since $T>0$ and thus for fixed R, z cannot exceed R. We shall be interested, however, only in the limit as $R\to\infty$, in which case, the contributions from the upper limits are negligible. The frequencies q_1 and q_2 will be chosen at our convenience. We note that the integrand in Eq. (2.18) is square integrable over the interval $-\infty$ to $+\infty$.

Consider now $G(R,z)$ for very large values of R. The contributions to the integral coming from portions of the contour for which $(\nu^2-\mu^2)^{\frac{1}{2}}$ and ν have the opposite algebraic sign will contain a rapidly varying exponential factor and make a vanishingly small contribution, $O(1/R)$, in comparison with the portions for which

$(\nu^2-\mu^2)^{\frac{1}{2}}$ and ν have the same sign. We may therefore discard the part of the contour below the real axis in Fig. 1, provided we retain only the lowest powers in $1/R$.[12] Suppose now we were to augment our contour by the inclusion of the strip from $-\mu$ to $+\mu$, staying slightly above the real axis. From our choice of cuts, $(\nu^2-\mu^2)^{\frac{1}{2}}=i(\mu^2-\nu^2)^{\frac{1}{2}}$, and consequently we have a decreasing exponential dependence on R as well as a rapidly varying oscillation from the factor $\exp(-i\nu R)$. Such contributions are clearly negligible in comparison with terms of order $1/R$ or larger coming from the outer portions of the contour. We may therefore replace the integral over C by one extending from $-\infty$ to ∞ on a line just above the real axis. Retaining only the leading term in powers of $1/R$, we conclude that we must have

$$\int_{-\infty}^{\infty} d\nu \frac{\sum_{l=0}^{\infty}[(2l+1)f_l\{(\nu^2-\mu^2)^{\frac{1}{2}}\}]}{(\nu-q_1)(\nu-q_2)} \times\exp\{i[(\nu^2-\mu^2)^{\frac{1}{2}}-\nu]R\}e^{i\nu z}=0, \quad z\geqslant 0. \quad (2.19)$$

We have, of course, assumed that $M(k,R)$ does not do anything spectacular on the strip $-\mu<\nu<\mu$ provided we stay slightly above the real axis. There may be singularities on the real axis and in fact if there are bound states there will be poles. This point will be discussed further below.

The sum in Eq. (2.19) is just the forward scattering amplitude $f(\nu)$ for a particle of momentum $k=(\nu^2-\mu^2)^{\frac{1}{2}}$. As is discussed in Sec. IV, we may conclude from (2.19) that the function $g(\nu,R)$ defined by

$$g(\nu,R)=\frac{f(\nu)}{(\nu-q_1)(\nu-q_2)}\exp\{i[(\nu^2-\mu^2)^{\frac{1}{2}}-\nu]R\}, \quad (2.20)$$

must be analytic in the upper half of the ν plane. The discussion in Sec. IV also shows that $g(\nu,R)$ is bounded in the upper half-plane and we shall now show that this boundedness is not dependent on the exponential factor. To see this, put $\nu=iy$ and consider the exponential for very large positive values of y. The exponential becomes $\exp(-\mu^2R/2y)$ and thus tends to unity for $y\to\infty$. We may conclude therefore that the function $\tilde{f}(\nu)$ given by

$$\tilde{f}(\nu)=f(\nu)/[(\nu-q_1)(\nu-q_2)] \quad (2.21)$$

is analytic in the upper half-plane (and is bounded for all values of ν, $0<\arg\nu<\pi$).

We must now generalize the above result to include also the possibilities of bound states and particle absorption. In case there are bound states, there are, as is well known, poles on the real ν axis from $-\mu$ to μ. However, these do not seriously trouble us because we always integrate on a contour slightly above the real axis. The contributions of the small indentations of the contour (made to avoid the poles) are precisely cancelled by the inclusion of the bound states in the sum over intermediate states detailed in Eq. (2.4). In the limit, then, as ν approaches the real axis in an integral such as in Eq. (2.19), one takes the principal value at the poles of the forward scattering amplitude $f(\nu)$.

If there is absorption of particles, we must imagine augmenting our considerations to allow for the additional channel (or channels) describing the alternate modes. This requires formal modifications of a variety familiar in nuclear reaction theory; roughly speaking, we must increase our set of eigenfunctions to include not only those states initiated by a plane wave in the elastic scattering channel, but also to include those states initiated by plane waves in other channels (i.e., the reactions inverse to the absorption processes) which have only outgoing waves in the elastic channel. The outcome of these manipulations is that the previous conclusions drawn from the function $f(\nu)$ in Eq. (2.21) continue to be true provided that $f(\nu)$ be interpreted as the coherent elastic forward scattering amplitude. In this case the phase shifts δ_l are, of course, complex.

The previous considerations relating to particles with mass do not appear to have very interesting applications. Of greater interest is the case of zero rest mass to which we now turn. The real physical problem of photons interacting with a quantized matter field will be discussed in the next section, but for the time being we shall continue the discussion with the amplified model of spin-zero "photons" and an external potential. All of our previous considerations remain valid but, of course, become simpler. We shall rewrite some of the equations for the special case $\mu=0$.

The equation analogous to Eq. (2.16) becomes

$$G(R,T)=\int_{-\infty}^{\infty}\frac{d\nu}{2}e^{-i\nu T}\epsilon(\nu)\{M(|\nu|,R)e^{i|\nu|R} -M(-|\nu|,R)e^{-i|\nu|R}\}, \quad (2.22)$$

which may be written in terms of $z=R-T$ as

$$G(R,z)=\int_{-\infty}^{\infty}\frac{d\nu}{2}e^{i\nu z}\{M(\nu,R)-M(-\nu,R)e^{-2i\nu R}\}. \quad (2.23)$$

The equation corresponding to (2.18) is obviously

$$H(R,z)=-e^{i(q_1+q_2)z}\int_{-\infty}^{\infty}\frac{d\nu}{2}\frac{e^{i\nu z}}{(\nu-q_1)(\nu-q_2)} \times\{M(\nu,R)-M(-\nu,R)e^{-2i\nu R}\}. \quad (2.24)$$

The argument now proceeds essentially as before. If we look first at the leading term in the $1/R$ expansion

[12] E. T. Whittaker and G. N. Watson, *Modern Analysis* (Cambridge University Press, New York, 1948), p. 172. The theorems referred to, the Riemann-Lebesgue lemmas, do not exactly cover the case at hand. The exact conditions on $M[(\nu^2-\mu^2)^{\frac{1}{2}}, R]$ which must obtain for the above remarks to be true have not been studied. The claims made seem very plausible, and in the only case where applications are made ($\mu=0$), the required extension of the Riemann-Lebesgue lemmas is trivial. See the discussion following Eq. (2.24).

of $M(\nu,R)$ (which is independent of $1/R$) we may conclude that the second term in Eq. (2.24) goes to zero in the limit $R\to\infty$. This may be seen by using the assumed square integrability of $M(-\nu,R)e^{i\nu z}/(\nu-q_1)\times(\nu-q_\sigma)$ together with Parseval's theorem. Imposing the condition that $H(R,z)$ should vanish for $z>0$ leads to the conclusion that the forward scattering amplitude, $f(\nu)$, is analytic in the upper half-plane and that our previously defined function $\bar{f}(\nu)$ is bounded in the upper half-plane.

Thus far we have considered only the leading term in the $1/R$ expansion of $M(\nu,R)$. This term is the forward scattering amplitude. One may well ask if anything can be said about directions other than forward. We have been unable to obtain any very simple relations, however some information may be found in the following way: If we had not made the the special choice of angle $\vartheta=\pi$ in Eq. (2.11), we would still have been able to carry through all the steps leading to Eqs. (2.18) and (2.24); the only difference that appears is that $M(\nu,R)$, say, in (2.24) becomes replaced by

$$M(\nu,R,\cos\vartheta)=\sum_{l=0}^{\infty}(2l+1)f_l(\nu)P_l(\cos\vartheta)q_l^2\left(\frac{\nu R}{2}\right), \quad (2.25)$$

where we have replaced ϑ by $\pi-\vartheta$. Note that the leading term in the $1/R$ expansion of $M(\nu,R,\cos\vartheta)$ is just the total scattering amplitude, $f(\vartheta)$. Our causality requirement takes the form

$$H(R,z,\cos\vartheta)=-e^{-i(q_1+q_2)z}\int_{-\infty}^{\infty}\frac{d\nu}{2}\frac{e^{i\nu z}}{(\nu-q_1)(\nu-q_2)}\times\{M(\nu,R,\cos\vartheta)-M(-\nu,R,\cos\vartheta)e^{-2i\nu R}\}=0, \quad \text{for} \quad R\cos(\vartheta/2)>T, \quad R>a. \quad (2.26)$$

We now differentiate H with respect to $\cos\vartheta$ and put $\vartheta=0$; an attempt to continue as before to isolate the leading term in the $1/R$ expansion of $\partial M/\partial\cos\vartheta$ leads to some difficulty in general. The reason is that $P_l'(1)=l(l+1)/2$, so that $\partial M/\partial\cos\vartheta$ will probably be proportional to ν^3 (for large ν) if $f(\nu)\sim\nu$ as has previously been assumed. Before applying the Riemann-Lebesgue theorem, we must supply two more powers of ν in the denominator by using our integration technique. [See procedure leading to Eq. (2.18).] When these are supplied, we may conclude that the function $g(\nu)$ defined by

$$g(\nu)=\frac{[\partial f(\nu,\cos\vartheta)/\partial\cos\vartheta]_{\cos\vartheta=1}}{(\nu-q_1)(\nu-q_2)(\nu-q_3)(\nu-q_4)}, \quad (2.27)$$

with the q's to be chosen conveniently, is analytic and bounded in the upper half ν plane. It is clear that there is an infinite sequence of such relations, obtained by carrying out the successive differentiations. In every case more powers of ν must be supplied in the denominator to insure the proper boundedness. We have made no attempt to solve in any sense for the individual scattering amplitudes $f_l(\nu)$ from this set of relations.

III. QUANTIZED ELECTROMAGNETIC AND MATTER FIELDS

We pass now to a consideration of the more interesting situation where the quantized electromagnetic field interacts with a quantized matter field. We shall consider a system whose interaction with the radiation field may be described by an interaction Hamiltonian density $-j_\mu(x)A_\mu(x)$, where $j_\mu(x)$ is the current density four-vector operator of the matter system and $A_\mu(x)$ the usual four-vector potential of the radiation field. The procedure we follow at this point is strictly analogous to that used in the previous section. We demand that the commutator of two Heiseberg field operators $\mathbf{A}_\lambda(x)$, $\mathbf{A}_\sigma(y)$ shall vanish for space-like separations of x and y. It is convenient to consider a matrix element of the commutator between an initial state for which there are no photons and the matter field is a state i and a final state with no photons and the matter system in a state f. We shall restrict our attention to such states i and f for which the energies E_i and E_f are equal. It is again convenient to restrict our attention to positive time intervals x_0-y_0 and to deal with the retarded function $\mathcal{G}_{\lambda\sigma}(x,y)$ defined by

$$\mathcal{G}_{\lambda\sigma}(x,y)=i\langle 0,f|[\mathbf{A}_\sigma(x),\mathbf{A}_\sigma(y)]|i,0\rangle\eta(x-y). \quad (3.1)$$

Our demand is that $\mathcal{G}_{\lambda\sigma}(x,y)$ be zero for $(x-y)^2>0$. There is, of course, no way known at present to compute the Heisenberg operators $\mathbf{A}$ except by perturbation theory. Fortunately this is not too serious since the lowest order perturbation calculations in the radiation field are very accurate. We shall work to second order in the electric charge e. It is unnecessary then for us to carry out any renormalizations. We assume that all interactions other than with the radiation field are taken into account exactly and we work in such an interaction representation. (For example, if we consider the scattering of γ rays by a hydrogen atom, we use the Furry interaction representation.)[13] To the second order in e, then, the Heisenberg operator $\mathbf{A}_\lambda(x)$ takes the well known form[14]

$$\mathbf{A}_\lambda(x)=A_\lambda(x)+i\int_{-\infty}^{\infty}d^4x'[H(x'),A_\lambda(x')]\eta(x-x')+i^2\int_{-\infty}^{\infty}d^4x'\int_{-\infty}^{\infty}d^4x''[H(x''),[H(x'),A_\lambda(x)]]\times\eta(x-x')\eta(x'-x''), \quad (3.2)$$

where $H(x)=-j_\mu(x)A_\mu(x)$ and the A's are now interaction representation operators. Substituting for $H(x)$,

[13] W. Furry, Phys. Rev. **81**, 115 (1951).
[14] J. Schwinger, Phys. Rev. **76**, 790 (1949).

and making use of such well known results as

$$[A_\lambda(x'),A_\sigma(x)]=i\delta_{\lambda\sigma}D(x-x'),$$
$$D_r(x)=-\eta(x)D(x), \tag{3.3}$$

we find

$$\mathfrak{A}_\lambda(x)=A_\lambda(x)+\int_{-\infty}^{\infty}d^4x'D_r(x-x')j_\lambda(x')$$
$$-i\int_{-\infty}^{\infty}d^4x'\int_{-\infty}^{\infty}d^4x''A_\mu(x'')$$
$$\times[j_\mu(x''),j_\lambda(x')]D_r(x-x')\eta(x'-x''). \tag{3.4}$$

We assume that the usual adiabatic switching on and off procedures are carried out in order to give meaning to the above integrals.

The commutator in Eq. (3.1) may now be evaluated easily, with the result

$$\mathcal{G}_{\lambda\sigma}(x,y)=\delta_{\lambda\sigma}D_r(x-y)\delta_{fi}$$
$$+\eta(x-y)\langle 0,f|G_{\lambda\sigma}(x,y)|i,0\rangle, \tag{3.5}$$

with $G_{\lambda\sigma}(x,y)$ given by

$$G_{\lambda\sigma}(x,y)=i\int_{-\infty}^{\infty}d^4x'\int_{-\infty}^{\infty}d^4x''[j_\lambda(x''),j_\sigma(x')]$$
$$\times\{D_r(x-x')D_r(y-x'')$$
$$+D_r(x-x')D(y-x'')\eta(x'-x'')$$
$$+D(x-x')D_r(y-x'')\eta(x''-x')\}. \tag{3.6}$$

In the limit as $x_0\to+\infty$, $y_0\to-\infty$, only the middle term survives, in accordance with the adiabatic hypothesis mentioned above. In this limit, $G_{\lambda\sigma}(x,y)$ becomes

$$G_{\lambda\sigma}(x,y)=i\int_{-\infty}^{\infty}d^4x'\int_{-\infty}^{\infty}d^4x''[j_\lambda(x''),j_\sigma(x')]$$
$$\times D(x-x')D(x''-y)\eta(x'-x''), \tag{3.7}$$

where we have used (3.3) and also $D(x)=-D(-x)$. Substituting the Fourier representation of the D's, namely,

$$D(x)=\frac{-i}{(2\pi)^3}\int d^4k\epsilon(k)\delta(k^2)e^{ik\cdot x}, \tag{3.8}$$

we have

$$\langle 0,f|G_{\lambda\sigma}(x,y)|i,0\rangle=-\int\frac{d^4k}{(2\pi)^3}\int\frac{d^4k'}{(2\pi)^3}e^{ik'\cdot x-ik\cdot y}$$
$$\times\epsilon(k)\epsilon(k')\delta(k^2)\delta(k'^2)\mathfrak{M}'^{i}(k',k), \tag{3.9}$$

where

$$\mathfrak{M}_{\lambda\sigma}{}^{fi}(k',k)=i\int d^4x'\int d^4x''\{\langle f|j_\lambda(x')j_\sigma(x'')|i\rangle$$
$$\times e^{-ik'\cdot x'+ik\cdot x''}\eta(x'-x'')-\langle f|j_\sigma(x')j_\lambda(x'')|i\rangle$$
$$\times e^{ik\cdot x''-ik'\cdot x''}\eta(x''-x')\}. \tag{3.10}$$

We write now:

$$\langle b|j_\mu(\mathbf{x})|a\rangle=\langle b|j_\mu(\mathbf{x})|a\rangle e^{-i(E_a-E_b)x_0},$$
$$\langle f|j_\lambda(x')j_\sigma(x'')|i\rangle=\sum_n\langle f|j_\lambda(\mathbf{x}')|n\rangle\langle n|j_\sigma(\mathbf{x}'')|i\rangle$$
$$\times e^{iE(x_0'-x_0'')}e^{-iE_n(x_0'-x_0'')}, \tag{3.11}$$
$$\eta(x)=\frac{1}{2\pi i}\int_{-\infty}^{\infty}da\frac{e^{iax_0}}{a-i\epsilon},$$

where n labels a complete set of state vectors for the matter system with the *positive* energies E_n and we have used $E_f=E_i=E$. The time integrations in (3.10) may be carried out immediately, with the result

$$\mathfrak{M}_{\lambda\sigma}{}^{fi}(k',k)=2\pi\delta(k_0-k_0')\sum_n\int d^3x'\int d^3x''$$
$$\times\left[\frac{\langle f|j_\lambda(\mathbf{x}')|n\rangle\langle n|j_\sigma(\mathbf{x}'')|i\rangle}{E+k_0-E_n+i\epsilon}e^{-ik'\cdot x+ik\cdot x''}\right.$$
$$\left.+\frac{\langle f|j_\sigma(\mathbf{x}')|n\rangle\langle n|j_\lambda(\mathbf{x}'')|i\rangle}{E-k_0-E_n-i\epsilon}e^{ik\cdot x'-ik\cdot x''}\right]. \tag{3.12}$$

This result is to be compared to the matrix element of the S matrix corresponding to a transition in which a photon of four-momentum k and polarization σ is scattered into a photon of four-momentum k' and polarization λ while the matter system makes a transition from the state i to state f of equal energy. Writing $S=1-iR$, we have

$$\mathfrak{F}_{\lambda\sigma}{}^{fi}(k',k)=\langle\lambda k'f|R|ik\sigma\rangle$$
$$=-i\int_{-\infty}^{\infty}d^4x'\int_{-\infty}^{\infty}d^4x''\langle\lambda k'f|H(x')$$
$$\times H(x'')|ik\sigma\rangle\eta(x'-x'')$$
$$=-i\int_{-\infty}^{\infty}d^4x'\int_{-\infty}^{\infty}d^4x''\{\langle f|j_\lambda(x')j_\sigma(x'')|i\rangle$$
$$\times e^{-ik'\cdot x'+ik\cdot x''}\eta(x'-x'')$$
$$+\langle f|j_\sigma(x')j_\lambda(x'')|i\rangle$$
$$\times e^{-ik'\cdot x''+ik\cdot x'}\eta(x'-x'')\}. \tag{3.13}$$

Using Eq. (3.11) as before, we find

$$\mathfrak{F}_{\lambda\sigma}{}^{fi}(k',k)=2\pi\delta(k_0-k_0')\sum_n\int d^3x'\int d^3x''$$
$$+\left[\frac{\langle f|j_\lambda(\mathbf{x}')|n\rangle\langle n|j_\sigma(\mathbf{x}'')|i\rangle}{E+k_0-E_n+i\epsilon}e^{-ik'\cdot x'+ik\cdot x''}\right.$$
$$\left.+\frac{\langle f|j_\sigma(\mathbf{x}')|n\rangle\langle n|j_\lambda(\mathbf{x}'')|i\rangle}{E-k_0-E_n+i\epsilon}e^{ik\cdot x'-ik'\cdot x''}\right]. \tag{3.14}$$

We see that except for the sign of ϵ in the second term, (3.14) and (3.12) are identical. If, for example, E is the ground state of the system, $E_n > E$ for all n, and $k_0 > 0$ (which is the case for real photon absorption as we have defined it), the difference between the two expressions is of no consequence, because in such a case the second denominator can never vanish. Of course, k_0 in Eq. (3.12) is not restricted to positive values and we may formally consider k_0 in Eq. (3.14) taking on negative values. We write for the coefficient of $2\pi\delta(k_0-k_0')$ in the two cases $M_{\lambda\sigma}{}^{fi}(k',k)$ and $F_{\lambda\sigma}{}^{fi}(k',k)$ for (3.12) and (3.14), respectively, and further introduce the dispersive and absorptive parts of $F_{\lambda\sigma}{}^{fi}$ according to the definition:

$$F_{\lambda\sigma}{}^{fi}(k'\cdot k) = D_{\lambda\sigma}{}^{fi}(k',k) + iA_{\lambda\sigma}{}^{fi}(k',k), \quad (3.15)$$

where the division is made according to whether the intermediate states in the sum are virtual (contributing to D) or real (contributing to A). Unless $i=f$, $\sigma=\lambda$, D and A will generally themselves be complex. We shall see examples of this in Sec. V. In terms of D and A, M can be written as

$$M_{\lambda\sigma}{}^{fi}(k',k) = D_{\lambda\sigma}{}^{fi}(k',k) + i\epsilon(k_0)A_{\lambda\sigma}{}^{fi}(k',k). \quad (3.16)$$

Thus, the factor $\epsilon(k_0)$ in the absorptive term reflects the previously noted differences in the energy denominators. It should be remarked that $F_{\lambda\sigma}{}^{fi}(k',k)$ is the scattering amplitude except for some easily supplied factors. For example, in Compton scattering, one must supply a factor of $(1/4\pi)(\nu'/\nu)$ if F is computed in the laboratory system, or a factor of $(1/4\pi)(m/W)$, where W is the total energy if F is computed in the barycentric system.

We now return to Eq. (3.9) which may be written, in virtue of the δ functions in the integrand and the definition of M, as

$$\langle 0,f|G_{\lambda\sigma}(x,y)|i,0\rangle = \int_{-\infty}^{\infty}\frac{dk_0 k_0^2}{(2\pi)^4}e^{-ik_0(x_0-y_0)}\int d\Omega_{\mathbf{n}}\int d\Omega_{\mathbf{n}'} \times e^{i|k_0|\mathbf{n}'\cdot\mathbf{x}-i|k_0|\mathbf{n}\cdot\mathbf{y}}M_{\lambda\sigma}{}^{ij}(k_0;|k_0|\mathbf{n}';|k_0|\mathbf{n}). \quad (3.17)$$

We have introduced a more explicit notation for the arguments of $M_{\lambda\sigma}{}^{ij}$. The k_0 refers to the "photon frequency" that appears in the energy denominators of Eq. (3.12); $|k_0|\mathbf{n}'$ was, before the above-mentioned δ functions were used, the momentum vector $\mathbf{k}'$ of the "emitted photon," and similarly $|k_0|\mathbf{n}$ was the momentum vector of the "absorbed photon," $\mathbf{k}$.

We have already imagined that $x_0\to+\infty$, $y_0\to-\infty$; we now consider removing $\mathbf{x}$,$\mathbf{y}$ to infinity. As in Sec. II, it is convenient to put $\mathbf{y}=-\mathbf{x}$ and for the purpose of carrying out the integrations over $\mathbf{n}$ and $\mathbf{n}'$ we choose the direction x as polar axis, and define a unit vector $\mathbf{n}_x$ parallel to x. In carrying out the angular integrations, we integrate by parts and retain only the leading terms in powers of $1/|x|$. We find

$$\langle 0,f|G_{\lambda\sigma}(x,y)|i,0\rangle = -\frac{1}{(2\pi)^2|\mathbf{x}|^2}\int_{-\infty}^{\infty}dk_0 e^{-ik_0(x_0-y_0)}\{e^{2i|k_0|\mathbf{x}|} \times M_{\lambda\sigma}{}^{ij}(k_0;k_0\mathbf{n}_x;k_0\mathbf{n}_x) - M_{\lambda\sigma}{}^{fi}(k_0;-\mathbf{n}_xk_0;\mathbf{n}_xk_0) \times M_{\lambda\sigma}{}^{fi}(k_0;\mathbf{n}_xk_0;-\mathbf{n}_xk_0) + e^{-2i|k_0|\mathbf{x}|} \times M_{\lambda\sigma}{}^{fi}(k_0;-\mathbf{n}_xk_0;-\mathbf{n}_xk_0)\}. \quad (3.18)$$

We now proceed exactly as we did in Sec. II: We introduce $z=2|x|-(x_0-y_0)$, multiply successively by the exponential factor $e^{-iq_1z}e^{-iq_2z}$ in each case integrating from z to ∞, and use the argument following Eq. (2.24). Imposing our condition that $\langle 0,f|G(x,y)|i\cdot 0\rangle$ vanish for $z>0$ yields, as our final condition,

$$\int_{-\infty}^{\infty}dk_0 e^{ik_0z}\frac{M_{\lambda\sigma}{}^{fi}(k_0;\mathbf{n}k_0;\mathbf{n}k_0)}{(k_0-q_1)(k_0-q_2)}=0, \quad z>0, \quad (3.19)$$

where we have dropped the subscript x of $\mathbf{n}_x$. This will furnish more general forms of the dispersion relations than are usually considered, since we need not confine ourselves to the completely coherent case $\lambda=\sigma$, $f=i$. Note that for $k_0>0$, $M_{\lambda\sigma}{}^{fi}(k_0;\mathbf{n}k_0;\mathbf{n}k_0)$ is, except for a factor $1/4\pi$, the forward scattering amplitude in the laboratory system. (See remarks following (3.16).)

It has not been necessary for us to make any assumptions about the evenness or oddness of M as a function of frequency k_0 up to this time. The precise dispersion relations which follow from Eq. (3.19) depend, however, on this question. We may deduce the behavior of M directly from its explicit form given in Eq. (3.12). Writing $\mathbf{k}=k_0\mathbf{n}$, $\mathbf{k}'=k_0\mathbf{n}'$ in accordance with Eq. (3.19), we see by inspection of Eq. (3.12) that

$$M_{\lambda\sigma}{}^{fi}(-k_0;-k_0\mathbf{n}';-k_0\mathbf{n}) = M_{\lambda\sigma}{}^{ij*}(+k_0;k_0\mathbf{n}',k_0\mathbf{n}). \quad (3.20)$$

If we regard M as an operator on the initial and final states, we see that changing k_0 into minus k_0 yields the Hermitian conjugate operator. There are similar relations which will not be used here but which are perhaps worth while pointing out. One of these is the direct counterpart of a relation recently used by Gell-Mann and Goldberger[15] in meson-nucleon scattering, namely

$$F_{\lambda\sigma}{}^{fi}(k',k) = F_{\sigma\lambda}{}^{fi}(-k,-k'). \quad (3.21)$$

Note that this relation is not true for $M_{\lambda\sigma}{}^{fi}$. Now the four-vectors k',k in (3.21) refer to real photon four-momenta, and in the case being considered here $k_0'=k_0$; we may write then $\mathbf{k}=|k_0|\mathbf{n}$ and $\mathbf{k}'=|k_0|\mathbf{n}'$, since the amplitude F is defined only for positive k_0 and we are free to decide whether $\mathbf{k},\mathbf{k}'$ shall change sign for

[15] M. Gell-Mann and M. L. Goldberger (to be published).

$k_0 \to -k_0$. Writing Eq. (3.21) very explicitly, we have

$$F_{\lambda\sigma}^{fi}(k_0; |k_0|\mathbf{n}'; |k_0|\mathbf{n}) = F_{\sigma\lambda}^{fi}(-k_0; -|k_0|\mathbf{n}; -|k_0|\mathbf{n}'). \quad (3.22)$$

It is easy to prove from our explicit formula, Eq. (3.14), that if $\lambda, \sigma = 1, 2$, or 3, which is the case for real photons,

$$F_{\sigma\lambda}^{fi}(-k_0; -|k_0|\mathbf{n}; -|k_0|\mathbf{n}') = \pm F_{\sigma\lambda}^{fi}(-k_0; |k_0|\mathbf{n}; |k_0|n'), \quad (3.23)$$

where one takes the plus or minus sign depending on whether the parities of the initial and final states are the same or different. Thus Eq. (3.22) becomes

$$F_{\lambda\sigma}^{fi}(k_0; |k_0|\mathbf{n}; |k_0|\mathbf{n}') = \pm F_{\sigma\lambda}^{fi}(-k_0; |k_0|\mathbf{n}; |k_0|\mathbf{n}'). \quad (3.24)$$

In exactly the same way one proves

$$M_{\lambda\sigma}^{fi}(-k_0; |k_0|\mathbf{n}'; |k_0|\mathbf{n}) = \pm M_{\lambda\sigma}^{if*}(k_0; |k_0|\mathbf{n}'; |k_0|\mathbf{n}). \quad (3.25)$$

Our principal result, Eq. (3.19), will be applied in Sec. V to a number of examples. In these applications we never go beyond the e^2 approximation under which (3.19) was derived.

IV. ANALYTICITY AND DISPERSION RELATIONS

In the previous sections we have shown that the requirements of commutativity of field operators taken at two space-like points have resulted in restrictions on what are essentially forward-scattering amplitudes of the variety that the functions are the Fourier transforms of other functions which vanish for positive values of their arguments. [See Eqs. (2.26) and (3.19).] The relation between the requirement that a function $h(w)$ be the Fourier transform of a function $g(z)$ which vanishes for positive values of z, and dispersion relations of the variety given by Kramers and Kronig, has been discussed in great detail by Toll and van Kampen. We shall give a short description of the mathematical theory, taking advantage of certain simplifications which we may introduce on the basis of physics.

We shall assume that the total cross section for any physical process either approaches a constant for high frequencies or approaches zero. Actually the theory we shall develop will remain valid even if the cross section were to increase with energy, provided this increase were not so rapid that the integral $\int_0^\infty d\nu\sigma^2(\nu)/\nu^2$ ceased to exist. With this limitation on the class of functions to be considered, we may use the rather weaker theorems from Fourier integral theory relating to functions which are square integrable.

In terms of the scattering amplitude $f(\nu)$, our assumption on the high-frequency dependence of the cross sections becomes

$$\int^\infty d\nu \left(\frac{\mathrm{Im} f(\nu)}{\nu^2}\right)^2 < \infty. \quad (4.1)$$

[We used the well-known relation $\sigma(\nu) = 4\pi \,\mathrm{Im}\, f(\nu)/\nu$.] We shall assume that $\mathrm{Re}\, f(\nu)$ satisfies the same requirement. In order to avoid difficulties at $\nu = 0$ we shall consider the conditions which may be imposed on a function $h(\nu)$ [which in our application is essentially the forward-scattering amplitude, and which we now assume has the boundedness property expressed in Eq. (4.1)] from the requirement

$$g(z) \equiv \int_{-\infty}^{\infty} d\nu \frac{h(\nu)}{(\nu - q_1)(\nu - q_2)} e^{i\nu z} = 0, \quad z > 0. \quad (4.2)$$

The frequencies q_1 and q_2 are complex with *negative* imaginary parts which will later be allowed to approach zero, and whose real parts will be chosen conveniently. The integrand in Eq. (4.2), $h(\nu)/(\nu - q_1)(\nu - q_2)$ may be expressed in terms of $g(z)$ by the Fourier theorem according to

$$\frac{h(\nu)}{(\nu - q_1)(\nu - q_2)} \equiv \bar{h}(\nu) = \frac{1}{2\pi} \int_{-\infty}^{0} dz g(z) e^{-i\nu z}. \quad (4.3)$$

From our original restrictions $h(\nu)$ we know that this integral is convergent for all values of ν. If we add to ν a positive imaginary part $i\gamma$ the integrand is multiplied by $e^{\gamma z}$ and the integral consequently converges even better. It follows that $\bar{h}(\nu)$ is the boundary value of a function which is analytic in the entire upper half ν plane. We now remark that not only is $\bar{h}(\nu)$ analytic, but it is also square integrable in the upper half-plane. To prove this, we observe that

$$\int_{-\infty}^{\infty} d\nu |\bar{h}(\nu + i\gamma)|^2 = \frac{1}{2\pi} \int_{-\infty}^{0} dz e^{2\gamma z} |g(z)|^2 \leqslant \int_{-\infty}^{\infty} d\nu |\bar{h}(\nu)|^2 < \infty, \quad (4.4)$$

independent of γ. Evidently the analyticity of $\bar{h}(\nu)$ implies that of $h(\nu)$, but of course not the integrability.

We wish now to express our requirement (4.2) as a dispersion relation of the familiar variety. This may be done in a variety of ways; one simple way is as follows: Let us simply evaluate the integral

$$\frac{\mathrm{P}}{i\pi} \int_{-\infty}^{\infty} d\nu' \frac{\bar{h}(\nu')}{\nu' - \nu}, \quad (4.5)$$

where P stands for the Cauchy principle value. Since $\bar{h}(\nu)$ has no poles in the upper half-plane, and because of (4.4),[16] the integral in (4.5) may be evaluated imme-

[16] It can be shown that Eq. (4.4) implies that the integral over an infinite semicircle above the real axis vanishes.

diately by contour integration, and it yields

$$\bar{h}(\nu)=\frac{\mathrm{P}}{i\pi}\int_{-\infty}^{\infty}d\nu'\frac{\bar{h}(\nu')}{\nu'-\nu}. \tag{4.6}$$

Let us now put in our explicit form for $\bar{h}(\nu)$ [Eq. (4.3)], taking $q_1=\nu_1-i\epsilon_1$, $q_2=i\epsilon_2$, and considering the limit as ϵ_1 and ϵ_2 approach zero. [Recall that $1/(x+i\epsilon)=\mathrm{P}(1/x)-i\pi\delta(x)$.] We find that

$$\frac{h(\nu)}{\nu(\nu-\nu_1)}-\frac{1}{\nu_1}\left[\frac{h(\nu_1)}{\nu-\nu_1}-\frac{h(0)}{\nu}\right]=\frac{\mathrm{P}}{i\pi}\int_{-\infty}^{\infty}d\nu'\frac{h(\nu')}{\nu'(\nu'-\nu_1)(\nu'-\nu)}, \tag{4.7}$$

where the principal value sign applies to all three singularities of the integrand. In our applications it will be convenient to consider the limit of both sides as $\nu_1\to 0$. Under these circumstances, we find

$$\frac{h(\nu)}{\nu^2}-\frac{h'(0)}{\nu}-\frac{h(0)}{\nu^2}=\lim_{\nu_1\to 0}\frac{\mathrm{P}}{i\pi}\int_{-\infty}^{\infty}d\nu'\frac{h(\nu')}{\nu'(\nu'-\nu_1)(\nu'-\nu)}. \tag{4.8}$$

There are two special cases of interest: (1) $h(\nu)=h^*(-\nu)$, and (2) $h(\nu)=-h^*(-\nu)$. In the first case, we have

$$\mathrm{Re}\,h(\nu)=\frac{2\nu^2}{\pi}\int_0^{\infty}d\nu'\frac{\mathrm{Im}\,h(\nu')}{\nu'(\nu'^2-\nu^2)}+\lim_{\nu_1\to 0}\frac{2\nu^2\nu_1(\nu_1+\nu)}{\pi}\mathrm{P}\int_0^{\infty}d\nu'\frac{\mathrm{Im}\,h(\nu')}{\nu'(\nu'^2-\nu_1^2)(\nu'^2-\nu_1)}; \tag{4.9}$$

whereas, in the second case,

$$\mathrm{Re}\,h(\nu)-\nu h'(0)=\frac{2\nu^2}{\pi}\lim_{\nu_1\to 0}\int_0^{\infty}d\nu'\frac{(\nu+\nu_1)\,\mathrm{Im}\,h(\nu')}{(\nu'^2-\nu_1^2)(\nu'^2-\nu^2)}. \tag{4.10}$$

In all of our applications we may pass to the limit of $\nu_1\to 0$ without difficulty because $\mathrm{Im}\,h(\nu)$ will invariably vanish for ν less than some threshold value. Equations (4.9) and (4.10) become then, respectively,

$$\begin{aligned}\mathrm{Re}\,h(\nu)-h(0)&=\frac{2\nu^2}{\pi}\mathrm{P}\int_0^{\infty}d\nu'\frac{\mathrm{Im}\,h(\nu')}{\nu'(\nu'^2-\nu^2)},\\ \mathrm{Re}\,h(\nu)-\nu h'(0)&=\frac{2\nu^3}{\pi}\mathrm{P}\int_0^{\infty}d\nu'\frac{\mathrm{Im}\,h(\nu')}{\nu'^2(\nu'^2-\nu^2)}.\end{aligned} \tag{4.11}$$

Case (1) in (4.11) becomes exactly the Kramers-Kronig dispersion relation provided we identify $h(\nu)$ with the quantity $N_{\lambda\sigma}{}^{ij}$ of Sec. III and consider the case of complete coherence, which we notice satisfies the appropriate condition $h(\nu)=h^*(\nu)$ [compare Eq. (3.20)]. Using the previously mentioned relation between the imaginary part of the coherent scattering amplitude and the total cross section, we have the result [in the notation of Eq. (3.15)]:

$$\begin{aligned}D_{\lambda\lambda}{}^{ii}(\nu)-D_{\lambda\lambda}{}^{ii}(0)&=\frac{2\nu^2}{\pi}\mathrm{P}\int_0^{\infty}d\nu'\frac{A_{\lambda\lambda}{}^{ii}(\nu')}{\nu'(\nu'^2-\nu^2)}\\ &=\frac{\nu^2}{-\pi^2}\mathrm{P}\int_0^{\infty}d\nu'\frac{\sigma(\nu')}{\nu'^2-\nu^2}.\end{aligned} \tag{4.12}$$

It should be remembered that our derivation was valid only to order e^2.

Before passing on to the applications of greatest interest, there are several simple observations worth making. Suppose we apply Eq. (4.12) to the case of a free electron. There is no e^2 cross section in such a case, and we see that coherent dispersive forward scattering amplitude is independent of frequency and takes on the value $D_{\lambda\lambda}{}^{ii}(0)=-e^2/m$ which is, of course, correct. Consider now the limit of (4.12) as the frequency approaches infinity:

$$D_{\lambda\lambda}{}^{ii}(\infty)-D_{\lambda\lambda}{}^{ii}(0)=-\frac{1}{2\pi^2}\int_0^{\infty}d\nu'\sigma(\nu'). \tag{4.13}$$

Either both sides are finite or they are both infinite. To order e^2, for a free electron, both sides are zero; the relation also checks to order e^4, incidentally. If the scattering is from a bound electron, say in a hydrogen atom, $D_{\lambda\lambda}{}^{ii}(0)=0$, since one must have Rayleigh scattering at low frequencies.[17] One might expect $D_{\lambda\lambda}{}^{ii}(\infty)$ to equal its value for a free electron, $-e^2/m$, which would yield the remarkable result:

$$\int_0^{\infty}d\nu\sigma(\nu)=2\pi^2e^2/m, \tag{4.14}$$

which is the well known Thomas-Reiche-Kuhn summation formula usually derived under the assumption of dipole transitions only and $\nu R\ll 1$. Unfortunately, there is some uncertainty as to whether $D_{\lambda\lambda}{}^{ii}(\infty)$ is equal to the value for a free electron. As has been pointed out by Toll[6] in the same connection, the photoelectric cross section for large frequencies goes like $1/\nu$ and this gives rise to a logarithmic frequency dependence in the dispersive amplitude. It is not completely clear that the published calculations of the photoeffect are reliable at very high frequencies. None of the existing direct calculations of the forward scattering amplitude are sufficiently accurate to decide if $D_{\lambda\lambda}{}^{ii}(\infty)$ takes the free electron value and this matter is being looked into further.

The causality condition (4.2) is not fulfilled for the scattering of light by a classical electron, as has been noted by Toll.[6] The same criticism applies to the scat-

[17] Note that the coefficient of the ν^2 Rayleigh scattering amplitude is simply $(1/2\pi^2)\int d\nu'\sigma(\nu')/\nu'^2$, where σ is the atomic absorption cross section for light. This is, of course, an old result, contained in the Kramers-Heisenberg dispersion formula.

tering formula obtained by Heitler's radiation damping theory. It turns out that in those cases the scattering amplitude has a pole in the upper half-plane. It gives a nonvanishing contribution to the commutator outside the light-cone which decays exponentially with a half-width of the order of the classical electron radius. This seems to be connected with the well known preacceleration of the classical electron.

It is important to note that one cannot in general expect to have a relation such as

$$\text{Re } f(\nu,\vartheta)-f(0,\vartheta)=\frac{2\nu^2}{\pi}\text{P}\int_0^\infty d\nu'\frac{\text{Im } f(\nu',\vartheta)}{\nu'(\nu'^2-\nu^2)}, \quad (4.15)$$

where $f(\nu,\vartheta)$ is the entire scattering amplitude valid for all angles ϑ. We consider only the case of zero mass. For if this were true, one would have such a relation for the individual f_l, which in turn leads to the conclusion that the phase shifts δ_l have for small frequencies a frequency dependence of the form $\delta_0\sim\nu$, $\delta_l\sim\nu^3$ for $l>0$. Such a situation leads to grave difficulties in that the integral in Eq. (2.22) is badly divergent near $\nu\sim0$. This is because the higher terms in the expansion in powers of $1/R$ carry also powers of $1/\nu$ at the same time. The weakest frequency dependence which can be tolerated is $\delta_l\sim\nu^{2l}$. (One customarily has $\delta_l\sim\nu^{2l+1}$ for scattering by a potential; it has been shown by van Kampen that in the limit of a point scatterer $\delta_l\sim\nu$.) The situation seems to be that although $f(\nu,\vartheta)$ is analytic in the upper half-plane, it does not have the requisite boundedness for a relation such as (4.15) to obtain. The proof of the above statements about the frequency dependence of the phase shifts is as follows: Assume that

$$\text{Re } f_l(\nu)=\frac{2\nu^2}{\pi}\text{P}\int_0^\infty d\nu'\frac{\text{Im } f_l(\nu')}{\nu'(\nu'^2-\nu^2)}, \quad (4.16)$$

and that $\sin^2\delta_l/\nu^2\to0$ for $\to0$ at least as rapidly as ν^2. We may write (4.16) as

$$\frac{\sin\delta_l(\nu)\cos\delta_l(\nu)}{\nu}=\frac{2\nu^2}{\pi}\text{P}\int_0^\infty d\nu'\frac{\sin^2\delta_l(\nu')/\nu'^2}{\nu'^2-\nu^2}. \quad (4.17)$$

We now remark that

$$\text{P}\int_0^\infty d\nu'\frac{1}{\nu'^2-\nu^2}=\frac{\pi^2}{4}\delta(\nu), \quad (4.18)$$

so that we may write, setting $\sin^2\delta_l/\nu^2=s^2(\nu)$, $\cos\delta_l(\nu)=c(\nu)$,

$$s(\nu)c(\nu)=\frac{2\nu^2}{\pi}\int_0^\infty d\nu'\frac{s^2(\nu')-s^2(\nu)}{\nu'^2-\nu^2}. \quad (4.19)$$

We no longer need the principle value sign since the singularity has been removed. We wish now to show that the integral in (4.19) has a nonzero limit as $\nu\to0$ and consequently that the low-frequency behavior of $s(\nu)c(\nu)$ is given by the explicit factor of ν^2. We write

$$\int_0^\infty d\nu'\frac{s^2(\nu')-s^2(\nu)}{\nu'^2-\nu^2}=\int_0^{\nu_0}d\nu'\frac{s^2(\nu')-s^2(\nu)}{\nu'^2-\nu^2}+\int_{\nu_0}^\infty d\nu'\frac{s^2(\nu')-s^2(\nu)}{\nu'^2-\nu^2}, \quad (4.20)$$

where ν_0 is a small frequency but greater than ν. Since this is the case, ν can certainly be put equal to zero in the second integral; and in the first integral, an expansion of $s^2(\nu')$ and $s^2(\nu)$ into a power series shows that one may safely pass to the limit of $\nu=0$ in it also. We have then, using $s(0)=0$, the result that

$$\lim_{\nu\to0}\text{P}\int_0^\infty d\nu'\frac{s^2(\nu')}{\nu'^2-\nu^2}=\int_0^\infty d\nu'\frac{s^2(\nu')}{\nu'^2}>0. \quad (4.21)$$

V. APPLICATIONS

We shall discuss several applications of the dispersion relations to practical situations. We consider first the case of the scattering of photons by a nucleus. The absorptive phenomena to be considered are photonuclear reactions and meson production. Our technique is to compare the dispersion relations for the nucleus to those of a collection of Z free protons and N free neutrons. We call the nuclear absorption cross section σ_A and the meson production cross sections for free nucleons σ_N and σ_P for neutrons and protons, respectively. (Notice that we are working to order e^2 only and hence need only e^2 cross sections.) The corresponding dispersive forward amplitudes are called D_A, D_P, and D_N. We have from Eq. (4.12) (dropping the subscripts and superscripts on the D's), subtracting from $D_A(\nu)$ the quantity $ZD_P(\nu)+ND_N(\nu)$,

$$D_A(\nu)-D_A(0)-Z[D_P(\nu)-D_P(0)]-N[D_N(\nu)-D_N(0)]=\frac{\nu^2}{2\pi^2}\text{P}\int_0^\infty d\nu'\frac{\sigma_A(\nu')-[Z\sigma_P(\nu')+N\sigma_N(\nu')]}{\nu'^2-\nu^2}. \quad (5.1)$$

The cross sections σ_N and σ_P are of course zero for frequencies less than the meson mass μ (or with recoil corrections about 155 Mev). To evaluate the left-hand side of (5.1), we first note that at zero frequency we have pure Thomson scattering,[18] so that

$$D_N(0)=0,\quad D_P(0)=-e^2/M,\qquad D_A(0)=-(Ze)^2/AM. \quad (5.2)$$

We next *assume* that in the limit of very large frequencies the scattering amplitude for the nucleus approaches that of equal number of free particles:

$$\lim_{\nu\to\infty}[D_A(\nu)-ZD_P(\nu)-ND_N(\nu)]=0. \quad (5.3)$$

[18] W. Thirring, Phil. Mag. 41, 1193 (1950); N. Kroll and M. Ruderman, Phys. Rev. 93, 233 (1954); Dser, Thirring, and Goldberger, Phys. Rev. 94, 711 (1954).

This conjecture cannot be verified in any simple way. As has already been pointed out, it appears not to be fulfilled for the scattering of photons by bound electrons. Aside from a logarithmic term in that case undoubtedly associated with the Coulomb field, the corrections for binding are said to be of the order of binding energy divided by electron mass.[19] Even if these binding effects actually exist in the present case, we would expect them to be of the order of binding energy/M or about a few percent and we shall neglect them here.

Above the threshold for meson production, the absorption cross section for a nucleus is mainly due to meson production. There are, of course, still some photonuclear processes which one would expect to have a rapidly decreasing cross section as the energy increases, and we shall neglect these contributions to the absorption when $\nu>\mu$. The average cross section per nucleon for a photomeson production from a nucleus is reduced in comparison to that of a free nucleon by[20] (a) the effect of binding, (b) Pauli principle, (c) reabsorption of produced mesons. The effect (c) essentially cancels out here since we ask for the total absorption cross section. In accordance with the above discussion we write for $\nu>\mu$,

$$[Z\sigma_P(\nu)+N\sigma_N(\nu)-\sigma_A(\nu)] \equiv[Z\sigma_P(\nu)+N\sigma_N(\nu)][1-R(\nu)], \quad (5.4)$$

$$R(\mu)=0, \quad R(\infty)=1.$$

The reduction factor $R(\nu)$ defined by the foregoing equations, because of effects (a) and (b) may be determined by existing experiments to about 20 percent. If now in Eq. (5.1) we substitute Eqs. (5.2), (5.3), and (5.4), and consider the limit as $\nu\to\infty$, we obtain

$$\frac{1}{2\pi^2}\int_0^\mu d\nu\sigma_A(\nu)=\frac{ZN}{A}\frac{e^2}{M}+\frac{1}{2\pi^2}\int_\mu^\infty d\nu \times[1-R(\nu)][Z\sigma_P(\nu)+N\sigma_N(\nu)]. \quad (5.5)$$

The structure of this sum rule may be understood in the following way: If the meson mass were infinite, so that there were no meson production, real or virtual, then Eq. (5.5) would reduce

$$\frac{1}{2\pi^2}\int_0^\infty d\nu\sigma_{A0}(\nu)=\frac{ZN}{A}\frac{e^2}{M}, \quad (5.6)$$

where $\sigma_{A0}(\nu)$ is the cross section for photodisintegration of the nucleus. This is precisely the sum rule given by Bethe and Levinger for *electric dipole transitions only*, in the case of ordinary forces between particles. In our derivation, the term ZNe^2/AM in Eq. (5.5) may be regarded as the contribution to the integrals of the absorption cross section arising from strictly nonmesonic processes, for in the absence of mesons the infinite-frequency forward-scattering amplitudes for free protons and neutrons would be expected to be $-e^2/M$ and zero, respectively. The second term in Eq. (5.5) presumably contains all of the mesonic effects such as modifications of the nucleon currents, exchange forces, etc.

We have evaluated the right-hand side of Eq. (5.5) using the available experimental data and assuming that $\sigma_N/\sigma_P\sim1.3$ in the important energy region between μ and 2μ. We find

$$\frac{1}{2\pi^2}\int_0^\mu d\nu\sigma_A(\nu)=\frac{ZN}{A}\frac{e^2}{M}\left[1+0.1\frac{A^2}{NZ}\right]. \quad (5.7)$$

The term $0.1A^2/NZ$ may be assumed accurate to about 30 percent on the basis of the present data. This is to be compared with the Bethe-Levinger sum rule,

$$\frac{1}{2\pi^2}\int_0^\infty d\nu\sigma_D(\nu)=\frac{ZN}{A}\frac{e^2}{M}(1+0.8x), \quad (5.8)$$

where $\sigma_D(\nu)$ is the electric dipole absorption cross section and x is the percentage of exchange forces in the two-body forces assumed to act between nucleons. Our sum rule, Eq. (5.7), has been derived under rather more general conditions than that of Bethe and Levinger, Eq. (5.8), and would appear to have some advantages over it: (1) All multiples are included automatically, (2) no assumptions whatsoever are made about nuclear forces or nuclear wave functions, (3) the upper limit of integration is clearly specified in (5.7), whereas σ_D in Eq. (5.8) can be regarded as the total nuclear absorption cross section only below the meson threshold, and finally, (4) only experimental quantities appear in (5.7) in comparison with the $0.8x$ in (5.8) which is a very "model-dependent" quantity. It is perhaps worth repeating that our only assumptions were that the forward-scattering amplitude for a bound nucleon approach that of a free nucleon for infinite-frequency photons, and that the absorption cross section for photonuclear processes not involving meson production may be neglected for photon frequencies above the threshold. (Simple estimates of direct nucleon ejection cross sections at these energies indicate that this neglect is well justified.) There are at present no experimental data for making an accurate test of Eq. (5.7). One finds by comparison with experiments with a maximum energy of about 50 Mev that there must be considerable absorption in the 50- to 150-Mev region, and there are practically no data in this energy range. It would be very useful to have the photodisintegration cross section for deuterium up to the threshold since the data on meson production in deuterium is quite extensive. For the time being, Eq. (5.7) can perhaps best be used to check the consistency of experimental

[19] J. S. Levinger, Phys. Rev. 87, 656 (1952).
[20] H. Feshbach and M. Lax, Phys. Rev. 81, 189 (1951); W. Thirring, Helv. Phys. Acta 26, 465 (1953).

data, since it is almost surely accurate to within 30 percent.

Our next application is to a study of the scattering of γ rays by protons. The amplitude for the forward scattering of photons from linear polarization state λ to state μ by a proton (or generally, any spin $\frac{1}{2}$ particle) must be of the general form

$$F_{\mu\lambda}(\nu)=f_1(\nu)\mathbf{e}_\mu\cdot\mathbf{e}_\lambda+if_2(\nu)\boldsymbol{\sigma}\cdot\mathbf{e}_\mu\times\mathbf{e}_\lambda, \tag{5.9}$$

where $\mathbf{e}_\mu$, $\mathbf{e}_\lambda$ are the photon polarization vectors and $\boldsymbol{\sigma}$ is the spin matrix of the proton. (We are regarding $F_{\mu\lambda}$ as a matrix in spin space.) The factor i is included so that if the frequency is below the threshold of particle production, $f_2(\nu)$ would be real. In general, of course, both $f_1(\nu)$ and $f_2(\nu)$ are complex, having dispersive and absorptive parts. From the scattering amplitude $F_{\mu\lambda}(\nu)$ given above, we construct the quantity $M_{\mu\lambda}$ of Sec. III (for forward scattering only) which differs from $F_{\mu\lambda}$ by having the absorptive parts of f_1 and f_2 multiplied by $\epsilon(\nu)$. Thus, writing $f_1=d_1+ia_1$, $f_2=d_2+ia_2$, we have

$$\begin{aligned}M_{\mu\lambda}(\nu)=&[d_1(\nu)+i\epsilon(\nu)a_1(\nu)]\mathbf{e}_\mu\cdot\mathbf{e}_\lambda\\&+i[d_2(\nu)+i\epsilon(\nu)a_2(\nu)]\boldsymbol{\sigma}\cdot\mathbf{e}_\mu\times\mathbf{e}_\lambda.\end{aligned} \tag{5.10}$$

The behavior of the various functions for negative values of the frequency is deduced from the general requirements, Eq. (3.20),

$$M_{\mu\lambda}(\nu)=M_{\mu\lambda}{}^\dagger(-\nu). \tag{5.11}$$

We deduce that

$$\begin{aligned}&d_1(\nu)=d_1(-\nu), \qquad a_1(\nu)=a_1(-\nu),\\&d_2(\nu)=-d_2(-\nu), \quad a_2(\nu)=-a_2(-\nu).\end{aligned} \tag{5.12}$$

Note that in the e^2 approximation, the d's and a's are real.

With this knowledge of the behavior of the functions for negative frequencies, we may apply the considerations of Sec. IV to the entire operator $M_{\mu\lambda}(\nu)$. If we apply our fundamental relation (4.11) to $M_{\mu\lambda}(\nu)$ given by (5.10), we notice that the coefficients of $\mathbf{e}_\mu\cdot\mathbf{e}_\lambda$ and $i\boldsymbol{\sigma}\cdot\mathbf{e}_\mu\times\mathbf{e}_\lambda$ separately satisfy the condition as may be seen by taking the trace of the entire expression. Using (5.12) we may write, finally,

$$\begin{aligned}d_1(\nu)-d_1(0)&=\frac{2\nu^2}{\pi}\int_0^\infty d\nu'\frac{a_1(\nu')}{\nu'(\nu'^2-\nu^2)},\\d_2(\nu)-\nu d_2'(0)&=\frac{2\nu^3}{\pi}\int_0^\infty d\nu'\frac{a_2(\nu')}{\nu'^2(\nu'^2-\nu^2)}.\end{aligned} \tag{5.13}$$

[The passage of the limit of ν_1 going to zero gives no trouble because both $a_1(\nu)$ and $a_2(\nu)$ are zero for zero frequency (in our e^2 approximation) and the zero lower limit in (5.13) is purely formal.]

Now it should be noted that only the quantity $a_1(\nu)$ bears any simple relation to the total cross section for γ rays, since it is only the coherent amplitude $\mu=\lambda$ that enters in the relation between the imaginary part of the scattering amplitude and the total cross section for unpolarized light. Thus the first of the relations (5.2) may be written (using $d_1(0)=-e^2/M$) as

$$d_1(\nu)=-e^2/M+\frac{\nu^2}{2\pi^2}\int_0^\infty d\nu'\frac{\sigma(\nu')}{\nu'^2-\nu^2}, \tag{5.14}$$

where $\sigma(\nu)$ is the total cross section to order e^2 and is thus composed of such processes as electron pair production, meson production, etc. This is the relation used in the first part of this section. The quantity $a_2(\nu)$ is not an experimental one in ordinary circumstances, but it can be given an experimental interpretation. If one introduces circular polarization for the photons (see Appendix B) one may define two coherent forward amplitudes corresponding to the cases where the polarization is parallel to the direction of the proton spin f_p and antiparallel f_a. (Note that there is no spin flip in the forward amplitude.) In terms of these coherent amplitudes we may write [in the notation of Eq. (5.9)],

$$f_1(\nu)=\tfrac{1}{2}[f_p(\nu)+f_a(\nu)], \quad f_2(\nu)=\tfrac{1}{2}[f_p(\nu)-f_a(\nu)], \tag{5.15}$$

and thus, since f_p and f_a are coherent amplitudes,

$$\begin{aligned}a_1(\nu)&=\frac{\nu}{4\pi}\frac{\sigma_p(\nu)+\sigma_a(\nu)}{2}=\frac{\nu}{4\pi}\sigma_{\text{unpolarized}},\\a_2(\nu)&=\frac{\nu}{4\pi}\frac{\sigma_p(\nu)-\sigma_a(\nu)}{2},\end{aligned}$$

where σ_p and σ_a are the total cross sections (or in the e^2 approximation, the various production cross sections) for photons polarized parallel or antiparallel to the proton spin.

Since the quantities σ_p and σ_a are not known experimentally, we cannot predict the forward scattering amplitude for γ rays with any real assurance, but can give only a lower limit, based on the neglect of f_2. In spite of the difficulties associated with making precise predictions, we felt that it would be worth while to pursue the problem further, going, as we shall see shortly, beyond the famework of our causality considerations when necessary. Before turning to this analysis, it should be noted that the relations (5.13) are of some theoretical interest since it is usually far easier to compute theoretically, from any model the absorptive terms a_1 and a_2 than to carry out a direct calculation of the dispersive amplitude. This point is well illustrated by the work of Rohrlich and Gluckstern.[21]

In our analysis of the γ-ray scattering, we shall consider the absorption cross section to be almost ex-

[21] R. Gluckstern and F. Rohrlich, Phys. Rev. 86, 1 (1952).

clusively the cross section for meson production. One should, of course, include the Delbrück scattering in order to obtain the total coherent scattering amplitude and we shall make some remarks about this later. We have used the data on photomeson production compiled by Nambu[22] to compute the dispersive and absorptive parts of the amplitude $f_1(\nu)$, according to (5.14) and $a_1(\nu)=(\nu/4\pi)\sigma(\nu)$. These functions are shown in Fig. 2. One sees that below the meson threshold, there is destructive interference between the Thomson amplitude and the anomalous amplitude so that the total forward scattering is quite small. The destructive interference arises from the fact that the meson amplitude is negative whereas the anomalous amplitude is positive, being caused by intermediate states with energies greater than the initial state. This is unfortunate since in principle we would like to use this result as a limitation on the phase shifts for γ-ray scattering below threshold: In the Appendix, a phase shift analysis is presented in terms of which the forward scattering amplitude may be expressed. Assuming that at low energies only a few multipoles need be considered (see below) and that the phase shifts are small, Eq. (5.14) for $d_1(\nu)$ gives a limitation on a certain combination of phase shifts. The cancellation just mentioned would not be expected at other angles; for example, if there are only multipoles other than those occurring in Thomson scattering ($E_{\frac{1}{2}}^1$, $E_{\frac{1}{2}}^1$) there must be constructive interference at other angles, since the total cross section must be larger than the Thomson cross section.

In order to illustrate the general features one might expect experimentally, we have made a calculation of the angular dependence and energy dependence of the scattering of photons by protons on the basis of a model suggested by the phenomenological analysis of photoproduction data.[23] At this point, of course, we must go far beyond our general considerations and the following discussion should be regarded only as giving qualitative features. The phase shift analysis given in the Appendix has been used with the following values for the phase shifts:

$$\text{Re}\,\delta_{\frac{1}{2}}^{E1}=-\frac{2\nu}{3}\frac{e^2}{M},\quad \text{Re}\,\delta_{\frac{1}{2}}^{E1}=-\frac{2\nu}{3}\frac{e^2}{M}(1-0.5\nu^2),$$

$$\text{Re}\,\delta_{\frac{1}{2}}^{M1}=\frac{2\nu}{3}\frac{e^2}{M}1\nu^2,\quad \text{Im}\,\delta_{\frac{1}{2}}^{E1}=0,$$

$$\text{Im}\,\delta_{\frac{1}{2}}^{E1}=1.4q\nu\frac{e^2}{M},\quad \nu>1 \qquad \text{Im}\,\delta_{\frac{1}{2}}^{M1}=1.4q^3\nu\frac{e^2}{M},\quad \nu>1$$

$$=0,\quad \nu<1, \qquad =0,\quad \nu<1,$$

$$\text{all other } \delta\text{'s}=0,$$

[22] Y. Nambu (unpublished).
[23] K. Brueckner and K. Watson, Phys. Rev. **86**, 926 (1952).

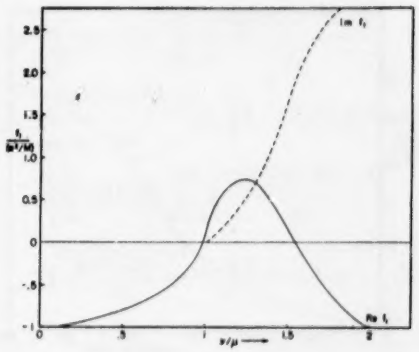

FIG. 2. The coherent forward scattering amplitude describing γ rays scattered by protons as a function of photon energy (in units of meson mass).

where we have written $q=(\nu^2-1)^{\frac{1}{2}}$, taking the meson mass as unity. At low energies (up to 150 Mev) it seems quite reasonable to consider only dipole phase shifts. The photoproduction data can be interpreted as involving mainly $E_{\frac{1}{2}}^1$ and $M_{\frac{1}{2}}^1$ for π^+ production and $M_{\frac{1}{2}}^1$ for π^0 production. In choosing the numerical value of the phase shifts we have used the dispersion relation for $d_1(\nu)$, Eq. (5.14) to fix a particular sum of the phase shifts and find (for low frequencies):

$$\frac{1}{\nu}\text{Re}\left[\delta_{\frac{1}{2}}^{E1}+\delta_{\frac{1}{2}}^{M1}+\tfrac{1}{2}(\delta_{\frac{1}{2}}^{E1}+\delta_{\frac{1}{2}}^{M1})\right]$$

$$=-\frac{e^2}{M}+\frac{\nu^2}{2\pi^2}\int_\mu^\infty d\nu'\frac{\sigma(\nu')}{\nu'^2}. \quad (5.16)$$

The sharing of the sum between $M_{\frac{1}{2}}^1$ and $E_{\frac{1}{2}}^1$ has been done in a way which seems in accordance with the photoproduction data. We have, however, made another assumption about the energy dependence of the anomalous part of the dipole phase shifts, and that is that they behave for small frequencies like ν^3. From the Appendix and Eq. (5), one finds:

$$\frac{1}{2\nu}\text{Re}[\delta_{\frac{1}{2}}^{E1}+\delta_{\frac{1}{2}}^{M1}-(\delta_{\frac{1}{2}}^{E1}+\delta_{\frac{1}{2}}^{M1})]$$

$$=\nu f_2'(0)+\frac{2\nu^3}{\pi}\int_\mu^\infty d\nu'\frac{a_2(\nu')}{\nu'^4}, \quad (5.17)$$

so that for that particular combination of phase shifts in Eq. (5.17) there may be a ν^3 frequency dependence. [A physical model which yields for $f_2(\nu)$ such a linear frequency dependence is a particle with a Pauli-type anomalous magnetic moment.] There appears to be no general principle to guide one at this point. [*Note added in proof.*—This statement is incorrect. It has been shown by two of us (M. G-M. and M.L.G.) and inde-

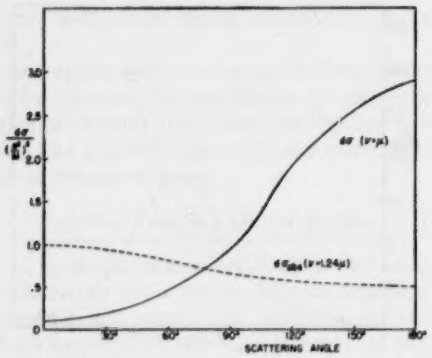

FIG. 3. The angular distribution of γ rays scattered by protons computed on the basis of phase shifts given in Sec. V.

pendently by F. E. Low that the linear term in $f_2(\nu)$ arising from the anomalous magnetic moment is exactly correct in any known theory. This term does not appear in a lowest-order calculation in meson theory, since it is proportional to the square of the anomalous magnetic moment. The formula is $f_2'(0)=-2(\mu_{\text{anom}})^2$.

The phase shifts suggested above must be corrected for this effect.] If one computes the forward scattering amplitude using pseudoscalar meson theory, charged mesons only, one finds[24] that the amplitude $f_2(\nu)$ is proportional to ν^3. This appears to be in contradiction to the work of Sachs and Foldy[25] who find $f_2(\nu)\sim\nu$, but we have been informed by Professor Sachs that an error has been found in the original work and they now find an ν^3 dependence.

In Figs. 3 and 4 we show the angular distribution and the energy dependence of the γ–P cross section which results from our assumed phase shifts. The angular distribution is very sensitive to the ratio of M_1^1 and E_1^1 phase shifts. The assumed dominance of M_1^1 results in a strong backward maximum which should simplify the experimental verification of the effects, since large-angle scatterings would be most easily observed. The energy dependence of the total cross section is to be contrasted with that given by Sachs and Foldy. They found that the cross section fell sharply for frequencies greater than μ, whereas our result shows a strong increase. Aside from the previously mentioned mistake in this paper, they inadvertantly dropped the absorptive part of the light-scattering amplitude. It should be emphasized that the results given in Figs. 3 and 4 are not to be taken too seriously, especially for energies above 1.5μ. They are based on rather *ad hoc* assumptions about phase shifts and are presented simply to give some qualitative ideas as to what one might expect.

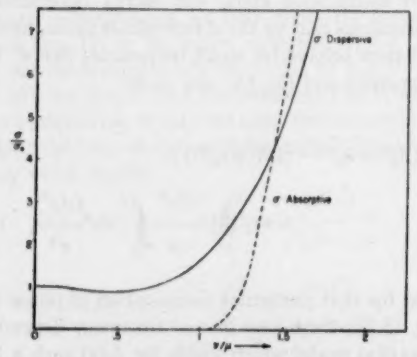

FIG. 4. The energy dependence of the total elastic scattering cross section for the scattering of γ rays by protons. σ_0 is the Thomson cross section, $8\pi e^4/3m^2$.

We must finally discuss the omission of the Delbrück scattering. In the forward direction the scattering by the Coulomb field actually has a greater amplitude than the entire Compton amplitude considered thus far. One has $d_1(\text{Delbrück})\sim 10^{-15}$ cm as compared to $d_1(\text{Compton})\sim 2\times 10^{-16}$ cm. The total cross section of the Delbrück scattering is, however, completely negligible ($\sim 10^{-34}$ cm^2). Furthermore, since the scattering is confined to very small angles, it should not affect the experimental search for anomalous γ–P scattering.

We have been unable to find any useful applications of the dispersion relations for particles with mass; these can presumably be constructed, since as a function of the total energy, the scattering amplitude satisfies all the requirements imposed in Sec. IV. There are at least two obstacles in the way of such applications: (1) One needs, in general, the scattering amplitude for nonphysical energies, ν, less than the mass, μ. Unless one makes further assumptions, one cannot get a formula involving only measurable quantities. (2) There is no small parameter analogous to e according to which one may separate the dispersive and absorptive effects. For example, an attempt to express the real part of the forward scattering amplitude for meson-nucleon scattering in terms of an integral over the total cross section [assuming point (1) is overcome] poses the problem that one knows neither side of the equation; the elastic scattering cross section is by no means negligible in comparison with the inelastic processes, as was the case for photons.

It is a pleasure to acknowledge several stimulating conversations with Professor E. P. Wigner. We are also indebted to Professor A. Wightman and to members of the Institute for Advanced Study for helpful conversations. One of us (W.T.) is grateful to the Institute for Advanced Study for a grant-in-aid and to Professor Robert Oppenheimer for the hospitality extended him at the Institute.

[24] M. L. Goldberger (unpublished).
[25] R. G. Sachs and L. Foldy, Phys. Rev. **80**, 824 (1950).

APPENDIX

We wish to describe the scattering of photons by a spin one-half particle. It is convenient to use a description in which the incident photons are circularly polarized parallel or antiparallel to the spin of the nucleon. We have in deriving these formulas neglected the possibility that the electric and magnetic multipoles mix. (Stated otherwise, we have not used the eigenphases of the scattering matrix.[26] The procedure is quite standard and we give only the result. The electric field vector $\mathbf{E}$ for the two cases of polarization becomes

$$\mathbf{E}_{p,a}=-e^{i\nu t}\chi_{+}\alpha_{\pm}+\frac{e^{i\nu r}}{r}\sum_{l=1}^{\infty}[2\pi(2l+1)]^{\frac{1}{2}}\times\sum_{j=l-\frac{1}{2}}^{j=l+\frac{1}{2}}C_{l\frac{1}{2}}(j,1\pm\tfrac{1}{2};1,\pm\tfrac{1}{2})\times\left\{\frac{\exp(2i\delta_{lj}{}^{\mathrm{mag}})-1}{2i\nu}+i\frac{\exp(2i\delta_{lj}{}^{el})-1}{2i\nu}\frac{\mathbf{r}\times}{r}\right\}\times\sum_{m=-\frac{1}{2}}^{m=\frac{1}{2}}C_{l\frac{1}{2}}(j,1\pm\tfrac{1}{2};1\pm\tfrac{1}{2}-m,m)\times\mathbf{X}_{l,1\pm\frac{1}{2}-m}\alpha_{m}. \quad (B.1)$$

The notation is that of Blatt and Weisskopf;[27] the $\alpha_{\pm}$ are the nucleon spin eigenfunctions. For the cross section, we obtain

$$d\sigma_{p}=2\pi\left\{\left|\sum_{l=1}^{\infty}(2l+1)^{\frac{1}{2}}\sum_{j=l-\frac{1}{2}}^{l+\frac{1}{2}}\left(\frac{\exp(2i\delta_{lj}{}^{\mathrm{mag}})-1}{2i\nu}+i\frac{\exp(2i\delta_{lj}{}^{el})-1}{2i\nu}\mathbf{r}\times\right)\mathbf{X}_{l,1}|C_{l\frac{1}{2}}(j,\tfrac{3}{2};1,\tfrac{1}{2})|^{2}\right|^{2}+\left|\sum_{l=1}^{\infty}(2l+1)^{\frac{1}{2}}\sum_{j=l-\frac{1}{2}}^{l+\frac{1}{2}}\left(\frac{\exp(2i\delta_{lj}{}^{\mathrm{mag}})-1}{2i\nu}+\frac{\exp(2i\delta_{lj}{}^{el})-1}{2i\nu}\mathbf{r}\times\right)\mathbf{X}_{l,2}C_{l\frac{1}{2}}(j,\tfrac{3}{2};1,\tfrac{1}{2})\times C_{l\frac{1}{2}}(j,\tfrac{3}{2};2,-\tfrac{1}{2})\right|^{2}\right\},$$

$$d\sigma_{a}=2\pi\left\{\left|\sum_{l=1}^{\infty}(2l+1)^{\frac{1}{2}}\sum_{j=l-\frac{1}{2}}^{l+\frac{1}{2}}\left(\frac{\exp(2i\delta_{lj}{}^{\mathrm{mag}})-1}{2i\nu}+i\frac{\exp(2i\delta_{lj}{}^{el})-1}{2i\nu}\mathbf{r}\times\right)\mathbf{X}_{l,1}|C_{l\frac{1}{2}}(j,\tfrac{1}{2};1,-\tfrac{1}{2})|^{2}\right|^{2}+\left|\sum_{l=1}^{\infty}(2l+1)^{\frac{1}{2}}\sum_{j=l-\frac{1}{2}}^{l+\frac{1}{2}}\left(\frac{\exp(2i\delta_{lj}{}^{\mathrm{mag}})-1}{2i\nu}=i\frac{\exp(2i\delta_{lj}{}^{el})-1}{2i\nu}\mathbf{r}\times\right)\mathbf{X}_{l,0}C_{l\frac{1}{2}}(j,\tfrac{1}{2};1,-\tfrac{1}{2})\times C_{l\frac{1}{2}}(j,\tfrac{1}{2};0,\tfrac{1}{2})\right|^{2}\right\}. \quad (B.2)$$

In (B.1) the first and second term correspond to the coherent and spin-flip amplitudes, respectively. In the forward direction we obtain for the scattering amplitudes f_p and f_a the values

$$f_{p}=\frac{3}{2\nu}(\delta_{\frac{1}{2}}{}^{M1}+\delta_{\frac{1}{2}}{}^{E1}),\qquad f_{a}=\frac{1}{2\nu}(\delta_{\frac{1}{2}}{}^{E1}+\delta_{\frac{1}{2}}{}^{M1})+\frac{1}{\nu}(\delta_{\frac{1}{2}}{}^{E1}+\delta_{\frac{1}{2}}{}^{M1}). \quad (B.3)$$

We have assumed that the phase shifts are small and that only dipole radiation need be considered. In deriving (B.3), we have used the fact that the spin-flip amplitude vanishes in the forward direction and that

$$\mathbf{X}_{l,\pm1}\Big|_{\vartheta=0}=\pm\frac{1}{\sqrt{2}}\left(\frac{2l+1}{4\pi}\right)^{\frac{1}{2}}\chi_{\pm},\qquad \frac{\mathbf{r}}{r}\times\mathbf{X}_{l,\pm1}\Big|_{\vartheta=0}=\frac{1}{\sqrt{2}}\left(\frac{2l+1}{4\pi}\right)^{\frac{1}{2}}\chi_{\pm}.$$

In our application we assumed also that $\delta_{\frac{1}{2}}{}^{M1}=0$. We find for the cross section for unpolarized light:

$$d\sigma=\frac{1}{8\nu^{2}}[(7+3\cos^{2}\vartheta)(|\delta_{\frac{1}{2}}{}^{M1}|^{2}+|\delta_{\frac{1}{2}}{}^{E1}|^{2})+4|\delta_{\frac{1}{2}}{}^{E1}|^{2}+2\,\mathrm{Re}\,\delta_{\frac{1}{2}}{}^{E1}\delta_{\frac{1}{2}}{}^{E1*}(3\cos^{2}\vartheta-1)+4\,\mathrm{Re}\,\delta_{\frac{1}{2}}{}^{M1}\delta_{\frac{1}{2}}{}^{E1*}(5+\cos\vartheta)],$$
$$\sigma=\frac{6\pi}{\nu^{2}}\{\tfrac{2}{3}(|\delta_{\frac{1}{2}}{}^{M1}|^{2}+|\delta_{\frac{1}{2}}{}^{E1}|^{2})+\tfrac{1}{3}|\delta_{\frac{1}{2}}{}^{E1}|^{2}\}. \quad (B.4)$$

In deducing (B.4) we used Eq. XII, (3.16) of reference 28 and

$$\mathbf{X}_{11}{}^{*}\cdot\frac{\mathbf{r}}{r}\times\mathbf{X}_{11}=\frac{3}{8\pi}\cos\vartheta,\quad \mathbf{X}_{10}{}^{*}\cdot\frac{\mathbf{r}}{r}\times\mathbf{X}_{10}=0.$$

[26] J. Blatt and L. Biedenharn, Revs. Modern Phys. **23**, 729 (1953).

[27] J. M. Blatt and V. F. Weisskopf, *Theoretical Nuclear Physics* (John Wiley and Sons, Inc., New York, 1952), Appendexes A and B.

Two-Nucleon Problem When the Potential Is Nonlocal but Separable. I

YOSHIO YAMAGUCHI*
Department of Physics, University of Illinois, Urbana, Illinois
(Received April 15, 1954)

The two-nucleon problem is considered in terms of an interaction of the form $(\mathbf{p}|V|\mathbf{p}')=-(\lambda/M)g(p)g(p')$. In this case we can find exact solutions both for bound states and for continuum states, and prescribe arbitrarily and independently the interaction effective in states of different angular momenta. This important feature makes the analysis of scattering straightforward and unambiguous. An example for $g(p)=(p^2+\beta^2)^{-1}$ is presented and compared with the low-energy neutron-proton data. The photodisintegration of the deuteron in our model is also discussed.

1. INTRODUCTION

IN the past several years, much (experimental and theoretical) work[1-4] has been published on the two-nucleon system. However, our information about nuclear forces is still rather small. From the theoretical point of view, this is partly due to the difficulty in solving the scattering problem. Therefore, it seems to us worthwhile to discuss a special nuclear potential for which we can get readily an exact solution. This potential[5] is nonlocal and thus of a fundamentally different form than those usually discussed, but since no one knows the correct form there remains room to test new types. If we choose our nonlocal potential to be without a long tail, we can depend upon the validity of the so-called effective range theory to guarantee a fit to the low-energy data for the two-nucleon system. Furthermore, our wave functions described below are convenient for the examination of various phenomena involving two nucleons. To illustrate this we will treat the photodisintegration of the deuteron in the last section.

2. FORMULATION OF THE PROBLEM

Let us consider the two-body nonrelativistic Schrödinger equation

$$\left\{E+\frac{1}{M}\Delta\right\}\psi(\mathbf{r})=\int(\mathbf{r}|V|\mathbf{r}')d\mathbf{r}'\psi(\mathbf{r}'), \tag{1}$$

E and M being, respectively, the total energy in the center-of-mass system and the nucleon mass. $(\mathbf{r}|V|\mathbf{r}')$ is the nuclear potential which, in general, is nonlocal.[6] Transforming to the momentum space representation, we have

$$(k^2/M-p^2/M)\psi(\mathbf{p})=\int(\mathbf{p}|V|\mathbf{p}')d\mathbf{p}'\psi(\mathbf{p}'), \tag{2}$$

where $\mathbf{k}$ is the incident momentum and $k=|\mathbf{k}|$, $k^2/M=E$. If $(\mathbf{p}|V|\mathbf{p}')$ depends only on $\mathbf{p}-\mathbf{p}'$, then our potential is "local," i.e., $(\mathbf{r}|V|\mathbf{r}')$ must be the function of $\mathbf{r}$ multiplied by $\delta(\mathbf{r}-\mathbf{r}')$; otherwise our potential becomes necessarily nonlocal. As stated before, we want to assume a nonlocal but separable potential[7]

$$(\mathbf{r}|V|\mathbf{r}')=-(\lambda/M)v^*(\mathbf{r})v(\mathbf{r}'), \tag{3}$$

or equivalently

$$(\mathbf{p}|V|\mathbf{p}')=-(\lambda/M)g^*(\mathbf{p})g(\mathbf{p}'),$$

where the asterisk designates complex conjugate. If we postulate time reversibility, $v(\mathbf{r})$ and $g(\mathbf{r})$ must be real in the sense defined by Wigner.[8] Equation (2) takes

---

* On leave of absence from Osaka City University, Osaka, Japan.

[1] G. F. Chew and M. L. Goldberger, Phys. Rev. **75**, 1637 (1949); J. M. Blatt and J. D. Jackson, Phys. Rev. **76**, 18 (1949); H. A. Bethe, Phys. Rev. **76**, 38 (1949); J. D. Jackson and J. M. Blatt, Revs. Modern Phys. **22**, 77 (1950); J. Schwinger, Phys. Rev. **78**, 135 (1950); E. E. Salpeter, Phys. Rev. **82**, 60 (1951); H. Feshbach and J. Schwinger, Phys. Rev. **84**, 194 (1951); Taketani, Nakamura, and Sasaki, Prog. Theoret. Phys. Japan **6**, 581 (1951); Taketani, Machida, and Onuma, Prog. Theoret. Phys. Japan **7**, 45 (1952); L. Hulthén and K. V. Laurikainen, Revs. Modern Phys. **23**, 1 (1951). For other references, see: L. Rosenfeld, *Nuclear Forces* (Interscience Publishers, Inc., New York—London, 1949); J. M. Blatt and V. F. Weisskopf, *Theoretical Nuclear Physics* (John Wiley and Sons, Inc., New York, 1952).

[2] Li, Whaling, Fowler, and Lauritsen, Phys. Rev. **83**, 512 (1951).

[3] E. Melkonian, Phys. Rev. **76**, 1744 (1949); Burgy, Ringo, and Hughes, Phys. Rev. **84**, 1160 (1950).

[4] Bailey, Bennett, Bergstrahl, Nuckolls, Richards, and Williams, Phys. Rev. **70**, 583 (1946); D. H. Frisch, Phys. Rev. **70**, 589 (1946); Lampi, Freier, and Williams, Phys. Rev. **80**, 853 (1950); Poss, Salant, Snow, and Yuan, Phys. Rev. **87**, 11 (1952); G. Snow, Phys. Rev. **87**, 21 (1952); Hafner, Hornyak, Falk, Snow, and Coor, Phys. Rev. **89**, 204 (1953). For other references, see Rosenfeld, or Blatt and Weisskopf, reference 1.

[5] This type of nuclear potential was discussed by E. P. Wigner (unpublished), quoted in Blatt and Weisskopf (reference 1, p. 139), Bloch, Gell-Mann, and Goldberger (unpublished).

[6] This nonlocal potential can be derived from the (unfamiliar) interaction between the nucleon field ψ and the meson field φ:

$$-\frac{\lambda}{M}\frac{1}{(2\pi)^3}\frac{\mu^2}{\beta^2}\frac{1}{4!}\left(\int\bar{\psi}\varphi\psi d\tau\right)^4,$$

providing that the nucleon has finite size:

$$\int\bar{\psi}\psi e^{-i\mathbf{p}\cdot\mathbf{r}}d\tau=\frac{\beta}{(\mu)^4}\frac{(p^2+\mu^2)^4}{(p^2+\beta^2)^4}\quad(\mu=\text{meson mass}),$$

and provided that we limit ourselves within the lowest order adiabatic nuclear force.

[7] This potential leads to the saturation of nuclear binding energies.

[8] E. Wigner, Nachr. Ges. Wiss. Göttingen **31**, 546 (1932).

the form

$$(k^2-p^2)\psi(\mathbf{p})=-\lambda g(\mathbf{p})\int g(\mathbf{p}')d\mathbf{p}'\psi(\mathbf{p}'). \quad (4)$$

In such a case, one can easily find the exact solution. To see this, let us consider the simplest case, $g(\mathbf{p})=g(|\mathbf{p}|)$. For the bound state we must replace $-k^2/M$ by the binding energy α^2/M. Thus

$$(\alpha^2+p^2)\psi(\mathbf{p})=\lambda g(p)\int g(p')d\mathbf{p}'\psi(\mathbf{p}'). \quad (5)$$

The desired solution must be[9]

$$\psi(\mathbf{p})=Ng(p)/(\alpha^2+p^2), \quad \frac{1}{N^2}=\int dq\frac{g^2(q)}{(\alpha^2+q^2)^2}; \quad (6)$$

and $\lambda=\lambda(\alpha)$ is now determined so as to fit the observed binding energy α^2/M of the deuteron:

$$\frac{1}{\lambda}=\int dq\frac{g^2(q)}{\alpha^2+q^2}. \quad (7)$$

Therefore, we see that the well-depth parameter s, defined by Blatt and Jackson,[1] is just

$$s=\lambda(\alpha)/\lim_{\alpha\to 0}\lambda(\alpha). \quad (7')$$

For the scattering problem

$$\psi(\mathbf{p})=\delta(\mathbf{p}-\mathbf{k})-\frac{\lambda g(k)}{1+\lambda\int dq\dfrac{g^2(q)}{k^2-q^2+i\epsilon}}\cdot\frac{g(p)}{k^2-p^2+i\epsilon}, \quad (8)$$

where $\mathbf{k}$ is the incident momentum and ϵ is an infinitesimal positive quantity which makes the second term of the right-hand side of (8) an outgoing wave. The differential cross section turns out to be

$$\begin{aligned} &d\sigma/d\omega=|f|^2,\\ &f=e^{i\delta}\sin\delta/k=1/(-ik+k\cot\delta)\\ &\quad=[2\pi^2\lambda g(k)g(p)]\Big/\left[1+\lambda\int dq\frac{g^2(q)}{k^2-q^2+i\epsilon}\right], \end{aligned} \quad (9)$$

where $\mathbf{p}$ is the momentum of scattered nucleon ($|\mathbf{p}|=k$).

In the more general case, where $g(p)$ depends not only on the magnitude of $\mathbf{p}$ but also on the direction, one can often find an exact solution. For example, if we assume the "central" plus "tensor" form:

$$g(\mathbf{p})=c(p)+1/\sqrt{8}\times\left\{\frac{3}{p^2}(\boldsymbol{\sigma}^{(1)}\cdot\mathbf{p})(\boldsymbol{\sigma}^{(2)}\cdot\mathbf{p})-(\boldsymbol{\sigma}^{(1)}\cdot\boldsymbol{\sigma}^{(2)})\right\}t(p), \quad (10)$$

where $c(p)$ and $t(p)$ are functions of $p=|\mathbf{p}|$, the exact solutions of the Schrödinger equation are readily obtainable. This case will be discussed in the following paper. A sufficient condition that the wave equation be soluble is as follows:

$$\int\frac{[g(\mathbf{k})\cdot g(\mathbf{p}')]d\mathbf{p}'[g(\mathbf{p}')\cdot g(\mathbf{p})]}{k^2-p'^2+i\epsilon}=[g(\mathbf{k})\cdot g(\mathbf{p})]\times(\text{function of } k=|\mathbf{k}|),$$

providing the integral exists.

If $g(p)$ depends on $p=|\mathbf{p}|$, we have just s scattering. In order to get scattering in a state of orbital angular momentum (without spin-orbit coupling), we must assume the potential

$$(\mathbf{p}|V_l|\mathbf{p}')=-\frac{\lambda}{M}\sum_{m=-l}^{l}Y_l^{m*}(\theta_p,\varphi_p)Y_l^m(\theta_{p'},\varphi_{p'})g(p)g(p'), \quad (11)$$

where $g(p)$ is dependent on $p=|\mathbf{p}|$. It is evident that we can also find the exact solution for this potential (11). It is very important to see that V_l causes scattering only for the lth partial wave, in other words, that the potential is completely "separable." We cannot have such separability in the case of a local potential. For example, the central local potential gives rise to scattering of all orders of spherical harmonics. This separability holds in terms of total angular momentum and parity also for the nonlocal potential involving spin-orbit coupling [e.g., (10)]. This fact makes the correlation of scattering phase shifts with the interaction quite definite and easy. Evidently this gain has been achieved by vastly extending the number of free parameters in the interaction.

One should note the seeming resemblance between the form of our wave function (8) and the second Born approximation to the usual local potential.

3. DETAILED DISCUSSION OF SPECIAL CASE $g(p)=(p^2+\beta^2)^{-1}$

If we assume, say, a rational function of $p=|\mathbf{p}|$ for $g(p)$, we can easily perform all integrations required in solving the two-body problem. In this section we consider in detail the simplest case,[10] where

$$g(p)=1/(p^2+\beta^2). \quad (12)$$

This interaction acts in the S state only.

[9] The factorable potential can have at most one bound state.

[10] This interaction was independently examined by F. Bloch and M. Gell-Mann (to be published). Their results are in agreement with ours.

(a) Bound State—Deuteron Problem

The Schrödinger equation takes the form

$$(\alpha^2+p^2)\psi(\mathbf{p})=\lambda\frac{1}{p^2+\beta^2}\int\frac{d\mathbf{p}'\psi(\mathbf{p}')}{p'^2+\beta^2}, \tag{13}$$

and its solution can readily be written down:

$$\psi(\mathbf{p})=N/[(\alpha^2+p^2)(\beta^2+p^2)], \quad N^2=\pi^{-2}\alpha\beta(\alpha+\beta)^3; \tag{14}$$

where N is the normalization constant. Here λ must be determined so as to fit the observed binding energy α^2/M of the deuteron. We get

$$\lambda=\pi^{-2}\beta(\alpha+\beta)^2=s\pi^{-2}\beta^3; \quad s=(\alpha+\beta)^2/\beta^2. \tag{15}$$

Curiously our deuteron function has exactly the same form as that for the well-known local potential of the Hulthén type; i.e., the deuteron function in the coordinate space is

$$\psi(\mathbf{r})=\left(\frac{\pi}{2}\right)^{\frac{1}{2}}\frac{N}{\beta^2-\alpha^2}\frac{e^{-\alpha r}-e^{-\beta r}}{r}, \quad r=|\mathbf{r}|. \tag{14'}$$

(b) Continuum State—Neutron-Proton Scattering

Our fundamental equation is

$$(k^2-p^2+i\epsilon)\psi(\mathbf{p})=-\lambda\frac{1}{\beta^2+p^2}\int d\mathbf{p}'\frac{1}{\beta^2+p'^2}\psi(\mathbf{p}'). \tag{16}$$

Putting

$$\psi(\mathbf{p})=\delta(\mathbf{p}-\mathbf{k})-\frac{k^2+p^2}{2\pi^2}f(k)\cdot\frac{1}{\beta^2+p^2}\cdot\frac{1}{k^2-p^2+i\epsilon} \tag{17}$$

and inserting this into (16), we can find $f(k)$:

$$f(k)=1\Big/\left[-ik+\left(-\beta+\frac{\beta^2+k^2}{2\beta}+\frac{(\beta^2+k^2)^2}{2\pi^2\lambda}\right)\right]. \tag{17'}$$

If we transform (17) into the $\mathbf{r}$ representation,

$$\psi(\mathbf{r})=e^{ikr}+f(k)\frac{e^{ikr}-e^{-\beta r}}{r}$$

$$=e^{i\delta}\left\{\frac{\sin(kr+\delta)-e^{-\beta r}\sin\delta}{kr}\right\}+\left(e^{ikr}-\frac{\sin kr}{kr}\right) \tag{17''}$$

(this form has often been used by many authors[1]), we can see that $f(k)$ is equal to the scattering amplitude;

$$f(k)=\frac{e^{i\delta}\sin\delta}{k}=\frac{1}{-ik+k\cot\delta}, \quad (\delta=\text{phase shift}).$$

Thus we find

$$k\cot\delta=-1/a+\tfrac{1}{2}r_0k^2-Pr_0^3k^4+Qr_0^5k^6+\cdots \tag{18}$$

$$=-\alpha+\tfrac{1}{2}r_d(\alpha^2+k^2)-P_dr_d^3(\alpha^2+k^2)^2$$
$$+Q_dr_d^5(\alpha^2+k^2)^3+\cdots; \tag{19}$$

and we can determine the scattering length a, the effective range r_0, etc.:

$$\frac{1}{a}=\frac{\beta}{2}\left(1-\frac{\beta^2}{\pi^2\lambda}\right), \qquad r_0=\frac{1}{\beta}\left(1+\frac{2\beta^2}{\pi^2\lambda}\right),$$
$$Pr_0^3=-\frac{1}{2\pi^2\lambda}, \qquad Qr_0^5=0, \quad \cdots. \tag{20}$$

For the triplet neutron-proton system, using (15), we find

$$a=\frac{2(\alpha+\beta)^2}{\alpha\beta(\alpha+2\beta)}, \qquad r_0=\frac{(\alpha+\beta)^2+2\beta^2}{\beta(\alpha+\beta)^2},$$
$$r_d=\frac{3\beta-\alpha}{\beta(\alpha+\beta)}, \qquad Pr_0^3=P_dr_d^3=-\frac{1}{2\beta(\alpha+\beta)^2}, \tag{20'}$$
$$Q=Q_d=0, \quad \cdots.$$

Here we can easily check the internal consistency:

$$1/a=\alpha-\tfrac{1}{2}r_d\alpha^2-P_dr_d^3\alpha^4, \quad r_0=r_d-4P_dr_d^3\alpha^2,$$
$$r_0=2\int_0^\infty dr[(1-r/a)^2-(1-r/a-e^{-\beta r})^2], \tag{20''}$$

and

$$r_d=2\int_0^\infty dr[(e^{-\alpha r})^2-(e^{-\alpha r}-e^{-\beta r})^2].$$

Note that P is negative for attractive potential $\lambda>0$. The intrinsic range b (see Blatt and Jackson[1]) is

$$b=\lim_{s\to1}r_0=\lim_{\alpha\to0}\left\{\frac{1}{\beta}+\frac{2\beta^2}{\pi^2\lambda(\alpha)}\right\}=\frac{3}{\beta}. \tag{21}$$

It is important to see that the expansion (18) does not contain terms higher than k^6. This feature is a result of our special assumption, (12), for the form of $g(p)$. In general, if we take $g(p)^{-1}$ as a polynomial in p^2 of order n (here we assume $g(p)^{-1}=0$ has no real roots), we find that our expansion (18) is a polynomial in k^2 of order $2n$. Furthermore, if $g(\mathbf{p})\propto p^l$ for small $p=|\mathbf{p}|$, we can prove that

$$k^{2l+1}\cot\delta=(\text{const})+(\text{const})k^2+\cdots.$$

(c) Comparison with Low-Energy Neutron-Proton Data

Let us distinguish the various quantities α, β, r_0, and so on, corresponding to the triplet or singlet state by the suffix t or s. We start with the triplet neutron-proton system. Adopting the value 938.9 Mev for M (this is equal to the average of the proton and neutron mass), and using $\alpha_t^2/M=2.225$ Mev,[2] we get

$$\alpha_t=2.316\times10^{12}\ \text{cm}^{-1}. \tag{22}$$

Then β_t can be determined from the experimental value[3] $a_t=5.378\times10^{-13}$ cm for the triplet scattering length a_t. We find

$$\beta_t=6.255\alpha_t=14.488\times10^{12}\text{ cm}^{-1}. \quad (23)$$

Inserting these values into (20′) we can calculate the triplet effective range r_{0t} and the shape-dependent factor P_t:

$$r_{0t}=1.716\times10^{-13}\text{ cm}, \quad (24)$$

$$P_t(r_{0t})^3=-0.122\times10^{-39}\text{ cm}^3=-0.024(r_{0t})^3. \quad (25)$$

These values may be compared with the corresponding parameters in Table I. Also the frequently used quantity $\rho_t=r_{0t}+2\alpha_t^2P_tr_{0t}^3=1.703\times10^{-13}$ cm. We get a very small value for P_t, because our nuclei potential does not have a long tail (the range β_t^{-1} is small compared with that of usually accepted local Yukawa well).

Secondly, let us examine the singlet neutron-proton scattering. For simplicity, we want to assume $\beta_s=\beta_t$. Then the singlet scattering length[3] $a_s=-23.69\times10^{-13}$ cm is sufficient to fix the value of strength λ_s of singlet potential. Using (20) we find the effective range r_{0s} and the shape-dependent factor P_s,

$$r_{0s}=2.151\times10^{-13}\text{ cm} \quad (26)$$

and

$$P_s(r_{0s})^3=-0.174\times10^{-39}\text{ cm}^3=-0.017(r_{0s})^3. \quad (27)$$

At present experimental information about the singlet neutron-proton system is rather poor, and the results (27) and (26), based on choosing $\beta_s=\beta_t$, are in agreement with existing knowledge[4] [see Table II]. If we want to have a different value for r_{0s}, we may take a different value for β_s [see Table II]. Figure 1 compares our theoretical total neutron-proton cross section with experimental results.[4]

We have not yet examined proton-proton scattering, because the combination of the local Coulomb potential with our nonlocal interaction presents a complicated problem.

4. PHOTODISINTEGRATION OF THE DEUTERON

We must consider the problem of gauge invariance when we take into account the electromagnetic field in our two-nucleon system, because we have assumed a nonlocal and therefore a velocity-dependent nuclear potential. That is to say, we must replace our nuclear potential (3) by a modified potential which is compatible with the gauge transformation. The most reasonable and simplest choice will be given by

$$(-\lambda/M)v(\mathbf{r}_p-\mathbf{r}_n)v(\mathbf{r}_p'-\mathbf{r}_n')\times\exp\left\{ie\int_{\mathbf{R}}^{r_p}\mathbf{A}\cdot d\mathbf{s}+ie\int_{r_p'}^{\mathbf{R}}\mathbf{A}\cdot d\mathbf{s}\right\}, \quad (28)$$

where $\mathbf{r}_p$ and $\mathbf{r}_n$ are the coordinates of proton and neutron, respectively, $\mathbf{r}=\mathbf{r}_p-\mathbf{r}_n$, $\mathbf{r}'=\mathbf{r}_p'-\mathbf{r}_n'$, $\mathbf{R}=(\mathbf{r}_p+\mathbf{r}_n)/2=(\mathbf{r}_p'+\mathbf{r}_n')/2$, and $\mathbf{A}$ is the electromagnetic potential acting on the proton. The integral over ds from **B** to **C** means the integral along the straight line from **B** to **C**. Of course the most general choice should have a form $(28)\times F+G$, where F and G are gauge-invariant quantities which approach limits $F\to1$ and $G\to0$ as the electromagnetic field vanishes (also see Sachs[11] and Osborne and Foldy[11]). For the sake of simplicity, however, we confine our discussion to an interaction of the form (28). Furthermore we want to adopt the special potential which is "spherically symmetric" (i.e., acts in S states only) when the electromagnetic potential vanishes. For this case, if we make a power series expansion in $\mathbf{A}$ and keep only zeroth- and first-order terms,

$$-\left\{\frac{\lambda_t}{M}v_t(r)v_t(r')\tfrac{1}{4}(3+\boldsymbol{\sigma}^p\cdot\boldsymbol{\sigma}^n)+\frac{\lambda_s}{M}v_s(r)v_s(r')\tfrac{1}{4}(1-\boldsymbol{\sigma}^p\cdot\boldsymbol{\sigma}^n)\right\}\times\left\{1+ie\int_0^1\tfrac{1}{2}\mathbf{r}\cdot\mathbf{A}(\mathbf{R}+\tfrac{1}{2}\mathbf{r}s)ds-ie\int_0^1\tfrac{1}{2}\mathbf{r}'\cdot\mathbf{A}(\mathbf{R}+\tfrac{1}{2}\mathbf{r}'(1-s))ds\right\}, \quad (29)$$

TABLE I. Parameters for the n-p triplet interaction.

	r_t (10^{-13} cm)	P_t	s_t	b_t (10^{-13} cm)
Square well[a]	1.724	−0.040	1.440	2.040
Exponential well[a]	1.687	+0.029	1.416	2.346
Yukawa well[a]	1.637	+0.137	1.419	2.913
Nonlocal $\beta_t=1.4488\times10^{12}$ cm^{-1}	1.716	−0.024	1.345	2.071

[a] G. Snow, Phys. Rev. **87**, 21 (1952).

TABLE II. Parameters for the n-p singlet interaction.

	r_s (10^{-13} cm)	P_s	s_s	b_s (10^{-13} cm)
Square well[a]	2.47 ±0.20	−0.03	0.926 ±6	2.58 ±6
Exponential well[a]	2.30 ±0.21	+0.010	0.937 ±6	2.51 ±6
Yukawa well[a]	2.03 ±0.23	+0.055	0.953 ±6	2.47 ±6
Nonlocal β_s/α_t				
6.2547	2.151	−0.01748	0.94494	2.071
6.25	2.153	−0.01747	0.94490	2.072
6.00	2.246	−0.01744	0.9427	2.159
5.75	2.348	−0.01739	0.9404	2.252
5.50	2.459	−0.01734	0.9379	2.345
5.25	2.581	−0.01729	0.9351	2.467
5.00	2.716	−0.01723	0.9321	2.590

[a] E. M. Hafner *et al.*, Phys. Rev. **89**, 204 (1953). Also see reference 1.

[11] R. G. Sachs, Phys. Rev. **74**, 433 (1948); R. K. Osborne and L. L. Foldy, Phys. Rev. **79**, 795 (1948).

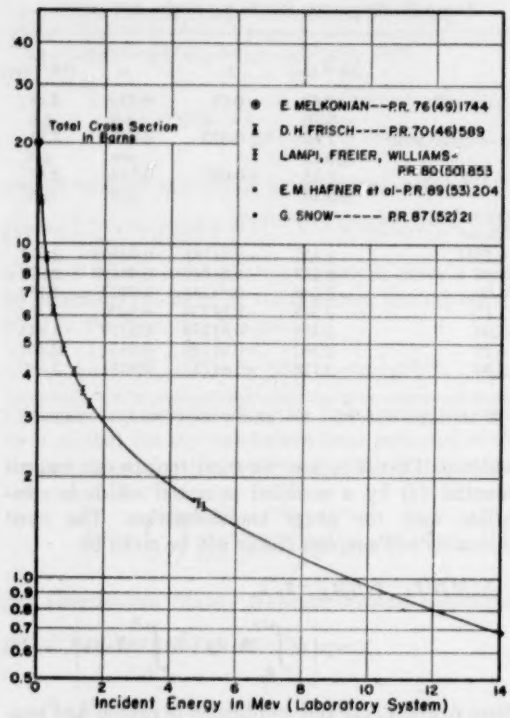
Total Cross Section in Barns
E. MELKONIAN--P.R. 76(49)1744
D.H. FRISCH----P.R. 70(46)589
LAMPI, FREIER, WILLIAMS-P.R. 80(50)853
E.M. HAFNER et al-P.R. 89(53)204
G. SNOW-----P.R. 87(52)21
Incident Energy in Mev (Laboratory System)

FIG. 1. Calculated n-p total cross section (triplet S plus singlet S only) is compared with observation. Here the S phase shifts are evaluated on the basis of following parameters (see Eqs. (24)–(27)):

	triplet	singlet
scattering length (in 10^{-13} cm)	5.378	−23.69
effective range (in 10^{-13} cm)	1.716	2.151
shape-dependent parameter	−0.024	−0.017

where $\boldsymbol{\sigma}_p$ and $\boldsymbol{\sigma}_n$ are the spins of proton and neutron, respectively; $-(\lambda_t/M)v_t(r)v_t(r')$ and $-(\lambda_s/M)v_s(r)v_s(r')$ are the nonlocal potentials for triplet and singlet states, respectively. This interaction then contributes to the radiative processes in neutron-proton system such as the photodisintegration of the deuteron,[12] aside from the usual electromagnetic interactions,

$$-(e/M)\mathbf{A}\cdot\mathbf{p}_p, \tag{30}$$

$$-[\mu_p\boldsymbol{\sigma}^p\cdot\mathrm{curl}\mathbf{A}(\mathbf{r}_p)+\mu_n\boldsymbol{\sigma}^n\cdot\mathrm{curl}\mathbf{A}(\mathbf{r}_n)]\mu_0,$$

and

$$\mu_p=2.793,\quad \mu_n=-1.913,\quad \mu_0=e/2M. \tag{31}$$

Since we assume no interactions except in ^3S and ^1S states and we know the correct S wave functions, we can easily calculate the photodisintegration cross section of the deuteron including all multipoles,

$$d\sigma/d\omega=d\sigma_e/d\omega+d\sigma_m/d\omega. \tag{32}$$

[12] The singlet part of (29) does not contribute to the deuteron photoeffect.

Here $d\sigma_e/d\omega$ is the spin-independent part [due to the interactions (29), (30)],

$$\frac{d\sigma_e}{d\omega}=\pi^2\frac{e^2}{4\pi}\frac{p_f^3}{M\nu}N^2\Bigg[\left\{\frac{g_t(p)}{\alpha^2+p^2}\right\}_{p=|\mathbf{p}_f-\frac{1}{2}\mathbf{v}|}-\int_0^1 ds\left\{\frac{\partial g_t(p)}{2p\partial p}\right\}_{p=|\mathbf{p}_f-(s/2)\mathbf{v}|}\Bigg]^2\sin^2\theta, \tag{32e}$$

and

$$g_t(p)=\frac{1}{(2\pi)^{\frac{1}{2}}}\int v_t(r)e^{-i\mathbf{p}\cdot\mathbf{r}}d\mathbf{r},\ N^2,\ \lambda_t\text{: see Eqs. (6), (7).}$$

$[g_t(p)/(\alpha^2+p^2)]$ comes from the usual interaction $\mathbf{A}\mathbf{p}_p$, (30), and $(1/2p)\partial g/\partial p$ comes from the modified nuclear interaction (29); while the spin-dependent cross section due to the magnetic interaction (31), which does not interfere with the spin-independent transition, is

$$\frac{d\sigma_m}{d\omega}=\frac{\pi^2}{6}\cdot\frac{e^2}{4\pi}\cdot\frac{p_f\nu}{M}\cdot N^2\{2|T|^2+|S|^2\}. \tag{32m}$$

In these expressions $\mathbf{p}_f(p_f=|\mathbf{p}_f|)$ is the final proton momentum, $\mathbf{v}(\nu=|\mathbf{v}|)$ is the incident photon momentum, $\theta=(\mathbf{p}_f\mathbf{v})/(p_f\nu)$; thus the energy balance is

$$\nu+\nu^2/4M=p_f^2/M+\alpha^2/M;$$

α^2/M is, as before, the binding energy of deuteron. All quantities are measured in the center-of-mass system. Note that $e^2/4\pi=1/137$. The quantities T and S are given by (T:$^3S\rightarrow$triplet, S:$^3S\rightarrow$singlet)

$$T=\mu_p\frac{g_t(p_-)}{\alpha^2+p_-^2}+\mu_n\frac{g_t(p_+)}{\alpha^2+p_+^2}-\frac{(\mu_p+\mu_n)\lambda_t g_t(p_f)}{1+\lambda_t J_t(p_f)}\times\int\frac{g_t(q)q_t(|\mathbf{q}-\frac{1}{2}\mathbf{v}|)}{(p_f^2-q^2+i\epsilon)(\alpha^2+|\mathbf{q}-\frac{1}{2}\mathbf{v}|^2)}d\mathbf{q}, \tag{32'}$$

$$S=\mu_p\frac{g_t(p_-)}{\alpha^2+p_-^2}-\mu_n\frac{g_t(p_+)}{\alpha^2+p_+^2}-\frac{(\mu_p-\mu_n)\lambda_s g_s(p_f)}{1+\lambda_s J_s(p_f)}\times\int\frac{g_s(\mathbf{q})g_t(|\mathbf{q}-\frac{1}{2}\mathbf{v}|)}{(p_f^2-q^2+i\epsilon)(|\mathbf{q}-\frac{1}{2}\mathbf{v}|^2+\alpha^2)}d\mathbf{q};$$

$$p_\pm=|\mathbf{p}_f\pm\tfrac{1}{2}\mathbf{v}|,$$

$$J_j(p_f)=\int d\mathbf{q}\frac{g_j^2(q)}{p_f^2-q^2+i\epsilon}\quad(j=t\text{ or }s).$$

If we are interested in the case where the incident photon energy is sufficiently small, (32) will reduce to the dipole cross sections

$$\frac{d\sigma_e}{d\omega}\rightarrow\frac{d\sigma(\text{E.D.})}{d\omega}=\frac{e^2}{4\pi}\frac{p_f^3}{\alpha^2+p_f^2}\pi^2N^2\sin^2\theta\times\left\{\frac{g_t(p_f)}{\alpha^2+p_f^2}-\frac{1}{2p_f}\frac{\partial g_t(p_f)}{\partial p_f}\right\}^2 \tag{33 E.D.}$$

and

$$\frac{d\sigma_m}{d\omega}\to\frac{d\sigma(\text{M.D.})}{d\omega}=\frac{e^2}{4\pi}\cdot\frac{p_f}{M^2(\alpha^2+p_f^2)}(\mu_p-\mu_n)^2\frac{N^2}{24\pi^2}$$
$$\times\left\{\sin\delta_s\frac{\lambda_t-\lambda_s}{\lambda_t\lambda_s}\cdot\frac{1}{g(p_f)}\right\}^2; \quad (33\text{ M.D.})$$

where δ_s=singlet phase shift (note that $T=0$). In (33 M.D.) we have assumed the same shape for the triplet and singlet nuclear forces:

$$g_t(p)=g_s(p)=g(p), \quad (34)$$

and used Eq. (7) for λ_t.

Special Case

As in the preceding section, let us assume

$$g_t(p)=1/(\beta_t^2+p^2) \text{ for the triplet potential,}$$

and

$$g_s(p)=1/(\beta_s^2+p^2) \text{ for the singlet potential,}$$

where β_t and β_s are constants which determine the ranges of nuclear potential. Then (32e) takes the form:

$$\frac{d\sigma_e}{d\omega}=\frac{e^2}{4\pi}\frac{\alpha p_f^3}{M\nu}\beta_t(\alpha+\beta_t)^3\sin^2\theta\left[\frac{1}{(\alpha^2+p_-^2)(\beta^2+p_-^2)}\right.$$
$$\left.-\left\{\frac{\partial}{2q\partial q}\left(\frac{1}{\frac{1}{2}\nu(\beta_t^2+q^2)^{\frac{1}{2}}}\right.\right.\right.$$
$$\left.\left.\left.\times\tan^{-1}\frac{\frac{1}{2}\nu(\beta_t^2+q^2)^{\frac{1}{2}}}{\beta_t^2+q^2-\{\frac{1}{2}\nu^2-(\mathbf{p}_f\nu)\}(\mathbf{p}_f\nu)\nu^{-2}}\right)\right\}_{q^2=p_f^2-\nu^{-2}(\mathbf{p}_f\nu)^2}\right]^2. \quad (35e)$$

For $d\sigma_m/d\omega$, we find

$$T=\frac{\mu_p}{(\alpha^2+p_-^2)(\beta_t^2+p_-^2)}+\frac{\mu_n}{(\alpha^2+p_+^2)(\beta_t^2+p_+^2)}$$
$$+\frac{(\mu_p+\mu_n)2f_t/\nu}{\beta_t^2-\alpha^2}\left[\tan^{-1}\left\{\frac{(\beta_t-\alpha)\frac{1}{2}\nu}{(\beta_t-ip_f)(\alpha-ip_f)+\frac{1}{4}\nu^2}\right\}\right.$$
$$\left.-\tan^{-1}\left\{\frac{(\beta_t-\alpha)\frac{1}{2}\nu}{2\beta_t(\alpha+\beta_t)+\frac{1}{4}\nu^2}\right\}\right] \quad (35')$$

$$S=\frac{\mu_p}{(\alpha^2+p_-^2)(\beta_t^2+p_-^2)}-\frac{\mu_n}{(\alpha^2+p_+^2)(\beta_t^2+p_+^2)}$$
$$+\frac{(\mu_p-\mu_n)2f_s/\nu}{\beta_t^2-\alpha^2}\left[\tan^{-1}\left\{\frac{(\beta_t-\alpha)\frac{1}{2}\nu}{(\beta_t-ip_f)(\alpha-ip_f)+\frac{1}{4}\nu^2}\right\}\right.$$
$$\left.-\tan^{-1}\left\{\frac{(\beta_t-\alpha)\frac{1}{2}\nu}{(\beta_t+\beta_s)(\alpha+\beta_s)+\frac{1}{4}\nu^2}\right\}\right];$$

where as before

$$p_\pm=|\mathbf{p}_f\pm\tfrac{1}{2}\boldsymbol{\nu}|,$$
$$f_j=1/(-ip_f+p_f\cot\delta_j) \quad (j=t \text{ or } s),$$
δ_t=triplet phase shift,

and

δ_s=singlet phase shift.

Here we have *not* assumed $g_t(p)=g_s(p)$, i.e., $\beta_t=\beta_s$.

At very low photon energy, we can approximate (35) by the dipole cross sections

$$\frac{d\sigma(\text{E.D.})}{d\omega}=\frac{e^2}{4\pi}\frac{\alpha p_f^3}{(\alpha^2+p_f^2)^3}\cdot\frac{\beta_t(\alpha+\beta_t)}{(\beta_t-\alpha)^2}$$
$$\times\left\{1-\left(\frac{\alpha^2+p_f^2}{\beta^2+p_f^2}\right)^2\right\}^2\sin^2\theta \quad (36\text{ E.D.})$$

and

$$\frac{d\sigma(\text{M.D.})}{d\omega}=\frac{1}{6}\frac{e^2}{4\pi}\frac{\alpha^2+p_f^2}{M^2}\cdot p_f(\mu_p-\mu_n)^2\alpha\beta_t(\alpha+\beta_t)^2\frac{\sin^2\delta_s}{p_f^2}$$
$$\times\left[\frac{p_f\cot\delta_s}{(\alpha^2+p_f^2)(\beta_t^2+p_f^2)}+\frac{1}{\beta_t+\alpha}\left\{\frac{\alpha\beta_t-p_f^2}{(\alpha^2+p_f^2)(\beta^2+p_f^2)}\right.\right.$$
$$\left.\left.-\frac{1}{(\alpha+\beta_s)(\beta_t+\beta_s)}\right\}\right]^2. \quad (36\text{ M.D.})$$

In the special case where $\beta_t=\beta_s=\beta$, we get, using Eq. (15),

$$\frac{d\sigma(\text{M.D.})}{d\omega}=\frac{1}{24}\frac{e^2}{4\pi}\left(\frac{\mu_p-\mu_n}{M}\right)^2\sin^2\delta_s\frac{\alpha p_f}{\beta(\alpha+\beta)}$$
$$\times\left(\frac{\lambda_t-\lambda_s}{\lambda_s}\right)^2\frac{\alpha^2+p_f^2}{p_f^2}\left(\frac{\beta^2+p_f^2}{\alpha^2+p_f^2}\right)^2.$$

Here we also put $M\nu$ equal to $\alpha^2+p_f^2$.

As is well-known, the electric dipole matrix element is always given by ($\boldsymbol{\varepsilon}$ is the polarization vector of the electromagnetic field)

$$\frac{i}{2}e\nu\int(^3P \text{ function})^*\boldsymbol{\varepsilon}\cdot\mathbf{r}(\text{deuteron function}).$$

Therefore, if we assume (i) a form of deuteron function, $Ng_t(p)/(\alpha^2+p^2)$, and (ii) no forces in ^3P states, the dipole cross section is just given by (33 E.D.), which is, in this sense, independent on a specific assumption of nonlocal nuclear potential. This fact holds for all electric multipole transitions (see an article of Sachs and Austern[13]) (for low photon energy).

[13] A. J. F. Siegert, Phys. Rev. **52**, 787 (1937); R. G. Sachs and N. Austern, Phys. Rev. **81**, 705 (1951).

Equation (36 E.D.) has very familiar form and in fact agrees with that reported by other authors[14] on the basis of the local Hulthén potential. In the magnetic dipole cross section (36 M.D.), we use familiar forms of wave functions both for the deuteron and the ^1S state, and so obtain a well-known result.

TABLE III. The thermal-neutron capture cross sections σ_{cap} by hydrogen, calculated from the formula (33 M.D.) multiplied by $(3/2)\nu^3/p_f^3$. For α_t and β_t we used Eqs. (22) and (23), while we assumed several values for β_s but fixed the value of the singlet scattering length as -23.69×10^{-13} cm.

β_s/α_t	$\sigma_{cap}\beta_n$ (10^{-20} cm^2/sec)	σ_{cap} (barns)
6.2547	7.069	0.32130
6.25	7.068	0.32126
6.00	7.019	0.3191
5.75	6.967	0.3167
5.50	6.909	0.3141
5.25	6.847	0.3112
5.00	6.778	0.3081

[14] H. A. Bethe and C. Longmire, Phys. Rev. **77**, 647 (1950); J. S. Levinger, Phys. Rev. **76**, 699 (1949); L. I. Schiff, Phys. Rev. **78**, 733 (1950); J. F. Marshall and E. Guth, Phys. Rev. **78**, 738 (1950); E. E. Salpeter, Phys. Rev. **82**, 60 (1951); J. G. Brennan and R. G. Sachs, Phys. Rev. **88**, 824 (1952); L. Hulthén and B. C. H. Nagel, Phys. Rev. **90**, 62 (1953).

Therefore, the content of Eqs. (35) and (36) is no greater than that of equations reached by other authors except that (35) includes *all multipoles*. For example, our cross sections cannot explain: (i) The experimental result (0.330 barn) for thermal neutron capture by hydrogen.[15] [In this case we must modify (36 M.D.) but in an obvious way (see Table III).] (ii) The large cross section at photon energy $\gtrsim$100 Mev. We do not repeat here, therefore, a detailed discussion based on the cross sections which we have derived.

In conclusion, we should like to emphasize again the usefulness of the wave functions examined in this paper. As was illustrated in Section 4 for the photodisintegration of deuteron, our wave functions are very convenient for the examination of various phenomena involving the two-nucleon system.

The author wishes to thank Professor G. F. Chew and Professor F. E. Low for their valuable suggestions and discussions.

[15] N. Austern, Phys. Rev. **92**, 670 (1953); Hamermesh, Ringo, and Wexler, Phys. Rev. **90**, 603 (1953); Harris, Muehlhause, Rose, Schroeder, Thomas, and Wexler, Phys. Rev. **91**, 125 (1953); G. von Dardel and A. W. Waltner, Phys. Rev. **91**, 1284 (1953).

Two-Nucleon Problem When the Potential Is Nonlocal but Separable. II

YOSHIO YAMAGUCHI AND YORIKO YAMAGUCHI
Department of Physics, University of Illinois, Urbana, Illinois
(Received April 15, 1954)

The two-nucleon problem is considered in terms of an interaction of the form $(\mathbf{p}|V|\mathbf{p}')=-(\lambda/M)g(\mathbf{p})g(\mathbf{p}')$, with $g(\mathbf{p})=C(p)+(1/\sqrt{8})\{3p^{-2}(\boldsymbol{\sigma}^p\cdot\mathbf{p})(\boldsymbol{\sigma}^n\cdot\mathbf{p})-(\boldsymbol{\sigma}^p\cdot\boldsymbol{\sigma}^n)\}T(p)$, where the second term gives rise to a mixture of D state with the S state determined by the first term. After deriving general results valid for any form of $g(\mathbf{p})$, we discuss in detail the special case of $C(p)=(p^2+\beta^2)^{-1}$ and $T(p)=-tp^2(\gamma^2+p^2)^{-2}$ and compared it with observed data. The photodisintegration of the deuteron is also discussed and it is found that the D-wave part of the deuteron plays an important role at high photon energies leading to a larger cross section than given by other calculations to date.

1. INTRODUCTION

IN the preceding paper[1] (cited as I hereafter) we have shown that the two-body Schrödinger equation can be easily solved with a nonlocal but separable nuclear interaction. In continuation of I, we want to discuss here the special case of a separable neutron-proton interaction with spin-orbit coupling. Adopting the algebraic notation of Rarita-Schwinger,[2] our nuclear interaction for the triplet state takes the form

$$(\mathbf{p}|V|\mathbf{p}')=-(\lambda/M)g(\mathbf{p})g(\mathbf{p}'),$$

$$g(\mathbf{p})=C(p)+(1/\sqrt{8})S(\mathbf{p})T(p),$$

and

$$S(\mathbf{p})=(3/p^2)(\boldsymbol{\sigma}^p\cdot\mathbf{p})(\boldsymbol{\sigma}^n\cdot\mathbf{p})-(\boldsymbol{\sigma}^p\cdot\boldsymbol{\sigma}^n), \qquad (1)$$

where $C(p)$ and $T(p)$ are the functions of $p=|\mathbf{p}|$, and $\boldsymbol{\sigma}^p$ or $\boldsymbol{\sigma}^n$ is the usual spin matrix for the proton or neutron. $C(p)$ and $T(p)$, or equivalently $g(\mathbf{p})$, must be real in the sense of Wigner.[3] As will be shown, the two-body problem can easily be solved for this interaction both for the bound and the continuum states. It seems therefore worth while to report the detailed discussion based on this potential to see the effects of the so-called tensor force. In the case of the usual local form, these effects are so complicated that they cannot be seen in a simple manner, because a local potential including tensor force requires tedious numerical integration[4] for solution.

It is evident that our triplet potential (1) acts in the $({}^3S_1+{}^3D_1)$ state only. Moreover, as will be seen in the next section, there is no room to find two independent solutions for $({}^3S_1+{}^3D_1)$ states, because the wave function is uniquely determined by $g(\mathbf{p})$. In other words, our potential acts just in the "eigen-S" state, following the terminology of Blatt and Biedenharn.[5] This striking feature is of course a direct consequence of the special assumption for the form of $g(\mathbf{p})$. To get an interaction acting in other states than the eigen-S, one may adopt another form for $(\mathbf{p}|V|\mathbf{p}')$, which necessarily contains further dependence upon the direction of $\mathbf{p}$. Nevertheless, for the time being let us confine our discussion to the nuclear potential (1).

If we choose our nonlocal potential involving spin-orbit coupling to be without a long tail, then we can depend upon the validity of the effective range theory,[6] just as in the case of local spin-orbit forces,[7] to guarantee a fit to the low-energy two-nucleon data. Since one gets the deuteron and continuum wave functions in very simple forms, one can easily apply them to high-energy regions which are outside of the validity of the shape-independent theory. Thus we shall calculate on the basis of our model the neutron-proton scattering and the photodisintegration of the deuteron at high energy. It turns out that the neutron-proton scattering up to 100 Mev is fairly well explained by the force (20) for the triplet eigen-S state and the singlet potential fixed in I, and it is shown that the D wave in the deuteron plays an important role in the high-energy photodisintegration. The photodisintegration cross section will be expressed in such a way as to make clear the dependence on the assumed deuteron function.

2. GENERAL FORMULATION

In this section we want to give relevant formulas for the neutron-proton system, without specifying the form of $g(\mathbf{p})$. In the next section we shall examine the two-nucleon system, assuming a simple form for $g(\mathbf{p})$. As in I, our problem can be treated more conveniently if the momentum-space representation is adopted rather than the coordinate representation.

(a) Deuteron Problem

Let us start with the deuteron problem. The deuteron function must take the form

$$\psi(\mathbf{p},\text{spin})=\{u(p)+(1/\sqrt{8})S(\mathbf{p})w(p)\}\chi_1^m, \qquad (2)$$

[1] Y. Yamaguchi, preceding paper [Phys. Rev. **95**, 1628 (1954)], cited as I.
[2] W. Rarita and J. Schwinger, Phys. Rev. **59**, 436, 556 (1941).
[3] E. Wigner, Nachr. Ges. Wiss. Göttingen **31**, 546 (1932).
[4] T. Miyazima, Proc. Phys.-Math. Soc. Japan **22**, 188 (1940); H. Feshbach and J. Schwinger, Phys. Rev. **84**, 194 (1951); J. M. Blatt and M. H. Kalos, Phys. Rev. **92**, 156 (1953); Fujii, Iwadare, Otsuki, Takotani, Tani, and Watari, Progr. Theoret. Phys. Japan **10**, 478 (1953). Other references will be found in J. M. Blatt and V. F. Weisskopf, *Theoretical Nuclear Physics* (John Wiley and Sons, Inc., New York, 1952).
[5] J. M. Blatt and L. C. Biedenharn, Phys. Rev. **86**, 399 (1952).
[6] E.g., see J. M. Blatt and V. F. Weisskopf, *Theoretical Nuclear Physics* (John Wiley and Sons, Inc., New York, 1952).
[7] R. S. Christian, Phys. Rev. **75**, 1675 (1949); Y. Yamaguchi, Progr. Theoret. Phys. Japan **6**, 439 (1951).

where $u(p)$ and $w(p)$ are the S and D wave functions, respectively, depending on $p=|\mathbf{p}|$; χ_1^m $(m=1, 0, -1)$ is the triplet spin function. Inserting (2) into the Schrödinger equation,

$$(\alpha^2+p^2)\{u(p)+(1/\sqrt{8})S(\mathbf{p})w(p)\}\chi_1^m$$
$$=\lambda\{C(p)+(1/\sqrt{8})S(\mathbf{p})T(p)\}\int d\mathbf{p}'\{C(p')u(p')$$
$$+T(p')w(p')\}\cdot\chi_1^m, \quad (3)$$

where $\alpha^2/M=$binding energy of the deuteron. One can readily find a solution

$$u(p)=NC(p)/(\alpha^2+p^2), \quad w(p)=NT(p)/(\alpha^2+p^2), \quad (4)$$

where N is a normalization constant fixed so that

$$\int d\mathbf{p}\{u^2(p)+w^2(p)\}=1,$$

or

$$N^{-2}=\int d\mathbf{p}\frac{C^2(p)+T^2(p)}{(\alpha^2+p^2)^2}. \quad (5)$$

One may determine the strength $\lambda=\lambda(\alpha)$ of our nuclear interaction so as to fit the observed binding energy α^2/M of the deuteron:

$$\frac{1}{\lambda}=\int d\mathbf{p}\frac{C^2(p)+T^2(p)}{\alpha^2+p^2}. \quad (6)$$

Thus the well-depth parameter s, defined by Blatt-Jackson,[7] is given by

$$s=\lambda(\alpha)/[\lim_{\alpha\to 0}\lambda(\alpha)].$$

The D-state probability P_D and the quadrupole moment of the deuteron Q are given by

$$P_D=\int d\mathbf{p}w^2(p)=4\pi N^2\int_0^\infty p^2dpT^2(p)(\alpha^2+p^2)^{-2}, \quad (7)$$

$$Q=-\frac{1}{4}\int d\mathbf{p}\left[\left\{u(p)+\frac{1}{\sqrt{8}}S(\mathbf{p})w(p)\right\}\chi_1^1\right]^*$$
$$\times\left\{3\frac{\partial^2}{\partial p_z^2}-\frac{\partial^2}{\partial\mathbf{p}^2}\right\}\left\{u(p)+\frac{1}{\sqrt{8}}S(\mathbf{p})w(p)\right\}\chi_1^1$$
$$=\frac{\sqrt{8}\pi}{5}\int_0^\infty dp\left\{p\frac{\partial u}{\partial p}w-p^2\frac{\partial^2 u}{\partial p^2}w\right\}$$
$$-\frac{\pi}{5}\int_0^\infty dp\left\{6w^2+p^2\left(\frac{\partial w}{\partial p}\right)^2\right\}. \quad (8)$$

(b) Neutron-Proton Scattering

Next let us examine the neutron-proton scattering. Our fundamental equation is

$$\psi_{\mathbf{k}}(\mathbf{p})=\varphi_{\mathbf{k}}(\mathbf{p})+\frac{M}{k^2-p^2+i\epsilon}\int(\mathbf{p}|V|\mathbf{p}')d\mathbf{p}'\psi_{\mathbf{k}}(\mathbf{p}'), \quad (9)$$

when $\mathbf{k}$ is the incident momentum, $k=|\mathbf{k}|$, $\varphi_{\mathbf{k}}(p)=\delta(\mathbf{p}-\mathbf{k})$ is the incident plane wave, and ϵ is a real positive infinitesimal quantity which makes the scattered part of $\psi_{\mathbf{k}}(\mathbf{p})$ only an outgoing wave. Introducing the T matrix,[8]

$$(\varphi_{\mathbf{p}},V\psi_{\mathbf{k}})=(\mathbf{p}|T|\mathbf{k}), \quad (10)$$

Eq. (9) takes the form

$$(\mathbf{p}|T|\mathbf{k})=(\mathbf{p}|V|\mathbf{k})+\int\frac{(\mathbf{p}|V|\mathbf{p}')d\mathbf{p}'(\mathbf{p}'|T|\mathbf{k})}{(k^2-p'^2+i\epsilon)/M}. \quad (11)$$

If $(\mathbf{p}|V|\mathbf{k})$ is factorable [see (1)], our Eq. (11) is easily solved:

$$(\mathbf{p}|T|\mathbf{k})=-\frac{\lambda}{M}\cdot\frac{g(\mathbf{p})g(\mathbf{k})}{1+\lambda J(k)}, \quad (12)$$

where $J(k)$ is given by

$$J(k)=\int d\mathbf{p}'\frac{C^2(p')+T^2(p')}{k^2-p^2+i\epsilon}. \quad (13)$$

It should be noted that the wave function which describes a scattering process is

$$\psi_{\mathbf{k}}(\mathbf{p},\text{spin})=\left\{\delta(\mathbf{p}-\mathbf{k})-\frac{\lambda}{1+\lambda J(k)}\cdot\frac{g(\mathbf{p})g(\mathbf{k})}{k^2-p^2+i\epsilon}\right\}\chi_1^m. \quad (14)$$

This wave function is determined uniquely from the potential (1) assumed and describes the eigen-^3S scattering.

From the T matrix (12), we can readily write down the desired cross section; for example the differential cross section in the c.m. system for an unpolarized triplet beam is as follows:

$$\frac{d\sigma}{d\omega}=\frac{1}{3}\text{Sp}\left[\frac{3+\boldsymbol{\sigma}^p\boldsymbol{\sigma}^n}{4}|2\pi^2M(\mathbf{p}|T|\mathbf{k})|^2\right], \quad (p=k), \quad (15)$$

or

$$\frac{d\sigma}{d\omega}=\frac{1}{3}\left|\frac{2\pi^2\lambda}{1+\lambda J(k)}\right|^2\text{Sp}\left[\frac{3+\boldsymbol{\sigma}^p\boldsymbol{\sigma}^n}{4}g(\mathbf{k})g(\mathbf{p})g(\mathbf{p})g(\mathbf{k})\right], \quad (16)$$

where $(3+\boldsymbol{\sigma}^p\cdot\boldsymbol{\sigma}^n)/4$ is the projection operator for the triplet state and $\mathbf{p}$ is the relative momentum after the

[8] B. A. Lippmann and J. Schwinger, Phys. Rev. **79**, 469 (1950).

scattering. More explicitly,

$$\frac{d\sigma}{d\omega}=\frac{\sigma_{\text{tot}}}{4\pi}\left\{1+\epsilon(k)\cdot\frac{3\cos^2\theta-1}{2}\right\},\quad \cos\theta=(\mathbf{p}\cdot\mathbf{k})/pk,$$

$$\sigma_{\text{tot}}=4\pi\left|\frac{2\pi^2\lambda}{1+\lambda J(k)}\right|^2\{C^2(k)+T^2(l)\}^2, \tag{17}$$

and

$$\epsilon(k)=\left\{\frac{2C(k)T(k)-(1/\sqrt{2})T^2(k)}{C^2(k)+T^2(k)}\right\}^2. \tag{18}$$

Here it should be noted that the asymmetry coefficient $\epsilon(k)$ is always positive.

The eigen S-phase shift δ can easily be calculated from the relation

$$\frac{2\pi^2\lambda\{C^2(k)+T^2(k)\}}{1+\lambda J(k)}=\frac{e^{i\delta}\sin\delta}{k}=\frac{1}{-ik+k\cot\delta}. \tag{19}$$

Then by expanding $k\cot\delta$ in a power series in k^2, one can derive the analytic expressions for the scattering length a, the effective range r_0, etc. We shall show this in the next section where a simple form for $g(\mathbf{p})$ is adopted.

3. DETAILED DISCUSSION OF THE SPECIAL CASE

In this section we want to examine our problem with a special form for $g(\mathbf{p})$. It is evident that if we assume rational functions for $C(p)$ and $T(p)$, then we can perform all integrations required in solving the two-body problem. It is natural to choose the simplest function in this category. At first sight the simplest choice seems to be

$$C(p)=1/(\beta^2+p^2),\quad T(p)=-l/(\gamma^2+p^2)$$

where β, γ, and l are constant parameters. This is, however, not a reasonable choice, because it corresponds to a long-tail potential in the $\mathbf{r}$ representation, which does not seem physically plausible and in fact leads to undesirable results: (i) the asymmetry coefficient $\epsilon(k)$ is insensitive to the incident momentum k and in general $\epsilon(k)\neq 0$ even at $k=0$ and (ii) the electric dipole photodisintegration cross section of the deuteron becomes anomalously large at very low photon energy. Therefore we choose the next simplest function, namely,

$$C(p)=1/(\beta^2+p^2),\quad T(p)=-lp^2/(\gamma^2+p^2)^2, \tag{20}$$

where β, γ, and l are constant parameters. This choice is quite reasonable, being free from the objections mentioned previously, and for the special case of D interaction only, i.e., $C(p)=0$, the scattering phase shift δ goes to the form $k^5\cot\delta=(\text{const})+(\text{const})k^2+\cdots$, which is of course the normal behavior for pure D wave scattering (see I, Sec. 3; this can easily be seen from Eq. (27) below if l is made very large). The form (20) is a natural generalization of the special interaction $g(p)=(\beta^2+p^2)^{-1}$ discussed in I, Sec. 3. In fact, if we put $l=0$, all of our results found below reduce to those of the "central" case of I, Sec. 3. Note that if $l>0$ our tensor force is attractive for parallel nucleon spins and gives a positive value for the quadrupole moment of the deuteron.

(a) Deuteron Problem

With this choice of potential, the deuteron function is

$$u(p)=\frac{N}{(\alpha^2+p^2)(\beta^2+p^2)},\qquad w(p)=-\frac{Nlp^2}{(\alpha^2+p^2)(\gamma^2+p^2)^2}, \tag{21}$$

where

$$\frac{1}{N^2}=\pi^2\left\{\frac{1}{\alpha\beta(\alpha+\beta)^3}+l^2\frac{5\alpha+\gamma}{8\gamma(\alpha+\gamma)^5}\right\}. \tag{22}$$

In our case the S wave function is again of Hulthén form. λ is determined by

$$\frac{1}{\lambda}=\pi^2\left\{\frac{1}{\beta(\alpha+\beta)^2}+\frac{l^2}{8}\cdot\frac{(5\alpha^2+4\alpha\gamma+\gamma^2)}{\gamma(\alpha+\gamma)^4}\right\}, \tag{23}$$

so that the well-depth parameter s is

$$s=\frac{\lambda}{\beta^{-3}+(l^2/8\gamma^3)}. \tag{24}$$

The D-state probability P_D and the quadrupole moment Q are easily calculated:

$$P_D=\frac{l^2(5\alpha+\gamma)}{8\gamma(\alpha+\gamma)^5}\Big/\left[\frac{1}{\alpha\beta(\alpha+\beta)^3}+\frac{l^2(5\alpha+\gamma)}{8\gamma(\alpha+\gamma)^5}\right], \tag{25}$$

$$\begin{aligned}Q=\frac{\sqrt{2}\pi^2N^2l}{10(\alpha+\beta)^4}\Bigg[&\frac{1}{(\beta+\gamma)^2(\alpha+\gamma)^5}\{\alpha\beta^2(5\alpha^2+4\alpha\beta+\beta^2)\\&+\beta\gamma(10\alpha^3+33\alpha^2\beta+22\alpha\beta^2+5\beta^3)\\&+\gamma^2(5\alpha^3+22\alpha^2\beta+33\alpha\beta^2+10\beta^3)\\&+\gamma^3(\alpha^2+4\alpha\beta+5\beta^2)\}\\&+\frac{2}{(\beta+\gamma)^3(\alpha+\gamma)^4}\{\alpha(\beta+\gamma)^3+4(\alpha^2+\beta\gamma)\\&\times(\beta^2+3\beta\gamma+\gamma^2)+16\alpha\beta\gamma(\beta+\gamma)\}\\&+\frac{2}{(\beta+\gamma)^4(\alpha+\gamma)^3}\{\beta(\alpha+\gamma)^3+4(\beta^2+\alpha\gamma)\\&\times(\alpha^2+3\alpha\gamma+\gamma^2)+16\alpha\beta\gamma(\alpha+\gamma)\}\Bigg]\\&-\frac{\pi^2N^2l^2}{160}\frac{(7\alpha^3+49\alpha^2\gamma+91\alpha\gamma^2+33\gamma^3)}{\gamma^3(\alpha+\gamma)^7}.\end{aligned} \tag{26}$$

(b) Scattering Problem

Since we have solved the scattering problem without specifying a form for $g(\mathbf{p})$, we can readily write down the unpolarized triplet cross section corresponding to the potential (20)

$$\frac{d\sigma}{d\omega}=\left|\frac{1}{-ik+k\cot\delta}\right|^2\left\{1+\epsilon(k)\cdot\frac{3\cos^2\theta-1}{2}\right\},$$

$$k\cot\delta=\left(\frac{1}{(\beta^2+k^2)^2}+\frac{l^2k^4}{(\gamma^2+k^2)^4}\right)^{-1}\left[\frac{1}{2\pi^2\lambda}-\frac{\beta^2-k^2}{2\beta(\beta^2+k^2)^2}-\frac{l^2(\gamma^6+5\gamma^4k^2+15\gamma^2k^4-5k^6)}{16\gamma(\gamma^2+k^2)^4}\right], \quad (27)$$

and

$$\epsilon(k)=\frac{\left[\frac{2}{(\beta^2+k^2)}\cdot\frac{tk^2}{(\gamma^2+k^2)^2}+\frac{1}{\sqrt{2}}\left\{\frac{tk^2}{(\gamma^2+k^2)^2}\right\}^2\right]^2}{\left[\left(\frac{1}{\beta^2+k^2}\right)^2+\left\{\frac{tk^2}{(\gamma^2+k^2)^2}\right\}^2\right]^2}. \quad (28)$$

The asymmetry factor has following features:

$$\epsilon(k)\simeq(4l^2\beta^4/\gamma^8)k^4, \quad (k\ll\beta,\gamma);$$

and

$$\epsilon(k)\to\left\{\frac{(2+l/\sqrt{2})l}{1+l^2}\right\}^2, \quad (k\to+\infty);$$

thus

$$\epsilon(k)=0 \quad \text{at} \quad k=0.$$

If we expand $k\cot\delta$, Eq. (27), in a power series in k^2, one can easily find the desired coefficients, the scattering length a, the effective range r_0, and the shape-dependent factor P;

$$\frac{1}{a}=-\frac{\beta^4}{2\pi^2\lambda}+\frac{\beta}{2}+\frac{l^2\beta^4}{16\gamma^3}=\frac{\alpha\beta(\alpha+2\beta)}{2(\alpha+\beta)^2}+\frac{l^2}{16}\cdot\frac{\beta^4}{\gamma^4}\cdot\frac{\alpha\gamma(\alpha^2+4\alpha\gamma+\gamma^2)}{(\alpha+\gamma)^4}, \quad (29)$$

TABLE I. Comparison with experiment of various quantities calculated with the parameters given in Eq. (33b).

Calculated	Experimental
$P_D=4.000$ percent	2–8 percent (due to Miyazawa's argument)[a] 5–10 percent (due to Machida's argument)[b]
$Q=2.7394\times10^{-27}$ cm^2	$(2.74\pm0.02)\times10^{-27}$ cm^2
$s=1.291_5$	
$b=2.122\times10^{-13}$ cm	
$a=5.378\times10^{-13}$ cm	$(5.378\pm0.021)\times10^{-13}$ cm
$r_0=1.704\times10^{-13}$	

[a] See reference 12.
[b] See reference 13.

$$r_0=\frac{2\beta^2}{\pi^2\lambda}+\frac{1}{\beta}-\frac{l^2}{8}\beta^2\left(\frac{\beta^2}{\gamma^5}+\frac{2}{\gamma^3}\right)=\frac{2\beta^2+(\alpha+\beta)^2}{\beta(\alpha+\beta)^2}+\frac{l^2}{8}\beta^2\left\{\frac{2(5\alpha^2+4\alpha\gamma+\gamma^2)}{\gamma(\alpha+\gamma)^4}-\frac{\beta^2}{\gamma^5}-\frac{2}{\gamma^3}\right\}, \quad (30)$$

$$Pr_0^3=-\frac{1}{2\pi^2\lambda}+\frac{l^2}{2}\frac{\beta^2}{\gamma^2}\left(\frac{1}{\pi^2\lambda}-\frac{1}{\beta^3}-\frac{l^2}{8\gamma^3}\right)+\frac{l^2}{16}\frac{1}{\gamma^3}\left(1+\frac{2\beta^2}{\gamma^2}+\frac{5\beta^4}{\gamma^4}\right)$$
$$=\frac{-1}{2\beta(\alpha+\beta)^2}-\frac{1}{2}l^2\left[\frac{5\alpha^2+4\alpha\gamma+\gamma^2}{8\gamma(\alpha+\gamma)^4}-\frac{1}{8\gamma^3}\left(1+\frac{2\beta^2}{\gamma^2}+\frac{5\beta^4}{\gamma^4}\right)+\frac{\beta^8}{\gamma^8}\left(\frac{1}{\beta^6}-\frac{1}{\beta(\alpha+\beta)^2}\right)\right]$$
$$-l^4\frac{\beta^8}{2\gamma^8}\left(\frac{1}{8\gamma^3}-\frac{5\alpha^2+4\alpha\gamma+\gamma^2}{8\gamma(\alpha+\gamma)^4}\right). \quad (31)$$

Thus the intrinsic range[6] b is given by

$$b=\frac{3}{\beta}-\frac{l^2\beta^4}{8\gamma^5}, \quad (32)$$

where we have used Eq. (23).

(c) Comparison with Experiments

Now we are in a position to compare our results with experimental data. To do this we must first find values of the parameters, α, β, γ, and l, which fit the low-energy neutron-proton data. This procedure can be performed conveniently as follows. First of all α can be fixed from the deuteron binding energy,[9] $\alpha^2/M=2.225$ Mev:

$$\alpha=2.316\times10^{12}\ \text{cm}^{-1}. \quad (33a)$$

Next, from formula (29) for the scattering length a and Eq. (25) for the D-state probability P_D, eliminating l, we get

$$\frac{2(1-P_D)}{P_D}\left(\frac{\alpha+\beta}{\beta}\right)^3\left[\frac{1}{a\alpha}-\frac{\beta(\alpha+2\beta)}{2(\alpha+\beta)^2}\right]=\frac{\alpha+\gamma}{\gamma(5\alpha+\gamma)}\left[2\alpha+\frac{(\alpha+\gamma)^2}{\gamma}\right].$$

[9] Li, Whaling, Fowler, and Lauritsen, Phys. Rev. **83**, 512 (1951).

Inserting P_D and the observed value[10] of $a=5.378\times10^{-13}$ cm in this equation, we can find a value of γ for an assumed value for β. Then, for any set of values for β and γ, we can calculate the value of t either from Eq. (29) for the scattering length [or equivalently from Eq. (25)] or from the Eq. (26) for the quadrupole moment. If these two values of t coincide for some set of β and γ, this set (β,γ,t) is the desired one. Unfortunately the D-state probability P_D has not been accurately determined up to the present time. Many authors, however, have adopted the value 4 percent,[11] and we shall tentatively do the same here. For a complete discussion of the D-state probability we refer the reader to existing articles.[12,13] Then we determine the values of parameters to be as follows:

$$\beta=5.759\alpha, \quad \gamma=6.771\alpha, \quad t=1.784. \qquad (33b)$$

For the sake of completeness, we list in Table I the values of various quantities (re-)calculated with these values for β, γ, and t. From these results it is evident that our model fits the low-energy neutron-proton data very well. As is seen from the form (20) for $T(p)$, the effect of tensor force is not appreciable at low energies [also see the formula just under (28)]. The total cross section for the triplet neutron-proton scattering is in agreement with that of the "central" case of I, Sec. 3 up to 20 Mev. However the tensor part $T(p)$ plays an important role at higher energies.

Let us compare our results with high-energy nucleon-nucleon collision experiments.[14,15] Figures 1 and 2 show the energy dependence of $\sigma_{\rm tot}/4\pi$ and $\epsilon(k)$, based on the parameters (33). We have determined in I, Sec. 3(c) the singlet neutron-proton interaction. Using this singlet interaction combined with the triplet interaction obtained here, we can calculate the high-energy neutron-proton scattering cross sections which, of course, contain contributions only from ^1S and eigen-^3S states (see Fig. 3). The deviation from the isotropic angular dependence is caused by the D wave in the eigen-^3S state. Furthermore, assuming charge dependence of nuclear interactions, one can compare the singlet S phase shift without Coulomb force with the observed one,[15] 50.2°, for proton-proton scattering at 30 Mev. (See Fig. 4.) As is seen from these figures, our calculated cross sections are in fair agreement with observations

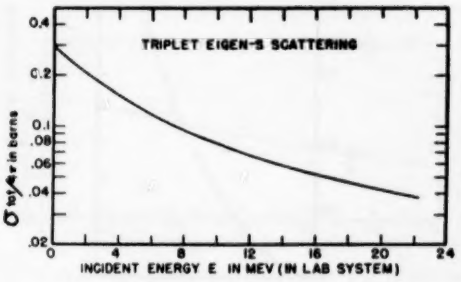

(a)

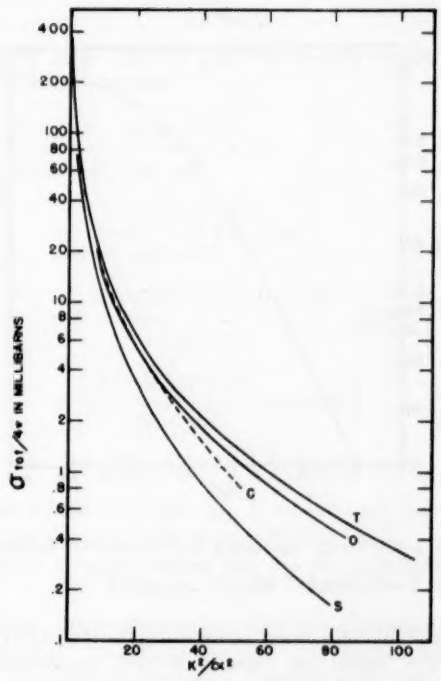

(b)

FIG. 1. (a) The n-p total cross section $\sigma_{\rm tot}$ divided by 4π for the triplet eigen-S scattering vs incident neutron energy E (in the laboratory system). This curve is in good agreement with that of the "central" case discussed in I, Sec. 3 [also see Fig. 1(b)]. (b) Curve T is the n-p total cross section $\sigma_{\rm tot}$ divided by 4π for the triplet eigen-S scattering [calculated from (27) and (33)]. Note that the triplet eigen-S scattering cross section is $d\sigma/d\omega=(\sigma_{\rm tot}/4\pi)\{1+\epsilon(k)(3\cos^2\vartheta-1/2)\}$. For comparison, we illustrated by curves C and S the triplet and singlet S-cross sections on the basis of the "central" interaction described in I, Sec. 3. The incident energy E in the laboratory system is given by $E=2k^2/M=(k^2/\alpha^2)\times4.45$ Mev. The curve O shows the average cross section of the triplet eigen-S and the singlet S scattering.

up to 100 Mev for the neutron-proton case and up to ~40 Mev for the proton-proton case. However, at still higher energies the calculated cross sections for both neutron-proton and proton-proton scattering are definitely smaller than the experimental values, indicating interactions in P or higher-order partial waves. This is of course the conclusion reached by Christian and

[10] E. Melkonian, Phys. Rev. **76**, 1744 (1949); Burgy, Ringo, and Hughes, Phys. Rev. **84**, 1160 (1951).

[11] This value is correct under two doubtful assumptions: (i) that the relativistic correction to the magnetic moment is small, and (ii) that there is complete additivity of the proton and the neutron moments.

[12] H. Miyazawa, Progr. Theoret. Phys. **7**, 207 (1952).

[13] S. Machida, Progr. Theoret. Phys. **9**, 683 (1953).

[14] Hardley, Kelly, Leith, Segrè, Wiegand, and York, Phys. Rev. **75**, 351 (1949); Kelly, Leith, Segrè, and Wiegand, Phys. Rev. **79**, 96 (1950); Randle, Tayler, and Wood, Proc. Roy. Soc. (London) **A213**, 392 (1952).

[15] W. K. H. Panofsky and F. L. Fillmore, Phys. Rev. **79**, 96 (1950); Cork, Johnston, and Richman, Phys. Rev. **79**, 57 (1950).

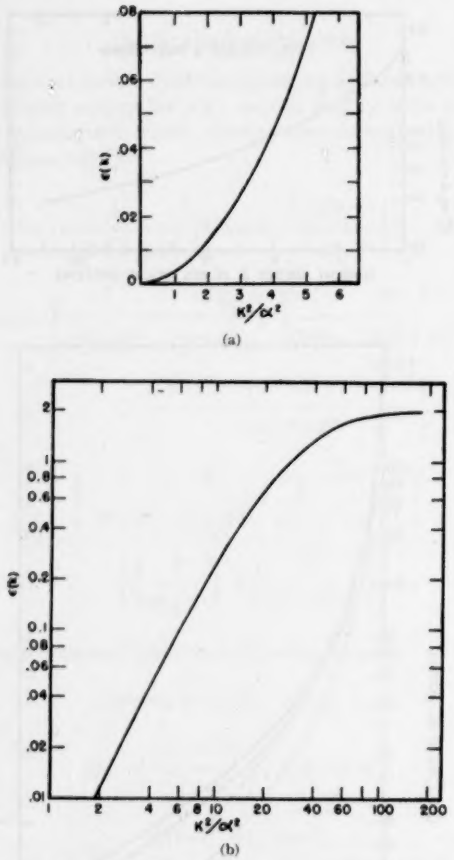

FIG. 2. The energy dependence of the asymmetry factor, $\epsilon(k)$, calculated from (28) and (33). Incident energy in laboratory system $E=(k^2/\alpha^2)\times 4.45$ Mev.

others.[16] Actually there is already some indication of a P wave interaction even in 90-Mev neutron-proton scattering, as is seen from the asymmetry around 90°. More detailed analysis of high-energy nucleon-nucleon scattering based on separable potentials is in progress.

4. PHOTODISINTEGRATION OF THE DEUTERON

Since we have found a nice form (21) for the deuteron function, it is interesting to apply it to the photodisintegration problem. As was shown in the preceding section, the neutron-proton interaction up to 100 Mev can be well expressed in terms of our separable potentials (20) for the eigen-^3S state and the singlet S potential described in I, and, as is well known, the forces acting in states higher than P are not important in this energy reaction. Thus it may be concluded that we are in a position to make a more accurate calculation of the electric dipole disintegration cross section up to 50-Mev photon energy (in the c.m. system) than has been reported so far.[17] The magnetic transition is partly due to an unknown effect, the so-called interaction magnetic moment.[18] However, neglecting this small effect, we can also calculate the magnetic transition using our wave functions. Therefore, keeping within the low and intermediate photon energies, we want to discuss here the dipole photodisintegration of the deuteron.

(a) Electric Dipole Transition

As stated previously, we want to use free ^3P waves and the deuteron function (4). According to Siegert's theorem,[19] the transition matrix for the electric dipole transition is given by $\int(^3P \text{ function})\mathbf{r}\cdot\boldsymbol{\varepsilon}(\text{deuteron function})$, where $\mathbf{r}$ is the relative coordinate between the proton and the neutron, and $\boldsymbol{\varepsilon}$ is the polarization vector of electromagnetic field. This matrix element can also be calculated using the argument of gauge invariance as was done in I, Sec. 4. These two methods naturally give the same results. Thus one can find the electric dipole disintegration cross section in the c.m. system

$$\frac{d\sigma_e}{d\omega}=\frac{e^2}{4\pi}\frac{\alpha p^3}{(\alpha^2+p^2)^3}\frac{\pi^2 N^2}{\alpha}[(E_1+E_2)\sin^2\theta+E_3(1+\cos^2\theta)],$$

$$E_1=\left\{C(p)-\frac{\alpha^2+p^2}{2p}\frac{\partial C}{\partial p}\right\}^2,$$

$$E_2=\left\{T(p)-\frac{\alpha^2+p^2}{2p}\frac{\partial T}{\partial p}\right\}^2, \tag{34}$$

and

$$E_3=\frac{3}{4}\left\{\frac{\alpha^2+p^2}{p^2}T(p)\right\}^2,$$

where θ is the angle between the photoproton and the incident photon, $\mathbf{p}$ is the relative momentum of the final neutron-proton system, E_1 represents the transition $^3S\to{}^3P$, and E_2 and E_3 correspond to the transition $^3D\to{}^3P$. It may be seen from this result that if $T(p)$ is constant for small p, the electric dipole cross section becomes proportional to $1/p$ at very low photon energy. In contrast to this, if $T(p)\propto p^2$ at small p as in the case of (20), the contribution from $^3D\to{}^3P$ is reasonably small at low photon energy.

Next let us compare our result (34) with that of the "central" potential. For this purpose, it is convenient

[16] R. S. Christian and E. W. Hart, Phys. Rev. **77**, 441 (1950); R. S. Christian and H. P. Noyes, Phys. Rev. **79**, 85 (1950); K. M. Case and A. Pais, Phys. Rev. **80**, 203 (1950); R. Jastrow, Phys. Rev. **81**, 165 (1951).

[17] A. Sugie and S. Yoshida, Progr. Theoret. Phys. **10**, 236 (1953); W. Rarita and J. Schwinger, Phys. Rev. **59**, 556 (1941); N. Austern, Phys. Rev. **85**, 283 (1952); T. M. Hu and H. S. W. Massey, Proc. Roy. Soc. (London) **A196**, 135 (1949). Other references will be found in I.

[18] N. Austern and R. G. Sachs, Phys. Rev. **81**, 710 (1951); N. Austern, reference 17.

[19] A. J. F. Siegert, Phys. Rev. **52**, 787 (1937); R. G. Sachs and N. Austern, Phys. Rev. **81**, 705, 710 (1951).

to introduce the "associated central potential" $-(\lambda_a/M)g_a(p)g_a(p')$, which is defined from the original interaction (1) including spin-orbit coupling as follows.

(i) The form of associated central potential is the same as the central part of the original potential; $g_a(p)=C(p)$.

(ii) The strength λ_a of the associated central potential is now determined so as to give the same value for the binding energy of the deuteron as that of the original interaction (1). Therefore the associated central potential does not exactly fit the low-energy data, even if the original potential (1) does fit. An example of this is given by the potential (20) with (33) fitted to low-energy neutron-proton data. The associated central potential has the value 5.759α for β, but the best-fit central potential has a different value, 6.255α, for β (see I, Sec. 3). It should be noted that the relation between the normalization constants N and N_a for the deuteron functions corresponding to the potential (1) and its associated central potential, respectively, is given by $N^2=N_a^2(1-P_D)$.

If we adopt the associated central potential, the electric dipole cross section turns out to be

$$\frac{d\sigma_e}{d\omega}=\frac{e^2}{4\pi}\frac{\alpha p^3}{(\alpha^2+p^2)^3}\frac{\pi^2N_a^2}{\alpha}E_1\sin^2\theta. \tag{35}$$

This form is, of course, the same as (33 E.D.) in I. Therefore, if in (34) we put $E_2=E_3=0$ and replace N by N_a [this fact is simply expressed by $t=0$, keeping in mind Eqs. (5), (6), and (7)], we find the result (35).

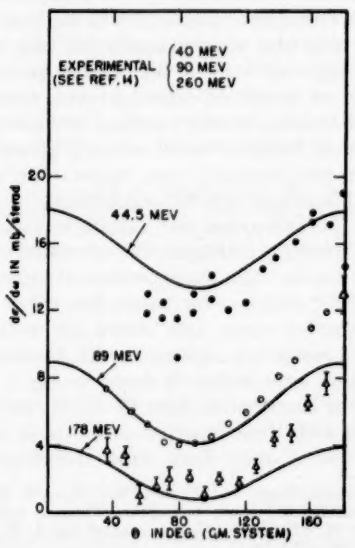

FIG. 3. The calculated average cross sections (triplet eigen-S plus singlet S scattering only) are compared with observation.

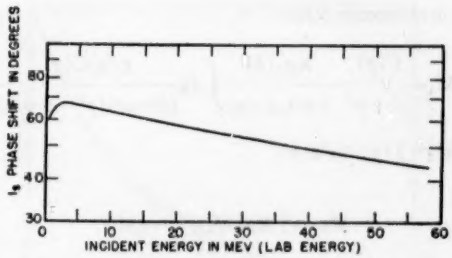

FIG. 4. ^1S phase shift is shown in this figure. This is calculated from Eqs. (18), (26), and (27) in I.

Example

If we adopt (20) for $g(\mathbf{p})$, the electric dipole cross section takes the form

$$\frac{d\sigma_e}{d\omega}=\frac{e^2}{4\pi}\frac{\alpha p^3}{(\alpha^2+p^2)^3}\frac{\beta(\alpha+\beta)}{(\beta-\alpha)^2}(1-P_D)$$
$$\times\left[\left\{1-\left(\frac{\alpha^2+p^2}{\beta^2+p^2}\right)^2\right\}^2\sin^2\theta\right.$$
$$+t^2\frac{(\beta^2-\alpha^2)^2(-\alpha^2\gamma^2+\alpha^2p^2+2p^4)^2}{(\gamma^2+p^2)^6}\sin^2\theta$$
$$\left.+\frac{3}{4}t^2\frac{(\beta^2-\alpha^2)^2(\alpha^2+p^2)^2}{(\gamma^2+p^2)^4}(1+\cos^2\theta)\right]$$
$$\equiv a_e+b_e\sin^2\theta, \tag{36}$$

where we use (22) and (25). If we put $t=0$, Eq. (36) has just the same form as Eq. (36 E.D.) in I.

(b) Magnetic Dipole Transition

As mentioned previously we shall not discuss here the effect of the interaction moment. The magnetic transition can then be evaluated unambiguously by using our wave functions. For future reference let us write down the singlet S potential $-(\lambda_s/M)g_s(p)g_s(p')$, and define $J_s(p)$ by

$$J_s(p)=\int d\mathbf{q}\frac{g_s^2(q)}{p^2-q^2+i\epsilon}.$$

The magnetic dipole cross section is

$$\frac{d\sigma_m}{d\omega}=\frac{1}{6}\frac{e^2}{4\pi}\left(\frac{\mu_p-\mu_n}{M}\right)^2\pi^2N^2p(\alpha^2+p^2)$$
$$\times\left[|M_1|^2+|M_2|^2+M_3\frac{3\cos^2\theta-1}{2}\right], \tag{37}$$

where θ is again the angle between the photonproton and the incident photon, M_1 and M_2 correspond to the $^3S\to{}^1S$ and $^3D\to{}^1S$ transitions, respectively, and M_3 is

the interference term:

$$M_1=\frac{C(p)}{\alpha^2+p^2}\frac{\lambda_s g_s(p)}{1+\lambda_s J_s(p)}\int dq\frac{g_s(q)C(q)}{(q^2+\alpha^2)(p^2-q^2+i\epsilon)},$$

$$M_2=T(p)/(\alpha^2+p^2),$$

and

$$M_3=\sqrt{2}\ \mathrm{Re}(M_1M_2)-\tfrac{1}{2}M_2^2.$$

If we replace our triplet interaction by the associated central interaction, we get the result (37) with $t=0$, i.e., $N^2=N_a^2$, $(M_2)^2=M_3=0$. If $T(p)=0$ at $p=0$, the effect of the D wave deuteron function is very small near threshhold. Therefore our magnetic dipole cross section is equal to that corresponding to the associated triplet central potential except for the factor $1-P_D$. This holds also in the case of thermal-neutron capture by hydrogen.

Example

Let us again use the deuteron function (21) and the singlet S wave function described in I, Sec. 3. To avoid confusion, let us write

$$g_s(p)=1/(\beta_s^2+p^2)\quad\text{and}\quad C(p)=1/(\beta_t^2+p^2).\tag{38}$$

Then the magnetic dipole cross section is

$$\frac{d\sigma_m}{d\omega}=\frac{1}{6}\frac{e^2}{4\pi}\left(\frac{\mu_p-\mu_n}{M}\right)^2\alpha\beta_t(\alpha+\beta_t)^3(1-P_D)p(\alpha^2+p^2)$$
$$\times\left[\frac{\sin^2\delta_s}{p^2}[\ \ ]^2+\frac{t^2p^4}{(\alpha^2+p^2)^2(\gamma^2+p^2)^4}\right.$$
$$\left.-\left\{\frac{\sqrt{2}\sin\delta_s\cos\delta_s}{p}[\ \ ]+\frac{tp^2}{2(\alpha^2+p^2)(\gamma^2+p^2)^2}\right\}\right.$$
$$\left.\times\frac{tp^2}{(\alpha^2+p^2)(\gamma^2+p^2)^2}\frac{3\cos^2\theta-1}{2}\right]$$
$$\equiv a_m+b_m\sin^2\theta,\tag{39}$$

TABLE II. The thermal-neutron capture cross sections calculated from (40) and (33).

β_s/α	Singlet effective range r_{0s} (10^{-13} cm)	Capture cross section multiplied by neutron velocity $\sigma_{cap}v_n$ (10^{-20} cm³/sec)
7.00	1.914	7.05
6.50	2.067	6.95
6.25	2.153	6.93
6.00	2.246	6.88
5.75	2.348	6.83
5.50	2.459	6.78

where δ_s is the singlet S phase shift and

$$[\ \ ]=\frac{p\cot\delta_s}{(\alpha^2+p^2)(\beta_t^2+p^2)}+\frac{1}{\beta_t+\alpha}\left\{\frac{\alpha\beta_t-p^2}{(\alpha^2+p^2)(\beta_t^2+p^2)}-\frac{1}{(\alpha+\beta_s)(\beta_t+\beta_s)}\right\}.$$

For thermal neutron capture by hydrogen we can neglect the ${}^3D\to{}^1S$ transition and obtain the total cross section σ_{cap} as

$$\sigma_{cap}v_n=2\pi\frac{e^2}{4\pi}\left(\frac{\mu_p-\mu_n}{M}\right)^2\left(\frac{\alpha}{M}\right)^3\frac{\alpha+\beta_t}{\beta_t}(1-P_D)(a_s\beta_t)^2$$
$$\times\left[-\frac{1}{a_s\beta_t}\frac{\alpha+\beta_t}{\beta_t}+\frac{\alpha}{\beta_t}\frac{1}{(\alpha+\beta_s)(\beta_t+\beta_s)}\right],\tag{40}$$

where v_n is the incident neutron velocity in the laboratory system and a_s is the singlet scattering length at zero energy.

(c) Discussion

We have seen that the photodisintegration cross section can be expressed in a tractable form, and our approach has the particular advantage of showing the effect of tensor force. Although the results obtained above were derived on the assumption of a separable potential, some aspects are valid quite generally. For example, our electric dipole cross section (34) depends only on the form of the deuteron function (4), which may be regarded as free from the assumption of a separable nuclear potential, and as the solution for a local potential if preferable. [Note that the Hulthén function is the bound-state solution for the local Hulthén potential and also simultaneously for the separable potential $g(p)=(p^2+\beta^2)^{-1}$.] We can also generalize the concept of an associated central potential for any type of potential with spin-orbit coupling. The photodisintegration cross sections based on such potentials will obey the relationships stated above. We are now interested in comparison with experiment.

Table II summarizes our calculation on thermal neutron capture by hydrogen. The calculated values are definitely smaller than the experimental value,[20] $\sigma_{cap}v_n=7.30\times10^{-20}$ cm³/sec, for reasonable values for the singlet effective range and shows the evidence for interaction moment in agreement with Austern.[21]

The dipole cross section is shown in Fig. 5. We can see that the contribution from ${}^3S\to{}^3P$ is essentially in agreement with those reported on the basis of a local Hulthén force,[22] apart from minor difference coming

[20] Hamermesh, Ringo, and Wexler, Phys. Rev. **90**, 603 (1953); Harris, Muehlhause, Rose, Schroeder, Thomas, and Wexler, Phys. Rev. **91**, 125 (1953); G. von Dardel and A. W. Waltner, Phys. Rev. **91**, 1284 (1953).

[21] N. Austern, Phys. Rev. **92**, 670 (1953).

[22] See I, where other references will be found.

from difference choices for the values of β_t and the factor $1-P_D$. The ${}^3D \rightarrow {}^3P$ transition becomes, however, more important with increasing photon energy and causes a rapid increase of the isotropic part $a=a_e+a_m$ in the angular distribution of photoprotons; see Fig. 5. In the magnetic dipole transition the D wave $w(p)$ of the deuteron gives some contribution. Thus we may conclude that the isotropic component $a=a_e+a_m \simeq a_e$ is a direct measure of $w(p)$ at a moderate photon energy. Up to the present there are no definite experimental results[23] about the isotropic part up to 20 Mev, and thus our results naturally do not contradict observation (the calculated total cross sections are in agreement with observation). At higher energies precise experiments by the Illinois group are now available.[24] Their total cross sections at 20–60 Mev photon energy are in reasonable agreement with our results but the angular distributions do not agree with our theoretical calculations. But one can expect to find larger values for a/b if one adopts a *larger* value for the D-state probability P_D than 4 percent.

At still higher energies the experimental cross sections are definitely larger than our prediction. However, at these energies we must certainly take into account effects disregarded so far; namely, (i) higher multipole transitions, (ii) forces in P or higher-angular-momentum states (see Austern[17]), and (iii) interaction moments or mesonic effects, and so on. One can hardly say anything without a careful examination of each of these points.

It should be noted that the smallness of P_D or Q does not necessarily mean that the D wave function $w(p)$ of the deuteron must be small at large p. Thus the possible and probable importance of D wave at large p remains one of our conclusions which is valid generally, because this statement follows directly from the form of deuteron function itself and is not dependent upon the assumption of a separable force.

Finally we should like to emphasize again the ease with which the approach presented in this paper handles the two-nucleon problem. The ability of the interaction (20) to fit observed results, in spite of its simple form, is remarkable. A slightly different separable nuclear potential with spin-orbit coupling was considered independently by Gell-Mann, Goldberger, and Bloch.[25] These authors started with the radial wave equations, in which the nuclear forces were assumed to be factorable.

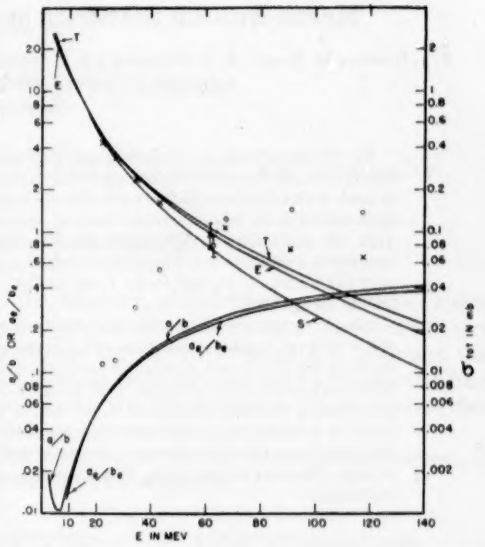

FIG. 5. The dipole cross section for $d(\gamma,p)n$ takes the form $d\sigma/d\omega=a+b\sin^2\theta$, $a=a_e+a_m$, $b=b_e+b_m$ [see Eqs. (36) and (39)]. The curves labeled T, E and S are T: the total cross section (E.D. plus M.D.), E: the total cross section for E.D. transition, and S: the contribution from ${}^3S \rightarrow {}^3P$ in the E.D. transition. The ratios a/b and a_e/b_e are also shown in this figure. It is noted that our calculations are based on the D-state probability P_D of 4 percent. Experimental results are shown by ×: total cross section, and o: a/b. The abscissa is the total energy E; E=(photon energy)+(kinetic energy of the incident deuteron) in the c.m. system.

We are deeply indebted to Professor G. F. Chew for his valuable discussions throughout this work. We also wish to thank Dr. A. O. Hanson, Mr. L. Allen, and Mr. E. A. Whalin for their discussion of the photodisintegration of the deuteron and for informing us of their results before publication.

[23] V. E. Krohn and E. F. Shrader, Phys. Rev. **86**, 391 (1952); H. Waffler and S. Younis, Helv. Phys. Acta **24**, 483 (1951); J. Halpern and E. V. Weinstock, Phys. Rev. **91**, 934 (1953).

[24] Allen, Hanson, and Whalin (private communication).

[25] Bloch, Gell-Mann, and Goldberger (unpublished).

Meson-Nucleon Scattering in the Tamm-Dancoff Approximation*

F. J. Dyson,† M. Ross,‡, E. E. Salpeter,§ S. S. Schweber,‖ M. K. Sundaresan, W. M. Visscher, and H. A. Bethe
Laboratory of Nuclear Studies, Cornell University, Ithaca, New York

(Received May 26, 1954)

An attempt is made to calculate meson-nucleon scattering by using charge-symmetric pseudoscalar meson theory with pseudoscalar coupling and without the use of perturbation theory. The Tamm-Dancoff formalism is used, with all states which are not directly coupled to the one-meson, one-nucleon state omitted. In this approximation an inhomogeneous integral equation in three-dimensional momentum space is derived for $g(\mathbf{p})$, the probability amplitude for relative momentum $\mathbf{p}$ between meson and nucleon. This equation is reduced to a separate one-dimensional integral equation for each of the six angular momentum and isotopic spin (T) states, $S_{\frac{1}{2}}$, $P_{\frac{1}{2}}$, and $P_{\frac{3}{2}}$ for $T=\frac{1}{2}, \frac{3}{2}$. The phase shifts for these states are given by the value of $g(p)$ on the energy-shell.

All self-energy and renormalization terms are omitted and the present method is inapplicable to the two states of total angular momentum and T equal to $\frac{1}{2}$. The integral equations are solved by semi-numerical methods for the $S_{\frac{3}{2}}$ and $P_{\frac{3}{2}}$ states with $T=\frac{3}{2}$, obtaining the shape of $g(p)$ and the variation of phase shift with energy and coupling constant. It is shown that only for the $P_{\frac{3}{2}}$, $T=\frac{3}{2}$ (corresponding to an attractive potential) is the phase shift much larger than in Born approximation and depends strongly on the coupling constant and on energy. For the other, repulsive, states the phase shift is less than in Born approximation. For energies of about 150 Mev or more and for a large enough coupling constant, the $P_{\frac{3}{2}}$, $T=\frac{3}{2}$ phase shift is larger than any of the others. This is in rough qualitative (but by no means quantitative) agreement with experiment.

I. INTRODUCTION

EXPERIMENTS on the angular distribution and total cross-section for ordinary and charge-exchange scattering of pions on protons have now been performed at various energies up to 135 Mev and higher.[1] An analysis of these experiments[1] indicates that they are compatible with the assumption of charge symmetry and that the results can be well represented in terms of six phase shifts (for each energy) α_1, α_{11}, α_{13}, the phase shifts for the $S_{\frac{1}{2}}$, $P_{\frac{1}{2}}$ and $P_{\frac{3}{2}}$ states of isotopic spin T equal to $\frac{1}{2}$, and α_3, α_{31}, α_{33}, the corresponding phase shifts for $T=\frac{3}{2}$. At energies approaching 150 Mev the dominating feature of such an analysis is the fact[1,2] that α_{33}, the $P_{\frac{3}{2}}$, $T=\frac{3}{2}$ phase shift, is much larger than any of the other five. On the other hand, if a second-order perturbation method is used on symmetric pseudoscalar meson theory, larger phase shifts are obtained for the S states than for P states, giving results not even in qualitative agreement with experiment. Chew[3] pointed out that, since the coupling constant used is very large, such a perturbation method is equivalent to using lowest-order Born approximation for the scattering from a very strong potential, which is well known to give misleading results. In particular the equivalent potential is attractive only for the $P_{\frac{3}{2}}$, $T=\frac{3}{2}$ state, so one would expect the correct phase shift α_{33} to be much larger than on Born approximation, but the phase shifts for all the other five "repulsive" states to be less than on Born approximation. This is in agreement with the earlier observation by Drell and Henley[4] that at least in the S states an effectively repulsive potential is obtained if the perturbation theory is avoided by a contact transformation, and that the S phase shifts are greatly reduced accordingly.

The present paper reports an attempt started[5] in the fall of 1952 to calculate pion-nucleon scattering phase shifts and using approximate methods but not using expansions in powers of the large coupling constant. The method used is essentially the Tamm-Dancoff treatment[6] of conventional three-dimensional field theory, involving an expansion of state vectors in terms of states corresponding to different numbers of virtual mesons and nucleon pairs present in the field. The treatment is applied to the charge-symmetric pseudoscalar meson theory with pseudoscalar coupling. To obtain relatively simple equations, only the states directly coupled to the principal one-meson, one-nucleon state are considered. This approximation is a drastic one but it goes much beyond perturbation theory.

With this approximation the problem can be reduced to an equation of motion in the form of a single integral equation for $g(\mathbf{p})$, the probability amplitude of a relative momentum $\mathbf{p}$ between pion and proton in the principal one-meson, one-nucleon state. This integral equation, derived in Sec. II, can be greatly simplified by using the

* Work supported in part by the U. S. Office of Naval Research.
† Now at the Institute for Advanced Study, Princeton, New Jersey.
‡ National Science Foundation Post-Doctoral Fellow now at Brookhaven National Laboratories, Upton, New York.
§ On leave of absence from Cornell at the Australian National University, Canberra, Australia.
‖ National Science Foundation Post-Doctoral Fellow.
[1] Anderson, Fermi, Martin and Nagle, Phys. Rev. **91**, 155 (1953); Fermi, Glicksman, Martin, and Nagle, Phys. Rev. **92**, 161 (1953); Barnes, Angell, Perry, Miller, Ring, and Nelson, Phys. Rev. **92**, 1327 (1953); Bodansky, Sachs, and Steinberger, Phys. Rev. **90**, 996 (1953); A. Roberts and J. Tinlot, Phys. Rev. **90**, 951 (1953).
[2] K. Brueckner, Phys. Rev. **86**, 106 (1952).
[3] G. F. Chew, Phys. Rev. **89**, 591 (1953).
[4] S. Drell and H. A. Henley, Phys. Rev. **88**, 1053 (1952).
[5] Dyson, Schweber, and Visscher, Phys. Rev. **90**, 372 (1953).
[6] I. Tamm, J. Phys. (U.S.S.R.) **9**, 449 (1945); S. Dancoff, Phys. Rev. **78**, 382 (1950).

conservation of isotopic spin, angular momentum, and parity (Secs. III to V), as was already pointed out by Chew.[3] For each value of T, j, and parity, the wave function $g(\mathbf{p})$ is thereby reduced to a function of a single variable, the magnitude of the momentum $\mathbf{p}$. In agreement with the general scattering theory of Lippmann and Schwinger[7] and Goldberger,[8] the function $g(\mathbf{p})$ is separated into an incident wave,

$$\delta(E-E(p)-\omega(p)),$$

and a scattered wave,

$$\mathrm{P}(1/[E-E(p)-\omega(p)])f(p)$$

(P=principal part), and it is shown (Sec. VI) that the scattering phase shift is directly related to the value of $f(p)$ on the energy shell, $f(k)$.

The integral equation for $f(p)$, Eq. (27), is an inhomogeneous one, and the Born approximation corresponds to carrying only the inhomogeneous term. Although the scattering phase shift is given directly by the value of $f(p)$ "on the energy shell," for its correct evaluation the integral equation has to be solved for all values of p (off the energy shell).

No attempt is made in the present paper to relate the Tamm-Dancoff formalism to more fully covariant four-dimensional treatments.[9] As a consequence all self-energy and renormalization terms had to be omitted, and the analysis could not be carried to completion for the two states of total angular momentum and isotopic spin of $\frac{1}{2}$. The integral equations are investigated in detail for two of the four remaining states, the $S_{\frac{1}{2}}$ and $P_{\frac{1}{2}}$ states with $T=\frac{3}{2}$, which experimentally show the largest phase shifts and most interesting energy dependence. Even these simplified equations cannot be solved by analytic means so that numerical or semi-numerical methods of solution had to be applied. Mainly to test the suitability of different numerical methods, the solutions for the two states of interest were carried out by slightly different means. In Secs. IX and X we give the approximations thus obtained for the shape of the "wave function" $g(\mathbf{p})$ and for the variation of phase shift with energy and with coupling constant. The results are discussed in Sec. XI.

II. DERIVATION OF THE EQUATION OF MOTION

An arbitrary state vector can be expanded in terms of the complete set of eigenfunctions of the number operators of the various free-field quanta. These are given by[10]

$$N^N=\int d^3p\sum_{i=1}^{2}a_i^*(\mathbf{p})a_i(\mathbf{p}),$$

$$N^{AN}=\int d^3p\sum_{i=1}^{2}b_i^*(\mathbf{p})b_i(\mathbf{p}),\quad\text{with}\quad b_i(\mathbf{p})=a_i^*(\mathbf{p}),\quad(1)$$

$$N_i^M=\int d^3k c_i^*(\mathbf{k})c_i(\mathbf{k}),$$

for the nucleons, antinucleons, and mesons, respectively. One readily establishes that these have as their eigenvalues the positive integers and zero, and that their eigenfunctions are obtained by repeated applications of the creation operators of the various field quanta on the vacuum state vector.

Our state vector for the meson-nucleon system, Ψ, can therefore be written as

$$\Psi=\psi^{(0,0;0)}\Phi_0+\frac{1}{(1!)^{\frac{1}{2}}}\sum_r\int d^3p\psi^{(1,0;0)}(\mathbf{p},r)a_r^*(\mathbf{p})\Phi_0$$
$$+\frac{1}{(1!)^{\frac{1}{2}}(1!)^{\frac{1}{2}}}\sum_r\sum_i\int d^3p\int d^3k\psi^{(1,0;1)}$$
$$\times(\mathbf{p},r;k,i)a_r^*(\mathbf{p})c_i^*(\mathbf{k})\Phi_0+\cdots.\quad(2)$$

The $\psi^{(m,n;l)}(\mathbf{p}_1s^{(1)},\mathbf{p}_2s^{(2)},\cdots\mathbf{p}_ms^{(m)};\mathbf{q}_1t^{(1)},\mathbf{q}_2t^{(2)},\cdots\mathbf{q}_nt^{(n)};\mathbf{k}_1i^{(1)},\mathbf{k}_2i^{(2)},\cdots\mathbf{k}_li^{(l)})$ are then the probability amplitudes for finding m "bare" nucleons with momenta and spins and isotopic spins specified by $\mathbf{p}_1$, $\mathbf{p}_2$, $\cdots\mathbf{p}_m$, $s^{(1)}$, $s^{(2)}$, $\cdots s^{(m)}$; n "bare" antinucleons specified by the $\mathbf{q}_1$, $\cdots\mathbf{q}_n$; $t^{(1)}$, $\cdots t^{(n)}$ variables; and l mesons specifield by the $\mathbf{k}$, i variables. This interpretation follows from the fact that the probability amplitude for finding for example a single nucleon of momentum p and spin and isotopic spin specified by s, in an experiment carried out on our system is given by

$$(a_s^*(\mathbf{p})\Phi_0,\Psi)=g^{(1,0;0)}(\mathbf{p},s).\quad(3)$$

Similarly the one-meson one-nucleon probability amplitude is given by

$$(a_s^*(\mathbf{p})c_i^*(\mathbf{k})\Phi_0,\Psi)=g^{(1,0;1)}(\mathbf{p},s;\mathbf{k},i).\quad(3a)$$

It should be noticed that $g^{(m,n;l)}(\mathbf{p}_1s^{(1)}\cdots\mathbf{p}_ms^{(m)};\mathbf{q}_1t^{(1)}\cdots\mathbf{q}_nt^{(n)};\mathbf{k}_1i^{(1)}\cdots\mathbf{k}_li^{(l)})$ is an antisymmetric function in the $\mathbf{p}s$ variables and $\mathbf{q}t$ variables, separately, and a symmetric function in the meson variables $\mathbf{k}i$.

The Schrödinger equation,

$$(H_0+H_I)\Psi=E\Psi,\quad(4)$$

where H_0=non-interacting free-field Hamiltonians and H_I=interaction Hamiltonian,

$$=iG\int d^3x\bar{\psi}(\mathbf{x})\gamma_5\tau_a\phi_a(\mathbf{x})\psi(\mathbf{x}),\quad(4a)$$

[7] B. Lippmann and J. Schwinger, Phys. Rev. **79**, 469 (1950).
[8] M. L. Goldberger, Phys. Rev. **84**, 929 (1951).
[9] M. Cini, Nuovo cimento **10**, 526 and 614 (1953); Karplus, Kievelson, and Martin, Phys. Rev. **90**, 1072 (1953); S. Deser and P. C. Martin, Phys. Rev. **90**, 1075 (1953); F. J. Dyson, Phys. Rev. **91**, 1543 (1953).
[10] See Appendix for the decomposition of operators.

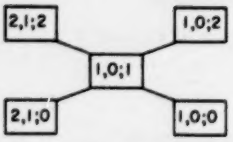

FIG. 1. The states directly coupled to the one-meson one-nucleon state.

can now be transcribed in terms of the amplitudes $g^{(m,n;I)}$. When this is done, an infinite set of coupled integral equations in the amplitudes $g^{(m,n;I)}$ is obtained. As such an infinite set of equations is not readily amenable to calculations when nucleon recoil effects are included, we have solved these equations in the lowest Tamm-Dancoff (hereafter abbreviated as T-D) approximation. The T-D approximation consists in describing the state vector Ψ in terms of only a finite number of amplitudes $g^{(m,n;I)}$ instead of in terms of an infinite set. Within this approximation, however, one then calculates all the amplitudes exactly. The particular approximation we have carried through consists in keeping only those amplitudes which are directly coupled to the one-meson one-nucleon amplitude in the state vector Ψ. This can be represented by Fig. 1. Stated concisely, we have described our state vector Ψ in terms of the amplitudes $g^{(1,0;1)}$, $g^{(1,0;0)}$, $g^{(1,0;2)}$, $g^{(2,1;2)}$, and $g^{(2,1;0)}$ only.

We shall now briefly indicate a method by which the equation of motion for these amplitudes can be obtained from the Schrödinger equation $(H_0+H_I)\Psi=E\Psi$ for the state vector. This equation is to be solved with the usual boundary condition imposed on a scattering state. In the calculations to be described, we have adopted the Goldberger[8] formalism for scattering theory in terms of standing waves. The integral equation for the state vector which incorporates the standing wave foundary condition is then given by

$$\Psi_a^{(1)}=\Phi_a+\mathrm{P}(1/[E_a-H_0])H_I\Psi_a^{(1)}, \tag{5}$$

where Φ_a is an eigenfunction of H_0 with eigenvalue E_a and corresponds to the incoming plane wave. P denotes the fact that the Cauchy principal value is to be taken for the resonance denominators. In the present problem,

$$\Phi_a=a_s^*(\mathbf{p}_0)c_i^*(\mathbf{k}_0)\Phi_0, \quad E_a=E(p_0)+\omega(k_0), \tag{6}$$

where $E(p_0)=(M^2+p_0^2)^{\frac{1}{2}}$, $\omega(k_0)=(\mu^2+k_0^2)^{\frac{1}{2}}$, p_0,s and k_0,i being the variables specifying the nucleon and meson, respectively, in the laboratory system. If we form the matrix element of Eq. (5) with the base vector $a_r^*(\mathbf{p})c_n^*(\mathbf{k})$, we obtain the equation for $g^{(1,0;1)}(\mathbf{p},r;\mathbf{k},n)$ in the form

$$\begin{aligned}(a_r^*(\mathbf{p})c_n^*(\mathbf{k})\Phi_0,\Psi_a^{(1)})&=g^{(1,0;1)}(\mathbf{p},r;\mathbf{k},n)\\&=(a_r^*(\mathbf{p})c_n^*(\mathbf{k})\Phi_0, a_s^*(\mathbf{p}_0)c_i^*(\mathbf{k}_0)\Phi_0)\\&\quad+(a_r^*(\mathbf{p})c_n^*(\mathbf{k})\Phi_0, \mathrm{P}(1/[E_a-H_0])H_I\Psi_a^{(1)}).\end{aligned} \tag{7}$$

Consider the last term in this expression which contains the interaction energy operator H_I. This operator can be expressed in terms of creation and destruction operators for the various field quanta according to the decompositions given in the Appendix. One of the terms in the decomposition of H_I corresponds to the creation of a meson with the scattering of the nucleon. We consider this term $H_I^{(a)}$ in detail. Explicitly, it is given by

$$\begin{aligned}H_I^{(a)}=iG\int d^3p_1\int d^3p_2\int d^3k\sum_{i,j}a_i^*(\mathbf{p}_1)a_j(\mathbf{p}_2)\\\times c_l^*(\mathbf{k})\delta(\mathbf{p}_1-\mathbf{p}_2+\mathbf{k})\bar{u}_i(\mathbf{p}_1)\gamma_5\tau_l u_j(\mathbf{p}_2).\end{aligned} \tag{8}$$

It is obvious that the only nonvanishing contribution to this matrix element comes from the $g^{(1,0;0)}$ amplitude of $\Psi_a^{(1)}$. One obtains for this

$$\begin{aligned}&iG\int d^3p_1\int d^3p_2\int d^3k_1\int d^3p'\sum_{i,j}(\Phi_0, a_r(\mathbf{p})c_n(\mathbf{k})\\&\quad\times\mathrm{P}(1/[E_a-H_0])a_i^*(\mathbf{p}_1)a_j(\mathbf{p}_2)c_l^*(\mathbf{k}_1)a_s^*(\mathbf{p}')\Phi_0)\\&\quad\cdot\delta(\mathbf{p}_1-\mathbf{p}_2+\mathbf{k}_1)\bar{u}_i(\mathbf{p}_1)\gamma_5\tau_l u_j(\mathbf{p}_2)g_s^{(1,0;0)}(\mathbf{p}')\\&=iG\int d^3p_1\int d^3p_2\int d^3k_1\int d^3p'\sum_{i,j}(\Phi_0, a_r(\mathbf{p})c_n(\mathbf{k})\\&\quad\cdot\mathrm{P}(1/[E_a-H_0])a_i^*(\mathbf{p}_1)\delta_{js}\delta(\mathbf{p}'-\mathbf{p}_2)c_l^*(\mathbf{k}_1)\Phi_0)\\&\quad\cdot\delta(\mathbf{p}_1-\mathbf{p}_2+\mathbf{k}_1)\bar{u}_i(\mathbf{p}_1)\gamma_5\tau_l u_j(\mathbf{p}_2)g_s^{(1,0;0)}(\mathbf{p}')\\&=iG\int d^3p_1\int d^3p_2\int d^3k_1\sum_i(\Phi_0, a_r(\mathbf{p})c_n(\mathbf{k})\\&\quad\cdot a_i^*(\mathbf{p}_1)c_l^*(\mathbf{k}_1)\Phi_0)\cdot\mathrm{P}(1/[E-E(p_1)-\omega(k_1)])\\&\quad\cdot\delta(\mathbf{p}_1-\mathbf{p}_2+\mathbf{k}_1)\bar{u}_i(\mathbf{p}_1)\gamma_5\tau_l u_j(\mathbf{p}_2)g_j^{(1,0;0)}(\mathbf{p}_2)\\&=iG\int d^3p_1\int d^3p_2\int d^3k_1\delta_{ri}\delta(\mathbf{p}_1-\mathbf{p})\delta_{nl}\delta(\mathbf{k}_1-\mathbf{k})\\&\quad\cdot\mathrm{P}(1/[E-E(p_1)-\omega(k_1)])\cdot\delta(\mathbf{p}_1-\mathbf{p}_2+\mathbf{k}_1)\\&\quad\times\bar{u}_i(\mathbf{p}_1)\gamma_5\tau_l u_j(\mathbf{p}_2)g_j^{(1,0;0)}(\mathbf{p}_2)\\&=iG\mathrm{P}(1/[E-E(p)-\omega(k)])\bar{u}_r(\mathbf{p})\gamma_5\tau_n\\&\quad\times u_j(\mathbf{p}_1+\mathbf{k}_1)g_j^{(1,0;0)}(\mathbf{p}_1+\mathbf{k}_1).\end{aligned} \tag{9}$$

Following this procedure, we obtain an equation for $g^{(1,0;1)}$ which involves coupling to the four other amplitudes. Similarly, one derives equations of motion for the amplitudes $g^{(1,0;0)}$, etc., which as a result of our particular approximation couple back only to the $g^{(1,0;1)}$ amplitude.[11] It is therefore possible to substitute the expression for these amplitudes back in the equation for $g^{(1,0;1)}$ and thus obtain an integral equation for $g^{(1,0;1)}(\mathbf{p},\mathbf{k})$ alone. This restates the Schrödinger equation in our approximation. The integral equation for the $g(\mathbf{p},\mathbf{k})$ [hereafter the superscript (1,0,1) will be

[11] If more states were kept, then one would have gotten a set of coupled integral equations, which could not be reduced to a single integral equation except by having the kernel in the form of an infinite sum with the coupling constant as the expansion parameter, which would be against the spirit of the present approach.

dropped, since we shall be concerned with this amplitude only] is

$$[E-E(p)-\omega(k)]g_{u\alpha}(\mathbf{p},\mathbf{k})=-\frac{G^2}{16\pi^3}\int d^3s\frac{M^2}{E(p)E(\mathbf{p}+\mathbf{s})\omega(s)}\bar{u}(\mathbf{p})\gamma_5\left\{\frac{3\Lambda_+(\mathbf{p}+\mathbf{s})}{E-E(\mathbf{p}+\mathbf{s})-\omega(k)-\omega(s)}\right.$$
$$\left.+\frac{3\Lambda_-(-\mathbf{p}-\mathbf{s})}{E-2E(p)-E(\mathbf{p}+\mathbf{s})-\omega(s)-\omega(k)}\right\}\gamma_5 u(\mathbf{p})g_{u\alpha}(\mathbf{p},\mathbf{k})+\frac{G^2}{16\pi^3}\int d^3s\frac{M^2}{E(s)E(\mathbf{s}+\mathbf{k})\omega(k)}$$
$$\times 2\,\mathrm{Sp}[\Lambda_+(\mathbf{s})\gamma_5\Lambda_-(-\mathbf{s}-\mathbf{k})\gamma_5]\cdot\left[\frac{1}{E-E(s)-E(\mathbf{s}+\mathbf{k})-E(p)}+\frac{1}{E-2E(p)-2\omega(k)-E(s)-E(\mathbf{s}+\mathbf{k})}\right]g_{u\alpha}(\mathbf{p},\mathbf{k})$$
$$+\frac{G^2}{16\pi^3}\int d^3s\int d^3t\frac{M^2}{E(s)E(t)\omega(\mathbf{s}+\mathbf{t})}\delta(0)\cdot\frac{6\,\mathrm{Sp}[\Lambda_+(\mathbf{s})\gamma_5\Lambda_-(\mathbf{t})\gamma_5]}{E-E(p)-\omega(k)-E(s)-E(t)-\omega(\mathbf{s}+\mathbf{t})}g_{u\alpha}(\mathbf{p},\mathbf{k})$$
$$-\frac{G^2}{16\pi^3}\int d^3s\left(\frac{M^4}{E(p)E^2(\mathbf{p}+\mathbf{k})E(\mathbf{p}+\mathbf{k}+\mathbf{s})\omega(k)\omega(s)}\right)^{\frac{1}{2}}\cdot\bar{u}(\mathbf{p})\gamma_5\left\{\frac{\tau_\alpha\Lambda_+(\mathbf{p}+\mathbf{k})\tau_\delta}{E-E(\mathbf{p}+\mathbf{k})}\right.$$
$$+\frac{\tau_\alpha\Lambda_-(-\mathbf{p}-\mathbf{k})\tau_\delta}{E-E(p)-E(\mathbf{p}+\mathbf{k})-E(\mathbf{p}+\mathbf{k}+\mathbf{s})-\omega(k)-\omega(s)}+\frac{\tau_\delta\Lambda_+(\mathbf{p}+\mathbf{s})\tau_\alpha}{E-E(\mathbf{p}+\mathbf{s})-\omega(k)-\omega(s)}$$
$$\left.+\frac{\tau_\delta\Lambda_-(-\mathbf{p}-\mathbf{s})\tau_\alpha}{E-E(\mathbf{p}+\mathbf{s})-E(\mathbf{p}+\mathbf{k}+\mathbf{s})-E(p)}\right\}\cdot\gamma_5 w(\mathbf{p}+\mathbf{s}+\mathbf{k})g_{w\delta}(\mathbf{p}+\mathbf{s}+\mathbf{k};-\mathbf{s}).\quad(10)$$

Here

$$\Lambda_+(\mathbf{p})=\frac{p+iM}{2iM}\quad\text{and}\quad\Lambda_-(\mathbf{p})=\frac{p-iM}{2iM}.\quad(11)$$

This equation contains nine terms describable by the following time-ordered Feynman graphs. The last four terms, which connect $g(\mathbf{p},\mathbf{k})$ with g for other momenta by an integral equation, arise from the graphs of Fig. 2

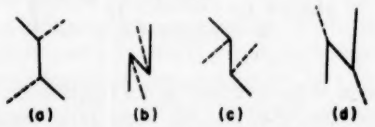

FIG. 2. The graphs responsible for meson-nucleon scattering.

which correspond to Compton scattering. The other five terms arise as a result of the self-energy processes indicated by the diagrams (α), (β), and (γ) of Fig. 3; (α) giving rise to the first two terms, (β) to the next two, and (γ) to the last one. These five terms, however, involve $g(\mathbf{p},\mathbf{k})$ only as a multiplicative factor. Since the $g(\mathbf{p},\mathbf{k})$ only occur in these five terms as a multiplicative factor, the correct treatment would be to transfer them to the left-hand side and obtain an equation of the form

$$[S_F(\mathbf{p})+\Delta_B(\mathbf{k})+\Delta E+1]g(\mathbf{p},\mathbf{k})=\int L(\mathbf{p},\mathbf{k};\mathbf{p}',\mathbf{k}')g(\mathbf{p}',\mathbf{k}')d^3\mathbf{k}'.\quad(12)$$

The first two factors on the left-hand side in a covariant treatment would correspond to using modified propagation functions (S_F' and Δ_F' rather than S_F and Δ_F), thus allowing for self-energy parts in the nucleon and meson lines in intermediary states. The ΔE term arises from graph (γ) and corresponds to a redefinition of the vacuum energy. In the present formalism we are prevented from evaluating these terms correctly since they diverge, and there exists at present no unambiguous method of subtracting all the self-energy parts.

The difficulty in renormalizing the vacuum self-energy term lies in the fact that we have diagonalized the total energy in the subspace of complete Hilbert space composed of not more than (2,1;2) particles. This means that the vacuum self energy is taken into account in the (1,0;1) state but not in the other intermediary states, thus causing a coupling between the physical system and the vacuum fluctuations. In this respect our present formalism is therefore wrong. A modified Tamm-Dancoff treatment, developed recently by one of us (F.J.D.)[9] bypasses this difficulty by defining the amplitudes with respect to the true vacuum state vector Ψ_0, rather than with respect to the bare vacuum state vector Φ_0 as done here. In such a treatment no vacuum self-energy term is present, and only the finite quantity $E-E_0$ (E_0=energy eigenvalue of true vacuum state) occurs. Furthermore, this modified form of the Tamm-Dancoff method has the great advantage that the self-energy parts can be unambiguously renormalized and the finite parts retained. In the present work we neglect the contribution due to the self energy terms.[12] The terms corresponding to the Compton

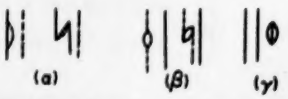

FIG. 3. The graphs involving renormalization corrections.

[12] Some of the renormalization terms have been evaluated by W. Visscher and will soon be published by him

diagrams (a), (b), (c), and (d) of Fig. 2 do not differ markedly in the "new" Tamm-Dancoff method from the ones evaluated in the present paper.

After neglect of the self-energy terms, we are left only with the last four terms in the integral equation (10). We write

$$\sum u(p)g_{u\alpha}(\mathbf{p},\mathbf{k})=g_\alpha'(\mathbf{p},\mathbf{k}),\quad Q_{\alpha\delta}'=\tau_\delta\tau_\alpha,\quad Q_{\alpha\delta}=\tau_\alpha\tau_\delta,$$

and go to the center-of-mass system, setting

$$g_\alpha'(\mathbf{p},\mathbf{k})\to g_\alpha'(\mathbf{p},\ -\mathbf{p})\equiv g_\alpha'(\mathbf{p}).$$

By utilizing the relations $\gamma_5\Lambda_+(\mathbf{p})\gamma_5=\Lambda_-(\mathbf{p})$; $\gamma_5\Lambda_-(\mathbf{p})\gamma_5=\Lambda_+(\mathbf{p})$, the equation may be written in the center-of-mass system as

$$[E-E(p)-\omega(p)]g'_\alpha(\mathbf{p})$$
$$=-\frac{G^2}{16\pi^3}\Lambda_+(\mathbf{p})\int d^3s\frac{M^2}{(E(p)\omega(p)E(s)\omega(s))^{\frac{1}{2}}}\Big\{Q_{\alpha\delta}\frac{\Lambda_-(0)}{E-M}+Q_{\alpha\delta}\frac{\Lambda_-(\mathbf{p}+\mathbf{s})\gamma_0\Lambda_+(0)}{E-E(p)-\omega(p)-E(s)-\omega(s)-M}$$
$$+Q_{\alpha\delta}'\frac{\Lambda_-(\mathbf{p}+\mathbf{s})}{E-E(\mathbf{p}+\mathbf{s})-\omega(p)-\omega(s)}+Q_{\alpha\delta}'\frac{\Lambda_+(-\mathbf{p}-\mathbf{s})}{E-E(\mathbf{p}+\mathbf{s})-E(p)-E(s)}\Big\}g_\delta'(\mathbf{s}).\quad(13)$$

Hereafter, since we are only going to deal with the amplitudes $g_\alpha'(\mathbf{p})$, we shall drop the prime on the g's, as there will be no confusion.

III. SEPARATION OF STATES OF DIFFERENT ISOTOPIC SPIN

The only operators in (13) involving isotopic spin are clearly Q and Q'. Their properties and eigenvalues may very easily be determined. $Q_{\alpha\delta}=\tau_\alpha\tau_\delta$, $Q_{\alpha\delta}^2=Q_{\alpha\beta}Q_{\beta\delta}=\tau_\alpha\tau_\beta\tau_\beta\tau_\delta=3Q_{\alpha\delta}$. Thus $Q_{\alpha\delta}$ has the eigenvalues 3 or 0. To assign these to isotopic spins, we note that $Q_{\alpha\delta}$ means the annihilation of the meson δ which is originally present, followed by the creation of a new meson, α. Now the annihilation can obviously only take place if $T=\frac{1}{2}$, because only for this isotopic spin do we have a state of the nucleon by itself. Hence $Q_{\frac{1}{2}}=3$ and $Q_{\frac{3}{2}}=0$. The other operator is

$$Q_{\alpha\delta}'=\tau_\delta\tau_\alpha=2-\tau_\alpha\tau_\delta,$$

and therefore has the eigenvalues,

$$Q_{\frac{1}{2}}'=-1,\quad Q_{\frac{3}{2}}'=2.$$

IV. REDUCTION OF WAVE FUNCTION TO LARGE COMPONENTS

Since $g(\mathbf{p})$ refers to a state of positive nucleon energy, it is clear that $\Lambda_-(\mathbf{p})g(\mathbf{p})=0$. We now write the four-component function

$$g(\mathbf{p})=\begin{pmatrix}g_+(\mathbf{p})\\ g_-(\mathbf{p})\end{pmatrix},$$

where $g_+(\mathbf{p})$ and $g_-(\mathbf{p})$ are two-component Pauli spinors. By eliminating the small components $g_-(\mathbf{p})$ in favor of the large components $g_+(\mathbf{p})$ we get

$$g(\mathbf{p})=\left(1+\frac{\gamma_5(\boldsymbol{\sigma}\cdot\mathbf{p})}{E(p)+N}\right)\begin{pmatrix}g_+(\mathbf{p})\\ 0\end{pmatrix}.$$

Since $(\boldsymbol{\sigma}\cdot\mathbf{p})$ is an invariant under rotations in 3-space, it is clear that $g(\mathbf{p})$ has the same total angular momentum as $g_+(\mathbf{p})$. It is convenient to make the reduction in this way, because $g_+(\mathbf{p})$ may be a function with definite orbital angular momentum, thus definite parity, while $g(\mathbf{p})$ clearly may not be.

Equation (13) then becomes

$$[E-E(p)-\omega(p)]g_\alpha(\mathbf{p})=-\frac{G^2}{16\pi^3}\frac{[-\beta\gamma_5(\boldsymbol{\sigma}\cdot\mathbf{p})+\beta E(p)+M]}{2M}\Big[\int d^3s\Big(\frac{M^4}{E(p)\omega(p)E(s)\omega(s)}\Big)^{\frac{1}{2}}\cdot\Big\{Q_{\alpha\delta}\frac{1-\beta}{2(E-M)}$$
$$+Q_{\alpha\delta}\frac{1+\beta}{2[E-E(p)-\omega(p)-E(s)-\omega(s)-M]}\Big\}+\int d^3s\frac{M^2}{[E^2(\mathbf{p}+\mathbf{s})E(p)\omega(p)E(s)\omega(s)]^{\frac{1}{2}}}$$
$$\cdot\Big\{Q_{\alpha\delta}'\frac{\beta\gamma_5[\boldsymbol{\sigma}\cdot(\mathbf{p}+\mathbf{s})]-\beta E(\mathbf{p}+\mathbf{s})+M}{2M[E-E(\mathbf{p}+\mathbf{s})-\omega(p)-\omega(s)]}+Q_{\alpha\delta}'\frac{\beta\gamma_5[\sigma\cdot(\mathbf{p}+\mathbf{s})]+\beta E(\mathbf{p}+\mathbf{s})+M}{2M[E-E(\mathbf{p}+\mathbf{s})-E(p)-E(s)]}\Big\}\Big]\Big(1+\frac{\gamma_5(\boldsymbol{\sigma}\cdot\mathbf{s})}{E(s)+M}\Big)g_\delta^+(\mathbf{s}).\quad(14)$$

To find the equation for $g_+(\mathbf{p})$ in terms of $g_+(\mathbf{s})$, we pick out the terms on the right-hand side which do not mix small and large components (i.e., those with Dirac matrices 1 or γ_5^2, and with any β's or σ's). Remembering that

$\gamma_\delta^2=1$, and that $\beta=1$ for the "large" component, we get

$$[E-E(p)-\omega(p)]g_{+\alpha}(\mathbf{p})=\frac{G^2}{64\pi^3}\Big[2\int d^3s\frac{1}{[E(p)\omega(p)E(s)\omega(s)]^{\frac{1}{2}}}\cdot Q_{\alpha\delta}\Big[\frac{(\boldsymbol{\sigma}\cdot\mathbf{p})(\boldsymbol{\sigma}\cdot\mathbf{s})}{(E-M)[E(s)+M]}$$
$$-\frac{E(p)+M}{E-E(p)-\omega(p)-E(s)-\omega(s)-M}\Big]+\int d^3s\frac{1}{[E^2(\mathbf{p}+\mathbf{s})E(p)\omega(p)E(s)\omega(s)]^{\frac{1}{2}}}Q_{\alpha\delta}'\Big\{\frac{1}{E-E(\mathbf{p}+\mathbf{s})-\omega(p)-\omega(s)}$$
$$\cdot\Big(\frac{(\boldsymbol{\sigma}\cdot\mathbf{p})(\boldsymbol{\sigma}\cdot\mathbf{s})[E(\mathbf{p}+\mathbf{s})+M]}{E(s)+M}-(\boldsymbol{\sigma}\cdot\mathbf{p})[\boldsymbol{\sigma}\cdot(\mathbf{p}+\mathbf{s})]+[E(p)+M][E(\mathbf{p}+\mathbf{s})-M]-\frac{[\boldsymbol{\sigma}\cdot(\mathbf{p}+\mathbf{s})](\boldsymbol{\sigma}\cdot\mathbf{s})[E(p)+M]}{E(s)+M}\Big)$$
$$-\frac{1}{E-E(\mathbf{p}+\mathbf{s})-E(p)-E(s)}\Big((\boldsymbol{\sigma}\cdot\mathbf{p})(\boldsymbol{\sigma}\cdot\mathbf{s})\frac{E(\mathbf{p}+\mathbf{s})-M}{E(s)+M}+(\boldsymbol{\sigma}\cdot\mathbf{p})[\boldsymbol{\sigma}\cdot(\mathbf{p}+\mathbf{s})]+[E(p)+M][E(\mathbf{p}+\mathbf{s})+M]$$
$$+[\boldsymbol{\sigma}\cdot(\mathbf{p}+\mathbf{s})](\boldsymbol{\sigma}\cdot\mathbf{s})\frac{E(p)+M}{E(s)+M}\Big)\Big\}\Big]g_{+\delta}(\mathbf{s}). \quad (15)$$

V. ELIMINATION OF ANGULAR AND SPIN DEPENDENCE OF THE INTEGRAL EQUATION

Let

$$A=E(p)+\omega(p)+E(s)+\omega(s)+M-E,$$
$$B=E(p)+E(s)-E,\quad C=\omega(p)+\omega(s)-E, \quad (16)$$

and let S_n and R_n be the operators defined by

$$S_ng(\mathbf{s})=\frac{1}{4\pi}\int d\Omega_s P_n(\Theta_s-\Theta_p)g(\mathbf{s})$$

and

$$R_ng(\mathbf{s})=\frac{1}{4\pi}\int d\Omega_s\frac{(\boldsymbol{\sigma}\cdot\mathbf{p})}{|p|}\frac{(\boldsymbol{\sigma}\cdot\mathbf{s})}{|s|}P_n(\Theta_s-\Theta_p)g(\mathbf{s}). \quad (17)$$

S_n clearly has the "eigenvalue" $1/(2n+1)$ for a state g with an orbital angular momentum $l=n$ in the sense that $S_ng(s,\Theta_s)=\delta_{nl}[1/(2l+1)]g(s,\Theta_p)$. The eigenvalues of R_n may be found as follows. Let $\phi(\mathbf{s})=[(\boldsymbol{\sigma}\cdot\mathbf{s})/|s|]g(\mathbf{s})$. Then, as has already been pointed out, $\phi(s)$ has the same total j as $g(\mathbf{s})$ but has the opposite parity. Thus if $g(s)$ has $l=j\pm\frac{1}{2}$, $\phi(s)$ has $l=j\mp\frac{1}{2}$ so that ϕ and g are symmetrically related to each other, and $g(\mathbf{s})=\phi(\mathbf{s})\cdot(\boldsymbol{\sigma}\cdot\mathbf{s})/|s|$, but inserting the definition of ϕ in (17), we may write $R_ng(\mathbf{s})=S_n\phi(\mathbf{s})(\boldsymbol{\sigma}\cdot\mathbf{p})/|p|$. Hence, R_n has eigenvalue $[1/(2n+1)]\delta_{n,l\pm1}$ in the same sense as before.

We define also:

$$[E(\mathbf{p}+\mathbf{s})]^{-1}=\sum_{n=0}^{\infty}X_nP_n(\Theta_s-\Theta_p),$$
$$[B+E(\mathbf{p}+\mathbf{s})]^{-1}=\sum_{n=0}^{\infty}Y_nP_n(\Theta_s-\Theta_p),$$

and

$$[C+E(\mathbf{p}+\mathbf{s})]^{-1}=\sum_{n=0}^{\infty}Z_nP_n(\Theta_s-\Theta_p). \quad (18)$$

Then we can evaluate such integrals as

$$\frac{1}{4\pi}\int d\Omega_s[E(\mathbf{p}+\mathbf{s})]^{-1}(\boldsymbol{\sigma}\cdot\mathbf{p})(\boldsymbol{\sigma}\cdot\mathbf{s})g(\mathbf{s})$$
$$=\sum_{n=0}^{\infty}|p||s|R_nX_ng(|s|),$$

and Eq. (18) becomes

$$[E-E(p)-\omega(p)]g(p)=\frac{G^2}{8\pi^2}\int_0^\infty\frac{s^2ds}{[E(p)\omega(p)E(s)\omega(s)]^{\frac{1}{2}}}\Big\{Q\frac{psR_0}{(E-M)(E(s)+M)}+Q\frac{[E(p)+M]S_0}{A}$$
$$+\frac{Q'}{2}\sum_n\Big[(Y_n-Z_n)\Big(S_n[E(p)+M]+\frac{psR_n}{E(s)+M}\Big)+\Big(\frac{1}{C}X_n+\frac{1}{B}X_n-\frac{1}{C}Z_n-\frac{1}{B}Y_n\Big)$$
$$\times\Big(\frac{psR_n[E(p)+E(s)+M]}{E(s)+M}+[E(p)+M][E(p)+E(s)-M]S_n\Big)\Big]\Big\}g(s). \quad (19)$$

The coefficients X_n, Y_n, and Z_n in the expression (18) can be easily determined. For this purpose write

$$E^2(\mathbf{p}+\mathbf{s})\equiv M^2+p^2+s^2+2psx\equiv\bar{E}^2(1+2rx+r^2), \quad (20a)$$

with $x=\cos(\Theta_s-\Theta_p)$. Then, clearly,

$$E(p+s)=\bar{E}(1+r),\quad E(p-s)=\bar{E}(1-r),$$

and

$$\bar{E}=[E(p+s)+E(p-s)]/2.$$

Also, by comparing coefficients in (20a),

$$r=ps/\bar{E}^2,\quad M^2+p^2+s^2=\bar{E}^2(1+r^2). \quad (20b)$$

Introducing further the abbreviations

$$z=E(\mathbf{p}+\mathbf{s})/\bar{E},\quad b=B/\bar{E},\quad\text{and}\quad c=C/\bar{E}, \quad (20c)$$

we get

$$x=(z^2-1-r^2)/2r;$$

and the coefficients become

$$X_n=(n+\tfrac{1}{2})(r\bar{E})^{-1}\int_{1-r}^{1+r}dzP_n\left(\frac{z^2-1-r^2}{2r}\right),$$

$$Y_n=(n+\tfrac{1}{2})(r\bar{E})^{-1}\int_{1-r}^{1+r}dz\left(\frac{z}{b+z}\right)P_n\left(\frac{z^2-1-r^2}{2r}\right),$$

and

$$Z_n=(n+\tfrac{1}{2})(r\bar{E})^{-1}\int_{1-r}^{1+r}dz\left(\frac{z}{c+z}\right)P_n\left(\frac{z^2-1-r^2}{2r}\right).$$

It is convenient to define the integrals

$$K_n(C)=\frac{1}{2ps}\int_{\bar{E}-R}^{\bar{E}+R}\frac{1}{C+Z}P_n\left(\frac{Z^2-\bar{E}^2-R^2}{2R}\right)dZ,$$

$$R=r\bar{E},\quad\text{and}\quad Z=z\bar{E},\tag{22}$$

and similarly $K_n(B)$. Then $X_n-Y_n=(2n+1)BK_n(B)$, and $X_n-Z_n=(2n+1)CK_n(C)$. Considering states with a definite l and j, we have seen above that the sum over n in (19) reduces to a single term, and S_n and R_n have the eigenvalues $\delta_{nl}/(2n+1)$ and $\delta_{n,l\pm1}/(2n+1)$, respectively, for $j=l\pm\frac{1}{2}$. Then (19) becomes

$$[E-E(p)-\omega(p)]g(p)=\frac{G^2}{8\pi^2}\int_0^\infty\frac{s^2ds}{[E(p)\omega(p)E(s)\omega(s)]^{\frac{1}{2}}}\cdot\Big\{Q\left(\frac{E(p)+M}{A}\right)_{S_{\frac{1}{2}}}+Q\left(\frac{1}{(E-M)}\frac{ps}{[E(s)+M]}\right)_{P_{\frac{1}{2}}}$$

$$+\tfrac{1}{2}Q'[E(p)+M][(A-2M)K_l(C)+(E-M)K_l(B)]+\tfrac{1}{2}Q'\frac{ps}{E(s)+M}[AK_{l\pm1}(C)+(E+M)K_{l\pm1}(B)]\Big\}g(s).\tag{23}$$

Thus finally we have an integral equation in one variable, the absolute momentum of the meson, which may be solved numerically. For scattering problems, $g(p)$ has a singularity because the factor $E-E(p)-\omega(p)$ becomes zero at a certain value of p, *viz.*, the momentum of the incident meson. Hence the integral equation has a singularity at this point, and its solution can be written in the form

$$g(p)=c\delta(E-E(p)-\omega(p))+\frac{1}{E-E(p)-\omega(p)}\times\int_0^\infty\frac{s^2ds}{[E(p)\omega(p)E(s)\omega(s)]^{\frac{1}{2}}}L(p,s)g(s),\tag{24}$$

where

$$L(p,s)=\text{expression in curly bracket in (23).}\tag{24a}$$

We may now define a nonsingular amplitude f by setting

$$g(p)=\delta(E-E(p)-\omega(p))+\mathrm{P}\frac{1}{E-E(p)-\omega(p)}f(p),\tag{25}$$

where we have set the normalization constant c in the previous expression equal to unity without any loss of generality since the normalization of $g(p)$ has not been fixed. In (25) we have chosen to take the principal value of the singular factor $[E-E(p)-\omega(p)]^{-1}$, since the use of purely real wave functions will simplify the numerical work. This means that $g(p)$ is required to be a standing wave (Lippmann and Schwinger,[7] Goldberger[8]). Next we shall find the relation of $f(p)$ to the scattering phase shift.

VI. RELATION OF $f(p)$ TO THE SCATTERING PHASE SHIFT

The asymptotic coordinate space wave function corresponding to $g(p)$ is determined wholly by the behavior of $\delta(E-E(p)-\omega(p))+\mathrm{P}(1/[E-E(p)-\omega(p)])$ near its singularity. If we designate the momentum of the incident meson by k, and assume that $f(p)$ is well-behaved near $p=k$, we may write

$$g(p)=\delta(p-k)+\mathrm{P}(1/[k-p])f(k)+R(p),$$

where $R(p)$ is a nonsingular function. A typical wave of angular momentum l behaves for large r as

$$g(\mathbf{r})\sim[j_l(kr)-\tan\delta\eta_l(kr)]Y_l^m(\mathbf{r})$$

(definition of the phase shift). Asymptotically, one finds that the singular part of the wave function is proportional to

$$g(\mathbf{r})=[\sin(kr-(l+\tfrac{1}{2})\pi/2)+\tan\delta_l\cos(kr-(l+\tfrac{1}{2})\pi/2)].$$

Expanding the radial function in terms of spherical Bessel functions $j_l(pr)$ whose asymptotic behavior is $\sin(pr-(l+\frac{1}{2})\pi/2)$, we find

$$g(p)=\delta(p-k)-(1/\pi)\tan\delta(1/[k-p])+R(p),$$

where R is a function of p which is regular at k. Therefore the identification may be made that

$$f(k)=-(1/\pi)\tan\delta,\tag{26}$$

and Eq. (24) becomes

$$f(p)=\frac{G^2}{8\pi^2}\int_0^\infty\frac{s^2}{[E(p)\omega(p)E(s)\omega(s)]^{\frac{1}{2}}}L(p,s)g(s)ds,\tag{27}$$

where $L(p,s)$ is given by the expression within the curly brackets of (23) and $g(s)$ stands for

$$g(s)=\delta(E-E(s)-\omega(s))+\mathrm{P}(1/[E-E(s)-\omega(s)])f(s).\tag{27a}$$

VII. DISCUSSION OF THE INTEGRAL EQUATION

The integral equation we have obtained after omitting all self-energy terms above for the meson-nucleon scat-

tering problem is an inhomogeneous one, and the terms therein arise as follows. The first and second terms in $L(p,s)$ arise from graphs (a) and (b), of Fig. 2, graph (a) contributing only to the $p_{\frac{1}{2}}$ state and (b) to the $S_{\frac{1}{2}}$ state respectively, and only for isotopic spin $\frac{1}{2}$. The next two terms arise from graphs (c) and (d), (c) giving the $K(C)$ terms and (d) giving the $K(B)$ terms.

The kernel L in the integral equation is real for $E<M+\mu$, where E is the actual energy of the system in the center-of-mass system. For energies greater than $M+\mu$, L becomes complex over the region of momenta for which the production of an additional real meson is possible. Thus for p (or s) between 0 and p_m, where p_m satisfies $\omega(p_m)+E(p_m)=E-\mu$, there is a pair of singularities in $\ln[(\bar{E}+C+R)/(\bar{E}+C-R)]$ at $[R/(C+\bar{E})]=\pm 1$, between which the logarithm is imaginary. Keeping the real and imaginary parts, one could calculate the total cross section for the production of an additional meson. This singularity in the kernel also affects the scattering problem. For simplicity, the principal part of the kernel alone was retained. If the energy is only slightly above threshold, $E-M-\mu\ll\mu$, the effect of the imaginary part of the kernel is small. Further, if we consider the cross section for meson production near threshold as small of first order, then the error made in the scattering calculation by retaining only the principal part is small of second order.

We now have the task of solving a one-dimensional integral equation with a real, nonsymmetric kernel $L(p,s)$ for the wave function $f(p)$, for each of the eigenstates of orbital and total angular momentum and isotopic spin. The quantity which can be compared directly with experiment is then the phase shift for each state δ, which is given in terms of the wave function "on the energy shell" $f(k)$ by the relation (26).

We focus our attention now on the S and P states. The functions K_l required for these states are

$$K_0(C)=\frac{1}{2ps}\ln\frac{\bar{E}+C+R}{\bar{E}+C-R},$$

$$K_1(C)=-\frac{1}{2ps}(M^2+p^2+s^2-C^2)K_0(C)+\frac{1}{2ps}\left(1-\frac{C}{\bar{E}}\right),$$

and

$$K_2(C)=-\frac{3}{4ps}(M^2+p^2+s^2-C^2)K_1(C)+\frac{C}{4\bar{E}^3}-\tfrac{1}{2}K_0(C); \tag{28}$$

and similarly for $K_l(B)$.

It will be convenient to compare our results with the equivalent Born approximation results. The lowest-order Born approximation can be obtained from Eq. (27) by retaining only the δ-function term in the expression for $f(s)$ in the integral on the right-hand side. The general expression for $f_B(p)$ is

$$f_B(p)=\frac{G^2}{8\pi^2}\left(\frac{E(k)\omega(k)}{E(p)\omega(p)}\right)^{\frac{1}{2}}\frac{k}{E}L(p,k);$$
$$E=E(k)+\omega(k). \tag{28a}$$

For the S and the P states, the expression for $L(p,k)$ involves K_0, K_1, and K_2 functions, for which the general expressions have been given above. If we now consider $(E-M)/M$ and μ/M small compared with unity, then the expansion parameters $R/(\bar{E}+C)$ or $R/(\bar{E}+B)$ involved in the logarithms in K_0, K_1, and K_2 are small,[13] hence the logarithms can be expanded in terms of the parameter, and the first terms retained. It may also be noticed[14] that $A-2M\sim\bar{E}+C$. Under these approximations the following simpler expressions for the first-order Born approximation are obtained.

$$S_{\frac{1}{2}}:\quad L(p,k)$$
$$=Q\frac{E(p)+M}{M}+\tfrac{1}{2}Q'\frac{E(p)+M}{\bar{E}}\left(1+\frac{E-M}{\bar{E}+B}\right),$$

$$P_{\frac{1}{2}}:\quad (pk)^{-1}L(p,k)$$
$$=Q\frac{1}{(E-M)(E(k)+M)}$$
$$+\tfrac{1}{2}Q'\left[-\frac{E(p)+M}{\bar{E}^2}\left(\frac{2\bar{E}+C}{3(\bar{E}+C)}+\frac{E-M}{2(\bar{E}+B)}\right)\right.$$
$$\left.+\frac{1}{\bar{E}[E(k)+M]}\left(1+\frac{2M}{\bar{E}+C}+\frac{E+M}{\bar{E}+B}\right)\right], \tag{29}$$

and

$$P_{\frac{1}{2}}:\quad (pk)^{-1}L(p,k)$$
$$=-\tfrac{1}{2}Q'\frac{E(p)+M}{\bar{E}^2}\left(\frac{2\bar{E}+C}{3(\bar{E}+C)}+\frac{E-M}{2(\bar{E}+B)}\right).$$

The quantity $\bar{E}$ which was previously a function of p and s is now a function of p and k. At low energies, i.e., $p<M$ it is found that the $K(B)$ terms arising from time ordered graph (d) are much smaller than the $K(C)$ terms arising from graph (c). The latter are particularly large as the denominators $\bar{E}+C$ are small. The Born approximation phase shifts are plotted against energy in Fig. 4. All these states are seen to imply a repulsive potential except the $P_{\frac{1}{2}}$, $T=\frac{3}{2}$ state. The use of Born approximation is based on the assumption that the effect of $f(s)$ in the integral equation is negligible compared to that of the delta function. But physically reasonable values of the coupling constant $G^2/4\pi$ are larger than unity rather than being small and the

[13] For $\bar{E}+C$ this is not quite obvious, since this quantity is small. If also $p\ll M$, then

$$\bar{E}+C\approx E(k)+\omega(k)+\omega(p)-E=\omega(p) \tag{a}$$

because of (28a). On the other hand,

$$R=r\bar{E}=pk/\bar{E}\sim pk/M, \tag{b}$$

and, since $p<\omega(p)$, we have $[R/(\bar{E}+C)]<k/M\ll 1$. If p is larger,

$$\bar{E}+C\approx E(p)+\omega(p)+\omega(k)-E\approx\omega(p)+E(p)-M, \tag{c}$$

which makes the result hold *a fortiori*.

[14] $A-2M=E(k)+\omega(k)-E+E(p)+\omega(p)-M$, which, by (28a) is equal to expression (c) in the preceding footnote.

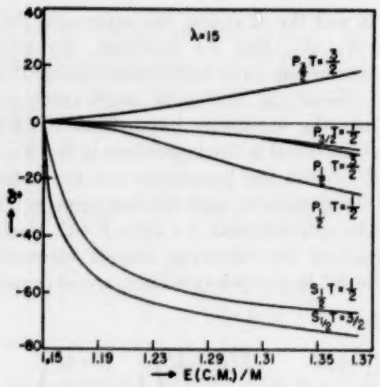

FIG. 4. Born approximation phase shifts as a function of c.m. energy $\lambda=15$.

effect of $f(s)$ is in fact quite large. The higher-order Born approximation could be obtained from Eq. (27) by using as initial trial wave function on the right-hand side the delta function instead of the whole $g(s)$, and then iterating the first-order Born approximation thus obtained. But since the $f(s)$ terms are so important this initial trial wave function is very poor, and the iteration procedure would converge very slowly, if at all. Because of the large G, we expect the first-order Born approximation results to be very poor, and direct solution of the integral equation is clearly necessary

VIII. GENERAL PROPERTIES OF THE INTEGRAL EQUATION

The kernel of our integral equation is a complicated function of the energy E as well as of the variables p and s. Therefore any accurate numerical solution of the equation will have to be found separately for each energy of interest. Before discussing such numerical solutions of our actual equation, however, some qualitative statements can be made on the general problem. Equation (27) may be rewritten by inserting (27a) and (28a) as

$$f(p)=f_B(p)-\frac{G^2}{8\pi^2}\int_0^\infty ds\frac{s^2}{[E(p)\omega(p)E(s)\omega(s)]^{\frac{1}{2}}}\times L(p,s)\frac{1}{E(s)+\omega(s)-E}f(s). \quad (30)$$

We shall now show that the determining feature of this equation is the *sign* of the integral on the right-hand side. If this is the same as the sign of $f(p)$, then the integral will tend to enhance $f(p)$ and the amplitude will be larger than the Born approximation amplitude f; if the integral has a sign opposite to that of $f(p)$, the reverse will be the case. Now $E(s)+\omega(s)-E$ is positive for most values of s; hence $L(p,s)$ must be *negative* in order to enhance f above the Born approximation value. From (29) it is seen that this will be the case, e.g., for the $P_{\frac{1}{2}}$ state if Q' is positive, which is true for $T=\frac{3}{2}$. Thus this state is apt to have a much higher phase shift than the Born approximation indicates, which offers hope that the observed large phase shift can be explained.

The situation for negative $L(p,s)$ is similar to that found in elementary problems with an attractive potential; in fact, the wave equation for the momentum wave function of the hydrogen atom has the form

$$[E-E(p)]g(\mathbf{p})=\int V(s-\mathbf{p})g(\mathbf{s})d^3s, \quad (31)$$

where $V(\mathbf{k})$ is the Fourier transform of the potential energy. The similarity with (23) is obvious, and it is also clear that $L(p,s)$, except for a factor, corresponds to $V(\mathbf{s}-\mathbf{p})$; hence negative L corresponds to a negative (attractive) potential. It is well known that in an attractive potential the scattering can be much larger than the Born approximation. In particular, we can have a *resonance* in which $(f/f_B)=\infty$. The same phenomenon can occur with our integral equation. If $L(p,s)$ is kept fixed and G is permitted to increase, a value of G will finally be reached at which the homogeneous equation, i.e., (30) without the term f_B, will have a solution. For this critical value of G, then, $f(k)=\infty$, and therefore [Eq. (26)] the phase shift δ is 90° as it should be for a resonance. (Incidentally, if L is negative, then also f_B is negative; therefore, as long as G is below its critical value, f is negative, and the phase shift is positive, as it should be for an attractive potential. For G greater than its critical value, f will have a sign opposite to f_B, hence positive, and δ is greater than 90°.)

If $L(p,s)$ is positive, we have the same situation as for a respulsive potential; f is less than the Born approximation, and a resonance cannot occur. An example is clearly the S state of $T=\frac{3}{2}$ for which (29) gives a positive $L(p,s)$. Thus the phase shift of this state will be less than the Born approximation which again gives hope for achieving agreement with experiment.

The $P_{\frac{1}{2}}$ state of $T=\frac{1}{2}$ is obviously also of repulsive character since $Q'=-1$ in this case. For the $P_{\frac{1}{2}}$ state we should consider primarily the terms with $\bar{E}+C$ in the denominator because this quantity is small compared with M, $\bar{E}$, etc. From (29) we find that

$$L(p,k)=pk\left\{Q\frac{1}{(E-M)[E(k)+M]}+\frac{Q'}{2}\left[-\frac{E(p)+M}{\bar{E}^3}\times\left(\frac{2\bar{E}+C}{3(\bar{E}+C)}\right)+\frac{1}{\bar{E}[E(k)+M]}\left(\frac{2M}{\bar{E}+C}\right)\right]\right\}.$$

This is clearly positive for $T=\frac{3}{2}$, $Q'=2$ so that this state is also repulsive. Both $P_{\frac{1}{2}}$, $T=\frac{1}{2}$ and $P_{\frac{3}{2}}$, $T=\frac{3}{2}$ are therefore expected to have small phase shifts in agreement with experiment.

This leaves the two states with $T=\frac{1}{2}$, $j=\frac{1}{2}$ (i.e. S and $P_{\frac{1}{2}}$). These cannot be treated by our present formalism. This is because for these states, and these

alone, it is possible for the meson to become absorbed by the nucleon in the intermediate state [graphs (a) and (b) of Fig. 2] (for all other quantum numbers this intermediate state is forbidden by conservation laws). Now the Tamm-Dancoff integral equation implies that the processes illustrated by the graphs can occur repeatedly, so that we are really considering graphs of the type shown in Fig. 5. These clearly contain self-energy graphs; hence they give the usual divergent results which must be removed by renormalization. But until now renormalization has only been carried out by perturbation theory, and this is not applicable in our strong-coupling problem. Therefore the two states in question of $T=\frac{1}{2}$ and $j=\frac{1}{2}$ are beyond the scope of this paper, and their treatment must be postponed to the future.

To get a better feeling for the working of the integral equation, we shall now discuss the solution of similar integral equations, but with kernels of a simplified form for which exact analytic solutions can be obtained. These cases illustrate the general relation between actual and Born-approximation wave functions as a function of the coupling constant and sign of the effective potential, but in a much simpler form than in our equation. One of these soluble cases is that in which the kernel has a maximum value when p and s are approximately equal to each other. The equation

$$f(p)=f_B(p)+\frac{G^2}{8\pi^2}\int_0^\infty dsL'(p,s)f(s)$$

may then be modified by taking $f(s)$ outside the integral sign, which gives

$$f(p)=f_B(p)/[1+(G^2/8\pi^2)I_1(p)], \qquad I_1(p)=-\int_0^\infty dsL'(p,s). \tag{32}$$

The second case is that in which $L(p,s)$ can be written as a product $L_1(p)L_2(s)$. Then $f_B(p)=L_1(p)\times$constant independent of p. If we let $a(p)=f(p)/L_1(p)$, then $a_B(p)=a_B=$a constant independent of p. Thus our equation is

$$a(p)=a_B+\frac{G^2}{8\pi^2}\int_0^\infty dsL_1(s)L_2(s)a(s).$$

The right-hand side is independent of p; therefore $a(p)$ is a constant and is equal to

$$a_B\Big/\left(1+\frac{G^2}{8\pi^2}I_2\right),$$

where

$$I_2=-\int_0^\infty dsL_1(s)L_2(s).$$

Finally,

$$f(p)=f_B(p)\Big/\left(1+\frac{G^2}{8\pi^2}I_2\right). \tag{32a}$$

FIG. 5. Modified propagator correction for the $j=\frac{1}{2}$, $T=\frac{1}{2}$ state.

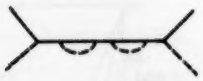

Although our equation is more complicated than the two simple cases mentioned above, yet we may make some qualitative statements about the nature of solutions for attractive and repulsive states. In the case of an attractive state, $f_B(p)$ and I_1 (or I_2) will be negative, and as $(G^2/8\pi^2)\cdot I_1$ (or I_2) reaches the value -1, a resonance occurs. This relation only crudely represents the actual case for the $P_{\frac{1}{2}}$, $T=\frac{3}{2}$ state. Here $(G^2/8\pi^2)\cdot I_1$ (or I_2) is negative and of the order of -1; the ratio $f(p)/f_B(p)$ is very large and is a very sensitive function of energy and coupling constant $G^2/4\pi$. However, we know that in the actual case $f(p)$ cannot be expressed in one of the simpler forms above, and therefore a resonance might not occur.

Another simple property of the kernel of our equation is that the important range of integration over s is of the order of M rather than μ. The integral is practically constant over values of $E-M-\mu\lesssim\mu$. Thus for states other than the sensitive $P_{\frac{1}{2}}$, $T=\frac{3}{2}$ state, the ratio of $f(p)$ to $f_B(p)$ is a slowly varying function in this energy range. Qualitatively, therefore, we can say that the forces represented by this theory have a range of order $1/M$. In an attempt to determine whether forces of longer range may be present, Mitra and Dyson[16] have considered the role of meson-meson interaction, so far with inconclusive results.

In the following section we discuss the solutions obtained for the $S_{\frac{1}{2}}$ and $P_{\frac{1}{2}}$ states for $T=\frac{3}{2}$ for laboratory energies up to 270 Mev by means of straightforward, largely numerical methods.

IX. NUMERICAL SOLUTION FOR THE S STATE WITH $T=3/2$

Two calculations were performed for the S state, one at zero energy and another for an energy of about 270 Mev (laboratory system). These correspond to values of k, the momentum in the center-of-mass system, of zero and $0.3M$, respectively. For the zero-energy case a seminumerical method was used for the solution of the one-dimensional integral equation, Eq. (30). This method only gives a fairly crude approximation, but is designed such that (1) the very lengthy kernel has to be evaluated only for a few values each of its two parameters p and s, (2) the integrals can be evaluated analytically, and (3) that solutions can be found easily for different values of the coupling constant $\lambda=G^2/4\pi$. The method proceeds as follows.

For a fixed value of p, the kernel $L(p,s)$ is evaluated for a few values of s and constants $a'(p)$, $b'(p)$, and $c'(p)$ are chosen such that the simple analytic function

$$a'(p)+[b'(p)/E(s)]+[c'(p)s/E^2(s)] \tag{33}$$

gives a reasonable approximation to the kernel $L(p,s)$.

[16] A. N. Mitra and F. J. Dyson, Phys. Rev. **90**, 372 (1953).

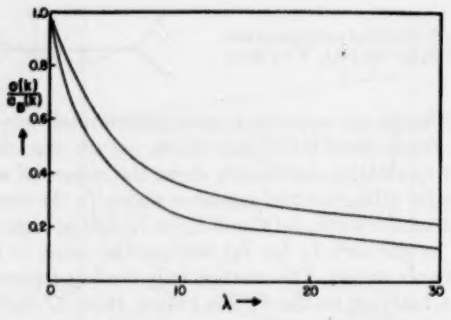

FIG. 6. Ratio of actual wave function to the Born approximation wave function on the energy shell as a function of the coupling constant λ. $(k/M)=0.3$ for upper curve and 0 for lower curve.

This fitting was done for a few values of (p/M) (0, 0.5, 1, and 2); the coefficients a', b', and c' are of course functions of p.

It is convenient to rewrite the integral equation in terms of a "wave function" $a(p)$, instead of $g(p)$, where $a(p)$ is defined by

$$a(p)=g(p)[E(p)\omega(p)]^{\frac{1}{2}}. \tag{34}$$

A form of iteration procedure is then adopted as follows. We choose an initial trial wave function $a_{tr}(p)$ of the form

$$a_{tr}(p)=a+[b/E(p)]+[cp/E^2(p)], \tag{35}$$

where the three constants a, b, and c are left unspecified for the moment. We substitute this function $a_{tr}(s)$ for $a(s)$ in the integral on the right-hand side of the integral equation and replace the kernel $L(p,s)$ by the approximate analytic expression, Eq. (33). For each of the values of p considered the integrals can now be carried out analytically, and an iterated wave function $a_{it}(p)$ obtained. This function $a_{it}(p)$ for each value of p considered consists of the sum of four terms, a known constant and known multiples of λa, λb, and λc. The three constants a, b, and c are then chosen by requiring the initial and iterated functions $a_{tr}(p)$ and $a_{it}(p)$ to agree for three values of p (these values were then adjusted very slightly to give the best overall fit between $a_{tr}(p)$ and $a_{it}(p)$ at all the values of p used.)

For a value of λ of 10 (the value used by M. Lévy in equivalent calculations on the neutron-proton system), for instance, the constants chosen were

$$a=-0.003, \quad b=0.271, \quad c=-0.084. \tag{36}$$

The initial and iterated functions were fairly similar and the result for the function on the energy shell, with the estimated error of this method of solution, is

$$a_{\text{actual}}(0)=(0.24\pm 0.01)a_{\text{Born}}(0), \tag{37}$$

where

$$a_{\text{Born}}(0)=1.075.$$

As expected for a "repulsive" state, Eq. (30) shows that the actual phase shift is very much smaller than its Born approximation value. As discussed above such a solution is easily obtained for a number of different values for the coupling constant λ and the ratio of actual phase shift to its Born approximation is plotted against λ in Fig. 6. It will be seen that this curve is similar to that represented by Eq. (31), the equivalent ratio for the simpler forms of the equation, although the actual curve has a slightly higher curvature than Eq. (31).

Similar calculations were carried out at a higher energy namely that corresponding to $k=0.3M$. An estimate of the contribution of the singularity due to the double meson production was made in this case by integrating the rapidly varying logarithm across the singularity. The contribution due to this singularity was found to be less than 10 percent of the value of the integral of the kernel found disregarding this singularity. Having found that this singularity did not contribute much to the scattering at least near the threshold, no effort was made to include this contribution accurately.

At this higher energy $(k=0.3M)$ essentially the same method was used as for the zero energy case, except that some of the integrations were carried out numerically. The iteration process described above was carried for values of (p/M) of 0, 0.3, 1, 2, and 4. For a coupling constant $\lambda=10$, the values of the constants in the trial wave function were found by requiring that the equations at the above-mentioned values of p be satisfied in the least-squares sense and one gets

$$a=-0.053, \quad b=0.454, \quad c=0.094. \tag{38}$$

The agreement between the initial and the iterated wave functions was not quite as close in this case as for zero energy, but was sufficiently good for the accuracy required. These two functions are plotted against p in Fig. 7, together with the Born approximation for this function. The value obtained for the wave function

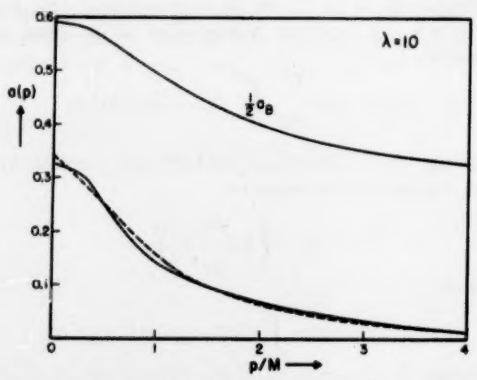

FIG. 7. Actual wave function together with the Born approximation wave function for the $S_{\frac{1}{2}}$, $T=\frac{1}{2}$ state, as a function of the momentum.

on the energy shell was (for $\lambda=\frac{1}{2}10$)

$$a_{\text{actual}}(0.3)=(0.365\pm0.020)a_{\text{Born}}(0.3),$$
$$a_{\text{Born}}(0.3)=1.172. \quad (39)$$

As will be seen from Fig. 6, the ratios of phase shift to their Born approximation for all the values of λ considered were not very different for the zero-energy case and for the 270-Mev case ($k=0.3M$). Since this ratio is such a slowly varying function of energy,[16] a simple interpolation procedure was used for intermediate energies. In Fig. 8 we plot the estimated phase shift as a function of energy together with their Born approximation for $\lambda=15$, (the order of magnitude of λ which will be shown in the next section to give best agreement with experiment for the $P_{\frac{1}{2}}$, $T=\frac{3}{2}$ state.)

X. THE $P_{\frac{1}{2}}$ INTEGRAL EQUATION

The $P_{\frac{1}{2}}$, $T=\frac{3}{2}$ integral equation was solved by expressing the solution $f(p)$ in a manner similar to (35), but with six parameters instead of three. The integral equation could then be satisfied for six different values of p; this yields six simultaneous ordinary linear equations for the six parameters in $f(p)$.

Several simplifications in the kernel were made before attempting this procedure. The kernel is a sum of terms $K_1(C)$, $K_2(C)$, $K_1(B)$, and $K_2(B)$. The $K(B)$ terms are generally 1/20 of the $K(C)$ terms (i.e., the interaction with the one-nucleon, two-meson configuration predominates). The $K(B)$ terms were, as a result, drastically approximated. The K_1 terms (associated with spin-independent processes) and the K_2 terms (associated with spin-dependent processes) are of the same order of magnitude for momenta much bigger than M, but the latter are relatively very small for low momenta. Therefore, the K_2 terms were neglected below the momentum of integration $s=(3/4)M$.

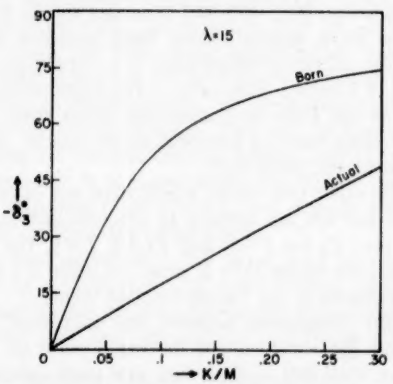

FIG. 8. Variation of $S_{\frac{1}{2}}$, $T=\frac{3}{2}$ phase shift (δ_3) with momentum k, in the c.m. system, for a coupling constant $\lambda=15$.

[16] It should be pointed out that this slow variation with energy may no longer hold for energies far in excess of the double meson production threshold energy, since the effect of the singularities, still small for 270 Mev, may become quite marked at these energies.

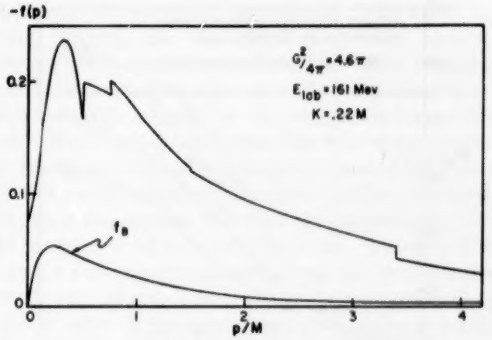

FIG. 9. Actual wave function together with the Born approximation wave function for the $P_{\frac{1}{2}}$, $T=\frac{3}{2}$ state.

The region of very high momenta ($p=10M$) was also neglected. This might be justified on the grounds that the error in the calculated phase shift associated with this neglect is less than about two percent. The singularities in the kernel associated with meson production were also neglected. Consider omission of the region of the integration variable from $[R/(\bar{E}+C)]=-\frac{1}{2}$ to $[R/(\bar{E}+C)]=\frac{1}{2}$ (which contains the singularities). It can be shown that the resulting error in the phase shift is $(\delta-\delta_{\text{calc}})/\delta\sim\{[\omega(k)-2\mu]/M\}^4$ for $k<M/2$. At these energies the error is then very small.

After the above approximations, the detailed method of the solution of the equation was as follows. The interval of integration was divided into four regions: 0 to $0.5M$, $0.5M$ to $1.5M$, $1.5M$ to $3.5M$, $3.5M$ to $10M$. The kernel was expanded in each of the regions as a function of s in a manner similar to (33), with the criterion that the error in the expansion be less than 10 percent at the boundaries of the regions. This was done for six values of p altogether. The form of the expansion for the solution $f(p)$ was chosen following roughly the indications from the expansion of the kernel; $f(p)$ was then taken to be a polynomial with 3, 1, 1, 1 undetermined coefficients in each of the four regions, respectively. The shape of this trial function was taken to be quadratic in $E-E(p)-\omega(p)$ in the region $p<M/2$. From $M/2$ to M, after some experimentation, it was taken as essentially constant. For $p>M$, the first trial function had a shape roughly of $1/p$, or more accurately $pf_B(p)$. The integrals were performed and the set of six simultaneous equations solved. The shape of the solution was then adjusted in the upper regions to improve the fit at the boundaries of the regions, and the equations were solved again. The solution thus obtained at 161 Mev for $G^2/4\pi=16$ is shown in Fig. 9. The solutions in Fig. 9 are represented very well (from about k to $5M$) by

$$f(p)=a(1+bp)f_B(p), \quad (40)$$

with $b=3/2M$ for $G^2/4\pi=16$. For $p\gg5M$, it is found that the behavior of $f(p)$ is independent of the energy. At the coupling constant in question ($G^2/4\pi=16$) we

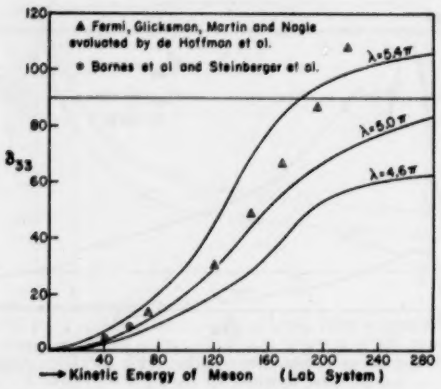
▲ Fermi, Glicksman, Martin and Nagle evaluated by de Hoffman et al.
• Barnes et al and Steinberger et al.
λ=5.4π
λ=5.0π
λ=4.6π
δ33
Kinetic Energy of Meson (Lab System)

FIG. 10. Variation of $P_{\frac{1}{2}}$, $T=\frac{3}{2}$ phase shift (δ_{33}) with kinetic energy of meson in laboratory system.

find

$$f(p)\approx p^{-1.4}\approx p^{0.6}f_B(p). \tag{41}$$

Solutions were obtained at four energies, 113, 161, 186, and 272 Mev in the laboratory system, corresponding to c.m. momenta $k=0.18M$, $0.22M$, $0.24M$, and $0.30M$. In addition, the slope $f(k)/k^3$ was roughly determined by using Eq. (39) at zero scattering energy. In this case the coefficient bM was 1.5, 2.0, for $G^2/4\pi=4.6\pi$, 5.0π, respectively. The calculated $P_{\frac{1}{2}}$, $T=\frac{3}{2}$ phase shift is plotted as a function of energy for several coupling constants in Fig. 10.

The accuracy of these solutions can be estimated very crudely in the following manner. Let the integral equation be written

$$f(p)=f_B(p)+\left[\int L'(p,s)\frac{f(s)}{f(p)}ds\right]f(p).$$

Then,

$$\Delta f(p)=\left\{\int\Delta[L'(p,s)]\frac{f(s)}{f(p)}ds + \int L'(p,s)\Delta\left[\frac{f(s)}{f(p)}\right]ds\right\}f(p)+\frac{f(p)-f_B(p)}{f(p)}\Delta f(p), \tag{42}$$

so that

$$\frac{\Delta f(p)}{f(p)}=\frac{f(p)}{f_B(p)}\{\epsilon_1+\epsilon_2\}, \tag{43}$$

where $\{\epsilon_1+\epsilon_2\}$ represents the two terms in curly brackets in Eq. (42). We have

$$\int ds L'(p,s)\frac{f(s)}{f(p)}\sim 1 \quad \text{for} \quad \frac{f(p)}{f_B(p)}\gg 1.$$

Then ϵ_1 is roughly given by the percentage error resulting from our approximations of L'. This error can be taken as about ± 3 percent. We may estimate ϵ_2 by examination of the deviation of the obtained solution, $f(p)$, from a smooth curve at the boundaries of the regions (see Fig. 9). This deviation is of the order of ± 20 percent. We shall take the average error in $f(s)/f(p)$, optimistically, as quadratic in this deviation, or $\epsilon_2\sim\pm 4$ percent. The ratio to the Born approximation $f(k)/f_B(k)\sim 6$ at 161 Mev. Then an error $\Delta f(k)/f(k)$ of about $\pm\frac{1}{3}$ is expected for a given coupling constant. As the ratio to the Born approximation increases, this error in $\tan\delta$ increases without limit. The error in the angle δ becomes the more meaningful quantity. For $\delta\approx 1$, $\tan\delta>1$, we can write

$$\frac{\Delta\delta}{\delta}=\frac{1}{\delta}\left(\frac{\Delta\tan\delta}{1+\tan^2\delta}\right)\sim-\frac{1}{\pi f_B(k)}\{\epsilon_1+\epsilon_2\}. \tag{44}$$

In the region of interest this error is also about $\pm\frac{1}{3}$. Since the coupling constant is varied in practice so that the solution obtained at one energy agrees with experiment, the question is how accurate is the relative phase shift determined at another energy? It might be expected that if the energy difference is of the order of the characteristic length of the solution obtained in the region 0 to $0.5M$ (say $\Delta k=0.2M$) then the error at the new energy would be of the order of that indicated in Eqs. (43) and (44).

XI. DISCUSSION

The numerical results for the two states investigated in detail, using the approximate equation of motion derived above, can be summarized as follows. For the $P_{\frac{1}{2}}$, $T=\frac{3}{2}$ state the calculated phase shift is appreciably larger than the Born approximation and is a very sensitive function of coupling constant $\lambda=G^2/4\pi$ and of energy. Rough agreement with experiment is obtained for a value of λ slightly larger than 15 (see Fig. 8 and below). For the $S_{\frac{1}{2}}$, $T=\frac{3}{2}$ state the ratio of phase shift to its Born approximation value is considerably less than unity, for $\lambda=15$ and decreases slowly with λ. Since the Born approximation itself increases slowly with λ, the calculated phase shift is a very insensitive function of λ indeed. This ratio to Born approximation, as well as the Born approximation phase shift itself, are also slowly varying functions of the energy, and so is the calculated phase shift.

For the other two states which were not calculated in detail but are not subject to renormalization difficulties, *viz.*, $P_{\frac{1}{2}}$ for $T=\frac{3}{2}$ and $P_{\frac{3}{2}}$ for $T=\frac{1}{2}$, the Born approximation phase shift is small (of order 5°) and is further reduced in the Tamm-Dancoff theory.

A direct comparison between the calculated phase shifts and the observed one for the S state of $T=\frac{3}{2}$, which we shall call δ_3, does not give good agreement. For example, at 136 Mev, the observed value is about $-15°$, while the calculated one is $-32°$ and $-34°$ for the two values of the coupling constant. This would indicate that the reduction as compared with the Born approximation is not nearly large enough. However, it is well known that the phase shift δ_3 has experimentally

a very complicated behavior at low energy which presumably cannot be explained by our theory, but which requires probably the introduction of an additional weak, long-range interaction[17,18] between nucleon and meson. This potential might be due to an interaction between the incident meson and the "bound" mesons in the nucleon, and one of us (M.R.) has found that a phenomenological theory based on this assumption accounts reasonably well for the behavior of δ_3 at low energies.

We therefore consider it more reasonable to compare our theory merely with the higher energy experiments. Above 40 Mev, the experimental phase shift δ_3 can be represented quite well by a straight line of the form[19]

$$\delta_3 = 11° - 130°(k/M). \tag{45}$$

Our theory, for $G^2/4\pi = 13$, gives very nearly

$$\delta_3 = -160°(k/M). \tag{46}$$

Therefore, the *slope* of the straight line δ_3 *vs* k is given quite well by the theory, as is the straight-line relation itself. By the way, this relation indicates that the interaction corresponds to a very strong repulsive core whose radius is given by the coefficient of k (in radians), and is therefore

$$2.3\hbar/Mc = 4.8\times10^{-14} \text{ cm from the experimental relation;} \tag{47}$$

$$2.8\hbar/Mc = 5.9\times10^{-14} \text{ cm from the theoretical relation.} \tag{48}$$

The *constant* term in (47) is attributed to the long-range attraction mentioned above.

Regarding the $P_{\frac{3}{2}}$ state there has been considerable controversy on the behavior of the phase shift above 120 Mev. It is now most likely[20] that there is a resonance at about 195 Mev, and that the phase shift goes nearly linearly with energy near the resonance. These experimental phase shifts are shown in Fig. 10. At energies up to about 150 Mev, these follow rather closely the theoretical curve for $G^2/4\pi = 5.1\pi = 16.0$ (not drawn). However, at higher energy, the theoretical curve does not increase steeply enough. This may be improved by including the renormalization terms as has been shown by Visscher.[21] It is also possible that higher configurations, involving more mesons, play a more important role and increase the phase shifts.

The work reported in this paper is to be considered purely as a pilot study for the following reasons. As discussed above, an unsophisticated three-dimensional approach was used throughout and hence all renormalization terms had to be omitted. It is hoped that work relating this formalism to a fully covariant approach will remove this difficulty.[9] More important still is the approximation of restricting ourselves to states directly coupled to the one-meson one-nucleon state. Nothing is known about the rate of convergence of the Tamm-Dancoff expansion in terms of the number of virtual mesons and nucleon pairs. A helpful fact in this respect is the increase of the energy denominators with the complexity of intermediate states. But even if the hope for convergence is justified, one will certainly need more terms of this expansion than were carried in the present paper to get quantitatively meaningful results. Higher terms could be included without essential modification in the method of deriving the equations of motion, but the solution of these coupled integral equations would be very lengthy, probably requiring the use of electronic computing machines. It was not felt worthwhile to carry such a program through until the renormalization difficulties have been removed.

One therefore should not expect any quantitative agreement between the present results and experiment, but we hope that the terms omitted in this paper will at least be qualitatively similar to those carried. In particular we expect that the distinction between effectively attractive and effectively repulsive interactions will remain, so that the phase shift for the $P_{\frac{3}{2}}$, $T=\frac{3}{2}$ state will continue to be the largest, and considerably enhanced compared with the Born approximation, while all other phase shifts will continue to be less than their Born approximation.

To sum up, the present work has by no means proved that pseudoscalar meson theory agrees with experiment, nor even that it is a self-consistent formalism. But at least it removes the impression given by perturbation theory calculations, that pseudoscalar meson theory with pseudoscalar coupling is incompatible with experiment.

ACKNOWLEDGMENTS

It is a great pleasure to express our hearty thanks to Dr. G. Chew and to Dr. S. D. Drell and Dr. E. Henley for showing us their work before publication. We thank Mr. A. N. Mitra for making available to us the results on the effects of meson-meson interaction. One of us (E.E.S.) is indebted to the Australian National University, where part of this work was completed.

APPENDIX

In the Schrödinger equation

$$(H_0+H_I)\Psi = E\Psi,$$

H_0 represents the free-field Hamiltonian and can be written in terms of the number operators of various field quanta in the form

$$H_0 = \sum_{\mathbf{p},u} N_u(\mathbf{p})E_u(\mathbf{p}) + \sum_{\mathbf{k},\alpha} N_\alpha{}^M(\mathbf{k})\omega_\alpha(\mathbf{k}),$$

[17] R. E. Marshak, Phys. Rev. **88**, 1208 (1952).
[18] J. Tinlot and A. Roberts, Phys. Rev. **90**, 951 (1953).
[19] Bethe, de Hoffman, and Schweber, *Introduction to Meson Theory* (Row, Peterson, & Company, Evanston, to be published).
[20] De Hoffmann, Metropolis, Alei, and Bethe, Phys. Rev. (to be published); M. Glicksman, Phys. Rev. **95**, 1335 (1954); R. L. Martin, Phys. Rev. (to be published).
[21] W. M. Visscher, Cornell University, thesis, 1953 (unpublished).

where $E(p)=+(M^2+p^2)^{\frac{1}{2}}$ and $\omega(k)=+(k^2+\mu^2)^{\frac{1}{2}}$, M and μ being the masses of nucleon and meson, respectively. The suffix α in the second term refers to the charge state of the meson. $N_u(\mathbf{p})$ is defined in terms of creation operators $[a_u^*(\mathbf{p})]$ and destruction operators $a_u(\mathbf{p})$ of nucleons in the form

$$N_u(\mathbf{p})=a_u^*(\mathbf{p})a_u(\mathbf{p}),$$

if u is a suffix referring to positive-energy states of the nucleon field. If u refers to negative-energy states, then

$$N_u(\mathbf{p})=a_u(\mathbf{p})a_u^*(\mathbf{p}).$$

The $a_u(p)$'s satisfy the relation

$$[a_u(\mathbf{p}),\, a_{u'}^*(\mathbf{p}')]_+=\delta_3(\mathbf{p}-\mathbf{p}')\delta_{uu'}.$$

Similarly the meson number operator is defined in terms of meson creation and destruction operators, $c_\alpha^*(\mathbf{k})$ and $c_\alpha(\mathbf{k})$ respectively, in the form

$$N_\alpha{}^M(\mathbf{k})=c_\alpha^*(\mathbf{k})c_\alpha(\mathbf{k}),$$

with the c's satisfying the commutation relations

$$[c_\alpha(\mathbf{k}),\, c_{\alpha'}^*(\mathbf{k}')]=\delta_3(\mathbf{k}-\mathbf{k}')\delta_{\alpha\alpha'}.$$

The nucleon field operator can be expanded in the form

$$\psi(\mathbf{x})=\frac{1}{(2\pi)^{\frac{1}{2}}}\int d^3p\left(\frac{M}{E(p)}\right)^{\frac{1}{2}}\times[\textstyle\sum_+ a_u(\mathbf{p})u(\mathbf{p})\exp(ip_\mu x_\mu)+\sum_- a_u(\mathbf{p})u(\mathbf{p})\exp(-ip_\mu x_\mu)].$$

The summation in the two terms extends over positive energy spinors and negative energy spinors, respectively. In the exponentials appears the four-dimensional scalar product of the vector p_u and x_u. The 0 component of p_μ, i.e., p_0, is defined as $+E(p)$. With the above decomposition for $\psi(\mathbf{x})$, $\bar{\psi}(\mathbf{x})$ takes the form

$$\bar{\psi}(\mathbf{x})=\frac{1}{(2\pi)^{\frac{1}{2}}}\int d^3p(M/E(p))^{\frac{1}{2}}\times[\textstyle\sum_+ a_u^*(\mathbf{p})\bar{u}(\mathbf{p})\exp(-ip_\mu x_\mu)+\sum_- a_u^*(\mathbf{p})\bar{u}(\mathbf{p})\exp(ip_\mu x_\mu)].$$

The meson operator $\phi_\alpha(\mathbf{x})$ is decomposed in the form

$$\phi_\alpha(\mathbf{x})=\frac{1}{[2(2\pi)^3]^{\frac{1}{2}}}\int d^3k\frac{1}{[\omega(k)]^{\frac{1}{2}}}[c_\alpha(\mathbf{k})\exp(ik_\mu x_\mu)+c_\alpha^*(\mathbf{k})\exp(-ik_\mu x_\mu)].$$

The Dirac spinors $u(p)$ are normalized in such a way that

$$\textstyle\sum_+ \bar{u}(\mathbf{p})u(\mathbf{p})=+1, \quad \text{and} \quad \sum_- \bar{u}(\mathbf{p})u(\mathbf{p})=-1.$$

The u's satisfy the Dirac equation $(\not{p}-iM)u(\mathbf{p})=0$ for positive energies, and $(\not{p}+iM)u(\mathbf{p})=0$ for negative energies. Substituting these expressions for the decomposition of the operators $\psi(\mathbf{x})$, $\bar{\psi}(\mathbf{x})$, and $\phi(\mathbf{x})$ in the expression for H_I, the interaction Hamiltonian, we can write it as the sum of the following eight terms:

$$\begin{aligned}H_I=iG(16\pi^3)^{-1}\int d^3p'\int d^3p\int d^3k\left(\frac{M^2}{E(p)E(p')\omega(k)}\right)^{\frac{1}{2}}&\cdot[\textstyle\sum_{+u'}\sum_{+u}\bar{u}(\mathbf{p}')\gamma_5\tau_\alpha u(\mathbf{p})a_{u'}^*(\mathbf{p}')\\&\cdot c_\alpha(\mathbf{k})a_u(\mathbf{p})\delta(\mathbf{p}-\mathbf{p}'+\mathbf{k})\\&+\textstyle\sum_{+u'}\sum_{+u}\bar{u}(\mathbf{p}')\gamma_5\tau_\alpha u(\mathbf{p})a_{u'}^*(\mathbf{p}')\\&\cdot c_\alpha^*(\mathbf{k})a_u(\mathbf{p})\delta(\mathbf{p}-\mathbf{p}'-\mathbf{k})\\&+\textstyle\sum_{+u'}\sum_{-u}\bar{u}(\mathbf{p}')\gamma_5\tau_\alpha u(\mathbf{p})a_{u'}^*(p')\\&\cdot c_\alpha(k)a_u(\mathbf{p})\delta(-\mathbf{p}-\mathbf{p}'+\mathbf{k})\\&+\textstyle\sum_{+u'}\sum_{-u}\bar{u}(\mathbf{p}')\gamma_5\tau_\alpha u(\mathbf{p})a_{u'}^*(\mathbf{p}')\\&\cdot c_\alpha^*(\mathbf{k})a_u(\mathbf{p})\delta(-\mathbf{p}-\mathbf{p}'-\mathbf{k})\\&+\textstyle\sum_{-u'}\sum_{+u}\bar{u}(\mathbf{p}')\gamma_5\tau_\alpha u(\mathbf{p})a_{u'}^*(\mathbf{p}')\\&\cdot c_\alpha(\mathbf{k})a_u(\mathbf{p})\delta(\mathbf{p}+\mathbf{p}'+\mathbf{k})\\&+\textstyle\sum_{-u'}\sum_{+u}\bar{u}(\mathbf{p}')\gamma_5\tau_\alpha u(\mathbf{p})a_{u'}^*(\mathbf{p}')\\&\cdot c_\alpha^*(\mathbf{k})a_\mu(\mathbf{p})\delta(\mathbf{p}+\mathbf{p}'-\mathbf{k})\\&+\textstyle\sum_{-u'}\sum_{-u}\bar{u}(\mathbf{p}')\gamma_5\tau_\alpha u(\mathbf{p})a_{u'}^*(\mathbf{p}')\\&\cdot c_\alpha(\mathbf{k})a_u(\mathbf{p})\delta(-\mathbf{p}+\mathbf{p}'+\mathbf{k})\\&+\textstyle\sum_{-u'}\sum_{-u}\bar{u}(\mathbf{p}')\gamma_5\tau_\alpha u(\mathbf{p})a_{u'}^*(\mathbf{p}')\\&\cdot c_\alpha^*(\mathbf{k})a_u(\mathbf{p})\delta(-\mathbf{p}+\mathbf{p}'-\mathbf{k})].\end{aligned}$$

Born-Type Rigid Motion in Relativity

G. SALZMAN AND A. H. TAUB
Physics Department and Mathematics Department, University of Illinois, Urbana, Illinois
(Received April 19, 1954)

Rigid motions of collections of particles as defined by Born, Herglotz, and Noether are studied in special and general relativity. An approximate method for solving the field equations of general relativity, the equations of motion of a perfect fluid undergoing a rigid motion, and the boundary condition $p=0$ is described and the first-order solution for the first two sets of equations is obtained. It is shown that in the classical limit the boundary conditions may be satisfied to this order.

1. INTRODUCTION

TO generalize the classical concept of rigid motion, Born[1] introduced a definition consistent with special and general relativity. As formulated by Herglotz[2] it states: For each pair of nearby particles of the body the orthogonal interval between the corresponding pair of world lines is constant during the motion. The orthogonal interval is the distance between the two world lines, measured along an infinitesimal hyperplane orthogonal to both lines in the sense of four dimensions, and calculated with the line element of the space time. It is shown in Fig. 1 in a Minkowski-type diagram, with one of the spatial dimensions suppressed.

Herglotz and Noether[3] then proved that in special relativity every Born-type rigid motion belongs to at least one of two classes. The world lines are either the orthogonal trajectories of a continuous one-parameter family of space-like hyperplanes, or segments of path curves of a continuous one-parameter family of Lorentz transformations of the four-dimensional Minkowski space-time R_4 into itself. We label these classes *plane motions* and *group motions*. Some motions belong to both classes. Any time-like curve determines one plane motion, but in order to determine a group motion the curve must be restricted.

2. NOTATION, DEFINITIONS, AND ASSUMPTIONS

A point (or event) is specified by four numbers x^α, the coordinate values of that point in the x^α-coordinate system. Lower case Greek indices have the range 1,2, 3, 4; Latin ones 1, 2, 3. The usual summation convention is used. The motion of each particle is described by parametric equations,

$$x^\alpha=\psi^\alpha(\xi^\nu,\theta), \tag{1}$$

where ξ^ν are parameters which label the particles and θ is any convenient *time-like* parameter, e.g., the time x^4 in the x^α-coordinate system. The points on a world line are obtained from (1) by holding ξ^ν fixed and allowing θ to run through its range of values. For any ξ^ν it is assumed that θ and $\psi^4(\xi^\nu,\theta)$ are monotone increasing functions of each other. Let θ_I be the smallest value that θ assumes; call it the initial value. The parameters ξ^ν are chosen to satisfy the equations

$$\psi^\alpha(\xi^\nu,\theta_I)=\xi^\alpha. \tag{2}$$

The particle located at ξ^α when $\theta=\theta_I$ is labeled by ξ^i, the *initial* values of its spatial coordinates x^i. To each particle ξ^i corresponds the *initial* value ξ^4 of x^4 for that particle, i.e.,

$$\xi^4=\sigma(\xi^i). \tag{3}$$

Substituting (3) into (1), we get

$$x^\alpha=\psi^\alpha(\xi^i,\sigma(\xi^i),\theta)$$

or simply,

$$x^\alpha=x^\alpha(\xi^i,\theta). \tag{4}$$

There is thus a three-parameter family $\{C_{\xi^i}\}$ of world lines for a motion of a system of particles. The *initial* hypersurface from which the world lines start, which we call the σ-hypersurface.

$$x^4=\sigma(x^i), \tag{5}$$

is assumed to be spacelike. All necessary differentiability of the functions $x^\alpha(\xi^i,\theta)$ and $\sigma(\xi^i)$ is assumed. Also, Eqs. (4) are assumed to define a nonsingular transformation between the coordinates x^α and the coordinates ξ^i,θ. The x^α-coordinate system has a metric tensor $g_{\alpha\beta}(x^\nu)$, however, in special relativity the coordinates will, unless otherwise specified, be chosen so as

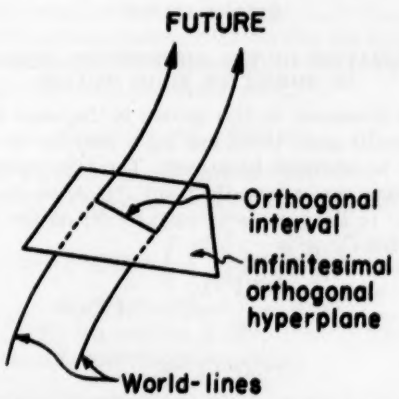

FIG. 1. The orthogonal interval between nearby particles. One of the spatial dimensions is suppressed.

[1] M. Born, Ann. Physik **30**, 1 (1909).
[2] G. Herglotz, Ann. Physik **31**, 393 (1909–1910).
[3] F. Noether, Ann. Physik **31**, 919 (1909–1910).

to have the metric tensor $g_{\alpha\beta}=\eta_{\alpha\beta}$, where

$$\eta_{11}=\eta_{22}=\eta_{33}=-\eta_{44}=1,$$
$$\eta_{\alpha\beta}=0 \quad \text{if} \quad \alpha\neq\beta, \tag{6}$$

i.e., they will be Galilean coordinates. The signature will always be taken as $(+\,+\,+\,-)$, i.e., space-like intervals will be positive.

For a family $\{C_{\xi^i}\}$ of world lines let $\mathcal{T}$ be the totality of those points of the space time that lie on world lines. At each point x^α of $\mathcal{T}$, a time like vector is defined by

$$U^\alpha=\partial x^\alpha(\xi^i,\theta)/\partial\theta=x^\alpha(\xi^i,\theta)_{,\theta}. \tag{7}$$

Because of the monotone relationship between $x^4(\xi^i,\theta)$ and θ, U^α points towards the future, i.e., $U^4>0$. Corresponding to this four-velocity vector field $U^\alpha(x^\nu)$ defined over $\mathcal{T}$, and to the choice of signature, is the unit vector field $u^\alpha(x^\nu)$ defined by

$$u^\alpha=(-U_\beta U^\beta)^{-\frac{1}{2}}U^\alpha, \tag{8}$$

where $U_\beta=g_{\alpha\beta}U^\alpha$. It follows from the definition that

$$u_\alpha u^\alpha=-1. \tag{9}$$

$u^\alpha(x^\nu)$ is the normalized four-velocity vector field. $U^\alpha(x^\nu)$ is an unnormalized four-velocity vector field. From Eq. (9) and from the fact that the $g_{\alpha\beta}$'s behave as constants with respect to covariant differentiation, we get

$$u_{\alpha;\beta}u^\alpha=0, \tag{10}$$

where $u_{\alpha;\beta}$ is the covariant derivative of $u_\alpha(x^\nu)$ with respect to x^β.

It is convenient to introduce a proper time s, which is defined by specifying its value on any hypersurface which intersects each of the world lines exactly once and by the equation

$$ds/d\theta=(-U_\beta U^\beta)^{\frac{1}{2}}. \tag{11}$$

It is assumed that a nonsingular transformation exists between the coordinates ξ^i,θ and the coordinates ξ^i,s. Equations (7), (8), and (11) imply that

$$\partial x^\alpha/\partial s=x^\alpha{}_{,s}=u^\alpha.$$

3. DERIVATION OF THE DIFFERENTIAL EQUATIONS OF BORN-TYPE RIGID MOTION

The discussion in this section is the same for flat and nonflat space times, and $g_{\alpha\beta}$ is used for the metric tensor to represent both cases. The infinitesimal displacement vector from the point $x^\alpha(\xi^i,\theta)$ on the world line C_{ξ^i} to the point $x^\alpha(\xi^i+d\xi^i,\theta+d\theta)$ on the nearby world line $C_{\xi^i+d\xi^i}$ is

$$dx^\alpha=\frac{\partial x^\alpha(\xi^i,\theta)}{\partial\xi^i}d\xi^i+x^\alpha(\xi^i,\theta)_\theta d\theta \tag{12}$$
$$=x^\alpha{}_{,i}d\xi^i+U^\alpha d\theta.$$

The component of dx^α parallel to $u^\alpha(\xi^i,\theta)$ is $(-dx^\beta u_\beta)u^\alpha$. Therefore the orthogonal displacement from C_{ξ^i} to $C_{\xi^i+d\xi^i}$ at $x^\alpha(\xi^i,\theta)$ is $dx^\alpha-(-dx^\beta u_\beta)u^\alpha$. Its length squared is

$$dl^2=g_{\alpha\beta}[dx^\alpha+dx^\nu u_\nu u^\alpha][dx^\beta+dx^\lambda u_\lambda u^\beta]$$
$$=g_{\alpha\beta}dx^\alpha dx^\beta+u_\nu dx^\nu u_\lambda dx^\lambda=(g_{\alpha\beta}+u_\alpha u_\beta)dx^\alpha dx^\beta. \tag{13}$$

Note the identity

$$(g_{\alpha\beta}+u_\alpha u_\beta)U^\alpha=0. \tag{14}$$

Substituting for dx^α from (12) into (13), and taking account of (14), we get for the square of the orthogonal interval

$$dl^2=(g_{\alpha\beta}+u_\alpha u_\beta)x^\alpha{}_{,i}x^\beta{}_{,j}d\xi^i d\xi^j. \tag{15}$$

If we regard the functions $g_{\nu\lambda}$, u_ν, and $x^\nu{}_{,k}$ in (15) as functions of ξ^k and θ, the statement that the motion is a Born-type rigid motion means that for all points ξ^i,θ in $\mathcal{T}$ and for all infinitesimal $d\xi^k$, dl is independent of θ, or equivalently,

$$[(g_{\alpha\beta}+u_\alpha u_\beta)x^\alpha{}_{,i}x^\beta{}_{,j}]_\theta=0. \tag{16}$$

Theorem: Equation (16) is equivalent to the covariant equation

$$u_{\mu;\nu}+u_{\nu;\mu}+u_{\mu;\lambda}u^\lambda u_\nu+u_{\nu;\lambda}u^\lambda u_\mu=0 \tag{17}$$

in which the functions $g_{\nu\lambda}$ (which enter in the covariant differentiation), and u_ν are regarded as functions of x^α.

Proof: From (11) it follows, since $U_\beta U^\beta\neq 0$, that Eq. (16) is equivalent to

$$[(g_{\alpha\beta}+u_\alpha u_\beta)x^\alpha{}_{,i}x^\beta{}_{,j}]_s=0. \tag{18}$$

If some dummy indices are changed, Eq. (18) becomes

$$[(g_{\alpha\mu}+u_\alpha u_\mu)u^\mu{}_{,\beta}+(g_{\beta\mu}+u_\beta u_\mu)u^\mu{}_{,\alpha}$$
$$+(g_{\alpha\beta,\mu}+u_{\alpha,\mu}u_\beta+u_\alpha u_{\beta,\mu})u_\mu]x^\alpha{}_{,i}x^\beta{}_{,j}=0.$$

Replacing $u_{\alpha,\mu}$ by $g_{\alpha\lambda,\mu}u^\lambda+g_{\alpha\lambda}u^\lambda{}_{,\mu}$; $g_{\alpha\beta,\gamma}$ by $g_{\mu\beta}\{{}_{\alpha\gamma}{}^\mu\}+g_{\alpha\mu}\{{}_{\beta\gamma}{}^\mu\}$, where $\{{}_{\beta\gamma}{}^\alpha\}$ are the Christoffel symbols of the second kind; changing dummies, collecting terms, using the fact that the covariant derivatives of $g_{\alpha\beta}$ vanish, and taking account of (10) we get

$$D_{\alpha\beta}x^\alpha{}_{,i}x^\beta{}_{,j}=0, \tag{19}$$

where

$$D_{\alpha\beta}=u_{\alpha;\beta}+u_{\beta;\alpha}+u_{\alpha;\lambda}u^\lambda u_\beta+u_{\beta;\lambda}u^\lambda u_\alpha.$$

Note the identities

$$D_{\alpha\beta}u^\alpha=0, \tag{20a}$$
$$D_{\alpha\beta}u^\beta=0. \tag{20b}$$

The Jacobian of the transformation from the coordinates x^α to the coordinates ξ^i,s is the determinant of the matrix $\|J^\alpha{}_\lambda\|$, where $J^\alpha{}_i=x^\alpha{}_{,i}$ and $J^\alpha{}_4=x^\alpha{}_{,s}=u^\alpha$. Equations (19), (20a), and (20b) imply that

$$D_{\alpha\beta}J^\alpha{}_\lambda J^\beta{}_\nu=0. \tag{21}$$

But by assumption $\|J^\alpha{}_\lambda\|$ is a nonsingular matrix. Therefore $D_{\alpha\beta}=0$, i.e., (16) implies (17). The reversibility of the steps in the proof insures that (17) implies (16), and therefore the two equations are equivalent.

There are only six independent equations contained in (17). This follows from the symmetry in μ and ν and from the fact that the equation obtained by multiplying (17) by u^μ is satisfied identically.

Equation (17) may be written in the equivalent form

$$(u_{\alpha;\beta}+u_{\beta;\alpha})(\delta^\alpha{}_\mu+u^\alpha u_\mu)(\delta^\beta{}_\nu+u^\beta u_\nu)=0, \tag{22}$$

where $\delta^\alpha{}_\mu$ is the Kronecker delta. If we define

$$P^\alpha=(\delta^\alpha{}_\mu+u^\alpha u_\mu)V^\mu,$$

where V^μ is an arbitrary vector, then P^α is an arbitrary vector orthogonal to u^α. (22) may then be written in the equivalent form

$$u_{\alpha;\beta}P^\alpha P^\beta=0. \tag{23}$$

(22) is also equivalent to

$$(U_{\alpha;\beta}+U_{\beta;\alpha})(\delta^\alpha{}_\mu+u^\alpha u_\mu)(\delta^\beta{}_\nu+u^\beta u_\nu)=0. \tag{24}$$

This can be seen as follows. Let

$$e^{2\psi}=-U_\alpha U^\alpha \tag{25}$$

define ψ. Note that $e^\psi\neq 0$. Then

$$u_\alpha=e^{-\psi}U_\alpha. \tag{26}$$

Differentiation of Eq. (25) gives

$$\psi_{,\beta}=-e^{-\psi}U_{\alpha;\beta}u^\alpha. \tag{27}$$

Differentiating Eq. (26) and using (26) and (27), we get

$$u_{\alpha;\beta}=e^{-\psi}U_{\mu;\beta}(\delta^\mu{}_\alpha+u^\mu u_\alpha). \tag{28}$$

Using the relation

$$(\delta^\sigma{}_\mu+u^\sigma u_\mu)(\delta^\mu{}_\alpha+u^\mu u_\alpha)=(\delta^\sigma{}_\alpha+u^\sigma u_\alpha),$$

we obtain from (28)

$$\begin{aligned}&(u_{\alpha;\beta}+u_{\beta;\alpha})(\delta^\alpha{}_\mu+u^\alpha u_\mu)(\delta^\beta{}_\nu+u^\beta u_\nu)\\&\quad=e^{-\psi}(U_{\alpha;\beta}+U_{\beta;\alpha})(\delta^\alpha{}_\mu+u^\alpha u_\mu)(\delta^\beta{}_\nu+u^\beta u_\nu).\end{aligned} \tag{29}$$

Since $e^{-\psi}\neq 0$, either (22) and (24) are each satisfied or they are each not satisfied by any given vector field $U_\alpha(x^\nu)$. They are thus equivalent.

4. THE RESULTS OF HERGLOTZ AND NOETHER

As already mentioned, Herglotz and Noether proved that in special relativity every Born-type rigid motion is either a plane motion or a group motion, or both.

A four-velocity field of a plane motion in special relativity can be characterized as follows. Let C_0 be a world line of the motion. C_0 is given by equations

$$x^\alpha=x^\alpha(\theta). \tag{30}$$

A four-velocity is determined along C_0, namely,

$$U^\alpha(\theta)=x^\alpha(\theta)_{,\theta}. \tag{31}$$

The hyperplane which intersects C_0 orthogonally at $x^\alpha(\theta)$ consists of those points x^ν which satisfy

$$U_\nu(\theta)[x^\nu-x^\nu(\theta)]=0. \tag{32}$$

Equation (32) can be regarded as assigning a value of θ to each point x^ν of $\mathcal{T}$, i.e., it defines a function $\theta(x^\nu)$. The vector field defined by

$$U^\alpha(x^\nu)=U^\alpha[\theta(x^\nu)], \tag{33}$$

where $\theta(x^\nu)$ is defined by Eq. (32), is a four-velocity vector field for the plane motion.

An important property of plane motions is that the local angular velocity four-vector a^μ vanishes identically, i.e.,

$$a^\mu=\tfrac{1}{2}(-g)^{-\frac{1}{2}}\epsilon^{\mu\alpha\beta\gamma}u_\alpha u_{\beta;\gamma}=0, \tag{34}$$

at all x^ν in $\mathcal{T}$, where g is the determinant of the matrix $\|g_{\alpha\beta}\|$, and $\epsilon^{\mu\alpha\beta\gamma}$ is the contravariant Levi-Civita tensor density, which equals $+1$ or -1 according as $\mu\alpha\beta\gamma$ is an even or odd permutation of the natural order 1, 2, 3, 4, and zero otherwise. Gödel showed[4] that a^μ represents the local angular velocity of matter relative to the compass of inertia, i.e, relative to the direction of the local proper time.

A four-velocity vector field of a group motion can be written

$$U^\alpha(x^\nu)=F^\alpha{}_\nu x^\nu+A^\alpha, \tag{35}$$

where $F^\alpha{}_\nu=F^{\alpha\lambda}\eta_{\lambda\nu}$, $F^{\alpha\lambda}=-F^{\lambda\alpha}$, $A^\alpha{}_{,\beta}=0$, and $F^{\alpha\lambda}{}_{,\beta}=0$.

We now verify that any vector field defined by (33) or by (35) satisfies (24). Differentiation of Eq. (32) gives

$$U_\nu(\theta)_{,\theta}\theta_{,\beta}[x^\nu-x^\nu(\theta)]+U_\nu(\theta)[\delta^\nu{}_\beta-U^\nu(\theta)\theta_{,\beta}]=0;$$

or, solving for $\theta_{,\beta}$,

$$\theta_{,\beta}=-\{U_\nu(\theta)_{,\theta}[x^\nu-x^\nu(\theta)]-U_\nu(\theta)U^\nu(\theta)\}^{-1}U_\beta(\theta). \tag{36}$$

Differentiation of Eq. (33) and use of (36) gives

$$\begin{aligned}U_{\alpha,\beta}=U_\alpha(\theta)_{,\theta}\{&U_\nu(\theta)_{,\theta}[x^\nu(\theta)-x^\nu]\\&+U_\nu(\theta)U^\nu(\theta)\}^{-1}U_\beta(\theta).\end{aligned} \tag{37}$$

It follows from (14) that the $U_{\alpha,\beta}$ given by (37) satisfies

$$U_{\alpha,\beta}(\delta^\beta{}_\nu+u^\beta u_\nu)=0.$$

From this equation and the fact that $U_{\alpha;\beta}=U_{\alpha,\beta}$ in a Galilean coordinate system it follows that the U_α given by (33) satisfies (24). For a group motion we have, from (35) and from the antisymmetry of $F_{\alpha\beta}$,

$$U_{\alpha,\beta}+U_{\beta,\alpha}=F_{\alpha\beta}+F_{\beta\alpha}=0. \tag{38}$$

Thus the U_α given by (35) satisfies (24).

For group motions the world lines are given by

$$x^\alpha=L^\alpha{}_\beta(\theta)\xi^\beta+\left(\int_{\theta_I}^{\theta}L^\alpha{}_\beta(\vartheta)d\vartheta\right)A^\beta, \tag{39}$$

where $\{L^\alpha{}_\beta(\theta)\}$ is a continuous one-parameter family of homogeneous Lorentz transformations.

[4] K. Gödel in *Proceedings of the Sixth International Congress of Mathematicians* (American Mathematical Society, Providence, 1950), Vol. 1, p. 175.

5. GROUP MOTIONS

For an appropriate choice of the parameter θ, the four-velocity vector field $U^\alpha(x^\sigma)$ of a group motion satisfies the ten Killing's equations,

$$U_{\alpha;\beta}+U_{\beta;\alpha}=0. \tag{40}$$

The concept of group motion is of course not restricted to flat space time. See, e.g., Eisenhart,[5] page 221 ff for a discussion of groups of motions. It is clear that any solution of (40) is a solution of (24), i.e., any group motion is a Born-type rigid motion.

To the four-velocity vector field $u^\alpha(x^\sigma)$ corresponds an unnormalized four-acceleration vector field $\dot{u}^\alpha = u^\alpha{}_{;\beta}u^\beta$.

Theorem: For a group motion,

$$\dot{u}_\alpha=(\log_e(-U_\beta U^\beta)^{\frac{1}{2}})_{,\alpha}, \tag{41}$$

where U_β satisfies (40).

Proof: Let ψ and u_α be defined by (25) and (26). Equation (40) implies that

$$U_{\alpha;\beta}u^\alpha u^\beta=0. \tag{42}$$

Multiplying Eq. (27) by u^β and taking account of (42), we get

$$\psi_{,\beta}u^\beta=0. \tag{43}$$

Differentiation of Eq. (26) gives

$$u_{\alpha;\beta}=-\psi_{,\beta}u_\alpha+e^{-\psi}U_{\alpha;\beta}. \tag{44}$$

Multiplying Eq. (44) by u^β, using (43), (40), and (27), we get

$$\dot{u}_\alpha=\psi_{,\alpha}$$

which, since $\psi=\log_e(-U_\beta U^\beta)^{\frac{1}{2}}$, is (41).

Theorem: A rigid motion is a group motion if and only if the normalized four-velocity vector field u^α satisfies the equation

$$\dot{u}_{\alpha,\beta}-\dot{u}_{\beta,\alpha}=0 \tag{45}$$

at all points x^σ of $\mathcal{V}$.

Proof: The four-acceleration $\dot{u}_\alpha$ of a group motion is the gradient of a scalar, which implies Eq. (45). This proves the *only if* part of the theorem.

Consider a rigid motion which satisfies (45). Equation (45) is the necessary and sufficient condition which insures that a function $\psi(x^\sigma)$ is defined by

$$\psi(x^\sigma)=\int^{x^\sigma}\dot{u}_\alpha dx^\alpha. \tag{46}$$

Let the vector field U_α be defined by $U_\alpha=e^\psi u_\alpha$. Then

$$U_{\alpha;\beta}+U_{\beta;\alpha}=e^\psi(u_{\alpha;\beta}+u_{\beta;\alpha}+u_\alpha\psi_{,\beta}+u_\beta\psi_{,\alpha}).$$

Substituting $\dot{u}_\beta$ for $\psi_{,\beta}$ and taking account of (17), we get (40). This proves the *if* part of the theorem.

[5] L. Eisenhart, *Riemannian Geometry* (Princeton University Press, Princeton, 1949).

The theorem proved by Herglotz and Noether can then be stated in the following manner. In special relativity a normalized four-velocity vector field $u_\mu(x^\sigma)$ which satisfies Eq. (17), must also satisfy at least one of the two equations (34) or (45).

The rigid motion equation, (17), may be written

$$u_{\mu;\nu}+u_{\nu;\mu}=-\dot{u}_\mu u_\nu-\dot{u}_\nu u_\mu. \tag{47}$$

From the definition of the local angular velocity four-vector a^μ given in Eq. (34), we obtain

$$\begin{aligned}2(-g)^{\frac{1}{2}}\epsilon_{\mu\nu\sigma\tau}a^\mu&=\delta_{\nu\sigma\tau}{}^{\alpha\beta\gamma}u_\alpha u_{\beta;\gamma}\\&=u_\nu(u_{\sigma;\tau}-u_{\tau;\sigma})+u_\sigma(u_{\tau;\nu}-u_{\nu;\tau})\\&\quad+u_\tau(u_{\nu;\sigma}-u_{\sigma;\nu}).\end{aligned} \tag{48}$$

From (9), (10), and (48), we find

$$2(-g)^{\frac{1}{2}}\epsilon_{\mu\nu\sigma\tau}a^\mu u^\tau=u_{\tau;\sigma}-u_{\sigma;\tau}+u_\sigma\dot{u}_\tau-u_\tau\dot{u}_\sigma,$$

or

$$u_{\mu;\nu}-u_{\nu;\mu}=-\dot{u}_\mu u_\nu+\dot{u}_\nu u_\mu+2(-g)^{\frac{1}{2}}\epsilon_{\sigma\tau\nu\mu}a^\sigma u^\tau. \tag{49}$$

Adding Eqs. (47) and (49) gives us

$$u_{\mu;\nu}=-\dot{u}_\mu u_\nu-(-g)^{\frac{1}{2}}\epsilon_{\mu\nu\sigma\tau}a^\sigma u^\tau. \tag{50}$$

From (10), (34), and (50) it follows that

$$\dot{u}_\mu u^\mu=a_\mu u^\mu=0. \tag{51}$$

From the antisymmetry of $\epsilon_{\mu\nu\sigma\tau}$ in μ and ν, it follows that any $u_\mu(x^\sigma)$ that satisfies (49) also satisfies (47), and therefore (17). Equations (50) and (51) are equivalent to Eq. (17). The Herglotz-Noether theorem can then be stated: In special relativity, if a normalized four-velocity vector field $u_\mu(x^\sigma)$ satisfies Eq. (49), i.e., if it is the field of a Born-type rigid motion, then at least one of the two conditions—

(1) $\dot{u}_\mu$ is the gradient of a scalar and the motion is a *group motion*; or

(2) a^σ vanishes and the motion is a *plane motion*; must hold throughout $\mathcal{V}$.

The geometrical properties of the world lines of Born type rigid motions in special relativity were examined in detail by Salzman.[6] In particular it was shown that a^μ does not vanish for the group motion which is such that the world lines of the particles undergoing the motion may be identified with the world lines of the particles constituting a rotating rigid disk. This means that there is no three-dimensional manifold orthogonal to this set of world lines. Hence the metric

$$dl^2=(g_{\alpha\beta}+u_\alpha u_\beta)x^\alpha{}_{,i}x^\beta{}_{,j}d\xi^i d\xi^j, \tag{15}$$

which measures the orthogonal distance between the world line of the particle ξ^i and that of the particle $\xi^i+d\xi^i$, is not the metric tensor of a three-space immersed in the Minkowski space time. Nevertheless, the quantity

$$l=\int dl \tag{52}$$

[6] G. Salzman, thesis, University of Illinois, 1953 (unpublished).

can be computed for any curve in the ξ^1, ξ^2, ξ^3 space and it will be independent of θ. We may take a curve such that

$$(\xi^1)^2+(\xi^2)^2=b^2, \quad \xi^3=0,$$

where b is a constant. This curve goes through the particles initially (i.e., for $\theta=\theta_l$) on the circumference of the rigid disk. When $\theta>\theta_l$ this curve is mapped into a locus described by Eqs. (39), where $L^\alpha{}_\beta(\theta)$ has been given by Herglotz. The value of l for this curve computed from Eqs. (15) and (52) has been called the *intrinsic circumference* of the rotating disk. The value of $l\neq 2\pi b$.

It should be pointed out that although it is possible to define other *intrinsic three-dimensional geometries* associated with a given three-parameter family of world lines with the *distance* between the particle ξ^i and $\xi^i+d\xi^i$ given by

$$dl^2=\mathcal{G}_{ij}d\xi^i d\xi^j,$$

the definition given by Eq. (15) has the virtue that dl is independent of θ.

6. THE DYNAMICAL EQUATIONS FOR A COMPRESSIBLE, NONVISCOUS, NON-HEAT CONDUCTING FLUID

Consider an isolated system of particles whose streamlines are the family $\{C_{\xi^i}\}$ of a rigid motion. Let $u^\alpha(x^\nu)$ be the unit four-velocity vector field defined by the streamlines. The system is described by a stress-energy tensor $T^{\alpha\beta}$ from which field quantities with correct relativistic transformation properties are defined. All field quantities, $T^{\alpha\beta}$ included, are understood to be the macroscopic averages of the corresponding microscopic quantities, and it is assumed that $T^{\alpha\beta}=T^{\beta\alpha}$. A method of performing Lorentz-invariant kinetic theory averages is given by Taub.[7] The result is that the macroscopic stress-energy tensor may be decomposed in the same way that Eckart[8] decomposed the corresponding microscopic stress-energy tensor, i.e.,

$$T^{\alpha\beta}=wu^\alpha u^\beta+Q^\alpha u^\beta+Q^\beta u^\alpha+S^{\alpha\beta}, \tag{53}$$

where

$$\begin{aligned} w&=T^{\alpha\beta}u_\alpha u_\beta,\\ Q^\alpha&=-T^{\lambda\beta}(\delta^\alpha{}_\lambda+u^\alpha u_\lambda)u_\beta,\\ S^{\alpha\beta}&=T^{\lambda\nu}(\delta^\alpha{}_\lambda+u^\alpha u_\lambda)(\delta^\beta{}_\nu+u^\beta u_\nu). \end{aligned} \tag{54}$$

These field quantities are interpreted as follows. The invariant w is the proper energy density, i.e., the energy density as determined by someone instantaneously at rest with respect to an element of the fluid, Q^α is the heat flow four vector, and $S^{\alpha\beta}$ is the stress tensor. If ρ is the proper density of matter then ϵ, the internal energy per unit rest mass of the fluid, is defined by

$$w=\rho(c^2+\epsilon). \tag{55}$$

[7] A. Taub, Phys. Rev. **74**, 328 (1948).
[8] C. Eckart, Phys. Rev. **58**, 919 (1940).

The invariant pressure p is defined by

$$S^\alpha{}_\alpha=3p. \tag{56}$$

In what follows it is assumed that the fluid being discussed is incapable of conducting heat or of maintaining shearing stresses. Thus $Q^\alpha=0$, and in the proper locally Lorentz coordinate system $S^{\alpha\beta}=0$ for $\alpha\neq\beta$, $S^{ii}=p$, and $S^{44}=0$. If we write $S^{\alpha\beta}=pg^{\alpha\beta}$, where $g_{\alpha\beta}$ is the metric tensor of the proper locally Lorentz coordinate system, then this is correct for all values of α and β except $\alpha=\beta=4$, when it gives $-p$ instead of 0. In these coordinates $u^\alpha u^\beta=0$ unless $\alpha=\beta=4$, when it equals 1. Thus

$$S^{\alpha\beta}=p(g^{\alpha\beta}+u^\alpha u^\beta) \tag{57}$$

is correct in the proper locally Lorentz coordinates, and since it is a tensor it is the correct form in any coordinates for the stress tensor of a fluid that can sustain only a pressure. Substituting Eqs. (55) and (57) into (53), and taking account of the assumption $Q^\alpha=0$, we get

$$T^{\alpha\beta}=\rho[c^2+\epsilon+(p/\rho)]u^\alpha u^\beta+pg^{\alpha\beta}. \tag{58}$$

Defining the dimensionless function

$$\mu=1+(1/c^2)[\epsilon+(p/\rho)] \tag{59}$$

enables us to write

$$T^{\alpha\beta}=\mu\rho c^2u^\alpha u^\beta+pg^{\alpha\beta}. \tag{60}$$

The equations of motion of the fluid are

$$T^{\alpha\beta}{}_{;\beta}=0, \tag{61}$$

and

$$(\rho u^\alpha)_{;\alpha}=0. \tag{62}$$

Equation (61) expresses the conservation of momentum and energy. Equation (62) states that no particles are created or annihilated.

Let the invariant absolute temperature τ and the invariant specific entropy S as measured by an observer at rest with respect to an element of the fluid be defined by

$$d\epsilon+pd(1/\rho)=\tau dS. \tag{63}$$

Then the conservation of energy equation, $T^{\alpha\beta}{}_{;\beta}u_\alpha=0$, and the conservation of matter imply conservation of entropy along the streamlines, $S_{,\alpha}u^\alpha=0$, as follows.

By use of (60) and (62), Eq. (61) becomes

$$\rho u^\beta(\mu c^2u^\alpha)_{;\beta}+(pg^{\alpha\beta})_{;\beta}=0.$$

By using the fact that $g^{\alpha\beta}{}_{;\beta}=0$, and taking account of (59), this becomes

$$\rho u^\beta[\epsilon+(p/\rho)]_{,\beta}u^\alpha+\mu\rho c^2\dot{u}^\alpha+p_{,\beta}g^{\alpha\beta}=0.$$

Multiplying by u_α, and noting Eqs. (9) and (10), we get

$$-\rho[\epsilon_{,\beta}+p(1/\rho)_{,\beta}]u^\beta=0,$$

which implies, since $-\rho\tau\neq 0$, that

$$S_{,\beta}u^\beta=0. \tag{64}$$

If all parts of the fluid are initially at the same entropy, then $S=constant$ holds throughout $\mathcal{T}$. In this case Eq. (63) determines p and ρ as functions of each other, once $\epsilon(p,\rho)$ is specified.

7. RIGID MOTION IN GENERAL RELATIVITY

The covariant derivatives that enter in Eqs. (61) and (62) are with respect to the coordinates in which the gravitational field is represented by the metric tensor $g_{\alpha\beta}$. We are concerned with problems in which this gravitational field is due to the fluid undergoing the motion described by Eqs. (61) and (62). Thus the $g_{\alpha\beta}$'s are determined by the Einstein field equations,

$$R_{\alpha\beta}-\tfrac{1}{2}g_{\alpha\beta}R=-kT_{\alpha\beta}, \tag{65}$$

in which the $T_{\alpha\beta}$ are the same as those occurring in Eq. (61).

The problem is then to solve the system of equations,

$$\left.\begin{aligned} R_{\alpha\beta}-\tfrac{1}{2}g_{\alpha\beta}R&=-kT_{\alpha\beta}, && (65)\\ u_{\alpha;\beta}+u_{\beta;\alpha}+\dot{u}_\alpha u_\beta+\dot{u}_\beta u_\alpha&=0, && (47)\\ u_\alpha u^\alpha&=-1, && (9)\\ T^{\alpha\beta}{}_{;\beta}&=0, && (61)\\ (\rho u^\alpha)_{;\alpha}&=0. && (62)\end{aligned}\right\}(66)$$

for the sixteen functions $g_{\alpha\beta}$, u_α, ρ, and p, where $T^{\alpha\beta}$ is assumed given by Eqs. (59) and (60) and ϵ is assumed to be a given function of p and ρ. Equation (61) is a consequence of Eq. (65), but is included in the system (66) because explicit use is made of it.

Theorem: A hydrodynamical system which satisfies the Eqs. of (66) and for which

$$\mu\partial\epsilon/\partial p\neq 0 \quad \text{and} \quad S=constant,$$

is performing a group motion.

Proof: Equation (9) implies (10). If Eq. (47) is multiplied by $g^{\alpha\beta}$ and (10) taken into account, then

$$u^\alpha{}_{;\alpha}=0. \tag{67}$$

Equations (62) and (67) imply that

$$p_{,\alpha}u^\alpha=0. \tag{68}$$

By using (60) and taking account of (62) and (68), Eq. (61) becomes

$$\rho p_{,\beta}u^\beta u^\alpha\partial\epsilon/\partial p+p_{,\beta}u^\alpha u^\beta+p_{,\beta}g^{\alpha\beta}+\mu\rho^2c^2\dot{u}^\alpha=0. \tag{69}$$

If Eq. (69) is multiplied by u_α, and (9) and (10) taken into account, then

$$-\rho p_{,\beta}u^\beta\partial\epsilon/\partial p=0,$$

or, since $\partial\epsilon/\partial p$ and ρ are nonzero throughout $\mathcal{T}$,

$$p_{,\beta}u^\beta=0 \tag{70}$$

throughout $\mathcal{T}$. Equation (69) then becomes, since $\mu\neq 0$

$$\dot{u}_\alpha=-p_{,\alpha}/(\mu\rho c^2). \tag{71}$$

From (71) we get

$$\dot{u}_{\alpha,\beta}-\dot{u}_{\beta,\alpha}=(\mu+\rho\partial\mu/\partial\rho)(p_{,\alpha}\rho_{,\beta}-p_{,\beta}\rho_{,\alpha})/(\mu\rho c^2).$$

But $S=constant$ implies that ρ and p are functions of each other, which in turn implies that $p_{,\alpha}\rho_{,\beta}-p_{,\beta}\rho_{,\alpha}=0$. Therefore Eq. (45) is satisfied at all x^ν in $\mathcal{T}$, and the motion is a group motion.

If $\epsilon(p,\rho)$ is any nonnegative function and if $\partial\epsilon/\partial p\neq 0$, then μ is a positive function and $\mu\partial\epsilon/\partial p\neq 0$. We will restrict ourselves to isentropic motions of fluids that satisfy this condition, and therefore we replace system (66) by

$$\left.\begin{aligned} R_{\alpha\beta}-\tfrac{1}{2}g_{\alpha\beta}R&=-kT_{\alpha\beta}, && (65)\\ U_{\alpha;\beta}+U_{\beta;\alpha}&=0, && (40)\\ u^\alpha&=(-g_{\alpha\nu}U^\alpha U^\nu)^{-\frac{1}{2}}U^\alpha, && (8)\\ T^{\alpha\beta}{}_{;\beta}&=0, && (61)\\ (\rho u^\alpha)_{;\alpha}&=0. && (62)\end{aligned}\right\}(72)$$

Equations (40) and (8) of system (72) imply (47) and (9), respectively, of system (66), and therefore every solution of (72) is a solution of (66).

8. A METHOD OF INTEGRATING THE SYSTEM OF EQS. (72)

The method we shall pursue is to reduce the system (72) to a set of equations for the $g_{\alpha\beta}$. In this set the U^α will be considered as known since the coordinate system may be chosen so that the U^α may be prescribed arbitrarily. The reduction is accomplished as follows: p and ρ may be expressed as functions of $g_{\alpha\beta}U^\alpha U^\beta$ if one assumes that $\mu\partial\epsilon/\partial p\neq 0$ and that the fluid is performing isentropic motion in accord with Eqs. (72). We examine solutions of (72) for which the U^α chosen is such that the angular velocity vector field given by (34) is nonvanishing. Since the motion is a group motion, the dynamical Eqs. (71) may be written

$$p_{,\alpha}/(\mu\rho c^2)=-[\log_e(-U_\beta U^\beta)^{\frac{1}{2}}]_{,\alpha}. \tag{73}$$

Since the motion is isentropic $p=p(\rho)$, which implies that the integrability conditions of Eq. (73) are satisfied. Therefore

$$\int(\mu\rho c^2)^{-1}dp=-\log_e(-U_\beta U^\beta)^{\frac{1}{2}}, \tag{74}$$

and we can explicitly obtain

$$\rho=\rho(g_{\alpha\beta}U^\alpha U^\beta), \quad p=p(g_{\alpha\beta}U^\alpha U^\beta), \tag{75}$$

where the right-hand members are known functions of $g_{\alpha\beta}U^\alpha U^\beta$. This enables us to eliminate the unknown functions ρ and p from $T_{\alpha\beta}$.

It is known (see, e.g., Eisenhart,[5] page 5) that given a vector field U^α, there exists a coordinate system in which $\bar{U}^\alpha=\delta^\alpha_4$. It is therefore no restriction at all to specify U^α, because $g_{\alpha\beta}$ is yet to be determined.

Thus, given a velocity field $U^\alpha(x^\nu)$, Eqs. (8) and (75) enable one to write $T_{\alpha\beta}$ explicitly in terms of the unknown functions $g_{\alpha\beta}$. Equations (65) then determine the $g_{\alpha\beta}$'s. Equations (40) are additional conditions on the first derivatives of the $g_{\alpha\beta}$'s. Equations (8) just

define $u^\alpha(x^\nu)$, and there is no question about satisfying them.

That Eq. (62) is automatically satisfied can be seen as follows. Since the motion is isentropic, $\rho=\rho(p)$ and

$$\rho_{,\alpha}=p_{,\alpha}d\rho/dp. \tag{76}$$

Equation (73) may be written

$$p_{,\alpha}=-\mu\rho c^2\dot{u}_\alpha.$$

It follows from this and from (10) that

$$p_{,\alpha}u^\alpha=0.$$

From this and from (76) we get

$$\rho_{,\alpha}u^\alpha=0,$$

which is Eq. (68). Since the motion is a group motion (67) holds, and (67) and (68) imply (62).

The problem is thus reduced to that of solving the system

$$\left.\begin{aligned} &R_{\alpha\beta}-\tfrac{1}{2}g_{\alpha\beta}R=-kT_{\alpha\beta}(g_{\mu\nu}U^\mu U^\nu), && (77)\\ &U_{\alpha;\beta}+U_{\beta;\alpha}=0, && (40)\end{aligned}\right\} \tag{78}$$

for the ten unknown $g_{\alpha\beta}$'s, the U^μ's being considered as given.

We will be interested in dynamical solutions which satisfy the condition $p=0$ on the boundary hypersurface of the region $\mathcal{T}$, which hypersurface can be described by equations of the form

$$x^i=h^i(b_1,b_2,ct).$$

The solutions will be required to be such that the functions p and ρ are nonnegative throughout $\mathcal{T}$.

9. THE ROTATING RIGID BODY IN GENERAL RELATIVITY

We assume that in the x^α-coordinates, which for heuristic reasons are called, r, z, ϕ, ct, the world lines are given by

$$\begin{aligned} x^1&=r=r_I,\\ x^2&=z=z_I,\\ x^3&=\phi=\phi_I+(\omega/c)ct,\\ x^4&=ct; \end{aligned} \tag{79}$$

i.e., the time coordinate ct is the parameter used to describe the motion, and the initial hypersurface from which the world lines start is $ct=0$. r_I, z_I, and ϕ_I are the parameters ξ^i that label the world lines.

The four-velocity vector field defined by Eqs. (79) with this choice of parameter is

$$\|U^\alpha\|=\|0,0,\omega/c,1\|. \tag{80}$$

Let $g_{\alpha\beta}(x^\nu)$ be the metric tensor of the x^α-coordinate system. Killing's Eqs. (40) can also be written as

$$g_{\alpha\beta,\lambda}U^\lambda+U^\lambda{}_{,\beta}g_{\lambda\alpha}+U^\lambda{}_{,\alpha}g_{\lambda\beta}=0. \tag{81}$$

Substituting Eq. (80) into Eq. (81) we get, since the second and third terms vanish,

$$g_{\alpha\beta,3}[\omega/c]+g_{\alpha\beta,4}=0.$$

The general solution of this equation is

$$g_{\alpha\beta}(x^\nu)=\chi_{\alpha\beta}(r,z,\phi-(\omega/c)ct),$$

where $\chi_{\alpha\beta}$ is an arbitrary function of r, z, and $\phi-(\omega/c)ct$ We restrict ourselves to looking for *steady state* motions with *cylindrical* symmetry, i.e., all the field quantities are assumed independent of ct and of ϕ, respectively. Therefore

$$g_{\alpha\beta}=g_{\alpha\beta}(r,z),$$

and this together with (80) insures that Killing's equations are satisfied. The problem is thus reduced to that of finding integrals of Eq. (77), i.e., sets of $g_{\alpha\beta}(r,z)$'s, which have the property that when they are substituted into Eqs. (75), nonnegative functions $\rho(x^\nu)$ and $p(x^\nu)$ are determined which vanish everywhere except in a region $\mathcal{T}$, and p is continuous on the boundary of $\mathcal{T}$. Also, U^α must be timelike throughout $\mathcal{T}$. In order to solve (77) an approximation method is used.

10. AN APPROXIMATION METHOD FOR INTEGRATING EQ. (77)

The method is based on the smallness of the constant k of Eq. (77). Newton's gravitational constant G is related to k by the equation (in our choice of units)

$$\begin{aligned} k=8\pi G/c^4&=[8\pi\times 6.67\times 10^{-8}\ \text{dyne cm}^2\ \text{gm}^{-2}]/\\ &\quad[(3\times 10^{10}\ \text{cm sec}^{-1})^4]\\ &=2.07\times 10^{-48}\ \text{g}^{-1}\ \text{cm}^{-1}\ \text{sec}^2. \end{aligned}$$

It is convenient to replace k by $\kappa\mathrm{k}$, with $\kappa=1\ \text{g}^{-1}\ \text{cm}^{-1}\ \text{sec}^2$, and k the pure number 2.07×10^{-48}, and to assume the metric tensor expanded in a power series in k,

$$g_{\alpha\beta}=\sum_{n=0}^{\infty}\mathrm{k}^n g^{(n)}{}_{\alpha\beta}=\sum_{n=0}^{\infty}\gamma^{(n)}{}_{\alpha\beta}. \tag{82}$$

Then, substituting this expression for $g_{\alpha\beta}$ into both members of (77), we seek a solution in which each equation obtained by equating the coefficients of like powers of k satisfied. This has the effect of replacing (77) by a sequence of equations of the form

$$\Theta_{\lambda\nu}{}^{\alpha\beta}\gamma^{(n)}{}_{\alpha\beta}=\mathrm{k}^n\phi^{(n)}{}_{\lambda\nu},\quad n=0,1,2,\cdots, \tag{83}$$

where $\Theta_{\lambda\nu}{}^{\alpha\beta}$ is a linear differential operator and $\phi^{(n)}{}_{\alpha\beta}$ is a known function which depends only on the $g^{(m)}{}_{\alpha\beta}$'s with $m<n$, and their derivatives. Thus if Eqs. (83) are solved in order, $\phi^{(n)}{}_{\alpha\beta}$ is a known function of x^ν at each step.

More explicitly, (77) may be written in the equivalent form

$$R_{\alpha\beta}=-\kappa\mathrm{k}\mathfrak{T}_{\alpha\beta}(g_{\lambda\nu}U^\lambda U^\nu), \tag{84}$$

where

$$\mathfrak{T}_{\alpha\beta}=T_{\alpha\beta}-\tfrac{1}{2}g_{\alpha\beta}[T_{\lambda\nu}g^{\lambda\nu}].$$

If it is assumed that $\gamma^{(0)}{}_{\alpha\beta}=\eta_{\alpha\beta}$, then Eqs. (83) are

$$\tfrac{1}{2}\Big[\eta^{\alpha\beta}\frac{\partial^2}{\partial x^\mu\partial x^\nu}+\delta^\alpha{}_\mu\delta^\beta{}_\nu\Box-\eta^{\alpha\sigma}\delta^\beta{}_\mu\frac{\partial^2}{\partial x^\sigma\partial x^\mu}-\eta^{\beta\sigma}\delta^\alpha{}_\nu\frac{\partial^2}{\partial x^\sigma\partial x^\mu}\Big]\gamma^{(n)}{}_{\alpha\beta}=\mathrm{k}^n\phi^{(n)}{}_{\mu\nu},\quad(85)$$

where

$$\phi^{(n)}{}_{\alpha\beta}=-\mathfrak{T}^{(n-1)}{}_{\alpha\beta}-\tfrac{1}{2}W^{(n)}{}_{\alpha\beta},$$

$\mathfrak{T}^{(n)}{}_{\alpha\beta}$ is defined by the equation

$$\mathfrak{T}_{\alpha\beta}=\sum_{n=0}^{\infty}\mathrm{k}^n\mathfrak{T}^{(n)}{}_{\alpha\beta},\quad\Box=\eta^{\alpha\beta}\frac{\partial^2}{\partial x^\alpha\partial x^\beta},$$

and $W^{(n)}{}_{\alpha\beta}$ is defined by the equation

$$R_{\alpha\beta}=\sum_{n=1}^{\infty}\mathrm{k}^n\big[\Theta_{\alpha\beta}{}^{\nu\lambda}\gamma^{(n)}{}_{\nu\lambda}+\tfrac{1}{2}W^{(n)}{}_{\alpha\beta}\big].$$

In this method the boundary condition $p=0$ is to be satisfied at the last step in the approximation.

11. USE OF THE APPROXIMATION METHOD IN THE CASE OF THE ROTATING RIGID BODY

Here the problem of Sec. 9 is examined in the first approximation, and it is shown that there exist in the classical limit of the theory rigidly rotating dynamical systems held together by their own gravitational fields.

We assume that

$$\gamma^{(0)}{}_{11}=\gamma^{(0)}{}_{22}=-\gamma^{(0)}{}_{44}=1,\ \gamma^{(0)}{}_{33}=r^2,\ \gamma^{(0)}{}_{\alpha\beta}=0\ \text{ if }\ \alpha\neq\beta.$$

This choice satisfies the zeroth order Eq. of (83) and Killing's equations, and enables us to get a formal expression for $\mathfrak{T}^{(0)}{}_{\alpha\beta}$.

The next step is to integrate the first-order field equations. To do this it is convenient to make a coordinate transformation which transforms $\gamma^{(0)}{}_{\alpha\beta}$ into $\eta_{\alpha\beta}$, the Minkowski metric tensor.

$$x^{*1}=x=r\cos\phi=x^1\cos x^3,$$
$$x^{*2}=y=r\sin\phi=x^1\sin x^3,$$
$$x^{*3}=z=z=x^2,$$
$$x^{*4}=ct=ct=x^4.$$

In this coordinate system the first order equation of (83) may be written

$$R^{*(1)}{}_{\alpha\beta}=-\mathrm{k}\mathfrak{T}^{*(0)}{}_{\alpha\beta},\quad(86)$$

where

$$R^{*(1)}{}_{\alpha\beta}=\Theta_{\alpha\beta}{}^{\mu\nu}\gamma^{*(1)}{}_{\mu\nu}=\tfrac{1}{2}[\Box\gamma^{*(1)}{}_{\alpha\beta}+\gamma^{*(1)}{}_{\sigma,\alpha\beta}-\gamma^{*(1)\nu}{}_{\alpha,\nu\beta}-\gamma^{*(1)\nu}{}_{\beta,\nu\alpha}],$$

$$\gamma^{*(1)}{}_{\alpha\beta}=(\partial x^\nu/\partial x^{*\alpha})(\partial x^\lambda/\partial x^{*\beta})\gamma^{(1)}{}_{\nu\lambda},$$

$$\gamma^{*(1)\nu}{}_{\alpha}=\eta^{\nu\beta}\gamma^{*(1)}{}_{\beta\alpha},$$

$$\gamma^{*(1)}=\eta^{\alpha\beta}\gamma^{*(1)}{}_{\alpha\beta}.$$

The homogeneous equation $R^{*(1)}{}_{\alpha\beta}=0$ has the solution $\gamma^{*(1)}{}_{\alpha\beta}=f^*{}_{\alpha,\beta}+f^*{}_{\beta,\alpha}$, where $f^*{}_\alpha$ are arbitrary functions. Therefore

$$\gamma^{*(1)}{}_{\alpha\beta}(x^{*\nu})=\mathrm{k}(2\pi)^{-1}\int[\![\mathfrak{T}^{*(0)}{}_{\alpha\beta}(x^{*\prime\nu})]\!]\times[\eta_{ij}(x^{*\prime i}-x^{*i})(x^{*\prime j}-x^{*j})]^{-\frac{1}{2}}dV^{*\prime}+\mathrm{k}(f^*{}_{\alpha,\beta}+f^*{}_{\beta,\alpha})\quad(87)$$

is a solution of Eq. (86) which has four arbitrary functions in accordance with the freedom of choice of a coordinate system. The three-dimensional volume element $dV^{*\prime}=dx^{*\prime}dy^{*\prime}dz^{*\prime}$. The expression $[\![\mathfrak{T}^{*(0)}{}_{\alpha\beta}(x^{*\prime\nu})]\!]$ is to be evaluated at the retarded time. The spatial distance between the field point and the variable integration point, evaluated in zeroth order, is

$$[\eta_{ij}(x^{*\prime i}-x^{*i})(x^{*\prime j}-x^{*j})]^{\frac{1}{2}}.$$

It can be verified that (87) is a solution of Eq. (86) for any choice of the region of integration.

The region over which the integration in (87) is carried out is related to the boundary condition $p^{(1)}=p([\gamma^{(0)}{}_{\alpha\beta}+\gamma^{(1)}{}_{\alpha\beta}]U^\alpha U^\beta)=0$ as follows: For any prescribed region of integration $p^{(1)}$ will be determined as a function of the coordinates, as will be shown below, the explicit functional form depending on the choice of the region of integration. The boundary described by the equation $p^{(1)}=0$ will then be determined by the region of integration and will vary as this region is varied. Thus, if the region of integration is given, the boundary $p^{(1)}=0$ is determined. It may not be a real boundary for some choices of the region of integration, in the sense that there may be no points in space time whose coordinates satisfy the equation of the boundary. Presumably, if one is given a real boundary $p^{(1)}=0$, one should be able to determine whether a region of integration exists for which the process described above leads to this boundary. This question will not be discussed further here.

In the subsequent discussion we shall assume that the region of integration in Eq. (87) is the interior of a sphere of radius $a^{(0)}$ and shall show that real boundaries exist for this case.

Because we are considering steady state motion the expression $[\![\mathfrak{T}^{*(0)}{}_{\alpha\beta}(x^{*\prime\nu})]\!]$ in Eq. (87) can be evaluated at any time. Transforming back to the x^α-coordinate system, we get

$$\gamma^{(1)}{}_{\alpha\beta}=(\partial x^{*\nu}/\partial x^\alpha)(\partial x^{*\lambda}/\partial x^\beta)\mathrm{k}\mathrm{k}(2\pi)^{-1}\times\int\mathfrak{T}^{*(0)}{}_{\nu\lambda}(x^{*\prime\sigma})[\eta_{ij}(x^{*\prime i}-x^{*i})(x^{*\prime j}-x^{*j})]^{-\frac{1}{2}}dV^{*\prime}+\mathrm{k}(f_{\alpha;\beta}+f_{\beta;\alpha}),\quad(88)$$

where

$$f_{\alpha;\beta}=(\partial x^{*\nu}/\partial x^\alpha)(\partial x^{*\lambda}/\partial x^\beta)f^*{}_{\nu,\lambda}=(\partial x^{*\nu}/\partial x^\alpha)(\partial x^{*\lambda}/\partial x^\beta)[f^*{}_{\nu,\lambda}+O(\mathrm{k})].$$

and of course the terms of order k with respect to $f^*_{\nu\lambda}$ are ignored.

The combination $(\gamma^{(0)}{}_{\alpha\beta}+\gamma^{(1)}{}_{\alpha\beta})U^\alpha U^\beta$ is required, rather than the individual $\gamma^{(1)}{}_{\alpha\beta}$'s. From (80) and the $\gamma^{(0)}{}_{\alpha\beta}$'s assumed,

$$(\gamma^{(0)}{}_{\alpha\beta}+\gamma^{(1)}{}_{\alpha\beta})U^\alpha U^\beta=(\omega r/c)^2-1+\Gamma, \tag{89}$$

where

$$\Gamma=\gamma^{(1)}{}_{44}+2(\omega/c)\gamma^{(1)}{}_{34}+(\omega/c)^2\gamma^{(1)}{}_{33}.$$

Using (88), straightforward calculation leads to

$$\Gamma(x^\nu)=\frac{\kappa k}{2\pi}\int\frac{\Omega(\mathbf{r},\mathbf{r}')}{|\mathbf{r}-\mathbf{r}'|}dV'+2\kappa k(\omega/c)rf_1, \tag{90}$$

where

$$\Omega(\mathbf{r},\mathbf{r}')=\frac{\mu^{(0)}\rho^{(0)}c^2\{1-[(\omega/c)^2rr'\cos(\phi-\phi')]\}^2}{1-(\omega r'/c)^2}$$
$$-(\tfrac{1}{2}\mu^{(0)}\rho^{(0)}c^2-p^{(0)})(1-(\omega r/c)^2),$$

$\mathbf{r}$ is the ordinary radial three vector, i.e., no time component, from the origin ($r=z=0$) to the point r,z,ϕ, and

$$|\mathbf{r}-\mathbf{r}'|=[r^2+r'^2+(z-z')^2-2rr'\cos(\phi-\phi')]^{\frac{1}{2}}.$$

The function f_1 may be taken to be zero, for if it is not we may go to another coordinate system related to the r,z,ϕ,ct coordinates as follows:

$$\bar{r}=\bar{r}(r,z),\quad \bar{z}=\bar{z}(r,z),\quad \bar{\phi}=\phi,\quad c\bar{t}=ct.$$

In this coordinate system the $\bar{U}^\sigma$ are still given by the right-hand sides of Eq. (80). Hence Eq. (90) will hold in the barred coordinate system. However we may choose the functions $\bar{r}(r,z)$ and $\bar{z}(r,z)$ so that

$$\bar{f}_1=f_1\partial r/\partial\bar{r}+f_2\partial z/\partial\bar{r}=0.$$

Therefore (90) becomes

$$\Gamma(x^\nu)=\frac{\kappa k}{2\pi}\int\frac{\Omega(\mathbf{r},\mathbf{r}')}{|\mathbf{r}-\mathbf{r}'|}dV'. \tag{91}$$

12. THE CLASSICAL LIMIT

Before specializing $\epsilon(p,\rho)$ or restricting ourselves to isentropic flow, we can determine the *classical limit* of $c^2\Gamma$. Note that

$$u^{(0)}=1+(1/c^2)[\epsilon^{(0)}+(p^{(0)}/\rho^{(0)})],$$
$$\tfrac{1}{2}\mu^{(0)}\rho^{(0)}c^2-p^{(0)}=\tfrac{1}{2}\rho^{(0)}c^2\{1+(1/c^2)[\epsilon^{(0)}-(p^{(0)}/\rho^{(0)})]\},$$
$$\kappa k=8\pi G/c^4.$$

Therefore, we get from (91)

$$\text{Limit}_{cl}\,c^2\Gamma=\underset{c\to\infty}{\text{Limit}}\,c^2\Gamma=2G\int\frac{\rho^{(0)}(\mathbf{r}')}{|\mathbf{r}-\mathbf{r}'|}dV'. \tag{92}$$

Equation (92) is useful in examining the classical limit ($c\to\infty$) of the first order approximation, i.e., the approximation to order k^1. The right-hand member of (92) is (-2) times the Newtonian gravitational potential of a distribution $\rho^{(0)}(\mathbf{r})$ of matter.

Under the assumption that the motion is isentropic and that $\epsilon(p,\rho)=p/[\rho(\gamma-1)]$, where γ is the ratio of the specific heats of the fluid and is assumed to be a constant, Eq. (63) gives

$$p=\kappa\rho^\gamma, \tag{93}$$

where κ is the constant of integration. Substituting this into (74), we find for Eqs. (75):

$$\left.\begin{aligned}\rho&=\{[(\gamma-1)/\kappa\gamma][A(-g_{\alpha\beta}U^\alpha U^\beta)^{-\frac{1}{2}}-c^2]\}^{1/(\gamma-1)},\\ p&=\kappa\{[(\gamma-1)/\kappa\gamma][A(-g_{\alpha\beta}U^\alpha U^\beta)^{-\frac{1}{2}}-c^2]\}^{\gamma/(\gamma-1)},\end{aligned}\right\} \tag{94}$$

where A is the constant of integration. Substituting from Eq. (89) for $g_{\alpha\beta}U^\alpha U^\beta$ into the above equation for p, we find the first order approximation to p, namely,

$$p^{(1)}=\kappa\{[(\gamma-1)/\kappa\gamma][A^{(1)}(1-(\omega r/c)^2-\Gamma)^{-\frac{1}{2}}-c^2]\}^{\gamma/(\gamma-1)}.$$

Let $[\chi]_0$ denote the value of a function χ at the origin ($r=z=0$). Then from the last equation,

$$A^{(1)}=\{[\kappa\gamma/(\gamma-1)][[p^{(1)}]_0/\kappa]^{(\gamma-1)/\gamma}+c^2\}(1-[\Gamma]_0)^{\frac{1}{2}},$$

and

$$p^{(1)}=\kappa\{[c^2(\gamma-1)/\kappa\gamma][\Lambda(1-[\Gamma]_0)^{\frac{1}{2}}$$
$$\times(1-(\omega r/c)^2-\Gamma)^{-\frac{1}{2}}-1]\}^{\gamma/(\gamma-1)}, \tag{95}$$

where

$$\Lambda=\frac{\kappa\gamma([p^{(1)}]_0/\kappa)^{(\gamma-1)/\gamma}}{(\gamma-1)c^2}+1.$$

If the square roots in Eq. (95) are expanded in powers of k (remembering that Γ and $[\Gamma]_0$ are of order k^1), terms of order k^2 or greater discarded and the classical limit taken, we find with the help of (92) that

$$\text{Limit}_{cl}\,p^{(1)}=\kappa\left\{\frac{\gamma-1}{\kappa\gamma}\left[\tfrac{1}{2}\omega^2r^2+B+G\int\frac{\rho^{(0)}(\mathbf{r}')}{|\mathbf{r}-\mathbf{r}'|}dV'\right]\right\}^{\gamma/(\gamma-1)}. \tag{96}$$

where

$$B=\frac{\kappa\gamma}{\gamma-1}\left(\frac{[p^{(1)}]_0}{\kappa}\right)^{(\gamma-1)/\gamma}-G\int\frac{\rho^{(0)}(\mathbf{r}')}{|\mathbf{r}'|}dV'.$$

Classically, a rigidly rotating body of gas which obeys the adiabatic law, Eq. (93), has a pressure p_{cl} given by

$$p_{cl}=\kappa\left\{\frac{\gamma-1}{\kappa\gamma}\left[\tfrac{1}{2}\omega^2r^2+B_{cl}+G\int\frac{\rho_{cl}(\mathbf{r}')}{|\mathbf{r}-\mathbf{r}'|}dV'\right]\right\}^{\gamma/(\gamma-1)}, \tag{97}$$

where

$$B_{cl}=\frac{\kappa\gamma}{\gamma-1}\left(\frac{[p_{cl}]_0}{\kappa}\right)^{(\gamma-1)/\gamma}-G\int\frac{\rho_{cl}(\mathbf{r}')}{|\mathbf{r}'|}dV'.$$

This is equivalent to Eq. (236.2) of Jean's *Astronomy and Cosmogony*.[9]

Consider the classical problem of a rigidly rotating body of gas which obeys the adiabatic law. If we attempted a perturbation approach in which the gravitational interaction was ignored in zeroth order, then we would have, from Eq. (97),

$$p_{cl}{}^{(0)}=\kappa\left\{\frac{\gamma-1}{\kappa\gamma}\left[\tfrac{1}{2}\omega^2r^2+\frac{\kappa\gamma}{\gamma-1}\left(\frac{[p_{cl}{}^{(0)}]_0}{\kappa}\right)^{(\gamma-1)/\gamma}\right]\right\}^{\gamma/(\gamma-1)}.$$

If the zeroth-order density $\rho_{cl}{}^{(0)}$ corresponding to this $p_{cl}{}^{(0)}$ was used to calculate a first approximate gravitational field and this field was used to calculate the first order pressure, we would get, from (97),

$$p_{cl}{}^{(1)}=\text{Limit}_{cl}p^{(1)}.$$

Thus the classical limit of the first order approximation gives the same density and pressure distribution as does the scheme described in this paragraph.

13. AN EXAMPLE

From (89) and (94) we see that

$$p^{(0)}=\kappa\{[c^2(\gamma-1)/\kappa\gamma][\Lambda(1-(\omega r/c)^2)^{-\frac{1}{2}}-1]\}^{\gamma/(\gamma-1)}.$$

This shows that $p^{(0)}$ is a monotone increasing function of r from 0 to c/ω, and that $p^{(0)}\to\infty$ as $r\to c/\omega$. There are thus no self-contained rotating rigid bodies in the zeroth approximation, i.e., an external cylindrical wall would be needed to keep the fluid moving in circular orbits rather than flowing outward. This is to be expected because in this approximation the particles are interacting only through the pressure.

The rest of the calculation is concerned with showing that in the classical limit there are self-contained dynamical solutions in the first approximation. We restrict ourselves to the case

$$\epsilon=p/[\rho(\gamma-1)],\quad p=\kappa\rho^\gamma,\quad\text{and}\quad\gamma=\tfrac{3}{2},$$

and to the classical limit.

The boundary of a self-contained dynamical solution in the first order approximation is defined by $p^{(1)}=0$. From Eq. (95) it follows that $p^{(1)}=0$ if and only if

$$\left(\frac{\omega r}{c}\right)^2+\Gamma-[\Gamma]_0+(1-[\Gamma]_0)\times\left[\frac{6\kappa}{c^2}\left(\frac{[p^{(1)}]_0}{\kappa}\right)^{\frac{1}{2}}+\left(\frac{3\kappa}{c^2}\right)^2\left(\frac{[p^{(1)}]_0}{\kappa}\right)^{\frac{1}{2}}\right]=0.$$

If this equation is multiplied through by c^2 and the classical limit taken, one obtains for the equation of the boundary in this case:

$$\omega^2r^2+\text{Limit}_{cl}c^2(\Gamma-[\Gamma]_0)+6\kappa([p^{(1)}]_0/\kappa)^{\frac{1}{2}}=0. \quad (98)$$

[9] J. Jeans, *Astronomy and Cosmogony* (Cambridge University Press, London, 1929), p. 259.

It can be shown[7] that the velocity of sound in a fluid of the type under consideration is

$$v=c\left(\frac{\rho}{\mu}\frac{d\mu}{d\rho}\right)^{\frac{1}{2}},$$

where μ must be expressed as a function of ρ alone. We then find that, in the classical limit,

$$\kappa=2v^2/(3\rho^{\frac{1}{2}})$$

which enables us to replace κ in Eq. (98).

If the integral of Eq. (91) is evaluated on the assumption of a spherical zero-order boundary of radius $a^{(0)}$, this result substituted into Eq. (98), the resulting equation brought into dimensionless form by dividing through by $2\omega^2(a^{(0)})^2$, the dimensionless constants

$$\alpha=2([v^{(1)}]_0/\omega a^{(0)})^2,$$
$$\alpha^{(0)}=2([v^{(0)}]_0/\omega a^{(0)})^2,$$
$$\beta=2\pi G[\rho^{(1)}]_0/\omega^2,$$

introduced, the replacements

$$\mathrm{r}=r/a^{(0)},\quad z=z/a^{(0)}$$

made, and the equation multiplied through by α^2, then the equation of the boundary is

$$f(\mathrm{r}^2,z^2)=0, \quad (99)$$

where

$$f(\mathrm{r}^2,z^2)=\alpha^3-\frac{\beta}{3}\left\{\frac{2}{5\cdot7}+\alpha^{(0)}[\alpha^{(0)}+\tfrac{2}{5}]\right\}z^2+\frac{\beta}{5\cdot7}\left[\frac{47}{9}-4\alpha^{(0)}\right]z^4-\frac{2\beta}{3\cdot7\cdot9\cdot11}z^6-\frac{\beta(2+9\alpha^{(0)})}{3\cdot5\cdot7}\mathrm{r}^2z^2+\frac{5\beta}{7\cdot9\cdot11}\mathrm{r}^2z^4-\frac{5\beta}{7\cdot11\cdot12}\mathrm{r}^4z^2+\left\{\frac{\alpha^2}{2}+\frac{\beta}{3}\left[\frac{1}{5\cdot7}+\alpha^{(0)}(\tfrac{1}{5}-\alpha^{(0)})\right]\right\}+\frac{\beta(1-48\alpha^{(0)})}{5\cdot7\cdot12}\mathrm{r}^4-\frac{113\beta}{7\cdot9\cdot11\cdot12}\mathrm{r}^6. \quad (100)$$

The function $f(\mathrm{r}^2,z^2)$ is related to the pressure in the classical limit of the first order approximation as follows: Substituting (92) into (96), and setting $\gamma=\frac{3}{2}$, we get

$$\text{Limit}_{cl}p^{(1)}=\kappa\{[1/(6\kappa)][(\omega r)^2+\text{Limit}_{cl}c^2(\Gamma-[\Gamma]_0)+6\kappa([p^{(1)}]_0/\kappa)^{\frac{1}{2}}]\}^3.$$

The expression in the second square bracket is

$$(2\omega^2(a^{(0)})^2/\alpha^2)f(\mathrm{r}^2,z^2),$$

as can be seen by tracing the steps from Eq. (98) to Eq. (99). Therefore,

$$\text{Limit}_{cl}p^{(1)}=\kappa\{[1/(3\kappa)](\omega a^{(0)}/\alpha)^2f(\mathrm{r}^2,z^2)\}^3. \quad (101)$$

Thus $\text{Limit}_{el}p^{(1)}$ and $f(r^2,z^2)$ are monotone increasing functions of each other and surfaces $f=constant$ surfaces are surfaces of uniform pressure.

The choice $\alpha^{(0)}=\alpha=2$ and $\beta=100$ gives a self-contained solution. Figure 2 shows the trace of the boundary on the positive part ($z>0$) of the r−z half plane. The fluid mass is in the shape—roughly speaking—of an ellipsoid of revolution about the minor axis. It differs from an ellipsoid to the extent that the equation of the boundary is

$$z=\pm 0.269(0.0684-r^2-0.967r^4)^{\frac{1}{2}},$$

whereas the boundary of an ellipsoid with the same axes is

$$z=\pm 0.277(0.0643-r^2)^{\frac{1}{2}}.$$

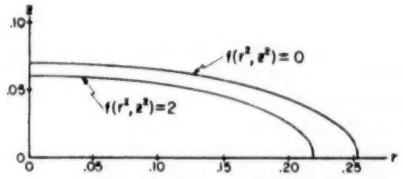

FIG. 2. A self-contained dynamical system in the first approximation.

It has been found that there are other choices of the parameters $\alpha^{(0)}$, α, and β which give non-self-contained solutions in this approximation.

Thus, the classical limit of the first order approximation in general relativity is a theory in which there exist self-contained dynamical systems which perform Born-type rigid motion.

PHYSICAL REVIEW VOLUME 95, NUMBER 6 SEPTEMBER 15, 1954

Comparison of the Cut-Off Meson Theory with Experiment*

GEOFFREY F. CHEW
Department of Physics, University of Illinois, Urbana, Illinois
(Received June 10, 1954)

The cut-off theory for the interaction of pions with nonrelativistic nucleons is tested against experiments involving a single nucleon, with and without the presence of an electromagnetic field. It is concluded that most of the existing information about the P-wave pion-nucleon interaction can be understood with a renormalized coupling constant, $f^2=0.058$ and a cut-off energy, $\omega_{max}=5.6\,\mu$. No light is shed on the S-wave pion-nucleon interaction.

I. INTRODUCTION

THE purpose of this paper is to compare with existing experimental data the so-called cut-off form of the Yukawa theory for the interaction of pions with nucleons. Although this form is not Lorentz-invariant[1] and is appropriate only when the nucleon velocity is small compared to the velocity of light, the meson velocity is unrestricted, so the theory can be applied to a very wide range of experiments. These include pion-nucleon scattering, photo-pion production, nucleon-nucleon scattering, and the ground-state properties of the deuteron, as well as the anomalous electromagnetic properties of nucleons (e.g., magnetic moments). It will be shown here that a large amount of the existing experimental information can be correlated by the meson theory with only two arbitrary parameters: a coupling constant and an energy cutoff.

The theory can most easily be characterized by writing down the interaction energy which it postulates between the pion field and a single fixed nucleon (at the origin of the coordinate system):

$$H_{\text{int}}=(4\pi)^{\frac{1}{2}}(f/\mu)\int d\mathbf{r}\rho(\mathbf{r})\sum_{\lambda=1}^{3}\tau_\lambda\boldsymbol{\sigma}\cdot\boldsymbol{\delta}\phi_\lambda(\mathbf{r}). \quad (1)$$

Here f is the dimensionless unrationalized coupling constant ($\hbar=c=1$), μ is the pion mass, $\rho(\mathbf{r})$ the "source" function, normalized so that $\int\rho(\mathbf{r})d\mathbf{r}=1$, $\boldsymbol{\sigma}$ and $\boldsymbol{\tau}$ are the Pauli spin and isotopic spin operators for the nucleon, and the ϕ_λ are the three real components of the pion field. The form (1) is often referred to as "gradient" coupling, but we prefer to call it simply "linear" coupling, since it is the only form compatible with the conservation of angular momentum, parity, and isotopic spin which at the same time is linear in the pion field and does not involve antinucleons. The effective nonrelativistic linear interactions of any field theory (including the γ_5 theory) must reduce to the form (1).

Although (1) has been written for an infinitely heavy nucleon, it is not hard to make the interaction Galilean invariant, that is, to include effects of order v/c, where v is the nucleon velocity. This has been done for some of the calculations discussed below, where it was felt that the accuracy of both experiment and calculation

* Supported by the U. S. Office of Naval Research.

[1] For a general discussion of the cut-off theory and more references, see W. Pauli, *Meson Theory of Nuclear Forces* (Interscience Publishers, Inc., New York—London, 1946), p. 12.

justified the extra care. However, the detailed construction of the Galilean invariant theory will be left for a subsequent paper. The consequences of the v/c corrections have never been found to change qualitative effects or conclusions.

The interaction (1) corresponds to a coupling between the nucleon and P-wave pions *only*. Recoil effects introduce small interactions in states of angular momenta different from 1, but the only way to put a strong S-wave interaction into a nonrelativistic theory is through terms of higher order in the pion field (e.g., terms proportional to ϕ^2). There is considerable arbitrariness in how such terms are to be written, so we have elected to concentrate here on P-wave phenomena. Fortunately for this approach, the dominant experimental effects are almost always in the P wave.

So long as the source function $\rho(r)$ is reasonably chosen, the theory characterized by (1) exists and calculations can in principle be made of any relevant physical experiment. The results of most such calculations may be expressed in terms of integrals over virtual pion momenta which will converge by virtue of the presence of factors $v(k)$, where $v(k)$ is the Fourier transform of the source function

$$v(k)=\int d\tau e^{-i\mathbf{k}\cdot\mathbf{r}}\rho(r).$$

For reasonable source shapes, $v(k)$ will be closely equal to unity from $k=0$ up to $k\approx k_{\max}$ and will then fall rapidly to zero. So long as $k_{\max}$ is substantially larger than the momenta of any real pions which occur in the problem, the exact way in which $v(k)$ falls to zero is usually unimportant and we may approximate it by a step function, i.e., $v(k)=1$ for $k<k_{\max}$, $v(k)=0$ for $k>k_{\max}$. Occasionally this procedure is dangerous, but in such cases the warning signals are fairly obvious. For the majority of the problems we shall consider, the theory may be said to contain only two constants, f^2 and $k_{\max}$ [or what is equivalent $\omega_{\max}=(k_{\max}{}^2+\mu^2)^{\frac{1}{2}}$].

It must be emphasized that the theory we are discussing here is not new, having been considered by many previous workers.[1] What is perhaps new is the method of evaluating its predictions. The group at Illinois has applied to it the coupling constant renormalization techniques invented by Dyson[2] and Ward[3] for use in relativistic theories, where there is no cutoff and where sensible results can be obtained *only* after renormalization. As explained in an earlier paper,[4] coupling constant renormalization is not necessary in the cut-off theory, but it makes possible the use of perturbation methods which are inapplicable in its absence.[5] Strictly speaking, the constant f occurring in (1) is not the constant to which we shall have reference hereafter. By our method of calculation only the renormalized f [referred to as f_r in reference (4)] occurs in expressions which are to be compared directly with experiment. We do not know and do not need to know the value of the unrenormalized coupling constant, although we suppose it to be considerably larger than the renormalized constant [see note added in proof].

The relationship of the cut-off theory to a more fundamental underlying theory is not clear. It is possible that the cutoff is nothing more than a rough approximation to damping effects which occur at high frequencies in the local γ_5 theory and whose existence eventually will be demonstrated by some extremely clever theorist. The author tends not to believe this, inclining more to the idea that the cutoff has something to do with the mysterious K particles and hyperons which have been discovered in the past few years, some of which have strong interactions (at least in pairs) with pions and nucleons. In other words we feel that the pion and the nucleon are probably only the lowest lying states in a complex system and that any theory which attempts to isolate them, as this one does, is bound to involve some characteristic energy corresponding to the states which are being ignored. We shall not delve deeper into such questions now, however, but confine our attention to the success of the cut-off theory as it stands.

Although some of the detailed calculations on which the results presented here are based already have been published; in several instances the work is still continuing or at least has not yet been written up. The author feels, however, that the success achieved so far is sufficiently interesting to make a preliminary general report worth while now, with the individual detailed calculations to appear later.

II. PION-NUCLEON SCATTERING

As reported in recent letters[6] the four P-wave phase shifts for pion-nucleon scattering have been calculated for laboratory energies up to 200 Mev. Specifically, the important terms up to fourth order in the sense of reference 4 have been kept and the scattering integral equation solved. Investigations of higher order effects have indicated that these will not be of great importance, even though the fourth-order terms were not negligible compared to those of second order. A detailed justification of these points will be given at a later time.

As already indicated by the variational treatment of second order terms alone,[7] the only phase shift which can become large in our theory is δ_{33}, since only in the

[1] F. J. Dyson, Phys. Rev. **75**, 1736 (1949).
[2] J. C. Ward, Proc. Phys. Soc. (London) **A64**, 54 (1951).
[3] G. F. Chew, Phys. Rev. **94**, 1749 (1954).

[5] The criterion for weak coupling in the absence of renormalization is that $f^2(k_{\max}/\mu)^2\ll 1$. After renormalization, it is only $f_r{}^2(k_{\max}/\mu)\ll 1$.
[6] G. F. Chew, Phys. Rev. **95**, 285 (1954); F. Salzman and J. Snyder, Phys. Rev. **95**, 286 (1954).
[7] G. F. Chew, Phys. Rev. **89**, 591 (1953).

state of $J=\frac{3}{2}, I=\frac{3}{2}$ is our scattering "potential" attractive. Recently Glicksman[8] and Bethe[9] have shown that a satisfactory analysis of the experimentally observed P-wave scattering can be made by neglecting all P phase shifts except δ_{33}, which means roughly that δ_{31}, δ_{13}, and δ_{11} can be assigned any values less than about one-tenth that of δ_{33} without violating observation. A possible interpretation is to say that δ_{33} is determined by the experiments, while the only thing we know about the other P phase shifts is that they are small. On this basis both Glicksman and Bethe find that δ_{33} passes through 90° near a laboratory energy of 200 Mev. This fact has been taken as one of two primary experimental data to determine the two parameters in the theory. The other datum is a phase shift $\delta_{33}=9.1°$ at 65 Mev, published by Bodansky, Sachs, and Steinberger.[10] Requiring our theory to give these two values for δ_{33} at the energies mentioned leads to a coupling constant,

$$f^2=0.058,$$

and an energy cutoff,

$$\omega_{\max}=5.6\,\mu.$$

In Fig. 1, the complete theoretical curves of δ_{33}, δ_{11}, δ_{13}, and δ_{31} (the latter two are always equal in our theory) are shown as a function of energy. The values of δ_{33} arrived at by Glicksman[8] and Bethe[9] as well as the Columbia result[10] are shown for comparison.

The rather substantial deviation of the coupling constant and cut-off used here from the earlier values ($f^2=0.2$, $\omega_{\max}=3.2\mu$) proposed by the author[7] needs some explanation. The major point is that when the earlier analysis was done, the existing experimental data seemed to indicate that δ_{33} did not actually pass through 90°. The fit given, in fact, corresponded to $\delta_{33}=53°$ at 200 Mev. Raising the cutoff was necessary to attain a 90° phase shift at the high energy, but this change required the coupling constant to be reduced to keep a fit at low energies. Also helping to lower the coupling constant were the fourth-order effects not considered in the earlier work and the exact solution of the integral equation. The variational approximation, used previously, systematically underestimates δ_{33}, as shown in detail by Gammel.[11]

It has been verified that for the earlier (low) cutoff the v/c corrections are not important, provided one calculates the phase shift directly and uses the center-of-mass pion energy. It is not clear that with the higher cutoff we may continue to ignore recoil and calculate accurately, but important corrections are unlikely.

[8] M. Glicksman, Phys. Rev. **95**, 1045 (1954).

[9] H. A. Bethe, Proceedings of the Fourth Annual Rochester Conference on High Energy Nuclear Physics (University of Rochester Press, Rochester, to be published), p. 134; de Hoffmann, Metropolis, Alei, and Bethe, Phys. Rev. **95**, 1586 (1954).

[10] Bodansky, Sachs, and Steinberger, Phys. Rev. **93**, 1367 (1954).

[11] J. Gammel, Phys. Rev. **95**, 209 (1954).

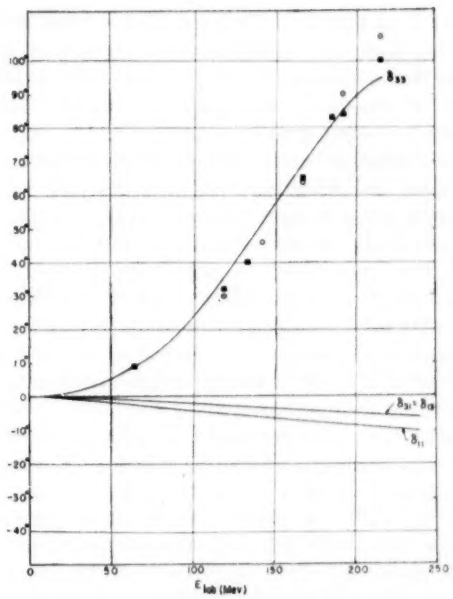

FIG. 1. The P phase shifts for pion-nucleon scattering, calculated from the cut-off theory. The upper six solid squares are Chicago values for δ_{33} given by Glicksman (see reference 8), while the point at 65 Mev was obtained by the Columbia group (see reference 10). The five open circles are due to de Hoffmann *et al.* (see reference 9).

The very complicated behavior of the S phase shifts in pion-nucleon scattering[9] is completely unexplained by the theory as it stands (with a linear interaction only). Recoil effects by themselves lead to results[12] which bear no resemblance to the experimental observations. A major extension of the theory is evidently required to explain the S-wave interaction.

It is not clear to how high an energy our nonrelativistic theory should be expected to be applicable. Calculations of pion-nucleon scattering will certainly become much more complicated as other processes, such as pion production, become energetically allowed. No thought has been given yet to the high energy problem, but it seems fair to say that the theory successfully describes the experimentally observed P-wave scattering up to 200 Mev.

III. PHOTO-PION PRODUCTION NEAR THRESHOLD

The cut-off theory gives a very simple result for charged photo-pion production close to threshold

$$\frac{d\sigma}{d\Omega}=2\frac{e^2f^2}{\mu^2}\frac{k}{\nu}. \tag{2}$$

Here $e^2=1/137$, while k and ν are the momenta of outgoing pion and incident photon, respectively. Formula (2) corresponds to an electric dipole transition with the production of an S-wave pion. Because in our theory

[12] E. Henley and M. Ruderman, Phys. Rev. **90**, 719 (1953).

there is no interaction between S-wave pions and nucleons, there are no higher order corrections to (2) after renormalization. One might worry that a modification of the theory to explain the observed S-wave scattering would spoil the simplicity of (2), i.e., introduce "radiative" corrections. However, a theorem due to Kroll and Ruderman[13] suggests that this will not happen. These workers have proved that for the kind of relativistic theory currently in fashion, the only radiative corrections to photo-pion production at threshold after renormalization are of order μ/M, where M is the nucleon mass. It does not require a great deal of optimism to believe that this feature will be present in the final correct theory which explains S-wave scattering along with everything else.

Since the v/c corrections to (2) are very simple and not quite negligible, we shall list them here. Kinematical effects give rise to a factor, $(1+\nu/M)^{-2}$, in the cross section, while the matrix element itself acquires a factor $(1\pm\nu/2M)$, the plus sign going with negative pion production (from neutrons) and the minus sign with positive pion production (from protons). Thus the $-/+$ ratio is $(1+2\nu/M)$, which is certainly not in serious disagreement with the values obtained so far from measurements near threshold on deuterium. For example, Beneventano, Bernardini, Lee, and Stoppini[14] find an average $-/+$ ratio of 1.5 ± 0.1 at 170 Mev, where the theoretical ratio is 1.3.

Modifying formula (2) by the v/c corrections listed above, we have for positive pion production near threshold,

$$\frac{d\sigma}{d\Omega_+}=2\frac{e^2f^2}{\mu^2}\frac{(1-\nu/M)}{(1+\nu/M)^2}\frac{k}{\nu}. \tag{2'}$$

Bernardini and Goldwasser[15] find that the low-energy S-wave positive photo-pion production from hydrogen can be fitted by formula (2') if f^2 is taken to be 0.066 ± 0.008, a value in satisfactory agreement with that obtained above from the P-wave scattering.

With respect to both the absolute value for photo-pion production and the positive negative ratio near threshold, therefore, the theory seems adequate.

IV. ANOMALOUS NUCLEON MAGNETIC MOMENTS

According to the cut-off theory, the pion field associated with single nucleons gives rise to anomalous magnetic moments which will be positive for protons and negative for neutrons, the absolute value being the same. The second-order formula for these anomalous moments is quite simple. In units of nuclear magnetons,

$$M_2=\pm\frac{8}{3\pi}\frac{M}{\mu}\frac{f^2}{\mu}\int_\mu^{\omega_{\max}}\frac{k^3}{\omega^3}d\omega, \tag{3}$$

and if formula (3) is evaluated with the constants determined from the scattering analysis, one finds $M_2=\pm1.15$. Friedman[16] has derived the formula for the fourth-order magnetic moment, which when evaluated for the same constants gives $M_4=\pm0.33$. Thus, up to fourth order the pion contribution to nucleon magnetic moments is ±1.48.

Experimentally, the total proton moment is $+2.79$ and the neutron moment -1.91 in these units. If one assumes the proton to have an intrinsic moment of one unit and the neutron to have zero intrinsic moment, then the residual or anomalous moments are $+1.79$ and -1.91, respectively. In this way of looking at the problem, therefore, one might say that the cut-off theory for pions explains a large fraction of the anomalous moments. The remainder could easily come from heavier mesons, together with nucleon recoil contributions.

V. PHOTO-PION PRODUCTION AT HIGHER ENERGIES

Above 200 Mev, the P-wave final state rapidly becomes important in photo-pion production and the simple formula (2) or (2') must be modified. The lowest order matrix element for charged photo-pion production, is

$$\mathcal{H}_2{}^+=2\pi ie\frac{\sqrt{2}f}{\mu}\frac{1}{\nu}\left\{\boldsymbol{\sigma}\cdot\boldsymbol{\varepsilon}-\frac{2\boldsymbol{\sigma}\cdot(\mathbf{k}-\mathbf{v})\boldsymbol{\varepsilon}\cdot\mathbf{k}}{\omega_{\mathbf{k}-\mathbf{v}}{}^2}\right\}, \tag{4}$$

where $\boldsymbol{\varepsilon}$ is the unit polarization vector of the incident photon, and

$$\begin{aligned}\omega_{\mathbf{k}-\mathbf{v}}{}^2&=\mu^2+(\mathbf{k}-\mathbf{v})^2\\&=2\nu^2(1-v\cos\theta),\end{aligned} \tag{5}$$

if $v=k/\nu$ is the velocity of the outgoing pion. (In this discussion we shall neglect recoil completely.) The matrix element for neutral photoproduction vanishes in this order.

The first term $\boldsymbol{\sigma}\cdot\boldsymbol{\varepsilon}$ in the bracket of (4) is the electric dipole matrix element already discussed, which leads to formula (2). The second term results from a mixture of many multipoles and gives infinitely many orders of outgoing pion angular momenta (because of the retardation factor in the denominator). By a remarkable cancellation, however, when (4) is squared and averaged over photon polarization and nucleon spin, interference between the two terms in (4) almost knocks out the square of the second term. The result for the cross

[13] N. Kroll and M. Ruderman, Phys. Rev. **93**, 233 (1954).
[14] Beneventano, Bernardini, Lee, and Stoppini (private communication).
[15] G. Bernardini and E. Goldwasser, Phys. Rev. **94**, 729 (1954) and private communication.
[16] M. H. Friedman (to be published). For a derivation of M_2, see reference 1, p. 38.

section in lowest order is[17]

$$\left(\frac{d\sigma}{d\Omega_2}\right)=\frac{2e^2f^2}{\mu^2}v\left\{1-\frac{\mu^2}{2v^2}\frac{v^2\sin^2\theta}{(1-v\cos\theta)^2}\right\}, \qquad (2'')$$

where one easily sees that the new contribution never amounts to more than a small fraction of that already given by (2).

Just as in the scattering problem, however, one must worry about higher order effects if intermediate states can exist which "resonate" with the final state. Salzman[18] has analyzed this problem and finds that those effects are large only if the final state has total angular momentum $\frac{3}{2}$ and total isotopic spin $\frac{3}{2}$.[19] One may say crudely that outgoing pions in this state suffer a strong secondary "scattering" by the nucleon, which amplifies their role tremendously and which must be represented by additional terms. At the same time, terms corresponding to exchange scattering must appear in the matrix element for neutral photo-pion production. It is well known from isotopic spin considerations that these will be exactly $\sqrt{2}$ times the extra terms appearing in the charged matrix element.

The corrected matrix elements now become

$$\mathcal{H}^+=ie\frac{\sqrt{2}f}{\mu}\frac{2\pi}{\nu}\left\{\boldsymbol{\sigma}\cdot\boldsymbol{\varepsilon}-\frac{2\boldsymbol{\sigma}\cdot(\mathbf{k}-\boldsymbol{\nu})\boldsymbol{\varepsilon}\cdot\mathbf{k}}{\omega_{k-\nu}{}^2}+2M_1\frac{i\mathbf{k}\cdot(\boldsymbol{\nu}\times\boldsymbol{\varepsilon})}{k\nu}\right.$$
$$\left.+(M_1+E_2)\frac{\boldsymbol{\sigma}\cdot\boldsymbol{\nu}\boldsymbol{\varepsilon}\cdot\mathbf{k}}{k\nu}-(M_1-E_2)\frac{\boldsymbol{\sigma}\cdot\boldsymbol{\varepsilon}\mathbf{k}\cdot\boldsymbol{\nu}}{k\nu}\right\} \qquad (6)$$

$$\mathcal{H}^0=ie\frac{2f}{\mu}\frac{2\pi}{\nu}\left\{2M_1\frac{i\mathbf{k}\cdot(\boldsymbol{\nu}\times\boldsymbol{\varepsilon})}{k\nu}+(M_1+E_2)\frac{\boldsymbol{\sigma}\cdot\boldsymbol{\nu}\boldsymbol{\varepsilon}\cdot\mathbf{k}}{k\nu}\right.$$
$$\left.-(M_1-E_2)\frac{\boldsymbol{\sigma}\cdot\boldsymbol{\varepsilon}\mathbf{k}\cdot\boldsymbol{\nu}}{k\nu}\right\}, \qquad (6')$$

where the symbols M_1 and E_2 represent the effective matrix elements for transitions to the 33 state due to magnetic dipole and electric quadrupole radiation, respectively. These matrix elements will be discussed in detail in the forthcoming paper by Salzman.[18] An evaluation is being carried out using the same kind of approximation employed to get the scattering phase shifts.

Squaring and averaging (6) and (6′), we obtain for the charged and neutral production cross sections

$$\left(\frac{d\sigma}{d\Omega}\right)_+=\frac{2e^2f^2}{\mu^2}v\left\{1-\frac{\mu^2}{2v^2}\frac{v^2\sin^2\theta}{(1-v\cos\theta)^2}+|M_1-E_2|^2\cos^2\theta\right.$$
$$-2\,\mathrm{Re}(M_1-E_2)\left(1-\frac{v^2/2\sin^2\theta}{1-v\cos\theta}\right)\cos\theta$$
$$\left.+[2|M_1|^2+\tfrac{1}{2}|M_1+E_2|^2+v\,\mathrm{Re}(M_1+E_2)]\sin^2\theta\right\}, \qquad (7)$$

$$\left(\frac{d\sigma}{d\Omega}\right)_0=\frac{4e^2f^2}{\mu^2}v\{|M_1-E_2|^2\cos^2\theta$$
$$+[2|M_1|^2+\tfrac{1}{2}|M_1+E_2|^2]\sin^2\theta\}. \qquad (7')$$

A preliminary test of these formulas has been made by assuming that

$$M_1=m_1(\mu\nu/k^2)e^{i\delta_{33}}\sin\delta_{33}$$
$$E_2=e_2(\mu\nu/k^2)e^{i\delta_{33}}\sin\delta_{33}, \qquad (8)$$

where m_1 and e_2 are real and energy-independent constants. The assumption (8) is certainly valid in the resonance region and appears, according to Salzman's early work, to be reasonable all the way from 200- to 400-Mev photon energy. Outside of these limits, the secondary scattering is unimportant anyway. By guessing at the values of certain complicated integrals, Salzman estimates $m_1=0.58$ and $e_2=0.18$ from the cut-off theory with $f^2=0.058$ and $\omega_{\max}=5.6\,\mu$. These numbers are subject to revision, but they will be used here to illustrate formulas (7) and (7′). A complete calculation which does not employ the simplifying assumption (8) and which includes states other than the $(\frac{3}{2},\frac{3}{2})$ will be published later by Dr. Salzman.

In Fig. 2 are plotted the theoretical and experimental[15,20–22] cross sections for positive photo-pion production up to 300-Mev photon energy at 90° in the barycentric system, as given by formula (7), with

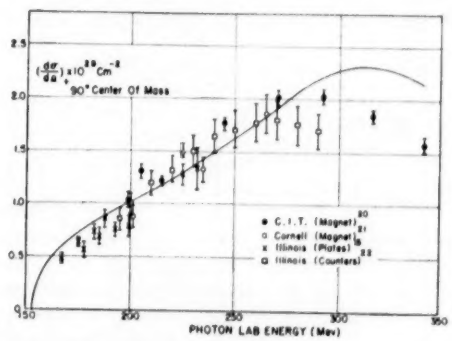

FIG. 2. A plot of formula (7), the theoretical prediction for charged photo-pion production at 90° in the center-of-mass system. The experimental points shown give a fairly representative sample of the more recent work (see references 15, 20–22).

[17] R. E. Marshak, *Meson Physics* (McGraw-Hill Book Company, Inc., New York, 1952), p. 13.
[18] F. Salzman (to be published).
[19] A conjecture that one need consider only the final state with $J=\frac{3}{2}$ and $I=\frac{3}{2}$ is the basis of a phenomenological approach developed by K. A. Brueckner and K. M. Watson, Phys. Rev. **86**, 923 (1952).
[20] V. Z. Peterson (private communication).
[21] Jenkins, Luckey, and Wilson, Phys. Rev. **94**, 755 (1954).
[22] J. E. Leiss and C. S. Robinson (private communication).

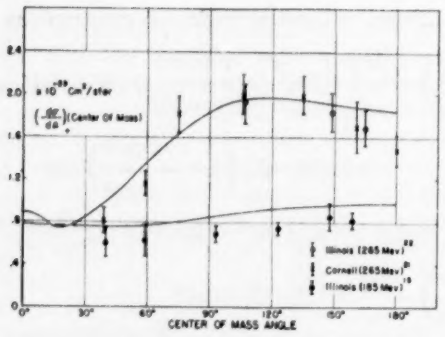

FIG. 3. The theoretical angular distribution for charged photo-pion production, compared to recent experiments at 185- and 265-Mev photon energies (see references 15 and 21).

$f^2=0.058$, and M_1 and E_2 approximated by formula (8). In other words, this is the prediction of the cut-off theory. There are no arbitrary constants once f^2 and ω_{max} are fixed, as they have been by the scattering. It is seen that the fit to experiment is adequate. The fact that the maximum occurs at too high an energy might be attributed to complete neglect of recoil effects such as those given in Eq. (2′) for the electric dipole term alone. The problem of including recoil in the secondary scattering terms is under investigation.

Further indication of the success of the theory is given by the comparison of theoretical and experimental angular distributions for charged photo-pions shown in Fig. 3. Remember that this is an absolute comparison; the normalization of the theoretical curves has not been adjusted.

In Fig. 4 the neutral photo-pion cross section at 90° is compared to the experiment of Silverman and Stearns.[23] It should be said here that more recent and still unpublished experiments at other laboratories indicate larger absolute values for the neutral cross sections. If these turn out to be correct, our agreement with the Cornell values is meaningless. One would have to hope, in that case, that the more accurate evaluation of M_1 and E_2 will yield larger numbers than have been used here.

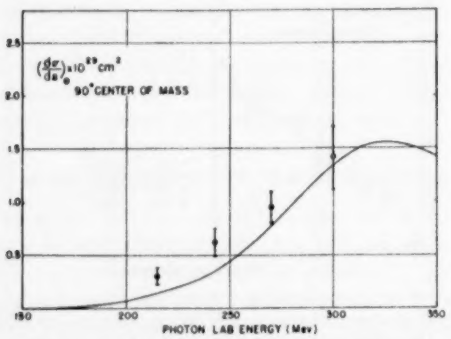

FIG. 4. The theoretical prediction for neutral photo-pion production at 90° in the center-of-mass system, compared to the experiment of Silverman and Stearns (see reference 23).

[23] A. Silverman and M. Stearns, Phys. Rev. **88**, 1228 (1952).

The angular distribution for neutral photo-pion production has also been measured. The results can be given in terms of ratios, A_0/A_2 and A_1/A_2, which refer to the angular distribution as expressed in the form

$$(d\sigma/d\Omega_0)=A_0+A_1\cos\theta+A_2\sin^2\theta.$$

A recent compilation of data,[21] based on results from Cornell and M.I.T.,[24] leads to $A_0/A_2=0.10\pm0.12$ and $A_1/A_2=-0.10\pm0.09$ in the energy range from 230 to 310 Mev. Formula (7′) predicts that $A_1=0$ and that with our guess for M_1 and E_2, $A_0/A_2=0.2$, with no energy dependence.

Although much more can be done with formulas (7) and (7′) in the way of comparison with experiment, especially at higher energies, we feel that until nucleon recoil is included only rougn tests are justified. In our judgment the comparisons described above indicate that the cut-off theory can describe photo-pion production with an accuracy of about 20 percent in the region of a few hundred Mev. In view of the neglect or incomplete treatment of nucleon recoil, this is the most that can be expected.

Before passing to the next subject it should be pointed out that even viewed as empirical formula, the expressions (7) and (7′) contain two qualitative features that distinguish them from certain earlier theoretical formulas which have been proposed.[19,25] The first is the inclusion of E_2 as well as M_1, which tends to make the neutral angular distribution almost a pure $\sin^2\theta$ and reduces the asymmetric $\cos\theta$ term in the charged angular distribution. The second feature is the inclusion of angular momenta greater than 1 in the outgoing charged pion wave. The most important consequence of the higher components is an added term in the $\sin^2\theta$ coefficient, due to interference with the scattered P wave. This term has its maximum for $\delta_{33}=45°$ rather than 90° and thereby causes the over-all maximum in the charged cross section to occur at a lower energy than that in the neutral.

VI. THE NEUTRON-ELECTRON INTERACTION

Another experimental datum to which one might be tempted to apply our theory is the interaction between electrons and slow neutrons. The most recently published result gives a depth, -3860 ± 370 ev,[26] for the effective neutron-electron potential of radius equal to the classical electron radius. Foldy[27] has pointed out

[24] G. Cocconi and A. Silverman, Phys. Rev. **88**, 1230 (1952); Goldschmidt-Clermont, Osborne, and Scott, Phys. Rev. **89**, 329 (1953).

[25] B. T. Feld, Phys. Rev. **89**, 330 (1953). Recently M. Ross, Phys. Rev. **94**, 454 (1954) has published a treatment which includes effects of the kind mentioned here.

[26] Hughes, Harvey, Goldberg, and Stafne, Phys. Rev. **90**, 497 (1953).

[27] L. Foldy, Phys. Rev. **83**, 688 (1951).

from relativistic considerations that the existence of a neutron magnetic moment implies an associated neutron-electron interaction of -4000 ev. Since the Foldy term is wholly relativistic (and completely outside our theory), one sees that the order of magnitude of the entire experimental effect is no larger than that of relativistic contributions to it.

One might conclude, then, that there is no point in applying a nonrelativistic theory to this problem. It is necessary to verify, however, that our theory does not predict a nonrelativistic contribution to the *n-e* interaction which is so much larger than the experimental value that one cannot reasonably expect it to be brought into agreement by uncalculated and unknown relativistic terms. Calculations by Salzman[28] show that the nonrelativistic contribution from the meson charge cloud is -8 kev. One will have to hope that a positive contribution of equal size will be forthcoming from the nucleonic core charge cloud when its effect can be calculated.

VII. NUCLEAR FORCES

No quantitative results have yet emerged from the application of the cut-off theory to the two nucleon problem, but it is worth pointing out that published calculations performed in other connections suggest that our theory may not fail this test. Almost all forms of meson theory attribute the majority of the tensor force in the deuteron to the exchange of a single (P wave) pion. Without cutoff, this exchange leads to the well known tensor force,[29]

$$V_t(\mathbf{r})=f^2\boldsymbol{\tau}_1\cdot\boldsymbol{\tau}_2\left(\frac{3\boldsymbol{\sigma}_1\cdot\mathbf{r}\boldsymbol{\sigma}_2\cdot\mathbf{r}}{r^2}-\boldsymbol{\sigma}_1\cdot\boldsymbol{\sigma}_2\right)\times\left(\frac{1}{\mu^2r^2}+\frac{1}{\mu r}+\frac{1}{3}\right)\frac{e^{-\mu r}}{r}. \quad (9)$$

With cutoff, the tensor potential is still given by (9) for $r\gg 2/k_{\max}$, but for $r\lesssim 2/k_{\max}$ the cutoff causes the potential to change sign (central part as well as tensor). Since Levy[30] was able to fit the observed properties of the deuteron using the tensor force (9) with $f^2=0.055$ and a repulsive core of radius, $0.38/\mu$, it is not unreasonable to hope that our potential, which already is determined by the constants $f^2=0.058$ and $\omega_{\max}=5.6\mu$, will give at least a rough fit to experiment $(2/k_{\max}=0.36/\mu)$.

It is less probable although not impossible that the central force also will be explained by this most primitive form of the cut-off theory. The difficulty here of course is that if S-wave pions, so far ignored, have an important interaction with nucleons they may be exchanged in pairs and make an important contribution to the central part of the two-nucleon interaction. At the very least, pairs of P-wave pions (i.e., fourth-order terms in f) must be considered,[31] since for a reason not well understood the exchange of single pions contributes almost nothing except a repulsive core to the central force.

VIII. CONCLUSION

It has been claimed that a renormalized coupling constant and cutoff can be found for the linear meson theory which successfully correlate a significant number of experiments involving nonrelativistic nucleons. The author believes the meaning of this success to be that, in some sense, *single* pion emission and absorption (real and virtual) are the dominant processes at energies below the nucleon rest energy. All our theory really amounts to is this assumption plus the observance of well known conservation laws. Heavier mesons and antinucleons seem not to intrude on the "low-energy" scene, except perhaps to help determine the magnitude of the cutoff.

The chief value of this kind of approach in the end probably will be to differentiate between those low-energy pion phenomena which give a real clue to the next big theoretical development and those which tell us nothing essentially new. For example, the low-energy P-wave phenomena seem to form a self-consistent group which may well lead nowhere in particular. We have the impression, on the other hand, that the low-energy S-wave pion-nucleon interaction cannot be disassociated from intrinsically high-energy questions such as the existence of antinucleons. Thus one might conclude that attention should be concentrated on the S wave, with the expectation that when a successful theory is constructed there, the P wave will follow in a natural fashion.

ACKNOWLEDGMENTS

The author is indebted to many friends and coworkers for assistance in preparing this discussion. In addition to those previously mentioned who actually have performed calculations discussed here and who will publish independently, particular thanks should be expressed to Dr. Francis Low who has provided encouragement and advice at every stage. Thanks are also due Dr. G. Bernadini and Dr. E. Goldwasser for a critical reading of the manuscript and to J. Leiss for helping in the numerical comparison with photomeson experiments.

Note added in proof.—T. D. Lee has recently communicated to the author a general proof that the renormalized coupling constant is smaller than the unrenormalized. A discussion of this point is to be published in *The Physical Review*.

[28] G. Salzman (private communication).
[29] See reference 1, p. 6.
[30] M. Levy, Phys. Rev. **86**, 806 (1952).
[31] Calculations by K. Brueckner and K. Watson, Phys. Rev. **92**, 1023 (1953), by E. Henley and M. Ruderman, Phys. Rev. **92**, 1036 (1953), as well as by M. Taketani *et al.* Progr. Theoret. Phys. (Japan) **7**, 45 (1952), suggest that the central force due to pairs of P-wave pions may be sufficient without any S-wave pairs. These calculations, however, do not consider a cutoff in the sense used here.

New Tamm-Dancoff Formalism

ABRAHAM KLEIN*
Harvard University, Cambridge, Massachusetts

(Received April 5, 1954; revised manuscript received June 25, 1954)

The problems of renormalization and imposition of the boundary condition that the vacuum state is the comparison state for all energies are examined, using the example of the one-particle system. The boundary condition difficulty is expressed by the apparent occurrence of undesirable singularities in the interaction kernel obtained after elimination of higher amplitudes. Rules are derived for the construction of this kernel to any order in the coupling constant. It is shown by direct calculation that at least through fourth order the kernel is actually free of such singularities. Arguments are presented which indicate that this result may be expected to hold generally if higher amplitudes are eliminated by a consistent application of successive approximations. Even after transformation, however, the kernel does not agree with that obtained from the covariant one-body equation, and a new renormalization procedure will be required.

I. INTRODUCTION

DYSON has proposed recently a new Tamm-Dancoff method[1] which has several patent advantages over the previous form.[2] The new procedure eliminates disconnected vacuum processes,[3] permits renormalizations to be carried out to lowest order,[4] and treats positive and negative energies on a symmetrical footing. One might expect, therefore, that it would provide a more suitable basis for a relativistic treatment of the meson-nucleon interaction than does the older formulation. There remain, nevertheless, certain grave questions pertaining to the renormalization of the equations to all orders and to the possibility of defining by suitable boundary conditions a state of lowest energy. The purpose of this paper is to explore these problems.

The amplitudes which enter the Dyson procedure are, formally at least, equal to the amplitudes that occur in the covariant methods,[5,6] if the time coordinates of all operators are equated in the latter. The equations satisfied by the covariant amplitudes can be renormalized,[7] in principle, because of the simple relationship of the kernels of these equations to the S matrix. One might expect to obtain information about the renormalization of Dyson's equations by comparison of the kernels in the respective methods. The covariant equations are, however, not reducible to single-time formalisms except by approximation methods.[2,8,9] The one-particle equation[5,10] forms a most useful exception to this rule, in that an exact three-dimensional equation for a stationary state can be deduced from the time-dependent form. The rules for constructing the kernel of this equation are, in all details, the same as those found from the work on the two-nucleon problem,[2,8,9] and lend credence to the results of that work. In particular, it is to be remarked that the singularities of the kernels occur only at the threshold for real processes.

On the other hand, the kernels in Dyson's formulation contain additional singularities at the threshold of processes which cannot take place, the so-called "spurious" singularities. These arise because in the derivation of the equations, no condition is imposed which assures that the true vacuum state is the comparison state for all energies. The appropriate condition must be appended as a boundary condition on allowed solutions. In the covariant case, the equations can also be derived without recourse explicitly to boundary conditions as shown clearly by the derivation of Schwinger.[5] Nevertheless, the identification of the Green's functions which occur in the kernel with those of Stueckelberg[11] and Feynman[12]—the outgoing wave condition in time—in itself establishes the required boundary condition for the one-particle problem; the additional consideration of the definition of the unequal time amplitude performs the same function for the two or more body problem, as has been emphasized recently by Wick.[13]

In order to obtain some information about boundary conditions in the new T.-D., we have investigated in Sec. II the one-particle problem for the simple case of a two-component spinor field in interaction with a boson field. Since no pairs can be created or destroyed, the vacuum state of the free-particle Hamiltonian coincides with the true vacuum. If we follow Dyson's procedure, nevertheless, without enforcing the coincidence of vacuum states, we find naturally that there is coupling to amplitudes involving creation operators (the minus particles). These express physically the presence of particles in the comparison state. It is important to remark that for the case considered, these amplitudes are never coupled *back* to the one-particle amplitude, as

* Society of Fellows.
[1] F. J. Dyson, Phys. Rev. **91**, 1543 (1954), referred to as D.
[2] M. M. Lévy, Phys. Rev. **88**, 72, 725 (1952).
[3] F. J. Dyson, Phys. Rev. **90**, 994 (1953).
[4] F. J. Dyson, Phys. Rev. **91**, 421 (1953).
[5] J. Schwinger, Proc. Natl. Acad. Sci. U. S. **37**, 452 (1951).
[6] E. E. Salpeter and H. A. Bethe, Phys. Rev. **84**, 1232 (1951).
[7] There are cases, such as that of meson-nucleon scattering, which require special treatment because of the dual role of meson as particle and field quantum.
[8] A. Klein, Phys. Rev. **90**, 1101 (1953). See also Phys. Rev. **94**, 1052 (1954).
[9] W. Macke, Z. Naturforsch. **89**, 599 (1953).
[10] R. P. Feynman, Phys. Rev. **80**, 440 (1950).
[11] E. C. G. Stueckelberg, Helv. Phys. Acta **19**, 242 (1946).
[12] R. P. Feynman, Phys. Rev. **76**, 749 (1949).
[13] G. C. Wick in Proceedings of the Fourth Annual Rochester Conference, 1954 (University of Rochester, Rochester).

an examination of the structure of the equations indicates.

The set of equations thus obtained comprehends a larger number of systems than does the set derived by the older T.-D. method. The reduction of the former to the latter is here trivial since it requires that a well-defined set of amplitudes be equated to zero. Because of the unidirectional coupling, the correct boundary condition can also be imposed by the method of successive elimination. The equation obtained for the one-particle amplitude at any stage of approximation is then the same for both methods. The full set of coupled equations for the new T.-D. method, however, contains information about the properties of any $n+1$ particle system compared to an n particle system. If primary attention had been focused on one of the amplitudes involving creation operators, the resulting equation would have contained "spurious" singularities.

In Sec. III the one-particle problem is treated utilizing the full relativistic Hamiltonian. In accordance with the discussion above, emphasis is placed on the equation which results from elimination of higher amplitudes. General rules are stated for constructing the kernel to any order; the derivation of these rules is relegated to Appendix A. The kernel of the covariant one-particle equation can also be written down to all orders (Sec. IV). One may then ask (Sec. V) whether the kernel of the new T.-D. equations can be transformed by partial fraction decomposition into the covariant one, thus rendering the "spurious" singularities indeed spurious. Detailed consideration of the fourth-order kernel—the second-order kernels agree—shows that such is not the case. It is a remarkable result, nevertheless, that the transformed interaction contains no spurious singularities. A similar result has been verified for the two-particle problem to fourth order. We surmise that the boundary conditions present no difficulty in the point of view taken here; the reasons for this are discussed. The renormalization is another question, since it does not follow by comparison, but rather it requires a separate investigation best carried out using a more covariant-looking form of the equations.[14]

The two-particle problem is considered briefly in Appendix B. We exhibit an approximate relative time dependence which, inserted into the covariant equation, reproduces the kernel of the new T.-D. method for the same problem to lowest order. This method fails in higher approximation.[15]

[14] The covariant time-dependent form of Dyson's equations has been found by S. S. Schweber, Phys. Rev. **94**, 1089 (1954). J. C. Taylor, Phys. Rev. (to be published) has shown that this formalism cannot be renormalized by the usual method, a result which can also be inferred from our work.

[15] A prescription for obtaining what is substantially the new T.-D. kernel from the covariant one is described by J. C. Taylor, reference 14. It involves, however, in addition to the assumption of a relative time dependence for the wave function, a redefinition of the physical content of the covariant kernel.

II. ONE-PARTICLE PROBLEM WITHOUT PAIRS

For this case the Hamiltonian has the form

$$H=H_0^N+H_0^M+H', \tag{1}$$

where

$$H_0^N=\sum_p\sum_u b_{pu}^*b_{pu}E_p, \tag{2}$$

$$H_0^M=\sum_k a_k^*a_k\omega_k, \tag{3}$$

and

$$H'=G\sum_k\sum_{k'}(2V\omega_k)^{-\frac{1}{2}}(a_k+a_{-k}^*)\times\sum_u\sum_v(u^*\gamma v):b_{k'u}^*b_{k'-kv}:. \tag{4}$$

The notation is the same as in D, except that γ is here a two-component matrix defining the coupling, and the sum is over positive energy spin states only. The operators of Eq. (4) are arranged in normal form.[16]

We define the one-particle wave function as the two-component quantity

$$\psi_\alpha(\mathbf{p})=\sum_u(\Psi_0^*b_{pu}\Psi)u_\alpha, \tag{5}$$

where Ψ_0 is the true vacuum state, Ψ the one-particle state vector. The state Ψ_0 equals the free vacuum state Φ_0,

$$b_{pu}\Phi_0=a_k\Phi_0=0. \tag{6}$$

The old and new T.-D. amplitudes are then identical, and we should expect the equations which they satisfy to coincide. For the sake of the investigation we shall, nevertheless, ape Dyson's procedure and derive a coupled set of equations involving $\psi_\alpha(\mathbf{p})$ without recourse to Eq. (6). The first three equations of this set are easily determined to be of the form

$$[\epsilon-E(\mathbf{p})]\psi_\alpha(\mathbf{p})=G\sum_{k_1}(2V\omega_1)^{-\frac{1}{2}}\gamma_{\alpha\beta}[\psi_\beta^+(\mathbf{p}-\mathbf{k}_1;\mathbf{k}_1)+\psi_\beta^-(\mathbf{p}-\mathbf{k}_1;\mathbf{k}_1), \tag{7}$$

$$[\epsilon-E(\mathbf{p}-\mathbf{k}_1)-\omega_1]\psi_\alpha^+(\mathbf{p}-\mathbf{k}_1;\mathbf{k}_1)=G(2V\omega_1)^{-\frac{1}{2}}\gamma_{\alpha\beta}\psi_\beta(\mathbf{p})+G\sum_{k_2}(2V\omega_2)^{-\frac{1}{2}}\gamma_{\alpha\beta}[\psi_\beta^{++}(\mathbf{p}-\mathbf{k}_1-\mathbf{k}_2;\mathbf{k}_2,\mathbf{k}_1)+\psi_\beta^{-+}(\mathbf{p}-\mathbf{k}_1-\mathbf{k}_2;\mathbf{k}_2,\mathbf{k}_1)]+G\sum_{k_2}(2V\omega_1)^{-\frac{1}{2}}\gamma_{\gamma\beta}\psi_{\gamma\beta\alpha}(\mathbf{k}_2^*,\mathbf{k}_1+\mathbf{k}_2,\mathbf{p}-\mathbf{k}_1), \tag{8}$$

$$[\epsilon-E(\mathbf{p}-\mathbf{k}_1)+\omega_1]\psi_\alpha^-(\mathbf{p}-\mathbf{k}_1,\mathbf{k}_1)=G\sum_{k_2}(2V\omega_2)^{-\frac{1}{2}}\gamma_{\alpha\beta}[\psi_\beta^{-+}(\mathbf{p}-\mathbf{k}_1-\mathbf{k}_2;\mathbf{k}_1,\mathbf{k}_2)+\psi_\beta^{--}(\mathbf{p}-\mathbf{k}_1-\mathbf{k}_2;\mathbf{k}_1,\mathbf{k}_2)]-G\sum_{k_2}(2V\omega_1)^{-\frac{1}{2}}\gamma_{\gamma\beta}\psi_{\gamma\beta\alpha}(\mathbf{k}_2^*,\mathbf{k}_1+\mathbf{k}_2,\mathbf{p}-\mathbf{k}_1). \tag{9}$$

[16] G. C. Wick, Phys. Rev. **80**, 268 (1950).

The amplitudes involved are defined, for example, by the expressions

$$\psi_\alpha^{-+}(\mathbf{p}-\mathbf{k}_1-\mathbf{k}_2;\,\mathbf{k}_2\mathbf{k}_1)$$
$$=\sum_u(\Psi_0^*:b(\mathbf{p}-\mathbf{k}_1-\mathbf{k}_2,u)a(-\mathbf{k}_2)^*a(\mathbf{k}_1):\Psi)u_\alpha, \quad (10)$$

and

$$\psi_{\gamma\beta\alpha}(\mathbf{k}_2^*,\mathbf{k}_1+\mathbf{k}_2,\mathbf{p}-\mathbf{k}_1)$$
$$=\sum_{u'',\,u',\,u}(\Psi_0^*:b(\mathbf{k}_2,u'')b(\mathbf{k}_1+\mathbf{k}_2,u')$$
$$\times b(\mathbf{p}-\mathbf{k}_1,u):\Psi)u_\gamma''^*u_\beta'u_\alpha. \quad (11)$$

Equations (7)–(9) exhibit the essential structure of the entire system of equations. Examination shows that amplitudes involving more than one nucleon operator and/or meson creation operators, of which the simplest example is $\psi^-(\mathbf{p}-\mathbf{k}_1;\,\mathbf{k}_1)$, are never coupled back to $\psi(\mathbf{p})$. That solution of the equations which results from successive elimination of all amplitudes except $\psi(\mathbf{p})$ then yields the same equation for the latter as does the old T.-D. method used in conjunction with Eq. (6). Moreover, in solving for the higher amplitudes it is consistent to equate to zero all those not coupled back to $\psi(\mathbf{p})$. Indeed, only by taking these spurious amplitudes to vanish do we obtain an eigenvalue equation for $\psi(\mathbf{p})$ which is identical with the old T.-D. case. On the other hand, Eqs. (7)–(9) . . . describe other systems, including those in which Ψ_0 is not the vacuum state. It is only in the latter cases that one encounters "spurious" singularities.

When we admit pair creation, the amplitudes that were found to vanish above lose this simplifying property. The kernel of the equation for $\psi(\mathbf{p})$ will contain contributions from these states which are all ultimately coupled back to the one-particle amplitude. In the next section we study the structure of this kernel.

III. ONE-PARTICLE PROBLEM WITH PAIRS

To be concrete we shall use the example of neutral pseudoscalar meson theory, the same as in D. In the appendix the equation of motion for the most general amplitude is constructed, of which the rules given below are a consequence. By successive elimination, we then obtain an equation for $\psi_\alpha(\mathbf{p})$, where α now takes on four values, of the form

$$[\epsilon-\eta(\mathbf{p})E(\mathbf{p})]\psi_\alpha(\mathbf{p})$$
$$=\sum_n[G^2/(2\pi)^3]^nK_{\alpha\beta}{}^n(\mathbf{p})\psi_\beta(\mathbf{p}). \quad (12)$$

$K_{\alpha\beta}{}^n(\mathbf{p})$ is the self-energy kernel of indicated order, the structure of which is specified completely by the set of rules which follow:

(1) Consider first the class of all irreducible[6] Feynman diagrams of order $2n$. There will be a set of contributions corresponding to each of these.

(2) For each Feynman diagram construct all time-ordered diagrams, with time conventionally increasing as we move toward the top of the page. The usual diagram will consist of a continuous nucleon line with segments directed either forwards or backwards in time, n meson lines, and one or more closed loops, the segments of which are also directed. We shall refer to the nucleon segments directed forwards and backwards in time as particles and antiparticles, respectively, although the terminology is not strictly accurate.[17] We shall then identify a process of pair creation or annihilation in the usual way.

(3) Omit all of the above diagrams in which a pair is annihilated and a meson *absorbed*. This rule is a direct consequence of the fact that we construct the kernel according to the equations of motions by proceeding backwards in time. From this point of view, the foregoing interaction appears as a disconnected vacuum process which is precluded by the structure of the equations of motion. This rule also has as a consequence that no diagrams are permitted in which there is an intermediate state in which nucleon lines are present with both the initial and final momentum.

(4) The full complement of contributions from each of the remaining time-ordered diagrams is obtained only by allowing both particles and antiparticles to propagate in positive and negative energy states. Consequently, label each nucleon segment (propagation between interactions) with a plus or minus sign, drawing separate diagrams for each possibility. The process of pair creation forms the sole exception to this rule. Here particle and antiparticle must be in energy states of opposite sign, but both choices are to be included. According to what has been stated above, this correlation is lost by either particle or antiparticle after its next interaction.

(5) The meson lines must also be given sign factors which will determine the sign of their contributions to energy denominators, and separate diagrams should again be drawn for each possibility. It is always the interaction associated with the emission of a meson which determines the sign. If a meson is emitted by a particle (antiparticle), label it with a sign which is the same as (opposite to) that associated with the propagation segment immediately following the emission.[18] In the destruction of a pair with the emission of a meson, both signs occur and must be tallied separately. For the creation of a pair and the emission of a meson, only the sign associated with the subsequent propagation of the *particle* occurs.

Figures 1(a)–(d) illustrate the rules to this point for a particular Feynman diagram. For conciseness, diagrams differing only in the assignment of sign factors have been lumped together with sign correlations indicated by connecting brackets. Disregarding the sign possibilities of the initial and final states, each diagram of Fig. 1

[17] The distinction here is between b and b^* operators.

[18] In the sense that propagation of both particle and antiparticle is always forward in time.

represents eight terms in the fourth-order kernel and their sum the contribution corresponding to the Feynman diagram which would be drawn as Fig. 1(a).

(6) Label each diagram with momentum variables as in Fig. 1(a). There is a three-momentum integral for each free variable, n in all. Except for signs, to be treated in rule (8), each vertex contributes a factor $\gamma(2\omega_i)^{-1}$. Each nucleon segment of momentum $\mathbf{p}'$ contributes $\Lambda_+(\mathbf{p}')$, a positive or negative energy projection operator, according to the sign determined by rule (4). These are sandwiched by γ matrices to form part of a matrix product which in its entirety either connects initial and final spin indices or constitutes a trace, one for each closed loop.

(7) There are $n-1$ intermediate states determined by drawing a horizontal line between successive interactions. Each such state contributes an energy denominator of the form

$$\epsilon-\sum(E-E'+\omega-\omega'), \tag{13}$$

wherein there is one term in the sum for each nucleon and meson line cut; E is the sum of energies of the particles (antiparticles) labeled plus (minus), E' the sum of the energies of the particles (antiparticles) labeled minus (plus), ω the sum of meson energies labeled plus, and ω' the sum of meson energies labeled minus. When the initial state of the nucleon occurs, both sign possibilities are conveniently included by writing $\eta(\mathbf{p})E(\mathbf{p})$ as a term of $\sum E$. The contributions to the kernel are now completely specified except for over-all sign.

(8) Count a factor of minus one for each of the following: a closed loop, a pair creation in which the particle is in a positive energy state (the antiparticle consequently in a negative energy state), destruction of a pair and emission of a meson labeled with a minus sign, emission of a meson by an antiparticle, and finally, the absorption of a meson by an antiparticle.

As a single further illustration of the rules, we record the two contributions of Fig. 1(d) for a particular spin dependence,

$$\begin{aligned}K_{+-+}{}^{d}(\mathbf{p})&=\int\frac{d\mathbf{k}_1 d\mathbf{k}_2}{2\omega_1 2\omega_2}\\&\times[\gamma\Lambda_+(\mathbf{p}-\mathbf{k}_1)\gamma\Lambda_-(\mathbf{p}-\mathbf{k}_1-\mathbf{k}_2)\gamma\Lambda_+(\mathbf{p}-\mathbf{k}_1)\gamma]\\&\times\{[\epsilon-E(\mathbf{p}-\mathbf{k}_1)-\omega_1]^{-1}\\&-[\epsilon-E(\mathbf{p}-\mathbf{k}_1)+\omega_1]^{-1}\}[\epsilon-\eta(\mathbf{p})E(\mathbf{p})]^{-1}\\&\times[\epsilon-\eta(\mathbf{p})E(\mathbf{p})-E(\mathbf{p}-\mathbf{k}_1)\\&\qquad-E(\mathbf{p}-\mathbf{k}_1-\mathbf{k}_2)-\omega_2]^{-1}.\end{aligned} \tag{14}$$

We shall return below in Sec. V to a discussion of the unusual structure of matrix elements of the type represented by Eq. (14). We merely note here that the rules stated above for the one-particle problem are applicable with trivial modification to the problem of any number of particles.

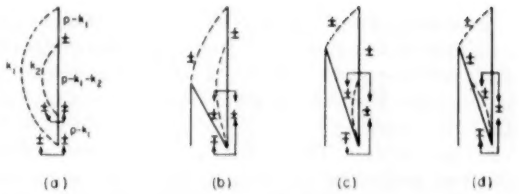

FIG. 1. Diagrams representing contributions to the fourth-order self-energy kernel for a prescribed order of emission and absorption of the mesons along the nucleon line.

IV. COVARIANT ONE-PARTICLE EQUATION

An equation for the one-particle system which incorporates the boundary condition that the comparison state is the vacuum state has been given by Schwinger.[6] We write it in the form

$$(-i\gamma_\mu\partial_\mu+m)\psi(x)+\int(dx')M(x,x')\psi(x')=0. \tag{15}$$

As a power series in the coupling constant, $M(x,x')$ is the sum of all irreducible diagrams.[6] Introducing the wave function for a stationary state,

$$\psi(x)=e^{-i\epsilon t}\psi(\mathbf{x}), \tag{16}$$

going over to momentum space, and integrating out the time dependence, we obtain the three-dimensional equation

$$\begin{aligned}[\epsilon-\eta(\mathbf{p})E(\mathbf{p})]\psi_\alpha(\mathbf{p})&\\=\sum_n[G^2/(2\pi)^3]^n M_{\alpha\beta}{}^n(\mathbf{p})\psi_\beta(\mathbf{p}),&\end{aligned} \tag{17}$$

where the contributions to $M_{\alpha\beta}{}^n(\mathbf{p})$ are determined by the same rules as have been given in detail for the two-body problem,[2,8,9] and will not be repeated again here. The structure of the kernel M, in particular of its energy denominators, suggests strongly that Eq. (17) cannot result, at least directly, from successive elimination carried out on a set of coupled three-dimensional equations. We turn now to an examination of the relationship between Eqs. (12) and (17).

V. COMPARISON OF KERNELS AND CONCLUSIONS

Since Eq. (17) incorporates the correct boundary conditions and can be renormalized, we adopt the following point of view: for Eq. (12) to be a useful formulation, it should be possible to transform the kernel K by partial fraction decomposition of energy denominators into a form in which all spurious singularities have been eliminated. Preferably, it should agree with the kernel M. Dyson has already shown that to order G^2 the two kernels are identical.

To obtain further information, we have examined in detail the contributions to K from Fig. 1 and compared these with the parts of M ($4!=24$ terms) corresponding to the same Feynman diagram. It is clear, first of all, that only contributions with the same spin dependence need be compared. There are eight sets characterized by the two possibilities for propagation with positive or negative energies for the nucleon in its intermediate states. Comparison shows that the sets $(+++)$ and $(---)$ are identical for K and M without any rearrangement. We remark next that we must not expect identity for the other arrangements because of one intrinsic difference between the kernels. The kernel M of Eq. (17) is the same whether the nucleon of momentum p is in a positive or a negative energy state. On the other hand, the rules of Sec. III show that such is not the case for the kernel K. Thus at best the kernels are equivalent up to differences that depend on $\epsilon-\eta(\mathbf{p})E(\mathbf{p})$. These differences are essential in the discussion of the renormalization,[14] since similar differences account for the failure of the renormalization method as applied to the old T.-D. method.[4] For the investigation of spurious singularities, however, it is reasonable to be content if the kernel K, after rearrangement, agrees with M when we set $\epsilon=\eta(\mathbf{p})E(\mathbf{p})$.

To this extent, we have found that the sets $(++-)$, $(-++)$, $(--+)$, and $(+--)$ are in agreement. On the other hand the sets $(+-+)$ and $(-+-)$, as computed from equations like (14), are definitely not. The origin of the discrepancy is to be sought in the fact that Eq. (14) and similar contributions become singular on the free-particle energy shell.[19] One still obtains a nonsingular (incorrect) result if one adds up all contributions before passing to the limit $\epsilon=\eta(\mathbf{p})E(\mathbf{p})$, but even this is not true when one turns to the consideration of contributions from diagrams with closed loops. A closer examination shows that the difficulty arises from an inversion of limiting processes. In carrying out the elimination of higher amplitudes, contributions like Eq. (14) actually occur in the schematic form,

$$\int d\mathbf{q}f(\mathbf{q})\delta(\mathbf{q}-\mathbf{q}')[\epsilon-\eta(\mathbf{p})E(\mathbf{p})+E(\mathbf{q})-E(\mathbf{q}')]^{-1}$$
$$=f(\mathbf{q}')[\epsilon-\eta(\mathbf{p})E(\mathbf{p})]^{-1}, \quad (18)$$

as long as $\epsilon\neq\eta E$. However if the latter limit is taken first, one obtains the confluence of two singularities, one a simple pole and the other a delta function. The principal part is taken at the pole. The correct value of the integral follows from the relation[20]

$$\mathrm{P}(1/x)\delta(x)=-\tfrac{1}{2}\delta'(x). \quad (19)$$

The correct value to be assigned to Eq. (18) is therefore

$$\lim(\epsilon\to\eta E)\int d\mathbf{q}f(\mathbf{q})\delta(\mathbf{q}-\mathbf{q}')$$
$$\times[\epsilon-\eta(\mathbf{p})E(\mathbf{p})+E(\mathbf{q})-E(\mathbf{q}')]^{-1}$$
$$=(\partial/\partial E(\mathbf{q}))f(\mathbf{q})\,|_{q=q'}. \quad (20)$$

By means of (20) the equivalence of Fig. 1 to the corresponding Feynman diagram can be established in the limit considered. Analogous results have been verified for other Feynman diagrams.

From the lack of complete identity of the kernels, we can conclude that a new renormalization scheme will be required; it may well encounter grave difficulties because of the discontinuities found in the discussion just completed. On the other hand, we have been uniformly successful in eliminating the spurious singularities. In other words the method of successive elimination correctly imposes the required boundary condition. Actually this result should not be surprising. It can be understood directly by using the relation between the old and new T.-D. amplitudes, D, Eq. (25),

$$a(N,N')=\textstyle\sum_M \beta^*(N+M)\alpha(N'+M)$$
$$\times\binom{N+M}{M}^{\frac{1}{2}}\binom{N'+M}{M}^{\frac{1}{2}}. \quad (21)$$

We first remark (still considering the one-particle problem) that every amplitude $a(N,N')$ coupled to $\psi_+(\mathbf{p})$ necessarily contains in the sum, Eq. (21), terms in which $\beta^*(N+M)$ and $\alpha(N+M)$ are amplitudes belonging to the vacuum and one-particle states, respectively. Considering $\psi_+(\mathbf{p})$ to be of order unity, we can assign to the other amplitudes orders of magnitude in powers of the coupling constant as follows: For each amplitude $a(N,N')$ determine the first term or terms in the sum, Eq. (20), which corresponds to the system of interest. Then assign to $a(N,N')$ an order of magnitude, $O(G^l)$, which is the product of the orders of magnitude of the β^*, α amplitudes that would be assigned to the latter by a weak coupling solution of the old T.-D. equations. The solution of the new T.-D. equations by construction of an equation for the amplitude of order unity involves the tacit assumption that the higher amplitudes are of the order of magnitude thus assigned. In this manner, at least the dominant contributions from other systems corresponding to smaller values of M in Eq. (20) are eliminated.

Our work indicates that the spurious singularities will disappear only if all amplitudes of the same order of magnitude are treated consistently. The partial success of the method of successive approximations may indeed be only one expression of this result. It may still be possible to utilize the set of coupled equations in other ways, as long as the amplitudes included form a consistent set in the sense explained earlier.

[19] The investigation which follows was stimulated by a communication from J. C. Taylor who has obtained similar results from the time-dependent formalism. The relevance of Eq. (20) was suggested to the author by M. L. Goldberger.

[20] W. Heitler, *Quantum Theory of Radiation* (Oxford University Press, Cambridge, 1954), third edition, p. 70.

It is a pleasure to acknowledge stimulating conversations and correspondence with F. J. Dyson, B. Kursunoglu, S. Schweber, and J. Schwinger.

APPENDIX A. EQUATIONS OF MOTION

We consider the equation of motion provided by the new T.-D. formalism for the most general amplitude which occurs in the one-particle problem,

$$\begin{aligned}
&\psi(\lambda_1\mu_1\cdots\lambda_n\mu_n\nu;(-)_1\cdots(-)_j(+)_{j+1}\cdots \\
&\qquad\times(+)_l;\mathbf{q}_1{}^*\mathbf{q}_1'\cdots\mathbf{q}_n{}^*\mathbf{q}_n',\mathbf{p};\mathbf{k}_1\cdots\mathbf{k}_l) \\
&=\sum_{u,v,w}(\Psi_0{}^*:a(-\mathbf{k}_1)^*\cdots a(-\mathbf{k}_j)^*a(\mathbf{k}_{j+1})\cdots \\
&\quad\times a(\mathbf{k}_l)b(\mathbf{q}_1u_1)^*b(\mathbf{q}_1'v_1)\cdots \\
&\quad\times b(\mathbf{q}_nu_n)^*b(\mathbf{q}_n'v_n)b(\mathbf{p},w):\Psi)u(\lambda_1)^*\cdots \\
&\qquad\times u(\lambda_n)^*v(\mu_1)\cdots v(\mu_n)w(\nu), \quad \text{(A.1)}
\end{aligned}$$

which contains a proton, n proton pairs, and l mesons. To include neutron pairs requires only that we eventually remember that a closed loop can be either of the proton or neutron variety. According to D, the equation of motion for the amplitude (A.1) is given by

$$\begin{aligned}
&[\epsilon+\eta^T(\mathbf{q}_1)E(\mathbf{q}_1)-\eta(\mathbf{q}_1')E(\mathbf{q}_1')+\cdots \\
&\quad+\eta^T(\mathbf{q}_n)E(\mathbf{q}_n)-\eta(\mathbf{q}_n')E(\mathbf{q}_n') \\
&\quad-\eta(\mathbf{p})E(\mathbf{p})+\omega_1+\cdots+\omega_j-\omega_{j+1}-\cdots-\omega_l] \\
&\quad\times\psi(\lambda_1\mu_1\cdots\nu;(-)_1\cdots(+)_l;\mathbf{Q}^*\mathbf{Q},\mathbf{p};\mathbf{K}) \\
&=\sum_{u,v,w}(\Psi_0{}^*[:A^*AB^*Bb(\mathbf{p},w):,H']\Psi) \\
&\qquad\times u(\lambda)^*v(\mu)w(\nu), \quad \text{(A.2)}
\end{aligned}$$

where we have introduced obvious shorthand notations for collections of momenta, of creation and annihilation operators, and of spin functions. The superscript T means transposed matrix. H' will be taken in a form which omits neutron operators and is thus of the form of Eq. (4) of the text, except that the sum is extended over positive and negative energy spin functions.

The essential task is to arrange the commutator in Eq. (A.2) in normal form. This is a straightforward but tedious task, and only the result will be quoted,

$$\begin{aligned}
&\sum_{u,v,w}[:A^*AB^*Bb_{p,w}:,H']u^*vw \\
&=\sum_{u,v,w,s,t}\sum_{k,k'}(2V\omega_k)^{-\frac{1}{2}}(s^*\gamma t)u^*vw \\
&\quad\times(\{:a_{-1}{}^*\cdots a_{-j}{}^*(a_{-k}{}^*+a_k)a_{j+1}\cdots a_l:\} \\
&\quad\times\{:B^*Bb_{p-k,t}:\delta_{w,s}(\mathbf{p}-\mathbf{k}') \\
&\qquad+\sum_{\beta=1}^{n}[:B^*B(b_\beta{}^*b_\beta)^{-1}b_\beta{}^*b_{\beta-k,t}b_{p,w}:\delta_{v(\beta),s}(\mathbf{q}_\beta'-\mathbf{k}') \\
&\qquad-:B^*B(b_\beta{}^*b_\beta)^{-1}b_{\beta+k,s}{}^*b_\beta b_{p,w}:\delta_{t,u(\beta)}(\mathbf{q}_\beta-\mathbf{k}'+\mathbf{k}) \\
&\qquad-:B^*B(b_\beta{}^*b_\beta)^{-1}b_\beta:[\delta_{w,s}{}^+(\mathbf{p}-\mathbf{k}')\delta_{t,u(\beta)}{}^-(\mathbf{q}_\beta-\mathbf{k}'+\mathbf{k}) \\
&\qquad-\delta_{t,u(\beta)}{}^+(\mathbf{q}_\beta-\mathbf{k}'+\mathbf{k})\delta_{w,s}{}^-(\mathbf{p}-\mathbf{k}')] \\
&\qquad+:B^*B(b_\beta{}^*b_\beta)^{-1}b_{p,w}: \\
&\qquad\times[\delta_{v(\beta),s}{}^+(\mathbf{q}_\beta'-\mathbf{k}')\delta_{t,u(\beta)}{}^-(\mathbf{q}_\beta-\mathbf{k}'+\mathbf{k}) \\
&\qquad-\delta_{t,u(\beta)}{}^+(\mathbf{q}_\beta-\mathbf{k}'+\mathbf{k})\delta_{v(\beta),s}{}^-(\mathbf{q}_\beta'-\mathbf{k}')] \\
&\qquad-\sum_{\alpha=1}^{n}\sum_{\beta=1}^{\alpha-1}[:B^*B(b_\beta{}^*b_\beta)^{-1}(b_\alpha{}^*b_\alpha)^{-1}b_\alpha{}^*b_\beta b_{p,w}: \\
&\qquad\times(\delta_{v(\alpha),s}{}^+(\mathbf{q}_\alpha'-\mathbf{k}')\delta_{t,u(\beta)}{}^-(\mathbf{q}_\beta-\mathbf{k}'+\mathbf{k}) \\
&\qquad-\delta_{t,u(\beta)}{}^+(\mathbf{q}_\beta-\mathbf{k}'+\mathbf{k})\delta_{v(\alpha),s}{}^-(\mathbf{q}_\alpha'-\mathbf{k}')+\alpha\leftrightarrow\beta]\} \\
&\qquad+\{\sum_{\rho=j+1}^{l}:A^*Aa_\rho{}^{-1}:\delta(\mathbf{k}+\mathbf{k}_\rho)\} \\
&\quad\times\{:b_{k',s}{}^*b_{k'-k,t}B^*Bb_{p,w}: \\
&\qquad+:B^*Bb_{p-k,t}:\delta_{w,s}{}^+(\mathbf{p}-\mathbf{k}') \\
&\qquad+\sum_{\beta=1}^{n}[:B^*B(b_\beta{}^*b_\beta)^{-1}b_\beta{}^*b_{\beta-k,t}b_{p,w}:\delta_{v(\beta),s}{}^+(\mathbf{q}_\beta'-\mathbf{k}') \\
&\qquad-:B^*B(b_\beta{}^*b_\beta)^{-1}b_{\beta+k,s}{}^*b_\beta b_{p,w}:\delta_{t,u(\beta)}{}^-(\mathbf{q}_\beta-\mathbf{k}'+\mathbf{k}) \\
&\qquad-:B^*B(b_\beta{}^*b_\beta)^{-1}b_\beta:\delta_{w,s}{}^+(\mathbf{p}-\mathbf{k}')\delta_{t,u(\beta)}{}^-(\mathbf{q}_\beta-\mathbf{k}'+\mathbf{k}) \\
&\qquad+:B^*B(b_\beta{}^*b_\beta)^{-1}b_{p,w}: \\
&\qquad\times\delta_{v(\beta),s}{}^+(\mathbf{q}_\beta'-\mathbf{k}')\delta_{t,u(\beta)}{}^-(\mathbf{q}_\beta-\mathbf{k}'+\mathbf{k}) \\
&\qquad-\sum_{\alpha=1}^{n}\sum_{\beta=1}^{\alpha-1}[:B^*B(b_\beta{}^*b_\beta)^{-1}(b_\alpha{}^*b_\alpha)^{-1}b_\alpha{}^*b_\beta b_{p,w}: \\
&\qquad\times\delta_{v(\alpha),s}{}^+(\mathbf{q}_\alpha'-\mathbf{k}')_{t,u}\delta_{(\beta)}{}^-(\mathbf{q}_\beta-\mathbf{k}'+\mathbf{k})+\alpha\leftrightarrow\beta]\} \\
&\qquad+\{\sum_{\rho=1}^{j}:A^*A(a_{-\rho}{}^*)^{-1}:\delta(\mathbf{k}+\mathbf{k}_\rho)\} \\
&\quad\times\{-:b_{k',s}{}^*b_{k'-k,t}B^*Bb_{p,w}: \\
&\qquad+:B^*Bb_{p-k,t}:\delta_{w,s}{}^-(p-k') \\
&\qquad+\sum_{\beta=1}^{n}[:B^*B(b_\beta{}^*b_\beta)^{-1}b_\beta{}^*b_{\beta-k,t}b_{p,w}:\delta_{v(\beta),s}{}^-(\mathbf{q}_\beta'-\mathbf{k}') \\
&\qquad-:B^*B(b_\beta{}^*b_\beta)^{-1}b_{\beta+k,s}{}^*b_\beta b_{p,w}:\delta_{t,u(\beta)}{}^+(\mathbf{q}_\beta-\mathbf{k}'+\mathbf{k}) \\
&\qquad+:B^*B(b_\beta{}^*b_\beta)^{-1}b_\beta:\delta_{t,u(\beta)}{}^+(\mathbf{q}_\beta-\mathbf{k}'+\mathbf{k})\delta_{w,s}{}^-(\mathbf{p}-\mathbf{k}') \\
&\qquad-:B^*B(b_\beta{}^*b_\beta)^{-1}b_{p,w}: \\
&\qquad\times\delta_{t,u(\beta)}{}^+(\mathbf{q}_\beta-\mathbf{k}'+\mathbf{k})\delta_{v(\beta),s}{}^-(\mathbf{q}_\beta'-\mathbf{k}') \\
&\qquad+\sum_{\alpha=1}^{n}\sum_{\beta=1}^{\alpha-1}[:B^*B(b_\beta{}^*b_\beta)^{-1}(b_\alpha{}^*b_\alpha)^{-1}b_\alpha{}^*b_\beta b_{p,w}: \\
&\qquad\times\delta_{t,u(\beta)}{}^+(\mathbf{q}_\beta-\mathbf{k}'+\mathbf{k}) \\
&\qquad\times\delta_{v(\alpha),s}{}^-(\mathbf{q}_\alpha'-\mathbf{k}')+\alpha\leftrightarrow\beta]\}). \quad \text{(A.3)}
\end{aligned}$$

The additional notation involves δ functions in spin and momentum with additional plus-or-minus sign super-

scripts indicating that both spin functions must be positive or negative energy states, and the use of inverse operators to indicate the omission of these operators from the complex B^*B.

The insertion of (A.3) into (A.2), the recollection that the diagrams or matrix elements are constructed from the equations of motion "backwards" in time, and the simple rundown of terms that occur, lead immediately to the rules of Sec. III. Thus, we see from the first three terms which describe the absorption of a meson by a "particle" (b operator) or an "antiparticle" (b^* operator) that there is no restriction on the sign of the energy of propagation after the absorption, but that absorption by an antiparticle contributes a factor of minus one. Further on, we see the restriction on the relative sign of the energies of particle and antiparticle in a pair creation, and so on.

APPENDIX B. TWO-PARTICLE PROBLEM

Dyson[1] has given the equation satisfied by the two-nucleon amplitude with kernel constructed to order G^2. We shall seek a relative time dependence for the covariant two-body equation which will reproduce the Dyson equation.

The covariant equation has the form (ladder approximation)

$$\chi(x_1,x_2)=-iG^2\int(dx_3)(dx_4)$$
$$\times G_+(x_1-x_3)G_+(x_2-x_4)\gamma_0{}^1\gamma_0{}^2$$
$$\times\gamma^1\gamma^2\Delta_+(x_3-x_4)\chi(x_3,x_4). \quad \text{(B.1)}$$

To reduce this to an approximate single-time equation, all previous workers[2,5,9] have assumed a relative time dependence determined for an instantaneous interaction. The equation thus obtained, consistent with hole theory, does not agree with the Dyson equation. Here we proceed differently.

We first rewrite (B.1) in the form ($t_1=t_2=t$):

$$(\epsilon-H_1-H_2)\chi(x_1,x_2,t)$$
$$=iG^2\int(dx_3)G_+(x_1-x_3)\gamma_0{}^1\gamma^1\gamma^2\Delta_+(x_3-x_2)\chi(x_3,x_2)$$
$$+iG^2\int(dx_4)G_+(x_2-x_4)$$
$$\times\gamma_0{}^2\gamma^1\gamma^2\Delta_+(x_1-x_4)\chi(x_1,x_4). \quad \text{(B.2)}$$

In each term of (B.2), one integrates over one of the two space-time points which occurs in the wave function. The following prescription, completely unjustified, will reproduce the Dyson equation to lowest order. Propagate the other point to this point with free-particle time dependence. Thus in the first term we write

$$\chi(x_3,x_2)=(2\pi)^{-3}\exp(-i\epsilon t_3)$$
$$\times\int d\mathbf{p}d\mathbf{q}\exp[i(\mathbf{p}\cdot\mathbf{x}_3+\mathbf{q}\cdot\mathbf{x}_2)$$
$$-i\eta^{(2)}(\mathbf{q})E(\mathbf{q})(t_2-t_3)]\psi(\mathbf{p},\mathbf{q}), \quad \text{(B.3)}$$

with a corresponding expression for $\chi(x_1,x_4)$. A simple calculation will now yield the required result. It can also be shown that the G^2 self-energy term can be treated similarly. It is clear that what we thereby achieve is not a derivation, that is, there is no unique approximate relative time dependence which will suffice to accomplish the end in view. Moreover the prescription given is no longer applicable to higher order terms, for in these no one of the two space-time points of the wave-function is given a preferred position by the linearization procedure that leads from (B.1) to (B.2).

Nevertheless the comparison of the two-body kernel of the new T.-D. method with the approximate single-time equation obtained from the covariant equation serves to reinforce the conclusions reached in Sec. V.[21]

[21] This problem is considered more fully by B. Kurşunoğlu, Phys. Rev. (to be published).

Letters to the Editor

PUBLICATION of brief reports of important discoveries in physics may be secured by addressing them to this department. The closing date for this department is five weeks prior to the date of issue. No proof will be sent to the authors. The Board of Editors does not hold itself responsible for the opinions expressed by the correspondents. Communications should not exceed 600 words in length and should be submitted in duplicate.

Overhauser Effect in a Free Radical

H. G. BELJERS, L. VAN DER KINT, AND J. S. VAN WIERINGEN
Philips Research Laboratories, N. V. Philips' Gloeilampenfabrieken, Eindhoven, Netherlands
(Received July 19, 1954)

ON theoretical grounds Overhauser[1] has predicted an interaction between paramagnetic and nuclear resonance. If the former is saturated, one of the processes trying to restore thermodynamic equilibrium is such that the change of angular momentum in an electron spin flip is compensated by a change in direction of a nuclear spin. Thus the ground state population of the nuclear spin system is increased. This increase can be detected by an enhanced nuclear resonance. According to Overhauser's first paper this effect would be confined to metals. It has been found in Li by Carver and Slichter.[2] Bloch[3] has pointed out that the effect might expected in nonmetals too. In this letter we give a brief description of a preliminary experiment in which the Overhauser effect was found in the free radical diphenylpicrylhydrazyl (DPPH).

The sample was placed in a glass tube inside a coil, that was inserted in a 3-cm resonant cavity, with the axis perpendicular to the magnetostatic field. The coil consisted of two groups of 20 windings each, separated by a gap of 2 mm in order to increase the penetration of the microwave field into the coil. The cavity, made of rectangular wave guide, was fed by a 70-watt klystron. The incident power could be measured by means of a calibrated attenuator in front of a monitor. Nuclear resonance in the coil was observed by a Thomas oscillator.[4] In DPPH a weak proton resonance was found, the peak height in 10 mm^3 being of the same order as that in 1 mm^3 H_2O with 2.5×10^{17} Fe^{3+} ions mm^{-3} added. In the field where paramagnetic resonance occurred (3300 oersted), the proton resonance was at about 14 Mc/sec.

At high microwave power levels the electron spin resonance showed saturation. At the same time the proton spin resonance increased by Overhauser effect (Fig. 1). During the experiment the sample was kept at room temperature by cooling with a jet of cold air, as it was found that towards higher temperatures the proton peak height increased as a result of decreasing line width. When the peak height was increased by Overhauser effect, no change in line width was observed. The temperature of the sample was checked by a thermocouple. The incident power was limited to 8 w by the cooling capacity of the air jet.

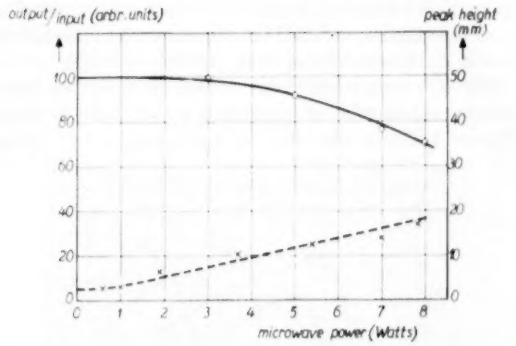

FIG. 1. Solid curve: output/input for electron spin resonance. Dotted curve: peak height of proton resonance on oscilloscope screen. Both are plotted against incident microwave power.

From paramagnetic resonance experiments it is well known that in DPPH there is an appreciable interaction between the electron hole and the nitrogen nuclear spin.[5] Therefore it would be interesting to see if the nitrogen nuclear resonance shows Overhauser effect. Unfortunately the nitrogen resonance will be extremely weak and cannot be detected by a simple oscillator.

We are indebted to Professor Casimir for suggesting the experiment, to Mr. van Iperen for providing the klystron, and to Dr. Klaassens for preparing the free radical sample.

[1] A. W. Overhauser, Phys. Rev. **92**, 411 (1953).
[2] T. R. Carver and C. P. Slichter, Phys. Rev. **92**, 212 (1953).
[3] F. Bloch, Phys. Rev. **93**, 944 (1954). See also J. Korringa, Phys. Rev. **94**, 1388 (1954).
[4] H. A. Thomas, Electronics **25**, 114 (1952).
[5] Hutchison, Pastor, and Kowalsky, J. Chem. Phys. **20**, 534 (1952).

Anomalous Optical Behavior of InSb and InAs

H. J. HROSTOWSKI, G. H. WHEATLEY, AND W. F. FLOOD, JR.
Bell Telephone Laboratories, Murray Hill, New Jersey
(Received July 26, 1954)

BURSTEIN[1] has recently proposed an explanation of the anomalous optical behavior of InSb observed by Tanenbaum and Briggs.[2] This explanation is based on the small effective electron mass m_n and the resultant low density of states in the conduction band. In degenerate n-type InSb, the lowest unfilled level in the conduction band rises above the bottom of the band as the electron concentration, n, increases. E_0, the optical energy gap, is determined by the energy separation between the lowest unoccupied level in the conduction band and the corresponding level in the valence band.

Thus E_0 is a function of n in degenerate n-type samples. A similar argument holds for degenerate p-type InSb in which E_0 should depend on p, the hole density.

We have observed room temperature transmission spectra of a number of degenerate n-type InSb samples. Figure 1 shows the effect of increasing n by doping

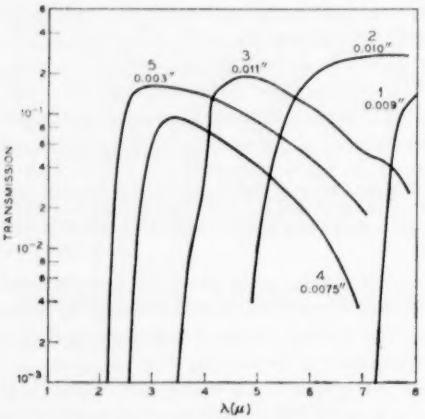

FIG. 1. Transmission spectra of n-type InSb samples; n ranges from 5×10^{15} cm^{-3} for curve 1 to about 10^{19} cm^{-3} for curves 4 and 5. Sample thicknesses are as shown.

with Te. Curve 1 is for "pure" InSb with an extrinsic electron density of 5×10^{15} cm^{-3}. All doped specimens were prepared from this material. Curves 2 through 5 demonstrate the increased displacement of the absorption edge to shorter wavelength as n is increased.

The observed dependence of E_0 on n at room temperature is shown by the solid curve in Fig. 2 which gives most weight to the single-crystal samples. The points at 1 and 2×10^{17} cm^{-3} were obtained from Ni- and Fe-doped samples, respectively. All others were determined from InSb doped with Te. To minimize errors arising from concentration gradients, optical measurements were taken on the same samples used for measurement of electron density after these had been ground thin

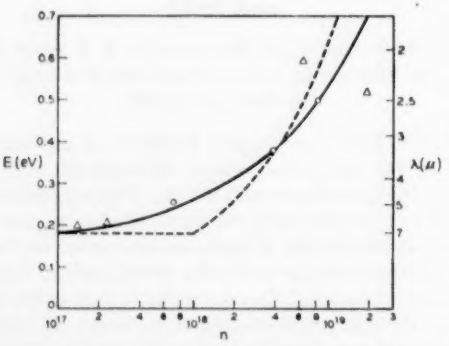

FIG. 2. Dependence of E_0 and λ on n(cm^{-3}) in InSb. – – – – calculated, ———— experimental, ○ single crystal samples, △ polycrystalline samples.

enough to give reasonable transmission. E_0 was calculated from the wavelength at 0.1 percent transmission. The dashed line in Fig. 2 is the theoretical curve calculated from the data of Tanenbaum and Maita[3] with the assumption of spherical energy surfaces. The experimental results agree with theory in the respect that E_0 seems to depend only on n. The consistency of results obtained from samples containing widely different impurities makes it appear very unlikely that the anomalous behavior of E_0 is caused by a specific impurity. An increase of 0.5 ev in E_0 was also obtained for a highly degenerate p-type sample. This ΔE_0 is in reasonable agreement with that predicted by Burstein.[1]

The discrepancies between theory and experiment are the observed ΔE_0 below $n=10^{18}$ cm^{-3} and the form of the dependence of E_0 on n. Explanation of the shift of the absorption edge below $n=10^{18}$ cm^{-3} requires the assumption that m_n is even smaller than the calculated value.[1] This implies that the effective hole mass and the thermal energy gap are also somewhat lower than previously reported.[1,3] Agreement between the slopes of the theoretical and experimental curves can be obtained by assuming that the effective electron mass increases linearly with the height of the Fermi level above the bottom of the conduction band. Exact calculations are unwarranted until more complete data are available and the theoretical uncertainties are resolved.

Since high electron mobilities have also been observed for InAs in this laboratory and by Folberth, Grimm, and Weiss,[4] a similar anomalous optical behavior might be expected for this compound. We have observed shifts of the absorption limit toward shorter wavelength with increasing electron density in InAs. However, the effect is not large and the maximum observed shift amounts to only 0.7 μ.

[1] E. Burstein, Phys. Rev. **93**, 632 (1954).
[2] M. Tanenbaum and H. B. Briggs, Phys. Rev. **91**, 1561 (1953).
[3] M. Tanenbaum and J. P. Maita, Phys. Rev. **91**, 1009 (1953).
[4] Folberth, Grimm, and Weiss, Z. Naturforsch. **8a**, 826 (1953).

Energy Losses of Electrons Passing through an MgO Foil

HIROSHI WATANABE
Hitachi Central Research Laboratory, Kokubunji-machi, Tokyo, Japan
(Received May 5, 1954; revised manuscript received July 12, 1954)

IT is well known that in the case of an insulator or a semiconductor there is a forbidden band above the valence band, and the width of this forbidden band is not known very accurately. Its measurement is regarded as an important problem for various reasons.

In the case of MgO, the width of the first forbidden band is believed to be certainly greater than 7.3 ev and,

as indicated by x-ray spectroscopy, may be as great as 10 to 15 ev.[1,2] An accurate value of the width of this band was obtained by the present experiment on the energy analysis of electrons which have passed through an MgO foil.[3] The electron velocity analyzer used in the

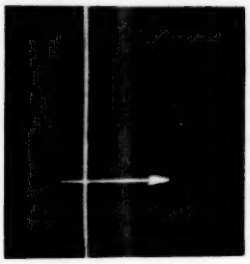

FIG. 1. Energy spectrum of 22-kev electrons which have passed through an MgO foil.

measurement is of the same type as that of Möllenstedt,[4] the details of which will be reported in the near future along with other experimental results. The accelerating voltage is 15–25 kv.

The MgO foil was prepared by leaving an unbacked Mg foil supported on a sheet mesh in an O_2-filled desiccator for 2–3 days at room temperature. The unbacked Mg foil was prepared by vacuum-evaporating Mg metal on a collodion film, and dissolving the latter in a 50 percent water-alcohol solution. The thickness of the film was about 200 A. Electron diffraction patterns showed that the Mg foil was converted completely into MgO. The formation of the hydroxide was prevented by use of a desiccator and prompt mounting in the vacuum column of the instrument at a pressure of 10^{-4} mm Hg or less.

Figures 1 and 2 are examples of the energy spectrum of 22-kev electrons after passing through the MgO foil. The photometric trace of Fig. 2 is along the arrow in Fig. 1. The main peak at 0 ev represents the primary electrons, and the peaks on the right represent the discrete energy losses of electrons transmitted through the specimen. The values of the discrete energy losses are measured on the photographic plates and are tabulated in Table I. Though the positions of the feeble or broad peaks cannot be determined very accurately, those of the sharp peaks such as the second peak at 11.4 ev, can be measured with sufficient accuracy, in this case, for example, with an accuracy of *ca* ± 0.1 ev. It can be concluded from Table I that the positions of the peaks are independent of the accelerating voltage of the incident electrons. The width of the second peak is also estimated from the energy spectrum and is given in Table I.

The discrete energy losses of electrons passing through the foil are considered to correspond to the transitions of electrons in MgO from the valence band to the empty band. The peak at *ca* 5.5 ev in Table I may correspond to a localized level in the first forbidden band, because its intensity is very weak and the energy distance from the main peak is small as compared with the hitherto accepted width of the first forbidden band. The existence of such peaks is shown by the measurements[5] of

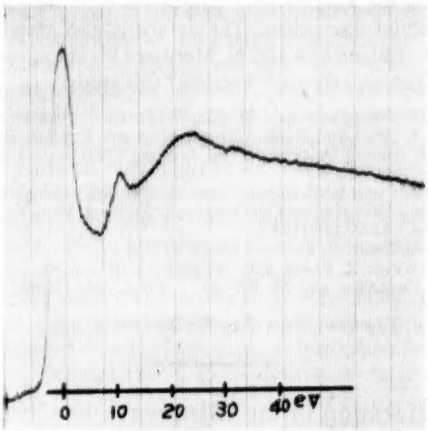

FIG. 2. The photometric curve of Fig. 1. The horizontal scale shows the energy loss in electron volts.

the spectral distribution of photoconductivity in MgO. The second peak at 11.4 ev is reasonably interpreted in that it corresponds to the electronic transitions to the first empty level. Thus the accurate value of the width of the first forbidden band above the valence band is

TABLE I. The energy distances of the peaks from the main peak and the estimated width of the second peak when the accelerating voltage of the incident electrons varies.

Accel. voltage kv	First peak	Second peak		Third peak	Number of measured plates
	Dist. ev	Dist. ev	Width ev	Dist. ev	
16	5.2	11.4_1	$1._7$	24.5	15
18	5.2	11.4_4	$1._9$	25.1	31
22	5.3	11.4_5	$1._9$	25.0	34
24.5	5.4	11.4_9	$1._9$	25.2	30

considered to be equal to 11.4 ev and the breadth of the empty level is *ca* 1.5 ev. Hitherto the width of the former band was taken to be about 10 to 15 ev from soft x-ray measurements. The author believes that an electron velocity analyzer of this type is a powerful tool for studying the electronic structure of nonconductive materials. It is also of interest to note that the ionization energy of the O^{--} ions in MgO has been calculated to be 11.8 ev.[6] The third peak at *ca* 25 ev is also considered to correspond to the second empty band above the valence band. The energy distance of the second empty band from the first empty band in MgO is obtainable from Townsend's experiment[7] on the *L*-absorption edge of x-rays. The fine structures of the

L-absorption edge of MgO show that a nearly forbidden range of energies is present at *ca* 12 ev above the first empty level. The energy separation, 13.6 ev, of the third peak from the second peak in Table I agrees well with the x-ray data.

The author wishes to express his thanks to Dr. N. Kato of the Kobayasi Institute of Physical Research for his helpful discussions. The author is also grateful to Dr. B. Tadano and Mr. N. Morito of his laboratory for their encouragement throughout this study.

[1] H. R. Day, Phys. Rev. **91**, 822 (1953).
[2] N. F. Mott and R. W. Gurney, *Electronic Processes in Ionic Crystals* (Oxford University Press, London, 1940), second edition, pp. 76–78.
[3] Measurements of energy losses of electrons passing through MgO foils have also been reported by E. Rudberg, Proc. Roy. Soc. (London) **A127**, 111 (1930).
[4] G. Möllenstedt, Optik **5**, 499 (1949).
[5] H. Weber, Z. Physik **130**, 392 (1951).
[6] J. Yamashita and M. Kojima, J. Phys. Soc. (Japan) **7**, 261 (1952).
[7] J. R. Townsend, Phys. Rev. **92**, 556 (1953).

Saturation in the Microwave Spectrum of Methyl Chloride*

GEORGE R. BIRD †
Mallinckrodt Chemical Laboratory, Harvard University, Cambridge, Massachusetts
(Received July 19, 1954)

THE saturation of the microwave transition $J=0\rightarrow1$ of CH_3Cl^{35} has been measured by the method of Baird and Bird.[1] The results constitute the first measurement on saturation of a rotational absorption line, all other microwave saturation measurements having been made on the $J=3$, $K=3$ line of the ammonia inversion spectrum.[2,3] As in the case of the ammonia line, the experimental results are described by the formula derived by Karplus and Schwinger.[4] Their derivation contains the assumption that collisions which broaden the absorption line are identical with collisions which transfer rotational energy and reduce the displacement from thermal equilibrium caused by the absorption of radiation. This corresponds to the case of diabatic (nonadiabatic or inelastic) collisions, which is expected to apply in the microwave region, but is known not to apply in the visible and ultraviolet regions.[5]

The experimental uncertainty in the actual measurement of the rate of saturation with increasing power is about 30 percent and is largely due to uncontrollable variations in the standing wave properties of the Stark-effect absorption cell. Reduction of the uncertainty requires the design of a more satisfactory wave guide, and work on this is now in progress. A detailed discussion of the measurements and calculations has been given elsewhere,[6] and will not be repeated.

The line breadth constant $\Delta\nu/p$ has been measured for each of the three quadrupole fine structure lines of this transition and found to be 21 ± 1 Mc/sec per mm Hg at 300°K, a result largely independent of the errors which enter into the saturation measurements. The intensity of the strongest line ($J=0\rightarrow1$, $F=3/2\rightarrow5/2$) is revised to 7.9×10^{-6} cm^{-1} from the figure of 6.6×10^{-6} cm^{-1} calculated by Kisliuk and Townes[7] for an assumed line breadth of 25 Mc/sec per mm Hg. If the line-broadening interactions are idealized as hard-sphere collisions, a collision diameter of 16.1 A may be calculated. This is much greater than the value of 5.6 A obtained from viscosity measurements and the kinetic theory of gases.[8] The large size of the microwave collision diameter indicates that dipole-dipole interactions are the principal mechanism for line broadening and rotational energy transfer.

The author gratefully acknowledges the help and encouragement of Professor E. Bright Wilson, Jr. A K-band thermistor and W bridge were kindly loaned by Dr. A. G. Hill of the Research Laboratory of Electronics, Massachusetts Institute of Technology.

* This research was supported in part by the Office of Naval Research.
† Formerly United States Rubber Company Predoctoral Fellow at Harvard University. Present address: Department of Chemistry, The Rice Institute, Houston, Texas.

[1] D. H. Baird and G. R. Bird, Rev. Sci. Instr. **25**, 319 (1954).
[2] B. Bleaney and R. P. Penrose, Proc. Roy. Soc. (London) **60**, 83 (1948).
[3] R. L. Carter and W. V. Smith, Phys. Rev. **73**, 1053 (1948).
[4] R. Karplus and J. Schwinger, Phys. Rev. **73**, 1020 (1948).
[5] W. V. Smith and R. R. Howard, Phys. Rev. **79**, 132 (1950).
[6] G. R. Bird, doctoral thesis, Harvard University, 1952 (unpublished).
[7] P. Kisliuk and C. H. Townes, National Bureau of Standards Circular 518 (June 23, 1952), p. 26.
[8] J. H. Jeans, *The Dynamical Theory of Gases* (Cambridge University Press, Cambridge, 1916), p. 295.

Electron Spin Resonance of an Impurity Level in Silicon*

A. HONIG AND A. F. KIP
Department of Physics, University of California, Berkeley, California
(Received July 19, 1954)

ELECTRON spin resonance has been observed in a sample of silicon containing 7×10^{16} lithium atoms per cm^3. The ionization energy of an electron in the impurity level is 0.033 ev, as determined from Hall effect measurements.[1]

A single resonance line was observed throughout the temperature range of 4°K to 20°K by using an rf frequency of about 8800 Mc/sec and a magnetic field of about 3200 oersteds. The same line was also observed on 300-Mc/sec equipment, kindly made available by Mr. G. Feher. Magnetic field modulation was used at both frequencies. The resonance line has a $g=1.999$, and a full width at half-maximum absorption of 1.5 oersteds; the line shape is approximately Gaussian. The resonance

shows rf power saturation behavior characteristic of inhomogeneously broadened lines, in which the spins are in thermal equilibrium only through the interaction with the lattice, rather than through spin-spin interaction. The observed line is actually a superposition of many overlapping narrow lines which saturate only over a small portion of the line, rather than over the whole line as in the homogeneous line-broadening situations. This situation is very similar to the one encountered in the F-center investigations of Kip, Kittel, Levy, and Portis[2,3]; the quantitative saturation behavior is thoroughly worked out by Portis in reference 3. The most probable mechanism for producing the inhomogeneous broadening of the line is magnetic hyperfine interaction of the electron with the Li and Si^{29} nuclei encompassed in its wave function.

The width of the resonance can be estimated on the basis of magnetic hyperfine interaction for an electron with ionization energy of 0.033 ev. Such an electron encompasses roughly about 600 Si atoms in its orbit, of which about 30 atoms are Si^{29}, the only stable magnetic isotope of silicon. Assuming that each of the silicon atoms share equally in the wave function and making an allowance for possible $\frac{1}{2}$ p character, one estimates an expected line width of about 1 oersted, which is of the order of magnitude of the observed width. If the Li shared equally with the Si in the wave function, there would be four Li hyperfine components of about 0.1 oersted separation between components. These would not be resolved due to the broadening of each component by the Si^{29}. However, the resonance line shape would be flattened at the top. This was not observed, and hence it is likely that Li gets a smaller share of the electron than Si. Upon calculating the line shape due to the Si^{29} and neglecting any width due to the Li hyperfine components, a closely Gaussian shape is found, in agreement with the experimental results. There appears to be a possibility of producing deeper-lying impurity levels by special treatment of the sample.[1] If these levels are connected with Li centers, resolved Li hyperfine structure might be obtained.

The resonance reported here seems to be clearly associated with a low ionization energy impurity level. It is of interest to note that the experimental evidence indicates that the electron is bound to the impurity atom rather than associated with an impurity band. This evidence is, of course, the magnetic hyperfine structure exhibited implicitly by the line.

The authors would like to thank Dr. F. J. Morin of Bell Telephone Laboratories for providing the sample and measuring its Hall effect, and Professor C. Kittel for several helpful discussions.

* Supported in part by the U. S. Office of Naval Research and the U. S. Signal Corps.

[1] Morin, Maita, Shulman, and Hannay, Bull. Am. Phys. Soc. **29**, No. 5, 22 (1954).

[2] Kip, Kittel, Levy, and Portis, Phys. Rev. **91**, 1066 (1953).

[3] A. M. Portis, Phys. Rev. **91**, 1071 (1953).

Meson-Meson Interaction in Meson Scattering*

MARC ROSS

Brookhaven National Laboratory, Upton, New York

(Received July 30, 1954)

THE purpose of this note is to discuss explicitly an interpretation of low-energy meson-nucleon scattering data which, though not new,[1] is different from that most frequently adopted. It shall be assumed that the meson-nucleon scattering arises from two sources: A, the meson-nucleon interaction neglecting any meson-meson collisions that might be suffered in the scattering process, and B, meson interaction directly with the mesons of the nucleon's proper field. This latter effect is associated with an interaction assumed to exist between free mesons, which we label C.

It seems proper to describe B by a potential whose range is of the order of the meson Compton wavelength $1/\mu$ (where $\hbar=c=1$). This type of description is indicated by the fact that C is, in the pseudoscalar (PS) theory, probably of range $1/M$ (where M is the nucleon mass). Thus the interaction with the meson cloud will

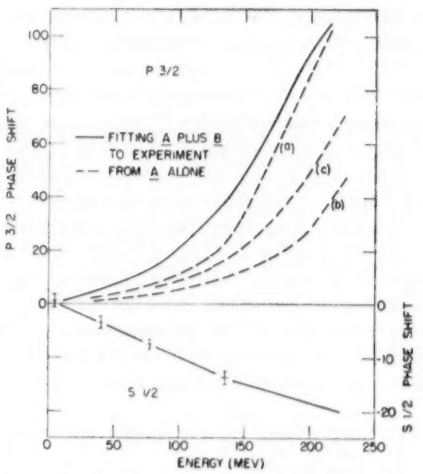

FIG. 1. $S_{\frac{1}{2}}$ and $P_{\frac{1}{2}}$ phase shifts for $T=\frac{3}{2}$ (see Table I). Referring to the S wave plot, the vertical bars show the phase angles obtained at various energies in fitting the S wave data. Exponential potentials (a) and (b) fit the more positive low-energy S phase shifts, while (c) fits the more negative. These S phase shifts obtained do not necessarily represent the best evaluation of recent results or the bars a good estimate of "experimental errors" at the energies in question.

be a point-by-point effect. This will be represented by a potential function in which is buried both the behavior of the probability density of the cloud and the strength of C. One can hope that the momentum dependence of C is smeared sufficiently by the momentum spread in the cloud to yield a constant potential over the range of incoming momenta in which we are interested. As a result of the short range of C we can assume that B is

TABLE I. Properties of satisfactory meson cloud potentials.

Well	Depth V	Range a	S core radius
Exp[a] (a)	0.15	1.0	0.26
Exp (b)	1.2	0.50	0.37
Exp (c)	0.6	0.50	0.30
Square	0.05	1.8	0.24

[a] Exp signifies $Ve^{-r/a}$. Units are $\hbar=c=\mu=1$.

independent of the total angular momentum of the system.

It is assumed that A is some kind of short range interaction (range order of $1/M$) in accordance with indications of the Tamm-Dancoff approximation of the PS theory.[2] We can describe the effect of A in each angular momentum isotopic spin state by satisfying equations derived approximately from the field theory, or phenomenologically. In the following we make the latter approach and take A to be a repulsive core[3] in the $T=\frac{3}{2}$, $S_{\frac{1}{2}}$ state and to yield a straight line behavior in an effective range type plot[4] in the $T=\frac{3}{2}$, $P_{\frac{1}{2}}$ state. It is hoped that the energy region under study is small enough so that this may well prove a satisfactory description. The problem then consists of solving the Klein-Gordon equation for a meson moving in the potential B, and of imposing the boundary condition that the phase shift is prescribed at small distances by A.

We will consider results deduced from meson-proton scattering and related experiments, for scattering energies up through about 200 Mev.[5,6] We assume that the correct phase shift analysis of this data is like that shown in Fig. 1, where all but $S_{\frac{1}{2}}$ and $P_{\frac{1}{2}}$ states for $T=\frac{3}{2}$ interact weakly. The parameters of exponential and square potentials B are determined by comparison with the $S_{\frac{1}{2}}$ and $P_{\frac{1}{2}}$ data for $T=\frac{3}{2}$. It is found that for each well there is a roughly triangular bounded region in range-depth space for which the data can be satisfied. Wells representative of the various types of behavior are listed in Table I along with the associated S wave core. The associated $P_{\frac{1}{2}}$, $T=\frac{3}{2}$ phase shift ascribed to A is plotted in Fig. 1. The predicted P and D wave phase shifts for $T=\frac{3}{2}$ due to B alone are given in Fig. 2.[7]

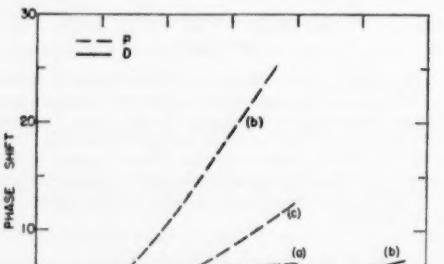

FIG. 2. P and D phase shifts predicted from B alone (see Table I). To obtain experimental predictions in $P_{\frac{1}{2}}$ and D states one could add the (small) Born approximation predictions for A from the PS theory (references 2, 8).

A similar program for $T=\frac{1}{2}$ cannot be carried out because there is too little experimental information. It is interesting to note, however, that the S wave phase shift behavior from a well B such as described in Table I is qualitatively of the form of the observed $S_{\frac{1}{2}}$, $T=\frac{1}{2}$ behavior. For $T=\frac{3}{2}$ it is of interest to consider adding to the (small) predicted $P_{\frac{1}{2}}$ and D wave phase shifts the (small) Born approximation results for A alone from the PS theory.[2,8] If this is done in the region considered in Fig. 2, the $P_{\frac{1}{2}}$ and D phase shifts remain attractive, although the $P_{\frac{1}{2}}$ and $D_{\frac{1}{2}}$ phase shifts associated with A are negative. Thus even a qualitative determination of these phase shifts would be indicative of meson-meson effects. It is felt that this prediction is not sensitive to the many assumptions made in the calculations. The $P_{\frac{1}{2}}$ phase shift is, unfortunately, difficult to determine experimentally since $P_{\frac{3}{2}}$ effects are so large. The D wave phase shifts are more promising of early determination. The term in the scattering angular distribution associated with D, $P_{\frac{3}{2}}$ interference is:

$$\lambda^2 2\,\mathrm{Re}\{[6a(D_{\frac{1}{2}})+9a(D_{\frac{3}{2}})]\cos^3\theta-5a(D_{\frac{1}{2}})\cos\theta\}a^*(P_{\frac{3}{2}}),$$

where the a's represent scattering amplitudes. Observation of this effect should not require great improvement in experimental techniques and statistics at energies beyond and even perhaps below the $P_{\frac{3}{2}}$ resonance, if the D wave phases add as predicted above.

One can try to carry these results further to examine, say, the two-meson system. There is little to go on, but assuming that there is an average probability of one meson in the cloud, one obtains the interesting result that the two-meson system is bound or close to being bound, depending on the range of C. In making this estimate it is assumed that C involves pairs of S wave mesons. If the one-meson state of the cloud is primarily concerned, then the two-meson state involved in our C is the $T=2$ state.

The author would like to thank the staff of the U. S. Atomic Energy Commission computing facilities at New York University for help in doing the computations.

* Work performed under the auspices of the U. S. Atomic Energy Commission.

[1] R. E. Marshak (unpublished remark). F. Dyson and A. Mitra, Phys. Rev. **90**, 372 (1953). The meson-meson interaction has been considered from the viewpoint of meson production by, among others, K. Brueckner and K. Watson, Phys. Rev. **87**, 621 (1952), and J. Kovacs, Phys. Rev. **93**, 252 (1954).

[2] H. A. Bethe and F. J. Dyson, and A. N. Mitra and F. J. Dyson, Phys. Rev. **90**, 372(A) (1953); Dyson, Ross, Salpeter, Schweber, Sundaresan, Visscher, and Bethe, Phys. Rev. **95**, 1644 (1954); G. Chew, Phys. Rev. **89**, 591 (1953); **94**, 1749, 1755 (1954) and **95**, 285 (1954).

[3] The same procedures carried through here for the $S_{\frac{1}{2}}$, $T=\frac{3}{2}$ state were originally considered by R. E. Marshak, Phys. Rev. **88**, 1208 (1952). A recent analysis of this kind has been made by P. Noyes and A. Woodruff, Phys. Rev. **94**, 1401 (1954).

[4] For discussion of the effective range theory for $l>0$ see G. Chew and M. Goldberger, Phys. Rev. **75**, 1637 (1949), and K. Brueckner, Phys. Rev. **87**, 1026 (1952).

[5] For a recent analysis of the data, see H. A. Bethe and F. de Hoffman, Phys. Rev. **95**, 1100 (1954).

[6] It is assumed that the $S_{\frac{1}{2}}$, $T=\frac{3}{2}$ phase shift is not proportional to momentum. J. Orear, Phys. Rev. **96**, 176 (1954) has shown, however, that the $S_{\frac{1}{2}}$ phase shifts may be proportional to momentum up to about 70 Mev, at which point there is a change in slope. This is somewhat high energy at which to have this change in slope, for the interpretation being considered here. This analysis of the data is not closely fitted in any of these calculations here.

[7] It must be noted that the predicted $P_{\frac{3}{2}}$ and D phase shifts are large enough to disturb many of the phase shift analyses on which their determination is based. A consistent treatment of all phase shifts would not qualitatively change the large S and $P_{\frac{1}{2}}$ effects but the quantitative results quoted above might be somewhat different. A more singular potential shape would reduce these $P_{\frac{3}{2}}$ and D wave predictions.

[8] F. Henley and M. Ruderman, Phys. Rev. **90**, 719 (1953); M. Nelkin (private communication).

Gyromagnetic Ratio of 10^{-8}-Second Ta^{181m}

S. Raboy and V. E. Krohn
Argonne National Laboratory, Lemont, Illinois
(Received July 26, 1954)

THE gyromagnetic ratio of the 480-kev isomeric state of Ta^{181} (1.1×10^{-8} sec) has been measured by the method used by the Swiss group[1] for a Cd^{111} isomeric state. The method involves a study of the angular correlation pattern for the 132-480 kev cascade (inset of Fig. 1) as a function of the magnetic field applied perpendicularly to the plane of the two gamma-ray detectors.

The source was prepared by irradiating hafnium metal in the new Argonne research reactor. The metal was dissolved in hydrofluoric acid and placed in Teflon holders covered with Scotch tape. The output of a fast coincidence circuit (10^{-7} sec) was fed into a slow triple-coincidence circuit, together with the outputs of two differential pulse-height analyzers. One of the analyzers had a 70-kev window straddling the 132-kev gamma ray, and the other analyzer had a window about 200 kev wide set with its lower edge at 450 kev. This eliminated detection of coincidences involving the 345-kev gamma ray. NaI(Tl) crystals with Lucite light pipes (six inches long) and 5819 photomultipliers were used as detectors. The Lucite light pipes, together with three layers of soft iron and one layer of mu-metal around the photomultiplier tubes, were sufficient to eliminate magnetic field effects on the photomultipliers.

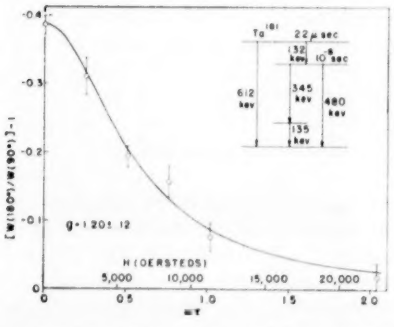

FIG. 1. Anisotropy calculated as a function of $\omega\tau$ (smooth curve) fitted to experimental points obtained as a function of magnetic field.

The magnitude of the gyromagnetic ratio for the 10^{-8}-sec state of Ta^{181} was obtained from a plot of the anisotropy of the 132–480 kev cascade *versus* the magnetic field (Fig. 1). The experimental points have been corrected for scattering from the magnet. This correction was based on a zero-field anisotropy $\{[W(180°)/W(90°)]-1\}$ determination in the presence of the magnet and the same measurement on a plywood table with scattering materials minimized. The latter determination gave an anisotropy in good agreement with the result of McGowan.[2] However, there was no decrease in the anisotropy during periods of up to twelve days following preparation of a source.

The anisotropy in a magnetic field was calculated by means of the following formula:

$$W(\theta,\omega\tau)=\int_0^\infty e^{-t/\tau}\{1+A_2P_2[\cos(\theta+\omega t)] +A_4P_4[\cos(\theta+\omega t)]\}dt,$$

where ω is the Larmor precession frequency, τ the lifetime of the 480-kev excited state, P_2 and P_4 are the second- and fourth-order Legendre polynomials, and A_2 and A_4 are their coefficients in the angular correlation function

$$W(\theta)=1+A_2P_2(\cos\theta)+A_4P_4(\cos\theta).$$

The magnetic field scale of Fig. 1 was then adjusted to fit the experimentally obtained points to the resultant smooth curve. The ratio of the magnetic field to $\omega\tau$ given by the scales of Fig. 1 was used to calculate the magnitude of the gyromagnetic ratio. The sign of the moment was determined by measuring coincidence rates at several angles for $H=5600$ oersteds (Fig. 2).

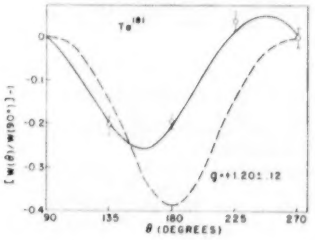

FIG. 2. Anisotropic part of the angular correlation pattern measured at a field of 5600 oersteds. The solid curve was calculated for $\omega\tau=0.51$ and the dashed curve for $\omega\tau=0$ (zero field).

The solid curve of the figure was calculated for a positive gyromagnetic ratio and $\omega\tau=0.51$ (as required by the fitting of the H and $\omega\tau$ scales of Fig. 1). Using $1.59\pm0.08\times10^{-8}$ sec for τ, we obtain

$$g=+1.20\pm0.12 \text{ nuclear units.}$$

We have used for A_2 and A_4 the values -0.280 and -0.058, respectively, as determined by McGowan.[2]

These values were corrected for the solid angle of our detectors. The calculation assumes that there is no attenuation of the angular correlation pattern caused by time dependent electric interactions in the liquid medium.[3,4] This assumption is inconsistent with McGowan's conclusions, but it can be justified by the following arguments: Consider two sets of operating conditions used by McGowan (Table II of reference 2); (a) resolving time, $2\tau_0=0.18\times10^{-6}$ sec, and zero delay; and (b) resolving time, $2\tau_0=1.32\times10^{-8}$ sec, and 6×10^{-9} sec delay. In an indirect manner McGowan arrived at attenuation factors $G_2=0.735$ and $G_4=0.497$. With these attenuation factors and formulas (72), (73), and (74) of Abragam and Pound[3] we calculate that the A_2 measured with operating conditions (b) should have been twenty percent higher than the A_2 measured with operating conditions (a). We also calculate that the A_4 for case (b) should be forty-five percent higher than the A_4 for case (a). These differences were not observed by McGowan.

We can obtain lower limits for G_2 and G_4 in the hydrofluoric acid medium by using McGowan's data. A difference of five percent in the A_2's or ten percent in the A_4's for the above pair of operating conditions would have been detected by McGowan. These differences correspond to $G_2=0.93$ and $G_4=0.86$, and we have taken these values as lower limits on the attenuation coefficients. If the attenuation factors actually fall at these lower limits, our result for g should be raised by about ten percent. The error quoted for g does not include the uncertainty arising from possible attenuation.

An additional argument in favor of values near unity for G_2 and G_4 in the hydrofluoric acid medium is that with such values the calculated "hard core" anisotropy does not fall significantly above the anisotropy measurements of McGowan for solid media.

At this time we are not prepared to make spin assignments to Ta^{181} but feel that this problem requires further study.

We wish to express our appreciation to Dr. F. Coester, with whom we have had many helpful discussions.

[1] Aeppli, Albers-Schönberg, Frauenfelder, and Scherrer, Helv. Phys. Acta **25**, 340 (1952).
[2] F. K. McGowan, Phys. Rev. **93**, 471 (1954).
[3] A. Abragam and R. V. Pound, Phys. Rev. **92**, 943 (1953).
[4] F. Coester, Phys. Rev. **93**, 1304 (1954).

Radiogenic Osmium fromRhenium-Containing Molybdenite

H. Hintenberger, W. Herr, and H. Voshage
Max-Planck-Institut für Chemie, Mainz, Germany
(Received July 26, 1954)

ACCORDING to Mattauch's[1] isobar rule either osmium or rhenium should have a naturally radioactive isotope of mass number 187, and in 1948 Naldrett and Libby[2] were able to establish a natural beta activity of rhenium to which they ascribed a half-life of 4×10^{12} years, and which was attributed to the isotope 187. If follows that rhenium-containing minerals must also contain radiogenic osmium. Professor Geilmann,[3] who from earlier investigations on the occurrence of rhenium[4] was in possession of minerals with high rhenium content, very kindly provided us with molybdenite with a rhenium content of 0.32 percent. To 139 g of this mineral we added 0.147 mg of ordinary osmium (made radioactive by cyclotron irradiation for control of the completeness of the osmium separation) and were able to recover altogether 2.26 mg osmium; 0.28 mg of this osmium was investigated in a 60-degree mass spectrometer. We identified the mass spectrogram of osmium in 5 different places with the

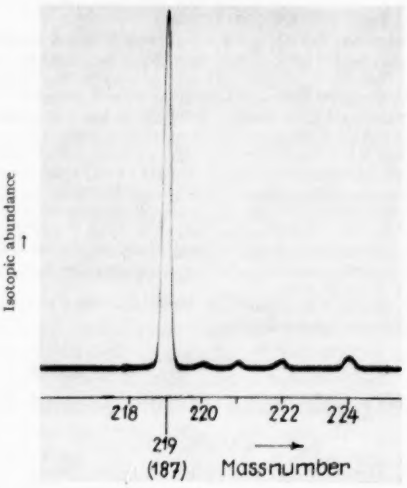

FIG. 1. Mass spectrum of radiogenic osmium in the mass range of OsO_2^+ ions.

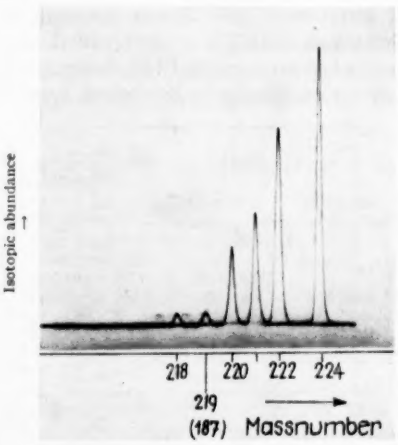

FIG. 2. Mass spectrum of normal osmium in the mass range of OsO_2^+ ions.

ions Os^+, OsO^+, OsO_2^+, OsO_3^+, and OsO_4^+. In each of these spectra the line corresponding to the isotope of mass 187 was greatly enhanced compared with that of ordinary osmium (see Figs. 1 and 2), from which it follows that, according to the isobar rule, the radioactivity of rhenium must be attributed to the isotope 187. Table I contains the abundances of the isotopes

TABLE I. Isotopic abundance of normal and of radiogenic osmium.

	184	186	187	188	189	190	192
Normal osmium (Nier)[a]	11	97	100	811	982	1610	2500
2.113 mg radiogenic Os plus 0.147 mg normal cyclotron-irradiated Os	···	···	100	1.1 ±0.2	1.5 ±0.3[b]	1.8 ±0.1	2.8 ±0.1

[a] A. O. Nier, Phys. Rev. **52**, 885 (1937).
[b] This error comes from an unknown disturbance line.

established by our measurements. The small amount of ordinary osmium visible in addition to the strong radiogenic amount can be accounted for quantitatively by the intentional addition of the cylcotron-irradiated osmium.[5] From the measured abundances of the isotopes and the quantities of added and recovered osmium, it follows that at least 99.5 percent of the osmium originally present in the mineral is radiogenic.

[1] J. Mattauch, Z. Physik. **91**, 361–371 (1934); Naturwiss. **25**, 738 (1937).
[2] S. N. Naldrett and W. F. Libby, Phys. Rev. **73**, 487, 929 (1948); see also N. Sugarman and H. Richter, Phys. Rev. **73**, 1411 (1948).
[3] We wish to thank Professor W. Geilmann for the material given to us and for valuable advice.
[4] W. Geilmann, Neues Jahrbuch für Mineralogie, 1945–1948, Abt. A, Heft 1–4, p. 3–9.
[5] We wish to thank Professor A. H. W. Aten, Jr., Amsterdam, for the active osmium.

Half-Life of Rhenium

W. HERR, H. HINTENBERGER, AND H. VOSHAGE
Max-Planck-Institut für Chemie, Mainz, Germany
(Received July 26, 1954)

NALDRETT and Libby[1] have given 4×10^{12} years as the half-life of Re^{187}. As, from the preceding paper,[2] the radiogenic part of osmium prepared from a rhenium-containing molybdenite is known, it is now possible by a chemical determination of the osmium and rhenium content of the mineral to calculate the half-life, provided reasonable assumptions about the age of the mineral can be made.

By the colorimetry method of Beeston and Lewis,[3] we found (0.32±0.01) percent of rhenium; an independent determination by neutron-activation confirmed this result. For the isolation of the radiogenic osmium, a procedure based on opening up by perchloric acid was developed. The measurement was made with a spectrophotometer by using the thio-urea complex of osmium. An osmium content of (0.00161±0.00009) percent was found, a value in accordance with the isotopic abundances appearing in the mass spectrometer after dilution of the radiogenic osmium by a known quantity (0.147 mg) of ordinary osmium.

From these figures one obtains the half-life

$$T(\mathrm{Re}^{187}) = 91.7t \quad (t = \text{age of the mineral}).$$

Unfortunately, the age of our molybdenite is unknown; we may, however, be sure that the mineral cannot be younger than 50 million years nor older than 2500 million years. This means, for the half-life T of Re^{187}, that

$$5\times10^9 \leqq T \leqq 2.5\times10^{11} \text{ years}.$$

The half-life is, therefore, definitely smaller than the value of 4×10^{12} years originally given by Naldrett and Libby which, by the way, is now considered to be too high also by Libby,[4] since it is difficult to determine the half-life by counter methods because of the extreme softness of the radiation. From an age of about 500 million years, which seems reasonable for these minerals,[5] one obtains a half-life of 5×10^{10} years.

[1] S. N. Naldrett and W. F. Libby, Phys. Rev. **73**, 487, 929 (1948); N. Sugarman and H. Richter, Phys. Rev. **73**, 1411 (1948).
[2] Hintenberger, Herr, and Voshage, preceding Letter [Phys. Rev. **95**, 1690 (1954)].
[3] Joseph M. Beeston and John R. Lewis, Anal. Chem. **25**, 651 (1953).
[4] Professor Libby (private communication).
[5] We are indebted to Professor Baier, Mainz, for valuable discussions.

Primary Alpha Particles in the Cosmic Radiation Near the Geomagnetic Equator*

MARTIN A. POMERANTZ†
Bartol Research Foundation of the Franklin Institute, Swarthmore, Pennsylvania
(Received July 19, 1954)

DURING a series of balloon flights in India, measurements of the flux of primary helium nuclei have been obtained with an apparatus consisting of a G-M counter coincidence train in which is interposed a high-pressure ionization chamber. Events characterized by a specific ionization at least as great as that of a primary alpha particle are recorded, whereas the slowest proton which can just penetrate the absorber beneath the chamber has an average specific ionization $I = 2.3I_{\min}$.

The measurements were conducted at Aligarh, Uttar Pradesh (latitude $\lambda = 18°$N), and Bangalore, Mysore ($\lambda = 3°$N). At each station, the intensity $N(I > 3.2I_{\min})$ of particles producing ionization-chamber pulses exceeding the bias setting corresponding to $3.2I_{\min}$, plotted on a logarithmic scale as a function of atmospheric depth, follows a straight line at high altitudes. The intensity N_{total} was also measured with counter-ion

chamber instruments equipped with an arrangement for removing the requirement $I>3.2I_{\min}$ at predetermined pressure intervals. By taking into account local nuclear interactions initiated by protons, knock-on electrons accompanying protons, and slow protons (albedo)[1] which actuate the apparatus, the alpha-particle flux is determined from the extrapolated values of N_{total} and $N(I>3.2I_{\min})$ at the "top of the atmosphere." The results are:

49 ± 13 particles m^{-2} sec^{-1} $sterad^{-1}$ at $\lambda=3°$,
81 ± 22 particles m^{-2} sec^{-1} $sterad^{-1}$ at $\lambda=18°$.

It is assumed in the analysis that every nuclear interaction initiated in the apparatus by a fast proton produces an ion-chamber pulse exceeding that characteristic of a relativistic particle with $Z=1$. The results of an experiment by McClure[2] at $\lambda=10°$ with a modified arrangement incorporating a multicounter shower detector and pulse-height recorder appear to be compatible with this hypothesis. Any alternative assumption would *increase* the value of the alpha-particle flux. The qualitative effect of the other presumably small systematic uncertainties is generally also in the direction of making the above values low.

Figure 1 shows previous measurements of the alpha-particle intensity at higher latitudes together with the present flux values plotted as a function of kinetic energy per nucleon. With one exception, the abscissa corresponds to the threshold energy, determined from geomagnetic theory, for entry in the vertical direction at the latitude at which the measurements were obtained. The indicated limits, along the energy axis, of the points at low latitudes are defined by the main cone and the Störmer cone plus earth's shadow cone, respectively, in view of the uncertainty regarding the contribution from the penumbral region. In the case of Linsley's measurement, the cutoff is determined by the Čerenkov detector rather than by the earth's magnetic field.

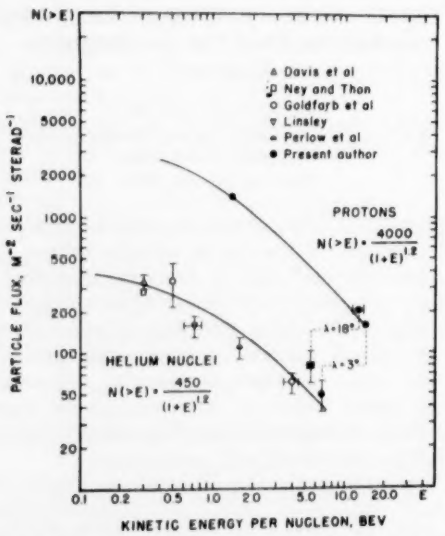

FIG. 1. Dependence upon threshold energy of the flux of primary protons and helium nuclei, respectively. References are as follows: Davis, Caulk, and Johnson, Phys. Rev. **91**, 431 (1953); E. P. Ney and D. M. Thon, Phys. Rev. **81**, 1069 (1951); Goldfarb, Bradt, and Peters, Phys. Rev. **77**, 751 (1950); J. Linsley, Phys. Rev. **93**, 899 (1954); Perlow, Davis, Kissinger, and Shipman, Phys. Rev. **88**, 321 (1952).

The proton points are the author's determinations of the total primary flux at geomagnetic latitudes 52°, 18°, and 3°, respectively, less the contribution from splash albedo[1] and nuclei with $Z>1$.

Both the protons with $1.5<E<15$ Bev and alpha particles with $0.3<E<7$ Bev/nucleon can be represented by an integral energy distribution of the form

$$N(>E)=k(1+E)^{-1.2},$$

where E is kinetic energy per nucleon, and $k=4000$ for protons and 450 for alpha particles. The available data relating to the heavier primaries in this energy interval likewise appear to be consistent with the same power-law relationship.

The anomaly in the total intensity at $\lambda=18°$ in India has been reported previously.[3] Within the experimental uncertainties, the ratio $N(I>3.2I_{\min})/N_{\text{total}}$ at a given altitude is constant between 3°N and 18°N, revealing that the composition of the primary cosmic radiation is not drastically different at these two stations. Thus, the enhanced intensity at $\lambda=18°$ does not appear to be attributable predominantly to a single component.

A complete account of these experiments will be published later, elsewhere.

* Supported by the joint program of the Office of Naval Research and the U. S. Atomic Energy Commission. Field expedition sponsored by National Geographic Society.

† Fulbright Professor, Muslim University, Aligarh, U.P., India, during the year 1952–1953.

[1] K. Anderson (private communication). The author wishes to thank Dr. Anderson for making his results available prior to publication.

[2] G. W. McClure (private communication).

[3] M. A. Pomerantz, Phys. Rev. **95**, 531 (1954).

Elastic Photoproduction of π^0 Mesons from Helium

E. L. GOLDWASSER, L. J. KOESTER, JR., AND F. E. MILLS
Department of Physics, University of Illinois, Urbana, Illinois
(Received July 26, 1954)

THE "elastic" photoproduction of π^0 mesons in helium near threshold has been observed. The term "elastic" denotes that process which may be written: $h\nu+He^4\rightarrow\pi^0+He^4$.

In general, when photomesons are created in the vicinity of a nucleon, the nucleon spin direction may or may not change. Since the helium nucleus has no bound excited states, a spin flip of one of its nucleons must

TABLE I. Threshold energies for the elastic process and several "inelastic" processes.

Process	Threshold energy (Mev)
$h\nu+He^4\rightarrow\pi^0+He^4$	137
$h\nu+He^4\rightarrow\pi^0+H^3+p$	158
$h\nu+He^4\rightarrow\pi^0+He^3+n$	159
$h\nu+He^4\rightarrow\pi^0+H^2+H^2$	162

result in disintegration, with an accompanying increase of about 20 Mev in the aggregate mass. Thresholds for the elastic process and for several "inelastic" processes are listed in Table I. The π^0 mass value used here is $\mu_0c^2=135$ Mev.[1]

Elastic photoproduction of S-wave mesons from helium would violate the $H=0\nleftrightarrow J=0$ selection rule. P-wave emission may then be expected to dominate at low energies. The only multipole absorption which can lead to this process ($\Delta l=1$, $\Delta s=0$, no parity change) is magnetic dipole.

The yield of π^0 photomesons from a 4-in. diameter cylinder of liquid helium was measured as the maximum energy of the betatron x-rays was varied between 150 and 190 Mev. The energies were known with an accuracy of the order of 1 percent. Detection of π^0 mesons was accomplished by observing the π^0 decay γ-ray pairs in two γ-ray telescopes.[2] All runs were made with the plane of the two telescopes making an angle $\theta=80°$ with the incident x-ray beam. The correlation angle, ϕ, between telescope axes was varied from 180° to 90° in 30° steps. Each telescope subtended an angle of 20° at the target. Counting rates from helium are presented in Figs. 1 and 2.

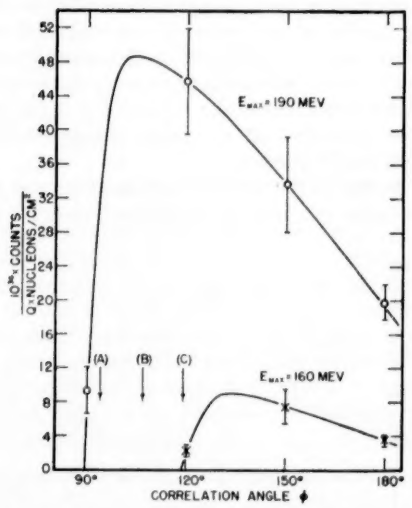

FIG. 1. Counting rates of γ-ray pairs from helium as a function of the angle ϕ between telescope axes. Arrows indicate minimum angles possible for (A) elastic production at 190 Mev; (B) inelastic production at 190 Mev; (C) elastic production at 160 Mev. Inelastic production is negligible at 160 Mev. Curves are arbitrarily drawn through experimental points.

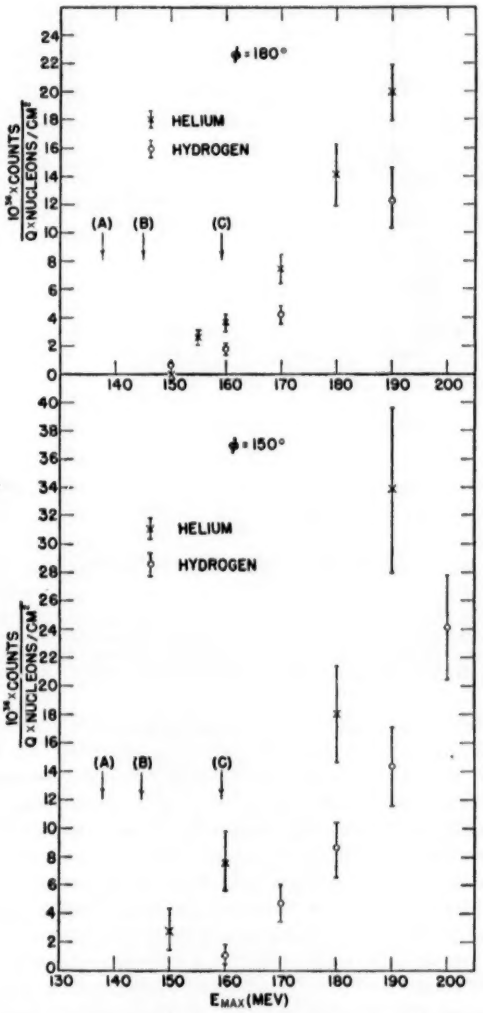

FIG. 2. Counting rates of γ-ray pairs from helium and hydrogen plotted against betatron energies for angles $\phi=180°$ and $\phi=150°$ between telescope axes. Arrows indicate: (A) elastic helium threshold, (B) hydrogen threshold, (C) inelastic helium threshold; all for zero-energy mesons.

The finite counting rates observed at betatron energies of 150, 155, and 160 Mev prove conclusively that elastic π^0 production occurs in helium. Of interest also are the relative contributions from the elastic and inelastic processes at energies above the inelastic production threshold. The angle ϕ between the two γ rays serves as a nonunique measure of the meson energy.[3] In particular, the smallest angle dynamically possible is given by the relation $\sin(\phi_c/2)=1/\gamma$, where the total energy of the meson is $E=\gamma\mu_0c^2$. The counting rates as functions of ϕ at 160 and at 190 Mev are plotted in Fig. 1, and the critical angles are indicated by arrows.

At 160 Mev, the π^0 production is confined almost entirely to the elastic process (Table I), so the lower

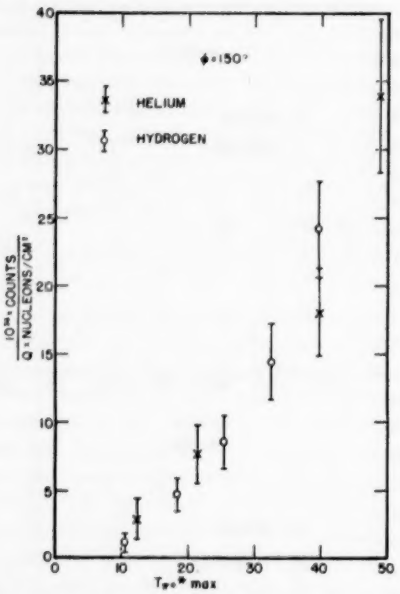

FIG. 3. Counting rates of γ-ray pairs from helium and hydrogen plotted against maximum π^0 kinetic energy in the center-of-mass system corresponding to E_{max} of betatron radiation. For helium, the dynamics for the elastic process have been used.

curve (Fig. 1) serves as an indication of the proper relation between observed counting rates and ϕ_e. At 190 Mev, both elastic and disintegration processes are allowed, but clearly the value of ϕ_e corresponding to elastic production fits better than the value corresponding to inelastic production. Apparently, therefore, the elastic process is still important at 190 Mev.

The counting rates shown in the graphs are normalized per equivalent quantum (Q) and per nucleon/cm² to permit some comparison with hydrogen production. Activation curves for helium and hydrogen at $\phi=180°$ and $\phi=150°$ are plotted in Fig. 2. The hydrogen points were observed with the same apparatus.[2] A valid comparison must take into account the difference between center-of-mass momenta in the hydrogen and helium cases. Figure 3 is obtained from Fig. 2 by changing the scale of abscissas from betatron energies to the corresponding π^0 kinetic energies in the center-of-mass system. All helium events are assumed to be elastic. If the hydrogen and helium cross sections depend on π^0 momentum in the same way, as they appear to do, then this is a meaningful comparison which indicates equal efficiencies per nucleon in hydrogen and helium at identical center-of-mass meson energies. This ratio of unity is in sharp contrast with the helium/hydrogen efficiency ratio of one-half obtained for charged mesons at higher energies.[4] Also, theoretical lower limits placed on the amount of S-wave production in hydrogen[5] suggest that the helium production efficiency should be relatively lower because of the absence of S-wave production. Cross-section calculations now in progress are necessary for a more accurate comparison.

[1] Smith, Birnbaum, and Barkas, Phys. Rev. **91**, 765 (1953); Chinowsky, Sachs, and Steinberger, Phys. Rev. **93**, 586 (1954).
[2] F. E. Mills and L. J. Koester (to be published).
[3] Panofsky, Steinberger, and Steller, Phys. Rev. **86**, 180 (1952).
[4] Jakobson, Schulz, and White, Phys. Rev. **91**, 695 (1953).
[5] K. M. Watson, Phys. Rev. **95**, 228 (1954).

Polarization in p-p Scattering at 415 Mev*†

J. A. KANE, R. A. STALLWOOD, R. B. SUTTON, T. H. FIELDS, AND J. G. FOX
Carnegie Institute of Technology, Pittsburgh, Pennsylvania
(Received July 19, 1954)

A POLARIZED proton beam has been obtained from the Carnegie synchrocyclotron by scattering the internal beam from a carbon target. Protons which were thereby scattered outward through an angle of about 13° passed through a 2 in. × 2 in. collimator in the shield wall. The intensity in the experimental area was measured with an ionization chamber to be about 10^5 protons cm^{-2} sec^{-1}. The beam energy as determined from a differential range curve was 415 Mev with a full width of 10 Mev.

We have measured the asymmetries produced when this beam underwent second scatterings coplanar with the first. The asymmetry, $\epsilon(\theta)$, is defined as $[I(\theta)-I(-\theta)]/[I(\theta)+I(-\theta)]$, where $I(\theta)$ is the intensity of protons scattered through an angle θ, and where positive values of θ are in the same sense as the first scattering.

Measurements of ϵ have been made by using carbon as the second scatterer in order to determine the degree of polarization of the beam. If the first and second scatterings were identical, the polarization, P, would be given by $P=\epsilon^{\frac{1}{2}}$, with ϵ the asymmetry observed in the second scattering. From the results of such an experiment we estimate that our beam polarization is between 40 and 50 percent.

The reality of the observed asymmetries was tested by scattering our normal unpolarized external beam[1]

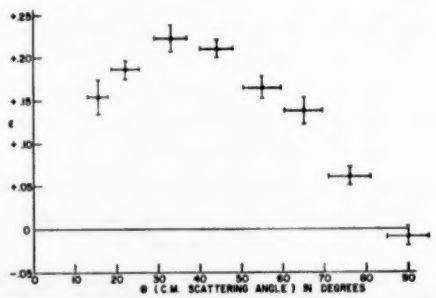

FIG. 1. Polarization in p-p scattering. The observed values for ϵ (defined in test) are shown *versus* the center-of-mass scattering angle. The vertical errors are the standard deviations from counting statistics. The horizontal bars indicate the angular resolution.

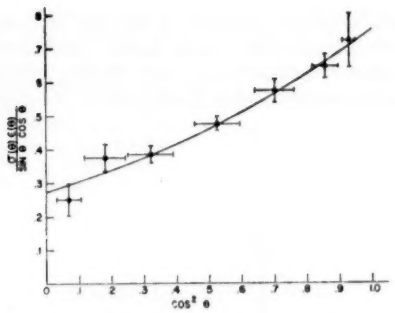

FIG. 2. The data of Fig. 1 are plotted in the form $\epsilon\sigma/\sin\theta\cos\theta$ *versus* $\cos^2\theta$. The equation of the solid line is given in the text.

from the second carbon target. The asymmetry observed was 0.004 ± 0.007 at a scattering angle of 10°.

A measurement has been made of the angular distribution of the asymmetry produced by scattering the polarized beam from liquid hydrogen. The scattered protons were detected with a counter telescope, which, at each angle θ, included a copper absorber of sufficient thickness such that only elastically scattered protons were counted, i.e., no particles accompanying meson production were counted.

Figure 1 shows the observed asymmetries. The polarization in p-p scattering can then be obtained from ϵ through the relation $P_H(\theta)=\epsilon(\theta)/(0.45\pm0.05)$. Figure 2 is a plot of $\sigma(\theta)\epsilon(\theta)/\sin\theta\cos\theta$ *vs* $\cos^2\theta$, where θ is the center-of-mass scattering angle, and $\sigma(\theta)$ is the unpolarized scattering cross section normalized to 1 at 90°.[2] If $\sigma(\theta)\epsilon(\theta)/\sin\theta\cos\theta$ is assumed to vary as $\alpha+\beta\cos^2\theta+\gamma\cos^4\theta$ (only ^3P and ^3F states contributing), a least squares fit to the observed values yields the solid line of Fig. 2.

The equation of this line gives

$$\sigma(\theta)P_H(\theta)=\frac{\sigma(\theta)\epsilon(\theta)}{(0.45\pm0.05)}$$

$$=K\sin\theta\cos\theta(1+b\cos^2\theta+c\cos^4\theta),$$

with $K=0.62\pm0.14$, $b=1.0\pm0.7$, $c=0.63\pm0.77$, where b and c are connected by the relation $c=1.6\pm0.3-0.98b$.

This contrasts with results at about 320 Mev[3,4] which seem to require considerably different values[5] for the coefficients of $\cos^2\theta$ and $\cos^4\theta$. Furthermore, our data agree with Chicago results[6] at 439 Mev within the somewhat larger statistical errors of the latter.

We are indebted to Professor L. Wolfenstein for many valuable discussions.

* This research was supported in part by the U. S. Atomic Energy Commission.

† To be submitted by J. A. Kane in partial fulfillment of the requirements for the degree of Doctor of Philosophy at Carnegie Institute of Technology.

[1] Kane, Stallwood, Sutton, Fields, and Fox, Phys. Rev. **95**, 662 (1954).

[2] Sutton, Fields, Fox, Kane, Mott, and Stallwood, Phys. Rev. **95**, 663 (1954). We have used this $\sigma(\theta)$, measured at 437 Mev, which shows a rise of about 20 percent from 90° c.m. to 17° c.m. At 415 Mev, $\sigma(\theta)$ may have less angular dependence. However, even a completely isotropic cross section would not change the expression for σP_H outside the quoted errors.

[3] Chamberlain, Segrè, Tripp, Wiegand, and Ypsilantis, Phys. Rev. **93**, 1430 (1954).

[4] Marshall, Marshall, and de Carvalho, Phys. Rev. **93**, 1431 (1954).

[5] L. Marshall in *Proceedings of the Fourth Annual Rochester Conference on High Energy Nuclear Physics* (University of Rochester Press, Rochester, 1954), p. 12.

[6] De Carvalho, Heiberg, Marshall, and Marshall, Phys. Rev. **94**, 1796 (1954).

Mesonic Corrections to the Beta-Decay Coupling Constants

R. J. FINKELSTEIN AND S. A. MOSZKOWSKI
University of California, Los Angeles, California

(Received July 29, 1954)

RECFNT analysis of the ft values in superallowed beta transitions have indicated that the Fermi and Gamow-Teller coupling constants (g_F and g_{GT}) are of approximately the same absolute magnitude.[1–5] Nevertheless, as several authors have pointed out,[6,7] the experimental data now require one to conclude that g_{GT}^2 is slightly larger than g_F^2. It is the purpose of this letter to suggest that such a difference may not be a property of the fundamental beta interaction itself, but that it is, at least partially, a consequence of certain radiative effects, involving primarily the emission and reabsorption of a π^0 meson.

The recently determined accurate ft values for O^{14} (3275 ± 75)[8] and C^{34} (3220 ± 200)[9,10] (which are almost certainly $0\to0$ transitions with $|\int 1|^2=2$, $|\int\boldsymbol{\sigma}|^2=0$, assuming only charge independence), provide a direct determination of g_F. In the notation of Gerhart[8] we have

$$[|\int 1|^2+R|\int\boldsymbol{\sigma}|^2]\times ft=6550\pm150\ \text{sec}, \qquad (1)$$

where $R=g_{GT}^2/g_F^2$.

For transitions between ground states of mirror nuclei which have closed shells of 0, 2, 8, 20 protons and neutrons ± one nucleon, the single-particle estimates[11] $|\int\boldsymbol{\sigma}|_{S.P.}^2$ for the G-T matrix elements should be reasonably good. We have used the four known mirror transitions of this kind for which the ft values are known fairly accurately[12] to attempt an approximate determination of the ratio R.[13] The results are shown in Table

TABLE I. Values of g_{GT}^2/g_F^2 deduced from beta transitions between nuclei with closed shells of protons and neutrons ±1 nucleon.

Transition	ft[a]	$\lvert\int 1\rvert^2$	$\lvert\int\boldsymbol{\sigma}\rvert_{S.P.}^2$	$R=g_{GT}^2/g_F^2$[b]
n^1-H^1	1280 ± 250	1	3	$1.37^{+0.4}_{-0.3}$
H^3-He^3	1014 ± 20	1	3	1.82 ± 0.1
$O^{15}-N^{15}$	3950 ± 200	1	0.33	1.97 ± 0.4
$F^{17}-O^{17}$	2320 ± 100	1	1.4	1.30 ± 0.15

[a] See reference 12.
[b] See reference 13.

I. These ratios are always larger than one. However, because of fluctuations, possibly associated with cooperative effects or experimental uncertainties, it is difficult to interpret them precisely. In order to make a rough comparison with theory, we might choose the arithmetic mean of the above ratios, namely 1.6. For other transitions in which the Gamow-Teller interaction participates, e.g., He^6, N^{13}, Ne^{19}, etc., the value of $|\int\boldsymbol{\sigma}|^2$ and thus the value of R as deduced from Eq. (1) depend sensitively on details of nuclear structure.

One should of course expect mesonic corrections to beta processes as well as to electromagnetic interactions; in fact the effect which alters R may be regarded as more elementary than the corresponding anomalies in the magnetic moment, since the virtual mesons do not interact. The lowest-order process involving a single π^0 is shown in Fig. 1. One might expect Chew's[14] approximate formulation of meson theory, involving a cutoff and renormalization, to apply perhaps about as well here as it does to the magnetic moment problem. According to this procedure the modified amplitude for beta decay is

$$(P\nu e|\Gamma|N)'=(P\nu e|\Gamma|N)+\sum_{\pi^0}[(P|V|P'\pi^0)\times(P\nu e|\Gamma|N')(N'\pi^0|V|N)]/(\epsilon_{\pi^0})^2, \quad (2)$$

where

$$(N'|V|N'\pi^0)=-(P|V|P'\pi^0)=(4\pi)^{\frac{1}{2}}(f/\mu)(2\epsilon)^{-\frac{1}{2}}(i\boldsymbol{\sigma}\cdot\mathbf{k}).$$

A straightforward calculation gives

$$\frac{(P\nu e|\Gamma|N)'}{(P\nu e|\Gamma|N)}=\begin{cases}1-3\delta & \text{for allowed Fermi transitions,}\\ 1+\delta & \text{for allowed Gamow-Teller transitions,}\end{cases} \quad (3)$$

where

$$\delta=(f^2/3\pi)\int_0^{x_{\max}}x^4(1+x^2)^{-\frac{1}{2}}dx$$

and $R^{\frac{1}{2}}=|g_{GT}/g_F|=1+4\delta$ to the second order in the coupling constant. To take all second-order processes into account one ought to add contributions from diagrams corresponding to wave function renormalization, but to the first order in δ these do not change $R^{\frac{1}{2}}$. More detailed calculations are planned. Using Chew's renormalized coupling constant and cutoff,[15] $f^2=0.058$ and $x_{\max}=5.51$, one obtains $\delta=0.079$ and $R_{\text{th}}^{\frac{1}{2}}=1.32$. The "mean" experimental $R^{\frac{1}{2}}$ is 1.25. In view of the experimental uncertainties and the crudeness of the theoretical estimate, this kind of agreement must be regarded as accidental. Of course, the above estimate refers to the free neutron and ignores cooperative effects such as exchange corrections, which may be significant in H^3, and quenching[16] which may become important in heavy nuclei. The existence of this mesonic perturbation of the correct sign and approximately right magnitude makes it possible to assume that the unperturbed Gamow-Teller and Fermi coefficients are exactly equal, in accordance with various hypotheses about the universal Fermi interaction.[17] We note also

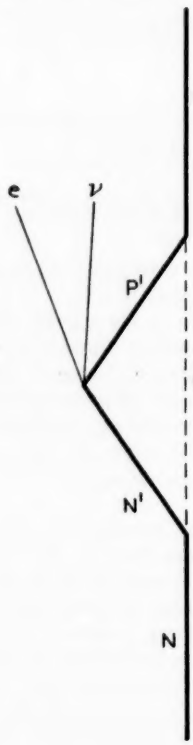

FIG. 1. Lowest-order mesonic correction to beta decay.

that this correction is present to the *same* extent in muon capture, but absent in muon decay; the effective Fermi constant for the μ decay should, for this reason, be slightly different from its value for μ capture and N decay. For example, if $R=1.6$, then the quantity[17,18] λ is changed from 1.2 to 1.0.

We would like to thank Professor N. Kroll, Professor M. Ruderman, and Professor R. Sherr for several illuminating discussions and Dr. J. B. Gerhart for informing us of his results before publication.

[1] O. Kofoed-Hansen and A. Winther, Kgl. Danske. Videnskab. Selskab, Mat.-fys. Medd. **26**, No. 14, (1953).
[2] G. L. Trigg, Phys. Rev. **86**, 506 (1952).
[3] R. Bouchez and R. Nataf, Compt. rend. **234**, 86 (1952).
[4] C. S. Wu, Physica **18**, 989 (1952).
[5] E. J. Konopinski and L. M. Langer, Ann. Rev. Nuclear Sci. **2**, 261 (1952).
[6] J. M. Blatt, Phys. Rev. **89**, 83 (1953).
[7] R. Sherr and J. B. Gerhart, Phys. Rev. **91**, 909 (1953).
[8] J. B. Gerhart, Phys. Rev. **95**, 288 (1954).
[9] D. Green and J. R. Richardson, Bull. Am. Phys. Soc. **29**, No. 6, 23 (1954).
[10] P. Stähelin, Phys. Rev. **92**, 1076 (1953).
[11] E. Wigner, Phys. Rev. **56**, 519 (1939).
[12] Data are taken from the compilation of Kofoed-Hansen and Winther (reference 1). There is a slight discrepancy between the *ft* value for O^{15} given in the present paper [calculated using the

formulas in E. Feenberg and G. Trigg, Revs. Modern Phys. **22**, 399 (1950)] and the value listed in reference 1.

[13] The values of R for the neutron and for H^3 have been previously given in reference 8 and reference 6, respectively.

[14] G. Chew, Phys. Rev. **94**, 1748, 1755 (1954).

[15] G. Chew, Phys. Rev. **95**, 285 (1954).

[16] H. Miyazawa, Progr. Theoret. Phys. (Japan) **6**, 801 (1951).

[17] L. Michel and A. Wightman, Phys. Rev. **93**, 354 (1954).

[18] L. Michel, *Progress in Cosmic Ray Physics* (North Holland Publishing Company, Amsterdam, 1952), Chap. 3, Eq. (43).

Antiproton Production

G. FELDMAN
Department of Mathematical Physics, University of Birmingham, Birmingham, England
(Received July 12, 1954)

RECENTLY a few Letters have appeared[1] which discuss the cross sections for antiproton production in nucleon-nucleon collisions, at energies which will soon be available at Berkeley. We should like to point out that there may be a more profitable way of producing antiprotons, by first producing a very energetic π meson which in turn produces an antiproton in colliding with a nucleon.

The reaction

$$p+N\rightarrow p+N+p+\bar{p}, \quad (1)$$

where N is a nucleon, has a threshold of $6Mc^2$ (5.6 Bev) for the incident proton. However, if we consider the two-step reaction,

$$\begin{aligned} &p+N\rightarrow N+N+\pi, \quad \text{(a)} \\ &\pi+N\rightarrow N+p+\bar{p}, \quad \text{(b)} \end{aligned} \quad (2)$$

the threshold for this double reaction, if we use the most energetic π produced in (a), is about $4.4\ Mc^2$ (4.1 Bev) for the incident proton in (a).

For the following reasons, then, we think that the reaction (2) may be more useful at Berkeley energies:

(i) If the N in (1) is a proton, the cross section is very small near threshold, since there are 3 final protons, one of which must be in at least a p-state.

(ii) For a given proton energy, say $\sim 7Mc^2$, reaction (2) will be a good deal above threshold, whereas (1) will not. Also in (b) of (2) there are only *three* final particles and thus the density-of-states factor will be considerably more favorable than for (1). The problem is then to produce the high-energy π mesons.

We can give a rough estimate for the cross sections for (1) and for (2b). We assume that we have protons of K.E.$\sim 7Mc^2$. Then we estimate the cross section for (1). The total energy in the c.m. system is about $4.24\ Mc^2$ and so the kinetic energy to be divided among the four final particles is $0.24\ Mc^2$. We estimate the matrix element crudely by conserving momentum at each vertex in Fig. 1 and putting in a factor $g/(2\omega)^{\frac{1}{2}}$ for each vertex, where g is the coupling constant and ω the meson energy. We can rearrange the vertices in 4! ways; we get $\frac{3}{2}g^4$ for the matrix element. Combining this result with the density-of-final-states factor, we get

FIG. 1. Feynman diagram of reaction (1).

$$\sigma_{pN}\approx 0.54(g^2/4\pi)^4(T_1/M)^{7/2}\ \text{mb},$$

where T_1 is the kinetic energy available in the c.m. system. In this example, $T_1\approx 0.24Mc^2$.

Now a proton of $7Mc^2$ could produce a meson of $6Mc^2$. The energy available in the c.m. system of (2b) is about $3.65Mc^2$ and thus the kinetic energy available is about $0.65Mc^2$. Using the same type of estimate for the matrix element as above, we get

$$\sigma_{\pi N}\approx 22(g^2/4\pi)^3(T_2/M)^2\ \text{mb}.$$

This gives

$$\frac{\sigma_{\pi N}}{\sigma_{pN}}\approx\frac{2000}{g^2/4\pi},$$

which is at least 200 if $g^2/4\pi\approx 10$. ($g^2/4\pi$ is quite likely smaller than 10.) Thus it seems that if more than about 0.1 percent of the protons can produce high-energy mesons, reaction (2) would be better.

[1] R. N. Thorn, Phys. Rev. **94**, 501 (1954); D. Fox, Phys. Rev. **94**, 499 (1954).

Modified Nucleon Propagators*

A. N. MITRA
Laboratory of Nuclear Studies, Cornell University, Ithaca, New York
(Received July 26, 1954)

THE need for nonperturbation methods in meson theory has been increasingly felt in recent years. There are, however, several difficulties associated with them, one of which has been recently pointed out by Feldman.[1] He has found that a new (nonrenormalizable) type of divergence appears when one uses modified

FIG. 1. Kernels for self-energy graphs.

nucleon propagators like S_F' instead of S_F. This divergence is, in turn, associated with certain complex poles of S_F' in addition to the usual ones of Feynman-Dyson theory. Feldman based his conclusions on a very simple form of S_F', *viz.*, one obtained by taking iterations of graphs like Fig. 1(a). It is conceivable, however, that a more complete expression for S_F' might remove this difficulty. One obvious modification would be to extend the kernel for S_F' to include some fourth-order processes as well, and to take iterations of the latter in the spirit of the Bethe-Salpeter approach.

An attempt has been made here to make this necessary extension of the kernel by including graphs of Fig. 1(b) in addition to those of Fig. 1(a). The calculations have been performed (like Feldman's) for the case $\mu/M \to 0$, which is a fairly good approximation. The result for the new S_F', after separating out the mass and charge renormalizations, is as follows:

$$S_F'(p) = S_F(p)[1-\beta\chi(y)+\beta^2\phi(y)]^{-1}, \tag{1}$$

$$\beta = (3/8\pi)(G^2/4\pi), \quad y = -i(\gamma p)/M, \tag{2}$$

$$\chi(y) = (1-y)[y^3+(1-y^2)\ln(1-y^2)]/y^3, \tag{3}$$

$$\phi(y) = [y^4 f(y^2)+y^2(1-y^2)\ln(1-y^2) - \tfrac{1}{2}(1-y^2)^2\ln(1-y^2) - \tfrac{1}{2}y^2(1-y^2) - y^3(1-y)]/y^3(1-y), \tag{4}$$

$$f(y^2) = \int_0^1 \ln[(1-uy^2)/(1-u)]\,(du/u). \tag{5}$$

The additional poles of $S_F'(p)$ are now given by

$$1-\beta\chi(y)+\beta^2\phi(y) = 0. \tag{6}$$

We denote the values of β, obtained from (6) as a function of y, by $\beta(y)$. $\beta(y)$ is plotted against y in Fig. 2.

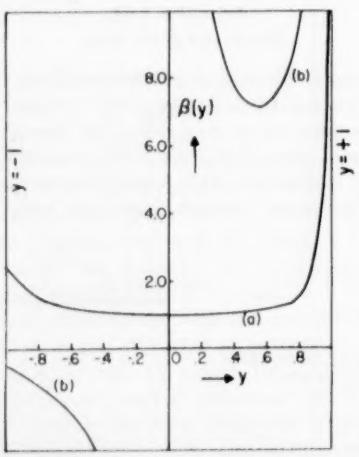

FIG. 2. Curves for $\beta(y)$ as a function of y. (a) Present calculation; (b) Feldman's result. $\beta(y)$ is complex for $|y|>1$.

Feldman's results, which are obtained by putting $\phi(y)=0$, are also given for comparison, One now finds that the minimum positive value of $\beta(y)$ is only 1.00, instead of Feldman's 7.25. Thus the condition for getting real poles of $S_F'(p)$ is now only $\beta>1$ instead of $\beta>7.25$. This seems quite compatible with the values allowed by the present-day pseudoscalar theory and has the consequence that the type of divergence envisaged by Feldman would not appear. This treatment does not claim to be as complete as it would be if all the fourth-order graphs, including the crossed self-energy and vacuum polarization graphs, were included. The calculations involving the latter are, however, much more complicated than the present one. An attempt is being made to include these effects and it is hoped that a detailed account will be published in the near future.

I am indebted to Dr. R. H. Dalitz for pointing out Feldman's results prior to publication.

* Assisted by the joint program of the Office of Naval Research and the U. S. Atomic Energy Commission.

[1] G. Feldman, Proc. Roy. Soc. (London) **A223**, 112 (1954).

Absolute Intensities of the Gamma Rays and X-Rays of Radium D†

P. E. DAMON AND R. R. EDWARDS

Departments of Physics and Chemistry, University of Arkansas, Fayetteville, Arkansas

(Received May 10, 1954)

RECENT studies[1,2] of the gamma-ray spectrum of RaD have failed to confirm the existence of low-intensity gamma rays previously reported. Intensity values for the 46.5-kev gamma ray, obtained by various observers using ionization chamber technique, are in good agreement,[3] averaging 3.5 ± 0.4 quanta per 100 disintegrations. The more recent discordant value reported by Wu *et al.*[2] is not a direct determination but depends on the L-fluorescence yield (f_x), and the contribution of L excitation (f_L) to the total conversion probability (N_T).

Reported values for the intensity of the L x-radiation (N_x), determined by ionization chamber measurements, are also in good agreement: 0.30,[4] 0.25,[5] and 0.27.[6] Values obtained by this method depend on the selection of an average energy per quantum. We have attempted to obtain a more precise value by using a quantum counter.

Wu *et al.*,[2] using a 180-degree beta-ray spectrometer with Geiger counter detector, found N_T to be 0.85 ± 0.05, and f_L to be 0.75. These values are in agreement with those reported by Cranberg,[7] and represent results of a technique inherently more reliable than those used in earlier work.

According to Lay,[8] the fluorescence yield from fluorescence excitation of bismuth is 0.40. Kinsey[9] finds some discrepancy between theoretical and experimental values of f_x in RaD, and a careful analysis of his work

indicates that it places the value only between the limits 0.30 and 0.50. Using the value of Wu *et al.* for the L conversion probability ($N_L=f_LN_T=0.64$), and Stahel's[5] value of N_x (0.25), one obtains $f_x=0.39$, considerably lower than the value 0.475 used by Wu *et al.* (attributed to Kinsey[9]) to obtain the intensity of the 46.5-kev gamma ray from their measured intensity ratio of L x-rays to gammas.

Using scintillation spectrometry and 2π alpha counting techniques we have measured absolute intensities of the gamma rays and L x-rays of RaD, and have obtained a total gamma-ray intensity of 4.4 ± 0.7 and an L x-ray intensity of 19 ± 3 per hundred disintegrations. A line at 31 ± 1 kev has been distinctly resolved by proportional spectrometry under conditions where pulse pile-up is eliminated. The intensity of this line is 0.6 ± 0.2, and that of the 46.5-kev line is 3.8 ± 0.6 per hundred disintegrations.

The intensity ratio of x-rays to 46.5-kev gammas obtained from the above results agrees with that reported by Wu *et al.*[2] Our value for N_x, together with their value for N_L, leads to a fluorescence yield of 0.30 ±0.05 which, in turn applied to their data, yields a 46.5-kev gamma intensity of 4 ± 1 instead of the reported 7 ± 2, thus bringing all reports into agreement.

Low-intensity gamma rays reported previously by us and others from proportional counter studies do not appear when pulse pile-up is eliminated by selective absorption techniques; these lines may thus be attributed, at least in part, to this effect. Limits may be set as follows: 43 kev, <0.2; 37 kev, <0.1; 23 kev, <0.1; 65 kev, <0.01; and K x-rays, <0.1 per hundred disintegrations. In addition, a thorough search for gamma rays in coincidence has been made, and no nonrandom coincidences have been found. In particular, it is clear that no line in the vicinity of 16 kev occurs in coincidence with the 31-kev gamma ray.

† This work was supported in part by the U. S. Atomic Energy Commission.

[1] G. T. Ewan and M. A. S. Ross, Nature **170**, 760 (1952).
[2] Wu, Boehm, and Nagel, Phys. Rev. **91**, 319 (1953).
[3] P. E. Damon and R. R. Edwards, Phys. Rev. **90**, 280 (1953).
[4] J. A. Gray, Nature **130**, 738 (1932).
[5] E. Stahel, Helv. Phys. Acta **8**, 651 (1935).
[6] Tsien San-Tsiang, Compt. rend. **218**, 503 (1944).
[7] L. Cranberg, Phys. Rev. **77**, 155 (1950).
[8] H. Lay, Z. Physik **91**, 533 (1934).
[9] B. B. Kinsey, Can. J. Research **A26**, 421 (1948).

Tau Meson Produced by 3.0-Bev Protons*

R. D. Hill, † E. O. Salant, and M. Widgoff
Brookhaven National Laboratory, Upton, New York
(Received August 2, 1954)

CONTINUED examination of the emulsions described in a first report[1] has disclosed ten stopping K mesons and, in addition, one τ meson. This τ meson was found in a stack of emulsions exposed at 90° to the 3.0-Bev proton beam, in position (a) of reference 1. In this stack, systematic scanning of 46 cm³ of emulsion showed, in addition to the τ meson, 5 stopping K^+ mesons, and 1578 stopping π and μ mesons.

The τ meson entered the stack, from the direction of the target, with an initial energy of 92 Mev. When allowance is made for its energy loss in the cosmotron wall, its minimum energy on leaving the target was 122 Mev. The particle traveled 3.4 cm in two emulsions before stopping and undergoing the typical τ-meson decay into three coplanar charged mesons.

Of the three outgoing mesons, only one came to rest in the stack. This was a π^+ meson, showing the characteristic $\pi-\mu-e$ decay after traversing 4.9 mm of emulsion and having, therefore, an initial energy of 15.4 Mev. One meson appeared to be almost stopping after traveling 4.6 mm. Its grain density variation with range was consistent with that of a pion of 17 Mev. The track of the third outgoing light meson showed no significant grain density variation in 8 mm of track length. Its grain density was consistent with that of a pion of 40 Mev. However, in both cases, the possibility of muons cannot be eliminated, as the steepness of the tracks prevented scattering measurements. Within the experimental error of 1°, the meson tracks were coplanar; the measured angles between the tracks were 61.3°, 150.0°, and 148.5°. From the momentum of the stopped pion, the momenta of the other mesons were computed to be 70.3 Mev/c and 118.2 Mev/c. If these two particles are accepted as pions, then these momenta correspond to energies of 16.8 and 43.4 Mev. The pion energies add up to (76 ± 5) Mev, in good agreement with the current value of 75 Mev for the Q of the τ-meson decay.[2]

It is advantageous to refer other K masses to the accurately known τ mass as a standard. In these measurements, the mean scattering angles of the τ, one K^- and one K^+ meson were $0.216°\pm0.015$, $0.215°\pm0.019°$, and $0.208°\pm0.020°$, respectively, determined for the same effective residual range[3] of 23.5 mm, and with approximately one hundred 100-μ cell lengths in each case. From the observed mean scattering angle of 0.216° and the correct τ mass of 965.5 m_e,[2] the scattering constant was calculated to be 25.8 ± 1.8 degree-Mev. With this scattering constant, the K^- mass was $(970\pm180)m_e$ and the K^+ mass $(1040\pm200)m_e$. These values are in satisfactory agreement with the masses obtained by the method of grain density-range comparisons with pion tracks, namely, $(960\pm190)m_e$ for the K^- and $(960\pm90)m_e$ for the K^+; this latter method gives $(960\pm80)m_e$ for the τ mass. Here the errors are standard statistical deviations and can be reduced by measuring more calibrating tracks.

The emission of a τ meson of 122 Mev at 90° to the 3.0-Bev proton beam makes unlikely the conclusion that this meson was produced, in a single nucleon-nucleon interaction, paired with another K meson; for if a target nucleon is assumed to have a Fermi energy even as high

as 25 Mev, there is not enough energy to produce a τ meson of 965.5 m_e and a K meson heavier than 800 m_e.[4]

We take pleasure in thanking Mrs. M. Carter and Mr. J. E. Smith for processing the emulsions, and Mrs. M. Hall, Mrs. B. Cozine, M. Bracker, A. Lea, and Miss M. Post for unsparing support in the microscopy.

* Research performed under the auspices of the U. S. Atomic Energy Commission.

† On leave from the University of Illinois, Urbana, Illinois.

[1] Hill, Salant, and Widgoff, Phys. Rev. **94**, 1794 (1954).
[2] Report of Padua Conference, 1954 (unpublished).
[3] K. Gottstein and J. H. Mulvey, Phil. Mag. **42**, 1089 (1951).
[4] R. Sternheimer, Phys. Rev. **93**, 642 (1954).

Primary Cosmic-Ray Spectrum Deduced from an Analysis of Jets

A. Engler and U. Haber-Schaim
Physikalisches Institut der Universität, Bern, Switzerland
(Received July 20, 1954)

During a systematic analysis of high-energy collisions, recorded in nuclear emulsions flown at high altitudes, sufficient data were obtained to attempt the determination of the energy spectrum of singly charged particles.

The method of selection was such as to inculde all stars with 5 shower particles or more having a "half-angle" of $\theta_{\frac{1}{2}} \leq 10°$. No restriction was imposed on the number of heavy or gray prongs. The only condition for the measurement of a star was that at least half the shower particles have a projected angle of $\leq 10°$ with respect to the direction of the primary. The angle of dip generally increases the true angle with the primary. Hence, from 75 stars measured hitherto, only 41 were selected as having $\theta_{\frac{1}{2}} \leq 10°$. We believe that in this way all events with that half-angle and $n_s \geq 5$ from the scanned area were included in our analysis. Only five stars of comparable energy having a neutral primary have been found. This fact as well as the high altitude at which the emulsion were flown ($\sim$30 km) suggest that the large majority of the singly charged particles are protons of primary origin.

The energies of the individual stars were estimated according to two different methods, both assuming multiple production. The first method does not involve a particular theory of meson production in nucleon-nucleon collision. It is based on the following assumptions: (a) all the shower particles have their origin in a single collision; (b) the angular distribution of the particles is symmetrical in the c.m. system and the velocity of most of them is larger than the velocity of the c.m. with respect to the laboratory system.

Since the incoming nucleon has to penetrate on the average a considerable length in nuclear matter (e.g., Ag, Br, or C, N, O nuclei), one may interpret assumption (a) to mean that the mesons that actually leave the nucleus are produced by a composite particle colliding with the last nucleon on the path. This composite particle is supposed to consist of that fraction of nucleons and pions already produced which are closely collimated in the forward direction.[1,2] The above-mentioned c.m. system refers to those two particles. If this is accepted, the energy of the primary is given by the well-known expression $E=2/\theta_{\frac{1}{2}}^2$ in nucleon mass units. Curve I (Fig. 1) shows the integral spectrum

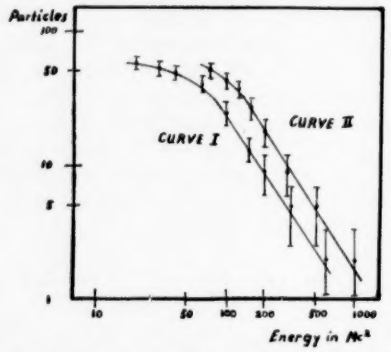

Fig. 1. The integral energy spectrum. In curve I, $E=2/\theta_{\frac{1}{2}}^2$, in curve II, $E=2k/\theta_{\frac{1}{2}}^2$.

obtained in this way. The large change of the slope below $E=65Mc^2$ is due to our method of selection. Therefore, with the lower limit of the spectrum taken at $E_0=65Mc^2$ (corresponding to $\theta_{\frac{1}{2}}=10°$) and the spectrum assumed to be of the form $N(>E)\sim E^{-s}$, the method of maximum likelihood gives for the 41 events $s=1.40_{-0.21}{}^{+0.23}$. The errors represent those values of s which are less probable by a factor of $e^{\frac{1}{2}}$ than the most probable one. This coincides with the standard deviation for a Gaussian distribution.

Our value for s is higher than that obtained recently by Hoang[3] by a similar method. The discrepancy is possibly due to the rejection of stars with $N_H \geqslant 4$ by Hoang.

For $E \geqslant 100Mc^2$ we have 25 events which by the same method yield $s=1.50_{-0.28}{}^{+0.31}$ in agreement with the results of Haber-Schaim[1] and Barrett *et al.*[4] for the same energy interval.

In the second method for the estimation of the energy, the possibility is taken into account that in the last and pertinent collision more than one nucleon (at rest) were hit simultaneously.[5,6] If k nucleons are hit, the energy of the primary as determined from the half-angle is $E=2k/\theta_{\frac{1}{2}}^2$. In order to determine k, one has to assume a relation between the observed multiplicity n_s and the energy. This has been done on the basis of Fermi's theory of meson production by Cocconi,[6] who obtained the relation

$$k=(n_s\sqrt{\theta_{\frac{1}{2}}})/2.6.$$

Let α_k be the probability for a collision with k nucleons $(=1\cdots4)$, $\sum_k \alpha_k=1$, and let the energy spectrum according to the first model have the form E^{-s}. Then we obtain for the spectrum, according to the second

model,

$$f(E)=\sum_k \alpha_k (E/k)^{-s}=E^{-s}\sum \alpha_k k^s.$$

In other words, if the spectrum in case I is well described by a power law, spectrum II will be described by the same power law provided the α_k are constant. This seems to be confirmed by our results (curve II, where the experimental bias is again responsible for the change of slope below $E=120Mc^2$). For $E \gtrsim 120Mc^2$ we obtain from 37 cases $s=1.45_{-0.23}{}^{+0.25}$. One should note that Cocconi[6] assumes the k nucleons to be arranged longitudinally in the direction of the primary, whereas we take them to be arranged transversely.[5] At present our results indicate that, assuming a geometrical mean free path in nuclear matter, the experimental values of α_k are very different from what one would expect to find for the Cocconi model applied to the emulsion nuclei. The detailed analysis of our data will be submitted for publication elsewhere.

We wish to express our gratitude to Professor F. G. Houtermans for his interest and encouragement and to Professor Charles Peyrou and Dr. M. Teucher for stimulating discussions. We are also indebted to Dr. Charles Houtermans who was associated with the early stages of this work. Finally we wish to thank Mrs. B. Mesmer, Mrs. R. Müller, and Mrs. G. Riesen for careful scanning of the plates.

[1] U. Haber-Schaim, Phys. Rev. **84**, 1199 (1951).
[2] M. F. Kaplon and D. M. Ritson, Phys. Rev. **85**, 932 (1952).
[3] T. F. Hoang, J. phys. et radium **15**, 5, 337 (1954).
[4] Barrett, Bollinger, Cocconi, Eisenberg, and Greisen, Revs. Modern Phys. **24**, 133 (1952).
[5] U. Haber-Schaim, Nuovo cimento, Padova Conference Supplement (to be published).
[6] G. Cocconi, Phys. Rev. **93**, 1107 (1954).

Asymmetry in Neutron Production by Bombarding Targets with 285-Mev Polarized Protons*

HUGH BRADNER AND ROBERT DONALDSON
Radiation Laboratory, Department of Physics, University of California, Berkeley, California
(Received June 21, 1954; revised manuscript received July 12, 1954)

AN asymmetry in neutron production has been observed in the quasi-elastic scattering of polarized protons on the nucleons of carbon, beryllium, and lithium targets.

The polarized proton beam was obtained by scattering the cyclotron beam on an internal beryllium target, using the arrangement of Chamberlain *et al.*[1] This resulting proton beam had a polarization of 65±3 percent, a mean energy of 285 Mev, and a flux of approximately 10^5 protons per second in the "cave" outside the cyclotron shielding.

When targets were bombarded by these polarized protons, neutrons (and protons) were ejected by nucleon-nucleon collisions. The neutrons were counted in 180° center-of-mass coincidence with their recoil protons, and only recoil protons of energy greater than $0.7\,E_0\cos^2\theta$ were accepted. Thus, only quasi-elastic proton-neutron events were recorded. One telescope subtended a solid angle of approximately 1/200 sterad, but the other needed to subtend 1/10 sterad to give good counting rates at large angles.

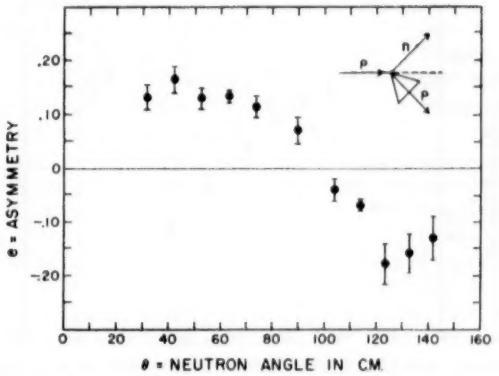

FIG. 1. Asymmetry e plotted as a function of the center-of-mass neutron angle for proton-neutron quasi-elastic scattering from carbon. The errors shown include only counting statistics.

The telescopes used for recording proton-neutron events could also be used for recording proton-proton events.

Alignment of the apparatus was checked by measuring the asymmetry of double scattered protons as in the experiment of Chamberlain *et al.*[1] Our data were found to agree within statistical errors, with their results.

In a p-n collision, it can be shown[2] that each of the scattered nucleons has the same polarization P_{np}, as long as the initial nucleons are unpolarized and nuclear forces are charge-independent. If the incident protons have a polarization P_p, the right-left asymmetry in the counting rate of neutrons is related to the polarization

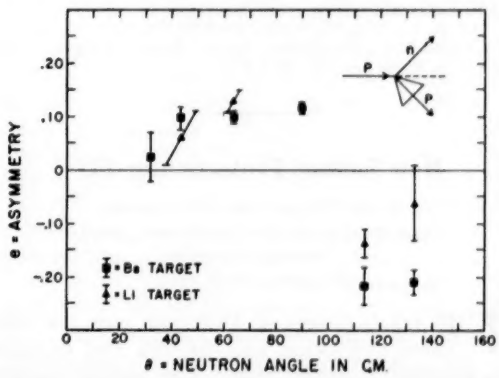

FIG. 2. Asymmetry e plotted as a function of the center-of-mass neutron angle for proton-neutron quasi-elastic scattering from lithium and beryllium. The errors shown include only counting statistics.

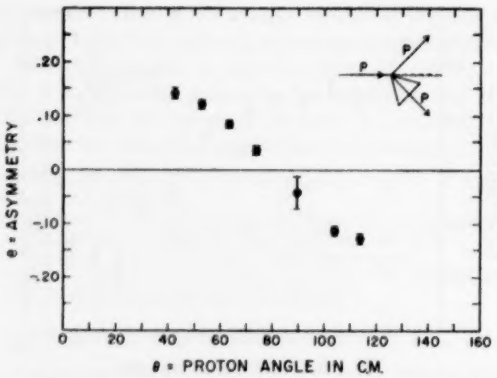

FIG. 3. Asymmetry e plotted as a function of the center-of-mass proton angle for the proton-proton quasi-elastic scattering off carbon. The errors shown include only counting statistics.

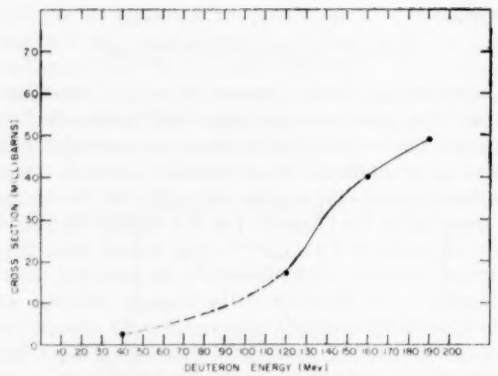

FIG. 1. Cross section for the production of Pa^{237} by deuteron bombardment of U^{238}.

P_{np} by the usual equation, $e=(L-R)/(L+R)=P_pP_{np}$; where e is the asymmetry, and L and R are the neutron counting rates at equal angles to the left and right. In the present experiment, this gives $P_{np}=e/0.65$.

Figures 1 and 2 give the quasi-elastic asymmetry e for neutrons from carbon, beryllium, and lithium targets. For angles greater than 90° center-of-mass the neutrons were defined by the telescope with poor angular resolution.

It should be noted that the nonzero neutron asymmetry at 90 degrees center-of-mass indicates[3] the presence of both odd and even terms in the scattering analysis. A subsequent experiment by Chamberlain *et al.*[4] using a liquid deuterium target gives results in good agreement with our data on carbon.

Figure 3 shows the asymmetry of quasi-elastic proton-proton scatters in carbon, obtained at the same time as the neutron data.

* This work was done under the auspices of the U. S. Atomic Energy Commission.

[1] Chamberlain, Segrè, Tripp, Wiegand, and Ypsilantis, Phys. Rev. **93**, 1430 (1954).

[3] M. Ruderman (private communication).

[3] Don R. Swanson, Phys. Rev. **84**, 1086 (1951).

[4] Chamberlain, Donaldson, Segrè, Tripp, Wiegand, and Ypsilantis, Phys. Rev. **95**, 580 (1954).

New Isotope Protactinium-237†

W. W. T. CRANE AND G. M. IDDINGS
Radiation Laboratory, University of California
Berkeley, California

(Received July 30, 1954)

THE bombardment of Th^{232} with energetic deuterons and helium ions has been used to study the isotopes of protactinium.[1] The heaviest isotope previously produced by this method was Pa^{235}, a negative beta particle emitting isotope with a twenty-three-minute half-life.[2] Until recently it has been assumed that reactions of the type $(d,2pxn)$ would have very small cross sections; consequently, little work has been done on the protactinium isotopes produced by high-energy deuteron bombardment of uranium.

In the bombardment of U^{238} with high-energy deuterons, the isotope Pa^{237} is produced by the reaction $(d,2pn)$. A sample of U^{238} was irradiated with 190-Mev deuterons, and a protactinium sample was chemically separated as soon as possible. From the decay of the negative beta particle emitted, one can determine that there is present an isotope with a half-life shorter than twenty-three minutes. However, accurate determination of the half-life of this isotope is difficult since large quantities of Pa^{235} are also produced. By chemically separating uranium from a protactinium fraction at fixed periods, the half-life and the mass assignment of this new short-lived protactinium isotope were determined. The uranium fractions were counted for β^- particles and gamma rays. The ratio β^-/γ in the separated uranium fraction was the same as that for a sample of U^{237} produced by other methods, and the separated uranium fractions decayed with the 6.7-day half-life of U^{237}. From this series of experiments, one obtains a half-life of 10.5 ± 1 min for Pa^{237}.

The cross section for the production of Pa^{237} was determined by bombarding one-mil uranium foils in the internal beam of the 184-inch cyclotron and then isolating the protactinium formed. The energy of the bombardments was determined by the radius of bombardment. The beam current was monitored by using the known cross section for the production of Na^{24} from aluminum.[3] The chemical yield was determined by adding a known amount of Pa^{231} to each sample. The amount of Pa^{231} present after purification was measured by pulse analyses of the alpha particles. The cross section as a function of energy is shown in Fig. 1.

It should be emphasized that these are only approximate cross sections. The largest errors enter in the resolution of the twenty-three minute Pa^{235} from the

ten-minute Pa^{237} and in the fact that very little is known about the radiation characteristics of Pa^{237}.

† This work was performed under the auspices of the U. S. Atomic Energy Commission.

[1] M. H. Studier and E. K. Hyde, Phys. Rev. **74**, 591 (1948).
[2] W. W. Meinke and G. T. Seaborg, Phys. Rev. **78**, 475 (1950).
[3] R. E. Batzel *et al.*, Phys. Rev. **91**, 939 (1953).

Isotopes of Curium, Berkelium, and Californium†

E. K. Hulet, S. G. Thompson, and A. Ghiorso
Radiation Laboratory and Department of Chemistry, University of California, Berkeley, California
(Received July 23, 1954)

SEVERAL new isotopes of curium, berkelium, and californium have been produced by charged-particle bombardments of pile-produced transplutonium isotopes, and their nuclear properties studied. The chemical procedures and counting methods used were essentially the same as those used in prior work of this nature at Berkeley.[1,2]

The existence of Cm^{245} was first proved by mass spectrographic analysis[3] of samples of curium subjected to long neutron irradiations in the Chalk River reactor. However, the electron capture decay of Bk^{245}, produced by helium ion bombardment of Cm^{242}, results in the formation of pure but small samples of Cm^{245}. This nuclide was found to decay by emitting alpha particles of 5.36 ± 0.05 Mev as measured by alpha-particle pulse-height analysis.[4] The energy measured probably does not represent the transition to the ground state of Am^{241}, but higher-energy alpha-particle groups were undetected in the samples of such low counting rates. The best approximation for the half-life of Cm^{245} is 20 000 years. This value is based on the counting of K and L x-rays arising from orbital electron capture by Bk^{245}, the use of approximate Auger conversion factors,[5,6] and the measurement of the alpha disintegration rate of the daughter. Elution of the material emitting 5.36-Mev alpha particles in the curium position (with Cm^{242}) from a cation exchange column with buffered ammonium citrate eluant proved that this new alpha-particle emitter is an isotope of curium.

A previously unknown isotope of californium, Cf^{248}, was made by helium ion bombardment of curium containing a small percentage of Cm^{245}.[3] This isotope decays by emission of 6.26 ± 0.03 Mev alpha particles with a half-life of 250 ± 20 days. Decay of the alpha radioactivity of the above energy was followed through two half-lives. A spontaneous fission half-life of about 7000 years was also measured, but this value is rather uncertain because of the extremely slow spontaneous fission rate of the sample. Observation of the growth of the 5.80-Mev alpha particles of Cm^{244} in the above sample proved the mass assignment of the Cf^{248}.

The bombardment of various mixtures of Am^{241} and Am^{243} with 27-Mev helium ions is believed to have produced a 1.8-day electron-capture isotope of berkelium which is tentatively assigned to Bk^{246}. The 1.8-day period was observed in the berkelium fraction from three different bombardments. A different chemical separation procedure was used in each case. This intermediate period was resolved from the 4.5-hour Bk^{243} (and Bk^{244}) and the 4.95-day Bk^{245} periods after following the decay in a windowless proportional counter. An 820 ± 10-kev gamma ray decaying with a 1.7-day half-life was observed in the berkelium fraction by means of a sodium iodide crystal scintillation counter connected to a 50-channel pulse-height analyzer.[7] It appeared that between 20 and 50 percent of the Bk^{246} electron-capture disintegrations passed through this 820-kev excited state of Cm^{246}, based on the total disintegration rate from the estimated counting yield of the windowless proportional counter and the best value[8,9] for the photoelectric yield from the sodium iodide crystal. K x-rays resulting from the berkelium decay were followed for decay with the sodium iodide scintillation counter and the L x-rays with a small xenon-filled proportional counter (90 percent xenon and 10 percent methane, at 1 atmos. connected to the 50-channel pulse-height analyzer. The approximate Bk^{246} decay period could be resolved from the 4.95-day component in both the K and L x-ray decay curves. A total disintegration energy of approximately 1.4 Mev is estimated from energy balances within closed decay cycles[10] to be available for orbital electron capture by Bk^{246}. The half-life thought to be associated with Bk^{246} seems reasonable for either a highly forbidden ground-state transition or if a large percentage of the disintegrations are forced to pass through a high-energy level of Cm^{246}.

Helium ion bombardment of curium containing a high percentage of Cm^{244} followed by a fast chemical separation of the californium fraction resulted in the detection of an orbital electron capture isotope of californium, Cf^{247}. This isotope was also observed in the products from nitrogen ion bombardments of U^{238} metal foils.[11] Decay of the K x-rays of this nuclide (followed in the presence of interfering Cf^{246} alpha radioactivity) with the aforementioned sodium iodide crystal scintillation spectrometer gave a half-life of 2.5 hours. A rough 3-hour half-life was obtained by resolving the decay curve of the L x-rays associated with the orbital electron capture of Cf^{247} and the alpha decay of Cf^{246}. The measured energies of the L x-rays ($L_\alpha=15.1$, $L_\beta=19.7$, and $L_\gamma=24.1$ kev) agree well with those expected from berkelium. No radioactivity could be detected from the daughter of Cf^{247}, namely Bk^{247}.

We would like to acknowledge the use of the pile facilities and the aid of the personnel of Atomic Energy of Canada Limited, Chalk River, Ontario, Canada, in the irradiation of americium and curium samples. We also wish to express our appreciation to Professor J. G. Hamilton, G. B. Rossi, W. B. Jones, and the operating crew of the 60-inch cyclotron for their special help in

the bombardment of americium and curium samples, and to Nelson B. Garden and the Health Chemistry Group for providing the protective equipment used for the handling of the radioactivity involved. It is a pleasure to acknowledge the valuable assistance by Dr. R. W. Hoff and Mr. A. Chetham-Strode, Jr., in some of the experiments. It is a privilege to acknowledge that this work was accomplished with the helpful guidance of Professor Glenn T. Seaborg.

† This work was performed under the auspices of the U. S. Atomic Energy Commission.

[1] Thompson, Ghiorso, and Seaborg, Phys. Rev. **80**, 781 (1950).
[2] Thompson, Street, Ghiorso, and Seaborg, Phys. Rev. **80**, 790 (1950).
[3] Mass spectrographic analysis by F. L. Reynolds.
[4] Ghiorso, Jaffey, Robinson, and Weissbourd, *The Transuranium Elements: Research Papers* (McGraw-Hill Book Company, Inc., New York, 1949), Paper No. 16.7. National Nuclear Energy Series, Plutonium Project Record, Vol. 14B, Div. IV.
[5] L. S. Germain, Phys. Rev. **78**, 90 (1950).
[6] B. B. Kinsey, Can. J. Research **A404** (1948).
[7] A. Ghiorso and A. E. Larsh, University of California Radiation Laboratory Unclassified Report UCRL-1959, September 25, 1952 (unpublished).
[8] P. W. Maguire and G. D O'Kelley, California Research and Development Corporation Report MTA-40, 1953 (unpublished).
[9] R. W. Hoff, Ph.D. thesis, University of California Radiation Laboratory Unclassified Report UCRL-2325, September, 1953 (unpublished).
[10] Seaborg, Glass, and Thompson (to be published).
[11] Ghiorso, Rossi, Harvey, and Thompson, Phys. Rev. **93**, 257 (1954).

Disintegration of Bismuth by 2.2-Bev Protons*

NATHAN SUGARMAN, † ROBERT B. DUFFIELD, ‡
G. FRIEDLANDER, AND J. M. MILLER §
Chemistry Department, Brookhaven National Laboratory, Upton, Long Island, New York

(Received July 23, 1954)

THE irradiation of bismuth with 2.2-Bev protons from the Brookhaven Cosmotron produces a large number of radioactive species. We report here on the cross sections for the formation of some of them.

Foils of bismuth metal were exposed in the circulating proton beam of the Cosmotron. During most of the irradiations, the beam intensity was approximately 10^{10} protons per pulse and the repetition rate was 1 pulse per 5 seconds. The number of protons striking the target was determined from the Na^{24} activity produced in a 0.003-inch aluminum monitor foil adjacent to the bismuth target. The cross section for the production of Na^{24} is approximately 9 millibarns at 2.2 Bev.[1]

Table I lists the products for which cross sections have been determined. After isolation from the target, the radioactivity of each species was measured by a calibrated proportional counter or a NaI scintillation counter. The alpha activity was measured directly in thin target foils.

The variation of cross section with mass number is strikingly different from that observed in the hundred-Mev range. Though only a few products have been measured at 2.2 Bev, there appears to be a monotonic decrease of cross section with decreasing Z of the product.[2] This is in contrast to the results obtained in the irradiation of bismuth with 190-Mev deuterons[3] or 340–450 Mev protons.[4] At the lower energies, there is a hump in the cross section curve centered at mass 95–100 with a total cross section of about 200 millibarns. This group of products, attributed to fission, is well separated from the spallation products. The present experiments at the higher energy indicate that, first, spallation with the emission of a large number of nucleons has become more probable, while, second, the division of the target nucleus into two fragments of approximately equal mass has become less probable, so that it is no longer possible to see in the yield *vs* mass curve a sharp division between the two processes. For example, the cross section for the production of Sr^{89} at 2.2 Bev is about 1/5 of that found with 190-Mev deuterons or ~400-Mev protons, while that for the production of mass number 149 is at least 100 times as large at 2.2 Bev as at 190 Mev. The absence, at 2.2 Bev, of a trough in the yield curve between spallation and fission regions has already been reported in preliminary work on reactions with lead.[5] Here a gross rare earth fraction (approximately representing mass numbers 130 to 180) was found to contain about 70 percent of the total x and γ activity of an irradiated lead target, while in a 380-Mev proton bombardment the corresponding fraction was of the order of one percent. The cross section for the formation of Ce^{141} from lead is about 100 times larger at 2.2-Bev than at 380-Mev proton energy.

A few very preliminary experiments have been done to determine the recoil momenta of the radioactive products. It has been found that the ranges in aluminum (mg/cm²) at 0° to the proton beam of some products are as follows: $Br^{80,82}$, ~3.2; $Sr^{91,92}$, ~3.3; $Ba^{128,129}$, ~1.5; Tb^{149}, ~1. From a thick bismuth target, approximately 5 times as many Tb^{149} recoils were found on a catcher foil in the forward direction as compared to the backward direction to the proton beam. The corresponding ratio in thick targets for $Ba^{128,129}$ was 3.8, and for $Sr^{91,92}$, 1.2. This would appear to mean that the cen-

TABLE I. Formation cross sections from 2.2-Bev protons in bismuth. All values are based on a cross section of 9 mb for the reaction $Al^{27}(p,3pn)Na^{24}$.

Product observed	σ(mb)	Product observed	σ(mb)
Pb^{203}	26	Ba^{129}	1.9
Tl^{202}	3	Ba^{128}	4.3
Tl^{201}	20	Sr^{91}	0.48
Tl^{200}	12	Sr^{89}	1.4
Tl^{199}	27	Br^{82}	0.22
Tl^{198}	15	Br^{80m}	0.67
Tb^{149}	0.95[a]	Ge^{75}	0.53
$Dy^{149-153}$ (19 min)	0.62[a]	Ge^{69}	0.65
$Dy^{149-153}$ (7 min)	1.77[a]	Ge^{66}	0.17
Ba^{131}	5.5		

[a] These nuclei were detected by their alpha activity. The cross sections are for the alpha branch only; the decay branching ratio is not accurately known. For this reason and also because these particular isotopes are highly neutron-deficient, the cross sections given represent only lower limits for the formation cross sections for these mass numbers.

ter-of-mass motion accounts for a large part of the range of the Ba and Tb recoils in the forward direction, but does not exclude the possibility that lighter products, such as Sr and Br, result largely from a fission reaction in which only a small portion of the kinetic energy of the incident proton is used for nuclear disintegration.

Finally, a detailed analysis of the results on the barium, strontium, and bromine nuclides at 2.2 Bev shows that the high-yield primary products are more neutron-deficient than those observed in the previously cited work[3,4] at lower energies. The $Tl^{200,201}$ activities in the present experiments, as at lower energy,[6] result primarily from the decay of lead and bismuth predecessors rather than from independent production. This probably accounts for the relatively low yield of Tl^{202}, a shielded nuclide.

We are grateful to many members of the staff of the Brookhaven National Laboratory for cooperation on these experiments, in particular, Dr. G. B. Collins and the operating staff of the Cosmotron.

* Research carried out under the auspices of the U. S. Atomic Energy Commission.

† Permanent address: Institute for Nuclear Studies, University of Chicago, Chicago, Illinois.

‡ Permanent address: Physics Department, University of Illinois, Urbana, Illinois.

§ Permanent address: Chemistry Department, Columbia University, New York, New York.

[1] A. Turkevich, Phys. Rev. **94**, 775 (1954).

[2] There are indications, especially from the x-ray spectra of the gross electron-capture activities, that the maximum yields occur several atomic numbers below Bi.

[3] R. H. Goeckermann and I. Perlman, Phys. Rev. **76**, 628 (1949).

[4] W. F. Biller (unpublished); P. Kruger, Ph.D. thesis, University of Chicago, March, 1954 (unpublished).

[5] J. M. Miller and G. Friedlander, Phys. Rev. **91**, 485 (1953).

[6] W. E. Bennett, Phys. Rev. **94**, 997 (1954).

Errata

New Absorption Lines of Crystals in Submicrowave Region, S. KOJIMA, K. TSUKADA, S. OGAWA, AND A. SHIMAUCHI [Phys. Rev. **92**, 1571 (1953)]. "Rock salt," which appeared three times in the printed text, should read "rock crystal (quartz)."

Reaction Concept in Electromagnetic Theory, V. H. RUMSEY [Phys. Rev. **94**, 1483 (1954)]. Equation (50) of this paper needs some further explanation. The reaction in anisotropic media was given in the form

$$\langle a,b\rangle=\int\int\int[\mathfrak{E}(b)\cdot d\mathbf{J}(a)-\mathfrak{K}(b)\cdot d\mathbf{K}(a)]. \quad \text{(E-1)}$$

Now the reciprocal relation for this class of fields is

$$\int\int\int[\mathfrak{E}(b)\cdot d\mathbf{J}(a)-\mathfrak{K}(b)\cdot d\mathbf{K}(a)]$$
$$=\int\int\int[\mathbf{E}(a)\cdot d\mathbf{J}(b)-\mathbf{H}(a)\cdot d\mathbf{K}(b)], \quad \text{(E-2)}$$

and $\langle a,b\rangle$ is not equal to $\langle b,a\rangle$ in general. However, the methods described in the paper for isotropic media can be carried over to anisotropic media without difficulty. To retain the same notation as for the isotropic case, it seems better to define $\langle a,b\rangle$ by the formula

$$\langle a,b\rangle=\int\int\int[\mathbf{E}(b)\cdot d\mathbf{J}(a)-\mathbf{H}(b)\cdot d\mathbf{K}(a)] \quad \text{(E-3)}$$

instead of (E-1), and use the notation

$$\langle a,b\rangle'=\int\int\int[\mathfrak{E}(b)\cdot d\mathbf{J}(a)-\mathfrak{K}(b)\cdot d\mathbf{K}(a)] \quad \text{(E-4)}$$

to denote the expression in (E-1). Thus

$$\langle a,b\rangle'=\langle b,a\rangle. \quad \text{(E-5)}$$

The quantity $\langle a,b\rangle$ can still be interpreted as the result of making an observation of the field generated by source b by using a as a test source, and thus the apparatus of the reaction theory still applies. The quantity $\langle a,b\rangle'$ represents the same thing, except that the environment in which the field generated by b exists is obtained from that to which $\langle a,b\rangle$ refers by transposing the tensors $\mu\epsilon$ and σ.

Elastic Scattering of 190-Mev Deuterons by Protons, OWEN CHAMBERLAIN AND MARTIN O. STERN [Phys. Rev. **94**, 666 (1954)]. In this paper, we presented experimental results on the elastic scattering of 190-Mev deuterons by protons, and attempted to compare these results with predictions based on the impulse approximation. Various potentials were used to represent the nucleon-nucleon interaction.

It has been called to our attention that an earlier publication of Daitch and French[1] also considered the relationship between nucleon-nucleon and nucleon-deuteron scattering. In particular, their relations (7) are equivalent to our Eq. (13) and Table V. These relations concern the energies and angles of nucleon-nucleon scattering to be used in calculating the deuteron-proton scattering.

We regret that, due to an oversight, reference to the work of these authors was not made.

[1] P. B. Daitch and J. B. French, Phys. Rev. **85**, 695 (1952).

Influence of the Earth's Magnetic Field on the Extensive Air Showers, GIUSEPPE COCCONI [Phys. Rev. **93**, 646 (1954)]. In the discussion of the importance of the displacement D_m of the electrons in an extensive air shower caused by the earth's magnetic field, two mistakes were made which have been pointed out to the author by Professor K. Greisen. (a) The fact that an electron of a certain sign can have had parents of different sign before reaching the detecting apparatus decreases D_m by

a factor of about 2. Using the same notation as in the original paper, it follows that $D_m/\mathfrak{D}_s=0.22\times(\cos\lambda)/P$ instead of $0.45(\cos\lambda)/P$. The old expression remains valid for other particles, e.g., mu mesons. (b) In evaluating the rms lateral displacement in the E−W direction, D_m must be added quadratically to $\mathfrak{D}_s$, and not linearly as was implicitly done in the discussion.

This reduces the ratio of the E−W to the N−S lateral displacement, for the electrons, to

$$\left[1+\left(\frac{0.22\cos\lambda}{P}\right)^2\right]^{\frac{1}{2}}\simeq 1+\frac{0.02\cos^2\lambda}{P^2}.$$

At sea level, the effect is practically negligible (~2 percent). It remains important, however, at high altitudes.

Quantum Theory of a Damped Electrical Oscillator and Noise. II. The Radiation Resistance, J. WEBER [Phys. Rev. **94**, 211 (1954)]. The following typographical errors appear on pages 212 and 213. In Eq. (6), the exponent 2 following the last bracket should be just inside the last bracket, making the last matrix element squared. In Eq. (9), the last matrix element, $\langle E_F|q_F/\sqrt{L}|E_F+\hbar\omega\rangle$, should be squared. In Eq. (13) on the right, the π^2 in the denominator should be π. In reference 2, page 213, the word "of" should be inserted after the word "propagation." On page 212, above Eq. (8), the statement "$\rho(E_{FR}+\hbar\omega)=\rho(E_{FR}-\hbar\omega)=\omega^2/2\pi^2\hbar c^3$ should be labeled Eq. (7).

Phase Shifts for High-Energy Nucleon-Nucleon Scattering, BURTON D. FRIED [Phys. Rev. **95**, 851 (1954)]. The line above Eq. (3) should read: "(b) the triplet D phase shifts are all equal." The letter D was inadvertently omitted.

Hyperfine Structure and Nuclear Moments of the Stable Bromine Isotopes, JOHN GORDON KING AND VINCENT JACCARINO [Phys. Rev. **94**, 1610 (1954)]. In Table I, the frequency $(1,0\leftrightarrow 0,0)^{81}$ appears incorrectly as 1275.271 instead of 1275.291. The quadrupole interaction constants, b, are listed with improper sign and superscript on page 1615. They are given correctly in the abstract.

THE PHYSICAL REVIEW

A journal of experimental and theoretical physics established by E. L. Nichols in 1893

VOLUME 95

Second Series

JULY 1–SEPTEMBER 15, 1954

Published for the

AMERICAN PHYSICAL SOCIETY

by the

AMERICAN INSTITUTE OF PHYSICS

Incorporated

THE PHYSICAL REVIEW

A journal of experimental and theoretical physics established by E. L. Nichols in 1893

Published by the American Institute of Physics for the

AMERICAN PHYSICAL SOCIETY

Officers

President

H. A. BETHE
Cornell University
Ithaca, New York

Vice-President

R. T. BIRGE
University of California,
Berkeley, California

Secretary

K. K. DARROW
Bell Telephone Laboratories
Office:
Columbia University
New York 27, New York

Treasurer

G. B. PEGRAM
Columbia University
New York 27, New York

Local Secretary for the Pacific Coast

J. KAPLAN
University of California at Los Angeles
Los Angeles, California

Managing Editor

S. A. GOUDSMIT
Brookhaven National Laboratory
Upton, Long Island
New York

BOARD OF EDITORS

Editor

S. A. GOUDSMIT

Assistant Editor

S. PASTERNACK

Associate Editors

1952–1954	*1953–1955*	*1954–1956*
W. P. ALLIS	W. A. FOWLER	P. G. BERGMANN
F. G. BRICKWEDDE	KENNETH GREISEN	GREGORY BREIT
W. B. FRETTER	CHARLES KITTEL	F. J. DYSON
CONYERS HERRING	R. E. MARSHAK	P. KUSCH
H. W. LEVERENZ	W. K. H. PANOFSKY	R. SMOLUCHOWSKI
ARNOLD NORDSIECK	V. F. WEISSKOPF	J. C. STREET

Manuscripts for publication should be submitted to S. A. GOUDSMIT, Brookhaven National Laboratory, Upton, Long Island, New York. The authors' institutions are requested to pay a publication charge of $15 per page which, if honored, entitles them to 100 free reprints. Instructions will be sent with galley proofs.

Proof and all correspondence concerning papers in the process of publication should be addressed to the Publication Manager, American Institute of Physics, 57 East 55 Street, New York 22, New York.

Subscription Price

United States and Canada $30.00
Elsewhere $32.00

Back Numbers[1]

Yearly back number rate when complete year is available:
Prior to 1949: **$25.00**
Thereafter: **$33.00**
Single copies: **$3.00** each, prior to July, 1929;
$1.50 each, July, 1929–December, 1941;
$3.00 each, January, 1942–December, 1946;
$1.50 each, thereafter.
General index, 1893–1920: **$4.00.**
1921–1950: Paper binding, **$10** (Members); **$14** (Nonmembers)
Cloth binding, **$12** (Members); **$16** (Nonmembers)

Subscriptions, renewals, and orders for back numbers should be addressed to the American Institute of Physics, 57 East 55 Street, New York 22, New York.

Changes of address in the case of members of the American Physical Society should be addressed to the Treasurer; in the case of other subscribers to the American Institute of Physics.

[1] For Series 1 inquire of Physics Department, Cornell University, Ithaca, New York.

The Physical Review is published semi-monthly at Prince and Lemon Streets, Lancaster, Pennsylvania.

Entered as second-class matter March 6, 1947, at the Post Office at Lancaster, Pennsylvania, under the Act of March 3, 1879.

Acceptance for mailing at special rate of postage provided for in paragraph (d-2), section 34.40, P. L. & R. of 1948, authorized January 27, 1933.

Author Index to Volume 95

References with (A) are to abstracts of papers presented at meetings of the American Physical Society; references with (T) designate title only. References with (L) are to Letters to the Editor. References with (E) are to Errata.

Aarons, M. W., M. Pobereskin, J. E. Gates, and E. B. Dale. Distribution of mass transported from collector into Ge crystal by forming process—1345(L)

Abeles, B. and S. Meiboom. Theory of galvanomagnetic effects in Ge—31

Abrahams, Elihu. Electron-electron scattering in alkali metals—839(L)

Abrahams, I. C. Color television (with demonstrations)—309(T)

Acton, Forman S. (see Herman, Frank)—371

Ajzenberg, Fay and Wolfgang Franzen. Neutrons from proton bombardment of B^{10}—1531

——, W. Franzen, and J. G. Likely. Neutrons from proton bombardment of B^{10}—641(A)

Akers, Lawrence K. and Ernest A. Jones. Vibrational spectra of pentafluorides of Sb, As, and Br—300(A)

Albert, R. D., M. L. Yeater, and E. R. Gaerttner. Neutron capture measurements with G. E. betatron velocity selector—644(A)

Albrecht, H. O. (see Mandeville, C. E.)—598(A)

Alburger, D. E. Experimental and theoretical studies of levels in Pb^{206}—632(T)

—— and M. H. L. Pryce. Energy levels in Pb^{206} from decay of Bi^{206}—1482

Alei, E. Felix (see Fermi, E.)—1581

Alei, E. P. (see de Hoffmann, F.)—1586

Alexander, B. H. (see Levitas, A.)—846(L)

Alford, W. Parker and Donald R. Hamilton. Recoil spectrum in β decay of Ne^{19}—1351(L)

Allen, Lew, Jr., and A. O. Hanson. Photodistintegration of deuterium by 95-Mev bremsstrahlung—629(A)

Allen, Robert C. Sphere measurements of neutron inelastic collision cross sections—637(A)

Allison, B. A. (see Scherrer, V. E.)—637(A)

—— (see Shapiro, P.)—751

Altshuler, Edward E. (see Sampson, John L.)—298(A); 617(A)

Altshuler, Saul and J. F. Carlson. Time-dependent variational principle—546

Ambler, E. and R. P. Hudson. Measurements on chromium potassium alum below 1°K—1143

——, R. P. Hudson, and G. M. Temmer. Anisotropic γ radiation from aligned Ce^{141} nuclei—625(A)

Anderson, C. D. (see van Lint, V. A. J.)—295(L)

Anderson, W. S. (see Sakai, M.)—101

Andrews, David H. Automatic electrostatic field plotter—633(A)

Ard, W. B. (see Fairbank, William M.)—566(L)

Arnowitt, Richard and S. Gasiorowicz. Approximate equations for meson-nucleon systems—618(A)

—— and S. Gasiorowicz. Covariant approximation scheme for Green's functions of coupled fields—538

Arons, Arnold. Amherst program: Experience with calculus-physics course required of all students—297(T)

Aschenbrenner, F. A. Particle selection technique used at M.I.T. cyclotron—600(A)

Ashkin, J. (see Blaser, J.)—624(A)

Aström, Björn (see Atterling, Hugo)—585(L)

Atkinson, W. R., R. G. Fowler, and W. R. Holden. Magneto-hydrodynamic flows in H and He—634(A)

Atterling, Hugo, Wilhelm Forsling, Lennart W. Holm, Lars Melander, and Björn Aström. Element 100 produced by means of cyclotron-accelerated oxygen ions—585(L)

Austern, N. and S. T. Butler. Coulomb effects in deuteron stripping—605(A)

Austin, Pauline M. Quantitative measurements of radar echoes from precipitation—297(A)

Autler, S. H. and W. F. Roat. Light decay from electroluminescent phosphors—599(A)

Axel, P. and J. D. Fox. Implications of photonuclear effect in Zr^{90}—613(A)

Babiskin, J. and M. C. Steele. Magnetic dependence of thermoelectric power of Bi at low temperatures—602(A)

Baer, W. Migration areas of Po-Be neutrons in H_2O-Zr mixtures—660(A)

Bair, Joe K. (see Willard, Harvey B.)—1359(L)

Baker, C. P. (see Draper, J. E.)—644(A)

Baker, E. (see Hudis, J.)—612(A)

Baker, N. and O. Bergmann. Decay scheme of τ meson—174

Balazs, N. L. General properties of solutions in Dirac's new electrodynamics—305(A)

—— Resolution of four-dimensional vector fields and tensor fields—305(A)

Baldwin, G. C., F. R. Elder, and W. F. Westendorp. Betatron orbit stability as function of n—600(A)

Balestrini, Silvio J. Mass-spectrometric study of deuteron-induced reactions in iodine—1502

Bandel, H. W. Measurement of current during formative time lag of sparks in uniform fields in air—1117

Bandtel, Kenneth C., Wilson J. Frank, Richard Madey, and Burton J. Moyer. Comparison of reactions $H^3(H^1, \pi^+)H^3$ and $H^3(H^1,\pi^0)He^3$ as test of charge independence—639(A)

Banta, H. E. (see Macklin, R. L.)—302(A)

Bardeen, J. (see Hall, L. H.)—559(L)

Baril, Alnert, Jr. Photolysis of para-diazo-N, N-dimethylaniline ZnCl dihydrate—306(A)

Barnett, C. F., P. M. Stier, and G. E. Evans. Relative secondary electron emission for ions and atoms—307(A)

—— (see Stier, P. M.)—303(A)

Barrett, C. S. (see Cohen, M. H.)—1094(L)

Barrett, P., G. Cocconi, Y. Eisenberg, and K. Greisen. Atmospheric temperature effect for mesons far underground—1573

——, G. Cocconi, Y. Eisenberg, and K. Greisen. Diurnal variations of intensity of cosmic rays far underground—1571

Bartholomew, G. A., F. Brown, H. E. Gove, A. E. Litherland, and E. B. Paul. Resonances in proton bombardment of C^{14}—649(A)

—— (see Gove, H. E.)—650(A)

Bartnoff, Shepard. Drop size distribution and visibility in clouds and rain—615(A)

—— (see Fish, Joseph K.)—297(A)

Barton, M. Q. and J. H. Smith. Proton-neutron coincidences in high-energy photodistintegration of Li—573(L)

—— (see Yamagata, T.)—574(L)

Bashkin, Stanley. $Li^7(d,p)Li^8$ yield curve—640(A); 1012

Baumann, N. P., F. W. Prosser, Jr., and R. W. Krone. γ-ray resonances in proton bombardment of Na^{23}—650(A)

Bazorgan, G. A., J. W. Irvine, Jr., and C. D. Coryell. Preparation and half-life of Cr^{52}—781

Beams, J. W. and J. B. Breazeale. Methods of spinning rotors at low temperatures—601(A)

Beard, C. I. (see Massey, J. T.)—622(A)

Beard, George and M. L. Wiedenbeck. Natural radioactivity of Sm^{147}—1246
Becker, R. A. (see Brown, H. N.)—626(A)
Bedo, D. E. and D. H. Tomboulian. *L*-absorption spectrum of Si and SiO_2—621(A)
Beeman, W. W. and R. H. Neynaber. Equipment for measurement of very small x-ray scattering cross sections —617(A)
Beer, A. C. (see Harman, T. C.)—596(A); 699
—— (see Willardson, R. K.)—597(A)
Béique, R. (see Lorrain, Paul)—599(A)
Belinfante, F. J. and J. C. Swihart. Quantized linear theory of gravitation. I—630(A)
—— (see Swihart, J. C.)—630(A)
Beljers, H. G., L. van der Kint, and J. S. van Wieringen. Overhauser effect in free radical—1683(L)
Bell, P. R. Recent advances in scintillation spectrometry—299(T)
—— (see Lazar, N. H.)—612(A)
Bell, R. E. Measurement of (p,xn) cross sections in Bi—651(A)
Belmont, E. and J. M. Miller. Reactions of 370-Mev protons with Co—1554
Belser, Richard B. and Margaret C. Chester. Structures and resistivities of sputtered films of Pt metals before and after aging by heating—307(A)
—— (see Brown, John L.)—308(A)
—— (see Chester, Margaret C.)—307(A)
Bender, R. S. (see Levine, S. H.)—640(A)
Bennett, A. Measurements of distribution of velocities in K molecular beams—608(A)
Bennett, W. E. (see Sugihara, T. T.)—298(A)
Bennett, W. H. and E. O. Hulburt. Theory of aurora based on magnetic self-focusing of solar ion streams—315
Bent, R. D., R. W. Bonner, and R. F. Sippel. Energy levels in C^{14} and N^{14}—649(A)
Bergmann, O. (see Baker, N.)—174
—— (see Green, H. S.)—516
Bergmann, Peter G. Quantum theory of gravitation—631(A)
Bergström, I. (see Passell, T. O.)—999
Beringer, R. and Mark A. Heald. Electron spin magnetic moment in atomic hydrogen—1474
Berkowitz, A. E., F. E. Jaumot, Jr., and F. C. Nix. Diffusion of Co^{60} in Ni-Al alloys containing excess vacancies —1185
Berlincourt, Ted G. and M. C. Steele. De Haas-van Alphen effect in Zn at liquid O_2 temperatures—603(A)
—— **and M. C. Steele.** Temperature-dependent de Haas-van Alphen parameters in Zn—1421
Berman, A. S. (see Lassettre, E. N.)—635(A)
Berman, R. and C. A. Swenson. Absolute temperature scale between 4.2° and 5.2°K—311
Bernardini, G. and E. L. Goldwasser. Photopion *S* wave near threshold and pion-nucleon coupling constant—857(L)
Bernstein, E. M. and H. W. Lewis. *L*-shell ionization by protons of 1.5- to 4.25-Mev energy—83
Bernstein, J. and A. Klein. Exchange current effects in deuteron—655(A)
Bernstein, S. (see Roberts, L. D.)—105
—— (see Stanford, C. P.)—302(A)
Bernstein, W., J. Weiss, and J. B. H. Kuper. Oxidation yield of ferrous sulfate dosimeter by x-rays—609(A)
Bersohn, R. Double bond character of C—Cl bond—614(A)
Bethe, H. A. and F. de Hoffmann. Meson-proton scattering phase shift analysis—1100(L)
—— (see de Hoffman, F.)—1586
—— (see Dyson, F. J.)—1644
—— (see Nelkin, M. S.)—618(A)
Bhatia, A. B. Minimum in electrical resistance of metals at low temperatures—914
Bhattacherjee, S. K., B. Waldman, and W. C. Miller. Energy determination of Cs^{137} *K* conversion electrons—404
Biedenharn, L. C., R. L. Gluckstern, and M. H. Hull, Jr. Coulomb wave functions for large values of parameter *n* —656(A)
Bird, George R. Saturation in microwave spectrum of methyl chloride—1686(L)
Birkhoff, R. D. (see Blackstock, A. W.)—303(A)
—— (see Hungerford, E. T.)—6
Birks, J. B. Temperature dependence of organic scintillation materials—277(L)
Birman, Joseph. Calculation of electrostatic lattice potentials, including ionic overlap—618(A)
Birnbaum, G. and A. A. Maryott. Microwave absorption in compressed gases—622(A)
Birnbaum, W., W. E. Crandall, G. P. Millburn, and R. V. Pyle. Excitation function for $C^{12}(d;\ p,2n)C^{11}$, $C^{12}(He^3;\ 2p,2n)C^{11}$, and $C^{12}(\alpha;\ 2p,3n)C^{11}$—649(A)
—— (see Crandall, W. E.)—620(A)
—— (see Millburn, G. P.)—620(A); 1268
Bitter, Francis (see Waymouth, John F.)—941
Bjørnerud, E. K. (see York, Carl M., Jr.)—159
Blackstock, A. W., R. D. Birkhoff, and M. Slater. Discrete electron energy losses in thin foils—303(A)
Blair, J. M. (see Holmgren, H. D.)—1544
Blair, J. S. Theory of elastic scattering of α particles by heavy nuclei—605(A); 1218
Blakewood, C. H. (see Dyba, R. V.)—1365
Blaser, J., J. Ashkin, F. Feiner, J. Gorman, and M. O. Stern. Total cross sections for scattering of positive pions by hydrogen—624(A)
Blatt, F. J. Properties of thin metallic films—13
—— (see Hall, L. H.)—559(L)
Blevins, Gilbert (see Jache, Albert)—299(A)
Bloch, Ingram (see Hsieh, Yu-Chang)—305(A)
Block, M. M. and D. T. King. Contributions of bremsstrahlung conversion in trident experiments—171
—— **and D. T. King.** Pairs formed by bremsstrahlung of great energy. II. Theoretical separation distribution—648(A)
—— (see King, D. T.)—648(A)
Bloembergen, N. and R. V. Pound. Radiation damping in magnetic resonance experiments—8
Bludman, Sidney A. Classical radiation from moving charges—654(A)
—— **and P. B. Daitch.** Validity of Born-Oppenheimer approximation—823
Blume, M. (see Treiman, S. B.)—646(A)
Boag, J. and B. Zendle. Scattered radiation contribution to depth dose data for 35- and 90-Mev synchrotron x-rays —608(A)
Boehm, F., P. Marmier, and J. W. M. DuMond. γ transitions in W^{185}—864(L)
Bok, Bart J. Radio studies of clouds in Milky Way—297(T)
Bollinger, L. M., R. R. Palmer, and D. A. Dahlberg. Total neutron cross sections of Bi and Mn—645(A)
—— (see Dahlberg, D. A.)—645(A)
Bolsterli, M. and E. Feenberg. Superallowed transitions in $4n$-type nuclides—612(A)
Bonner, R. W. (see Bent, R. D.)—649(A)
Bonner, T. W. (see Cook, C. F.)—639(A)
Borowitz, Sidney. Perturbation calculation of elastic exchange scattering of electrons by H atoms—656(A)
Bortner, T. E. and G. S. Hurst. Ionization of pure gases and mixtures of gases by 5-Mev α particles—609(A)
—— **and G. S. Hurst.** w value in electron volts for 5-Mev α particles in gases and gas mixtures—303(A)

Box, Harold C. and G. Stanley Klaiber. γ-ray spectrum of Ac^{228}—1247
Boyd, G. E. Tc activities at mass 97—113
Bozorth, R. M. (see McSkimin, H. J.)—616(A)
Braams, C. M. (d,p) reactions of Ca^{42} and Ca^{44}—650(A)
Braden, C. H., E. T. Patronis, Jr., and L. D. Wyly. Decay of Hg^{195}—627(A)
——, **L. D. Wyly, and E. T. Patronis, Jr.** Activities produced in Au by proton bombardment—758
Bradner, Hugh and Robert Donaldson. Asymmetry in neutron production by bombardment targets with 285-Mev polarized protons—1701(L)
—— **and R. E. Donaldson.** Search for polarization in charge exchange scattering—663(A)
Brattain, W. H. (see Garrett, C. G. B.)—1091(L)
Bray, P. J. Method for detection of pure quadrupole resonances—606(A)
Breazeale, J. B. (see Beams, J. W.)—601(A)
Brentano, J. C. M. and J. D. Richards. Evaporated multiple layers with semiconductor properties—841(L)
Breton, A. (see Lorrain, Paul)—599(A)
Bridge, H. S., H. Courant, B. Dayton, H. C. DeStaebler, Jr., B. Rossi, and D. Willard. Recent results on S particles—662(A)
——, **H. Courant, H. DeStaebler, Jr., and B. Rossi.** Possible example of annihilation of heavy particle—1101(L)
—— (see DeStaebler, H. C., Jr.)—662(A)
Brisbout, Françoise A. (see Parsons, R. W.)—193
Brody, Selma B. Aging of crushed Si and Ge powders—298(A)
Broida, H. P. and J. R. Pellam. Phosphorescence of atoms and molecules of solid N_2 at 4.2°K—845(L)
Brolley, J. E., Jr., W. C. Dickinson, and R. L. Henkel. Angular distribution of U^{235} fragments from neutron-induced fission as function of incident neutron energy—651(A)
Brown, Fielding and Charles L. Gravel. Domain rotation in sintered Ni ferrite—652(A)
—— (see Bartholomew, G. A.)—649(A)
Brown, H. A. and J. M. Luttinger. Calculation of ferromagnetic and antiferromagnetic Curie temperatures—652(A)
Brown, H. N., F. B. Smith, and R. A. Becker. Radiations from Ho^{164}—626(A)
Brown, John L. and Richard B. Belser. Electron microscope and diffraction traversing technique for examination of bimetal films—308(A)
Brown, L. Carlton and Dudley Williams. Magnetic resonance spectra of beryl crystals—1110(L)
Brown, Sanborn C. (see Champion, K. S. W.)—634(A)
—— (see Gould, Lawrence)—897
—— (see Reder, Fritz H.)—885
Browne, Cornelius P. Energy levels of Al^{26}—860(L)
—— (see Buechner, W. W.)—609(A)
Broyles, A. A. W.K.B. approximation through turning point—656(A)
Brueckner, K., C. Levinson, and H. Mahmoud. Two-body forces and nuclear saturation. I. Method—655(A)
—— (see Levinson, C.)—655(A)
Brysk, Henry (see Goldman, David T.)—305(A)
Buechner, W. W., C. P. Browne, H. Enge, M. Mazari, and C. D. Buntschuh. Magnetic spectrograph for nuclear disintegration studies—609(A)
Bunker, M. E., J. W. Starner, and J. P. Mize. Disintegration of Ga^{70}—612(A)
—— (see Mize, J. P.)—627(A)
Buntschuh, C. D. (see Buechner, W. W.)—609(A)
Burford, A. O., J. F. Perkins, and S. K. Haynes. Intensities of radiations from Hf^{175}—303(A)
Burgess, James H. Magnetic resonance enhancement in multilevel system—608(A)
Burgus, Warren H., George A. Cowan, J. W. Hadley, Wilmot Hess, Theodore Shull, M. L. Stevenson, and H. F. York. Cross sections for reactions $Ti^{48}(d,2n)V^{48}$; $Cr^{52}(d,2n)Mn^{52}$; and $Fe^{57}(d,2n)Co^{58}$—750
Burgwald, G. M. (see Reiffel, L.)—1294
Burkhardt, J. L. and E. J. Winhold. $In^{115}(\gamma,\gamma')In^{115m}$ cross section—629(A)
Burrus, Charles A., Albert Jache, and Walter Gordy. Mm wave spectrum of phosphine—299(A)
——, **Albert Jache, and Walter Gordy.** 1–2 mm wave spectroscopy. V. PH_3 and PD_3—706
Burson, S. B., W. C. Jordan, and J. M. LeBlanc. Isomeric states in $_{32}Ge^{73}$ and $_{32}Ge^{77}$—613(A)
—— (see LeBlanc, J. M.)—627(A)
Burwell, J. R. (see Kim, Y. B.)—661(A)
—— (see Thompson, R. W.)—661(A); 1576
Butler, S. T. (see Austern, N.)—605(A)

Callaway, Joseph. Approximate correlation potential—656(A)
—— (see Herman, Frank)—371
Camac, M. (see McGuire, A. D.)—625(A)
Cameron, A. G. W. (see Katz, L.)—464
Campbell, E. C. (see Stelson, P. H.)—301(A)
Campbell, J. G. Resonance absorption of γ radiation by O^{16} nuclei—1357(L)
Cap, Ferdinand. Nonlinear meson theory of nuclear forces—287(L)
Cap, C. (see Rohrer, R. H.)—302(A)
Caren, R. P. and C. E. Nielsen. Vapor expansion chamber using ammonia and water. II—601(A)
Cargill, W. H. (see Rohrer, R. H.)—308(A)
Carlson, B. C. (see Talmi, I.)—606(A)
Carlson, J. F. (see Altshuler, Saul)—546
Carlson, R. R. and E. B. Nelson. Capture γ rays from 315-kev proton bombardment of Be^9—641(A)
—— (see Nelson, E. B.)—650(A)
Carroll, Thomas J. Air-guided propagation of short radio waves around earth bulge—623(A)
Carter, R. S. and J. A. Harvey. Parameters of neutron resonances in Cs, In, Sn, and Pr—645(A)
—— (see Pilcher, V. E.)—645(A)
Carver, T. R. (see Schumacher, R. T.)—1089(L)
Case, K. M. Some generalizations of Foldy-Wouthuysen transformation—1323
Castle, J. G., Jr. Paramagnetic resonance absorption in soft carbon—846(L)
Chamberlain, Owen, Robert Donaldson, Emilio Segrè, Robert Tripp, Clyde Wiegand, and Thomas Ypsilantis. Experiments on nucleon-nucleon scattering with 312-Mev polarized protons—850(L)
—— **and John D. Garrison.** p-p scattering experiments at 170 and 260 Mev—1349(L)
——, **G. Pettengill, E. Segrè, and C. Wiegand.** Small-angle p-p cross sections and polarization at 300 Mev—1348(L)
——, **Emilio Segrè, Robert Tripp, Clyde Wiegand, and Thomas Ypsilantis.** Mechanism of proton polarization in high-energy collisions—1105(L)
——, **Emilio Segrè, Robert Tripp, Clyde Wiegand, and Thomas Ypsilantis.** Polarization of high-energy deuterons—1104(L)
—— **and Martin O. Stern.** Elastic scattering of 190-Mev deuterons by protons—1705(E)
Champion, K. S. W. and S. C. Brown. Phenomena of plasma resonance—634(A)

Chang, W. Y. Sea level mesons stopped in thin Pb and Al foils. I. Possible emission of charged nuclear particles and related events—1282; II. Low-energy (1–5 Mev) γ-rays —1288
Chase, C. E. and Melvin A. Herlin. Ultrasonic measurements in magnetically cooled He—565(L)
Chase, D. M. Equations of motion of charged test particles in general relativity—243
Chaudhury, N. K. (see Ganguly, S. C.)—1148
Chen, F. F. (see Shapiro, A. M.)—663(A)
Chester, Margaret C. (see Belser, Richard B.)—307(A)
—— **and Richard B. Belser.** Solder-shear tests to metal films deposited on glass substrates by evaporation and sputtering—308(A)
—— (see Belser, Richard B.)—307(A)
Chester, P. F. and J. S. Dugdale. Melting curves of deuterium and hydrogen—278(L)
Cheston, W. B. Compton scattering—247
Chew, Geoffrey F. Comparison of cut-off meson theory with experiment—1669
—— Improved calculation of p-wave pion-nucleon scattering phase shifts in cut-off theory—285(L)
Chinowsky, W. and J. Steinberger. Absorption of negative pions in deuterium: Parity of pion—1561
—— **and Jack Steinberger.** Parity of pion—623(A)
—— (see Steinberger, Jack)—623(A)
Choppin, G. R. (see Harvey, B. G.)—581(L)
Christian, Schuyler M. (see Johnson, Everett R.)—560(L)
Church, E. L. and M. Goldhaber. Low-energy transitions in Gd and related rare-earth activities—626(A)
Clark, Arnold F. (see Kao, S. K.)—662(A)
—— (see Mann, Leonard A.)—648(A)
Clarke, Edward N. Oxygen and surface energy-level structure on Ge—284(L)
Class, C. M. (see Eisinger, J.)—628(A)
—— (see Hanna, S. S.)—110
Cleland, J. W. and J. H. Crawford, Jr. Neutron irradiation of InSb—1177
Clement, J. R. Effect of temperature scales on low-temperature calorimetric data—601(A)
—— (see Overton, W. C., Jr.)—602(A)
Clifford, Joseph M. and R. B. Sawyer. Analysis of Forbes bar method for measuring thermal conductivity of metals —665(A)
Cocconi, Giuseppe. Influence of earth's magnetic field on extensive air showers—1705(E)
—— (see Barrett, P.)—1571, 1573
Cochran, Lewis W. (see Stone, W. G.)—304(A)
Codrington, R. S., J. D. Olds, and H. C. Torrey. Paramagnetic resonance in organic free radicals at low fields —607(A)
Coester, F. Hyperquantization of Feynman amplitudes—631(A); 1318
Cohen, B. L., D. J. Coombe, and B. L. Ferrell. Recent progress in fission fragment angular distribution measurements—303(A)
——, **G. H. McCormick, T. H. Handley, and E. Newman.** $(p,2n)$, $(p,2p)$, (p,t), (p,He^3) and (p,f) cross sections and excitation functions—639(A)
—— (see Handley, T. H.)—611(A)
Cohen, David, Burton J. Moyer, Harlan Shaw, and Charles Waddell. Proton bremsstrahlung and high-energy γ emission from C—664(A)
Cohen, M. H. Decomposition of scalar product of 2 symmetric tensors—674
—— **and C. S. Barrett.** Interaction of electrons with grain boundaries—1094(L)
Cohen, Marshall H. Electromagnetic scattering by dielectric bodies—657(A)
Cohen, V. W. and D. A. Gilbert. Nuclear spin and hfs interaction of 3.1-hr Cs^{134} isomer—569(L)
Cohn, H. O. (see Kim, Y. B.)—661(A)
—— (see Thompson, R. W.)—661(A)
Colli, L. Uv photons in decay of metastable A atoms—892
Collier, Robert J. Direct l-doublet transition of HCN in 10-cm wavelength region—1201
Collins, T. L., T. T. Scolman, and A. O. Nier. Precision double-focusing mass spectrometer—615(A)
Collinson, J. A. and W. W. Watson. Spectroscopic isotope shift in Hf I and Hf II—621(A)
Cook, C. F., T. W. Bonner, and J. B. Marion. Neutron thresholds from (d,n) and (p,n) reactions—639(A)
—— (see Eisinger, J.)—628(A)
Coombe, D. J. (see Cohen, B. L.)—303(A)
Cooper, Daniel I. (see Zimmerman, Robert L.)—662(A)
Cooper, John N. (see Green, D. W.)—610(A)
—— (see Russell, Leonard N.)—99
Cooper, Leon N. and James Rainwater. Theory of multiple Coulomb scattering from extended nuclei—1107(L)
Corenzwit, E. (see Matthias, B. T.)—1435
Cork, J. M. (see LeBlanc, J. M.)—627(A)
Cormack, A. M. Heat generation in earth by solar neutrinos —580(L)
Coryell, Charles D. (see Bazorgan, G. A.)—781
—— (see Richter, Harold G.)—1550
—— (see Sugihara, T. T.)—298(A)
Courant, H. (see Bridge, H. S.)—662(A); 1101(L)
—— (see DeStaebler, H. C., Jr.)—662(A)
Cowan, D. A. (see Winnemore, B. J.)—301(A)
Cowan, George A. (see Burgus, Warren H.)—750
Cox, John, W. J. Orville Thomas, and Walter Gordy. Centrifugal distortion in methyl halides—299(A)
Cox, S. A. (see Goldburg, W. I.)—628(A)
Crandall, W. E., W. Birnbaum, L. Schecter, and G. P. Millburn. Nuclear radii and transparencies from inelastic cross-section measurements. II. Interpretation—620(A)
—— (see Birnbaum, W.)—649(A)
—— (see Millburn, G. P.)—620(A); 1268
—— (see Schecter, L.)—659(A)
Crane, W. W. T. and G. M. Iddings. New isotope protactinium-237—1702(L)
Crawford, F. S., Jr., and M. L. Stevenson. Reaction $p+p\rightarrow\pi^{+}+d$ with polarized protons—1112(L)
Crawford, J. H., Jr. (see Cleland, J. W.)—1177
Croft, G. T., W. F. Love, and F. C. Nix. De Haas-van Alphen effect in Sn and Sn-Sb alloys—1403
Cronemeyer, Donald C. Recombination center density measurements in Ge—309(T)
Cross, W. G. and T. A. Eastwood. γ radiation from the decay of UX_2 (Pa^{234})—628(A)
Crussard, J., M. F. Kaplon, J. Klarmann, and J. H. Noon. Heavy unstable particles in stripped emulsions—584(L)
——, **W. D. Walker, and M. Koshiba.** π^{-} interactions at 1.5 Bev. II—624(A)
—— (see Kaplon, M. F.)—660(A)
—— (see Noon, J. H.)—1103(L)
—— (see Walker, W. D.)—624(A); 852(L)
Culler, Vaughn and R. W. Waniek. Total cross sections for high-energy neutrons—585(L)
—— (see Hillman, Peter)—462
—— (see Waniek, R. W.)—659(A)
Cummerow, Robert L. Photovoltaic effect in p-n junctions —16
—— Use of Si p-n junctions for converting solar energy to electrical energy—561(L)
Cunnell, F. A. and E. E. Schneider. Ionic conductivity and x-ray coloration of alkali halides—598(A)
Cure, J. W. and G. S. Hurst. Neutron scattering—302(A)

Curtis, C. D. (see Winnemore, B. J.)—301(A)
Cutkosky, R. E. Internal bremsstrahlung—1222
—— Solutions of Bethe-Salpeter equation—653(A)

Dabbs, J. W. T. and L. D. Roberts. Method for brute force polarization of H nuclei—307(A)
—— **and L. D. Roberts.** Polarization of Mn^{55} nuclei; cryogenic aspects—970
—— (see Roberts, L. D.)—105; 307(A)
Daggett, E. H. and G. R. Grove. γ-ray spectrum of Po^{209}—627(A)
Dahlberg, D. A. and L. M. Bollinger. Analyses of neutron resonances in Zn isotopes—645(A)
—— (see Bollinger, L. M.)—645(A)
Daitch, P. B. (see Bludman, S.)—823
Dale, E. B. (see Aarons, M. W.)—1345(L)
Dalitz, R. H. Sachs exchange moment—799
Damon, P. E. and R. R. Edwards. Absolute intensities of γ rays and x-rays of RaD—1698(L)
Davies, R. W. Energy spectrum of turbulence for entire range—912
Davis, Charles F., Jr., and M. W. P. Strandberg. Paramagnetic resonance absorption in ammonium chrome alum—607(A)
Davis, L., Jr., G. A. deMars, L. G. Rubin, and W. D. Straub. Some electrical properties of several Si-Ge alloys—597(A)
Dawson, J. M. and Z. I. Slawsky. Effect of intermolecular forces on rapid expansion of gas from initial condition of very high density and temperature—614(A)
Day, E. A. (see Johnston, L. H.)—599(A)
Day, Robert B. and Torben Huus. γ radiation from B^{10} bombarded by protons—1003
Dayton, B. (see Bridge, H. S.)—662(A)
Dayton, Irving E. Elastic scattering of 18-Mev protons by Al, Fe, Ni, and Cu—754
DeBenedetti, S. (see Stearns, M. B.)—625(A); 1353(L)
de Boisblanc, D. R. and K. A. McCollom. MTR time-of-flight instrumentation—609(A)
Deeds, W. E. Vibrational analysis of polypeptide chains—300(A)
de Hoffmann, F., N. Metropolis, E. P. Alei, and H. A. Bethe. Pion-hydrogen phase shift analysis between 120 and 217 Mev—1586
—— (see Bethe, H. A.)—1100(L)
DeLuca, Lloyd B. Self-diffusion coefficient of nitrogen—306(A)
deMars, G. A. (see Davis, L., Jr.)—597(A)
Dempsey, E. and D. ter Haar. Statistics of face-centered cubic ferromagnet—651(A)
De Pangher, J. n-p scattering at 300 Mev—578(L)
der Mateosian, E. Applications of "internal source" scintillation spectrometer—646(A)
—— **and C. S. Wu.** β spectrum of I^{130} and its decay scheme—458
—— (see Muehlhause, C. O.)—598(A)
DeStaebler, Herbert, Jr. Nuclear absorption of negative K particles—1110(L)
——, **H. S. Bridge, H. Courant, and B. Rossi.** Unusual cosmic-ray event—662(A)
—— (see Bridge, H. S.)—662(A); 1101(L)
Dettman, J. W. and A. Schild. Conservation theorems in modified electrodynamics—631(A); 1057
Deverall, G. V., K. W. Meissner, and G. J. Zissis. Precision wavelength and isotopic shift measurements of Ge arc lines—1463
Devlin, G. E. (see Schawlow, A. L.)—1344(L)
DeWire, J. W. (see Edwards, D. A.)—629(A)
Dexter, R. N., H. J. Zeiger, and Benjamin Lax. Anisotropy of cyclotron resonance of holes in Ge—557(L)
——, **H. J. Zeiger, Benjamin Lax, and E. S. Rosenblum.** Anisotropy of cyclotron resonance in Ge. Part II. Experiment—597(A)
—— (see Lax, Benjamin)—597(A)
Diamond, R. M. New isotopes of Nb: Nb^{89} and Nb^{90m}—410
Dizk, J. L. (see Sakai, M.)—101
Dickinson, W. C. (see Brolley, J. E., Jr.)—651(A)
Dillinger, J. R. (see Knudsen, W. C.)—279(L)
Dillon, J. A., Jr. (see Sheridan, W. F.)—635(A)
Dolan, W. W. and W. P. Dyke. Temperature-and-field emission of electrons from metals—327
Domenicali, C. A. and F. A. Otter. Thermoelectric power and electron scattering in metal alloys—1134
Donaghy, Charles F. and Clark Goodman. Determination of thickness of Li targets from position of geometric peak—298(A)
Donahoe, F. J. and F. C. Nix. Temperature and field dependence of de Haas-van Alphen effect—1395
Donaldson, Robert E. (see Bradner, H.)—663(A); 1701(L)
—— (see Chamberlain, Owen)—850(L)
Dondes, S. (see Harteck, P.)—320
Dorain, Paul B. (see Thacher, H. C., Jr.)—615(A)
Dorfman, Leon M. Absorption of tritium β particles in hydrogen and other gases—393
Drachman, R. J. and D. C. Peaslee. Isotopic spin factors in nuclear reactions—605(A)
Draper, J. E. and C. P. Baker. Self-indication measurement of σ_{1s} for 5.2-ev neutron resonance in Ag—644(A)
Dratz, A. F. (see Rohrer, R. H.)—308(A)
Dresden, M. Estimate of lifetime of positrons in superconductors—603(A)
Dresselhaus, G., A. F. Kip, and C. Kittel. Spin-orbit interaction and effective masses of holes in Ge—568(L)
Drisko, R. M. Angular dependence of annihilation quanta from magnetic substates of triplet positronium—611(A)
Dropkin, J. J. and S. Orgel. Ac photoconductivity in phosphors—597(A)
Drougard, M. E. and D. R. Young. Dielectric constant behavior of single-domain single crystals of $BaTiO_3$ in vicinity of Curie point—1152
Dudziak, Walter F. Charged pion production from C by protons—866(L)
—— (see Sagane, Ryokichi)—863(L)
Duffield, Robert B. (see Huizenga, J. R.)—1009
—— (see Sugarman, Nathan)—1704(L)
Dugdale, J. S. (see Chester, P. F.)—278(L)
DuMond, Jesse W. M. (see Boehm, F.)—864(L)
—— (see Snelgrove, Philip)—1203
Dunlap, W. C., Jr. (see Leifer, H. N.)—51
Dyba, R. V., C. T. Lane, and C. H. Blakewood. Film flow and bulk formation of He II in capillaries—1365
Dyke, W. P. (see Dolan, W. W.)—327
Dyson, F. J., M. Ross, E. E. Salpeter, S. S. Schweber, M. K. Sundaresan, W. M. Visscher, and H. A. Bethe. Meson-nucleon scattering in Tamm-Dancoff approximation—1644

Eastwood, T. A. (see Cross, W. G.)—628(A)
Edwards, D. A., B. Wolfe, A. Silverman, and J. W. DeWire. Angular distributions of photodeuterons—629(A)
Edwards, R. R. (see Damon, P. E.)—1698(L)
Efremov, N. Role of principal quantum number (n) in calculation of radii of ions with low (1^+,2^+,3^+,4^+) valence—614(A)
Eggler, C. and C. M. Huddleston. Gaseous scintillation counter—600(A)
Eisberg, R. M., H. Palevsky, M. E. Rickey, and T. I. Taylor. Total cross section of O_2 for cold neutrons—659(A)

—— (see Palevsky, H.)—659(A)
Eisenberg, Y. Interaction of heavy primaries in Pb—647(A)
—— (see Barrett, P.)—1571; 1573
Eisinger, J., C. F. Cook, and C. M. Class. Electric excitation of Au—628(A)
Elbek, B., K. O. Nielsen, and O. B. Nielsen. Determination of maximum β energy in decay of P^{32}—96
Elder, F. R. (see Baldwin, G. C.)—600(A)
El-Hussaini, Jassim (see Snelgrove, Philip)—1203
Ellis, R. A., Jr., M. B. Gottlieb, and J. A. Van Allen. Low-momentum end of spectrum of heavy primary cosmic rays—304(A)
Elsasser, Walter M. Dimensional relations in magnetohydrodynamics—1
Enatsu, Hiroshi, Hiroichi Hasegawa, and Pong Yul Pac. Theory of unstable heavy particles—263
Endt, P. M., J. C. Kluyver, and C. van der Leun. γ rays from $Si^{30}(p,\gamma)P^{31}$—580(L)
Enge, H. (see Buechner, W. W.)—609(A)
Engel, Olive G. Some aspects of dynamics of waterdrop collisions with solids—615(A)
Engler, A. and U. Haber-Schaim. Primary cosmic-ray spectrum deduced from analysis of jets—1700(L)
Ennis, Malcolm E. and Arthur Hemmendinger. Small-angle cross sections for scattering of protons by tritons —772
Enright, Dorothy P. (see Talley, Robert M.)—1092(L)
Eriksen, Erik (see Foldy, Leslie L.)—1048
Evans, G. E. (see Barnett, C. F.)—307(A)
—— (see Stier, P. M.)—303(A)

Fafarman, A. and M. H. Shamos. Cosmic-ray μ-meson low-energy differential range spectrum—648(A)
Fairbank, Henry A. and J. Wilks. Thermal conductivity of liquid He below 1.0°K—277(L)
Fairbank, William M., W. B. Ard, and G. K. Walters. Fermi-Dirac degeneracy in liquid He^3 below 1°K—566(L)
Falkoff, D. L. Random pulses and electron-spin line widths in metals—607(A)
Fan, H. Y., W. Kaiser, E. E. Klontz, K. Lark-Horowitz, and R. R. Pepper. Energy levels and photoconductivity in electron-bombarded Ge—1087(L)
Fang, P. H. Variance properties of general field operator —631(A)
Fano, U. Ionizing collisions of very fast particles and dipole strength of optical transitions—1198
Farney, G. K. (see Givin, H. H.)—302(A); 641(A)
Farwell, George W. and Harvey E. Wegner. Elastic scattering of intermediate-energy α particles by heavy nuclei —664(A); 1212
Faust, W. R. (see Scherrer, V. E.)—637(A)
—— (see Shapiro, P.)—751
Feenberg, E. (see Bolsterli, M.)—612(A)
Feeny, Harold (see Trambarulo, Ralph)—622(A)
Feher, G. and A. F. Kip. Electron spin resonance in Be —1343(L)
Feiner, F. (see Blaser, J.)—624(A)
Feingold, A. M. (see Lyons, D. H.)—606(A)
Feldman, G. Antiproton production—1697(L)
Ferguson, G. A., J. Halpern, R. Nathans, and P. F. Yergin. Photoneutron cross sections in He, N, O, F, Ne, and A—659(A); 776
Fermi, E., N. Metropolis, and E. Felix Alei. Phase shift analysis of scattering of negative pions by hydrogen— 1581
Ferrell, B. L. (see Cohen, B. L.)—303(A)
Fields, P. R. (see Friedman, A. M.)—1501
Fields, T. H., J. G. Fox, J. A. Kane, R. A. Stallwood, and R. B. Sutton. π^+ production in H by 437-Mev protons—638(A)
—— (see Kane, J. A.)—662(A); 1694(L)
Fine, S. (see Hendee, C. F.)—281(L)
Finkelstein, R. J. and S. A. Moszkowski. Mesonic corrections to β-decay coupling constants—1695(L)
Finlay-Freundlich, E. Red-shifts in spectra of celestial bodies—654(A)
Firor, J. W., J. A. Simpson, and S. B. Treiman. Production of cosmic radiation at sun—1015
Fischer, David and Gerson Goldhaber. Small angle p-p scattering at 330 Mev—1350(L)
Fischer, G. E. Scattering of 10-Mev protons on Mg and C —664(A)
Fischer, Vera Kistiakowsky. Disintegration of Pm^{150}— 626(A)
Fish, Joseph K. and Shepard Bartnoff. Study of drop-size frequency distribution in clouds and rain—297(A)
Fisher, L. H. Buildup processes in sparks and positive corona—620(T)
Fitch, V. (see Koslov, S.)—291(L); 625(A)
Fitzpatrick, P. M. (see Howard, R. A.)—661(A)
Fleming, J. R. (see Hourd, R. F.)—647(A)
Fletcher, R. C., W. A. Yager, G. L. Pearson, and F. R. Merritt. Hyperfine splitting in spin resonance of Group V donors in Si—844(L)
Fletcher, William H. and W. E. Shuler. Infrared spectrum of allene-d_2—300(A)
Flood, W. F., Jr. (see Hrostowski, H. J.)—1683(L)
Fluharty, R. G. MTR fast chopper—609(A)
Foldy, Leslie L. and Erik Eriksen. Physical consequences of vacuum polarization—1048
Foley, H. M. (see Sucher, J.)—966
Foner, Simon. Measuring magnetic properties of ferromagnetic materials by means of Hall effect—652(A)
Ford, Kenneth W. Nuclear deformation and moment of inertia of nuclear rotational states—1250
Forsling, Wilhelm (see Atterling, Hugo)—585(L)
Fowler, Charles A., Jr., and Edward M. Fryer. Magnetic domains in CO by longitudinal Kerr effect—564(L); 652(A)
Fowler, J. L. (see Johnson, C. H.)—637(A)
Fowler, R. G. (see Atkinson, W. R.)—634(A)
Fowler, W. B., R. P. Shutt, A. M. Thorndike, and W. L. Whittemore. Meson production in n-p collisions at Cosmotron energies—1026
Fox, J. D. (see Axel, P.)—613(A)
Fox, J. G. (see Fields, T. H.)—638(A)
—— (see Kane, J. A.)—662(A); 1694
Frank, Wilson J. (see Bandtel, Kenneth C.)—639(A)
Frankel, Sherman (see Golden, Robert K.)—613(A)
Franzen, Wolfgang (see Ajzenberg, F.)—641(A); 1531
Fraser, J. S. (see Milton, J. C. D.)—628(A)
Frenkiel, F. N. Theory of turbulent diffusion—658(T)
Fried, Burton D. Phase shifts for high-energy nucleon-nucleon scattering—851(L); 1706(E)
Friedlander, G. (see Hudis, J.)—612(A)
—— (see Sugarman, Nathan)—1704(L)
Friedman, A. M., A. L. Harkness, P. R. Fields, M. H. Studier, and J. R. Huizenga. α half-lives of Cm^{244}, Cm^{245}, and Cm^{246}—1501
Friedman, A. S. (see Haar, Lester)—614(A)
Frisch, David H. 2-body forces and nuclear stability— 865(L)
—— (see Pugh, G. E.)—590(L); 611(A)
—— (see Storrs, C. L.)—1252
—— (see Zimmerman, Robert L.)—662(A)
Frisch, Harry L. and Joel L. Lebowitz. Simplified model of stationary nonequilibrium process—643(A)
Fryer, Edward M. (see Fowler, Charles A., Jr.)—564(L); 652(A)
Fuchs, L. (see Primak, W.)—22

Fujino, Takuzo (see Ishiguro, Masakazu)—1347(L)
Fuller, E. G. (see Hayward, Evans)—1106(L)
Fulton, Thomas and Paul C. Martin. Two-body system in quantum electrodynamics. Energy levels of positronium—811
Fung, Si-Chang and Anthony Turkevich. Radiochemical evidence for the $Cu^{65}(p,p\pi^+)Ni^{65}$ reaction—176
Furlong, L. R. Low-temperature luminescence of CdS—1086(L)
Furuichi, Jiro (see Mitsui, Toshio)—558(L)
Fuson, Nelson, Marie-Louise Josien, and Essie M. Shelton. Infrared spectroscopic study of influence of molecular structure upon ν(NH), ν(CO), and $\nu(CH_3)$ in benzopyrroles and their analogs—300(A)

Gaerttner, E. R. (see Albert, R. D.)—644(A)
Gaffney, John and W. C. Overton, Jr. Temperature variations of elastic constants of Cu single crystals from 4.2°K to 300°K—602(A)
Ganguly, S. C. and N. K. Chaudhury. Anisotropy of fluorescence of some organic crystals—1148
Garber, M. and D. E. Mapother. Effect of pressure on superconducting transition of Sn—603(A)
Garlick, G. F. J. (see Halperin, A.)—1098(L)
Garrett, C. and G. N. Whyte. Build-up measurements on Co^{60} γ radiation in Fe and Pb—889
Garrett, C. G. B. and W. H. Brattain. Self-powered semiconductor amplifier—1091(L)
Garrison, John D. (see Chamberlain, Owen)—1349(L)
Gasiorowicz, S. (see Arnowitt, Richard)—538; 618(A)
Gates, J. E. (see Aarons, M. W.)—1345(L)
Geballe, T. H. and F. J. Morin. Ionization energies of groups III and V elements in Ge—1085(L)
—— (see Matthias, B. T.)—1435
Geer, E. H. (see Nelson, E. B.)—650(A)
Geiger, K. W. and D. C. Rose. Neutron multiplicity from spontaneous fission of U—646(A)
Geller, K., J. Halpern, and Paul F. Yergin. Photoneutron angular distribution—659(A)
Geller, S. (see Matthias, B. T.)—1435
Gell-Mann, M., M. L. Goldberger, and W. E. Thirring. Use of causality conditions in quantum theory—1612
—— **and F. E. Low.** Quantum electrodynamics at small distances—1300
—— (see Goldberger, M. L.)—654(A)
Gerardo, H. (see Toms, M. E.)—629(A)
Gerhart, J. B. O^{14} decay and Fermi coupling constant in β decay—288(L)
Ghiorso, A., S. G. Thompson, G. H. Higgins, B. G. Harvey, and G. T. Seaborg. Evidence for subshell at $N = 152$—293(L)
—— (see Harvey, B. G.)—581(L)
—— (see Hulet, E. K.)—1703(L)
Ghosh, S. N. (see Sheridan, W. F.)—635(A)
Gibbons, J. H. and H. W. Newson. Total neutron cross sections in kev region: Tl^{208} and Tl^{206}—644(A)
—— (see Newson, H. W.)—640(A)
—— (see Rohrer, R. H.)—302(A)
Gibson, G. and P. Stehle. Interference effects in annihilation process—657(A)
Gilbert, D. A. (see Cohen, V. W.)—569(L)
Gilmore, P. (see Lorrain, Paul)—599(A)
Gilvarry, J. J. Relativistic Thomas-Fermi atom model—71
Gindler, J. E. (see Huizenga, J. R.)—1009
Girard, P. E. (see Lorrain, Paul)—599(A)
Givin, H. H., G. K. Farney, T. M. Hahn, and B. D. Kern. Angular distribution of 12-Mev and 16-Mev γ rays from proton bombardment of boron—641(A)
——, **G. K. Farney, B. D. Kern, and T. M. Hahn.** Angular distribution of 12-Mev γ rays from reaction $B^{11}(p,\gamma)C^{12}$—302(A)
Glasser, R. G. (see Schein, Marcel)—855(L)
Glauber, R. J. and P. C. Martin. Radiative capture of orbital electrons—572(L)
—— (see Zemach, A. C.)—605(A)
Glendenin, L. E. (see Steinberg, E. P.)—431; 867(L)
Glicksman, Maurice. Scattering of 187-Mev negative pions by hydrogen—1045
Gluckstern, R. L. (see Biedenharn, L. C.)—656(A)
Gold, R. (see Koerts, L.)—612(A)
Goldberger, M. L., M. Gell-Mann, and W. E. Thirring. General conditions on scattering matrix—654(A)
—— (see Gell-Mann, M.)—1612
Goldburg, W. I., S. A. Cox, and R. M. Williamson. Coulomb excitation of Au—628(A)
—— **and R. M. Williamson.** Coulomb excitation of Ta, W, and Au—767
Goldemberg, J. and L. Katz. Fine structure in neutron yield curves from (γ,n) reactions in Li^7, C^{13}, O^{16}, and F^{19}—471
—— (see Spicer, B. M.)—629(A)
Golden, Robert K. and Sherman Frankel. K-conversion electron—γ angular correlation in Sn^{117}—613(A)
Goldhaber, Gerson (see Fischer, David)—1350(L)
Goldhaber, M. (see Church, E. L.)—626(A)
—— (see Sunyar, A. W.)—570(L)
Goldman, David T. and Henry Brysk. Spatial distribution of energy dissipation by bremsstrahlung spectrum—305(A)
Goldman, J. E. (see Urquhart, H. M. A.)—653(A)
Goldschmidt-Clermont, Y. (see Osborne, L. S.)—637(A)
Goldstein, J. H. (see Slayton, George R.)—299(A)
Goldstein, Louis. Theory of liquid He^3–He^4 mixtures—869
Goldwasser, E. L., L. J. Koester, Jr., and F. E. Mills. Elastic photoproduction of π^0 mesons from He—1692(L)
—— (see Bernardini, G.)—857(L)
Gomez, R. (see Pugh, G. E.)—590(L); 611(A)
Good, W. M. (see Kunz, W. E.)—640(A)
—— (see Moak, C. D.)—641(A)
Goodenough, John B. Theory of domain creation and coercive force in polycrystalline ferromagnetics—917
—— (see Loeb, A. L.)—616(A)
Goodman, Clark (see Donaghy, Charles F.)—298(A)
—— (see Guernsey, Janet B.)—297(A); 636(A)
—— (see Kiehn, Robert M.)—636(A); 989
—— (see Mark, Hans)—628(A)
Goodman, L. S. and S. Wexler. Nuclear spin and moment of 3.1-hr Cs^{134m}—570(L)
Gordon, Carroll K. Electrical conductivity of S—306(A)
Gordon, J. P., H. J. Zeiger, and C. H. Townes. Molecular microwave oscillator and new hfs in microwave spectrum of NH_3—282(L)
Gordy, Walter (see Burrus, Charles A.)—299(A); 706
—— (see Cox, John)—299(A)
—— (see Jache, Albert)—299(A)
Gorman, J. (see Blaser, J.)—624(A)
Gottlieb, M. B. (see Ellis, R. A., Jr.)—304(A)
Gould, Lawrence and Sanborn C. Brown. Microwave determination of probability of collision of electrons in He—897
Gourary, B. S. and R. W. Hart. Spherical model of antiferromagnet—652(A); 676
Gove, H. E., E. B. Paul, A. E. Litherland, and G. A. Bartholomew. Some spin assignments and partial width measurements of resonances in S^{33} from reaction $P^{31}(p,\gamma)S^{32}$—650(A)
—— (see Bartholomew, G. A.)—649(A)
Grandey, Ray A. (see Mann, Leonard A.)—648(A)

Gravel, Charles L. (see Brown, Fielding)—652(A)
Graves, Ernest D. and H. C. Thomas. Proportional counter for Auger electrons—304(A)
Green, Alex E. S. Coulomb radius constant from nuclear masses—1006
Green, C. D. and D. Ter Haar. Statistical aspects of second law of thermodynamics—643(A)
Green, D. W., J. N. Cooper, and J. C. Harris. Stopping powers of metals for low-energy protons—610(A)
Green, F. L. and J. A. Martin. High-intensity beam of low-energy protons in ORNL 86-inch cyclotron—304(A)
Green, H. S. Integral equations of quantized field theory—548
—— **and O. Bergmann.** Core structure in soft component showers—516
Greenberg, J. Mayo. High-energy electron scattering—619(A)
Greenberg, L. H., J. G. V. Taylor, and R. N. H. Haslam. Yield of α particles from photonuclear reactions at 23-Mev bremsstrahlung—1540
Greenblatt, M. H. Time delay in secondary emission—633(A)
Greisen, K. (see Barrett, P.)—1571; 1573
Griffith, Gordon L. De-excitation γ rays from inelastic scattering of neutrons—636(A)
Grove, G. R. (see Daggett, E. H.)—627(A)
Guernsey, Janet B. and Clark Goodman. Low-lying states in nuclei from $(n,n'\gamma)$ interactions—297(A)
—— **and Clark Goodman.** Neutron inelastic scattering in Ta and I—636(A)
Gupta, Suraj N. Electromagnetic interaction of particles of spin $\frac{1}{2}$—630(A)
—— Fierz-Pauli theory of particles of spin 3/2—1334
Gursky, H. (see Winnemore, B. J.)—301(A)
Guss, Donald, Lawrence Killion, and F. T. Porter. β spectra of Re^{186} and Re^{188}—627(A)
Gutowsky, H. S. Structural determinations by nuclear magnetism—596(T)

Haar, Lester and A. S. Friedman. General method for high-speed machine computation of ideal gas thermal properties. Diatomic free radicals of isotopic hydrides—614(A)
Haber-Schaim, U. (see Engler, A.)—1700(L)
Hadley, J. W. (see Burgus, Warren H.)—750
Hafner, Everett Mark. Refinement of uniform model—604(A)
—— (see Roberts, A.)—663(A); 1099(L)
Hahn, B. (see Hofstadter, R.)—512
Hahn, T. M. (see Givin, H. H.)—302(A); 641(A)
—— (see Lafferty, D. L.)—637(A)
—— (see Rayburn, L. A.)—301(A); 637(A)
Halbert, M. L. (see McGuire, A. D.)—625(A)
Hall, Harold H. Analysis of proton-proton scattering at 9.7 Mev—424
Hall, L. H., J. Bardeen, and F. J. Blatt. Infrared absorption spectrum of Ge—559(L)
Hall, T., M. Siegel, L. M. Sharpe, and D. Pressman. Production of I^{124} by deuteron bombardment of Te—1208
Halperin, A. and G. F. J. Garlick. Low-temperature bleaching and restoration of color centers—1098(L)
Halpern, I. (see Sugihara, T. T.)—630(A)
Halpern, J., R. Nathans, and P. F. Yergin. $A^{40}(\gamma,n)$ threshold and mass of A^{39}—1529
—— (see Ferguson, G. A.)—659(A); 776
—— (see Geller, K.)—659(A)
—— (see Weinstock, E. V.)—630(A)
Hamermesh, Bernard (see Recksiedler, Arthur)—650(A)
Hamilton, Donald R. (see Alford, W. Parker)—1351(L)
Hamlin, D. (see Merritt, J.)—638(A)
Handley, T. H. and B. L. Cohen. New isotope identification program on Oak Ridge 86-inch cyclotron—611(A)
—— (see Cohen, B. L.)—639(A)
Hanna, S. S., E. C. LaVier, and C. M. Class. β-α correlation in decay of Li^8—110
—— (see Shafroth, S. M.)—86; 641(A)
Hanson, A. O. (see Allen, Lew, Jr.)—629(A)
—— (see Yamagata, T.)—574(L)
Hanson, H. P. and J. R. Knight. K-absorption edge studies of compounds—621(A)
Hanson, W. B. and J. R. Pellam. Second sound attenuation in liquid He II—321; 604(A)
Hardy, W. A. and G. Silvey. Microwave spectrum of TeCS and masses of stable Te isotopes—385
Harkness, A. L. (see Friedman, A. M.)—1501
Harman, T. C., R. K. Willardson, and A. C. Beer. Analysis of magnetoresistance and Hall coefficient in p-type InSb and p-type Ge—699
——, **R. K. Willardson, and A. C. Beer.** Comparison of Hall and magnetoresistance phenomena in InSb with those in Ge—596(A)
—— (see Willardson, R. K.)—597(A)
Harris, D. R. and A. L. Hodson. Production of V^0 particles in Cu—661(A)
Harris, J. (see Green, D. W.)—610(A)
Hart, Edward W. Electronic energy of ordered alloys—666(A)
Hart, Robert W. (see Gourary, Barry S.)—652(A); 676
Harteck, P. and S. Dondes. Origin of N_2O in atmosphere—320
Hartman, P. L. (see Tomboulian, D. H.)—600(A)
Hartzler, A. J. and R. T. Siegel. 400-Mev n-p scattering—185
——, **R. T. Siegel, and W. Opitz.** Small-angle n-p scattering at 400 Mev—591(L)
Harvey, B. G., H. P. Robinson, S. G. Thompson, A. Ghiorso, and G. R. Choppin. Some pile neutron cross sections of isotopes of americium, berkelium, californium, and element 99—581(L)
—— (see Ghiorso, A.)—293(L)
Harvey, J. A., C. E. Porter, and D. J. Hughes. Variation of $\bar{\Gamma}_n^0/\bar{D}$ ratio with atomic weight—645(A)
—— (see Carter, R. S.)—645(A)
Hasegawa, Hirochi (see Enatsu, Hiroshi)—263
Haskin, D. M. (see Schein, Marcel)—855(L)
Haslam, R. N. H. (see Greenberg, L. H.)—1540
—— (see Katz, L.)—464
Hayden, R. J. (see Steinberg, E. P.)—867(L)
Haynes, Sherwood K. (see Burford, A. O.)—303(A)
—— (see Meneely, George R.)—308(A)
Hayward, Evans and E. G. Fuller. Nuclear elastic scattering of photons—1106(L)
Heald, Mark A. (see Beringer, R.)—1474
Hebb, Elizabeth (see Mitchell, Allan C. G.)—727
Heckrotte, Warren. Nuclear cross sections and size of nucleus—619(A); 1279
—— **and Joseph V. Lepore.** Polarization of nucleons elastically scattered from nuclei—1109(L)
Heinz, O. Range and specific ionization for high-energy protons in nuclear emulsions—610(A)
Hellens, R. L. (see Jennings, B.)—636(A)
Hemmendinger, Arthur (see Ennis, Malcolm E.)—772
Hendee, C. F. and S. Fine. Moseley's law applied to proportional counter resolution of adjacent elements—281(L)
Henkel, John H. Equation of state and thermal dependence of elastic coefficients of crystalline argon—617(A)
Henkel, R. L. (see Brolley, J. E., Jr.)—651(A)

Hennig, G. R. Thermal neutron capture cross section of C^{13}—92
——, **B. Smaller, and E. L. Yasaitis.** Paramagnetic resonance absorption in graphite—1088(L)
Henry, Warren E. Low-temperature magnetization of two Ce salts—603(A)
—— Strong field induced paramagnetic anomaly in $NiSiF_6 \cdot 6H_2O$—1449
Herber, R. H. (see Sugihara, T. T.)—298(A)
Hereford, Frank L. Annihilation of positrons in liquid He—1097(L)
—— (see McMaster, William H.)—723
Herlin, Melvin A. (see Chase, C. E.)—565(L)
Herman, Frank. Speculations on energy band structure of Ge-Si alloys—847(L)
——, **Joseph Callaway, and Forman S. Acton.** Comparison of various approximate exchange potentials—371
Herman, R. C., L. L. Mador, R. F. Wallis, and M. C. Williams. X-ray production of *F* centers in NaCl and LiF—598(A)
Herr, W., H. Hintenberger, and H. Voshage. Half-life of rhenium—1691(L)
—— (see Hintenberger, H.)—1690(L)
Herring, Conyers. Role of low-energy phonons in thermal conduction—954
Herwig, Lloyd O. and Glenn H. Miller. Relative ionization yields for fission fragments in various gases—413
Hesketh, R. V. and E. E. Schneider. Shape of *F* band—837(L)
—— **and E. E. Schneider.** Thermal restoration of color centers at low temperature—598(A)
Hess, Wilmot (see Burgus, Warren H.)—750
Heydenburg, N. P. and G. M. Temmer. Coulomb excitation of energy levels in Rh and Ag—861(L)
—— **and G. M. Temmer.** Coulomb excitation *vs* compound nucleus formation in the lighter elements—629(A)
Hibi, Tadatosi and Kazuo Ishikawa. Spectral dependence of thermionic emission with activation from (Ba−Sr)O cathodes over 0.6–3.5 ev region—1183
Hickam, W. M. Ionization probability curves near threshold for Zn, Cd, and Hg—703
Hidalgo, John U., Sr. Measurements of solvent volume changes in sugar factory using radioactive tracer technic—306(A)
Higgins, G. H. (see Ghiorso, A.)—293(L)
Hill, R. D., E. O. Salant, and M. Widgoff. τ meson produced by 3.0-Bev protons—1699(L)
Hillman, Peter, Vaughn Culler, and N. F. Ramsey. Polarization in high-energy *p-n-n* double scattering—462
Hinnov, Einar and Hedwig Kohn. Intensity measurements of resonance lines in flame source—301(A)
—— (see Kohn, Hedwig)—301(A)
Hintenberger, H., W. Herr, and H. Voshage. Radiogenic Os from Re-containing molybdenite—1690(L)
—— (see Herr, W.)—1691(L)
Hodson, A. L. (see Harris, D. R.)—661(A)
Hoffman, H. E. (see Howard, R. A.)—661(A)
Hofstadter, R., B. Hahn, A. W. Knudsen, and J. A. McIntyre. High-energy electron scattering and nuclear structure determinations. II—512
Holden, W. R. (see Atkinson, W. R.)—634(A)
Holm, D. M. (see Terrell, J.)—650(A)
Holm, Lennart W. (see Atterling, Hugo)—585(L)
Holmes, John R. and Leon Pape. Pressure shift in He λ5875—621(A)
Holmgren, H. D., J. M. Blair, B. E. Simmons, T. F. Stratton, and R. V. Stuart. Differential cross sections for $C^{13}(d,p)C^{14}$ and $C^{13}(d,t)C^{12}$—1544
Honig, A. and A. F. Kip. Electron spin resonance of impurity level in silicon—1686(L)
Hood, H. P. (see Sands, R. H.)—607(A)
Hopper, V. D. (see Parsons, R. W.)—193
Hopson, J. E. and C. E. Nielsen. Vapor expansion chamber using pure water. I—601(A)
—— (see Nielsen, C. E.)—601(A)
Horrocks, D. L. and A. F. Voigt. Half-life of Tl^{204}—1205
Horsley, R. J. (see Katz, L.)—464
Horton, G. K. and E. Phibbs. Effect of nuclear charge on internally produced pairs—604(A)
Hourd, R. F., J. R. Fleming, and J. J. Lord. Flux of primary heavy nuclei at equator—647(A)
Howard, R. A., P. M. Fitzpatrick, H. E. Hoffman, and J. S. Urban. Decay of heavy neutral particle—661(A)
Howland, P. R. and W. E. Kreger. γ-ray absorption coefficients for NaI, Cu, Ta, and W—407
Hoyle, Fred. Observational tests in cosmology—309(T)
Hrostowski, H. J., G. H. Wheatley, and W. F. Flood, Jr. Anomalous optical behavior in InSb and InAs—1683(L)
Hsieh, Yu-Chang and Ingram Bloch. Normal coordinates in nuclear photoeffect—305(A)
Huddleston, C. M. (see Eggler, C.)—600(A)
Hudis, J., E. Baker, and G. Friedlander. Production of Be^7 in high-energy reactions—612(A)
Hudson, R. P. and C. K. McLane. Magnetic and thermal properties of chromic methylamine alum below 1°K—932
—— (see Ambler, E.)—625(A); 1143
Huebner, W. F. (see Phelps, John)—441
Huggett, R. W. (see Thompson, R. W.)—661(A); 1576
Hughes, D. J. (see Harvey, J. A.)—645(A)
—— (see Levin, J. S.)—645(A)
—— (see Seidl, F. G. P.)—476
Hughes, Raymond H. Isotope shift in Li I spectrum—621(A)
Hughes, Vernon W. (see Marder, S.)—611(A)
—— (see Teutsch, Werner B.)—1461
—— (see Weinreich, Gabriel)—1451
Huizenga, J. R., J. E. Gindler, and R. B. Duffield. Relative photofission yields of several fissionable materials—1009
—— (see Friedman, A. M.)—1501
Hulburt, E. O. (see Bennett, W. H.)—315
Hulet, E. K., S. G. Thompson, and A. Ghiorso. Isotopes of curium, berkelium, and californium—1703(L)
Hull, M. H., Jr. (see Biedenharn, L. C.)—656(A)
Hungerford, E. T. and R. D. Birkhoff. Electron straggling in thin foils—6
Hunt, W. A., R. M. Kline, and D. J. Zaffarano. β endpoint energies and half-lives for some mirror transitions—611(A)
Hurley, J. P. and P. S. Jastram. γ ray studies of Re^{186}—627(A)
Hurst, G. S. (see Bortner, T. E.)—303(A); 609(A)
—— (see Cure, J. W.)—302(A)
Hurwitz, H., Jr. (see Zweifel, P. F.)—660(A)
Hutchinson, Franklin (see Phelps, John)—441
Hutchison, Clyde A., Jr., and W. Burton Lewis. Paramagnetic resonance absorption in sodium plutonyl acetate—1096(L)
Huus, Torben (see Day, Robert B.)—1003
Hyde, Earl K. (see Mathur, Hirdaya B.)—708

Iddings, G. M. (see Crane, W. W. T.)—1702(L)
Igo, G. and M. S. Wertheim. Isotope shift in x-ray spectra of heavy elements—1097(L)
Inghram, M. G. (see Steinberg, E. P.)—867(L)
—— (see Malm, R.)—641(A); 993
Inoki, M., T. Yasaki, and Y. Matsukawa. Mass measurements of slow cosmic-ray mesons—1565
Irvine, J. W., Jr. (see Bazorgan, G. A.)—781

Ise, J. (see Schecter, L.)—659(A)
Ishiguro, Masakazu, Fujio Oda, and Takuzo Fujino. Plastic flow and low-frequency dispersion in alkali halide crystal—1347(L)
Ishikawa, Kazuo (see Hibi, Tadatosi)—1183

Jaccarino, Vincent (see King, John Gordon)—1706(E)
Jache, Albert, Gilbert Blevins, and Walter Gordy. Mm wave spectrum of arsine—299(A)
—— (see Burrus, Charles A.)—299(A); 706
Jackson, J. David. Schematic calculation of (p,xn) cross sections of heavy elements—651(A)
Jackson, J. L. Equations of motion of coupled ordered and dissipative systems—642(A)
Jacobs, Donald H. and Milton E. Pugh. JAINCOMP-C and -D digital computers—616(A)
Jacobsohn, B. A. Nuclear rotational levels and μ-mesonic atom—654(A)
Jakobson, M. and J. H. Manley. Phase properties of deflected ion beam from fixed-frequency cyclotron—600(A)
Jan, J.-P. and J. S. Koehler. Small angle x-ray scattering from cold-worked Al-Ag and Al-Zn alloys—665(A)
Jancovici, B. G. Coulomb energy and nuclear radius—389; 619(A)
—— **and I. Talmi.** Tensor forces and β decay of C^{14} and O^{14}—289(L)
Jansen, L. and Z. I. Slawsky. Deviations from additivity of intermolecular field at high densities—614(A)
Jastram, P. S. (see Hurley, J. P.)—627(A)
Jaumot, F. E., Jr. (see Berkowitz, A. E.)—1185
Jen, C. K. (see Massey, J. T.)—622(A)
Jenkins, T. L., D. Luckey, T. R. Palfrey, and R. R. Wilson. Photoproduction of charged π mesons from hydrogen and deuterium—179
Jennings, B., J. B. Weddell, and R. L. Hellens. Inelastic scattering of 4.3-Mev neutrons by Fe^{56}—636(A)
Jensen, E. N. (see Pohm, A. V.)—1523
Jentschke, W. (see Robinson, W. H.)—1412
Johnson, C. H. and J. L. Fowler. Differential cross section for elastic scattering of neutrons from N—637(A)
—— (see Trail, Carroll C.)—640(A); 1363(L)
Johnson, Everett R. and Schuyler M. Christian. Properties of Ge-Si alloys—560(L)
Johnson, F. S., J. D. Purcell, and R. Tousey. Extension of extreme uv solar spectrum—621(A)
Johnson, Peter D. and Ferd E. Williams. Effect of pressure on optical absorption of activator in luminescent solid—598(A)
—— **and Ferd E. Williams.** Effect of pressure on optical absorption of activator system in KCl: Tl—69
Johnson, T. H. AEC research programs and policies—299(T)
Johnston, L. H., E. A. Day, and J. H. Williams. Proposed design of 50-Mev proton linear accelerator—599(A)
Jones, D. R. Production of neutrons by negative μ mesons by complex nuclei—624(A)
Jones, Ernest A. (see Akers, Lawrence K.)—300(A)
—— (see Lovell, R. J.)—300(A)
Jones, Harry. Electronic wave functions in metals in relation to nuclear magnetic resonance—606(T)
Jordan, W. C. (see Burson, S. B.)—613(A)
Josien, Marie-Louise. Application of infrared spectroscopy to study of molecular interactions in solutions—299(T)
—— (see Fuson, Nelson)—300(A)

Kaiser, H. F. Microtron maximum particle energy—667(A)
—— Microtrons (electron cyclotrons for X and K band operation)—600(A)
—— Recent progress in microtron research—632(T)
Kaiser, W. (see Fan, H. Y.)—1087(L)
Kalos, M. (see Tobocman, W.)—605(A)
Kammer, E. W. Effect of small strains on electrical resistance of U wire—307(A)
Kanda, Eizo (see Sugawara, Tadashi)—1355(L)
Kanda, Teinosuke (see Sugawara, Tadashi)—1355(L)
Kane, J. A., R. A. Stallwood, R. B. Sutton, T. H. Fields, and J. G. Fox. External proton beam of Carnegie synchrocyclotron—662(A)
——, **R. A. Stallwood, R. B. Sutton, T. H. Fields, and J. G. Fox.** Polarization in p-p scattering at 415 Mev—1694(L)
—— (see Fields, T. H.)—638(A)
Kao, S. K. and A. F. Clark. p-p scattering in nuclear emulsions—662(A)
Kaplon, M. F., J. Crussard, J. Klarmann, and J. Noon. Observations on unstable particles in photographic emulsion—660(A)
—— (see Crussard, J.)—584(L)
—— (see Koshiba, M.)—647(A)
—— (see Noon, J. H.)—647(A); 1103(L)
Karle, I. L. Electron-diffraction studies of internal motion in molecules—633(T)
Karp, Samuel N. (see Shmoys, Jerry)—656(A)
Karplus, Robert. Hall effect in ferromagnetics—297(T)
—— **and J. M. Luttinger.** Hall effect in ferromagnetics—1154
Karzmark, C. J. (see Kim, Y. B.)—661(A)
—— (see Thompson, R. W.)—661(A); 1576
Kasper, J. S. (see Wilson, V. C.)—1408
Kato, Susumu (see Shinoda, Gunji)—840(L)
Kato, W. Y. (see Seidl, F. G. P.)—476
Katz, L., R. N. H. Haslam, R. J. Horsley, A. G. W. Cameron, and R. Montalbetti. Fine structure in $C^{13}(\gamma,n)C^{12}$ and $O^{18}(\gamma,n)O^{17}$ activation curves—464
—— (see Goldemberg, J.)—471
Keller, J. M. and E. Koenigsberg. Electronic quadrupole-quadrupole interactions in Ce metal—665(A)
Kelly, W. H. (see Lu, D. C.)—121; 1533
Kennedy, J. M. and W. T. Sharp. γ radiation from reactions induced by polarized particles—440
Kent, D. C. (see Levinger, J. S.)—418
Kereiakes, J. G. and A. T. Krebs. Use of scintillation counters in studies on luminous efficiency of biological materials—308(A)
Kern, B. D. (see Givin, H. H.)—302(A); 641(A)
—— (see Lamarsh, J. R.)—307(A)
Kerner, Edward H. Periodic impurities in periodic lattice—687
Kerr, Robert J. (see Meneely, George R.)—308(A)
Keuffel, J. W. (see Mezzetti, L.)—858(L)
Kiehn, Robert M. and Clark Goodman. Neutron inelastic scattering—636(A); 989
Killion, Lawrence (see Guss, Donald)—627(A)
Kim, Y. B., J. R. Burwell, H. O. Cohn, C. J. Karzmark, and R. W. Thompson. Magnetic cloud-chamber observation of V particles. I. Charged V particles—661(A)
King, Allen L. Rheological problem—298(A)
King, D. T. and M. M. Block. Pairs formed by bremsstrahlung of great energy. I. Experimental—648(A)
—— (see Block, M. M.)—171; 648(A)
King, Jean I. F. Potential theory formulation of radiant heat transfer—298(A)
King, John Gordon and Vincent Jaccarino. Hfs and nuclear moments of stable Br isotopes—1706(E)
Kington, Joe D. (see Willard, Harvey B.)—1359(L)
Kip, A. F. (see Dresselhaus, G.)—568(L)
—— (see Feher, G.)—1343(L)
—— (see Honig, A.)—1686(L)
Kirkwood, Robert L. Gravitational field equations—1051

Kittel, C. Statistical mechanics and Overhauser nuclear polarization effect—589(L)
—— (see Dresselhaus, G.)—568(L)
Klaiber, G. Stanley (see Box, Harold C.)—1247
Klarmann, J. (see Crussard, J.)—584(L)
—— (see Kaplon, M. F.)—660(A)
Klein, Abraham. Dyson's new Tamm-Dancoff method—654(A)
—— New Tamm-Dancoff formalism—1676
—— Suppression of pair coupling in nuclear forces—1061
—— Suppression of pair effects in nuclear forces—667(A)
—— (see Bernstein, J.)—655(A)
Klein, Martin J. and Paul H. E. Meijer. Principle of minimum entropy production—642(A)
Kleinman, D. A. (see Ryder, E. J.)—1342(L)
Kline, R. M. (see Hunt, W. A.)—611(A)
Klontz, E. E. (see Fan, H. Y.)—1087(L)
Kluyver, J. C. (see Endt, P. M.)—580(L)
Knight, J. R. (see Hanson, H. P.)—621(A)
Knowles, C. Harry and R. T. Lagemann. Some thermodynamic constants of liquid HF—306(A)
Knudsen, A. W. (see Hofstadter, R.)—512
Knudsen, W. C. and J. R. Dillinger. Experimental evidence for structure in He II film—279(L)
Koehler, J. S. (see Jan, J.-P.)—665(A)
Koehler, W. C. and E. O. Wollan. Neutron magnetic diffraction studies of La, Ca manganites—653(A)
—— **and E. O. Wollan.** Search for antiferromagnetism in V_3Si, Cr_3Si, and Mo_3Si—280(L)
Koenigsberg, E. (see Keller, J. M.)—665(A)
Koerts, Leo. Ground state of Re^{188}—1358(L)
——, **A. Schwarzschild, R. Gold, and C. S. Wu.** β spectrum of K^{42}—612(A)
Koester, L. J., Jr. (see Goldwasser, E. L.)—1692(L)
Kohn, Hedwig and Einar Hinnov. Photoelectric measurement of reversal temperature—301(A)
—— (see Hinnov, Einar)—301(A)
Kojima, S., K. Tsukada, S. Ogawa, and A. Shimauchi. New absorption lines of crystals in submicrowave region—1705(E)
Kooi, Clarence. Hall effect in ferromagnetics—843(L)
Korff, Serge A. Effect of melting of polar ice on length of day—296(L)
Kortright, J. M. (see Yearian, H. J.)—653(A)
Koshiba, M. and M. F. Kaplon. Observations on high-energy soft cascade—647(A)
—— (see Crussard, J.)—624(A)
—— (see Walker, W. D.)—624(A); 852(L)
Koslov, S., V. Fitch, and J. Rainwater. Experimental study of μ^--meson mass and vacuum polarization in mesonic atoms—291(L)
——, **V. Fitch, and J. Rainwater.** Mass of μ^- meson from mesonic x-rays—625(A)
Koster, G. F. Theory of scattering in solids—1436
—— **and J. C. Slater.** Wave functions for impurity levels—1167
Krasnow, M. E. (see Lassettre, E. N.)—635(A)
Kraushaar, J. J., J. W. Mihelich, and A. W. Sunyar. Directional correlation of γ rays of A^{36}—456
Krebs, A. T. (see Kereiakes, J. G.)—308(A)
Kreger, W. E. (see Howland, P. R.)—407
Krohn, V. E. and S. Raboy. Decay scheme of Pb^{204m}—1354(L)
—— **and S. Raboy.** Magnetic moment of first-excited state of Pb^{204}—608(A)
—— (see Raboy, S.)—1689(L)
Krone, R. W. (see Baumann, N. P.)—650(A)
Kruse, U. E. and J. M. Teem. p-p cross section at 95 Mev—662(A)
—— (see J. M. Teem)—664(A)
Kunz, W. E., C. D. Moak, and W. M. Good. $Li^7(He^3,p)Be^9$ reaction—640(A)
—— (see Moak, C. D.)—641(A)
Kuper, J. B. H. (see Bernstein, W.)—609(A)
Kurbatov, J. D. (see Sakai, M.)—101

Lackner, Henry (see Trambarulo, Ralph)—622(A)
Lafferty, D. L., L. A. Rayburn, and T. M. Hahn. γ-ray spectrum from inelastic scattering of fast neutrons in Fe—637(A)
—— (see Rayburn, L. A.)—301(A); 637(A)
Lagemann, R. T. (see Knowles, C. Harry)—306(A)
Lamarsh, J. R. and B. D. Kern. Metastable magnetic states—307(A)
Landsberg, P. T. Statistical mechanics of temperature-dependent energy levels—643(A)
Lane, C. T. (see Dyba, R. V.)—1365
Langenheim, R. H. (see Yearian, H. J.)—653(A)
Laporte, Otto. Interaction of shock waves—658(T)
Lark-Horowitz, K. (see Fan, H. Y.)—1087(L)
Lassettre, E. N., A. S. Berman, S. Silverman, and M. E. Krasnow. Electron spectrometer for study of inelastic collision cross sections—635(A)
LaVier, E. C. (see Hanna, S. S.)—110
Lawson, J. R. and M. B. Towns. Molecular association in perfluoroalkyl carboxylic acids—300(A)
Lax, Benjamin, H. J. Zeiger, and R. N. Dexter. Anisotropy of cyclotron resonance in Ge. I. Theory—597(A)
—— (see Dexter, R. N.)—557(L); 597(A)
Lax, Melvin. Infrared absorption in semiconductors—309(T)
—— **and Joel L. Lebowitz.** Vibration spectra of crystal lattices—617(A)
Lazar, N. H. Decay of Sb^{124}—292(L)
—— **and P. R. Bell.** γ radiation from K^{42}—612(A)
Leavitt, C. P. (see Shapiro, A. M.)—663(A)
LeBlanc, J. M., J. M. Cork, and S. B. Burson. Decay of Pt^{189}—627(A)
—— (see Burson, S. B.)—613(A)
Lebowitz, Joel L. (see Frisch, Harry L.)—643(A)
—— (see Lax, Melvin)—617
Leder, Lewis B. and L. Marton. Characteristic energy loss of electrons—634(A)
—— **and L. Marton.** Effect of chemical combination on characteristic energy loss of electrons—1345(L)
Lee, T. D. Some special examples in renormalizable field theory—1329
Lehner, J. and G. M. Wing. Solution of transport equation for case of slab geometry—642(A)
Leifer, H. N. and W. C. Dunlap, Jr. Some properties of p-type GaSb between 15°K and 925°K—51
Leighton, R. B. (see van Lint, V. A. J.)—295(L)
—— (see York, Carl M., Jr.)—159
Leipuner, L. (see Stearns, M. B.)—625(A); 1353(L)
Leiss, J. E. and C. S. Robinson. Photoproduction of π^+ mesons from hydrogen—638(A)
—— (see Penfold, A. S.)—637(A)
—— (see Robinson, C. S.)—638(A)
Lemonick, Aaron and Francis M. Pipkin. Spins and hyperfine splittings of Ag^{111} and Cu^{64}—1356(L)
Lepore, Joseph V. (see Heckrotte, Warren)—1109(L)
Lesk, I. A. Survey of Ge and Si devices—309(T)
Levin, J. S. and D. J. Hughes. Measurements of neutron resonance parameters in U, Th, Hg, and Au—645(A)
—— (see Seidl, F. G. P.)—476
Levine, S. H., R. S. Bender, J. N. McGruer, and W. F. Vogelsang. Reaction particles from 14.5-Mev deuteron bombardment of Li^7 and Li^6—640(A)

Levinger, J. S. and D. C. Kent. Independent particle model and nuclear photoeffect—418
Levinson, C., K. Brueckner, and H. Mahmoud. Two-body forces and nuclear saturation. II. Results—655(A)
—— (see Brueckner, K.)—655(A)
Levinson, John. Generator of linearly varying current for electromagnet—651(A)
Levinthal, Cyrus. Molecular structure and biological control mechanism—606(T)
Levitas, A., C. C. Wang, and B. H. Alexander. Energy gap of Ge-Si alloys—846(L)
Lewis, H. W. (see Bernstein, E. M.)—83
—— (see Schawlow, A. L.)—1344(L)
Lewis, W. Burton (see Hutchison, Clyde A., Jr.)—1096(L)
Lewis, W. E. (see Pohm, A. V.)—1523
Libby, W. F. (see Suttle, A. D., Jr.)—866(L)
Likely, J. G. (see Ajzenberg, F.)—641(A)
Lindenbaum, S. J. and Luke C. L. Yuan. Production of positive and negative pions in Be by 1.0 and 2.3-Bev protons—638(A)
Lindqvist, Torsten and Allan C. G. Mitchell. Disintegration of K^{45}—444; 612(A)
—— **and Allan C. G. Mitchell.** Nuclear levels in Ca^{45}—1535
Lindsay, John C. and A. V. Masket. High-speed transient dynamic analysis—665(A)
Linsley, John. Čerenkov counter measurement of fast multiply charged cosmic rays—647(A)
Litherland, A. E. (see Bartholomew, G. A.)—649(A)
—— (see Gove, H. E.)—650(A)
Loeb, A. L. and J. B. Goodenough. Influence of covalence on ion ordering and distortion in spinels—616(A)
Loeb, L. B. Some fundamental processes of gaseous electronics—620(T)
Loeliger, H. R. and L. R. Sarles. Magnetic moment of Os^{189}—291(L)
Lokanathan, S., J. Steinberger, and H. B. Wolfe. High-energy electrons in the capture of μ^- mesons by complex nuclei—624(A)
Lord, J. J. (see Fleming, J. R.)—647(A)
—— (see Orear, Jay)—624(A)
Lorrain, Paul, R. Béique, P. Gilmore, P. E. Girard, A. Breton, and P. Piché. Pressurized 500-kv high-frequency Cockroft-Walton accelerator—599(A)
Love, W. F. (see Croft, G. T.)—1403
—— (see Passaglia, E.)—666(A)
Lovell, R. J. and E. A. Jones. Potential constants for carbonyl fluoride—300(A)
Low, F. E. (see Gell-Mann, M.)—1300
Lu, D. C., W. H. Kelly, and M. L. Wiedenbeck. Decay schemes of Cd^{114} and Te^{125}—121
——, **W. H. Kelly, and M. L. Wiedenbeck.** γ-ray spectra following β-decay of Br^{80}, Sb^{124}, and I^{131}—1533
Luckey, D. (see Jenkins, T. L.)—179
Luckey, G. W. Formation of photographic latent image in Ag halides—309(T)
Lutes, O. S. (see Maxwell, E.)—333
Luttinger, J. M. (see Brown, H. A.)—652(A)
—— (see Karplus, Robert)—1154
Lyon, W. S. and J. E. Strain. Decay of Rb^{86}—1500
Lyons, D. H. and A. M. Feingold. Level structure of Li^8—606(A)
Lyons, Harold. Recent determinations of velocity of light—633(T)

Macdonald, J. Ross and John E. Robinson. Ac Hall and magnetoresistive effects in photoconducting alkali halides—44
Mackin, R. J. (see Mills, W. R., Jr.)—1206
Macklin, R. L. and H. E. Banta. $Li^6(d,t)$ reaction—302(A)
Madey, Richard (see Bandtel, Kenneth C.)—639(A)
Mador, L. L. (see Herman, R. C.)—598(A)
Magnuson, D. W. Molar polarization, dipole moment, and nonideality of trichloroheptafluorobutane vapor—301(A)
Mahmoud, H. (see Brueckner, K.)—655(A)
—— (see Levinson, C.)—655(A)
Malenka, Bertram J. Polarization in high-energy elastic nucleon-nucleus scattering—522
—— Polarization in scattering by nuclei at high energies—620(A)
Malm, R. and D. R. Inglis. Conservation of isobaric spin in reaction $Be^9(p,\alpha)Li^6$—993
—— **and D. R. Inglis.** Magnetic analysis indicating charge symmetry in reaction $Be^9(p,\alpha)Li^6$—641(A)
Malmberg, P. R. (see Sun, K. H.)—600(A)
Mandeville, C. E. and H. O. Albrecht. Phosphorescence of and energy storage in some uv-emitting phosphors—598(A)
Manley, J. H. (see Jakobson, M.)—600(A)
Mann, D. E. and Earle K. Plyler. Vibrational spectrum of fluorotrichloroethylene—622(A)
Mann, Leonard A., Ray A. Grandey, and Arnold F. Clark. Cross sections for meson-induced stars in Ilford G5 nuclear emulsions—648(A)
Mapother, D. E. (see Garber, M.)—603(A)
—— (see Mould, R. E.)—604(A)
Marcus, Jules A. (see Plumb, Harmon H.)—602(A)
Marder, S., V. W. Hughes, and C. S. Wu. Effect of angular dependence of annihilation radiation of orthopositronium in magnetic field—611(A)
Marion, J. B. (see Cook, C. F.)—639(A)
Mark, Hans, Clyde McClelland, and Clark Goodman. Electric excitation of Mn^{55} with protons—628(A)
Marmier, P. (see Boehm, F.)—864(L)
Marquez, Luis. Disintegration of Rh^{103}—67
Marshall, J. F., R. A. Shatas, and M. A. Pomerantz. Target-thickness dependence of δ-ray emission produced by 1.3-Mev electrons—634(A)
—— (see Pomerantz, M. A.)—633(A)
Marshall, John. Polarization of high-energy protons—644(T)
——, **L. Marshall, D. Nagle, and W. Skolnik.** Scattering of 314-Mev polarized protons by deuterium—1020
—— (see Nagle, D.)—663(A)
Marshall, L. (see Marshall, J.)—1020
—— (see Nagle, D.)—663(A)
Martin, J. A. (see Green, F. L.)—304(A)
Martin, P. C. (see Fulton, Thomas)—811
—— (see Glauber, R. J.)—572(L)
Martin, Ronald L. Phase shift analysis of scattering of negative pions on H—1606
Marton, L. Survey of characteristic energy losses of electrons—620(T)
——, **Tommy F. McCraw, and J. Arol Simpson.** Electron scattering in solids at 20 kev—634(A)
—— (see Leder, Lewis B.)—634(A); 1345(L)
Maryott, A. A. (see Birnbaum, G.)—622(A)
Masket, A. V. Interior value problems—305(A)
—— (see Lindsay, John C.)—665(A)
Massey, J. T., C. I. Beard, and C. K. Jen. Microwave spectral series of deuterated hydrogen peroxide—622(A)
Masuda, Yoshika (see Sugawara, Tadashi)—1355(L)
Mathur, Hirdaya B. and Earl K. Hyde. Spectrometer studies of radiation of neutron-deficient isotopes of Cs and of $E3$ isomers, Xe^{127m} and Xe^{135m}—708
Matsukawa, Y. (see Inoki, M.)—1565
Matthias, B. T. Superconducting compounds—633(T)

—, **T. H. Geballe, S. Geller, and E. Corenzwit.** Superconductivity of Nb_3Sn—1435
— (see Schawlow, A. L.)—1344(L)
Maxwell, E. and O. S. Lutes. Threshold field properties of some superconductors—333
Mayburg, Sumner. Precipitation of impurities at dislocations in heat-treated Si—838(L)
— Vacancies and interstitials in heat-treated Ge—38
Mayo, E. E. Generalization of theorem by Pappus—305(A)
Mazari, M. (see Buechner, W. W.)—609(A)
McCarthy, John T. Mass differences for isobars capable of double-β decay—447
McClelland, Clyde (see Mark, Hans)—628(A)
McClure, J. W. Axial ratios in hexagonal metals—665(A)
McCollom, K. A. (see de Boisblanc, D. R.)—609(A)
McCormick, G. H. (see Cohen, B. L.)—639(A)
McCormick, Philip T. Theoretical energy and angular distributions of bremsstrahlung electrons—657(A)
McCraw, Tommy F. (see Marton, L.)—634(A)
McGruer, J. N. (see Levine, S. H.)—640(A)
McGuire, A. D., M. Camac, M. L. Halbert, and J. B. Platt. X-rays from π mesonic atoms—625(A)
McIntyre, J. A. (see Hofstadter, R.)—512
McKeown, Michael (see Muehlhause, C. O.)—598(A)
— (see Scharff-Goldhaber, Gertrude)—613(A)
McLane, C. K. (see Hudson, R. P.)—932
McMaster, William H. and Frank L. Hereford. Angular distribution of photoelectrons produced by 0.4–0.8 Mev polarized photons—723
McReynolds, A. W. and T. Riste. Magnetic neutron diffraction from Fe_3O_4—1161
McSkimin, H. J., A. J. Williams, and R. M. Bozorth. Elastic constants of Co and of CoZn ferrite crystals—616(A)
Meiboom, S. (see Abeles, B.)—31
Meijer, Paul H. E. Calculation of wavefunctions in symmetrical crystalline field—1443
— (see Klein, Martin J.)—642(A)
Meissner, K. W. (see Deverall, G. V.)—1463
Melander, Lars (see Atterling, Hugo)—585(L)
Melton, Charles E. Measurements of ionization produced by 5-Mev α particles in argon mixtures—303(A)
Melvin, M. Avramy. Law of impact for generally shaped bodies—615(A)
Meneely, George R., Robert J. Kerr, Jesse E. Hoffman, and Sherwood K. Haynes. Rotating-sphere solid-angle scanner for γ rays—308(A)
Meneghetti, David and S. S. Sidhu. Neutron diffraction study of Cu-Mn system—666(A)
Mercer, C. F. (see Williams, Jack H.)—306(A)
Merritt, F. R. (see Fletcher, R. C.)—844(L)
Merritt, J. and D. Hamlin. Yield of π^+ mesons by 335-Mev protons as function of atomic number—638(A)
Merz, Walter J. Domain formation and domain wall motions in ferroelectric $BaTiO_3$ single crystals—690
Metropolis, N. (see de Hoffmann, F.)—1586
— (see Fermi, E.)—1581
Metzger, F. R. and W. B. Todd. Nuclear resonance fluorescence in Hg^{198} and lifetime of 411-kev excited state of Hg^{198}—853(L)
— **and W. B. Todd.** Resonance fluorescence with nuclei: Tl^{203}—627(A)
— (see Swann, C. P.)—636(A)
Meyerott, R. E. Approximate Hartree type wave functions and matrix elements for K and L shells of atoms and ions—12
Mezzetti, L. and J. W. Keuffel. Decay curve of K particles—858(L)
Michel, M. C. (see Passell, T. O.)—999
Mihelich, J. W. Disintegration of Ta^{182}—626(A)
—, **A. W. Schardt, and E. Segrè.** Energy levels in Po^{210}—1508
— (see Kraushaar, J. J.)—456
— (see Sunyar, A. W.)—570(L)
Millburn, G. P., W. Birnbaum, W. E. Crandall, and L. Schecter. Nuclear radii and transparencies from inelastic cross-section measurements. I. Method—620(A)
—, **W. Birnbaum, W. E. Crandall, and L. Schecter.** Nuclear radii from inelastic cross-section measurements—1268
— (see Birnbaum, W.)—649(A)
— (see Crandall, W. E.)—620(A)
— (see Schecter, L.)—659(A)
Miller, D. W., V. K. Rasmussen, and M. B. Sampson. Energy levels of C^{13} by inelastic α scattering—649(A)
Miller, Glenn H. (see Herwig, Lloyd O.)—413
Miller, J. M. (see Belmont, E.)—1554
— (see Sugarman, Nathan)—1704(L)
Miller, R. C. High-energy, large-angle distribution of pair electrons produced by bremsstrahlung—796
Miller, W. C. (see Bhattacherjee, S. K.)—404
— (see Noyes, J. C.)—396
Mills, F. E. (see Goldwasser, E. L.)—1692(L)
Mills, R. (see Yang, C. N.)—631(A)
Mills, W. R., Jr., and R. J. Mackin, Jr. Observations on 4.43-Mev γ-rays from C^{13}—1206
Milton, J. C. D. and J. S. Fraser. α-γ angular correlation in decay of Ra^{224}, Ra^{226}, and Pu^{238}—628(A)
Mingins, Charles R. (see Sampson, John L.)—617(A)
Miskel, J. A. and M. L. Perlman. Double vacancies in K shell associated with K-electron capture in A^{37}—612(A)
Mitchell, Allan C. G. and Elizabeth Hebb. Disintegration of Ba^{139}—727
— (see Lindqvist, Torsten)—444, 612(A); 1535
Mitra, A. N. Modified nucleon propagators—1697(L)
Mitsui, Toshio and Jiro Furuichi. Kinetic properties of domains in Rochelle salt—558(L)
Mize, J. P., J. W. Starner, and M. E. Bunker. Radiations of Ir^{190m}—627(A)
— (see Bunker, M. E.)—612(A)
Moak, C. D., W. M. Good, and W. E. Kunz. Be^9+He^4 reactions—641(A)
— (see Kunz, W. E.)—640(A)
Montalbetti, R. (see Katz, L.)—464
Morin, F. J. (see Geballe, T. H.)—1085(L)
Morrison, P. Solar-connected variations of cosmic rays—646(A)
Moser, Paul (see Trambarulo, Ralph)—622(A)
Moses, H. E. Canonical transformation for electron-positron field coupled to time-independent electromagnetic field. II—237
Moszkowski, Steven A. Energy levels in spheroidal well—604(A)
— (see Finkelstein, R. J.)—1695(L)
Mould, R. E. and D. E. Mapother. Superconductivity of precipitation hardening Al alloy—604(A)
Moyer, Burton J. (see Bandtel, Kenneth C.)—639(A)
— (see Cohen, David)—664(A)
— (see Wilcox, J. M.)—664(A)
Moyer, James W. (see Ruth, Ralph P.)—562(L)
Muckenthaler, F. (see Neiler, J. H.)—640(A)
Muehlhause, C. O., E. der Mateosian, and Michael McKeown. Effects of preparation and temperature on response of NaI phosphors—598(A)
Murray, R. B. Specific heat of $MnCl_2$ at temperatures of liquid He—307(A)
Muschlitz, E. E., Jr. Scattering of H^- ions in range 20–400 ev—635(A)

Myers, H., A. Odian, P. C. Stein, and A. Wattenberg. Neutrons in coincidence with high-energy photoprotons—576(L)

Nagle, D., J. Marshall, L. Marshall, and W. Skolnik. Polarization of 310-Mev protons by deuterium—663(A)
—— (see Marshall, J.)—1020
Nathans, R. (see Ferguson, G. A.)—659(A); 776
—— (see Halpern, J.)—1529
Neaves, A. and D. ter Haar. Thermal conductivity of semiconductors—596(A)
Neiler, J. H., F. Muckenthaler, and James Schenck. Fast neutron scintillation spectra of $Li^6(n,\alpha)H^3$ reaction in LiI(Eu)—640(A)
Nelkin, M. S. and H. A. Bethe. Meson production in meson-proton scattering—618(A)
Nelson, E. B., E. H. Geer, and R. R. Carlson. Scintillation counter study of γ rays from proton capture in Na—650(A)
—— (see Carlson, R. R.)—641(A)
Neufeld, Jacob. Bohr's theory of energy losses of moving charged particles—1128
Newkirk, J. B. Growth of CdI_2 crystals—616(A)
Newman, E. (see Cohen, B. L.)—639(A)
Newson, H. W. and J. H. Gibbons. Resonance near $Li^7(p,n)$ threshold—640(A)
—— (see Gibbons, J. H.)—644(A)
—— (see Rohrer, R. H.)—302(A)
Newson, Henry. Shell effects in highly excited nuclei—299(T)
Neynaber, R. H. (see Beeman, W. W.)—617(A)
Nickell, William E. Yield and angular distribution of protons from $Li^6(d,p)Li^7$—426
Nicklas, J. P. Isotope shift in neutral C—1469
Nielsen, Alvin H. Infrared spectrum of σ_3 for $B^{10}F_3$ and $B^{11}F_3$—300(A)
Nielsen, C. E. and J. E. Hopson. Vapor expansion chamber using pure gases at low temperatures. III—601(A)
—— (see Caren, R. P.)—601(A)
—— (see Hopson, J. E.)—601(A)
Nielsen, K. O. (see Elbek, B.)—96
Nielsen, O. B. (see Elbek, B.)—96
Nier, A. O. (see Collins, T. L.)—615(A)
Nix, F. C. (see Berkowitz, A. E.)—1185
—— (see Croft, G. T.)—1403
—— (see Donahoe, F. J.)—1395
Noon, J. H. and M. F. Kaplon. Fragmentation of heavy primary nuclei into light elements—647(A)
——, **M. F. Kaplon, and J. Crussard.** Anomalous event observed in photographic emulsion—1103(L)
—— (see Crussard, J.)—584(L)
—— (see Kaplon, M. F.)—660(A)
Noyes, H. P. Pion-nucleon S phase shifts at low energy—619(A)
Noyes, J. C., J. E. Van Hoomissen, W. C. Miller, and B. Waldman. Photodisintegration thresholds of D_2O and Be—396
Nyborg, Wesley L. Self-maintained oscillations in fluid flow—297(T)

Oda, Fujio (see Ishiguro, Masakazu)—1347(L)
Odian, A. (see Myers, H.)—576(L)
Ogawa, S. (see Kojima, S.)—1705(E)
O'Kelley, G. D. (see Olsen, J. L.)—1539
Olds, J. D. (see Codrington, R. S.)—607(A)
Olsen, J. L. and G. D. O'Kelley. Decay of Cs^{136}—1539
O'Neill, Gerard K. Time-of-flight measurements of inelastic neutron scattering—635(A)
—— Time-of-flight measurements on inelastic scattering of 14.8-Mev neutrons—1235
Opitz, W. (see Hartzler, A. J.)—591(L)
Orear, Jay, C. H. Tsao, J. J. Lord, and A. B. Weaver. Scattering of 145-Mev π^+ by H in emulsion—624(A)
Orgel, S. (see Dropkin, J. J.)—597(A)
Osborne, L. S., Y. Goldschmidt-Clermont, and G. Parker. Photoproduction of π^+ mesons near threshold—637(A)
Otter, F. A. (see Domenicali, C. A.)—1134
Overton, W. C., Jr., and J. R. Clement. Correlation techniques for testing Born-von Kármán theory of specific heats—602(A)
—— (see Gaffney, John)—602(A)
Owen, Henry R. (see Schaeffer, Oliver A.)—615(A)

Pac, Pong Yul (see Enatsu, Hiroshi)—263
Packard, M. E. Chemical applications of nuclear magnetic resonance—596(T)
Palevsky, H. and R. M. Eisberg. Magnetic scattering of cold neutrons by gaseous oxygen—659(A)
—— (see Eisberg, R. M.)—659(A)
—— (see Seidl, F. G. P.)—476
Palfrey, T. R. (see Jenkins, T. J.)—179
Palma, M. B., M. U. Palma, and D. Palumbo. Paramagnetic resonance absorption of $VOSO_4 \cdot 5H_2O$—608(A)
Palma, M. U. (see Palma, M. B.)—608(A)
Palmer, R. R. (see Bollinger, L. M.)—645(A)
Palumbo, D. (see Palma, M. B.)—608(A)
Pape, Leon (see Holmes, John R.)—621(A)
Park, David. Ferrimagnetic resonance in sintered masses—652(A)
Parker, G. (see Osborne, L. S.)—637(A)
Parker, Vincent E. (see Snyder, Conway W.)—635(A)
Parratt, L. G. Solid surface studies by total reflection of x-rays—617(A)
—— Surface studies of solids by total reflection of x-rays—359
Parsons, R. W., Françoise A. Brisbout, and V. D. Hopper. Meson showers and high-energy interactions in light and heavy nuclei—193
Passaglia, E. and W. F. Love. Resistivity of ordered and disordered Cu-Au alloys at low temperatures—666(A)
Passell, T. O., M. C. Michel, and I. Bergström. Decay of odd-odd isomer Tl^{198m}—999
Patronis, E. T., Jr. (see Braden, C. H.)—627(A); 758
Patterson, Reid. (p,n) reactions on As, Y, Nb, and Rh—303(A)
Paul, E. B. (see Bartholomew, G. A.)—649(A)
—— (see Gove, H. E.)—650(A)
Pearson, G. L. (see Fletcher, R. C.)—844(L)
Peaslee, D. C. Coulomb energies of light nuclei—717
—— Pion production ratios. II—1580
—— Supermultiplet evidence from isotopic spin spacing—605(A)
—— (see Drachman, R. J.)—605(A)
Pecjak, F. A. (see Sun, K. H.)—600(A)
Peck, R. A., Jr. Rf Cockroft-Walton generator for neutron production—599(A)
Pellam, J. R. (see Broida, H. P.)—845(L)
—— (see Hanson, W. B.)—321; 604(A)
Penfold, A. S. and J. E. Leiss. Determination of photo cross sections from bremsstrahlung activation curves—637(A)
—— (see Spicer, B. M.)—629(A)
Pepper, R. R. (see Fan, H. Y.)—1087(L)
Percus, Jerome K. and George J. Yevick. Domain of action of collective coordinates in new approach to many-body problem—642(A)
—— (see Yevick, George J.)—642(A)
Perkins, J. F. (see Burford, A. O.)—303(A)
Perlman, M. L. and Joan P. Welker. Disintegration of I^{126}—133; 613(A)

—— (see Miskel, J. A.)—612(A)
Perry, Robert W. (see Sampson, John L.)—298(A)
Peter, Martin and M. W. P. Strandberg. Microwave spectrum of OCS—622(A)
Pettengill, G. (see Chamberlain, O.)—1348(L)
Pfann, W. G. and W. Van Roosbroeck. Radioactive and photoelectric *p-n* junction power sources—597(A)
Phelps, John, W. F. Huebner, and Franklin Hutchinson. Stopping power of organic foils for 6-Mev alphas—441
Phibbs, E. (see Horton, G. K.)—604(A)
Piché, P. (see Lorrain, Paul)—599(A)
Pilcher, V. E., R. S. Carter, and A. Stolovy. Neutron resonances in Ho, Tm, and Lu—645(A)
Pines, David. Electron interaction in solids—620(T)
—— Paramagnetic and diamagnetic susceptibility of conduction electrons—1090(L)
Pipkin, Francis M. (see Lemonick, Aaron)—1356(L)
Platt, J. B. (see McGuire, A. D.)—625(A)
Pleasonton, Frances (see Snell, Arthur H.)—304(A)
Plumb, Harmon H. and Jules A. Marcus. Thermal conductivity of Ga single crystals at low temperatures—602(A)
Plyler, Earle K. (see Mann, D. E.)—622(A)
Pobereskin, M. (see Aarons, M. W.)—1345(L)
Pohm, A. V., W. E. Lewis, J. H. Talboy, Jr., and E. N. Jensen. β spectra of Pr^{142}, Tm^{170}, and Rb^{86}—1523
Pomerantz, Martin A. Cosmic radiation at very high altitudes near geomagnetic equator—531
—— Primary α particles near geomagnetic equator—1691(L)
——, **J. F. Marshall, and R. A. Shatas.** Forward-backward ratio of secondary emission produced by 1.3-Mev electrons—633(A)
—— (see Marshall, J. F.)—634(A)
Porter, C. E. (see Harvey, J. A.)—645(A)
Porter, F. T. (see Guss, Donald)—627(A)
Posener, D. W. and M. W. P. Strandberg. Centrifugal distortion in asymmetric top molecules. III. H_2O, D_2O, and HDO—374
Pound, R. V. (see Bloembergen, N.)—8
Pratt, William W. Energy and angular distribution of protons from deuteron bombardment of Ni—1517
Pressman, D. (see Hall, T.)—1208
Preston, W. M. (see Stelson, P. H.)—974
Price, P. J. Electronic thermal conduction in semiconductors—596(A)
Primak, William. The metamict state—837(L)
—— **and L. Fuchs.** Electrical conductivities of natural graphite crystals—22
Pringle, R. W., W. Turchinetz, and H. W. Taylor. Further study of decay scheme of Ir^{189}—115
Prosser, F. W. (see Baumann, N. P.)—650(A)
Pruett, C. H. and R. G. Wilkinson. Disintegration of Ce^{139}—625(A)
Pryce, M. H. L. (see Alburger, D. E.)—1482
Pugh, G. E., D. H. Frisch, and R. Gomez. Nuclear scattering of γ rays below meson threshold—590(L)
——, **D. H. Frisch, and R. Gomez.** Scattering of x-rays by nuclei—611(A)
Pugh, Milton E. (see Jacobs, Donald H.)—616(A)
Pulvari, C. F. Propagation of displacement in solid, having crystalline structure with bistable states—617(A)
Purcell, J. D. (see Johnson, F. S.)—621(A)
Pyle, R. V. (see Birnbaum, W.)—649(A)

Quimby, S. L. Temperature variation of mean Debye temperature of Cu_3Au, 20°C to 450°C—916

Raboy, S. and V. E. Krohn. Gyromagnetic ratio of 10^{-9}-second Ta^{181m}—1689(L)
—— (see Krohn, V.)—608(A); 1354(L)
Rainwater, James (see Cooper, Leon N.)—1107(L)
—— (see Koslov, S.)—291(L); 625(A)
Ramsey, N. F. Molecular-beam studies of molecules—596(T)
—— (see Hillman, Peter)—462
Rankin, Bayard. Simplifying approximation for determining cascade shower distributions—657(A)
Rao, K. Narahari. Near uv absorption spectrum of 1,2,4-trifluorobenzene—299(A)
Rasmussen, V. K. (see Miller, D. W.)—649(A)
Ravenhall, D. G. (see Yennie, D. R.)—500
Rayburn, L. A., D. L. Lafferty, and T. M. Hahn. γ rays produced by inelastic scattering of *d*-D neutrons in Cu, Al, and Mg—637(A)
——, **D. L. Lafferty, and T. M. Hahn.** Inelastic scattering of *d*-D neutrons by Fe and Cu—301(A)
—— (see Lafferty, D. L.)—637(A)
Rayne, John. Specific heats of metals below one degree absolute—1428
Recksiedler, Arthur and Bernard Hamermesh. Capture γ-ray studies using scintillation coincidence spectrometer—650(A)
Reder, Fritz H. and Sanborn C. Brown. Energy distribution function of electrons in pure He—885
Rediker, Robert H. Ionization chamber measurements at 10,600 feet of absorption of *N* component in carbon and hydrocarbon—526
Redlich, Martin G. Interactions between some two-nucleon configurations—448
—— **and Eugene P. Wigner.** β-decay matrix element for deformed core model—122
Reier, Melvin and Morris H. Shamos. Neutron-capture γ-ray spectra—636(A)
Reiffel, L. and G. M. Burgwald. Low-energy events—1294
Reynolds, H. L., D. W. Scott, and A. Zucker. Range and charge of energetic nitrogen ions in Ni—671
—— **and A. Zucker.** Equilibrium charge distribution of stripped 26-Mev N ions—1353(L)
—— **and A. Zucker.** Excitation function for reaction $Be^9(N^{14})F^{18}He^5$—302(A)
Reynolds, J. B. and K. G. Standing. Angular distribution of deuterons from (*p,d*) reactions in light nuclei—639(A)
Ribe, F. L. and J. D. Seagrave. Pickup reactions $B^{10}(n,d)Be^9$ for 14-Mev neutrons—649(A)
Richards, J. D. (see Brentano, J. C. M.)—841(L)
Richter, Harold G. and Charles D. Coryell. Low-energy photofission yields for U^{238}—1550
Rickey, M. E. (see Eisberg, R. M.)—659(A)
Ringo, G. R. and S. Wexler. Standards for thermal neutron capture measurements—660(A)
Riste, T. (see McReynolds, A. W.)—1161
Roat, W. F. (see Autler, S. H.)—599(A)
Roberts, A., J. Tinlot, and E. M. Hafner. Polarization in *n-p* scattering at 100–200 Mev—1099(L)
——, **J. Tinlot, and E. M. Hafner.** Polarization of 170-Mev neutrons—663(A)
—— (see Tinlot, J.)—137
Roberts, James H. (see Weddell, James B.)—117
Roberts, L. D., S. Bernstein, J. W. T. Dabbs, and C. P. Stanford. Capture of polarized neutrons by polarized Sm^{149} nuclei—105
—— **and J. W. T. Dabbs.** Approximate partition function for certain iron group salts at low temperatures—307(A)
—— (see Dabbs, J. W. T.)—307(A); 970
Robinson, C. S. and J. E. Leiss. Photoproduction of π^+ mesons from H near threshold—638(A)
—— (see Leiss, J. E.)—638(A)
Robinson, H. P. (see Harvey, B. G.)—581(L)
Robinson, John E. (see Macdonald, J. Ross)—44

Robinson, W. H. and W. Jentschke. Response of anthracene scintillation crystals to mono-energetic soft x-rays—1412
Rogers, F. T., Jr. General relations in fluid convection theory. I. Similarity theory for flow onset—305(A)
Rogers, T. F. Microwave and far infrared atmospheric water-vapor absorption—622(A)
Rogosa, G. L. (see Schwarz, G.)—950
Rohrer, R. H., W. H. Cargill, and A. F. Dratz. Applications of NaI γ-ray spectrometer to blood volume determinations—308(A)
——, **H. W. Newson, J. H. Gibbons, and P. Cap.** Activation of Al and Se^{80} by p-neutron capture in kev region—302(A)
Rohrlich, F. Pair production and bremsstrahlung in field of electron—657(A)
Rose, D. C. (see Geiger, K. W.)—646(A)
Rosenblum, E. S. (see Dexter, R. N.)—597(A)
Rosenfeld, Arthur H. Pion production by 440-Mev protons incident upon H and C—638(A)
—— (see Warshaw, S. D.)—649(A)
Rosenstock, Herbert B. Counting lattice frequencies—617(A)
Rosenthal, Jenny E. New technique for solving three-dimensional electron optics potential problems with axial symmetry—633(A)
Ross, A. W. and D. ter Haar. Volume changes in substitutional alloys—665(A)
Ross, I. M. (see Ryder, E. J.)—1342(L)
Ross, Marc H. Meson-meson effects in meson-nucleon scattering—619(A)
—— Meson-meson interaction in meson scattering—1687(L)
—— (see Dyson, F. J.)—1644
Rossi, B. (see Bridge, H. S.)—662(A); 1101(L)
—— (see DeStaebler, H. C., Jr.)—662(A)
Rothstein, Jerome. Can well-informed heat engine (WHE) have free will?—643(A)
—— Possible macroscopic effects of single lattice defects—370
Roys, P. A., K. Shure, and J. J. Taylor. Penetration of 6-Mev γ rays in water—911
—— (see Shure, K.)—610(A)
Ruark, Arthur E. Electrodynamic equations symmetrical in respect to charges and poles; with remarks on monopoles—305(A)
—— Properties of hypothetical atoms composed of magnetic poles—632(A)
Rubin, L. G. (see Davis, L., Jr.)—597(A)
Rubin, Robert J. Excluded-volume problem—642(T)
—— Quantum-mechanical molecular distribution functions in one-dimensional fluid composed of hard spheres—643(A)
Rumsey, V. H. Reaction concept in electromagnetic theory—1705(E)
Rushworth, F. A. Nuclear magnetic resonance in some solid hydrocarbons—608(A)
Russell, Leonard N., Warren E. Taylor, and John N. Cooper. γ radiation from Mg^{28} under proton bombardment—99
Russell, Paul N. Nonmetallic ferromagnetic materials—309(T)
Ruth, Ralph P. and James W. Moyer. Power efficiency for photovoltaic effect in Ge-grown junction—562(L)
Ryder, E. J., I. M. Ross, and D. A. Kleinman. Electron multiplication in Ge at low temperature—1342(L)

Sachs, R. G. Structure of nucleon. II. Pion-nucleon scattering—1065
Sagane, Ryokichi. Positrons from decay of μ mesons—660(T)
——, **Walter F. Dudziak, and James Vedder.** Positron spectrum from decay of μ meson—863(L)
Sakai, M., J. L. Dick, W. S. Anderson, and J. D. Kurbatov. Decay scheme of Co^{56}—101
Salant, E. O. (see Hill, R. D.)—1699(L)
Salpeter, E. E. (see Dyson, F. J.)—1644
Salzman, Freda F. and James N. Snyder. Numerical calculation of 3/2−3/2 pion-nucleon reaction matrix and phase shifts—286(L)
Salzman, G. and A. H. Taub. Born-type rigid motion in relativity—1659
Sampson, John L., Edward E. Altshuler, and Charles R. Mingins. Granular structure of $BaTiO_3$ ceramic—617(A)
——, **Edward E. Altshuler, and Robert W. Perry.** Replication of $BaTiO_3$ ceramic surfaces for electron microscopy—298(A)
Sampson, M. B. (see Miller, D. W.)—649(A)
Sands, Matthew, J. G. Teasdale, and Robert L. Walker. Negative-to-positive ratio of photomesons from deuterium—592(L)
Sands, R. H., J. Townsend, and H. P. Hood. Paramagnetic resonances in glasses—607(A)
Saraf, Babulal. Inner bremsstrahlung in A^{37} and Ge^{71}—612(A)
—— Inner bremsstrahlung in electron capture process—Ge^{71}—97
Sarles, L. R. (see Loeliger, H. R.)—291(L)
Sawamoto, K. (see Yamaka, E.)—848(L)
Sawyer, R. B. (see Clifford, Joseph M.)—665(A)
Saxon, David S. (see Woods, Roger D.)—577(L)
Schaeffer, Oliver A. and Henry R. Owen. Electron impact studies of isotopic O_2 and CO_2 molecules—615(A)
Schardt, A. W. (see Mihelich, J. W.)—1508
Scharff, Morris F. Moments of Na^{23}—1114(L)
—— Regularity in magnetic moments of odd nuclei—1112(L)
Scharff-Goldhaber, Gertrude and Michael McKeown. New isomers in Br and Cl—613(A)
Schawlow, A. L., B. T. Matthias, H. W. Lewis, and G. E. Devlin. Structure of intermediate state in superconductors—1344(L)
Schecter, L., W. E. Crandall, G. P. Millburn, and J. Ise. Cross section for producing high-energy neutrons from C targets bombarded by protons, deuterons, and He^3 particles—659(A)
—— (see Crandall, W. E.)—620(A)
—— (see Millburn, G. P.)—620(A); 1268
Schein, Marcel, D. M. Haskin, and R. G. Glasser. Narrow shower of pure photons at 100 000 feet—855(L)
Schenck, James (see Neiler, J. H.)—640(A)
Scherrer, V. E., B. A. Allison, and W. R. Faust. γ radiation from interaction of 3.1-Mev neutrons—637(A)
—— (see Shapiro, P.)—751
Schild, A. (see Dettman, J. W.)—631(A); 1057
Schluter, Robert A. Neutral pion-deuteron production in high-energy n-p collisions—639(A)
—— (see Wright, S. C.)—639(A)
Schmitt, Roman A. and Nathan Sugarman. U photofission yields—1260
Schneider, E. E. (see Cunnell, F. A.)—598(A)
—— (see Hesketh, R. V.)—598(A); 837(L)
Schumacher, R. T., T. R. Carver, and C. P. Slichter. Measurement of spin paramagnetism of conduction electrons—1089(L)
Schwarz, G. and G. L. Rogosa. Transmission of x-rays through calcite in Laue diffraction—950
Schwarzschild, A. (see Koerts, L.)—612(A)
Schweber, S. S. (see Dyson, F. J.)—1644
Schweitzer, W. G., Jr. (see Zahn, C. T.)—633(A)
Scolman, T. T. (see Collins, T. L.)—615(A)
Scott, D. W. (see Reynolds, H. L.)—671

Scott, F. R., D. B. Thomson, and W. Wright. Thermal neutron capture cross sections of hydrogen, B, and Ag—582(L)
Seaborg, G. T. (see Ghiorso, A.)—293(L)
Seagrave, J. D. (see Ribe, F. L.)—649(A)
Seeger, R. J. AEC research policies of National Science Foundation—299(T)
—— Role of physics in engineering education—309(T)
Segall, Benjamin. Nuclear shapes at half-filled shells—605(A)
Segrè, Emilio (see Chamberlain, Owen)—850(L); 1348(L); 1104(L); 1105(L)
—— (see Mihelich, J. W.)—1508
Seidl, F. G. P., D. J. Hughes, H. Palevsky, J. S. Levin, W. Y. Kato, and N. G. Sjöstrand. "Fast chopper" time-of-flight measurement of neutron resonances—476
Seliger, H. H. Transmission of monoenergetic positrons and electrons—610(A)
Selove, W. Pickup deuterons produced from 95-Mev protons—663(A)
Senitzky, I. R. Harmonic oscillator wave functions—1115
—— Quantum effects in interaction between electrons and high-frequency fields. I—904
Shaforth, S. M. and S. S. Hanna. Decay scheme and γ-γ correlations in B^{10}—86
—— **and S. S. Hanna.** γ-γ correlation in $Be^9(d,n)B^{10*}(\gamma)B^{10}$—641(A)
Shamos, Morris H. (see Fafarman, A.)—648(A)
—— (see Reier, Melvin)—636(A)
Shapiro, A. M., C. P. Leavitt, and F. F. Chen. Total p-p cross section above 400 Mev—663(A)
Shapiro, I. I. and J. M. Teem. Interpretation of scattering of high-energy nucleons by complex nuclei—619(A)
Shapiro, Maurice M. Recent results from study of cosmic rays with nuclear emulsions—299(T)
Shapiro, P., V. E. Scherrer, B. A. Allison, and W. R. Faust. n-γ coincidences produced by inelastic scattering of neutrons—751
Sharp, W. T. (see Kennedy, J. M.)—440
Sharpe, L. M. (see Hall, T.)—1208
Shatas, R. A. (see Marshall, J. F.)—634(A)
—— (see Pomerantz, M. A.)—633(A)
Shaw, C. H. (see Soules, Jack)—621(A)
Shaw, Harlan (see Cohen, David)—664(A)
Shelton, Essie M. (see Fuson, Nelson)—300(A)
Sheridan, Walter F. Rf mass spectrometer as rocket-borne instrument for atmospheric composition studies—298(A)
——, **J. A. Dillon, Jr., and S. N. Ghosh.** Experimental determination of charge transfer cross sections—635(A)
Shibuya, Motoichi. Magnetoresistance effect in cubic semiconductors with spheroidal energy surfaces—1385
Shimauchi, A. (see Kojima, S.)—1705(E)
Shinoda, Gunji, Tatsuro Suzuki, and Susumu Kato. Two types of band emission curves of Cu in soft x-ray region—840(L)
Shmoys, Jerry and Samuel N. Karp. Calculation of potential from transit time—656(A)
Shuler, W. E. (see Fletcher, William H.)—300(A)
Shull, Theodore (see Burgus, Warren H.)—750
Shure, K., P. A. Roys, and J. J. Taylor. Penetration of 6-Mev γ rays in Pb and Fe—610(A)
—— (see Roys, P. A.)—911
Shutt, R. P. (see Fowler, W. B.)—1026
Sidhu, S. S. (see Meneghetti, David)—666(A)
Siegel, M. (see Hall, T.)—1208
Siegel, R. T. (see Hartzler, A. J.)—185; 591(L)
Silver, E. G. and R. W. Waniek. Interactions of high-energy neutrons in Mo—586(L)
Silverman, A. (see Edwards, D. A.)—629(A)
Silverman, S. (see Lassettre, E. N.)—635(A)
Silvey, G. (see Hardy, W. A.)—385
Simmons, B. E. (see Holmgren, H. D.)—1544
Simmons, J. W. (see Slayton, George R.)—299(A)
Simon, Albert. High-speed computation of angular momentum functions—657(A)
Simpson, Arol (see Marton, L.)—634(A)
Simpson, J. A. (see Firor, J. W.)—1015
Simpson, O. D. Measurement of time jitter in BF_3 counters—600(A)
Singer, S. F. Storm decrease of cosmic radiation at pole—647(A)
Sippel, R. F. (see Bent, R. D.)—649(A)
Sjöstrand, N. G. (see Seidl, F. G. P.)—476
Skolnik, W. (see Marshall, J.)—1020
—— (see Nagle, D.)—663(A)
Sladek, Ronald J. Thermal conductivity of In-Tl alloys at liquid He temperatures—603(A)
Slater, J. C. (see Koster, G. F.)—1167
Slater, M. (see Blackstock, A. W.)—303(A)
Slawsky, Z. I. (see Dawson, J. M.)—614(A)
—— (see Jansen, L.)—614(A)
Slayton, George R., J. W. Simmons, and J. H. Goldstein. Microwave spectrum and dipole moment of vinylene carbonate—299(A)
Slichter, C. P. (see Schumacher, R. T.)—1089(L)
Smaller, B. (see Hennig, G. R.)—1088(L)
Smith, Alan W. Low-temperature thermal conductivity of Canadian natural graphite—1095(L)
—— (see Brown, H. N.)—626(A)
Smith, J. F. Electrostatic energy calculations for (Na_2WO_3)—1369
Smith, J. H. Nuclear scattering of high-energy electrons—271
—— (see Barton, M. Q.)—573(L)
—— (see Yamagata, T.)—574(L)
Smith, J. R. Scattering of 14.1-Mev neutrons in He, H, and N—730
Smith, Lyle. Research with Cosmotron—299(T)
Snelgrove, Philip, Jassim El-Hussaini, and Jesse W. M. DuMond. Corrected values of W K-series x-ray wavelengths with 2-meter curved crystal diffraction spectrometer—1203
Snell, Arthur H. and Frances Pleasonton. Magnetic spectrometer for recoil spectrometry—304(A)
Snyder, Conway W. and Vincent E. Parker. System for measuring flight times of fast neutrons—635(A)
Snyder, James N. (see Salzman, Freda F.)—286(L)
Solbrig, A. W., Jr. Effects of certain 3-body nuclear interactions in H^3 and He^3—831
Solt, I. H., Jr., and M. W. P. Strandberg. Conduction electron spin resonance absorption in Na—607(A)
Soules, Jack and C. H. Shaw. X-ray absorption in solid argon—621(A)
Spear, Vincent. New technique for visualizing thyroid outline using I^{131} and scintillation counter—308(A)
Spencer, L. V. Calculations on penetration of high-energy electrons—610(A)
Spicer, B. M., A. S. Penfold, and J. Goldemberg. Fine structure of $O^{16}(\gamma,n)O^{15}$ activation curve—629(A)
Spohr, D. A. and R. T. Webber. Electrical and thermal conductivity of Mg and Mg alloy at low temperatures—602(A)
Spry, W. J. Total cross section for charge exchange scattering of π^- mesons by H at 42, 30, and 20 Mev—1295
Squire, Charles F. Velocity of sound in superconducting Sn—1126
Stahl, R. H. n-p scattering at 91 Mev—664(A)
Stallwood, R. A. (see Fields, T. H.)—638(A)
—— (see Kane, J. A.)—662(A); 1694(L)
Standing, K. G. (see Reynolds, J. B.)—639(A)

Stanford, C. P., T. E. Stephenson, and S. Bernstein. Demonstration of neutron spin from Bloch-Alvarez-type experiment—302(A)
—— (see Roberts, L. D.)—105
Starner, J. W. (see Bunker, M. E.)—612(A)
—— (see Mize, J. P.)—627(A)
Stearns, M., M. B. Stearns, S. DeBenedetti, and L. Leipuner. Limits on π^0-meson mass from mesonic x-rays—1353(L)
—— (see Stearns, M. B.)—625(A)
Stearns, M. B., M. Stearns, L. Leipuner, and S. DeBenedetti. Energy measurements of meson x-rays—625(A)
—— (see Stearns, M.)—1353(L)
Steele, M. C. (see Babiskin, J.)—602(A)
—— (see Berlincourt, Ted G.)—603(A); 1421
Steenberg, N. R. Reorientation of aligned nuclei—605(A); 982
Steffen, Rolf M. Mixed $E1+M2$ γ transition in Nd^{144}—614(A)
Stehle, P. (see Gibson, G.)—657(A)
Stein, Irving. Completed quantum theory—632(A)
Stein, P. C. (see Myers, H.)—576(L)
Steinberg, E. P. and L. E. Glendenin. Radiochemical investigation of spontaneous fission of Cm^{242}—431
——, **L. E. Glendenin, M. G. Inghram, and R. J. Hayden.** Fine structure in U^{233} fission—867(L)
Steinberger, Jack and William Chinowsky. Charge exchange scattering of stopped π^- mesons in deuterium—623(A)
—— (see Chinowsky, William—623(A); 1561
—— (see Lokanathan, S.)—624(A)
Stelson, P. H. and E. C. Campbell. Cross section for excitation of Pb^{207m} by inelastic neutron scattering—301(A)
—— **and W. M. Preston.** Resonant states of Mg^{24} excited by protons on Na—974
Stephens, William E. (see Toms, M. Elaine)—629(A); 1209
Stephenson, T. E. (see Stanford, C. P.)—302(A)
Stern, A. W. Invariance and isotopic spin—632(A)
Stern, Martin O. (see Blaser, J.)—624(A)
—— (see Chamberlain, Owen)—1705(E)
Sternglass, E. J. Energy expenditure per ion pair in solids—609(A)
Sternheimer, R. M. Effect of atomic core on nuclear quadrupole coupling—736
—— Electronic polarizabilities of ions from Hartree-Fock wave functions—655(A)
—— Polarization of nucleons elastically scattered from nuclei—587(L)
Stevenson, M. L. (see Burgus, Warren H.)—750
—— (see Crawford, F. S., Jr.)—1112(L)
Stier, P. M., C. F. Barnett, and G. E. Evans. Electron capture and loss cross sections for protons—303(A)
—— (see Barnett, C. F.)—307(A)
Stix, Thomas H. Primary heavy nuclei—782
St. John, Robert M. and J. G. Winans. Motion of arc cathode spot in a magnetic field—634(A)
Stolovy, A. (see Pilcher, V. E.)—645(A)
Stone, W. G. and Lewis W. Cochran. Energy per ion pair for recoil atoms in methane—304(A)
Storrs, C. L. and D. H. Frisch. Scattering of 1.32-Mev neutrons by protons—1252
Strain, J. E. (see Lyon, W. S.)—1500
Straley, Joseph W. Intensity of infrared absorption bands in methylene chloride—300(A)
Strandberg, M. W. P. and M. Tinkham. Effects of deviation of O_3 from Hund (b)—623(A)
—— (see Davis, Charles F., Jr.)—607(A)
—— (see Peter, Martin)—622(A)
—— (see Posener, D. W.)—374
—— (see Solt, I. H., Jr.)—607(A)
—— (see Tinkham, M.)—622(A)
Stratton, T. F. (see Holmgren, H. D.)—1544
Straub, W. D. (see Davis, L., Jr.)—597(A)
Strauch, K. and W. F. Titus. Scattering of 96-Mev protons from light nuclei—854(L)
Straumanis, M. E. Remark concerning absolute value of Avogadro's number—566(L)
Stuart, R. V. (see Holmgren, H. D.)—1544
Studier, M. H. (see Friedman, A. M.)—1501
Sucher, J. and H. M. Foley. Relativistic and magnetic spin interactions in He-like atoms—966
Sugarman, Nathan, Robert B. Duffield, G. Friedlander, and J. M. Miller. Disintegration of bismuth by 2.2-Bev protons—1704(L)
—— (see Schmitt, Roman A.)—1260
Sugawara, Tadashi, Yoshika Masuda, Teinosuke Kanda, and Eizo Kanda. Nuclear magnetic resonance in solid hydrogen with various *ortho* concentrations—1355(L)
Sugihara, T. T. and I. Halpern. Energy dependence of some photonuclear reactions—630(A)
——, **R. H. Herber, W. E. Bennett, and C. D. Coryell.** Absence of K capture in decay scheme of Pb^{205}—298(A)
Sun, K. H., P. R. Malmberg, and F. A. Pecjak. Scintillation detector for thermal and epithermal neutrons—600(A)
Sundaresan, M. K. (see Dyson, F. J.)—1644
Sunyar, A. W. Lifetime measurements of fast $E2$ transitions in even-even nuclei—626(A)
——, **J. W. Mihelich, and M. Goldhaber.** Decay of Cs^{134m} (3.1 hr)—570(L)
—— (see Kraushaar, J. J.)—456
Suttle, A. D., Jr., and W. F. Libby. Natural radioactivity of Re—866(L)
Sutton, R. B. (see Fields, T. H.)—638(A)
—— (see Kane, J. A.)—662(A); 1694(L)
Suzuki, Tatsuro (see Shinoda, Gunji)—840(L)
Swann, C. P. and F. R. Metzger. Inelastic scattering of neutrons by Ba^{137} and Hg^{199}—636(A)
Swann, W. F. G. Acquirement of cosmic-ray energies by betatron action—646(A)
Swanson, R. A. (see Warshaw, S. D.)—649(A)
Swenson, C. A. (see Berman, R.)—311
Swetnick, Martin Jay. Cosmic-ray neutrons in water at altitude of 10 600 feet—793
Swihart, J. C. and F. J. Belinfante. Quantized linear theory of gravitation. II—630(A)
—— (see Belinfante, F. J.)—630(A)

Takeda, Gyo. Application of intermediate coupling theory to scattering of pseudoscalar mesons by a nucleon—1078
Talboy, J. H., Jr. (see Pohm, A. V.)—1523
Talley, Robert M. and Dorothy P. Enright. Photovoltaic effect in InAs—1092(L)
Talmi, I. and B. C. Carlson. Pairing effects in Coulomb energies of mirror nuclei—606(A)
—— (see Jancovici, B.)—289(L)
Tamor, S. Polarization effects in high-energy proton-deuteron scattering—620(A)
Taub, A. H. (see Salzman, G.)—1659
Tauc, J. Theory of thermoelectric power in semiconductors—1394
Taylor, H. W. (see Pringle, R. W.)—115
Taylor, J. C. Tamm-Dancoff method—1313
Taylor, J. G. V. (see Greenberg, L. H.)—1540
Taylor, J. J. (see Roys, P. A.)—911
—— (see Shure, K.)—610(A)
Taylor, T. I. (see Eisberg, R. M.)—659(A)
Taylor, Warren E. (see Russell, Leonard N.)—99
Taylor, William J. Lattice distortion and x-ray diffraction intensities in dilute solid solutions—666(A)

Teasdale, J. G. (see Sands, Matthew)—592(L)
Teem, J. M. and U. E. Kruse. Elastic proton-deuteron scattering at 95 Mev—664(A)
—— (Kruse, U. E.)—662(A)
—— (see Shapiro, I. I.)—619(A)
Teller, Edward. Classical field theory of nuclei—632(T)
Temmer, G. M. Coulomb excitation of nuclear energy levels by α particles—628(T)
—— (see Ambler, E.)—625(A)
—— (see Heydenburg, N. P.)—629(A); 861(L)
ter Haar, D. Atomic theory of λ transition in liquid He—633(T)
—— Atomic theory of liquid He—604(A)
—— λ transition of liquid He—895
—— (see Dempsey, E.)—651(A)
—— (see Green, C. D.)—643(A)
—— (see Neaves, A.)—596(A)
—— (see Ross, A. W.)—665(A)
Terrell, J. and D. M. Holm. Excitation function for $Fe^{56}(n,p)Mn^{56}$—650(A)
Teutsch, Werner B. and Vernon W. Hughes. Hfs of He^3 in metastable triplet state—1461
Thacher, H. C., Jr., and Paul B. Dorain. Dielectric constant of dioctyl phthalate smoke—615(A)
Thirring, W. E. Classical limit of pseudoscalar coupling—653(A)
—— (see Gell-Mann, M.)—1612
—— (see Goldberger, M. L.)—654(A)
Thomas, H. C. (see Graves, Ernest D.)—304(A)
Thomas, W. J. Orville (see Cox, John)—299(A)
Thompson, R. W., J. R. Burwell, H. O. Cohn, R. W. Huggett, and C. J. Karzmark. Magnetic cloud chamber observations of V-particles. II. Status of work on θ^0 meson—661(A)
——, **J. R. Burwell, R. W. Huggett, and C. J. Karzmark.** Evidence for double production of V^0 particles—1576
—— (see Kim, Y. B.)—661(A)
Thompson, S. G. (see Ghiorso, A.)—293(L)
—— (see Harvey, B. G.)—581(L)
—— (see Hulet, E. K.)—1703(L)
Thomson, D. B. (see Scott, F. R.)—582(L)
Thorndike, A. M. (see Fowler, W. B.)—1026
Ting, Yu and Dudley Williams. Intensities of Zeeman components of quadrupole transitions in $NaClO_3$—607(A)
Tinkham, M. and M. W. P. Strandberg. Selection rules in the microwave magnetic resonance spectrum of O_2—622(A)
—— (see Strandberg, M. W. P.)—623(A)
Tinlot, John. Polarization in neutron-proton collisions—644(T)
—— **and A. Roberts.** Angular distribution of charge-exchange scattering of 40-Mev π^- mesons by hydrogen—137
—— (see Roberts, A.)—663(A); 1099(L)
Tittman, Jay. Neutron moderation in SiO_2—660(A)
Titus, W. F. (see Strauch, K.)—854(L)
Tobias, Cornelius. Radiation and dynamics of cell division—606(T)
Tobocman, W. and M. Kalos. Numerical calculation of stripping angular distribution—605(A)
Todd, W. B. (see Metzger, F. R.)—627(A); 853(L)
Tomboulian, D. H. and P. L. Hartman. Spectral distribution curves of far uv radiation from Cornell synchrotron—600(A)
—— (see Bedo, D. E.)—621(A)
Toms, M. Elaine, H. Gerardo, and W. E. Stephens. Photoprotons from Co—629(A)
—— **and William E. Stephens.** Photoprotons from Co—1209
Torrey, H. C. (see Codrington, R. S.)—607(A)
Tousey, R. (see Johnson, F. S.)—621(A)
Townes, C. H. Recent applications of microwave spectroscopy to study of molecules—596(T)
—— (see Gordon, J. P.)—282(L)
Towns, M. B. (see Lawson, J. R.)—300(A)
Townsend, J. (see Sands, R. H.)—607(A)
Trail, Carroll C. and C. H. Johnson. Energy levels in Be^8 from $Li^7(d,n)Be^8$—1363(L)
—— **and C. H. Johnson.** Proton recoil telescope for observing neutron spectra—640(A)
Trainor, L. E. H. Phenomenological many-body exchange forces—801
Trambarulo, Ralph, Henry Lackner, Paul Moser, and Harold Feeny. Pressure broadening of cyanogen bromide in microwave region—622(A)
Trammell, G. T. Electron scattering from nuclei—619(A)
Treanor, Charles E. Isotope shift in neutral O—1472
Treiman, S. B. Radiative decay of θ^0 particle—1360(L)
—— **and M. Blume.** Galactic rf radiation and cosmic-ray electrons—646(A)
—— (see Firor, J. W.)—1015
Trilling, G. H. (see van Lint, V. A. J.)—295(L)
Tripp, Robert (see Chamberlain, Owen)—850(L); 1104(L); 1105(L)
Tsao, C. H. (see Orear, Jay)—624(A)
Tsukada, K. (see Kojima, S.)—1705(E)
Turchinetz, W. (see Pringle, R. W.)—115
Turkevich, Anthony (see Fung, Si-Chang)—176
Turner, C. M. Ionization loading of electrostatic generators—599(A)

Underwood, Newton and G. F. Zindler, Jr. Small current dc amplifier—304(A)
Urban, J. S. (see Howard, R. A.)—661(A)
Urquhart, H. M. A. and J. E. Goldman. Magnetostrictive effects in α-Fe_2O_3—653(A)

Van Allen, J. A. (see Ellis, R. A., Jr.)—304(A)
van der Kint, L. (see Beljers, H. G.)—1683(L)
van der Leun, C. (see Endt, P. M.)—580(L)
Van Hoomissen, J. E. (see Noyes, J. C.)—396
Van Hove, Léon. Correlations in space and time and Born approximation scattering in systems of interacting particles—249
—— Time-dependent correlations between spins and neutron scattering in ferromagnetic crystals—1374
van Lint, V. A. J., G. H. Trilling, R. B. Leighton, and C. D. Anderson. Q value of Λ^0 decay—295(L)
Van Roosbroeck, W. (see Pfann, W. G.)—597(A)
van Wieringen, J. S. (see Beljers, H. G.)—1683(L)
Varma, Jagdish. Radiations from Cd^{115} (43-days)—613(A)
Vasileff, H. D. Thermal ionization of impurities in polar crystals—618(A)
Vedder, James (see Sagane, Ryokichi)—863(L)
Visscher, W. M. (see Dyson, F. J.)—1644
Vogelsang, W. F. (see Levine, S. H.)—640(A)
Vogt, Erich and Gregory H. Wannier. Scattering of ions by polarization forces—1190
Voigt, A. F. (see Horrocks, D. L.)—1205
Voshage, H. (see Hintenberger, H.)—1691(L)
Voyvodic, L. Charged heavy mesons from nuclear collisions—661(A)

Wacker, Paul F. SCF treatment of unclosed shells, operators containing spin, and radial correlation—656(A)
Wada, W. Internal pair production in radiative absorption of π^- mesons by H atoms—618(A)
Waddell, Charles (see Cohen, David)—664(A)
Wahl, John S. Energy distribution of fragments from fission of U^{235}, U^{238}, and Pu^{239} by fast neutrons—126

Waldman, B. (see Bhattacherjee, S. K.)—404
—— (see Noyes, J. C.)—396
Walker, Robert L. (see Sands, Matthew)—592(L)
Walker, W. D., J. Crussard, and M. Koshiba. π^--p collisions at 1.5 Bev. I—624(A)
——, **J. Crussard, and M. Koshiba.** π-meson production in π-nucleon collisions at 1.5 Bev—852(L)
—— (see Crussard, J.)—624(A)
Wallis, R. F. (see Herman, R. C.)—598(A)
Walters, G. K. (see Fairbank, William M.)—566(L)
Wang, C. C. (see Levitas, A.)—846(L)
Wangsness, Roald K. Susceptibility tensor and Faraday effect in ferrimagnetics—339
Waniek, R. W. and Vaughn Culler. Total cross sections for high-energy neutrons—659(A)
—— (see Culler, Vaughn)—585(L)
—— (see Silver, E. G.)—586(L)
Wannier, Gregory H. (see Vogt, Erich)—1190
Warshaw, S. D., R. A. Swanson, and A. H. Rosenfeld. Cross sections for reactions $C^{12}(p,pn)(n,2n)C^{11}$—649(A)
Watanabe, Hiroshi. Energy losses of electrons passing through MgO foil—1684(L)
Watanabe, Satosi. Superselection rule regarding spinor particle numbers—631(A)
Watson, Kenneth M. Some general relations between photoproduction and scattering of π mesons—228
Watson, W. W. (see Collinson, J. A.)—621(A)
Wattenberg, A. (see Myers, H.)—576(L)
Waymouth, John F. and Francis Bitter. Experiments on electroluminescence—941
Weaver, A. B. (see Orear, Jay)—624(A)
Webber, R. T. (see Spohr, D. A.)—602(A)
Weber, J. Quantum theory of damped electrical oscillator and noise. II. Radiation resistance—1706(E)
Weddell, James B. and James H. Roberts. Angular distribution of $Li^6(n,\alpha)H^3$—117
—— (see Jennings, B.)—636(A)
Wegner, Harvey E. (see Farwell, George W.)—664(A); 1212
Weinreich, Gabriel and Vernon W. Hughes. Hfs of He^3 in metastable triplet state—1451
Weinstock, E. V. and J. Halpern. Systematics of photoproton yields—630(A)
Weiss, J. (see Bernstein, W.)—609(A)
Welker, Joan P. (see Perlman, Morris L.)—133; 613(A)
Welton, T. A. Formulation of quantum electrodynamics in Minkowski space—632(A)
—— Theory of nuclear reactions with radioactive product—302(A)
Wertheim, M. S. (see Igo, G.)—1097(L)
Westendorp, W. F. (see Baldwin, G. C.)—600(A)
Wexler, S. (see Goodman, L. S.)—570(L)
—— (see Ringo, G. R.)—660(A)
Whalin, E. A., Jr. Photodisintegration of deuterium by 165-Mev x-rays—1362(L)
Wheatley, G. H. (see Hrostowski, H. J.)—1683(L)
White, M. G. (see Yntema, J. L.)—1226
Whittemore, W. L. (see Fowler, W. B.)—1026
Whyte, G. N. (see Garrett, C.)—889
Wick, G. C. Properties of Bethe-Salpeter wave functions—653(A)
Widgoff, M. (see Hill, R. D.)—1699(L)
Wiedenbeck, M. L. (see Beard, George)—1246
—— (see Lu, D. C.)—121; 1533
Wiegand, Clyde. High-energy experiments on polarization of protons—644(T)
—— (see Chamberlain, Owen)—850(L); 1348(L); 1104(L); 1105(L)
Wigner, Eugene P. (see Redlich, Martin G.)—122
Wilcox, J. M. and B. J. Moyer. Nuclear internal momentum distributions—664(A)
Wilkinson, R. G. (see Pruett, C. H.)—625(A)
Wilks, J. (see Fairbank, Henry A.)—277(L)
Willard, D. Momentum of S-particle secondaries—661(A)
—— (see Bridge, H. S.)—662(A)
Willard, Harvey B. Elastic scattering angular distributions and polarization of fast neutrons—299(T)
——, **Joe K. Bair, and Joe D. Kington.** Polarization of fast neutrons from nuclear reactions—1359(L)
Willardson, R. K., T. C. Harman, and A. C. Beer. Application of three-carrier model to Hall effect in Ge—597(A)
—— (see Harman, T. C.)—596(A); 699
Williams, A. J. (see McSkimin, H. J.)—616(A)
Williams, Dudley (see Brown, L. Carlton)—1110(L)
—— (see Ting, Yu)—607(A)
Williams, Ferd E. (see Johnson, Peter D.)—69; 598(A)
Williams, Jack H. and C. F. Mercer. Seismology in southeast—306(A)
—— (see Johnston, L. H.)—599(A)
Williams, M. C. (see Herman, R. C.)—598(A)
Williams, Robert W. Nuclear size and cross sections at cosmic-ray energies—647(A)
Williamson, R. M. (see Goldburg, W. I.)—628(A); 767
Wilson, R. N. (see Yennie, D. R.)—500
Wilson, R. R. (see Jenkins, T. L.)—179
Wilson, V. C. and J. S. Kasper. Neutron diffraction studies of NiZn ferrite—1408
Winans, J. C. (see St. John, Robert M.)—634(A)
Wing, G. M. (see Lehner, J.)—642(A)
Winhold, E. J. (see Burkhardt, J. L.)—629(A)
Winnemore, B. J., H. Gursky, D. A. Cowan, and C. D. Curtis. Further study of Po-Be neutron spectrum—301(A)
Winsberg, Lester. Interaction of negative muons with iodine—205
—— Interaction of negative pions with iodine—198
Witmer, Enos E. Formula for nuclear masses in terms of electron mass involving only rational numbers for light nuclei—610(A)
—— Nuclear masses as rational multiples of electron mass—667(A)
Wolfe, B. (see Edwards, D. A.)—629(A)
Wolfe, H. B. (see Lokanathan, S.)—624(A)
Wolfenstein, Lincoln. Theoretical considerations about polarization experiments—644(T)
Wolff, P. A. Theory of electron multiplication in Si and Ge—1415
—— Theory of secondary electron cascade in metals—56
Wollan, E. O. (see Koehler, W. C.)—280(L); 653(A)
Wong, Calvin. β decay of F^{17} and C^{11}—765
—— β decay of F^{20}—761
Wood, R. E. Eu activation studies with monochromatic neutrons—453
—— Resonance scattering of Ag and Au—644(A)
Woods, Roger D. and David S. Saxon. Diffuse surface optical model for nucleon-nuclei scattering—577(L)
Wright, S. C. and R. A. Schluter. Negative pion production in n-p collisions—639(A)
Wright, W. (see Scott, F. R.)—582(L)
Wu, C. S. (see der Mateosian, E.)—458
—— (see Koerts, L.)—612(A)
—— (see Marder, S.)—611(A)
Wyly, L. D. (see Braden, C. H.)—627(A); 758

Yager, W. A. (see Fletcher, R. C.)—844(L)
Yagoda, Herman. Ratio of π^-/π^+ meson production in cosmic-ray disintegrations of emulsion nuclei—648(A)
Yamagata, T., M. Q. Barton, A. O. Hanson, and J. H. Smith. Photodisintegration of deuterium by 265-Mev bremsstrahlung—574(L)

Yamaguchi, Yoriko and Yoshio Yamaguchi. Factorable neutron-proton interaction—654(A)
—— (see Yamaguchi, Yoshio)—1635
Yamaguchi, Yoshio. 2-nucleon problem when potential is nonlocal but separable. I—1628
—— **and Yoriko Yamaguchi.** 2-nucleon problem when potential is nonlocal but separable. II—1635
—— (see Yamaguchi, Yoriko)—654(A)
Yamaka, E. and K. Sawamoto. Electrical conductivity of MgO single crystals—848(L)
Yang, C. N. and R. Mills. Isotopic spin conservation and generalized gauge invariance—631(A)
Yasaitis, E. L. (see Hennig, G. R.)—1088(L)
Yasaki, T. (see Inoki, M.)—1565
Yearian, H. J., J. M. Kortright, and R. H. Langenheim. Lattice parameters of $FeFe_{(2-\rho)}Cr_\rho O_4$ spinel system—653(A)
Yeater, M. L. (see Albert, R. D.)—644(A)
Yennie, D. R., D. G. Ravenhall, and R. N. Wilson. Phase shift calculation of high-energy electron scattering—500
Yergin, Paul F. (see Ferguson, G. A.)—659(A); 776
—— (see Geller, K.)—659(A)
—— (see Halpern, J.)—1529
Yevick, George J. and Jerome K. Percus. Dynamical behavior of collective coordinates in new approach to many-body problem—642(A)
—— (see Percus, Jerome K.)—642(A)
Yntema, J. L. and M. G. White. Scattering of protons by H near 18 Mev—1226
Yokota, Ryosuke. Color centers in alkali silicate and borate glasses—1145
York, Carl M., Jr., R. B. Leighton, and E. K. Bjørnerud. Cloud-chamber study of charged V particles—159
York, H. F. (see Burgus, Warren H.)—750
Young, D. R. (see Drougard, M. E.)—1152
Ypsilantis, Thomas (see Chamberlain, Owen)—850(L); 1104(L); 1105(L)
Yuan, Luke C. L. (see Lindenbaum, S. J.)—638(A)

Zaffarano, D. J. (see Hunt, W. A.)—611(A)
Zahn, C. T. and Schweitzer, W. G., Jr. Excitation and separation of pure high-order modes in large high-Q cavities—633(A)
Zeiger, H. J. (see Dexter, R. N.)—557(L); 597(A)
—— (see Gordon, J. P.)—282(L)
—— (see Lax, Benjamin)—597(A)
Zemach, A. C. and R. J. Glauber. Spin correlations in neutron scattering by gases—605(A)
Zendle, B. (see Boag, J.)—608(A)
Zimmerman, Robert L., David H. Frisch, and Daniel I. Cooper. p-p scattering near interference minimum—662(A)
Zindler, G. F., Jr. (see Underwood, Newton)—304(A)
Zirkle, R. E. Effects of irradiating small fractions of individual dividing cells—606(T)
Zissis, G. J. (see Deverall, G. V.)—1463
Zucker, A. (see Reynolds, H. L.)—302(A); 671; 1353(L)
Zweifel, Paul F. Second-order corrections to β spectra—112
—— **and H. Hurwitz, Jr.** Slowing-down of neutrons in hydrogenous moderators—660(A)

PHYSICAL REVIEW VOLUME 95, NUMBER 6 SEPTEMBER 15, 1954

Analytic Subject Index to Volume 95

References with (A) are to abstracts of papers presented at meetings of the American Physical Society; references with (L) are to Letters to the Editor; references with (E) are to Errata. Items are listed under the following categories.

Acoustics
Astrophysics
Atomic and Molecular Beams
Atomic Mass and Abundance
Atomic Structure and Spectra
Biophysics
Chemical Effects and Properties
Constants, Standards, Units
Cosmic Radiation
Crystalline State
Dielectrics and Dielectric Properties
Diffraction
Diffusion
Elasticity and Plasticity
Electrical Conductivity and Resistance
Electrical Discharges
Electrical Properties
Electromagnetic Theory and Electrodynamics
Electrons and Positrons
Elementary Particle Interactions
Errata
Field Theory
Films, Properties
Fluid Dynamics
Gamma Rays
Gases
Geophysics
Helium, Liquid
Imperfections in Solids
Ionization
Ions
Ions and Electrons, Mobility
Liquids
Luminescence
Magnetic Properties
Magnetic Resonance
Mathematical Methods
Mechanics
Mesons
Methods and Instruments
Microwaves
Miscellaneous
Molecular Aggregates
Molecular Structure and Spectra
Neutrino
Noise
Nuclear Fission
Nuclear Moments and Spin
Nuclear Photoeffects
Nuclear Reactions, General
Nuclear Reactions Induced by α Particles and He^3
Nuclear Reactions Induced by Deuterons and Tritons
Nuclear Reactions Induced by Mesons
Nuclear Reactions Induced by Neutrons
Nuclear Reactions Induced by Protons
Nuclear Spectra
Nuclear Structure Theory
Optical Properties
Proceedings of the American Physical Society
Quantum Electrodynamics
Quantum Mechanics
Radiation
Radioactivity
Range and Energy Loss
Relativity and Gravitation
Scattering, General
Scattering of α Particles
Scattering of Deuterons
Scattering of Electrons and Positrons
Scattering of Mesons
Scattering of Neutrons
Scattering of Protons
Semiconductors
Spectra, General
Statistical Mechanics and Thermodynamics
Superconductivity
Thermal Properties
X-Rays

Absorption of Radiation (see **Radiation**)
Acoustics
Ultrasonic measurements in magnetically cooled He, C. E. Chase and Melvin A. Herlin—565(L)
Velocity of sound in superconducting Sn, Charles F. Squire—1126
Adsorption (see **Gases**)
Aerodynamics (see **Fluid Dynamics**)
Afterglow (see **Electrical Discharges**)
Alloys (see **Crystalline State**)
Annihilation (see **Electrons and Positrons**)
Antiferroelectric Phenomena (see **Dielectrics and Dielectric Properties**)
Antiferromagnetism (see **Magnetic Properties**)
Arcs (see **Electrical Discharges**)
Astrophysics
Acquirement of cosmic-ray energies by betatron action, W. F. G. Swann—646(A)
Dimensional relations in magnetohydrodynamics, Walter M. Elsasser—1
Extension of extreme ultraviolet solar spectrum, F. S. Johnson, J. D. Purcell, and R. Tousey—621(A)
Galactic rf radiation and cosmic-ray electrons, S. B. Treiman and M. Blume—646(A)
Production of cosmic radiation at sun, J. W. Firor, J. A. Simpson, and S. B. Treiman—1015
Red-shifts in spectra of celestial bodies, E. Finlay-Freundlich—654(A)
Solar-connected variations of cosmic rays, P. Morrison—646(A)
Theory of aurora based on magnetic self-focusing of solar ion streams, W. H. Bennett and E. O. Hulburt—315
Atmosphere (see **Geophysics**)
Atomic and Molecular Beams
Distribution of velocities in K molecular beams, A. Bennett—608(A)
Hfs and nuclear moments of stable Br isotopes, John Gordon King and Vincent Jaccarino—1706(E)
Hfs of He^5 in metastable triplet state, Werner B. Teutsch and Vernon W. Hughes—1461; Gabriel Weinreich and Vernon W. Hughes—1451
Nuclear spin and hfs interaction of 3.1-hr Cs^{134} isomer, V. W. Cohen and D. A. Gilbert—569(L)
Nuclear spin and magnetic moment of 3.1-hr Cs^{134m}, L. S. Goodman and S. Wexler—570(L)
Spins and hyperfine splittings of Ag^{111} and Cu^{64}, Aaron Lemonick and Francis M. Pipkin—1356(L)
Atomic Mass and Abundance
$A^{40}(\gamma,n)$ threshold and mass of A^{39}, J. Halpern, R. Nathans, and P. F. Yergin—1529
Formula for nuclear masses in terms of electron mass involving only rational numbers for light nuclei, Enos E. Witmer—610(A)
Mass differences for isobars capable of double-β decay, John T. McCarthy—447
Microwave spectrum of TeCS and masses of stable Te isotopes, W. A. Hardy and G. Silvey—385
Nuclear masses as rational multiples of electron mass, Enos E. Witmer—667(A)
Precision double-focusing mass spectrometer, T. L. Collins, T. T. Scolman, and A. O. Nier—615(A)
Atomic Structure and Spectra
Angular dependence of annihilation quanta from magnetic substates of triplet positronium, R. M. Drisko—611(A)
Approximate Hartree type wave functions and matrix elements for K and L shells of atoms and ions, R. E. Meyerott—72
Effect of angular dependence of annihilation radiation of orthopositronium in magnetic field, S. Marder, V. W. Hughes, and C. S. Wu—611(A)
Effect of atomic core on nuclear quadrupole coupling, R. M. Sternheimer—736
Electron spin magnetic moment in atomic hydrogen, R. Beringer and Mark A. Heald—1474
Energy measurements of meson x-rays, M. B. Stearns, M. Stearns, L. Leipuner, and S. DeBenedetti—625(A)
Experimental study of μ^- meson mass and vacuum polarization in mesonic atoms, S. Koslov, V. Fitch, and J. Rainwater—291(L)
Hfs of He^5 in metastable triplet state, Werner B. Teutsch and Vernon W. Hughes—1461; Gabriel Weinreich and Vernon W. Hughes—1451
Intensity measurements of resonance lines in flame source, Einar Hinnov and Hedwig Kohn—301(A)
Ionization probability curves near threshold for Zn, Cd, and Hg, W. M. Hickam—703
Isotope shift in Li I spectrum, Raymond H. Hughes—621(A)
Isotope shift in neutral C, J. P. Nicklas—1469
Isotope shift in neutral O, Charles E. Treanor—1472
Isotope shift in x-ray spectra of heavy elements, G. Igo and M. S. Wertheim—1097(L)
Limits on π^- meson mass from mesonic x-rays, M. Stearns, M. B. Stearns, S. DeBenedetti, and L. Leipuner—1353(L)
Mass of μ^- meson from mesonic x-rays, S. Koslov, V. Fitch, and J. Rainwater—625(A)
Nuclear rotational levels and μ mesonic atom, B. A. Jacobsohn—654(A)
Nuclear spin and hfs interaction of 3.1-hr Cs^{134} isomer, V. W. Cohen and D. A. Gilbert—569(L)
Nuclear spin and magnetic moment of 3.1-hr Cs^{134m}, L. S. Goodman and S. Wexler—570(L)
Photoelectric measurement of reversal temperature, Hedwig Kohn and Einar Hinnov—301(A)
Physical consequences of vacuum polarization, Leslie L. Foldy and Erik Eriksen—1048
Precision wavelength and isotopic shift measurements of Ge arc lines, G. V. Deverall, K. W. Meissner, and G. J. Zissis—1463
Pressure shift in He λ5875, John R. Holmes and Leon Pape—621(A)
Properties of hypothetical atoms composed of magnetic poles, Arthur E. Ruark—632(A)
Relativistic and magnetic spin interactions in He-like atoms, J. Sucher and H. M. Foley—966
Relativistic Thomas-Fermi atom model, J. J. Gilvarry—71
Spectroscopic isotope shift in Hf I and Hf II, J. A. Collinson and W. W. Watson—621(A)
Two-body system in quantum electrodynamics. Energy levels of positronium, Thomas Fulton and Paul C. Martin—811
Uv photons in decay of metastable A atoms, L. Colli—892
X-rays from π mesonic atoms, A. D. McGuire, M. Camac, M. L. Halbert, and J. B. Platt—625(A)
Aurora (see **Astrophysics; Geophysics**)

Barkhausen Effect (see **Magnetic Properties**)
Biophysics
Applications of NaI γ-ray spectrometer to blood volume determinations, R. H. Rohrer, W. H. Cargill, and A. F. Dratz—308(A)
New technique for visualizing thyroid outline using I^{131} and scintillation counter, Vincent Spear—308(A)
Rheological problem, Allen L. King—298(A)
Use of scintillation counters in studies on luminous efficiency of biological materials, J. G. Kereiakes and A. T. Krebs—308(A)
Boson Theory (see **Field Theory**)
Bremsstrahlung (see **Radiation**)

Broadening of Spectral Lines (see **Atomic Structure and Spectra; Molecular Structure and Spectra; Spectra, General**)

Capture Cross Sections (see **Electrons and Positrons; Nuclear Reactions; Radiation**)
Čerenkov Effect (see **Radiation**)
Chemical Effects and Properties
Double bond character of C—Cl bond, R. Bersohn—614(A)
Electron impact studies of isotopic and CO_2 molecules, Oliver A. Schaeffer and Henry R. Owen—615(A)
General method for high-speed machine computation of ideal gas thermal properties. Diatomic free radicals of isotopic hydrides, Lester Haar and A. S. Friedman—614(A)
Origin of N_2O in atmosphere, P. Harteck and S. Dondes—320
Photolysis of para-diazo-N, N-dimethylaniline ZnCl dihydrate, Alnert Baril, Jr.—306(A)
Role of principal quantum number (n) in calculation of radii of ions with low (1^+,2^+,3^+,4^+) valence, N. Efremov—614(A)
Chemical Reactions (see **Chemical Effects and Properties**)
Chemiluminescence (see **Luminescence**)
Cold Emission (see **Electrical Properties**)
Colloids (see **Chemical Effects and Properties; Molecular Aggregates**)
Compton Effect (see **Radiation**)
Conductivity, Electrical (see **Electrical Conductivity and Resistance**)
Conductivity, Thermal (see **Thermal Properties**)
Constants, Standards, Units
Avogadro's number, M. E. Straumanis—566(L)
Effect of temperature scales on low-temperature calorimetric data, J. R. Clement—601(A)
Standards for thermal neutron capture measurements, G. R. Ringo and S. Wexler—660(A)
Cosmic Radiation
Acquirement of cosmic-ray energies by betatron action, W. F. G. Swann—646(A)
Anomalous event observed in photographic emulsion, J. H. Noon, M. F. Kaplon, and J. Crussard—1103(L)
Atmospheric temperature effect for mesons far underground, P. Barrett, G. Cocconi, Y. Eisenberg, and K. Greisen—1573
Čerenkov counter measurement of fast multiply charged cosmic rays, John Linsley—647(A)
Charged heavy mesons from nuclear collisions, L. Voyvodic—661(A)
Cloud-chamber study of charged V particles, Carl M. York, R. B. Leighton, and E. K. Bjørnerud—159
Cosmic radiation at very high altitudes near geomagnetic equator, Martin A. Pomerantz—531
Cosmic-ray μ-meson low-energy differential range spectrum, A. Fafarman and M. H. Shamos—648(A)
Cosmic-ray neutrons in water at altitude of 10 600 feet, Martin Jay Swetnick—793
Cross sections for meson-induced stars in Ilford G5 nuclear emulsions, Leonard A. Mann, Ray A. Grandey, and Arnold F. Clark—648(A)
Decay of heavy neutral particle, R. A. Howard, P. M. Fitzpatrick, H. E. Hoffman, and J. S. Urban—661(A)
Diurnal variations of intensity of cosmic rays far underground, P. Barrett, G. Cocconi, Y. Eisenberg, and K. Greisen—1571
Evidence for double production of V^0 particles, R. W. Thompson, J. R. Burwell, R. W. Huggett, and C. J. Karzmark—1576
Flux of primary heavy nuclei at equator, R. F. Hourd, J. R. Fleming, and J. J. Lord—647(A)
Fragmentation of heavy primary nuclei into light elements, J. H. Noon and M. F. Kaplon—647(A)
Galactic rf radiation and cosmic-ray electrons, S. B. Treiman and M. Blume—646(A)
Heavy unstable particles in stripped emulsions, J. Crussard, M. F. Kaplon, J. Klarmann, and J. H. Noon—584(L)
Influence of earth's magnetic field on extensive air showers, Giuseppe Cocconi—1705(E)
Interaction of heavy primaries in Pb, Y. Eisenberg—647(A)
Ionization chamber measurements at 10 600 feet of absorption of N component in carbon and hydrocarbon, Robert H. Rediker—526
Low-energy events, L. Reiffel and G. M. Burgwald—1294
Low-momentum end of spectrum of heavy primary cosmic rays, R. A. Ellis, Jr., M. B. Gottlieb, and J. A. Van Allen—304(A)
Magnetic cloud-chamber observation of V particles. I. Charged V particles, Y. B. Kim, J. R. Burwell, H. O. Cohn, C. J. Karzmark, and R. W. Thompson—661(A); II. Status of work on θ^0 meson, R. W. Thompson, J. R. Burwell, H. O. Cohn, R. W. Huggett, and C. J. Karzmark—661(A)
Mass measurements of slow cosmic-ray mesons, M. Inoki, T. Yasaki, and Y. Matsukawa—1565
Meson showers and high-energy interactions in light and heavy nuclei, R. W. Parsons, Françoise A. Brisbout, and V. D. Hopper—193
Momentum of S-particle secondaries, D. Willard—661(A)
Narrow shower of pure photons at 100 000 feet, Marcel Schein, D. M. Haskin, and R. G. Glasser—855(L)
Nuclear absorption of negative K particles, Herbert DeStaebler, Jr.—1110(L)
Nuclear size and cross sections at cosmic-ray energies, Robert W. Williams—647(A)
Observations on high-energy soft cascade, M. Koshiba and M. F. Kaplon—647(A)
Pairs formed by bremsstrahlung of great energy. I. Experimental, D. T. King and M. M. Block—648(A); II. Theoretical separation distribution, M. M. Block and D. T. King—648(A)
Possible example of annihilation of heavy particle, H. S. Bridge, H. Courant, H. DeStaebler, Jr., and B. Rossi—1101(L)
Primary α particles near geomagnetic equator, Martin A. Pomerantz—1691(L)
Primary cosmic-ray spectrum deduced from analysis of jets, A. Engler and U. Haber-Schaim—1700(L)
Primary heavy nuclei, Thomas H. Stix—782
Production of cosmic radiation at sun, J. W. Firor, J. A. Simpson, and S. B. Treiman—1015
Production of V^0 particles in Cu, D. R. Harris and A. L. Hodson—661(A)
Ratio of π^-/π^+ meson production in cosmic-ray disintegrations of emulsion nuclei, Herman Yagoda—648(A)
Recent results on S particles, H. S. Bridge, H. Courant, B. Dayton, H. C. DeStaebler, Jr., B. Rossi, and D. Willard—662(A)
Sea level mesons stopped in thin Pb and Al foils. I. Possible emission of charged nuclear particles and related events, W. Y. Chang—1282; II. Low-energy (1–5 Mev) γ rays, W. Y. Chang—1288
Simplifying approximation for determining cascade shower distributions, Bayard Rankin—657(A)
Solar-connected variations of cosmic rays, P. Morrison—646(A)

Cosmic Radiation (Continued)
Storm decrease of cosmic radiation at pole, S. F. Singer —647(A)
Unstable particles in photographic emulsion, M. F. Kaplon, J. Crussard, J. Klarmann, and J. Noon—660(A)
Unusual cosmic-ray event, H. C. DeStaebler, Jr., H. S. Bridge, H. Courant, and B. Rossi—662(A)
Cosmology (see **Astrophysics; Relativity and Gravitation**)
Critical Potentials (see **Atomic Structure and Spectra; Molecular Structure and Spectra**)
Cross Section (see **Electrons and Positrons; Nuclear Reactions; Radiation; Scattering**)
Crystal Counters (see **Methods and Instruments**)
Crystalline State (see also **Electrical Properties; Imperfections in Solids; Magnetic Properties; Semiconductors;** etc.)
Aging of crushed Si and Ge powders, Selma B. Brody—298(A)
Analysis of Forbes bar method for measuring thermal conductivity of metals, Joseph M. Clifford and R. B. Sawyer—665(A)
Anisotropy of fluorescence of some organic crystals, S. C. Ganguly and N. K. Chaudhury—1148
Approximate correlation potential, Joseph Callaway—656(A)
Avogadro's number, M. E. Straumanis—566(L)
Axial ratios in hexagonal metals, J. W. McClure—665(A)
Calculation of electrostatic lattice potentials, including ionic overlap, Joseph Birman—618(A)
Calculation of wavefunctions in symmetrical crystalline field, Paul H. E. Meijer—1443
Comparison of various approximate exchange potentials, Frank Herman, Joseph Callaway, and Forman S. Acton —371
Correlation techniques for testing Born-von Karman theory of specific heats, W. C. Overton, Jr., and J. R. Clement —602(A)
Counting lattice frequencies, Herbert B. Rosenstock—617(A)
Diffusion of Co^{60} in Ni-Al alloys containing excess vacancies, A. E. Berkowitz, F. E. Jaumot, Jr., and F. C. Nix —1185
Electron-electron scattering in alkali metals, Elihu Abrahams—839(L)
Electronic energy of ordered alloys, Edward W. Hart—666(A)
Electronic quadrupole-quadrupole interactions in Ce metal, J. M. Keller and E. Koenigsberg—665(A)
Electrostatic energy calculations for (Na_xWO_3), J. F. Smith—1369
Energy losses of electrons passing through MgO foil, Hiroshi Watanabe—1684(L)
Equation of state and thermal dependence of elastic coefficients of crystalline argon, John H. Henkel—617(A)
Evaporated multiple layers with semiconductor properties, J. C. M. Brentano and J. D. Richards—841(L)
Granular structure of $BaTiO_3$ ceramic, John L. Sampson, Edward E. Altshuler, and Charles R. Mingins—617(A)
Growth of CdI_2 crystals, J. B. Newkirk—616(A)
Influence of covalence on ion ordering and distortion in spinels, A. L. Loeb and J. B. Goodenough—616(A)
Interaction of electrons with grain boundaries, M. H. Cohen and C. S. Barrett—1094(L)
Ionic conductivity and x-ray coloration of alkali halides, F. A. Cunnell and E. E. Schneider—598(A)
K-absorption edge studies of compounds, H. P. Hanson and J. R. Knight—621(A)
L-absorption spectrum of Si and SiO_2, D. E. Bedo and D. H. Tomboulian—621(A)
Lattice distortion and x-ray diffraction intensities in dilute solid solutions, William J. Taylor—666(A)
Lattice parameters of $FeFe_{(2-x)}Cr_xO_4$ spinel system, H. J. Yearian, J. M. Kortright, and R. H. Langenheim—653(A)
Low-temperature bleaching and restoration of color centers, A. Halperin and G. F. J. Garlick—1098(L)
Low-temperature thermal conductivity of Canadian natural graphite, Alan W. Smith—1095(L)
Magnetic neutron diffraction from Fe_3O_4, A. W. McReynolds and T. Riste—1161
Metamict state, William Primak—837(L)
Minimum in electrical resistance of metals at low temperatures, A. B. Bhatia—914
Neutron diffraction studies of NiZn ferrite, V. C. Wilson and J. S. Kasper—1408
Neutron diffraction study of Cu-Mn system, David Meneghetti and S. S. Sidhu—666(A)
New absorption lines of crystals in submicrowave region, S. Kojima, K. Tsukada, S. Ogawa, and A. Shimauchi —1705(E)
Paramagnetic and diamagnetic susceptibility of conduction electrons, David Pines—1090(L)
Paramagnetic resonance absorption in soft carbon, J. G. Castle, Jr.—846(L)
Periodic impurities in periodic lattice, Edward H. Kerner —687
Possible macroscopic effects of single lattice defects, Jerome Rothstein—370
Propagation of displacement in solid, having crystalline structure with bistable states, C. F. Pulvari—617(A)
Properties of Ge-Si alloys, Everett R. Johnson and Schuyler M. Christian—560(L)
Role of low-energy phonons in thermal conduction, Conyers Herring—954
SCF treatment of unclosed shells, operators containing spin, and radial correlation, Paul F. Wacker—656(A)
Shape of *F* band, R. V. Hesketh and E. E. Schneider—837(L)
Small angle x-ray scattering from cold-worked Al-Ag and Al-Zn alloys, J.-P. Jan and J. S. Koehler—665(A)
Solid surface studies by total reflection of x-rays, L. G. Parratt—617(A)
Specific heats of metals below one degree absolute, John Rayne—1428
Surface studies of solids by total reflection of x-rays, L. G. Parratt—359
Temperature variation of mean Debye temperature of Cu_3Au, 20°C to 450°C, S. L. Quimby—916
Temperature variations of elastic constants of Cu single crystals from 4.2°K to 300°K, John Gaffney and W. C. Overton, Jr.—602(A)
Theory of domain creation and coercive force in polycrystalline ferromagnetics, John B. Goodenough—917
Theory of scattering in solids, G. F. Koster—1436
Thermal ionization of impurities in polar crystals, H. D. Vasileff—618(A)
Thermal restoration of color centers at low temperature, R. V. Hesketh and E. E. Schneider—598(A)
Thermoelectric power and electron scattering in metal alloys, C. A. Domenicali and F. A. Otter—1134
Two types of band emission curves of Cu in soft x-ray region, Gunji Shinoda, Tatsuro Suzuki, and Susumu Kato—840(L)
Vacancies and interstitials in heat-treated Ge, Sumner Mayburg—38
Vibration spectra of crystal lattices, Melvin Lax and Joel L. Lebowitz—617(A)
Volume changes in substitutional alloys, A. W. Ross and D. ter Haar—665(A)

Wave functions for impurity levels, G. F. Koster and J. C. Slater—1167
X-ray absorption in solid argon, Jack Soules and C. H. Shaw—621(A)
X-ray production of F centers in NaCl and LiF, R. C. Herman, L. L. Mador, R. F. Wallis, and M. C. Williams —598(A)

Diamagnetism (see **Magnetic Properties**)
Dielectrics and Dielectric Properties
Dielectric constant behavior of single-domain single crystals of $BaTiO_3$ in vicinity of Curie point, M. E. Drougard and D. R. Young—1152
Dielectric constant of dioctyl phthalate smoke, H. C. Thacher, Jr., and Paul B. Dorain—615(A)
Domain formation and domain wall motions in ferroelectric $BaTiO_3$ single crystals, Walter J. Merz—690
Electromagnetic scattering by dielectric bodies, Marshall H. Cohen—657(A)
Electronic polarizabilities of ions from Hartree-Fock wave functions, R. M. Sternheimer—655(A)
Granular structure of $BaTiO_3$ ceramic, John L. Sampson, Edward E. Altshuler, and Charles E. Mingins—617(A)
Kinetic properties of domains in Rochelle salt, Toshio Mitsui and Jiro Furuichi—558(L)
Molar polarization, dipole moment, and nonideality of trichloroheptafluorobutane vapor, D. W. Magnuson—301(A)
Plastic flow and low-frequency dispersion in alkali halide crystal, Masakazu Ishiguro, Fujio Oda, and Takuzo Fujino—1347(L)
Propagation of displacement in a solid, having a crystalline structure with bistable states, C. F. Pulvari—617(A)
Diffraction (see also **Scattering**)
Lattice distortion and x-ray diffraction intensities in dilute solid solutions, William J. Taylor—666(A)
Magnetic neutron diffraction from Fe_3O_4, A. W. McReynolds and T. Riste—1161
Neutron diffraction studies of NiZn ferrite, V. C. Wilson and J. S. Kasper—1408
Neutron diffraction study of Cu-Mn system, David Meneghetti and S. S. Sidhu—666(A)
Neutron magnetic diffraction studies of La, Ca manganites, W. C. Koehler and E. O. Wollan—653(A)
Search for antiferromagnetism in V_3Si, Cr_3Si, and Mo_3Si, W. C. Koehler and E. O. Wollan—280(L)
Transmission of x-rays through calcite in Laue diffraction, G. Schwarz and G. L. Rogosa—950
Diffusion
Diffusion of Co^{60} in some Ni-Al alloys containing excess vacancies, A. E. Berkowitz, F. E. Jaumot, Jr., and F. C. Nix—1185
Self-diffusion coefficient of nitrogen, Lloyd B. DeLuca—306(A)
Discharge of Electricity in Gases (see **Electrical Discharges**)
Disintegration and Excitation of Nucleus (see **Nuclear Reactions**)
Dynamics (see **Mechanics**)

Elasticity and Plasticity (see also **Molecular Aggregates**)
Effect of small strains on electrical resistance of U wire, E. W. Kammer—307(A)
Elastic constants of Co and of CoZn ferrite crystals, H. J. McSkimin, A. J. Williams, and R. M. Bozorth—616(A)
Equation of state and thermal dependence of elastic coefficients of crystalline argon, John H. Henkel—617(A)
Law of impact for generally shaped bodies. M. Avramy Melvin—615(A)
Plastic flow and low-frequency dispersion in alkali halide crystal, Masakazu Ishiguro, Fujio Oda, and Takuzo Fujino—1347(L)
Temperature variations of elastic constants of Cu single crystals from 4.2°K to 300°K, John Gaffney and W. C. Overton, Jr.—602(A)
Electrical Breakdown (see **Dielectrics and Dielectric Properties; Electrical Discharges**)
Electrical Conductivity and Resistance (see also **Semiconductors; Superconductors**)
Ac Hall and magnetoresistive effects in photoconducting alkali halides, J. Ross Macdonald and John E. Robinson —44
Ac photoconductivity in phosphors, J. J. Dropkin and S. Orgel—597(A)
Effect of small strains on electrical resistance of U wire, E. W. Kammer—307(A)
Electrical and thermal conductivity of Mg and Mg alloy at low temperatures, D. A. Spohr and R. T. Webber—602(A)
Electrical conductivities of natural graphite crystals, W. Primak and L. Fuchs—22
Electrical conductivity of MgO single crystals, E. Yamaka and K. Sawamoto—848(L)
Electrical conductivity of sulfur, Carroll K. Gordon—306(A)
Evaporated multiple layers with semiconductor properties, J. C. M. Brentano and J. D. Richards—841(L)
Hall effect in ferromagnetics, Clarence Kooi—843(L); Robert Karplus and J. M. Luttinger—1154
Interaction of electrons with grain boundaries, M. H. Cohen and C. S. Barrett—1094(L)
Ionic conductivity and x-ray coloration of alkali halides, F. A. Cunnell and E. E. Schneider—598(A)
Minimum in electrical resistance of metals at low temperatures, A. B. Bhatia—914
Resistivity of ordered and disordered Cu-Au alloys at low temperatures, E. Passaglia and W. F. Love—666(A)
Theory of galvanomagnetic effects in Ge, B. Abeles and S. Meiboom—31
Electrical Discharges
Measurement of current during formative time lag of sparks in uniform fields in air, H. W. Bandel—1117
Energy distribution function of electrons in pure He, Fritz H. Reder and Sanborn C. Brown—885
Magnetohydrodynamic flows in H and He, W. R. Atkinson, R. G. Fowler, and W. R. Holden—634(A)
Microwave determination of probability of collision of electrons in He, Lawrence Gould and Sanborn C. Brown —897
Motion of arc cathode spot in magnetic field, Robert M. St. John and J. G. Winans—634(A)
Phenomena of plasma resonance, K. S. W. Champion and S. C. Brown—634(A)
Phosphorescence of atoms and molecules of solid N_2 at 4.2°K, H. P. Broida and J. R. Pellam—845(L)
Uv photons in decay of metastable A atoms, L. Colli—892
Electrical Properties (see also **Dielectrics and Dielectric Properties; Electrical Conductivity and Resistance; Semiconductors; Superconductors**)
Angular distribution of photoelectrons produced by 0.4–0.8 Mev polarized photons, William H. McMaster and Frank L. Hereford—723
Forward-backward ratio of secondary emission produced by 1.3-Mev electrons, M. A. Pomerantz, J. F. Marshall, and R. A. Shatas—633(A)
Magnetic dependence of thermoelectric power of Bi at low temperatures, J. Babiskin and M. C. Steele—602(A)
Relative secondary electron emission for ions and atoms, C. F. Barnett, P. M. Stier, and G. E. Evans—307(A)

Electrical Properties (Continued)
Spectral dependence of thermionic emission with activation from (Ba–Sr)O cathodes over 0.6–3.5 ev region, Tadatosi Hibi and Kazuo Ishikawa—1183
Target-thickness dependence of δ-ray emission produced by 1.3-Mev electrons, J. F. Marshall, R. A. Shatas, and M. A. Pomerantz—634(A)
Temperature-and-field emission of electrons from metals, W. W. Dolan and W. P. Dyke—327
Theory of secondary electron cascade in metals, P. A. Wolff—56
Theory of thermoelectric power in semiconductors, J. Tauc —1394
Thermoelectric power and electron scattering in metal alloys, C. A. Domenicali and F. A. Otter—1134
Time delay in secondary emission, M. H. Greenblatt—633(A)
Electrodynamics (see **Electromagnetic Theory and Electrodynamics**)
Electrolysis (see **Chemical Effects and Properties**)
Electromagnetic Theory and Electrodynamics
Automatic electrostatic field plotter, David H. Andrews —633(A)
Betatron orbit stability as function of n, G. C. Baldwin, F. R. Elder, and W. F. Westendorp—600(A)
Calculation of potential from transit time, Jerry Shmoys and Samuel N. Karp—656(A)
Classical radiation from moving charges, Sidney A. Bludman—654(A)
Conservation theorems in modified electrodynamics, J. W. Dettman and A. Schild—1057
Dimensional relations in magnetohydrodynamics, Walter M. Elsasser—1
Electrodynamic equations symmetrical in respect to charges and poles; with remarks on monopoles, Arthur E. Ruark —305(A)
Electromagnetic scattering by dielectric bodies, Marshall H. Cohen—657(A)
Equations of motion of coupled ordered and dissipative systems, J. L. Jackson—642(A)
Excitation and separation of pure high-order modes in large high-Q cavities, C. T. Zahn and W. G. Schweitzer, Jr.—633(A)
General properties of solutions in Dirac's new electrodynamics, N. L. Balazs—305(A)
Microtron maximum particle energy, H. F. Kaiser—667(A)
New technique for solving three-dimensional electron optics potential problems with axial symmetry, Jenny E. Rosenthal—633(A)
Phase properties of deflected ion beam from fixed-frequency cyclotron, M. Jakobson and J. H. Manley—600(A)
Quantum theory of damped electrical oscillator and noise. II. Radiation resistance, J. Weber—1706(E)
Reaction concept in electromagnetic theory, V. H. Rumsey —1705(E)
Resolution of four-dimensional vector fields and tensor fields, N. L. Balazs—305(A)
Theory of aurora based on magnetic self-focusing of solar ion streams, W. H. Bennett and E. O. Hulburt—315
Electron Diffraction (see **Diffraction; Scattering of Electrons and Positrons**)
Electron Optics (see **Electromagnetic Theory and Electrodynamics**)
Electronic Tubes (see **Methods and Instruments**)
Electrons and Positrons (see also **Electromagnetic Theory and Electrodynamics; Elementary Particle Interactions; Scattering of Electrons and Positrons**)
Angular dependence of annihilation quanta from magnetic substates of triplet positronium, R. M. Drisko—611(A)
Annihilation of positrons in liquid He, Frank L. Hereford —1097(L)
Bremsstrahlung conversion in trident experiments, M. M. Block and D. T. King—171
Effect of angular dependence of annihilation radiation of orthopositronium in magnetic field, S. Marder, V. W. Hughes, and C. S. Wu—611(A)
Effect of nuclear charge on internally produced pairs, G. K. Horton and E. Phibbs—604(A)
Electron-positron scattering in alkali metals, Elihu Abrahams—839(L)
Estimate of lifetime of positrons in superconductors, M. Dresden—603(A)
High-energy, large-angle distribution of pair electrons produced by bremsstrahlung, R. C. Miller—796
Interference effects in annihilation process, G. Gibson and P. Stehle—657(A)
Pair production and bremsstrahlung in field of electron, F. Rohrlich—657(A)
Pairs formed by bremsstrahlung of great energy. I. Experimental, D. T. King and M. M. Block—648(A); II. Theoretical separation distribution, M. M. Block and D. T. King—648(A)
Theoretical energy and angular distributions of bremsstrahlung electrons, Philip T. McCormick—657(A)
Two-body system in quantum electrodynamics. Energy levels of positronium, Thomas Fulton and Paul C. Martin—811
Electrons, Mobility (see **Ions and Electrons, Mobility**)
Electrons, Scattering of (see **Scattering of Electrons and Positrons**)
Electrons, Secondary (see **Electrical Properties**)
Electrons, Thermionic (see **Electrical Properties**)
Electro-Optical Effects (see **Optical Properties**)
Electrostriction (see **Dielectrics and Dielectric Properties**)
Elementary Particle Interactions
Angular distribution of charge-exchange scattering of 40-Mev π^- mesons by hydrogen, J. Tinlot and A. Roberts —137
Antiproton production, G. Feldman—1697(L)
Application of intermediate coupling theory to scattering of pseudoscalar mesons by nucleon, Gyo Takeda—1078
Approximate equations for meson-nucleon systems, Richard Arnowitt and S. Gasiorowicz—618(A)
Bremsstrahlung conversion in trident experiments, M. M. Block and D. T. King—171
Charge exchange scattering of stopped π^- mesons in deuterium, Jack Steinberger and William Chinowsky—623(A)
Classical limit of pseudoscalar coupling, W. E. Thirring —653(A)
Comparison of cut-off meson theory with experiment, Geoffrey F. Chew—1669
Conservation theorems in modified electrodynamics, J. W. Dettman and A. Schild—1057
Covariant approximation scheme for Green's functions of coupled fields, R. Arnowitt and S. Gasiorowicz—538
Effects of certain 3-body nuclear interactions in H^3 and He^4, A. W. Solbrig, Jr.—831
Elastic scattering of pions by nucleons and pion production in nucleon-nucleon collisions, John L. Gammel—209
Evidence for double production of V^0 particles, R. W. Thompson, J. R. Burwell, R. W. Huggett, and C. J. Karzmark—1576
Factorable n-p interaction, Yoriko Yamaguchi and Yoshio Yamaguchi—654(A)
400-Mev n-p scattering, A. J. Hartzler and R. T. Siegel —185

General relations between photoproduction and scattering of π mesons, Kenneth M. Watson—228
Internal pair production in radiative absorption of π^- mesons by H atoms, W. Wada—618(A)
Meson-meson effects in meson-nucleon scattering, Marc H. Ross—619(A)
Meson-meson interaction in meson scattering, Marc Ross—1687(L)
Meson-nucleon scattering in Tamm-Dancoff approximation, F. J. Dyson, M. Ross, E. E. Salpeter, S. S. Schweber, M. K. Sundaresan, W. M. Visscher, and H. A. Bethe—1644
Meson production in meson-proton scattering, M. S. Nelkin and H. A. Bethe—618(A)
Meson production in n-p collisions at Cosmotron energies, W. B. Fowler, R. P. Shutt, A. M. Thorndike, and W. L. Whittemore—1026
Meson-proton scattering phase shift analysis, H. A. Bethe and F. de Hoffmann—1100(L)
Meson showers and high-energy interactions in light and heavy nuclei, R. W. Parsons, Françoise A. Brisbout, and V. D. Hopper—193
Negative pion production in n-p collisions, S. C. Wright and R. A. Schluter—639(A)
Negative-to-positive ratio of photomesons from deuterium, Matthew Sands, J. G. Teasdale, and Robert L. Walker—592(L)
Neutral pion-deuteron production in high-energy n-p collisions, Robert A. Schluter—639(A)
New Tamm-Dancoff formalism, Abraham Klein—1676
Nonlinear meson theory of nuclear forces, Ferdinand Cap—287(L)
n-p scattering at 91 Mev, R. H. Stahl—664(A)
n-p scattering at 300 Mev, J. DePangher—578(L)
Nucleon-nucleon scattering with 312-Mev polarized protons, Owen Chamberlain, Robert Donaldson, Emilio Segrè, Robert Tripp, Clyde Wiegand, and Thomas Ypsilantis—850(L)
Numerical calculation of 3/2−3/2 pion-nucleon reaction matrix and phase shifts, Freda F. Salzman and James N. Snyder—286(L)
Parity of pion, William Chinowsky and Jack Steinberger—623(A)
Phase shift analysis of scattering of negative pions by hydrogen, E. Fermi, N. Metropolis, and E. Felix Alei—1581; Donald L. Martin—1606
Phase shifts for high-energy nucleon-nucleon scattering, Burton D. Fried—851(L); 1706(E)
Phenomenological many-body exchange forces, L. E. H. Trainor—801
Photopion S wave near threshold and pion-nucleon coupling constant, G. Bernardini and E. L. Goldwasser—857(L)
Photoproduction of charged π mesons from hydrogen and deuterium, T. L. Jenkins, D. Luckey, T. R. Palfrey, and R. R. Wilson—179
Photoproduction of π^+ mesons from hydrogen, J. E. Leiss and C. S. Robinson—638(A)
Photoproduction of π^+ mesons from H near threshold, C. S. Robinson and J. E. Leiss—638(A)
Photoproduction of π^+ mesons near threshold, L. S. Osborne, Y. Goldschmidt-Clermont, and G. Parker—637(A)
Physical consequences of vacuum polarization, Leslie L. Foldy and Erik Eriksen—1048
π^- interactions at 1.5 Bev. II, J. Crussard, W. D. Walker, and M. Koshiba—624(A)
π-meson production in π-nucleon collisions at 1.5 Bev, W. D. Walker, J. Crussard, and M. Koshiba—852(L)
π^--p collisions at 1.5 Bev. I, W. D. Walker, J. Crussard, and M. Koshiba—624(A)
Pion-hydrogen phase shift analysis between 120 and 217 Mev, F. de Hoffmann, N. Metropolis, E. P. Alei, and H. A. Bethe—1586
Pion production by 440-Mev protons incident upon H and C, Arthur H. Rosenfeld—638(A)
Pion production ratios. II, D. C. Peaslee—1580
Polarization in high-energy p-n-n double scattering, Peter Hillman, Vaughn Culler, and N. F. Ramsey—462
Polarization in p-p scattering at 415 Mev, A. Kane, R. A. Stallwood, R. B. Sutton, T. H. Fields, and J. G. Fox—1694(L)
Possible example of annihilation of heavy particle, H. S. Bridge, H. Courant, H. DeStaebler, Jr., and B. Rossi—1101(L)
p-p cross section at 95 Mev, U. E. Kruse and J. M. Teem—662(A)
p-p scattering at 9.7 Mev, analysis, Harold H. Hall—424
p-p scattering experiments at 170 and 260 Mev, Owen Chamberlain and John D. Garrison—1349(L)
p-p scattering in nuclear emulsions, S. K. Kao and A. F. Clark—662(A)
p-p scattering near interference minimum, Robert L. Zimmerman, David H. Frisch, and Daniel I. Cooper—662(A)
Properties of Bethe-Salpeter wave functions, G. C. Wick—653(A)
p-wave pion-nucleon scattering phase shifts in cut-off theory, Geoffrey F. Chew—285(L)
Reaction $p+p\rightarrow\pi^++d$ with polarized protons, F. S. Crawford, Jr., and M. L. Stevenson—1112(L)
Scattering of 1.32-Mev neutrons by protons, C. L. Storrs and D. H. Frisch—1252
Scattering of 145-Mev π^+ by H in emulsion, Jay Orear, C. H. Tsao, J. J. Lord, and A. B. Weaver—624(A)
Scattering of 187-Mev negative pions by hydrogen, Maurice Glicksman—1045
Scattering of 314-Mev polarized protons by deuterium, J. Marshall, L. Marshall, D. Nagle, and W. Skolnik—1020
Scattering of protons by H near 18 Mev, J. L. Yntema and M. G. White—1226
Small-angle n-p scattering at 400 Mev, A. J. Hartzler, R. T. Siegel, and W. Opitz—591(L)
Small-angle p-p cross sections and polarization at 300 Mev, O. Chamberlain, G. Pettengill, E. Segrè, and C. Wiegand—1348(L)
Small-angle p-p scattering at 330 Mev, David Fischer and Gerson Goldhaber—1350(L)
Solutions of Bethe-Salpeter equation, R. E. Cutkosky—653(A)
Structure of nucleon. II. Pion-nucleon scattering, R. G. Sachs—1065
Suppression of pair coupling in nuclear forces, Abraham Klein—1061
Suppression of pair effects in nuclear forces, Abraham Klein—667(A)
Tamm-Dancoff method, J. C. Taylor—1313
Theory of unstable heavy particles, Hiroshi Enatsu, Hiroichi Hasegawa, and Pong Pul Pac—263
Total cross section for charge exchange scattering of π^- mesons by H at 42, 30, and 20 Mev, W. J. Spry—1295
Total cross sections for scattering of positive pions by hydrogen, J. Blaser, J. Ashkin, F. Feiner, J. Gorman, and M. O. Stern—624(A)
Total p-p cross section above 400 Mev, A. M. Shapiro, C. P. Leavitt, and F. F. Chen—663(A)

Elementary Particle Interactions (Continued)
Two-nucleon problem when potential is nonlocal but separable. I, Yoshio Yamaguchi—1628; II, Yoshio Yamaguchi and Yoriko Yamaguchi—1635
Use of causality conditions in quantum theory, M. Gell-Mann, M. L. Goldberger, and W. E. Thirring—1612
Elements (see **Atomic Mass and Abundance**)
Energy Loss of Particles (see **Range and Energy Loss**)
Energy States of Atoms (see **Atomic Structure and Spectra**)
Energy States of Molecules (see **Molecular Structure and Spectra**)
Energy States of Nucleus (see **Nuclear Reactions; Nuclear Spectra; Nuclear Structure Theory**)
Equations of State (see **Chemical Effects and Properties**)
Errata
Elastic scattering of 190-Mev deuterons by protons, Owen Chamberlain and Martin O. Stern—1705(E)
Hfs and nuclear moments of stable Br isotopes, John Gordon King and Vincent Jaccarino—1706(E)
Influence of earth's magnetic field on extensive air showers, Giuseppe Cocconi—1705(E)
New absorption lines of crystals in submicrowave region, S. Kojima, K. Tsukada, S. Ogawa, and A. Shimauchi —1705(E)
Phase shifts for high-energy nucleon-nucleon scattering, Burton D. Fried—1706(E)
Quantum theory of damped electrical oscillator and noise. II. Radiation resistance, J. Weber—1706(E)
Reaction concept in electromagnetic theory, V. H. Rumsey —1705(E)
Errors of Measurement (see **Methods and Instruments**)
Evaporation (see **Liquids**)
Excitation of Atoms (see **Atomic Structure and Spectra**)
Excitation of Molecules (see **Molecular Structure and Spectra**)
Excitation of Nucleus (see **Nuclear Reactions; Nuclear Spectra; Nuclear Structure Theory**)
Explosion Phenomena (see **Fluid Dynamics**)

Faraday Effect (see **Optical Properties**)
Ferroelectric Phenomena (see **Dielectrics and Dielectric Properties**)
Ferromagnetism (see **Magnetic Properties**)
Field Emission (see **Electrical Properties**)
Field Theory (see also **Quantum Electrodynamics; Relativity and Gravitation**)
Antiproton production, G. Feldman—1697
Application of intermediate coupling theory to scattering of pseudoscalar mesons by nucleon, Gyo Takeda—1078
Approximate equations for meson-nucleon systems, Richard Arnowitt and S. Gasiorowicz—618(A)
Canonical transformation for electron-positron field coupled to time-independent electromagnetic field. II, H. E. Moses—237
Classical limit of pseudoscalar coupling, W. E. Thirring —653(A)
Comparison of cut-off meson theory with experiment, Geoffrey F. Chew—1669
Conservation theorems in modified electrodynamics, J. W. Dettman and A. Schild—1057
Covariant approximation scheme for Green's functions of coupled fields, R. Arnowitt and S. Gasiorowicz—538
Dyson's new Tamm-Dancoff method, Abraham Klein—654(A)
Electromagnetic interaction of particles of spin 3/2, Suraj N. Gupta—630(A)
Factorable n-p interaction, Yoriko Yamaguchi and Yoshio Yamaguchi—654(A)
Fierz-Pauli theory of particles of spin 3/2, Suraj N. Gupta —1334
Formation of quantum electrodynamics in Minkowski space, T. A. Welton—632(A)
General conditions on scattering matrix, M. L. Goldberger, M. Gell-Mann, and W. E. Thirring—654(A)
General relations between photoproduction and scattering of π mesons, Kenneth M. Watson—228
Hyperquantization of Feynman amplitudes, F. Coester—631(A); 1318
Integral equations of quantized field theory, H. S. Green —548
Invariance and isotopic spin, A. W. Stern—632(A)
Isotopic spin conservation and generalized gauge invariance, C. N. Yang and R. Mills—631(A)
Meson-meson effects in meson-nucleon scattering, Marc H. Ross—619(A)
Meson-meson interaction in meson scattering, Marc Ross —1687(L)
Meson-nucleon scattering in Tamm-Dancoff approximation, F. J. Dyson, M. Ross, E. E. Salpeter, S. S. Schweber, M. K. Sundaresan, W. M. Visscher, and H. A. Bethe—1644
Meson production in meson-proton scattering, M. S. Nelkin and H. A. Bethe—618(A)
Modified nucleon propagators, A. N. Mitra—1697(L)
New Tamm-Dancoff formalism, Abraham Klein—1676
Nonlinear meson theory of nuclear forces, Ferdinand Cap —287(L)
Properties of Bethe-Salpeter wave functions, G. C. Wick —653(A)
p-wave pion-nucleon scattering phase shifts in cut-off theory, Geoffrey F. Chew—285(L)
Quantized linear theory of gravitation. I, F. J. Belinfante and J. C. Swihart—630(A); II, J. C. Swihart and F. J. Belinfante—630(A)
Quantum electrodynamics at small distances, M. Gell-Mann and F. E. Low—1300
Quantum theory of gravitation, Peter G. Bergmann—631(A)
Sachs exchange moment, R. H. Dalitz—799
Solutions of Bethe-Salpeter equation, R. E. Cutkosky—653(A)
Special examples in renormalizable field theory, T. D. Lee —1329
Superselection rule regarding spinor particle numbers, Satosi Watanabe—631(A)
Suppression of pair coupling in nuclear forces, Abraham Klein—1061
Suppression of pair effects in nuclear forces, Abraham Klein—667(A)
Tamm-Dancoff method, J. C. Taylor—1313
Theory of unstable heavy particles, Hiroshi Enatsu, Hiroichi Hasegawa, and Pong Yul Pac—263
Two-nucleon problem when potential is nonlocal but separable. I, Yoshio Yamaguchi—1628; II, Yoshio Yamaguchi and Yoriko Yamaguchi—1635
Variance properties of general field operator, P. H. Fang —631(A)
Films, Properties
Electron microscope and diffraction traversing technique for examination of bimetal films, John L. Brown and Richard B. Belser—308(A)
Evaporated multiple layers with semiconductor properties, J. C. M. Brentano and J. D. Richards—841(L)
Properties of thin metallic films, F. J. Blatt—13
Replication of $BaTiO_3$ ceramic surfaces for electron microscopy, John L. Sampson, Edward E. Altshuler, and Robert W. Perry—298(A)

Solder-shear tests to metal films deposited on glass substrates by evaporation and sputtering, Margaret C. Chester and Richard B. Belser—308(A)
Structures and resistivities of sputtered films of Pt metals before and after aging by heating, Richard B. Belser and Margaret C. Chester—307(A)
Fine Structure (see **Atomic Structure and Spectra**)
Fission of Nucleus (see **Nuclear Fission**)
Fluctuation Phenomena (see **Noise**)
Fluid Dynamics
Dimensional relations in magnetohydrodynamics, Walter M. Elsasser—1
Dynamics of waterdrop collisions with solids, Olive G. Engel—615(A)
Energy spectrum of turbulence for entire range, R. W. Davies—912
General relations in fluid convection theory. I. Similarity theory for flow onset, F. T. Rogers, Jr.—305(A)
Magnetohydrodynamic flows in H and He, W. R. Atkinson, R. G. Fowler, and W. R. Holden—634(A)
Rheological problem, Allen L. King—298(A)
Fluorescence (see **Luminescence**)
Friction (see **Mechanics**)

Galvanomagnetic Effect (see **Magnetic Properties**)
Gamma Rays (see also **Nuclear Reactions; Nuclear Spectra; Range and Energy Loss**)
Build-up measurements on Co^{60} γ radiation in Fe and Pb, C. Garrett and G. N. Whyte—889
4.43-Mev γ rays from C^{12}, W. R. Mills, Jr., and R. J. Mackin, Jr.—1206
γ-ray absorption coefficients for NaI, Cu, Ta, and W, P. R. Howland and W. E. Kreger—407
Nuclear scattering of γ rays below meson threshold, G. E. Pugh, D. H. Frisch, and R. Gomez—590(L)
Penetration of 6-Mev γ rays in Pb and Fe, K. Shure, P. A. Roys, and J. J. Taylor—610(A)
Penetration of 6-Mev γ rays in water, P. A. Roys, K. Shure, and J. J. Taylor—911
Rotating-sphere solid-angle scanner for γ rays, George R. Meneely, Robert J. Kerr, Jesse E. Hoffman, and Sherwood K. Haynes—308(A)
Gases
Deviations from additivity of intermolecular field at high densities, L. Jansen and Z. I. Slawsky—614(A)
Effect of intermolecular forces on rapid expansion of gas from initial condition of very high density and temperature, J. M. Dawson and Z. I. Slawsky—614(A)
General method for high-speed machine computation of ideal gas thermal properties. Diatomic free radicals of isotopic hydrides, Lester Haar and A. S. Friedman—614(A)
Geophysics
Air-guided propagation of short radio waves around earth bulge, Thomas J. Carroll—623(A)
Drop-size distribution and visibility in clouds and rain, Shepard Bartnoff—615(A)
Drop-size frequency distribution in clouds and rain, Joseph K. Fish and Shepard Bartnoff—297(A)
Effect of melting of polar ice on length of day, Serge A. Korff—296(L)
Heat generation in earth by solar neutrinos, A. M. Cormack—580(L)
Microwave and far infrared atmospheric water-vapor absorption, T. F. Rogers—622(A)
Origin of N_2O in atmosphere, P. Harteck and S. Dondes—320
Radar echoes from precipitation, Pauline M. Austin—297(A)
Rf mass spectrometer as rocket-borne instrument for atmospheric composition studies, Walter F. Sheridan—298(A)
Seismology in southeast, Jack H. Williams and C. F. Mercer—306(A)
Theory of aurora based on magnetic self-focusing of solar ion streams, W. H. Bennett and E. O. Hulburt—315
Glasses (see **Molecular Aggregates**)
Gravitation (see **Relativity and Gravitation**)
Gyromagnetization (see **Magnetic Properties**)

Hall Effect (see **Electrical Conductivity and Resistance; Semiconductors**)
Heat Capacity (see **Thermal Properties**)
Heat Conduction (see **Thermal Properties**)
Heat of Dissociation and Formation (see **Molecular Structure and Spectra**)
Heat of Fusion (see **Thermal Properties**)
Heat of Vaporization (see **Thermal Properties**)
Helium, Liquid
Absolute temperature scale between 4.2° and 5.2°K, R. Berman and C. A. Swenson—311
Annihilation of positrons in liquid He, Frank L. Hereford—1097(L)
Atomic theory of liquid He, D. ter Haar—604(A)
Experimental evidence for structure in He II film, W. C. Knudsen and J. R. Dillinger—279(L)
Fermi-Dirac degeneracy in liquid He^3 below 1°K, William M. Fairbank, W. B. Ard, and G. K. Walters—566(L)
Film flow and bulk formation of He II in capillaries, R. V. Dyba, C. T. Lane, and C. H. Blakewood—1365
λ transition of liquid He, D. ter Haar—895
Second sound attenuation in liquid He II, W. B. Hanson and J. R. Pellam—321; 604(A)
Theory of liquid He^3–He^4 mixtures, Louis Goldstein—869
Thermal conductivity of liquid He below 1.0°K, Henry A. Fairbank and J. Wilks—277(L)
Ultrasonic measurements in magnetically cooled He, C. E. Chase and Melvin A. Herlin—565(L)
High Voltage Tubes and Machines (see **Methods and Instruments**)
Hydrodynamics (see **Fluid Dynamics**)
Hyperfine Structure (see **Atomic Structure and Spectra; Molecular Structure and Spectra; Nuclear Moments and Spin**)

Imperfections in Solids (see also **Crystalline State; Electrical Conductivity and Resistance; Luminescence; Semiconductors**)
Ac Hall and magnetoresistive effects in photoconducting alkali halides, J. Ross Macdonald and John E. Robinson—44
Anomalous optical behavior of InSb and InAs, H. J. Hrostowski, G. H. Wheatley, and W. F. Flood, Jr.—1683(L)
Color centers in alkali silicate and borate glasses, Ryosuke Yokota—1145
Diffusion of Co^{60} in some Ni-Al alloys containing excess vacancies, A. E. Berkowitz, F. E. Jaumot, Jr., and F. C. Nix—1185
Electrical conductivity of MgO single crystals, E. Yamaka and K. Sawamoto—848(L)
Energy levels and photoconductivity in electron-bombarded Ge, H. Y. Fan, W. Kaiser, E. E. Klontz, K. Lark-Horowitz, and R. R. Pepper—1087(L)
Ionic conductivity and x-ray coloration of alkali halides, F. A. Cunnell and E. E. Schneider—598(A)
Lattice parameters of $FeFe_{(2-x)}Cr_xO_4$ spinel system, H. J. Yearian, J. W. Kortright, and R. H. Langenheim—653(A)

Imperfections in Solids (Continued)
Low-temperature bleaching and restoration of color centers, A. Halperin and G. F. J. Garlick—1098(L)
Metamict state, William Primak—837(L)
Neutron irradiation of InSb, J. W. Cleland and J. H. Crawford, Jr.—1177
Paramagnetic resonance absorption in soft carbon, J. G. Castle, Jr.—846(L)
Plastic flow and low-frequency dispersion in alkali halide crystal, Masakazu Ishiguro, Fujio Oda, and Takuzo Fujino—1347(L)
Possible macroscopic effects of single lattice defects, Jerome Rothstein—370
Precipitation of impurities at dislocations in heat-treated Si, Sumner Mayburg—838(L)
Propagation of displacement in solid, having crystalline structure with bistable states, C. F. Pulvari—617(A)
Shape of *F* band, R. V. Hesketh and E. E. Schneider—837(L)
Small angle x-ray scattering from cold-worked Al-Ag and Al-Zn alloys, J.-P. Jan and J. S. Koehler—665(A)
Spectral dependence of thermionic emission with activation from (Ba–Sr)O cathodes over 0.6–3.5 ev region, Tadatosi Hibi and Kazuo Ishikawa—1183
Thermal ionization of impurities in polar crystals, H. D. Vasileff—618(A)
Thermal restoration of color centers at low temperature, R. V. Hesketh and E. E. Schneider—598(A)
Vacancies and interstitials in heat-treated Ge, Sumner Mayburg—38
X-ray production of *F* centers in NaCl and LiF, R. C. Herman, L. L. Mador, R. F. Wallis, and M. C. Williams—598(A)
Inelastic Scattering (see **Nuclear Reactions; Scattering**)
Instruments (see **Methods and Instruments**)
Internal Conversion (see **Nuclear Spectra**)
Ionization (see also **Electrical Discharges; Range and Energy Loss**)
Absorption of tritium β particles in hydrogen and other gases, Leon M. Dorfman—393
Energy expenditure per ion pair in solids, E. J. Sternglass—609(A)
Energy per ion pair for recoil atoms in methane, W. G. Stone and Lewis W. Cochran—304(A)
Ionization energies of groups III and V elements in Ge, T. H. Geballe and F. J. Morin—1085(L)
Ionization of pure gases and mixtures of gases by 5-Mev α particles, T. E. Bortner and G. S. Hurst—609(A)
Ionization probability curves near threshold for Zn, Cd, and Hg, W. M. Hickam—703
Ionization produced by 5-Mev α particles in argon mixtures, Charles E. Melton—303(A)
Ionizing collisions of very fast particles and dipole strength of optical transitions, U. Fano—1198
L-shell ionization by protons of 1.5- to 4.5-Mev energy, E. M. Bernstein and H. W. Lewis—83
Range and specific ionization for high-energy protons in nuclear emulsions, O. Heinz—610(A)
Relative ionization yields for fission fragments in various gases, Lloyd O. Herwig and Glenn H. Miller—413
w value in electron volts for 5-Mev α particles in gases and gas mixtures, T. E. Bortner and G. S. Hurst—303(A)
Ionization Potentials of Atoms (see **Atomic Structure and Spectra**)
Ionization Potentials of Molecules (see **Molecular Structure and Spectra**)
Ionosphere (see **Geophysics**)
Ions (see also **Electrical Discharges**)
Approximate Hartree type wave functions and matrix elements for *K* and *L* shells of atoms and ions, R. E. Meyerott—72
Electronic polarizabilities of ions from Hartree-Fock wave functions, R. M. Sternheimer—655(A)
Equilibrium charge distribution of stripped 26-Mev N ions, H. L. Reynolds and A. Zucker—1353(L)
Experimental determination of charge transfer cross sections, W. F. Sheridan, J. A. Dillon, Jr., and S. N. Ghosh—635(A)
Range and charge of energetic nitrogen ions in Ni, H. L. Reynolds, D. W. Scott, and A. Zucker—671
Role of principal quantum number (n) in calculation of radii of ions with low (1^+,2^+,3^+,4^+) valence, N. Efremov—614(A)
Scattering of H^- ions in range 20–400 ev, E. E. Muschlitz, Jr.—635(A)
Scattering of ions by polarization forces, Erich Vogt and Gregory H. Wannier—1190
Theory of aurora based on magnetic self-focusing of solar ion streams, W. H. Bennett and E. O. Hulburt—315
Ions and Electrons, Mobility (see also **Semiconductors**)
Isobars (see **Atomic Mass and Abundance**)
Isomers, Molecular (see **Molecular Structure and Spectra**)
Isomers, Nuclear (see **Nuclear Spectra**)
Isotopes (see **Atomic Mass and Abundance; Radioactivity**)

Kerr Effect (see **Optical Properties**)
Kinetic Theory of Gases (see **Gases**)

Liquid Helium (see **Helium, Liquid**)
Liquids
Measurements of solvent volume changes in sugar factory using radioactive tracer technic, John U. Hidalgo, Sr.—306(A)
Luminescence
Anisotropy of fluorescence of some organic crystals, S. C. Ganguly and N. K. Chaudhury—1148
Effect of pressure on optical absorption of activator in luminescent solid, Peter D. Johnson and Ferd E. Williams—598(A)
Effect of pressure on optical absorption of activator system in KCl: Tl, Peter D. Johnson and Ferd E. Williams—69
Effects of preparation and temperature on response of NaI phosphors, C. O. Muehlhause, E. der Mateosian, and Michael McKeown—598(A)
Experiments on electroluminescence, John F. Waymouth and Francis Bitter—941
Light decay from electroluminescent phosphors, S. H. Autler and W. F. Roat—599(A)
Low-temperature luminescence of CdS, L. R. Furlong—1086(L)
Phosphorescence of and energy storage in some uv-emitting phosphors, C. E. Mandeville and H. O. Albrecht—598(A)
Phosphorescence of atoms and molecules of solid N_2 at 4.2°K, H. P. Broida and J. R. Pellam—845(L)
Photoconductivity in phosphors, J. J. Dropkin and S. Orgel—597(A)
Response of anthracene scintillation crystals to monoenergetic soft x-rays, W. H. Robinson and W. Jentschke—1412
Temperature dependence of organic scintillation materials, J. B. Birks—277(L)
Use of scintillation counters in studies on luminous efficiency of biological materials, J. G. Kereiakes and A. T. Krebs—308(A)

Magnetic Fields (see **Electromagnetic Theory and Electrodynamics**)

Magnetic Properties

Approximate partition function for certain iron group salts at low temperatures, L. D. Roberts and J. W. T. Dabbs—307(A)

Calculation of ferromagnetic and antiferromagnetic Curie temperatures, H. A. Brown and J. M. Luttinger—652(A)

Chromium potassium alum below 1°K, E. Ambler and R. P. Hudson—1143

de Haas-van Alphen effect in Sn and Sn-Sb alloys, G. T. Croft, W. F. Love, and F. C. Nix—1403

de Haas-van Alphen effect in Zn at liquid O_2 temperatures, Ted G. Berlincourt and M. C. Steele—603(A)

Domain rotation in sintered Ni ferrite, Fielding Brown and Charles L. Gravel—652(A)

Ferrimagnetic resonance in sintered masses, David Park—652(A)

Hall effect in ferromagnetics, Clarence Kooi—843(L); Robert Karplus and J. M. Luttinger—1154

Influence of covalence on ion ordering and distortion in spinels, A. L. Loeb and J. B. Goodenough—616(A)

Lattice parameters of $FeFe_{(2-x)}Cr_xO_4$ spinel system, H. J. Yearian, J. M. Kortright, and R. H. Langenheim—653(A)

Low-temperature magnetization of two Ce salts, Warren E. Henry—603(A)

Magnetic and thermal properties of chromic methylamine alum below 1°K, R. P. Hudson and C. K. McLane—932

Magnetic domains in Co by longitudinal Kerr effect, Charles A. Fowler, Jr., and Edward M. Fryer—564(L); 652(A)

Magnetic neutron diffraction from Fe_3O_4, A. W. McReynolds and T. Riste—1161

Magnetostrictive effects in α-Fe_2O_3, H. M. A. Urquhart and J. E. Goldman—653(A)

Measuring magnetic properties of ferromagnetic materials by means of Hall effect, Simon Foner—652(A)

Metastable magnetic states, J. R. Lamarsh and B. D. Kern—307(A)

Method for brute force polarization of H nuclei, J. W. T. Dabbs and L. D. Roberts—307(A)

Neutron diffraction studies of NiZn ferrite, V. C. Wilson and J. S. Kasper—1408

Neutron diffraction study of Cu-Mn system, David Meneghetti and S. S. Sidhu—666(A)

Neutron magnetic diffraction studies of La, Ca manganites, W. C. Koehler and E. O. Wollan—653(A)

Paramagnetic and diamagnetic susceptibility of conduction electrons, David Pines—1090(L)

Polarization of Mn^{56} nuclei: cryogenic aspects, J. W. T. Dabbs and L. D. Roberts—970

Properties of thin metallic films, F. J. Blatt—13

Search for antiferromagnetism in silicides V_3Si, Cr_3Si, and Mo_3Si, W. C. Koehler and E. O. Wollan—280(L)

Spherical model of antiferromagnet, B. S. Gourary and R. W. Hart—652(A); 676

Spin paramagnetism of conduction electrons, R. T. Schumacher, T. R. Carver, and C. P. Slichter—1089(L)

Statistics of face-centered cubic ferromagnet, E. Dempsey and D. ter Haar—651(A)

Strong field induced paramagnetic anomaly in $NiSiF_6 \cdot 6H_2O$, Warren E. Henry—1449

Susceptibility tensor and Faraday effect in ferrimagnetics, Roald K. Wangsness—339

Temperature and field dependence of de Haas-van Alphen effect, F. J. Donahoe and F. C. Nix—1395

Temperature-dependent de Haas-van Alphen parameters in Zn, Ted G. Berlincourt and M. C. Steele—1421

Theory of domain creation and coercive force in polycrystalline ferromagnetics, John B. Goodenough—917

Theory of galvanomagnetic effects in Ge, B. Abeles and S. Meiboom—31

Time-dependent correlations between spins and neutron scattering in ferromagnetic crystals, Léon Van Hove—1374

Magnetic Resonance (see also **Nuclear Moments and Spin**)

Anisotropy of cyclotron resonance in Ge. I. Theory, Benjamin Lax, H. J. Zeiger, and R. N. Dexter—597(A); II. Experiment, R. N. Dexter, H. J. Zeiger, Benjamin Lax, and E. S. Rosenblum—597(A)

Anisotropy of cyclotron resonance of holes in Ge, R. N. Dexter, H. J. Zeiger, and Benjamin Lax—557(L)

Conduction electron spin resonance absorption in Na, I. H. Solt, Jr., and M. W. P. Strandberg—607(A)

Demonstration of neutron spin from Bloch-Alvarez-type experiment, C. P. Stanford, T. E. Stephenson, and S. Bernstein—302(A)

Detection of pure quadrupole resonances, P. J. Bray—606(A)

Electron spin magnetic moment in atomic hydrogen, R. Beringer and Mark A. Heald—1474

Electron spin resonance in Be, G. Feher and A. F. Kip—1343(L)

Electron spin resonance of impurity level in Si, A. Honig and A. F. Kip—1686(L)

Ferrimagnetic resonance in sintered masses, David Park—652(A)

Hfs and nuclear moments of stable Br isotopes, John Gordon King and Vincent Jaccarino—1706(E)

Hfs of He^3 in metastable triplet state, Werner B. Teutsch and Vernon W. Hughes—1461; Gabriel Weinreich and Vernon W. Hughes—1451

Hyperfine splitting in spin resonance of Group V donors in Si, R. C. Fletcher, W. A. Yager, G. L. Pearson, and F. R. Merritt—844(L)

Intensities of Zeeman components of quadrupole transitions in $NaClO_3$, Yu Ting and Dudley Williams—607(A)

Magnetic resonance enhancement in multilevel system, James H. Burgess—608(A)

Magnetic resonance spectra of beryl crystals, L. Carlton Brown and Dudley Williams—1110(L)

New absorption lines of crystals in submicrowave region, S. Kojima, K. Tsukada, S. Ogawa, and A. Shimauchi—1705(E)

Nuclear magnetic resonance in solid hydrogen with various *ortho* concentrations, Tadashi Sugawara, Yoshika Masuda, Teinosuke Kanda, and Eizo Kanda—1355(L)

Nuclear magnetic resonance in some solid hydrocarbons, F. A. Rushworth—608(A)

Nuclear spin and hfs interaction of 3.1-hr Cs^{134} isomer, V. W. Cohen and D. A. Gilbert—569(L)

Nuclear spin and magnetic moment of 3.1-hr Cs^{134m}, L. S. Goodman and S. Wexler—570(L)

Os^{189} magnetic moment, H. R. Loeliger and L. R. Sarles—291(L)

Overhauser effect in free radical, H. G. Beljers, L. van der Kint, and J. S. van Wieringen—1683(L)

Paramagnetic and diamagnetic susceptibility of conduction electrons, David Pines—1090(L)

Paramagnetic resonance absorption in ammonium chrome alum, Charles F. Davis, Jr., and M. W. P. Strandberg—607(A)

Paramagnetic resonance absorption in graphite, G. R. Hennig, B. Smaller, and E. L. Yasaitis—1088(L)

Paramagnetic resonance absorption in sodium plutonyl acetate, Clyde A. Hutchison, Jr., and W. Burton Lewis—1096(L)

Magnetic Resonance (Continued)
Paramagnetic resonance absorption in soft C, J. G. Castle, Jr.—846(L)
Paramagnetic resonance absorption of $VOSO_4 \cdot 5H_2O$, M. B. Palma, M. U. Palma, and D. Palumbo—608(A)
Paramagnetic resonance in organic free radicals at low fields, R. S. Codrington, J. D. Olds, and H. C. Torrey —607(A)
Paramagnetic resonances in glasses, R. H. Sands, J. Townsend, and H. P. Hood—607(A)
Radiation damping in magnetic resonance experiments, N. Bloembergen and R. V. Pound—8
Random pulses and electron-spin line widths in metals, D. L. Falkoff—607(A)
Spin paramagnetism of conduction electrons, R. T. Schumacher, T. R. Carver, and C. P. Slichter—1089(L)
Spin-orbit interaction and effective masses of holes in Ge, G. Dresselhaus, A. F. Kip, and C. Kittel—568(L)
Spins and hyperfine splittings of Ag^{111} and Cu^{64}, Aaron Lemonick and Francis M. Pipkin—1356(L)
Statistical mechanics and Overhauser nuclear polarization effect, C. Kittel—589(L)
Magneto-Optical Effects (see **Optical Properties**)
Magnetoresistance (see **Electrical Conductivity and Resistance; Semiconductors**)
Magnetostriction (see **Magnetic Properties**)
Mass Defects (see **Atomic Mass and Abundance**)
Mass Spectroscopy (see **Atomic Mass and Abundance; Methods and Instruments**)
Mathematical Methods
Calculation of potential from transit time, Jerry Shmoys and Samuel N. Karp—656(A)
Decomposition of scalar product of 2 symmetric tensors, M. H. Cohen—674
High-speed computation of angular momentum functions, Albert Simon—657(A)
Interior value problems, A. V. Masket—305(A)
Resolution of four-dimensional vector fields and tensor fields, N. L. Balazs—305(A)
W.K.B. approximation through turning point, A. A. Broyles—656(A)
Measurements (see **Methods and Instruments**)
Mechanics
Generalization of theorem by Pappus, E. E. Mayo—305(A)
Law of impact for generally shaped bodies. M. Avramy Melvin—615(A)
Mechanics, Quantum—Atomic Structure and Spectra (see **Atomic Structure and Spectra**)
Mechanics, Quantum—General (see **Quantum Mechanics**)
Mechanics, Quantum—Molecular Structure and Spectra (see **Molecular Structure and Spectra**)
Mechanics, Quantum—Nuclear (see **Nuclear Structure Theory**)
Mechanics, Quantum—of Solid Bodies (see **Crystalline State**)
Mechanics, Statistical (see **Statistical Mechanics and Thermodynamics**)
Meson Field Theory (see **Field Theory**)
Mesons (see also **Cosmic Radiation; Elementary Particle Interactions; Nuclear Reactions Induced by Mesons; Scattering of Mesons**)
Absorption of negative pions in deuterium: Parity of pion, W. Chinowsky and J. Steinberger—1561
Anomalous event observed in photographic emulsion, J. H. Noon, M. F. Kaplon, and J. Crussard—1103(L)
Charge exchange scattering of stopped π^- mesons in deuterium, Jack Steinberger and William Chinowsky—623(A)
Charged heavy mesons from nuclear collisions, L. Voyvodic—661(A)
Charged pion production from C by protons, Walter F. Dudziak—866(L)
Cloud-chamber study of charged V particles, Carl M. York, Jr., R. B. Leighton, and E. K. Bjørnerud—159
Comparison of reactions $H^2(H^1,\pi^+)H^3$ and $H^2(H^1,\pi^0)He^3$ as test of charge independence, Kenneth C. Bandtel, Wilson J. Frank, Richard Madey, and Burton J. Moyer —639(A)
Cosmic-ray μ meson low-energy differential range spectrum, A. Fafarman and M. H. Shamos—648(A)
Decay curve of K particles, L. Mezzetti and J. W. Keuffel —858(L)
Decay of heavy neutral particle, R. A. Howard, P. M. Fitzpatrick, H. E. Hoffman, and J. S. Urban—661(A)
Elastic photoproduction of π^0 mesons from He, E. L. Goldwasser, L. J. Koester, Jr., and F. E. Mills—1692(L)
Elastic scattering of pions by nucleons and pion production in nucleon-nucleon collisions, John L. Gammel—209
Energy measurements of meson x-rays, M. B. Stearns, M. Stearns, L. Leipuner, and S. DeBenedetti—625(A)
Evidence for double production of V^0 particles, R. W. Thompson, J. R. Burwell, R. W. Huggett, and C. J. Karzmark—1576
Experimental study of μ^- meson mass and vacuum polarization in mesonic atoms, S. Koslov, V. Fitch, and J. Rainwater—291(L)
General relations between photoproduction and scattering of π mesons, Kenneth M. Watson—228
Heavy unstable particles in stripped emulsions, J. Crussard, M. F. Kaplon, J. Klarmann, and J. H. Noon—584(L)
Limits on π^- meson mass from mesonic x-rays, M. Stearns, M. B. Stearns, S. DeBenedetti, and L. Leipuner—1353(L)
Magnetic cloud-chamber observation of V particles. I. Charged V particles, Y. B. Kim, J. R. Burwell, H. O. Cohn, C. J. Karzmark, and R. W. Thompson—661(A); II. Status of work on θ^0 meson, R. W. Thompson, J. R. Burwell, H. O. Cohn, R. W. Huggett, and C. J. Karzmark—661(A)
Mass measurements of slow cosmic-ray mesons, M. Inoki, T. Yasaki and Y. Matsukawa—1565
Mass of μ^- meson from mesonic x-rays, S. Koslov, V. Fitch, and J. Rainwater—625(A)
Meson production in meson-proton scattering, M. S. Nelkin and H. A. Bethe—618(A)
Meson production in n-p collisions at Cosmotron energies, W. B. Fowler, R. P. Shutt, A. M. Thorndike, and W. L. Whittemore—1026
Meson showers and high-energy interactions in light and heavy nuclei, R. W. Parsons, Françoise A. Brisbout, and V. D. Hopper—193
Meson-meson effects in meson-nucleon scattering, Marc H. Ross—619(A)
Momentum of S-particle secondaries, D. Willard—661(A)
Negative pion production in n-p collisions, S. C. Wright and R. A. Schluter—639(A)
Negative-to-positive ratio of photomesons from deuterium, Matthew Sands, J. G. Teasdale, and Robert L. Walker —592(L)
Neutral pion-deuteron production in high-energy n-p collisions, Robert A. Schluter—639(A)
Nuclear absorption of negative K particles, Herbert DeStaebler, Jr.—1110(L)
Parity of pion, William Chinowsky and Jack Steinberger —623(A)

Photopion S wave near threshold and pion-nucleon coupling constant, G. Bernardini and E. L. Goldwasser—857(L)
Photoproduction of charged π mesons from hydrogen and deuterium, T. L. Jenkins, D. Luckey, T. R. Palfrey, and R. R. Wilson—179
Photoproduction of π^+ mesons from H, J. E. Leiss and C. S. Robinson—638(A)
Photoproduction of π^+ mesons from hydrogen near threshold, C. S. Robinson and J. E. Leiss—638(A)
Photoproduction of π^+ mesons near threshold, L. S. Osborne, Y. Goldschmidt-Clermont, and G. Parker—637(A)
π^+ production in H by 437-Mev protons, T. H. Fields, J. G. Fox, J. A. Kane, R. A. Stallwood, and R. B. Sutton—638(A)
π-meson production in π-nucleon collisions at 1.5 Bev, W. D. Walker, J. Crussard, and M. Koshiba—852(L)
Pion production by 440-Mev protons incident upon H and C, Arthur H. Rosenfeld—638(A)
Pion production ratios. II, D. C. Peaslee—1580
Positron spectrum from decay of μ meson, Ryokichi Sagane, Walter F. Dudziak, and James Vedder—863(L)
Possible example of annihilation of heavy particle, H. S. Bridge, H. Courant, H. DeStaebler, Jr., and B. Rossi—1101(L)
Production of positive and negative pions in Be by 1.0 and 2.3-Bev protons, S. J. Lindenbaum and Luke C. L. Yuan—638(A)
Production of V^0 particles in Cu, D. R. Harris and A. L. Hodson—661(A)
Q value of Λ^0 decay, V. A. J. van Lint, G. H. Trilling, R. B. Leighton, and C. D. Anderson—295(L)
Radiative decay of θ^0 particle, S. B. Treiman—1360(L)
Radiochemical evidence for $Cu^{65}(p,p\pi^+)Ni^{65}$ reaction, Si-Chang Fung and Anthony Turkevich—176
Ratio of π^-/π^+ meson production in cosmic ray disintegrations of emulsion nuclei, Herman Yagoda—648(A)
Reaction $p+p\rightarrow\pi^++d$ with polarized protons, F. S. Crawford, Jr., and M. L. Stevenson—1112(L)
Recent results on S particles, H. S. Bridge, H. Courant, B. Dayton, H. C. DeStaebler, Jr., B. Rossi, and D. Willard—662(A)
Sea level mesons stopped in thin Pb and Al foils. I. Possible emission of charged nuclear particles and related events, W. Y. Chang—1282; II. Low-energy (1–5 Mev) γ rays, W. Y. Chang—1288
τ-meson decay scheme, N. Baker and O. Bergmann—174
τ meson produced by 3.0-Bev protons, R. D. Hill, E. O. Salant, and M. Widgoff—1699(L)
Theory of unstable heavy particles, Hiroshi Enatsu, Hiroichi Hasegawa, and Pong Yul Pac—263
Unstable particles in photographic emulsion, M. F. Kaplon, J. Crussard, J. Klarmann, and J. Noon—660(A)
Unusual cosmic-ray event, H. C. DeStaebler, Jr., H. S. Bridge, H. Courant, and B. Rossi—662(A)
X-rays from π mesonic atoms, A. D. McGuire, M. Camac, M. L. Halbert, and J. B. Platt—625(A)
Yield of π^+ mesons by 335-Mev protons as function of atomic number, J. Merritt and D. Hamlin—638(A)

Metals (see **Crystalline State**)
Metastable Atoms (see **Atomic Structure and Spectra**)
Metastable Molecules (see **Molecular Structure and Spectra**)
Meteorology (see **Geophysics**)
Methods and Instruments

Applications of "internal source" scintillation spectrometer, E. der Mateosian—646(A)
Automatic electrostatic field plotter, David H. Andrews—633(A)
Betatron orbit stability as function of n, G. C. Baldwin, F. R. Elder, and W. F. Westendorp—600(A)
Detection of pure quadrupole resonances, P. J. Bray—606(A)
Determination of thickness of Li targets from position of geometric peak, Charles F. Donaghy and Clark Goodman—298(A)
Electron microscope and diffraction traversing technique for examination of bimetal films, John L. Brown and Richard B. Belser—308(A)
Electron spectrometer for study of inelastic collision cross sections, E. N. Lassettre, A. S. Berman, S. Silverman, and M. E. Krasnow—635(A)
Equipment for measurement of very small x-ray scattering cross sections, W. W. Beeman and R. H. Neynaber—617(A)
Excitation and separation of pure high-order modes in large high-Q cavities, C. T. Zahn and W. G. Schweitzer, Jr.—633(A)
External proton beam of Carnegie synchrocyclotron, J. A. Kane, R. A. Stallwood, R. B. Sutton, T. H. Fields, and J. G. Fox—662(A)
Forbes bar method for measuring thermal conductivity of metals, Joseph M. Clifford and R. B. Sawyer—665(A)
Gaseous scintillation counter, C. Eggler and C. M. Huddleston—600(A)
General method for high-speed machine computation of ideal gas thermal properties. Diatomic free radicals of isotopic hydrides, Lester Haar and A. S. Friedman—614(A)
Generator of linearly varying current for electromagnet, John Levinson—651(A)
High-intensity beam of low-energy protons in ORNL 86-inch cyclotron, F. L. Green and J. A. Martin—304(A)
High-speed transient dynamic analysis, John C. Lindsay and A. V. Masket—665(A)
Ionization loading of electrostatic generators, C. M. Turner—599(A)
JAINCOMP-C and -D digital computers, Donald H. Jacobs and Milton E. Pugh—616(A)
Magnetic spectrograph for nuclear disintegration studies, W. W. Buechner, C. P. Browne, H. Enge, M. Mazari, and C. D. Buntschuh—609(A)
Magnetic spectrometer for recoil spectrometry, Arthur H. Snell and Frances Pleasonton—304(A)
Measuring magnetic properties of ferromagnetic materials by means of Hall effect, Simon Foner—652(A)
Methods of spinning rotors at low temperatures, J. W. Beams and J. B. Breazeale—601(A)
Microtron maximum particle energy, H. F. Kaiser—667(A)
Microtrons (electron cyclotrons for X and K band operation) II, H. F. Kaiser—600(A)
Molecular microwave oscillator and new hfs in microwave spectrum of NH_3, J. P. Gordon, H. J. Zeiger, and C. H. Townes—282(L)
Moseley's law applied to proportional counter resolution of adjacent elements, C. F. Hendee and S. Fine—281(L)
MTR fast chopper, R. G. Fluharty—609(A)
MTR time-of-flight instrumentation, D. R. deBoisblanc and K. A. McCollom—609(A)
Oxidation yield of ferrous sulfate dosimeter by x-rays, W. Bernstein, J. Weiss, and J. B. H. Kuper—609(A)
Particle selection technique used at M.I.T. cyclotron, F. A. Aschenbrenner—600(A)
Phase properties of deflected ion beam from fixed-frequency cyclotron, M. Jakobson and J. H. Manley—600(A)

Methods and Instruments (Continued)
Photoelectric measurement of reversal temperature, Hedwig Kohn and Einar Hinnov—301(A)
Polarization of Mn^{56} nuclei: cryogenic aspects, J. W. T. Dabbs and L. D. Roberts—970
Precision double-focusing mass spectrometer, T. L. Collins, T. T. Scolman, and A. O. Nier—615(A)
Pressurized 500-kv high-frequency Cockroft-Walton accelerator, Paul Lorrain, R. Béique, P. Gilmore, P. E. Girard, A. Breton, and P. Piché—599(A)
Proportional counter for Auger electrons, Ernest D. Graves and H. C. Thomas—304(A)
Proposed design of 50-Mev proton linear accelerator, L. H. Johnston, E. A. Day, and J. H. Williams—599(A)
Proton recoil telescope for observing neutron spectra, Carroll C. Trail and C. H. Johnson—640(A)
Radioactive and photoelectric *p-n* junction power sources, W. G. Pfann and W. Van Roosbroeck—597(A)
Replication of $BaTiO_3$ ceramic surfaces for electron microscopy, John L. Sampson, Edward E. Altshuler, and Robert W. Perry—298(A)
Response of anthracene scintillation crystals to monoenergetic soft x-rays, W. H. Robinson and W. Jentschke —1412
Rf Cockroft-Walton generator for neutron production, R. A. Peck, Jr.—599(A)
Rf mass spectrometer as rocket-borne instrument for atmospheric composition studies, Walter F. Sheridan—298(A)
Rotating-sphere solid-angle scanner for γ rays, George R. Meneely, Robert J. Kerr, Jesse E. Hoffman, and Sherwood K. Haynes—308(A)
Scattered radiation contribution to depth dose data for 35- and 90-Mev synchrotron x-rays, J. Boag and B. Zendle —608(A)
Scintillation detector for thermal and epithermal neutrons, K. H. Sun, P. R. Malmberg, and F. A. Pecjak—600(A)
Self-powered semiconductor amplifier, C. G. B. Garrett and W. H. Brattain—1091(L)
Small current dc amplifier, Newton Underwood and G. F. Zindler, Jr.—304(A)
Spectral distribution curves of far uv radiation from Cornell synchrotron, D. H. Tomboulian and P. L. Hartman—600(A)
System for measuring flight times of fast neutrons, Conway W. Snyder and Vincent E. Parker—635(A)
Time jitter in BF_3 counters, O. D. Simpson—600(A)
Use of scintillation counters in studies on luminous efficiency of biological materials, J. G. Kereiakes and A. T. Krebs—308(A)
Use of Si *p-n* junctions for converting solar energy to electrical energy, R. L. Cummerow—561(L)
Vapor expansion chamber using pure water. I, J. E. Hopson and C. E. Nielsen—601(A)
Vapor expansion chamber using ammonia and water. II, R. P. Caren and C. E. Nielsen—601(A)
Vapor expansion chamber using pure gases at low temperatures. III, C. E. Nielsen and J. E. Hopson—601(A)

Microwaves (see also **Atomic Structure and Spectra; Magnetic Resonance; Molecular Structure and Spectra; Nuclear Moments and Spin**)
Microwave determination of probability of collision of electrons in He, Lawrence Gould and Sanborn C. Brown —897
Molecular microwave oscillator and new hfs in microwave spectrum of NH_3, J. P. Gordon, H. J. Zeiger, and C. H. Townes—282(L)
Phenomena of plasma resonance, K. S. Champion and S. C. Brown—634(A)
Quantum effects in interaction between electrons and high-frequency fields. I, I. R. Senitzky—904

Miscellaneous
Can well-informed heat engine (WHE) have free will?, Jerome Rothstein—643(A)

Mobility of Ions and Electrons (see **Ions and Electrons, Mobility**)

Molecular Aggregates
Color centers in alkali silicate and borate glasses, Ryosuke Yokota—1145
Metamict state, William Primak—837(L)
Paramagnetic resonances in glasses, R. H. Sands, J. Townsend, and H. P. Hood—607(A)

Molecular Beams (see **Atomic and Molecular Beams**)

Molecular Structure and Spectra
Centrifugal distortion in asymmetric top molecules, III. H_2O, D_2O, and HDO, D. W. Posener and M. W. P. Strandberg—374
Centrifugal distortion in methyl halides, John Cox, W. J. Orville Thomas, and Walter Gordy—299(A)
Direct *l*-doublet transition of HCN in 10-cm wavelength region, Robert J. Collier—1201
Double bond character of C—Cl bond, R. Bersohn—614(A)
Effects of deviation of O_2 from Hund (*b*), M. W. P. Strandberg and M. Tinkham—623(A)
Electron impact studies of isotopic O_2 and CO_2 molecules, Oliver A. Schaeffer and Henry R. Owen—615(A)
Infrared spectroscopic study of influence of molecular structure upon ν(NH), ν(CO), and $\nu(CH_3)$ in benzopyrroles and their analogs, Nelson Fuson, Marie-Louise Josien, and Essie M. Shelton—300(A)
Infrared spectrum of allene-d_2, William H. Fletcher and W. E. Shuler—300(A)
Infrared spectrum of σ_2 for $B^{10}F_3$ and $B^{11}F_3$, Alvin H. Nielsen—300(A)
Intensity of infrared absorption bands in methylene chloride, Joseph W. Straley—300(A)
Microwave absorption in compressed gases, G. Birnbaum and A. A. Maryott—622(A)
Microwave and far infrared atmospheric water-vapor absorption, T. F. Rogers—622(A)
Microwave spectral series of deuterated hydrogen peroxide, J. T. Massey, C. I. Beard, and C. K. Jen—622(A)
Microwave spectrum and dipole moment of vinylene carbonate, George R. Slayton, J. W. Simmons, and J. H. Goldstein—299(A)
Microwave spectrum of OCS, Martin Peter and M. W. P. Strandberg—622(A)
Microwave spectrum of TeCS and masses of stable Te isotopes, W. A. Hardy and G. Silvey—385
Mm wave spectrum of arsine, Albert Jache, Gilbert Blevins, and Walter Gordy—299(A)
Mm wave spectrum of phosphine, Charles A. Burrus, Albert Jache, and Walter Gordy—299(A)
Molecular association in perfluoroalkyl carboxylic acids, J. R. Lawson and M. B. Towns—300(A)
Molecular microwave oscillator and new hfs in microwave spectrum of NH_3, J. P. Gordon, H. J. Zeiger, and C. H. Townes—282(L)
Near uv absorption spectrum of 1,2,4-trifluorobenzene, K. Narahari Rao—299(A)
Nuclear magnetic resonance in solid H_2 with various *ortho* concentrations, Tadashi Sugawara, Yoshika Masuda, Teinosuke Kanda, and Eizo Kanda—1355(L)
1–2 mm wave spectroscopy. V. PH_3 and PD_3, Charles Burrus, Albert Jache, and Walter Gordy—706
Photolysis of para-diazo-N,N-dimethylaniline ZnCl dihydrate, Alnert Baril, Jr.—306(A)
Potential constants for carbonyl fluoride, R. J. Lovell and E. A. Jones—300(A)

Pressure broadening of cyanogen bromide in microwave region, Ralph Trambarulo, Henry Lackner, Paul Moser, and Harold Feeny—622(A)
Saturation in microwave spectrum of methyl chloride, George R. Bird—1686(L)
Selection rules in microwave magnetic resonance spectrum of O_3, M. Tinkham and M. W. P. Strandberg—622(A)
Vibrational analysis of polypeptide chains, W. E. Deeds—300(A)
Vibrational spectra of pentafluorides of Sb, As, and Br, Lawrence K. Akers and Ernest A. Jones—300(A)
Vibrational spectrum of fluorotrichloroethylene, D. E. Mann and Earle K. Plyer—622(A)

Moments, Nuclear (see **Nuclear Moments and Spin**)
Moments of Molecules (see **Molecular Structure and Spectra**)

Neutrino (see also **Nuclear Spectra; Radioactivity**)
Heat generation in earth by solar neutrinos, A. M. Cormack—580(L)
Recoil spectrum in β decay of Ne^{19}, W. Parker Alford and Donald R. Hamilton—1351(L)

Neutron Diffraction (see **Diffraction; Scattering of Neutrons**)
Neutrons (see **Elementary Particle Interactions**)
Noise
Quantum theory of damped electrical oscillator and noise. II. Radiation resistance, J. Weber—1706(E)

Nuclear Fission
Angular distribution of U^{235} fragments from neutron-induced fission as function of incident neutron energy, J. E. Brolley, Jr., W. C. Dickinson, and R. L. Henkel—651(A)
Energy distributions of fragments from fission of U^{235}, U^{238}, and Pu^{239} by fast neutrons, John S. Wahl—126
Fine structure in U^{233} fission, E. P. Steinberg, L. E. Glendenin, M. G. Inghram, and R. J. Hayden—867(L)
Fission-fragment angular distribution measurements, B. L. Cohen, D. J. Coombe, and B. L. Ferrell—303(A)
Low-energy photofission yields for U^{238}, Harold G. Richter and Charles D. Coryell—1550
Neutron multiplicity from spontaneous fission of uranium, K. W. Geiger and D. C. Rose—646(A)
$(p,2n)$, $(p,2p)$, (p,t), (p,He^3) and (p,f) cross sections and excitation functions, B. L. Cohen, G. H. McCormick, T. H. Handley, and E. Newman—639(A)
Radiochemical investigation of spontaneous fission of Cm^{242}, E. P. Steinberg and L. E. Glendenin—431
Relative ionization yields for fission fragments in various gases, Lloyd O. Herwig and Glenn H. Miller—413
Relative photofission yields of several fissionable materials, J. R. Huizenga, J. E. Gindler, and R. B. Duffield—1009
U photofission yields, Roman A. Schmitt and Nathan Sugarman—1260

Nuclear Forces (see **Elementary Particle Interactions; Field Theory; Nuclear Structure Theory**)
Nuclear Induction (see **Magnetic Resonance; Nuclear Moments and Spin**)
Nuclear Isomers (see **Nuclear Spectra; Radioactivity**)
Nuclear Moments and Spin
Effect of atomic core on nuclear quadrupole coupling, R. M. Sternheimer—736
Electron spin magnetic moment in atomic hydrogen, R. Beringer and Mark A. Heald—1474
Exchange current effects in deuteron, J. Bernstein and A. Klein—655(A)
Gyromagnetic ratio of 10^{-6}-second Ta^{181m}, S. Raboy and V. E. Krohn—1689(L)
Hfs and nuclear moments on stable Br isotopes, John Gordon King and Vincent Jaccarino—1706(E)
Magnetic moment of first-excited state of Pb^{204}, V. Krohn and S. Raboy—608(A)
Magnetic resonance spectra of beryl crystals, L. Carlton Brown and Dudley Williams—1110(L)
Method for brute force polarization of H nuclei, J. W. T. Dabbs and L. D. Roberts—307(A)
Na^{23} moments, Morris F. Scharff—1114(L)
Neutron spin from Bloch-Alvarez type experiment, C. P. Stanford, T. E. Stephenson, and S. Bernstein—302(A)
Nuclear spin and hfs interaction of 3.1-hr Cs^{136} isomer, V. W. Cohen and D. A. Gilbert—569(L)
Nuclear spin and magnetic moment of 3.1-hr Cs^{134m}, L. S. Goodman and S. Wexler—570(L)
Os^{189} magnetic moment, H. R. Loeliger and L. R. Sarles—291(L)
Polarization of Mn^{55} nuclei: cryogenic aspects, J. W. T. Dabbs and L. D. Roberts—970
Regularity in magnetic moments of odd nuclei, Morris F. Scharff—1112(L)
Relativistic and magnetic spin interactions in He-like atoms, J. Sucher and H. M. Foley—966
Reorientation of aligned nuclei, N. R. Steenberg—605(A); 982
Sachs exchange moment, R. H. Dalitz—799
Spins and hyperfine splittings of Ag^{111} and Cu^{64}, Aaron Lemonick and Francis M. Pipkin—1356(L)

Nuclear Photoeffects
$A^{40}(\gamma,n)$ threshold and mass of A^{39}, J. Halpern, R. Nathans, and P. F. Yergin—1529
Angular distributions of photodeuterons, D. A. Edwards, B. Wolfe, A. Silverman, and J. W. DeWire—629(A)
Determination of photo cross sections from bremsstrahlung activation curves, A. S. Penfold and J. E. Leiss—637(A)
Elastic photoproduction of π^0 mesons from He, E. L. Goldwasser, L. J. Koester, Jr., and F. E. Mills—1692(L)
Energy dependence of some photonuclear reactions, T. T. Sugihara and I. Halpern—630(A)
Fine structure in $C^{12}(\gamma,n)C^{11}$ and $O^{16}(\gamma,n)O^{15}$ activation curves, L. Katz, R. N. H. Haslam, R. J. Horsley, A. G. W. Cameron, and R. Montalbetti—464
Fine structure in neutron yield curves from (γ,n) reactions in Li^7, C^{13}, O^{16}, and F^{19}, J. Goldemberg and L. Katz—471
Fine structure of $O^{16}(\gamma,n)O^{15}$ activation curve, B. M. Spicer, A. S. Penfold, and J. Goldemberg—629(A)
Hg^{198} nuclear resonance fluorescence and lifetime of 411-kev excited state, F. R. Metzger and W. B. Todd—853(L)
Implications of photonuclear effect in Zr^{90}, P. Axel and J. D. Fox—613(A)
$In^{115}(\gamma,\gamma')In^{115m}$ cross section, J. L. Burkhardt and E. J. Winhold—629(A)
Independent particle model and nuclear photoeffect, J. S. Levinger and D. C. Kent—418
Low-energy photofission yields for U^{238}, Harold G. Richter and Charles D. Coryell—1550
Negative-to-positive ratio of photomesons from deuterium, Matthew Sands, J. G. Teasdale, and Robert L. Walker—592(L)
Neutrons in coincidence with high-energy photoprotons, H. Myers, A. Odian, P. C. Stein, and A. Wattenberg—576(L)
Normal coordinates in nuclear photoeffect, Yu-Chang Hsieh and Ingram Bloch—305(A)
Nuclear scattering of γ rays below meson threshold, G. E. Pugh, D. H. Frisch, and R. Gomez—590(L)
Photodisintegration of deuterium by 95-Mev bremsstrahlung, Lew Allen, Jr., and A. O. Hanson—629(A)
Photodisintegration of deuterium by 165-Mev x-rays, E. A. Whalin, Jr.—1362(L)

Nuclear Photoeffects (Continued)
Photodisintegration of deuterium by 265-Mev bremsstrahlung, T. Yamagata, M. Q. Barton, A. O. Hanson, and J. H. Smith—574(L)
Photodisintegration thresholds of D_2O and Be, J. C. Noyes, J. E. Van Hoomissen, W. C. Miller, and B. Waldman—396
Photoneutron angular distributions, K. Geller, J. Halpern, and Paul F. Yergin—659(A)
Photoneutron cross sections in He, N, O, F, Ne, and A, G. A. Ferguson, J. Halpern, R. Nathans, and P. F. Yergin—659(A); 776
Photopion S wave near threshold and pion-nucleon coupling constant, G. Bernardini and E. L. Goldwasser—857(L)
Photoproduction of charged π mesons from hydrogen and deuterium, T. L. Jenkins, D. Luckey, T. R. Palfrey, and R. R. Wilson—179
Photoproduction of π^+ mesons from H, J. E. Leiss and C. S. Robinson—638(A)
Photoproduction of π^+ mesons from H near threshold, C. S. Robinson and J. E. Leiss—638(A)
Photoproduction of π^+ mesons near threshold, L. S. Osborne, Y. Goldschmidt-Clermont, and G. Parker—637(A)
Photoprotons from Co, M. E. Toms, H. Gerardo, and W. E. Stephens—629(A); M. Elaine Toms and William E. Stephens—1209
Proton-neutron coincidences in high-energy photodisintegration of Li, M. Q. Barton and J. H. Smith—573(L)
Relative photofission yields of several fissionable materials, J. R. Huizenga, J. E. Gindler, and R. B. Duffield—1009
Resonance absorption of γ radiation by O^{16} nuclei, J. G. Campbell—1357(L)
Systematics of photoproton yields, E. V. Weinstock and J. Halpern—630(A)
U photofission yields, Roman A. Schmitt and Nathan Sugarman—1260
Use of causality conditions in quantum theory, M. Gell-Mann, M. L. Goldberger, and W. E. Thirring—1612
Yield of α particles from photonuclear reactions at 23-Mev bremsstrahlung, L. H. Greenberg, J. G. V. Taylor, and R. N. H. Haslam—1540

Nuclear Reactions, General (see also **Elementary Particle Interactions; Scattering**)
$Be^9(N^{14})F^{19}He^5$ excitation function, H. L. Reynolds and A. Zucker—302(A)
Determination of thickness of Li targets from position of geometric peak, Charles F. Donaghy and Clark Goodman—298(A)
γ radiation from reactions induced by polarized particles, J. M. Kennedy and W. T. Sharp—440
High-speed computation of angular momentum functions, Albert Simon—657(A)
Isotopic spin factors in nuclear reactions, R. J. Drachman and D. C. Peaslee—605(A)
Magnetic spectrograph for nuclear disintegration studies, W. W. Buechner, C. P. Browne, H. Enge, M. Mazari, and C. D. Buntschuh—609(A)
Nuclear cross sections and size of nucleus, Warren Heckrotte—1279
Nuclear radii and transparencies from inelastic cross-section measurements. I. Method, G. P. Millburn, W. Birnbaum, W. E. Crandall, and L. Schecter—620(A); II. Interpretation, W. E. Crandall, W. Birnbaum, L. Schecter, and G. P. Millburn—620(A)
Nuclear radii from inelastic cross-section measurements, G. P. Millburn, W. Birnbaum, W. E. Crandall, and L. Schecter—1268
Polarization of fast neutrons from nuclear reactions, Harvey B. Willard, Joe K. Bair, and Joe D. Kington—1359(L)
Theory of nuclear reactions with radioactive product, T. A. Welton—302(A)

Nuclear Reactions Induced by α Particles and He^3 (see also **Scattering of α Particles**)
Be^9+He^3 reactions, C. D. Moak, W. M. Good, and W. E. Kunz—641(A)
Coulomb excitation of energy levels in Rh and Ag, N. P. Heydenburg and G. M. Temmer—861(L)
Coulomb excitation *vs* compound nucleus formation in lighter elements, N. P. Heydenburg and G. M. Temmer—629(A)
Cross section for producing high-energy neutrons from C targets bombarded by protons, deuterons, and He^3 particles, L. Schecter, W. E. Crandall, G. P. Millburn, and J. Ise—659(A)
Energy levels of C^{13} by inelastic α scattering, D. W. Miller, V. K. Rasmussen, and M. B. Sampson—649(A)
Excitation function from $C^{13}(d;p,2n)C^{13}$, $C^{13}(He^3;2p,2n)C^{13}$, and $C^{13}(\alpha;2p,3n)C^{13}$, W. Birnbaum, W. E. Crandall, G. P. Millburn, and R. V. Pyle—649(A)
4.43-Mev γ-rays from C^{13}, W. R. Mills, Jr., and R. J. Mackin, Jr.—1206
$Li^7(He^3,p)Be^9$ reaction, W. E. Kunz, C. D. Moak, and W. M. Good—640(A)
Nuclear radii from inelastic cross-section measurements, G. P. Millburn, W. Birnbaum, W. E. Crandall, and L. Schecter—620(A); 1268
Po-Be neutron spectrum, B. J. Winnemore, H. Gursky, D. A. Cowan, and C. D. Curtis—301(A)

Nuclear Reactions Induced by Deuterons and Tritons (see also **Scattering of Deuterons**)
Al^{26} energy levels, Cornelius P. Browne—860(L)
Be^8 energy levels from $Li^7(d,n)Be^8$, Carroll C. Trail and C. H. Johnson—1363(L)
Ca^{42} and $Ca^{44}(d,p)$ reactions, C. M. Braams—650(A)
Coulomb effects in deuteron stripping, N. Austern and S. T. Butler—605(A)
Cross section for producing high-energy neutrons from C targets bombarded by protons, deuterons, and He^3 particles, L. Schecter, W. E. Crandall, G. P. Millburn, and J. Ise—658(A)
Differential cross sections for $C^{13}(d,p)C^{14}$ and $C^{13}(d,t)C^{12}$, H. D. Holmgren, J. M. Blair, B. E. Simmons, T. F. Stratton, and R. V. Stuart—1544
Energy and angular distribution of protons from deuteron bombardment of Ni, William W. Pratt—1517
Energy levels in C^{14} and N^{14}, R. D. Bent, R. W. Bonner, and R. F. Sippel—649(A)
Excitation function for $C^{13}(d;p,2n)C^{13}$, $C^{13}(He^3;2p,2n)C^{13}$, and $C^{13}(\alpha;2p,3n)C^{13}$, W. Birnbaum, W. E. Crandall, G. P. Millburn, and R. V. Pyle—649(A)
γ-γ correlation in $Be^9(d,n)B^{10*}(\gamma)B^{10}$, S. M. Shafroth and S. S. Hanna—641(A)
$Li^6(d,t)$ reaction, R. L. Macklin and H. E. Banta—302(A)
$Li^7(d,p)Li^8$ yield curve, Stanley Bashkin—640(A); 1012
Mass-spectrometric study of deuteron-induced reactions in iodine, Silvio J. Balestrini—1502
Neutron thresholds from (d,n) and (p,n) reactions, C. F. Cook, T. W. Bonner, and J. B. Marion—639(A)
Nuclear cross sections and size of nucleus, Warren Heckrotte—619(A); 1279
Nuclear radii from inelastic cross-section measurements, G. P. Millburn, W. Birnbaum, W. E. Crandall, and L. Schecter—620(A); 1268
Numerical calculation of stripping angular distribution, W. Tobocman and M. Kalos—605(A)

New isotope protactinium-237, W. W. T. Crane and G. M. Iddings—1702(L)
Production of I^{124} by deuteron bombardment of Te, T. Hall, M. Siegel, L. M. Sharpe, and D. Pressman—1208
Proton recoil telescope for observing neutron spectra, Carroll C. Trail and C. H. Johnson—640(A)
Reaction particles from 14.5-Mev deuteron bombardment of Li^7 and Li^6, S. H. Levine, R. S. Bender, J. N. McGruer, and W. F. Vogelsang—640(A)
$Ti^{48}(d,2n)V^{48}$, $Cr^{52}(d,2n)Mn^{52}$, and $Fe^{56}(d,2n)Co^{56}$ cross sections, Warren H. Burgus, George A. Cowan, J. W. Hadley, Wilmot Hess, Theodore Shull, M. L. Stevenson, and H. F. York—750
Yield and angular distribution of protons from $Li^6(d,p)Li^7$, William E. Nickell—426

Nuclear Reactions Induced by Mesons (see also **Elementary Particle Interactions; Mesons; Scattering of Mesons**)

Absorption of negative pions in deuterium: Parity of pion, W. Chinowsky and J. Steinberger—1561
Charge exchange scattering of stopped π^- mesons in deuterium, Jack Steinberger and William Chinowsky—623(A)
Cross sections for meson-induced stars in Ilford G5 nuclear emulsions, Leonard A. Mann, Ray A. Grandey, and Arnold F. Clark—648(A)
High-energy electrons in capture of μ^- mesons by complex nuclei, S. Lokanathan, J. Steinberger, and H. B. Wolfe—624(A)
Interaction of negative muons with iodine, Lester Winsberg—205
Interaction of negative pions with iodine, Lester Winsberg—198
Internal pair production in radiative absorption of π^- mesons by H atoms, W. Wada—618(A)
Nuclear absorption of negative K particles, Herbert DeStaebler, Jr.—1110(L)
Numerical calculation of 3/2−3/2 pion-nucleon reaction matrix and phase shifts, Freda F. Salzman and James N. Snyder—286(L)
Parity of pion, William Chinowsky and Jack Steinberger—623(A)
π^- interactions at 1.5 Bev. II, J. Crussard, W. D. Walker, and M. Koshiba—624(A)
π-meson production in π-nucleon collisions at 1.5 Bev, W. D. Walker, J. Crussard, and M. Koshiba—852(L)
π^--p collisions at 1.5 Bev. I, W. D. Walker, J. Crussard, and M. Koshiba—624(A)
Production of neutrons by negative μ mesons by complex nuclei, D. R. Jones—624(A)
Scattering of 145-Mev π^+ by H in emulsion, Jay Orear, C. H. Tsao, J. J. Lord, and A. B. Weaver—624(A)
Total cross section for charge exchange scattering of π^- mesons by H at 42, 30, and 20 Mev, W. J. Spry—1295
Total cross sections for scattering of positive pions by H, J. Blaser, J. Ashkin, F. Feiner, J. Gorman, and M. O. Stern—624(A)

Nuclear Reactions Induced by Neutrons (see also **Elementary Particle Interactions; Scattering of Neutrons**)

Activation of Al and Se^{80} by p-neutron capture in kev region, R. H. Rohrer, H. W. Newson, J. H. Gibbons, and P. Cap—302(A)
Angular distribution of U^{235} fragments from neutron-induced fission as function of incident neutron energy, J. E. Brolley, Jr., W. C. Dickinson, and R. L. Henkel—651(A)
C^{13} thermal neutron capture cross section, G. R. Hennig—92
Capture γ-ray studies using scintillation coincidence spectrometer, Arthur Recksiedler and Bernard Hamermesh—650(A)
Capture of polarized neutrons by polarized Sm^{149}, L. D. Roberts, S. Bernstein, J. W. T. Dabbs, and C. P. Stanford—105
Cr^{55} preparation and half-life, G. A. Bazorgan, J. W. Irvine, Jr., and C. D. Coryell—781
Cross section for excitation of Pb^{207m} by inelastic neutron scattering, P. H. Stelson and E. C. Campbell—301(A)
Cross sections for reactions $C^{13}(p,pn)(n,2n)C^{11}$, S. D. Warshaw, R. A. Swanson, and A. H. Rosenfeld—649(A)
De-excitation γ rays from inelastic scattering of neutrons, Gordon L. Griffith—636(A)
Energy distributions of fragments from fission of U^{235}, U^{238}, and Pu^{239} by fast neutrons, John S. Wahl—126
Eu activation studies with monochromatic neutrons, R. E. Wood—453
"Fast chopper" time-of-flight measurement of neutron resonances, F. G. P. Seidl, D. J. Hughes, H. Palevsky, J. S. Levin, W. Y. Kato, and N. G. Sjöstrand—476
Fast neutron scintillation spectra of $Li^6(n,\alpha)H^3$ reaction in LiI(Eu), J. H. Neiler, F. Muckenthaler, and James Schenck—640(A)
$Fe^{56}(n,p)Mn^{56}$ excitation function, J. Terrell and D. M. Holm—650(A)
γ radiation from interaction of 3.1-Mev neutrons, V. E. Scherrer, B. A. Allison, and W. R. Faust—637(A)
γ-ray spectrum from inelastic scattering of fast neutrons in Fe, D. L. Lafferty, L. A. Rayburn, and T. M. Hahn—637(A)
γ rays produced by inelastic scattering of d-D neutrons in Cu, Al, and Mg, L. A. Rayburn, D. L. Lafferty, and T. M. Hahn—637(A)
Inelastic scattering of d-D neutrons by Fe and Cu, L. A. Rayburn, D. L. Lafferty, and T. M. Hahn—301(A)
Inelastic scattering of 4.3-Mev neutrons by Fe^{56}, B. Jennings, J. B. Weddell, and R. L. Hellens—636(A)
Inelastic scattering of neutrons by Ba^{137} and Hg^{199}, C. P. Swann and F. R. Metzger—636(A)
Interactions of high-energy neutrons in Mo, E. G. Silver and R. W. Waniek—586(L)
$Li^6(n,\alpha)H^3$ angular distribution, James B. Weddell and James H. Roberts—117
Low-lying states in nuclei from $(n,n'\gamma)$ interactions, Janet B. Guernsey and Clark Goodman—297(A)
Meson production in n-p collisions at Cosmotron energies, W. B. Fowler, R. P. Shutt, A. M. Thorndike, and W. L. Whittemore—1026
Negative pion production in n-p collisions, S. C. Wright and R. A. Schluter—639(A)
Neutral pion-deuteron production in high-energy n-p collisions, Robert A. Schluter—639(A)
Neutron-capture γ-ray spectra, Melvin Reier and Morris H. Shamos—636(A)
Neutron capture measurements with G. E. betatron velocity selector, R. D. Albert, M. L. Yeater, and E. R. Gaerttner—644(A)
Neutron inelastic scattering, Robert M. Kiehn and Clark Goodman—636(A); 989
Neutron inelastic scattering in Ta and I, Janet B. Guernsey and Clark Goodman—636(A)
Neutron resonance parameters in Cs, In, Sn, and Pr, R. S. Carter and J. A. Harvey—645(A)
Neutron resonance parameters in U, Th, Hg, and Au, J. S. Levin and D. J. Hughes—645(A)
Neutron resonance scattering by Ag and Au, R. E. Wood—644(A)

Nuclear Reactions Induced by Neutrons (Continued)
Neutron resonances in Ho, Tm, and Lu, V. E. Pilcher, R. S. Carter, and A. Stolovy—645(A)
Neutron resonances in Zn isotopes, D. A. Dahlberg and L. M. Bollinger—645(A)
New isotope identification program on Oak Ridge 86-inch cyclotron, T. H. Handley and B. L. Cohen—611(A)
n-γ coincidences produced by inelastic scattering of neutrons, P. Shapiro, V. E. Scherrer, B. A. Allison, and W. R. Faust—751
Nuclear size and cross sections at cosmic-ray energies, Robert W. Williams—647(A)
Pickup reactions $B^{10}(n,d)Be^9$ for 14-Mev neutrons, F. L. Ribe and J. D. Seagrave—649(A)
Pile neutron cross sections of isotopes of Am, Bk, Cf, and element 99, B. G. Harvey, H. P. Robinson, S. G. Thompson, A. Ghiorso, and G. R. Choppin—581(L)
Polarization in n-p scattering at 100–200 Mev, A. Roberts, J. Tinlot, and E. M. Hafner—1099(L)
Polarization of Mn^{56} nuclei: cryogenic aspects, J. W. T. Dabbs and L. D. Roberts—970
Scattering of 14.1-Mev neutrons in He, H, and N, J. R. Smith—730
Search for polarization in charge exchange scattering, H. Bradner and R. E. Donaldson—663(A)
Self-indication measurement of σ_{t_0} for 5.2-ev neutron resonance in Ag, J. E. Draper and C. P. Baker—644(A)
Sphere measurements of neutron inelastic collision cross sections, Robert C. Allen—637(A)
Standards for thermal neutron capture measurements, G. R. Ringo and S. Wexler—660(A)
Thermal neutron capture cross sections of hydrogen, B, and Ag, F. R. Scott, D. B. Thomson, and W. Wright—582(L)
Time-of-flight measurements of inelastic neutron scattering, Gerard K. O'Neill—635(A)
Time-of-flight measurements on inelastic scattering of 14.8-Mev neutrons, Gerard K. O'Neill—1235
Total cross section of O_2 for cold neutrons, R. M. Eisberg, H. Palevsky, M. E. Rickey, and T. I. Taylor—659(A)
Total cross sections for high-energy neutrons, Vaughn Culler and R. W. Waniek—585(L); R. W. Waniek and Vaughn Culler—659(A)
Total neutron cross sections in kev region: Tl^{205} and Tl^{205}, J. H. Gibbons and H. W. Newson—644(A)
Total neutron cross sections of Bi and Mn, L. M. Bollinger, R. R. Palmer, and D. A. Dahlberg—645(A)
Variation of $\bar{\Gamma}_n^0/\bar{D}$ ratio with atomic weight, J. A. Harvey, C. E. Porter, and D. J. Hughes—645(A)

Nuclear Reactions Induced by Protons (see also **Elementary Particle Interactions; Scattering of Protons**)
Activities produced in Au by proton bombardment, C. H. Braden, L. D. Wyly, and E. T. Patronis, Jr.—758
Angular distribution of deuterons from (p,d) reactions in light nuclei, J. B. Reynolds and K. G. Standing—639(A)
Angular distribution of 12-Mev and 16-Mev γ rays from proton bombardment of boron, H. H. Givin, G. K. Farney, T. M. Hahn, and B. D. Kern—641(A)
Angular distribution of 12-Mev γ rays from reaction $B^{11}(p,\gamma)C^{12}$, H. H. Givin, G. K. Farney, B. D. Kern, and T. M. Hahn—302(A)
Antiproton production, G. Feldman—1697(L)
Assymetry in neutron production by bombarding targets with 285-Mev polarized protons, Hugh Bradner and Robert Donaldson—1701(L)
Capture γ rays from 315-kev proton bombardment of Be^9, R. R. Carlson and E. B. Nelson—641(A)
Charged pion production from C by protons, Walter F. Dudziak—866(L)
Comparison of reactions $H^3(H^1,\pi^+)H^3$ and $H^3(H^1,\pi^0)He^3$ as test of charge independence, Kenneth C. Bandtel, Wilson J. Frank, Richard Madey, and Burton J. Moyer—639(A)
Conservation of isobaric spin in reaction $Be^9(p,\alpha)Li^6$, R. Malm and D. R. Inglis—993
Coulomb excitation of Au, W. I. Goldburg, S. A. Cox, and R. M. Williamson—628(A)
Coulomb excitation of Ta, W, and Au, W. I. Goldburg and R. M. Williamson—767
Cross section for producing high-energy neutrons from C targets bombarded by protons, deuterons, and He^4 particles, L. Schecter, W. E. Crandall, G. P. Millburn, and J. Ise—658(A)
Cross sections for reactions $C^{12}(p,pn)(n,2n)C^{11}$, S. D. Warshaw, R. A. Swanson, and A. H. Rosenfeld—649(A)
Determination of thickness of Li targets from position of geometric peak, Charles F. Donaghy and Clark Goodman—298(A)
Disintegration of bismuth by 2.2-Bev protons, Nathan Sugarman, Robert B. Duffield, G. Friedlander, and J. M. Miller—1704(L)
Electric excitation of Au, J. Eisinger, C. F. Cook, and C. M. Class—628(A)
Electric excitation of Mn^{55} with protons, Hans Mark, Clyde McClelland, and Clark Goodman—628(A)
γ radiation from B^{10} bombarded by protons, Robert B. Day and Torben Huus—1003
γ radiation from Mg^{26} under proton bombardment, Leonard N. Russell, Warren E. Taylor, and John N. Cooper—99
γ-ray resonances in proton bombardment of Na^{23}, N. P. Baumann, F. W. Prosser, Jr., and R. W. Krone—650(A)
γ-rays from $Si^{30}(p,\gamma)P^{30}$ reaction, P. M. Endt, J. C. Kluyver, and C. van der Leun—580(L)
Magnetic analysis indicating charge symmetry in reaction $Be^9(p,\alpha)Li^6$, R. Malm and D. R. Inglis—641(A)
Mechanism of proton polarization in high-energy collisions, Owen Chamberlain, Emilio Segrè, Robert Tripp, Clyde Wiegand, and Thomas Ypsilantis—1105(L)
Neutron thresholds from (d,n) and (p,n) reactions, C. F. Cook, T. W. Bonner, and J. B. Marion—639(A)
Neutrons from proton bombardment of B^{10}, F. Ajzenberg, W. Franzen, and J. G. Likely—641(A); Fay Ajzenberg and Wolfgang Franzen—1531
New isotope identification program on Oak Ridge 86-inch cyclotron, T. H. Handley and B. L. Cohen—611(A)
Nuclear radii from inelastic cross-section measurements, G. P. Millburn, W. Birnbaum, W. E. Crandall, and L. Schecter—620(A); 1268
Nuclear size and cross sections at cosmic-ray energies, Robert W. Williams—647(A)
π^+ production in H by 437-Mev protons, T. H. Fields, J. G. Fox, J. A. Kane, R. A. Stallwood, and R. B. Sutton—638(A)
Pickup deuterons produced from 95-Mev protons, W. Selove—663(A)
Pion production by 440-Mev protons incident upon H and C, Arthur H. Rosenfeld—638(A)
Pion production ratios. II, D. C. Peaslee—1580
(p,n) reactions on As, Y, Nb, and Rh, Reid Patterson—303(A)
$(p,2n)$, $(p,2p)$, (p,t), (p,He^3), and (p,f) cross sections and excitation functions, B. L. Cohen, G. H. McCormick, T. H. Handley, and E. Newman—639(A)
Polarization in high-energy p-n-n double scattering, Peter Hillman, Vaughn Culler, and N. F. Ramsey—462

Polarization of fast neutrons from nuclear reactions, Harvey B. Willard, Joe K. Bair, and Joe D. Kington —1359(L)
Polarization of 170-Mev neutrons, A. Roberts, J. Tinlot, and E. M. Hafner—663(A)
p-p cross section at 95 Mev, U. E. Kruse and J. M. Teem —662(A)
p-p scattering in nuclear emulsions, S. K. Kao and A. F. Clark—662(A)
p-p scattering near interference minimum, Robert L. Zimmerman, David H. Frisch, and Daniel I. Cooper—662(A)
Production of Be^7 in high-energy reactions, J. Hudis, E. Baker, and G. Friedlander—612(A)
Production of positive and negative pions in Be by 1.0 and 2.3-Bev protons, S. J. Lindenbaum and Luke C. L. Yuan —638(A)
Proton bremsstrahlung and high-energy γ emission from C, David Cohen, Burton J. Moyer, Harlan Shaw, and Charles Waddell—664(A)
(p,xn) cross sections in Bi, R. E. Bell—651(A)
Radiochemical evidence for $Cu^{65}(p,pn\pi^+)Ni^{65}$ reaction, Si-Chang Fung and Anthony Turkevich—176
Reaction $p+p\rightarrow\pi^++d$ with polarized protons, F. S. Crawford, Jr., and M. L. Stevenson—1112(L)
Reactions of 370-Mev protons with Co, E. Belmont and J. M. Miller—1554
Resonance near $Li^7(p,n)$ threshold, H. W. Newson and J. H. Gibbons—640(A)
Resonances in proton bombardment of C^{14}, G. A. Bartholomew, F. Brown, H. E. Gove, A. E. Litherland, and E. B. Paul—649(A)
Resonant states of Mg^{24} excited by protons on Na, P. H. Stelson and W. M. Preston—974
Scattering of 10-Mev protons on Mg and C, G. E. Fischer —664(A)
Scattering of 96-Mev protons from light nuclei, K. Strauch and W. F. Titus—854(L)
Scattering of 314-Mev polarized protons by deuterium, J. Marshall, L. Marshall, D. Nagle, and W. Skolnik —1020
Schematic calculation of (p,xn) cross sections of heavy elements, J. David Jackson—651(A)
Scintillation counter study of γ rays from proton capture in Na, E. B. Nelson, E. H. Geer, and R. R. Carlson—650(A)
Search for polarization in charge exchange scattering, H. Bradner and R. E. Donaldson—663(A)
Spin assignments and partial width measurements of resonances in S^{33} from reaction $P^{31}(p\gamma)S^{32}$, H. E. Gove, E. B. Paul, A. E. Litherland, and G. A. Bartholomew—650(A)
τ meson produced by 3.0-Bev protons, R. D. Hill, E. O. Salant and M. Widgoff—1699(L)
Total p-p cross section above 400 Mev, A. M. Shapiro, C. P. Leavitt, and F. F. Chen—663(A)
Yield of π^+ mesons by 335-Mev protons as function of atomic number, J. Merritt and D. Hamlin—638(A)
Nuclear Scattering (see **Scattering**)
Nuclear Spectra (see also **Nuclear Reactions; Radioactivity**)
Absence of K capture in decay scheme of Pb^{205}, T. T. Sugihara, R. H. Herber, W. E. Bennett, and C. D. Coryell—298(A)
Absolute intensities of γ rays and x-rays of radium D, P. E. Damon and R. R. Edwards—1698(L)
Ac^{228} γ-ray spectrum, Harold C. Box and G. Stanley Klaiber—1247
Al^{26} energy levels, Cornelius P. Browne—860(L)
α-γ angular correlation in decay of Ra^{224}, Ra^{226}, and Pu^{240}, J. C. D. Milton and J. S. Fraser—628(A)
Angular distribution of 12-Mev γ rays from reaction $B^{11}(p,\gamma)C^{12}$, H. H. Givin, G. K. Farney, B. D. Kern, and T. M. Hahn—302(A)
Anisotropic γ radiation from aligned Ce^{141} nuclei, E. Ambler, R. P. Hudson, and G. M. Temmer—625(A)
Applications of "internal source" scintillation spectrometer, E. der Mateosian—646(A)
B^{10} decay scheme and γ-γ correlations, S. M. Shafroth and S. S. Hanna—86
Ba^{139} disintegration, Allan C. G. Mitchell and Elizabeth Hebb—727
Be^8 energy levels from $Li^7(d,n)Be^8$, Carroll C. Trail and C. H. Johnson—1363(L)
β-α correlation in decay of Li^8, S. S. Hanna, E. C. LaVier, and C. M. Class—110
β-decay matrix element for deformed core model, Martin G. Redlich and Eugene P. Wigner—122
β end-point energies and half-lives for some mirror transitions, W. A. Hunt, R. M. Kline, and D. J. Zaffarano —611(A)
β spectra of Pr^{142}, Tm^{170}, and Rb^{86}, A. V. Pohm, W. E. Lewis, J. H. Talboy, Jr., and E. N. Jensen—1523
Br and Cl new isomers, Gertrude Scharff-Goldhaber and Michael McKeown—613(A)
Ca^{42} nuclear levels, Torsten Lindqvist and Allan C. G. Mitchell—1535
Capture γ-ray studies using scintillation coincidence spectrometer, Arthur Recksiedler and Bernard Hamermesh —650(A)
Capture γ rays from 315-kev proton bombardment of Be^9, R. R. Carlson and E. B. Nelson—641(A)
Cd^{114} and Te^{126} decay schemes, D. C. Lu, W. H. Kelly, and M. L. Wiedenbeck—121
Cd^{115} decay (43-day), Jagdish Varma—613(A)
Ce^{139} disintegration, C. H. Pruett and R. G. Wilkinson —625(A)
$Cm^{244, 245, 246}$, α half-lives, A. M. Friedman, A. L. Harkness, P. R. Fields, M. H. Studier, and J. R. Huizenga—1501
Co^{60} decay scheme, M. Sakai, J. L. Dick, W. S. Anderson, and J. D. Kurbatov—101
Coulomb excitation of Au, W. I. Goldburg, S. A. Cox, and R. M. Williamson—628(A)
Coulomb excitation of energy levels in Rh and Ag, N. P. Heydenburg and G. M. Temmer—861(L)
Coulomb excitation of Ta, W, and Au, W. I. Goldburg and R. M. Williamson—767
Coulomb excitation *vs* compound nucleus formation in lighter elements, N. P. Heydenburg and G. M. Temmer —629(A)
Cs^{130} decay, J. L. Olsen and G. D. O'Kelley—1539
Cs^{137} K conversion electron energy, S. K. Bhattacherjee, B. Waldman, and W. C. Miller—404
Decay of Cs^{134m} (3.1 hr), A. W. Sunyar, J. W. Mihelich, and M. Goldhaber—570(L)
Directional correlation of γ rays of A^{38}, J. J. Kraushaar, J. W. Mihelich, and A. W. Sunyar—456
Double vacancies in K shell associated with K-electron capture in A^{37}, J. A. Miskel and M. L. Perlman—612(A)
Effect of nuclear charge on internally produced pairs, G. K. Horton and E. Phibbs—604(A)
Electric excitation of Au, J. Eisinger, C. F. Cook, and C. M. Class—628(A)
Electric excitation of Mn^{55} with protons, Hans Mark, Clyde McClelland, and Clark Goodman—628(A)
Element 100 produced by means of cyclotron-accelerated oxygen ions, Hugo Atterling, Wilhelm Forsling, Lennart W. Holm, Lars Melander, and Björn Åström—585(L)

Nuclear Spectra (Continued)
Energy levels in C^{14} and N^{14}, R. D. Bent, R. W. Bonner, and R. F. Sippel—649(A)
Energy levels in Pb^{206} from decay of Bi^{206}, D. E. Alburger and M. H. L. Pryce—1482
Evidence for subshell at N=152, A. Ghiorso, S. G. Thompson, G. H. Higgins, B. G. Harvey, and G. T. Seaborg —29?(L)
F^{17} and C^{11} β decay, Calvin Wong—765
F^{20} β decay, Calvin Wong—761
4.43-Mev γ-rays from C^{13}, W. R. Mills, Jr., and R. J. Mackin, Jr.—1206
Further applications of "internal source" scintillation spectrometer, E. der Mateosian—646(A)
Ga^{70} disintegration, M. E. Bunker, J. W. Starner, and J. P. Mize—612(A)
γ radiation from B^{10} bombarded by protons, Robert B. Day and Torben Huus—1003
γ radiation from interaction of 3.1-Mev neutrons, V. E. Scherrer, B. A. Allison, and W. R. Faust—637(A)
γ radiation from Mg^{26} under proton bombardment, Leonard N. Russell, Warren E. Taylor, and John N. Cooper—99
γ radiation from reactions induced by polarized particles, J. M. Kennedy and W. T. Sharp—440
γ-ray spectra following β decay of Br^{82}, Sb^{124}, and I^{131}, D. C. Lu, W. H. Kelly, and M. L. Wiedenbeck—1533
γ rays from $Si^{29}(p,\gamma)P^{30}$, P. M. Endt, J. C. Kluyver, and C. van der Leun—580(L)
γ rays produced by inelastic scattering of d-D neutrons in Cu, Al, and Mg, L. A. Rayburn, D. L. Lafferty, and T. M. Hahn—637(A)
Ge^{71} inner bremsstrahlung in electron capture process, Babulal Saraf—97
Ge^{75} and Ge^{77} isomeric states, S. B. Burson, W. C. Jordan, and J. M. LeBlanc—613(A)
Gyromagnetic ratio of 10^{-8}-second Ta^{181m}, S. Raboy and V. E. Krohn—1689(L)
Hf^{175} radiations, intensities, A. O. Burford, J. F. Perkins, and S. K. Haynes—303(A)
Hg^{198} decay, C. H. Braden, E. T. Patronis, Jr., and L. D. Wyly—627(A)
Hg^{198} nuclear resonance fluorescence and lifetime of 411-kev excited state, F. R. Metzger and W. B. Todd—853(L)
Ho^{164} radiations, H. N. Brown, F. B. Smith, and R. A. Becker—626(A)
I^{126} disintegration, M. L. Perlman and Joan P. Welker—133; 613(A)
I^{126} β spectrum and decay scheme, E. der Mateosian and C. S. Wu—458
$In^{115}(\gamma,\gamma')In^{115m}$ cross section, J. L. Burkhardt and E. J. Winhold—629(A)
Inner bremsstrahlung in A^{37} and Ge^{71}, Babulal Saraf—612(A)
Internal bremsstrahlung, R. E. Cutkosky—1222
Ir^{192} decay scheme, R. W. Pringle, W. Turchinetz, and H. W. Taylor—115
Ir^{192m} radiations, J. P. Mize, J. W. Starner, and M. E. Bunker—627(A)
K^{42} β spectrum, L. Koerts, A. Schwarzschild, R. Gold, and C. S. Wu—612(A)
K^{42} decay, γ radiation, N. H. Lazar and P. R. Bell—612(A)
K^{42} disintegration, Torsten Lindqvist and Allan C. G. Mitchell—444; 612(A)
Lifetime measurements of fast $E2$ transitions in even-even nuclei, A. W. Sunyar—626(A)
Low-energy transitions in Gd and related rare-earth activities, E. L. Church and M. Goldhaber—626(A)
Low-lying states in nuclei from $(n,n'\gamma)$ interactions, Janet B. Guernsey and Clark Goodman—297(A)
Magnetic moment of first-excited state of Pb^{204}, V. Krohn and S. Raboy—608(A)
Mesonic corrections to β-decay coupling constants, R. J. Finkelstein and S. A. Moszkowski—1695(L)
Nb^{90} and Nb^{90m}, R. M. Diamond—410
Nd^{144} mixed $E1+M2$ γ transition, Rolf M. Steffen—614(A)
Neutron-capture γ-ray spectra, Melvin Reier and Morris H. Shamos—636(A)
n-γ coincidences produced by inelastic scattering of neutrons, P. Shapiro, V. E. Scherrer, B. A. Allison, and W. R. Faust—751
Nuclear deformation and moment of inertia of nuclear rotational states, Kenneth W. Ford—1250
O^{14} decay and Fermi coupling constant in β decay, J. B. Gerhart—288(L)
P^{32} maximum β energy, B. Elbek, K. O. Nielsen, and O. B. Nielsen—96
Pb^{204m} decay scheme, V. E. Krohn and S. Raboy—1689(L)
Pm^{150} disintegration, Vera Kistiakowsky Fischer—626(A)
Po^{209} γ-ray spectrum, E. H. Daggett and G. R. Grove—627(A)
Po^{210} energy levels, J. W. Mihelich, A. W. Schardt, and E. Segrè—1508
Po-Be neutron spectrum, B. J. Winnemore, H. Gursky, D. A. Cowan, and C. D. Curtis—301(A)
Proportional counter for Auger electrons, Ernest D. Graves—304(A)
Pt^{189} decay, J. M. LeBlanc, J. M. Cork, and S. B. Burson —627(A)
Radiation of neutron-deficient isotopes of Cs and of $E3$ isomers, Xe^{127m} and Xe^{129m}, Hirdaya B. Mathur and Earl K. Hyde—708
Radiative capture of orbital electrons, R. J. Glauber and P. C. Martin—572(L)
Rb^{86} decay, W. S. Lyon and J. E. Strain—1500
Re^{186} and Re^{188} β spectra, Donald Guss, Lawrence Killion, and F. T. Porter—627(A)
Re^{186} γ-ray studies, J. P. Hurley and P. S. Jastram—627(A)
Re^{186} ground state, Leo Koerts—1358(L)
Recoil spectrum in β decay of Ne^{19}, W. Parker Alford and Donald R. Hamilton—1351(L)
Reorientation of aligned nuclei, N. R. Steenberg—605(A); 982
Resonance fluorescence with nuclei: Tl^{203}, F. R. Metzger and W. B. Todd—627(A)
Resonant states of Mg^{24} excited by protons on Na, P. H. Stelson and W. M. Preston—974
Rh^{102} disintegration, Luis Marquez—67
Rotating-sphere solid-angle scanner for γ rays, George R. Meneely, Robert J. Kerr, Jesse E. Hoffman, and Sherwood K. Haynes—308(A)
Sb^{124} decay, N. H. Lazar—292(L)
Scintillation counter study of γ rays from proton capture in Na, E. B. Nelson, E. H. Geer, and R. R. Carlson —650(A)
Sm^{147} natural radioactivity, George Beard and M. L. Wiedenbeck—1245
Sn^{117} K-conversion electron-γ angular correlation, Robert K. Golden and Sherman Frankel—613(A)
Spin assignments and partial width measurements of resonances in S^{32} from reaction $P^{31}(p,\gamma)S^{32}$, H. E. Gove, E. B. Paul, A. E. Litherland, and G. A. Bartholomew —650(A)
Superallowed transitions in $4n$-type nuclides, M. Bolsterli and E. Feenberg—612(A)

Ta^{182} disintegration, J. W. Mihelich—626(A)
Tc activities at mass 97, G. E. Boyd—113
Tensor forces and β decay of C^{14} and O^{14}, B. Jancovici and I. Talmi—289(L)
Tl^{198m} decay, T. O. Passell, M. C. Michel, and I. Bergström—999
UX_2 (Pa^{234}) decay, (γ radiation), W. G. Cross and T. A. Eastwood—628(A)
W^{182} γ transitions, F. Boehm, P. Marmier, and J. W. M. DuMond—864(L)

Nuclear Structure Theory (see also **Nuclear Reactions; Nuclear Spectra**)
β-decay matrix element for deformed core model, Martin G. Redlich and Eugene P. Wigner—122
Coulomb energies of light nuclei, D. C. Peaslee—717
Coulomb energy and nuclear radius, B. G. Jancovici—389; 619(A)
Coulomb radius constant from nuclear masses, Alex E. S. Green—1006
Diffuse surface optical model for nucleon-nuclei scattering, Roger D. Wood and David S. Saxon—577(L)
Effects of certain 3-body nuclear interactions in H^3 and He^3, A. W. Solbrig, Jr.—831
Energy levels in spheroidal well, Steven A. Moszkowski—604(A)
Exchange current effects in deuteron, J. Bernstein and A. Klein—655(A)
Formula for nuclear masses in terms of electron mass involving only rational numbers for light nuclei, Enos E. Witmer—610(A)
Independent particle model and nuclear photoeffect, J. S. Levinger and D. C. Kent—418
Interactions between some two-nucleon configurations, Martin G. Redlich—448
Interpretation of scattering of high-energy nucleons by complex nuclei, I. I. Shapiro and J. M. Teem—619(A)
Li^9 level structure, D. H. Lyons and A. M. Feingold—606(A)
Mesonic corrections to β-decay coupling constants, R. J. Finkelstein and S. A. Moszkowski—1695(L)
Normal coordinates in nuclear photoeffect, Yu-Chang Hsieh and Ingram Bloch—305(A)
Nuclear cross sections and size of nucleus, Warren Heckrotte—619(A); 1279
Nuclear deformation and moment of inertia of nuclear rotational states, Kenneth W. Ford—1250
Nuclear internal momentum distributions, J. M. Wilcox and B. J. Moyer—664(A)
Nuclear masses as rational multiples of electron mass, Enos E. Witmer—667(A)
Nuclear radii and transparencies from inelastic cross-section measurements. II. Interpretation, W. E. Crandall, W. Birnbaum, L. Schecter, and G. P. Millburn—620(A)
Nuclear rotational levels and μ-mesonic atom, B. A. Jacobsohn—654(A)
Nuclear shapes at half-filled shells, Benjamin Segall—605(A)
Pairing effects in Coulomb energies of mirror nuclei, I. Talmi and B. C. Carlson—606(A)
Phenomenological many-body exchange forces, L. E. H. Trainor—801
Physical consequences of vacuum polarization, Leslie L. Foldy and Erik Eriksen—1048
Polarization in high-energy elastic nucleon-nucleus scattering, Bertram J. Malenka—522
Refinement of uniform model, Everett Mark Hafner—604(A)
Sachs exchange moment, R. H. Dalitz—799
Structure of nucleon. II. Pion-nucleon scattering, R. G. Sachs—1065
Superallowed transitions in $4n$-type nuclides, M. Bolsterli and E. Feenberg—612(A)
Supermultiplet evidence from isotopic spin spacing, D. C. Peaslee—605(A)
Tensor forces and β decay of C^{14} and O^{14}, B. Jancovici and I. Talmi—289(L)
Theory of unstable heavy particles, Hiroshi Enatsu, Hiroichi Hasegawa, and Pong Yul Pac—263
Two-body forces and nuclear saturation. I. Method, K. Brueckner, C. Levinson, and H. Mahmoud—655(A); II. Results, C. Levinson, K. Brueckner, and H. Mahmoud—655(A)
Two-body forces and nuclear stability, David H. Frisch—865(L)

Optical Instruments (see **Methods and Instruments**)
Optical Properties (see also **Luminescence**)
Anomalous optical behavior of InSb and InAs, H. J. Hrostowski, G. H. Wheatley, and W. F. Flood, Jr.—1683(L)
Color centers in alkali silicate and borate glasses, Ryosuke Yokota—1145
Effect of pressure on optical absorption of activator in luminescent solid, Peter D. Johnson and Ferd E. Williams—598(A)
Effect of pressure on optical absorption of activator system in KCl: Tl, Peter D. Johnson and Ferd E. Williams—69
Infrared absorption spectrum of Ge, L. H. Hall, J. Bardeen, and F. J. Blatt—559(L)
Ionic conductivity and x-ray coloration of alkali halides, F. A. Cunnell and E. E. Schneider—598(A)
Ionizing collisions of very fast particles and dipole strength of optical transitions, U. Fano—1198
Low-temperature bleaching and restoration of color centers, A. Halperin and G. F. J. Garlick—1098(L)
Magnetic domains in Co by longitudinal Kerr effect, Charles A. Fowler, Jr., and Edward M. Fryer—564(L); 652(A)
Plastic flow and low-frequency dispersion in alkali halide crystal, Masakazu Ishiguro, Fujio Oda, and Takuzo Fujino—1347(L)
Shape of F band, R. V. Hesketh and E. E. Schneider—837(L)
Spectral dependence of thermionic emission with activation from (Ba—Sr)O cathodes over 0.6–3.5 ev region, Tadatosi Hibi and Kazuo Ishikawa—1183
Susceptibility tensor and Faraday effect in ferrimagnetics, Roald K. Wangsness—339
Thermal restoration of color centers at low temperature, R. V. Hesketh and E. E. Schneider—598(A)
X-ray production of F centers in NaCl and LiF, R. C. Herman, L. L. Mador, R. F. Wallis, and M. C. Williams—598(A)

Pair Production (see **Electrons and Positrons**)
Phosphors and Phosphorescence (see **Luminescence**)
Photoconductivity (see **Electrical Conductivity and Resistance**)
Photodisintegration (see **Nuclear Photoeffects**)
Photoelasticity (see **Elasticity and Plasticity**)
Photoelectric Effect (see **Electrical Properties**)
Photography and Photographic Emulsions (see **Methods and Instruments**)
Photometry (see **Methods and Instruments**)
Photons (see **Radiation**)
Photovoltaic Effect (see **Electrical Properties; Semiconductors**)

Piezoelectric Effect (see **Dielectrics and Dielectric Properties**)
Plasticity (see **Elasticity and Plasticity**)
Polarization, Electrical (see **Dielectrics and Dielectric Properties**)
Polymers (see **Molecular Aggregates**)
Positrons (see **Electrons and Positrons**)
Probability (see **Mathematical Methods**)
Proceedings of the American Physical Society
Spring Meeting of the New England Section at Wellesley, Massachusetts on March 20, 1954—297
Meeting of the Southeastern Section at Knoxville, Tennessee, April 1–3, 1954—299
Spring Meeting of the New York State Section at Syracuse, New York, April 9 and 10, 1954—309
Spring Meeting at Washington, D. C., April 29 and 30, and May 1, 1954—594
Protons (see **Elementary Particle Interactions**)

Quantum Electrodynamics (see also **Field Theory**)
Canonical transformation for electron-positron field coupled to time-independent electromagnetic field. II, H. E. Moses—237
Conservation theorems in modified electrodynamics, J. W. Dettman and A. Schild—631(A)
Formulation of quantum electrodynamics in Minkowski space, T. A. Walton—632(A)
Physical consequences of vacuum polarization, Leslie L. Foldy and Erik Eriksen—1048
Quantum effects in interaction between electrons and high-frequency fields. I, I. R. Senitzky—904
Quantum electrodynamics at small distances, M. Gell-Mann and F. E. Low—1300
Two-body system in quantum electrodynamics. Energy levels of positronium, Thomas Fulton and Paul C. Martin—811
Quantum Mechanics
Calculation of wave functions in symmetrical crystalline field, Paul H. E. Meijer—1443
Completed quantum theory, Irving Stein—632(A)
Coulomb wave functions for large values of parameter n, L. C. Biedenharn, R. L. Gluckstern, and M. H. Hull, Jr. —656(A)
Generalizations of Foldy-Wouthuysen transformation, K. M. Case—1323
Harmonic oscillator wave functions, I. R. Senitzky—1115
High-speed computation of angular momentum functions, Albert Simon—657(A)
Quantum effects in interaction between electrons and high-frequency fields. I, I. R. Senitzky—904
Quantum theory of damped electrical oscillator and noise. II. Radiation resistance, J. Weber—1706(E)
Relativistic Thomas-Fermi atom model, J. J. Gilvarry—71
SCF treatment of unclosed shells, operators containing spin, and radial correlation, Paul F. Wacker—656(A)
Time-dependent variational principle, Saul Altshuler and J. F. Carlson—546
Use of causality conditions in quantum theory, M. Gell-Mann, M. L. Goldberger, and W. E. Thirring—1612
Validity of Born-Oppenheimer approximation, S. Bludman and P. B. Daitch—823
W.K.B. approximation through turning point, A. A. Broyles—656(A)
Quenching of Radiation (see **Radiation**)

Radar (see **Methods and Instruments; Radiation**)
Radiation (see also **Gamma Rays; Range and Energy Loss; X-Rays**)
Air-guided propagation of short radio waves around earth bulge, Thomas J. Carroll—623(A)
Bremsstrahlung conversion in trident experiments, M. M. Block and D. T. King—171
Build-up measurements on Co^{60} γ radiation in Fe and Pb, C. Garrett and G. N. Whyte—889
Compton scattering, W. B. Cheston—247
Galactic rf radiation and cosmic-ray electrons, S. B. Treiman and M. Blume—646(A)
Hg^{198} nuclear resonance fluorescence and lifetime of 411-kev excited state, F. R. Metzger and W. B. Todd—853(L)
High-energy, large-angle distribution of pair electrons produced by bremsstrahlung, R. C. Miller—796
Inner bremsstrahlung in A^{37} and Ge^{71}, Babulal Saraf—612(A)
Internal bremsstrahlung, R. E. Cutkosky—1222
Nuclear elastic scattering of photons, Evans Hayward and E. G. Fuller—1106(L)
Nuclear scattering of γ rays below meson threshold, G. E. Pugh, D. H. Frisch, and R. Gomez—590(L)
Pair production and bremsstrahlung in field of electron, F. Rohrlich—657(A)
Pairs formed by bremsstrahlung of great energy. I. Experimental, D. T. King and M. M. Block—648(A); II. Theoretical separation distribution, M. M. Block and D. T. King—648(A)
Penetration of 6-Mev γ rays in water, P. A. Roys, K. Shure, and J. J. Taylor—911
Potential theory formulation of radiant heat transfer, Jean I. F. King—298(A)
Proton bremsstrahlung and high-energy γ emission from C, David Cohen, Burton J. Moyer, Harlan Shaw, and Charles Waddell—664(A)
Radar echoes from precipitation, Pauline M. Austin—297(A)
Radiative capture of orbital electrons, R. J. Glauber and P. C. Martin—572(L)
Scattering of x-rays by nuclei, G. Pugh, D. H. Frisch, and R. Gomez—611(A)
Small-angle x-ray scattering from cold-worked Al-Ag and Al-Zn alloys, J.-P. Jan and J. S. Koehler—665(A)
Spatial distribution of energy dissipation by bremsstrahlung spectrum, David T. Goldman and Henry Brysk—305(A)
Spectral distribution curves of far uv radiation from Cornell synchrotron, D. H. Tomboulian and P. L. Hartman—600(A)
Theoretical energy and angular distributions of bremsstrahlung electrons, Philip T. McCormick—657(A)
Radio Waves (see **Radiation**)
Radioactivity (see also **Nuclear Spectra**)
Absolute intensities of γ rays and x-rays of RaD, P. E. Damon and R. R. Edwards—1698(L)
Ac^{228} γ-ray spectrum, Harold C. Box and G. Stanley Klaiber—1247
α-γ angular correlation in decay of Ra^{224}, Ra^{226}, and Pu^{238}, J. C. D. Milton and J. S. Fraser—628(A)
Cm, Bk, and Cf isotopes, E. K. Hulet, S. G. Thompson, and A. Ghiorso—1703(L)
$Cm^{244, 245, 246}$, α half-lives, A. M. Friedman, A. L. Harkness, P. R. Fields, M. H. Studier, and J. R. Huizenga —1501
Cr^{55} preparation and half-life, G. A. Bazorgan, J. W. Irvine, Jr., and C. D. Coryell—781
Element 100 produced by means of cyclotron-accelerated oxygen ions, Hugo Atterling, Wilhelm Forsling, Lennart W. Holm, Lars Melander, and Björn Åström—585(L)
Evidence for subshell at N=152, A. Ghiorso, S. G. Thompson, G. H. Higgins, B. G. Harvey, and G. T. Seaborg —293(L)

I^{124} production by deuteron bombardment of Te, T. Hall, M. Siegel, L. M. Sharpe, and D. Pressman—1208
Mass differences for isobars capable of double-β decay, John T. McCarthy—447
Nb^{89} and Nb^{89m}, R. M. Diamond—410
New isotope identification program on Oak Ridge 86-inch cyclotron, T. H. Handley and B. L. Cohen—611(A)
Pa^{227}, W. W. T. Crane and G. M. Iddings—1702(L)
Po^{209} γ-ray spectrum, E. H. Daggett and G. R. Grove —627(A)
Proportional counter for Auger electrons, Ernest D. Graves and H. C. Thomas—304(A)
Radiogenic Os from Re-containing molybdenite, H. Hintenberger, W. Herr, and H. Voshage—1690(L)
Re half-life, W. Herr, H. Hintenberger, and H. Voshage —1691(L)
Re natural radioactivity, A. D. Suttle, Jr., and W. F. Libby—866(L)
Sm^{147} natural radioactivity, George Beard and M. L. Wiedenbeck—1246
Tl^{204} half-life, D. L. Horrocks and A. F. Voigt—1205
UX_2 (Pa^{234}) decay, γ radiation, W. G. Cross and T. A. Eastwood—628(A)
Raman Spectra (see **Molecular Structure and Spectra**)
Range and Energy Loss (see also **Ionization; Scattering**)
Absorption of tritium β particles in hydrogen and other gases, Leon M. Dorfman—393
Bohr's theory of energy losses of moving charged particles, Jacob Neufeld—1128
Calculations on penetration of high-energy electrons, L. V. Spencer—610(A)
Characteristic energy loss of electrons, Lewis B. Leder and L. Marton—634(A)
Discrete electron energy losses in thin foils, A. W. Blackstock, R. D. Birkhoff, and M. Slater—303(A)
Effect of chemical combination on characteristic energy loss of electrons, Lewis B. Leder and L. Marton—1345(L)
Electron capture and loss cross sections for protons, P. M. Stier, C. F. Barnett, and G. E. Evans—303(A)
Electron straggling in thin foils, E. T. Hungerford and R. D. Birkhoff—6
Energy expenditure per ion pair in solids, E. J. Sternglass —609(A)
Energy losses of electrons passing through MgO foil, Hiroshi Watanabe—1684(L)
Equilibrium charge distribution of stripped 26-Mev N ions, H. L. Reynolds and A. Zucker—1353(L)
γ-ray absorption coefficients for NaI, Cu, Ta, and W, P. R. Howland and W. E. Kreger—407
Ionization of pure gases and mixtures of gases by 5-Mev α particles, T. E. Bortner and G. S. Hurst—609(A)
L-shell ionization by protons of 1.5- to 4.24-Mev energy, E. M. Bernstein and H. W. Lewis—83
Migration areas of Po-Be neutrons in H_2O-Zn mixtures, W. Baer—660(A)
Neutron moderation in SiO_2, Jay Tittman—660(A)
Penetration of 6-Mev γ rays in Pb and Fe, K. Shure, P. A. Roys, and J. J. Taylor—610(A)
Penetration of 6-Mev γ rays in water, P. A. Roys, K. Shure, and J. J. Taylor—911
Range and charge of energetic nitrogen ions in Ni, H. L. Reynolds, D. W. Scott, and A. Zucker—671
Range and specific ionization for high-energy protons in nuclear emulsions, O. Heinz—610(A)
Relative ionization yields for fission fragments in various gases, Lloyd O. Herwig and Glenn H. Miller—413
Slowing-down of neutrons in hydrogenous moderators, P. F. Zweifel and H. Hurwitz, Jr.—660(A)
Spatial distribution of energy dissipation by bremsstrahlung spectrum, David T. Goldman and Henry Brysk—305(A)
Stopping power of organic foils for 6-Mev alphas, John Phelps, W. F. Huebner, and Franklin Hutchinson—441
Stopping powers of metals for low-energy protons, D. W. Green, J. N. Cooper, and J. C. Harris—610(A)
Target-thickness dependence of δ-ray emission produced by 1.3-Mev electrons, J. F. Marshall, R. A. Shatas, and M. A. Pomerantz—634(A)
Transmission of monenergetic positrons and electrons, H. H. Seliger—610(A)
Recombination (see **Molecular Structure and Spectra**)
Rectifiers (see **Electrical Conductivity and Resistance; Semiconductors**)
Relativity and Gravitation
Born-type rigid motion in relativity, G. Salzman and A. H. Taub—1659
Equation of motion of charged test particles in general relativity, D. M. Chase—243
Gravitational field equations, Robert L. Kirkwood—1051
Quantized linear theory of gravitation. I, F. J. Belinfante and J. C. Swihart—630(A); II, J. C. Swihart and F. J. Belinfante—630(A)
Quantum theory of gravitation, Peter G. Bergmann—631(A)
Red-shifts in spectra of celestial bodies, E. Finlay-Freundlich—654(A)
Resolution of four-dimensional vector fields and tensor fields, N. L. Balazs—305(A)
Resistance, Electrical (see **Electrical Conductivity and Resistance**)
Resonance Radiation (see **Radiation**)

Scattering, General (see also **Diffraction; Elementary Particle Interactions; Nuclear Reactions; Range and Energy Loss**)
Correlations in space and time and Born approximation scattering in systems of interacting particles, Léon Van Hove—249
Diffuse surface optical model for nucleon-nuclei scattering, Roger D. Woods and David S. Saxon—577(L)
General conditions on scattering matrix, M. L. Goldberger, M. Gell-Mann, and W. E. Thirring—654(A)
Phase shifts for high-energy nucleon-nucleon scattering, B. D. Fried—851(L); 1706(E)
Polarization in high-energy elastic nucleon-nucleus scattering, Bertram J. Malenka—522
Polarization of nucleons elastically scattered from nuclei, R. M. Sternheimer—587(L); Warren Heckrotte and Joseph V. Lepore—1279(L)
Scattering of H^- ions in range 20–400 ev, E. E. Muschlitz, Jr.—635(A)
Scattering of ions by polarization forces, Erich Vogt and Gregory H. Wannier—1190
Theory of multiple Coulomb scattering from extended nuclei, Leon N. Cooper and James Rainwater—1107(L)
Theory of scattering in solids, G. F. Koster—1436
Time-dependent variational principle, Saul Altshuler and J. F. Carlson—546
Scattering of α Particles (see also **Nuclear Reactions Induced by α Particles and He^4**)
Elastic scattering of intermediate-energy α particles by heavy nuclei, George W. Farwell and Harvey E. Wegner —664(A); 1212
Energy levels of C^{12} by inelastic α scattering, D. W. Miller, V. K. Rasmussen, and M. B. Sampson—649(A)
Theory of elastic scattering of α particles by heavy nuclei, J. S. Blair—605(A); 1218

Scattering of Atoms and Molecules (see **Atomic and Molecular Beams**)

Scattering of Deuterons (see also **Nuclear Reactions Induced by Deuterons and Tritons**)

Elastic scattering of 190-Mev deuterons by protons, Owen Chamberlain and Martin O. Stern—1705(E)

Polarization of high-energy deuterons, Owen Chamberlain, Emilio Segrè, Robert Tripp, Clyde Wiegand, and Thomas Ypsilantis—1104(L)

Scattering of Electrons and Positrons (see also **Electrons and Positrons**)

Electron-electron scattering in alkali metals, Elihu Abrahams—839(L)

Electron scattering from nuclei, G. T. Trammell—619(A)

Electron scattering in solids at 20 kev, L. Marton, Tommy F. McCraw, and J. Arol Simpson—634(A)

Electron spectrometer for study of inelastic collision cross sections, E. N. Lassettre, A. S. Berman, S. Silverman, and M. E. Krasnow—635(A)

Electron straggling in thin foils, E. T. Hungerford and R. D. Birkhoff—6

High-energy electron scattering, J. Mayo Greenberg—619(A)

High-energy electron scattering and nuclear structure determinations. II, R. Hofstadter, B. Hahn, A. W. Knudsen, and J. A. McIntyre—512

Nuclear scattering of high-energy electrons, J. H. Smith—271

Perturbation calculation of elastic exchange scattering of electrons by H atoms, Sidney Borowitz—656(A)

Phase shift calculation of high-energy electron scattering, D. R. Yennie, D. G. Ravenhall, and R. N. Wilson—500

Theory of scattering in solids, G. F. Koster—1436

Scattering of Mesons (see also **Mesons; Nuclear Reactions Induced by Mesons**)

Angular distribution of charge-exchange scattering of 40-Mev π^- mesons by H, J. Tinlot and A. Roberts—137

Application of intermediate coupling theory to scattering of pseudoscalar mesons by nucleon, Gyo Takeda—1078

Comparison of cut-off meson theory with experiment, Geoffrey F. Chew—1669

Elastic scattering of pions by nucleons and pion production in nucleon-nucleon collisions, John L. Gammel—209

General relations between photoproduction and scattering of π mesons, Kenneth M. Watson—228

Meson-meson effects in meson-nucleon scattering, Marc H. Ross—619(A)
—1687(L)

Meson-nucleon scattering in Tamm-Dancoff approximation, F. J. Dyson, M. Ross, E. E. Salpeter, S. S. Schweber, M. K. Sundaresan, W. M. Visscher, and H. A. Bethe—1644

Meson production in meson-proton scattering, M. S. Nelkin and H. A. Bethe—618(A)

Meson-proton scattering phase shift analysis, H. A. Bethe and F. de Hoffmann—1100(L)

Numerical calculation of 3/2−3/2 pion-nucleon reaction matrix and phase shifts, Freda F. Salzman and James N. Snyder—286(L)

Phase shift analysis of scattering of negative pions by H, E. Fermi, N. Metropolis, and E. Felix Alei—1581; Ronald L. Martin—1606

π^- interactions at 1.5 Bev. II, J. Crussard, W. D. Walker, and M. Koshiba—624(A)

π^--p collisions at 1.5 Bev. I, W. D. Walker, J. Crussard, and M. Koshiba—624(A)

Pion-hydrogen phase shift analysis between 120 and 217 Mev, F. de Hoffmann, N. Metropolis, E. P. Alei, and H. A. Bethe—1586

Pion-nucleon S phase shifts at low energy, H. P. Noyes—619(A)

P-wave pion-nucleon scattering phase shifts in cut-off theory, Geoffrey F. Chew—285(L)

Scattering of 145-Mev π^+ by H in emulsion, Jay Orear, C. H. Tsao, J. J. Lord, and A. B. Weaver—624(A)

Scattering of 187-Mev negative pions by H, Maurice Glicksman—1045

Structure of nucleon. II. Pion-nucleon scattering, R. G. Sachs—1065

Theory of multiple Coulomb scattering from extended nuclei, Leon N. Cooper and James Rainwater—1107(L)

Total cross section for charge exchange scattering of π^- mesons by H at 42, 30, and 20 Mev, W. J. Spry—1295

Total cross sections for scattering of positive pions by H, J. Blaser, J. Ashkin, F. Feiner, J. Gorman, and M. O. Stern—624(A)

Scattering of Neutrons (see also **Nuclear Reactions Induced by Neutrons**)

Correlations in space and time and Born approximation scattering in systems of interacting particles, Léon Van Hove—249

Cross section for excitation of Pb^{207m} by inelastic neutron scattering, P. H. Stelson and E. C. Campbell—301(A)

De-excitation γ rays from inelastic scattering of neutrons, Gordon L. Griffith—636(A)

Differential cross section for elastic scattering of neutrons from N, C. H. Johnson and J. L. Fowler—637(A)

400-Mev n-p scattering, A. J. Hartzler and R. T. Siegel—185

γ-ray spectrum from inelastic scattering of fast neutrons in Fe, D. L. Lafferty, L. A. Rayburn, and T. M. Hahn—637(A)

γ rays produced by inelastic scattering of d-D neutrons in Cu, Al, and Mg, L. A. Rayburn, D. L. Lafferty, and T. M. Hahn—637(A)

Inelastic scattering of d-D neutrons by Fe and Cu, L. A. Rayburn, D. L. Lafferty, and T. M. Hahn—301(A)

Inelastic scattering of 4.3-Mev neutrons by Fe^{56}, B. Jennings, J. B. Weddell, and R. L. Hellens—636(A)

Inelastic scattering of neutrons by Ba^{137} and Hg^{199}, C. P. Swann and F. R. Metzger—636(A)

Interpretation of scattering of high-energy nucleons by complex nuclei, I. I. Shapiro and J. M. Teem—619(A)

Low-lying states in nuclei from $(n,n'\gamma)$ interactions, Janet B. Guernsey and Clark Goodman—297(A)

Magnetic scattering of cold neutrons by gaseous oxygen, H. Palevsky and R. M. Eisberg—659(A)

Migration areas of Po-Be neutrons in H_2O-Zn mixtures, W. Baer—660(A)

Neutron inelastic scattering, Robert M. Kiehn and Clark Goodman—636(A); 989

Neutron inelastic scattering in Ta and I, Janet B. Guernsey and Clark Goodman—636(A)

Neutron moderation in SiO_2, Jay Tittman—660(A)

Neutron scattering, J. W. Cure and G. S. Hurst—302(A)

n-γ coincidences produced by inelastic scattering of neutrons, P. Shapiro, V. E. Scherrer, B. A. Allison, and W. R. Faust—751

n-p scattering at 91 Mev, R. H. Stahl—664(A)

n-p scattering at 300 Mev, J. De Pangher—578(L)

Polarization in high-energy p-n-n double scattering, Peter Hillman, Vaughn Culler, and N. F. Ramsey—462

Polarization of fast neutrons from nuclear reactions, Harvey B. Willard, Joe K. Bair, and Joe D. Kington—1359(L)

Polarization of 170-Mev neutrons, A. Roberts, J. Tinlot, and E. M. Hafner—663(A)

Scattering of 1.32-Mev neutrons by protons, C. L. Storrs and D. H. Frisch—1252

Scattering of 14.1-Mev neutrons in He, H, and N, J. R. Smith—730
Search for polarization in charge exchange scattering, H. Bradner and R. E. Donaldson—663(A)
Slowing-down of neutrons in hydrogenous moderators, P. F. Zweifel and H. Hurwitz, Jr.—660(A)
Small-angle n-p scattering at 400 Mev, A. J. Hartzler, R. T. Siegel, and W. Opitz—591(L)
Solution of transport equation for case of slab geometry, J. Lehner and G. M. Wing—642(A)
Sphere measurements of neutron inelastic collision cross sections, Robert C. Allen—637(A)
Spin correlations in neutron scattering by gases, A. C. Zemach and R. J. Glauber—605(A)
Time-dependent correlations between spins and neutron scattering in ferromagnetic crystals, Léon Van Hove —1374
Time-of-flight measurements of inelastic neutron scattering, Gerard K. O'Neill—635(A)
Time-of-flight measurements on inelastic scattering of 14.8-Mev neutrons, Gerard K. O'Neill—1235
Scattering of Protons (see also **Nuclear Reactions Induced by Protons**)
Asymmetry in neutron production by bombarding targets with 285-Mev polarized protons, Hugh Bradner and Robert Donaldson—1701(L)
Diffuse surface optical model for nucleon-nuclei scattering, Roger D. Woods and David S. Saxon—577(L)
Elastic proton-deuteron scattering at 95 Mev, J. M. Teem and U. E. Kruse—664(A)
Elastic scattering of 18-Mev protons by Al, Fe, Ni, and Cu, Irving E. Dayton—754
Electron capture and loss cross sections for protons, P. M. Stier, C. F. Barnett, and G. E. Evans—303(A)
400-Mev neutron-proton scattering, A. J. Hartzler and R. T. Siegel—185
Interpretation of scattering of high-energy nucleons by complex nuclei, I. I. Shapiro and J. M. Teem—619(A)
Mechanism of proton polarization in high-energy collisions, Owen Chamberlain, Emilio Segrè, Robert Tripp, Clyde Wiegand, and Thomas Ypsilantis—1105(L)
Nuclear internal momentum distributions, J. M. Wilcox and B. J. Moyer—664(A)
Nucleon-nucleon scattering with 312-Mev polarized protons, Owen Chamberlain, Robert Donaldson, Emilio Segrè, Robert Tripp, Clyde Wiegand, and Thomas Ypsilantis—850(L)
Phase shifts for high-energy nucleon-nucleon scattering, Burton D. Fried—851(L); 1706(E)
Polarization effects in high-energy proton-deuteron scattering, S. Tamor—620(A)
Polarization in high-energy elastic nucleon-nucleus scattering, Bertram J. Malenka—522
Polarization in n-p scattering at 100–200 Mev, A. Roberts, J. Tinlot, and E. M. Hafner—1099(L)
Polarization in p-p scattering at 415 Mev, A. Kane, R. A. Stallwood, R. B. Sutton, T. H. Fields, and J. G. Fox —1694(L)
Polarization in scattering by nuclei at high energies, B. J. Malenka—620(A)
Polarization of nucleons elastically scattered from nuclei, R. M. Sternheimer—587(L); Warren Heckrotte and Joseph V. Lepore—1109(L)
Polarization of 170-Mev neutrons, A. Roberts, J. Tinlot, and E. M. Hafner—663(A)
Polarization of 310-Mev protons by deuterium, D. Nagle, J. Marshall, L. Marshall, and W. Skolnik—663(A)
p-p scattering at 9.7 Mev, analysis, Harold H. Hall—424
p-p scattering experiments at 170 and 260 Mev, Owen Chamberlain and John D. Garrison—1349(L)
Scattering of 96-Mev protons from light nuclei, K. Strauch and W. F. Titus—854(L)
Scattering of protons by H near 18 Mev, J. L. Yntema and M. G. White—1226
Scattering of 10-Mev protons on Mg and C, G. E. Fischer —664(A)
Scattering of 314-Mev polarized protons by deuterium, J. Marshall, L. Marshall, D. Nagle, and W. Skolnik —1020
Search for polarization in charge exchange scattering, H. Bradner and R. E. Donaldson—663(A)
Small-angle cross sections for scattering of protons by tritons, Malcolm E. Ennis and Arthur Hemmendinger —772
Small-angle p-p cross sections and polarization at 300 Mev, O. Chamberlain, G. Pettengill, E. Segrè, and C. Wiegand—1348(L)
Small-angle p-p scattering at 330 Mev, David Fischer and Gerson Goldhaber—1350(L)
Scattering of Radiation (see **Gamma Rays; Radiation; Range and Energy Loss; X-Rays**)
Scintillation Counters (see **Methods and Instruments; Luminescence**)
Secondary Emission (see **Electrical Properties**)
Semiconductors
Aging of crushed Si and Ge powders, Selma B. Brody—298(A)
Analysis of magnetoresistance and Hall coefficient in p-type InSb and p-type Ge, T. C. Harman, R. K. Willardson, and A. C. Beer—699
Anisotropy of cyclotron resonance of holes in Ge, R. N. Dexter, H. J. Zeiger, and Benjamin Lax—557(L)
Anisotropy of cyclotron resonance in Ge. I. Theory, Benjamin Lax, H. J. Zeiger, and R. N. Dexter—597(A); II. Experiment, R. N. Dexter, H. J. Zeiger, Benjamin Lax, and E. S. Rosenblum—597(A)
Anomalous optical behavior of InSb and InAs, H. J. Hrostowski, G. H. Wheatley, and W. F. Flood, Jr. —1683(L)
Application of three-carrier model to Hall effect in Ge, R. K. Willardson, T. C. Harman, and A. C. Beer—597(A)
Comparison of Hall and magnetoresistance phenomena in InSb with those in Ge, T. C. Harman, R. K. Willardson, and A. C. Beer—596(A)
Distribution of mass transported from collector into Ge crystal by forming process, M. W. Aarons, M. Poberesкin, J. E. Gates, and E. B. Dale—1345(L)
Electrical properties of several Si-Ge alloys, L. Davis, Jr., G. A. deMars, L. G. Rubin, and W. D. Straub—597(A)
Electron multiplication in Ge at low temperature, E. J. Ryder, I. M. Ross, and G. A. Kleinman—1342(L)
Electron spin resonance of impurity level in Si, A. Honig and A. F. Kip—1686(L)
Electronic thermal conduction in semiconductors, P. J. Price—596(A)
Energy band structure of Ge-Si alloys, Frank Herman—847(L)
Energy gap of Ge-Si alloys, A. Levitas, C. C. Wang, and B. H. Alexander—846(L)
Energy levels and photoconductivity in electron-bombarded Ge, H. Y. Fan, W. Kaiser, E. E. Klontz, K. Lark-Horowitz, and R. R. Pepper—1087(L)
Evaporated multiple layers with semiconductor properties, J. C. M. Brentano and J. D. Richards—841(L)
Hyperfine splitting in spin resonance of Group V donors in Si, R. C. Fletcher, W. A. Yager, G. L. Pearson, and F. R. Merritt—844(L)

Semiconductors (Continued)
Infrared absorption spectrum of Ge, L. H. Hall, J. Bardeen, and F. J. Blatt—559(L)
Ionization energies of groups III and V elements in Ge, T. H. Geballe and F. J. Morin—1085(L)
Magnetoresistance effect in cubic semiconductors with spheroidal energy surfaces, Motoichi Shibuya—1385
Neutron irradiation of InSb, J. W. Cleland and J. H. Crawford, Jr.—1177
Oxygen and surface energy level structure on Ge, Edward N. Clarke—284(L)
Photovoltaic effect in InAs, Robert M. Talley and Dorothy P. Enright—1092(L)
Photovoltaic effect in *p-n* junctions, Robert L. Cummerow—16
Power efficiency for photovoltaic effect in Ge-grown junction, Ralph P. Ruth and James W. Moyer—562(L)
Precipitation of impurities at dislocations in heat-treated Si, Sumner Mayburg—838(L)
Properties of Ge-Si alloys, Everett R. Johnson and Schuyler M. Christian—560(L)
Properties of *p*-type GaSb between 15°K and 925°K, H. N. Leifer and W. C. Dunlap, Jr.—51
Radioactive and photoelectric *p-n* junction power sources, W. G. Pfann and W. Van Roosbroeck—597(A)
Self-powered semiconductor amplifier, C. G. B. Garrett and W. H. Brattain—1091(L)
Spin-orbit interaction and effective masses of holes in Ge, G. Dresselhaus, A. F. Kip, and C. Kittel—568(L)
Theory of electron multiplication in Si and Ge, P. A. Wolff—1415
Theory of galvanomagnetic effects in Ge, B. Abeles and S. Meiboom—31
Theory of thermoelectric power in semiconductors, J. Tauc—1394
Thermal conductivity of semiconductors, A. Neaves and D. ter Haar—596(A)
Use of Si *p-n* junctions for converting solar energy to electrical energy, R. L. Cummerow—561(L)
Vacancies and interstitials in heat-treated Ge, Sumner Mayburg—38
Shock Waves (see **Fluid Dynamics**)
Solid State (see **Crystalline State**)
Solutions (see **Liquids**)
Sound (see **Acoustics**)
Spallation (see **Nuclear Reactions**)
Spark Discharge (see **Electrical Discharges**)
Specific Heat (see **Thermal Properties**)
Spectra, Atomic (see **Atomic Structure and Spectra**)
Spectra, General
Extension of extreme uv solar spectrum, F. S. Johnson, J. D. Purcell, and R. Tousey—621(A)
Photoelectric measurement of reversal temperature, Hedwig Kohn and Einar Hinnov—301(A)
Spectra, Molecular (see **Molecular Structure and Spectra**)
Spectra, Nuclear (see **Nuclear Spectra**)
Spectroscopy Technique (see **Methods and Instruments**)
Spinor Fields (see **Field Theory**)
Standards (see **Constants, Standards, Units**)
Stark Effect (see **Atomic Structure and Spectra**)
Statistical Mechanics and Thermodynamics
Absolute temperature scale between 4.2° and 5.2°K, R. Berman and C. A. Swenson—311
Approximate partition function for certain Fe group salts at low temperatures, L. D. Roberts and J. W. T. Dabbs—307(A)
Can well-informed heat engine (WHE) have free will?, Jerome Rothstein—643(A)
Domain of action of collective coordinates in new approach to many-body problem, Jerome K. Percus and George J. Yevick—642(A)
Dynamical behavior of collective coordinates in new approach to many-body problem, George J. Yevick and Jerome K. Percus—642(A)
Effect of temperature scales on low-temperature calorimetric data, J. R. Clement—601(A)
Equations of motion of coupled ordered and dissipative systems, J. L. Jackson—642(A)
General method for high-speed machine computation of ideal gas thermal properties. Diatomic free radicals of isotopic hydrides, Lester Haar and A. S. Friedman—614(A)
Molar polarization, dipole moment, and nonideality of trichloroheptafluorobutane vapor, D. W. Magnuson—301(A)
Principle of minimum entropy production, Martin J. Klein and Paul H. E. Meijer—642(A)
Quantum-mechanical molecular distribution functions in one-dimensional fluid composed of hard spheres, Robert J. Rubin—643(A)
Simplified model of stationary nonequilibrium process, Harry L. Frisch and Joel L. Lebowitz—643(A)
Solution of transport equation for case of slab geometry, J. Lehner and G. M. Wing—642(A)
Spherical model of antiferromagnet, B. S. Gourary and R. W. Hart—652(A); 676
Statistical aspects of second law of thermodynamics, C. D. Green and D. ter Haar—643(A)
Statistical mechanics and Overhauser nuclear polarization effect, C. Kittel—589(L)
Statistical mechanics of temperature-dependent energy levels, P. T. Landsberg—643(A)
Statistics of face-centered cubic ferromagnet, E. Dempsey and D. ter Haar—651(A)
Thermodynamic constants of liquid HF, C. Harry Knowles and R. T. Lagemann—306(A)
Statistical Methods (see **Mathematical Methods**)
Superconductivity
Effect of pressure on superconducting transition of Sn, M. Garber and D. E. Mapother—603(A)
Estimate of lifetime of positrons in superconductors, M. Dresden—603(A)
Intermediate state in superconductors, A. L. Schawlow, B. T. Matthias, H. W. Lewis, and G. E. Devlin—1344(L)
Superconductivity of Nb_3Sn, B. T. Matthias, T. H. Geballe, S. Geller, and E. Corenzwit—1435
Superconductivity of precipitation hardening Al alloy, R. E. Mould and D. E. Mapother—604(A)
Threshold field properties of some superconductors, E. Maxwell and O. S. Lutes—333
Velocity of sound in superconducting Sn, Charles F. Squire—1126
Supersonics (see **Fluid Dynamics**)

Thermal Conductivity (see **Thermal Properties**)
Thermal Diffusion (see **Diffusion**)
Thermal Expansion (see **Thermal Properties**)
Thermal Properties
Correlation techniques for testing Born-von Karman theory of specific heats, W. C. Overton, Jr., and J. R. Clement—602(A)
Electrical and thermal conductivity of Mg and Mg alloy at low temperatures, D. A. Spohr and R. T. Weber—602(A)
Forbes bar method for measuring thermal conductivity of metals, Joseph M. Clifford and R. B. Sawyer—665(A)

Low-temperature thermal conductivity of Canadian natural graphite, Alan W. Smith—1095(L)
Magnetic and thermal properties of chromic methylamine alum below 1°K, R. P. Hudson and C. K. McLane—932
Melting curves of deuterium and hydrogen, P. F. Chester and J. S. Dugdale—278(L)
Potential theory formulation of radiant heat transfer, Jean I. F. King—298(A)
Role of low-energy phonons in thermal conduction, Conyers Herring—954
Specific heat of $MnCl_2$ at temperatures of liquid He, R. B. Murray—307(A)
Specific heats of metals below one degree absolute, John Rayne—1428
Thermal conductivity of Ga single crystals at low temperatures, Harmon H. Plumb and Jules A. Marcus—602(A)
Thermal conductivity of In-Tl alloys at liquid He temperatures, Ronald J. Sladek—603(A)
Thermal conductivity of liquid He below 1.0°K, Henry A. Fairbank and J. Wilks—277(L)
Thermodynamic constants of liquid HF, C. Harry Knowles and R. T. Lagemann—306(A)

Thermal Radiation (see **Radiation**)
Thermionic Emission (see **Electrical Properties**)
Thermodynamics (see **Statistical Mechanics and Thermodynamics**)
Thermoelectric Effect (see **Electrical Properties; Semiconductors**)
Thermoluminescence (see **Luminescence**)
Thermomagnetic Effect (see **Magnetic Properties**)
Total Cross Sections (see **Electrons and Positrons; Nuclear Reactions**)
Transmutation (see **Nuclear Reactions**)

Uncertainty Principle (see **Quantum Mechanics**)
Units (see **Constants, Standards, Units**)

Vacuum Tubes (see **Methods and Instruments**)
Van der Waals Forces (see **Molecular Structure and Spectra**)
Viscosity (see **Liquids**)

Wave Mechanics (see **Quantum Mechanics**)
Work Function (see **Electrical Properties**)

X-Rays
Avogadro's number, M. E. Straumanis—566(L)
Corrected values of W *K*-series x-ray wavelengths with 2-meter curved crystal diffraction spectrometer, Philip Snelgrove, Jassim El-Hussaini, and Jesse W. M. DuMond—1203
Energy measurements of meson x-rays, M. B. Stearns, M. Stearns, L. Leipuner, and S. DeBenedetti—625(A)
Equipment for measurement of very small x-ray scattering cross sections, W. W. Beeman and R. H. Neynaber—617(A)
Isotope shift in x-ray spectra of heavy elements, G. Igo and M. S. Wertheim—1097(L)
K-absorption edge studies of compounds, H. P. Hanson and J. R. Knight—621(A)
L-absorption spectrum of Si and SiO_2, D. E. Bedo and D. H. Tomboulian—621(A)
Limits on π^--meson mass from mesonic x-rays, M. Stearns, M. B. Stearns, S. DeBenedetti, and L. Leipuner—1353(L)
L-shell ionization by protons of 1.5- to 4.25-Mev energy, E. M. Bernstein and H. W. Lewis—83
Mass of μ^- meson from mesonic x-rays, S. Koslov, V. Fitch, and J. Rainwater—625(A)
Moseley's law applied to proportional counter resolution of adjacent elements, C. F. Hendee and S. Fine—281(L)
Response of anthracene scintillation crystals to monoenergetic soft x-rays, W. H. Robinson and W. Jentschke—1412
Scattered radiation contribution to depth dose data for 35- and 90-Mev synchrotron x-rays, J. Goag and B. Zendle—608(A)
Scattering of x-rays by nuclei, G. Pugh, D. H. Frisch, and R. Gomez—611(A)
Small-angle x-ray scattering from cold-worked Al-Ag and Al-Zn alloys, J.-P. Jan and J. S. Koehler—665(A)
Solid surface studies by total reflection of x-rays, L. G. Parratt—617(A)
Spatial distribution of energy dissipation by bremsstrahlung spectrum, David T. Goldman and Henry Brysk—305(A)
Surface studies of solids by total reflection of x-rays, L. G. Parratt—359
Transmission of x-rays through calcite in Laue diffraction, G. Schwarz and G. L. Rogosa—950
2 types of band emission curves of Cu in soft x-ray region, Gunji Shinoda, Tatsuro Suzuki, and Susumu Kato—840(L)
X-ray absorption in solid argon, Jack Soules and C. H. Shaw—621(A)
X-rays from π mesic atoms, A. D. McGuire, M. Camac, M. L. Halbert, and J. B. Platt—625(A)

CONTENTS—*continued*

Letters to the Editor:

Overhauser Effect in a Free Radical . . . . . H. G. Beljers, L. van der Kint, and J. S. van Wieringen 1683

Anomalous Optical Behavior of InSb and InAs . . . . . H. J. Hrostowski, G. H. Wheatley, and W. F. Flood, Jr. 1683

Energy Losses of Electrons Passing through an MgO Foil . . . . . Hiroshi Watanabe 1684

Saturation in the Microwave Spectrum of Methyl Chloride . . . . . George R. Bird 1686

Electron Spin Resonance of an Impurity Level in Silicon . . . . . A. Honig and A. F. Kip 1686

Meson-Meson Interaction in Meson Scattering . . . . . Marc Ross 1687

Gyromagnetic Ratio of 10^{-9}-Second Te^{121m} . . . . . S. Rabey and V. E. Krohn 1689

Radiogenic Osmium from Rhenium-Containing Molybdenite . . . . . H. Hintenberger, W. Herr, and H. Voshage 1690

Half-Life of Rhenium . . . . . W. Herr, H. Hintenberger, and H. Voshage 1691

Primary Alpha Particles in the Cosmic Radiation near the Geomagnetic Equator . . . . . Martin A. Pomerantz 1691

Elastic Photoproduction of π^0 Mesons from Helium . . . . . E. L. Goldwasser, L. J. Koester, Jr., and F. E. Mills 1692

Polarization in p-p Scattering at 415 Mev . . . . . J. A. Kane, R. A. Stallwood, R. B. Sutton, T. H. Fields, and J. G. Fox 1694

Mesonic Corrections to the Beta-Decay Coupling Constants . . . . . R. J. Finkelstein and S. A. Moszkowski 1695

Antiproton Production . . . . . G. Feldman 1697

Modified Nucleon Propagators . . . . . A. N. Mitra 1697

Absolute Intensities of the Gamma Rays and X-Rays of Radium D . . . . . P. E. Damon and R. R. Edwards 1698

Test Meson Produced by 3.0-Bev Protons . . . . R. D. Hill, E. O. Salant, and M. Widgoff 1699

Primary Cosmic-Ray Spectrum Deduced from an Analysis of Jets . . . . . A. Eagler and U. Haber-Schaim 1700

Asymmetry in Neutron Production by Bombarding Targets with 285-Mev Polarized Protons . . . . . Hugh Bradner and Robert Donaldson 1701

New Isotope Protactinium-237 . . . . . W. W. T. Crane and G. M. Iddings 1702

Isotopes of Curium, Berkelium, and Californium . . . . . E. K. Hulet, S. G. Thompson, and A. Ghiorso 1703

Disintegration of Bismuth by 2.2-Bev Protons . . . . . Nathan Sugarman, Robert B. Duffield, G. Friedlander, and J. M. Miller 1704

Errata 1705

Author Index to Volume 96 1707

Analytic Subject Index to Volume 96 1727

L. V. Heilbron, C. T. Lane, and C. H. Blakewood 1363
J. F. Smith 1369
Léon Van Hove 1374
Motoichi Shibuya 1385
J. Tate 1394
F. J. Dunkee and F. C. Nix 1395
E. T. Goth, W. P. Low, and F. C. Nix 1403
H. C. Wilson and J. S. Koeger 1408
W. E. Ramsden and W. Jentschke 1412
P. A. Wolff 1413
Hal G. Mohrmann and M. C. Steele 1421
John Rayne 1428
R. Gaudin, B. Géller, and E. Corenswit 1433
G. F. Koster 1436
Paul H. E. Meijer 1443
Warren E. Henry 1449
Gabriel Matzkanin and Vernon W. Hughes 1451
Werner R. Trumpis and Vernon W. Hughes 1461
R. V. Pound, E. W. Mclennan, and G. J. Zissis 1463
James P. Nicklas 1469
Charles E. Treanor 1472
Robert Beringer and Mark A. Heald 1474
D. S. Allsopp and M. H. L. Pryce 1482
W. K. Lyon and J. E. Stanis 1489
P. B. Hicks, M. H. Studier, and J. R. Huizenga 1501
Silvio J. Balestrini 1502
J. F. Mulligan, A. W. Schardt, and E. Segrè 1506
William W. Pratt 1517
R. A. Lewis, J. H. Tawney, Jr., and E. N. Jensen 1523
J. Hodgson, R. Nathans, and P. F. Yergin 1529
Roy Aldenkamp and Wolfgang Franzen 1534
J. A. W. K. Ridley, and M. L. Wiedenbeck 1537
Thomas Lincoln and Allen C. C. Mitchell 1538
J. L. Olsen and G. D. O'Kelley 1539
J. G. V. Taylor, and E. N. H. Haskin 1540
R. E. Simmons, T. F. Stratton, and R. V. Stuart 1546
Harold G. Hughes and Charles D. Coryell 1550
E. Balmont and J. M. Miller 1554
W. Colgrovsky and J. Steinberger 1561
T. Yamaki, and Y. Matsubara 1565
Gerson, Y. Rimoldini, and K. Grahm 1571
Gerson, Y. Rimoldini, and K. Grahm 1572
J. W. Kennedy, and C. J. Kevranian 1576
D. C. Peaslee 1580
M. Mahapatra, and E. Felix Alai 1584
M. Mahapatra, K. F. Alai, and H. A. Bethe 1586
Ronald L. Martin 1603
E. Goldberger, and W. E. Thirring 1612
Yoshio Yamaguchi 1626
Yoshio Yamaguchi and Yoriko Yamaguchi 1635
F. J. Dyson, 1636
W. M. Visscher, and H. A. Bethe 1646
G. Salzberg and A. H. Taub 1659
Geoffrey F. Chew 1668
Abraham Klein 1670

LANCASTER PRESS, INC., LANCASTER, Pa.